frontiers | Research Topics

The neural basis of hyper-adaptability in humans and animals

Edited by
Jun Izawa, Jun Ota, Tomohiko Takei and Belén Rubio Ballester

Published in
Frontiers in Systems Neuroscience
Frontiers in Human Neuroscience
Frontiers in Computational Neuroscience

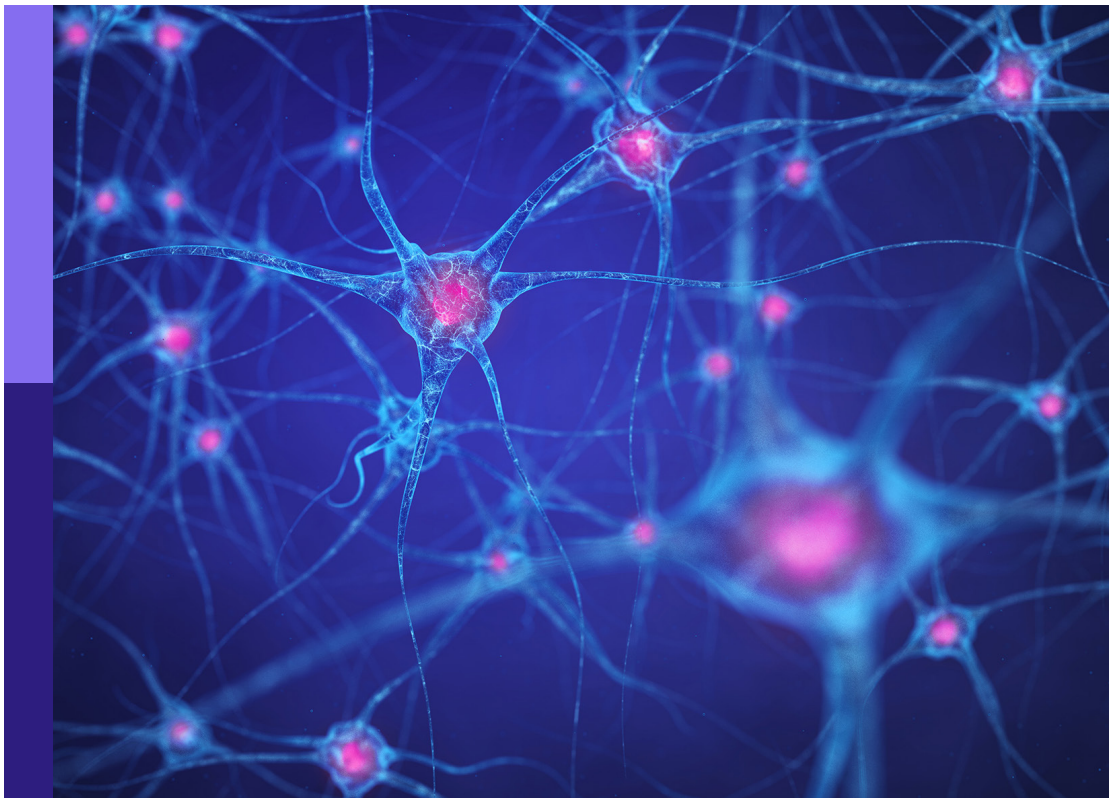

FRONTIERS EBOOK COPYRIGHT STATEMENT

The copyright in the text of individual articles in this ebook is the property of their respective authors or their respective institutions or funders. The copyright in graphics and images within each article may be subject to copyright of other parties. In both cases this is subject to a license granted to Frontiers.

The compilation of articles constituting this ebook is the property of Frontiers.

Each article within this ebook, and the ebook itself, are published under the most recent version of the Creative Commons CC-BY licence. The version current at the date of publication of this ebook is CC-BY 4.0. If the CC-BY licence is updated, the licence granted by Frontiers is automatically updated to the new version.

When exercising any right under the CC-BY licence, Frontiers must be attributed as the original publisher of the article or ebook, as applicable.

Authors have the responsibility of ensuring that any graphics or other materials which are the property of others may be included in the CC-BY licence, but this should be checked before relying on the CC-BY licence to reproduce those materials. Any copyright notices relating to those materials must be complied with.

Copyright and source acknowledgement notices may not be removed and must be displayed in any copy, derivative work or partial copy which includes the elements in question.

All copyright, and all rights therein, are protected by national and international copyright laws. The above represents a summary only. For further information please read Frontiers' Conditions for Website Use and Copyright Statement, and the applicable CC-BY licence.

ISSN 1664-8714
ISBN 978-2-83251-873-1
DOI 10.3389/978-2-83251-873-1

About Frontiers

Frontiers is more than just an open access publisher of scholarly articles: it is a pioneering approach to the world of academia, radically improving the way scholarly research is managed. The grand vision of Frontiers is a world where all people have an equal opportunity to seek, share and generate knowledge. Frontiers provides immediate and permanent online open access to all its publications, but this alone is not enough to realize our grand goals.

Frontiers journal series

The Frontiers journal series is a multi-tier and interdisciplinary set of open-access, online journals, promising a paradigm shift from the current review, selection and dissemination processes in academic publishing. All Frontiers journals are driven by researchers for researchers; therefore, they constitute a service to the scholarly community. At the same time, the *Frontiers journal series* operates on a revolutionary invention, the tiered publishing system, initially addressing specific communities of scholars, and gradually climbing up to broader public understanding, thus serving the interests of the lay society, too.

Dedication to quality

Each Frontiers article is a landmark of the highest quality, thanks to genuinely collaborative interactions between authors and review editors, who include some of the world's best academicians. Research must be certified by peers before entering a stream of knowledge that may eventually reach the public - and shape society; therefore, Frontiers only applies the most rigorous and unbiased reviews. Frontiers revolutionizes research publishing by freely delivering the most outstanding research, evaluated with no bias from both the academic and social point of view. By applying the most advanced information technologies, Frontiers is catapulting scholarly publishing into a new generation.

What are Frontiers Research Topics?

Frontiers Research Topics are very popular trademarks of the *Frontiers journals series*: they are collections of at least ten articles, all centered on a particular subject. With their unique mix of varied contributions from Original Research to Review Articles, Frontiers Research Topics unify the most influential researchers, the latest key findings and historical advances in a hot research area.

Find out more on how to host your own Frontiers Research Topic or contribute to one as an author by contacting the Frontiers editorial office: frontiersin.org/about/contact

The neural basis of hyper-adaptability in humans and animals

Topic editors

Jun Izawa — University of Tsukuba, Japan

Jun Ota — The University of Tokyo, Japan

Tomohiko Takei — Tamagawa University, Japan

Belén Rubio Ballester — Institute for Bioengineering of Catalonia (IBEC), Spain

Citation

Izawa, J., Ota, J., Takei, T., Ballester, B. R., eds. (2023). *The neural basis of hyper-adaptability in humans and animals*. Lausanne: Frontiers Media SA.

doi: 10.3389/978-2-83251-873-1

Table of contents

07 Motility Profile of Captive-Bred Marmosets Revealed by a Long-Term In-Cage Monitoring System
Masashi Koizumi, Naotake Nogami, Kensuke Owari, Akiyo Kawanobe, Terumi Nakatani and Kazuhiko Seki

22 Enhanced Visual Feedback Using Immersive VR Affects Decision Making Regarding Hand Use With a Simulated Impaired Limb
Naoko Sakabe, Samirah Altukhaim, Yoshikatsu Hayashi, Takeshi Sakurada, Shiro Yano and Toshiyuki Kondo

30 Contralateral and Ipsilateral Interactions in the Somatosensory Pathway in Healthy Humans
Daisuke Ishii, Kiyoshige Ishibashi, Hiroshi Yuine, Kotaro Takeda, Satoshi Yamamoto, Yuki Kaku, Arito Yozu and Yutaka Kohno

36 Interaction of the Left–Right Somatosensory Pathways in Patients With Thalamic Hemorrhage: A Case Report
Daisuke Ishii, Kiyoshige Ishibashi, Kotaro Takeda, Hiroshi Yuine, Satoshi Yamamoto, Yuki Kaku, Arito Yozu and Yutaka Kohno

44 Non-human Primate Models to Explore the Adaptive Mechanisms After Stroke
Noriyuki Higo

52 Brain Processes Involved in Motor Planning Are a Dominant Factor for Inducing Event-Related Desynchronization
Kosei Nakayashiki, Hajime Tojiki, Yoshikatsu Hayashi, Shiro Yano and Toshiyuki Kondo

64 It Is Time to Study Overlapping Molecular and Circuit Pathophysiologies in Alzheimer's and Lewy Body Disease Spectra
Noritaka Wakasugi and Takashi Hanakawa

85 A Model of Predictive Postural Control Against Floor Tilting in Rats
Akira Konosu, Tetsuro Funato, Yuma Matsuki, Akihiro Fujita, Ryutaro Sakai and Dai Yanagihara

96 Brain Activity Reflects Subjective Response to Delayed Input When Using an Electromyography-Controlled Robot
Hyeonseok Kim, Yeongdae Kim, Makoto Miyakoshi, Sorawit Stapornchaisit, Natsue Yoshimura and Yasuharu Koike

104 Distribution of Large and Small Dorsal Root Ganglion Neurons in Common Marmosets
Moeko Kudo, Sidikejiang Wupuer, Shinji Kubota and Kazuhiko Seki

111 Evaluation of Postural Sway in Post-stroke Patients by Dynamic Time Warping Clustering
Dongdong Li, Kohei Kaminishi, Ryosuke Chiba, Kaoru Takakusaki, Masahiko Mukaino and Jun Ota

124 Musculoskeletal Modeling and Inverse Dynamic Analysis of Precision Grip in the Japanese Macaque
Tsuyoshi Saito, Naomichi Ogihara, Tomohiko Takei and Kazuhiko Seki

134 Individual Optimal Attentional Strategy in Motor Learning Tasks Characterized by Steady-State Somatosensory and Visual Evoked Potentials
Takeshi Sakurada, Masataka Yoshida and Kiyoshi Nagai

148 Effect of Walking Adaptability on an Uneven Surface by a Stepping Pattern on Walking Activity After Stroke
Yusuke Sekiguchi, Keita Honda and Shin-Ichi Izumi

160 Efficiency and Stability of Step-To Gait in Slow Walking
Kento Hirayama, Yohei Otaka, Taichi Kurayama, Toru Takahashi, Yutaka Tomita, Seigo Inoue, Kaoru Honaga, Kunitsugu Kondo and Rieko Osu

168 Model-Based Analyses for the Causal Relationship Between Post-stroke Impairments and Functional Brain Connectivity Regarding the Effects of Kinesthetic Illusion Therapy Combined With Conventional Exercise
Yu Miyawaki, Masaki Yoneta, Megumi Okawada, Michiyuki Kawakami, Meigen Liu and Fuminari Kaneko

180 Excitatory-Inhibitory Homeostasis and Diaschisis: Tying the Local and Global Scales in the Post-stroke Cortex
Francisco Páscoa dos Santos and Paul F. M. J. Verschure

199 Preceding Postural Control in Forelimb Reaching Movements in Cats
Mirai Takahashi, Toshi Nakajima and Kaoru Takakusaki

217 Decreased Tactile Sensitivity Induced by Disownership: An Observational Study Utilizing the Rubber Hand Illusion
Kota Ataka, Tamami Sudo, Ryoji Otaki, Eizaburo Suzuki and Shin-Ichi Izumi

227 Body-Specific Attention to the Hands and Feet in Healthy Adults
Naoki Aizu, Ryoji Otaki, Kazuhiro Nishii, Takumi Kito, Runhong Yao, Kenya Uemura, Shin-ichi Izumi and Kouji Yamada

237 Reinforcement Learning Model With Dynamic State Space Tested on Target Search Tasks for Monkeys: Self-Determination of Previous States Based on Experience Saturation and Decision Uniqueness
Tokio Katakura, Mikihiro Yoshida, Haruki Hisano, Hajime Mushiake and Kazuhiro Sakamoto

259 "Tricking the Brain" Using Immersive Virtual Reality: Modifying the Self-Perception Over Embodied Avatar Influences Motor Cortical Excitability and Action Initiation
Karin A. Buetler, Joaquin Penalver-Andres, Özhan Özen, Luca Ferriroli, René M. Müri, Dario Cazzoli and Laura Marchal-Crespo

278 Individual Sensory Modality Dominance as an Influential Factor in the Prefrontal Neurofeedback Training for Spatial Processing: A Functional Near-Infrared Spectroscopy Study
Takeshi Sakurada, Mayuko Matsumoto and Shin-ichiroh Yamamoto

292 Neuroimaging Examination of Driving Mode Switching Corresponding to Changes in the Driving Environment
Ryu Ohata, Kenji Ogawa and Hiroshi Imamizu

303 Relationship Between Body-Specific Attention to a Paretic Limb and Real-World Arm Use in Stroke Patients: A Longitudinal Study
Ryoji Otaki, Yutaka Oouchida, Naoki Aizu, Tamami Sudo, Hiroshi Sasahara, Yuki Saito, Sunao Takemura and Shin-Ichi Izumi

318 Real-Time Detection and Feedback of Canonical Electroencephalogram Microstates: Validating a Neurofeedback System as a Function of Delay
Tomohisa Asai, Takamasa Hamamoto, Shiho Kashihara and Hiroshi Imamizu

333 A Neural Controller Model Considering the Vestibulospinal Tract in Human Postural Control
Yuichiro Omura, Kohei Kaminishi, Ryosuke Chiba, Kaoru Takakusaki and Jun Ota

353 Clarify Sit-to-Stand Muscle Synergy and Tension Changes in Subacute Stroke Rehabilitation by Musculoskeletal Modeling
Ruoxi Wang, Qi An, Ningjia Yang, Hiroki Kogami, Kazunori Yoshida, Hiroshi Yamakawa, Hiroyuki Hamada, Shingo Shimoda, Hiroshi R. Yamasaki, Moeka Yokoyama, Fady Alnajjar, Noriaki Hattori, Kouji Takahashi, Takanori Fujii, Hironori Otomune, Ichiro Miyai, Atsushi Yamashita and Hajime Asama

369 Neural Network Models for Spinal Implementation of Muscle Synergies
Yunqing Song, Masaya Hirashima and Tomohiko Takei

382 Hyper-Adaptation in the Human Brain: Functional and Structural Changes in the Foot Section of the Primary Motor Cortex in a Top Wheelchair Racing Paralympian
Tomoyo Morita, Satoshi Hirose, Nodoka Kimura, Hiromasa Takemura, Minoru Asada and Eiichi Naito

397 Stochastic Physiological Gaze-Evoked Nystagmus With Slow Centripetal Drift During Fixational Eye Movements at Small Gaze Eccentricities
Makoto Ozawa, Yasuyuki Suzuki and Taishin Nomura

412 Design of an Isometric End-Point Force Control Task for Electromyography Normalization and Muscle Synergy Extraction From the Upper Limb Without Maximum Voluntary Contraction
Woorim Cho, Victor R. Barradas, Nicolas Schweighofer and Yasuharu Koike

426 Reinforcement Learning Model With Dynamic State Space Tested on Target Search Tasks for Monkeys: Extension to Learning Task Events
Kazuhiro Sakamoto, Hinata Yamada, Norihiko Kawaguchi, Yoshito Furusawa, Naohiro Saito and Hajime Mushiake

438 EMG space similarity feedback promotes learning of expert-like muscle activation patterns in a complex motor skill
Victor R. Barradas, Woorim Cho and Yasuharu Koike

frontiers in Systems Neuroscience

METHODS
published: 15 April 2021
doi: 10.3389/fnsys.2021.645308

Motility Profile of Captive-Bred Marmosets Revealed by a Long-Term In-Cage Monitoring System

*Masashi Koizumi, Naotake Nogami, Kensuke Owari, Akiyo Kawanobe, Terumi Nakatani and Kazuhiko Seki**

Department of Neurophysiology, National Institute of Neuroscience, National Center of Neurology and Psychiatry, Tokyo, Japan

A quantitative evaluation of motility is crucial for studies employing experimental animals. Here, we describe the development of an in-cage motility monitoring method for new world monkeys using off-the-shelf components, and demonstrate its capability for long-term operation (e.g., a year). Based on this novel system, we characterized the motility of the common marmoset over different time scales (seconds, hours, days, and weeks). Monitoring of seven young animals belonging to two different age groups (sub-adult and young-adult) over a 231-day period revealed: (1) strictly diurnal activity (97.3% of movement during daytime), (2) short-cycle (∼20 s) transition in activity, and (3) bimodal diurnal activity including a "siesta" break. Additionally, while the mean duration of short-cycle activity, net daily activity, and diurnal activity changed over the course of development, 24-h periodicity remained constant. Finally, the method allowed for detection of progressive motility deterioration in a transgenic marmoset. Motility measurement offers a convenient way to characterize developmental and pathological changes in animals, as well as an economical and labor-free means for long-term evaluation in a wide range of basic and translational studies.

Keywords: non-human primate, marmoset, home-cage activity, neurodegenerative diseases, passive infrared pyroelectric motion sensor, intermittency of movement, daily activity profile

OPEN ACCESS

Edited by:
Jun Izawa,
University of Tsukuba, Japan

Reviewed by:
Masatoshi Yoshida,
Hokkaido University, Japan
Corinna Ross,
Texas Biomedical Research Institute, United States

***Correspondence:**
Kazuhiko Seki
seki@ncnp.go.jp

Received: *22 December 2020*
Accepted: *26 March 2021*
Published: *15 April 2021*

Citation:
Koizumi M, Nogami N, Owari K, Kawanobe A, Nakatani T and Seki K (2021) Motility Profile of Captive-Bred Marmosets Revealed by a Long-Term In-Cage Monitoring System. Front. Syst. Neurosci. 15:645308. doi: 10.3389/fnsys.2021.645308

INTRODUCTION

To move and explore the surrounding environment is crucial for animals. Motility is vital for maintaining strength and the flexibility of behaviors required to survive under a constantly changing environment. Motility declines following functional deterioration of multiple body parts (Ferrucci et al., 2016; Buchman et al., 2018). Movement disorder often accompanies certain neurologic diseases (Taroni and Didonato, 2004; Nóbrega and De Almeida, 2012), severely limiting an individual's viability (Barlow et al., 1996; Robinson et al., 2013). Behavioral phenotyping of experimental animal models of human disease aims to quantitatively characterize the motor behavior and its disease-specific deviation from healthy animals (Lin et al., 2001; Pratte et al., 2011; Urbach et al., 2014). Measurement of bodily movement (e.g., locomotion or ambulation) is often included in the established battery of assays used to evaluate an animal's behavior (Crawley and Paylor, 1997; Rogers et al., 1997). It offers a practical way to compare the level of motility among individuals with different genetic backgrounds (Tang et al., 2002), disease or disease progression (Portal et al., 2013). Motility measurements can reflect various factors, such as changes in the

external environment (Casadesus et al., 2001; Barbosa and Mota, 2009) or internal metabolic states (Garland et al., 2011). Traditionally, measurements of this type have been performed though multiple iterated sessions under strictly controlled protocols, i.e., duration and interval of measurement, dimension and condition of measurement field (Wahlsten, 2001), so as to minimize test-irrelevant variation. However, this kind of measurement is highly labor-intensive for both the animal and the experimenter. This is particularly taxing when performing repeated, rigorous tests to evaluate alterations in longitudinal motility, which frequently occur with a very slow time constant (e.g., over months and years) during maturation, aging, and disease progression (Carter et al., 1999; Yhnell et al., 2016). An easy and efficient way to measure the motility of animals through their life span is, therefore, essential to overcome this limitation.

In-cage motility evaluation, whereby the experimenter measures motility exclusively within the home cage, in which each animal spends their normal life, has been applied recently in rodents (Spruijt and Devisser, 2006; Redfern et al., 2017). This method has a number of advantages over traditional iterated measurements. First, it is more labor friendly. Second, it achieves a remarkable gain in long-term consecutive output, enabling the evaluation of time dependency, periodicity, and long-lasting, slowly developing alterations, such as those associated with aging or progressive disease. Third, by introducing automated, continuous measurement without involvement of the experimenter during evaluation, it improves the reproducibility and replicability, which were typically sacrificed in the iterated approach because of uncontrollable fluctuation of environmental factors as well as experimental procedures (Crabbe et al., 1999).

Here, we report an in-cage motility measurement method specifically developed for non-human primates. These species represent superior models of human disease owing to their phylogenetic proximity, as well as structural and functional similarity to humans (Capitanio and Emborg, 2008; Kishi et al., 2014; Phillips et al., 2014; Walker et al., 2017). Specifically, the common marmoset (Callithrix jacchus) has become a valuable primate species in translational studies of human disease ('t Hart et al., 2015; Galvao-Coelho et al., 2017), including those relating to movement disorder (Emborg, 2017). Their small body size makes them easy to handle, saves space, and allows breeding a number of disease models in a single laboratory. Their husbandry is comparable to that of rodents, which is particularly advantageous in comparison with larger primate species such as macaque monkeys. However, so far, behavioral phenotyping of marmosets has been more challenging than for rodent models. There are no established battery tests. The number of animals per study is limited by ethical (Prescott, 2010) and economic reasons. A divergent genetic (Barr et al., 2003) and environmental (Johnson et al., 1996) background leads to different physiological and psychological profiles among individuals (Slipogor et al., 2016; Koski et al., 2017). The common marmoset is generally a stress-sensitive primate species and is readily disturbed by an unusual situation or following separation from mates (Norcross and Newman, 1999; Bassett et al., 2003; Kaplan et al., 2012). Marmosets are arboreal animals (Garber, 1992; Larson, 2018) and thus they prefer to move vertically, not only horizontally. Finally, their longer life span (Abbott et al., 2003; Nishijima et al., 2012) makes frequent measurement for each stage of life very challenging. Consequently, so far, phenotyping marmoset behavior has relied on *ad hoc* methods (Marshall and Ridley, 2003; Verhave et al., 2009; Choudhury and Daadi, 2018) or on mere objective descriptions.

The in-cage motility monitoring system we propose here is intended to overcome these limitations as it is specific to non-human primates. It enables motility to be assessed with minimal stress by performing measurements daily under a familiar environment for both marmosets and human experimenters, it avoids inter-individual differences in habituation to the specific measurement field and equipment, it can easily capture any movement that occurs within the three-dimensional space of the home cage, and could potentially measure the motility continuously throughout an animal's life span. The aim of this study was to validate in-cage motility measurement on various marmoset age groups (from adolescent to elderly), healthy and disease model, and under different times of diurnal and annual cycles. We developed an off-the-shelf measurement system based on a passive infrared movement detector and data-logger capable of running uninterrupted 24 h a day for months. Using this novel system, we successfully characterized the motility of healthy common marmosets and transgenic models of human disease, on different time scales ranging from second to weeks.

METHODS

Experimental Set-Up

Ethics Statement

This study compared the motility of wild-type marmosets from two different age groups (Experiment 1), and that of a transgenic marmoset model of human ataxia with age-matched control groups (Experiment 2). All procedures and housing conditions were approved by the committee on the ethical issue in animal experiments of the National Center of Neurology and Psychiatry (NCNP) and were carried out in accordance with its guideline for the care and use of primates. The latter complied with the guideline issued by the Japanese Ministry of Education, Culture, Sports, Science and Technology (2006) and the National Institutes of Health guide for the care and use of Laboratory animals (National Research Council (US) Institute for Laboratory Animal Research, 1996).

Housing Environment

All marmosets used in this study were housed in a breeding room of the primate research facility at the NCNP. In the breeding room, 54 cages were divided into two series and placed along the walls. This layout facilitated social contact as it allowed marmosets to hear or see each other. The room was maintained at 28°C and 50% humidity by an automatic air conditioning system. Lighting was kept under a constant artificial 12-h dark/12-h light cycle managed by a control timer that regulated the fluorescent lamps on the ceiling. Illuminance near the floor of the room was 450 lux. Water was freely supplied via a feeding bulb attached to the cage. The diet consisted mainly of pellets adjusted for new world monkeys (CMS, Oriental Yeast, Tokyo, Japan) and was given regularly twice a day together with wet mash, supplements,

and a favorite food into a cup attached to the cage. Pellets were given every morning (9–10 AM) and another meal was served at around 4 PM. The cage was cleaned by service staff every day before noon.

Animals

Ten marmosets were used for this study. Details about each marmoset as well as duration of the experiment (age on the first and last day) are reported in **Table 1**.

Seven marmosets housed in the same room were recruited from the breeding colony to measure baseline activity and compare daily activity in different age groups (Experiment 1). To facilitate their habituation, they were moved to the single housing environment at least a week before starting the measurements. We divided the monkeys in two groups according to their age: sub-adults and young-adults (Missler et al., 1992). Three marmosets (one male and two females, aged 208 ± 8 days on the first day of daily activity measurements) were assigned to the sub-adult group; whereas another four marmosets (three males and one female, aged 398 ± 34 days) were assigned to the young-adult group.

For Experiment 2, three marmosets (three males, aged 184 ± 1.4 days) were recruited from the polyglutamine disease model transgenic marmoset line (second generation) recently established in our laboratory (Tomioka et al., 2017). Polyglutamine diseases are heritable neurodegenerative disorders caused by expansion of trinucleotide repeats for the polyglutamine tract (Nóbrega and De Almeida, 2012). This animal model typically shows a variety of motor disease symptoms characterized by progressively lower daily activity (Tomioka et al., 2017). To compile an age-matched wild-type control group, we used data from the young-adult group.

Period of Daily Activity Measurement

Information about the duration of each experiment and the animals enrolled is provided in **Table 1**. In both experiments, animals were moved from the large cage for family housing to the individual cage (30 cm W × 60 cm H × 50 cm D) located in the same breeding room.

Equipment

A commercially available passive infrared pyroelectric motion sensor (AMN32111; Panasonic, Osaka, Japan) was used to detect the movement of each marmoset within their cage (**Figures 1A,B**). Although this sensor was originally designed to detect subtle movements made by humans from more than two meters above, it can also detect the movements of small animals such as rodents (Brown et al., 2016). We were able to confirm that it can also detect the movements of the common marmoset with a precision of several centimeter (**Supplementary Document 1** and **Supplementary Videos 1, 2**). To send TTL-level count pulses to a data-logger upon occurrence of every movement, we attached a transistor buffer circuit (**Figure 1C**) housed inside a small plastic box (35 × 53 × 11 mm) together with the sensor (**Figures 1B,C**). Then, the TTL pulse from the circuit was wired to a compact-sized pulse logger (LR8512; Hioki, Nagano, Japan). This type of data-logger can count the number of TTL pulses within a pre-fixed time bin (from 100 ms to 60 min) and store the cumulative number of pulses for each time bin until it reaches the upper limit of sampling bin capacity (500,000 times). We chose 2 s as the minimum resolution for time domain analysis. This allowed us to compile TTL events over 10 days without any interruption. A single data-logger could receive TTL signals from two sensors simultaneously. The data-logger could work without any external controller and function for an indefinite time. Data were transferred

TABLE 1 | Period of study and age range for each marmoset participating in either *Experiment 1* or *Experiment 2*.

Animal	Entire monitoring period		Experiment 1		Experiment 2	
	Start date (age in days)	End date	Start age (days)	End age (days)	Start age (days)	End age (days)
Sub-adult						
Chomo ♂	2017/8/1 (195)	2018/3/31	204	435		
Lungma ♀	2017/8/1 (195)	2018/3/31	204	435		
Azuma ♀	2017/8/1 (218)	2018/3/31	218	449		
mean (SD)			208.67 (8.08)	439.67 (8.08)		
Young-adult						
Matter ♂	2017/1/23 (167)	2018/3/31	368	599	187	480
Horn ♂	2017/1/23 (167)	2018/3/31	368	599	187	480
Turumi ♂	2016/11/20 (163)	2018/3/31	428	659	184	477
Kano ♀	2016/11/20 (163)	2018/3/31	428	659	184	477
mean (SD)			398.00 (34.64)	629.00 (34.64)	185.50 (1.73)	478.50 (1.73)
Symptomatic transgenic						
Kirishima ♂	2016/9/18 (185)	2017/7/8			185	478
Asymptomatic transgenic						
Ibuki ♂	2016/9/18 (185)	2018/3/31			185	478
Zao ♂	2016/12/19 (170)	2018/3/31			183	476
mean (SD)					184.00 (1.41)	477.00 (1.41)

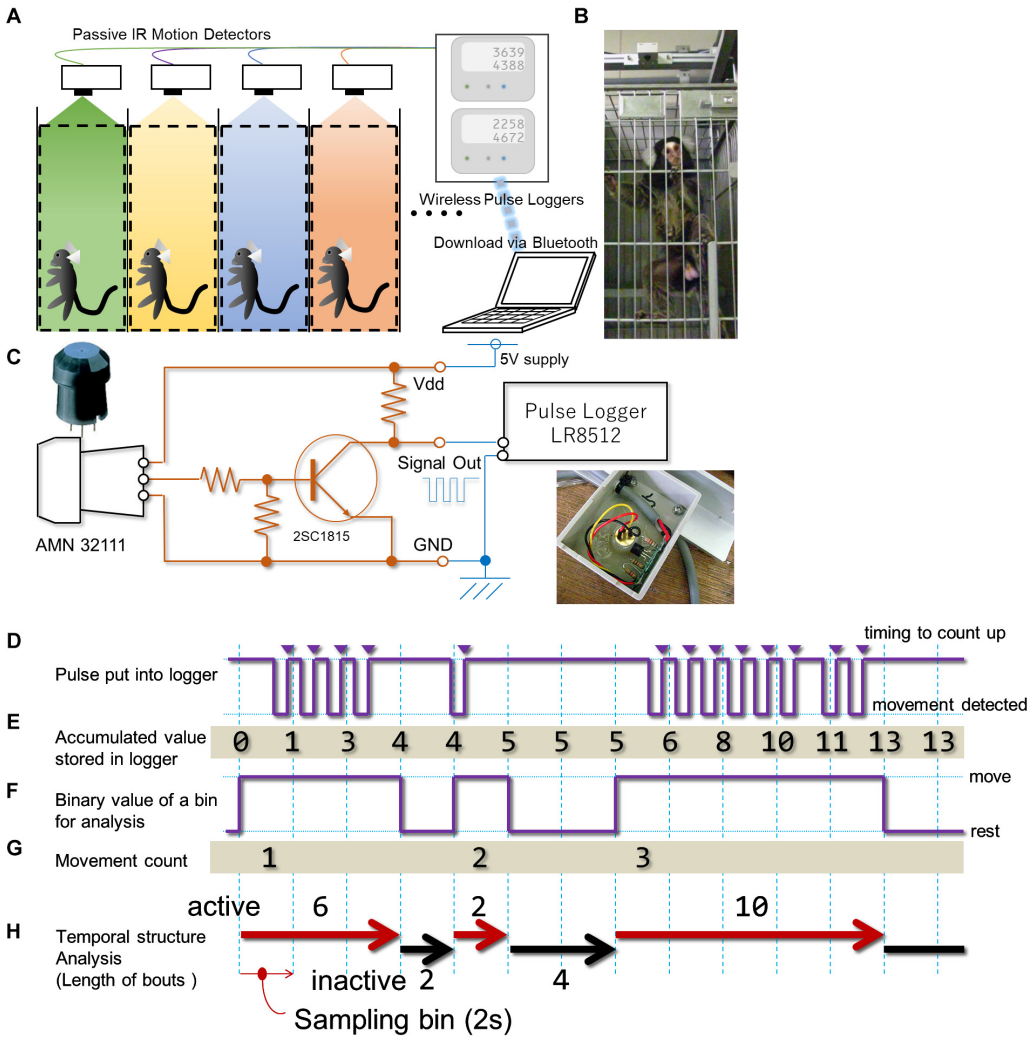

FIGURE 1 | In-cage continuous motility monitoring system for marmosets. **(A)** A schematic diagram of the in-cage continuous motility monitoring system for marmosets. A passive infra-red pyroelectric motion sensor was attached above the ceiling of each cage. Signal from four animals were concurrently and continuously stored by two data loggers, which was downloaded once a week by a PC via blue tooth interface. **(B)** Photo image of the motion sensor (top) and marmoset. **(C)** A circuit diagram of the custom-made buffer amplifier inserted between each motion sensor and data logger. Inset, a photo image of actual installation of the circuit board. **(D)** The sensor sends a negative logic pulse when a movement is detected. This example shows movements of a single marmoset detected during a 28-s period by the sensor. **(E)** The logger counts pulses at each occasion when the logic signal level reaches a high voltage level (triangles) and adds the counts in an incrementally accumulating manner at every 2-s intervals (sampling bin). For the period presented in this example, 13 pulses were detected and accumulated. **(F-H)** Offline processing of the accumulated value from the data logger. **(F)** We converted the accumulated value retrieved from the data logger into a series of binary queue so that it could represent whether or not the increase in the accumulated value occurred every 2 s. **(G)** With our definition of movement, three movements were detected. **(H)** From the binary queue of movement **(F)**, we computed indexes for the successiveness of each phase (active and inactive phases, length of movement bout, length of the inactive phase). See methodology for details.

approximately once a week to an external personal computer via blue-tooth.

Each sensor was mounted 170 mm above the cage's ceiling and 170 mm behind the front of the cage (**Figure 1B** and **Supplementary Figure 1**). This location of the sensor covers about 96% of the entire space inside of each cage for detecting the animal's movement (**Supplementary Figure 1**). A system consisting of 16 sensors and eight data-loggers enabled the monitoring of up to 16 marmosets at the same time. To prevent detection of movements made by marmosets housed in the neighboring cages, we placed stainless-steel separation-boards at both sides of each cage. Each cage row was separated by a passage (2600 mm width), thus any movement of marmosets housed in the cages on the other side was entirely out of detection range of the sensor. Since the sensor's range of detection is larger than the cage space, human motion (e.g., feeding or cleaning of the cage) was also detected, and it was not easy to dissociate these movements from those made by the marmoset. The estimated period for each operation is up to two minutes for each animal (corresponding to less than fifty to thirty counts (see

next section) per day). Marmosets were kept under continuous 24-h monitoring throughout the assessment period.

Analysis

Dataset

Data retrieved from each data-logger were converted to csv format and were subjected to statistical analysis in R[1]. Although this system allowed for continuous uninterrupted recording during the entire experimental period, some animals had to be occasionally taken from their cage for a routine health examination by a veterinarian. Therefore, we manually excluded daily recorded data if such break exceeded 30 min.

Data Processing for Analysis

Data sets were composed of a series of values representing the accumulation of TTL pulse counts (**Figure 1D**) for each sampling bin (i.e., 2 s) and the number of TTL events per sampling bin was counted (**Figure 1E**). Due to the intrinsic property of the sensor, we noticed that the single sequence of an animal's movement could generate multiple TTL pulses. Therefore, each single TTL pulse *per se* might not correspond to a single movement. To deal with this sensor's property, we had to decrease the precision of time for assessment within the movement count. Specifically, we converted this series to a binary queue encoding whether a single detection of movement occurred in each sampling period (2 s, **Figure 1F**), and concatenate bins until detecting a state where no movement was detected within a single sampling period. We defined this concatenated bin as the "bout," and it was used as a basic unit to count the amount of the marmoset's activity. Subsequently, the following indices were used to parameterize the day-long, binary time-series. a. Gross activity per day (day-long activity) representing the number of movements (**Figure 1G**) per day (24 h). b. Diurnal activity per day (day-time activity) representing the number of movements during daytime for each day (from 7 AM to 7 PM, light period of the colony room). c. Diurnal index obtained by dividing daytime activity by day-long activity. d. Daily cyclic activity representing the duration of motility in a daily cycle. This index was derived by counting the number of movements per minute (**Figure 1G**) throughout the experimental period, segmented on a weekly basis (from Sunday to Saturday), and the auto-correlation analysis yields for this weekly time series after applying smoothing (moving average around 9 bins weighted homogeneously). e. Hourly activity representing the number of movements per clock hour throughout the experimental period (represented as weekly average).

Intermittent Bursts of Movement (Length of the Movement Bout and Inactive Phase)

While deriving the above indices (**Figures 1D,E**), we noticed that each movement frequently lasted more than one bin (i.e., more than 2 s, **Figure 1F**). This intermittency was quantified by computing the length of movement bout and inactive phase. The length of movement bout was quantified by counting the number of back-to-back bins with an active state, followed by unit conversion from bin numbers to seconds (**Figure 1H**). The length of the inactive phase was quantified by counting the number of bins interposed between two active states, followed by the same unit conversion as for the active state (**Figure 1H**). To evaluate longitudinal changes with respect to the length of movement bout or inactive phase, the third quartile point of these phases in weekly data was obtained for the entire period.

Statistical Analysis

A probability <0.01 was considered significant for all statistical tests unless otherwise mentioned. In Experiment 1, a two-way ANOVA was conducted for effects on individuals and age differences in day-long activities, and the Kruskal-Wallis rank sum test was used for assessing the inter-individual difference in diurnal index. The Friedman test was used to assess the inter-week difference of the length of movement bout and inactive phase. The Wilcoxon rank sum test was used for assessing the difference between two age groups with respect to day-long activity. The paired *t*-test was applied when comparing hourly activity in daytime activity profiles. In Experiment 2, the Wilcoxon rank sum test was used to compare each index before and after the onset of symptoms. The Friedman test was used for assessing the inter-week difference of daytime activity, as well as the length of movement bout and inactive phase. All statistical analyses were carried out using built-in functions in R or the "exactRankTests" package in R.

RESULTS

Experiment 1

Different Day-Long Activity Between Sub-Adult and Young-Adult Animals

First, we compared each animal's amount of day-long activity by plotting the data compiled during the entire recording period separately for all healthy animals (**Figure 2**).

Using two-way ANOVA, we found a significant main effect in both individuals [$F(5, 1606) = 126.84$, $p < 0.01$] and age-groups [$F(1,1606) = 2216.8$, $p < 0.01$]. This result suggests that the amount of day-long activity changes during development even among young marmosets.

Marmosets' Behavior Is Characterized by a Periodicity of 24 h

Next, we evaluated the periodicity of activity during the circadian cycle. As before, we compared the amount of day-long activity for each animal during the entire recording period. A representative example over a one-week period for a single animal is shown in **Figure 3**. The activity count was limited during the light period and almost zero during the dark period (**Figure 3A**). A time series for every week throughout the recording period (re-binned for every minute) was constructed and the auto-correlogram for one week for each monkey was computed (**Figure 3B**). This autocorrelation analysis yielded an estimate of the duration of a single cycle; in the specific case presented, it amounted to 23.97 h. A comparison for all seven marmosets (**Figure 3C**) revealed a median daily cycle of 24.001 h for the sub-adult group and

[1]https://www.r-project.org/

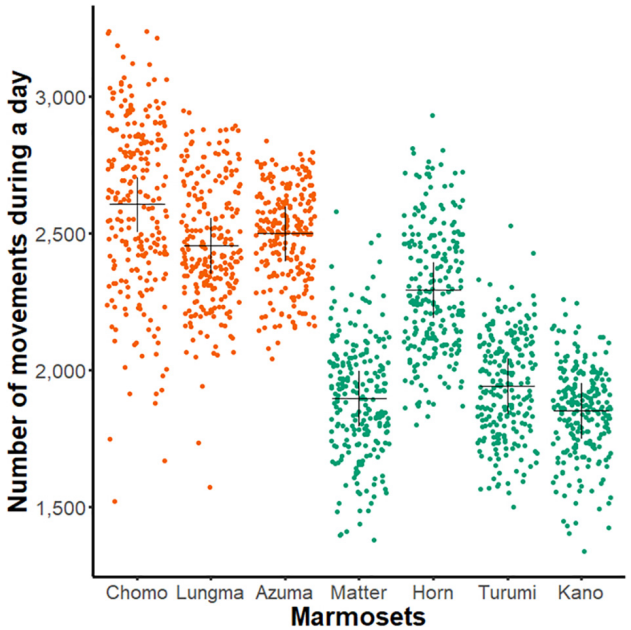

FIGURE 2 | Day-long activity of sub-adult and young-adult marmosets. A comparison of day-long activities (ordinate, aggregated number of movements, see **Figure 1G**) of each marmoset (abscissa, $n = 7$, name of each marmoset is specified). Each dot represents the net activity for a single day. The black cross indicates mean for all measurement days for each animal; orange, sub-adult group and green, young-adult group.

23.996 h for the young-adult group (Wilcoxon rank sum test, $W = 7132$, $p = 0.1895$). These results indicate that marmoset daily life is marked by light cycles in the colony room; however, this periodicity is equal between the two marmoset groups.

Pattern of Diurnal Activity and Activity During Daylight

We further characterized the pattern of activity in the active period within each daily cycle (diurnal activity pattern). Although we found some variation in the diurnal index among subjects (from 0.9518 to 0.9870, Kruskal-Wallis rank sum test, Chi-squared = 798.68, $df = 6$, $p < 0.01$), this result indicates that almost all activity was observed during the light period (**Figure 4A**). Such finding is consistent with the common marmoset being a diurnal animal. Moreover, as the diurnal index was higher in the young-adult group (Wilcoxon rank sum test, $W = 134440$, $p < 0.01$), night time activity was relatively higher in the sub-adult group, suggesting that the diurnal pattern formed during development.

Next, we computed and compared activity per hour during daytime for each marmoset (**Figure 4B**). Activity was triggered by turning on the light of the housing room and reached its first peak around 9 AM. Then, it decreased until reaching the trough (termed a "siesta" break) around noon. After that, activity increased again, culminating in a second peak around 3–4 PM. Averaging this hourly activity (converted to z score) for each animal (**Figure 4C**) revealed a remarkable bimodal daily pattern. This bimodality indicates that daytime activity could be divided into two segments: before and after the "siesta" break. Following the second peak around 3–4 PM, four marmosets comprising three young-adults and one sub-adult started exhibiting a decline in activity 2 h before the light went off (paired t-test, $t = 3.0151$, $df = 12$, $p = 0.01076$); whereas three marmosets comprising two sub-adults and one young adult kept active even as the light went off (**Figure 4B**). This result might suggest that the diurnal, bimodal rhythm had not yet developed in the latter three marmosets. Overall, the lower diurnal index in the sub-adult group could indicate a not yet developed day-night cycle; whereas a smaller variance of activity during daytime could reflect an immature intra-daytime cycle in younger animals. These findings suggest that the daily activity cycle of marmosets is shaped progressively during this age interval.

Decreased Daily Activity During the Developmental Period

Longitudinal variations in daytime activity throughout the recording period are shown in **Figure 5**. Each point indicates the weekly mean (±SD) of daytime activity for each marmoset as a function of the individual's age. Animals in the sub-adult group exhibited a progressive decrease in activity during a measurement period (reddish color), which was then merged to the level in the young-adult groups (bluish color). By assuming a monotonic decrease in activity as a function of age, we computed a linear regression for both animal groups throughout the recording period. We detected a steeper decrease in the sub-adult group ($y = -14.625x + 2679.45$, $p < 0.01$, $R^2 = 0.415$) than in the young-adult group ($y = -6.50x + 2064.99$, $p < 0.01$, $R^2 = 0.079$), where y is the number of movements and x is the age in weeks.

Intermittent Nature of Marmoset Activity

Figure 6A shows the length of movement bouts during the entire recording period in each marmoset. As indicated by the median score (interrupted vertical line), each activity bout lasted several seconds. The third quartile point (red line) indicates a trend associated with long-lasting movements. By tracing the scores for the entire assessment period (**Figure 6C**), we found that the movement bout decreased as a function of age in the sub-adult group (Chi-squared = 62.873, $df = 32$, $p < 0.01$) but not in the young-adult group (Chi-squared = 44.936, $df = 32$, $p = 0.6421$) by the Friedman test. These results suggest that the length of each movement bout decreases during the early marmoset developmental period.

We made a similar comparison for the inactive phase (**Figures 6B,D**). In contrast to the movement bout, the length of the inactive phase became progressively longer within the observed age range. Based on the Friedman test, this longitudinal change occurred in the sub-adult group (Chi-squared = 74.708, $df = 32$, $p < 0.01$), as well as in the young-adult group (Chi-squared = 53.732, $df = 32$, $p = 0.009451$).

Overall, the length of movement bout indicates that marmoset activity is intermittent and consists of a bout of several seconds

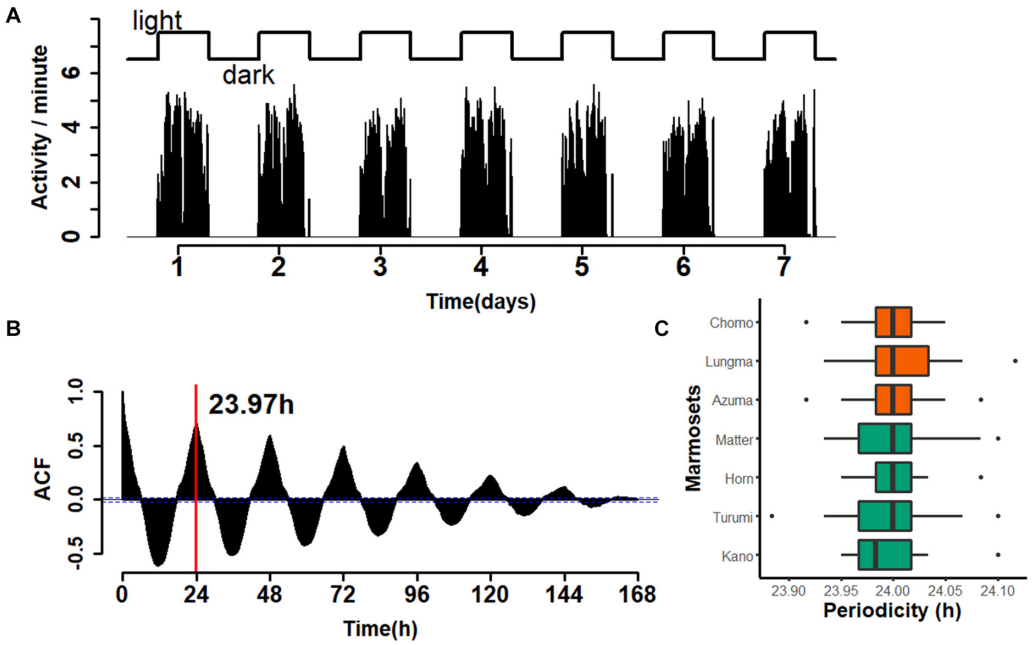

FIGURE 3 | Periodicity of 24 h for marmoset activity. **(A)** An example of a week-long, continuous recording for a single animal (Kano, recorded in week 23). Top, light–dark cycle of the breeding room. Bottom, aggregated number of movements for each minute. Movements were highly restricted during the light period. **(B)** Auto-correlogram of marmoset activity in the same week of the same animal as in panel **(A)**. Red line, estimated duration of a single cycle (23.97 h for the week). **(C)** Median ± inter-quartile range of the cycle duration for each marmoset is shown with the ordinal box plot. The color codes are the same as those used in **Figure 2**.

followed by an inactive period. It also suggests that the decrease in activity during development may be explained by both a shorter activity bout as well as a longer resting period between bouts.

Experiment 2

Changes in Motility in a Disease Marmoset Model During Progression of Motor Symptoms

So far, we analyzed the pattern of in-cage activity in healthy wild-type marmosets (**Table 1**). Next, we analyzed the development of the symptom of a transgenic marmoset model of ataxia (n = 3). A symptomatic animal (**Figure 7A**, black line) was diagnosed with onset of symptoms around 33 weeks of age (arrow) (Owari et al., 2016). Daily activity differed dramatically between the period preceding the onset of symptoms or their earlier phase (left) and a later phase (right) of progression. Indeed, the motility of the symptomatic animal, as quantified by the daytime activity count, decreased during symptom progression until it dropped to half the initial value. During the latter part of the recording, a steeper monotonic reduction was observed in this symptomatic marmoset, but not in four age-matched wild-type controls (blue line, Chi-squared = 38.314, df = 19, p = 0.00541) or two pre-symptomatic transgenic marmosets (orange line, Chi-squared = 27.486, df = 19, p = 0.09384) according to the Friedman test. This result indicates that the method of measuring daily movement developed in this study is sufficiently sensitive to characterize the progressive deterioration of motor symptoms typical of this disease.

Alternation of the Intermittent Nature of Daily Activity During Progression of Motor Symptoms

Finally, we evaluated the intermittent nature in daily activity of the symptomatic marmoset during progression of motor symptom (**Figures 7B,C**) in a similar way as during development (**Figure 6**). We found a shorter movement bout in the symptomatic transgenic marmoset during the latter weeks, but this decrement was not obtained in both age-matched asymptomatic transgenic marmosets (orange line, Chi-squared = 18.732, df = 19, p = 0.4741) or age-matched wild-type controls (blue line, Chi-squared = 24.858, df = 19, p = 0.1653) by the Friedman test. As this measurement may be influenced by the difficulty of maintaining movement for a given period, the changes could reflect the weakening of motor ability caused by disease progression. In addition, we found a gradual lengthening of the inactive phase only in the symptomatic animal (**Figure 7C**). The increased length of the inactive phase may represent the transient immobilization of movement caused by ataxia and observed also in human patients. Furthermore, this result suggests that measuring intermittent movements could serve as a convenient biomarker of disease progression in the ataxia model, as it could be evaluated based on a shorter assessment period of daily activity.

DISCUSSION

We developed an in-cage motility monitoring method for marmosets using a passive infrared motion detector, and

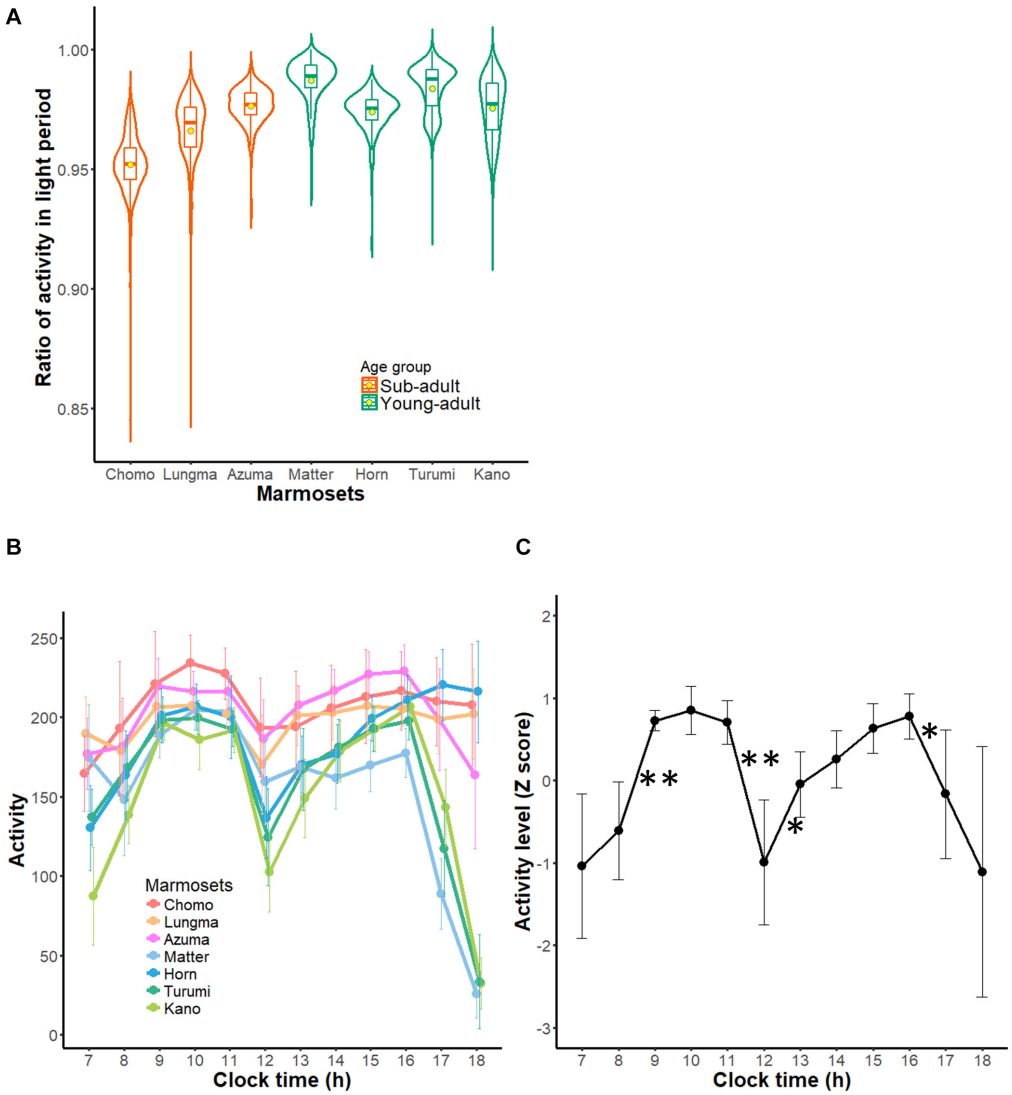

FIGURE 4 | Diurnal activity pattern of common marmosets. **(A)** Diurnal index of each marmoset during all recording periods is represented in the form of a violin plot. Contour indicates the histogram for indexes during all recording periods and the box plot within each contour indicates the medians (horizontal bars) and means (circles). **(B)** Hourly activity of each marmoset during daytime (mean ± SD). Each color represents each marmoset (warm colors for sub-adult groups and cold colors for young adult group are used to match those of other figures). **(C)** A collective profile of daytime activity of marmosets. This plot shows mean ± SD of all seven marmosets from each marmoset's Z-scored profile. **1% significant difference from the next hour, *5% significant difference from the next hour.

examined its feasibility during long-term operation (**Figure 1**). Monitoring of seven animals was successful and without any interruption over 231 days. Activity profiles, including gross daily activity and daytime hourly activity, could be extracted from the data obtained for each marmoset. Furthermore, this method successfully assessed the slow, long-term changes in motility occurring in a marmoset model of human disease. We conclude that the in-cage motility monitoring system is suitable for the longitudinal assessment of marmoset motility.

In the past, various methods for measuring animal motility have been devised. One approach is to use a wearable, microfabricated tiny logger device packaged with micro sensors (Mann et al., 2005; Sri Kantha and Suzuki, 2006; Hoffmann et al., 2012; Melo et al., 2016), whereby changes in acceleration are detected and accumulated over several seconds. The main limitations are the capacity of the data logger and a practical resolution < 0.1 Hz. A popular alternative is to place the sensor in the space surrounding the animals, rather than on the animal itself. Video tracking is commonly used in assays such as the open field test, whereby the travel distance is derived from the locomotion trajectory (Noldus et al., 2001). Recent technological advances have made video tracking devices sufficiently small for their use as an in-cage monitoring system for rodents (Singh et al., 2019). Further, by using multiple cameras or with an additional depth sensor, it is possible to track an animal's whereabouts in the three dimensional space,

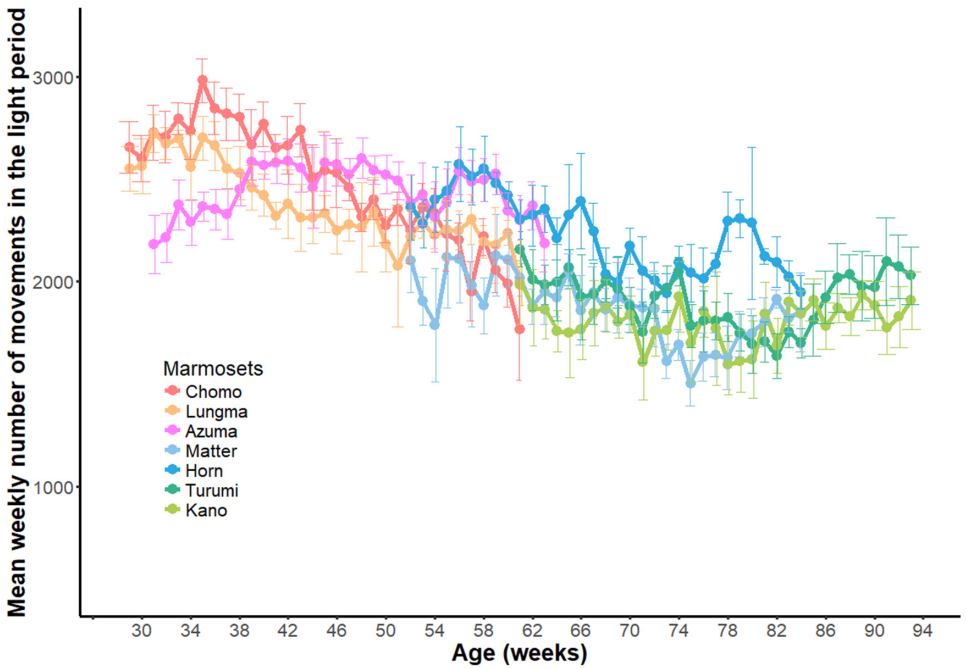

FIGURE 5 | Developmental changes in daytime activity. Longitudinal changes in daytime activities throughout the experiment period (33 weeks) for all seven marmosets. Weekly mean (±SD) for each marmoset was plotted against age.

including in primates (Ballesta et al., 2014). The disadvantage of such a system is its rather large, fragile, and complex structure when applied in the cage (Yabumoto et al., 2019). Unless it is built a new, it is difficult to make major modifications to an existing animal husbandry facility as it may affect an animal's physical and mental status. In this study, we overcame this problem by employing a passive movement detector.

Selection of the Motion Detection Mechanism

Currently, an animal's movement is detected by physically interrupting the photo-beam, or by recording changes in thermal distribution in space as a function of time. The "photo-beam" method senses the interruption of a near-infrared light beam upon the animal's passage. However, the area of detection is limited by the width of the photo beam (typically < 10 mm) and, therefore, numerous sensors are required to cover a large three dimensional space when detecting marmoset movement (Pearce et al., 1995). In contrast, the second method locates the animal based on a particular infrared wavelength emitted by the organism. Accordingly, the signals sent back at every change in position are used to track the animal's movement. Importantly, one sensor can cover a wide three dimensional space, meaning that a single sensor is sufficient to cover almost the entire area of a typical marmoset cage without any modification to the cage itself. This type of sensor is used to evaluate rodents' activity within a single enclosure (Masuo et al., 1997) and has been recently applied to measure the activity of single animals housed simultaneously in different cages (Brown et al., 2016; Matikainen-Ankney et al., 2019). Based on these characteristics, we chose this method to detect marmoset movement in their home cage.

Long-Term Recording

A continuous series of data points obtained by in-cage measurements can potentially unmask the periodicity hidden in animal behavior. The profiles obtained from all marmosets in this study showed a cyclic, 24-h transition in activity level, with almost all activity occurring during the light period. These findings match the diurnal nature of marmosets (Menezes et al., 1993; Hoffmann et al., 2012) and are in line with studies on their circadian rhythm (Erkert, 1989).

The bimodal profile of daily activity is consistent with the reported profiles of two prominent active phases during daytime (Erkert, 1989; Castro et al., 2003; Melo et al., 2013). Although peak level before noon may be affected here by the husbandry routine, lower activity around noon may reflect the marmoset's specific behavioral pattern previously observed in free-ranging individuals (Castro et al., 2003). The hourly variation in daily activity observed here implies that any comparison in motility among or within subjects might be validated only if data are recorded at a comparable time of the day. In this sense, in-cage 24-h measurements provide an excellent source of information.

The marmoset's moderately long lifespan is advantageous when investigating primate aging or slowly progressive diseases (Maclean et al., 2000; Tardif et al., 2011). Recently, alternations in the daily rhythm have been associated with neurodegenerative disease (Leng et al., 2019). An altered synchronization to light has

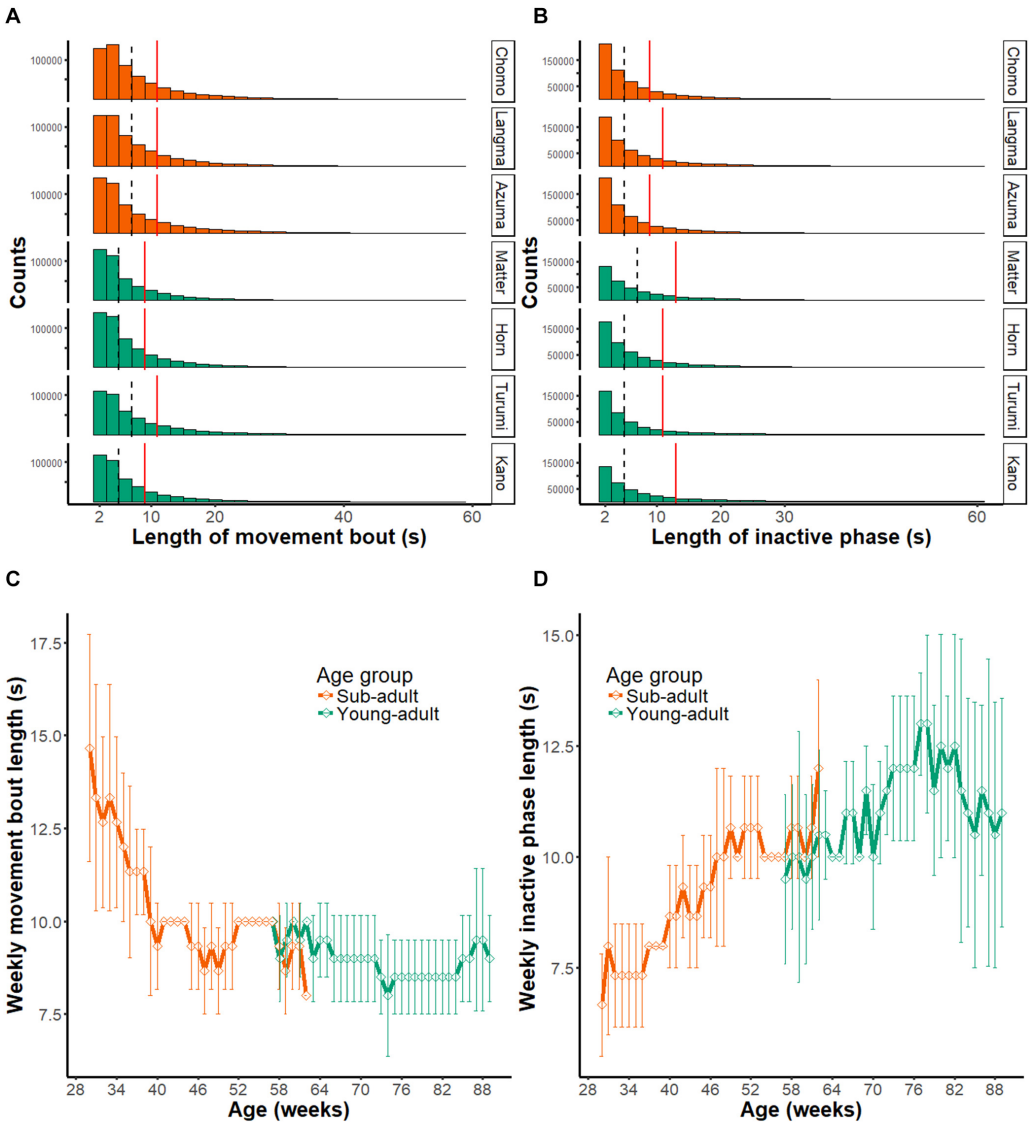

FIGURE 6 | Intermittent nature of marmoset activity. **(A)** Histograms showing the distribution of movement bout lengths during daytime at all periods of monitoring (231 days). The results of seven animals are presented separately. Note that bouts longer than 60 s (0.2% of all data) are not included in the histogram. Dashed line, median of all movement bouts; red solid line; third quantile point of all movement bouts. **(B)** Histograms showing the length of inactive phase during daytime at all periods of monitoring (231 days). Note that inactive phases longer than 60 s (2.6% of all data) are not included in the histogram. Dashed line, median of all movement bouts; red solid line, third quantile point of all movement bouts. **(C)** Longitudinal changes in the length of movement bout. Group mean (±SD) of the index is plotted as a function of mean age of animals. Note that the movement bout decreased as a function of age in the sub-adult group, but the young adult group did not show a significant change. **(D)** Length of the inactive phase is shown in the same format as in panel **(C)**. Note that the length of inactive phase continuously extended throughout the observed age range.

been observed in aged marmosets (Gonçalves et al., 2016) and REM sleep behavioral disorder has been reported in a Parkinson's disease marmoset model (Verhave et al., 2011). Considering the monophasic pattern of sleep (Hoffmann et al., 2012), marmoset is an ideal species for studying sleep disorder. Our system for long-term continuous recording could evaluate changes characterized by such relatively slow time constant.

We found that marmoset activity differed among two age groups. Various stages are proposed as developmental milestones in marmosets (Missler et al., 1992; De Castro Leao et al., 2009; Schultz-Darken et al., 2016). The animals used in the present study corresponded to the sub-adult and young-adult developmental phases (Missler et al., 1992). Lower overall activity in the relatively more mature young-adult group suggests that the motility measurement obtained with this system reflects the profile of each developmental stage. Melo et al. (2016) reported higher daily activity in juvenile marmosets compared to their parents. A gradual decline in activity from sub-adults to young-adults may be a function of development. Even though early maturity of marmoset behavior has been reported

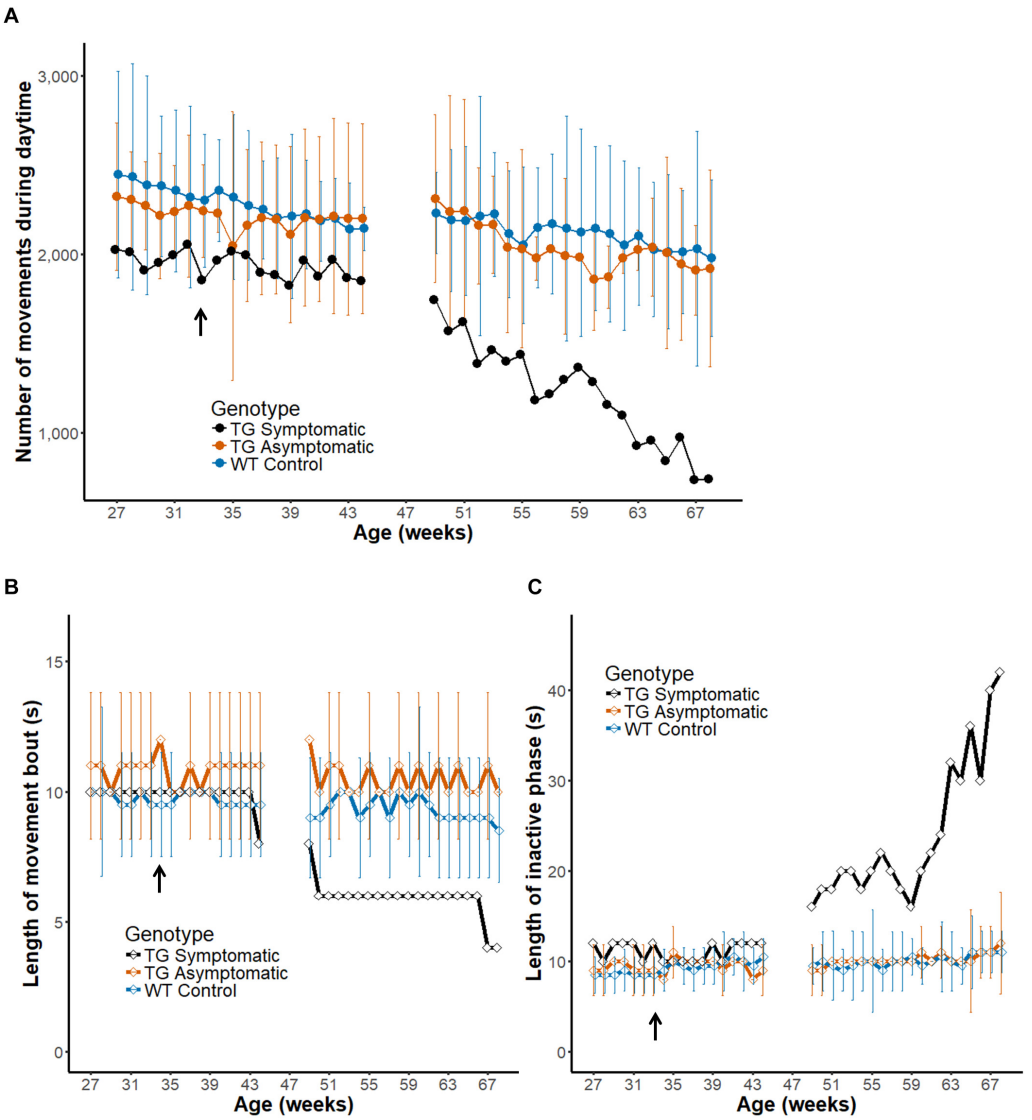

FIGURE 7 | Intermittent nature of activity represents the progression of disease in a transgenic marmoset. **(A)** Number of movements during daytime before and after the onset of diagnosed symptoms (33 weeks of age, arrow in the horizontal axis) in a transgenic marmoset (n = 1, black) and age-matched asymptomatic (n = 2, orange) and wild-type (n = 4, blue) animals (group mean ± 2 SD). Note that the measurement was paused from weeks 45 to 48 as the transgenic animal was temporality transferred to another cage for a neuroimaging experiment. **(B,C)** Longitudinal changes in the length of movement bout **(B)** and inactive phase **(C)**. Group mean (±2 SD) of the index is plotted as a function of mean age. The movement bout decreased and the inactive phase increased as a function of age after disease onset in the symptomatic transgenic animal. Note that the score obtained for a symptomatic marmoset after disease onset was generally beyond the 2 SD range of that obtained for wildtype controls or asymptomatic marmosets.

(Wang et al., 2014), the time-course of subsequent motor development is less known. Hence, the proposed movement monitoring system may help gather life-long data essential when using marmoset as the animal model of human disease at different developmental stages.

Measurement From a Transgenic Marmoset Model of Human Ataxia

Our system was capable of quantifying the monotonic decline in motility of transgenic marmosets mimicking human polyglutamine disorder (Tomioka et al., 2017) during the entire course of disease progression (Owari et al., 2016). In a previous study, using a rodent model of human neurodegenerative disorder, the onset and time-course of disease progression were identified by measuring animal motility (Norflus et al., 1998; Rudenko et al., 2009; Holter et al., 2013). Our study upgraded those observations in two important ways. First, we applied the method to the marmoset monkey, which is a closer relative to humans. Second, we covered the entire life span of each transgenic marmoset and successfully characterized the pre- and post-symptomatic state.

It should be noted that scattered sampling of motility has already been reported in a pharmacologically induced marmoset model (Pearce et al., 1995; Ando et al., 2008; Verhave et al., 2011; Phillips et al., 2017). However, this is the first such study on genetically induced animals. Using linear regression, we successfully estimated the quantitative time constant of disease progression at -46.74 per week during the last 20 weeks of measurement (**Figure 7A**). The ability to accurately quantify the decline in motility is crucial for establishing new intervention strategies and assessing the effectiveness of therapeutic agents.

Temporal Structure Analysis

Animal motility can be characterized by analyzing its temporal structure (De Visser et al., 2006; Umemori et al., 2009; Blum et al., 2014). Aside from the circadian rhythm, an animal's behavior can exhibit cycles of activity and inactivity, as well as include a shorter "ultradian" rhythm (Honma and Hiroshige, 1978; Blum et al., 2014) or sub-hour and sub-minutes cycles. The circadian rhythm and the shorter cycle could be controlled by distinct brain mechanisms (Blum et al., 2014) and deteriorate independently under specific brain disorders (Nakamura et al., 2007). Intermittency of movement, i.e., the short-cycle rhythm, has been successfully used to characterize motility profiles among different rodent strains (De Visser et al., 2006), as well as symptom progression in the transgenic motor disease model (Hickey et al., 2005). Using a comparable time resolution, Goulding et al. (2008) found a specific "temporal structure" within a short active cluster for intake behavior, which differed in mutant obesity mice.

Time resolution of our system enabled us to characterize short-cycle movement in the marmoset home cage (**Figure 1**). Indeed, we found that the duration of both active and inactive phases varied with animal age and there was a steep increase in the length of the inactive phase after symptom progression in a transgenic marmoset. From these results, we conclude that short-cycle movement could serve as a marker to characterize the motility of both wild-type and transgenic model marmosets. Moreover, it could be applied to evaluate the extent of ataxia as a function of disease progression in other model animals (Hickey et al., 2005) or to characterize the motility of non-human primates using temporal structure analysis (Goulding et al., 2008).

Simultaneous Measurement From Various Marmosets in the Same Colony

The most important advantage of our system is its simplicity. It is made exclusively by off-the-shelf electrical parts and can be easily installed on the marmoset's home cage, making it possible to simultaneously monitor the motility of numerous animals at low cost. The measurement of large numbers of animals has a clear advantage for non-human primates. For example, their intricate, albeit highly evolved, structure of the musculoskeletal and neural systems renders their behavioral pattern highly complex. For this reason, quantitative evaluation of behavior has been challenging, as well as time- and energy-consuming due to a one-by-one approach. Sample size is becoming crucial for contemporary studies of non-human primates (Prescott, 2010).

Another advantage arising from simultaneous behavioral recording of many animals is the possibility to extract "common-mode noise" originating from a shared housing environment, and purify the recorded measurement by eliminating such noise. Generally speaking, animal's behavior is driven either by the internal state of the body or by stimuli arising from the external environment A classical, session-based measurement (Wahlsten, 2001) aims to dissociate the latter from the former. To assess auditory response, for example, the experimenter presents the same auditory stimulus repetitively in a sound-proof chamber and extracts the ensuing common neural response (Bendor and Wang, 2007). The disadvantage of behavioral measurement in the home cage is represented by the difficulty to control environmental factors. In a normal marmoset colony, a number of auditory stimuli (e.g., vocal calls, movement of other animals or human staff providing daily care) may occur at times that are fairly unpredictable by the experimenter. Therefore, repetitive presentation of the same sound may generate a type of behavior that was actually triggered by other external events occurring coincidentally with the experimental sound. As a consequence, results manifest lower reproducibility between trials or individuals. One way to overcome this limitation is to monitor stimuli-driven behaviors concurrently in all animals. Known as the yoked control design, this method records the behavior triggered by the same controlled and uncontrolled environmental stimuli in all animals. The experimenter then obtains purified data by subtracting the component associated to the same environmental signal from all subjects.

Finally, the proposed method has another advantage in terms of reproducibility. Some marmosets are difficult to habituate to the experimental set-up, and the way and extent of habituation may differ between individuals. Measurement in our method is performed in the most familiar space for the animals and cancels out the irrelevant variance generated by acquiring data from a large number of subjects.

Limitations

Lastly, it is worth mentioning the four potential limitations of the proposed activity sensing system. Firstly, our system cannot assess the activity of individual marmoset when they are housed with other animals. This is because the sensor system we used cannot track a specific heat source. There are other systems that are dedicated to this objective (Mann et al., 2005). Secondly, the sensor used in this study was originally designed for the precise detection of human movements, but not for small and versatile animals like a common marmoset. Consequently, it is not assured that the system can detect a variety of movements without failure even when animals were within the field of detection of sensor. Third, due to the intrinsic properties of the sensor, the sensitivity of detection changes as a function of distance between the sensor and animals (**Supplementary Figures 2C,D**). Therefore, movement detection could be biased toward a situation when animals stayed in the upper part of the cage. Fourth, the system cannot dissociate different types of movement (e.g., locomotion or movement of body parts, **Supplementary Videos 1, 2**) because the sensor

simply detects the variance of temperature within the field. The pose estimation-based motion analysis approach (Mathis et al., 2018; Mathis and Mathis, 2019), for example, is superior for this objective. Overall, a potential user of this system needs to be aware that our system can provide a relative, but not absolute, evaluation of an animal's motility. While it is useful to compare the motility among different animals or that of the same animal on a different day, it may not be straightforward to compare with the motility evaluated by other systems.

DATA AVAILABILITY STATEMENT

The original contributions presented in the study are included in the article/**Supplementary Material**, further inquiries can be directed to the corresponding author.

ETHICS STATEMENT

The animal study was reviewed and approved by the committee on the ethical issue in animal experiments of the National Center of Neurology and Psychiatry.

AUTHOR CONTRIBUTIONS

MK and KS designed, manufactured, installed the in-cage motility measurement system, and wrote a draft of the manuscript. MK and AK performed the measurements. MK analyzed the data. TN, NN, KO, and KS generated the transgenic animal used in the study. All authors contributed to the final version of this manuscript.

FUNDING

This work was supported by research grants from the Japan Agency for Medical Research and Development (JP20dm0207092, JP20dm0207066, JP19ek0109216, and JP16ak0101027), Intramural Research Grants (26-11, 29-5) for Neurological and Psychiatric Disorders at NCNP, and the JSPS KAKENHI, Grant-in-Aid for Scientific Research on Innovative Areas "Hyper-adaptability for overcoming body-brain dysfunction: Integrated empirical and system theoretical approaches" (Grant Number 19H05724 to KS).

ACKNOWLEDGMENTS

The authors would like thank Drs. Ryoichi Saito and Yuko Katakai (Administrative Section of Primate Research Facility, NCNP) for helping install the sensor and manage animals, as well as Dr. Hidetoshi Ishibashi (Tokyo Medical University) for establishing the previous version of the monitoring system.

SUPPLEMENTARY MATERIAL

The Supplementary Material for this article can be found online at: https://www.frontiersin.org/articles/10.3389/fnsys.2021.645308/full#supplementary-material

REFERENCES

Abbott, D. H., Barnett, D. K., Colman, R. J., Yamamoto, M. E., and Schultz-Darken, N. J. (2003). Aspects of common marmoset basic biology and life history important for biomedical research. *Comp. Med.* 53, 339–350.

Ando, K., Maeda, J., Inaji, M., Okauchi, T., Obayashi, S., Higuchi, M., et al. (2008). Neurobehavioral protection by single dose l-deprenyl against MPTP-induced parkinsonism in common marmosets. *Psychopharmacology* 195, 509–516. doi: 10.1007/s00213-007-0929-2

Ballesta, S., Reymond, G., Pozzobon, M., and Duhamel, J. R. (2014). A real-time 3D video tracking system for monitoring primate groups. *J. Neurosci. Methods* 234, 147–152. doi: 10.1016/j.jneumeth.2014.05.022

Barbosa, M. N., and Mota, M. T. (2009). Behavioral and hormonal response of common marmosets, Callithrix jacchus, to two environmental conditions. *Primates* 50, 253–260. doi: 10.1007/s10329-009-0137-2

Barlow, C., Hirotsune, S., Paylor, R., Liyanage, M., Eckhaus, M., Collins, F., et al. (1996). Atm-deficient mice: a paradigm of ataxia telangiectasia. *Cell* 86, 159–171. doi: 10.1016/s0092-8674(00)80086-0

Barr, C. S., Newman, T. K., Becker, M. L., Parker, C. C., Champoux, M., Lesch, K. P., et al. (2003). The utility of the non-human primate; model for studying gene by environment interactions in behavioral research. *Genes Brain Behav.* 2, 336–340.

Bassett, L., Buchanan-Smith, H. M., Mckinley, J., and Smith, T. E. (2003). Effects of training on stress-related behavior of the common marmoset (Callithrix jacchus) in relation to coping with routine husbandry procedures. *J. Appl. Anim. Welf. Sci.* 6, 221–233. doi: 10.1207/s15327604jaws0603_07

Bendor, D., and Wang, X. (2007). Differential neural coding of acoustic flutter within primate auditory cortex. *Nat. Neurosci.* 10, 763–771. doi: 10.1038/nn1888

Blum, I. D., Zhu, L., Moquin, L., Kokoeva, M. V., Gratton, A., Giros, B., et al. (2014). A highly tunable dopaminergic oscillator generates ultradian rhythms of behavioral arousal. *Elife* 3:e05105.

Brown, L. A., Hasan, S., Foster, R. G., and Peirson, S. N. (2016). COMPASS: Continuous Open Mouse Phenotyping of Activity and Sleep Status. *Wellcome Open Res.* 1:2. doi: 10.12688/wellcomeopenres.9892.2

Buchman, A. S., Dawe, R. J., Yu, L., Lim, A., Wilson, R. S., Schneider, J. A., et al. (2018). Brain pathology is related to total daily physical activity in older adults. *Neurology* 90, 1911–1919e.

Capitanio, J. P., and Emborg, M. E. (2008). Contributions of non-human primates to neuroscience research. *Lancet* 371, 1126–1135. doi: 10.1016/s0140-6736(08)60489-4

Carter, R. J., Lione, L. A., Humby, T., Mangiarini, L., Mahal, A., Bates, G. P., et al. (1999). Characterization of progressive motor deficits in mice transgenic for the human Huntington's disease mutation. *J. Neurosci.* 19, 3248–3257. doi: 10.1523/jneurosci.19-08-03248.1999

Casadesus, G., Shukitt-Hale, B., and Joseph, J. A. (2001). Automated measurement of age-related changes in the locomotor response to environmental novelty and home-cage activity. *Mech. Ageing Dev.* 122, 1887–1897. doi: 10.1016/s0047-6374(01)00324-4

Castro, C. S. S., Menezes, A. L., and Moreira, L. F. S. (2003). Locomotor Activity Rhythm in Free-ranging Common Marmosets (Callithrix jacchus). *Biol. Rhythm Res.* 34, 23–30. doi: 10.1076/brhm.34.1.23.14084

Choudhury, G. R., and Daadi, M. M. (2018). Charting the onset of Parkinson-like motor and non-motor symptoms in nonhuman primate model of Parkinson's disease. *PLoS One* 13:e0202770. doi: 10.1371/journal.pone.0202770

Crabbe, J. C., Wahlsten, D., and Dudek, B. C. (1999). Genetics of mouse behavior: interactions with laboratory environment. *Science* 284, 1670–1672. doi: 10.1126/science.284.5420.1670

Crawley, J. N., and Paylor, R. (1997). A proposed test battery and constellations of specific behavioral paradigms to investigate the behavioral phenotypes of transgenic and knockout mice. *Horm. Behav.* 31, 197–211. doi: 10.1006/hbeh.1997.1382

De Castro Leao, A., Duarte, D., Neto, A., and De Sousa, M. B. (2009). New developmental stages for common marmosets (Callithrix jacchus) using mass and age variables obtained by K-means algorithm and self-organizing maps (SOM). *Comput. Biol. Med.* 39, 853–859. doi: 10.1016/j.compbiomed.2009.05.009

De Visser, L., Van Den Bos, R., Kuurman, W. W., Kas, M. J., and Spruijt, B. M. (2006). Novel approach to the behavioural characterization of inbred mice: automated home cage observations. *Genes Brain Behav.* 5, 458–466. doi: 10.1111/j.1601-183x.2005.00181.x

Emborg, M. E. (2017). Nonhuman Primate Models of Neurodegenerative Disorders. *ILAR J.* 58, 190–201. doi: 10.1093/ilar/ilx021

Erkert, H. G. (1989). Characteristics of the circadian activity rhythm in common marmosets (Callithrix j. jacchus). *Am. J. Primatol.* 17, 271–286. doi: 10.1002/ajp.1350170403

Ferrucci, L., Cooper, R., Shardell, M., Simonsick, E. M., Schrack, J. A., and Kuh, D. (2016). Age-Related Change in Mobility: Perspectives From Life Course Epidemiology and Geroscience. *J. Gerontol. Biol. Sci. Med. Sci.* 71, 1184–1194. doi: 10.1093/gerona/glw043

Galvao-Coelho, N. L., Galvao, A. C. M., Da Silva, F. S., and De Sousa, M. B. C. (2017). Common Marmosets: A Potential Translational Animal Model of Juvenile Depression. *Front. Psychiatry* 8:175. doi: 10.3389/fpsyt.2017.00175

Garber, P. A. (1992). Vertical clinging, small body size, and the evolution of feeding adaptations in the Callitrichinae. *Am. J. Phys. Anthropol.* 88, 469–482. doi: 10.1002/ajpa.1330880404

Garland, T. Jr., Schutz, H., Chappell, M. A., Keeney, B. K., Meek, T. H., Copes, L. E., et al. (2011). The biological control of voluntary exercise, spontaneous physical activity and daily energy expenditure in relation to obesity: human and rodent perspectives. *J. Exp. Biol.* 214, 206–229. doi: 10.1242/jeb.048397

Gonçalves, F. B., Borges, G. R., Gonçalves, B. S. B., Cavalcante, J. S., Menezes, A. A. L., and Azevedo, C. V. M. (2016). Evidence for age-related changes in the circadian activity rhythm of the diurnal primate Callithrix jacchus: a case report. *Biol. Rhythm Res.* 47, 395–399. doi: 10.1080/09291016.2015.1129695

Goulding, E. H., Schenk, A. K., Juneja, P., Mackay, A. W., Wade, J. M., and Tecott, L. H. (2008). A robust automated system elucidates mouse home cage behavioral structure. *Proc. Natl. Acad. Sci. U S A.* 105, 20575–20582. doi: 10.1073/pnas.0809053106

Hickey, M. A., Gallant, K., Gross, G. G., Levine, M. S., and Chesselet, M. F. (2005). Early behavioral deficits in R6/2 mice suitable for use in preclinical drug testing. *Neurobiol. Dis.* 20, 1–11. doi: 10.1016/j.nbd.2005.01.024

Hoffmann, K., Coolen, A., Schlumbohm, C., Meerlo, P., and Fuchs, E. (2012). Remote long-term registrations of sleep-wake rhythms, core body temperature and activity in marmoset monkeys. *Behav. Brain Res.* 235, 113–123. doi: 10.1016/j.bbr.2012.07.033

Holter, S. M., Stromberg, M., Kovalenko, M., Garrett, L., Glasl, L., Lopez, E., et al. (2013). A broad phenotypic screen identifies novel phenotypes driven by a single mutant allele in Huntington's disease CAG knock-in mice. *PLoS One* 8:e80923. doi: 10.1371/journal.pone.0080923

Honma, K. I., and Hiroshige, T. (1978). Endogenous ultradian rhythms in rats exposed to prolonged continuous light. *Am. J. Physiol.* 235, R250–R256.

Johnson, E. O., Kamilaris, T. C., Calogero, A. E., Gold, P. W., and Chrousos, G. P. (1996). Effects of early parenting on growth and development in a small primate. *Pediatr. Res.* 39, 999–1005. doi: 10.1203/00006450-199606000-00012

Kaplan, G., Pines, M. K., and Rogers, L. J. (2012). Stress and stress reduction in common marmosets. *Appl. Anim. Behav. Sci.* 137, 175–182. doi: 10.1016/j.applanim.2011.04.011

Kishi, N., Sato, K., Sasaki, E., and Okano, H. (2014). Common marmoset as a new model animal for neuroscience research and genome editing technology. *Dev. Growth Differ.* 56, 53–62. doi: 10.1111/dgd.12109

Koski, S. E., Buchanan-Smith, H. M., Ash, H., Burkart, J. M., Bugnyar, T., and Weiss, A. (2017). Common marmoset (Callithrix jacchus) personality. *J. Comp. Psychol.* 131, 326–336.

Larson, S. G. (2018). Nonhuman Primate Locomotion. *Am. J. Phys. Anthropol.* 165, 705–725. doi: 10.1002/ajpa.23368

Leng, Y., Musiek, E. S., Hu, K., Cappuccio, F. P., and Yaffe, K. (2019). Association between circadian rhythms and neurodegenerative diseases. *Lancet Neurol.* 18, 307–318. doi: 10.1016/s1474-4422(18)30461-7

Lin, C. H., Tallaksen-Greene, S., Chien, W. M., Cearley, J. A., Jackson, W. S., Crouse, A. B., et al. (2001). Neurological abnormalities in a knock-in mouse model of Huntington's disease. *Hum. Mol. Genet.* 10, 137–144. doi: 10.1093/hmg/10.2.137

Maclean, C. J., Baker, H. F., Ridley, R. M., and Mori, H. (2000). Naturally occurring and experimentally induced beta-amyloid deposits in the brains of marmosets (Callithrix jacchus). *J. Neural. Transm.* 107, 799–814. doi: 10.1007/s007020070060

Mann, T. M., Williams, K. E., Pearce, P. C., and Scott, E. A. (2005). A novel method for activity monitoring in small non-human primates. *Lab. Anim.* 39, 169–177. doi: 10.1258/0023677053739783

Marshall, J. W., and Ridley, R. M. (2003). Assessment of cognitive and motor deficits in a marmoset model of stroke. *ILAR J.* 44, 153–160. doi: 10.1093/ilar.44.2.153

Masuo, Y., Matsumoto, Y., Morita, S., and Noguchi, J. (1997). A novel method for counting spontaneous motor activity in the rat. *Brain Res. Brain Res. Protoc.* 1, 321–326. doi: 10.1016/s1385-299x(97)00005-6

Mathis, A., Mamidanna, P., Cury, K. M., Abe, T., Murthy, V. N., Mathis, M. W., et al. (2018). DeepLabCut: markerless pose estimation of user-defined body parts with deep learning. *Nat. Neurosci.* 21, 1281–1289. doi: 10.1038/s41593-018-0209-y

Mathis, M. W., and Mathis, A. (2019). Deep learning tools for the measurement of animal behavior in neuroscience. *Curr. Opin. Neurobiol.* 60, 1–11. doi: 10.1016/j.conb.2019.10.008

Matikainen-Ankney, B. A., Garmendia-Cedillos, M., Ali, M., Krynitsky, J., Salem, G., Miyazaki, N. L., et al. (2019). Rodent Activity Detector (RAD), an Open Source Device for Measuring Activity in Rodent Home Cages. *eNeuro* 6, ENEURO.160–ENEURO.119.

Melo, P. R., Goncalves, B. S., Menezes, A. A., and Azevedo, C. V. (2016). Circadian activity rhythm in pre-pubertal and pubertal marmosets (Callithrix jacchus) living in family groups. *Physiol. Behav.* 155, 242–249. doi: 10.1016/j.physbeh.2015.12.023

Melo, P., Goncalves, B., Menezes, A., and Azevedo, C. (2013). Socially adjusted synchrony in the activity profiles of common marmosets in light-dark conditions. *Chronobiol. Int.* 30, 818–827. doi: 10.3109/07420528.2013.767823

Menezes, A. A. L., Moreira, L. F. S., Azevedo, C. V. M., Costa, S. F., and Castro, C. S. S. (1993). Behavioral rhythms in the captive common marmoset (Callithrix jacchus) under natural environmental conditions. *Braz. J. Med. Biol. Res.* 26, 741–745.

Missler, M., Wolff, J. R., Rothe, H., Heger, W., Merker, H. J., Treiber, A., et al. (1992). Developmental biology of the common marmoset: proposal for a "postnatal staging". *J. Med. Primatol.* 21, 285–298. doi: 10.1111/j.1600-0684.1992.tb00593.x

Nakamura, T., Kiyono, K., Yoshiuchi, K., Nakahara, R., Struzik, Z. R., and Yamamoto, Y. (2007). Universal scaling law in human behavioral organization. *Phys. Rev. Lett.* 99:138103.

National Research Council (US) Institute for Laboratory Animal Research (1996). "Guide for the care and use of laboratory animals," in *Animal Environment, Housing, and Management*, (Washington, DC: National Academies Press (US)), Available online at: https://www.ncbi.nlm.nih.gov/books/NBK232587/

Nishijima, K., Saitoh, R., Tanaka, S., Ohsato-Suzuki, M., Ohno, T., and Kitajima, S. (2012). Life span of common marmoset (Callithrix jacchus) at CLEA Japan breeding colony. *Biogerontology* 13, 439–443. doi: 10.1007/s10522-012-9388-1

Nóbrega, C., and De Almeida, L. (2012). "Machado-Joseph Disease / Spinocerebellar Ataxia Type 3," in *Spinocerebellar Ataxia*, ed. J. Gazulla (Rijeka: IntechOpen).

Noldus, L. P., Spink, A. J., and Tegelenbosch, R. A. (2001). EthoVision: a versatile video tracking system for automation of behavioral experiments. *Behav. Res. Methods Instrum. Comput.* 33, 398–414. doi: 10.3758/bf03195394

Norcross, J. L., and Newman, J. D. (1999). Effects of separation and novelty on distress vocalizations and cortisol in the common marmoset (Callithrix jacchus). *Am. J. Primatol.* 47, 209–222. doi: 10.1002/(sici)1098-2345(1999)47:3<209::aid-ajp3>3.0.co;2-0

Norflus, F., Tifft, C. J., Mcdonald, M. P., Goldstein, G., Crawley, J. N., Hoffmann, A., et al. (1998). Bone marrow transplantation prolongs life span and

ameliorates neurologic manifestations in Sandhoff disease mice. *J. Clin. Invest.* 101, 1881–1888. doi: 10.1172/jci2127

Owari, K., Nogami, N., Nakatani, T., Koizumi, M., Ishibashi, H., Nagai, Y., et al. (2016). "Generation of transgenic marmoset line with polyglutamine disease and behavioral phenotyping," in *Society for Neuroscience Annual Meeting*, (San Diego: Society for Neuroscience).

Pearce, R. K., Jackson, M., Smith, L., Jenner, P., and Marsden, C. D. (1995). Chronic L-DOPA administration induces dyskinesias in the 1-methyl-4- phenyl-1,2,3,6-tetrahydropyridine-treated common marmoset (Callithrix Jacchus). *Mov. Disord.* 10, 731–740. doi: 10.1002/mds.870100606

Phillips, K. A., Bales, K. L., Capitanio, J. P., Conley, A., Czoty, P. W., Hart, B. A., et al. (2014). Why primate models matter. *Am. J. Primatol.* 76, 801–827. doi: 10.1002/ajp.22281

Phillips, K. A., Ross, C. N., Spross, J., Cheng, C. J., Izquierdo, A., Biju, K. C., et al. (2017). Behavioral phenotypes associated with MPTP induction of partial lesions in common marmosets (Callithrix jacchus). *Behav. Brain Res.* 325, 51–62. doi: 10.1016/j.bbr.2017.02.010

Portal, E., Riess, O., and Nguyen, H. P. (2013). Automated home cage assessment shows behavioral changes in a transgenic mouse model of spinocerebellar ataxia type 17. *Behav. Brain Res.* 250, 157–165. doi: 10.1016/j.bbr.2013.04.042

Pratte, M., Panayotis, N., Ghata, A., Villard, L., and Roux, J. C. (2011). Progressive motor and respiratory metabolism deficits in post-weaning Mecp2-null male mice. *Behav. Brain Res.* 216, 313–320. doi: 10.1016/j.bbr.2010.08.011

Prescott, M. J. (2010). Ethics of primate use. *Adv. Sci. Res.* 5, 11–22. doi: 10.5194/asr-5-11-2010

Redfern, W. S., Tse, K., Grant, C., Keerie, A., Simpson, D. J., Pedersen, J. C., et al. (2017). Automated recording of home cage activity and temperature of individual rats housed in social groups: The Rodent Big Brother project. *PLoS One* 12:e0181068. doi: 10.1371/journal.pone.0181068

Robinson, L., Plano, A., Cobb, S., and Riedel, G. (2013). Long-term home cage activity scans reveal lowered exploratory behaviour in symptomatic female Rett mice. *Behav. Brain Res.* 250, 148–156. doi: 10.1016/j.bbr.2013.04.041

Rogers, D. C., Fisher, E. M., Brown, S. D., Peters, J., Hunter, A. J., and Martin, J. E. (1997). Behavioral and functional analysis of mouse phenotype: SHIRPA, a proposed protocol for comprehensive phenotype assessment. *Mamm. Genome* 8, 711–713. doi: 10.1007/s003359900551

Rudenko, O., Tkach, V., Berezin, V., and Bock, E. (2009). Detection of early behavioral markers of Huntington's disease in R6/2 mice employing an automated social home cage. *Behav. Brain Res.* 203, 188–199. doi: 10.1016/j.bbr.2009.04.034

Schultz-Darken, N., Braun, K. M., and Emborg, M. E. (2016). Neurobehavioral development of common marmoset monkeys. *Dev. Psychobiol.* 58, 141–158. doi: 10.1002/dev.21360

Singh, S., Bermudez-Contreras, E., Nazari, M., Sutherland, R. J., and Mohajerani, M. H. (2019). Low-cost solution for rodent home-cage behaviour monitoring. *PLoS One* 14:e0220751. doi: 10.1371/journal.pone.0220751

Slipogor, V., Gunhold-De Oliveira, T., Tadic, Z., Massen, J. J., and Bugnyar, T. (2016). Consistent inter-individual differences in common marmosets (Callithrix jacchus) in Boldness-Shyness, Stress-Activity, and Exploration-Avoidance. *Am. J. Primatol.* 78, 961–973. doi: 10.1002/ajp.22566

Spruijt, B. M., and Devisser, L. (2006). Advanced behavioural screening: automated home cage ethology. *Drug Discov. Today Technol.* 3, 231–237. doi: 10.1016/j.ddtec.2006.06.010

Sri Kantha, S., and Suzuki, J. (2006). Sleep quantitation in common marmoset, cotton top tamarin and squirrel monkey by non-invasive actigraphy. *Comp. Biochem. Physiol. Mol. Integr. Physiol.* 144, 203–210. doi: 10.1016/j.cbpa.2006.02.043

't Hart, B. A., Van Kooyk, Y., Geurts, J. J., and Gran, B. (2015). The primate autoimmune encephalomyelitis model; a bridge between mouse and man. *Ann. Clin. Transl. Neurol.* 2, 581–593.

Tang, X., Orchard, S. M., and Sanford, L. D. (2002). Home cage activity and behavioral performance in inbred and hybrid mice. *Behav. Brain Res.* 136, 555–569. doi: 10.1016/s0166-4328(02)00228-0

Tardif, S. D., Mansfield, K. G., Ratnam, R., Ross, C. N., and Ziegler, T. E. (2011). The marmoset as a model of aging and age-related diseases. *ILAR J.* 52, 54–65. doi: 10.1093/ilar.52.1.54

Taroni, F., and Didonato, S. (2004). Pathways to motor incoordination: the inherited ataxias. *Nat. Rev. Neurosci.* 5, 641–655. doi: 10.1038/nrn1474

Tomioka, I., Ishibashi, H., Minakawa, E. N., Motohashi, H. H., Takayama, O., Saito, Y., et al. (2017). Transgenic Monkey Model of the Polyglutamine Diseases Recapitulating Progressive Neurological Symptoms. *eNeuro* 4, ENEURO.250–ENEURO.216.

Umemori, J., Nishi, A., Lionikas, A., Sakaguchi, T., Kuriki, S., Blizard, D. A., et al. (2009). QTL analyses of temporal and intensity components of home-cage activity in KJR and C57BL/6J strains. *BMC Genet.* 10:40. doi: 10.1186/1471-2156-10-40

Urbach, Y. K., Raber, K. A., Canneva, F., Plank, A. C., Andreasson, T., Ponten, H., et al. (2014). Automated phenotyping and advanced data mining exemplified in rats transgenic for Huntington's disease. *J. Neurosci. Methods* 234, 38–53. doi: 10.1016/j.jneumeth.2014.06.017

Verhave, P. S., Jongsma, M. J., Van Den Berg, R. M., Vis, J. C., Vanwersch, R. A., Smit, A. B., et al. (2011). REM sleep behavior disorder in the marmoset MPTP model of early Parkinson disease. *Sleep* 34, 1119–1125. doi: 10.5665/sleep.1174

Verhave, P. S., Vanwersch, R. A., Van Helden, H. P., Smit, A. B., and Philippens, I. H. (2009). Two new test methods to quantify motor deficits in a marmoset model for Parkinson's disease. *Behav. Brain Res.* 200, 214–219. doi: 10.1016/j.bbr.2009.01.022

Wahlsten, D. (2001). Standardizing tests of mouse behavior: reasons, recommendations, and reality. *Physiol. Behav.* 73, 695–704. doi: 10.1016/s0031-9384(01)00527-3

Walker, J., Maclean, J., and Hatsopoulos, N. G. (2017). The marmoset as a model system for studying voluntary motor control. *Dev. Neurobiol.* 77, 273–285. doi: 10.1002/dneu.22461

Wang, Y., Fang, Q., and Gong, N. (2014). Motor assessment of developing common marmosets. *Neurosci. Bull.* 30, 387–393. doi: 10.1007/s12264-013-1395-y

Yabumoto, T., Yoshida, F., Miyauchi, H., Baba, K., Tsuda, H., Ikenaka, K., et al. (2019). MarmoDetector: A novel 3D automated system for the quantitative assessment of marmoset behavior. *J. Neurosci. Methods* 322, 23–33. doi: 10.1016/j.jneumeth.2019.03.016

Yhnell, E., Dunnett, S. B., and Brooks, S. P. (2016). A Longitudinal Motor Characterisation of the HdhQ111 Mouse Model of Huntington's Disease. *J. Huntingtons Dis.* 5, 149–161. doi: 10.3233/jhd-160191

Conflict of Interest: The authors declare that the research was conducted in the absence of any commercial or financial relationships that could be construed as a potential conflict of interest.

Copyright © 2021 Koizumi, Nogami, Owari, Kawanobe, Nakatani and Seki. This is an open-access article distributed under the terms of the Creative Commons Attribution License (CC BY). The use, distribution or reproduction in other forums is permitted, provided the original author(s) and the copyright owner(s) are credited and that the original publication in this journal is cited, in accordance with accepted academic practice. No use, distribution or reproduction is permitted which does not comply with these terms.

frontiers in Human Neuroscience

ORIGINAL RESEARCH
published: 11 June 2021
doi: 10.3389/fnhum.2021.677578

Enhanced Visual Feedback Using Immersive VR Affects Decision Making Regarding Hand Use With a Simulated Impaired Limb

Naoko Sakabe[1†], *Samirah Altukhaim*[2,3†], *Yoshikatsu Hayashi*[2], *Takeshi Sakurada*[4], *Shiro Yano*[1] *and Toshiyuki Kondo*[1*]

[1] *Department of Computer and Information Sciences, Graduate School of Engineering, Tokyo University of Agriculture and Technology, Tokyo, Japan,* [2] *Biomedical Science and Biomedical Engineering, School of Biological Sciences, University of Reading, Reading, United Kingdom,* [3] *Physiotherapy Group in Stroke Unit, Alamiri Hospital, Kuwait City, Kuwait,* [4] *College of Science and Engineering, Ritsumeikan University, Shiga, Japan*

The long-term effects of impairment have a negative impact on the quality of life of stroke patients in terms of not using the affected limb even after some recovery (i.e., learned non-use). Immersive virtual reality (IVR) has been introduced as a new approach for the treatment of stroke rehabilitation. We propose an IVR-based therapeutic approach to incorporate positive reinforcement components in motor coordination as opposed to constraint-induced movement therapy (CIMT). This study aimed to investigate the effect of IVR-reinforced physical therapy that incorporates positive reinforcement components in motor coordination. To simulate affected upper limb function loss in patients, a wrist weight was attached to the dominant hand of participant. Participants were asked to choose their right or left hand to reach toward a randomly allocated target. The movement of the virtual image of the upper limb was reinforced by visual feedback to participants, that is, the participants perceived their motor coordination as if their upper limb was moving to a greater degree than what was occurring in everyday life. We found that the use of the simulated affected limb was increased after the visual feedback enhancement intervention, and importantly, the effect was maintained even after gradual withdrawal of the visual amplification. The results suggest that positive reinforcement within the IVR could induce an effect on decision making in hand usage.

Keywords: immersive virtual reality, learned non-use, constraint-induced movement therapy, reinforcement-induced movement therapy, visual amplification

OPEN ACCESS

Edited by:
Jun Izawa,
University of Tsukuba, Japan

Reviewed by:
Wen Wen,
The University of Tokyo, Japan
Aviv Elor,
University of California, Santa Cruz, United States

***Correspondence:**
Toshiyuki Kondo
t_kondo@cc.tuat.ac.jp

[†]These authors have contributed equally to this work

Specialty section:
This article was submitted to Motor Neuroscience, a section of the journal Frontiers in Human Neuroscience

Received: *07 March 2021*
Accepted: *18 May 2021*
Published: *11 June 2021*

Citation:
Sakabe N, Altukhaim S, Hayashi Y, Sakurada T, Yano S and Kondo T (2021) Enhanced Visual Feedback Using Immersive VR Affects Decision Making Regarding Hand Use With a Simulated Impaired Limb. Front. Hum. Neurosci. 15:677578. doi: 10.3389/fnhum.2021.677578

1. INTRODUCTION

Stroke is one of the leading causes of long-term disability, and it has a higher prevalence in older people. It has been reported that the number of stroke survivors is increasing in the aging society (Mukherjee and Patil, 2011). Stroke patients may suffer from upper limb impairment and experience many of challenges while undergoing treatment for this impairment (Adamovich et al., 2004), and often such treatment requires several different approaches (Dobkin, 2008). There is great variability in terms of functional outcome; some patients are unable to regain full functionality, and they must manage with varying levels of lifelong upper limb paresis (Faria-Fortini et al., 2011).

Therefore, there is a need to develop rehabilitation methods that can offer more effective treatment and a better chance of higher-level functional recovery.

One of the most appreciated rehabilitation processes is motor coordination (MC), which plays a vital role in the musculoskeletal system, and leads to movement of body parts (Levin et al., 2008). Motor coordination is facilitated by the forces of kinetic features and kinematic actions that work together to achieve voluntary movements (Arbib, 1981). For most of stroke patients, rehabilitation primarily involves physical therapy (PT). The foremost role of PT is to achieve coordination of the affected parts of the body. This can be investigated in depth by discussing the role of neuroplasticity in the rehabilitation of neurons of stroke patients (Mang et al., 2013). Physiotherapy sessions mainly involve task-oriented exercises that can restore healthy activities such as pouring water into a glass and drinking or reacquiring skills (Rensink et al., 2009; Ordahan et al., 2015).

Constraint-Induced Movement Therapy (CIMT) is one of the most effective treatment procedures for stroke patients. This method involves physical constraining of unaffected limb and compelling the patient to use the affected limb. Based on previous studies, a noticeable improvement is observed in experimental patients as compared to other therapies (Kwakkel et al., 2015). Although this method is successful, researchers have argued that CIMT processes are often intensive and involve a grueling therapeutic schedule that may affect a patient's adherence to a therapy regimen, which affects the efficacy of the treatment (Lannin et al., 2003; Kwakkel et al., 2015). Virtual reality (VR) has shown promising results in terms of recovery of stroke patients and clinical feasibility (Burdea, 2003; Perez-Marcos et al., 2017). The use of VR technology allows for the use of more dynamic environmental setups in which targets can be reliably and rapidly modified (Viau et al., 2004).

Immersive virtual reality (IVR) continues to show great promise when applied to CIMT as part of post-stroke rehabilitation. Numerous studies have shown that IVR rehabilitation could greatly improve affordability and accessibility of post-stroke motor treatment in an immersive and interesting way, while also providing incredibly valuable, individualized bio-feedback to therapists to improve the rehabilitation process.

The IVR environment significantly improves patient motivation to perform repetitive, motor-intensive tasks that are a crucial component of the rehabilitation process (Elor et al., 2018a,b). It was shown how a simple game with adaptive difficulty could lead to improved mobility, motor performance, and psychological health when compared to standard rehabilitation techniques. Elor et al. used IVR incorporating modified constraint-induced movement therapy (mCIMT), and the results showed that the proposing system was beneficial for stroke patients by encouraging them to use the affected hand without constraining the unaffected side (Both hands are free to move). Another study aims to determine the feasibility and measure safety and outcomes of combining IVR and mCIMT (Borstad et al., 2018). They used the "Recovery Rapids" kayaking game in the Virtual Environment to provide a motivating environment. From the outcome measures, the combination between IVR and mCIMT could be greatly improved for patients with chronic hemiparesis. The patients were much more likely to engage with rehabilitation when done in this sort of engaging and interactive way (Borstad et al., 2018). In regards to implementation, another study showed that a head-mounted display (HMD) was a much more effective tool for physiological rehabilitation and encouraging task-based exercise than a dedicated interactive room environment which projected the games onto the four walls of the room (Elor and Kurniawan, 2020; Elor et al., 2020). This is because the HMD-based system was perceived to have a higher sense of immersion, ease of use, and enjoyment of gameplay than the room-scale alternative.

As a direct relevance to our study, Ballester et al. (2016) offered a new treatment alternative that incorporates CIMT and another therapeutic approach known as reinforcement induced movement therapy (RIMT). Using the goal-oriented reaching task, they amplified the speed of the impaired hand within the VR environment and showed the efficacy of the RIMT. Even though the improvement of the motor coordination of stroke patients was demonstrated in the Fugle-Mayer scores after the RIMT intervention, the subjective experience of being fully immersed in the VR environment was not realized in their study. Although they introduced positive reinforcement in their pioneering work using computer simulated limb in the display, the concept of the RIMT should be extended to use the Immersive VR. In IVR, visual feedback is set up to show only the simulated upper limb. It is important that participants observe only the simulated hand during the task. If they observe their real hand moving in front of them while watching the simulated hand on the display, the mismatch in visual feedback of the motor coordination would create a sense of loss of ownership of the simulated upper limb, or, in some cases, the subjective awareness of loss of controlling one's own body.

The learning process entails the creation of new connections. This process is made possible by neuroplasticity (Mang et al., 2013). Task-oriented training increases activation in parts of the brain, such as the inferior parietal cortex, the premotor cortex, and the sensorimotor cortex; therefore increasing neuroplasticity in the motor and sensory neural pathways (Nelles et al., 2001; Jang et al., 2003; Rensink et al., 2009). In addition, body representation in a coordinated system of the body based on the visual information. This plays a critical role in the subjective experience of motor coordination in goal-oriented tasks. Thus, in this study, we explored the RIMT paradigm by using the IVR to produce the subjective experiences. This study presents a new therapeutic approach for IVR that incorporates RIMT by simulating impaired conditions in healthy participants.

2. MATERIALS AND METHODS

2.1. Participants

The experiments were conducted at two sites: Tokyo University of Agriculture and Technology (TUAT), Japan and the University of Reading (UoR), UK. Seventeen healthy individuals (nine female and eight male) participated in the experiment at the TUAT, while 29 healthy individuals (17 female and 12 male) participated in the experiments at the UoR. In total,

46 healthy participants were recruited. All were right-handed, and their mean age was 27.5 ± 7.9 (mean ± sd). Participants provided written informed consent after being informed about the aims and procedure of the experiment. The experimental protocols were approved by the ethics committees of both TUAT (No.191204-3145) and UoR (No.SBS18-19 17), and the devices, programs, and protocol of participant experiments were identical at both sites.

2.2. Experimental Setup

We developed an IVR system (**Figure 1A**) integrated with a HMD (Oculus Rift DK2) and a markerless motion capture system (Leap Motion). The motion capture device was fixed on the front of the HMD to measure the real hands movements in the frontal space. Participants were asked to wear the HMD, and sit comfortably on a high-back chair and rest their upper limbs on a table placed in front of them. Through the IVR system, the participants could experience a fully embodied avatar, and the virtual hand was controlled to coincide with the captured real hand position in real-time using the Leap Motion Core Assets (version: 4.3.2; **Figure 1B**). The VR environment and virtual upper limbs were implemented using Unity (version: Unity2018.2.9) and Blender (version: 2.79b) software. The virtual upper limb posture (i.e., the shoulder and elbow angles) in the IVR environment was adjusted by an inverse kinematics program (Final IK, version: 1.8) in the Unity environment. Thus, participants were able to execute the reaching task in the IVR environment from the first-person perspective.

To realize visual enhancement intervention, we introduced a visual amplification function in the IVR system, in which the virtual hand was displayed at α times linearly apart, that is, the position vector of the virtual hand starting from a home position was extended α times with respect to the actual hand position vector. Even in the visual enhancement condition, the appearance of the virtual upper limb posture was adjusted by the inverse kinematics program.

2.3. Task

In the VR environment, the participants engaged in a hand-choice reaching task (**Figure 2A**). At the beginning of each trial, participants were instructed to set both virtual hands at a home position. A half-second after the initialization, a virtual target (red sphere) randomly appeared in one of seven candidate positions (0, ±15, ±30, and ±45° from midline). They were asked to reach for the target immediately by choosing their right or left hand. The target turned in blue when reached by the virtual hand and immediately disappeared. To prevent in-depth consideration for choice, the experimental system checked that the reaction time was between 150 and 500 ms after the appearance. If this condition is not fulfilled, the target will disappear and the trial is invalidated.

To investigate whether the enhanced visual feedback in the IVR system affects decision making in choice of hand use among impaired persons, we introduced a virtual impairment condition aimed at simulating stroke patients with degradation of upper limb function. We attached a heavy wrist weight (1.0 kg) to the distal portion of the dominant forearm of the healthy participants. To determine the mass of the wrist weight, we performed a pilot study. The weight of 0.5 kg did not affect the usage of the hand (i.e., hand choice), but the weight of 1.0 kg showed the effect of the weight to simulate the impaired upper limb.

2.4. Procedure

The experiment consisted of four phases: baseline, pre-test, Intervention, and post-test (**Figure 3**).

The baseline phase aimed to familiarize participants with the task procedure and measure their baseline performance, including two practice sessions and one test session. In the first practice session, we asked participants to perform the reaching task using their right hand. Each target appeared twice in a fixed order (left to right). Thereafter, they repeated the same procedure with their left hand. Through this practice session, participants could perform the reaching task toward all the target with each hand. In the second practice session, participants were instructed to reach their hand to a randomly appearing target by freely choosing the right or left hand. This was repeated 5 times for each target. After these practice sessions, participants completed a total of 70 trials (10 times per target) with randomly appearing targets as the test session. Results from the test session were used as the baseline performance for the free choice reaching paradigm without wrist weight and visual amplification.

The pre-test phase included one practice and one test session with wrist weight, but no visual amplification, and aimed to quantify the effect of the attached wrist weight in choosing their right or left hand. The practice session contained 35 trials, that is, 5 times for each target, and was introduced to endow the participants with the experience of the reaching task with the wrist weight. After the practice session, participants executed a test session following the same protocol as the test session of the baseline phase.

In the intervention phase, we repeated the same procedure as in the pre-test phase, but with the visual amplification ($\alpha = 1.4$).

After the intervention phase, one gradual withdrawal session was conducted with gradually reducing the visual amplification to $\alpha = 1.0$ at the end. Finally, the post-test phase was executed without visual amplification, following the same protocol as in the test session of the pre-test phase.

In each session, the participants repeated the reaching task at their own pace. It was <3 min for 70 trials. To minimize their fatigue, two minutes breaks were provided between phases. The entire procedure takes 35–40 min.

2.5. Analysis and Statistics

As shown in **Figure 2A**, targets appeared in a semi-circular array at seven predetermined angles separated by 15°. To analyze the effects of the wrist weight and the visual enhancement, we quantified participants' usage of their left and right hands in the test session of each phase. To this end, first, the probability of right hand usage was plotted as a function of the target angles, and then a psychometric function was fitted to these plots (**Figure 2B**). The angle at which the psychometric function corresponds to a 50% probability was defined as the border angle.

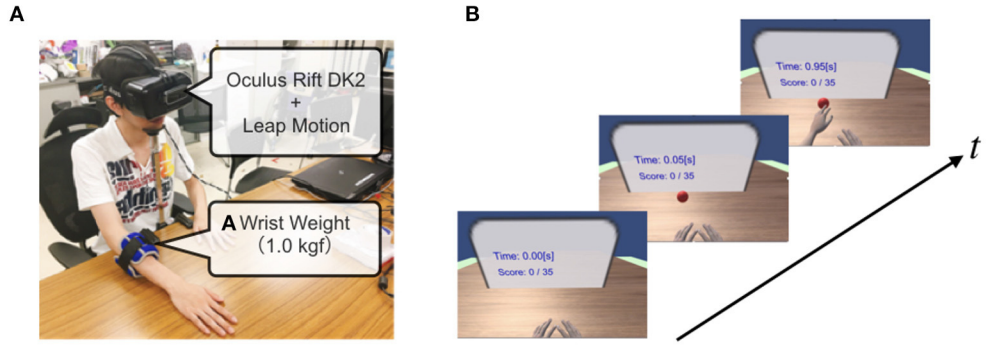

FIGURE 1 | Immersive Virtual Reality system integrated with motion capture. **(A)** A 1.0 kg wrist weight was attached to the distal portion of the dominant forearm of the healthy participant to simulate the affected upper limb of stroke patients. A head-mounted display (HMD) was attached to the head with a strap, and a motion capture system (Leap motion) was attached to the front part of the HMD. **(B)** The participant placed their hands at the home positions, and the target appeared randomly along with the semi-circle. The participant was asked to reach for the target immediately by choosing their virtually impaired or unaffected hand.

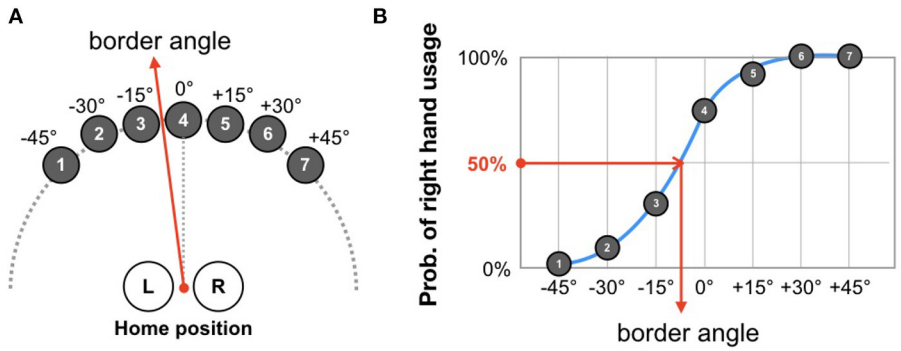

FIGURE 2 | Definition of border angle. **(A)** At each trial, participants were asked to reach toward a target that was randomly drawn from seven candidate positions. The task was repeated until 70 trials were completed (10 times for each target). **(B)** According to the probability distribution of right-hand usage, the border angle is determined as the angle-approximated psychometric function that results in a probability of 50%.

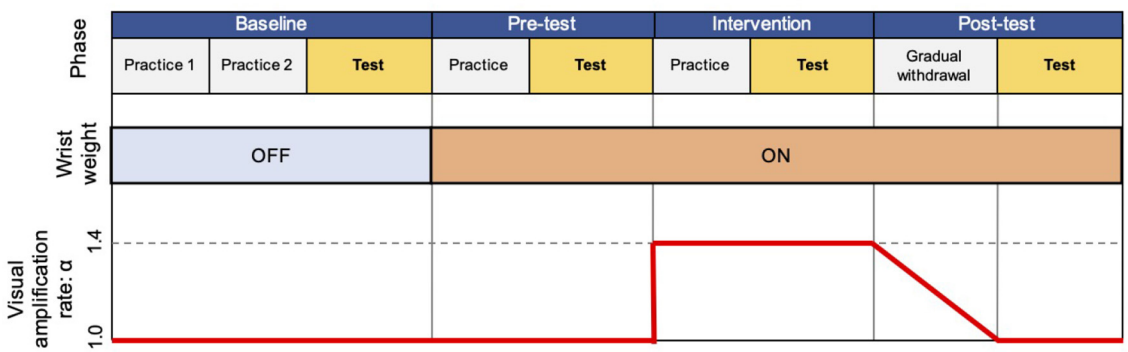

FIGURE 3 | Flow of experiment. The experiment consisted of four experimental phases (baseline, pre-test, intervention, and post-test), each of which includes practice or gradual withdrawal session, and a test session.

To test if the wrist weight leads to less usage of the dominant hand and visual enhancement causes recovery of the usage, the border angles during the four experimental phases were statistically evaluated using the Friedman test. For further analysis, we conducted paired comparisons of the border angle distributions in each phase. The Shapiro-Wilk test was used to check the normality of the distribution, and the Wilcoxon signed-rank test was applied to evaluate

statistical significance among phases. The significance level was set to $p = 0.05$.

3. RESULTS

Three out of 46 participants were excluded from further analysis for the reason that the border angle could not be calculated because they chose an inappropriate strategy, for example, they decided to use their right or left hand for all the targets in any phases.

To reveal the effects of wrist weight and visual amplification on the distributions of border angles among the four experimental phases, we performed the Friedman test for the remaining 43 participants. As a result, we confirmed statistical significance among the four phases ($F_r = 33.795$, $df = 3$, $p < 0.01$). Before the paired comparison analysis, we performed the Shapiro–Wilk test to check if the data met the normal distribution criteria. The resultant p-value of the normality test was $p = 0.006251$, $p = 0.001783$, $p = 0.06966$, and $p = 0.06293$ for the baseline, pre-test, intervention, and post-test phases, respectively. Since the data for the border angles in some phases were not normally distributed, we decided to use the Wilcoxon signed-rank test for the paired sample comparison among the phases.

As shown in **Figure 4**, the statistical comparison between the baseline and pre-test phases was significant ($p < 0.01$). This suggests that attaching a wrist weight reduced the frequency of using their dominant (i.e., right) hand to reach for the target. Thus, it was a successful manipulation to simulate impaired function of a stroke patient, whereas the effect was not confirmed in six participants. Moreover, the statistical comparison between the pre-test and intervention phases was also significant ($p = 0.01347$). This implies that visual amplification affected the usage of their dominant hand when performing the task. Importantly, the result of the comparison between the pre-test and post-test phases was significant ($p = 0.02432$). This indicates that the visual amplification in the intervention phase induced a positive effect on the use of the simulated impaired hand even after the visual amplification was removed (i.e., post-test).

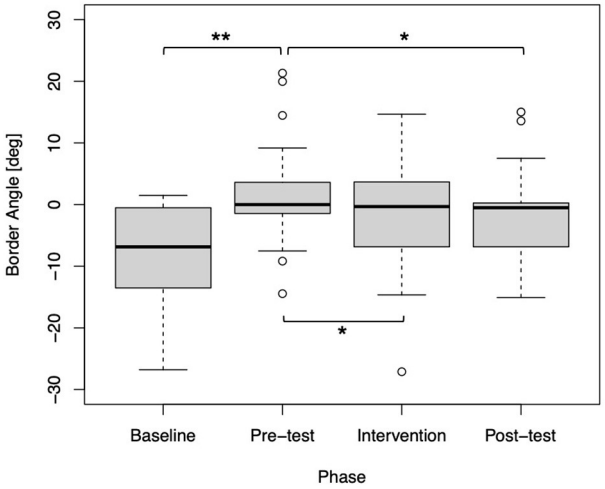

FIGURE 4 | Box plot of the border angles for each phase ($N = 43$). Statistical significance was confirmed between the baseline and pre-test phases (**$p < 0.01$), the pre-test and intervention phases (*$p < 0.05$), and the pre-test and post-test phases ($p < 0.05$).

4. DISCUSSION

This study aimed to test the validity of a new therapeutic approach that uses IVR technology. Ballester et al. (2016) offered a new treatment alternative that incorporates CIMT and another therapeutic approach known as reinforcement induced movement therapy (RIMT). Our IVR approach incorporates this positive reinforcement in physical rehabilitation as opposed to other conventional CIMT. In this study, we tested whether the visual enhancement intervention realized by the IVR system causes positive reinforcement in a hand-choice reaching task. To simulate the impaired upper limb function of stroke patients in healthy participants, we introduced a virtual impairment setting by attaching a heavy weight to the wrist of the dominant forearm.

Our study had three key findings; First, the border angle where the hand choice probability equals 50% significantly shifted toward the dominant-side after the virtual impairment (i.e., comparison between baseline and pre-test), indicating that the participants had to use their non-dominant side after attaching a wrist weight. Second, the border angle significantly recovered after visual enhancement intervention using the IVR system (i.e., comparison between pre-test and intervention). Third, and most importantly, the border angle was maintained even after the gradual withdrawal of visual amplification (i.e., comparison between pre-test and pos-test), suggesting that the visual enhancement induced a positive and strong effect on the deciding on which hand to use even when the visual amplification was set to 1.0, i.e., no amplification The third point was never reported before, and is promising for the clinical study with stroke patients, as this result indicates that the decision-making process would be biased to use the impaired hand in their daily life after the VR enhanced physical therapy.

Previous studies assert that people suffering from stroke tend to have pre-defined preferences when executing tasks that require manipulation of hands; in most cases, the affected hand is not used (Stoloff et al., 2011; Ballester et al., 2016). The perpetual non-use of a particular hand can harm a patient's quality of life. Indeed, Ballester et al. (2016) claims that stroke patients are sensitive to self-perceived failure; specifically, that the hesitation in using the affected limb is due to a fear of failure and sensitivity about their perceived limitation. In the IVR environment, user can "look around" the artificial world and interact with virtual features or objects. Through iterative visual-motor loops in the brain, the person can have a feeling of controlling the virtual image of their body in such a way that the virtual world would be perceived as a real one. As a result, this technology might support the feeling of embodiment toward the virtual avatar that

can be observed from a first-person perspective (Abtahi et al., 2019).

Gonzalez-Franco et al. (2020) explore the impact of motor behavior based on the avatar embodiment. Motor behavior of subjects might be affected when there is discrepancy of the avatar movement that is temporally or spatially deviated from the executed action. In their study, they implement an effect in which the avatar hand drifts either gradually or instantly. Their results show that when there is a mismatch between the real body movement and the virtual avatar, participants try to compensate such a mismatch. This is an example of the "power of the follower effect" which is an active strategy to reduce the conflict of the visuo-proprioceptive feedback coming from spatial mismatch, so users will change their behaviors as much as they can (Gonzalez-Franco et al., 2020).

In this study, it is intriguing that most of participants were not aware of the visual enhancement during the intervention. Within the IVR, the coordinated systems between body representation and vision provides a matching and, based on the findings, the moderate visual enhancement was subconsciously embedded into the cognitive functions of participants' lower-level motor coordination. This enhanced motor performance likely affected the neural pathway of decision-making in the usage of the affected and unaffected upper limbs.

Over the years, many studies have been conducted to investigate the impact of modified visual feedback on body consciousness and behavior (Slater et al., 2008; Burin et al., 2019; Keenaghan et al., 2020; Aoyagi et al., 2021), indicating that sense of agency is affected by the visual feedback. This is because the mismatch between the intended motion and the actual visual feedback directly affects the level of the sense of agency. In our study, we think that the reaching motion within the IVR can contribute to mask the mismatch between the actual upper limb motion and the visually amplified feedback, because the participants do not observe their own upper limb motion in reality. Thus, the participants could feel the higher sense of agency during the visual feedback intervention, resulting in the biased-decision making process to use the impaired upper limb after the removal of the visual amplification.

There can be different reasons why positive visual feedback facilitates the usage of the affected upper limb. Karsh and Eitam (2015) found that the positive judgment of agency over actions encourages the individual to adapt into the continuous changing environment and achieve desired goals, and they discussed that a positive judgement of agency activates the brain's reward system that in turn biases action selection toward actions that were associated with the largest amount of agency. Thus, in the future study, the sense of the agency in the IVR before and after the intervention will be a very interesting point to explore.

Our findings indicated that once the visual enhancement activates a neuronal pathway of using the affected hand in terms of the decision-making process, this neural pathway continues to be active even after the visual enhancement is taken away. Further, this findings was observed even though the intervention (using the enhanced visual feedback) was made available for only a certain period of time. Therefore, our IVR visual enhancement training system could potentially offer a new type of intervention for stroke rehabilitation, incorporating the immersive subjective experience of motor coordination.

Like all other studies, this study also had its limitations. For instance, applying the wrist weight on the dominant hand of some participants encouraged them to manipulate it more as an exercise. Excessive manipulation of the simulated hand with weight does not simulate the features of the paretic limb. In future studies, the hand grip test might be used to determine a suitable weight for individual participants. Secondly, statistics indicate that stroke is more prevalent in people of advanced ages, besides the sense of agency tends to reduce with age (Moore, 2016). A study found that older adults (mean age 78.47 years) were more sensitive to changes in the experimental variables, lag between cursor and mouse movements of 250 or 500 ms turbulence less compared to college students. The possible reason could be college students are more experienced in handling mouse control on computer. Future studies should include a higher percentage of older participants to ensure that the sense of agency suggested by this study is perpetuated to other age groups, specifically the target patient age group (Metcalfe et al., 2010). In summary, the future study will help us understand how the sense of agency is maintained and how motor adaptation can be created when training within the IVR environment.

DATA AVAILABILITY STATEMENT

The raw data supporting the conclusions of this article will be made available by the authors, without undue reservation.

ETHICS STATEMENT

The experimental protocols in this study were approved by the ethics committees of Tokyo University of Agriculture and Technology (No.191204-3145) and the University of Reading (No.SBS18-19 17). The participants provided written informed consent to participate in the study. Written informed consent was obtained from the individual in **Figure 1** for the publication.

AUTHOR CONTRIBUTIONS

TK conceived and supervised the study. NS designed the experiment, developed the experimental system, signal processing, and statistical analysis. NS and SA performed the participant experiments. NS, SA, YH, and TK contributed to the discussion of the results. SA and TK wrote the draft of the manuscript. YH, TS, and SY provided critical review of the experimental procedure and analysis. All authors have read and approved the final manuscript.

FUNDING

This research was supported by Japan Society for the Promotion of Science Grants-in-Aid for Scientific Research (JSPS

KAKENHI) (Grant numbers JP19H05727, JP18K19732, and JP17KK0064), and a research grant from the Institute of Global Innovation Research at TUAT. This research project is also funded by the Kuwait government by means of a studentship.

ACKNOWLEDGMENTS

The authors would like to thank all individuals who participated in this study.

REFERENCES

Abtahi, P., GonzalezFranco, M., Ofek, E., and Steed, A. (2019). "I'm a Giant: walking in large virtual environments at high speed gains," in *Proceedings of the 2019 CHI Conference on Human Factors in Computing Systems* (Glasgow), 1–13. doi: 10.1145/3290605.3300752

Adamovich, S. V., Merians, A. S., Boian, R., Tremaine, M., Burdea, G. S., Recce, M., et al. (2004). A virtual reality based exercise system for hand rehabilitation post-stroke: transfer to function. *Conf. Proc. IEEE Eng. Med. Biol. Soc.* 7, 4936–4939. doi: 10.1109/IEMBS.2004.1404364

Aoyagi, K., Wen, W., An, Q., Hamasaki, S., Yamakawa, H., Tamura, Y., et al. (2021). Modified sensory feedback enhances the sense of agency during continuous body movements in virtual reality. *Sci. Rep.* 11:2553. doi: 10.1038/s41598-021-82154-y

Arbib, M. (1981). "Perceptual structures and distributed motor control," in *Handbook of Physiology, Section I: The Nervous System. 2: Motor Control*, ed V. B. Brooks (Baltimore, MD: Williams and Wilkins).

Ballester, B. R., Maier, M., San Segundo Mozo, R. M., Castaneda, V., Duff, A., and Verschure, P. F. (2016). Counteracting learned non-use in chronic stroke patients with reinforcement-induced movement therapy. *J. Neuroeng. Rehabil.* 13:74. doi: 10.1186/s12984-016-0178-x

Borstad, A. L., Crawfis, R., Phillips, K., Pax Lowes, L., Maung, D., McPherson, R., et al. (2018). In-home delivery of constraint-induced movement therapy via virtual reality gaming. *J. Patient Center. Res. Rev.* 5, 6–17. doi: 10.17294/2330-0698.1550

Burdea, G. C. (2003). Virtual rehabilitation-benefits and challenges. *Methods Inf. Med.* 42, 519–523. doi: 10.1055/s-0038-1634378

Burin, D., Kilteni, K., Rabuffetti, M., Slater, M., and Pia, L. (2019). Body ownership increases the interference between observed and executed movements. *PLoS ONE* 14:e0209899. doi: 10.1371/journal.pone.0209899

Dobkin, B. H. (2008). Training and exercise to drive poststroke recovery. *Nat. Clin. Pract. Neurol.* 4, 76–85. doi: 10.1038/ncpneuro0709

Elor, A., and Kurniawan, S. (2020). The ultimate display for physical rehabilitation: a bridging review on immersive virtual reality. *Front. Virt. Real.* 1:585993. doi: 10.3389/frvir.2020.585993

Elor, A., Kurniawan, S., and Teodorescu, M. (2018a). "Towards an immersive virtual reality game for smarter post-stroke rehabilitation," in *IEEE International Conference on Smart Computing (SMARTCOMP)* (Taormina), 219–225. doi: 10.1109/SMARTCOMP.2018.00094

Elor, A., Powell, M., Mahmoodi, E., Hawthorne, N., Teodorescu, M., and Kurniawan, S. (2020). On shooting stars: comparing CAVE and HMD immersive virtual reality exergaming for adults with mixed ability. *ACM Trans. Comput. Healthc.* 1, 1–22. doi: 10.1145/3396249

Elor, A., Teodorescu, M., and Kurniawan, S. (2018b). Project star catcher: a novel immersive virtual reality experience for upper limb rehabilitation. *ACM Trans. Access. Comput.* 11, 1–25. doi: 10.1145/3265755

Faria-Fortini, I., Michaelsen, S. M., Cassiano, J. G., and Teixeira-Salmela, L. F. (2011). Upper extremity function in stroke subjects: relationships between the international classification of functioning, disability, and health domains. *J. Hand Ther.* 24, 257–265. doi: 10.1016/j.jht.2011.01.002

Gonzalez-Franco, M., Cohn, B., Ofek, E., Burin, D., and Maselli, A. (2020). "The self-avatar follower effect in virtual reality," in *IEEE Conference on Virtual Reality and 3D User Interfaces (VR)* (Atlanta, GA), 18–25. doi: 10.1109/VR46266.2020.00019

Jang, S. H., Kim, Y.-H., Cho, S.-H., Lee, J.-H., Park, J.-W., and Kwon, Y.-H. (2003). Cortical reorganization induced by task-oriented training in chronic hemiplegic stroke patients. *Neuroreport* 14, 137–141. doi: 10.1097/00001756-200301200-00025

Karsh, N., and Eitam, B. (2015). I control therefore I do: judgments of agency influence action selection. *Cognition* 138, 122–131. doi: 10.1016/j.cognition.2015.02.002

Keenaghan, S., Bowles, L., Crawfurd, G., Thurlbeck, S., Kentridge, R. W., and Cowie, D. (2020). My body until proven otherwise: Exploring the time course of the full body illusion. *Conscious. Cogn. Neurosci.* 78:102882. doi: 10.1016/j.concog.2020.102882

Kwakkel, G., Veerbeek, J. M., van Wegen, E. E., and Wolf, S. L. (2015). Constraint-induced movement therapy after stroke. *Lancet Neurol.* 14, 224–234. doi: 10.1016/S1474-4422(14)70160-7

Lannin, N. A., Horsley, S. A., Herbert, R., McCluskey, A., and Cusick, A. (2003). Splinting the hand in the functional position after brain impairment: a randomized, controlled trial. *Arch. Phys. Med. Rehabil.* 84, 297–302. doi: 10.1053/apmr.2003.50031

Levin, M. F., Kleim, J. A., and Wolf, S. L. (2008). What do motor "recovery" and "compensation" mean in patients following stroke? *Neurorehabil. Neural Rep.* 23, 313–319. doi: 10.1177/1545968308328727

Mang, C. S., Campbell, K. L., Ross, C. J., and Boyd, L. A. (2013). Promoting neuroplasticity for motor rehabilitation after stroke: considering the effects of aerobic exercise and genetic variation on brain-derived neurotrophic factor. *Phys. Ther.* 93, 1707–1716. doi: 10.2522/ptj.20130053

Metcalfe, J., Eich, T. S., and Castel, A. D. (2010). Metacognition of agency across the lifespan. *Cognition* 116, 267–282. doi: 10.1016/j.cognition.2010.05.009

Moore, J. W. (2016). What is the sense of agency and why does it matter? *Front. Psychol.* 7:1272. doi: 10.3389/fpsyg.2016.01272

Mukherjee, D., and Patil, C. G. (2011). Epidemiology and the global burden of stroke. *World Neurosurg.* 76(6 Suppl.), 85–90. doi: 10.1016/j.wneu.2011.07.023

Nelles, G., Jentzen, W., Jueptner, M., Müller, S., and Diener, H. (2001). Arm training induced brain plasticity in stroke studied with serial positron emission tomography. *Neuroimage* 13, 1146–1154. doi: 10.1006/nimg.2001.0757

Ordahan, B., Karahan, A., Basaran, A., Turkoglu, G., Kucuksarac, S., Cubukcu, M., et al. (2015). Impact of exercises administered to stroke patients with balance trainer on rehabilitation results: a randomized controlled study. *Hippokratia* 19:125.

Perez-Marcos, D., Chevalley, O., Schmidlin, T., Garipelli, G., Serino, A., Vuadens, P., et al. (2017). Increasing upper limb training intensity in chronic stroke using embodied virtual reality: a pilot study. *J. Neuroeng. Rehabil.* 14:119. doi: 10.1186/s12984-017-0328-9

Rensink, M., Schuurmans, M., Lindeman, E., and Hafsteinsdóttir, T. (2009). Task-oriented training in rehabilitation after stroke: systematic review. *J. Adv. Nurs.* 65, 737–754. doi: 10.1111/j.1365-2648.2008.04925.x

Slater, M., Perez-Marcos, D., Ehrsson, H. H., and Sanchez-Vives, M. V. (2008). Towards a digital body: the virtual arm illusion. *Front. Hum. Neurosci.* 2:6. doi: 10.3389/neuro.09.006.2008

Stoloff, R., Taylor, J., Xu, J., Ridderikhoff, A., and Ivry, R. (2011). Effect of reinforcement history on hand choice in an unconstrained reaching task. *Front. Neurosci.* 5:41. doi: 10.3389/fnins.2011.00041

Viau, A., Feldman, A. G., McFadyen, B. J., and Levin, M. F. (2004). Reaching in reality and virtual reality: a comparison of

movement kinematics in healthy subjects and in adults with hemiparesis. *J. Neuroeng. Rehabil.* 1:11. doi: 10.1186/1743-000 3-1-11

Conflict of Interest: The authors declare that the research was conducted in the absence of any commercial or financial relationships that could be construed as a potential conflict of interest.

Copyright © 2021 Sakabe, Altukhaim, Hayashi, Sakurada, Yano and Kondo. This is an open-access article distributed under the terms of the Creative Commons Attribution License (CC BY). The use, distribution or reproduction in other forums is permitted, provided the original author(s) and the copyright owner(s) are credited and that the original publication in this journal is cited, in accordance with accepted academic practice. No use, distribution or reproduction is permitted which does not comply with these terms.

frontiers in Systems Neuroscience

BRIEF RESEARCH REPORT
published: 17 August 2021
doi: 10.3389/fnsys.2021.698758

Contralateral and Ipsilateral Interactions in the Somatosensory Pathway in Healthy Humans

Daisuke Ishii[1,2], Kiyoshige Ishibashi[3], Hiroshi Yuine[4], Kotaro Takeda[5], Satoshi Yamamoto[6], Yuki Kaku[1], Arito Yozu[1] and Yutaka Kohno[1]*

[1]*Center for Medical Sciences, Ibaraki Prefectural University of Health Sciences, Ami, Japan,* [2]*Department of Cognitive Behavioral Physiology, Chiba University Graduate School of Medicine, Chiba, Japan,* [3]*Department of Physical Therapy, Ibaraki Prefectural University of Health Sciences Hospital, Ami, Japan,* [4]*Department of Occupational Therapy, School of Health Sciences, Ibaraki Prefectural University of Health Sciences, Ami, Japan,* [5]*Faculty of Rehabilitation, School of Healthcare, Fujita Health University, Toyoake, Japan,* [6]*Department of Physical Therapy, School of Health Sciences, Ibaraki Prefectural University of Health Sciences, Ami, Japan*

Hyper-adaptability, the ability to adapt to changes in the internal environment caused by neurological disorders, is necessary to recover from various disabilities, such as motor paralysis and sensory impairment. In the recovery from motor paralysis, the pre-existing neural pathway of the ipsilateral descending pathway, which is normally suppressed and preserved in the course of development, is activated to contribute to the motor control of the paretic limb. Conversely, in sensory pathways, it remains unclear whether there are compensatory pathways which are beneficial for the recovery of sensory impairment due to damaged unilateral somatosensory pathways, such as thalamic hemorrhage. Here, we investigated the interaction between the left and right somatosensory pathways in healthy humans using paired median nerve somatosensory evoked potentials (SEPs). Paired median nerve SEPs were recorded at CP3 and CP4 with a reference of Fz in the International 10–20 System. The paired median nerve stimulation with different interstimulus intervals (ISIs; 1, 2, 3, 5, 10, 20, 40, 60, and 100 ms) was performed to test the influence of the first stimulus (to the right median nerve) on the P14, P14/N20, and N20/P25 components induced by the second stimulus (left side). Results showed that the first stimulation had no effect on SEP amplitudes (P14, P14/N20, and N20/P25) evoked by the second stimulation in all ISI conditions, suggesting that there might not be a neural connectivity formed by a small number of synapses in the left–right interaction of the somatosensory pathway. Additionally, the somatosensory pathway may be less diverse in healthy participants.

Keywords: evoked potentials, somatosensory, corpus callosum, median nerve, humans

OPEN ACCESS

Edited by:
Jun Izawa,
University of Tsukuba, Japan

Reviewed by:
Hidenori Aizawa,
Hiroshima University, Japan
Satoshi Kodama,
The University of Tokyo, Japan

****Correspondence:***
Daisuke Ishii
ishiid@ipu.ac.jp

Received: *22 April 2021*
Accepted: *26 July 2021*
Published: *17 August 2021*

Citation:
Ishii D, Ishibashi K, Yuine H, Takeda K, Yamamoto S, Kaku Y, Yozu A and Kohno Y (2021) Contralateral and Ipsilateral Interactions in the Somatosensory Pathway in Healthy Humans. Front. Syst. Neurosci. 15:698758. doi: 10.3389/fnsys.2021.698758

INTRODUCTION

Hyper-adaptability can be defined as the ability to adapt to changes in the internal environment caused by neurological disorders (e.g., stroke and spinal cord injury); it is essential for recovery from various disabilities. Corticospinal neurons in the forelimb region of the primary motor cortex project to contralateral and ipsilateral spinal interneurons (Yoshino-Saito et al., 2010). This ipsilateral descending pathway plays an important role in the recovery from motor paralysis after stroke (Netz et al., 1997; Levy et al., 2001). Moreover, previous studies on monkeys with spinal

cord-lesions showed that the sprouting of midline-crossing axons of the corticospinal tract occurs in the spinal cord rostral to the lesion, and the sprouting was associated with improvement in hand function and locomotion (Courtine et al., 2005; Rosenzweig et al., 2010). Additionally, functional motor representation maps around the damage and remote cortical regions change with rehabilitative motor training after focal damage in the forelimb movement area of the motor cortex (Nudo et al., 1996; Frost et al., 2003; Ramanathan et al., 2006; Barbay et al., 2013). These studies suggest that a pathway normally suppressed and preserved in the course of development may participate in the control of the paretic limb to adapt to changes in the internal environment (Murata et al., 2015; Isa, 2017, 2019; Isa et al., 2019; Yamamoto et al., 2019; Kato et al., 2020).

A functional magnetic resonance imaging (fMRI) study of sensory pathways revealed that not only the contralateral primary somatosensory cortex (SI) but also the ipsilateral SI was activated following the median nerve stimulation (Nihashi et al., 2005). In macaque monkeys, bilateral receptive fields have been found in the somatosensory area 2, which is considered to be the homolog of Brodmann's area 2 in human SI (Iwamura et al., 2001, 2002). Neural responses in the bilateral receptive fields were not found after making postcentral gyrus lesions in the contralateral hemisphere, suggesting that the neurons in the bilateral receptive fields receive the sensory information from the contralateral brain through interhemispheric transfer (Iwamura et al., 1994). The presence of a left–right interaction at various levels is important for recovery from hypoesthesia because the left–right interaction through the corpus callosum does not contribute to the recovery of hypoesthesia in cases where somatosensory pathways are damaged at the subcortical level, such as the thalamus. Several studies investigated the interactions between contralateral and ipsilateral activations using a paired median nerve somatosensory evoked potential (p-SEP) protocol (Ragert et al., 2011; Brodie et al., 2014). In this protocol, peripheral stimulation of the unilateral median nerve as conditioning stimulus (CS) always preceded the stimulation of the other median nerve as the test stimulus (TS) with some interstimulus intervals (ISIs). In the presence of a left–right interaction, the SEP evoked by the TS is attenuated by the interference of the CS. The levels of the left–right interaction in the somatosensory pathway were estimated by the length of the ISI (Ragert et al., 2011; Brodie et al., 2014). It is unclear whether the amplitude of SEPs evoked by the second median nerve stimulation is attenuated or eliminated by the first median nerve stimulation in cases of short ISIs, especially in those less than 5 ms. On the other hand, Ragert et al. showed that the first stimulation to the left median nerve decreased the SEP amplitudes (N20) evoked by the second stimulation to the right median nerve with an ISI of 20–25 ms (Ragert et al., 2011). Additionally, Brodie et al. showed that the first stimulation to the right median nerve decreased the SEP amplitudes (P14/N20 and N20/P25) evoked by the second stimulation to the left median nerve with ISIs of 25–35 and 15–35 ms, respectively (Brodie et al., 2014). These studies indicate that interhemispheric inhibitory interactions in the SI occur between the two hemispheres through the corpus callosum in the critical time interval of 20–25 ms or 15–35 ms after median nerve stimulation (Ragert et al., 2011; Brodie et al., 2014). Moreover, the results of these two previous studies are inconsistent, and there is no consensus on the ISI interval regarding the left–right interaction of somatosensory pathways. In addition, the commissural fibers between the left and right sides of the hemispheres comprise not only the corpus callosum but also other commissural fibers such as the anterior and posterior commissural fibers. It is necessary to elucidate whether there are somatosensory pathways that provide input to the contralateral SI over a long period of time through these routes. Therefore, p-SEP recordings were obtained at nine different ISIs (1, 2, 3, 5, 10, 20, 40, 60, and 100 ms) to investigate the interaction between contralateral and ipsilateral activations at various levels in healthy humans.

MATERIALS AND METHODS

Participants

Fourteen healthy right-handed males (mean age: 30.6; range: 25–39 years) participated in this study. The total sample size (n = 14) was calculated using the G*Power 3.1.9.2 software (repeated measures, within factors, F-tests, effect size f: 0.25, α error: 0.05, Power: 0.8, number of measurements: 10; Faul et al., 2007). No participants had a history of neurological or psychiatric problems. The present study was approved by the Ethics Committee of Ibaraki Prefectural University of Health Sciences (approval no. 893 and e278).

SEP Recording

To investigate the interactions between contralateral and ipsilateral activations at a level below the brainstem, single median nerve SEPs (s-SEPs) and paired median nerve SEPs (p-SEPs) were recorded using a previously described protocol with minor modifications (Ragert et al., 2011; Brodie et al., 2014; **Figures 1A,B**). In the s-SEP paradigm, s-SEPs were obtained by stimulating the right and left median nerve at the wrist. In the p-SEP paradigm, peripheral stimulation of the right median nerve as conditioning stimulus (CS) always preceded the left median nerve stimulation as the test stimulus (TS) with nine different ISIs (1, 2, 3, 5, 10, 20, 40, 60, and 100 ms). Electroencephalogram (EEG) data from three-channel electrodes (Fz, CP3, and CP4) were recorded using a BrainAmp DC (Brain Products, Gilching, Germany) and TMS-compatible EEG electrode caps. The ground electrode was placed on the skin over the midpoint between the radius and ulna at the height of the proximal 1/2 of the right forearm, and the linked ear was used as a reference. The impedance of each electrode was set at < 5 kΩ. EEG signals were recorded at a sampling frequency of 5 kHz with a bandpass of DC–1 kHz.

A Neuropack X1 (Nihon kohden, Tokyo, Japan) was used to deliver electrical stimuli of 0.2 ms duration at a rate of 3 Hz. The stimulus intensity was set three times the perceptual threshold [7.46 ± 1.21 mA for the right median nerve, 7.58 ± 0.52 mA for the left median nerve (mean ± standard deviation SD)]. During the p-SEP condition, the right median nerve stimulation always proceeded the left median nerve stimulation using nine different ISIs (1–100 ms). During the s-SEP condition, a test stimulus (TS

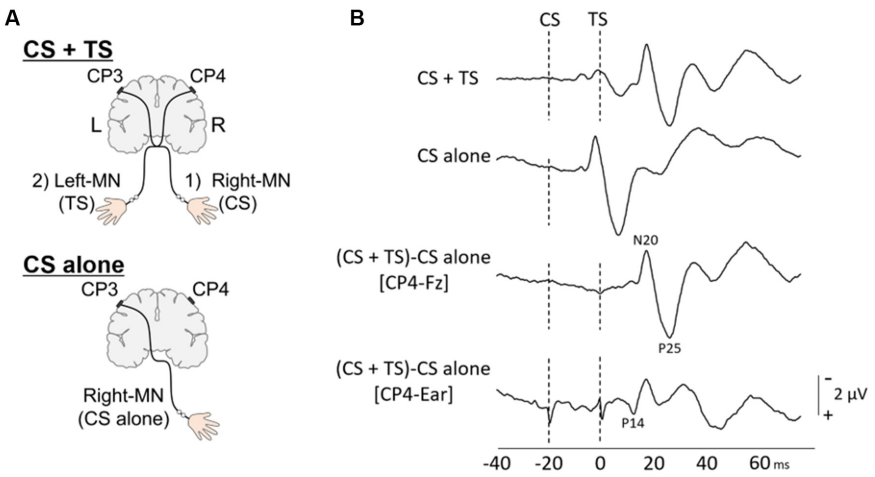

FIGURE 1 | Paired median nerve somatosensory evoked potential (p-SEP). **(A)** To investigate the effect of conditioning stimulus (CS) on the SEP induced by the test stimulus (TS) (upper panel), the paired median nerve SEPs (p-SEPs) and (lower panel) the single median nerve SEPs (s-SEPs) were recorded at CP4 electrodes. In the p-SEP recording: (1) the right median nerve (right-MN) stimulation as CS always preceded; (2) the left median nerve (Left-MN) stimulation as TS with nine different interstimulus intervals (ISIs; 1, 2, 3, 5, 10, 20, 40, 60, and 100 ms). **(B)** Typical p-SEP (ISI; 20 ms) and s-SEP waveforms at CP4 from a representative individual. Dotted line: the time of stimulation. The p-SEP data were analyzed using the following formula: p-SEPs = (SEP response of CS + TS at CP4) – (SEP response of CS alone at CP4).

alone, left median nerve) and a control stimulus (CS alone, right median nerve) were applied. The order of conditions [CS + TS (1–100 ms), TS alone, and CS alone] was pseudo-randomized during the experiment. A total of five, 500 stimulus-related epochs were recorded with 500 epochs for each condition [9 ISIs (CS + TS), TS alone, and CS alone]. We asked the patients to count the electrical stimuli during SEP recordings to counteract the attention effect.

Data Analysis

Epochs were digitally filtered using a band-pass Butterworth filter (1–200 Hz), and each condition was averaged (Ragert et al., 2011). Each SEP component was calculated by montages described below using Matlab R2019a (MathWorks, Natick, MA, United States; Mauguiere et al., 1999; Cruccu et al., 2008). The subcortical component (P14) = CP3 or CP4-linked earlobes; the cortical components (P14-peak–N20-peak and N20-peak–P25) = CP3 or CP4 − Fz. Amplitudes of the subcortical component (P14) were measured as the P14-onset to P14-peak. Amplitudes of cortical components (P14-peak–N20-peak and N20-peak–P25) were measured from peak to peak.

To evaluate the effect of CS (right median nerve stimulation) on TS (left median nerve stimulation), the p-SEP data were analyzed using the following formula:

p-SEPs at CP3 or CP4 = (SEP response of CS + TS) – (SEP response of CS only)

Statistical Analyses

All analyses were conducted using the SPSS 12.0 for Windows (SPSS, Chicago, Illinois). Data are shown as mean ± SD for all results (**Figure 2**). Data distribution was evaluated using the Shapiro–Wilk normality test. All data were normally distributed. Data of each amplitude (P14, P14/N20, N20/P25) were analyzed using one-way repeated-measures analysis of variance with factor ISI conditions (TS alone, 1, 2, 3, 5, 10, 20, 40, 60, and 100 ms). Dunnett's test was used for *post hoc* comparisons. Statistical significance was set at $p < 0.05$.

RESULTS

Supplementary Figures 1–14 show the s-SEP and analyzed p-SEP (s-SEP subtracted) waveforms at CP3 and CP4 from all participants. The Shapiro–Wilk test showed that all data were normally distributed ($p > 0.05$). **Figures 2A–F** show no significant main effects on ISI conditions in all amplitudes at CP3 and CP4 (P14: CP3, $F_{(9,117)} = 1.421$, $p = 0.187$; CP4, $F_{(9,117)} = 1.236$, $p = 0.280$; P14/N20: CP3, $F_{(9,117)} = 1.574$, $p = 0.131$; CP4, $F_{(9,117)} = 0.947$; $p = 0.487$; and N20/P25: CP3, $F_{(9,117)} = 0.730$, $p = 0.681$; CP4, $F_{(9,117)} = 0.938$; $p = 0.495$). Dunnett's test showed no significant differences between each ISI and TS alone condition in all amplitudes at CP3 and CP4 ($p > 0.05$).

DISCUSSION

In this study, we investigated the interaction between contralateral and ipsilateral somatosensory pathways in healthy humans. The major findings of this study were that the right median nerve stimulation (CS) did not interfere with SEP amplitude (P14, P14/N20, N20/P25) induced by left median nerve stimulation (TS) in all ISI conditions (1, 2, 3, 5, 10, 20, 40, 60, and 100 ms).

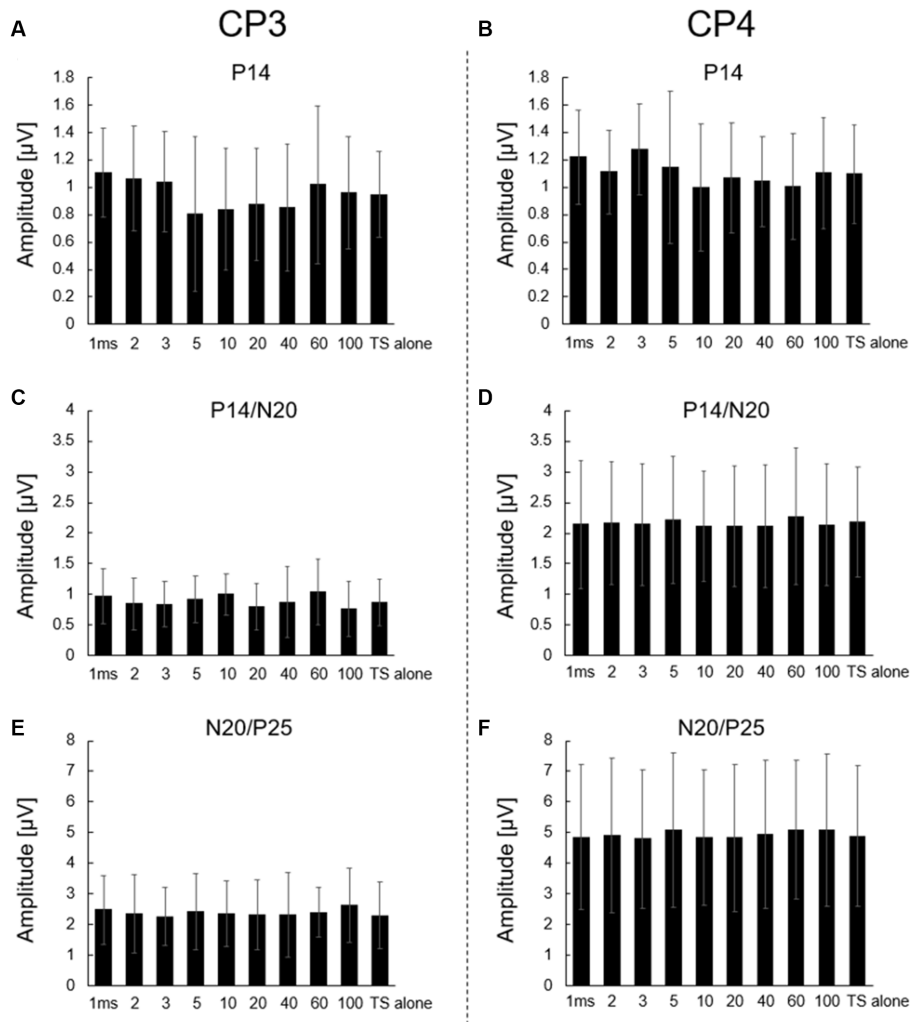

FIGURE 2 | Effect of CS to the right median nerve on P14, P14/N20, and N20/P25 responses of CP3 and CP4 electrodes. Averaged **(A,B)** P14, **(C,D)** P14/N20, and **(E,F)** N20/P25 amplitudes for TS alone and all ISI conditions (1, 2, 3, 5, 10, 20, 40, 60, and 100 ms). Left panels: CP3 electrode; right panels: CP4 electrode. No significant differences were observed between each ISI condition and TS alone condition in all amplitudes. All data are presented as means ± SD.

If a direct connection between bilateral ascending pathways exists, the amplitude of SEP induced by the second median nerve TS would be attenuated or eliminated by the refractory period under the short ISI condition (Hoshiyama and Kakigi, 2002). However, in our result, the right median nerve stimulation (CS) did not decrease the cortical and subcortical components of the SEP induced by the left median nerve TS in short ISI conditions (1, 2, 3, and 5 ms). This result suggests the absence of a neural connectivity formed by a small number of synapses in the left–right interaction of the somatosensory pathway.

Regarding our results in the middle ISI condition (10–40 ms), Ragert et al. showed decreased N20 SEP amplitude with an ISI of 20–25 ms (Ragert et al., 2011). In contrast, Brodie et al. showed decreased P14/N20 SEP amplitude with an ISI of 25–35 ms and decreased N20/P25 SEP amplitude with an ISI of 15–35 ms, respectively (Brodie et al., 2014). In the present study, the right median nerve stimulation (CS) did not interfere with SEPs induced by the left median nerve stimulation (TS) in mid-length ISI conditions (10, 20, and 40 ms). This finding is inconsistent with the results of the two previous studies, and there is no consensus on the ISI interval regarding the left–right interaction of somatosensory pathways. However, the number of trials that were averaged was different between the previous studies and the current study (Ragert et al., 150 epochs; Brodie et al., 300 epochs; current study, 500 epochs). Importantly, increasing the number of SEP recordings improves the signal-to-noise ratio, suggesting that we were able to record SEPs by median nerve stimulation with a higher signal-to-noise ratio within the measurement conditions of the current study. Whether differences in the order of stimulation to the median nerve (Ragert et al., left to right; Brodie et al., right to left; current study, right to left) may account for conflicting results remains unclear.

The commissural fibers between the left and right hemispheres comprise not only the corpus callosum but

also other commissural fibers such as the anterior and posterior commissural fibers. To investigate the left–right interaction of somatosensory pathways by polysynaptic connections, we included long ISIs (60 and 100 ms) in our evaluations and found no significant inhibitory effects of the first stimulation to the right median nerve on the SEP evoked by the second stimulation to the left median nerve. This finding suggests that there may not be a pathway to input to the contralateral SI over a long period of time or that investigating the long left–right connectivity by polysynaptic connections might be difficult using the p-SEP method.

A study with cortical surface SEP recordings in patients undergoing epileptogenic tissue resection revealed that four of 41 patients showed ipsilateral SEPs, which were very localized, were of considerably lower amplitude, had a longer latency (1.2–17.8 ms), and did not show an initial negativity (Noachtar et al., 1997). The uncrossed ipsilateral afferent system from the upper extremities includes the spinoreticular and spinomesencephalic tract, which may reach the ipsilateral somatosensory cortex (Scheibel, 1984; Noachtar et al., 1997). Although any changes in SEPs could not be identified with the electrode ipsilateral to the median nerve TS, somatosensory information may actually be directly inputted to the ipsilateral cerebrum. The existence of pathways that transfer somatosensory information to the contralateral hemisphere without involving the corpus callosum is important for recovery from hypoesthesia because when somatosensory pathways are damaged at the subcortical level, such as the thalamus, left–right interaction through the corpus callosum does not contribute to the recovery of hypoesthesia. Therefore, the presence of ipsilateral ascending pathways, which are very localized and have considerably lower amplitude using a multi-channel electrode in healthy adults, should be investigated. They should also be investigated in stroke patients, in whom large-scale changes in neural networks occur.

This study has several limitations. First, we performed a total of 5, 500 stimuli to the median nerve, which may have affected the activation or inhibition of somatosensory pathways. However, to minimize the order effect, each ISI condition was randomized. Second, all participants were men. The structure and function of the brain differs between men and women (Zaidi, 2010). Therefore, future studies should investigate sex differences in the interaction between contralateral and ipsilateral activations. Finally, the CS and TS were set to the same intensity and it remains possible that CS was not strong enough to affect the ipsilateral hemisphere. Future studies will include different CS intensities.

DATA AVAILABILITY STATEMENT

The original contributions presented in the study are included in the article/**Supplementary Material**, further inquiries can be directed to the corresponding author.

ETHICS STATEMENT

The studies involving human participants were reviewed and approved by the Ibaraki Prefectural University of Health Sciences Review Board (approval no. 893 and e278). The patients/participants provided their written informed consent to participate in this study.

AUTHOR CONTRIBUTIONS

Conceptualization: DI, KI, HY, KT, AY, and YKo. Methodology and investigation: DI, KI, HY, and YKa. Formal analysis: DI, KT, and SY. Writing the original draft: DI. Review and editing of manuscript: KI, HY, KT, SY, YKa, AY, and YKo. All authors contributed to the article and approved the submitted version.

FUNDING

This work was supported by JSPS KAKENHI (Nos. 18K17725 and 21H03305 to DI; and No. 19H05730 to AY) and a Grant-in-Aid for Project Research (No. 1962-1 to YKo) from the Ibaraki Prefectural University of Health Sciences.

SUPPLEMENTARY MATERIAL

The Supplementary Material for this article can be found online at: https://www.frontiersin.org/articles/10.3389/fnsys.2021.698758/full#supplementary-material.

REFERENCES

Barbay, S., Guggenmos, D. J., Nishibe, M., and Nudo, R. J. (2013). Motor representations in the intact hemisphere of the rat are reduced after repetitive training of the impaired forelimb. *Neurorehabil. Neural Repair* 27, 381–384. doi: 10.1177/1545968312465193

Brodie, S. M., Villamayor, A., Borich, M. R., and Boyd, L. A. (2014). Exploring the specific time course of interhemispheric inhibition between the human primary sensory cortices. *J. Neurophysiol.* 112, 1470–1476. doi: 10.1152/jn.00074.2014

Courtine, G., Roy, R. R., and Raven, J. (2005). Performance of locomotion and foot grasping following a unilateral thoracic corticospinal tract lesion in monkeys *(Macaca mulatta)* . *Brain* 128,2338–2358. doi: 10.1093/brain/awh604

Cruccu, G., Aminoff, M. J., Curio, G., Guerit, J. M., Kakigi, R., Mauguiere, F., et al. (2008). Recommendations for the clinical use of somatosensory-evoked potentials. *Clin. Neurophysiol.* 119, 1705–1719. doi: 10.1016/j.clinph.2008.03.016

Faul, F., Erdfelder, E., Lang, A. G., and Buchner, A. (2007). G*Power 3: a flexible statistical power analysis program for the social, behavioral and biomedical sciences. *Behav. Res. Methods* 39, 175–191. doi: 10.3758/bf03193146

Frost, S. B., Barbay, S., Friel, K. M., Plautz, E. J., and Nudo, R. J. (2003). Reorganization of remote cortical regions after ischemic brain injury: a potential substrate for stroke recovery. *J. Neurophysiol.* 89, 3205–3214. doi: 10.1152/jn.01143.2002

Hoshiyama, M., and Kakigi, R. (2002). New concept for the recovery function of short-latency somatosensory evoked cortical potentials following median nerve stimulation. *Clin. Neurophysiol.* 113, 535–541. doi: 10.1016/s1388-2457(02)00039-1

Isa, T. (2017). The brain is needed to cure spinal cord injury. *Trends Neurosci.* 40, 625–636. doi: 10.1016/j.tins.2017.08.002

Isa, T. (2019). Dexterous hand movements and their recovery after central nervous system injury. *Annu. Rev. Neurosci.* 42, 315–335. doi: 10.1146/annurev-neuro-070918-050436

Isa, T., Mitsuhashi, M., and Yamaguchi, R. (2019). Alternative routes for recovery of hand functions after corticospinal tract injury in primates and rodents. *Curr. Opin. Neurol.* 32, 836–843. doi: 10.1097/WCO.0000000000000749

Iwamura, Y., Iriki, A., and Tanaka, M. (1994). Bilateral hand representation in the postcentral somatosensory cortex. *Nature* 369, 554–556. doi: 10.1038/369554a0

Iwamura, Y., Tanaka, M., Iriki, A., Taoka, M., and Toda, T. (2002). Processing of tactile and kinesthetic signals from bilateral sides of the body in the postcentral gyrus of awake monkeys. *Behav. Brain Res.* 135, 185–190. doi: 10.1016/s0166-4328(02)00164-x

Iwamura, Y., Taoka, M., and Iriki, A. (2001). Bilateral activity and callosal connections in the somatosensory cortex. *Neuroscientist* 7, 419–429. doi: 10.1177/107385840100700511

Kato, J., Yamada, T., Kawaguchi, H., Matsuda, K., and Higo, N. (2020). Functional near-infrared-spectroscopy-based measurement of changes in cortical activity in macaques during post-infarct recovery of manual dexterity. *Sci. Rep.* 10:6458. doi: 10.1038/s41598-020-63617-0

Levy, C. E., Nichols, D. S., Schmalbrock, P. M., Keller, P., and Chakeres, D. W. (2001). Functional MRI evidence of cortical reorganization in upper-limb stroke hemiplegia treated with constraint-induced movement therapy. *Am. J. Phys. Med. Rehabil.* 80, 4–12. doi: 10.1097/00002060-200101000-00003

Mauguiere, F., Allison, T., Babiloni, C., Buchner, H., Eisen, A. A., Goodin, D. S., et al. (1999). Somatosensory evoked potentials. The international federation of clinical neurophysiology. *Electroencephalogr. Clin. Neurophysiol.* 52, 79–90.

Murata, Y., Higo, N., Hayashi, T., Nishimura, Y., Sugiyama, Y., Oishi, T., et al. (2015). Temporal plasticity involved in recovery from manual dexterity deficit after motor cortex lesion in macaque monkeys. *J. Neurosci.* 35, 84–95. doi: 10.1523/JNEUROSCI.1737-14.2015

Netz, J., Lammers, T., and Homberg, V. (1997). Reorganization of motor output in the non-affected hemisphere after stroke. *Brain* 120, 1579–1586. doi: 10.1093/brain/120.9.1579

Nihashi, T., Naganawa, S., Sato, C., Kawai, H., Nakamura, T., Fukatsu, H., et al. (2005). Contralateral and ipsilateral responses in primary somatosensory cortex following electrical median nerve stimulation—an fMRI study. *Clin. Neurophysiol.* 116, 842–848. doi: 10.1016/j.clinph.2004.10.011

Noachtar, S., Luders, H. O., Dinner, D. S., and Klem, G. (1997). Ipsilateral median somatosensory evoked potentials recorded from human somatosensory cortex. *Electroencephalogr. Clin. Neurophysiol.* 104, 189–198. doi: 10.1016/s0168-5597(97)00013-0

Nudo, R. J., Wise, B. M., SiFuentes, F., and Milliken, G. W. (1996). Neural substrates for the effects of rehabilitative training on motor recovery after ischemic infarct. *Science* 272, 1791–1794. doi: 10.1126/science.272.5269.1791

Ragert, P., Nierhaus, T., Cohen, L. G., and Villringer, A. (2011). Interhemispheric interactions between the human primary somatosensory cortices. *PLoS One* 6:e16150. doi: 10.1371/journal.pone.0016150

Ramanathan, D., Conner, J. M., and Tuszynski, M. H. (2006). A form of motor cortical plasticity that correlates with recovery of function after brain injury. *Proc. Natl. Acad. Sci. U S A* 103, 11370–11375. doi: 10.1073/pnas.0601065103

Rosenzweig, E. S., Courtine, G., Jindrich, D. L., Brock, J. H., Ferguson, A. R., Strand, S. C., et al. (2010). Extensive spontaneous plasticity of corticospinal projections after primate spinal cord injury. *Nat. Neurosci.* 13, 1505–1510. doi: 10.1038/nn.2691

Scheibel, A. B. (1984). *The Brain Stem Reticular Core and Sensory Function*. Bethesda, MD: American Physiology Society.

Yamamoto, T., Hayashi, T., Murata, Y., Ose, T., and Higo, N. (2019). Premotor cortical-cerebellar reorganization in a macaque model of primary motor cortical lesion and recovery. *J. Neurosci.* 39, 8484–8496. doi: 10.1523/JNEUROSCI.0077-19.2019

Yoshino-Saito, K., Nishimura, Y., Oishi, T., and Isa, T. (2010). Quantitative inter-segmental and inter-laminar comparison of corticospinal projections from the forelimb area of the primary motor cortex of macaque monkeys. *Neuroscience* 171, 1164–1179. doi: 10.1016/j.neuroscience.2010.10.007

Zaidi, Z. F. (2010). Gender differences in human brain: a review. *Open Anat. J.* 2, 37–55. doi: 10.2174/1877609401002010037

Conflict of Interest: The authors declare that the research was conducted in the absence of any commercial or financial relationships that could be construed as a potential conflict of interest.

Publisher's Note: All claims expressed in this article are solely those of the authors and do not necessarily represent those of their affiliated organizations, or those of the publisher, the editors and the reviewers. Any product that may be evaluated in this article, or claim that may be made by its manufacturer, is not guaranteed or endorsed by the publisher.

Copyright © 2021 Ishii, Ishibashi, Yuine, Takeda, Yamamoto, Kaku, Yozu and Kohno. This is an open-access article distributed under the terms of the Creative Commons Attribution License (CC BY). The use, distribution or reproduction in other forums is permitted, provided the original author(s) and the copyright owner(s) are credited and that the original publication in this journal is cited, in accordance with accepted academic practice. No use, distribution or reproduction is permitted which does not comply with these terms.

frontiers in Human Neuroscience

CASE REPORT
published: 01 November 2021
doi: 10.3389/fnhum.2021.761186

Interaction of the Left–Right Somatosensory Pathways in Patients With Thalamic Hemorrhage: A Case Report

Daisuke Ishii[1,2], Kiyoshige Ishibashi[3], Kotaro Takeda[4], Hiroshi Yuine[5], Satoshi Yamamoto[6], Yuki Kaku[1], Arito Yozu[1] and Yutaka Kohno[1]*

[1] Center for Medical Sciences, Ibaraki Prefectural University of Health Sciences, Inashiki-gun, Japan, [2] Department of Cognitive Behavioral Physiology, Chiba University Graduate School of Medicine, Chiba, Japan, [3] Department of Physical Therapy, Ibaraki Prefectural University of Health Sciences Hospital, Inashiki-gun, Japan, [4] Faculty of Rehabilitation, School of Healthcare, Fujita Health University, Toyoake, Japan, [5] Department of Occupational Therapy, School of Health Sciences, Ibaraki Prefectural University of Health Sciences, Inashiki-gun, Japan, [6] Department of Physical Therapy, School of Health Sciences, Ibaraki Prefectural University of Health Sciences, Inashiki-gun, Japan

OPEN ACCESS

Edited by:
Tomohiko Takei,
Tamagawa University, Japan

Reviewed by:
Satoko Koganemaru,
Kyoto University, Japan
Mitsunari Abe,
Fukushima Medical University, Japan

***Correspondence:**
Daisuke Ishii
ishiid@ipu.ac.jp

Specialty section:
This article was submitted to Motor Neuroscience, a section of the journal Frontiers in Human Neuroscience

Received: *19 August 2021*
Accepted: *12 October 2021*
Published: *01 November 2021*

Citation:
Ishii D, Ishibashi K, Takeda K, Yuine H, Yamamoto S, Kaku Y, Yozu A and Kohno Y (2021) Interaction of the Left–Right Somatosensory Pathways in Patients With Thalamic Hemorrhage: A Case Report. Front. Hum. Neurosci. 15:761186. doi: 10.3389/fnhum.2021.761186

Neural plasticity compensates for the loss of motor function after stroke. However, whether neural plasticity occurs in the somatosensory pathways after stroke is unknown. We investigated the left–right somatosensory interaction in two hemorrhagic patients using a paired somatosensory evoked potentials (p-SEPs) recorded at CP3 and CP4, which was defined as an amplitude difference between the SEPs of paired median nerve stimulations to both sides and that of single stimulation to the affected side. Patient 1 (61-year-old, left thalamic hemorrhage) has a moderate motor impairment, severe sensory deficit, and complained of pain in the affected right upper limb. Patient 2 (72-year-old, right thalamic hemorrhage) had slight motor and sensory impairments with no complaints of pain. Single SEPs (s-SEPs) were obtained by stimulation of the right and left median nerves, respectively. For paired stimulations, 1 ms after the first stimulation to the non-affected side, followed by a second stimulation to the affected side. In patient 1, a s-SEP with stimulation to the non-affected side and a p-SEP were observed in CP4. However, a s-SEP was not observed in either hemisphere with stimulation to the affected side. On the other hand, in patient 2, a s-SEP in CP3 with stimulation to the non-affected side and in CP4 with stimulation to the affected side were observed; however, a p-SEP was not observed. In addition, to investigate the mechanism by which ipsilateral median nerve stimulation enhances contralateral p-SEP in patient 1, we compared the SEP averaged over the first 250 epochs with the SEP averaged over the second 250 epochs (total number of epochs recorded: 500). The results showed that in the patient 1, when the bilateral median nerve was stimulated continuously, the habituation did not occur and the response was larger than that of the s-SEP with unilateral median nerve stimulation. In the current case report, the

damage to the thalamus may cause neuroplasticity in terms of the left–right interaction (e.g., left and right S1). The somatosensory input from the affected side may interfere with the habituation of the contralateral somatosensory system and conversely increase the response.

Keywords: stroke, somatosensory evoked potentials, neural plasticity, paired somatosensory evoked potentials, thalamic hemorrhage

INTRODUCTION

The human nervous system has acquired some adaptive responses, defined as "hyper-adaptability," that are activated with significant changes in the internal environment (it does not work under normal conditions). For example, neural plasticity in the central nervous system plays an important role in the recovery of motor paralysis caused by corticospinal tract damage. Previous studies on spinal cord-lesioned monkeys showed that the sprouting of midline-crossing axons in the corticospinal tract occurs in the spinal cord rostral to the lesion, and the sprouting was associated with improvement in hand function and locomotion (Courtine et al., 2005; Rosenzweig et al., 2010). In addition, the functional motor representation maps around the damage and remote cortical regions change with rehabilitative motor training after focal damage in the forelimb movement area of the motor cortex (Nudo et al., 1996; Frost et al., 2003; Ramanathan et al., 2006; Barbay et al., 2013). These studies suggest that an unusual neural route is created, which then controls the paretic limb (Murata et al., 2015; Isa, 2017; Yamamoto et al., 2019; Kato et al., 2020). Conversely, no compensatory mechanism for sensory information processing after damage to the somatosensory pathway has been identified.

Neurons in the unilateral S1 receive sensory information from the contralateral brain through interhemispheric transfer (Iwamura et al., 1994, 2001, 2002; Nihashi et al., 2005). Recently, three previous studies, including our study, investigated interactions between contralateral and ipsilateral activations using a paired median nerve somatosensory evoked potential (p-SEP) protocol in a healthy human (Ragert et al., 2011; Brodie et al., 2014; Ishii et al., 2021). In this protocol, peripheral stimulation of the unilateral median nerve preceded the stimulation of the other median nerve with some interstimulus intervals (ISIs). When left–right interaction is presented, the SEP evoked by the stimulation to the unilateral median nerve is modulated by interference of the stimulation to the median nerve on the other side. Ragert et al. (2011) and Brodie et al. (2014) showed that interhemispheric inhibitory interactions in the S1 occur between two hemispheres *via* the corpus callosum in a critical time interval of 20–25 or 15–35 ms after median nerve stimulation. However, we recently investigated the effect of ISIs (1–100 ms) on p-SEPs in more detail and concluded that no interaction occurs between left and right somatosensory pathways in healthy subjects with any ISI (Ishii et al., 2021). We further demonstrated that no interaction occurs between the bilateral somatosensory pathways of healthy subjects with short ISI conditions (<5 ms), which indicates that there is also no left–right transmission of a small number of synapses in the pathways (Ishii et al., 2021). In stroke patients, in whom large-scale changes in neural networks occur, the existence of a left–right interaction of somatosensory pathways at a level other than the corpus callosum has not been established. However, left–right somatosensory interaction at a level other than the corpus callosum might contribute to recovery from hypoesthesia. This is because when the somatosensory pathways are damaged at the subcortical level, such as in the thalamus, left–right interaction through the corpus callosum may not contribute to the recovery of hypoesthesia.

We hypothesized that the neural connectivity formed by a small number of synapses in the left–right interaction of the somatosensory pathway would be present in patients with recovered sensory impairment. Therefore, we investigated the interaction of the left–right of somatosensory pathways in two patients with thalamic hemorrhage using the p-SEPs protocol under short ISI (Ragert et al., 2011; Brodie et al., 2014; Ishii et al., 2021).

CASE DESCRIPTION

This study was reviewed and approved by the Ibaraki Prefectural University of Health Sciences Review Board (approval nos. 893 and e278). The patients provided their written informed consent to participate in this study.

Timeline for Clinical and Laboratory Findings

Table 1 shows the clinical episodes and evaluation results from the onset of symptoms to the time of SEP recording.

Patient 1

A 61-year-old right-handed Japanese man was admitted to the acute care hospital due to right upper and lower limb paresis, facial paresis, and speech disturbance. On admission, the Glasgow Coma Scale (GCS) for the eye-opening, verbal, and motor responses was 3, 5, and 6 points, respectively. Head computed tomography (CT) showed a high-density area in the left thalamus (**Figure 1A**). On the second day post-onset, acute rehabilitation (occupational, physical, and speech therapy) was initiated. The physical examination revealed the following findings: right upper and lower limb paresis (Brunnstrom stage 2 for arm, 2 for hand, and 2 for leg), and severe hypoesthesia with deep (thumb-localizing test: 3) and superficial sensation. The patient was subsequently transferred to a convalescent rehabilitation hospital at 4 weeks post-onset. Evaluation at the time of transfer showed a GCS of 15 points, paralysis of the

right upper and lower limbs (Brunnstrom stage 3 for arm, 3–4 for hand, and 3–4 for foot), severe hypoesthesia with deep sensation (thumb-localizing test: 2), and superficial sensation. In addition, he complained of pain in the right upper limb (affected side).

Patient 2

A 72-year-old right-handed Japanese man was admitted to the acute care hospital due to left upper and lower limb paresis. On admission, the GCS for the eye-opening, verbal, and motor responses was 4, 5, and 6 points, respectively. Head CT showed a high-density area in the right thalamus (**Figure 1A**). On the day of onset, acute rehabilitation (occupational, physical, and speech therapy) was initiated. The physical examination revealed the following findings: left upper and lower limb paresis (Brunnstrom stage 2 for arm, 3 for hand, and 2 for leg), and severe hypoesthesia with deep and superficial sensations. The patient was subsequently transferred to a convalescent rehabilitation hospital at 20 days post-onset. Evaluation at the time of transfer showed paralysis of the left upper and lower limbs (Brunnstrom stage 3 for arm, 4 for hand, and 5 for foot), slight hypoesthesia with deep and superficial sensations, and no complaints of pain in the left upper limb (affected side).

Physical Examination at SEP Recording

On the 107th (patient 1) or 152th (patient 2) day of onset, we performed a physical examination using the Brunnstrom stage (for paresis), sense of passive movement and position sense of thumb (for deep sensations), and Semmes–Weinstein Monofilament (SWM) test (Sakai Medical, Tokyo) for superficial sensation as previously described (Mima et al., 2004). The SWM applies stimulation with constant pressure and evaluates tactile thresholds using several levels of stimulus intensity (Bell-Krotoski et al., 1995). Briefly, monofilaments of 20 different sizes (1.65–2.83, 3.22–3.61, 3.84–4.31, 4.54–6.45, and 6.65 expressed as the log of the bending force in mg) were applied to the index finger (three points), mother finger (one point), middle finger (three points), and palm (five points) (**Figure 1B**).

Somatosensory Evoked Potential Recording

To investigate the interactions between contralateral and ipsilateral activations, single SEP (s-SEP), and p-SEP were recorded using a previously described protocol with minor modifications (Ragert et al., 2011; Brodie et al., 2014; Ishii et al., 2021). In the s-SEP paradigm, s-SEPs were obtained by stimulation of the right and left median nerves at the wrist (**Figures 2**, **3**). In the p-SEP paradigm, peripheral stimulation to the median nerve of the affected side (conditioning stimulus: CS) was performed 1 ms after the stimulation to the non-affected side (test stimulus: TS). A BrainAmp DC (Brain Products, Gilching, Germany) and TMS-compatible EEG electrode caps were used for SEP recordings. The ground electrode was placed on the skin over the right biceps brachii. The impedance of each electrode was set below 5 kΩ. EEG signals were recorded at a sampling frequency of 5 kHz with 1 kHz low-pass analog filter.

A Neuropack X1 (Nihon Kohden, Tokyo, Japan) was used to deliver electrical stimuli of 0.2 ms duration at a rate of 3 Hz (Ishibashi et al., 2020). The stimulus intensity was set at three times the perceptual threshold of the non-affected side (patient 1: 10.5 mA for bilateral median nerve; patient 2: 11.4 mA for bilateral median nerve). During stimulation for s-SEP, TS (non-affected side), and CS (affected side) were applied to the median nerve. A total of 1,500 stimulus-related epochs were recorded with 500 epochs for each condition [(TS + CS), TS only, and CS only]. We asked the subjects to count the electrical stimuli during the SEP recordings to counteract the attention effect.

Data Analysis

Epochs were digitally filtered using a bandpass Butterworth filter (1–200 Hz) (Ragert et al., 2011; Brodie et al., 2014; Ishii et al., 2021). We calculated and compared the average of the SEP from 1 to 250 epochs with those from 251 to 500 epochs (**Figures 2**, **3**). Each SEP component was calculated using the montages described below using MATLAB R2019a (MathWorks, Natick, MA, United States) (Mauguiere et al., 1999; Cruccu et al., 2008). The cortical components of short latency SEP (P14-peak–N20-peak amplitude, N20-peak–P25-peak amplitude, and P25-peak–N33-peak amplitude) from CP3 or CP4 (Fz reference) were calculated.

To evaluate the effect of the CS (stimulation to the affected side) on TS (stimulation to the non-affected side), the p-SEPs in the contralateral and ipsilateral pathways (data at CP3 and CP4, respectively) were calculated using the following equation (Ragert et al., 2011; Brodie et al., 2014; Ishii et al., 2021):

$$\text{p-SEP} = (\text{SEP of TS} + \text{CS}) - \big(\text{SEP of CS only}\big)$$

RESULTS

Motor Paralysis and Sensory Impairment at the Day of SEP Recording

Patient 1

Brunnstrom stages of the paretic limbs were 3 for arm, 4 for hand, and 4 for leg, respectively. Hypoesthesia was severe in deep (sense of passive movement and position sense of thumb) and superficial sensations (**Figure 1B**). During the evaluation of deep sensation, the patient remarked, "I can vaguely tell that it is moving, but I cannot identify the direction or the finger that is moving." Moreover, numbness and pain in the upper limb on the affected side increased since admission to the convalescent rehabilitation hospital.

Patient 2

Brunnstrom stages of the paretic limbs were 5 for arm, 5 for hand, and 4 for leg. Hypoesthesia was mild in deep and superficial sensations (**Figure 1B**). At the time of the SEP recording, the patient said, "I felt the sensation more strongly with (the single than) the paired stimulation." Moreover, he complained of numbness in the ball of the left thumb and no pain in the affected upper limb.

TABLE 1 | Clinical and laboratory findings on patients 1 and 2.

Patient 1		Patient 2	
Days	**Clinical and laboratory findings**	**Days**	**Clinical and laboratory findings**
0 (onset)	Admission to the acute care hospital due to right upper and lower limb paresis, facial paresis, and speech disturbance.	0 (onset)	Admission to the acute care hospital due to left upper and lower limb paresis.
2	Starting the acute rehabilitation (occupational, physical, and speech therapy). Brunnstrom stage: 2 (arm), 2 (hand), and 2 (leg) Deep sensations: severe (thumb-localizing test: 3) Superficial sensation: severe		Starting the acute rehabilitation (occupational, physical, and speech therapy). Brunnstrom stage: 2 (arm), 3 (hand), and 2 (leg) Deep sensations: severe Superficial sensation: severe
33	Transferred to a convalescent rehabilitation hospital. Brunnstrom stage: 3 (arm), 3–4 (hand), and 3–4 (foot) Deep sensations: severe (thumb-localizing test: 2) Superficial sensation: severe Pain: affected upper limb	20	Transferred to a convalescent rehabilitation hospital. Brunnstrom stage: 3 (arm), 4 (hand), and 5 (foot) Deep sensations: mild Superficial sensation: mild
107 (SEP recording)	Brunnstrom stage: 3 (arm), 4 (hand), and 4 (foot) Deep sensations: severe Superficial sensation: severe Pain: affected upper limb	152 (SEP recording)	Brunnstrom stage: 5 (arm), 5 (hand), and 4 (foot) Deep sensations: mild Superficial sensation: mild

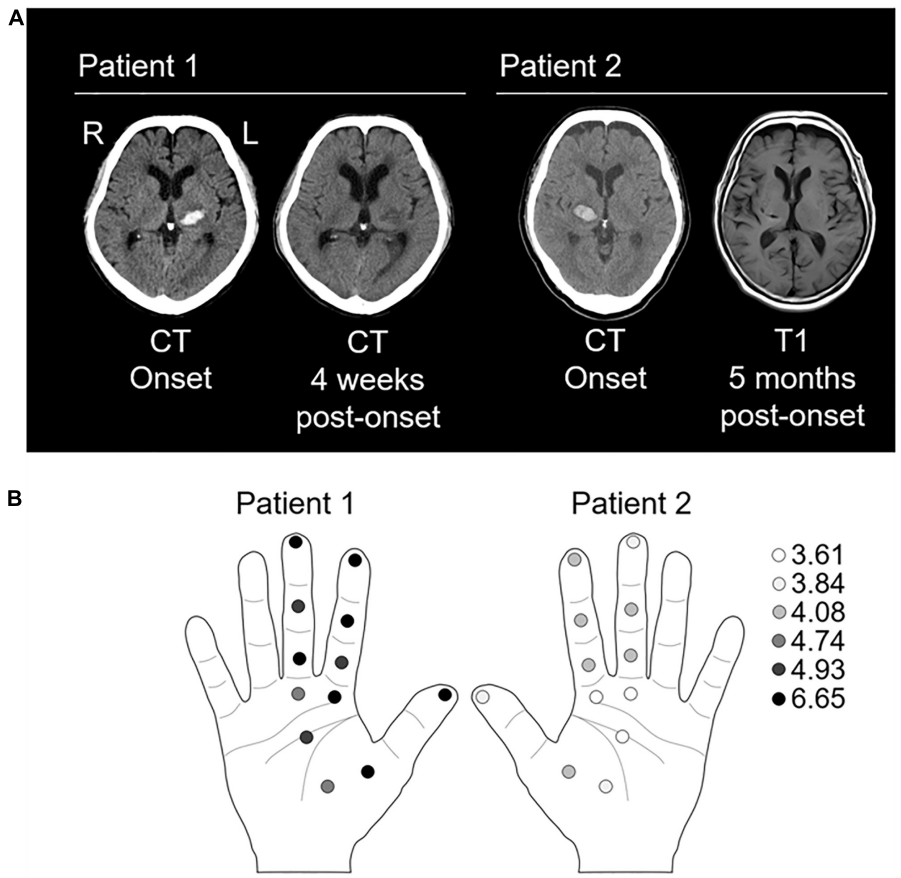

FIGURE 1 | Evaluation of lesioned site and tactile threshold. **(A)** *Left panel*: the computed tomography (CT) images of patient 1 at onset and 4 weeks post-onset show a high-and low-density area in the left thalamus, respectively. *Right panel*: the CT image at onset and T1-weighted magnetic resonance image at 5 weeks post-onset in patient 2 show a high-density area and a low signal-intensity area in the right thalamus, respectively. **(B)** Left panel showing tactile thresholds in patient 1. Right panel showing tactile thresholds in patient 2. The monofilaments of 20 different sizes (1.65–2.83, 3.22–3.61, 3.84–4.31, 4.54–6.45, and 6.65 expressed as the log of the bending force in mg) were applied to the index finger (three points), mother finger (one point), middle finger (three points), and palm (five points). Normal: 1.65–2.83; diminished light touch: 3.22–3.61; diminished protective sensation: 3.84–4.31; loss of protective sensation: 4.56–6.45; deep pressure sensation: 6.65; and unmeasurable: >6.65 (Bell-Krotoski and Tomancik, 1987; Jerosch-Herold, 2005).

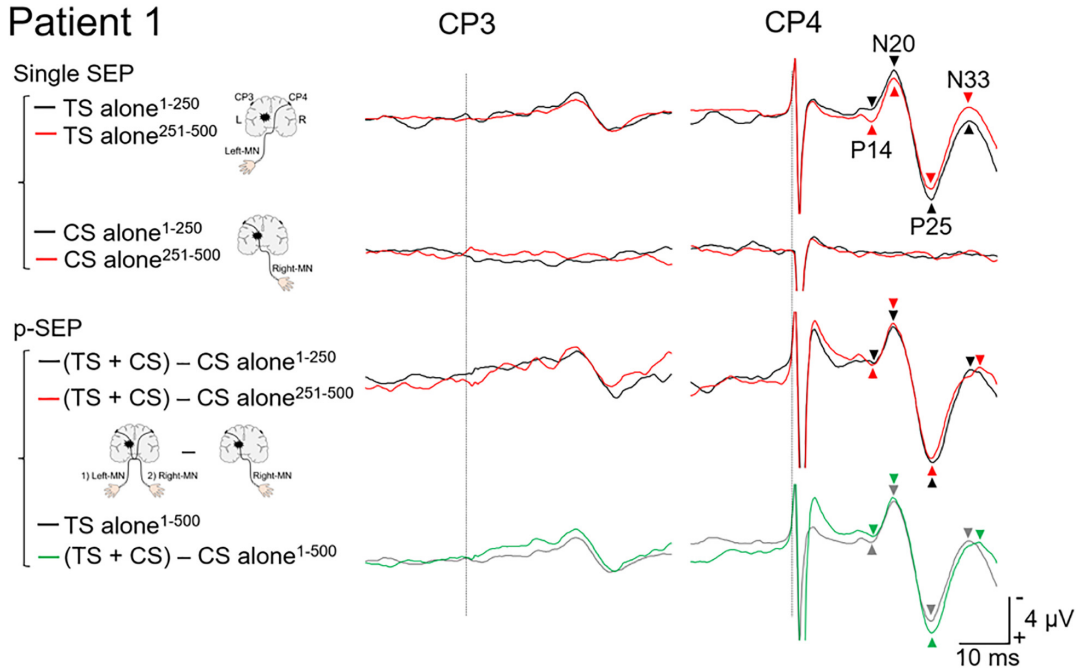

FIGURE 2 | Paired median nerve somatosensory evoked potential in patient 1. *Left panels*: to investigate the effect of the conditioning stimulus (CS) on the SEP induced by the test stimulus (TS), the single median nerve SEPs (single SEP) (right-MN: CS alone), and the paired median nerve SEPs (p-SEP) were recorded at the CP3 and CP4 electrodes (Ragert et al., 2011). In the p-SEP recording, the right-MN stimulus (CS) was performed 1 ms after the left-MN stimulus (TS). *Right panels*: all SEP waveforms at CP3 and CP4 from patient 1. We compared the SEP averaged over the first 250 epochs with the SEP averaged over the second 250 epochs (total number of epochs recorded: 500). Black line: the SEP averaged over the first 250 epochs. Red line: the SEP averaged over the second 250 epochs. Gray line: the SEP averaged over all epochs (500 epochs) (TS alone condition). Green line: the SEP averaged over all epochs (500 epochs) [(TS + CS) − CS alone condition]. Dotted line: the time duration of stimulation. MN, median nerve.

Evaluation of Somatosensory Pathway After Stroke

Patient 1

In the TS alone condition (non-affected side) at CP4 (**Figure 2**), the amplitude of N20/P25 averaged over the second half (251–500 epochs; 9.5 μV) was smaller than that over the first half (1–250 epochs; 11.2 μV), despite the other components showing less difference between the first (P14/N20, 3.4 μV and P25/N33, 6.8 μV) and second halves (P14/N20, 3.7 μV and P25/N33, 7.0 μV). In the CS alone condition (affected side) at CP3, no cortical components were recorded. After subtracting the CS alone condition from the TS + CS condition for each half, a small difference was observed between the first (P14/N20, 3.7 μV; N20/P25, 11.7 μV; and P25/N33, 7.9 μV) and second halves (P14/N20, 3.1 μV; N20/P25, 11.7 μV; and P25/N33, 8.0 μV). However, in terms of the average over 1–500 epochs, the amplitude of the N20/P25 (11.6 μV) and P25/N33 (7.8 μV) for "(TS + CS) − CS alone" was larger than that for TS alone (N20/P25, 10.4 μV and P25/N33, 6.9 μV). On the other hand, there was less difference between the TS alone (3.6 μV) and p-SEP (3.3 μV).

Patient 2

In the TS alone condition at CP3 (**Figure 3**), the amplitudes of the second half (N20/P25, 7.1 μV and P25/N33, 2.4 μV) were extremely smaller than those of the first half (N20/P25, 8.0 μV and P25/N33, 3.6 μV). On the other hand, in the P14/N20 component, a small difference was observed between the first (1.9 μV) and second half (2.1 μV). In the "(TS + CS) − CS" conditions at CP3, the amplitudes of the second half (N20/P25, 6.8 μV) were extremely smaller than those of the first half (N20/P25, 9.1 μV). In the P14/N20 component, few differences between the first (2.5 μV) and second half (1.8 μV) were observed. N33 component of the second half could not be identified due to uncertainty. These results of the "(TS + CS) − CS" condition were different from that of patient 1. Consequently, in the average over 1–500 epochs, there were few differences between the TS alone (P14/N20, 2.0 μV and N20/P25, 7.6 μV) and "(TS + CS) − CS" (P14/N20, 2.2 μV and N20/P25, 7.9 μV) conditions. In the CS alone condition at CP4, the cortical components recorded in the first half (P14/N20, 0.7 μV; N20/P25, 2.3 μV; and P25/N33, 0.6 μV) disappeared in the second half.

DISCUSSION

In this case report, we investigated the interaction between contralateral and ipsilateral activations in the somatosensory pathways in two patients with thalamic hemorrhage. When the left and right somatosensory pathways are directly connected,

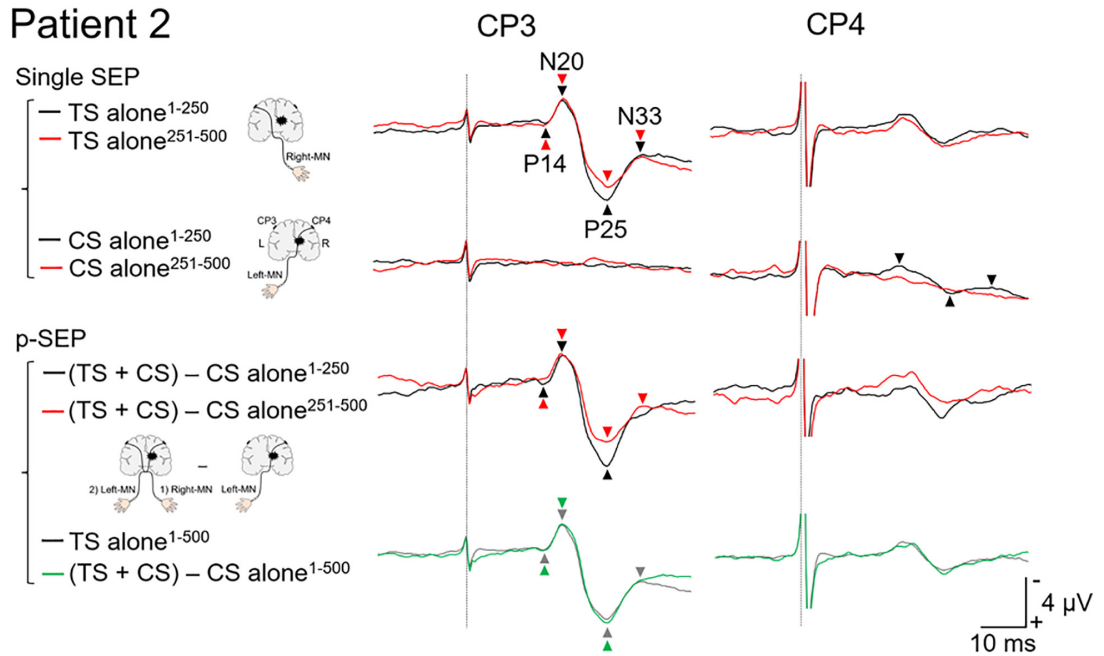

FIGURE 3 | Paired median nerve somatosensory evoked potential in patient 2. *Left panels*: to investigate the effect of conditioning stimulus (CS) on the SEP induced by the test stimulus (TS), the single median nerve SEPs (single SEP) (left-MN: CS alone), and the paired median nerve SEPs (p-SEP) were recorded at the CP3 and CP4 electrodes (Ragert et al., 2011). In the p-SEP recording, the left-MN stimulus (CS) was performed 1 ms after the right-MN stimulus (TS). *Right panels*: all SEP waveforms at CP3 and CP4 from patient 2. We compared the SEP averaged over the first 250 epochs with the SEP averaged over the second 250 epochs (total number of epochs recorded: 500). Black line: the SEP averaged over the first 250 epochs. Red line: the SEP averaged over the second 250 epochs. Gray line: the SEP averaged over all epochs (500 epochs) (TS alone condition). Green line: the SEP averaged over all epochs (500 epochs) [(TS + CS) − CS alone condition]. Dotted line: the time duration of stimulation. MN, median nerve.

the ipsilateral SEPs would be recorded (Noachtar et al., 1997). Additionally, the amplitude of these ipsilateral SEPs evoked by the second median nerve stimulus (affected side) would be attenuated or eliminated (during the refractory period) by the first median nerve stimulus (non-affected side) under short ISI conditions (e.g., 1–5 ms). No cortical components had been previously identified when the ISI of the paired stimulation to the same median nerve was short (Hoshiyama and Kakigi, 2002). In the present case report, no ipsilateral SEPs were recorded from the two patients (**Figures 2**, **3**).

In patient 1, the amplitude of N20/P25 of the p-SEP with bilateral median nerve stimulation was larger than that of the s-SEP with unilateral median nerve stimulation. On the other hand, in patient 2, the amplitudes of N20/P25 of the p-SEP and s-SEP were of the same degree. These results suggest that left and right somatosensory pathway may have formed a connection in patient 1. Moreover, to investigate this phenomenon in more detail, we calculated and compared the average of the SEP from 1 to 250 epochs with the average of the SEP from 251 to 500 epochs (**Figures 2**, **3**). As a results, in patients 1 and 2, the amplitude of N20/P25 with continuous stimulation to the non-affected side was smaller in the second half than in the first half. In addition, in patent 2, after subtracting the CS alone condition (left median nerve stimulation) from the TS + CS condition (p-SEP), the amplitude of N20/P25 was smaller in the second half than in the first half. On the other hand, in patient 1, the amplitude of the p-SEP "(TS + CS) − CS" in the first and second half were same level. We have previously reported that continuous electrical stimulation of the median nerve decreases the amplitude of N20/P25 of the SEPs (Ishibashi et al., 2021a). This may be caused by habituation to continuous electrical stimulation, resulting in an attenuated central nervous system response to electrical stimulation. In current case report and our previous study, the patient 1 had left–right interaction after thalamic hemorrhage, and somatosensory input from the affected side interfered with the habituation of the contralateral somatosensory system, and conversely increases the response.

In mild cases of thalamus injury, the amplitude of N20/P25 of the SEP induced by the stimulation of the affected side was attenuated when the non-affected side was stimulated by vibration in the early stage (Staines et al., 2002). This indicates that patients with thalamocortical stroke have reduced ability to gate competing sensory information from the non-affected side when sensory stimulation is applied to both affected and non-affected sides. In addition, the decrease in SEPs is normalized with recovery of symptoms. Patient 1 in our case report was a severe case, and it is possible that the abnormalities in the gating mechanisms of left and right somatosensory pathway persist.

The difference between patients 1 and 2 was that patient 2 had better recovery of sensory deficits than patient 1. As for other symptoms, patient 1 had pain in the affected upper limb, but patient 2 did not complain of pain. Chronic pain caused by

the thalamic nucleus after stroke is the maladaptive plasticity of the central nervous system that constitutes a pain-related network (Willoch et al., 2004; Seghier et al., 2005; Kumar et al., 2009; Casey et al., 2012; Ohn et al., 2012; Krause et al., 2016; Nagasaka et al., 2021). Based on this information and the SEP results, it is possible that interactions between the left and right somatosensory pathways observed in a patient with thalamic hemorrhage are related to pain rather than recovery. However, the details are still unclear because other factors have not been thoroughly investigated.

This case report has several limitations. First, we were unable to identify the factors causing the interaction between the left and right somatosensory pathway in patient 1 because patients 1 and 2 had different degrees of recovery and symptoms (e.g., presence of pain) as well as different hemispheres of injury. A large body of evidence from studies on healthy individuals and patients with brain injury shows that structural and functional asymmetry exists between the left and right hemispheres of the human brain (Kinsbourne, 1977; Corbetta et al., 1993; Thiebaut de Schotten et al., 2011; Duecker and Sack, 2015; Ishii et al., 2019; Ishibashi et al., 2021b). In addition, 5 months had passed since the onset of symptoms in patient 2, and about 3 months had passed since the onset of symptoms in patient 1. Future studies involving a large number of patients are necessary to establish the presence or absence of the left–right interaction of somatosensory pathways after stroke. Second, we have not been able to identify the site where the left and right somatosensory pathways were connected. The current case report indicates that damage to the thalamus may cause neuroplasticity in the left–right interaction (e.g., left and right S1). The somatosensory input from the affected side may interfere with the habituation of the contralateral somatosensory system and conversely increase the response. Third, the blindness of evaluators of SEPs was incomplete. Finally, only patients with thalamic hemorrhage were included in this study. Further validation is needed, which can be achieved by applying the results of this study to patients with central nervous system injury.

DATA AVAILABILITY STATEMENT

The original contributions presented in the study are included in the article/supplementary material, further inquiries can be directed to the corresponding author.

ETHICS STATEMENT

This study was reviewed and approved by the Ibaraki Prefectural University of Health Sciences Review Board (approval nos. 893 and e278). The patients/participants provided their written informed consent to participate in this study. Written informed consent was obtained from the individual(s) for the publication of any potentially identifiable images or data included in this article.

AUTHOR CONTRIBUTIONS

DI, KI, KT, HY, AY, and YKo: conceptualization. DI, KI, KT, and YKa: methodology and investigation. DI, KT, and SY: formal analysis. DI: writing – original draft. KI, KT, HY, SY, YKa, AY, and YKo: writing – review and editing. All authors contributed to the article and approved the submitted version.

FUNDING

This work was supported by the JSPS KAKENHI (Nos. 18K17725 and 21H03305 to DI; and No. 19H05730 to AY) and a Grant-in-Aid for Project Research (No. 1962-1 to YKo) from the Ibaraki Prefectural University of Health Sciences.

REFERENCES

Barbay, S., Guggenmos, D. J., Nishibe, M., and Nudo, R. J. (2013). Motor representations in the intact hemisphere of the rat are reduced after repetitive training of the impaired forelimb. *Neurorehabil. Neural Repair* 27, 381–384. doi: 10.1177/1545968312465193

Bell-Krotoski, J., and Tomancik, E. (1987). The repeatability of testing with Semmes-Weinstein monofilaments. *J. Hand Surg. Am.* 12, 155–161. doi: 10.1016/s0363-5023(87)80189-2

Bell-Krotoski, J. A., Fess, E. E., Figarola, J. H., and Hiltz, D. (1995). Threshold detection and Semmes-Weinstein monofilaments. *J. Hand Ther.* 8, 155–162. doi: 10.1016/s0894-1130(12)80314-0

Brodie, S. M., Villamayor, A., Borich, M. R., and Boyd, L. A. (2014). Exploring the specific time course of interhemispheric inhibition between the human primary sensory cortices. *J. Neurophysiol.* 112, 1470–1476. doi: 10.1152/jn.00074.2014

Casey, K. L., Geisser, M., Lorenz, J., Morrow, T. J., Paulson, P., and Minoshima, S. (2012). Psychophysical and cerebral responses to heat stimulation in patients with central pain, painless central sensory loss, and in healthy persons. *Pain* 153, 331–341. doi: 10.1016/j.pain.2011.10.029

Corbetta, M., Miezin, F. M., Shulman, G. L., and Petersen, S. E. (1993). A PET study of visuospatial attention. *J. Neurosci.* 13, 1202–1226. doi: 10.1523/jneurosci.13-03-01202.1993

Courtine, G., Roy, R. R., Raven, J., Hodgson, J., Mckay, H., Yang, H., et al. (2005). Performance of locomotion and foot grasping following a unilateral thoracic corticospinal tract lesion in monkeys (*Macaca mulatta*). *Brain* 128, 2338–2358. doi: 10.1093/brain/awh604

Cruccu, G., Aminoff, M. J., Curio, G., Guerit, J. M., Kakigi, R., Mauguiere, F., et al. (2008). Recommendations for the clinical use of somatosensory-evoked potentials. *Clin. Neurophysiol.* 119, 1705–1719.

Duecker, F., and Sack, A. T. (2015). The hybrid model of attentional control: new insights into hemispheric asymmetries inferred from TMS research. *Neuropsychologia* 74, 21–29. doi: 10.1016/j.neuropsychologia.2014.11.023

Frost, S. B., Barbay, S., Friel, K. M., Plautz, E. J., and Nudo, R. J. (2003). Reorganization of remote cortical regions after ischemic brain injury: a potential substrate for stroke recovery. *J. Neurophysiol.* 89, 3205–3214. doi: 10.1152/jn.01143.2002

Hoshiyama, M., and Kakigi, R. (2002). New concept for the recovery function of short-latency somatosensory evoked cortical potentials following median nerve stimulation. *Clin. Neurophysiol.* 113, 535–541. doi: 10.1016/s1388-2457(02)00039-1

Isa, T. (2017). The Brain Is Needed to Cure Spinal Cord Injury. *Trends Neurosci.* 40, 625–636. doi: 10.1016/j.tins.2017.08.002

Ishibashi, K., Ishii, D., Yamamoto, S., Noguchi, A., Tanamachi, K., and Kohno, Y. (2020). Opposite modulations of corticospinal excitability by intermittent and

continuous peripheral electrical stimulation in healthy subjects. *Neurosci. Lett.* 740:135467.

Ishibashi, K., Ishii, D., Yamamoto, S., Noguchi, A., Tanamachi, K., and Kohno, Y. (2021a). Opposite modulations of corticospinal excitability by intermittent and continuous peripheral electrical stimulation in healthy subjects. *Neurosci. Lett.* 740:135467. doi: 10.1016/j.neulet.2020.135467

Ishibashi, K., Ishii, D., Yamamoto, S., Okamoto, Y., Wakatabi, M., and Kohno, Y. (2021b). Asymmetry of Interhemispheric Connectivity during Rapid Movements of Right and Left Hands: a TMS-EEG Study. *J. Mot. Behav.* doi: 10.1080/00222895.2021.1930993 [Epub Online ahead of print].

Ishii, D., Ishibashi, K., Yuine, H., Takeda, K., Yamamoto, S., Kaku, Y., et al. (2021). Contralateral and Ipsilateral Interactions in the Somatosensory Pathway in Healthy Humans. *Front. Syst. Neurosci.* 15:698758. doi: 10.3389/fnsys.2021.698758

Ishii, D., Takeda, K., Yamamoto, S., Noguchi, A., Ishibashi, K., Tanamachi, K., et al. (2019). Effect of Visuospatial Attention on the Sensorimotor Gating System. *Front. Behav. Neurosci.* 13:1. doi: 10.3389/fnbeh.2019.00001

Iwamura, Y., Iriki, A., and Tanaka, M. (1994). Bilateral hand representation in the postcentral somatosensory cortex. *Nature* 369, 554–556. doi: 10.1038/369554a0

Iwamura, Y., Tanaka, M., Iriki, A., Taoka, M., and Toda, T. (2002). Processing of tactile and kinesthetic signals from bilateral sides of the body in the postcentral gyrus of awake monkeys. *Behav. Brain Res.* 135, 185–190. doi: 10.1016/s0166-4328(02)00164-x

Iwamura, Y., Taoka, M., and Iriki, A. (2001). Bilateral activity and callosal connections in the somatosensory cortex. *Neuroscientist* 7, 419–429. doi: 10.1177/107385840100700511

Jerosch-Herold, C. (2005). Assessment of sensibility after nerve injury and repair: a systematic review of evidence for validity, reliability and responsiveness of tests. *J. Hand Surg. Br.* 30, 252–264. doi: 10.1016/j.jhsb.2004.12.006

Kato, J., Yamada, T., Kawaguchi, H., Matsuda, K., and Higo, N. (2020). Functional near-infrared-spectroscopy-based measurement of changes in cortical activity in macaques during post-infarct recovery of manual dexterity. *Sci. Rep.* 10:6458.

Kinsbourne, M. (1977). Hemi-neglect and hemisphere rivalry. *Adv. Neurol.* 18, 41–49.

Krause, T., Asseyer, S., Taskin, B., Floel, A., Witte, A. V., Mueller, K., et al. (2016). The Cortical Signature of Central Poststroke Pain: gray Matter Decreases in Somatosensory, Insular, and Prefrontal Cortices. *Cereb. Cortex* 26, 80–88. doi: 10.1093/cercor/bhu177

Kumar, B., Kalita, J., Kumar, G., and Misra, U. K. (2009). Central poststroke pain: a review of pathophysiology and treatment. *Anesth. Analg.* 108, 1645–1657. doi: 10.1213/ane.0b013e31819d644c

Mauguiere, F., Allison, T., Babiloni, C., Buchner, H., Eisen, A. A., Goodin, D. S., et al. (1999). Somatosensory evoked potentials. The International Federation of Clinical Neurophysiology. *Electroencephalogr. Clin. Neurophysiol. Suppl.* 52, 79–90.

Mima, T., Oga, T., Rothwell, J., Satow, T., Yamamoto, J., Toma, K., et al. (2004). Short-term high-frequency transcutaneous electrical nerve stimulation decreases human motor cortex excitability. *Neurosci. Lett.* 355, 85–88. doi: 10.1016/j.neulet.2003.10.045

Murata, Y., Higo, N., Hayashi, T., Nishimura, Y., Sugiyama, Y., Oishi, T., et al. (2015). Temporal plasticity involved in recovery from manual dexterity deficit after motor cortex lesion in macaque monkeys. *J. Neurosci.* 35, 84–95. doi: 10.1523/jneurosci.1737-14.2015

Nagasaka, K., Nemoto, K., Takashima, I., Bando, D., Matsuda, K., and Higo, N. (2021). Structural Plastic Changes of Cortical Gray Matter Revealed by Voxel-Based Morphometry and Histological Analyses in a Monkey Model of Central Post-Stroke Pain. *Cereb. Cortex* 31, 4439–4449. doi: 10.1093/cercor/bhab098

Nihashi, T., Naganawa, S., Sato, C., Kawai, H., Nakamura, T., Fukatsu, H., et al. (2005). Contralateral and ipsilateral responses in primary somatosensory cortex following electrical median nerve stimulation–an fMRI study. *Clin. Neurophysiol.* 116, 842–848. doi: 10.1016/j.clinph.2004.10.011

Noachtar, S., Luders, H. O., Dinner, D. S., and Klem, G. (1997). Ipsilateral median somatosensory evoked potentials recorded from human somatosensory cortex. *Electroencephalogr. Clin. Neurophysiol.* 104, 189–198. doi: 10.1016/s0168-5597(97)00013-0

Nudo, R. J., Wise, B. M., Sifuentes, F., and Milliken, G. W. (1996). Neural substrates for the effects of rehabilitative training on motor recovery after ischemic infarct. *Science* 272, 1791–1794. doi: 10.1126/science.272.5269.1791

Ohn, S. H., Chang, W. H., Park, C. H., Kim, S. T., Lee, J. I., Pascual-Leone, A., et al. (2012). Neural correlates of the antinociceptive effects of repetitive transcranial magnetic stimulation on central pain after stroke. *Neurorehabil. Neural Repair* 26, 344–352. doi: 10.1177/1545968311423110

Ragert, P., Nierhaus, T., Cohen, L. G., and Villringer, A. (2011). Interhemispheric interactions between the human primary somatosensory cortices. *PLoS One* 6:e16150. doi: 10.1371/journal.pone.0016150

Ramanathan, D., Conner, J. M., and Tuszynski, M. H. (2006). A form of motor cortical plasticity that correlates with recovery of function after brain injury. *Proc. Natl. Acad. Sci. U. S. A.* 103, 11370–11375.

Rosenzweig, E. S., Courtine, G., Jindrich, D. L., Brock, J. H., Ferguson, A. R., Strand, S. C., et al. (2010). Extensive spontaneous plasticity of corticospinal projections after primate spinal cord injury. *Nat. Neurosci.* 13, 1505–1510. doi: 10.1038/nn.2691

Seghier, M. L., Lazeyras, F., Vuilleumier, P., Schnider, A., and Carota, A. (2005). Functional magnetic resonance imaging and diffusion tensor imaging in a case of central poststroke pain. *J. Pain* 6, 208–212.

Staines, W. R., Black, S. E., Graham, S. J., and Mcilroy, W. E. (2002). Somatosensory gating and recovery from stroke involving the thalamus. *Stroke* 33, 2642–2651.

Thiebaut de Schotten, M., Dell'acqua, F., Forkel, S. J., Simmons, A., Vergani, F., Murphy, D. G., et al. (2011). A lateralized brain network for visuospatial attention. *Nat. Neurosci.* 14, 1245–1246.

Willoch, F., Schindler, F., Wester, H. J., Empl, M., Straube, A., Schwaiger, M., et al. (2004). Central poststroke pain and reduced opioid receptor binding within pain processing circuitries: a [11C]diprenorphine PET study. *Pain* 108, 213–220.

Yamamoto, T., Hayashi, T., Murata, Y., Ose, T., and Higo, N. (2019). Premotor Cortical-Cerebellar Reorganization in a Macaque Model of Primary Motor Cortical Lesion and Recovery. *J. Neurosci.* 39, 8484–8496.

Conflict of Interest: The authors declare that the research was conducted in the absence of any commercial or financial relationships that could be construed as a potential conflict of interest.

Publisher's Note: All claims expressed in this article are solely those of the authors and do not necessarily represent those of their affiliated organizations, or those of the publisher, the editors and the reviewers. Any product that may be evaluated in this article, or claim that may be made by its manufacturer, is not guaranteed or endorsed by the publisher.

Copyright © 2021 Ishii, Ishibashi, Takeda, Yuine, Yamamoto, Kaku, Yozu and Kohno. This is an open-access article distributed under the terms of the Creative Commons Attribution License (CC BY). The use, distribution or reproduction in other forums is permitted, provided the original author(s) and the copyright owner(s) are credited and that the original publication in this journal is cited, in accordance with accepted academic practice. No use, distribution or reproduction is permitted which does not comply with these terms.

frontiers in Systems Neuroscience

MINI REVIEW
published: 08 November 2021
doi: 10.3389/fnsys.2021.760311

Non-human Primate Models to Explore the Adaptive Mechanisms After Stroke

*Noriyuki Higo**

Human Informatics and Interaction Research Institute, National Institute of Advanced Industrial Science and Technology, Tsukuba, Japan

The brain has the ability to reconstruct neural structures and functions to compensate for the brain lesions caused by stroke, although it is highly limited in primates including humans. Animal studies in which experimental lesions were induced in the brain have contributed to the current understanding of the neural mechanisms underlying functional recovery. Here, I have highlighted recent advances in non-human primate models using primate species such as macaques and marmosets, most of which have been developed to study the mechanisms underlying the recovery of motor functions after stroke. Cortical lesion models have been used to investigate motor recovery after lesions to the cortical areas involved in movements of specific body parts. Models of a focal stroke at the posterior internal capsule have also been developed to bridge the gap between the knowledge obtained by cortical lesion models and the development of intervention strategies because the severity and outcome of motor deficits depend on the degree of lesions to the region. This review will also introduce other stroke models designed to study the plastic changes associated with development and recovery from cognitive and sensory impairments. Although further validation and careful interpretation are required, considering the differences between non-human primate brains and human brains, studies using brain-lesioned non-human primates offer promise for improving translational outcomes.

Keywords: brain lesions, functional recovery, macaque monkey, marmoset, pain, plasticity, rehabilitation, voluntary movements

OPEN ACCESS

Edited by:
Belén Rubio Ballester, Institute for Bioengineering of Catalonia (IBEC), Spain

Reviewed by:
Jihane Homman-Ludiye, Monash University, Australia
Riki Matsumoto, Kobe University, Japan

***Correspondence:**
Noriyuki Higo
n.higo@aist.go.jp

Received: *18 August 2021*
Accepted: *20 October 2021*
Published: *08 November 2021*

Citation:
Higo N (2021) Non-human Primate Models to Explore the Adaptive Mechanisms After Stroke. Front. Syst. Neurosci. 15:760311. doi: 10.3389/fnsys.2021.760311

INTRODUCTION

The regeneration of lost neural circuitry after stroke, the most frequent cause of brain lesions, is poor because mature neurons do not divide to replace the lost neurons and also because the presence of inhibitory factors prevents functional and structural recovery of the lesioned neuronal tissue (Buchli and Schwab, 2005; Galtrey and Fawcett, 2007). Nevertheless, functional recovery often occurs in patients with stroke and physical and cognitive deficits. In addition to the acute management of stroke to prevent the expansion of irreversible tissue lesions, rehabilitation treatment during the subacute and chronic phases is important to promote functional recovery. Plastic changes of the nervous system and functional compensation in the remaining intact brain areas are thought to underlie the functional recovery after brain lesions, and the concept of neurorehabilitation, which focuses on enhancing plasticity following brain lesions, has

received considerable attention over the past decades. However, for the development of effective neurorehabilitation strategies, the functional compensation mechanisms should be elucidated in detail. In addition to clinical studies in stroke patients, studies using animal models in which lesions are experimentally induced in the brain have made major contributions in this research field. Experimental animals can be used to investigate the micro- and macroscopic changes that occur during functional recovery after stroke, including the changes involving gene and protein expression, nervous system structures, and brain activity. Rodents such as mice and rats are the most commonly used vertebrates in biomedical research because of their low cost and ease of genetic manipulation. However, in addition to studies using rodents, investigations using non-human primates such as macaques and marmosets are likely to facilitate translational outcomes because of the proximity of these primates to humans in terms of genetics, anatomy, physiology, and behavior (Kuypers, 1982; Alstermark et al., 2004; Courtine et al., 2007; Isa et al., 2007; Lemon, 2008; Yamamoto et al., 2013; Higo, 2014). Especially, the similarity in the pattern of myelination (Van Essen et al., 2019) is essential because the debris of myelin is produced after stroke and they are toxic to neurons (Marin and Carmichael, 2019). Moreover, recent comparative transcriptomic studies have reported higher genetic similarities in both neurons and microglia among primates as compared to rodents (Geirsdottir et al., 2019; Krienen et al., 2020). This review highlights recent advances in the development of non-human primate models used to explore the adaptive mechanisms after stroke.

PRIMATE SPECIES

Macaque monkeys, a genus of Old World monkeys that include rhesus monkeys (*Macaca mulatta*), Japanese monkeys (*Macaca fuscata*), and cynomolgus monkeys (*Macaca fascicularis*), are the most commonly used group of primate species in this research field, although other Old World monkeys, such as olive baboons (*Papio anubis*) and vervet monkeys (*Chlorocebus pygerythrus*), have also been used historically (Vilensky and Gilman, 2002). Old World monkeys have a gyrencephalic brain, i.e., brains with a highly folded cortex (**Table 1**), and cortical and subcortical anatomy similar to that in humans. The neuronal structures of the motor cortex and corticospinal tract of these monkeys are especially more compatible with humans than the other experimental primate species described below (Kuypers, 1982; Alstermark et al., 2004; Courtine et al., 2007; Isa et al., 2007; Lemon, 2008). The combination of this homology of the motor system with the relatively large brains enables acquisition of imaging data on par with those evaluated in clinical research. Macaque monkeys and other Old World monkeys are highly dexterous and capable of precision grip, which is exemplified by the ability to hold small objects between the tips of the index finger and the thumb (**Table 1**) (Heffner and Masterton, 1975). The common marmoset (*Callithrix jacchus*), a small New World monkey species, has also been used as an animal model. Although common marmosets show a lower degree of dexterity than macaque monkeys, as characterized by the absence of a precision grip (**Table 1**) (Heffner and Masterton, 1975), their small body size makes them easy to handle. In addition, the brain of common marmosets has a smaller number of cortical sulci, which is referred to as the lissencephalic brain. This characteristic provides advantages over the macaque monkey in experiments such as electrophysiological recording and cortical surface imaging. Moreover, genetic engineering techniques have gradually become applicable to common marmosets (Sasaki et al., 2009). Squirrel monkeys (*Saimiri sciureus*) and capuchin monkeys (*Cebus apella*) are New World monkey species classified as lissencephalic and gyrencephalic primates, respectively (**Table 1**). Their body sizes are larger than those of common marmosets and smaller than those of macaques. Capuchin monkeys are highly dexterous and use a precision grip, whereas squirrel monkeys have moderately dexterous hands with pseudo-opposable thumbs that can be opposed to the side of the index finger (Heffner and Masterton, 1975). Differences in the extent of corticospinal terminations within the ventral horn are thought to underlie the differences in dexterity between squirrel and capuchin monkeys (Bortoff and Strick, 1993). The species of non-human primates should be selected depending on the purpose of the research. Comparison of the recovery after brain lesions among the different primate species will provide information on how difference in neuronal structures affects the adaptability, which is essential for extrapolating findings obtained by animal studies to human patients. The comparison is, however, difficult at present because the size and location of lesions are highly variable among studies depending on methods of lesion induction as described in the next section. Induction of controlled focal lesions to a specific brain region will enable the comparison among different species.

TABLE 1 | Non-human primate species used to investigate adaptive mechanisms after stroke.

Species	Body weight (kg)*	Gyrification**	Precision grip
Rhesus monkey	8.3	Gyrencephalic	Capable
Japanese monkey	9.9	Gyrencephalic	Capable
Cynomolgus monkey	4.7	Gyrencephalic	Capable
Olive baboon	25.0	Gyrencephalic	Capable
Vervet monkey	4.0	Gyrencephalic	Capable
Common marmoset	0.4	Lissencephalic	Incapable
Squirrel monkey	0.8	Lissencephalic	Incapable
Capuchin monkey	1.3	Gyrencephalic	Capable

**The information of the average body weight is referred from the articles (Heffner and Masterton, 1975; Bonadio, 2000; Fooden and Aimi, 2005).*
***Images of cerebral cortex of the non-human primates can be viewed in the article (Gonzales et al., 2015).*

METHODS OF LESION INDUCTION

Since more than 100 years ago, experimental lesions have been made in the motor cortex of macaque monkeys by using various methods such as subpial aspiration, electric thermocautery, and excision with scalpel, and subsequent motor recovery has been investigated (Ogden and Franz, 1917; Travis and Woolsey, 1956; Passingham et al., 1983;

Liu and Rouiller, 1999; Vilensky and Gilman, 2002). Because of the presence of a topographically organized map of body parts in the primary motor cortex, which is often identified by intracortical microstimulation techniques (Stoney et al., 1968; Kwan et al., 1978; Higo et al., 2016), it is possible to create a lesion in the cortical areas involved in movements of specific body parts. In recent decades, ibotenic acid, which selectively excites and destroys cell bodies (Curtis et al., 1979), has also been used to create specific gray matter lesions without damaging the white matter (Liu and Rouiller, 1999; Murata et al., 2008, 2015a,b; Yamamoto et al., 2019). However, the pathophysiology of these lesion models may differ from that of stroke patients because the stroke is caused by a blood clot or bleeding, *i.e.,* ischemic and hemorrhagic strokes, respectively. To imitate ischemic stroke, electrocoagulation techniques have been used to occlude the superficial blood vessels supplying the motor cortex (Nudo et al., 1996; Frost et al., 2003; Dancause et al., 2005, 2006). Photothrombotic stroke is another model of superficial blood vessel occlusion (Ikeda et al., 2013; Khateeb et al., 2019). In this method, hydrophilic dyes, such as Rose Bengal, induce platelet aggregation and occlusion of microvessels by light exposure, impairing blood flow within the area exposed to light (Jourdan et al., 1995; Saniabadi et al., 1995). In addition, focal cerebral ischemia was induced in the visual cortex of marmoset through intracortical injections of endothelin-1 (Teo and Bourne, 2014), a vasoconstrictor peptide (Yanagisawa et al., 1988).

Clinically, the middle cerebral artery (MCA) is the most common artery involved in stroke (Nogles and Galuska, 2021). To reproduce the pathology of MCA occlusion, arterial blockade can be induced in the MCA of macaque monkeys by using various methods, including occlusion by a clip or ligature, intra-arterial insertion of filaments or catheters, injection of endothelin-1, or electrocoagulation (Frykholm et al., 2000; Enblad et al., 2001; Virley et al., 2004; Sasaki et al., 2011; Yin et al., 2013; Mcentire et al., 2016; Fan et al., 2017; Yeo et al., 2019). These MCA occlusion models show behavioral and motor function deficits that resemble those seen in stroke patients and are characterized by a relatively large volume of brain lesions, although the volume of lesions differs depending on the nature (permanent or transient), duration, and position of the occlusion. Therefore, MCA occlusion models are associated with a high risk of mortality, and even if the animals do not die, their functional recovery is generally limited because of the severe brain lesions. Although these MCA occlusion models have contributed to the development of strategies for preventing the expansion of irreversible tissue lesions in the acute phase of cerebral infarction, most MCA occlusion models are not ideal for investigating the plastic changes associated with recovery of function by rehabilitation treatments. To investigate the recovery mechanisms after stroke, a smaller focal stroke was induced in the posterior internal capsule, which carries the corticospinal tracts. In comparison with models involving motor cortex lesions, capsular infarct models are expected to be useful for exploring key factors that regulate motor recovery after infarcts in stroke patients because the severity and outcome of motor deficits depend on the degree of lesions to the region (Wenzelburger et al., 2005; Schiemanck et al., 2008; Rosso et al., 2011). In the marmoset capsular infarct model, electrocoagulation was performed in the anterior choroidal artery, which irrigates the internal capsule (Puentes et al., 2015). On the other hand, in the macaque model, focal infarcts were induced at the posterior internal capsule by injection of endothelin-1 (**Figure 1A**) (Murata and Higo, 2016). Hemorrhage, another major cause of stroke, has also been induced by the injection of collagenase type IV, which disrupts the basal lamina of blood vessels (Rosenberg et al., 1990), into the posterior internal capsule of macaque monkeys.

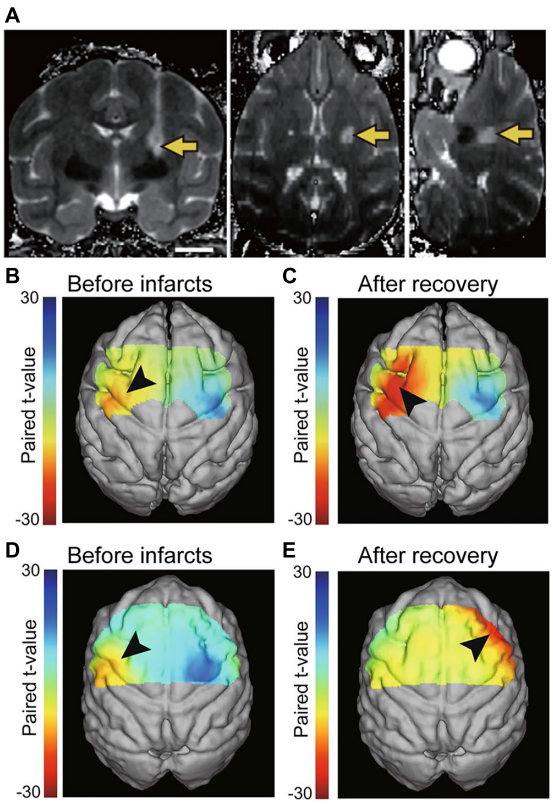

FIGURE 1 | (A) T2-weighted MRI showing the location of infarcts in the posterior internal capsule one day after endothelin-1 injection (coronal, axial, and sagittal images). The arrows indicate the infarct. Scale bars = 10 mm. Reproduced from **Figure 1** of the study by Murata and Higo (2016). **(B–E)** Brain activation during voluntary hand movements before infarcts **(B,D)** and after motor recovery from the internal capsular infarcts. Before infarcts, focal activation was observed in the hand area of the primary motor cortex (arrowhead in **B,D**). After motor recovery, increased activation of the premotor area was identified (arrowhead in **C,E**). The cortex contralateral to the stroke plays a greater role in recovery when lesions are more severe **(E)**. Reproduced from Figures 2, 4 of the study by Kato et al. (2020b).

MOTOR DYSFUNCTION AND RECOVERY

Most brain-lesioned non-human primates have been used to study the mechanisms underlying deficits and recovery of motor function after stroke. This is because severe motor deficits are the predominant cause of long-term disability, and motor recovery is the most crucial aspect influencing the quality of

life of stroke survivors. Another reason is the experimental ease; objective evaluations of motor performance are more accessible than those of other brain functions. Studies using the motor cortex lesion models described above have indicated recovery of motor performance after paralysis, and therefore the models have been used to investigate mechanisms of motor recovery after lesions to specific brain regions. To date, compensatory changes in brain activity during voluntary movements, movement representations, projections, and gene expression in the motor cortex are reported in such motor cortex lesioned models (Nudo et al., 1996; Liu and Rouiller, 1999; Frost et al., 2003; Dancause et al., 2005, 2006 #17; Murata et al., 2008, 2015a,b; Yamamoto et al., 2019).

A recent study used the macaque model of internal capsular infarcts to report compensatory changes in motor cortical activity during voluntary movements (**Figures 1B,C**) (Kato et al., 2020b). Similar changes in motor cortical activity have also been reported in stroke patients during motor recovery (Loubinoux et al., 2007; Horn et al., 2016); therefore, the macaque internal capsular infarct model is thought to reproduce the plastic neural changes that occur in stroke patients. Especially, the results of the macaque model of internal capsular infarcts are consistent with stroke patients in that the cortex contralateral to stroke plays a greater role in recovery when lesions are more severe (**Figures 1D,E**) (Johansen-Berg et al., 2002; Schaechter and Perdue, 2008; Bestmann et al., 2010; Rehme et al., 2011; Bradnam et al., 2012; Kantak et al., 2012; Bajaj et al., 2016; Touvykine et al., 2016; Dodd et al., 2017). Uncovering compensatory mechanisms that occur in the contralesional hemisphere will contribute to understanding hyper-adaptability of the brain, i.e., dynamic reconstruction of the neural structure to compensate for the loss of neural function due to brain lesions. Moreover, brain imaging technologies to monitor brain activity changes in both hemispheres after stroke will be useful to estimate the progress of rehabilitation on functional recovery of stroke patients.

COGNITIVE AND SENSORY DYSFUNCTIONS

Stroke patients usually show deficits in multiple functions, including cognitive and sensory functions; therefore, development of relevant animal models that reproduce these deficits is desirable. The anatomical structures and functions involved in cognitive processing in non-human primates are also more similar to those in humans than in rodents. For

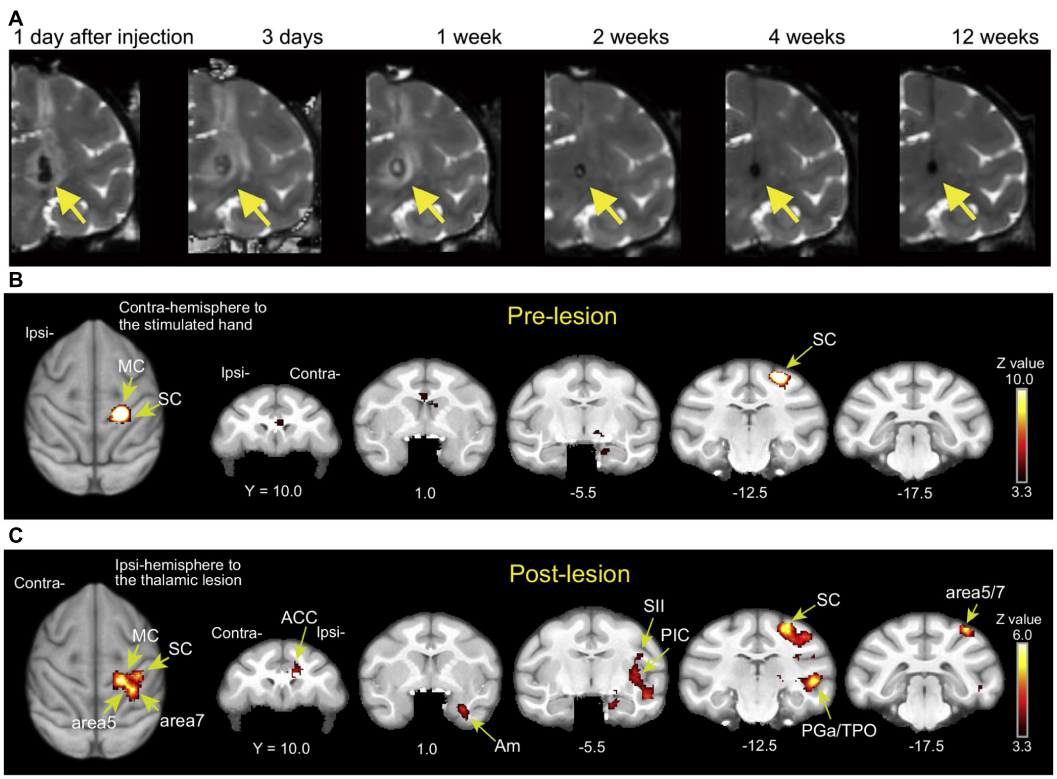

FIGURE 2 | (A) T2-weighted MRI showing the time course of hemorrhagic stroke after collagenase type IV induction (coronal images). A hematoma and edema were seen as the hypointense stroke core in the VPL of the thalamus (arrows) and the surrounding hyperintense rim. Reproduced from **Figure 1** of the study by Nagasaka et al. (2017). **(B,C)** Brain activity changes associated with CPSP. Brain activity associated with mechanical stimulation to the hand contralateral to the lesioned hemisphere (or the corresponding hand before stroke) during the pre-lesion and post-lesion periods when CPSP was developed. ACC, anterior cingulate cortex; Am, amygdala; MC, primary motor cortex; PGa, anterior subdivisions of the angular gyrus; PIC, posterior insular cortex; SC, primary somatosensory cortex; SII, secondary somatosensory cortex; TPO, temporo-parieto-occipital junction. Reproduced from **Figure 3** of the study by Nagasaka et al. (2020).

example, macaques and humans share homologous anatomical and physiological features of the prefrontal cortex, whereas no obvious homologous areas of the prefrontal cortex are found in rodents (Preuss, 1995; Ongur and Price, 2000). The sensory processing system of non-human primates is also more similar to that of humans than those of rodents; for example, the primary somatosensory cortex is well developed in macaque monkeys and clearly differentiated into four subdivisions (areas 3a, 3b, 1, and 2), which are not observed in rodents (Kaas, 2004). Therefore, brain-lesioned non-human primate models designed to study plastic changes associated with the development of and recovery from both cognitive and sensory impairments have also been sought to improve translational outcomes of treating cognitive disorders after physical brain lesions.

In comparison with rodents, non-human primates have a higher potential to perform complex tasks requiring higher cognitive skills, such as planning, decision-making, and problem-solving, and cognitive dysfunction after stroke can be assessed by the performance on cognitive tasks using apparatus such as the touchscreen-equipped operant chamber. To date, cognitive and motor dysfunctions have been assessed in MCA occlusion models with a relatively large volume of brain lesions. One study using an MCA occlusion model in macaque monkeys reported a decline in motor-planning ability for the non-paretic extremity (Roitberg et al., 2003). The marmoset MCA occlusion model also exhibited a neglect of the contralesional side of space (Marshall and Ridley, 2003), which is similar to hemispatial neglect syndrome seen in stroke patients. Hemispatial neglect has also been reproduced in macaque monkeys by inducing reversible lesions of the parietal cortex using the $GABA_A$ receptor agonist muscimol (Kubanek et al., 2015). These models are important for developing effective neurorehabilitation strategies because hemispatial neglect is a common disabling condition following stroke. However, the studies to date have not addressed the neurological mechanisms underlying both development of and recovery from hemispatial neglect, necessitating further investigation to obtain knowledge for treating cognitive impairment in stroke patients.

Pain is a complex phenomenon that involves sensory, cognitive, and emotional neuronal processing. Pathological pain commonly occurs after stroke and is referred to as central post-stroke pain (CPSP). CPSP occurs over a variable period, usually weeks to months, after stroke in the thalamic nucleus and other areas involved in the somatosensory pathways (Kumar et al., 2009; Hosomi et al., 2015). A dominant theory of the pathophysiology underlying this pain condition is the maladaptive plasticity of the central nervous system, which constitutes a pain-related network. Identification of CPSP-associated plastic changes in the brain can therefore facilitate an understanding of both the pathogenetic mechanism and the therapeutic strategy. In the macaque model of CPSP (Nagasaka et al., 2017), a hemorrhagic stroke lesion was created by injection of collagenase type IV into the ventral posterolateral nucleus (VPL) of the thalamus, which relays somatosensory information (**Figure 2A**). Behavioral analysis indicated that this model reproduces late-onset allodynia and hyperalgesia similar to those observed in human patients over several weeks and more following the stroke, and both the withdrawal threshold for mechanical stimulation and the withdrawal latency for thermal stimulation on the hand contralateral to the lesioned hemisphere are significantly decreased relative to those before the stroke induction (Nagasaka et al., 2017). A functional MRI study in the macaque CPSP model showed changes in somatosensory stimuli-induced brain activation, which is similar to the findings observed in CPSP patients (**Figures 2B,C**) (Peyron et al., 1998; Seghier et al., 2005; Ducreux et al., 2006; Ohn et al., 2012; Nagasaka et al., 2020). The brain activation, combined with behavioral results, indicated that the macaque CPSP model faithfully reproduces the pain in CPSP patients. Using the macaque CPSP model, a recent study indicated that a significant reduction in synaptic terminals in pain-related cortical areas is associated with the development of CPSP (Nagasaka et al., 2021). Another recent study using the macaque CPSP model showed that functional connectivity is inappropriately strengthened between the mediodorsal nucleus of the thalamus and the amygdala, which are thought to be involved in the emotional aspects of pain, and that repetitive transcranial magnetic stimulation (rTMS) over the primary motor cortex normalizes this strengthened connectivity (Kadono et al., 2021).

CONCLUDING REMARKS

Investigations of the adaptive mechanisms after stroke using non-human primate models are ongoing, as described above. Further elucidation of these mechanisms may facilitate the development of novel and innovative therapeutic approaches for stroke patients. Non-human primate models are also used to evaluate the clinical efficacy of existing drugs and other therapeutic interventions. Although rodents are the most commonly used vertebrate species in biomedical research, drugs and therapeutics that were proven to be effective in rodent models frequently failed clinical trials (Endres et al., 2008). In addition to the previously described differences in the anatomical structures and functions of the brain between primates and rodents, these models have also shown differences in the post-lesion responses in studies using brain-lesioned animals. For example, the time course of the proliferation of macrophages/microglia after brain lesions as well as their function has been suggested to differ between macaques and rodents (Wang et al., 2013; Nagasaka et al., 2017; Yeo et al., 2019; Yew et al., 2019; Kato et al., 2020a). Moreover, neurogenesis is robustly induced in response to stroke in rodents, whereas neurogenesis after stroke is much lower in non-human primates (Liu et al., 1998; Kee et al., 2001; Tonchev et al., 2003). The time course of macrophage/microglia proliferation as well as the low rates of neurogenesis after brain lesions in non-human primates are consistent with those reported in human stroke patients (Thiel et al., 2010; Huttner et al., 2014). A recent study also reported that responses of astrocytes, another crucial player in the pathogenesis of brain lesions, to stroke differ between rodents and primates (Boghdadi et al., 2020). These differences between rodents and primates may underlie failures in clinical trials.

The results of brain imaging studies, in which activity changes during motor recovery and CPSP development are consistent between macaque stroke models and stroke patients as described

above (Loubinoux et al., 2007; Horn et al., 2016; Kato et al., 2020b), may indicate the high translational potential of the primate models. Notably, however, the brains of non-human primates are still different from human brains. For example, MRI tractography analysis showed differences in the frontal network anatomy between humans and non-human primate species, including macaque monkeys (Barrett et al., 2020), and transcriptome analyses have indicated differences in gene expression between human and non-human primate brains (Bakken et al., 2016; He et al., 2017). Although further validation and careful interpretation of these findings are required, studies using brain-lesioned non-human primates have the potential to improve translational outcomes.

AUTHOR CONTRIBUTIONS

The author confirms sole responsibility for the conception and preparation of this review.

FUNDING

This work was supported by a Grant-in-Aid for Scientific Research on Innovative Areas "Hyper-adaptability for overcoming body-brain dysfunction: Integrated empirical and system theoretical approaches" (No. 20H05490) from the Ministry of Education, Culture, Sports, Science and Technology, Japan.

REFERENCES

Alstermark, B., Ogawa, J., and Isa, T. (2004). Lack of monosynaptic corticomotoneuronal EPSPs in rats: disynaptic EPSPs mediated via reticulospinal neurons and polysynaptic EPSPs via segmental interneurons. *J. Neurophysiol.* 91, 1832–1839. doi: 10.1152/jn.00820.2003

Bajaj, S., Housley, S. N., Wu, D., Dhamala, M., James, G. A., and Butler, A. J. (2016). Dominance of the Unaffected Hemisphere Motor Network and Its Role in the Behavior of Chronic Stroke Survivors. *Front. Hum. Neurosci.* 10:650. doi: 10.1371/journal.pone.0154752

Bakken, T. E., Miller, J. A., Ding, S. L., Sunkin, S. M., Smith, K. A., Ng, L., et al. (2016). A comprehensive transcriptional map of primate brain development. *Nature* 535, 367–375.

Barrett, R. L. C., Dawson, M., Dyrby, T. B., Krug, K., Ptito, M., D'arceuil, H., et al. (2020). Differences in Frontal Network Anatomy Across Primate Species. *J. Neurosci.* 40, 2094–2107. doi: 10.1523/jneurosci.1650-18.2019

Bestmann, S., Swayne, O., Blankenburg, F., Ruff, C. C., Teo, J., Weiskopf, N., et al. (2010). The role of contralesional dorsal premotor cortex after stroke as studied with concurrent TMS-fMRI. *J. Neurosci.* 30, 11926–11937. doi: 10.1523/JNEUROSCI.5642-09.2010

Boghdadi, A. G., Spurrier, J., Teo, L., Li, M., Skarica, M., Cao, B., et al. (2020). Primate-specific response of astrocytes to stroke limits peripheral macrophage infiltration. *Biorxiv* 083501. doi: 10.1101/2020.05.08.083501

Bonadio, C. (2000). *Macaca Fascicularis*. Animal Diversity Web. Available online at: http://animaldiversity.org/accounts/Macaca_fascicularis/ (accessed September 27, 2021).

Bortoff, G. A., and Strick, P. L. (1993). Corticospinal terminations in two new-world primates: further evidence that corticomotoneuronal connections provide part of the neural substrate for manual dexterity. *.J Neurosci.* 13, 5105–5118. doi: 10.1523/JNEUROSCI.13-12-05105.1993

Bradnam, L. V., Stinear, C. M., Barber, P. A., and Byblow, W. D. (2012). Contralesional hemisphere control of the proximal paretic upper limb following stroke. *Cereb. Cortex* 22, 2662–2671. doi: 10.1093/cercor/bhr344

Buchli, A. D., and Schwab, M. E. (2005). Inhibition of Nogo: a key strategy to increase regeneration, plasticity and functional recovery of the lesioned central nervous system. *Ann. Med.* 37, 556–567. doi: 10.1080/07853890500407520

Courtine, G., Bunge, M. B., Fawcett, J. W., Grossman, R. G., Kaas, J. H., Lemon, R., et al. (2007). Can experiments in nonhuman primates expedite the translation of treatments for spinal cord injury in humans? *Nat. Med.* 13, 561–566. doi: 10.1038/nm1595

Curtis, D. R., Lodge, D., and Mclennan, H. (1979). The excitation and depression of spinal neurones by ibotenic acid. *J. Physiol.* 291, 19–28. doi: 10.1113/jphysiol.1979.sp012796

Dancause, N., Barbay, S., Frost, S. B., Plautz, E. J., Chen, D., Zoubina, E. V., et al. (2005). Extensive cortical rewiring after brain injury. *J. Neurosci.* 25, 10167–10179. doi: 10.1523/jneurosci.3256-05.2005

Dancause, N., Barbay, S., Frost, S. B., Zoubina, E. V., Plautz, E. J., Mahnken, J. D., et al. (2006). Effects of small ischemic lesions in the primary motor cortex on neurophysiological organization in ventral premotor cortex. *J. Neurophysiol.* 96, 3506–3511. doi: 10.1152/jn.00792.2006

Dodd, K. C., Nair, V. A., and Prabhakaran, V. (2017). Role of the Contralesional vs. Ipsilesional Hemisphere in Stroke Recovery. *Front. Hum. Neurosci.* 11:469. doi: 10.3389/fnhum.2017.00469

Ducreux, D., Attal, N., Parker, F., and Bouhassira, D. (2006). Mechanisms of central neuropathic pain: a combined psychophysical and fMRI study in syringomyelia. *Brain* 129, 963–976. doi: 10.1093/brain/awl016

Enblad, P., Frykholm, P., Valtysson, J., Silander, H. C. S., Andersson, J., Fasth, K. J., et al. (2001). Middle cerebral artery occlusion and reperfusion in primates monitored microdialysis and sequential positron emission tomography. *Stroke* 32, 1574–1580. doi: 10.1161/01.str.32.7.1574

Endres, M., Engelhardt, B., Koistinaho, J., Lindvall, O., Meairs, S., Mohr, J. P., et al. (2008). Improving outcome after stroke: overcoming the translational roadblock. *Cerebrovasc. Dis.* 25, 268–278. doi: 10.1159/000118039

Fan, J., Li, Y., Fu, X., Li, L., Hao, X., and Li, S. (2017). Nonhuman primate models of focal cerebral ischemia. *Neural. Regen. Res.* 12, 321–328. doi: 10.4103/1673-5374.200815

Fooden, J., and Aimi, M. (2005). Systematic review of Japanese macaques, *Macaca fuscata*. *Field. Zool.* 104, 1–198.

Frost, S. B., Barbay, S., Friel, K. M., Plautz, E. J., and Nudo, R. J. (2003). Reorganization of remote cortical regions after ischemic brain injury: a potential substrate for stroke recovery. *J. Neurophysiol.* 89, 3205–3214. doi: 10.1152/jn.01143.2002

Frykholm, P., Andersson, J. L. R., Valtysson, J., Silander, H. C., Hillered, L., Persson, L., et al. (2000). A metabolic threshold of irreversible ischemia demonstrated by PET in a middle cerebral artery occlusion-reperfusion primate model. *Acta Neurol. Scand.* 102, 18–26. doi: 10.1034/j.1600-0404.2000.102001018.x

Galtrey, C. M., and Fawcett, J. W. (2007). The role of chondroitin sulfate proteoglycans in regeneration and plasticity in the central nervous system. *Brain Res. Rev.* 54, 1–18. doi: 10.1016/j.brainresrev.2006.09.006

Geirsdottir, L., David, E., Keren-Shaul, H., Weiner, A., Bohlen, S. C., Neuber, J., et al. (2019). Cross-Species Single-Cell Analysis Reveals Divergence of the Primate Microglia Program. *Cell* 179, 1609–1622.e16.

Gonzales, L. A., Benefit, B. R., Mccrossin, M. L., and Spoor, F. (2015). Cerebral complexity preceded enlarged brain size and reduced olfactory bulbs in Old World monkeys. *Nat. Commun.* 6:7580. doi: 10.1038/ncomms8580

He, Z., Han, D., Efimova, O., Guijarro, P., Yu, Q., Oleksiak, A., et al. (2017). Comprehensive transcriptome analysis of neocortical layers in humans, chimpanzees and macaques. *Nat. Neurosci.* 20, 886–895. doi: 10.1038/nn.4548

Heffner, R., and Masterton, B. (1975). Variation in form of the pyramidal tract and its relationship to digital dexterity. *Brain Behav. Evo.l* 12, 161–200. doi: 10.1159/000124401

Higo, N. (2014). Effects of rehabilitative training on recovery of hand motor function: a review of animal studies. *Neurosci. Res.* 78, 9–15. doi: 10.1016/j.neures.2013.09.008

Higo, N., Kunori, N., and Murata, Y. (2016). Neural Activity during Voluntary Movements in Each Body Representation of the Intracortical Microstimulation-Derived Map in the Macaque Motor Cortex. *PLoS One* 11:e0160720. doi: 10.1371/journal.pone.0160720

Horn, U., Roschka, S., Eyme, K., Walz, A. D., Platz, T., and Lotze, M. (2016). Increased ventral premotor cortex recruitment after arm training in an fMRI study with subacute stroke patients. *Behav. Brain Res.* 308, 152–159. doi: 10.1016/j.bbr.2016.04.040

Hosomi, K., Seymour, B., and Saitoh, Y. (2015). Modulating the pain network–neurostimulation for central poststroke pain. *Nat. Rev. Neurol.* 11, 290–299. doi: 10.1038/nrneurol.2015.58

Huttner, H. B., Bergmann, O., Salehpour, M., Racz, A., Tatarishvili, J., Lindgren, E., et al. (2014). The age and genomic integrity of neurons after cortical stroke in humans. *Nat. Neurosci.* 17, 801–803. doi: 10.1038/nn.3706

Ikeda, S., Harada, K., Ohwatashi, A., Kamikawa, Y., Yoshida, A., and Kawahira, K. (2013). A new non-human primate model of photochemically induced cerebral infarction. *PLoS One* 8:e60037. doi: 10.1371/journal.pone.0060037

Isa, T., Ohki, Y., Alstermark, B., Pettersson, L. G., and Sasaki, S. (2007). Direct and indirect cortico-motoneuronal pathways and control of hand/arm movements. *Physiology* 22, 145–152. doi: 10.1152/physiol.00045.2006

Johansen-Berg, H., Rushworth, M. F., Bogdanovic, M. D., Kischka, U., Wimalaratna, S., and Matthews, P. M. (2002). The role of ipsilateral premotor cortex in hand movement after stroke. *Proc. Natl. Acad. Sci. U. S. A.* 99, 14518–14523. doi: 10.1073/pnas.222536799

Jourdan, A., Aguejouf, O., Imbault, P., Doutremepuich, F., Inamo, J., and Doutremepuich, C. (1995). Experimental thrombosis model induced by free radicals. Application to aspirin and other different substances. *Thromb. Res.* 79, 109–123. doi: 10.1016/0049-3848(95)91519-q

Kaas, J. H. (2004). Evolution of the large, complex sensorimotor systems of anthropoid primates. *Int. J. Comp. Psychol.* 17, 34–52.

Kadono, Y., Koguchi, K., Okada, K. I., Hosomi, K., Hiraishi, M., Ueguchi, T., et al. (2021). Repetitive transcranial magnetic stimulation restores altered functional connectivity of central poststroke pain model monkeys. *Sci. Rep.* 11:6126. doi: 10.1038/s41598-021-85409-w

Kantak, S. S., Stinear, J. W., Buch, E. R., and Cohen, L. G. (2012). Rewiring the brain: potential role of the premotor cortex in motor control, learning, and recovery of function following brain injury. *Neurorehabil. Neural. Repair* 26, 282–292. doi: 10.1177/1545968311420845

Kato, J., Murata, Y., Takashima, I., and Higo, N. (2020a). Time- and area-dependent macrophage/microglial responses after focal infarction of the macaque internal capsule. *Neurosci. Res.* 170, 350–359. doi: 10.1016/j.neures.2020.12.001

Kato, J., Yamada, T., Kawaguchi, H., Matsuda, K., and Higo, N. (2020b). Functional near-infrared-spectroscopy-based measurement of changes in cortical activity in macaques during post-infarct recovery of manual dexterity. *Sci. Rep.* 10:6458. doi: 10.1038/s41598-020-63617-0

Kee, N. J., Preston, E., and Wojtowicz, J. M. (2001). Enhanced neurogenesis after transient global ischemia in the dentate gyrus of the rat. *Exp. Brain Res.* 136, 313–320. doi: 10.1007/s002210000591

Khateeb, K., Yao, Z., Kharazia, V. N., Burunova, E. P., Song, S., Wang, R., et al. (2019). A Practical Method for Creating Targeted Focal Ischemic Stroke in the Cortex of Nonhuman Primates. *Annu. Int. Conf. IEEE Eng. Med. Biol. Soc.* 2019, 3515–3518. doi: 10.1109/EMBC.2019.8857741

Krienen, F. M., Goldman, M., Zhang, Q., Del Rosario, C. H. R., Florio, M., Machold, R., et al. (2020). Innovations present in the primate interneuron repertoire. *Nature* 586, 262–269. doi: 10.1038/s41586-020-2781-z

Kubanek, J., Li, J. M., and Snyder, L. H. (2015). Motor role of parietal cortex in a monkey model of hemispatial neglect. *Proc. Natl. Acad. Sci. U. S. A.* 112, E2067–E2072. doi: 10.1073/pnas.1418324112

Kumar, B., Kalita, J., Kumar, G., and Misra, U. K. (2009). Central poststroke pain: a review of pathophysiology and treatment. *Anesth. Analg.* 108, 1645–1657. doi: 10.1213/ane.0b013e31819d644c

Kuypers, H. G. (1982). A new look at the organization of the motor system. *Prog. Brain Res.* 57, 381–403. doi: 10.1016/S0079-6123(08)64138-2

Kwan, H. C., Mackay, W. A., Murphy, J. T., and Wong, Y. C. (1978). An intracortical microstimulation study of output organization in precentral cortex of awake primates. *J. Physiol.* 74, 231–233.

Lemon, R. N. (2008). Descending pathways in motor control. *Annu. Rev. Neurosci.* 31, 195–218. doi: 10.1146/annurev.neuro.31.060407.125547

Liu, J., Solway, K., Messing, R. O., and Sharp, F. R. (1998). Increased neurogenesis in the dentate gyrus after transient global ischemia in gerbils. *J. Neurosci.* 18, 7768–7778. doi: 10.1523/jneurosci.18-19-07768.1998

Liu, Y., and Rouiller, E. M. (1999). Mechanisms of recovery of dexterity following unilateral lesion of the sensorimotor cortex in adult monkeys. *Exp. Brain Res.* 128, 149–159. doi: 10.1007/s002210050830

Loubinoux, I., Dechaumont-Palacin, S., Castel-Lacanal, E., De Boissezon, X., Marque, P., Pariente, J., et al. (2007). Prognostic value of FMRI in recovery of hand function in subcortical stroke patients. *Cereb. Cortex* 17, 2980–2987. doi: 10.1093/cercor/bhm023

Marin, M. A., and Carmichael, S. T. (2019). Mechanisms of demyelination and remyelination in the young and aged brain following white matter stroke. *Neurobiol. Dis.* 126, 5–12. doi: 10.1016/j.nbd.2018.07.023

Marshall, J. W., and Ridley, R. M. (2003). Assessment of cognitive and motor deficits in a marmoset model of stroke. *ILAR J.* 44, 153–160. doi: 10.1093/ilar.44.2.153

Mcentire, C. R., Choudhury, G. R., Torres, A., Steinberg, G. K., Redmond, D. E. Jr., and Daadi, M. M. (2016). Impaired Arm Function and Finger Dexterity in a Nonhuman Primate Model of Stroke: Motor and Cognitive Assessments. *Stroke* 47, 1109–1116. doi: 10.1161/STROKEAHA.115.012506

Murata, Y., and Higo, N. (2016). Development and characterization of a macaque model of focal internal capsular infarcts. *PLoS One* 11:e0154752.

Murata, Y., Higo, N., Hayashi, T., Nishimura, Y., Sugiyama, Y., Oishi, T., et al. (2015a). Temporal plasticity involved in recovery from manual dexterity deficit after motor cortex lesion in macaque monkeys. *J. Neurosci.* 35, 84–95. doi: 10.1523/JNEUROSCI.1737-14.2015

Murata, Y., Higo, N., Oishi, T., and Isa, T. (2015b). Increased expression of the growth-associated protein-43 gene after primary motor cortex lesion in macaque monkeys. *Neurosci. Res.* 98, 64–69. doi: 10.1016/j.neures.2015.04.007

Murata, Y., Higo, N., Oishi, T., Yamashita, A., Matsuda, K., Hayashi, M., et al. (2008). Effects of motor training on the recovery of manual dexterity after primary motor cortex lesion in macaque monkeys. *J. Neurophysiol.* 99, 773–786. doi: 10.1152/jn.01001.2007

Nagasaka, K., Nemoto, K., Takashima, I., Bando, D., Matsuda, K., and Higo, N. (2021). Structural Plastic Changes of Cortical Gray Matter Revealed by Voxel-Based Morphometry and Histological Analyses in a Monkey Model of Central Post-Stroke Pain. *Cereb. Cortex.* 31, 4439–4449. doi: 10.1093/cercor/bhab098

Nagasaka, K., Takashima, I., Matsuda, K., and Higo, N. (2020). Brain activity changes in a monkey model of central post-stroke pain. *Exp. Neurol.* 323:113096. doi: 10.1016/j.expneurol.2019.113096

Nagasaka, K., Yamanaka, K., Ogawa, S., Takamatsu, H., and Higo, N. (2017). Brain activity changes in a macaque model of oxaliplatin-induced neuropathic cold hypersensitivity. *Sci. Rep.* 7:4305. doi: 10.1038/s41598-017-04677-7

Nogles, T. E., and Galuska, M. A. (2021). *Middle Cerebral Artery Stroke*. Treasure Island: StatPearls.

Nudo, R. J., Wise, B. M., Sifuentes, F., and Milliken, G. W. (1996). Neural substrates for the effects of rehabilitative training on motor recovery after ischemic infarct. *Science* 272, 1791–1794. doi: 10.1126/science.272.5269.1791

Ogden, R., and Franz, S. I. (1917). On cerebral motor control: The recovery from experimentally produced hemiplesia. *Psychobiology* 1, 33–47. doi: 10.1037/h0074814

Ohn, S. H., Chang, W. H., Park, C. H., Kim, S. T., Lee, J. I., Pascual-Leone, A., et al. (2012). Neural correlates of the antinociceptive effects of repetitive transcranial magnetic stimulation on central pain after stroke. *Neurorehabil. Neural. Repair* 26, 344–352. doi: 10.1177/1545968311423110

Ongur, D., and Price, J. L. (2000). The organization of networks within the orbital and medial prefrontal cortex of rats, monkeys and humans. *Cereb. Cortex.* 10, 206–219. doi: 10.1093/cercor/10.3.206

Passingham, R. E., Perry, V. H., and Wilkinson, F. (1983). The long-term effects of removal of sensorimotor cortex in infant and adult rhesus monkeys. *Brain* 106, 675–705. doi: 10.1093/brain/106.3.675

Peyron, R., Garcia-Larrea, L., Gregoire, M. C., Convers, P., Lavenne, F., Veyre, L., et al. (1998). Allodynia after lateral-medullary (Wallenberg) infarct. A PET study. *Brain* 121, 345–356. doi: 10.1093/brain/121.2.345

Preuss, T. M. (1995). Do Rats Have Prefrontal Cortex - the Rose-Woolsey-Akert Program Reconsidered. *J. Cogn. Neurosci.* 7, 1–24. doi: 10.1162/jocn.1995.7.1.1

Puentes, S., Kaido, T., Hanakawa, T., Ichinohe, N., Otsuki, T., and Seki, K. (2015). Internal capsule stroke in the common marmoset. *Neuroscience* 284, 400–411. doi: 10.1016/j.neuroscience.2014.10.015

Rehme, A. K., Fink, G. R., Von Cramon, D. Y., and Grefkes, C. (2011). The role of the contralesional motor cortex for motor recovery in the early days after stroke assessed with longitudinal FMRI. *Cereb. Cortex.* 21, 756–768. doi: 10.1093/cercor/bhq140

Roitberg, B., Khan, N., Tuccar, E., Kompoliti, K., Chu, Y., Alperin, N., et al. (2003). Chronic ischemic stroke model in cynomolgus monkeys: behavioral, neuroimaging and anatomical study. *Neurol. Res.* 25, 68–78. doi: 10.1179/016164103101200950

Rosenberg, G. A., Mun-Bryce, S., Wesley, M., and Kornfeld, M. (1990). Collagenase-induced intracerebral hemorrhage in rats. *Stroke* 21, 801–807. doi: 10.1161/01.str.21.5.801

Rosso, C., Colliot, O., Valabregue, R., Crozier, S., Dormont, D., Lehericy, S., et al. (2011). Tissue at risk in the deep middle cerebral artery territory is critical to stroke outcome. *Neuroradiology* 53, 763–771. doi: 10.1007/s00234-011-0916-5

Saniabadi, A. R., Umemura, K., Matsumoto, N., Sakuma, S., and Nakashima, M. (1995). Vessel wall injury and arterial thrombosis induced by a photochemical reaction. *Thromb. Haemost.* 73, 868–872. doi: 10.1055/s-0038-1653883

Sasaki, E., Suemizu, H., Shimada, A., Hanazawa, K., Oiwa, R., Kamioka, M., et al. (2009). Generation of transgenic non-human primates with germline transmission. *Nature* 459, 523–527. doi: 10.1038/nature08090

Sasaki, M., Kudo, K., Honjo, K., Hu, J. Q., Wang, H. B., and Shintaku, K. (2011). Prediction of infarct volume and neurologic outcome by using automated multiparametric perfusion-weighted magnetic resonance imaging in a primate model of permanent middle cerebral artery occlusion. *J. Cereb. Blood Flow Metabol.* 31, 448–456. doi: 10.1038/jcbfm.2010.106

Schaechter, J. D., and Perdue, K. L. (2008). Enhanced cortical activation in the contralesional hemisphere of chronic stroke patients in response to motor skill challenge. *Cereb. Cortex* 18, 638–647. doi: 10.1093/cercor/bhm096

Schiemanck, S. K., Kwakkel, G., Post, M. W., Kappelle, L. J., and Prevo, A. J. (2008). Impact of internal capsule lesions on outcome of motor hand function at one year post-stroke. *J. Rehabil. Med.* 40, 96–101. doi: 10.2340/16501977-0130

Seghier, M. L., Lazeyras, F., Vuilleumier, P., Schnider, A., and Carota, A. (2005). Functional magnetic resonance imaging and diffusion tensor imaging in a case of central poststroke pain. *J. Pain* 6, 208–212. doi: 10.1016/j.jpain.2004.11.004

Stoney, S. D. Jr., Thompson, W. D., and Asanuma, H. (1968). Excitation of pyramidal tract cells by intracortical microstimulation: effective extent of stimulating current. *J. Neurophysiol.* 31, 659–669. doi: 10.1152/jn.1968.31.5.659

Teo, L., and Bourne, J. A. (2014). A reproducible and translatable model of focal ischemia in the visual cortex of infant and adult marmoset monkeys. *Brain Pathol.* 24, 459–474. doi: 10.1111/bpa.12129

Thiel, A., Radlinska, B. A., Paquette, C., Sidel, M., Soucy, J. P., Schirrmacher, R., et al. (2010). The temporal dynamics of poststroke neuroinflammation: a longitudinal diffusion tensor imaging-guided PET study with 11C-PK11195 in acute subcortical stroke. *J. Nucl. Med.* 51, 1404–1412. doi: 10.2967/jnumed.110.076612

Tonchev, A. B., Yamashima, T., Zhao, L., Okano, H. J., and Okano, H. (2003). Proliferation of neural and neuronal progenitors after global brain ischemia in young adult macaque monkeys. *Mol. Cell Neurosci.* 23, 292–301. doi: 10.1016/s1044-7431(03)00058-7

Touvykine, B., Mansoori, B. K., Jean-Charles, L., Deffeyes, J., Quessy, S., and Dancause, N. (2016). The Effect of Lesion Size on the Organization of the Ipsilesional and Contralesional Motor Cortex. *Neurorehabil. Neural. Repair.* 30, 280–292. doi: 10.1177/1545968315585356

Travis, A. M., and Woolsey, C. N. (1956). Motor performance of monkeys after bilateral partial and total cerebral decortications. *Am. J. Phys. Med.* 35, 273–310.

Van Essen, D. C., Donahue, C. J., Coalson, T. S., Kennedy, H., Hayashi, T., and Glasser, M. F. (2019). Cerebral cortical folding, parcellation, and connectivity in humans, nonhuman primates, and mice. *Proc. Natl. Acad. Sci. U. S. A.* 116, 26173–26180. doi: 10.1073/pnas.1902299116

Vilensky, J. A., and Gilman, S. (2002). Lesion of the precentral gyrus in nonhuman primates: a pre-medline bibliography. *Int. J. Primatol.* 23, 1319–1333.

Virley, D., Hadingham, S. J., Roberts, J. C., Farnfield, B., Elliott, H., Whelan, G., et al. (2004). A new primate model of focal stroke: endothelin-1-induced middle cerebral artery occlusion and reperfusion in the common marmoset. *J. Cereb. Blood Flow Metab.* 24, 24–41. doi: 10.1097/01.WCB.0000095801.98378.4A

Wang, G., Zhang, J., Hu, X., Zhang, L., Mao, L., Jiang, X., et al. (2013). Microglia/macrophage polarization dynamics in white matter after traumatic brain injury. *J. Cereb. Blood Flow Metab.* 33, 1864–1874. doi: 10.1038/jcbfm.2013.146

Wenzelburger, R., Kopper, F., Frenzel, A., Stolze, H., Klebe, S., Brossmann, A., et al. (2005). Hand coordination following capsular stroke. *Brain* 128, 64–74. doi: 10.1093/brain/awh317

Yamamoto, T., Hayashi, T., Murata, Y., Ose, T., and Higo, N. (2019). Premotor Cortical-Cerebellar Reorganization in a Macaque Model of Primary Motor Cortical Lesion and Recovery. *J. Neurosci.* 39, 8484–8496. doi: 10.1523/JNEUROSCI.0077-19.2019

Yamamoto, T., Oishi, T., Higo, N., Murayama, S., Sato, A., Takashima, I., et al. (2013). Differential expression of secreted phosphoprotein 1 in the motor cortex among primate species and during postnatal development and functional recovery. *PLoS One* 8:e65701. doi: 10.1371/journal.pone.0065701

Yanagisawa, M., Kurihara, H., Kimura, S., Tomobe, Y., Kobayashi, M., Mitsui, Y., et al. (1988). A novel potent vasoconstrictor peptide produced by vascular endothelial cells. *Nature* 332, 411–415. doi: 10.1038/332411a0

Yeo, H. G., Hong, J. J., Lee, Y., Yi, K. S., Jeon, C. Y., Park, J., et al. (2019). Increased CD68/TGFbeta Co-expressing Microglia/ Macrophages after Transient Middle Cerebral Artery Occlusion in Rhesus Monkeys. *Exp. Neurobiol.* 28, 458–473. doi: 10.5607/en.2019.28.4.458

Yew, W. P., Djukic, N. D., Jayaseelan, J. S. P., Walker, F. R., Roos, K. A. A., Chataway, T. K., et al. (2019). Early treatment with minocycline following stroke in rats improves functional recovery and differentially modifies responses of peri-infarct microglia and astrocytes. *J. Neuroinflamma.* 16:6. doi: 10.1186/s12974-018-1379-y

Yin, Y., Gu, Z., Pan, L., Gan, L., Qin, D., Yang, B., et al. (2013). How does the motor relearning program improve neurological function of brain ischemia monkeys? *Neural. Regen. Res.* 8, 1445–1454.

Conflict of Interest: The author declares that the research was conducted in the absence of any commercial or financial relationships that could be construed as a potential conflict of interest.

Publisher's Note: All claims expressed in this article are solely those of the authors and do not necessarily represent those of their affiliated organizations, or those of the publisher, the editors and the reviewers. Any product that may be evaluated in this article, or claim that may be made by its manufacturer, is not guaranteed or endorsed by the publisher.

Copyright © 2021 Higo. This is an open-access article distributed under the terms of the Creative Commons Attribution License (CC BY). The use, distribution or reproduction in other forums is permitted, provided the original author(s) and the copyright owner(s) are credited and that the original publication in this journal is cited, in accordance with accepted academic practice. No use, distribution or reproduction is permitted which does not comply with these terms.

frontiers in Human Neuroscience

ORIGINAL RESEARCH
published: 11 November 2021
doi: 10.3389/fnhum.2021.764281

Brain Processes Involved in Motor Planning Are a Dominant Factor for Inducing Event-Related Desynchronization

Kosei Nakayashiki[1], Hajime Tojiki[1], Yoshikatsu Hayashi[2], Shiro Yano[1] and Toshiyuki Kondo[1]*

[1] Department of Computer and Information Sciences, Graduate School of Engineering, Tokyo University of Agriculture and Technology, Tokyo, Japan, [2] Biomedical Science and Biomedical Engineering, School of Biological Sciences, University of Reading, Whiteknights, Reading, United Kingdom

OPEN ACCESS

Edited by:
Jun Ota,
The University of Tokyo, Japan

Reviewed by:
Ryosuke Chiba,
Asahikawa Medical University, Japan
Yuichi Kobayashi,
Shizuoka University, Japan

****Correspondence:***
Kosei Nakayashiki
nakayashiki@livingsyslab.org

Specialty section:
This article was submitted to Motor Neuroscience, a section of the journal Frontiers in Human Neuroscience

Received: *25 August 2021*
Accepted: *18 October 2021*
Published: *11 November 2021*

Citation:
Nakayashiki K, Tojiki H, Hayashi Y, Yano S and Kondo T (2021) Brain Processes Involved in Motor Planning Are a Dominant Factor for Inducing Event-Related Desynchronization. Front. Hum. Neurosci. 15:764281. doi: 10.3389/fnhum.2021.764281

Event-related desynchronization (ERD) is a relative attenuation in the spectral power of an electroencephalogram (EEG) observed over the sensorimotor area during motor execution and motor imagery. It is a well-known EEG feature and is commonly employed in brain-computer interfaces. However, its underlying neural mechanisms are not fully understood, as ERD is a single variable correlated with external events involving numerous pathways, such as motor intention, planning, and execution. In this study, we aimed to identify a dominant factor for inducing ERD. Participants were instructed to grasp their right hand with three different (10, 25, or 40%MVF: maximum voluntary force) levels under two distinct experimental conditions: a closed-loop condition involving real-time visual force feedback (VF) or an open-loop condition in a feedforward (FF) manner. In each condition, participants were instructed to repeat the grasping task a certain number of times with a timeline of Rest (10.0 s), Preparation (1.0 s), and Motor Execution (4.0 s) periods, respectively. EEG signals were recorded simultaneously with the motor task to evaluate the time-course of the event-related spectrum perturbation for each condition and dissect the modulation of EEG power. We performed statistical analysis of mu and beta-ERD under the instructed grasping force levels and the feedback conditions. In the FF condition (i.e., no force feedback), mu and beta-ERD were significantly attenuated in the contralateral motor cortex during the middle of the motor execution period, while ERD in the VF condition was maintained even during keep grasping. Only mu-ERD at the somatosensory cortex tended to be slightly stronger in high load conditions. The results suggest that the extent of ERD reflects neural activity involved in the motor planning process for changing virtual equilibrium point rather than the motor control process for recruiting motor neurons to regulate grasping force.

Keywords: brain-computer interface, EEG, grasping, isometric, event-related desynchronization

1. INTRODUCTION

Brain-computer interface (BCI) technology has been extensively investigated over the last decade (Graimann et al., 2010; Do et al., 2011; Lebedev and Nicolelis, 2017). BCIs establish direct communication channels from the brain to control external devices. Especially, this technology is expected to facilitate neuro-rehabilitation for stroke patients, which is on the rise in an aging society. For example, BCI has been used to detect motor intention from brain activity and control medical/assistive devices such as exoskeleton or electrical stimulation to intentionally move paralyzed limbs (Tacchino et al., 2017; Bai et al., 2020). A widely used feature of brain signals to detect the motor intention is event-related desynchronization/synchronization (ERD/S) (Pfurtscheller and Lopes da Silva, 1999; Pfurtscheller, 2001), where ERD is a relative spectral power attenuation of electroencephalogram (EEG) during motor execution and motor imagery (Ron-Angevin et al., 2011; Formaggio et al., 2013), while ERS is a relative spectral power increase like a rebound mainly after the motor execution (Nakamura et al., 2021). Pioneering work by Takahashi et al. (2012) revealed that increasing the strength of functional electrical stimulation (FES) in response to the detection of ERD enabled the paralyzed ankle to bend spontaneously after the intervention, whereas the FES alone cannot induce such motor recovery of the stroke patients. This result indicates the critical function of closing the sensorimotor loop via the feedback loops between the motor intention and the somatosensory feedback. Ono et al. (2015) reported that M1 and supplementary motor area of stroke patients were activated after patients were trained for 1 month using ERD-based BCI to provide a motion picture or motor drive right after detecting the motor imagination. Ramos-Murguialday et al. (2013) performed BCI rehabilitation for patients with the severe chronic stroke conditions. They tested two groups; one group whose fingers were assisted to move in accordance with brain activity and the other group whose fingers were moved randomly. The former group indicated improvement in motor function, while the latter showed no improvement. Thus, the successful BCI-based neuro-rehabilitation depends on accurate and reliable detection of motor intention, and closing of sensorimotor loops which can provide a feedback signal immediately after motor intention.

In order to detect motor intent from ERD, it is critical to elucidate the dominant neural processes underscoring motor execution reflected in ERD generation. Relevant candidates are "motor intention," "motor planning," and "motor command generation" (Kitazawa et al., 1997; Sober and Sabes, 2003, 2005; Desmurget and Sirigu, 2012). Motor execution can be performed via two distinct pathways. One pathway involves a feedforward-based control loop termed open-loop control. One such example is when intending to generate a given level of grasping force, motor plan is initially generated at upstream neural systems followed by a corresponding series of motor commands generated downstream in motor areas, thereby recruiting muscles in the motor units. In contrast, the other pathway involves a feedback-based control loop in which motor planning is adjusted to the real-time input from the limbs interacting with tools or the environment. The former control loop is unidirectional motor coordination after motor intention and planning are generated, which may be suitable for repetitive motion in a steady environment. Conversely, the latter requires the constant monitoring of the resultant components after motor execution and involves real-time regulation of motor planning.

Another point to note in the elucidation of ERD is that it occurs not only during exercise but also during motor imagery. Motor imagery has been widely used in the context of BCI training. Participants are typically instructed to imagine "execution of motion." Previous studies have indicated that an increase in ERD strength is correlated with the success of imagining the kinetic aspects of motion such as strength of force and velocity of motion. Wang et al. recently reported that ERD induced by motor imagery may be modulated by the intensity of movement (Wang et al., 2017, 2019). Yuan et al. (2010) reported that ERD was correlated with the speed of periodic grasping motion in motor imagery and motor execution.

Most BCI studies have focused on training motor imagery in healthy participants. Nevertheless, this experimental protocol itself remains controversial, as participants must imagine moving their body parts yet remain motionless. Raffin et al. (2012) reported that brain activation detected by fMRI was different when comparing two populations of patients for executed and imagined movements of amputated limbs. The same issue holds for cases of paralyzed limbs; therefore, we hypothesized that motor imagery of healthy participants and motor attempts to move the paralyzed limbs are underpinned by different neurological pathways. In neuro-rehabilitation, stroke patients are engaged in motor attempts during therapeutic intervention. The neurological pathways involved should be similar to motor execution pathways in healthy participants. Therefore, we focused on training sessions of motor execution, rather than motor imagery in healthy participants.

In our previous study, we performed EEG experiments for studying the ERD during actual hand grasping with different motor loads (0, 2, 10, and 15 kgf) and grasping speeds ("Slow," "Fast," and "Hold" conditions in the paper) (Nakayashiki et al., 2014). We found that ERD was continuously generated during periodic execution ("Slow" and "Fast" conditions), while it tended to decrease when the participants keep their hand holding ("Hold" condition). Since ERD decreases even though it continues to exert exercise during maintenance, it is presumed that ERD does not directly reflect muscle strength exertion. On the other hand, Fry et al. (2016) reported ERD continues to occur in isometric movement. There are many differences in these experiments, but we focused the difference that our experiment was feedforward-controlled movement, while Fry's experiment was feedback-controlled movement. In the feedback control, the level of muscle strength exertion or hand position are displayed as visual feedback with respect to a target value (Kristeva et al., 2007); i.e., closed-loop visual motor control is performed in the brain, and errors from the target value are constantly fed back to the participants, and corrected. For the feedforward control, participants have to perform the task only by relying on tactile or somatosensory feedback (Gwin and Ferris, 2012). However, it is difficult for the participants to fine-tune the force output without visual feedback; thus, they adjusts the force based on the prior

practice of the task. In this study, the ERD/S induced with or without real-time visual feedback of grasping force (i.e., feedback or feedforward control) is compared to investigate the effect of an error correction process in the brain on resultant ERD.

Another result of our previous studies suggested that grasping force and resultant ERD were not correlated. However, several ambiguities in the experimental procedure remained. For instance, since the strength of motor load was determined by choosing several hand-grippers, the grasping forces that the participants actually generated could not be confirmed. Therefore, in this experiment, an electronic grip dynamometer was used to measure the actual grasping force and to give the real-time feedback of grasping force level to the participants. In addition, the motor load was adjusted individually based on the maximum grip force of each participant.

In this study, we systematically investigate the effects of feedback and feedforward control on resulting mu and beta-ERD while participants are instructed to control grasping force. First, we investigate how the ERD can be generated when the closed-loop visuomotor control or feedforward control is imposed to participants. We hypothesize that the generation of mu-ERD reflects the motor planning rather than the motor intention, because it can be expected that the mu-ERD indicates the rebound during isometric contraction, same as "Hold" condition in our previous study (Nakayashiki et al., 2014). Second, we investigate the relationship between the grasping force level and resultant ERD amplitude. If the ERD is not related to the motor commands that would control the recruitment of muscle, it is expected that this relationship indicates no correlation.

2. MATERIALS AND METHODS

2.1. Participants

Ten healthy male participants (aged 22–25 years, mean age: 23.1 years) took part in the experiment. All were right-handed, as assessed by the Edinburgh Handedness Inventory (Oldfield, 1971) and had no record of any neurological disorders. Participant recruitment and experimental procedures were approved by the ethics committee of the Tokyo University of Agriculture and Technology. Participants were informed of the aims and procedures of the experiment, and provided written informed consent prior to participation in the experiment.

2.2. Experimental Setup

Participants were seated in a comfortable chair with their right arm placed on a table, such that their forearm muscles were relaxed against gravity (**Figure 1**). Participants were instructed to grasp a digital grip dynamometer (T.K.K.5710b, TAKEI Scientific Instruments Co., Ltd., Japan) with their right hand. Their grasping force level was measured using a strain amplifier (DMP-911B, Kyowa Electronic Instruments Co., Ltd., Japan) and stored in a personal computer. The grasping force data were analyzed online using original MATLAB and Simulink (MathWorks, MA) scripts to enable online visual force feedback. An LCD monitor was located in front of the participants to enable to present visual cues and grasping force level on the display according to the experimental condition.

During the experiment, participants wore an EEG cap with 64-channel active EEG electrodes (g.SCARABEO, g.tec, Vienna, Austria); the ground and reference electrodes were placed on the forehead (AFz) and left mastoids, respectively. The EEG signals were amplified using a digital bio-signal amplifier (g.HIamp, g.tec, Austria), and band-pass filtered between 0.1 and 100 Hz in the amplifier. Throughout the experiment, EEG activity was sampled at 512 Hz for the offline analysis.

2.3. Experimental Procedure

We designed an experimental paradigm to investigate how kinetic properties and sensory feedback conditions during grasping movement affected the resulting ERD. In the experiment, participants were instructed to grasp their right hand at one of three different force levels (10, 25, or 40%MVF: maximum voluntary force) under two visual feedback conditions: VF (with visual feedback of grasping force level displayed as the length of a red horizontal bar) or FF (without visual feedback, i.e., feedforward control). To avoid the effects of muscle fatigue, the following six experimental conditions were conducted in a fixed order for all participants, i.e., starting from the VF condition and 10%MVF, followed by the FF condition and 10%MVF, VF condition and 25%MVF, and so on. In each condition, participants were instructed to repeat the experimental tasks for 30 times. As participants were tasked to perform the VF condition first, this provided sufficient training opportunities to obtain self-regulatory ability of grasping force level in the subsequent FF conditions.

Each task consisted of Rest (10.0 s), Preparation (1.0 s), and Motor Execution (4.0 s) periods (**Figure 2**). During the Rest period, participants were instructed to relax while looking at a blue fixation cross on the screen. 1.0 s before the Motor Execution period, a beep sound was played to indicate the task initiation. During the Motor Execution period, the fixation cross turned red, and participants were instructed to grasp their right hand and maintain their grasping force level within a pre-specified range. Note that the participants had to keep clenching their hand for 4.0 s until the Motor Execution period was terminated (i.e., the fixation cross turned blue). In the FF condition; i.e., without the visual force feedback condition, verbal feedback was displayed on the screen for 2.0 s just after the Motor Execution period. For example, "Good" represented that the grasping force level was within the $\pm$ 10% range of the pre-specified target force level (see **Figure 2**). Other verbal expressions included "Too Strong" (20% or more), "Strong" (10% or more), "Too Weak" ($-$20% or less), and "Weak" ($-$10% or less).

2.4. EEG Signal Processing

We evaluated the time-course of event-related spectral perturbations to determine the modulation of ERD/S, according to each experimental condition.

The experimental trials in which the absolute EEG amplitude exhibited over 100 μV were discarded from further analysis, as these signals were artifacts reflecting the eye-blink and/or body sway. The remaining EEG data were pre-processed using EEGLAB software (Delorme and Makeig, 2004). The acquired EEG data were subjected to 1 Hz high-pass filter, 40 Hz low-pass

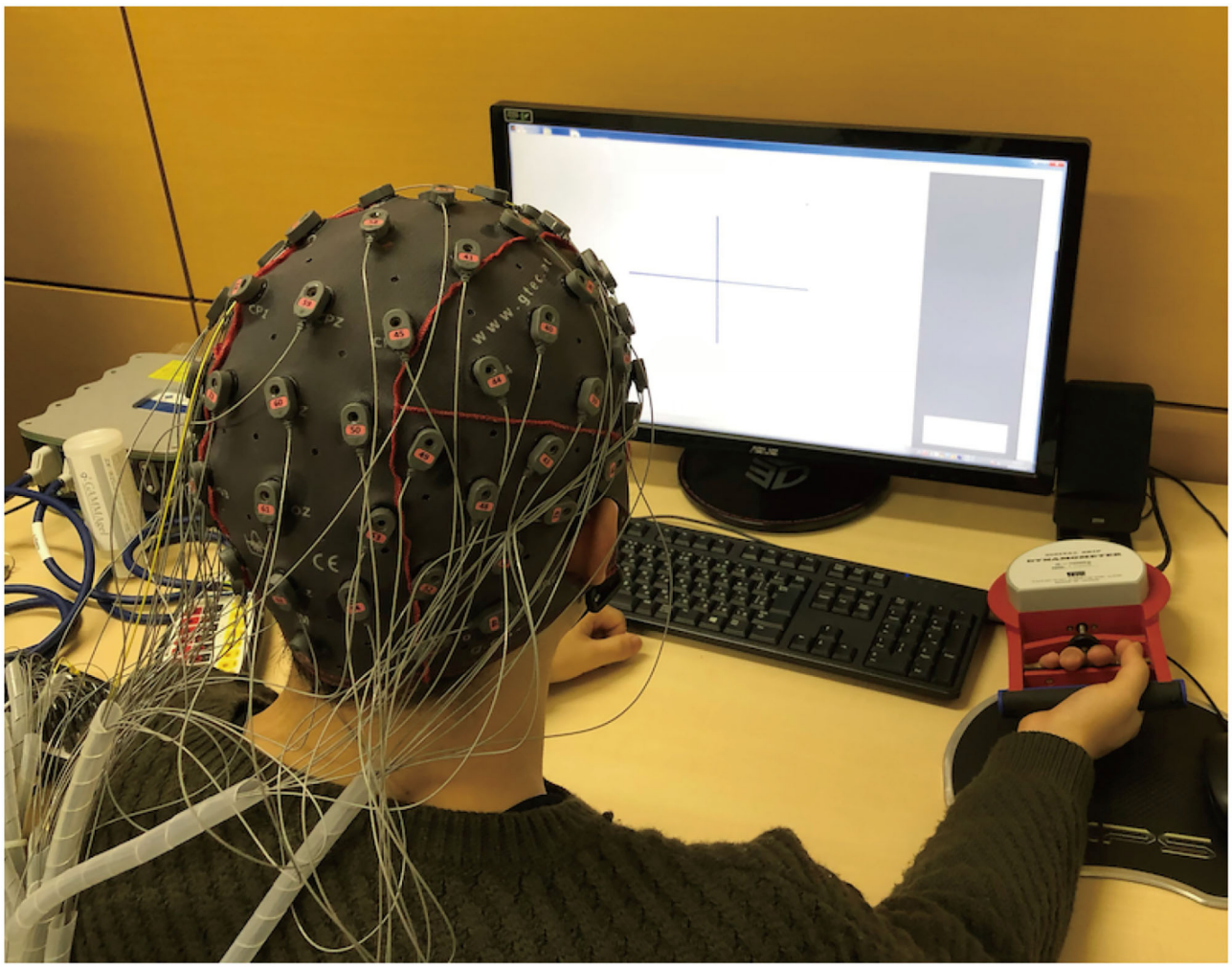

FIGURE 1 | Experimental setup. Participants wore an EEG cap with 64-channel active electrodes (g.Tec Inc., Austria). Participants were seated in a comfortable chair and placed their right arm on a table such that a group of muscles of their upper limb were relaxed against gravity. An LCD monitor was located in front of them, enabling viewing of a visual cue on the display.

filter, and 50 Hz notch filter. EEG data were binned into 11.0 s epochs (−4.0 to 7.0 s) with respect to the onset of grasping force which aligned to 0.0 s. Epochs were visually checked and epochs that were estimated to have a lot of noise in them were removed. The Noise was confirmed in many epochs of the 40%MVF condition, and the majority of epochs were removed from some participants. Therefore, the 40%MVF condition data was considered inappropriate as EEG data and was excluded from the analysis.

We used Independent Component Analysis (ICA) as a method to remove artifacts in EEG, such as ocular electrograms, electromyograms, and body movements (Jung et al., 2000a). The ICA is a computational method for separating a multivariate signal into multiple independent components. By applying the ICA to the scalp electrode data, the activities at the signal sources can be estimated, and artifacts such as blinking can be separated from the estimated activity (independent components) at each signal source. In this study, denoising was adapted in the following manner. For each participant, EEG signals from four conditions were merged into a single data set, except for the 40%MVF condition. These data were adapted to *runica* function of EEGLAB using the infomax ICA algorithm (Bell and Sejnowski, 1995). If the topography, time course, or frequency spectrum of each independent component was inferred to reflect EMG, body motion, or eye movement artifacts, these component was excluded (Jung et al., 2000a,b; Allison et al., 2012), and the EEG signal for each channel was reconstructed with the remaining components.

Time-frequency maps were calculated using the wavelet transform. The ERD was calculated by normalization with respect to the time-averaged power during the most recent Rest period (i.e., −4.0 to −2.0 s).

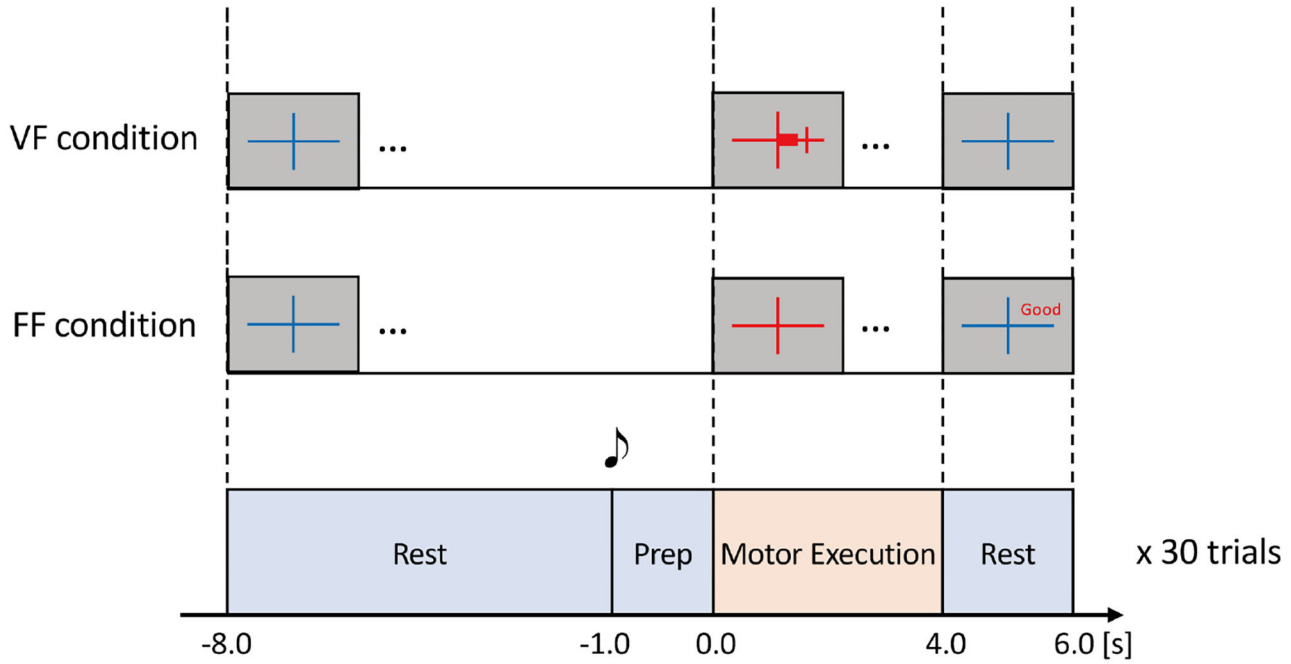

FIGURE 2 | Experimental task. The task comprised Rest, Prep, and Motor Execution periods. During the Rest period, participants were instructed to relax. 1.0 s before the Motor Execution period, a beep sound was played for notification. During the Motor Execution period, the participants were instructed to grasp their right hand and maintain the grasping force within a specified range chosen from 10, 25, or 40%MVF with visual feedback (VF) or a feedforward (FF) condition. In the VF condition, a red horizontal bar indicated the extent of grasping force in real-time. In the FF condition, no online feedback was provided, but the precision of grasping force (i.e., the extent of error) was shown after the Motor Execution period. Thus, there were six experimental conditions according to the combination of %MVF × the way of feedback. In each condition, the experimental task was repeated 30 times to obtain sufficient EEG signals.

2.5. Statistical Analysis

For the comparison of behavioral measures of grasping force across the three %MVF levels and two feedback conditions (VF and FF), a 3 × 2 two-way repeated measures ANOVA was conducted with the significance level sets at 0.01. As described in the EEG signal processing section, we excluded the artifacts from the recorded signals, because there was substantial amount of noise from the body motion in the EEG data under 40%MVF condition. However, we included the grasping force data under the 40%MVF condition into the statistical analysis to confirm the success or failure of the grasping force demonstration in the entire experiment.

Regarding the EEG data analysis, we chose a specific frequency band in which the strongest ERD was generated across each participant and condition, since the range of the frequency band for the ERD generation differs from participant to participant. After moving-averaging the intensity of the power spectra over the frequency at a width of 3 Hz, the frequency band with the strongest ERD at the beginning of the grasping (0.0–1.0 s) was calculated, and the ERD during the grasping (2.0–3.0 s) in that frequency band of interest was tested. Mu-ERD and beta-ERD were calculated for each frequency range of the mu band (8–13 Hz) and beta band (14–30 Hz). The calculated values of the ERD were summarized under the feedback and force level conditions, and statistically tested in the following manner; Shapiro-Wilk test was used to check whether the ERD of all participants (averaged by channel and condition) could be a normal distribution. If the results were rejected with the threshold of 0.01 in some cases, Wilcoxon signed-rank test was used for the statistical tests.

3. RESULTS

3.1. Grasping Force

To clarify the relationship between the grasping force level and the EEG feature, we firstly analyzed the grasping forces that the participants actually exerted in the experiments.

Figure 3A indicates the time-series of grasping forces in %MVF measures of a typical participant (Participant B) under the FF and FB experimental condition. Each graph includes the trajectories of the resultant grasping force of 30 trials. As shown in **Figure 3A**, the grasping forces were maintained more or less precisely during the Motor Execution period, although relatively large variability was observed in the FF condition due to the lack of visual force feedback.

Figure 3B represents the mean and standard error of grasping forces during 1.0–4.0 s of the Motor Execution period across participants in each condition. To verify whether participants were able to produce the exact instructed level of force, we statistically analyzed the resultant grasping forces. A 3 × 2 two-way repeated measures ANOVA (*force level* × *feedback condition*) revealed a significant main effect on *force level* [$F_{(2,18)} = 8076.9$, $p < 0.01$], but no interaction effect [$F_{(2,18)} = 0.4567$,

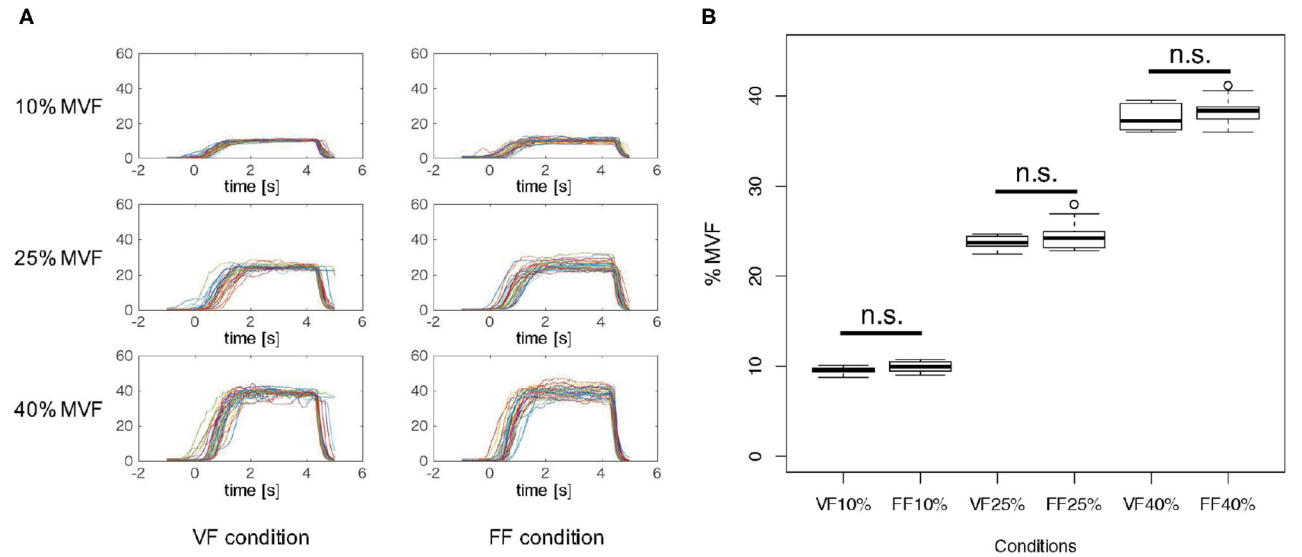

FIGURE 3 | Grasping force in %MVF measure. **(A)** Grasping force time-series of a typical participant (Participant B) in %MVF measured under each experimental condition. Each graph includes 30 trials. As shown in these graphs, the grasping forces were maintained during 1.0–4.0 s, and a relatively large variability was observed in the FF condition. **(B)** Mean and standard error of grasping forces during 1.0–4.0 s across participants in each condition. Two-way ANOVA revealed a significant main effect of %MVF levels, but no significant difference was observed between feedback conditions. This implies that the participants exerted identical motor outputs in both VF and FF conditions.

$p = 0.54588$] and significant main effect of *feedback condition* [$F_{(1,18)} = 2.3941, p = 0.1562$] were noted. These results indicated that participants indeed exerted precise motor outputs according to the instructed force level in both FF and FB conditions.

Moreover, we investigated whether visual force feedback induced increase of frequency of grasping force adjustment. The %MVF between 2.0 and 4.0 s of the task period was extracted, and the number of zero-crossing with respect to the mean value was counted. A moving average of 16 points (about 0.03 s wide) was applied in order to eliminate fluctuations due to hand tremor and spinal reflex instead of control by visual and tactile force feedback. The median number of zero-crossing in all trials was calculated for each subject in each session, and Wilcoxon signed-rank test was performed under the VF and FF conditions. As a result, we found that the number of zero-crossing under the VF condition was significantly higher than that under the FF condition ($p = 0.0312$) (**Supplementary Figure 1**). These results suggested that participants performed a relatively large number of adjustments on their grasping force through the visual feedback. In addition, the comparison of the number of zero-crossing in the first half (15 trials) and the last half (15 trials) in the VF condition revealed there was no significant difference ($p = 0.4161$), leading to the conclusion that there is no learning effect in controlling the grasping force (**Supplementary Figure 2**).

3.2. Time-Frequency Map of the Event-Related Spectral Perturbation

Time-courses of the relative power decrease (ERD) and increase (ERS) in primary motor cortex (C3, Cz, and C4) under each visual feedback and grasping force level condition were depicted in the left two column of **Figure 4**. The horizontal axis indicates the time aligned at the onset of the task period (0.0 s), and the vertical axis represents the frequency. The color bar indicates the relative power.

As can be seen in the results of contralateral hemisphere (C3) which would reflect right hand movements, apparent mu-rebound (i.e., disappearance of ERD in 8–13 Hz) was observed at the middle of the task period (1.0–3.0 s) in the FF condition (i.e., without visual force feedback), whereas mu-ERD was continuously confirmed in the VF condition.

3.3. Effects of Two Factors (Force and Feedback Conditions) at C3

To confirm the effect of the force levels and the feedback conditions on the resulting ERD at C3 channel, we statistically compared mu and beta-ERD in each condition (right two column in **Figure 4**). These notched box-plots represent the results of factor-by-factor testing of ERD during maintenance of grasping period (i.e., 2.0–3.0 s) calculated according to the process described in the statistical analysis section ($^{**}p < 0.01$). For example, the graph of "Mu-ERD FF-VF" represents the comparison of mu-ERD in the FF and VF conditions without discriminating the grasping force levels (i.e., all the data of 10 and 25%MVF were used.). These results showed that mu-ERD was significantly stronger in the VF condition than that in the FF condition ($p = 0.0003$). On the other hand, there was no significant difference in mu-ERD between the "force condition" ($p = 0.65$). This trend was also true for beta-ERD, with a significant difference for "feedback condition" ($p = 0.010$)

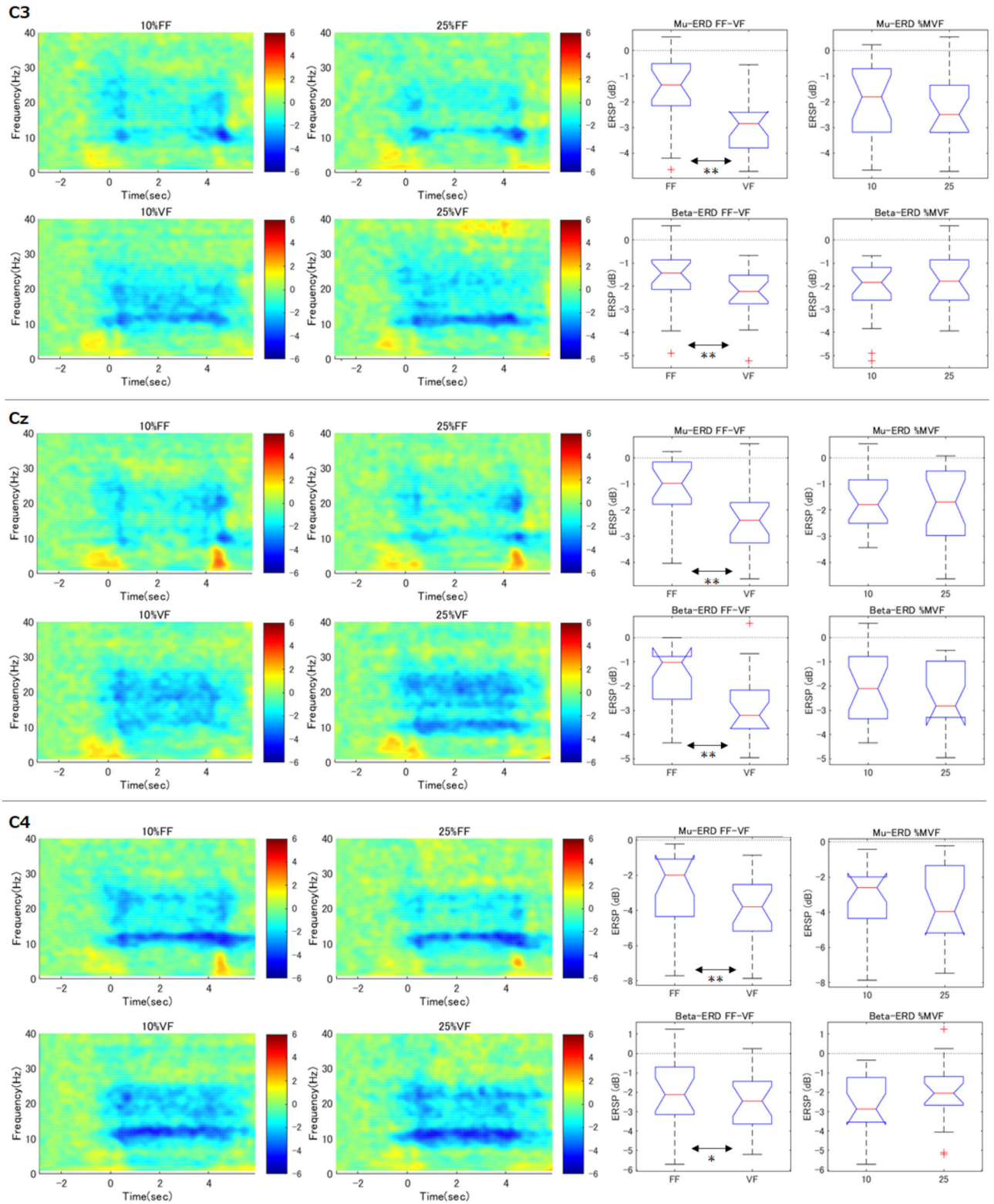

FIGURE 4 | Time-frequency maps of ERD/S and comparison of ERD during maintenance of grasping (C3, Cz, C4). The graphs in the left two columns show the time course of relative power decreases (ERD) and increases (ERS) in the motor cortex under each condition. The horizontal axis is the time aligned with the beginning of the task period (0.0 s), and the vertical axis represents the frequency. The color bar indicates the relative power. In the FF condition, mu-ERD disappeared in the

(Continued)

FIGURE 4 | middle of the exercise execution period (1.0–3.0 s). The graphs in the right two columns demonstrate, for each participant and each condition, the ERD during the maintenance of grasping (2.0–3.0 s) was calculated and statistically processed for all participants (**$p < 0.01$). These results indicate that the mu-ERD in the VF condition was significantly stronger than that in the FF condition. On the other hand, there was no significant difference in mu-ERD between the force conditions. Beta-ERD showed the same trend as mu-ERD.

and no difference for "magnitude of force" ($p = 0.062$). In addition, no interaction between the two factors was confirmed (mu: $p = 0.872$, beta: $p = 0.773$). These results showed that ERD decreased during the exercise execution period only in the FF condition.

3.4. Effects of Two Factors in Surrounding Channels

Similar to right hand primary motor cortex (C3), we further analyzed the surrounding channels: Fz (supplementary motor cortex), FC3 (premotor cortex), C4 (left hand primary motor cortex), Cz (foot primary motor cortex), and CP3 (right hand somatosensory motor cortex) (see **Figures 4**, **5**). As shown in the time-frequency map, in the FF condition, the mu-ERD of each channel tended to decrease in the middle of the task period (1.0–3.0 s). The statistical results were similar to those of C3 in FCz, Fz, C4, and Cz (both mu and beta-ERD were significantly stronger in the VF condition than in the FF condition). In FC3, mu-ERD tended to be significantly stronger in the VF condition as in C3, while beta-ERD showed a similar trend but no significant difference. In CP3, there was no significant difference in mu-ERD between the FF and VF conditions, while mu-ERD was significantly stronger in the 25%MVF condition than the 10%MVF condition. Beta-ERD tended to be significantly stronger in the VF condition as in C3. No interaction between the two factors (force and feedback) was observed in any of the channels.

4. DISCUSSION

We investigated event-related spectral power decrease in the mu and beta frequency bands elicited by actual motion of the hand grasping under several force levels. In addition, by displaying the %MVF to the participants in real-time, we examined the effect of feedback or feedforward control on the ERD under maintaining grasping force. Experimental results showed that (1) grasping force level had no significant effect on the intensity of the mu and beta-ERD on motor cortex as a result of motor execution, and (2) online visual feedback of grasping force had a positive effect on inducing continuous mu-ERD.

Kilavik et al. (2013) reported that during stable object holding, beta oscillations display a relative increase in power and are phase-synchronized with the EMG of tonically contracting muscles. Stancák et al. (1997) used a finger lifting movement against several motor loads as the motor task, and reported that the duration of mu-ERD (not the time-averaged mu-ERD level) was significantly longer under the heaviest load condition and that post-movement beta-synchronization was also longer under the heaviest load compared to the no-load condition. The authors concluded that the ERD/S was influenced by the applied external load. Neurophysiological research by Tan et al. (2013) demonstrated that neural activity in sub-cortical areas was linked to motor effort. Furthermore, functional MRI studies indicated that cortical BOLD signal may correlate with grasping force levels (Cramer et al., 2002; Keisker et al., 2009). Pistohl et al. (2012) reported that the movement of a cup of two different weights performed by epileptic patients can be classified, albeit with low accuracy, by combining ECoG signals below 6 Hz and above 14 Hz. In their another study, they reported that ECoG of the human motor cortex could successfully distinguish two different grasping movements (precision vs. whole-hand grip) even if the weights of the manipulating objects were different (Pistohl et al., 2013). Wang et al. (2017) reported that motor imagery of different muscle strengths can be classified in real-time by beta-ERD but not mu-ERD. Tatti et al. (2019) reported that impulse forces to reach a target at different distances were different, but, the generated forces were not correlated with beta-ERD during a reaching task. Gwin and Ferris (2012) reported a slightly stronger ERD in the supplementary motor area at high load in isotonic and isometric movements of the foot. To summarize, in previous studies, there are some findings stating that fMRI and ECoG can distinguish the brain activities related to the weight of the load, but in the studies using EEG ERD, the tendency is different depending on the conditions. The different trends from our results where ERD in the motor cortex does not affect the level of muscle strength exertion are found in the results of Wang and Gwin. The major differences between those two experimental designs are motor imagery and foot movements. To our knowledge, the work that most closely resembles our results was reported by Chakarov et al. (2009) who indicated that EEG and EMG spectral power did not show any significant differences among the three force conditions, although the beta range EEG-EMG coherence increased as the load increased.

Although the above work appears controversial, the modulation of ERD may be dependent on several factors including (1) experimental paradigm, such as single execution or repetitive motion; (2) frequency range; (3) motor performance over task duration; and (4) brain region, including invasive or non-invasive approaches.

Human sensorimotor processing consists of sub-processes including motor intention, planning of motion trajectory, motor command generation, and receiving sensory feedback. Our findings demonstrated that ERD of the motor cortex may not reflect the strength of the motor load. We propose that the strength of mu and beta-ERD may reflect the motor planning process rather than motor command generation which recruits

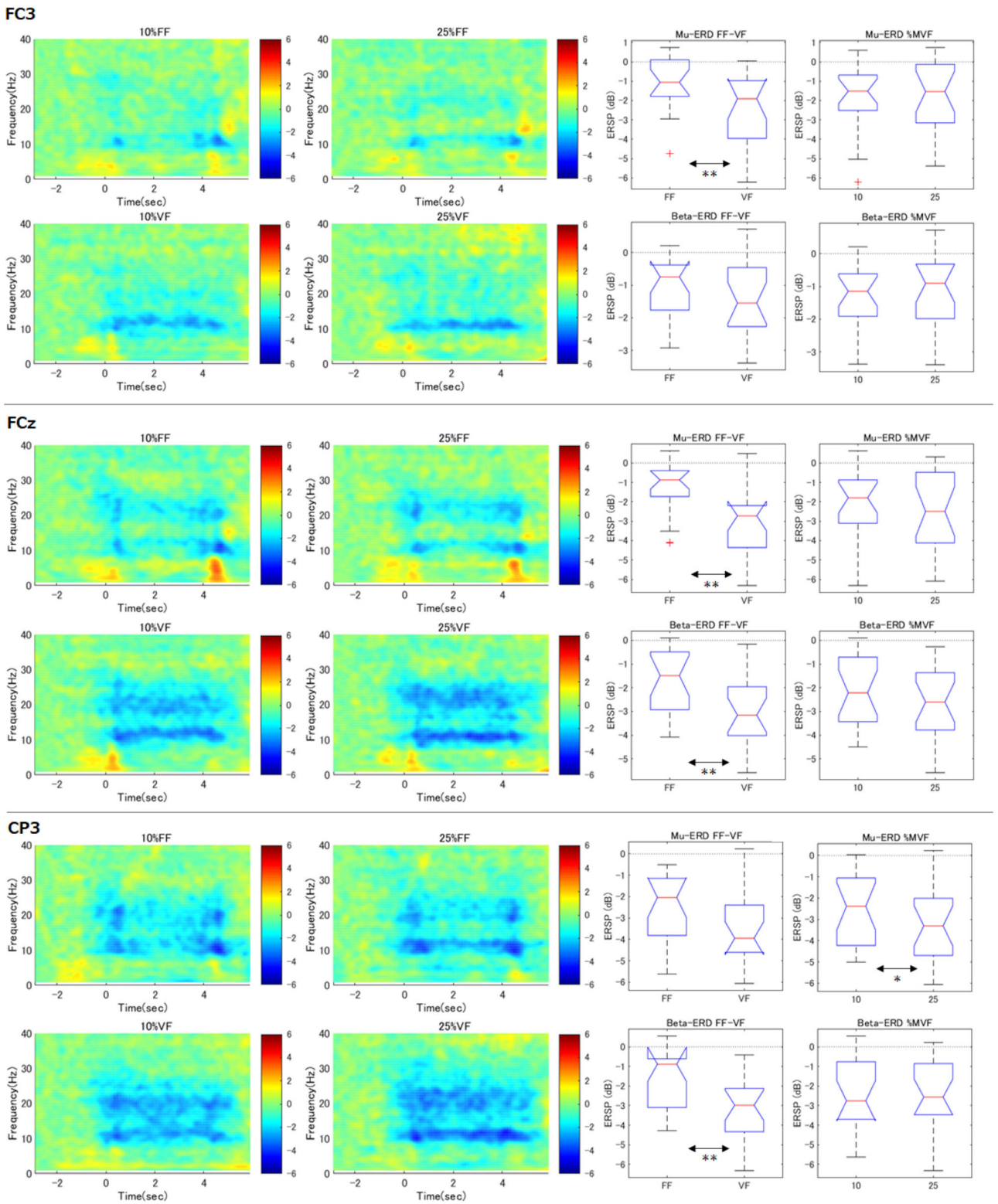

FIGURE 5 | Time-frequency maps of ERD/S and comparison of ERD during maintenance of grasping (FC3, FCz, CP3). The same analysis as for C3 was performed for the surrounding channels. The trend of the tilt time-frequency map is similar to that of C3. Statistical tests on the resultant ERD during maintenance of grasping in FF condition showed that mu/beta-ERD for FCz, mu-ERD for FC3, and beta-ERD disappeared for CP3. only in CP3, mu-ERD occurred significantly more strongly when the load was strong (**$p < 0.01$, *$p < 0.05$).

a group of motor neurons. On the other hand, our results also indicated that mu-ERD in the somatosensory cortex may reflect the intensity of the motor load; Mu-ERD in the somatosensory area may reflect the strength of the skin sensation that changes depending on the strength of the load. However, our result is different in terms of the frequency band and location of the channels found from the results of Wang, Gwin, and Pistohl, who found differences in brain activity with motor load introduced in the previous section (Gwin and Ferris, 2012; Pistohl et al., 2012; Wang et al., 2017). This may indicate that the processing of the load may differ, depending on the type of exercise. The difference may stem from the fact that motor imagery was used in Wang's experiment while motor execution was used in our experiment, thus the brain processes for the both might be different with each other. In addition, it is still a question of how to prove if subjects were able to imagine different grasping forces by motor imagery. Gwin also reported that the extent of ERD correlates with the force level, but they only compared the ERD immediately after the muscle exertion in both isometric and isotonic conditions. Therefore, the brain processes may differ between instantaneous and continuous exertion of force. Furthermore, Pistohl used ECoG for motion classification experiment, and the channel range they analyzed included not only the motor cortex but also the somatosensory area. If the classification result comes from the information in the area, their finding is consistent with our result that the strength of the load is related to the mu-ERD of the somatosensory area rather than the motor area. However, signals of 5 Hz or less and 54 Hz or more mainly contribute to classification accuracy, these are considered to be a neural process different from mu and beta-ERD.

Our experimental results demonstrated that online visual force feedback during grasping movement has positive effects on inducing the mu and beta-ERD. Similar results have been reported in previous studies. Gwin and Ferris (2012) investigated whether the ICA of high-density EEG could classify lower limb motor tasks, and reported that ERD decreased during isometric movement in the motor tasks. There was no visual feedback that allowed the foot position to be fine-tuned. Their experimental conditions and results are similar to the FF condition in our study. Fry et al. (2016) investigated whether force strength and force development rate affect MEG beta-ERD / ERS. In this experiment, isometric wrist flexion movement was performed, and the amount exerted was visually feedback in real-time. As a result, it has been reported that beta-ERD continued to occur during movement. Their experimental conditions and results are similar to the VF condition in our study. Mayhew et al. (2017) examined the physiological brain activity of Grasping with and without Visual Feedback using fMRI BOLD signals. They reported that premotor cortex and parietal lobe BOLD are activated by visual feedback compared to without visual feedback during maintenance of grasping. Although not exactly in line with the brain regions in our study, EEG has lower spatial resolution than fMRI Considering this point, Mayhew's physiological finding seems to be similar to our result. From these results, in our study, in the case of no visual feedback while controlling the grasping force, mu-ERD was probably produced in correlation with motor intention or a few times motor planning for kinematic control of virtual equilibrium points. In the case of real-time visual force feedback, participants can monitor the difference between the current grasping force and target value of the force, and they continue to adjust the grasping force, thereby controlling their virtual equilibrium points. It is plausible that the continuous planning of virtual equilibrium points resulted in continuous mu-ERD generation. As a concern, in this study, the order of experimental conditions was fixed in order to avoid fatigue. In particular, the VF condition is a practice for the FF condition, and it cannot be denied that learning of tactile force control may affect the ERD. However, since there was no significant difference in the number of zero crosses in the first and the last half of VF trials, it is presumed that visual force feedback is still dominant in the last half and the influence of the learning effect is low.

Now, let us discuss the possibility of applying BCI-based neuro-rehabilitation. As discussed in the Introduction, the neurological pathways of motor execution in healthy participants are presumed to be similar to the motor training of patients, as patients with hemiparetic conditions actually attempt to move their body parts, thereby, generating the motor intention and the motor planning. Thus, our study with the focus on motor execution may contribute to the development of the BCI applications for the training of patients. Monitoring the mu-ERD during the motor training and the continuous ERD generation indicated that the real-time control of the target posture involved the re-planning of body posture/kinematics. Future studies should investigate how the re-planning of body posture monitored by BCIs can benefit recovery of motor coordination. Since our experimental paradigm was conducted only on healthy young participants, in the future study, it is necessary to confirm if the same principal of closing the sensorimotor loops applies to paraplegics and the elderly.

DATA AVAILABILITY STATEMENT

The raw data supporting the conclusions of this article will be made available by the authors, without undue reservation.

ETHICS STATEMENT

The studies involving human participants were reviewed and approved by the Ethics Committee of the Tokyo University of Agriculture and Technology. The patients/participants provided their written informed consent to participate in this study. Written informed consent was obtained from the individual in **Figure 1** for the publication.

AUTHOR CONTRIBUTIONS

KN supervised the study and designed the experiment. KN and HT developed the experimental system, performed the experiments, and statistical analysis. KN and TK contributed to discussion of the obtained results. KN, TK, and YH wrote the manuscript. SY provided fruitful comments for the experimental

procedure and analysis. All authors have read and approved the final manuscript.

FUNDING

This research was supported by JSPS KAKENHI (Grant Numbers: JP17KK0064, JP18K19732, JP19H05727, JP20H02111, and JP20J10024) and a research grant from the Institute of Global Innovation Research at TUAT.

ACKNOWLEDGMENTS

We are grateful to all of the participants in the experiment.

SUPPLEMENTARY MATERIAL

The Supplementary Material for this article can be found online at: https://www.frontiersin.org/articles/10.3389/fnhum.2021.764281/full#supplementary-material

REFERENCES

Allison, B. Z., Dunne, S., Leeb, R., Millán, J. D. R., and Nijholt, A. (2012). *Towards Practical Brain-Computer Interfaces: Bridging the Gap from Research to Real-World Applications*. Berlin; Heidelberg: Springer Science & Business Media. doi: 10.1007/978-3-642-29746-5

Bai, Z., Fong, K. N. K., Zhang, J. J., Chan, J., and Ting, K. H. (2020). Immediate and long-term effects of BCI-based rehabilitation of the upper extremity after stroke: a systematic review and meta-analysis. *J. Neuroeng. Rehabil.* 17:57. doi: 10.1186/s12984-020-00686-2

Bell, A. J., and Sejnowski, T. J. (1995). An information-maximization approach to blind separation and blind deconvolution. *Neural Comput.* 7, 1129–1159. doi: 10.1162/neco.1995.7.6.1129

Chakarov, V., Naranjo, J. R., Schulte-Monting, J., Omlor, W., Huethe, F., and Kristeva, R. (2009). Beta-range EEG-EMG coherence with isometric compensation for increasing modulated low-level forces. *J. Neurophysiol.*, 102, 1115–1120. doi: 10.1152/jn.91095.2008

Cramer, S. C., Weisskoff, R. M., Schaechter, J. D., Nelles, G., Foley, M., Finklestein, S. P., et al. (2002). Motor cortex activation is related to force of squeezing. *Hum. Brain Mapp.* 16, 197–205. doi: 10.1002/hbm.10040

Delorme, A., and Makeig, S. (2004). EEGLAB: an open source toolbox for analysis of single-trial EEG dynamics including independent component analysis. *J. Neurosci. Methods* 134, 9–21. doi: 10.1016/j.jneumeth.2003.10.009

Desmurget, M., and Sirigu, A. (2012). Conscious motor intention emerges in the inferior parietal lobule. *Curr. Opin. Neurobiol.* 22, 1004–1011. doi: 10.1016/j.conb.2012.06.006

Do, A. H., Wang, P. T., King, C. E., Abiri, A., and Nenadic, Z. (2011). Brain-computer interface controlled functional electrical stimulation system for ankle movement. *J. Neuroeng. Rehabil.* 8:49. doi: 10.1186/1743-0003-8-49

Formaggio, E., Storti, S. F., Boscolo Galazzo, I., Gandolfi, M., Geroin, C., Smania, N., et al. (2013). Modulation of event-related desynchronization in robot-assisted hand performance: brain oscillatory changes in active, passive and imagined movements. *J. Neuroeng. Rehabil.* 10:24. doi: 10.1186/1743-0003-10-24

Fry, A., Mullinger, K. J., O'Neill, G. C., Barratt, E. L., Morris, P. G., Bauer, M., et al. (2016). Modulation of post-movement beta rebound by contraction force and rate of force development: modulation of PMBR by force & RFD. *Hum. Brain Mapp.* 37, 2493–2511. doi: 10.1002/hbm.23189

Graimann, B., Allison, B., and Pfurtscheller, G. (2010). "Brain-computer interfaces: a gentle introduction," in *Brain-Computer Interfaces: Revolutionizing Human-Computer Interaction*, eds B. Graimann, G. Pfurtscheller, and B. Allison (Berlin; Heidelberg Springer), 1–27. doi: 10.1007/978-3-642-02091-9

Gwin, J. T., and Ferris, D. P. (2012). An EEG-based study of discrete isometric and isotonic human lower limb muscle contractions. *J. Neuroeng. Rehabil.* 9:35. doi: 10.1186/1743-0003-9-35

Jung, T.-P., Makeig, S., Humphries, C., Lee, T.-W., McKeown, M. J., Iragui, V., et al. (2000a). Removing electroencephalographic artifacts by blind source separation. *Psychophysiology* 37, 163–178. doi: 10.1111/1469-8986.3720163

Jung, T.-P., Makeig, S., Westerfield, M., Townsend, J., Courchesne, E., and Sejnowski, T. J. (2000b). Removal of eye activity artifacts from visual event-related potentials in normal and clinical subjects. *Clin. Neurophysiol.* 111, 1745–1758. doi: 10.1016/S1388-2457(00)00386-2

Keisker, B., Hepp-Reymond, M.-C., Blickenstorfer, A., Meyer, M., and Kollias, S. S. (2009). Differential force scaling of fine-graded power grip force in the sensorimotor network. *Hum. Brain Mapp.* 30, 2453–2465. doi: 10.1002/hbm.20676

Kilavik, B. R. E., Zaepffel, M., Brovelli, A., MacKay, W. A., and Riehle, A. (2013). The ups and downs of β oscillations in sensorimotor cortex. *Exp. Neurol.* 245, 15–26. doi: 10.1016/j.expneurol.2012.09.014

Kitazawa, S., Kimura, T., and Uka, T. (1997). Prism adaptation of reaching movements: specificity for the velocity of reaching. *J. Neurosci.* 17, 1481–1492. doi: 10.1523/JNEUROSCI.17-04-01481.1997

Kristeva, R., Patino, L., and Omlor, W. (2007). Beta-range cortical motor spectral power and corticomuscular coherence as a mechanism for effective corticospinal interaction during steady-state motor output. *Neuroimage* 36, 785–792. doi: 10.1016/j.neuroimage.2007.03.025

Lebedev, M. A., and Nicolelis, M. A. L. (2017). Brain-machine interfaces: from basic science to neuroprostheses and neurorehabilitation. *Physiol. Rev.* 97, 767–837. doi: 10.1152/physrev.00027.2016

Mayhew, S. D., Porcaro, C., Tecchio, F., and Bagshaw, A. P. (2017). fMRI characterisation of widespread brain networks relevant for behavioural variability in fine hand motor control with and without visual feedback. *NeuroImage* 148, 330–342. doi: 10.1016/j.neuroimage.2017.01.017

Nakamura, A., Suzuki, Y., Milosevic, M., and Nomura, T. (2021). Long-lasting event-related beta synchronizations of electroencephalographic activity in response to support-surface perturbations during upright stance: a pilot study associating beta rebound and active monitoring in the intermittent postural control. *Front. Syst. Neurosci.* 15:660434. doi: 10.3389/fnsys.2021.660434

Nakayashiki, K., Saeki, M., Takata, Y., Hayashi, Y., and Kondo, T. (2014). Modulation of event-related desynchronization during kinematic and kinetic hand movements. *J. Neuroeng. Rehabil.* 11:90. doi: 10.1186/1743-0003-11-90

Oldfield, R. C. (1971). The assessment and analysis of handedness: the Edinburgh inventory. *Neuropsychologia* 9, 97–113. doi: 10.1016/0028-3932(71)90067-4

Ono, T., Tomita, Y., Inose, M., Ota, T., Kimura, A., Liu, M., et al. (2015). Multimodal sensory feedback associated with motor attempts alters BOLD responses to paralyzed hand movement in chronic stroke patients. *Brain Topogr.* 28, 340–351. doi: 10.1007/s10548-014-0382-6

Pfurtscheller, G. (2001). Functional brain imaging based on ERD/ERS. *Vision Res.* 4, 1257–1260. doi: 10.1016/S0042-6989(00)00235-2

Pfurtscheller, G., and Lopes da Silva, F. H. (1999). Event-related EEG/MEG synchronization and desynchronization: basic principles. *Clin. Neurophysiol.* 110, 1842–1857. doi: 10.1016/S1388-2457(99)00141-8

Pistohl, T., Schmidt, T. S. B., Ball, T., Schulze-Bonhage, A., Aertsen, A., and Mehring, C. (2013). Grasp detection from human ECoG during natural reach-to-grasp movements. *PLoS ONE* 8:e54658. doi: 10.1371/journal.pone.0054658

Pistohl, T., Schulze-Bonhage, A., Aertsen, A., Mehring, C., and Ball, T. (2012). Decoding natural grasp types from human ECoG. *Neuroimage* 59, 248–260. doi: 10.1016/j.neuroimage.2011.06.084

Raffin, E., Mattout, J., Reilly, K. T., and Giraux, P. (2012). Disentangling motor execution from motor imagery with the phantom limb. *Brain* 135, 582–595. doi: 10.1093/brain/awr337

Ramos-Murguialday, A., Broetz, D., Rea, M., Läer, L., Yilmaz, Ö., Brasil, F. L., et al. (2013). brain-machine interface in chronic stroke rehabilitation: a controlled study: BMI in chronic stroke. *Ann. Neurol.* 74, 100–108. doi: 10.1002/ana.23879

Ron-Angevin, R., Velasco-Alvarez, F., Sancha-Ros, S., and da Silva-Sauer, L. (2011). "A two-class self-paced bci to control a robot in four directions," in *Proceedings of the IEEE International Conference on Rehabilitation Robotics* (Zurich), 977–982. doi: 10.1109/ICORR.2011.5975486

Sober, S. J., and Sabes, P. N. (2003). Multisensory integration during motor planning. *J. Neurosci.* 23, 6982–6992. doi: 10.1523/JNEUROSCI.23-18-06982.2003

Sober, S. J., and Sabes, P. N. (2005). Flexible strategies for sensory integration during motor planning. *Nat. Neurosci.* 8, 490–497. doi: 10.1038/nn1427

Stancák, A., Riml, A., and Pfurtscheller, G. (1997). The effects of external load on movement-related changes of the sensorimotor EEG rhythms. *Electroencephalogr. Clin. Neurophysiol.* 102, 495–504. doi: 10.1016/S0013-4694(96)96623-0

Tacchino, G., Gandolla, M., Coelli, S., Barbieri, R., Pedrocchi, A., and Bianchi, A. M. (2017). EEG analysis during active and assisted repetitive movements: evidence for differences in neural engagement. *IEEE Trans. Neural Syst. Rehabil. Eng.* 25, 761–771. doi: 10.1109/TNSRE.2016.2597157

Takahashi, M., Takeda, K., Otaka, Y., Osu, R., Hanakawa, T., Gouko, M., et al. (2012). Event related desynchronization-modulated functional electrical stimulation system for stroke rehabilitation: a feasibility study. *J. Neuroeng. Rehabil.* 9:56. doi: 10.1186/1743-0003-9-56

Tan, H., Pogosyan, A., Anzak, A., Ashkan, K., Bogdanovic, M., Green, A. L., et al. (2013). Complementary roles of different oscillatory activities in the subthalamic nucleus in coding motor effort in Parkinsonism. *Exp. Neurol.* 248, 187–195. doi: 10.1016/j.expneurol.2013.06.010

Tatti, E., Ricci, S., Mehraram, R., Lin, N., George, S., Nelson, A. B., et al. (2019). Beta modulation depth is not linked to movement features. *Front. Behav. Neurosci.* 13:49. doi: 10.3389/fnbeh.2019.00049

Wang, K., Wang, Z., Guo, Y., He, F., Qi, H., Xu, M., et al. (2017). A brain-computer interface driven by imagining different force loads on a single hand: an online feasibility study. *J. Neuroeng. Rehabil.* 14:93. doi: 10.1186/s12984-017-0307-1

Wang, Z., Zhou, Y., Chen, L., Gu, B., Yi, W., Liu, S., et al. (2019). BCI monitor enhances electroencephalographic and cerebral hemodynamic activations during motor training. *IEEE Trans. Neural Syst. Rehabil. Eng.* 27, 780–787. doi: 10.1109/TNSRE.2019.2903685

Yuan, H., Perdoni, C., and He, B. (2010). Relationship between speed and EEG activity during imagined and executed hand movements. *J. Neural Eng.* 7:26001. doi: 10.1088/1741-2560/7/2/026001

Conflict of Interest: The authors declare that the research was conducted in the absence of any commercial or financial relationships that could be construed as a potential conflict of interest.

Publisher's Note: All claims expressed in this article are solely those of the authors and do not necessarily represent those of their affiliated organizations, or those of the publisher, the editors and the reviewers. Any product that may be evaluated in this article, or claim that may be made by its manufacturer, is not guaranteed or endorsed by the publisher.

Copyright © 2021 Nakayashiki, Tojiki, Hayashi, Yano and Kondo. This is an open-access article distributed under the terms of the Creative Commons Attribution License (CC BY). The use, distribution or reproduction in other forums is permitted, provided the original author(s) and the copyright owner(s) are credited and that the original publication in this journal is cited, in accordance with accepted academic practice. No use, distribution or reproduction is permitted which does not comply with these terms.

frontiers in Systems Neuroscience

REVIEW
published: 18 November 2021
doi: 10.3389/fnsys.2021.777706

It Is Time to Study Overlapping Molecular and Circuit Pathophysiologies in Alzheimer's and Lewy Body Disease Spectra

Noritaka Wakasugi[1] *and Takashi Hanakawa*[1,2]*

[1] *Integrative Brain Imaging Center, National Center of Neurology and Psychiatry, Tokyo, Japan,* [2] *Department of Integrated Neuroanatomy and Neuroimaging, Graduate School of Medicine, Kyoto University, Kyoto, Japan*

Alzheimer's disease (AD) is the leading cause of dementia due to neurodegeneration and is characterized by extracellular senile plaques composed of amyloid β_{1-42} (Aβ) as well as intracellular neurofibrillary tangles consisting of phosphorylated tau (p-tau). Dementia with Lewy bodies constitutes a continuous spectrum with Parkinson's disease, collectively termed Lewy body disease (LBD). LBD is characterized by intracellular Lewy bodies containing α-synuclein (α-syn). The core clinical features of AD and LBD spectra are distinct, but the two spectra share common cognitive and behavioral symptoms. The accumulation of pathological proteins, which acquire pathogenicity through conformational changes, has long been investigated on a protein-by-protein basis. However, recent evidence suggests that interactions among these molecules may be critical to pathogenesis. For example, Aβ/tau promotes α-syn pathology, and α-syn modulates p-tau pathology. Furthermore, clinical evidence suggests that these interactions may explain the overlapping pathology between AD and LBD in molecular imaging and post-mortem studies. Additionally, a recent hypothesis points to a common mechanism of prion-like progression of these pathological proteins, via neural circuits, in both AD and LBD. This suggests a need for understanding connectomics and their alterations in AD and LBD from both pathological and functional perspectives. In AD, reduced connectivity in the default mode network is considered a hallmark of the disease. In LBD, previous studies have emphasized abnormalities in the basal ganglia and sensorimotor networks; however, these account for movement disorders only. Knowledge about network abnormalities common to AD and LBD is scarce because few previous neuroimaging studies investigated AD and LBD as a comprehensive cohort. In this paper, we review research on the distribution and interactions of pathological proteins in the brain in AD and LBD, after briefly summarizing their clinical and neuropsychological manifestations. We also describe the brain functional and connectivity changes following abnormal protein accumulation in AD and LBD. Finally, we argue for the necessity of neuroimaging studies that examine

OPEN ACCESS

Edited by:
Tomohiko Takei,
Tamagawa University, Japan

Reviewed by:
Yashar Zeighami,
McGill University, Canada
Yuhei Takado,
National Institute of Radiological Sciences (NIRS), Japan

***Correspondence:**
Takashi Hanakawa
hanakawa.takashi.2s@kyoto-u.ac.jp

Received: *15 September 2021*
Accepted: *28 October 2021*
Published: *18 November 2021*

Citation:
Wakasugi N and Hanakawa T (2021) It Is Time to Study Overlapping Molecular and Circuit Pathophysiologies in Alzheimer's and Lewy Body Disease Spectra. Front. Syst. Neurosci. 15:777706. doi: 10.3389/fnsys.2021.777706

AD and LBD cases as a continuous spectrum especially from the proteinopathy and neurocircuitopathy viewpoints. The findings from such a unified AD and Parkinson's disease (PD) cohort study should provide a new comprehensive perspective and key data for guiding disease modification therapies targeting the pathological proteins in AD and LBD.

Keywords: Alzheimer's disease, Parkinson's disease, MRI, functional connectivity, fluid biomarkers, PET, SPECT, longitudinal cohort design

INTRODUCTION

In parallel with global aging, the number of elderly patients with neurodegenerative diseases is rapidly increasing worldwide. Among others, Alzheimer's disease (AD) is the most common, followed by Parkinson's disease (PD) (Hou et al., 2019). AD is the most common cause of dementia (Jansen et al., 2015). People with AD have memory impairment and deficits of self-awareness as the core clinical symptoms. People with AD also exhibit behavioral and psychological symptoms of dementia (BPSD), including anxiety, depression and hallucinations (Jack et al., 2018). AD has key neuropathological hallmarks, including extracellular senile plaques composed mainly of amyloid β_{1-42} ($A\beta_{1-42}$) and intracellular neurofibrillary tangles (NFTs) consisting of phosphorylated tau (p-tau) (Buckner et al., 2005; Jansen et al., 2015; Teipel et al., 2015; Demirtaş et al., 2017; Ishii et al., 2019). Abnormal Aβ and tau are considered key molecules in the etiopathogenesis of AD. However, it remains unclear how disease-specific the abnormal Aβ and tau proteins are in AD because these molecules are also involved in the pathophysiology of geriatric diseases other than AD (Galvin et al., 2011). Now it is widely recognized that AD is a disease spectrum spanning from preclinical AD, amnestic mild cognitive impairment (aMCI) and fully developed AD (Weiner et al., 2017).

Parkinson's disease is the second most common neurodegenerative disorder, characterized by motor symptoms, including akinesia, rigidity, and resting tremor. Non-motor symptoms include cognitive impairment, depression, anhedonia, anxiety, visual hallucination, and pain (Postuma et al., 2015). Moreover, People with PD usually have autonomic dysfunctions, including constipation, urinary disturbance, and orthostatic hypotension (Postuma et al., 2015). In PD, Lewy neurites, neurites with accumulations of protein aggregates mainly composed of α-synuclein (α-syn), are present in both the central and peripheral nervous systems. These protein accumulations are considered to give rise to the various neurological symptoms (Henderson et al., 2019; Mendoza-Velásquez et al., 2019). Furthermore, it is known that systemic symptoms of PD not only coexist with motor symptoms, but also appear before the onset of motor symptoms (Heinzel et al., 2019). Currently, dementia in advanced PD is commonly referred to as PD dementia (PDD). As part of the PD spectrum, dementia with Lewy bodies (DLB) may start from cognitive decline leading to dementia before or almost at the same time as the development of parkinsonism. Thus, PD is also a disease spectrum spanning from prodromal PD without motor symptoms to fully developed PD/PDD and DLB (Heinzel et al., 2019), which may be comprehensively called Lewy body disease (LBD), a synonym of the PD spectrum here, from an etiopathological perspective.

Alzheimer's disease and PD spectra include many common cognitive and psychiatric symptoms and risk factors. Recently, the core pathology of AD and LBD (i.e., PD/DLB) has been hypothesized to share the same mechanism, called the protein propagation hypothesis (Dagher and Zeighami, 2018; Colin et al., 2020). The hypothesis posits that neurodegeneration progresses by cross-synaptic transmission of abnormal proteins with altered conformation. This could explain the observation that in both PD and AD, various clinical signs gradually appear with aging, which allows the propagation of abnormal proteins. Even if this hypothesis is correct, many issues remain unresolved, such as differences in the neural circuits involved. Furthermore, the coexistence of AD and PD pathology is common in sporadic cases (Irwin et al., 2013). This coexistence may be the key to elucidating the molecular pathology of sporadic cases of LBD and AD.

In previous studies, AD and PD cases have typically been enrolled in different and independent cohorts. The Alzheimer's Disease Neuroimaging Initiative (ADNIs) is a series of cohort studies of AD (Petersen et al., 2010; Weiner et al., 2017; Veitch et al., 2019), as The Parkinson Progression Markers Initiative is for PD (Marek et al., 2011). However, considering the shared pathological mechanisms, many important questions may only be resolved by studies that include both AD and PD spectra in the same cohort. For example, mild cognitive impairment (MCI) may herald dementia (Flicker et al., 1991). MCI initially drew attention in the field of AD research. However, the background pathology of MCI is not limited to AD, but includes various pathological conditions such as PD (Dichgans and Leys, 2017; Baiano et al., 2020). A comprehensive cohort including different types of MCIs will likely cast new light on the prodromal stage of dementia.

In this article, we review basic research on the distribution and interactions of pathological proteins in the brains of AD and LBD, after briefly summarizing their clinical and neuropsychological manifestations. We also describe functional and connectivity changes in the brain in AD and LBD. Finally, we will argue for the necessity for a neuroimaging cohort treating the AD spectrum and the PD spectrum as a continuum. The findings, which will be obtained from the proposed cohort study, should provide a new comprehensive perspective for these two most important neurodegenerative disorders.

ALZHEIMER'S DISEASE

Alzheimer's disease is the most common dementia in the population over 65 years of age. The core clinical symptom of AD is impaired recent memory, which supposedly results from dysfunctions of the medial temporal lobe (MTL) and the hippocampus. Most patients with AD first present with impaired episodic memory, followed by more extensive cognitive dysfunctions, including amnesia, apraxia, and visuospatial deficits (Eramudugolla et al., 2017). These cognitive symptoms are ascribed to the dysfunctions of the temporal lobe, parietal lobe, and occipital lobe. Semantic memory problems caused by lateral temporal lobe dysfunction and insight and spontaneity deficits resulting from frontal lobe dysfunction may also be observed (Hodges and Patterson, 1997; Boublay et al., 2020).

Diagnostic Criteria

Alzheimer's disease is diagnosed primarily by clinical history. Multiple markers, including cerebrospinal fluid (CSF), neuroimaging, and genetic tests, are used as supportive findings (Jack et al., 2018). For the clinical diagnosis of AD, the following two criteria are used: (i) finding of major neurocognitive disorder (NCD), as defined by the fifth edition of the Diagnostic and Statistical Manual of Mental Disorders (DSM-5) (Eramudugolla et al., 2017), and (ii) the diagnostic guidelines of the National Institute on Aging and Alzheimer's Association (NIA-AA) (Jack et al., 2018). The common item in the two criteria is slowly progressive dementia.

DSM-5 criteria make use of genetic risks, including family history and identification of the causative genes. Cognitive dysfunctions need to be shown in two or more cognitive domains centered on the memory/learning disorders. NIA-AA criteria also consider the genetic risks and clinical symptoms, similar to DSM-5. NIA-AA also takes into consideration evidence for the existence of AD pathology indicated by fluid biomarkers such as CSF and imaging biomarkers such as positron emission tomography (PET).

For research purposes, the International Working Group-2 (IWG-2) criteria for AD may be used (Dubois et al., 2014). The criteria broadly classify AD into typical AD, in which patients initially develop episodic memory impairment, and atypical AD, in which patients develop unique symptoms such as logopenic aphasia and frontal lobe signs. In addition, the evaluation of Aβ and tau, using CSF or PET, is also essential.

Mild cognitive impairment is a condition where slight cognitive impairment is recognized objectively compared with a condition before illness, but the patients' activities of daily living are independent. MCI centered on memory deficits is clinically diagnosed as amnestic MCI (aMCI) presumably caused by AD pathology (Petersen et al., 1999, 2001). In addition, if there are findings from fluid/imaging markers indicating abnormalities in Aβ/tau, this condition is defined as AD-MCI (Albert et al., 2011).

Neuropsychological Testing

Neuropsychological tests for AD are used for screening, differential diagnosis, and severity assessment. In clinical practice, screening for dementia or MCI is performed by tests for general cognitive functions. Mini Mental State Examination (MMSE), a simple test for assessing multiple cognitive domains, is used with a cutoff value of 23/24 for dementia (Trivedi, 2017). To diagnose MCI, Montreal Cognitive Assessment (MoCA) may be used with a cutoff value of 25/26 (Davis et al., 2015). These tests are helpful not only for screening through the assessment of total scores, but also for evaluating cognitive subcategories, including memory, attention, and visuospatial cognition.

As the disease progresses, patients with AD who initially had only memory impairment begin to show impairment involving multiple cognitive domains, including visuospatial cognition and language. Therefore, the Wechsler Adult Intelligence Scale (WAIS) and the Wechsler Memory Scale (WMS-R) are performed for a more detailed and comprehensive evaluation. However, because these advanced tests take more than 1 h, they are not suitable for screening.

Differential diagnosis to estimate the background pathology of dementia cannot solely rely on the neuropsychological examination, and is accordingly usually performed in combination with the assessment of clinical course and diagnostic imaging. In clinical practice, it is important to distinguish AD from other dementias such as DLB. Typical early symptoms are predominantly memory deficits in AD; executive function and visuospatial cognition are impaired only after memory deficits become apparent (Jack et al., 2018). Therefore, for differential diagnosis of AD, patients should undergo tests of memory, attention, executive functions, and visuospatial cognition to distinguish from DLB, in which executive function and visuospatial cognition are impaired at the early stage. However, because half of the cases of DLB are complicated by AD pathology, the possibility that DLB patients have AD-like memory impairment from the onset needs to be taken into account (Yoshizawa et al., 2013).

The severity assessment is essential for selecting rehabilitation and welfare services, and for longitudinal cognitive assessment in clinical research. Clinical Dementia Rating (CDR) (Morris, 1993) is a scale that evaluates general cognitive functions and community affairs, home/hobbies, and personal care. CDR yields a global scale (CDR-GS) and a sum of boxes (CDR-SB). CDR-GS is a general severity calculated by weighting the results of each subscale and is commonly used for disease staging. On the CDR, CDR-GS 0.5 corresponds to MCI, and 1.0 or larger corresponds to dementia (Chang et al., 2011). CDR-SB provides more information in terms of quantitative evaluation than CDR-GS, especially in MCI and early AD (O'Bryant et al., 2010). A feature of CDR is that it also refers to interviews with family members. Thus, CDR provides accurate information for understanding disease severity and significantly impaired function when evaluated by a proficient examiner that is well informed by the caregiver. Alzheimer's Disease Assessment Scale-Cognitive Subscale (ADAS-cog) is an assessment of 11 cognitive subcategories related to AD symptoms (Kueper et al., 2018). It is time-consuming, yet suitable for observing changes in cognitive function over time and is often used in clinical trials.

Genetics

Most AD cases are sporadic, and the most prominent risk factor is aging (Angelova and Brown, 2019). AD also has familial cases,

and many genetic risk factors are known. In autosomal dominant AD, mutations in proteins related to Aβ production, such as presenilin 1/2 (*PSEN1/PSEN2*) and amyloid precursor protein (*APP*) have been reported (Robinson et al., 2017). The mutation of *PSEN1* accounts for the most common form of familial AD. *PSEN1* is a component of the γ-secretase complex, which plays an essential role in the production of Aβ. *APP* mutations were first reported as an etiological factor in intracranial hemorrhage with amyloid pathology (amyloid angiopathy) and subsequently identified in familial AD cases. Patients with autosomal dominant AD (AD-AD) with *PSEN1/PSEN2* and *APP* mutations may exhibit predominantly motor symptoms of akinetic-right type caused by Aβ deposition in the basal ganglia (Vöglein et al., 2019). Therefore, it may be difficult to distinguish some AD-AD cases from patients with PDD and DLB.

The ε*4* allele of the *APOE* gene is the most important risk factor for sporadic AD (Jansen et al., 2015), being present in more than half of all AD cases, compared with a frequency of ∼14% in the general population (Pontifex et al., 2018). The ApoE protein functions as a ligand for the low-density lipoprotein (LDL) receptor family on the cell, and its abnormality causes atherosclerosis. In the brain, ApoE is mainly produced by astrocytes and is involved in transporting and removing cholesterol (Hauser et al., 2011). Furthermore, ApoE was reported to be involved in the degradation of Aβ (Jiang et al., 2008). Humans carry the ε*2*,ε*3*, and ε*4* alleles with a worldwide frequency of 8.4, 77.9 and 13.7%, respectively (Liu et al., 2013). Compared with ε*3*/ε*3*, ε*4* hetero carriers have an odds ratio (OR) of 2.8 [95% confidence interval (CI) 2.3–3.5], whereas homo carriers (ε*4*/ε*4*) have an OR of 11.8 (95% CI 7.0–19.8) (Pontifex et al., 2018). Conversely, *APOEε2* is considered a protective factor for AD symptoms and pathology (Liu et al., 2013; Jindal and Bansal, 2016). *APOEε4* has been reported to be involved in abnormal Aβ accumulation and perturbed functional connectivity (FC) (Sheline et al., 2010a).

Recent whole-exome sequencing and genome-wide association studies (GWAS) revealed a rare variant of the triggering receptor expressed on myeloid cells 2 (*TREM2*) in AD (Guerreiro et al., 2013; Jonsson et al., 2013). Interestingly, TREM2, which is expressed by microglia, could be involved in the removal of Aβ. It is expected that advances in genetic research will continue to reveal novel AD risk genes.

Fluid Biomarkers

Aβ and tau, which constitute the hallmark senile plaques and NFTs, respectively, are the most important biomarkers of AD (Hampel et al., 2010; Olsson et al., 2016). The Alzheimer's Disease Neuroimaging Initiative (ADNI) revealed that CSF can be used to detect the earliest changes in AD pathology (Weiner et al., 2012). Another study found decreased CSF-Aβ more than 25 years before the onset of AD (Bateman et al., 2012). These findings are incorporated into clinical diagnostic criteria, such as the NIA/AA criteria, for preclinical AD, which is the prodromal stage with normal cognition before MCI. As such, CSF-Aβ is considered a promising AD biomarker for early diagnosis, and is widely used in both the clinical and research laboratory settings. Lower $A\beta_{1-42}$ level and higher total tau (t-tau) or p-tau are reliable CSF biomarkers of AD pathology. Also, several reports suggest that the ratio of $A\beta_{1-42}/A\beta_{1-40}$ (Blennow and Hampel, 2003), t-tau/$A\beta_{1-42}$ (Shaw et al., 2009) or p-tau/$A\beta_{1-42}$ (De Meyer et al., 2010) more accurately reflect AD pathology than $A\beta_{1-42}$ or tau alone. In p-tau, CSF-tau phosphorylated at serine 181 (p-tau 181) is regarded as an AD-specific biomarker (Hampel and Teipel, 2004). As a CSF marker under development, Aβ oligomers might become a useful biomarker. Aβ oligomers are formed during the polymerization process of Aβ fibrils and are suggested to cause synaptic dysfunction. However, a hurdle to quantitative evaluation is the limited amount of Aβ oligomers in CSF (Hampel et al., 2010).

It has been suggested that plasma p-tau 181 is a potential AD-specific marker for predicting neurodegeneration and cognitive decline (Barthélemy et al., 2020; Moscoso et al., 2021). The results of a meta-analysis of blood biomarkers showed increased t-tau, p-tau 181, p-tau 217, neurofilament light protein (NFL) and decreased $A\beta_{1-42}$ in patients with AD and AD-MCI (Qu et al., 2021).

Neuroimaging

Blood Flow/Metabolism Changes

Detecting changes in cerebral perfusion using single-photon emission computed tomography (SPECT) is widely used in the clinical field to distinguish AD from other dementias. ^{18}F-fluorodeoxyglucose positron emission tomography (FDG PET) detects patterns of regional glucose metabolism associated with AD pathology (neuronal loss). The core finding is similar between perfusion SPECT and FDG-PET. Decreased perfusion or glucose metabolism in the temporal lobe, the parietal lobe and the posterior cingulate gyrus (PCC) is indicative of AD (Bloudek et al., 2011). The sensitivity of perfusion SPECT to distinguish patients with AD from healthy subjects is 80%, and the specificity is 85% (McKhann et al., 2011). FDG-PET discriminates between AD and healthy subjects with a sensitivity of 90% and a specificity of 89% (Bloudek et al., 2011).

Amyloid Positron Emission Tomography

Visualization of deposition of Aβ or tau in the brain is strong evidence of AD pathology. Both amyloid-PET and tau-PET provide indispensable information for the classification and interpretation of the underlying pathophysiology as well as for the early diagnosis. Recently, the removal of Aβ fibrils and tau accumulation is considered a promising disease-modifying therapy, and thus the visualization of abnormal Aβ or tau in the brain is becoming even more important from the viewpoint of treatment. Aβ deposition can be visualized using PET. There are several standard probes, including Pittsburgh compound B (^{11}C-PiB) and several ^{18}F agents (florbetapir and florbetaben), for amyloid-PET (Chételat et al., 2020). ^{11}C-PiB has been used as a standard PET probe for a long time and has substantially advanced our knowledge of the disease. However, because ^{11}C-PiB has a half-life of only 20 min, its use is limited to hospitals with a cyclotron and synthesis unit. Currently, multiple ^{18}F-probes, which have a longer half-life of 110 min, and is thus deliverable from a factory, have been developed so that amyloid-PET can be performed at more hospitals than before.

Both CSF-Aβ and amyloid-PET are tests for identifying AD pathology related to senile (amyloid) plaques. In a report comparing PiB-PET and CSF biomarkers, PiB-positive patients had significantly lower Aβ and significantly higher t-tau and p-tau in CSF compared with PiB-negative subjects (Shimada et al., 2011). There is a negative correlation between PET Aβ levels and CSF Aβ levels. The diagnostic value of amyloid-PET and CSF-Aβ is comparable, but they differ slightly in the information they provide. Unlike CSF-Aβ, amyloid-PET can visualize the spatial extent of amyloid deposition. In AD, the core imaging findings are amyloid accumulation in the frontal lobe, PCC and precuneus. The amyloid burden in these regions can explain the pathophysiology of AD well and can provide a key to differential diagnosis from other dementias. PET probe injection is less invasive than a lumbar puncture, so that cognitively healthy people may undergo amyloid-PET more comfortably than CSF collection for screening or possibly prodromal interventions. Conversely, CSF-Aβ is suggested to reflect AD pathology earlier than amyloid-PET (Mattsson et al., 2015). Even if amyloid-PET is negative, CSF measurements may identify earlier amyloid pathology. Furthermore, if a promising CSF biomarker is developed in the future (Hampel et al., 2010), additional tests can be performed if the frozen CSF sample is preserved. Thus, past patient conditions can be evaluated using the latest testing method with CSF. CSF and amyloid-PET are thus complementary, and it is important to combine the two tests to assess amyloid pathology more comprehensively than before.

Tau Positron Emission Tomography

Although tau-PET has faced some problems, such as difficulty in developing a probe with a high affinity for AD-tau and a low affinity for $A\beta_{1-42}$ (Valotassiou et al., 2018), multiple nuclides, including ^{11}C-PBB3/^{18}F-PM-PBB (Maruyama et al., 2013; Tagai et al., 2021) and ^{18}F-flortaucipir (Leuzy et al., 2019) are now available. The intracerebral accumulation rate of tau-PET nuclides correlates well with the severity of the disease. Therefore, it attracts attention as a modality with favorable characteristics compared with other biomarker candidates (Joie et al., 2020).

Tau-PET is a promising imaging method for the diagnosis of various neurodegenerative disorders including the AD spectrum. Amyloid burden visualized by PET is affected by aging and the *ApoE* allele, and hence the specificity of AD diagnosis with amyloid PET is relatively low especially in the elderly aged over 80 years old (Ossenkoppele et al., 2015). Contrastingly, tau-PET has been reported to show high specificity in differentiating AD from other neurodegenerative disorders (Ossenkoppele et al., 2018). Moreover, tau-PET positivity can be a better predictor of cognitive decline in AD as compared with CSF-p-tau 181 or amyloid PET (Bucci et al., 2021). Another study using ^{11}C-PBB3 PET revealed cases with tau accumulation without $A\beta_{1-42}$ accumulation by amyloid-PET (Shimada et al., 2017). This amyloid-negative and tau-positive state may represent an entity called primary age-related tauopathy (PART) (Crary et al., 2014). Dementia with PART overlaps with senile dementia of the NFT type (SD-NFT), which is tau-related dementia distinct from AD. Patients with SD-NFT are sometimes misdiagnosed as AD, and hence tau-PET may be useful for differential diagnosis.

The PET can provide data most closely related to the neuropathological diagnosis. Yet, PET is an expensive tool and thus may not be affordable in many places in the world. Therefore, early biomarkers using relatively easy-to-perform tests, such as blood tests and magnetic resonance imaging (MRI), should be explored. Until such surrogate markers become available, PET will remain one of the most important tools in cohort studies of neurodegenerative disorders. In the meantime, it is important to organize comprehensive and high-quality cohort studies to acquire multiple PET scan along with fluid samples (both blood and CSF) and MRI.

Structural Magnetic Resonance Imaging

Hippocampal and MTL atrophy in structural MRI is frequently used as an adjunct to clinical diagnosis of AD. In a systematic review, MTL atrophy was discriminative between AD and healthy persons with a sensitivity of 85% and a specificity of 88% (Scheltens et al., 2002). In AD, the accumulation of $A\beta_{1-42}$ and p-tau is thought to become saturated before the onset of symptoms such as cognitive decline and cerebral atrophy, which become apparent later (Weiner et al., 2015). Reflecting this time course, changes in brain structure occur mainly after the onset of cognitive decline, and therefore, structural MRI primarily provides imaging markers for diagnosis and severity assessment after onset.

Reduced hippocampal volume is a consistent finding across structural MRI studies as previously observed in postmortem brains. A voxel-based morphometry (VBM) analysis of structural MRI suggested that the progression of cerebral atrophy in AD parallels the putative propagation of neurofibrillary tangle implicated by Braak staging (Matsuda, 2016). A combining a neuropsychological battery with VBM analysis of MRI data from ADNI found correlations between memory loss and mediolateral temporal lobe atrophy as well as between executive dysfunction and parietotemporal atrophy (Nho et al., 2012). White matter changes in AD are reported to be less significant than gray matter changes. However, a meta-analysis of VBM suggests that in patients with AD, there is considerable volume loss in the white matter beneath the parahippocampal gyrus and in the posterior corpus callosum (Matsuda, 2016).

Diffusion Tensor Imaging

Tau is a microtubule-associated protein that is involved in stabilizing the microtubule structure of neuronal axons (Guo et al., 2017). DTI is a method for capturing changes in the microstructure of the white matter, and it may be able to detect axonal changes related to tau pathology. In AD, reduced fractional anisotropy (FA) is most pronounced in fiber tracts in the limbic area, such as the fornix, and in the temporal lobe (Teipel et al., 2015). This abnormality in white matter microstructure is an early change seen in the process of AD neurodegeneration. Moreover, an FA reduction in PCC has been reported in patients in the prodromal stage,

including subjective cognitive impairment (SCI) and mild MCI (Stenset et al., 2011).

Functional Magnetic Resonance Imaging

Functional MRI can be used to observe brain activities non-invasively via blood-oxygen-level-dependent (BOLD) signals, which reflect local fluctuations in the oxygenation of cerebral blood (Ogawa et al., 1990). Task-related changes in BOLD signals and synchronous BOLD fluctuations across multiple regions at resting state exhibit changes associated with the onset and progression of neurodegenerative diseases, including AD. In fMRI studies with a memory task, patients with early MCI show increased activation in the MTL (Dickerson et al., 2004, 2005; Chhatwal and Sperling, 2012) and hippocampus (Celone et al., 2006), compared with healthy controls. This hyperactivation may be lost at follow-up (O'Brien et al., 2010; Bai et al., 2011). Therefore, it is hypothesized that temporary hyperactivation is a compensatory mechanism in the early stage of AD (Clment and Belleville, 2010).

Resting-state functional connectivity MRI (rsfcMRI) is a promising imaging modality for pre-symptomatic diagnosis of AD. This type of MRI focuses on the co-fluctuation of BOLD signals across brain regions in the low-frequency band below 0.1 Hz (Liu, 2013). Thus, rsfcMRI studies assume that brain regions with mutually interwoven networks should show similar fluctuations in low-frequency BOLD signals, reflecting concerted fluctuation of synaptic activity propagated through the neural network. Another assumption is that the level of coordination of signals across brain regions reflect specific functions subserved by the network. Interestingly, FC can be detected between regions without known direct fiber connections (Honey et al., 2009), meaning that rsfcMRI may detect network abnormalities that cannot be discovered by studies of structural connectivity. Thus, rsfcMRI is valuable as a biomarker of AD because brain networks are differentially affected by various factors, including the stage of the disease (Wang et al., 2006; Sheline and Raichle, 2013; Kim et al., 2015; Córdova-Palomera et al., 2017; Palmqvist et al., 2017), symptoms (Adriaanse et al., 2014), treatments (Ochmann et al., 2017), pathology (Sheline et al., 2010a,b; Robinson et al., 2017; Shi and Holtzman, 2018) and genetic factors (Vöglein et al., 2019). In AD, various types of network alterations, including those of the default mode network (DMN), are reported (**Figure 1A**).

The most well-established finding is that hippocampal–default mode network (DMN) connectivity is reduced compared with healthy people (Hohenfeld et al., 2018). Among the nodes within the DMN, the importance of connectivity between the precuneus and PCC has been demonstrated in numerous studies (Greicius et al., 2003; Wu et al., 2011; Teipel et al., 2015; Palmqvist et al., 2017; Ibrahim et al., 2021). The precuneus plays a central role in visuospatial imagery, episodic memory retrieval, and processing of self-related information (Cavanna and Trimble, 2006). The PCC is related to internally-directed thinking and helps allocate attention efficiently in collaboration with the ECN (Leech et al., 2011). Abnormal connectivity between the PCC and precuneus likely reflects pathological changes in AD as substantial abnormalities are detected in these regions, such as decreased glucose metabolism and perfusion, and accumulation of abnormal proteins (Bloudek et al., 2011; Daerr et al., 2017). Indeed, the FC abnormality in AD is, at least in part, associated with amyloid accumulation. Changes in AD-like connectivity have been found in amyloid-positive non-AD patients (Sheline et al., 2010b). Surprisingly, *APOEε4* carriers have reduced connectivity at the stage of no amyloid accumulation (Sheline et al., 2010a).

The pattern of DMN FC abnormality may depend on the age of onset. Early-onset AD shows impairment among a wide range of connectivities, including visual network, auditory network, sensorimotor network (SMN), DMN, executive control network (ECN), and dorsal attention network (DAN), compared with senile-onset AD (Adriaanse et al., 2014).

Several rsfcMRI studies have attempted to classify categories within the AD spectrum (e.g., AD-MCI vs. AD), AD from other dementia spectra, or from healthy elderlies (Zhou et al., 2010; Wee et al., 2016; Zhang et al., 2019). Conventional static FC, dynamic FC (reflecting changes in FC over time), and amplitude of low-frequency fluctuations (ALFF) have been used for classification. The combination of these different modalities slightly improves classification accuracy (de Vos et al., 2018). Machine learning (ML) classification using PCC-FC can classify AD and healthy elderlies with a sensitivity of 75.2% and a specificity of 74.9% (Ibrahim et al., 2021). The ICA-based ML technique can classify AD patients and healthy elderlies with a sensitivity of 78.2% and a specificity of 83.2% (Ibrahim et al., 2021). In classifying AD patients from healthy elderlies, the classification performance is significantly improved when multiple MR modalities (structural MRI, DTI, and rsfMRI) are combined, compared with a single imaging modality (Schouten et al., 2016).

PARKINSON'S DISEASE

The core condition of the LBD/PD spectrum, PD, is the most common movement disorder and is caused primarily by the loss of nigrostriatal dopaminergic neurons, associated with the intracellular deposition of α-syn (Postuma et al., 2015). The cardinal clinical symptom is a movement disorder comprehensively called parkinsonism, with features of akinesia, rigidity, resting tremor, and postural instability. The PD spectrum may also present with cognitive disturbance and dementia. In PD, the prevalence of MCI is reported to be 40% (Baiano et al., 2020), and that of dementia is 30% (Hanagasi et al., 2017). Dementia in PD spectrum is characterized by hallucination with highly specific content and temporal fluctuations in cognitive function centered on attention and arousal (Dickson et al., 2017). DLB is diagnosed if dementia is already present from the onset, and PD with dementia (PDD) is diagnosed if cognitive decline occurs after the onset of motor symptoms. In general, 1 year after the onset of PD is used as the boundary between PDD and DLB (1-year rule) (Bonanni et al., 2006; McKeith et al., 2017). Thus, PDD and DLB may constitute a spectrum (Jellinger and Korczyn, 2018). Some reports indicate differences in clinical features between PDD and DLB. Patients with DLB tend to have severer visuospatial cognitive, executive, and attentional decline

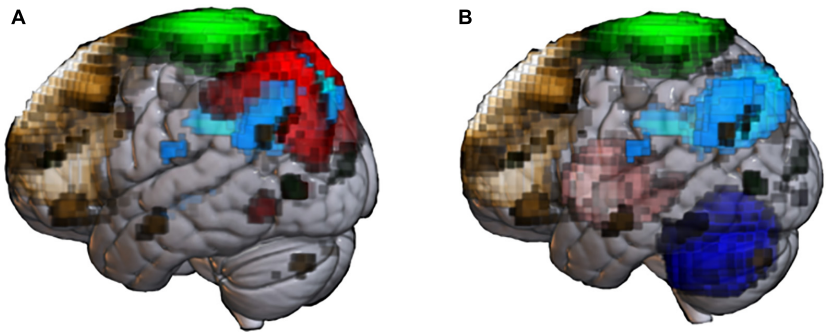

FIGURE 1 | Abnormal resting-state networks in Alzheimer's disease (AD) and Parkinson's disease (PD). Functional network templates were extracted from the MRI database (70 healthy elderly) at the National Center of Neurology and Psychiatry' to display network abnormality reported in past AD **(A)** and PD **(B)** studies. **(A)** Default mode network (DMN, light blue) is the representative network impaired in patients with senile-onset AD. Early- onset AD shows impaired not only DMN, but also executive control network (brown), sensory-motor network (SMN, green) and dorsal-attention network (red). **(B)** Patients with PD shows extensive network impairment, including basal ganglia (pink), cerebellum network (blue), and SMN. PD patients with cognitive impairment shows impaired DMN and ECN.

than people with PDD (Morra and Donovick, 2014). In terms of the motor symptoms, resting tremor and laterality are less evident in DLB than in PDD.

Symptoms common in AD, including olfactory dysfunction, apathy, and anxiety depression, are also common in dementia in the PD spectrum (Attems et al., 2014; Le Heron et al., 2018; Galts et al., 2019). As described later, DLB/PDD is associated with various degrees of AD pathology, and this shared pathology may be the reason for the clinical similarity between AD and PDD/DLB.

Diagnostic Criteria

There are two widely used diagnostic criteria for PD—the United Kingdom Parkinson's Disease Society Brain Bank (UKPDSBB) clinical diagnostic criteria (Gibb and Lees, 1988; Hughes et al., 1992) and the International Parkinson and Movement Disorder Society (MDS) clinical diagnostic criteria for PD (Postuma et al., 2015). Both require bradykinesia as a core symptom.

UKPDSBB criteria diagnose PD with the following three steps: presence of parkinsonism (step 1), exclusion of other parkinsonian syndromes (step 2), and existence of supportive features (step 3). These criteria are used worldwide and have had their accuracy verified by postmortem pathological diagnoses. The MDS diagnostic criteria include criteria for clinical diagnosis and research criteria for probabilistic prediction of PD before the diagnosis, according to risk factors and mild symptoms. Multiple studies have reported a high concordance rate for PD diagnosis between UKPDSBB criteria and MDS criteria (Malek et al., 2017; Postuma et al., 2018). Neither criterion mentions PDD, which requires an independent assessment (Sachdev et al., 2014).

Motor and Neuropsychological Tests

In the PD spectrum, the MDS-Sponsored Revision of the Unified Parkinson's Disease Rating Scale (MDS-UPDRS) is widely used for the evaluation of motor and non-motor symptoms (Goetz et al., 2008). MDS-UPDRS is divided into the following four sections: questionnaire for non-motor symptoms in daily life (Part 1), motor symptoms in daily life (Part 2), motor examination by a physician (Part 3), and questionnaire for motor complications (Part 4). The score is used for evaluation of disease severity and response to treatment.

Because of the difference in clinical symptoms, PD has been traditionally subjected to neuropsychological tests slightly different from those for AD. A condition consistent with MCI is found in nearly half of people with PD (Goldman et al., 2018). A longitudinal study reported that 80% of people with PD eventually show dementia (Williams-Gray et al., 2007). In PD, executive function is particularly vulnerable. Executive dysfunction is found from the prodromal stage and is more pronounced than memory impairment. Therefore, in the cognitive evaluation of PD, a test of frontal lobe functions such as Frontal Assessment Battery (FAB) (Dubois et al., 2000) is often added to a general cognitive test such as MMSE. Otherwise, it is recommended to perform MoCA, in which executive functions are tested in more detail than MMSE (Weintraub et al., 2015).

To assess cognitive dysfunctions in early PD (such as PD-MCI), it is recommended to examine five cognitive domains—memory, executive, attention/working memory, language, and visuospatial function (Litvan et al., 2012). To this end, thorough testing with WAIS and WMS may be considered (Tang et al., 2016).

In PDD, psychiatric symptoms are often directly linked to a decrease in Activities of Daily Living (ADL), and it is essential to evaluate the severity of psychiatric symptoms properly (Rosenthal et al., 2010). MDS-UPDRS Part 1 evaluates these symptoms. Questionnaires such as Beck Depression Inventory (BDI) (Beck et al., 1961), Questionnaire for Impulsive-Compulsive Disorders (QUIP) (Probst et al., 2014), and State-Trait Anxiety Inventory (STAI) (Caillava-Santos et al., 2015) are often used for the assessment of psychiatric symptoms in the PD spectrum.

Genetics

Like AD, PD is primarily a sporadic disease. Multiple genetic and environmental factors appear to be involved in the onset of

PD. Approximately 5% of PD cases are familial, some of which are inherited in a Mendelian fashion, including *SNCA*, *PKRN,* and *LRRK2* (Singleton and Hardy, 2019). Studies of PD genetics have revealed some of the mechanisms including abnormal α-syn deposition, oxidative stress, mitochondrial dysfunction, and abnormalities in the ubiquitin-proteasome system leading eventually to cell death (Ganguly et al., 2021). Genome-wide association studies (GWASs) have identified many single nucleotide polymorphisms (SNPs) as risk factors for PD (Nalls et al., 2014; Blauwendraat et al., 2020). However, it is still unclear how and to what extent each of these genes is related to PD pathology.

GBA has recently been recognized as a risk gene for PD. *GBA* is the causative gene of Gaucher's disease, an autosomal recessive lysosomal disorder caused by glucocerebrosidase (GBA) deficiency (Hruska et al., 2008). It is reported that decreased GBA activity increases soluble α-syn oligomers (Mazzulli et al., 2011). Interestingly, decreased GBA activity in the brain is also seen in patients with sporadic PD (Gegg et al., 2012). The OR for any *GBA* mutation in PD patients vs. controls was reported to be 5.43 (Sidransky et al., 2009). Carriers of *GBA* mutations are reported to represent 4–29% of patients with PD, and *GBA* may be related to the early onset of PD (Lees et al., 2009).

Fluid Biomarkers

There are few established serum biomarkers for PD. However, several reports have pointed out the association between PD and inflammatory markers. For example, a study found a correlation between the development of sporadic PD and elevated inflammatory biomarkers such as serum TNF-α and IL-6 (Ferrari and Tarelli, 2011). Another study found that decreased apolipoprotein A1 and increased C-reactive protein (CRP) were associated with severe motor symptoms, depression, and sleep disorders (Ferrari and Tarelli, 2011; Lawton et al., 2020).

The most straightforward fluid biomarker should be the direct measurement of α-syn. However, there are some difficulties in measuring the protein in body fluids. Blood has the advantage of easy collection, but simple measurement of α-syn using a blood sample is not currently helpful in distinguishing PD from healthy population. Although there are multiple reports of elevated plasma or serum α-syn levels in PD patients compared with healthy people (Chang et al., 2020), reports on the correlation between α-syn levels and clinical symptoms are inconsistent. There is even a report of decreased plasma α-syn in PD patients (Li et al., 2007). Technical problems may underlie the discrepancies, including contamination of α-syn from erythrocytes due to hemolysis, differences in assay technique, and differences in the binding ability of the antibodies to α-syn (Ganguly et al., 2021). More recently, α-syn oligomers and aggregated α-syn have drawn attention as biomarkers for the progression of PD (Maass et al., 2019). The α-syn oligomers and aggregated α-syn may be involved in the transcellular transmission of α-syn (Okuzumi et al., 2021).

Measurement of α-syn in CSF should be established. Many studies have reported that total α-syn is lower in patients with PD than in healthy controls (Tokuda et al., 2006; Mollenhauer et al., 2013; Wennström et al., 2013). However, the specificity of this finding is not high enough to distinguish PD from healthy controls or from other parkinsonian syndromes (Zhou et al., 2015). Measurement of phosphorylated α-syn or the ratio of phosphorylated α-syn to total α-syn might be helpful in distinguishing PD from healthy controls and from other parkinsonian syndromes (Majbour et al., 2016). CSF studies also show an increase in α-syn oligomers and an increase in the ratio of α-syn oligomer to total α-syn in PD (Tokuda et al., 2010; Majbour et al., 2016; Kakuda et al., 2019). The development of measurement methods has seen recent progress (Kakuda et al., 2019; Okuzumi et al., 2021). Recently, real-time quaking-induced conversion (RT-QuIC), a technique originally developed to detect the self-aggregating ability of proteins in prion diseases, was used for detecting α-syn aggregation with a sensitivity of 92% (DLB) and 95% (PD), and a specificity of 100% (Fairfoul et al., 2016). The use of the novel assays, including RT-QuIC and α-syn oligomers, currently promises the most useful biomarker to precisely capture synuclein deposition.

Neuroimaging

Blood Flow/Metabolism Changes

Changes in cerebral perfusion are used primarily for the auxiliary diagnosis of PDD. Using SPECT, decreased perfusion is observed along with disease progression and impaired cognitive function in patients with PDD. In particular, perfusion in the frontal, parietal and occipital lobes is reduced in patients with PDD (Spampinato et al., 1991; Sawada et al., 1992). Furthermore, in PDD patients with impaired visual cognitive function, decreased perfusion in the occipital lobe is remarkable (Abe et al., 2003). In FDG-PET, glucose hypermetabolism is observed mainly in the putamen, motor cortex and cerebellum, and hypometabolism is seen in the posterior temporoparietal and occipital lobes (Meyer et al., 2017; Thobois et al., 2019). An FDG-PET study revealed that DLB had higher glucose metabolism in PCC and precuneus than did AD, irrespective of amyloid deposition (Graff-Radford et al., 2014).

Positron Emission Tomography/Single-Photon Emission Computed Tomography to Detect Monoaminergic Dysfunction in Parkinson's Disease Spectrum

Single-photon emission computed tomography can visualize PD-derived neurodegeneration, such as the reduction in dopaminergic nerve endings and the loss of the epicardial sympathetic nerve.

^{123}I-meta-iodobenzylguanidine (MIBG)-SPECT captures the loss of postganglionic sympathetic neurons in the PD spectrum. It was reported that abnormalities in ^{123}I-MIBG-SPCET could be diagnostic in PD, with a sensitivity of 84.3% and a specificity of 89.5% (Sawada et al., 2009). ^{123}I-MIBG-SPECT abnormality can be observed at the early stages, even before the onset of definitive motor symptoms in PD (Heinzel et al., 2019). However, it should be noted that some patients can show a false negative finding in the early stages (Sawada et al., 2009).

Presynaptic dopaminergic neuronal loss can be detected using dopamine transporter (DAT)-SPECT. Of the many radiotracers, ^{123}I-Ioflupane is the easiest to access. There are multiple reports

that the sensitivity and specificity for loss of dopaminergic nerve terminals using DAT-SPECT are 90% or higher (Pirker, 2003; Brigo et al., 2014; O'Brien et al., 2014). Still, false-negative cases have been pointed out (Ba and Martin, 2015). Although it is challenging to distinguish PD from other parkinsonian syndromes using the results from DAT-SPECT only, some studies reported that visual inspection and evaluation of specific binding ratio (SBR) over time can help distinguish PD from other synucleinopathies (Sakakibara et al., 2020). It has been reported that the combined use of DAT-SPECT and MIBG SPECT enhances the specificity of the diagnosis of PD (Yoshii et al., 2017). Therefore, if clinical diagnosis of PD is challenging, the combined use of DAT-SPECT and MIBG SPECT may be considered. Semi-quantified values are available in the form of heart-mediastinal ratio in MIBG-SPECT and SBR of DAT-SPECT. Furthermore, a correction method of these values across different facilities has been proposed for multicenter research (Nakajima et al., 2012; Matsuda et al., 2018).

Positron Emission Tomography to Detect Abnormal Protein Deposition in Parkinson's Disease Spectrum

The PET imaging technology for visualizing α-syn accumulation has not been established yet (Verdurand et al., 2018). Several PET tracers are under development, and animal experiments have confirmed the affinity of the tracers for α-syn aggregates (Kuebler et al., 2021). If an α-syn tracer is developed for humans, it will be possible to identify patients in the preclinical/prodromal stage, to evaluate changes in α-syn deposition in the course of disease progression, and to distinguish PD from other parkinsonian syndromes. Further research and development are urgently needed.

In terms of Aβ/tau accumulation, patients with PDD/DLB have many similarities with AD from multiple perspectives. In a cross-sectional amyloid PET study, PDD and DLB showed moderate to prominent amyloid burden in most cases whereas PD with normal cognition had little amyloid burden (Mashima et al., 2017). The spatial distribution of amyloid in PDD/DLB was similar to that in AD (Shimada et al., 2013). It was also reported that the uptake pattern of tau PET tracer in the temporal-lobe is different between AD and DLB (Kantarci et al., 2017). This discrepancy between PDD/DLB and AD is still under investigation and is going to be discussed in detail in the UNRESOLVED QUESTIONS AND FUTURE DIRECTIONS section.

Structural Magnetic Resonance Imaging

Previously in the PD research, structural MRI was performed only to rule out other parkinsonian syndromes such as vascular parkinsonism. This poor performance was partly due to the difficulty in detecting PD-specific structural abnormalities using conventional sequences with low-field MRI imaging below 1.5 T (Sterling et al., 2016). With a higher magnetic field of 3 T, group-level analyses revealed a loss of volume in the putamen (Tinaz et al., 2011), midbrain, basal ganglia, basal forebrain and medial temporal lobe (Zeighami et al., 2015), occipital lobe and head of the caudate nucleus (Sterling et al., 2013; Lewis et al., 2016). As symptom–structure correlates, motor symptoms have been associated with frontal lobe atrophy (Burton et al., 2004; Rosenberg-Katz et al., 2013), and occipital lobe atrophy with hallucinations (Pagonabarraga et al., 2014). Cognitive impairment is related to atrophy of widely distributed structures (Zeighami et al., 2019), including the hippocampus (Laakso et al., 1996; Camicioli et al., 2003; Junqué et al., 2005; Tam et al., 2005; Ibarretxe-Bilbao et al., 2008), the anterior cingulate cortex (Nagano-Saito et al., 2005), the temporal cortex (Summerfield et al., 2005), the frontal cortex (Burton et al., 2004; Nagano-Saito et al., 2005), and the parietal cortex (Sanchez-Castaneda et al., 2009).

The substantia nigra pars compacta (SNc), where the cell bodies of the nigrostriatal dopamine neurons reside, is critical in the clinical evaluation of PD. Recently, technology with high-field MRI of 3 T or higher has allowed visualization of pathological processes in the SNc (Wang et al., 2016). For the assessment of the SNc, susceptibility-weighted imaging (SWI), quantitative susceptibility mapping (QSM) and neuromelanin (NM) imaging may have a diagnostic value. SWI is sensitive to the iron content in the brain. In patients with PD, iron is accumulated in the brain; therefore, iron-deposition imaging may be useful. SWI studies suggest that iron deposition is higher in patients with PD than in healthy people in the SNc, caudate nucleus, red nucleus, putamen and globus pallidus (Zhang et al., 2009; Wu et al., 2014; Wang et al., 2016). QSM is another iron mapping technique through the modeling of magnetic susceptibility sources. QSM studies indicate increased iron deposition in the SNc (Ahmadi et al., 2020; Poston et al., 2020), red nucleus (Cheng et al., 2020), prefrontal cortex, caudate (Chen et al., 2019) and putamen (Thomas et al., 2020) in PD. In a meta-analysis of the iron deposition imaging in PD, iron deposition in the SNc was shown with both SWI and QSM. Moreover, positive correlation between QSM iron deposition and the total UPDRS score has been reported (Pyatigorskaya et al., 2020).

Neuromelanin-contrast MRI might provide a promising biomarker for the PD spectrum. NM is present in dopaminergic neurons in the SNc. Turbo spin echo T1-weighted MRI sequence with magnetization transfer (Sasaki et al., 2008) and gradient recalled echo with magnetization transfer (van der Pluijm et al., 2021) are currently used to yield a contrast sensitive to NM. NM MRI signals increase with age in the healthy population, but are markedly decreased in PD, reflecting the loss of dopamine neurons (Sasaki et al., 2008; Zucca et al., 2014).

Diffusion Tensor Imaging

In PD, many studies have reported correlations between decreased FA in the SN and severe motor symptoms (Prakash et al., 2012; Schuff et al., 2015; Langley et al., 2016). FA abnormalities have been reported also for non-motor symptoms, and these are associated with cognitive symptoms, mood disorders, hyposmia, hallucinations, and REM sleep behavior disorder (RBD) (Hall et al., 2016).

Patients with PDD show decreased FA and increased mean diffusivity throughout the cerebral white matter compared with healthy people (Melzer et al., 2013). Reduced hippocampal FA is also reported in patients with PDD compared with patients with

PD and those with normal cognitive functions (Chen B. et al., 2015). Others have reported an association of general cognitive decline evaluated by MMSE and MoCA with lower FA in the corpus callosum, the anterior cingulate cortex, and the frontal white matter regions (Kamagata et al., 2012; Chen B. et al., 2015).

Functional Magnetic Resonance Imaging

In PD, various alterations are reported in motor-related resting-state networks, including the basal ganglia (Helmich et al., 2010; Hacker et al., 2012; Agosta et al., 2014; Rolinski et al., 2015), cerebellum (Hu et al., 2015; O'Callaghan et al., 2016) and SMN (Fling et al., 2014; Bell et al., 2015; Canu et al., 2015) (**Figure 1B**). A meta-analysis suggests that decreased FC in the posterior putamen in PD may be a consistent finding (Herz et al., 2014).

Changes in FC may reflect a specific type of motor symptom. Tremor-dominant PD patients, compared with patients without tremor, show increased FC within the striatum (Dirkx et al., 2016), between the subthalamic nucleus and motor and primary somatosensory cortices (Baudrexel et al., 2011), and among the cerebellum, thalamus and motor cortex (Helmich et al., 2011). Nevertheless, decreased FC in tremor-dominant PD has also been reported in the cerebellum (Hu et al., 2015), putamen (Chen H.M. et al., 2015) and primary somatosensory cortex (Zhang et al., 2015). Akinetic-rigid subtype patients, compared with healthy controls, show increased FC in the left putamen, bilateral angular gyri, bilateral medial prefrontal cortices (MPFC) (Zhang et al., 2015) and anterior DMN (Hou et al., 2018b), while they show decreased FC in the precuneus, amygdala (Guan et al., 2017), the left inferior parietal cortex and PCC within the DMN (Karunanayaka et al., 2016; Hou et al., 2018b), and the precentral gyrus (Hu et al., 2015). In summary, the akinetic-rigid subtype shows more widespread alterations in FC, especially in the DMN, compared with the tremor-dominant subtype. This finding may be related to the observation that patients with the akinetic-rigid subtype are more likely to develop cognitive impairment than those with the tremor-dominant subtype (Karunanayaka et al., 2016). Freezing of gait (FOG) is a PD-related gait disturbance characterized by sudden and temporary inability to walk forward or turn (Vandenbossche et al., 2012). A study reported a correlation between severer FOG and lower FC in the SMN (Canu et al., 2015) whereas another study showed increased FC in the SMN in patients with PD-FOG (Fling et al., 2014).

Functional connectivity alterations in PD vary depending on the disease stage. Patients with early drug-naive PD show altered functional connectivity in the cerebello-thalamo-cortical network (Hou et al., 2018a). Similar changes were reported in several prodromal PD studies before the onset of motor symptoms (Rolinski et al., 2016; Yamada et al., 2019; Wakasugi et al., 2021). Focusing on the subsequent changes over time in disease progression, it has been reported that the temporal progression of PD motor symptoms is correlated with reduced FC between the anterior putamen and the midbrain and increased FC between the cerebellum and the motor cortex (Manza et al., 2016). Furthermore, a study suggested that advanced PD patients may show decreased FC between the putamen, caudate and midbrain (Hacker et al., 2012). In terms of treatment, it is known that levodopa, the most commonly used medication for PD, increases motor network connectivity, which is opposite to the changes associated with the progression of motor symptoms in PD (Wu et al., 2009; Esposito et al., 2013; Agosta et al., 2014). A relationship between FC and cognitive symptoms has also been reported.

Patients with PDD show impaired FC of the DMN, compared with PD patients without dementia and healthy participants (Gorges et al., 2015). Decreased DMN-FC in PDD was also reported in a meta-analysis (Wolters et al., 2019). Patients with PDD also showed decreased ECN-FC (Filippi et al., 2019), and similar abnormality was reported at the prodromal stage (Wakasugi et al., 2021) (**Figure 1B**). Further reports showed disrupted connectivity in the frontoparietal network (Amboni et al., 2015; Borroni et al., 2015) and dorsal attention network (Baggio et al., 2015) in PDD. While a correlation between FC reduction in motor networks and reduced α-syn in the CSF has been reported (Campbell et al., 2015), this finding should be interpreted with caution because reliable CSF biomarkers for PD are not yet established.

In summary, rsfcMRI studies in PD have yielded some consistent findings, such as decreased FC in the putamen in most PD cases and DMN in cognitively impaired PD cases. Further research is needed to clarify the connectivity changes in many other networks, particularly as the observed connectivity changes in a particular network differ among reports. This inconsistency in FC findings may be caused by differences in the predominant clinical symptoms and disease stage (Hohenfeld et al., 2018; Filippi et al., 2019; Wolters et al., 2019). In this regard, it remains unclear if increases in FC reflect a compensatory mechanism or pathological processes. The inconsistency among previous rsfMRI studies may also be ascribed to technical issues: insufficient pre-processing, modulation of FC by medications including levodopa (Tahmasian et al., 2015), and insufficient sample size (Chen et al., 2018). These problems should be overcome by accumulating high-quality rsfMRI data with sufficiently large sample size, followed by cutting-edge preprocessing such as Human Connectome Project (HCP)-style MRI protocol (Glasser et al., 2016) and the adjustment of medication.

Summary

Till now, AD and PD have been studied independently, and most findings have been obtained independently.

In AD, memory impairment identified by clinical interview and neuropsychological testing is the core clinical symptom. Responsible genes for familial cases and risk genes for sporadic cases have been found, but more are yet to be identified. The identification of reliable biological or imaging markers for sporadic cases is of great importance in AD research to advance the development of disease-modifying therapies. Blood biomarkers are under development, and promising methods have been reported (Nakamura et al., 2018). Measurements of CSF can reveal alterations in key proteins (Aβ and tau) underlying AD pathology. To visualize the spatial distribution of Aβ, amyloid-PET has been established for its utility in

clinical studies. A few tracers have been proposed for tau-PET. Structural MRI and perfusion SPECT/FDG-PET are used to detect brain atrophy and reduced blood flow/energy requirement, respectively, both of which indicate neuronal loss. The analysis of brain connectivity by rsfcMRI consistently shows abnormality in the DMN. Moreover, ML combined with FC has permitted discrimination between AD and healthy controls with a degree of accuracy.

Parkinson's disease is characterized by movement disorder possibly complicating cognitive impairment. In cognitive disturbance in PD, executive function is particularly impaired. Many responsible genes for familial cases and risk genes for sporadic cases have been identified. MIBG-SPECT and DAT-SPECT are widely performed to detect the neurodegeneration of monoaminergic neuronal systems, which is a hallmark of PD pathology. Structural MRI with high magnetic field has utility in PD research for revealing the iron deposition and neurodegeneration in the SNc, which are the core pathological changes in PD. Detection methods for the other pathological hallmark, α-syn, are not established yet. Imaging measures of brain atrophy and blood flow/energy requirement show variable findings, depending in part on the motor subtype and presence of cognitive decline. Decreased perfusion is shown by SPECT in PD with cognitive decline. A group analysis using structural MRI revealed cerebral atrophy, especially in patients with substantial non-motor symptoms. Many rsfcMRI studies are reported, but again, the results vary, depending on the subtype and stage. Yet, network abnormalities of the basal ganglia, frontal lobe, and cerebellum, corresponding to movement disorders, and DMN/frontal lobe abnormalities corresponding to cognitive disorders have been consistently reported.

Because AD and PD are regarded distinct and independent disorders with different core clinical symptoms (cognitive vs. motor), different neuropsychological tests and imaging methods have been traditionally applied to each disease. Unfortunately, different evaluation methods have been applied to symptoms common to AD/PD as well, including cognitive and psychiatric symptoms. Therefore, it remains unclear which pathophysiological mechanisms are common, and which are unique to each disorder, despite the shared symptoms and the putatively common pathological mechanisms.

UNRESOLVED QUESTIONS AND FUTURE DIRECTIONS

Research on AD and PD has substantially progressed in the last few decades, but major questions remain unresolved. Given the overlaps between AD and PD in many aspects, the commonalities and differences between AD and PD need to be clarified, especially from the viewpoints of clinical manifestation, proteinopathy, vasculopathy, and neurocircuitopathy. To this end, it is necessary to construct a cohort containing both AD spectrum and PD spectrum. Related approach has been recently proposed for nation-wide cohort studies including AD and other dementia in Canada and United Kingdom (Chertkow et al., 2019; Morton et al., 2019; Koychev et al., 2020).

Clinical Viewpoints

Now, it is recognized that patients in the PD spectrum may show AD-like symptoms, and those in the AD spectrum could also exhibit PD-like symptoms, including anosmia and movement disorders. Anosmia is present in both AD and PD. Patients with AD were reported to perform worse than patients with PD in an odor recognition task (Lehrner et al., 1997). Anosmia in AD is common in cases with Lewy body accumulation in the postmortem brain (Olichney et al., 2005). However, it is not clear how α-syn, which constitutes Lewy bodies, is involved in olfaction problems in AD, in contrast to PD, in which neuronal loss occurs in the locus coeruleus, the raphe nuclei, and the nucleus basalis of Meynart (Doty, 2012).

In contrast to the common clinical conception, patients with PD may present with AD-like memory-dominant cognitive decline (Das et al., 2019). Conversely, some patients with AD may display parkinsonism (Sasaki, 2018). In a longitudinal study of AD with a mean follow-up of 3.6 years, 12.3% of patients had clinically apparent parkinsonism at the initial visit, and 22.6% at the final visit (Portet et al., 2009). Interestingly, patients with AD complicated with mild parkinsonism exhibit decreased DAT in the caudate nucleus, the pattern of which is closer to DLB than PD (Chung et al., 2019). To our knowledge, no study has directly examined prodromal PD pathology in AD with motor symptoms using CSF-α-syn or α-syn-PET. BPSD with hallucinations, suggestive of monoamine system dysfunction, a hallmark of PD pathology, is also present in AD.

Similarities in clinical manifestations are clearly seen between AD and PD. Anosmia may point to the common pathophysiology underlying the two. However, since few, if any, large-scale studies used a common clinical scale to compare AD and PD, it is unclear exactly how similar or different are these common symptoms in the two disorders.

Proteinopathy Viewpoints

Mounting evidence indicates α-syn pathology in the AD spectrum and Aβ/tau pathology in the PD spectrum. In animal experiments, many forms of interactions between AD-related proteins and PD-related proteins are reported, and such molecular interactions may explain the mixed AD and PD pathology common in humans. It has been suggested that Aβ directly affects the toxicity of α-syn. Aβ-rich AD-transgenic mice, including PSEN1/2 and APP mutation, show rapid and widespread aggregation of α-syn (Bassil et al., 2020). This finding suggests that Aβ plaques may promote seeding and spreading of α-syn. Tau and α-syn directly interact with each other to promote co-assembly (Bassil et al., 2021). Thus, each abnormal protein promotes the formation of other abnormal proteins.

Most postmortem brains in patients with PDD are complicated by varying degrees of AD pathology (Dickson et al., 2017). Thus, it is widely accepted that a certain degree of PD cognitive impairment may be associated with AD pathology. In AD, however, approximately 33% of the patients exhibit

significant Lewy body pathology alongside Aβ (Deture and Dickson, 2019), especially the presence of Lewy pathology in the olfactory bulb and the amygdala in patients with AD (Serrano-Pozo et al., 2011; Deture and Dickson, 2019). Also, patients in the PD spectrum show accompanying AD pathology (Kosaka and Manabe, 2010). A multicenter-cohort study of DLB examined Aβ and p-tau with CSF and PET. Among the patients, 32% were Aβ positive, 13% were p-tau positive, and 15% were positive for both Aβ and p-tau (Ferreira et al., 2020). Aβ and p-tau were found to be independent risk factors for cognitive decline in DLB. Interestingly, in the same study, p-tau was associated with a lower likelihood of parkinsonism and RBD in DLB.

While amyloid pathology in PDD/DLB is common, the complications of amyloid pathology in non-demented PD remain unclear. In a study using amyloid-PET, the prevalence rate of Aβ was rather low in non-demented PD patients compared with the healthy population (Mashima et al., 2017). It is possible that the involvement of Aβ pathology may be different in non-demented PD and PDD/DLB, but further studies are needed.

Because interactions of abnormal proteins in advanced stages of AD/PD-related dementia may occur, it is important to examine overlapping or interacting proteinopathies even in the preclinical and prodromal stages. In aMCI, which is considered a prodromal stage of AD, patients show cognitive decline that correlates with increased CSF α-syn levels (Twohig and Nielsen, 2019). Although few studies have evaluated protein interactions in prodromal PD, the coexistence of Aβ and tau pathology may promote the progression of prodromal PD to DLB (Berg et al., 2021). Protein interactions in prodromal AD and PD remain unclear, and this requires research attention. Considering that the therapeutic target of each disease is shifting to the early stage, a more thorough understanding of the disease, including protein interactions in the preclinical/prodromal stage, is urgently needed.

Vasculopathy Viewpoints

Cerebrovascular lesions cause cognitive or motor impairment. However, the significance of vascular lesions including white matter hyperintensities (WMHs) is often underestimated in the pathogenesis of dementia in comparison with, e.g., the proteinopathy viewpoint (Prins and Scheltens, 2015). In the AD spectrum, multiple studies indicated the presence of vascular lesions as an important background pathology (Prins and Scheltens, 2015; Saito et al., 2015; Muddapu et al., 2020). Decreased amyloid clearance has been proposed for the involvement of WMHs in AD pathogenesis (Saito et al., 2015). WMHs are also considered to underlie dementia in PD (Bohnen and Albin, 2011; Liu et al., 2021).

Neurocircuitopathy Viewpoints

In AD, many abnormalities in connectivity centering on the hippocampus and DMN, related to Aβ pathology, have been reported (Takamura and Hanakawa, 2017). In PD, abnormalities in the motor networks, including the basal ganglia and SMN, have been consistently reported. Importantly, DMN abnormalities have been observed in both the AD and PD spectra with cognitive impairment. AD features abnormalities mainly in the precuneus and PCC within the DMN (Ibrahim et al., 2021) whereas DLB has more widespread network abnormalities involving the DMN and the occipital lobe (Wolters et al., 2019).

It seems important to investigate the relationship between proteinopathic abnormalities and neuropsychological indices in the AD and PD spectra, and their relationship with the neurocircuitopahty viewpoint, including the DMN abnormality. Existing MRI cohort studies do not allow us to perform such an analysis because they recruit AD and PD cohorts independently with different evaluation metrics. Therefore, it remains unknown how Aβ, tau and α-syn are involved in the differences in DMN abnormalities between AD and PD. By performing network analysis using biomarkers of both AD and PD, it may be possible to assess the degree to which each AD/PD pathology contributes to network changes. In particular, little is known about the relationship between PD network abnormalities and proteinopathy.

Summary

Although the presence of substantial overlaps has been demonstrated, AD and PD cohorts have been recruited and evaluated separately. In particular, there is a marked discrepancy between the evaluation metrics for cognitive and neuropsychiatric functions, which limits the utility of existing cohorts for comparing AD and PD. Therefore, we recommend that a new cohort should be designed to resolve this problem. Each AD/PD spectrum should be evaluated throughout the preclinical, prodromal, early, and advanced stages.

Accumulating evidence indicates that the comorbidity of AD and PD pathology is common in elderly people. Many questions remain unanswered. For example, it is not yet known if the comorbidity is simply coincidental to the aging process *per se* or if it is caused by the interactions of the key common molecules in AD and PD. It is not clear when and how the mixed AD and PD pathology (i.e., co-pathology) emerges and progresses. Furthermore, it is unclear how the co-pathology affects clinical symptoms, brain structure, and circuit pathology.

To answer these questions, we should first consider merging data from existing cohorts targeting a single disease spectrum for efficiency. There are renown MRI cohorts including ADNI and PPMI (Petersen et al., 2010; Marek et al., 2011; Weiner et al., 2017; Veitch et al., 2019), which have evaluated the AD and PD spectrum separately in depth. For biomarker/genetic studies, it may be worthwhile evaluating a common set of proteins or risk genes from originally distinct cohort. However, it is known that technical differences such as a way to collect, store and measure samples may limit the reliability of the results. For imaging studies, it is still difficult to perform accurate statistical analysis of MRI data obtained from different MR scanners and protocols (Duchesne et al., 2019). Although image analysis methods to remove the scanner difference have been proposed, such methods will remove the difference across the disease spectra when AD is heavily sampled in some sites and PD is heavily sampled in the others. Also, since each cohort tend to focus on spectral-specific clinical and neuropsychological indices, it is difficult to compare network indices correlated with a common set of neuropsychological indices. Recently, some

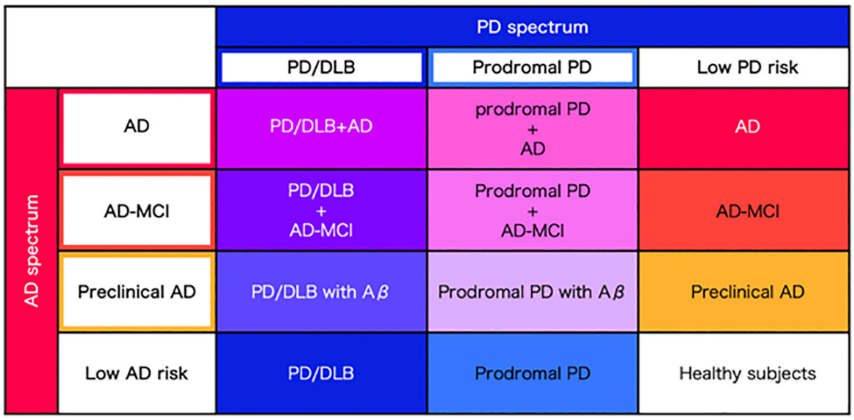

FIGURE 2 | Precise classification of AD and PD spectrum. Regarding AD and PD as spectra, precise disease classification will be performed based on the severity of abnormal protein accumulation and clinical data, derived from each AD and PD spectrum.

PD cohorts employed amyloid and tau PET. It is intriguing to compare spatial distribution of pathological protein across spectra; however, it is still difficult to associate the findings with neuropsychiatric indices with different batteries.

Considering the homology of AD and PD spectra in terms of abnormal proteins, vascular factors, motor sand cognitive symptoms, it is most reasonable to perform the same elaborate evaluation in a single cohort employing the same evaluation measures across the spectra. Here we propose to establish a newly designed cohort combining both the AD and PD spectra (**Figure 2**). Then, symptoms, biomarkers, brain structure and circuit pathology should be evaluated. The unified AD and PD cohort is expected to overcome the limitation of the existing AD cohort and PD cohort combined.

To investigate the similarities and differences between AD and PD, it is important to design a cohort study with a few key characteristics. First, it is necessary to apply the same behavioral, cognitive, and neuropsychiatric scales to AD and PD. Behaviorally, because parkinsonism is sometimes seen in AD, it may be needed to evaluate motor functions of both AD and PD with MDS-UPDRS. CDR and ADAS, which are used for AD, and FAB and MoCA, which are used for early PD, may need to be jointly used. It would be interesting to compare the results between PD-MCI in AD-MCI with tests for the five cognitive domains. Unified questionnaire must be used for assessment of behavioral and psychiatric symptoms such as anxiety, depression, and sleep problems, which are common to both AD and PD. The same olfactory test should be applied to AD and PD to test anosmia.

Next, Aβ/p-tau and α-syn should be evaluated for both AD and PD. To date, Aβ and p-tau have been mostly measured for AD only, and α-syn has been measured for PD cohorts only. The same assay methods of these proteins should be applied to blood and spinal fluid obtained from AD and PD. In postmortem brain research, NFTs appear in the locus coeruleus and entorhinal cortex first, and then spread to the limbic system and neocortex as dementia progresses (Braak and Braak, 1991). To evaluate the spatial distribution of abnormal protein accumulations over time, longitudinal PET imaging is important.

Finally, network and structural abnormalities of the brain should be compared in detail, preferably using the HCP-style MRI protocol (Glasser et al., 2016; Koike et al., 2021). This modern MRI technology should be combined with the standardized assessment of clinical scales and proteinopathies with fluid biomarkers and SPECT/PET. The effects of Aβ, tau and α-syn accumulation on network connectivity and their association with symptoms should be examined.

Here are cases where the unified AD and PD cohort may provide new knowledge. Clinically, aMCI is often presumed to have AD pathology (Petersen et al., 1999, 2001). The unified AD and PD cohort will provide data to suggest how common is aMCI without evidence for AD pathology but, for example, decreased DAT indicative of the PD spectrum (presumably prodromal DLB). Then, markers of the circuit pathology of such non-AD MCI may be compared with those of PD-MCI "neuroimaged" in the cohort to examine if the markers of neurocircuitopathy could serve as early markers differentiating AD-MCI and non-AD MCI. In the unified AD and PD cohort, vascular burden as a common background pathology to AD and PD can be evaluated from multiple perspectives, such as interactions of WMH burden with the proteinopathy, symptoms or circuit pathology. We can then ask how WMH burden similarly or differentially modulates manifestation of the AD spectrum and PD spectrum. The unified AD and PD cohort may also clarify the specific roles of the DMN in cognitive decline in the AD spectrum and PD spectrum since DMN is implicated for both AD and PDD.

CONCLUSION

Indispensable knowledge has been garnered from previously established AD cohorts and LBD cohorts. Nevertheless, evaluating abnormalities within each disease category only, without knowing the similarities or differences between the two, cannot provide a clear understanding of their pathophysiologies, from protein interactions and disease-spectrum crossovers. Constructing a cohort with multifaceted evaluations for both

AD and LBD is not an easy task. However, longitudinal cohort studies, which meet the requirements proposed above, should provide novel insight into the pathophysiologies of AD and LBD. This knowledge will in turn provide much-needed data for guiding the development of disease-modifying therapies targeting the pathological proteins in AD and LBD.

AUTHOR CONTRIBUTIONS

NW drafted the manuscript. NW and TH wrote the manuscript. Both authors contributed to the article and approved the submitted version.

FUNDING

This article was in part supported by the Japan Agency for Medical Research and Development (AMED, https://www.amed.go.jp/en/index.html) (21dm0307003h0004 and 21dm0307004h0004), and the Japan Society for the Promotion of Science (JSPS, www.jsps.go.jp) KAKENHI (19H05726).

ACKNOWLEDGMENTS

We thank Barry Patel, from Edanz (https://jp.edanz.com/ac), for editing a draft of this manuscript.

REFERENCES

Abe, Y., Kachi, T., Kato, T., Arahata, Y., Yamada, T., Washimi, Y., et al. (2003). Occipital hypoperfusion in Parkinson's disease without dementia: Correlation to impaired cortical visual processing. *J. Neurol. Neurosurg. Psychiatry* 74, 419–422. doi: 10.1136/jnnp.74.4.419

Adriaanse, S. M., Binnewijzend, M. A. A., Ossenkoppele, R., Tijms, B. M., Van Der Flier, W. M., Koene, T., et al. (2014). Widespread disruption of functional brain organization in early-onset Alzheimer's disease. *PLoS One* 9:102995. doi: 10.1371/journal.pone.0102995

Agosta, F., Caso, F., Stankovic, I., Inuggi, A., Petrovic, I., Svetel, M., et al. (2014). Cortico-striatal-thalamic network functional connectivity in hemiparkinsonism. *Neurobiol. Aging* 35, 2592–2602. doi: 10.1016/j.neurobiolaging.2014.05.032

Ahmadi, S. A., Bötzel, K., Levin, J., Maiostre, J., Klein, T., Wein, W., et al. (2020). Analyzing the co-localization of substantia nigra hyper-echogenicities and iron accumulation in Parkinson's disease: A multi-modal atlas study with transcranial ultrasound and MRI. *NeuroImage Clin.* 26, 102185. doi: 10.1016/j.nicl.2020.102185

Albert, M. S., DeKosky, S. T., Dickson, D., Dubois, B., Feldman, H. H., Fox, N. C., et al. (2011). The diagnosis of mild cognitive impairment due to Alzheimer's disease: recommendations from the National Institute on Aging-Alzheimer's Association workgroups on diagnostic guidelines for Alzheimer's disease. *Alzheimers. Dement.* 7, 270–279. doi: 10.1016/j.jalz.2011.03.008

Amboni, M., Tessitore, A., Esposito, F., Santangelo, G., Picillo, M., Vitale, C., et al. (2015). Resting-state functional connectivity associated with mild cognitive impairment in Parkinson's disease. *J. Neurol.* 262, 425–434. doi: 10.1007/s00415-014-7591-5

Angelova, D. M., and Brown, D. R. (2019). Microglia and the aging brain: are senescent microglia the key to neurodegeneration? *J. Neurochem.* 151, 676–688. doi: 10.1111/jnc.14860

Attems, J., Walker, L., and Jellinger, K. A. (2014). Olfactory bulb involvement in neurodegenerative diseases. *Acta Neuropathol.* 127, 459–475. doi: 10.1007/s00401-014-1261-7

Ba, F., and Martin, W. R. W. (2015). Dopamine transporter imaging as a diagnostic tool for parkinsonism and related disorders in clinical practice. *Park. Relat. Disord.* 21, 87–94. doi: 10.1016/j.parkreldis.2014.11.007

Baggio, H.-C., Segura, B., Sala-Llonch, R., Marti, M.-J., Valldeoriola, F., Compta, Y., et al. (2015). Cognitive impairment and resting-state network connectivity in Parkinson's disease. *Hum. Brain Mapp.* 36, 199–212. doi: 10.1002/hbm.22622

Bai, F., Xie, C., Watson, D. R., Shi, Y., Yuan, Y., Wang, Y., et al. (2011). Aberrant hippocampal subregion networks associated with the classifications of aMCI subjects: A longitudinal Resting-State study. *PLoS One* 6:29288. doi: 10.1371/journal.pone.0029288

Baiano, C., Barone, P., Trojano, L., and Santangelo, G. (2020). Prevalence and clinical aspects of mild cognitive impairment in Parkinson's disease: A meta-analysis. *Mov. Disord.* 35, 45–54. doi: 10.1002/mds.27902

Barthélemy, N. R., Horie, K., Sato, C., and Bateman, R. J. (2020). Blood plasma phosphorylated-tau isoforms track CNS change in Alzheimer's disease. *J. Exp. Med.* 217, 1–12. doi: 10.1084/JEM.20200861

Bassil, F., Brown, H. J., Pattabhiraman, S., Iwasyk, J. E., Maghames, C. M., Meymand, E. S., et al. (2020). Amyloid-Beta (Aβ) Plaques Promote Seeding and Spreading of Alpha-Synuclein and Tau in a Mouse Model of Lewy Body Disorders with Aβ Pathology. *Neuron* 105, 260.e–275.e. doi: 10.1016/j.neuron.2019.10.010

Bassil, F., Meymand, E. S., Brown, H. J., Xu, H., Cox, T. O., Pattabhiraman, S., et al. (2021). α-Synuclein modulates tau spreading in mouse brains. *J. Exp. Med.* 218:20192193. doi: 10.1084/jem.20192193

Bateman, R. J., Xiong, C., Benzinger, T. L. S., Fagan, A. M., Goate, A., Fox, N. C., et al. (2012). Clinical and Biomarker Changes in Dominantly Inherited Alzheimer's Disease. *N. Engl. J. Med.* 367, 795–804. doi: 10.1056/nejmoa1202753

Baudrexel, S., Witte, T., Seifried, C., von Wegner, F., Beissner, F., Klein, J. C., et al. (2011). Resting state fMRI reveals increased subthalamic nucleus-motor cortex connectivity in Parkinson's disease. *Neuroimage* 55, 1728–1738. doi: 10.1016/j.neuroimage.2011.01.017

Beck, A. T., Ward, C. H., Mendelson, M., Mock, J., and Erbaugh, J. (1961). An inventory for measuring depression. *Arch. Gen. Psychiatry* 4, 561–571. doi: 10.1001/archpsyc.1961.01710120031004

Bell, P. T., Gilat, M., O'Callaghan, C., Copland, D. A., Frank, M. J., Lewis, S. J. G., et al. (2015). Dopaminergic basis for impairments in functional connectivity across subdivisions of the striatum in Parkinson's disease. *Hum. Brain Mapp.* 36, 1278–1291. doi: 10.1002/hbm.22701

Berg, D., Borghammer, P., Fereshtehnejad, S. M., Heinzel, S., Horsager, J., Schaeffer, E., et al. (2021). Prodromal Parkinson disease subtypes — key to understanding heterogeneity. *Nat. Rev. Neurol.* 17, 349–361. doi: 10.1038/s41582-021-00486-9

Blauwendraat, C., Nalls, M. A., and Singleton, A. B. (2020). The genetic architecture of Parkinson's disease. *Lancet Neurol.* 19, 170–178. doi: 10.1016/S1474-4422(19)30287-X

Blennow, K., and Hampel, H. (2003). CSF markers for incipient Alzheimer's disease. *Lancet. Neurol.* 2, 605–613. doi: 10.1016/s1474-4422(03)00530-1

Bloudek, L. M., Spackman, D. E., Blankenburg, M., and Sullivan, S. D. (2011). Review and meta-analysis of biomarkers and diagnostic imaging in Alzheimer's disease. *J. Alzheimers. Dis.* 26, 627–645. doi: 10.3233/JAD-2011-110458

Bohnen, N. I., and Albin, R. L. (2011). White matter lesions in Parkinson disease. *Nat. Rev. Neurol.* 7, 229–236. doi: 10.1038/nrneurol.2011.21

Bonanni, L., Thomas, A., and Onofrj, M. (2006). Diagnosis and management of dementia with Lewy bodies: Third report of the DLB Consortium. *Neurology* 66:1455. doi: 10.1212/01.wnl.0000224698.67660.45

Borroni, B., Premi, E., Formenti, A., Turrone, R., Alberici, A., Cottini, E., et al. (2015). Structural and functional imaging study in dementia with Lewy bodies and Parkinson's disease dementia. *Parkinsonism Relat. Disord.* 21, 1049–1055. doi: 10.1016/j.parkreldis.2015.06.013

Boublay, N., Bouet, R., Dorey, J.-M., Padovan, C., Makaroff, Z., Fédérico, D., et al. (2020). Brain Volume Predicts Behavioral and Psychological Symptoms

in Alzheimer's Disease. *J. Alzheimers. Dis.* 73, 1343–1353. doi: 10.3233/JAD-190612

Braak, H., and Braak, E. (1991). Neuropathological stageing of Alzheimer-related changes. *Acta Neuropathol.* 82, 239–259. doi: 10.1007/BF00308809

Brigo, F., Matinella, A., Erro, R., and Tinazzi, M. (2014). [^{123}I]FP-CIT SPECT (DaTSCAN) may be a useful tool to differentiate between Parkinson's disease and vascular or drug-induced parkinsonisms: a meta-analysis. *Eur. J. Neurol.* 21, 1369–e90. doi: 10.1111/ene.12444

Bucci, M., Chiotis, K., and Nordberg, A. (2021). Alzheimer's disease profiled by fluid and imaging markers: tau PET best predicts cognitive decline. *Mol. Psychiatry* 2021:2. doi: 10.1038/s41380-021-01263-2

Buckner, R. L., Snyder, A. Z., Shannon, B. J., LaRossa, G., Sachs, R., Fotenos, A. F., et al. (2005). Molecular, structural, and functional characterization of Alzheimer's disease: Evidence for a relationship between default activity, amyloid, and memory. *J. Neurosci.* 25, 7709–7717. doi: 10.1523/JNEUROSCI.2177-05.2005

Burton, E. J., McKeith, I. G., Burn, D. J., Williams, E. D., and O'Brien, J. T. (2004). Cerebral atrophy in Parkinson's disease with and without dementia: A comparison with Alzheimer's disease, dementia with Lewy bodies and controls. *Brain* 127, 791–800. doi: 10.1093/brain/awh088

Caillava-Santos, F., Margis, R., and de Mello Rieder, C. R. (2015). Wearing-off in Parkinson's disease: Neuropsychological differences between on and off periods. *Neuropsychiatr. Dis. Treat.* 11, 1175–1180. doi: 10.2147/NDT.S77060

Camicioli, R., Moore, M. M., Kinney, A., Corbridge, E., Glassberg, K., and Kaye, J. A. (2003). Parkinson's disease is associated with hippocampal atrophy. *Mov. Disord.* 18, 784–790. doi: 10.1002/mds.10444

Campbell, M. C., Koller, J. M., Snyder, A. Z., Buddhala, C., Kotzbauer, P. T., and Perlmutter, J. S. (2015). CSF proteins and resting-state functional connectivity in Parkinson disease. *Neurology* 84, 2413–2421. doi: 10.1212/WNL.0000000000001681

Canu, E., Agosta, F., Sarasso, E., Volontè, M. A., Basaia, S., Stojkovic, T., et al. (2015). Brain structural and functional connectivity in Parkinson's disease with freezing of gait. *Hum. Brain Mapp.* 36, 5064–5078. doi: 10.1002/hbm.22994

Cavanna, A. E., and Trimble, M. R. (2006). The precuneus: A review of its functional anatomy and behavioural correlates. *Brain* 129, 564–583. doi: 10.1093/brain/awl004

Celone, K. A., Calhoun, V. D., Dickerson, B. C., Atri, A., Chua, E. F., Miller, S. L., et al. (2006). Alterations in memory networks in mild cognitive impairment and Alzheimer's disease: An independent component analysis. *J. Neurosci.* 26, 10222–10231. doi: 10.1523/JNEUROSCI.2250-06.2006

Chang, C. W., Yang, S. Y., Yang, C. C., Chang, C. W., and Wu, Y. R. (2020). Plasma and Serum Alpha-Synuclein as a Biomarker of Diagnosis in Patients With Parkinson's Disease. *Front. Neurol.* 10:1–7. doi: 10.3389/fneur.2019.01388

Chang, Y. L., Bondi, M. W., McEvoy, L. K., Fennema-Notestine, C., Salmon, D. P., Galasko, D., et al. (2011). Global clinical dementia rating of 0.5 in MCI masks variability related to level of function. *Neurology* 76, 652–659. doi: 10.1212/WNL.0b013e31820ce6a5

Chen, B., Fan, G. G., Liu, H., and Wang, S. (2015). Changes in anatomical and functional connectivity of Parkinson's disease patients according to cognitive status. *Eur. J. Radiol.* 84, 1318–1324. doi: 10.1016/j.ejrad.2015.04.014

Chen, H. M., Wang, Z. J., Fang, J. P., Gao, L. Y., Ma, L. Y., Wu, T., et al. (2015). Different Patterns of Spontaneous Brain Activity between Tremor-Dominant and Postural Instability/Gait Difficulty Subtypes of Parkinson's Disease: A Resting-State fMRI Study. *CNS Neurosci. Ther.* 21, 855–866. doi: 10.1111/cns.12464

Chen, Q., Chen, Y., Zhang, Y., Wang, F., Yu, H., Zhang, C., et al. (2019). Iron deposition in Parkinson's disease by quantitative susceptibility mapping. *BMC Neurosci.* 20, 1–8. doi: 10.1186/s12868-019-0505-9

Chen, X., Lu, B., and Yan, C.-G. (2018). Reproducibility of R-fMRI metrics on the impact of different strategies for multiple comparison correction and sample sizes. *Hum. Brain Mapp.* 39, 300–318. doi: 10.1002/hbm.23843

Cheng, Q., Huang, J., Liang, J., Ma, M., Zhao, Q., Lei, X., et al. (2020). Evaluation of abnormal iron distribution in specific regions in the brains of patients with Parkinson's disease using quantitative susceptibility mapping and R2* mapping. *Exp. Ther. Med.* 2020, 3778–3786. doi: 10.3892/etm.2020.8645

Chertkow, H., Borrie, M., Whitehead, V., Black, S. E., Feldman, H. H., Gauthier, S., et al. (2019). The comprehensive assessment of neurodegeneration and dementia: Canadian cohort study. *Can. J. Neurol. Sci.* 46, 499–511. doi: 10.1017/cjn.2019.27

Chételat, G., Arbizu, J., Barthel, H., Garibotto, V., Law, I., Morbelli, S., et al. (2020). Amyloid-PET and 18F-FDG-PET in the diagnostic investigation of Alzheimer's disease and other dementias. *Lancet Neurol.* 19, 951–962. doi: 10.1016/S1474-4422(20)30314-8

Chhatwal, J. P., and Sperling, R. A. (2012). Functional MRI of mnemonic networks across the spectrum of normal aging, mild cognitive impairment, and Alzheimer's disease. *J. Alzheimers. Dis.* 31(Suppl. 3), S155–S167. doi: 10.3233/JAD-2012-120730

Chung, S. J., Lee, Y. H., Yoo, H. S., Sohn, Y. H., Ye, B. S., Cha, J., et al. (2019). Distinct FP-CIT PET patterns of Alzheimer's disease with parkinsonism and dementia with Lewy bodies. *Eur. J. Nucl. Med. Mol. Imaging* 46, 1652–1660. doi: 10.1007/s00259-019-04315-6

Clment, F., and Belleville, S. (2010). Compensation and disease severity on the memory-related activations in mild cognitive impairment. *Biol. Psychiatry* 68, 894–902. doi: 10.1016/j.biopsych.2010.02.004

Colin, M., Dujardin, S., Schraen-Maschke, S., Meno-Tetang, G., Duyckaerts, C., Courade, J. P., et al. (2020). From the prion-like propagation hypothesis to therapeutic strategies of anti-tau immunotherapy. *Acta Neuropathol.* 139, 3–25. doi: 10.1007/s00401-019-02087-9

Córdova-Palomera, A., Kaufmann, T., Persson, K., Alnæs, D., Doan, N. T., Moberget, T., et al. (2017). Disrupted global metastability and static and dynamic brain connectivity across individuals in the Alzheimer's disease continuum. *Sci. Rep.* 7, 1–14. doi: 10.1038/srep40268

Crary, J. F., Trojanowski, J. Q., Schneider, J. A., Abisambra, J. F., Abner, E. L., Alafuzoff, I., et al. (2014). Primary age-related tauopathy (PART): a common pathology associated with human aging. *Acta Neuropathol.* 128, 755–766. doi: 10.1007/s00401-014-1349-0

Daerr, S., Brendel, M., Zach, C., Mille, E., Schilling, D., Zacherl, M. J., et al. (2017). Evaluation of early-phase [18F]-florbetaben PET acquisition in clinical routine cases. *NeuroImage Clin.* 14, 77–86. doi: 10.1016/j.nicl.2016.10.005

Dagher, A., and Zeighami, Y. (2018). Testing the Protein Propagation Hypothesis of Parkinson Disease. *J. Exp. Neurosci.* 12, 0–3. doi: 10.1177/1179069518786715

Das, T., Hwang, J. J., and Poston, K. L. (2019). Episodic recognition memory and the hippocampus in Parkinson's disease: A review. *Cortex* 113, 191–209. doi: 10.1016/j.cortex.2018.11.021

Davis, D., Creavin, S., Yip, J., Noel-Storr, A., and Cullum, S. (2015). Montreal Cognitive Assessment for the diagnosis of Alzheimer's disease and other dementias. *Cochrane Database Syst. Rev. Montr.* 2015:10775. doi: 10.1002/14651858.CD010775.pub2.www.cochranelibrary.com

De Meyer, G., Shapiro, F., Vanderstichele, H., Vanmechelen, E., Engelborghs, S., Paul, et al. (2010). *Diagnosis-Independent Alzheimer Disease Biomarker Signature in Cognitively Normal Elderly People*. Available online at: www.loni.ucla.edu [Accessed June 19, 2021]

de Vos, F., Koini, M., Schouten, T. M., Seiler, S., van der Grond, J., Lechner, A., et al. (2018). A comprehensive analysis of resting state fMRI measures to classify individual patients with Alzheimer's disease. *Neuroimage* 167, 62–72. doi: 10.1016/j.neuroimage.2017.11.025

Demirtaş, M., Falcon, C., Tucholka, A., Gispert, J. D., Molinuevo, J. L., and Deco, G. (2017). A whole-brain computational modeling approach to explain the alterations in resting-state functional connectivity during progression of Alzheimer's disease. *NeuroImage Clin.* 16, 343–354. doi: 10.1016/j.nicl.2017.08.006

Deture, M. A., and Dickson, D. W. (2019). The neuropathological diagnosis of Alzheimer's disease. *Mol. Neurodegener.* 14, 1–18. doi: 10.1186/s13024-019-0333-5

Dichgans, M., and Leys, D. (2017). Vascular Cognitive Impairment. *Circ. Res.* 120, 573–591. doi: 10.1161/CIRCRESAHA.116.308426

Dickerson, B. C., Salat, D. H., Bates, J. F., Atiya, M., Killiany, R. J., Greve, D. N., et al. (2004). Medial temporal lobe function and structure in mild cognitive impairment. *Ann. Neurol.* 56, 27–35. doi: 10.1002/ana.20163

Dickerson, B. C., Salat, D. H., Greve, D. N., Chua, E. F., Rand-Giovannetti, E., Rentz, D. M., et al. (2005). Increased hippocampal activation in mild cognitive impairment compared to normal aging and AD. *Neurology* 65, 404–411. doi: 10.1212/01.wnl.0000171450.97464.49

Dickson, D. W., Halliday, G., Aarsland, D., Attems, J., Ballard, C. G., Bayston, A., et al. (2017). Diagnosis and management of dementia with Lewy bodies: Fourth consensus report of the DLB Consortium. *Neurology* 89, 1–14.

Dirkx, M. F., den Ouden, H., Aarts, E., Timmer, M., Bloem, B. R., Toni, I., et al. (2016). The cerebral network of parkinson's tremor: An effective connectivity fMRI study. *J. Neurosci.* 36, 5362–5372. doi: 10.1523/JNEUROSCI.3634-15.2016

Doty, R. L. (2012). Olfactory dysfunction in Parkinson disease. *Nat. Rev. Neurol.* 8, 329–339. doi: 10.1038/nrneurol.2012.80

Dubois, B., Feldman, H. H., Jacova, C., Hampel, H., Molinuevo, J. L., Blennow, K., et al. (2014). Advancing research diagnostic criteria for Alzheimer's disease: the IWG-2 criteria. *Lancet. Neurol.* 13, 614–629. doi: 10.1016/S1474-4422(14)70090-0

Dubois, B., Slachevsky, A., Litvan, I., and Pillon, B. (2000). The FAB. *Neurology* 55, 1621–1626.

Duchesne, S., Chouinard, I., Potvin, O., Fonov, V. S., Khademi, A., Bartha, R., et al. (2019). The Canadian Dementia Imaging Protocol: Harmonizing National Cohorts. *J. Magn. Reson. Imaging* 49, 456–465. doi: 10.1002/jmri.26197

Eramudugolla, R., Mortby, M. E., Sachdev, P., Meslin, C., Kumar, R., and Anstey, K. J. (2017). Evaluation of a research diagnostic algorithm for DSM-5 neurocognitive disorders in a population-based cohort of older adults. *Alzheimer's Res. Ther.* 9, 1–12. doi: 10.1186/s13195-017-0246-x

Esposito, F., Tessitore, A., Giordano, A., De Micco, R., Paccone, A., Conforti, R., et al. (2013). Rhythm-specific modulation of the sensorimotor network in drug-naive patients with Parkinson's disease by levodopa. *Brain* 136, 710–725. doi: 10.1093/brain/awt007

Fairfoul, G., McGuire, L. I., Pal, S., Ironside, J. W., Neumann, J., Christie, S., et al. (2016). Alpha-synuclein RT-QuIC in the CSF of patients with alpha-synucleinopathies. *Ann. Clin. Transl. Neurol.* 3, 812–818. doi: 10.1002/acn3.338

Ferrari, C. C., and Tarelli, R. (2011). Parkinson's disease and systemic inflammation. *Parkinsons. Dis.* 2011:436813. doi: 10.4061/2011/436813

Ferreira, D., Przybelski, S. A., Lesnick, T. G., Lemstra, A. W., Londos, E., Blanc, F., et al. (2020). β-Amyloid and tau biomarkers and clinical phenotype in dementia with Lewy bodies. *Neurology* 95, e3257–e3268. doi: 10.1212/WNL.0000000000010943

Filippi, M., Sarasso, E., and Agosta, F. (2019). Resting-state Functional MRI in Parkinsonian Syndromes. *Mov. Disord Clin. Pr.* 6, 104–117. doi: 10.1002/mdc3.12730

Flicker, C., Ferris, S. H., and Reisberg, B. (1991). Mild cognitive impairment in the elderly: predictors of dementia. *Neurology* 41, 1006–1009. doi: 10.1212/wnl.41.7.1006

Fling, B. W., Cohen, R. G., Mancini, M., Carpenter, S. D., Fair, D. A., Nutt, J. G., et al. (2014). Functional reorganization of the locomotor network in parkinson patients with freezing of gait. *PLoS One* 9:291. doi: 10.1371/journal.pone.0100291

Galts, C. P. C., Bettio, L. E. B., Jewett, D. C., Yang, C. C., Brocardo, P. S., Rodrigues, A. L. S., et al. (2019). Depression in neurodegenerative diseases: Common mechanisms and current treatment options. *Neurosci. Biobehav. Rev.* 102, 56–84. doi: 10.1016/j.neubiorev.2019.04.002

Galvin, J. E., Price, J. L., Yan, Z., Morris, J. C., and Sheline, Y. I. (2011). Resting bold fMRI differentiates dementia with Lewy bodies vs Alzheimer disease. *Neurology* 76, 1797–1803. doi: 10.1212/WNL.0b013e31821ccc83

Ganguly, U., Singh, S., Pal, S., Prasad, S., Agrawal, B. K., Saini, R. V., et al. (2021). Alpha-Synuclein as a Biomarker of Parkinson's Disease: Good, but Not Good Enough. *Front. Aging Neurosci.* 13, 1–19. doi: 10.3389/fnagi.2021.702639

Gegg, M. E., Burke, D., Heales, S. J. R., Cooper, J. M., Hardy, J., Wood, N. W., et al. (2012). Glucocerebrosidase deficiency in substantia nigra of parkinson disease brains. *Ann. Neurol.* 72, 455–463. doi: 10.1002/ana.23614

Gibb, W. R., and Lees, A. J. (1988). The relevance of the Lewy body to the pathogenesis of idiopathic Parkinson's disease. *J. Neurol. Neurosurg. Psychiatry* 51, 745–752. doi: 10.1136/jnnp.51.6.745

Glasser, M. F., Smith, S. M., Marcus, D. S., Andersson, J. L. R., Auerbach, E. J., Behrens, T. E. J., et al. (2016). The Human Connectome Project's neuroimaging approach. *Nat. Neurosci.* 19, 1175–1187. doi: 10.1038/nn.4361

Goetz, C. G., Tilley, B. C., Shaftman, S. R., Stebbins, G. T., Fahn, S., Martinez-Martin, P., et al. (2008). Movement Disorder Society-sponsored revision of the Unified Parkinson's Disease Rating Scale (MDS-UPDRS): scale presentation and clinimetric testing results. *Mov. Disord* 23, 2129–2170. doi: 10.1002/mds.22340

Goldman, J. G., Vernaleo, B. A., Camicioli, R., Dahodwala, N., Dobkin, R. D., Ellis, T., et al. (2018). Cognitive impairment in Parkinson's disease: a report from a multidisciplinary symposium on unmet needs and future directions to maintain cognitive health. *npj Park. Dis.* 4, 1–11. doi: 10.1038/s41531-018-0055-3

Gorges, M., Müller, H.-P., Lulé, D., Pinkhardt, E. H., Ludolph, A. C., and Kassubek, J. (2015). To rise and to fall: functional connectivity in cognitively normal and cognitively impaired patients with Parkinson's disease. *Neurobiol. Aging* 36, 1727–1735. doi: 10.1016/j.neurobiolaging.2014.12.026

Graff-Radford, J., Murray, M. E., Lowe, V. J., Boeve, B. F., Ferman, T. J., Przybelski, S. A., et al. (2014). Dementia with Lewy bodies: basis of cingulate island sign. *Neurology* 83, 801–809. doi: 10.1212/WNL.0000000000000734

Greicius, M. D., Krasnow, B., Reiss, A. L., and Menon, V. (2003). Functional connectivity in the resting brain: A network analysis of the default mode hypothesis. *Proc. Natl. Acad. Sci. U. S. A.* 100, 253–258. doi: 10.1073/pnas.0135058100

Guan, X., Zeng, Q., Guo, T., Wang, J., Xuan, M., Gu, Q., et al. (2017). Disrupted functional connectivity of basal ganglia across tremor-dominant and akinetic/rigid-dominant Parkinson's disease. *Front. Aging Neurosci.* 9, 1–11. doi: 10.3389/fnagi.2017.00360

Guerreiro, R., Wojtas, A., Bras, J., Carrasquillo, M., Rogaeva, E., Majounie, E., et al. (2013). TREM2 Variants in Alzheimer's Disease. *N. Engl. J. Med.* 368, 117–127. doi: 10.1056/nejmoa1211851

Guo, T., Noble, W., and Hanger, D. P. (2017). Roles of tau protein in health and disease. *Acta Neuropathol.* 133, 665–704. doi: 10.1007/s00401-017-1707-9

Hacker, C. D., Perlmutter, J. S., Criswell, S. R., Ances, B. M., and Snyder, A. Z. (2012). Resting state functional connectivity of the striatum in Parkinson's disease. *Brain* 135, 3699–3711. doi: 10.1093/brain/aws281

Hall, J. M., Ehgoetz Martens, K. A., Walton, C. C., O'Callaghan, C., Keller, P. E., Lewis, S. J. G., et al. (2016). Diffusion alterations associated with Parkinson's disease symptomatology: A review of the literature. *Park. Relat. Disord.* 33, 12–26. doi: 10.1016/j.parkreldis.2016.09.026

Hampel, H., Frank, R., Broich, K., Teipel, S. J., Katz, R. G., Hardy, J., et al. (2010). Biomarkers for alzheimer's disease: Academic, industry and regulatory perspectives. *Nat. Rev. Drug Discov.* 9, 560–574. doi: 10.1038/nrd3115

Hampel, H., and Teipel, S. J. (2004). Total and phosphorylated tau proteins: evaluation as core biomarker candidates in frontotemporal dementia. *Dement. Geriatr. Cogn. Disord.* 17, 350–354. doi: 10.1159/000077170

Hanagasi, H. A., Tufekcioglu, Z., and Emre, M. (2017). Dementia in Parkinson's disease. *J. Neurol. Sci.* 374, 26–31. doi: 10.1016/j.jns.2017.01.012

Hauser, P. S., Narayanaswami, V., and Ryan, R. O. (2011). Apolipoprotein E: from lipid transport to neurobiology. *Prog. Lipid Res.* 50, 62–74. doi: 10.1016/j.plipres.2010.09.001

Heinzel, S., Berg, D., Gasser, T., Chen, H., Yao, C., and Postuma, R. B. (2019). Update of the MDS research criteria for prodromal Parkinson's disease. *Mov. Disord.* 34, 1464–1470. doi: 10.1002/mds.27802

Helmich, R. C., Derikx, L. C., Bakker, M., Scheeringa, R., Bloem, B. R., and Toni, I. (2010). Spatial remapping of cortico-striatal connectivity in parkinson's disease. *Cereb. Cortex* 20, 1175–1186. doi: 10.1093/cercor/bhp178

Helmich, R. C., Janssen, M. J. R., Oyen, W. J. G., Bloem, B. R., and Toni, I. (2011). Pallidal dysfunction drives a cerebellothalamic circuit into Parkinson tremor. *Ann. Neurol.* 69, 269–281. doi: 10.1002/ana.22361

Henderson, M. X., Trojanowski, J. Q., and Lee, V. M. Y. (2019). α-Synuclein pathology in Parkinson's disease and related α-synucleinopathies. *Neurosci. Lett.* 709:134316. doi: 10.1016/j.neulet.2019.134316

Herz, D. M., Eickhoff, S. B., Løkkegaard, A., and Siebner, H. R. (2014). Functional neuroimaging of motor control in parkinson's disease: A meta-analysis. *Hum. Brain Mapp.* 35, 3227–3237. doi: 10.1002/hbm.22397

Hodges, J. R., and Patterson, K. (1997). Semantic memory disorders. *Trends Cogn. Sci.* 1, 68–72. doi: 10.1016/S1364-6613(97)01022-X

Hohenfeld, C., Werner, C. J., and Reetz, K. (2018). Resting-state connectivity in neurodegenerative disorders: Is there potential for an imaging biomarker? *NeuroImage Clin.* 18, 849–870. doi: 10.1016/j.nicl.2018.03.013

Honey, C. J., Sporns, O., Cammoun, L., Gigandet, X., Thiran, J. P., Meuli, R., et al. (2009). Predicting human resting-state functional connectivity from structural connectivity. *Proc. Natl. Acad. Sci. U. S. A.* 106, 2035–2040. doi: 10.1073/pnas.0811168106

Hou, Y., Dan, X., Babbar, M., Wei, Y., Hasselbalch, S. G., Croteau, D. L., et al. (2019). Ageing as a risk factor for neurodegenerative disease. *Nat. Rev. Neurol.* 15, 565–581. doi: 10.1038/s41582-019-0244-7

Hou, Y., Yang, J., Luo, C., Ou, R., Zou, Y., Song, W., et al. (2018b). Resting-state network connectivity in cognitively unimpaired drug-naïve patients with rigidity-dominant Parkinson's disease. *J. Neurol. Sci.* 395, 147–152. doi: 10.1016/j.jns.2018.10.003

Hou, Y., Ou, R., Yang, J., Song, W., Gong, Q., and Shang, H. (2018a). Patterns of striatal and cerebellar functional connectivity in early-stage drug-naïve patients with Parkinson's disease subtypes. *Neuroradiology* 60, 1323–1333. doi: 10.1007/s00234-018-2101-6

Hruska, K. S., LaMarca, M. E., Scott, C. R., and Sidransky, E. (2008). Gaucher disease: Mutation and polymorphism spectrum in the glucocerebrosidase gene (GBA). *Hum. Mutat.* 29, 567–583. doi: 10.1002/humu.20676

Hu, X., Zhang, J., Jiang, X., Zhou, C., Wei, L., Yin, X., et al. (2015). Decreased interhemispheric functional connectivity in subtypes of Parkinson's disease. *J. Neurol.* 262, 760–767. doi: 10.1007/s00415-014-7627-x

Hughes, A. J., Daniel, S. E., Kilford, L., and Lees, A. J. (1992). Accuracy of clinical diagnosis of idiopathic Parkinson's disease: A clinico-pathological study of 100 cases. *J. Neurol. Neurosurg. Psychiatry* 55, 181–184. doi: 10.1136/jnnp.55.3.181

Ibarretxe-Bilbao, N., Ramírez-Ruiz, B., Tolosa, E., Martí, M. J., Valldeoriola, F., Bargalló, N., et al. (2008). Hippocampal head atrophy predominance in Parkinson's disease with hallucinations and with dementia. *J. Neurol.* 255, 1324–1331. doi: 10.1007/s00415-008-0885-8

Ibrahim, B., Suppiah, S., Ibrahim, N., Mohamad, M., Hassan, H. A., Nasser, N. S., et al. (2021). Diagnostic power of resting-state fMRI for detection of network connectivity in Alzheimer's disease and mild cognitive impairment: A systematic review. *Hum. Brain Mapp.* 42, 2941–2968. doi: 10.1002/hbm.25369

Irwin, D. J., Lee, V. M. Y., and Trojanowski, J. Q. (2013). Parkinson's disease dementia: Convergence of α-synuclein, tau and amyloid-β pathologies. *Nat. Rev. Neurosci.* 14, 626–636. doi: 10.1038/nrn3549

Ishii, M., Hiller, A. J., Pham, L., McGuire, M. J., Iadecola, C., and Wang, G. (2019). Amyloid-Beta Modulates Low-Threshold Activated Voltage-Gated L-Type Calcium Channels of Arcuate Neuropeptide Y Neurons Leading to Calcium Dysregulation and Hypothalamic Dysfunction. *J. Neurosci.* 39, 8816–8825. doi: 10.1523/JNEUROSCI.0617-19.2019

Jack, C. R. Jr., Bennett, D. A., Blennow, K., Carrillo, M. C., Dunn, B., Haeberlein, S. B., et al. (2018). NIA-AA Research Framework: Toward a biological definition of Alzheimer's disease. *Alzheimers Dement* 14, 535–562. doi: 10.1016/j.jalz.2018.02.018

Jansen, W. J., Ossenkoppele, R., Knol, D. L., Tijms, B. M., Scheltens, P., Verhey, F. R. J., et al. (2015). Prevalence of cerebral amyloid pathology in persons without dementia: A meta-analysis. *JAMA - J. Am. Med. Assoc.* 313, 1924–1938. doi: 10.1001/jama.2015.4668

Jellinger, K. A., and Korczyn, A. D. (2018). Are dementia with Lewy bodies and Parkinson's disease dementia the same disease? *BMC Med.* 16:1–16. doi: 10.1186/s12916-018-1016-8

Jiang, Q., Lee, C. Y. D., Mandrekar, S., Wilkinson, B., Cramer, P., Zelcer, N., et al. (2008). ApoE Promotes the Proteolytic Degradation of Aβ. *Neuron* 58, 681–693. doi: 10.1016/j.neuron.2008.04.010

Jindal, K., and Bansal, A. (2016). APOEε2 is associated with milder clinical and pathological Alzheimer's disease. *Ann. Neurosci.* 23:112. doi: 10.1159/000443572

Joie, R., La, Visani, A. V., Baker, S. L., Brown, J. A., Bourakova, V., et al. (2020). Prospective longitudinal atrophy in Alzheimer's disease correlates with the intensity and topography of baseline tau-PET. *Sci. Transl. Med.* 12, 1–13. doi: 10.1126/scitranslmed.aau5732

Jonsson, T., Stefansson, H., Steinberg, S., Jonsdottir, I., Jonsson, P. V., Snaedal, J., et al. (2013). Variant of TREM2 Associated with the Risk of Alzheimer's Disease. *N. Engl. J. Med.* 368, 107–116. doi: 10.1056/nejmoa1211103

Junqué, C., Ramírez-Ruiz, B., Tolosa, E., Summerfield, C., Martí, M. J., Pastor, P., et al. (2005). Amygdalar and hippocampal MRI volumetric reductions in Parkinson's disease with dementia. *Mov. Disord.* 20, 540–544. doi: 10.1002/mds.20371

Kakuda, K., Ikenaka, K., Araki, K., So, M., Aguirre, C., Kajiyama, Y., et al. (2019). Ultrasonication-based rapid amplification of α-synuclein aggregates in cerebrospinal fluid. *Sci. Rep.* 9, 1–10. doi: 10.1038/s41598-019-42399-0

Kamagata, K., Motoi, Y., Abe, O., Shimoji, K., Hori, M., Nakanishi, A., et al. (2012). White matter alteration of the cingulum in Parkinson disease with and without dementia: Evaluation by diffusion tensor tract-specific analysis. *Am. J. Neuroradiol.* 33, 890–895. doi: 10.3174/ajnr.A2860

Kantarci, K., Lowe, V. J., Boeve, B. F., Senjem, M. L., Tosakulwong, N., Lesnick, T. G., et al. (2017). AV-1451 tau and β-amyloid positron emission tomography imaging in dementia with Lewy bodies. *Ann. Neurol.* 81, 58–67. doi: 10.1002/ana.24825

Karunanayaka, P. R., Lee, E. Y., Lewis, M. M., Sen, S., Eslinger, P. J., Yang, Q. X., et al. (2016). Default mode network differences between rigidity- and tremor-predominant Parkinson's disease. *Cortex* 81, 239–250. doi: 10.1016/j.cortex.2016.04.021

Kim, H. K., Yoo, K., Na, D. L., Seo, S. W., Jeong, J., and Jeong, Y. (2015). Non-monotonic reorganization of brain networks with Alzheimer's disease progression. *Front. Aging Neurosci.* 7:1–10. doi: 10.3389/fnagi.2015.00111

Koike, S., Tanaka, S. C., Okada, T., Aso, T., Yamashita, A., Yamashita, O., et al. (2021). Brain/MINDS beyond human brain MRI project: A protocol for multi-level harmonization across brain disorders throughout the lifespan. *NeuroImage Clin.* 2021:102600. doi: 10.1016/j.nicl.2021.102600

Kosaka, K., and Manabe, Y. (2010). The first autopsied case of diffuse Lewy body disease (DLBD): Re-examination by recent immunostaining methods: The 50th Anniversary of Japanese Society of Neuropathology. *Neuropathology* 30, 458–462. doi: 10.1111/j.1440-1789.2010.01128.x

Koychev, I., Young, S., Holve, H., Ben Yehuda, M., and Gallacher, J. (2020). Dementias Platform UK Clinical Studies and Great Minds Register: Protocol of a targeted brain health studies recontact database. *BMJ Open* 10, 1–10. doi: 10.1136/bmjopen-2020-040766

Kuebler, L., Buss, S., Leonov, A., Ryazanov, S., Schmidt, F., Maurer, A., et al. (2021). [11C]MODAG-001—towards a PET tracer targeting α-synuclein aggregates. *Eur. J. Nucl. Med. Mol. Imaging* 48, 1759–1772. doi: 10.1007/s00259-020-05133-x

Kueper, J. K., Speechley, M., and Montero-Odasso, M. (2018). The Alzheimer's Disease Assessment Scale-Cognitive Subscale (ADAS-Cog): Modifications and Responsiveness in Pre-Dementia Populations. A Narrative Review. *J. Alzheimers Dis.* 63, 423–444. doi: 10.3233/jad-170991

Laakso, M. P., Partanen, K., Riekkinen, P., Lehtovirta, M., Helkala, E. L., Hallikainen, M., et al. (1996). Hippocampal volumes in Alzheimer's disease, Parkinson's disease with and without dementia, and in vascular dementia: An MRI study. *Neurology* 46, 678–681. doi: 10.1212/wnl.46.3.678

Langley, J., Huddleston, D. E., Merritt, M., Chen, X., McMurray, R., Silver, M., et al. (2016). Diffusion tensor imaging of the substantia nigra in Parkinson's disease revisited. *Hum. Brain Mapp.* 37, 2547–2556. doi: 10.1002/hbm.23192

Lawton, M., Baig, F., Toulson, G., Morovat, A., Evetts, S. G., Ben-Shlomo, Y., et al. (2020). Blood biomarkers with Parkinson's disease clusters and prognosis: The oxford discovery cohort. *Mov. Disord.* 35, 279–287. doi: 10.1002/mds.27888

Le Heron, C., Apps, M. A. J., and Husain, M. (2018). The anatomy of apathy: A neurocognitive framework for amotivated behaviour. *Neuropsychologia* 118, 54–67. doi: 10.1016/j.neuropsychologia.2017.07.003

Leech, R., Kamourieh, S., Beckmann, C. F., and Sharp, D. J. (2011). Fractionating the default mode network: Distinct contributions of the ventral and dorsal posterior cingulate cortex to cognitive control. *J. Neurosci.* 31, 3217–3224. doi: 10.1523/JNEUROSCI.5626-10.2011

Lees, A. J., Hardy, J., and Revesz, T. (2009). Parkinson's disease. *Lancet* 373, 2055–2066. doi: 10.1016/S0140-6736(09)60492-X

Lehrner, J. P., Brücke, T., Dal-Bianco, P., Gatterer, G., and Kryspin-Exner, I. (1997). Olfactory Functions in Parkinson's Disease and Alzheimer's Disease. *Chem. Senses* 22, 105–110. doi: 10.1093/chemse/22.1.105

Leuzy, A., Chiotis, K., Lemoine, L., Gillberg, P. G., Almkvist, O., Rodriguez-Vieitez, E., et al. (2019). Tau PET imaging in neurodegenerative tauopathies—still a challenge. *Mol. Psychiatry* 24, 1112–1134. doi: 10.1038/s41380-018-0342-8

Lewis, M. M., Du, G., Lee, E. Y., Nasralah, Z., Sterling, N. W., Zhang, L., et al. (2016). The pattern of gray matter atrophy in Parkinson's disease differs in cortical and subcortical regions. *J. Neurol.* 263, 68–75. doi: 10.1007/s00415-015-7929-7

Li, Q. X., Mok, S. S., Laughton, K. M., McLean, C. A., Cappai, R., Masters, C. L., et al. (2007). Plasma α-synuclein is decreased in subjects with Parkinson's disease. *Exp. Neurol.* 204, 583–588. doi: 10.1016/j.expneurol.2006.12.006

Litvan, I., Goldman, J. G., Tröster, A. I., Schmand, B. A., Weintraub, D., Petersen, R. C., et al. (2012). Diagnostic criteria for mild cognitive impairment in Parkinson's disease: Movement Disorder Society Task Force guidelines. *Mov. Disord.* 27, 349–356. doi: 10.1002/mds.24893

Liu, C. C., Kanekiyo, T., Xu, H., and Bu, G. (2013). Apolipoprotein e and Alzheimer disease: Risk, mechanisms and therapy. *Nat. Rev. Neurol.* 9, 106–118. doi: 10.1038/nrneurol.2012.263

Liu, H., Deng, B., Xie, F., Yang, X., Xie, Z., Chen, Y., et al. (2021). The influence of white matter hyperintensity on cognitive impairment in Parkinson's disease. *Ann. Clin. Transl. Neurol.* 8, 1917–1934. doi: 10.1002/acn3.51429

Liu, T. T. (2013). Neurovascular factors in resting-state functional MRI. *Neuroimage* 80, 339–348. doi: 10.1016/j.neuroimage.2013.04.071

Maass, F., Schulz, I., Lingor, P., Mollenhauer, B., and Bähr, M. (2019). Cerebrospinal fluid biomarker for Parkinson's disease: An overview. *Mol. Cell. Neurosci.* 97, 60–66. doi: 10.1016/j.mcn.2018.12.005

Majbour, N. K., Vaikath, N. N., Van Dijk, K. D., Ardah, M. T., Varghese, S., Vesterager, L. B., et al. (2016). Oligomeric and phosphorylated alpha-synuclein as potential CSF biomarkers for Parkinson's disease. *Mol. Neurodegener.* 11, 1–15. doi: 10.1186/s13024-016-0072-9

Malek, N., Lawton, M. A., Grosset, K. A., Bajaj, N., Barker, R. A., Ben-Shlomo, Y., et al. (2017). Utility of the new Movement Disorder Society clinical diagnostic criteria for Parkinson's disease applied retrospectively in a large cohort study of recent onset cases. *Park. Relat. Disord* 40, 40–46. doi: 10.1016/j.parkreldis.2017.04.006

Manza, P., Zhang, S., Li, C. S., and Leung, H. C. (2016). Resting-state functional connectivity of the striatum in early-stage Parkinson's disease: Cognitive decline and motor symptomatology. *Hum. Brain Mapp.* 37, 648–662. doi: 10.1002/hbm.23056

Marek, K., Jennings, D., Lasch, S., Siderowf, A., Tanner, C., Simuni, T., et al. (2011). The Parkinson Progression Marker Initiative (PPMI). *Prog. Neurobiol.* 95, 629–635. doi: 10.1016/j.pneurobio.2011.09.005

Maruyama, M., Shimada, H., Suhara, T., Shinotoh, H., Ji, B., Maeda, J., et al. (2013). Imaging of tau pathology in a tauopathy mouse model and in Alzheimer patients compared to normal controls. *Neuron* 79, 1094–1108. doi: 10.1016/j.neuron.2013.07.037

Mashima, K., Ito, D., Kameyama, M., Osada, T., Tabuchi, H., Nihei, Y., et al. (2017). Extremely Low Prevalence of Amyloid Positron Emission Tomography Positivity in Parkinson's Disease without Dementia. *Eur. Neurol.* 77, 231–237. doi: 10.1159/000464322

Matsuda, H. (2016). MRI morphometry in Alzheimer's disease. *Ageing Res. Rev.* 30, 17–24. doi: 10.1016/j.arr.2016.01.003

Matsuda, H., Murata, M., Mukai, Y., Sako, K., Ono, H., Toyama, H., et al. (2018). Japanese multicenter database of healthy controls for [(123)I]FP-CIT SPECT. *Eur. J. Nucl. Med. Mol. Imaging* 45, 1405–1416. doi: 10.1007/s00259-018-3976-5

Mattsson, N., Insel, P. S., Donohue, M., Landau, S., Jagust, W. J., Shaw, L. M., et al. (2015). Independent information from cerebrospinal fluid amyloid-β and florbetapir imaging in Alzheimer's disease. *Brain* 138, 772–783. doi: 10.1093/brain/awu367

Mazzulli, J. R., Xu, Y. H., Sun, Y., Knight, A. L., McLean, P. J., Caldwell, G. A., et al. (2011). Gaucher disease glucocerebrosidase and α-synuclein form a bidirectional pathogenic loop in synucleinopathies. *Cell* 146, 37–52. doi: 10.1016/j.cell.2011.06.001

McKeith, I. G., Boeve, B. F., Dickson, D. W., Halliday, G., Taylor, J. P., Weintraub, D., et al. (2017). Diagnosis and management of dementia with Lewy bodies: Fourth consensus report of the DLB Consortium. *Neurology* 89, 88–100. doi: 10.1212/wnl.0000000000004058

McKhann, G. M., Knopman, D. S., Chertkow, H., Hyman, B. T., Jack, C. R. J., Kawas, C. H., et al. (2011). The diagnosis of dementia due to Alzheimer's disease: recommendations from the National Institute on Aging-Alzheimer's Association workgroups on diagnostic guidelines for Alzheimer's disease. *Alzheimers. Dement.* 7, 263–269. doi: 10.1016/j.jalz.2011.03.005

Melzer, T. R., Watts, R., Macaskill, M. R., Pitcher, T. L., Livingston, L., Keenan, R. J., et al. (2013). White matter microstructure deteriorates across cognitive stages in Parkinson disease. *Neurology* 80, 1841–1849. doi: 10.1212/WNL.0b013e3182929f62

Mendoza-Velásquez, J. J., Flores-Vázquez, J. F., Barrón-Velázquez, E., Sosa-Ortiz, A. L., Illigens, B. M. W., and Siepmann, T. (2019). Autonomic dysfunction in α-synucleinopathies. *Front. Neurol.* 10, 1–8. doi: 10.3389/fneur.2019.00363

Meyer, P. T., Frings, L., Rücker, G., and Hellwig, S. (2017). 18F-FDG PET in Parkinsonism: Differential diagnosis and evaluation of cognitive impairment. *J. Nucl. Med.* 58, 1888–1898. doi: 10.2967/jnumed.116.186403

Mollenhauer, B., Trautmann, E., Taylor, P., Manninger, P., Sixel-Döring, F., Ebentheuer, J., et al. (2013). Total CSF α-synuclein is lower in de novo Parkinson patients than in healthy subjects. *Neurosci. Lett.* 532, 44–48. doi: 10.1016/j.neulet.2012.11.004

Morra, L. F., and Donovick, P. J. (2014). Clinical presentation and differential diagnosis of dementia with Lewy bodies: a review. *Int. J. Geriatr. Psychiatry* 29, 569–576. doi: 10.1002/gps.4039

Morris, J. C. (1993). The Clinical Dementia Rating (CDR): current version and scoring rules. *Neurology* 43, 2412–2414. doi: 10.1212/wnl.43.11.2412-a

Morton, R. E., St John, P. D., and Tyas, S. L. (2019). Migraine and the risk of all-cause dementia, Alzheimer's disease, and vascular dementia: A prospective cohort study in community-dwelling older adults. *Int. J. Geriatr. Psychiatry* 34, 1667–1676. doi: 10.1002/gps.5180

Moscoso, A., Grothe, M. J., Ashton, N. J., Karikari, T. K., Lantero Rodríguez, J., Snellman, A., et al. (2021). Longitudinal Associations of Blood Phosphorylated Tau181 and Neurofilament Light Chain with Neurodegeneration in Alzheimer Disease. *JAMA Neurol.* 78, 396–406. doi: 10.1001/jamaneurol.2020.4986

Muddapu, V. R., Dharshini, S. A. P., Chakravarthy, V. S., and Gromiha, M. M. (2020). Neurodegenerative Diseases – Is Metabolic Deficiency the Root Cause? *Front. Neurosci.* 14, 1–19. doi: 10.3389/fnins.2020.00213

Nagano-Saito, A., Washimi, Y., Arahata, Y., Kachi, T., Lerch, J. P., Evans, A. C., et al. (2005). Cerebral atrophy and its relation to cognitive impairment in Parkinson disease. *Neurology* 64, 224–229. doi: 10.1212/01.WNL.0000149510.41793.50

Nakajima, K., Okuda, K., Matsuo, S., Yoshita, M., Taki, J., Yamada, M., et al. (2012). Standardization of metaiodobenzylguanidine heartto mediastinum ratio using a calibration phantom: Effects of correction on normal databases and a multicentre study. *Eur. J. Nucl. Med. Mol. Imaging* 39, 113–119. doi: 10.1007/s00259-011-1963-1

Nakamura, A., Kaneko, N., Villemagne, V. L., Kato, T., Doecke, J., Doré, V., et al. (2018). High performance plasma amyloid-β biomarkers for Alzheimer's disease. *Nature* 554, 249–254. doi: 10.1038/nature25456

Nalls, M. A., Pankratz, N., Lill, C. M., Do, C. B., Hernandez, D. G., Saad, M., et al. (2014). Large-scale meta-analysis of genome-wide association data identifies six new risk loci for Parkinson's disease. *Nat. Genet.* 46, 989–993. doi: 10.1038/ng.3043

Nho, K., Risacher, S. L., Crane, P. K., DeCarli, C., Glymour, M. M., Habeck, C., et al. (2012). Voxel and surface-based topography of memory and executive deficits in mild cognitive impairment and Alzheimer's disease. *Brain Imaging Behav.* 6, 551–567. doi: 10.1007/s11682-012-9203-2

O'Brien, J. L., O'Keefe, K. M., Laviolette, P. S., Deluca, A. N., Blacker, D., Dickerson, B. C., et al. (2010). Longitudinal fMRI in elderly reveals loss of hippocampal activation with clinical decline. *Neurology* 74, 1969–1976. doi: 10.1212/WNL.0b013e3181e3966e

O'Brien, J. T., Oertel, W. H., McKeith, I. G., Grosset, D. G., Walker, Z., Tatsch, K., et al. (2014). Is ioflupane I123 injection diagnostically effective in patients with movement disorders and dementia? Pooled analysis of four clinical trials. *BMJ Open* 4:5122. doi: 10.1136/bmjopen-2014-005122

O'Bryant, S. E., Lacritz, L. H., Hall, J., Waring, S. C., Chan, W., Khodr, Z. G., et al. (2010). Validation of the new interpretive guidelines for the clinical dementia rating scale sum of boxes score in the National Alzheimer's Coordinating Center database. *Arch. Neurol.* 67, 746–749. doi: 10.1001/archneurol.2010.115

O'Callaghan, C., Hornberger, M., Balsters, J. H., Halliday, G. M., Lewis, S. J. G., and Shine, J. M. (2016). Cerebellar atrophy in Parkinson's disease and its implication for network connectivity. *Brain* 139, 845–855. doi: 10.1093/brain/awv399

Ochmann, S., Dyrba, M., Grothe, M. J., Kasper, E., Webel, S., Hauenstein, K., et al. (2017). Does Functional Connectivity Provide a Marker for Cognitive Rehabilitation Effects in Alzheimer's Disease? An Interventional Study. *J. Alzheimer's Dis.* 57, 1303–1313. doi: 10.3233/JAD-160773

Ogawa, S., Lee, T.-M., Nayak, A. S., and Glynn, P. (1990). Oxygenation−sensitive contrast in magnetic resonance image of rodent brain at high magnetic fields. *Magn. Reson. Med.* 14, 68–78. doi: 10.1002/mrm.1910140108

Okuzumi, A., Hatano, T., Fukuhara, T., Ueno, S., Nukina, N., Imai, Y., et al. (2021). α-Synuclein Seeding Assay Using RT-QuIC. *Methods Mol. Biol.* 2322, 3–16. doi: 10.1007/978-1-0716-1495-2_1

Olichney, J. M., Murphy, C., Hofstetter, C. R., Foster, K., Hansen, L. A., Thal, L. J., et al. (2005). Anosmia is very common in the Lewy body variant of Alzheimer's disease. *J. Neurol. Neurosurg. Psychiatry* 76, 1342–1347. doi: 10.1136/jnnp.2003.032003

Olsson, B., Lautner, R., Andreasson, U., Öhrfelt, A., Portelius, E., Bjerke, M., et al. (2016). CSF and blood biomarkers for the diagnosis of Alzheimer's disease: a systematic review and meta-analysis. *Lancet Neurol.* 15, 673–684. doi: 10.1016/S1474-4422(16)00070-3

Ossenkoppele, R., Jansen, W. J., Rabinovici, G. D., Knol, D. L., van der Flier, W. M., van Berckel, B. N., et al. (2015). Prevalence of amyloid PET positivity in dementia syndromes: a meta-analysis. *Jama* 313, 1939–1949. doi: 10.1001/jama.2015.4669

Ossenkoppele, R., Rabinovici, G. D., Smith, R., Cho, H., Scholl, M., Strandberg, O., et al. (2018). Discriminative accuracy of [18F]flortaucipir positron emission tomography for Alzheimer disease vs other neurodegenerative disorders. *JAMA - J. Am. Med. Assoc.* 320, 1151–1162. doi: 10.1001/jama.2018.12917

Pagonabarraga, J., Soriano-Mas, C., Llebaria, G., López-Solà, M., Pujol, J., and Kulisevsky, J. (2014). Neural correlates of minor hallucinations in non-demented patients with Parkinson's disease. *Park. Relat. Disord.* 20, 290–296. doi: 10.1016/j.parkreldis.2013.11.017

Palmqvist, S., Schöll, M., Strandberg, O., Mattsson, N., Stomrud, E., Zetterberg, H., et al. (2017). Earliest accumulation of β-amyloid occurs within the default-mode network and concurrently affects brain connectivity. *Nat. Commun.* 8:1150. doi: 10.1038/s41467-017-01150-x

Petersen, R. C., Aisen, P. S., Beckett, L. A., Donohue, M. C., Gamst, A. C., Harvey, D. J., et al. (2010). Alzheimer's Disease Neuroimaging Initiative (ADNI): Clinical characterization. *Neurology* 74, 201–209. doi: 10.1212/WNL.0b013e3181cb3e25

Petersen, R. C., Doody, R., Kurz, A., Mohs, R. C., Morris, J. C., Rabins, P. V., et al. (2001). Current concepts in mild cognitive impairment. *Arch. Neurol.* 58, 1985–1992. doi: 10.1001/archneur.58.12.1985

Petersen, R. C., Smith, G. E., Waring, S. C., Ivnik, R. J., Tangalos, E. G., and Kokmen, E. (1999). Mild cognitive impairment: clinical characterization and outcome. *Arch. Neurol.* 56, 303–308. doi: 10.1001/archneur.56.3.303

Pirker, W. (2003). Correlation of dopamine transporter imaging with parkinsonian motor handicap: How close is it? *Mov. Disord.* 18:10579. doi: 10.1002/mds.10579

Pontifex, M., Vauzour, D., and Minihane, A. M. (2018). The effect of APOE genotype on Alzheimer's disease risk is influenced by sex and docosahexaenoic acid status. *Neurobiol. Aging* 69, 209–220. doi: 10.1016/j.neurobiolaging.2018.05.017

Portet, F., Scarmeas, N., Cosentino, S., Helzner, E. P., and Stern, Y. (2009). Extrapyramidal signs before and after diagnosis of incident Alzheimer disease in a prospective population study. *Arch. Neurol.* 66, 1120–1126. doi: 10.1001/archneurol.2009.196

Poston, K. L., Ua Cruadhlaoich, M. A. I., Santoso, L. F., Bernstein, J. D., Liu, T., Wang, Y., et al. (2020). Substantia Nigra Volume Dissociates Bradykinesia and Rigidity from Tremor in Parkinson's Disease: A 7 Tesla Imaging Study. *J. Parkinsons. Dis.* 10, 591–604. doi: 10.3233/JPD-191890

Postuma, R. B., Berg, D., Stern, M., Poewe, W., Olanow, C. W., Oertel, W., et al. (2015). MDS clinical diagnostic criteria for Parkinson's disease. *Mov. Disord.* 30, 1591–1601. doi: 10.1002/mds.26424

Postuma, R. B., Poewe, W., Litvan, I., Lewis, S., Lang, A. E., Halliday, G., et al. (2018). Validation of the MDS clinical diagnostic criteria for Parkinson's disease. *Mov. Disord.* 33, 1601–1608. doi: 10.1002/mds.27362

Prakash, B. D., Sitoh, Y. Y., Tan, L. C. S., and Au, W. L. (2012). Asymmetrical diffusion tensor imaging indices of the rostral substantia nigra in Parkinson's disease. *Park. Relat. Disord.* 18, 1029–1033. doi: 10.1016/j.parkreldis.2012.05.021

Prins, N. D., and Scheltens, P. (2015). White matter hyperintensities, cognitive impairment and dementia: An update. *Nat. Rev. Neurol.* 11, 157–165. doi: 10.1038/nrneurol.2015.10

Probst, C. C., Winter, L. M., Moller, B., Weber, H., Weintraub, D., Witt, K., et al. (2014). Validation of the questionnaire for impulsive-compulsive disorders in Parkinson's disease (QUIP) and the QUIP-rating scale in a German speaking sample. *J. Neurol.* 261, 936–942. doi: 10.1007/s00415-014-7299-6

Pyatigorskaya, N., Sanz-Morère, C. B., Gaurav, R., Biondetti, E., Valabregue, R., Santin, M., et al. (2020). Iron imaging as a diagnostic tool for parkinson's disease: A systematic review and meta-analysis. *Front. Neurol.* 11:366. doi: 10.3389/fneur.2020.00366

Qu, Y., Ma, Y. H., Huang, Y. Y., Ou, Y. N., Shen, X. N., Chen, S. D., et al. (2021). Blood biomarkers for the diagnosis of amnestic mild cognitive impairment and Alzheimer's disease: A systematic review and meta-analysis. *Neurosci. Biobehav. Rev.* 128, 479–486. doi: 10.1016/j.neubiorev.2021.07.007

Robinson, M., Lee, B. Y., and Hane, F. T. (2017). Recent Progress in Alzheimer's Disease Research, Part 2: Genetics and Epidemiology. *J. Alzheimers. Dis.* 57, 317–330. doi: 10.3233/JAD-161149

Rolinski, M., Griffanti, L., Piccini, P., Roussakis, A. A., Szewczyk-Krolikowski, K., Menke, R. A., et al. (2016). Basal ganglia dysfunction in idiopathic REM sleep behaviour disorder parallels that in early Parkinson's disease. *Brain* 139, 2224–2234. doi: 10.1093/brain/aww124

Rolinski, M., Griffanti, L., Szewczyk-Krolikowski, K., Menke, R. A. L., Wilcock, G. K., Filippini, N., et al. (2015). Aberrant functional connectivity within the basal ganglia of patients with Parkinson's disease. *NeuroImage Clin.* 8, 126–132. doi: 10.1016/j.nicl.2015.04.003

Rosenberg-Katz, K., Herman, T., Jacob, Y., Giladi, N., Hendler, T., and Hausdorff, J. M. (2013). Gray matter atrophy distinguishes between Parkinson disease motor subtypes. *Neurology* 80, 1476–1484. doi: 10.1212/WNL.0b013e31828cfaa4

Rosenthal, E., Brennan, L., Xie, S., Hurtig, H., Milber, J., Weintraub, D., et al. (2010). Association between cognition and function in patients with Parkinson disease with and without dementia. *Mov. Disord.* 25, 1170–1176. doi: 10.1002/mds.23073

Sachdev, P. S., Blacker, D., Blazer, D. G., Ganguli, M., Jeste, D. V., Paulsen, J. S., et al. (2014). Classifying neurocognitive disorders: The DSM-5 approach. *Nat. Rev. Neurol.* 10, 634–642. doi: 10.1038/nrneurol.2014.181

Saito, S., Yamamoto, Y., and Ihara, M. (2015). Mild Cognitive Impairment: At the Crossroad of Neurodegeneration and Vascular Dysfunction. *Curr. Alzheimer Res.* 12, 507–512. doi: 10.2174/1567205012666150530202508

Sakakibara, S., Hashimoto, R., Katayama, T., Kenjyo, M., Yokokawa, Y., Saito, Y., et al. (2020). Longitudinal Change of DAT SPECT in Parkinson's Disease and Multiple System Atrophy. *J. Parkinsons. Dis.* 10, 123–130. doi: 10.3233/JPD-191710

Sanchez-Castaneda, C., Rene, R., Ramirez-Ruiz, B., Campdelacreu, J., Gascon, J., Falcon, C., et al. (2009). Correlations between gray matter reductions and cognitive deficits in dementia with lewy bodies and Parkinson's disease with dementia. *Mov. Disord.* 24, 1740–1746. doi: 10.1002/mds.22488

Sasaki, M., Shibata, E., Kudo, K., and Tohyama, K. (2008). Neuromelanin-sensitive MRI: Basics, technique, and clinical applications. *Clin. Neuroradiol.* 18, 147–153. doi: 10.1007/s00062-008-8018-4

Sasaki, S. (2018). High prevalence of parkinsonism in patients with MCI or mild Alzheimer's disease. *Alzheimers. Dement.* 14, 1615–1622. doi: 10.1016/j.jalz.2018.06.3054

Sawada, H., Oeda, T., Yamamoto, K., Kitagawa, N., Mizuta, E., Hosokawa, R., et al. (2009). Diagnostic accuracy of cardiac metaiodobenzylguanidine scintigraphy in Parkinson disease. *Eur. J. Neurol.* 16, 174–182. doi: 10.1111/j.1468-1331.2008.02372.x

Sawada, H., Udaka, F., Kameyama, M., Seriu, N., Nishinaka, K., Shindou, K., et al. (1992). SPECT findings in Parkinson's disease associated with dementia. *J. Neurol. Neurosurg. Psychiatry* 55, 960–963. doi: 10.1136/jnnp.55.10.960

Scheltens, P., Fox, N., Barkhof, F., and De Carli, C. (2002). Structural magnetic resonance imaging in the practical assessment of dementia: Beyond exclusion. *Lancet Neurol.* 1, 13–21. doi: 10.1016/S1474-4422(02)00002-9

Schouten, T. M., Koini, M., De Vos, F., Seiler, S., Van Der Grond, J., Lechner, A., et al. (2016). Combining anatomical, diffusion, and resting state functional magnetic resonance imaging for individual classification of mild and moderate Alzheimer's disease. *NeuroImage Clin.* 11, 46–51. doi: 10.1016/j.nicl.2016.01.002

Schuff, N., Wu, I. W., Buckley, S., Foster, E. D., Coffey, C. S., Gitelman, D. R., et al. (2015). Diffusion imaging of nigral alterations in early Parkinson's disease with dopaminergic deficits. *Mov. Disord.* 30, 1885–1892. doi: 10.1002/mds.26325

Serrano-Pozo, A., Frosch, M. P., Masliah, E., and Hyman, B. T. (2011). Neuropathological alterations in Alzheimer disease. *Cold Spring Harb. Perspect. Med.* 1, 1–24. doi: 10.1101/cshperspect.a006189

Shaw, L. M., Vanderstichele, H., Knapik-Czajka, M., Clark, C. M., Aisen, P. S., Petersen, R. C., et al. (2009). Cerebrospinal fluid biomarker signature in alzheimer's disease neuroimaging initiative subjects. *Ann. Neurol.* 65, 403–413. doi: 10.1002/ana.21610

Sheline, Y. I., Morris, J. C., Snyder, A. Z., Price, J. L., Yan, Z., D'Angelo, G., et al. (2010a). APOE4 allele disrupts resting state fMRI connectivity in the absence of amyloid plaques or decreased CSF Aβ42. *J. Neurosci.* 30, 17035–17040. doi: 10.1523/JNEUROSCI.3987-10.2010

Sheline, Y. I., and Raichle, M. E. (2013). Resting state functional connectivity in preclinical Alzheimer's disease. *Biol. Psychiatry* 74, 340–347. doi: 10.1016/j.biopsych.2012.11.028

Sheline, Y. I., Raichle, M. E., Snyder, A. Z., Morris, J. C., Head, D., Wang, S., et al. (2010b). Amyloid Plaques Disrupt Resting State Default Mode Network Connectivity in Cognitively Normal Elderly. *Biol. Psychiatry* 67, 584–587. doi: 10.1016/j.biopsych.2009.08.024

Shi, Y., and Holtzman, D. M. (2018). Interplay between innate immunity and Alzheimer disease: APOE and TREM2 in the spotlight. *Nat. Rev. Immunol.* 18, 759–772. doi: 10.1038/s41577-018-0051-1

Shimada, H., Ataka, S., Takeuchi, J., Mori, H., Wada, Y., Watanabe, Y., et al. (2011). Pittsburgh compound B-negative dementia: a possibility of misdiagnosis of patients with non-alzheimer disease-type dementia as having AD. *J. Geriatr. Psychiatry Neurol.* 24, 123–126. doi: 10.1177/0891988711409410

Shimada, H., Kitamura, S., Shinotoh, H., Endo, H., Niwa, F., Hirano, S., et al. (2017). Association between Aβ and tau accumulations and their influence on clinical features in aging and Alzheimer's disease spectrum brains: A [(11)C]PBB3-PET study. *Alzheimer's Dement* 6, 11–20. doi: 10.1016/j.dadm.2016.12.009

Shimada, H., Shinotoh, H., Hirano, S., Miyoshi, M., Sato, K., Tanaka, N., et al. (2013). β-Amyloid in Lewy body disease is related to Alzheimer's disease-like atrophy. *Mov. Disord.* 28, 169–175. doi: 10.1002/mds.25286

Sidransky, E., Nalls, M. A., Aasly, J. O., Aharon-Peretz, J., Annesi, G., Barbosa, E. R., et al. (2009). Multicenter analysis of glucocerebrosidase mutations in Parkinson's disease. *N. Engl. J. Med.* 361, 1651–1661. doi: 10.1056/NEJMoa0901281

Singleton, A., and Hardy, J. (2019). Progress in the genetic analysis of Parkinson's disease. *Hum. Mol. Genet.* 28, R215–R218. doi: 10.1093/hmg/ddz183

Spampinato, U., Habert, M. O., Mas, J. L., Bourdel, M. C., Ziegler, M., De Recondo, J., et al. (1991). (99mTc)-HM-PAO SPECT and cognitive impairment in Parkinson's disease: A comparison with dementia of the Alzheimer type. *J. Neurol. Neurosurg. Psychiatry* 54, 787–792. doi: 10.1136/jnnp.54.9.787

Stenset, V., Bjørnerud, A., Fjell, A. M., Walhovd, K. B., Hofoss, D., Due-Tønnessen, P., et al. (2011). Cingulum fiber diffusivity and CSF T-tau in patients with subjective and mild cognitive impairment. *Neurobiol. Aging* 32, 581–589. doi: 10.1016/j.neurobiolaging.2009.04.014

Sterling, N. W., Du, G., Lewis, M. M., Dimaio, C., Kong, L., Eslinger, P. J., et al. (2013). Striatal shape in Parkinson's disease. *Neurobiol. Aging* 34, 2510–2516. doi: 10.1016/j.neurobiolaging.2013.05.017

Sterling, N. W., Lewis, M. M., Du, G., and Huang, X. (2016). Structural imaging and Parkinson's disease: Moving toward quantitative markers of disease progression. *J. Parkinsons. Dis.* 6, 557–567. doi: 10.3233/JPD-160824

Summerfield, C., Junqué, C., Tolosa, E., Salgado-Pineda, P., Gómez-Ansón, B., Martí, M. J., et al. (2005). Structural Brain Changes in Parkinson Disease With Dementia. *Arch. Neurol.* 62:281. doi: 10.1001/archneur.62.2.281

Tagai, K., Ono, M., Kubota, M., Kitamura, S., Takahata, K., Seki, C., et al. (2021). High-Contrast In Vivo Imaging of Tau Pathologies in Alzheimer's and Non-Alzheimer's Disease Tauopathies. *Neuron* 109, 42.e–58.e. doi: 10.1016/j.neuron.2020.09.042

Tahmasian, M., Bettray, L. M., van Eimeren, T., Drzezga, A., Timmermann, L., Eickhoff, C. R., et al. (2015). A systematic review on the applications of resting-state fMRI in Parkinson's disease: Does dopamine replacement therapy play a role? *Cortex* 73, 80–105. doi: 10.1016/j.cortex.2015.08.005

Takamura, T., and Hanakawa, T. (2017). Clinical utility of resting-state functional connectivity magnetic resonance imaging for mood and cognitive disorders. *J. Neural Transm.* 124, 821–839. doi: 10.1007/s00702-017-1710-2

Tam, C. W. C., Burton, E. J., McKeith, I. G., Burn, D. J., and O'Brien, J. T. (2005). Temporal lobe atrophy on MRI in Parkinson disease with dementia: A comparison with Alzheimer disease and dementia with Lewy bodies. *Neurology* 64, 861–865. doi: 10.1212/01.WNL.0000153070.82309.D4

Tang, H., Huang, J., Nie, K., Gan, R., Wang, L., Zhao, J., et al. (2016). Cognitive profile of Parkinson's disease patients: a comparative study between early-onset and late-onset Parkinson's disease. *Int. J. Neurosci.* 126, 227–234. doi: 10.3109/00207454.2015.1010646

Teipel, S., Drzezga, A., Grothe, M. J., Barthel, H., Chételat, G., Schuff, N., et al. (2015). Multimodal imaging in Alzheimer's disease: Validity and usefulness for early detection. *Lancet Neurol.* 14, 1037–1053. doi: 10.1016/S1474-4422(15)00093-9

Thobois, S., Prange, S., Scheiber, C., and Broussolle, E. (2019). What a neurologist should know about PET and SPECT functional imaging for parkinsonism: A practical perspective. *Park. Relat. Disord.* 59, 93–100. doi: 10.1016/j.parkreldis.2018.08.016

Thomas, G. E. C., Leyland, L. A., Schrag, A. E., Lees, A. J., Acosta-Cabronero, J., and Weil, R. S. (2020). Brain iron deposition is linked with cognitive severity in Parkinson's disease. *J. Neurol. Neurosurg. Psychiatry* 91, 418–425. doi: 10.1136/jnnp-2019-322042

Tinaz, S., Courtney, M. G., and Stern, C. E. (2011). Focal cortical and subcortical atrophy in early Parkinson's disease. *Mov. Disord.* 26, 436–441. doi: 10.1002/mds.23453

Tokuda, T., Qureshi, M. M., Ardah, M. T., Varghese, S., Shehab, S. A. S., Kasai, T., et al. (2010). Detection of elevated levels of α-synuclein oligomers in CSF from patients with Parkinson disease. *Neurology* 75, 1766–1772. doi: 10.1212/WNL.0b013e3181fd613b

Tokuda, T., Salem, S. A., Allsop, D., Mizuno, T., Nakagawa, M., Qureshi, M. M., et al. (2006). Decreased α-synuclein in cerebrospinal fluid of aged individuals and subjects with Parkinson's disease. *Biochem. Biophys. Res. Commun.* 349, 162–166. doi: 10.1016/j.bbrc.2006.08.024

Trivedi, D. (2017). Cochrane Review Summary: Mini-Mental State Examination (MMSE) for the detection of dementia in clinically unevaluated people aged 65 and over in community and primary care populations. *Prim. Heal. Care Res. Dev.* 2017, 1–2. doi: 10.1017/S1463423617000202

Twohig, D., and Nielsen, H. M. (2019). α-synuclein in the pathophysiology of Alzheimer's disease. *Mol. Neurodegener.* 14:23. doi: 10.1186/s13024-019-0320-x

Valotassiou, V., Malamitsi, J., Papatriantafyllou, J., Dardiotis, E., Tsougos, I., Psimadas, D., et al. (2018). SPECT and PET imaging in Alzheimer's disease. *Ann. Nucl. Med.* 32, 583–593. doi: 10.1007/s12149-018-1292-6

van der Pluijm, M., Cassidy, C., Zandstra, M., Wallert, E., de Bruin, K., Booij, J., et al. (2021). Reliability and Reproducibility of Neuromelanin-Sensitive Imaging of the Substantia Nigra: A Comparison of Three Different Sequences. *J. Magn. Reson. Imaging* 53, 712–721. doi: 10.1002/jmri.27384

Vandenbossche, J., Deroost, N., Soetens, E., Coomans, D., Spildooren, J., Vercruysse, S., et al. (2012). Freezing of gait in Parkinson's disease: Disturbances in automaticity and control. *Front. Hum. Neurosci.* 6:1–19. doi: 10.3389/fnhum.2012.00356

Veitch, D. P., Weiner, M. W., Aisen, P. S., Beckett, L. A., Cairns, N. J., Green, R. C., et al. (2019). Understanding disease progression and improving Alzheimer's disease clinical trials: Recent highlights from the Alzheimer's Disease Neuroimaging Initiative. *Alzheimers. Dement.* 15, 106–152. doi: 10.1016/j.jalz.2018.08.005

Verdurand, M., Levigoureux, E., Zeinyeh, W., Berthier, L., Mendjel-Herda, M., Cadarossanesaib, F., et al. (2018). In Silico, in Vitro, and in Vivo Evaluation of New Candidates for α-Synuclein PET Imaging. *Mol. Pharm.* 15, 3153–3166. doi: 10.1021/acs.molpharmaceut.8b00229

Vöglein, J., Paumier, K., Jucker, M., Preische, O., McDade, E., Hassenstab, J., et al. (2019). Clinical, pathophysiological and genetic features of motor symptoms in autosomal dominant Alzheimer's disease. *Brain* 142, 1429–1440. doi: 10.1093/brain/awz050

Wakasugi, N., Togo, H., Mukai, Y., Nishikawa, N., Sakamoto, T., Murata, M., et al. (2021). Prefrontal network dysfunctions in rapid eye movement sleep behavior disorder. *Park. Relat. Disord.* 85, 72–77. doi: 10.1016/j.parkreldis.2021.03.005

Wang, L., Zang, Y., He, Y., Liang, M., Zhang, X., Tian, L., et al. (2006). Changes in hippocampal connectivity in the early stages of Alzheimer's disease: Evidence

from resting state fMRI. *Neuroimage* 31, 496–504. doi: 10.1016/j.neuroimage.2005.12.033

Wang, Z., Luo, X. G., and Gao, C. (2016). Utility of susceptibility-weighted imaging in Parkinson's disease and atypical Parkinsonian disorders. *Transl. Neurodegener.* 5, 1–8. doi: 10.1186/s40035-016-0064-2

Wee, C. Y., Yang, S., Yap, P. T., and Shen, D. (2016). Sparse temporally dynamic resting-state functional connectivity networks for early MCI identification. *Brain Imaging Behav.* 10, 342–356. doi: 10.1007/s11682-015-9408-2

Weiner, M. W., Veitch, D. P., Aisen, P. S., Beckett, L. A., Cairns, N. J., Cedarbaum, J., et al. (2015). 2014 Update of the Alzheimer's Disease Neuroimaging Initiative: A review of papers published since its inception. *Alzheimers. Dement.* 11, e1–e120. doi: 10.1016/j.jalz.2014.11.001

Weiner, M. W., Veitch, D. P., Aisen, P. S., Beckett, L. A., Cairns, N. J., Green, R. C., et al. (2012). The Alzheimer's Disease Neuroimaging Initiative: a review of papers published since its inception. *Alzheimers. Dement.* 8, S1–S68. doi: 10.1016/j.jalz.2011.09.172

Weiner, M. W., Veitch, D. P., Aisen, P. S., Beckett, L. A., Cairns, N. J., Green, R. C., et al. (2017). The Alzheimer's Disease Neuroimaging Initiative 3: Continued innovation for clinical trial improvement. *Alzheimers. Dement.* 13, 561–571. doi: 10.1016/j.jalz.2016.10.006

Weintraub, D., Simuni, T., Caspell-Garcia, C., Coffey, C., Lasch, S., Siderowf, A., et al. (2015). Cognitive performance and neuropsychiatric symptoms in early, untreated Parkinson's disease. *Mov. Disord.* 30, 919–927. doi: 10.1002/mds.26170

Wennström, M., Surova, Y., Hall, S., Nilsson, C., Minthon, L., Boström, F., et al. (2013). Low CSF Levels of Both α-Synuclein and the α-Synuclein Cleaving Enzyme Neurosin in Patients with Synucleinopathy. *PLoS One* 8:53250. doi: 10.1371/journal.pone.0053250

Williams-Gray, C. H., Foltynie, T., Brayne, C. E. G., Robbins, T. W., and Barker, R. A. (2007). Evolution of cognitive dysfunction in an incident Parkinson's disease cohort. *Brain* 130, 1787–1798. doi: 10.1093/brain/awm111

Wolters, A. F., van de Weijer, S. C. F., Leentjens, A. F. G., Duits, A. A., Jacobs, H. I. L., and Kuijf, M. L. (2019). Resting-state fMRI in Parkinson's disease patients with cognitive impairment: A meta-analysis. *Park. Relat. Disord.* 62, 16–27. doi: 10.1016/j.parkreldis.2018.12.016

Wu, S. F., Zhu, Z. F., Kong, Y., Zhang, H. P., Zhou, G. Q., Jiang, Q. T., et al. (2014). Assessment of cerebral iron content in patients with Parkinson's disease by the susceptibility-weighted MRI. *Eur. Rev. Med. Pharmacol. Sci.* 18, 2605–2608.

Wu, T., Long, X., Zang, Y., Wang, L., Hallett, M., Li, K., et al. (2009). Regional homogeneity changes in patients with Parkinson's disease. *Hum. Brain Mapp.* 30, 1502–1510. doi: 10.1002/hbm.20622

Wu, X., Li, R., Fleisher, A. S., Reiman, E. M., Guan, X., Zhang, Y., et al. (2011). Altered default mode network connectivity in Alzheimer's disease-A resting functional MRI and Bayesian network study. *Hum. Brain Mapp.* 32, 1868–1881. doi: 10.1002/hbm.21153

Yamada, G., Ueki, Y., Oishi, N., Oguri, T., Fukui, A., Nakayama, M., et al. (2019). Nigrostriatal Dopaminergic Dysfunction and Altered Functional Connectivity in REM Sleep Behavior Disorder With Mild Motor Impairment. *Front Neurol* 10:802. doi: 10.3389/fneur.2019.00802

Yoshii, F., Ryo, M., Baba, Y., Koide, T., and Hashimoto, J. (2017). Combined use of dopamine transporter imaging (DAT-SPECT) and (123)I-metaiodobenzylguanidine (MIBG) myocardial scintigraphy for diagnosing Parkinson's disease. *J. Neurol. Sci.* 375, 80–85. doi: 10.1016/j.jns.2017.01.042

Yoshizawa, H., Vonsattel, J. P. G., and Honig, L. S. (2013). Early neuropsychological discriminants for Lewy body disease: An autopsy series. *J. Neurol. Neurosurg. Psychiatry* 84, 1326–1330. doi: 10.1136/jnnp-2012-304381

Zeighami, Y., Fereshtehnejad, S. M., Dadar, M., Collins, D. L., Postuma, R. B., Mišiæ, B., et al. (2019). A clinical-anatomical signature of Parkinson's disease identified with partial least squares and magnetic resonance imaging. *Neuroimage* 190, 69–78. doi: 10.1016/j.neuroimage.2017.12.050

Zeighami, Y., Ulla, M., Iturria-Medina, Y., Dadar, M., Zhang, Y., Larcher, K. M. H., et al. (2015). Network structure of brain atrophy in de novo parkinson's disease. *Elife* 4, 1–20. doi: 10.7554/eLife.08440

Zhang, J., Wei, L., Hu, X., Xie, B., Zhang, Y., Wu, G.-R., et al. (2015). Akinetic-rigid and tremor-dominant Parkinson's disease patients show different patterns of intrinsic brain activity. *Parkinsonism Relat. Disord.* 21, 23–30. doi: 10.1016/j.parkreldis.2014.10.017

Zhang, T., Zhao, Z., Zhang, C., Zhang, J., Jin, Z., and Li, L. (2019). Classification of early and late mild cognitive impairment using functional brain network of resting-state fMRI. *Front. Psychiatry* 10, 1–16. doi: 10.3389/fpsyt.2019.00572

Zhang, W., Sun, S. G., Jiang, Y. H., Qiao, X., Sun, X., and Wu, Y. (2009). Determination of brain iron content in patients with Parkinson's disease using magnetic susceptibility imaging. *Neurosci. Bull.* 25, 353–360. doi: 10.1007/s12264-009-0225-8

Zhou, B., Wen, M., Yu, W. F., Zhang, C. L., and Jiao, L. (2015). The diagnostic and differential diagnosis utility of cerebrospinal fluid α -synuclein levels in Parkinson's disease: A meta-analysis. *Parkinsons. Dis.* 2015:567386. doi: 10.1155/2015/567386

Zhou, J., Greicius, M. D., Gennatas, E. D., Growdon, M. E., Jang, J. Y., Rabinovici, G. D., et al. (2010). Divergent network connectivity changes in behavioural variant frontotemporal dementia and Alzheimer's disease. *Brain* 133, 1352–1367. doi: 10.1093/brain/awq075

Zucca, F. A., Basso, E., Cupaioli, F. A., Ferrari, E., Sulzer, D., Casella, L., et al. (2014). Neuromelanin of the human substantia Nigra: An update. *Neurotox. Res.* 25, 13–23. doi: 10.1007/s12640-013-9435-y

Conflict of Interest: The authors declare that the research was conducted in the absence of any commercial or financial relationships that could be construed as a potential conflict of interest.

Publisher's Note: All claims expressed in this article are solely those of the authors and do not necessarily represent those of their affiliated organizations, or those of the publisher, the editors and the reviewers. Any product that may be evaluated in this article, or claim that may be made by its manufacturer, is not guaranteed or endorsed by the publisher.

Copyright © 2021 Wakasugi and Hanakawa. This is an open-access article distributed under the terms of the Creative Commons Attribution License (CC BY). The use, distribution or reproduction in other forums is permitted, provided the original author(s) and the copyright owner(s) are credited and that the original publication in this journal is cited, in accordance with accepted academic practice. No use, distribution or reproduction is permitted which does not comply with these terms.

frontiers in Systems Neuroscience

ORIGINAL RESEARCH
published: 25 November 2021
doi: 10.3389/fnsys.2021.785366

A Model of Predictive Postural Control Against Floor Tilting in Rats

Akira Konosu[1], Tetsuro Funato[2], Yuma Matsuki[2], Akihiro Fujita[2], Ryutaro Sakai[1] and Dai Yanagihara[1]**

[1] Department of Life Sciences, The University of Tokyo, Meguro-ku, Japan, [2] Department of Mechanical Engineering and Intelligent Systems, The University of Electro-Communications, Chofu, Japan

Humans and animals learn the internal model of bodies and environments from their experience and stabilize posture against disturbances based on the predicted future states according to the internal model. We evaluated the mechanism of predictive control during standing, by using rats to construct a novel experimental system and comparing their behaviors with a mathematical model. In the experiments, rats (n = 6) that were standing upright using their hindlimbs were given a sensory input of light, after a certain period, the floor under them tilted backward. Initially, this disturbance induced a large postural response, including backward rotation of the center-of-mass angle and hindlimb segments. However, the rats gradually adjusted to the disturbance after experiencing 70 sequential trials, and a reduction in the amplitude of postural response was noted. We simulated the postural control of the rats under disturbance using an inverted pendulum model and model predictive control (MPC). MPC is a control method for predicting the future state using an internal model of the control target. It provides control inputs that optimize the predicted future states. Identification of the predictive and physiological parameters so that the simulation corresponds to the experiment, resulted in a value of predictive horizon (0.96 s) close to the interval time in the experiment (0.9–1.15 s). These results suggest that the rats predict posture dynamics under disturbance based on the timing of the sensory input and that the central nervous system provides plasticity mechanisms to acquire the internal model for MPC.

Keywords: predictive postural control, bipedal rats, motor learning, model predictive control, simulation

OPEN ACCESS

Edited by:
Jun Izawa,
University of Tsukuba, Japan

Reviewed by:
Taishin Nomura,
Osaka University, Japan
Kamran Iqbal,
University of Arkansas at Little Rock, United States

***Correspondence:**
Tetsuro Funato
funato@uec.ac.jp
Dai Yanagihara
dai-y@idaten.c.u-tokyo.ac.jp

Received: *29 September 2021*
Accepted: *01 November 2021*
Published: *25 November 2021*

Citation:
Konosu A, Funato T, Matsuki Y, Fujita A, Sakai R and Yanagihara D (2021) A Model of Predictive Postural Control Against Floor Tilting in Rats. Front. Syst. Neurosci. 15:785366. doi: 10.3389/fnsys.2021.785366

INTRODUCTION

Most daily activities and skillful motor performance require predictive postural control to stabilize the posture against internal and external disturbances. Predictive postural controls are based on neuroplasticity, which enables learning of the internal models, namely, the relationship between motor output and the resulting posture changes in a certain environment. Although a wide range of nervous system areas, centered in the cerebellum, have been suggested to be involved in predictive postural control (Diener et al., 1992; Yakovenko et al., 2011; Ng et al., 2013; Yanagihara, 2014; Bolzoni et al., 2015), the detailed mechanisms remain unclear.

In humans, one of the most important and challenging tasks in postural control is to maintain an upright standing posture against gravity. Disturbance systems, in which a floor tilts backward

while participants maintain a static standing posture, greatly contribute to understanding the stabilization mechanisms of the upright posture and finding automatic responses with a latency of approximately 100 ms (Nashner, 1976; Carpenter et al., 1999). Several studies have examined predictive postural controls for external disturbances while incorporating classical conditioning into floor-tilting systems. In the association between floor tiles and the preceding sensory inputs, muscle activities around the leg joints and center of pressure (CoP) started to fluctuate just before the tilt (Kolb et al., 2002). In addition, even without the floor tilt, the sensory input alone evoked predictive movement to cancel the upcoming postural response and suppress the excessive stretch reflex as a result of this association (Campbell et al., 2009). Furthermore, it has been found that patients with cerebellar defects cannot establish these predictive controls (Kolb et al., 2004).

Neuroscience has evolved as a result of powerful research methods, these include recording neural activities, genetic manipulation, and temporal and/or region-specific inactivation in rodents. Developing experimental systems for predictive postural control in rodents would greatly advance the understanding of these mechanisms. We have developed a system for evaluating predictive postural controls for voluntary movements has been developed in mice (Yamaura et al., 2013). Recent advances in the identification of the genetic basis of hereditary cerebellar ataxias have made it possible to produce mouse models for these diseases. Spinocerebellar ataxia is a type of cerebellar disease associated with an autosomal dominant pattern of inheritance. The most common type is spinocerebellar ataxia type 3, also known as Machado-Joseph disease. We generated a conditional transgenic mouse model with spinocerebellar ataxia type 3 mice, which have defective cerebellar Purkinje cells due to the induced expression of the Purkinje cell-specific L7 promoter (Yamaura et al., 2013). In the voluntary reaching task, that performed dorsiflexion of the neck as the prime movement, to reach and drink from a water flask while standing, spinocerebellar ataxia type 3 mice showed postural deficits that are characterized by considerable variation in the trajectory of the mouth, terrible swaying posture, and delayed electromyography activities in the hindlimb muscles. This study demonstrated that predictive postural controls can be kinematically and physiologically evaluated in rodents. However, to our knowledge, an experimental system to evaluate predictive controls against external disturbances has not yet been established. To understand the neural basis of it, applying the systems of upright standing and floor tilting in rodents could be effective. We have previously established an experimental environment in which rats maintained an upright posture using hindlimbs on a static floor, confirming that the intersegmental coordination and frequency characteristics of the CoP are consistent with those of humans (Funato et al., 2017). In the present study, we establish a novel experimental task in rats by incorporating a floor tilting disturbance and a conditioning paradigm into this system.

To approach the control mechanism for predictive behavior, we used a mathematical model of postural control. In previous studies, we developed a postural control model for bipedally standing rats with lesions in the olivo-cerebellar system (Funato et al., 2021), and showed that the decreased non-linear control, possibly due to lesions in the internal model, caused instability. The current experiment conducted on rats is based on this study, thereby the mathematical model is also based on this study. The same body model of rats can be used, and an additional component for predictive behavior is needed. To model the predictive behavior of rats, a mathematical model of postural control requires prediction control. One such control system is the model predictive control (MPC). MPC predicts the future state using an internal model of the control target and determines the control inputs so that the predicted state becomes optimal. MPC has been used for the gait and postural control of humanoid robots (Alcaraz-Jiménez et al., 2013; Scianca et al., 2020) and has been used as a model for human quiet standing (Yao and Levine, 2009), walking (Sun et al., 2018), and arm movement during standing (Shen et al., 2021). Prediction time, which is the extent to which future behavior is predicted for control, is a major parameter for determining the behavior by MPC. By comparing the behavior of the mathematical model with the simulation and the behavior of rats in the experiment, we can evaluate the prediction time of rats in the experiment. A comparison of the estimated prediction time of the rats and the experimental conditions will show the control characteristics of the prediction behavior in rats.

In this study, we numerically evaluated the neural mechanism of predictive postural controls against external disturbances through a combination of experiments in rats and simulation with MPC.

MATERIALS AND METHODS

Experimental Animals

Six Wistar rats (male, 19 $\pm$ 2 weeks old, 404 $\pm$ 28 g body weight) supplied by CLEA (Tokyo, Japan) were used for this experiment. They were kept in a room with a constant temperature and a light and dark cycle of 12 h, with access to food and water *ad libitum*. The experiment was approved by the Ethical Committee for Animal Experiments at the University of Tokyo and was conducted in accordance with the Guidelines for Research with Experimental Animals of the University of Tokyo.

Experimental Protocols

Postural tasks were performed on a custom-made rotating floor in a dark room (**Figure 1A**). The rats were habituated to the experimental environment and learned to stand upright using hindlimbs. This was followed by 70 sequential tilting trials performed during 1 day. The paradigm of one trial was as follows (**Figure 1B**). First, the lights installed in front of the rat were turned on, simultaneously, 4% sucrose water was supplied as a reward through a flexible tube suspended above the center of the floor and accumulated at the tip. The rat stood upright on the hindlimbs in the direction of light to drink the water. The measurer entered an electrical trigger into the experimental system after confirming that the rat was in the proper posture (the body was stationary and the stomach was facing the light). This

trigger turned the light off, and the floor began to rotate backward (toes-up, **Figure 1C**) about 0.9 (0.91 ± 0.04) s later. This interval time was within the range in which classical conditioning can be established (Kolb et al., 2002). The floor rotated by 8.8 degrees over 0.25 s, with a constant angular velocity.

The height of the water supply port was determined during the habituation period for each rat, to ensure that the heel did not float and the hip did not touch the floor in the upright position (24.0 ± 0.3 cm).

Measurement of Kinematics

Prior to the measurements, the right-sided body surface of the rats was shaved, and markers using black ink were applied to eight body landmarks [4th metatarsophalangeal (MTP) joint, lateral malleolus, knee joint, greater trochanter, iliac crest, scapula, the midpoint between the iliac crest and scapula, and the temporomandibular joint] under anesthesia with 2.5% isoflurane gas. Six high-speed cameras (Prime 13 and 13 W, NaturalPoint Inc., United States) recorded the movements of the right side of their body, at 200 Hz in infrared mode, after the trigger.

Motion Analysis

The two-dimensional coordinates of nine markers (the above eight markers and nose, black points in **Figure 1D**) on the image were calculated using DeepLabCut, an image analysis software based on deep learning (Mathis et al., 2018), for the video of each camera in the trials. The three-dimensional coordinates of each marker were calculated using the direct linear transformation method (Abdel-Aziz and Karara, 2015). The coordinates were then smoothed with a 15 Hz 4th-order Butterworth low-pass filter. Sagittal plane motion analyses were performed using a 5-segment rigid link model consisting of the foot, leg, lower trunk, upper trunk, and head segments (**Figure 1D**). The inertial parameters of the segments were determined using the following procedure. First, a rat was frozen in the upright position with the markers applied as in the experiment and dismantled into the segments. Then, for each segment, the mass was measured, and the center of mass (CoM) was determined as a fulcrum, balancing the segment when it was hung with a string. These procedures were performed on three individuals, including those used for the experiment (440 ± 28 g body weight), and an average of the parameters was used for the analysis (**Table 1**).

For each trial, the CoM angle (the angle of the vector from the MTP joint to the whole-body CoM) and the angles and angular velocities of the segments were calculated. These parameters are shown as the angles with the perpendicular line and backward rotation (**Figure 1E**).

In addition, the effects of segment rotations on the CoM angle (E_i) were estimated using the following formula:

$$E_i = \int_0^{0.3} dt \frac{m_i}{M} \cdot \frac{\boldsymbol{r}(t) \cdot \boldsymbol{r_i}(t)}{|\boldsymbol{r}(t)|\,|\boldsymbol{r_i}(t)|} \omega_i(t) \quad (1)$$

where i is the segment of interest, m_i is the mass of the body part above the segment i (e.g., collection of the leg, lower trunk, upper trunk, and head segments when i is the leg segment), M is the mass of the whole body,$\mathbf{r}(\mathbf{t})$ is the vector from the MTP joint to the whole body CoM, $\mathbf{r_i}(\mathbf{t})$ is the vector from the lower end marker of the segment i (e.g., lateral malleolus when i is the leg segment) to the CoM of the body part above segment i, and $\omega_i(t)$ is the angular velocity of segment i. The integrand of this equation was calculated for each frame based on the experimental data, and a discrete-time integration was performed for the interval from the start of floor tilt to 0.3 s later. It was assumed that the body part above the segment of interest was a rigid body and rotated around the lower end of the segment.

Model Predictive Control Model and Simulation

We used a mathematical model to reproduce the behavior of the rats to control with the prediction of future disturbances after a light stimulus. A block diagram of the mathematical model is presented in **Figure 2**.

The body of the rat was modeled as an inverted pendulum with one link from the MTP joint to the CoM.

$$J\ddot{\theta} = mgh\sin\theta + \tau + \tau_{Floor} + \sigma\xi \quad (2)$$

where θ is the angle of the body from the vertical (elevation angle), J is the moment of inertia, and m, h, and g are the mass of the rat, the length from the MTP joint to the CoM, and the acceleration of gravity, respectively. The control torque is τ, the torque due to biological noise is σξ, where time-variant function ξ(t) is a Gaussian white noise and time-invariant coefficient σ is the intensity (Asai et al., 2009). τ_{Floor} is the torque input to the body according to the floor inclination and is explained below.

The stability of the rat's body is partially supported by the physical stiffness of the muscles around the MTP joint during standing (Winter et al., 1998). The torque generated at this time is modeled by the elasticity k_P and viscosity k_D of the muscles around the MTP joint.

$$\tau_{Floor} = -k_P(\theta - \phi) - k_D\left(\dot{\theta} - \dot{\phi}\right) \quad (3)$$

where ϕ is the angle of the floor from the horizontal line. In the stationary standing position, it is zero and acts to stabilize, whereas when the floor is inclined, τ_{Floor} acts as a disturbance torque according to the inclination.

TABLE 1 | Inertial parameters of the segments.

Segments	Mass (%)	Ls (%)	Lv (%)
Foot	1	32	–
Leg	9	68	–
Lower trunk	53	18	33
Upper trunk	29	40	10
Head	8	33	−7

*The masses are shown as percentages of the whole body, and those of the foot and leg segments are the sum of both hindlimbs. As shown in **Figure 1D**, the center of mass of each segment is shown as coordinates in the coordinate systems formed by the direction of the segment line and the direction orthogonal to it and as the percentages of the line lengths (Ls and Lv, respectively). Because the foot and leg segments were linear in shape and too small to hang with a string, the Lv was assumed to be 0.*

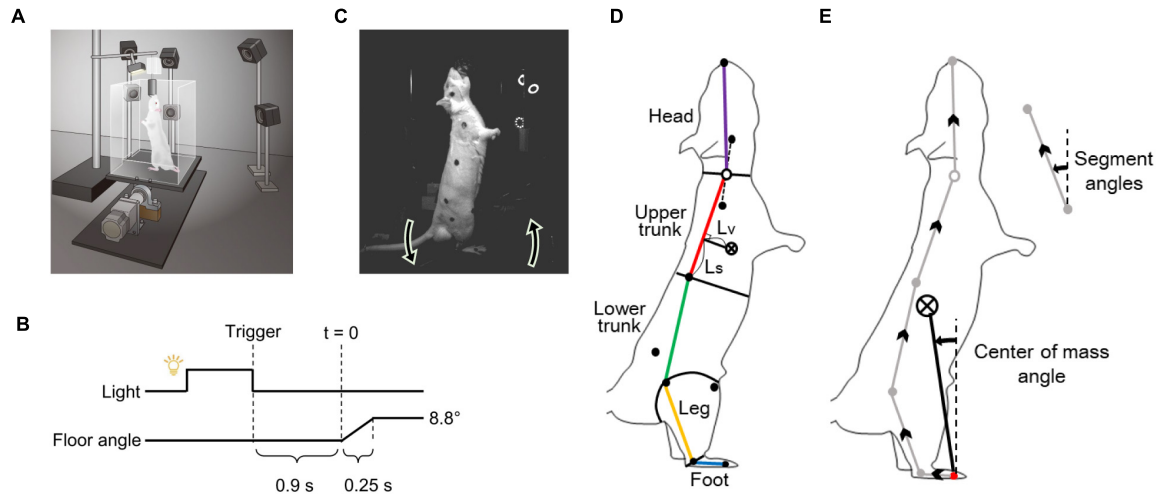

FIGURE 1 | Experimental methods. **(A)** Experimental apparatus. **(B)** Paradigm of the floor tilting trial. **(C)** A rat maintaining upright posture and rotation direction of the floor. **(D)** Definition of body segments. **(E)** Definitions of center-of-mass angle and segment angles.

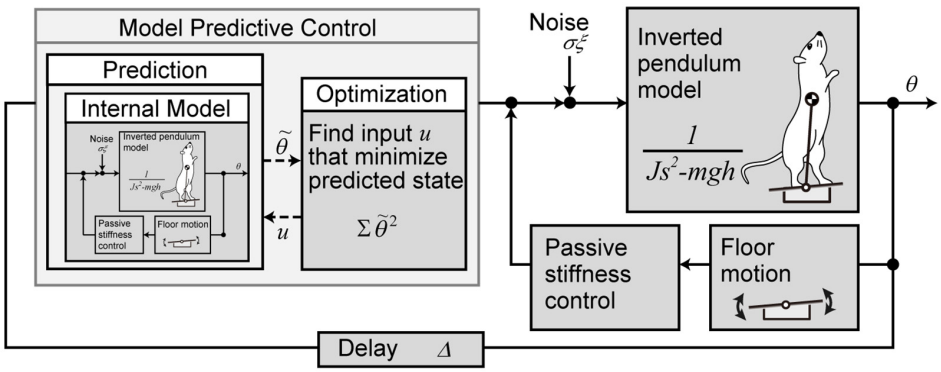

FIGURE 2 | Mathematical model of the postural motion of a rat with the prediction for tilting disturbance. The body is modeled with a single link inverted pendulum, and the control system is modeled with model predictive control.

The control system with prediction was modeled with MPC. MPC predicts the state from the current time to H_p steps later, based on the internal model. It also derives the control inputs that optimize the predicted states by providing control inputs with different values for H_u steps. MPC performs this prediction and optimization in each time step and uses the input of only the first step as the actual control input. Here, H_p is called prediction horizon, and H_u is called control horizon. In our model, the inverted pendulum model (Eq. 2) and the floor model (Eq. 3) are used as the internal model for prediction, assuming that the internal model has been created accurately by sufficient learning. The target value of the predicted state $\tilde{\theta}$ for the state θ, is always set to zero. For optimization, an evaluation function is set to minimize the sum of the squares of $\tilde{\theta}$ for the H_p step interval.

The proposed model has five unknown parameters other than the parameters determined by the physical properties of the rat's body: the prediction horizon H_p, the control horizon H_u, the elastic and viscous coefficients k_P and k_D around the MTP joint, and the noise magnitude σ. By simulating the mathematical model, we investigated the effects of these parameters on the behavior of the model. In the simulation, we used the average values of the body parameters of the rats (n = 6) used in the experiment (m = 0.404 kg, h = 0.107 m). The sensory delay was set to 40 ms based on a previous study on rats (Muramatsu et al., 2009). The sampling time of the simulation and MPC is set to 0.001 s. Model Predictive Control Toolbox of Matlab/Simulnk is used to implement the MPC.

To compare the behavior of proposed model with conventional feedback control models, we further simulated the conventional model with floor disturbance using Eq. (3). The control models included the PD controller based on the Peterka's gains [$\tau = -k_P\theta - k_D\dot{\theta}$, $k_P = 1.46mgh$, $k_D = 0.3mgh$; (Peterka, 2002)], and the non-linear PD controller for standing rats [$\tau = -k_{P2}\theta^2 - k_{P0}\theta - k_D\dot{\theta}$, $k_{P2} = 196mgh$, $k_{P0} = 0.88mgh$, $k_D = 0.11mgh$; (Funato et al., 2021)]. Here, the control gains were normalized with mgh to eliminate differences in the body.

Quantitative Evaluation of the Rats' Behavior From the Mathematical Model

We compared the behavior of the constructed mathematical model with that of the rat and examined the characteristics of the controller that reproduces the behavior of the rat. For this purpose, we identified the unknown parameters (prediction horizon H_p, control horizon H_u, elastic coefficient around the MTP joint k_P, viscous coefficient k_D, and noise magnitude σ) of the mathematical model that best reproduced the behavior of the rat.

To identify the parameters, we compared the time series of the CoM angle from the experiment with that of the body angle θ from the simulation, and searched for the parameters that minimize the squared error. Specifically, the time sequences of CoM angle from −0.35 s to 0.45 s (here, 0 s is the start of floor tilt) of the terminal 3 trials in each rat are extracted (18 in total), and are compared with the simulation for identification. To reduce the effect of noise variation in the parameter search, the simulation was repeated for five trials and averaged for each evaluation. We used a genetic algorithm (GA) for parameter searching. The "ga" function of Matlab Global Optimization Toolbox was used for GA. In summary, MPC searches were conducted to identify the optimal control input in each simulation step (every 0.001 ms), and simulation with real-time optimal input was repeated five times with same parameters. Then, the average of the simulation result was compared with the experiment for updating the parameter values once. Subsequently, the next simulation with real-time optimization was started for the next update of parameters. The parameters were identified by repeating these sequences using the GA.

Statistical Analysis

Trials in which the rats lifted their feet off the floor during the tilt were excluded from the analyses. Parameters calculated based on marker coordinates that may not have been calculated accurately by DeepLabCut ("likelihood" <0.9) were also excluded. The results of the analysis are shown as the mean ± standard deviation of the six rats. For the displacements of CoM and segment angles from the start of the tilt to 0.3 s later, the differences in the average of the initial and terminal eight trials were tested with the paired *t*-test using SPSS (IBM, United States), in which $p < 0.05$ was considered as significant.

By comparing the experimental results and the simulation results of the proposed model, the values for five unknown parameters were identified. To validate the significance of the identification results, we used a two-way ANOVA with experimental sequences and parameters.

RESULTS

Experimental Results

In the initial trials, the rats experienced a significant response of the whole body due to the floor tilt, but the amplitude of this response was reduced in the later trials (**Figure 3A**). **Figure 3B** shows the time series of the CoM angles of all trials in a representative individual. The CoM angle monotonically increased after the start of the tilt, but this fluctuation gradually decreased with repeated trials. We quantified the increase in the CoM angle from the start of the tilt to 0.3 s (**Figures 3C,D**). The increase was significantly smaller in the terminal eight trials than in the initial eight trials. The difference in the increase between the first and 11th trial (9.9 deg in average) was larger than the difference between the 11th and final trial (3.6 deg in average), suggesting that the rats primarily learned to compensate for the floor tilt in the initial 10 trials.

In the initial trials, the foot and leg segments rotated backward along with the backward tilt of the floor, whereas the upper trunk and head segments rotated forward (**Figures 4A,B**). These rotations decreased significantly during the trials. We estimated the effects of segment rotation on the CoM angle using Eq. (1). It was found that, in the initial trials, the backward rotations of the foot and leg segments largely affected the increase in the CoM angle after the start of floor tilts (**Figure 4C**).

Simulation of the Proposed Model

To approach the mechanism of the rats' predictive control for tilt disturbance, we constructed a mathematical model using MPC and investigated the behavior of the model by simulation. **Figure 5A** shows the results of the CoM angle and torque in the simulation. The blue line in the CoM angle of **Figure 5A** is the result of the simulation, and the red line shows the rats' CoM angle from the experiment (the average of 17 sequences out of the measured 18 sequences, excluding one sequence in which the rat's behavior was different from the other sequences [Rat 5 Sequence 1]; a comparison of the results for each sequence is shown in **Supplementary Figure 1**). The unknown parameters of the mathematical model used in the simulation were set to the optimal values (**Figure 6**), which will be described later in detail. The mean (SD) of the correlation coefficient (cosine correlation) between the CoM angle from the simulation and from the experiment for all the 18 sequences were 0.99 (± 0.01, **Supplementary Figure 1** shows the correlation coefficient for each sequence). These results show that the proposed system using MPC successfully reproduced the behavior of the rat.

Figure 5B shows the reaction of the conventional controller, PD controller with Peterka's gain parameters (Peterka, 2002) and a non-linear PD controller for standing rats (Funato et al., 2021). Both models could stabilize the body after floor disturbances, but the behaviors were slightly different from the experiment. When we focus on the control torque τ, the control torque of every controller gradually increases after the floor torque τ_{Floor} increased, and the control torque τ becomes larger than the floor torque τ_{Floor}. The disturbance *via* floor torque τ_{Floor} terminates when time = 0.2 s and the CoM angle gradually returns to the vertical position. Here, the controllers react differently to the termination of the disturbance. The MPC controller smoothly reacted to the change in the floor torque τ_{Floor}, while conventional controllers drastically changed the control torque.

Next, we investigated the features of the proposed model to reproduce the behavior of the rats. The proposed model has two MPC parameters, that is, the prediction horizon H_p and control horizon H_u, and three parameters related to the body system, the

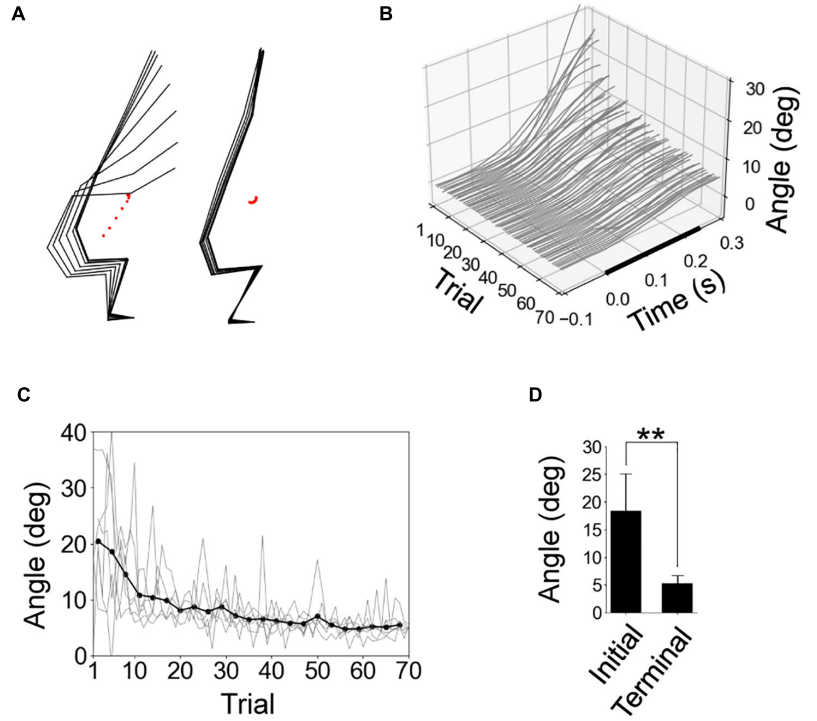

FIGURE 3 | Reduction of postural response due to experience of tilting trials. **(A)** Stick pictures of first and last trials in a representative rat. The period from the start of floor tilt to 0.28 s later was shown using black-point markers in **Figure 1C**. **(B)**. Time series of center-of-mass (CoM) angles of all 70 trials in a representative individual, with the start time of the tilting at time 0. **(C)** Fluctuation in CoM angle from the start of tilt to 0.3 s later for all individuals (gray line; $n = 6$) and the average (black line, the averages of 3 peripheral trials). **(D)** Statistical comparison of fluctuation in CoM angle from the start of tilt to 0.3 s between the average of initial and terminal eight trials by paired t-test ($n = 6$). $^{**}P < 0.01$.

MTP stiffness k_P, the MTP viscosity k_D, and the magnitude of the noise σ. The effect of the two MPC parameters on the behavior is shown in **Figures 5C–G**.

Figure 5C shows the CoM angle and control torque τ of the simulation with the prediction horizon H_p from 30 ms to 1,300 ms. Here, the system became unstable when the prediction horizon was lower than 30 ms and higher than 1,300 ms. Each line in **Figure 5C** is the result of the simulation at each prediction horizon (the average of ten simulations to reduce the CoM variation due to noise). The CoM and torque patterns with a different prediction horizon H_p were similar to each other, but there were differences in the peak values. **Figure 5D** shows the maximum CoM angle, and **Figure 5E** shows the maximum torque (**Figures 5D,E** show the result of one sequence (Rat 1 Sequence 1), and **Supplementary Figure 2** shows the result of whole sequences). These figures indicate that the maximum CoM decreases while the maximum torque decreases as the prediction horizon H_p increases. In other words, as the prediction horizon increases, the motion is designed to suppress the fluctuation in the CoM with less torque. This characteristic of prediction horizon H_p was consistent for 16 of 18 sequences (see also **Supplementary Figure 2**).

Following this, the control horizon H_u was varied from 2 ms to 50 ms, as shown in **Figure 5F**. Each line in the figure represents the simulation result according to each control horizon H_u (the average of ten simulations to reduce the CoM variation due to noise). Subsequently, the pattern changes gradually with increasing H_u values, and the fluctuation in the CoM and maximum torque become smaller with higher control horizon H_u. **Figure 5G** shows the correlation coefficient (cosine correlation) between the time series of the CoM angle with a control horizon of 50 ms and the time series of the CoM angle with each control horizon H_u (**Figure 5G** shows the result of one sequence (Rat 1 Sequence 1), and **Supplementary Figure 3** shows the result of whole sequences). **Figure 5G** shows that the change in the time series of the CoM angle is obvious up to 20 ms, and becomes less obvious after 30 ms. This characteristic of control horizon H_u was consistent for all sequences (see also **Supplementary Figure 3**).

In summary, the longer control and prediction horizons suppressed the variation in the CoM angle with a smaller torque. Furthermore, the prediction horizon H_p affected the peak value, whereas the control horizon H_u affected the pattern. Based on the characteristics of these control parameters, we identified five unknown parameters.

Identification Results of the Prediction Behavior

We searched for model parameters (prediction horizon H_p, control horizon H_u, MTP stiffness k_P, MTP viscosity k_D, and noise magnitude σ) whose simulation reproduces the

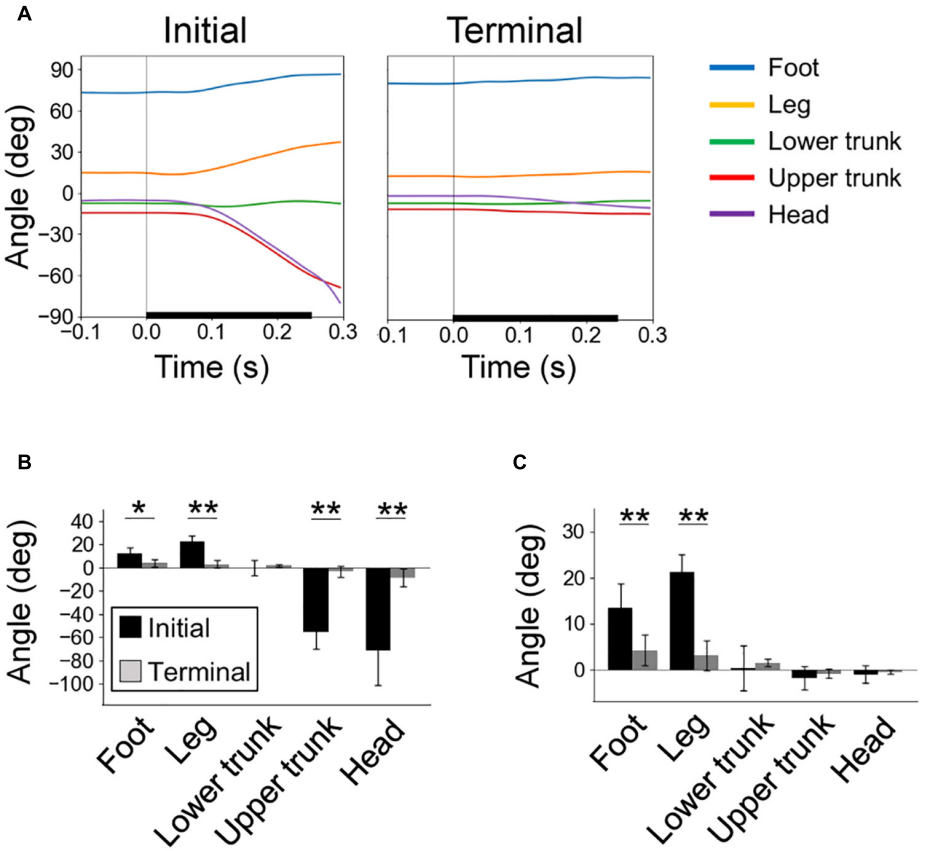

FIGURE 4 | Rotation of body segments due to perturbation. **(A)** Time series of segment angles in the initial (left) and terminal (right) trials, with the start time of floor tilting at time 0. Definitions of segment angles are in **Figure 1E**. **(B)** Rotation angles of segments from the start of floor tilt to 0.3 s later. **(C)** Effects of segment rotations on the CoM angle calculated by Eq. (1). In **(A–C)**, individual averages (n = 6) of trial averages (initial and terminal eight) are shown. *P < 0.05; **P < 0.01.

measured time series of the rat's CoM angle. **Figure 6** shows the results, and the time series of the simulation with these parameters is shown in **Figure 5A**. The significance of the identified parameters was tested using a two-way ANOVA with the parameters and experimental sequences. The results did not show significant differences among experimental sequences (P = 0.47, f = 1.00, df = 17), but showed significant differences with the parameters (P < 0.001, f = 474.0, df = 4), implying the robustness of the identification results to different experimental sequences.

The top row of **Figure 6** shows the MPC parameters. The mean (SD) of the result of the prediction horizon was 0.96 (± 0.19) s. This result indicates that the postural control can be predicted up to 0.96 s prior to the state. In the experiment, the rats received a light stimulus 0.9 s before the tilt disturbance of 0.25 s. The interval time between the sensory input and the disturbance was 0.9–1.15 s, which is close to the identified length of the prediction horizon. The mean (SD) of the result of the control horizon was 24.4 (± 8.6) ms. This result indicates that the prediction of the control input could change for 24.4 ms. Simulations with different control horizons (**Figures 5F,G**) showed that the CoM angle hardly changed when the control horizon was greater than 20 ms. This indicates that the identified control horizon is long enough to produce sufficiently complex inputs.

The lower portion of **Figure 6** shows the parameters related to the body model. The mean (SD) value of the MTP stiffness k_P was 0.34 (± 0.13) *mgh*. This value is normalized with body mass (*m*), acceleration of gravity (*g*), and the length from the MTP joint to the CoM (*h*). Previous studies showed that ankle stiffnesses in humans to be approximately 0.3 *mgh* (Hof, 1998) to approximately 0.7 *mgh* (Morasso and Sanguineti, 2002). The identified value was almost comparable, which supports the validity of the identification results. The mean (SD) value of the MTP viscosity k_D was 0.03 (± 0.02) *mgh*. Previous studies (Asai et al., 2009; Suzuki et al., 2012) have assumed that the ankle viscosity is less than a tenth of the stiffness. The mean (SD) value of the noise magnitude σ was 0.50 (± 0.23) mNm. This value was in close agreement with the previously identified noise magnitude in the quiet standing rats (Funato et al., 2021).

DISCUSSION

In this study, we constructed a floor-tilting task for upright standing rats and compared these behaviors with a simulation

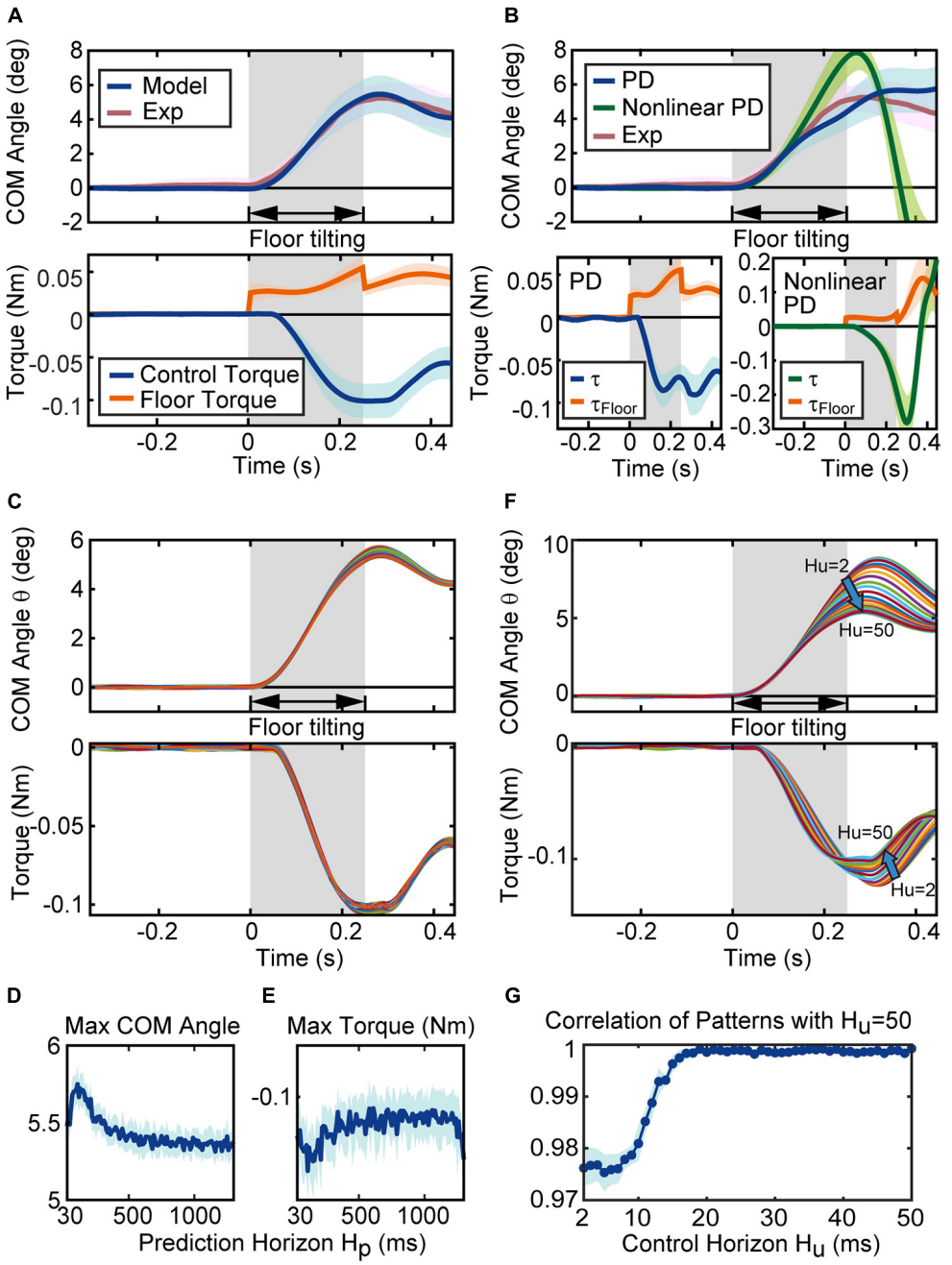

FIGURE 5 | Behavior of the proposed mathematical model. **(A)** Simulation results of the model. The blue and red lines in the figure of CoM angle are the average of the CoM angles for the 17 simulated (Model) and experimental (Exp) sequences. The blue and red regions represent their standard deviation (SD). The blue and orange line in the torque figure represent the average of the control torque τ and the floor torque τ_{Floor}, respectively. The surrounding blue and orange regions represent the associated SD. **(B)** Simulation results of the conventional models. Blue lines, green lines and red lines in the figure of CoM angle are the average results of the PD controller with Peterka's gain parameters, the average results of the non-linear PD controller for standing rats, and the average of the experimental sequences, respectively. Blue, green, red regions represent their SD. The blue, green, and orange line in the figure of torque represent the average of the control torque τ and the floor torque τ_{Floor}, respectively. The blue, green and orange regions represent their SD. **(C)** Time series of the CoM angle and torque with different prediction horizons. Each line in the figure is the simulation result of the model with a prediction horizon from 30 ms to 1,300 ms (average of ten simulation results with same parameters). The maximum CoM angle and the maximum torque for each parameter are shown in **(D,E)**, respectively. **(D,E)** Are the results for one sequence, and **Supplementary Figure 2** shows the results for complete sequences. **(F)** Time series of the CoM angle and torque with the control horizon from 2 ms to 50 ms. Each line is the average of ten simulations with the same prediction horizon. **(G)** The correlation coefficient (cosine correlation) between the time series of the CoM angle (average of ten trials) with control horizon 50 ms and the time series of the CoM angle with each control horizon. The line is the average of ten correlation coefficients for each control horizon, and the area represents SD. **(G)** Is the results for one sequence, and **Supplementary Figure 2** shows the results for complete sequences.

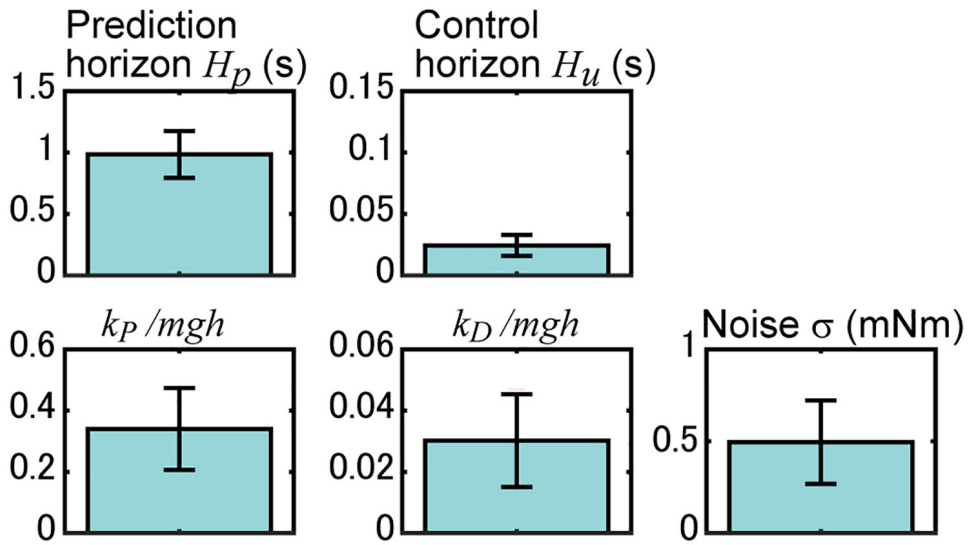

FIGURE 6 | Identified parameters of the proposed model. Results for the prediction horizon H_p, control horizon H_u, MTP stiffness k_P, MTP viscosity k_D, and noise magnitude σ are shown. Here, the results of MTP stiffness and viscosity are normalized with m body mass, g acceleration of gravity, and h length from MTP joint to CoM. Blue bars and their error bars represent the average and standard deviation of the identified results for 18 experimental sequences of rats.

that was based on MPC. In the experiment, the postural response of the rats due to disturbance dramatically reduced after experiencing 70 sequential trials, indicating that they acquired predictive control against the disturbance. The simulation showed that prolonging the predictive and control horizons allowed a reduction in the fluctuation of the CoM and peak control torque. The predictive horizon identified to match the simulation with the measured CoM data was close to the interval time, from the light turning off to the disturbance, suggesting that the rats predicted posture dynamics under the disturbance based on the timing of the sensory input.

During the initial trials in the experiment, the foot and leg segments rotated backward, contributing to increase in the CoM angle (**Figures 3**, **4**). Similarly, in the bipedal standing of humans, the backward tilt of the floor displaces the CoP backward and rotates the shank backward (Diener et al., 1992; Carpenter et al., 1999; Kolb et al., 2002; Campbell et al., 2009). Regarding the movement of the segments above the trunk, the lower trunk did not significantly rotate on average, but the upper trunk and head rotated forward (**Figure 4B**). In human studies, the trunk is simplified into one segment. However, as it has been reported to rotate forward with the backward tilt of floors (Carpenter et al., 1999), the overall direction of rotation is consistent with this study. In rodents, the mass and length of the trunk account for greater proportions of the whole body than in humans (**Table 1**; Winter, 2009), and the trunk is not adapted to maintain upright positions as in humans. These characteristics seem to have led to the bending of the trunk as a result of the disturbance (**Figure 3A**). In any case, the overall mechanics by which a floor rotation evokes postural response is by the transmission of the rotation to the legs, giving backward momentum to the pelvis and lower trunk. This is common between bipedal humans and rodents.

The experience of 70 sequential disturbance trials dramatically reduced postural response, including backward rotation of the foot and the leg segments (**Figures 3**, **4**). These results indicate that flexing of the ankle and the MTP joints at proper timing and amplitudes according to the floor tilt contributed to a reduction in the response. During the tilting tasks for humans, the entire sole was in contact with the floor, and the joints above the ankle determined the postural movement. On the other hand, it seems relatively easy for rodents to tiptoe on the hindlimbs (Funato et al., 2017), indicating that movements of the MTP joints can be significantly involved in postural control. Therefore, we used an inverted pendulum model around the MTP joint in this simulation. In humans, under the association of tilting disturbance and preceding sensory input, fluctuation of activities immediately before the tilting, suppression of stretch reflexes, and automatic postural response with a latency of approximately 100 ms are evoked at muscles around the ankle, knee, and hip joints (Kolb et al., 2002; Campbell et al., 2009). Although the present study is limited to measuring kinematics, similar adjustments are likely to be evoked in the muscles around the MTP joints.

We modeled the behavior of predictive postural control of rats using MPC. The postural control system of quiet standing has been modeled using feedback control such as proportional-integral-derivative (PID) control (Peterka, 2000, 2002) or intermittent control considering the dead zone of the sensory system (Asai et al., 2009; Gawthrop et al., 2014). The bipedal standing of the rats was also modeled using PID-based feedback control. To model the prediction of disturbances, the control needs to include a prediction mechanism. However, the postural control model with prediction has hardly been discussed. One study adopted MPC to model human postural control from the viewpoint of optimal control (Yao and Levine, 2009) and

showed the time correlation of the body sway (estimated by Stabilogram-Diffusion Function) and the amplitude of the body sway were reproduced by the model with MPC. More recent research used MPC to model arm movement during a standing position and showed the contribution of the arm to achieve stabilization (Shen et al., 2021). MPC consists of the prediction of future states based on internal models and the optimization of the predicted states. Researches have demonstrated that the internal forward model (Miall and Wolpert, 1996) can be produced as the activity of Purkinje cells (Laurens et al., 2013; Herzfeld and Shadmehr, 2014), thus proving that prediction of the state could be possible. It is also possible to control optimization in the nervous system (Scott, 2004; Todorov, 2004). Therefore, the nervous system is equipped with a mechanism that enables MPC, and it is reasonable to model postural control with prediction using MPC. Our simulation results successfully reproduced the predictive behavior of rats, and the identification results for the MPC parameters were consistent with the experimental conditions and past identification results for postural control.

One of the advantages of our MPC model over the conventional PID-based feedback control models is that our model explicitly considers the internal model for prediction. This enables us to discuss the effect of learning the internal model on posture control. However, at the same time, flexibility in the internal model causes uncertainty. The internal model is composed of learning; thus, it could cause a large uncertainty, particularly during the learning process. Only one point that can determine the property of the internal model is after learning. After complete learning, the internal model is assumed to be a good copy of the actual body and environment. Therefore, in this study, we used them as an internal model. As a limitation, this system model can simulate only the behavior of rats after learning, and thus, we compared simulation results with the experimental results after learning. This model minimizes the uncertainty in the internal model and succeeds in the discussion of prediction control. However, the learning process in rats could not be discussed using the current model. To overcome this limitation, the internal model should include learning. The internal model used in our model is based on the equation of motion of the body and environment, and these equations can be learned by machine learning. Therefore, by including machine learning in our model, approaching the learning mechanism of rats using the model will become possible.

The interval time between the sensory input of light and the floor tilting was set within the range, allowing classical conditioning (Kolb et al., 2002) and our simulation results support the establishment of these associations. However, non-associative processes, such as habituation or adaptation, may also have contributed to the reduction in the amplitude of postural response due to disturbance (Nashner, 1976; Kolb et al., 2002, 2004). It will be important to experimentally distinguish between associative and non-associative learning in the future. The first strategy is to focus on preparatory activities before the disturbance (Kolb et al., 2002). In the experiment, a rat trembled in the interval time of several trials in the middle of learning (data not shown), suggesting that an association was about to be established. As a previous study pointed out that movement before floor tilt can be disadvantageous to postural stabilization (Kolb et al., 2002), it may be difficult to detect preparatory movements before disturbance at a kinematic level. However, examining muscle activities in antagonist muscles may capture these activities. The second strategy was to conduct control experiments. Experimental conditions without sensory input would quantify the rate of learning that is based on only non-associative learning, and conversely, giving sensory input alone under association would induce canceling movements at the time of the disturbance, which is based on association (Clark et al., 2002; Campbell et al., 2009). These refinements in experiments will play an important role in neuroscientific research on predictive postural control in the future. That is, the inactivation of specific areas in the nervous system clarifies the responsibilities for associative and non-associative learning, and identifying neural activities synchronizing with sensory input, disturbance, and muscle activities will help understand the coding and processing mechanisms of predictive postural controls in the nervous system.

DATA AVAILABILITY STATEMENT

The raw data supporting the conclusions of this article will be made available by the authors, without undue reservation.

ETHICS STATEMENT

The animal study was reviewed and approved by the Ethical Committee for Animal Experiments at the University of Tokyo.

AUTHOR CONTRIBUTIONS

AK, DY, YM, and AF designed and conducted the experiment. TF, YM, and AF designed and executed the simulation. RS contributed to programming for the simulation. DY and TF conceptualized and supervised the whole study. AK, TF, and DY wrote the manuscript. All authors reviewed the manuscript.

FUNDING

This study was partially supported by Grants-in-Aid for Scientific Research on Innovative Areas (No. 19H05728), for Scientific Research (C) (Nos. 18K10955 and 21K03932), for Young Scientists (No. 20K19592), and for the Promotion of Joint International Research [Fostering Joint International Research (B)] (No. 20KK0226) funded by the Ministry of Education, Culture, Sports, Science, and Technology of Japan.

SUPPLEMENTARY MATERIAL

The Supplementary Material for this article can be found online at: https://www.frontiersin.org/articles/10.3389/fnsys.2021.785366/full#supplementary-material

REFERENCES

Abdel-Aziz, Y. I., and Karara, H. M. (2015). Direct linear transformation from comparator coordinates into object space coordinates in close-range photogrammetry. *Photogramm. Eng. Remote Sensing* 81, 103–107. doi: 10.14358/pers.81.2.103

Alcaraz-Jiménez, J. J., Herrero-Pérez, D., and Martínez-Barberá, H. (2013). Robust feedback control of ZMP-based gait for the humanoid robot Nao. *Int. J. Robot. Res.* 32, 1074–1088. doi: 10.1177/0278364913487566

Asai, Y., Tasaka, Y., Nomura, K., Nomura, T., Casadio, M., and Morasso, P. (2009). A model of postural control in quiet standing: robust compensation of delay-induced instability using intermittent activation of feedback control. *PLoS One* 4:e6169. doi: 10.1371/journal.pone.0006169

Bolzoni, F., Bruttini, C., Esposti, R., Castellani, C., and Cavallari, P. (2015). Transcranial direct current stimulation of SMA modulates anticipatory postural adjustments without affecting the primary movement. *Behav. Brain Res.* 291, 407–413. doi: 10.1016/j.bbr.2015.05.044

Campbell, A. D., Dakin, C. J., and Carpenter, M. G. (2009). Postural responses explored through classical conditioning. *Neuroscience* 164, 986–997. doi: 10.1016/j.neuroscience.2009.07.042

Carpenter, M. G., Allum, J. H., and Honegger, F. (1999). Directional sensitivity of stretch reflexes and balance corrections for normal subjects in the roll and pitch planes. *Exp. Brain Res.* 129, 93–113. doi: 10.1007/s002210050940

Clark, R. E., Manns, J. R., and Squire, L. R. (2002). Classical conditioning, awareness, and brain systems. *Trends Cogn. Sci.* 6, 524–531. doi: 10.1016/s1364-6613(02)02041-7

Diener, H. C., Dichgans, J., Guschlbauer, B., Bacher, M., Rapp, H., and Klockgether, T. (1992). The coordination of posture and voluntary movement in patients with cerebellar dysfunction. *Mov. Disord.* 7, 14–22. doi: 10.1002/mds.870070104

Funato, T., Sato, Y., Fujiki, S., Sato, Y., Aoi, S., Tsuchiya, K., et al. (2017). Postural control during quiet bipedal standing in rats. *PLoS One* 12:e0189248. doi: 10.1371/journal.pone.0189248

Funato, T., Sato, Y., Sato, Y., Fujiki, S., Aoi, S., Tsuchiya, K., et al. (2021). Quantitative evaluation of posture control in rats with inferior olive lesions. *Sci. Rep.* 11:20362. doi: 10.1038/s41598-021-99785-w

Gawthrop, P., Loram, I., Gollee, H., and Lakie, M. (2014). Intermittent control models of human standing: similarities and differences. *Biol. Cybern.* 108, 159–168. doi: 10.1007/s00422-014-0587-5

Herzfeld, D. J., and Shadmehr, R. (2014). Cerebellum estimates the sensory state of the body. *Trends Cogn. Sci.* 18, 66–67. doi: 10.1016/j.tics.2013.10.015

Hof, A. L. (1998). *In vivo* measurement of the series elasticity release curve of human triceps surae muscle. *J. Biomech.* 31, 793–800. doi: 10.1016/s0021-9290(98)00062-1

Kolb, F. P., Lachauer, S., Maschke, M., and Timmann, D. (2002). Classical conditioning of postural reflexes. *Pflugers Arch.* 445, 224–237. doi: 10.1007/s00424-002-0892-z

Kolb, F. P., Lachauer, S., Maschke, M., and Timmann, D. (2004). Classically conditioned postural reflex in cerebellar patients. *Exp. Brain Res.* 158, 163–179. doi: 10.1007/s00221-004-1889-y

Laurens, J., Meng, H., and Angelaki, D. E. (2013). Computation of linear acceleration through an internal model in the macaque cerebellum. *Nat. Neurosci.* 16, 1701–1708. doi: 10.1038/nn.3530

Mathis, A., Mamidanna, P., Cury, K. M., Abe, T., Murthy, V. N., Mathis, M. W., et al. (2018). DeepLabCut: markerless pose estimation of user-defined body parts with deep learning. *Nat. Neurosci.* 21, 1281–1289. doi: 10.1038/s41593-018-0209-y

Miall, R. C., and Wolpert, D. M. (1996). Forward models for physiological motor control. *Neural Netw.* 9, 1265–1279. doi: 10.1016/s0893-6080(96)00035-4

Morasso, P. G., and Sanguineti, V. (2002). Ankle muscle stiffness alone cannot stabilize balance during quiet standing. *J. Neurophysiol.* 88, 2157–2162. doi: 10.1152/jn.2002.88.4.2157

Muramatsu, H., Suzuki, K., Sasaki, T., Matsumoto, M., Sakuma, J., Oinuma, M., et al. (2009). Evoked potentials elicited on the cerebellar cortex by electrical stimulation of the rat spinocerebellar tract. *Surg. Neurol.* 72, 395–400; discussion 400. doi: 10.1016/j.surneu.2009.04.015

Nashner, L. M. (1976). Adapting reflexes controlling the human posture. *Exp. Brain Res.* 26, 59–72. doi: 10.1007/BF00235249

Ng, T. H., Sowman, P. F., Brock, J., and Johnson, B. W. (2013). Neuromagnetic brain activity associated with anticipatory postural adjustments for bimanual load lifting. *Neuroimage* 66, 343–352. doi: 10.1016/j.neuroimage.2012.10.042

Peterka, R. J. (2000). Postural control model interpretation of stabilogram diffusion analysis. *Biol. Cybern.* 82, 335–343. doi: 10.1007/s004220050587

Peterka, R. J. (2002). Sensorimotor integration in human postural control. *J. Neurophysiol.* 88, 1097–1118. doi: 10.1152/jn.2002.88.3.1097

Scianca, N., De Simone, D., Lanari, L., and Oriolo, G. (2020). MPC for humanoid gait generation: stability and feasibility. *IEEE Trans. Robot.* 36, 1171–1188. doi: 10.1109/tro.2019.2958483

Scott, S. H. (2004). Optimal feedback control and the neural basis of volitional motor control. *Nat. Rev. Neurosci.* 5, 532–546. doi: 10.1038/nrn1427

Shen, K., Chemori, A., and Hayashibe, M. (2021). Reproducing human arm strategy and its contribution to balance recovery through model predictive control. *Front. Neurorobot.* 15:679570. doi: 10.3389/fnbot.2021.679570

Sun, J., Wu, S., and Voglewede, P. A. (2018). Dynamic simulation of human gait model with predictive capability. *J. Biomech. Eng.* 140:031008. doi: 10.1115/1.4038739

Suzuki, Y., Nomura, T., Casadio, M., and Morasso, P. (2012). Intermittent control with ankle, hip, and mixed strategies during quiet standing: a theoretical proposal based on a double inverted pendulum model. *J. Theor. Biol.* 310, 55–79. doi: 10.1016/j.jtbi.2012.06.019

Todorov, E. (2004). Optimality principles in sensorimotor control. *Nat. Neurosci.* 7, 907–915. doi: 10.1038/nn1309

Winter, D. A. (2009). *Biomechanics and Motor Control of Human Movement*. New York, NY: Wiley.

Winter, D. A., Patla, A. E., Prince, F., Ishac, M., and Gielo-Perczak, K. (1998). Stiffness control of balance in quiet standing. *J. Neurophysiol.* 80, 1211–1221. doi: 10.1152/jn.1998.80.3.1211

Yakovenko, S., Krouchev, N., and Drew, T. (2011). Sequential activation of motor cortical neurons contributes to intralimb coordination during reaching in the cat by modulating muscle synergies. *J. Neurophysiol.* 105, 388–409. doi: 10.1152/jn.00469.2010

Yamaura, H., Hirai, H., and Yanagihara, D. (2013). Postural dysfunction in a transgenic mouse model of spinocerebellar ataxia type 3. *Neuroscience* 243, 126–135. doi: 10.1016/j.neuroscience.2013.03.044

Yanagihara, D. (2014). Role of the cerebellum in postural control. *J. Phys. Fitness Sports Med.* 3, 169–172. doi: 10.7600/jpfsm.3.169

Yao, L., and Levine, W. S. (2009). "An optimal model predictive control model for human postural regulation," in *Proceedings of the 17th Mediterranean Conference on Control and Automation*, Thessaloniki, 1143–1148. doi: 10.1109/MED.2009.5164700

Conflict of Interest: The authors declare that the research was conducted in the absence of any commercial or financial relationships that could be construed as a potential conflict of interest.

Publisher's Note: All claims expressed in this article are solely those of the authors and do not necessarily represent those of their affiliated organizations, or those of the publisher, the editors and the reviewers. Any product that may be evaluated in this article, or claim that may be made by its manufacturer, is not guaranteed or endorsed by the publisher.

Copyright © 2021 Konosu, Funato, Matsuki, Fujita, Sakai and Yanagihara. This is an open-access article distributed under the terms of the Creative Commons Attribution License (CC BY). The use, distribution or reproduction in other forums is permitted, provided the original author(s) and the copyright owner(s) are credited and that the original publication in this journal is cited, in accordance with accepted academic practice. No use, distribution or reproduction is permitted which does not comply with these terms.

frontiers in Systems Neuroscience

ORIGINAL RESEARCH
published: 29 November 2021
doi: 10.3389/fnsys.2021.767477

Brain Activity Reflects Subjective Response to Delayed Input When Using an Electromyography-Controlled Robot

*Hyeonseok Kim[1,2], Yeongdae Kim[3], Makoto Miyakoshi[2], Sorawit Stapornchaisit[4], Natsue Yoshimura[1] and Yasuharu Koike[1]**

[1]*Institute of Innovative Research, Tokyo Institute of Technology, Yokohama, Japan,* [2]*Swartz Center for Computational Neuroscience, Institute for Neural Computation, University of California, San Diego, San Diego, CA, United States,* [3]*Department of Industrial Engineering and Economics, Tokyo Institute of Technology, Tokyo, Japan,* [4]*Department of Artificial Intelligence, Application Division, EAGLYS Inc., Tokyo, Japan*

In various experimental settings, electromyography (EMG) signals have been used to control robots. EMG-based robot control requires intrinsic parameters for control, which makes it difficult for users to understand the input protocol. When a proper input is not provided, the response time of the system varies; as such, the user's subjective delay should be investigated regardless of the actual delay. In this study, we investigated the influence of the subjective perception of delay on brain activation. Brain recordings were taken while subjects used EMG signals to control a robot hand, which requires a basic processing delay. We used muscle synergy for the grip command of the robot hand. After controlling the robot by grasping their hand, one of four additional delay durations (0 ms, 50 ms, 125 ms, and 250 ms) was applied in every trial, and subjects were instructed to answer whether the delay was natural, additional, or whether they were not sure. We compared brain activity based on responses ("sure" and "not sure"). Our results revealed a significant power difference in the theta band of the parietal lobe, and this time range included the interval in which the subjects could not feel the delay. Our study provides important insights that should be considered when constructing an adaptive system and evaluating its usability.

Keywords: electromyography (EMG), electroencephalogram (EEG), delay, subjective response, parietal, robot, robot hand, independent component

OPEN ACCESS

Edited by:
Jun Izawa,
University of Tsukuba, Japan

Reviewed by:
Toshiyuki Kondo,
Tokyo University of Agriculture and Technology, Japan
Isao Nambu,
Nagaoka University of Technology, Japan

****Correspondence:***
Yasuharu Koike
koike@pi.titech.ac.jp

Received: *30 August 2021*
Accepted: *18 October 2021*
Published: *29 November 2021*

Citation:
Kim H, Kim Y, Miyakoshi M, Stapornchaisit S, Yoshimura N and Koike Y (2021) Brain Activity Reflects Subjective Response to Delayed Input When Using an Electromyography-Controlled Robot. Front. Syst. Neurosci. 15:767477. doi: 10.3389/fnsys.2021.767477

INTRODUCTION

In general, when using a human interface system, there are often delays in control, which is an issue that can reduce trust in the utility of the system. For example, time delays in controlling robotic hands are inevitable, leading to lower user satisfaction (Yang and Dorneich, 2015) and performance (Selvidge et al., 2002; Rank et al., 2010). Thus, delays play a critical

Abbreviations: EMG, electromyography; EEG, electroencephalogram; ERSP, event-related spectral perturbation.

role in the efficiency of this process. Using questionnaires, several behavioral studies have investigated subjective evaluations of delayed output in specific situations such as first-person shooter games (Quax et al., 2004) and webpage loading (Guse et al., 2015). It was reported that in a real-time cursor control task, subtle and large delays in visual feedback were associated with different brain regions (Kim et al., 2020). Thus, a delay in the general human interface is a key factor that determines the subjective impression of the trustworthiness of the system, which also determines the user experience.

The use of electromyography (EMG) readings as an input to the human-robot interface has been widely used in various applications, including the control of various body parts such as the hands (Yang et al., 2009), fingers (Hussain et al., 2016), and an exoskeleton robot (Lenzi et al., 2012; Peternel et al., 2016). Various methods have been developed to improve the performance of the control, which has been evaluated based on task performance and technological factors (Choi et al., 2009; Al-Timemy et al., 2016; Ao et al., 2017). However, in real-world applications, users are unaware of the EMG activation patterns or the signal processing used to control the robot. Unlike the control using extrinsic parameters such as position, EMG-based control is somewhat counterintuitive for users. Users anticipate real-time movement when controlling the computer cursor or video on the screen; however, in EMG-based control, the control method is rather difficult to understand, and users are unaware of the natural delay. We are not aware when EMG signals start to activate. Thus, in EMG-based control, not only system performance but also subjective usability should be carefully evaluated and investigated. If users cannot control the system, they need to change the muscles that are used to optimize input commands so that the control becomes more efficient. Visual feedback is the most critical information in the process of establishing a reliable input protocol to establish the correct set of muscles that cause a responsive reaction in the robot hand. Although undesirable, confirming a replicable delay is still useful in terms of (meta-level) confirmation of the reliability of the input-output relations. Irregularity in this expected delay makes users skeptical about the effectiveness of the EMG input ("Is my particular use of muscles easily readable to the system?") and/or reduces trust in the system ("Is this system functioning as expected?"). These negative concerns have a negative impact on user experience. If users do not understand exactly how the system works, this might happen even if the system followed the command configuration well. However, the relationship between the subjective perception of delay and its neural representation under EMG-based robot control is poorly understood. In other words, subjective awareness of the delay may change subsequent neural processes, but this process has rarely been investigated.

To evaluate the influence of the subjective perception of delay on brain activation, we designed an electroencephalogram (EEG) study using EMG-based robot control. We extracted muscle synergy from EMG signals that were used as the grip command of a robot hand that had the necessary basic delay to move. One of four additional delays (0 ms, 50 ms, 125 ms, and 250 ms) was applied in each trial, and subjects were instructed to answer whether the delay was natural or additional or whether they were not sure after they controlled the robot by grasping their hand. We compared the brain activities based on the responses ("sure" and "not sure").

MATERIALS AND METHODS

Subjects

Nine subjects (six men and three women; mean age ± standard deviation: 26.56 ± 3.17 years) participated in the experiment. All subjects were right-handed and did not have any neurological or motor function disorders. All subjects provided written informed consent prior to the experiment. This study was approved by the ethics committee of the Tokyo Institute of Technology and was conducted in accordance with the Declaration of Helsinki.

Experimental Apparatus and Data Acquisition

Figure 1 is a schematic of the experimental environment. During the experiment, the subjects sat on a chair, and their right arm was placed on a supportive surface. They wore an EEG cap, EMG sensor, and markers for motion sensors, and a face cover with a black paper was attached to subjects such that they could not see their right hand. Visual instructions or questions were presented on a screen in front of them, and subjects could make choices by pressing the keyboard button with their left hand. A robot hand (qb SoftHand, qb robotics, Italy) was fixed to a table and was in the subjects' view. The robot hand and the monitor were placed for subjects to see them without having to move their heads.

Motion data were acquired using the OptiTrack motion capture system (NaturalPoint Inc., Corvallis, OR). Markers were attached to the subjects' wrist, back of the hand, and middle finger to measure human motion; sensors were placed at the robot's wrist, back of the hand, and middle finger to measure its motion. We measured EMG signals from 32 channels using an array EMG sensor (Koike et al., 2020) that covers the muscles of the forearm. According to the international 10–20 system (Klem et al., 1999), we measured EEG signals from 64 channels (Fp1, Fp2, Fpz, AF3, AF4, AF7, AF8, AFz, F1, F2, F3, F4, F5, F6, F7, F8, Fz, FT7, FT8, FC1, FC2, FC3, FC4, FC5, FC6, FCz, C1, C2, C3, C4, C5, C6, Cz, T7, T8, TP7, TP8, CP1, CP2, CP3, CP4, CP5, CP6, CPz, P1, P2, P3, P4, P5, P6, P7, P8, P9, P10, Pz, PO3, PO4, PO7, PO8, POz, O1, O2, Oz, and Iz) using the Biosemi ActiveTwo system (Biosemi, Amsterdam, Netherlands).

Robot Control

Before the actual task, we conducted a calibration session to determine the proper input command of the robot for each subject. Before the calibration began, the subjects placed their right arm on the arm support and relaxed. During calibration, they grasped and opened their hands three times. They were instructed to grip naturally, not exert maximally, and spread their fingers such that their joints did not bend. While they performed the motion, the EMG signals and the angle of the

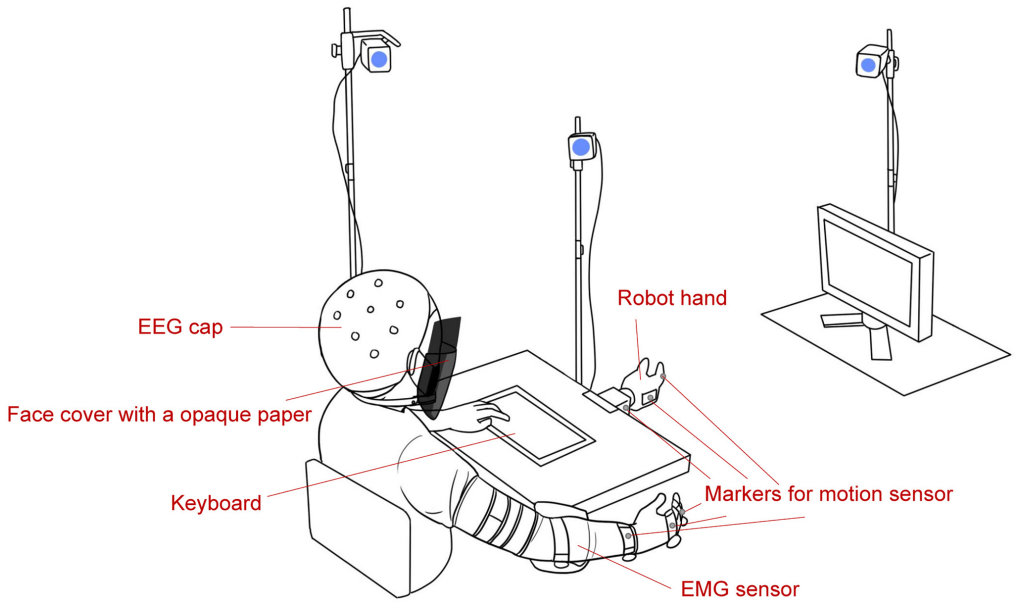

FIGURE 1 | Experimental environment (not to scale). EMG, electromyography; EEG, electroencephalogram.

metacarpophalangeal joint of the middle finger were measured. Noisy EMG channels were rejected during the inspection. The remaining EMG channels were rectified and filtered using a second-order Butterworth low-pass filter with a cutoff frequency of 5 Hz. We extracted two muscle synergies from the filtered EMG signals using the HALS algorithm (Cichocki and Phan, 2009). The number of synergies was increased if the synergies were not relevant to hand motion. We used the musculoskeletal model (Kawase et al., 2017) to estimate the joint angle with the corresponding muscle synergies. The estimated joint angle was used as the input command for the robot hand during the task session. After calibration, the subjects practiced long enough to learn how to control the robot that was imitating the human grip. To ensure natural movement control, the robot control was tested immediately after calibration, and recalibration was performed if necessary. We instructed subjects to remember their own way to control the robot and not to change their method during the experiment because we wanted to evaluate how subjects responded to delayed movement compared with the robot with no manipulation of their input commands. In addition, the interval between the human's movement and the robot's movement was defined as the response time, where the initiation of movements was detected based on position data. Thus, the response time includes the durations for signal processing and additional delay in some cases.

Task Description

At the beginning of the experiment, the "wait" message was shown on the screen, instructing subjects to put their right hand on the arm supporter and relax. When their hand was in the resting state, the message was changed into either "natural delay" or "??" When a natural delay was shown on the screen, subjects knew no additional artificial delay would be applied in this trial. Trials showing "natural delay" were set for subjects to know and feel the necessary time required for robot control, which included EMG signal processing and transferring signals to the robot so that they could compare this to when an input command was intentionally delayed in other trials. When "??" was shown on the screen, subjects did not know whether an additional delay would be applied. "additional delay" meant input commands would be intentionally lagged further in addition to a natural delay that is the minimal time required to control the robot for the experiment. When subjects saw either message, they were instructed to look at the robot and control it by grasping their hand and feeling the delay. After the robot had completely gripped, the robot went back to a resting position, and the message was changed into the following: "(1) natural delay; (2) I am not sure; and (3) natural delay + additional delay." The subjects were instructed to push one of the corresponding buttons (1, 2, or 3) on the keyboard. When subjects felt that the delay was the same as a natural delay or if they knew the delay was natural, they selected 1. When they were not sure whether an additional delay was applied, they selected 2. When they were sure that they felt an additional delay, they selected 3. Further, they were instructed to push either button without thinking and push 2 whenever they found themselves hesitant to select. After making their selections, the participants pushed the space bar to confirm their choice. If subjects pushed the space bar, the message said "Relax," instructing them to relax until the next trial. This procedure was repeated for all trials.

Each trial had one of four additional delay durations: no delay, 50 ms, 125 ms, and 250 ms. As mentioned above, "natural delay" was displayed on the screen during some trials where no delay was applied and subjects were aware of the nature of the delay

before they moved. This was set for subjects so that they do not forget the feeling of a natural delay. Thus, there were five types of trials for each run (one where "natural delay" was shown and four where "??" was shown on the screen). Each run consisted of 24 trials per type of trial where the delay was not indicated ("??") and 29 trials without an additional delay where the subjects knew a delay was not applied. In each run, the first five trials had no delay, and subjects were informed of this, and the first few trials included additional delays, because if they forgot how the natural delay felt, they would not be able to make a comparison with the trials with additional delay. In total, each run had 125 trials, and we conducted three runs for each subject in the experiment. There was a rest period between the runs.

EEG Preprocessing

EEGLAB was used for EEG preprocessing. First, EEG signals were resampled at 256 Hz to match the data format for further analysis. Then, the EEG signals were obtained using a high-pass filter with a cutoff frequency of 1 Hz. We used cleanLineNoise (Bigdely-Shamlo et al., 2015) to eliminate line noise and artifact subspace reconstruction for data cleaning (Mullen et al., 2015; Blum et al., 2019). Cleaned signals were re-referenced to an average, and we performed independent component analysis. Each independent component was used to fit an equivalent current dipole model with fit Two Dipoles (Piazza et al., 2016) and identified using ICLabel (Pion-Tonachini et al., 2019).

Data Analysis

EEG preprocessing was conducted at the single-subject level, whereas analysis from the clustering was conducted at the group level. Independent components, identified as brain components, were used for k-means clustering based on dipole locations. There were 11 clusters, as determined by the silhouette index (Rousseeuw, 1987). We extracted epochs between 0.5 s before the onset of the human's movement and 2 s after the onset, and we calculated event-related spectral perturbation (ERSP) on independent components related to each cluster using the Morse wavelet (MATLAB Wavelet Toolbox).

For the statistical analysis, trials where delay information ("natural delay" on the screen) was presented were not used. For comparison, three responses (natural delay, not sure, and additional delay) were employed and categorized into two groups, namely, sure (natural and additional delay) and not sure. We combined "natural" and "additional" to identify factors that are not related to the amount of delay but make users feel strange, which could be used to evaluate usability. We thought that we could exclude brain activity related to delay perception by combining both options. In addition, we aimed to help subjects understand the natural delay by providing them with the option to select "natural delay" so that we could exclude the effects of basic delay in controlling. Thus, we provided separate response options ("natural," "not sure," and "additional"). These options enabled subjects to unconsciously select "not sure" when they do not know whether this delay is "natural" or "additional". We used time-frequency points between 1 and 50 Hz within an epoch from each cluster for analysis. We used a cluster-based permutation test with weak control of the familywise error rate (Groppe et al., 2011) to determine whether each comparison of the two conditions was statistically significant. The threshold of the p-value for preselection was set to 0.01, and the permutation was repeated 5,000 times for each comparison. For comparison based on the response, three subjects were not included because they did not select "not sure" enough much, and the resulting number of samples was not sufficient for analysis.

TABLE 1 | Frequency of each response.

	Natural	Not sure	Additional
S1	145	41	102
S2	101	60	127
S3	147	39	102
S4	161	47	80
S5	94	41	153
S6	39	79	170

RESULTS

Table 1 shows the frequency of each response. **Figure 2** shows the proportion of behavioral results for each subject. The summation of the four types of delay is 100% in each response. **Figure 3** shows the interval between the human's movement and the robot's movement. The mean values were about 0.77 s in both cases, and the standard deviation was 0.22 and 0.28, respectively. The difference was not statistically significant (t-test; $p > 0.1$). We found a cluster showing significant differences between "sure" and "not sure." **Figure 4** shows the ERSP of the cluster based on the participants' responses and significantly different masks. A value of 0 s represents the initiation of human movement. We observed a significant power difference (not sure) between 5 and 7 Hz immediately after movement onset. This significant power difference was sustained until 0.7 s. From 0.5 s, a significant power difference of approximately 3.5 Hz was observed. In both cases, a power decrease in the beta band of the cluster was observed from the onset of the subjects' movement. **Figure 5** shows the density of the current dipoles corresponding to each independent component that the cluster consisted of. The cluster was composed of 21 independent components from six subjects. Estimated by the dipoles taking up the head model, anatomical brain regions related to the cluster were the paracentral lobule with a probability of 21%, the postcentral gyrus with a probability of 19%, and the precuneus with a probability of 16%.

DISCUSSION

In this study, we investigated how subjective delay perception is reflected in the brain using subjects' responses, regardless of an actual delay. We found that the cluster showing significant differences was associated with the paracentral lobule, postcentral gyrus, and precuneus. The cluster showed significant power differences around 5–7 Hz and 3–4 Hz in the "not sure" condition compared with those in the "sure" condition. The standard deviation of the robot's response time, which is the interval between human and robot movement, was 0.2–0.3 s in

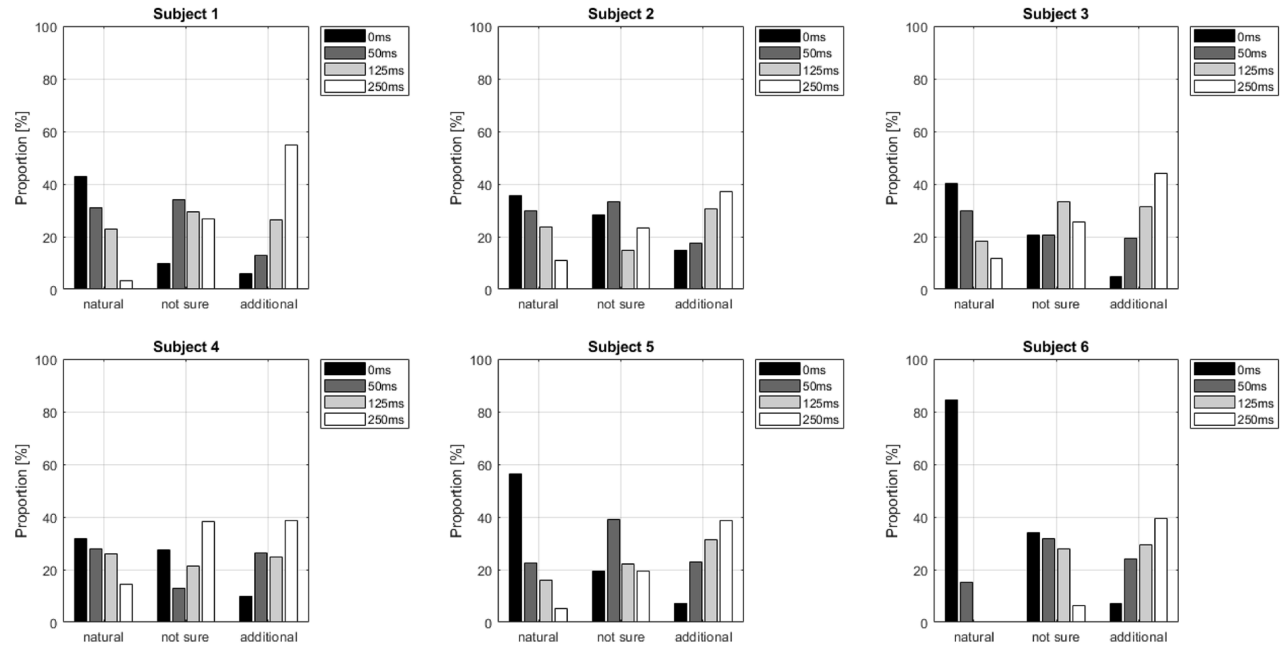

FIGURE 2 | Delay proportion for each response. The summation of the four types of delay is 100% in each response.

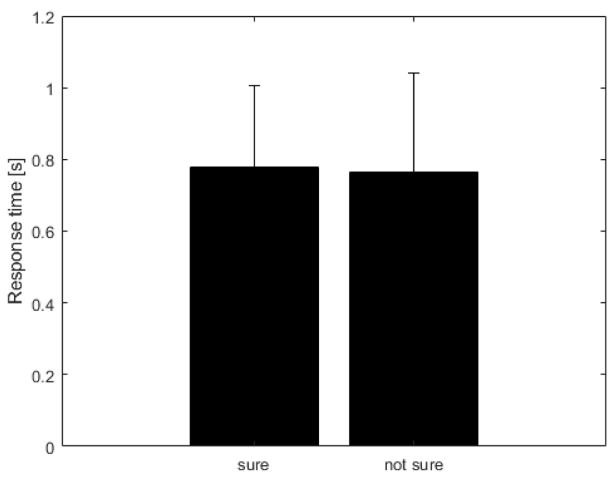

FIGURE 3 | The interval between human movement and robot movement. Unit is seconds (s). The mean value was calculated from six subjects selected for analysis. The error bar represents the standard deviation of the means of subjects.

both conditions. This may reflect an individual's behavior, which includes different ways to input a command to the robot hand.

We observed two significant power differences, at 0–0.7 s and 0.5–0.9 s. This significant power difference could be a reason why the subjects did not have certainty about their response. Uncertainty about subjects' responses was reflected in the error-related potential, which means that two types of errors can occur (Scheffers and Coles, 2000). Awareness of response errors is also reflected in the brain (Nieuwenhuis et al., 2001). Likewise, awareness of a delay might be different from the delay itself, which could also be reflected in the brain. The length of the delay is associated with a sense of agency and has previously been used to raise a sense of agency (Haering and Kiesel, 2015; Osumi et al., 2019; Bu-Omer et al., 2021). Brain activation related to a sense of agency has been reported in several brain regions, evidenced by a power decrease in the central and bilateral parietal regions (Kang et al., 2015), parieto-occipital regions (Bu-Omer et al., 2021), and pre-supplementary motor areas (Moore et al., 2010). If we consider that the sense of agency refers to a high-level representation that can be related to non-unique neurocognitive phenomena, our results might be related to a sense of agency.

Because our analysis was based on the subjects' responses, we could consider the cluster in terms of metacognition. A previous work has shown that judgment of agency and judgment of performance were differently related to the brain and can, therefore, be dissociated (Miele et al., 2011). In our experiment, the subjects were instructed to answer whether the delay was natural or additional. They had to identify delays, which could be related to both agency and performance. Another study reported that when subjects felt and did not feel the delay, different activation patterns were observed in the cerebellum, which provided accurate timing information (Leube et al., 2003). This physiological basis, which is not related to actual delay but may influence motor command, supports that delay perception should be considered.

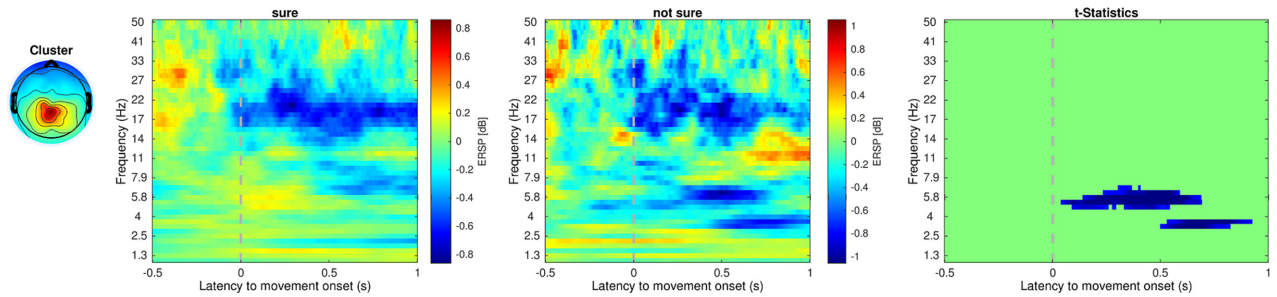

FIGURE 4 | Event-related spectral perturbation of the cluster that showed significant regions within the epoch. Unit is decibel [dB]. The dotted line at 0 s indicates the initiation of the human movement. Cluster 5 includes 21 independent components from six subjects. The power difference (not sure-sure) between about 5–7 Hz was statistically significant.

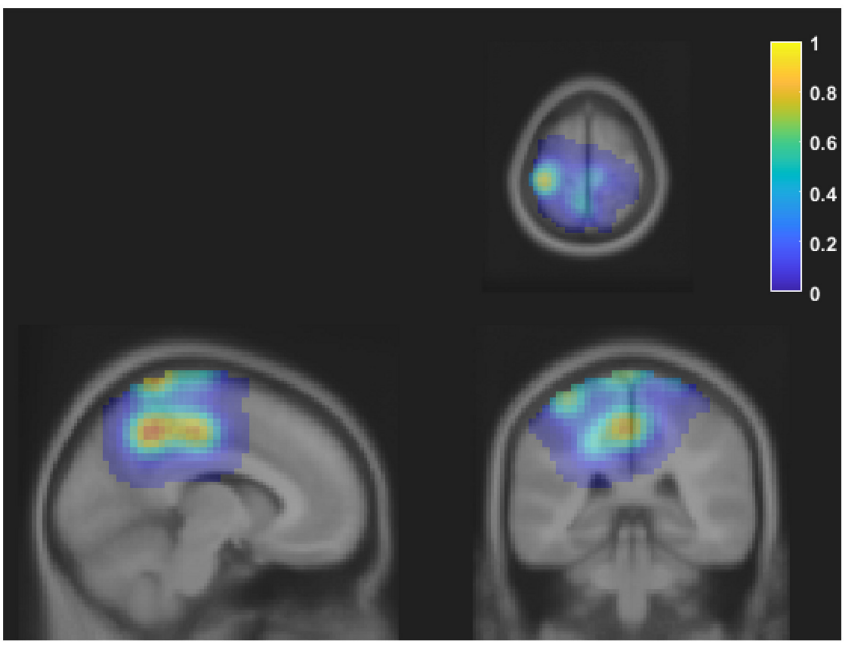

FIGURE 5 | The density of the current dipoles corresponding to each independent component of the cluster. The values were normalized to the maximum value. The cluster includes 21 independent components from six subjects. The mean MNI coordinate was [−9 −35 64], and the standard deviation was [16 14 16]. Each image is shown on axial, sagittal, and coronal planes. Estimated locations of each dipole were the paracentral lobule, postcentral gyrus, and precuneus. MNI, Montreal Neurological Institute.

Our significant period included the time range before an input command reached. This suggests that subjects sometimes felt that the robot was not controlled well, regardless of the actual performance of the system. Subjects' conscious responses might be dominated by their current feeling rather than the actual delay of the system. There have been several studies on brain activity before a stimulus. Pre-stimulus oscillation, in the context of visual perception performance, has also been investigated (Hanslmayr et al., 2007). These results showed that the pre-stimulus alpha power of "perceivers" was lower than that of "non-perceivers." Additionally, the phases of the alpha at the stimulus onset were related to visual perception (Milton and Pleydell-Pearce, 2016). It has been reported that an increase in pre-stimulus theta oscillations is associated with retrieving successful source memory (Addante et al., 2011), and this phase was associated with the subsequent successful encoding of memory (Cruzat et al., 2021). This evidence may support our results, indicating a significant change in power during the interval when subjects cannot feel a delay.

Previous studies have focused on the stimulus; however, in our study, the users decided the onset of the time. Users expect robots to move and compare to the experience from previous trials, known as trials with natural delay. This situation

makes it difficult to understand the results completely, and brain activity dominating perception, such as the pre-stimulus oscillations introduced in previous studies, partially contributed to our results. For EMG-controlled systems, such brain activity dominating perception could be ignored during proper usability evaluation as the user's response during that trial may not be driven by the actual performance of the system. In addition, this mechanism would be sensitive to brain-machine interfaces requiring human intention, such as the intention to brake when driving a car (Teng et al., 2017), directional intention (Kim et al., 2019), motor imagery intention (Xu et al., 2020), and gait intention (Hasan et al., 2020).

In this study, we have categorized the responses into two groups, namely, "sure" (natural and additional delay) and "not sure". Out of the nine subjects, only six were considered for analysis as the other three did not select "not sure" enough times. The cluster we found included information for all the subjects but the three subjects' brain activity during the experiment might not have included the information related to the cluster. Our current experimental paradigm was not optimal to derive "not sure," and we did not expect the results obtained in this study. For future studies, the number of subjects should be increased for a better understanding, and a proper experimental paradigm should be designed for investigating our result related to pre-stimulus oscillation.

In this study, we investigated how subjective feelings of delay are reflected in the brain. Our results showed that the power of the theta band in the parietal lobe was significantly changed, suggesting that users might evaluate the system in advance without feeling the response of the system. This should be considered when constructing an adaptive system and evaluating its usability. For further study, delays that can occur when using an EMG interface should be categorized, and the response to each type of delay should be investigated.

DATA AVAILABILITY STATEMENT

The original contributions presented in the study are included in the article/**Supplementary Material**, further inquiries can be directed to the corresponding author.

ETHICS STATEMENT

The studies involving human participants were reviewed and approved by the ethics committee of the Tokyo Institute of Technology. The patients/participants provided their written informed consent to participate in this study.

AUTHOR CONTRIBUTIONS

HK, NY, and YKo developed the concept and designed the experiment. HK, YKi, and SS acquired the data. HK and MM analyzed the data. HK, YKi, and MM drafted the manuscript. All authors contributed to the article and approved the submitted version.

FUNDING

This work was supported by the JSPS KAKENHI (grant no. 19H05728), Tateishi Science and Technology Foundation (grant no. 2188001), JST PRESTO (Precursory Research for Embryonic Science and Technology; grant no. JPMJPR17JA), JST MIRAI (grant no. JPMJM18C8), and Tokyo Tech Fellowship for Young Doctoral Researchers.

SUPPLEMENTARY MATERIALS

The Supplementary Material for this article can be found online at: https://www.frontiersin.org/articles/10.3389/fnsys.2021.767477/full#supplementary-material.

REFERENCES

Addante, R. J., Watrous, A. J., Yonelinas, A. P., Ekstrom, A. D., and Ranganath, C. (2011). Prestimulus theta activity predicts correct source memory retrieval. *Proc. Natl Acad. Sci. U S A* 108, 10702–10707. doi: 10.1073/pnas.1014528108

Al-Timemy, A. H., Khushaba, R. N., Bugmann, G., and Escudero, J. (2016). Improving the performance against force variation of EMG controlled multifunctional upper-limb prostheses for transradial amputees. *IEEE Trans. Neural Syst. Rehabil. Eng.* 24, 650–661. doi: 10.1109/TNSRE.2015.2445634

Ao, D., Song, R., and Gao, J. (2017). Movement performance of human-robot cooperation control based on EMG-driven hill-type and proportional models for an ankle power-assist exoskeleton robot. *IEEE Trans. Neural Syst. Rehabil. Eng.* 25, 1125–1134. doi: 10.1109/TNSRE.2016.2583464

Bigdely-Shamlo, N., Mullen, T., Kothe, C., Su, K. M., and Robbins, K. A. (2015). The PREP pipeline: standardized preprocessing for large-scale EEG analysis. *Front. Neuroinform.* 9:16. doi: 10.3389/fninf.2015.00016

Blum, S., Jacobsen, N. S. J., Bleichner, M. G., and Debener, S. (2019). A riemannian modification of artifact subspace reconstruction for EEG artifact handling. *Front. Hum. Neurosci.* 13:141. doi: 10.3389/fnhum.2019.00141

Bu-Omer, H. M., Gofuku, A., Sato, K., and Miyakoshi, M. (2021). Parieto-occipital alpha and Low-Beta EEG power reflect sense of agency. *Brain Sci.* 11:743. doi: 10.3390/brainsci11060743

Choi, C., Micera, S., Carpaneto, J., and Kim, J. (2009). Development and quantitative performance evaluation of a noninvasive EMG computer interface. *IEEE Trans. Biomed. Eng.* 56, 188–191. doi: 10.1109/TBME.2008.2005950

Cichocki, A., and Phan, A. H. (2009). Fast local algorithms for large scale nonnegative matrix and tensor factorizations. *IEICE Trans. Fundam. Electron. Commun. Comput. Sci.* 92, 708–721. doi: 10.1587/transfun.E92.A.708

Cruzat, J., Torralba, M., Ruzzoli, M., Fernández, A., Deco, G., and Soto-Faraco, S. (2021). The phase of theta oscillations modulates successful memory formation at encoding. *Neuropsychologia* 154:107775. doi: 10.1016/j.neuropsychologia.2021.107775

Groppe, D. M., Urbach, T. P., and Kutas, M. (2011). Mass univariate analysis of event-related brain potentials/fields I: a critical tutorial review. *Psychophysiology* 48, 1711–1725. doi: 10.1111/j.1469-8986.2011.01273.x

Guse, D., Schuck, S., Hohlfeld, O., Raake, A., and Möller, S. (2015). "Subjective quality of webpage loading: the impact of delayed and missing elements on quality ratings and task completion time" in *2015 Seventh International Workshop on Quality of Multimedia Experience (QoMEX)*, (Pilos, Greece: IEEE), 1–6. doi: 10.1109/QoMEX.2015.7148094

Haering, C., and Kiesel, A. (2015). Was it me when it happened too early? Experience of delayed effects shapes sense of agency. *Cognition* 136, 38–42. doi: 10.1016/j.cognition.2014.11.012

Hanslmayr, S., Aslan, A., Staudigl, T., Klimesch, W., Herrmann, C. S., and Bäuml, K. H. (2007). Prestimulus oscillations predict visual perception

performance between and within subjects. *NeuroImage* 37, 1465–1473. doi: 10.1016/j.neuroimage.2007.07.011

Hasan, S. S., Siddiquee, M. R., Atri, R., Ramon, R., Marquez, J. S., and Bai, O. (2020). Prediction of gait intention from pre-movement EEG signals: a feasibility study. *J. Neuroeng. Rehabil.* 17:50. doi: 10.1186/s12984-020-00675-5

Hussain, I., Spagnoletti, G., Salvietti, G., and Prattichizzo, D. (2016). An EMG interface for the control of motion and compliance of a supernumerary robotic finger. *Front. Neurorobot.* 10:18. doi: 10.3389/fnbot.2016.00018

Kang, S. Y., Im, C. H., Shim, M., Nahab, F. B., Park, J., Kim, D. W., et al. (2015). Brain networks responsible for sense of agency: an EEG study. *PLoS One* 10:e0135261. doi: 10.1371/journal.pone.0135261

Kawase, T., Sakurada, T., Koike, Y., and Kansaku, K. (2017). A hybrid BMI-based exoskeleton for paresis: EMG control for assisting arm movements. *J. Neural Eng.* 14:016015. doi: 10.1088/1741-2552/aa525f

Kim, H., Yoshimura, N., and Koike, Y. (2019). Classification of movement intention using independent components of premovement EEG. *Front. Hum. Neurosci.* 13:63. doi: 10.3389/fnhum.2019.00063

Kim, H., Yoshimura, N., and Koike, Y. (2020). Investigation of delayed response during real-time cursor control using electroencephalography. *J. Health. Eng.* 2020:1418437. doi: 10.1155/2020/1418437

Klem, G. H., Lüders, H. O., Jasper, H., and Elger, C. (1999). The ten-twenty electrode system of the international federation. *Electroencephalogr. Clin. Neurophysiol.* 52, 3–6.

Koike, Y., Kim, Y., Staporn chaisit, S., Qin, Z., Kawase, T., and Yoshimura, N. (2020). Development of multi-sensor array electrodes for measurement of deeper muscle activation. *Sens. Mater.* 32, 959–966. doi: 10.18494/SAM.2020.2636

Lenzi, T., De Rossi, S. M. M., Vitiello, N., and Carrozza, M. C. (2012). Intention-based EMG control for powered exoskeletons. *IEEE Trans. Biomed. Eng.* 59, 2180–2190. doi: 10.1109/TBME.2012.2198821

Leube, D. T., Knoblich, G., Erb, M., Grodd, W., Bartels, M., and Kircher, T. T. (2003). The neural correlates of perceiving one's own movements. *NeuroImage* 20, 2084–2090. doi: 10.1016/j.neuroimage.2003.07.033

Miele, D. B., Wager, T. D., Mitchell, J. P., and Metcalfe, J. (2011). Dissociating neural correlates of action monitoring and metacognition of agency. *J. Cogn. Neurosci.* 23, 3620–3636. doi: 10.1162/jocn_a_00052

Milton, A., and Pleydell-Pearce, C. W. (2016). The phase of pre-stimulus alpha oscillations influences the visual perception of stimulus timing. *NeuroImage* 133, 53–61. doi: 10.1016/j.neuroimage.2016.02.065

Moore, J. W., Ruge, D., Wenke, D., Rothwell, J., and Haggard, P. (2010). Disrupting the experience of control in the human brain: pre-supplementary motor area contributes to the sense of agency. *Proc. Biol. Sci.* 277, 2503–2509. doi: 10.1098/rspb.2010.0404

Mullen, T. R., Kothe, C. A. E., Chi, Y. M., Ojeda, A., Kerth, T., Makeig, S., et al. (2015). Real-time neuroimaging and cognitive monitoring using wearable dry EEG. *IEEE Trans. Biomed. Eng.* 62, 2553–2567. doi: 10.1109/TBME.2015.2481482

Nieuwenhuis, S., Ridderinkhof, K. R., Blom, J., Band, G. P., and Kok, A. (2001). Error-related brain potentials are differentially related to awareness of response errors: evidence from an antisaccade task. *Psychophysiology* 38, 752–760. doi: 10.1111/1469-8986.3850752

Osumi, M., Nobusako, S., Zama, T., Yokotani, N., Shimada, S., Maeda, T., et al. (2019). The relationship and difference between delay detection ability and judgment of sense of agency. *PLoS One* 14:e0219222. doi: 10.1371/journal.pone.0219222

Peternel, L., Noda, T., Petrič, T., Ude, A., Morimoto, J., and Babič, J. (2016). Adaptive control of exoskeleton robots for periodic assistive behaviours based on EMG feedback minimisation. *PLoS One* 11:e0148942. doi: 10.1371/journal.pone.0148942

Piazza, C., Miyakoshi, M., Akalin-Acar, Z., Cantiani, C., Reni, G., Bianchi, A. M., et al. (2016). "An automated function for identifying EEG independent components representing bilateral source activity," in *IFMBE Proc. XIV Mediterranean Conference on Medical and Biological Engineering and Computing*, eds E. Kyriacou, S. Christofides and C. S. Pattichis (Cham: Springer International Publishing), 105–109.

Pion-Tonachini, L., Kreutz-Delgado, K., and Makeig, S. (2019). ICLabel: an automated electroencephalographic independent component classifier, dataset and website. *NeuroImage* 198, 181–197. doi: 10.1016/j.neuroimage.2019.05.026

Quax, P., Monsieurs, P., Lamotte, W., De Vleeschauwer, D., and Degrande, N. (2004). "Objective and subjective evaluation of the influence of small amounts of delay and jitter on a recent first person shooter game," in *Proceedings of the 3rd Workshop on Network and System Support for Games* (Portland, OR, United States), 152–156.

Rank, M., Shi, Z., and Hirche, S. (2010). Perception of delay in haptic telepresence systems. *PRESENCE: Teleoperators Vir. Environ.* 19, 389–399. doi: 10.1162/pres_a_00021

Rousseeuw, P. J. (1987). Silhouettes: a graphical aid to the interpretation and validation of cluster analysis. *J. Comput. Appl. Math.* 20, 53–65. doi: 10.1016/0377-0427(87)90125-7

Scheffers, M. K., and Coles, M. G. H. (2000). Performance monitoring in a confusing world: error-related brain activity, judgments of response accuracy and types of errors. *J. Exp. Psychol. Hum. Percept. Perform.* 26, 141–151. doi: 10.1037//0096-1523.26.1.141

Selvidge, P. R., Chaparro, B. S., and Bender, G. T. (2002). The world wide wait: effects of delays on user performance. *Int. J. Ind. Ergon.* 29, 15–20. doi: 10.1016/S0169-8141(01)00045-2

Teng, T., Bi, L., and Liu, Y. (2017). EEG-based detection of driver emergency braking intention for brain-controlled vehicles. *IEEE Trans. Intell. Transp. Syst.* 19, 1766–1773. doi: 10.1109/TITS.2017.2740427

Xu, J., Zheng, H., Wang, J., Li, D., and Fang, X. (2020). Recognition of EEG signal motor imagery intention based on deep multi-view feature learning. *Sensors (Basel)* 20:3496. doi: 10.3390/s20123496

Yang, E., and Dorneich, M. C. (2015). The effect of time delay on emotion, arousal, and satisfaction in human-robot interaction. *Proc. Hum. Factors Ergon. Soc. Annu. Meet.* 59, 443–447. doi: 10.1177/1541931215591094

Yang, D. P., Zhao, J. D., Gu, Y. K., Wang, X. Q., Li, N., Jiang, L., et al. (2009). An anthropomorphic robot hand developed based on underactuated mechanism and controlled by EMG signals. *J. Bionic Eng.* 6, 255–263. doi: 10.1016/S1672-6529(08)60119-5

Conflict of Interest: SS was employed by the company EAGLYS Inc.

The remaining authors declare that the research was conducted in the absence of any commercial or financial relationships that could be construed as a potential conflict of interest.

Publisher's Note: All claims expressed in this article are solely those of the authors and do not necessarily represent those of their affiliated organizations, or those of the publisher, the editors and the reviewers. Any product that may be evaluated in this article, or claim that may be made by its manufacturer, is not guaranteed or endorsed by the publisher.

Copyright © 2021 Kim, Kim, Miyakoshi, Staporn chaisit, Yoshimura and Koike. This is an open-access article distributed under the terms of the Creative Commons Attribution License (CC BY). The use, distribution or reproduction in other forums is permitted, provided the original author(s) and the copyright owner(s) are credited and that the original publication in this journal is cited, in accordance with accepted academic practice. No use, distribution or reproduction is permitted which does not comply with these terms.

frontiers in Systems Neuroscience

BRIEF RESEARCH REPORT
published: 02 December 2021
doi: 10.3389/fnsys.2021.801492

Distribution of Large and Small Dorsal Root Ganglion Neurons in Common Marmosets

*Moeko Kudo, Sidikejiang Wupuer, Shinji Kubota and Kazuhiko Seki**

Department of Neurophysiology, National Institute of Neuroscience, National Center of Neurology and Psychiatry, Kodaira, Japan

The aim of this study was to elucidate the size and distribution of dorsal root ganglion (DRG) neurons in non-human primates and to compare them with those of rodent DRG neurons. By measuring the size of NeuN-, NF200-, and peripherin-positive DRG neurons in the lumbar spinal cord of rats and marmosets, we found that the cell size distribution pattern was comparable in both species, although DRG neurons in marmosets were larger than those of rodents. This is the first demonstration that DRG neurons in marmosets have a bimodal size distribution, which has been well established in rodents and humans.

Keywords: dorsal root ganglion (DRG), nonhuman primate, rat, size distribution, NF200, peripherin

OPEN ACCESS

Edited by:
Jun Izawa,
University of Tsukuba, Japan

Reviewed by:
Pascal Darbon,
Université de Strasbourg, France
Takahiro Kondo,
Keio University, Japan
Hiroyuki Miyawaki,
Osaka City University, Japan

****Correspondence:***
Kazuhiko Seki
seki@ncnp.go.jp

Received: *25 October 2021*
Accepted: *12 November 2021*
Published: *02 December 2021*

Citation:
Kudo M, Wupuer S, Kubota S and Seki K (2021) Distribution of Large and Small Dorsal Root Ganglion Neurons in Common Marmosets. Front. Syst. Neurosci. 15:801492. doi: 10.3389/fnsys.2021.801492

INTRODUCTION

It is widely accepted that cell body size is an accurate marker to characterize the morphological characteristics of dorsal root ganglion (DRG) neurons (Warrington and Griffith, 1904; Lawson, 1979). Large cells are associated with thicker, myelinated Aβ sensory axons, while small cells are associated with thinner, unmyelinated C fibers (Yoshida and Matsuda, 1979; Harper and Lawson, 1985; Lawson and Waddell, 1991). Thus, a strong correlation has been observed repeatedly between DRG cell size and axonal conduction velocity (Yoshida and Matsuda, 1979; Harper and Lawson, 1985; Lawson and Waddell, 1991; McCarthy and Lawson, 1997).

Although our understanding of the cell size-dependent characteristics of DRG neurons is largely based on rodent experiments, the size of DRG cells in humans has also been measured in a few studies (Josephson et al., 2001; Feliciano et al., 2007; Zhang et al., 2017), which reported that DRG neurons are larger in humans than in rodents (Josephson et al., 2001; Haberberger et al., 2019). Anatomically, the larger size of human DRG neurons may represent a simple correlation with their larger cell bodies (Toossi et al., 2021); however, functionally speaking, larger DRG neurons are advantageous for humans to make quick sensorimotor reactions according to environmental changes using their larger bodies, if the correlation between anatomical (cell size) and functional (e.g., conduction velocity) properties is also applicable in humans. Indeed, among mammals, humans are known to possess higher tactile and kinesthetic acuity and rich behavioral repertoires compared to rodents, irrespective of body size. However, to date, the link between DRG neuron size and function (i.e., conduction speed) is less established in humans because of the difficulty in assessing their function *in vivo* (but see Pruszynski and Johansson, 2014). This limitation could be addressed by establishing a non-human primate model for analyzing DRG neuron

anatomy and function. To this end, we have established electrophysiological (Umeda et al., 2012) and immunohistochemical assays for DRG neurons of non-human primates (Kudo et al., 2021). In this short report, we elucidated the size and distribution of DRG neurons in non-human primates and compared them with those of rodent DRG neurons.

MATERIALS AND METHODS

Experimental Animals

We used 14 adult common marmosets (1–12 years old, body weight 282–409 g, four males and 10 females) and eight young male Jcl:Wistar rats (8 weeks old, body weight 251–326 g) in the present study. The animals were housed under standard conditions with food and water available *ad libitum* and a 12-h:12-h light:dark cycle. All experiments were conducted in accordance with protocols approved by the Ethics Committee for Animal Research of the National Institute of Neuroscience, National Center of Neurology and Psychiatry, Japan.

Dissection

We anesthetized the marmosets with sodium pentobarbital (50 mg/kg) and perfused them transcardially with phosphate-buffered saline (PBS; pH 7.4), followed by 300–400 ml of 4% paraformaldehyde.

To expose the sciatic nerve, we placed the marmosets in a prone position. We cut the skin over the gluteus muscles and performed a blunt dissection to separate both heads of the biceps femoris. Once we identified the sciatic nerve below the biceps femoris, we further exposed the nerve proximally until its departure from the pelvis. Then, we removed the skin, viscera, and muscle to expose the vertebral, sacral, and medial iliac bones, which we cleared of overlying tissue in order to identify the sites of fusion of the lower lumbar vertebrae. We denoted the most caudal vertebra that lacked an articulation with a rib at its rostral margin as the first lumbar (L1) vertebra.

Immunohistochemistry

We collected tissue from the lumbar region of the spinal cord, together with the DRG and sciatic nerve, which we post-fixed in 4% paraformaldehyde overnight at 4°C and transferred to 30% sucrose in PBS at 4°C. We cut DRG sections at 20-μm thickness on a cryostat (Microm HM550; Thermo Fisher Scientific, Waltham, MA) and mounted them on amino silane-coated slides. After we washed the sections three times with PBS, we incubated them with PBS containing 2% normal goat serum (NGS) for 1 h at room temperature, followed by incubation with a primary antibody, diluted in 2% NGS and 0.1% Triton X-100 in PBS, overnight at 4°C. Then, we washed the sections with PBS three times and incubated them with a secondary antibody, diluted in 2% NGS in PBS, for 1 h at room temperature. We washed the sections with PBS and covered them with a glass coverslip. We stained control sections using the same protocol but omitted the primary antibodies. All processes were performed in a dark chamber. We used the following primary antibodies: rabbit anti-NeuN (1:2,000; Abcam, Cambridge, MA), mouse anti-neurofilament 160/200 (NF200; 1:2,000; N2912; Sigma-Aldrich, St. Louis, MO), and rabbit anti-peripherin (1:400; AB1530; Millipore, Burlington, MA). We used the following secondary antibodies (all diluted 1:500): donkey anti-rabbit IgG (Alexa Fluor 555; Abcam) and goat anti-mouse IgG (Alexa Fluor 555; Molecular Probes, Eugene, OR).

Histological Quantification

We acquired fluorescence images using fluorescent microscopy (BZ-X700; Keyence, Osaka, Japan) at fixed settings using a 10× or 20× objective. We performed image analysis and quantification using BZ-X710 image analysis software (BZ-H3M; Keyence). For the cell size distribution of NeuN-, NF200-, and peripherin-positive neurons, we selected every 10th DRG section spaced by 200 μm from the serial sections, and we examined four to six sections for rats or three to eight sections for marmosets in each animal. In each selected section, we measured the cross-sectional area of the labeled cells.

Before sectioning, we measured the size of lumbar DRGs (Ebraheim and Lu, 1998; Silav et al., 2016) in some of the marmosets ($n = 4$) and all of the rats ($n = 12$). We measured the L4 DRG in rats and L6 DRG in marmosets since these were the largest of those innervated by the sciatic nerve. We evaluated the cross-sectional area of the entire DRG (Beom et al., 2019) for each section of the corresponding DRG.

Statistical Analysis

We tested the difference of DRG cell size for each neural marker (NeuN, NF200, and peripherin) between rats and marmosets by either the Wilcoxon rank-sum test (for mean cell size) or a two-sample Kolmogorov–Smirnov test (for the distribution pattern). We considered $p < 0.05$ as significant in all statistical analyses.

RESULTS

Figure 1 shows the sciatic nerve and its segmental origin in marmosets. In this dissection, the segmental origin of the sciatic nerve, together with those of the femoral and saphenous nerves, were clearly visible (**Figure 1A**). We found that the sciatic nerve of marmosets originated mainly from the 5th, 6th, and 7th lumbar spinal roots (**Figures 1B,C**). This result was different from that observed in rodents, which originates from the 3rd and 4th (mice) or 4th and 5th (rats) lumbar spinal roots (Rigaud et al., 2008). Therefore, in our comparison of DRG neuron size, we focused on the DRGs of L4–6 in rats and L5–7 in marmosets.

Figure 2 shows examples of immunostained sections containing DRG neurons in rats (**Figures 2A–C**) and marmosets (**Figures 2D–F**). We stained each DRG slice for NeuN (**Figures 2A,D**), a neuronal marker, NF200 (**Figures 2B,E**), a marker for myelinated primary afferents that convey somatosensory signals other than nociception (Ma, 2002), and peripherin (**Figures 2C,F**), a marker for unmyelinated primary afferents that convey nociceptive signals (Amaya et al., 2000). In these examples, cells with a larger diameter were found frequently in sections of marmoset DRGs (**Figures 2D–F**). Then, we evaluated the size of each DRG cell stained in each

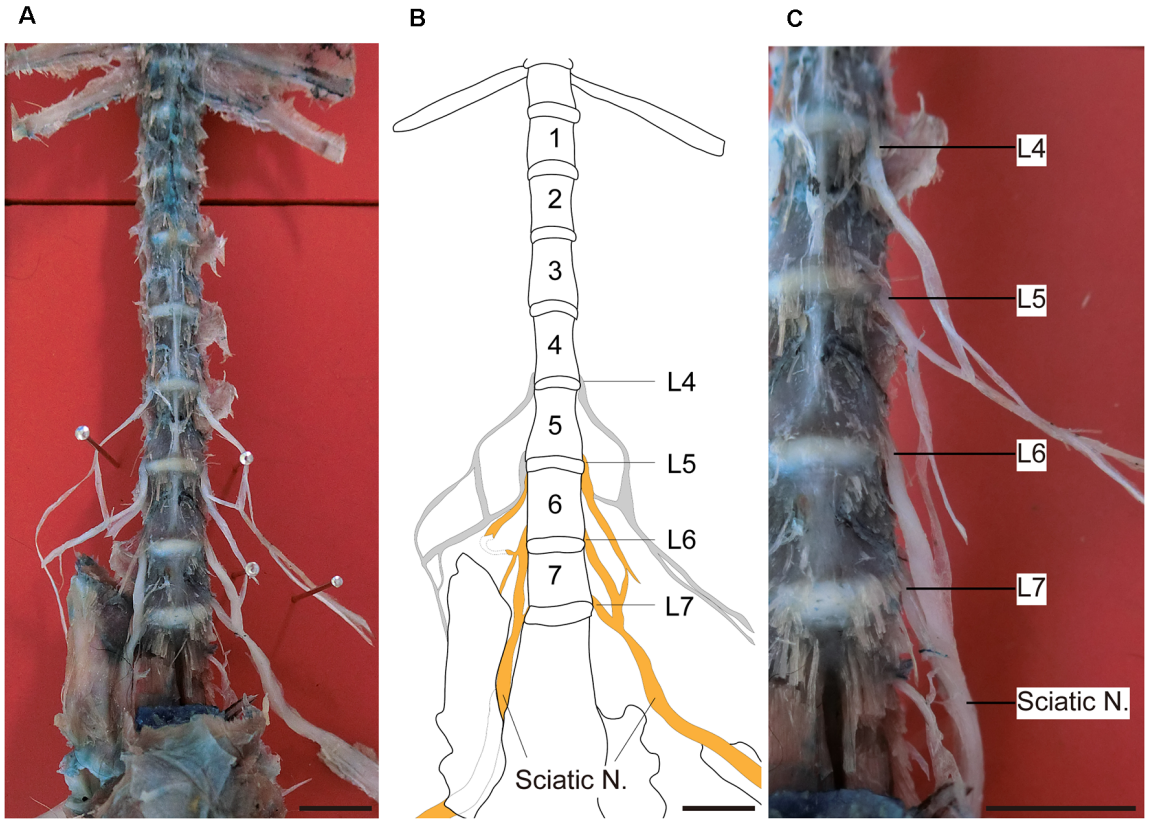

FIGURE 1 | Sciatic nerve and DRGs of marmosets. Ventral views of the dissection and reference line drawing made from a marmoset, showing the sciatic nerve and its segmental origins. **(A)** Photograph showing the lower thoracic and lumbar spinal cord. The sciatic nerve is formed by the combination of several nerves in the lumbar spine. **(B)** A line drawing of the photograph shown in **(A)**. The lumbar region of this specimen contained seven vertebrae. The L5, L6, and L7 spinal nerves contributed to the sciatic nerve. Gray lines: nerves hidden by the overlying pelvic bone. **(C)** Right side of the lower lumbar vertebrae as shown in **(A)** (enlarged). Orange: sciatic nerve. Scale bars: 10 mm.

section from all animals (shown in **Figures 2G–L**). In general, we confirmed the well-established bimodal distribution of DRG cell body size (Warrington and Griffith, 1904; Lawson, 1979; Ohnishi and Ogawa, 1986; Schmalbruch, 1987; Verge et al., 1990) in rats (**Figures 2G–I**). In rats, the size distribution of DRG cells labeled with NF200 (**Figure 2H**) was comparable with that of large "light" cells, which were also labeled with RT97, another antibody specific for this subpopulation of DRG neurons (Lawson et al., 1984). The peripherin-labeled DRG neurons tended to be small (**Figure 2I**), which again is comparable with the distribution of small "dark" cells. These large and small DRG subpopulations seemed to underlie the bimodal property of NeuN-labeled DRG neurons (**Figure 2G**). The cell type distribution of marmosets (**Figures 2J–L**) was comparable with that of rats. The cell size distribution patterns of the peripherin-positive and NF200-positive neurons were not different between rats and marmosets (two-sample Kolmogorov–Smirnov test, $p = 0.996$ and $p = 0.101$, respectively, **Figure 2**), which fundamentally composed the bimodal distribution of NeuN-positive neurons. This result suggests that the bimodal cell size distribution of DRG neurons reported in rodents is also applicable to marmoset DRG neurons.

Figure 3 summarizes the average size in each subcategory of DRG cells in rats (black) and marmosets (white). The average size of NeuN-positive DRG neurons in rats was $716.9 \pm 114\ \mu m^2$ ($n = 3{,}902$ cells), which was significantly smaller than that in marmosets ($1{,}181.7 \pm 188.3\ \mu m^2$, $n = 6{,}422$ cells, $p < 0.005$; **Figure 3A**). Similarly, we found significant differences in the average size of NF200- or peripherin-labeled cells between rats and marmosets. The average size of NF200-positive DRG neurons in rats and marmosets was $1{,}224.1 \pm 288.8\ \mu m^2$ ($n = 2{,}290$ cells) vs. $1{,}528.6 \pm 231.8\ \mu m^2$ ($n = 3{,}677$ cells), respectively (**Figure 3B**), and the average size of peripherin-positive DRG neurons was $393.6 \pm 34.8\ \mu m^2$ ($n = 2{,}658$ cells) vs. $499.8 \pm 64.4\ \mu m^2$ ($n = 3{,}295$ cells), respectively (**Figure 3C**). Therefore, we concluded that DRG cell size was generally larger in marmosets, but it may not be ascribed to the biased distribution of neither large nor small DRG cells.

The size of DRG neurons in rats and marmosets are shown in **Figures 4A,B,C**. The results showed that marmosets possessed larger DRG neurons, which were especially longer than those in rats. Since body weight (**Figure 4D**) was also larger in marmosets, the size of DRG neurons might increase as a function of body size.

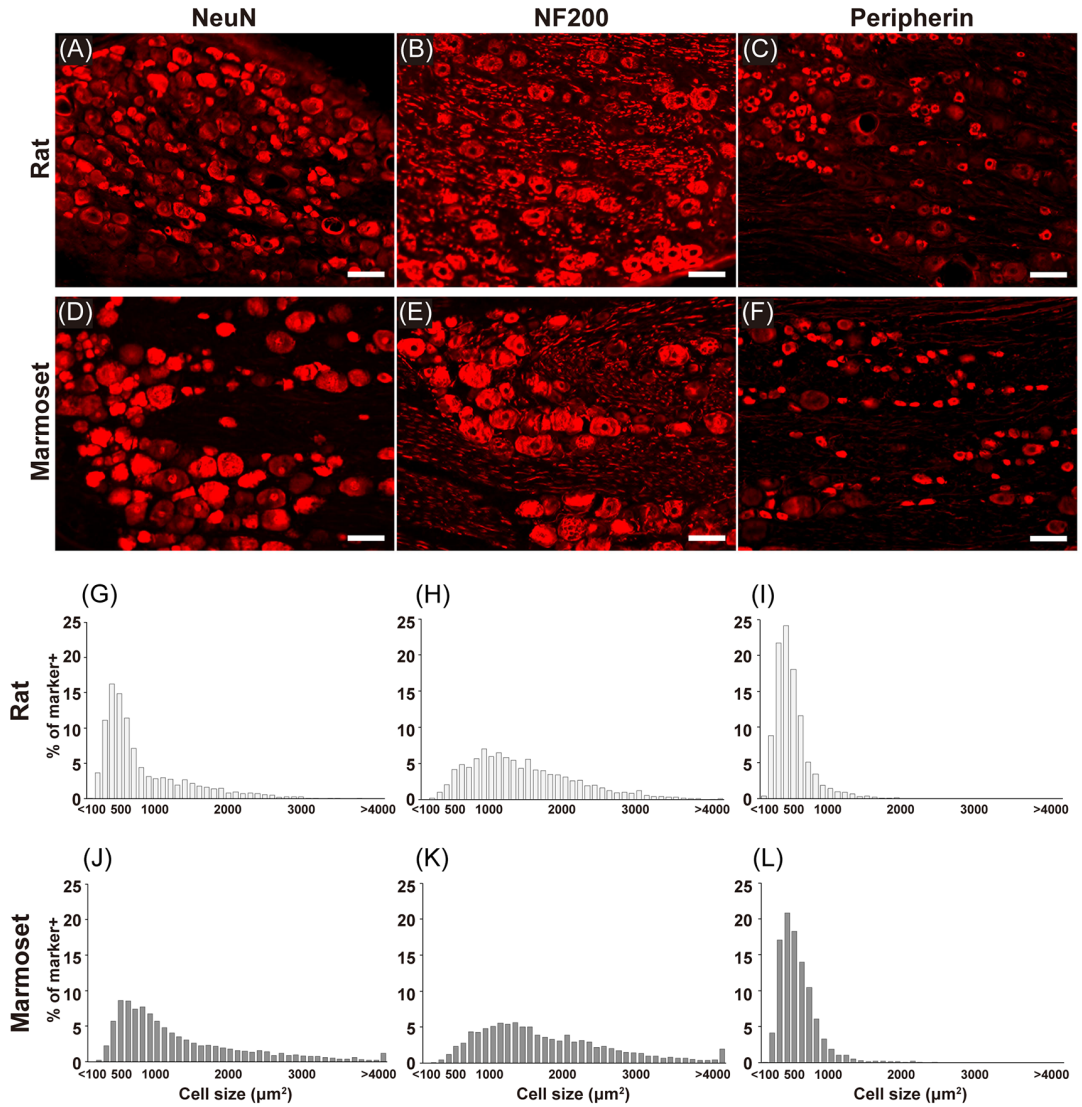

FIGURE 2 | Immunohistochemistry. Immunostaining for NeuN **(A,D)**, NF200 **(B,E)**, and peripherin **(C,F)** in the DRGs of rats **(A–C)** and marmosets **(D–F)**. Histograms showing the size distribution of NeuN- **(G,J)**, NF200- **(H,K)**, and peripherin-positive **(I,L)** cells. Scale bars: 100 μm.

DISCUSSION

In this study, we found that the sciatic nerve of marmosets originated mainly from DRGs of the 5th, 6th, and 7th lumbar spinal cord. Compared with the DRGs of rodents, in which the sciatic nerve originates from the 3rd and 4th (mice) or 4th and 5th (rats) lumbar spinal roots (Rigaud et al., 2008), we suggest that the segmental origin of the sciatic nerve in marmosets is shifted caudally. A number of studies have compared the anatomy of peripheral nerves for the lower limbs between macaque monkeys and rodents (Janjua and Leong, 1984, 1987; Yeong et al., 1998). These studies consistently reported that the segmental origins of the sciatic nerve or its downstream nerves are biased caudally in macaques compared to rats. For example, sciatic neurons are distributed to L4–7 in macaques and L3–6 in rats (Janjua and Leong, 1984). Interestingly, the human sciatic nerve originates from more caudal segments (L5–S1; Baumer et al., 2015). These comparisons among rodents, marmosets, and humans suggest that the caudal shift of sciatic nerve innervation correlates with the evolutionary status of vertebrates. Since the segmental origin of the sciatic nerve in marmosets is similar to that of macaques, which is closer to the characteristics of humans compared to rodents. The common marmoset (*Callithrix jacchus*) has attracted considerable attention in the research fields of biomedical science (Okano et al., 2012) and behavioral science (Prins et al., 2017). Furthermore, transgenic marmoset models of human disease have been developed recently (Sasaki et al., 2009; Sato et al., 2016; Tomioka et al., 2017). Our results add another example to the similarities between marmosets and humans and suggest that marmosets could be an animal model for human

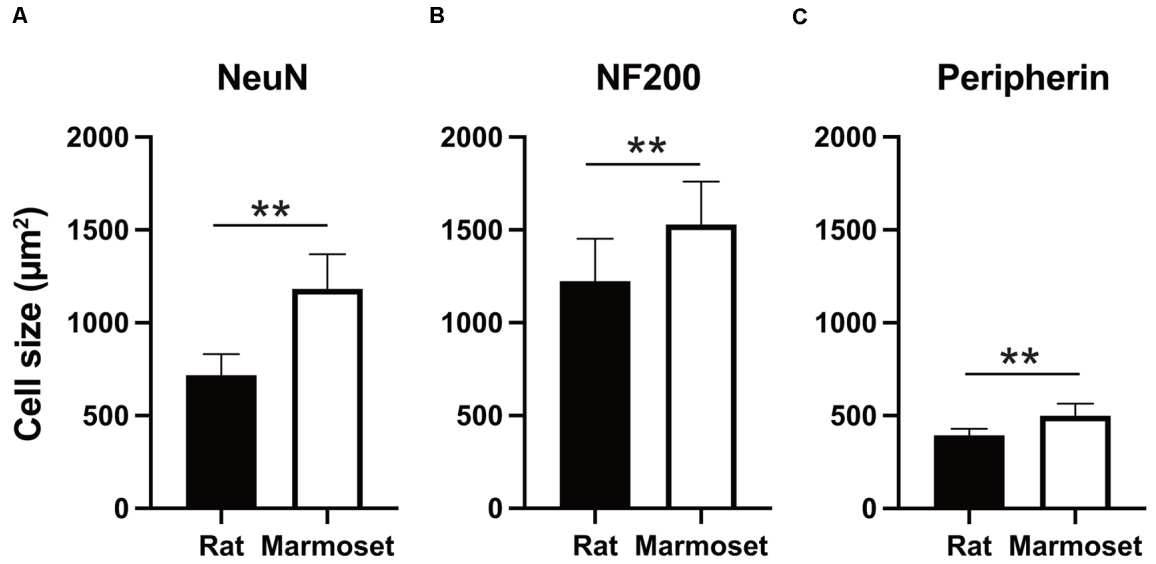

FIGURE 3 | Cell size comparison. Comparison of the size of NeuN- **(A)**, NF200- **(B)**, and peripherin-positive cells **(C)** between rats and marmosets. $^{**}p < 0.01$.

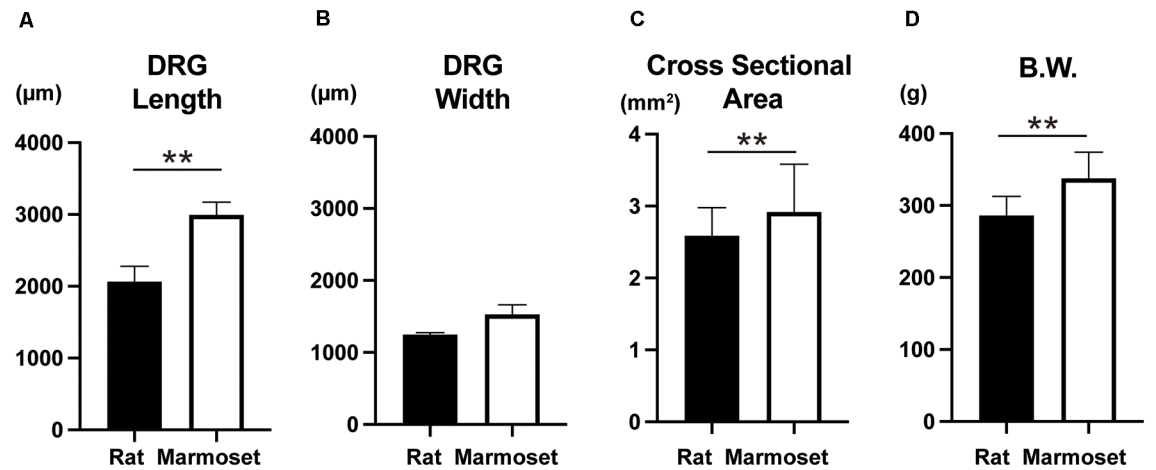

FIGURE 4 | Whole DRG size and body weight. Comparison of the whole DRG length **(A)**, width **(B)**, cross-sectional area **(C)**, and body weight **(D)** between rats ($n = 8$) and marmosets ($n = 4$ for **A**,**B**,**C** and $n = 12$ for **D**). $^{**}p < 0.01$.

peripheral nerve disorders and their treatment (Kudo et al., 2021).

In this study, we confirmed the bimodal size distribution of large and small DRG neurons in marmosets. Since comparable observations have been reported repeatedly in other species, this result was expected. Nevertheless, this finding provides invaluable information for future studies using New World monkeys as a model of the human peripheral nervous system and for the establishment of therapeutic strategies for neuronal diseases such as chronic pain syndrome. In contrast, we found that marmoset DRG cells were larger than those of rats (**Figure 3**), which is in agreement with previous studies comparing humans and rodents (Josephson et al., 2001; Haberberger et al., 2019). We hypothesize that this finding may provide support for the higher acuity and cognitive function of non-human primates for non-noxious inputs from the lower limbs compared to rats, because the relative increase in the size of large DRG neurons, and thus myelinated afferents, will increase conduction velocity in non-human primates. However, we found no difference in the size of two subpopulations of DRG neurons between rats and marmosets. This result may suggest that the size of DRG neurons with myelinated and nonmyelinated axons is increased proportionally, and thus affects the cognitive profile to noxious and non-noxious sensory inputs comparably. We rather suggest that the difference in cell size between rats and marmosets may simply correspond to the greater size of the body and peripheral nervous system of marmosets, which leads to the requirement for sensory nerves with higher conduction velocities

to perform proper sensorimotor actions using their larger bodies and limbs.

DATA AVAILABILITY STATEMENT

The original contributions presented in the study are included in the article, further inquiries can be directed to the corresponding author.

ETHICS STATEMENT

The animal study was reviewed and approved by the Ethics Committee for Animal Research of the National Institute of Neuroscience, National Center of Neurology and Psychiatry, Japan.

AUTHOR CONTRIBUTIONS

MK and SW performed the dissections. SW and MK performed the histological analyses. SK and MK performed the statistical analyses. KS conceived and designed the study and was responsible for the experiments, analyses, and interpretation of the data, as well as manuscript drafting, editing, and revising.

FUNDING

This work was supported by Grants-in-Aid from the Japan Society for the Promotion of Science, grant numbers JP19H01092, 19H05724, and 19K21825 (to KS) and JP17J05310 (to SK), and research grants from the Japan Agency for Medical Research and Development (JP21dm0207092, JP21dm0207066, and JP21dm0207077 to KS).

ACKNOWLEDGMENTS

We would like thank Drs. Ryoichi Saito and Yuko Katakai (Administrative Section of the Primate Research Facility, NCNP) for helping with the surgeries and post-surgical animal care in the marmoset experiments.

REFERENCES

Amaya, F., Decosterd, I., Samad, T. A., Plumpton, C., Tate, S., Mannion, R. J., et al. (2000). Diversity of expression of the sensory neuron-specific TTX-resistant voltage-gated sodium ion channels SNS and SNS2. *Mol. Cell Neurosci.* 15, 331–342. doi: 10.1006/mcne.1999.0828

Baumer, P., Weiler, M., Bendszus, M., and Pham, M. (2015). Somatotopic fascicular organization of the human sciatic nerve demonstrated by MR neurography. *Neurology* 84, 1782–1787. doi: 10.1212/WNL.0000000000001526

Beom, J., Kim, S., Suh, H. C., Kim, D. K., Kang, S. H., Lee, S. U., et al. (2019). Association between sensory nerve action potential and lumbar dorsal root ganglion area. *J. Clin. Neurosci.* 59, 37–40. doi: 10.1016/j.jocn.2018.11.019

Ebraheim, N. A., and Lu, J. (1998). Morphometric evaluation of the sacral dorsal root ganglia. a cadaveric study. *Surg. Radiol. Anat.* 20, 105–108.

Feliciano, C., Sosa, I., Reyes, O., Berrios, I., and Kuffler, D. P. (2007). Morphological characterization of six subpopulations of adult human DRG neurons at the light microscopic level. *P R Health. Sci. J.* 26, 7–11.

Haberberger, R. V., Barry, C., Dominguez, N., and Matusica, D. (2019). Human dorsal root ganglia. *Front. Cell Neurosci.* 13: 271. doi: 10.3389/fncel.2019.00271

Harper, A. A., and Lawson, S. N. (1985). Conduction velocity is related to morphological cell type in rat dorsal root ganglion neurones. *J. Physiol.* 359, 31–46. doi: 10.1113/jphysiol.1985.sp015573

Janjua, M. Z., and Leong, S. K. (1984). Organization of neurons forming the femoral, sciatic, common peroneal and tibial nerves in rats and monkeys. *Brain Res.* 310, 311–323. doi: 10.1016/0006-8993(84)90154-9

Janjua, M. Z., and Leong, S. K. (1987). Sensory, motor and sympathetic neurons forming the common peroneal and tibial nerves in the macaque monkey (*Macaca fascicularis*). *J. Anat.* 153, 63–76.

Josephson, A., Widenfalk, J., Trifunovski, A., Widmer, H. R., Olson, L., and Spenger, C. (2001). GDNF and NGF family members and receptors in human fetal and adult spinal cord and dorsal root ganglia. *J. Comp. Neurol.* 440, 204–217. doi: 10.1002/cne.1380

Kudo, M., Wupuer, S., Fujiwara, M., Saito, Y., Kubota, S., Inoue, K. I., et al. (2021). Specific gene expression in unmyelinated dorsal root ganglion neurons in nonhuman primates by intra-nerve injection of AAV 6 vector. *Mol. Ther. Methods Clin. Dev.* 23, 11–22. doi: 10.1016/j.omtm.2021.07.009

Lawson, S. N. (1979). The postnatal development of large light and small dark neurons in mouse dorsal root ganglia: a statistical analysis of cell numbers and size. *J. Neurocytol.* 8, 275–294. doi: 10.1007/BF01236123

Lawson, S. N., Harper, A. A., Harper, E. I., Garson, J. A., and Anderton, B. H. (1984). A monoclonal antibody against neurofilament protein specifically labels a subpopulation of rat sensory neurones. *J. Comp. Neurol.* 228, 263–272. doi: 10.1002/cne.902280211

Lawson, S. N., and Waddell, P. J. (1991). Soma neurofilament immunoreactivity is related to cell size and fibre conduction velocity in rat primary sensory neurons. *J. Physiol.* 435, 41–63. doi: 10.1113/jphysiol.1991.sp018497

Ma, Q. P. (2002). Expression of capsaicin receptor (VR1) by myelinated primary afferent neurons in rats. *Neurosci. Lett.* 319, 87–90. doi: 10.1016/s0304-3940(01)02537-x

McCarthy, P. W., and Lawson, S. N. (1997). Differing action potential shapes in rat dorsal root ganglion neurones related to their substance P and calcitonin gene-related peptide immunoreactivity. *J. Comp. Neurol.* 388, 541–549.

Ohnishi, A., and Ogawa, M. (1986). Preferential loss of large lumbar primary sensory neurons in carcinomatous sensory neuropathy. *Ann. Neurol.* 20, 102–104. doi: 10.1002/ana.410200119

Okano, H., Hikishima, K., Iriki, A., and Sasaki, E. (2012). The common marmoset as a novel animal model system for biomedical and neuroscience research applications. *Semin. Fetal Neonatal Med.* 17, 336–340. doi: 10.1016/j.siny.2012.07.002

Prins, N. W., Pohlmeyer, E. A., Debnath, S., Mylavarapu, R., Geng, S., Sanchez, J. C., et al. (2017). Common marmoset (Callithrix jacchus) as a primate model for behavioral neuroscience studies. *J. Neurosci. Methods* 284, 35–46. doi: 10.1016/j.jneumeth.2017.04.004

Pruszynski, J. A., and Johansson, R. S. (2014). Edge-orientation processing in first-order tactile neurons. *Nat. Neurosci.* 17, 1404–1409. doi: 10.1038/nn.3804

Rigaud, M., Gemes, G., Barabas, M. E., Chernoff, D. I., Abram, S. E., Stucky, C. L., et al. (2008). Species and strain differences in rodent sciatic nerve anatomy: implications for studies of neuropathic pain. *Pain* 136, 188–201. doi: 10.1016/j.pain.2008.01.016

Sasaki, E., Suemizu, H., Shimada, A., Hanazawa, K., Oiwa, R., Kamioka, M., et al. (2009). Generation of transgenic non-human primates with germline transmission. *Nature* 459, 523–527. doi: 10.1038/nature08090

Sato, K., Oiwa, R., Kumita, W., Henry, R., Sakuma, T., Ito, R., et al. (2016). Generation of a nonhuman primate model of severe combined immunodeficiency using highly efficient genome editing. *Cell Stem Cell* 19, 127–138. doi: 10.1016/j.stem.2016.06.003

Schmalbruch, H. (1987). The number of neurons in dorsal root ganglia L4–L6 of the rat. *Anat. Rec.* 219, 315–322. doi: 10.1002/ar.1092190313

Silav, G., Arslan, M., Comert, A., Acar, H. I., Kahilogullari, G., Dolgun, H., et al. (2016). Relationship of dorsal root ganglion to intervertebral foramen in lumbar region: an anatomical study and review of literature. *J. Neurosurg. Sci.* 60, 339–344.

Tomioka, I., Ishibashi, H., Minakawa, E. N., Motohashi, H. H., Takayama, O., Saito, Y., et al. (2017). Transgenic monkey model of the polyglutamine diseases recapitulating progressive neurological symptoms. *eNeuro* 4:ENEURO.0250-16.2017. doi: 10.1523/ENEURO.0250-16.2017

Toossi, A., Bergin, B., Marefatallah, M., Parhizi, B., Tyreman, N., Everaert, D. G., et al. (2021). Comparative neuroanatomy of the lumbosacral spinal cord of the rat, cat, pig, monkey and human. *Sci. Rep.* 11:1955. doi: 10.1038/s41598-021-81371-9

Umeda, T., Seki, K., Sato, M. A., Nishimura, Y., Kawato, M., and Isa, T. (2012). Population coding of forelimb joint kinematics by peripheral afferents in monkeys. *PLoS One* 7:e47749. doi: 10.1371/journal.pone.0047749

Verge, V. M., Tetzlaff, W., Bisby, M. A., and Richardson, P. M. (1990). Influence of nerve growth factor on neurofilament gene expression in mature primary sensory neurons. *J. Neurosci.* 10, 2018–2025. doi: 10.1523/JNEUROSCI.10-06-02018.1990

Warrington, W. B., and Griffith, F. (1904). On the cells of the spinal ganglia and on the relationship of their histological structure to the axonal distribution. *Brain* 27, 297–326. doi: 10.1093/brain/27.3.297

Yeong, S. O., Subramaniam, K., and Vrbova, G. (1998). Organization of common peroneal nerve motoneurones in the rat and monkey: a comparative study. *Neuroreport* 9, 1085–1088. doi: 10.1097/00001756-199804200-00023

Yoshida, S., and Matsuda, Y. (1979). Studies on sensory neurons of the mouse with intracellular-recording and horseradish peroxidase-injection techniques. *J. Neurophysiol.* 42, 1134–1145. doi: 10.1152/jn.1979.42.4.1134

Zhang, X., Priest, B. T., Belfer, I., and Gold, M. S. (2017). Voltage-gated Na(+) currents in human dorsal root ganglion neurons. *eLife* 6:e23235. doi: 10.7554/eLife.23235

Conflict of Interest: The authors declare that the research was conducted in the absence of any commercial or financial relationships that could be construed as a potential conflict of interest.

Publisher's Note: All claims expressed in this article are solely those of the authors and do not necessarily represent those of their affiliated organizations, or those of the publisher, the editors and the reviewers. Any product that may be evaluated in this article, or claim that may be made by its manufacturer, is not guaranteed or endorsed by the publisher.

Copyright © 2021 Kudo, Wupuer, Kubota and Seki. This is an open-access article distributed under the terms of the Creative Commons Attribution License (CC BY). The use, distribution or reproduction in other forums is permitted, provided the original author(s) and the copyright owner(s) are credited and that the original publication in this journal is cited, in accordance with accepted academic practice. No use, distribution or reproduction is permitted which does not comply with these terms.

frontiers in Human Neuroscience

ORIGINAL RESEARCH
published: 03 December 2021
doi: 10.3389/fnhum.2021.731677

Evaluation of Postural Sway in Post-stroke Patients by Dynamic Time Warping Clustering

Dongdong Li[1]*, *Kohei Kaminishi*[2], *Ryosuke Chiba*[3], *Kaoru Takakusaki*[3], *Masahiko Mukaino*[4] and *Jun Ota*[2]

[1] Department of Precision Engineering, School of Engineering, The University of Tokyo, Tokyo, Japan, [2] Research Into Artifacts, Center for Engineering (RACE), School of Engineering, The University of Tokyo, Tokyo, Japan, [3] Division of Neuroscience, Department of Physiology, Asahikawa Medical University, Asahikawa, Japan, [4] Department of Rehabilitation Medicine I, School of Medicine, Fujita Health University, Toyoake, Japan

Post-stroke complications are the second most frequent cause of death and the third leading cause of disability worldwide. The motor function of post-stroke patients is often assessed by measuring the postural sway in the patients during quiet standing, based on sway measures, such as sway area and velocity, which are obtained from temporal variations of the center of pressure. However, such approaches to establish a relationship between the sway measures and patients' demographic factors have hardly been successful (e.g., days after onset). This study instead evaluates the postural sway features of post-stroke patients using the clustering method of machine learning. First, we collected the stroke patients' multi-variable motion-capture standing-posture data and processed them into *t* s long data slots. Then, we clustered the *t*-s data slots into *K* cluster groups using the dynamic-time-warping partition-around-medoid (DTW-PAM) method. The DTW measures the similarity between two temporal sequences that may vary in speed, whereas PAM identifies the centroids for the DTW clustering method. Finally, we used a *post-hoc* test and found that the sway amplitudes of markers in the shoulder, hip, knee, and center-of-mass are more important than their sway frequencies. We separately plotted the marker amplitudes and frequencies in the medial-lateral direction during a 5-s data slot and found that the post-stroke patients' postural sway frequency lay within the bandwidth of 0.5–1.5 Hz. Additionally, with an increase in the onset days, the cluster index of cerebral hemorrhage patients gradually transits in a four-cluster solution. However, the cerebral infarction patients did not exhibit such pronounced transitions over time. Moreover, we found that the postural-sway amplitude increased in clusters 1, 3, and 4. However, the amplitude of cluster 2 did not follow this pattern, owing to age effects related to the postural sway changes with age. A rehabilitation doctor can utilize these findings as guidelines to direct the post-stroke patient training.

Keywords: clustering, dynamic time-warping, post-stroke, postural sway, standing posture

OPEN ACCESS

Edited by:
Giovanni Di Pino,
Campus Bio-Medico University, Italy

Reviewed by:
Taishin Nomura,
Osaka University, Japan
Luca Paolo Ardigò,
University of Verona, Italy

***Correspondence:**
Dongdong Li
li@race.t.u-tokyo.ac.jp

Specialty section:
This article was submitted to Motor Neuroscience, a section of the journal Frontiers in Human Neuroscience

Received: *28 June 2021*
Accepted: *09 November 2021*
Published: *03 December 2021*

Citation:
Li D, Kaminishi K, Chiba R, Takakusaki K, Mukaino M and Ota J (2021) Evaluation of Postural Sway in Post-stroke Patients by Dynamic Time Warping Clustering. Front. Hum. Neurosci. 15:731677. doi: 10.3389/fnhum.2021.731677

1. INTRODUCTION

A stroke is mainly caused by a lack of oxygen when the brain's blood flow is interrupted by a blockage (i.e., cerebral infarction, CI) or an artery rupture (i.e., cerebral hemorrhage, CH). Stroke patients tend to inherit an irregular postural sway during quiet standing (Chern et al., 2010), which increases the risk of falling. In this regard, evaluation of their quiet standing postural sway is essential.

Researchers have evaluated the quiet standing postural sway of post-stroke patients for many years. However, the postural sway features (e.g., sway amplitude) of the patients can be different because of different patient demographic factors (e.g., days after onset, age, and the influence of the level of damage in lesion regions) (Bansil et al., 2012; Cho et al., 2014; Halmi et al., 2020). Unfortunately, the relationship between postural sway features and patient demographic factors has not been well-studied. Some researchers focused only on sway amplitude. For example, Mizrahi et al. (1989) measured and analyzed the bilateral forces of the supporting limbs of stroke patients and found that they had significantly higher sway activity compared with normal controls. In the anterior-posterior and medial-lateral (ML) directions, (Wang et al., 2017) found that stroke patients had a more pronounced center-of-pressure (COP) sway than healthy people. Paillex and So (2005) demonstrated that temporal patterns of the difference between the COP and center-of-gravity could be characterized differently for healthy subjects and patients. Some researchers revealed greater sway activity in hemiplegic subjects compared with normal controls (Mizrahi et al., 1989).

Furthermore, machine-learning methods (e.g., multivariate time-series clustering) can find postural sway features using complete time-series data. For Parkinson's disease, Das et al. (2011) explored the motor symptoms of patients using a motion-capture system and a support vector machine. However, only a few studies have thus far analyzed the differences in post-stroke patients' quiet standing postural sway. Furthermore, there is no consensus with regards to the best method or feature set for analyzing motion-capture data to understand and assess post-stroke postural sway.

Hence, this study evaluates postural-sway features of post-stroke patients using a motion-capture system with a multivariate time-series machine-learning clustering technique.

The remainder of this paper is organized as follows. Section 2 reports the method of clustering and parameter distribution calculation. Section 3 presents the results. Section 4 discusses the implications of the results. Finally, we present the conclusions in section 5.

2. METHODS

In this section, we describe our research method (**Figure 1**). First, the kinematic posture data of patients are measured, as detailed in section 2.1. Then, we extract features, as presented in section 2.2. Next, the clustering method is described in section 2.3. Finally, we calculate the parameter distribution, as detailed in section 2.4.

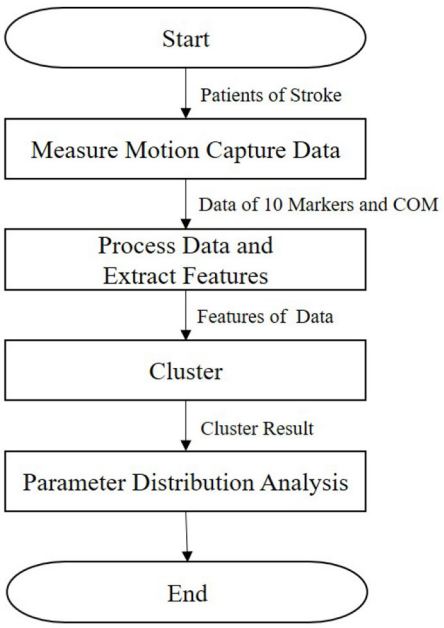

FIGURE 1 | Workflow of the methods used in this study.

2.1. Motion-Capture Measurement

2.1.1. Study Population

Fujita Health University recruited the study subjects for our research. According to the agreement approved by the University Ethics Committee, all subjects provided informed written consent (HM18-467). We hired 10 male subjects. Five were CH, and five were CI; their statistical information is shown in **Table 1**. We added new data to previous research results (Li et al., 2021), including ages, days after onset, and hemiplegia. In our previous work (Li et al., 2021), we assumed that CH and CI presented differences in standing posture and leveraged a support vector machine for classification. However, in this paper, we evaluate the postural sway of post-stroke patients in a quiet standing position via clustering.

2.1.2. Patient Data Collection

A 3-dimensional (3D) motion analysis system, KinemaTracer© (KISSEI COMTEC, Matsumoto, Japan), was used to precisely measure the quiet standing posture of post-stroke patients. The system hardware leveraged one recording/analyzing laptop and four charge-coupled-device cameras arranged around a standing platform on a level floor without a handrail. As shown in **Figure 2**, we attached the markers (30-mm diameter) to the acromion on both sides of the subject: the hip joint (positioned on the line connecting the superior anterior iliac spine and greater trochanter at 1/3 of the distance from greater trochanter), the knee joint (the AP midpoint of the lateral epicondyle of the femur), the ankle joint (exterior), and the toes (fifth metatarsal head). The measurement sampling frequency was 60 *Hz* for 30 *s*. A more detailed description of our methodology and

TABLE 1 | Subject information.

Name index	Disease	Age	Days after onset	Hemiplegia side
CH1	Cerebral hemorrhage	54	1108/1150	Right
CH2	Cerebral hemorrhage	48	122/129/136/143	Left
CH3	Cerebral hemorrhage	59	51/58/65/79/93	Left
CH4	Cerebral hemorrhage	63	520/527/534	Either
CH5	Cerebral hemorrhage	54	315/340/358	Right
CI1	Cerebral infarction	52	74/88/109/176	Right
CI2	Cerebral infarction	75	132/147	Left
CI3	Cerebral infarction	80	69/80	Right
CI4	Cerebral infarction	63	91/108	Left
CI5	Cerebral infarction	69	992/1007/1020/1051	Right

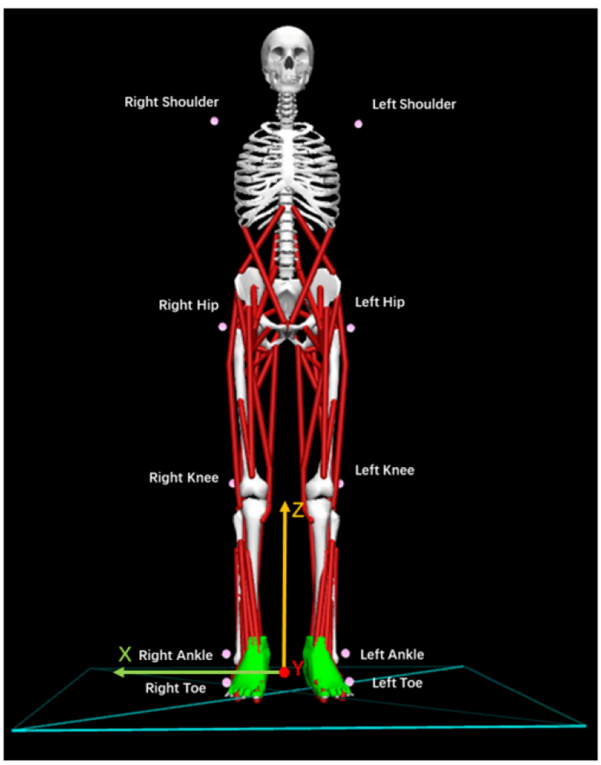

FIGURE 2 | Location and names of markers attached to the patients. Ten pink markers were attached to the body symmetrically.

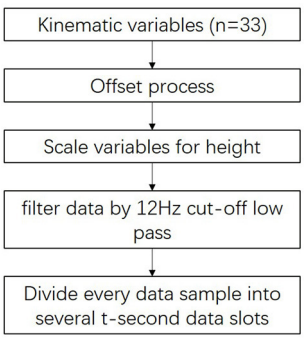

FIGURE 3 | Methodology framework of the feature extraction described in section 2.2.

mathematical formulas for data collection can be found in Matsuda et al. (2016) and Li et al. (2021).

2.2. Data Processing and Feature Extraction

2.2.1. Kinematic Collected Variables

In this study, we utilized 33 kinematic variables extracted from the 3D motion analysis system for post-stroke patients' postural-sway evaluation. The kinematic variables contain 3D displacements (X-axis, Y-axis, Z-axis) of the center of mass (COM) and 3D displacements of 10 markers during the 30-s period. Hence, we collected 33 kinematic variables.

2.2.2. Feature Extraction

We extracted features for use when clustering post-stroke patient data with high performance. The methodology of this process is described in **Figure 3**.

First, the variables were offset by setting the location of the ankle markers as midpoints as the patient stands on the front part of the level floor.

Next, we eliminated the anthropometric differences between subjects using the distance between shoulder and ankle markers using Equation (1):

$$p_i^{'} = \frac{p_i}{l_1 + l_2 + l_3}, i = 1, 2, ..., n, \quad (1)$$

where p_i is the i-th X/Y/Z-axis position of the kinematic variable; $p_i^{'}$ is the i-th X/Y/Z scaled marker position; l_1 is the average distance between the shoulder and hip markers; l_2 is the average distance between the hip and knee markers; and l_3 is the average distance between the knee and ankle markers. n is the number of kinematic variables, and the value of n was set to 33.

Next, we used a double-pass, second-order Butter-worth low-pass filter with a cutoff frequency of 12 Hz to filter the $p^{'}$ data.

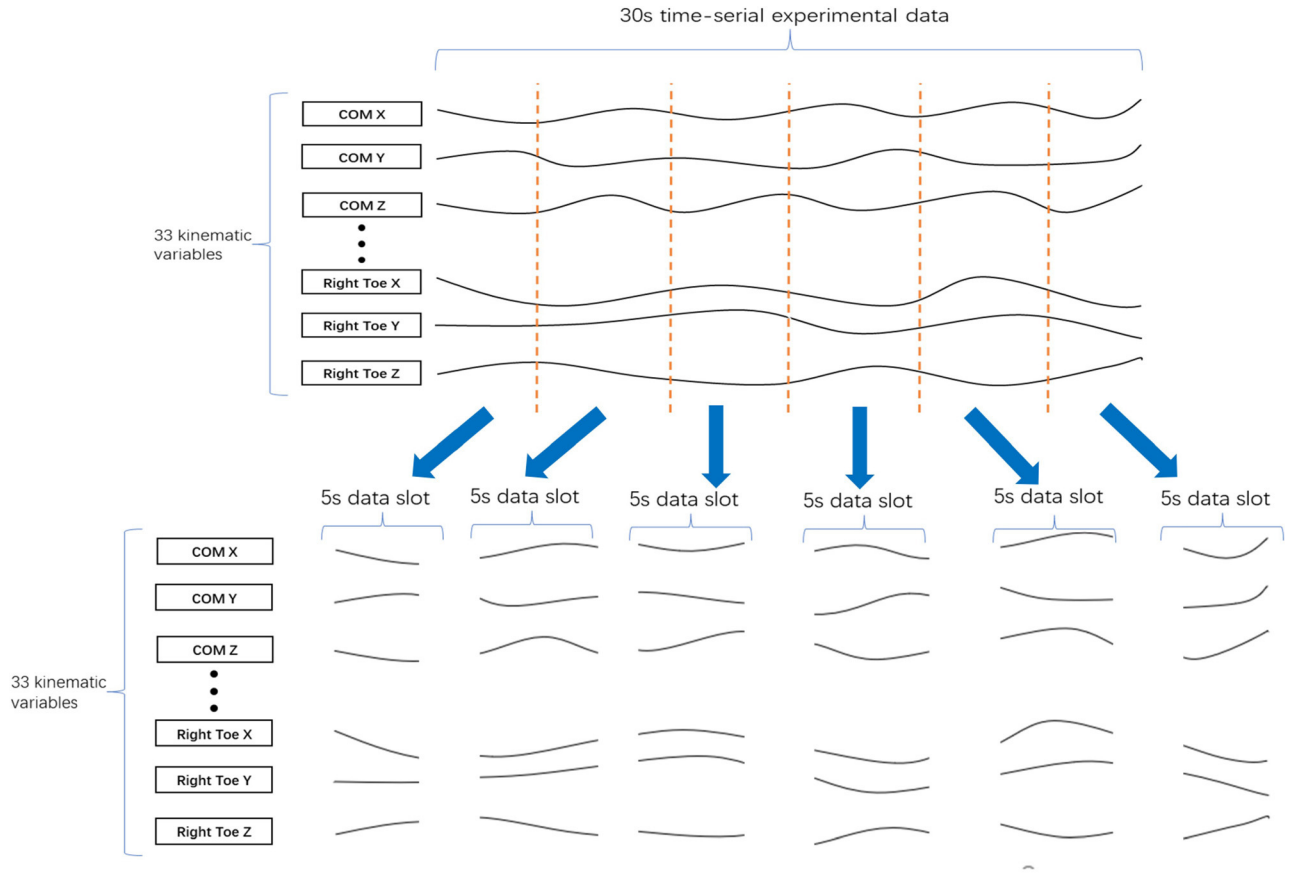

FIGURE 4 | Division of 30 s of data into six 5-s data slots. A 30 s set of experimental data with 33 kinematic variables was divided into six of 5-s data slots, where each data slot has 33 kinematic variables.

Thus, the noise arising from changes in the orientation of the subject's body and other factors during measurement (Abdulhay et al., 2018) were removed.

Finally, to increase the data set size for each cluster, we divided every 30-s data sample into several data slots t seconds in length. For example, the division of a 30-s data sample into six 5-s data slots is shown in **Figure 4**. To determine the best value of t, we tested a range (t = 3, 5, 6, and 10) by evaluating the clustering results.

2.3. Clustering

To find the postural-sway patterns of the post-stroke patients and to identify the relationships between the patient body displacement and their different characteristics (e.g., age, days after onset, and hemiplegia side), we used the multivariate time-series (MTS) clustering method. In a related field, numerous MTS methods have been explored (Montero and Vilar, 2014; Brandmaier, 2015; Genolini et al., 2015; Sardá-Espinosa, 2019).

As one method of MTS clustering, partitioning clustering with dynamic time warping (DTW) clustering is used to evaluate the similarity of different data slots (Malik and Lai, 2017; Rybarczyk et al., 2018). In **Figure 5**, the DTW compares the similarity between two temporal sequences (Data A and B), which may vary in speed. The DTW is used for temporal sequences, such as video, audio, and graphics data. Moreover, compared with other MTS clustering methods (e.g., a permutation distribution cluster), DTW provides faster calculations (Montero and Vilar, 2014; Sardá-Espinosa, 2019). Therefore, we used the DTW method to evaluate the similarity of data slots from different patients. To illustrate the similarity exhibited by data slots of 5 s in length in the case of postural sway, we present **Figures 5B–D** which show the similarity in 5-s slot data taken from individuals as well as from different patients. Moreover, we can evaluate the sway amplitude and frequency measured from the data slot as its similarity feature via DTW. Furthermore, this method calculates the distance between all points in the data; hence, the smaller the gap, the closer the match. The DTW could work well on the 33 kinematic variables because the postural sway of human is periodic (Giveans et al., 2011). All periods of sway data are similar. Thus, we assumed they can be detected by DTW. Moreover, to avoid the cut off of such periods, based on the period, we divide the 30 s of data into t-s data slots. Another researcher also used DTW to detect hip sway (Cuntoor et al., 2003).

After assessing the similarity between different slots, DTW clustering divides data slots into K clusters, and each cluster

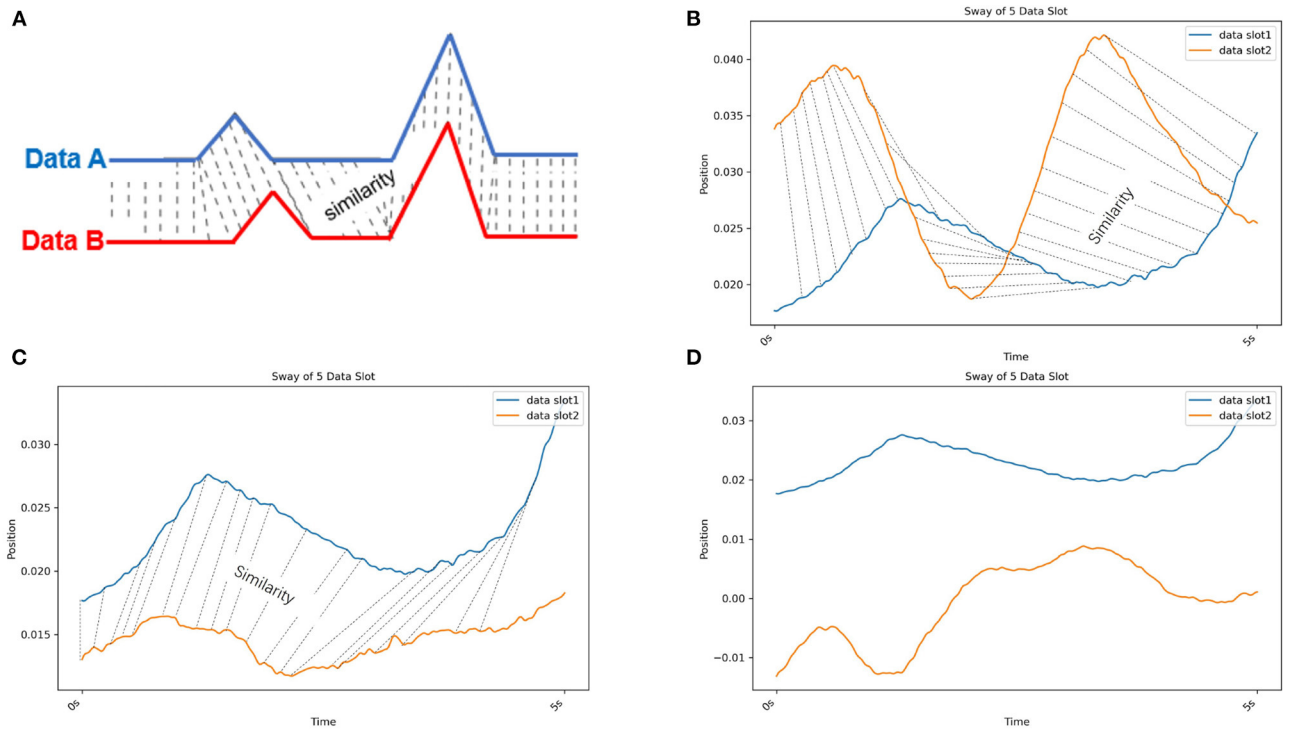

FIGURE 5 | (A) Dynamic time warping (DTW). DTW compares the similarity between two temporal sequences (Data A in blue and B in red) that can vary in speed. **(B)** Dynamic time warping (DTW) with real postural sway data from the same individual. The blue and orange lines are the COM X data of different data slots from CH2. **(C)** Dynamic time warping (DTW) with real postural sway data from different patients in the same cluster. The blue line is the COM X data of a data slot from CH2. Orange line is the COM X data of a data slot from CH3. **(D)** Dynamic time warping (DTW) with real postural sway data from different patients in different clusters. The blue line is the COM X data of a data slot from CH2. The orange line is the COM X data of a data slot from CH5. Because the similarity of these two data slots is low, no similarity lines could be drawn.

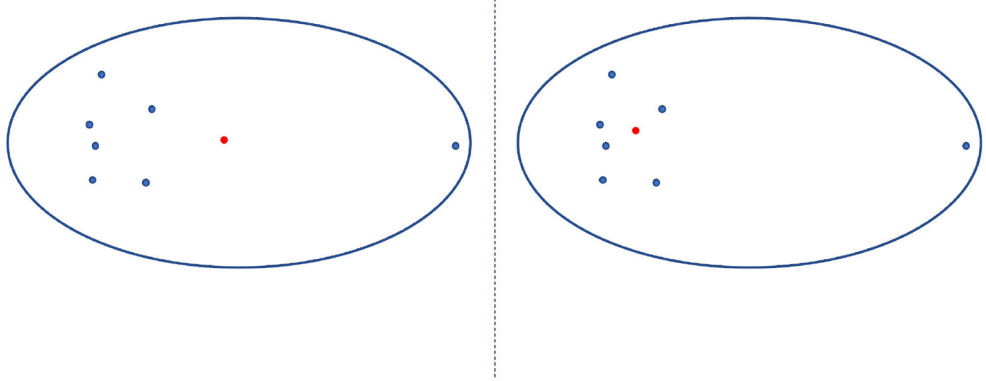

FIGURE 6 | Mean center vs. medoid center. The mean center is indicated by the red dot in the left panel and differs the medoid center (indicated by the red dot in the right panel), which is the most central object in the clusters with the smallest sum of distances from other data.

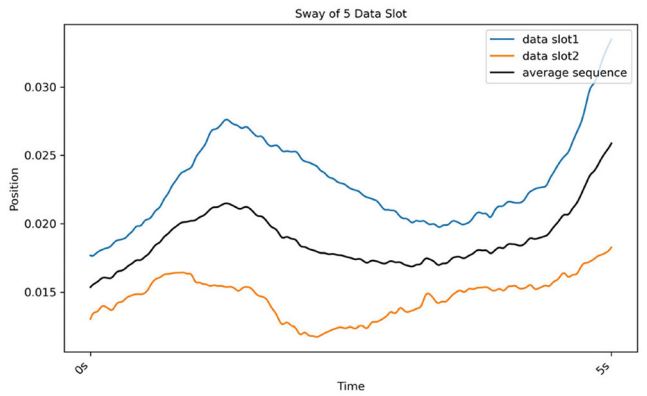

FIGURE 7 | Results of DBA, which gradually determines the average sequence (black line) of two sequences (red line from CH2 and blue line from CH3).

has a centroid. Here, the cluster implies a group wherein the data slots are more similar than those in other groups. Moreover, the centroid is the cluster center. We attempted two different centroid calculation methods. One is the partition-around-medoid (PAM) method, and another is DTW barycenter averaging (DBA) (Sardá-Espinosa, 2019).

The PAM is a method to find K-medoids point of clustering (Mannor et al., 2011). First, PAM selects K representative medoids (the most central clusters) to construct an initial cluster. Then, it continuously changes the medoids to find a better cluster representative with more significant reductions in distortion function. In each iteration, the set of best medoids for each cluster forms a new respective medoid. As shown in a 2-dimensional example of **Figure 6**, the medoid center in the red dot in the right figure is the most central object in the clusters with the smallest sum of distances from other data, which differs from the mean center in the red dot in the left figure.

The DBA refines another method of finding the K-medoids method. Here, medoids were defined as an average sequence of sets of sequences. The cluster was divided based on the distance between the average sequence and sets of sequences (Petitjean et al., 2011). Real postural sway (marker) data is used to further illustrate this process in **Figure 7**.

We present the set of 5-s data slots as an example. The input data consisted of 186 sets of 33 × 300-dimensional vector data representing the standardized X/Y/Z-axis positions of 10 markers and a COM from 31 sets of 30 s of experimental data. We had 31 of 30 s experimental data. Every 30 s of data was divided into six slots of 5-s data. Hence, we had a total of 31 × 6 (186) sets of (33 × 300)-dimensional vector data. Because the measurement sampling frequency was 60 Hz for 30 s, for 5 s data, the number of columns is 60 Hz × 5 s (300). The DTW clustering compared each vector of one data slot and its corresponding vector of another. We randomly initialized the centroid of the cluster, and to avoid the effect of random errors in a centroid and to choose the best clustering solution, we repeated the process 10 times for the data set.

TABLE 2 | DTW-PAM result.

Data slot time t	Cluster number K	Cluster validity		
		C-H index	DB index	D index
3 s	3	98.70	1.73	0.03
	4	76.70	1.63	0.02
	5	63.78	1.29	0.03
5 s	3	58.70	1.55	0.06
	4	60.84	1.45	0.01
	5	45.36	1.19	0.06
6 s	3	47.90	1.76	0.09
	4	34.78	2.37	0.02
	5	35.88	1.42	0.03
10 s	3	27.89	1.85	0.22
	10	18.15	1.30	0.05
	5	19.87	2.19	0.03

TABLE 3 | DTW-DBA result.

Data slot time t	Cluster number K	Cluster validity		
		C-H index	DB index	D index
3 s	3	103.38	1.60	0.04
	4	83.89	1.69	0.04
	5	83.17	1.53	0.04
5 s	3	63.80	1.57	0.24
	4	53.48	1.49	0.04
	5	40.92	1.10	0.24
6 s	3	52.39	1.98	0.06
	4	43.24	1.45	0.09
	5	37.20	1.24	0.11
10 s	3	28.32	1.56	0.08
	4	24.44	1.72	0.09
	5	23.17	1.35	0.27

TABLE 4 | Characteristics of cluster under data time slot = 5 s, $K = 4$.

Cluster index	Days after onset	Age	Disease-type percentage
Cluster 1	1,108	54	CH: 0.6, CI: 0.4
Cluster 2	520	63	CH: 0.75, CI: 0.25
Cluster 3	340	54	CH: 0.95, CI: 0.05
Cluster 4	109	59	CH: 0.43, CI: 0.57

Afterwards, the method of determination of the best K clusters was introduced. First, to avoid the effect of random centroid behaviors and to choose the best clustering solution, we repeated the process 10 times for each data slot. Next, we evaluated the cluster solution using three cluster indices, including the Davies-Bouldin (DB) index (Davies and Bouldin, 1979), the Calinski-Harabasz (C-H) index (Caliński and Harabasz, 1974), and the Dunn (D) index (Dunn, 1974), separately. These three indices

evaluated the minimum value of the product of mean and the SD of the intra-cluster gap.

The DB is shown in Equation (2), where K is the number of clusters. In cluster i, δ_i is the mean gap between data units to their cluster centers, c_i. In cluster j, δ_j is the mean gap between all data units to their cluster centers, c_j. $d(c_i, c_j)$ is the gap of cluster centers, c_i and c_j. The best cluster solution has the minimum DB value.

$$DB = \frac{1}{K} \sum_{i=1, i \neq j}^{K} max \left(\frac{(\delta_i + \delta_j)}{d(c_i, c_j)} \right). \quad (2)$$

The C-H index is defined Equation (3), where K is the number of clusters and N is the volume of the data set. The BGSS indicates the sum of squares of the partition between clusters, and WGSS represents the sum of squares of the partition within a cluster. The best cluster result has the biggest indicator value.

$$C - H = \frac{(N - K)}{(K - 1)} \times \frac{BGSS}{WGSS}. \quad (3)$$

In the cluster, the D index is defined as value calculated by dividing the smallest distance (d_{min}) within the cluster to the biggest distance (d_{max}), as shown in 4:

$$D = \frac{d_{min}}{d_{max}}. \quad (4)$$

2.4. Parameter Distribution Calculation

After obtaining clustering solutions of the ts data slot and the K cluster, we analyzed the sway features of each kinematic variable of t-s data slots between clusters by applying a *post-hoc* test.

Here, based on previous research (Petri, 2002; Paillex and So, 2005; Abdulhay et al., 2018), we calculated three kinds of sway feature parameters for each kinematic variable of t-s data slots: amplitude, standard deviation (SD), and sway frequency. Amplitude is defined as the gap between maximum and minimum values of one kinematic variable in one t-s data slot. The SD is defined as the standard deviation of one kinematic variable in one t-s data slot. Sway frequency is defined as the frequency value corresponding to the first most prominent peak in frequency domain map by the fast Fourier transform.

Before implementing the *post-hoc* test, we first determined the *post-hoc* test method by observing distribution and the homogeneity level of parameters using Shapiro-Wilk (Mohd Razali and Bee Wah, 2011) and Bartlett's tests (Tobias and Carlson, 1969). If the parameter data follow a normal distribution and display homogeneity of variance, we can use Turkey-Kramer *post-hoc* method. Otherwise, we use a pairwise Wilcoxon test (Pohlert, 2014) with a Benjamini-Hochberg p-value adjustment method. Therefore, we performed a *post-hoc* test to find which cluster pairs were significant to each parameter.

We consider the case of the left shoulder marker when the data slot is 5 s and K = 4 as an example. First, based on the clustering result, we grouped the 186 data slots into four groups. Then for each group, we extracted the 5-s left-shoulder markers' x, y, and z values from each slot. Then, we calculated amplitude, SD, and sway frequency for each kinematic variable in each data slot. Finally, we implemented the *post-hoc* to find the significant kinematic variables for discussion.

3. RESULTS

3.1. General Cluster Performance

In this work, we used two models, DTW-PAM and DTW-DBA. Based on the cluster validity evaluation, we compared the cluster results in which the data-slot time, t, was in the range of 3, 5, 6, and 10 s; K was in the range of 3, 4, and 5; and the method was DTW-PAM or DTW-DBA, as shown in **Tables 2**, **3**. Then, we found that the DTW-PAM model of the t = 5-s data slot with K = 4 was better than the other results. Hence, we inferred from the clustered index that there was a difference in the standing postures of post-stroke patients. Then, only the detailed solution of DTW-PAM was introduced.

Finally, based on the clustering result of the t = 5-s data slot with K = 4 on the DTW-PAM model, we observed and calculated the median value of days after onset, age, and disease-type percentage from the first to the fourth clusters, as shown in **Table 4**.

3.2. Parameter Distribution Analysis

To analyze the sway features of each kinematic variable of t-s data slots between clusters, first, using the Shapiro-Wilk test, we found that the parameters did not follow a normal distribution and displayed homogeneity of variance. Therefore, we used the pairwise Wilcoxon test (Pohlert, 2014) to perform the *post-hoc* test to find clusters representing significant differences. In **Table 5**, the *post-hoc* test subjects and results are listed. For each axis of each body on the left or right side (indexed from 1 to 33), we performed a *post-hoc* test to determine which cluster pairs had significant differences. The result shows that the differences between clusters are mainly explained by amplitude and SD. In **Table 5**, the contribution of the shoulder, hip, knee, and COM variables that are particularly significant are colored blue. As a result, we present **Figures 8**, **9**, whose x-axes represent the ML amplitude after normalization and postural-sway frequency, respectively. The kinematic variables of the three axes (x, y, z) are likely to be strongly correlated with each other in **Table 5**. Thus, only the values of the index in the X-axis (ML) are shown. The left and right sides are similar; only the left side is shown.

Meanwhile, from **Table 4**, we find that from clusters 1 to 4, the days after onset value decreased. From **Figure 8**, we observed a pattern from clusters 1, 3, and 4 in which the amplitude increased, meaning that as days from post-stroke onset decreased, the postural-sway amplitude increased.

Then, we created the days-after-onset cluster table to explore the transition pattern of days after onset in CH and CI separately in **Table 6**, where we used numbers 1–4 and colors from blue to red to represent the clustered data from days after onset. The numbers from 0 to 1,000 indicate the days after onset for

TABLE 5 | *Post-hoc* test results for each axis of each body on the left or right side to determine significant kinematic variables.

Amplitude					SD					Frequency				
Index	**Part**	**L/R**	**Axis**	***Post-hoc* test result**	**Index**	**Part**	**L/R**	**Axis**	***Post-hoc* test result**	**Index**	**Part**	**L/R**	**Axis**	***Post-hoc* test result**
1	COM	None	X	1&2, 1&3, 1&4, 2&3, 2&4	1	COM	None	X	1&2, 1&3, 1&4, 2&3, 2&4	1	COM	None	X	None
2	COM	None	Y	1&2, 1&3, 1&4, 2&3, 2&4	2	COM	None	Y	1&2, 1&3, 1&4, 2&3, 2&4	2	COM	None	Y	None
3	COM	None	Z	1&2, 1&3, 1&4, 2&4, 3&4	3	COM	None	Z	1&2, 1&3, 1&4, 2&4, 3&4	3	COM	None	Z	None
4	Shoulder	Left	X	1&2, 1&3, 1&4, 2&3, 2&4	4	Shoulder	Left	X	1&2, 1&3, 1&4, 2&3, 2&4	4	Shoulder	Left	X	None
5	Shoulder	Left	Y	1&2, 1&3, 1&4, 2&3, 2&4	5	Shoulder	Left	Y	1&2, 1&3, 1&4, 2&3, 2&4	5	Shoulder	Left	Y	1&4
6	Shoulder	Left	Z	1&2, 1&3, 1&4, 2&3, 2&4	6	Shoulder	Left	Z	1&2, 1&3, 1&4, 2&3, 2&4	6	Shoulder	Left	Z	None
7	Shoulder	Right	X	1&2, 1&3, 1&4, 2&3, 2&4	7	Shoulder	Right	X	1&2, 1&3, 1&4, 2&3, 2&4	7	Shoulder	Right	X	None
8	Shoulder	Right	Y	1&2, 1&3, 1&4	8	Shoulder	Right	Y	1&2, 1&3, 1&4	8	Shoulder	Right	Y	3&4
9	Shoulder	Right	Z	1&2, 1&3, 1&4, 2&4	9	Shoulder	Right	Z	1&2, 1&3, 1&4, 2&4	9	Shoulder	Right	Z	None
10	Hip	Left	X	1&2, 1&3, 1&4, 2&3, 2&4	10	Hip	Left	X	1&2, 1&3, 1&4, 2&3	10	Hip	Left	X	None
11	Hip	Left	Y	1&2, 1&3, 1&4, 2&3, 2&4	11	Hip	Left	Y	1&2, 1&3, 1&4, 2&3, 2&4	11	Hip	Left	Y	None
12	Hip	Left	Z	1&2, 1&3, 1&4, 2&4	12	Hip	Left	Z	1&2, 1&3, 1&4, 2&4	12	Hip	Left	Z	None
13	Hip	Right	X	1&2, 1&3, 1&4, 2&3	13	Hip	Right	X	1&2, 1&3, 1&4, 2&3	13	Hip	Right	X	None
14	Hip	Right	Y	1&2, 1&3, 1&4, 2&3, 2&4	14	Hip	Right	Y	1&2, 1&3, 1&4	14	Hip	Right	Y	None
15	Hip	Right	Z	1&2, 1&3, 1&4	15	Hip	Right	Z	1&2, 1&3, 1&4	15	Hip	Right	Z	None
16	Knee	Left	X	1&2, 1&3, 1&4, 2&3, 3&4	16	Knee	Left	X	1&2, 1&3, 1&4, 2&3, 3&4	16	Knee	Left	X	None
17	Knee	Left	Y	1&2, 1&3, 1&4	17	Knee	Left	Y	1&2, 1&3, 1&4	17	Knee	Left	Y	None
18	Knee	Left	Z	1&2, 1&3, 1&4, 2&4	18	Knee	Left	Z	1&2, 1&3, 1&4, 2&4	18	Knee	Left	Z	1&2, 2&4
19	Knee	Right	X	1&2, 1&3, 1&4, 2&3	19	Knee	Right	X	1&2, 1&3, 1&4	19	Knee	Right	X	None
20	Knee	Right	Y	1&2, 1&3, 1&4	20	Knee	Right	Y	1&2, 1&3, 1&4	20	Knee	Right	Y	None
21	Knee	Right	Z	None	21	Knee	Right	Z	None	21	Knee	Right	Z	None
22	Ankle	Left	X	3&4	22	Ankle	Left	X	None	22	Ankle	Left	X	1&4
23	Ankle	Left	Y	1&2, 2&3, 2&4	23	Ankle	Left	Y	1&2, 2&3, 2&4	23	Ankle	Left	Y	None
24	Ankle	Left	Z	1&2, 2&3, 2&4	24	Ankle	Left	Z	1&2	24	Ankle	Left	Z	None
25	Ankle	Right	X	1&3, 1&4, 2&3, 2&4	25	Ankle	Right	X	1&3, 2&3	25	Ankle	Right	X	1&2
26	Ankle	Right	Y	1&4, 2&4	26	Ankle	Right	Y	None	26	Ankle	Right	Y	None
27	Ankle	Right	Z	1&2, 1&3, 1&4, 2&4	27	Ankle	Right	Z	1&3, 1&4	27	Ankle	Right	Z	None
28	Toe	Left	X	1&3, 1&4, 2&3, 2&4	28	Toe	Left	X	1&3, 1&4, 2&3	28	Toe	Left	X	None
29	Toe	Left	Y	None	29	Toe	Left	Y	None	29	Toe	Left	Y	None
30	Toe	Left	Z	None	30	Toe	Left	Z	None	30	Toe	Left	Z	None
31	Toe	Right	X	1&2, 1&4, 2&3, 2&4	31	Toe	Right	X	1&2, 2&3, 2&4	31	Toe	Right	X	None
32	Toe	Right	Y	1&2, 1&4, 2&4	32	Toe	Right	Y	1&2, 2&3, 2&4	32	Toe	Right	Y	None
33	Toe	Right	Z	None	33	Toe	Right	Z	None	33	Toe	Right	Z	None

Taking the first line of Amplitude as an example, "1&2" means the kinematic variable COM X was shown to be significant in clusters 1 and 2 by the post-hoc test. The contribution of the shoulder, hip, knee, and COM variables were particularly significant (indicated by blue).

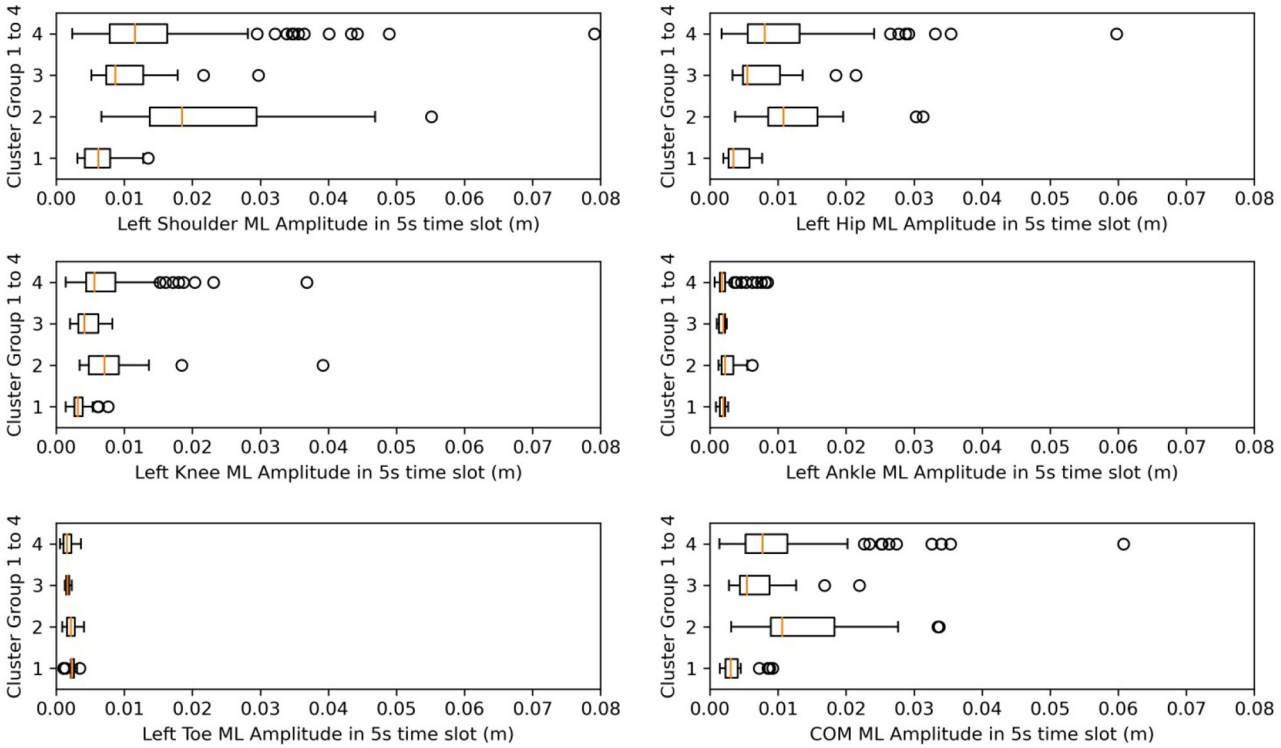

FIGURE 8 | Box plots for amplitude in ML. X-axes represent the amplitude after normalization in the ML direction.

each cluster group. We can see that as the days after onset increased, CH patients transited from clusters 4 to 3, to 2, and to 1, in order, whereas for CI patients, they did not show a pronounced transition over time. Moreover, in **Table 6**, CH3, CI1, CI2, and CI4 was the cluster which was clustered into different clusters, because it is difficult to cluster them perfectly in machine learning. Clusters in which many data slots are clustered are considered to be the main clusters.

4. DISCUSSION

This study aimed to determine and understand the postural-sway features of post-stroke patients in quiet standing postures. Using DTW-PAM, differences were observed between patient clusters. The markers' amplitude, SD, and frequency indicated that disease-days after onset and disease subtypes (CH or CI) contributed more to postural-sway features than did other features.

After analyzing **Table 5**, we determined that amplitude had a similar significance performance as the SD, and it had greater significance than did frequency in the clusters, meaning that amplitude and SD were more valuable than the frequency in the clusters. In particular, the differences were more pronounced in the shoulder, hip, and knee. This finding may provide a focus area for post-stroke patient therapy. From **Figure 8**, we found that the upper parts of limbs (e.g., shoulder, hip, and COM) had significantly larger amplitude values than did the lower parts of limbs (e.g., knee, ankle, and toes). This finding is similar to a previous study that showed that waist sway was more significant than leg sway (Dickstein and Abulaffio, 2000). From **Table 4** and **Figure 8**, we found that as days from post-stroke onset decreased; the postural-sway amplitude increased in clusters 1, 3, and 4. However, the amplitude of cluster 2 did not follow this pattern, which may be due to age effects that there was a relationship between postural sway changing with age (Kim et al., 2010).

Frequency was not significantly different in the *post-hoc* test, but we found that the frequency of postural sway fell in 0.5–1.5 Hz for COM, and from cluster 3, CH subjects of lower age and lower days after onset kept their sway frequencies within 0.6–0.7 Hz. A previous researcher found that frequency of body sway fell in the range of 0.1–0.2 Hz (Koltermann et al., 2019), and because they also found that post-stroke increases sway frequency (Mizrahi et al., 1989), our finding was found to be reasonable.

Furthermore, in **Table 6**, we observed that CH-patient body postural sway gradually changed as days after onset increased (clusters 4 to 1). Meanwhile, CI-patient body postural sway did not show the same onset-days correlation. Another researcher found that CH patients made more significant recovery gains, although they had more excellent functional (motor) impairments (e.g., standing and walking) than CI patients. They also found that CH patients having the most severe disability improved more than those with CI of comparable severity (Kelly et al., 2003; Katrak et al., 2009). From this knowledge, we

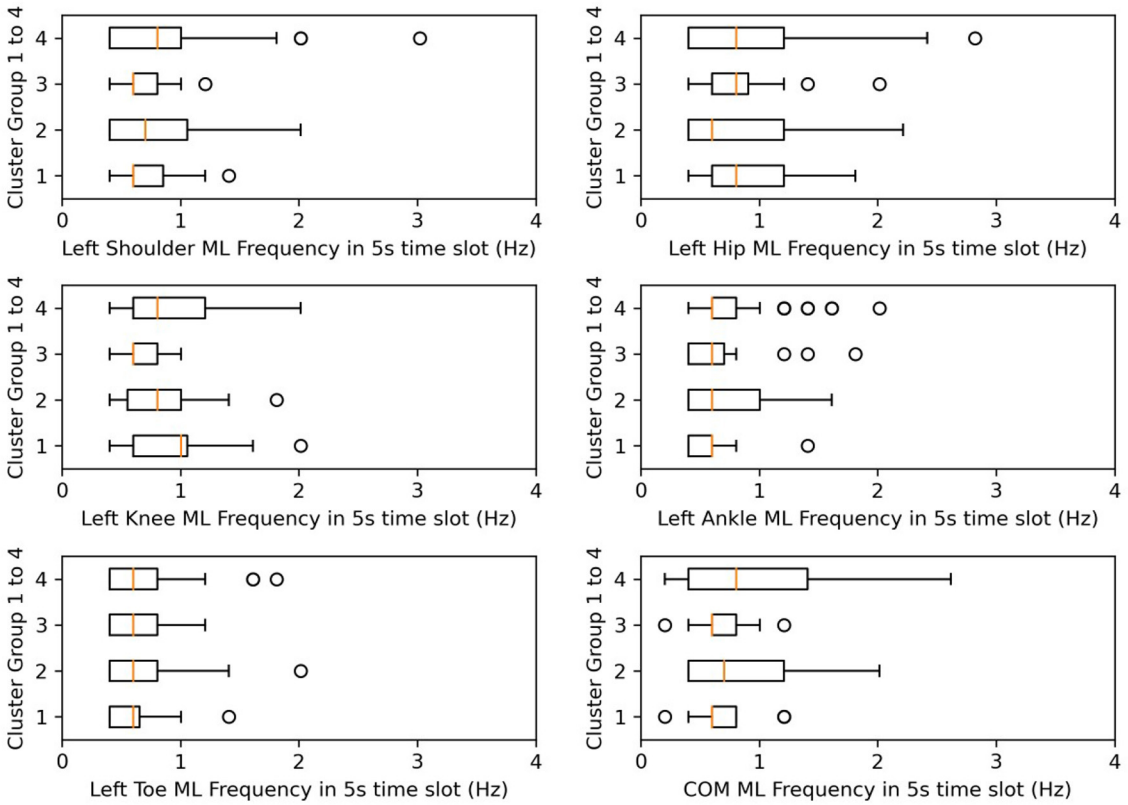

FIGURE 9 | Box plots for frequency in ML. X-axes represent the postural-sway frequency in the ML direction.

assumed that a CH onset-days correlation might emerge from their better recovery ability. This finding may give researchers and practitioners new ideas about sway-pattern changes during post-stroke patient rehabilitation. In addition, **Table 6** shows that the group formed of CH3, CI1, CI2, and CI4 were clustered into different clusters. After observing their data plots and analyzing the patient demographic factors, we found they all had fewer days after onset (less than 180 days, subacute phases). During the subacute phases, the stroke patient recovers more noticably and is more unstable in muscle force than in the chronic phase (Kiran, 2012; Chow and Stokic, 2014). Hence, these patients exhibit different sway patterns, even over the same experiment duration, and data from the subacute phase patients is considered to be difficult to cluster. This hence might be reason why different slots for one person were clustered into different clusters.

This study has certain limitations. The first is that the number of subjects was only 10. With more subjects, more calculations and analyses could be performed. The second is that we only considered male patients. We plan to investigate more subjects, including female patients, and analyze their postural-sway characteristics in future research. The third is that we did not perform clustering for the healthy age-matched and young subjects. If we add such subjects, we could compared the postural sway among healthy human and stroke patients to determine which postural-sway characteristics are important, which will add meaning to the study.

5. CONCLUSION

This study evaluated the postural-sway features of post-stroke patients using a motion-capture system to collect standing posture data. After collecting stroke patients' multi-variable motion-capture standing posture data, we processed them into data slots of t seconds long. Subsequently, we determined the optimal length of the data slots and number of clusters, and clustered the t-s data slots into K cluster groups using the DTW-PAM method. Finally, to find the critical kinematic variables, we performed a *post-hoc* test. We found that the shoulder, hip, knee, and COM played essential roles in clustering, and the amplitude of the marker was more helpful than its frequency. Furthermore, we created a days-from-onset clustering table and a box plot of the shoulder, hip, knee, and COM variable amplitudes and frequency separately in ML direction using 5-s data slots. We found that as the days after onset increased, CH patients transited from cluster four to clusters 3, 2, and 1 of a four-cluster solution, whereas for CI patients, they did not show such pronounced transitions over time.

TABLE 6 | Clustering by days after onset to explore the transition pattern of days after onset in CH and CI.

Name index	Days after onset	0	100	200	300	400	500	600	700	800	900	1,000	1100
CH3	51	4 4 4 4 4 4											
CH3	58	4 4 4 4 2 2											
CH3	65	4 4 4 4 4 2											
CH3	79	4 4 4 4 4 4											
CH3	93	4 4 4 4 4 4											
CH2	122		4 4 4 4 4 4										
CH2	129		4 4 4 4 4 4										
CH2	136		4 4 4 4 4 4										
CH2	143		4 4 4 4 4 4										
CH5	315				3 3 3 3 3 3								
CH5	340				3 3 3 3 3 3								
CH5	358				3 3 3 3 3 3								
CH4	520						2 2 2 2 2						
CH4	527						2 2 2 2 2						
CH4	534						2 2 2 2 2						
CH1	1108												1 1 1 1 1 1
CH1	1150												1 1 1 1 1 1
CI3	69	4 4 4 4 4 4											
CI3	80	4 4 4 4 4 4											
CI1	74	4 4 4 4 4 4											
CI1	88	4 4 4 4 4 4											
CI4	91	2 2 2 2 2 2											
CI4	108	4 4 4 4 4 4											
CI1	109		4 4 4 4 4 4										
CI1	176		4 3 1 1 1 1										
CI2	132		4 4 4 4 4 2										
CI2	147		4 4 1 1 1 1										
CI5	992									4 4 4 4 4 4			
CI5	1007										4 4 4 4 4 4		
CI5	1020										4 4 4 4 4 4		
CI5	1051										4 4 4 4 4 4		

Numbers 1–4 and colors from blue to red represent the clustered data from days after onset. The numbers from 0 to 1,000 indicate the days after onset for each cluster.

The above finding would provide researchers new ideas about sway-pattern changes for post-stroke patient rehabilitation. In the following research, we plan to increase the number of subjects.

DATA AVAILABILITY STATEMENT

The original contributions presented in the study are included in the article/**Supplementary Material**, further inquiries can be directed to the corresponding author/s.

ETHICS STATEMENT

The studies involving human participants were reviewed and approved by Fujita Health University, the University Ethics Committee. The patients/participants provided their written informed consent to participate in this study. Written informed consent was obtained from the individual(s) for the publication of any potentially identifiable images or data included in this article.

AUTHOR CONTRIBUTIONS

DL conceived the ideas, designed the methodology, performed the programming, and wrote the paper. JO and KK supervised the paper and provided comments on the research directions. MM preformed the experiments and provided study materials. RC and KT reviewed and edited the paper. All authors have read and approve the final manuscript.

FUNDING

This work has been partially supported by JSPS KAKENHI 19H05730 and the Mohammed bin Salman Center for Future Science and Technology for Saudi–Japan Vision 2030 at The University of Tokyo (MbSC2030).

SUPPLEMENTARY MATERIAL

The Supplementary Material for this article can be found online at: https://www.frontiersin.org/articles/10.3389/fnhum.2021.731677/full#supplementary-material

REFERENCES

Abdulhay, E., Arunkumar, N., Narasimhan, K., Vellaiappan, E., and Venkatraman, V. (2018). Gait and tremor investigation using machine learning techniques for the diagnosis of Parkinson disease. *Future Gen. Comput. Syst.* 83, 366–373. doi: 10.1016/j.future.2018.02.009

Bansil, S., Prakash, N., Kaye, J., Wrigley, S., Manata, C., Stevens-Haas, C., et al. (2012). Movement disorders after stroke in adults: a review. *Tremor Other Hyperkinet. Movements* 2:02. doi: 10.5334/tohm.110

Brandmaier, A. M. (2015). PDC: an R package for complexity-based clustering of time series. *J. Stat. Softw.* 67, 1–23. doi: 10.18637/jss.v067.i05

Caliński, T., and Harabasz, J. (1974). "A dendrite method foe cluster analysis," in *Commun. Stat.* 3, 1–27. doi: 10.1080/03610927408827101

Chern, J. S., Lo, C. Y., Wu, C. Y., Chen, C. L., Yang, S., and Tang, F. T. (2010). Dynamic postural control during trunk bending and reaching in healthy adults and stroke patients. *Am. J. Phys. Med. Rehabil.* 89, 186–197. doi: 10.1097/PHM.0b013e3181c56287

Cho, K., Lee, K., Lee, B., Lee, H., and Lee, W. (2014). Relationship between postural sway and dynamic balance in stroke patients. *J. Phys. Therapy Sci.* 26, 1989–1992. doi: 10.1589/jpts.26.1989

Chow, J. W., and Stokic, D. S. (2014). Variability, frequency composition, and complexity of submaximal isometric knee extension force from subacute to chronic stroke. *Neuroscience* 273, 189–198. doi: 10.1016/j.neuroscience.2014.05.018

Cuntoor, N., Kale, A., and Chellappa, R. (2003). "Combining multiple evidences for gait recognition," in *ICASSP, IEEE International Conference on Acoustics, Speech and Signal Processing - Proceedings* (College Park, MD: IEEE), 33–36.

Das, S., Trutoiu, L., Murai, A., Alcindor, D., Oh, M., De La Torre, F., et al. (2011). "Quantitative measurement of motor symptoms in Parkinson's disease: a study with full-body motion capture data," in *Proceedings of the Annual International Conference of the IEEE Engineering in Medicine and Biology Society, EMBS* (Pittsburgh, PA), 6789–6792. doi: 10.1109/IEMBS.2011.6091674

Davies, D. L., and Bouldin, D. W. (1979). A cluster separation measure. *IEEE Trans. Pattern Anal. Mach. Intell.* 1, 224–227. doi: 10.1109/TPAMI.1979.4766909

Dickstein, R., and Abulaffio, N. (2000). Postural sway of the affected and nonaffected pelvis and leg in stance of hemiparetic patients. *Arch. Phys. Med. Rehabil.* 81, 364–367. doi: 10.1016/S0003-9993(00)90085-6

Dunn, J. C. (1974). Well-separated clusters and optimal fuzzy partitions. *J. Cybernet.* 4, 95–104. doi: 10.1080/01969727408546059

Genolini, C., Alacoque, X., Sentenac, M., and Arnaud, C. (2015). Kml and kml3d: R packages to cluster longitudinal data. *J. Stat. Softw.* 65, 1–34. doi: 10.18637/jss.v065.i04

Giveans, M. R., Yoshida, K., Bardy, B., Riley, M., and Stoffregen, T. A. (2011). Postural sway and the amplitude of horizontal eye movements. *Ecol. Psychol.* 23, 247–266. doi: 10.1080/10407413.2011.617215

Halmi, Z., Stone, T. W., Dinya, E., and Málly, J. (2020). Postural instability years after stroke. *J. Stroke Cerebrovasc. Dis.* 29, 1–6. doi: 10.1016/j.jstrokecerebrovasdis.2020.105038

Katrak, P. H., Black, D., and Peeva, V. (2009). Do stroke patients with intracerebral hemorrhage have a better functional outcome than patients with cerebral infarction? *PM R* 1, 427–433. doi: 10.1016/j.pmrj.2009.03.002

Kelly, P. J., Furie, K. L., Shafqat, S., Rallis, N., Chang, Y., and Stein, J. (2003). Functional recovery following rehabilitation after hemorrhagic and ischemic stroke. *Arch. Phys. Med. Rehabil.* 84, 968–972. doi: 10.1016/S0003-9993(03)00040-6

Kim, J. W., Eom, G. M., Kim, C. S., Kim, D. H., Lee, J. H., Park, B. K., et al. (2010). Sex differences in the postural sway characteristics of young and elderly subjects during quiet natural standing. *Geriatr. Gerontol. Int.* 10, 191–198. doi: 10.1111/j.1447-0594.2009.00582.x

Kiran, S. (2012). What is the nature of poststroke language recovery and reorganization? *ISRN Neurol.* 2012, 1–13. doi: 10.5402/2012/786872

Koltermann, J. J., Gerber, M., Beck, H., and Beck, M. (2019). Validation of different filters for center of pressure measurements by a cross-section study. *Technologies* 7:68. doi: 10.3390/technologies7040068

Li, D., Kaminishi, K., Chiba, R., Takakusaki, K., Mukaino, M., and Ota, J. (2021). Evaluating quiet standing posture of post-stroke patients by classifying cerebral infarction and cerebral hemorrhage patients. *Adv. Robot.* 35, 878–888. doi: 10.1080/01691864.2021.1893218

Malik, O. A., and Lai, D. T. C. (2017). "Multivariate time series clustering analysis for human balance data," in *Lecture Notes in Computer Science*, eds S. Phon-Amnuaisuk, S. P. Ang, and S. Y. Lee, (Seri Begawan: Springer), 112–125. doi: 10.1007/978-3-319-69456-6_10

Mannor, S., Jin, X., Han, J., Jin, X., Han, J., Jin, X., et al. (2011). "K-medoids clustering," in *Encyclopedia of Machine Learning*, eds C. Sammut and G. I. Webb (Boston, MA: Springer US), 564–565. doi: 10.1007/978-0-387-30164-8_426

Matsuda, F., Mukaino, M., Ohtsuka, K., Tanikawa, H., Tsuchiyama, K., Teranishi, T., et al. (2016). Analysis of strategies used by hemiplegic stroke patients to achieve toe clearance. *Jpn. J. Comp. Rehabil. Sci.* 7, 111–118.

Mizrahi, J., Solzi, P., Ring, H., and Nisell, R. (1989). Postural stability in stroke patients: vectorial expression of asymmetry, sway activity and relative sequence of reactive forces. *Med. Biol. Eng. Comput*. 27, 181–190. doi: 10.1007/BF02446228

Mohd Razali, N., and Bee Wah, Y. (2011). Power comparisons of Shapiro-Wilk, Kolmogorov-Smirnov, Lilliefors and Anderson-Darling tests. *J. Stat. Model. Anal*. 2, 13–14.

Montero, P., and Vilar, J. A. (2014). TSclust: an R package for time series clustering. *J. Stat. Softw*. 62, 1–43. doi: 10.18637/jss.v062.i01

Paillex, R., and So, A. (2005). Changes in the standing posture of stroke patients during rehabilitation. *Gait Post*. 21, 403–409. doi: 10.1016/j.gaitpost.2004.04.011

Petitjean, F., Ketterlin, A., and Gançarski, P. (2011). A global averaging method for dynamic time warping, with applications to clustering. *Pattern Recogn*. 44, 678–693. doi: 10.1016/j.patcog.2010.09.013

Petri, D. (2002). Frequency-domain testing of waveform digitizers. *IEEE Trans. Instrument. Measure*. 51, 445–453. doi: 10.1109/TIM.2002.1017714

Pohlert, T. (2014). The pairwise multiple comparison of mean ranks package (PMCMR). *R Package* 27:27.

Rybarczyk, Y., Deters, J. K., Gonzalo, A. A., Esparza, D., Gonzalez, M., Villarreal, S., et al. (2018). Recognition of physiotherapeutic exercises through DTW and low-cost vision-based motion capture. *Adv. Intell. Syst. Comput*. 592, 348–360. doi: 10.1007/978-3-319-60366-7_33

Sardá-Espinosa, A. (2019). Time-series clustering in R Using the dtwclust package. *R J*. 11:41. doi: 10.32614/RJ-2019-023

Tobias, S., and Carlson, J. E. (1969). Brief report: Bartlett's test of sphericity and chance findings in factor analysis. *Multivar. Behav. Res*. 4, 375–377. doi: 10.1207/s15327906mbr0403_8

Wang, W., Li, K., Wei, N., Yin, C., and Yue, S. (2017). "Evaluation of postural instability in stroke patient during quiet standing," in *Proceedings of the Annual International Conference of the IEEE Engineering in Medicine and Biology Society, EMBS* (Jinan), 2522–2525. doi: 10.1109/EMBC.2017.8037370

Conflict of Interest: The authors declare that the research was conducted in the absence of any commercial or financial relationships that could be construed as a potential conflict of interest.

Publisher's Note: All claims expressed in this article are solely those of the authors and do not necessarily represent those of their affiliated organizations, or those of the publisher, the editors and the reviewers. Any product that may be evaluated in this article, or claim that may be made by its manufacturer, is not guaranteed or endorsed by the publisher.

Copyright © 2021 Li, Kaminishi, Chiba, Takakusaki, Mukaino and Ota. This is an open-access article distributed under the terms of the Creative Commons Attribution License (CC BY). The use, distribution or reproduction in other forums is permitted, provided the original author(s) and the copyright owner(s) are credited and that the original publication in this journal is cited, in accordance with accepted academic practice. No use, distribution or reproduction is permitted which does not comply with these terms.

frontiers in Systems Neuroscience

ORIGINAL RESEARCH
published: 08 December 2021
doi: 10.3389/fnsys.2021.774596

Musculoskeletal Modeling and Inverse Dynamic Analysis of Precision Grip in the Japanese Macaque

Tsuyoshi Saito[1], Naomichi Ogihara[1,2], Tomohiko Takei[3] and Kazuhiko Seki[4]**

[1] Department of Mechanical Engineering, Faculty of Science and Technology, Keio University, Yokohama, Japan, [2] Department of Biological Sciences, Graduate School of Science, The University of Tokyo, Tokyo, Japan, [3] Brain Science Institute, Tamagawa University, Tokyo, Japan, [4] Department of Neurophysiology, National Institute of Neuroscience, National Center of Neurology and Psychiatry, Tokyo, Japan

Toward clarifying the biomechanics and neural mechanisms underlying coordinated control of the complex hand musculoskeletal system, we constructed an anatomically based musculoskeletal model of the Japanese macaque (*Macaca fuscata*) hand, and then estimated the muscle force of all the hand muscles during a precision grip task using inverse dynamic calculation. The musculoskeletal model was constructed from a computed tomography scan of one adult male macaque cadaver. The hand skeleton was modeled as a chain of rigid links connected by revolute joints. The path of each muscle was defined as a series of points connected by line segments. Using this anatomical model and a model-based matching technique, we constructed 3D hand kinematics during the precision grip task from five simultaneous video recordings. Specifically, we collected electromyographic and kinematic data from one adult male Japanese macaque during the precision grip task and two sequences of the precision grip task were analyzed based on inverse dynamics. Our estimated muscular force patterns were generally in agreement with simultaneously measured electromyographic data. Direct measurement of muscle activations for all the muscles involved in the precision grip task is not feasible, but the present inverse dynamic approach allows estimation for all the hand muscles. Although some methodological limitations certainly exist, the constructed model analysis framework has potential in clarifying the biomechanics and neural control of manual dexterity in macaques and humans.

Keywords: hand, motor control, grasping, optimization, muscle force

OPEN ACCESS

Edited by:
Karl Thomas Bates, University of Liverpool, United Kingdom

Reviewed by:
Shouhei Shirafuji, The University of Tokyo, Japan
Mitsuhiro Hayashibe, Tohoku University, Japan

****Correspondence:***
Naomichi Ogihara
ogihara@bs.s.u-tokyo.ac.jp
Kazuhiko Seki
seki@ncnp.go.jp

Received: *12 September 2021*
Accepted: *12 November 2021*
Published: *08 December 2021*

Citation:
Saito T, Ogihara N, Takei T and Seki K (2021) Musculoskeletal Modeling and Inverse Dynamic Analysis of Precision Grip in the Japanese Macaque. Front. Syst. Neurosci. 15:774596. doi: 10.3389/fnsys.2021.774596

INTRODUCTION

A complex hand musculoskeletal system enables humans to execute highly coordinated movements, such as firmly grasping and skillfully manipulating objects using the thumb and other fingers. Precision grip is frequently chosen as the subject of experiments focused on the neural control mechanisms underlying human dexterous grip. Precision grip is computationally demanding compared with other grasp types, e.g., power grip. By measuring brain activity during

precision grip tasks in macaques, researchers have identified several regions in the central nervous system that contribute to dexterous hand movements. For example, corticospinal projection neurons in the primary motor cortex (e.g., Muir and Lemon, 1983; Bennett and Lemon, 1996; Schieber and Rivlis, 2005) and neurons in the spinal cord (Takei and Seki, 2010, 2013; Alstermark et al., 2011; Takei et al., 2017; Oya et al., 2020) have been implicated in dexterous hand movements.

Precision grip is a very complex mechanical phenomenon. As a result, the relationship between neural activities and the generation of finger force is difficult to define, and can be counterintuitive (Wannier et al., 1991; Maier et al., 1993). For example, cortico-motoneuronal cells in the primary motor cortex, which have an excitatory output effect on finger muscles, are sometimes negatively correlated with the exerted finger force even though their target muscles are positively correlated (Maier et al., 1993). Therefore, an understanding of the dynamic and complex interactions between the nervous system and musculoskeletal system is essential for clarifying the neural mechanisms of primate hand control.

Inverse dynamics analysis is a useful method for investigating the dynamic interactions between the neural system and the musculoskeletal system (Chan and Moran, 2006; Cheng and Loeb, 2008; Jindrich et al., 2011). In this method, muscle forces are estimated by entering motion data into equations describing the motion of a mechanical body system (Erdemir et al., 2007). Such biomechanical modeling and inverse dynamic analyses have (a) been successfully used to describe reaching movements in macaques (Chan and Moran, 2006; Cheng and Loeb, 2008; Jindrich et al., 2011), (b) been useful in distinguishing intrinsic, extrinsic, kinematic, and kinetic variables (Chan and Moran, 2006), and (c) improved the interpretation of kinematic and electrophysiological data (Cheng and Loeb, 2008). However, to the best of our knowledge, no researchers have attempted to construct a hand musculoskeletal model for biomechanical analysis of precision grip in macaques, although musculoskeletal models of the human hand have been developed recently (e.g., Lee et al., 2015; Sachdeva et al., 2015; Mirakhorlo et al., 2018).

In the present study, we constructed an anatomically based, 3D musculoskeletal model of the Japanese macaque hand and biomechanically analyzed macaque's precision grip based on inverse dynamic calculation, toward clarifying the biomechanics and neural mechanisms underlying coordinated control of the complex hand musculoskeletal system. Specifically, we tested the hypothesis that the inverse dynamic analysis would enable estimation of all the hand muscles involved in the precision grip task. The primate hand possesses an especially complex musculoskeletal structure with at least 39 muscles (Tubiana, 1981), many of which are very difficult to access during *in vivo* experiments. Thus, a complete hand musculoskeletal model could be useful in describing hand muscle activities related to precision grip control. Such research could lead to a deeper understanding of how muscle activities are coordinated within the nervous system for effective control of the complex hand musculoskeletal system.

MATERIALS AND METHODS

Hand Musculoskeletal Model

We constructed a 3D musculoskeletal model of the Japanese macaque (*Macaca fuscata*) hand from a computed tomography scan of one adult male cadaver. The deceased macaque used to be a performing monkey and died naturally as a result of acute respiratory tract infection after living in retirement for more than 10 years. The body mass at the time of death was ∼10 kg. This cadaver had previously been CT scanned to construct a whole-body musculoskeletal model for locomotion studies (Ogihara et al., 2009), but for the present study, we rescanned the cryonically preserved right hand and forearm at a higher resolution ($0.096 \times 0.096 \times 0.095$ mm) using a micro CT scanner (ScanXmate-A080S, Comscantecno, Yokohama, Japan). Consecutive cross-sectional images were then transferred to medical imaging software (Analyze 9.0; Biomedical Imaging Resource Mayo Clinic, Rochester, MN, United States) and the 3D surface models of each of the bones were generated as a triangular mesh model using the marching cube method. The experiments took place at the Laboratory of Physical Anthropology, Kyoto University. The use of CT images contributes to reduce the errors of estimated joint moments and muscle forces because it contributes to correct identifications of the locations of joint centers and the orientations of the axes of joint rotations.

We defined the bone coordinate systems embedded in each of the metacarpals (MC) or phalanges (P) using the bone principal axes, the origins of which were located at the centroid, with the *z*-axis as the major axis corresponding to the orientation of the shaft, and the *x*- and *y*-axes corresponding to the radial-ulnar and extension-flexion rotational axes, respectively. Carpal bones were treated as a single mass, ignoring inter-carpal mobility. The origin of the carpal coordinate system was set at the centroid, with the *x*-, *y*-, and *x*-axes facing the dorsal, ulnar, and distal directions, respectively.

We modeled the hand skeleton as a chain of 20 rigid-body bone segments connected by revolute joints. We modeled the interphalangeal (IP) joint as a hinge joint with 1 degree-of-freedom (DOF), capable only of flexion and extension. We approximated the distal articular surface of the phalanges with a cylinder to estimate the joint center. The hinge axis was defined as parallel to the distal *y*-coordinate axis. The metacarpophalangeal (MCP) joints were modeled as joints with 2 DOF, capable of flexion and extension, and radial and ulnar deviation (a universal joint). We approximated the distal articular surface of the metacarpals with a sphere to estimate the joint center. The two rotational joints were assumed to correspond to the *x*- and *y*-axes of the proximal phalanx. The saddle-shaped 1st carpometacarpal (CMC) joint was approximated by a paraboloid surface and modeled as a universal joint with 2 DOF, capable of flexion and extension, and radial and ulnar deviation (Ogihara et al., 2009; Matsuura et al., 2010). The joint center was assumed to be at the apex of the paraboloid and the axes were determined

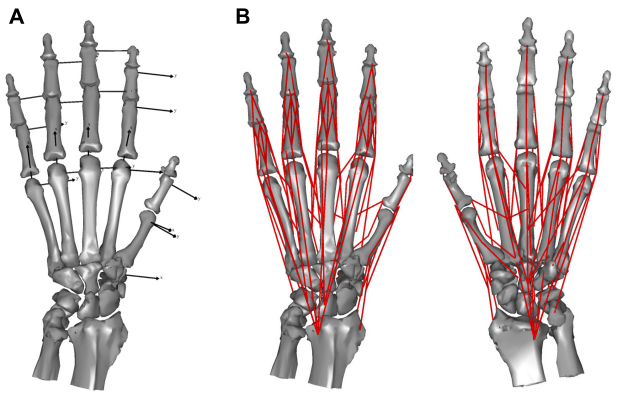

FIGURE 1 | Skeletal model **(A)** and musculoskeletal model **(B)** of the Japanese macaque hand.

TABLE 1 | Inertial parameters for Japanese macaque hand segments.

	Mass (g)	Principal moment of inertia (g mm^2)		
		Ix	Iy	Iz
Carpus	16.50	2.05.E+03	1.41.E+03	2.36.E+03
1MC	4.70	2.55.E+02	3.73.E+02	1.96.E+02
2MC	6.68	6.77.E+02	8.44.E+02	2.78.E+02
3MC	7.42	9.13.E+02	1.10.E+03	3.09.E+02
4MC	7.10	8.05.E+02	9.82.E+02	2.96.E+02
5MC	6.16	5.38.E+02	6.92.E+02	2.57.E+02
1PP	1.31	4.90.E+01	3.87.E+01	2.15.E+01
1DP	0.43	5.22.E+00	3.41.E+00	4.13.E+00
2PP	2.00	8.18.E+01	9.67.E+01	3.90.E+01
2MP	0.60	9.92.E+00	9.18.E+00	4.89.E+00
2DP	0.43	5.40.E+00	4.50.E+00	3.05.E+00
3PP	3.79	2.37.E+02	2.86.E+02	1.16.E+02
3MP	0.85	2.04.E+01	2.17.E+01	7.80.E+00
3DP	0.68	1.09.E+01	1.20.E+01	6.09.E+00
4PP	3.60	2.13.E+02	2.55.E+02	9.96.E+01
4MP	0.95	2.55.E+01	2.37.E+01	9.37.E+00
4DP	0.62	1.01.E+01	1.04.E+01	4.85.E+00
5PP	2.62	9.63.E+01	1.05.E+02	7.31.E+01
5MP	0.54	9.11.E+00	8.10.E+00	4.15.E+00
5DP	0.41	5.02.E+00	4.38.E+00	2.75.E+00

based on the orientation of the paraboloid. The remaining four CMC joints were represented as gimbal joints (joints with three rotational axes intersecting one another), with the joint locations defined as the center of the articular surface. The mobility of CMC joints 2–5 is negligible during precision grip. Thus, for the purposes of this study we treated these and the carpal segment as a single segment. The kinematic skeleton of the macaque hand was thus mathematically described as an open chain of 16 rigid links connected by revolute joints (**Figure 1A**).

We calculated the mass and the principal moment of inertia for each phalangeal segment as in Ogihara et al. (2009). Briefly, the skin surface model of the hand was divided into phalangeal segments, and the inertial parameters were numerically calculated using each segmented surface model, assuming homogeneous segment composition and a density of 1.0 g/cm^3 (**Table 1**). The mass and the principal moment of inertia of the metacarpal and carpal segments were calculated by approximating the corresponding volumes with rectangular solids. The principal axes of inertia of each segment were assumed to be coincident with the bone principal axes, and the center of mass was approximated to be at the origin of the bone fixed-coordinate system.

We defined the muscle-tendon path of each of the 23 hand muscles listed in **Table 2** as a series of points connected by line segments (**Figure 1B**) as in previous studies (e.g., Mirakhorlo et al., 2018; Michaud et al., 2021). Each point, fixed to a corresponding bone coordinate system, was obtained based on our dissection records of the Japanese macaque hand (Ogihara and Oishi, 2012). Origin and insertion points were digitized at the estimated centroids of muscle attachment sites. Intermediate points were determined to properly constrain the muscle-tendon path. Therefore, the muscle-tendon paths do not slide on the bones in the present model. Although there have been some attempts to model such sliding phenomena based on continuum mechanics (e.g., Sachdeva et al., 2015), such complex models usually require additional parameters which possibly introduce additional uncertainties in the model. In addition, previous studies suggested the slight changes in the muscle paths did not markedly affect the results of the simulations (Valente et al., 2014; Kainz et al., 2021). Hence, each muscle-tendon path was represented as a series of points connected by line segments. We modeled muscles that are divided or split along the muscle path, such as the FDP, FDS, and EDC (see **Table 2** for abbreviations), as groups of several independent muscle paths. Maximum muscle force was assumed to be proportional to the physiological cross-sectional area (PCSA), and was calculated by multiplying the PCSA by the maximum muscle stress (23 N/cm^2) (Spector et al., 1980) as in Delp et al. (1990) and Lemay and Crago (1996), although no study has validated that the muscle stress value measured from cat soleus (Spector et al., 1980) can be applicable to primate hand muscles. The PCSA of each muscle was obtained from Macaque A in Ogihara and Oishi (2012) since this was the same macaque that had been CT scanned for the construction of the present model. We set the PCSA of the FDP1 and CD2 to zero as these muscles are absent in the Japanese macaque (Ogihara and Oishi, 2012). Pennation angle was not considered in the calculation because this value is typically very small for hand muscles and thus is not expected to significantly affect the force-generating capacity of the muscles. The extensor mechanism (dorsal aponeurosis) on the dorsal side of each long finger was modeled as a net structure, based on the methods of Garcia-Elias et al. (1991) and Sancho-Bru et al. (2001). We determined the load transmission of muscles to the extensor mechanism based on the methods of Chao et al. (1989). **Figure 2** illustrates how the extensor mechanisms were connected with the interosseous and extensor digitorum muscles to generate torques around the IP joints. We did not include lumbrical muscles in this model because

TABLE 2 | Muscle parameters for the Japanese macaque hand.

	muscle name	Abb	PCSA (cm^2)	max. force (*N*)
1	Flexor digitorum superficialis	FDS		
	FDS2	FDS2	0.45	10.4
	FDS3	FDS3	0.85	19.6
	FDS4	FDS4	0.95	21.9
	FDS5	FDS5	1.23	28.3
2	Flexor digitorum profundus	FDP		
	FDP1	FDP1	0.00	0.0
	FDP2	FDP2	1.81	41.6
	FDP3	FDP3	1.39	32.0
	FDP4	FDP4	1.29	29.7
	FDP5	FDP5	1.63	37.5
3	Extensor digitorum communis	EDC		
	EDC2	EDC2	0.29	6.7
	EDC3	EDC3	0.08	1.8
	EDC4	EDC4	0.12	2.8
	EDC5	EDC5	0.32	7.4
4	Extensor digiti secundi & tertii proprius			
	ED2P	ED2P	0.23	5.3
	ED3P	ED3P	0.08	1.8
5	Extensor digiti quarti & quinti proprius			
	ED4P	ED4P	0.22	5.1
	ED5P	ED5P	0.19	4.4
6	Abductor pollicis longus	ABPL	2.67	61.4
7	Extensor pollicis longus	EPL	0.19	4.4
8	Abductor pollicis brevis	ABPB	0.71	16.3
9	Flexor pollicis brevis	FPB	0.32	7.4
10	Opponens pollicis	OP	0.34	7.8
11	Adductor pollicis	ADP		
	ADP oblique	ADPo	0.17	3.9
	ADP transverse	ADPt	0.43	9.9
12	Abductor digiti minimi	ABDM	1.17	26.9
13	Flexor digiti minimi brevis	FDMB	0.33	7.6
14	Opponens digiti minimi	ODM	0.63	14.5
15	Dorsal interosseous 1 radial head	1DIOr	0.52	12.0
	Dorsal interosseous 1 ulnar head	1DIOu	0.52	12.0
16	Dorsal interosseous 2 radial head	2DIOr	0.40	9.1
	Dorsal interosseous 2 ulnar head	2DIOu	0.40	9.1
17	Dorsal interosseous 3 radial head	3DIOr	0.30	6.9
	Dorsal interosseous 3 ulnar head	3DIOu	0.30	6.9
18	Dorsal interosseous 4 radial head	4DIOr	0.23	5.3
	Dorsal interosseous 4 ulnar head	4DIOu	0.23	5.3
19	Palmar interosseous 1	1PIO	0.56	12.9
20	Palmar interosseous 2	2PIO	0.18	4.1
21	Palmar interosseous 3	3PIO	0.24	5.5
22	Contrahens digiti quarti	CD4	0.21	4.8
23	Contrahens digiti quinti	CD5	0.22	5.1
	Contrahens digiti scundi	CD2	0.00	0.0

Abb, abbreviation; PCSA, physiological cross-sectional area of muscle.

the force generating capacity of these muscles is very small. In addition, lumbrical muscles are difficult to emulate because they originate from the FDP tendons, but are not directly connected to a bone segment.

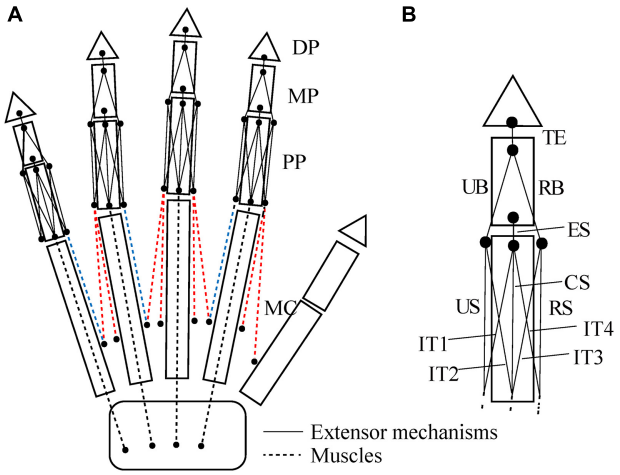

FIGURE 2 | Schematic diagram showing how the interosseous and extensor muscles are connected to extensor mechanisms in this model **(A)**. Extensor mechanisms of the index finger **(B)**. TE, terminal extensor tendon; UB, ulnar band; RB, radial band; ES, extensor slip; US, ulnar slip; CS, central slip; RS, radial slip; IT, interosseous tendon. Tensions of the TE, UB, RB and ES, f_{TE}, f_{UB}, f_{RB}, and f_{ES} are calculated as follows: $f_{TE} = f_{RB} + f_{UB}$; $f_{RB} = 0.167 \times f_{EDC2}$; $f_{UB} = 0.167 \times f_{EDC2} + 0.333 \times f_{1PIO}$; $f_{ES} = 0.167 \times f_{EDC2} + 0.333 \times f_{1PIO} + 0.333 \times f_{1DIOr} + 0.333 \times f_{1DIOu}$. Radial and ulnar components of the 1DIO inserting into the extensor mechanism are denoted by *r* and *u*, respectively.

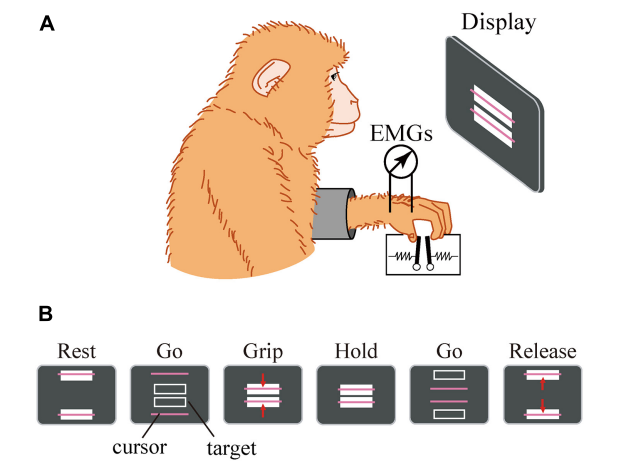

FIGURE 3 | Experimental setup. The macaque sat in front of a computer screen **(A)**. The lever positions were displayed on a computer screen as cursors, and the macaque was required to grip, hold, and release the levers using the thumb and index finger according to the movement of a target displayed on the screen **(B)**.

Our anatomically accurate model of the Japanese macaque hand was entered into the musculoskeletal simulation software package Anybody Modeling System (AnyBody Technology, Aalborg, Denmark) (Damsgaard et al., 2006). This software is capable of constructing a musculoskeletal model using a programming language (Anyscript) and the inverse dynamic analysis of the developed musculoskeletal system.

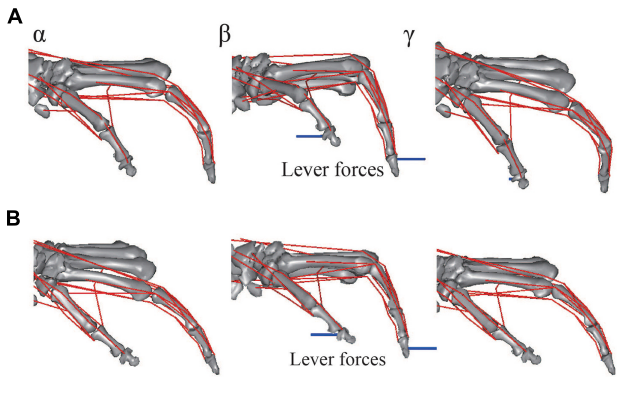

FIGURE 4 | Graphical representation of reconstructed hand musculoskeletal kinematics of the Japanese macaque during the precision grip task. **(A)** Trial 1. **(B)** Trial 2. α, β, and γ correspond to the moments at which the levers had just been gripped (α), the maximum forces had been applied by the index finger (β), and the levers had been released (γ), respectively. Red lines, muscle paths; blue lines, lever forces. Joint angles were defined as positive for extension and adduction of the 1CMC and MCP joints and for extension of the IP joints. Joint angles were defined as zero at $t = 0$.

Precision Grip Task

We collected electromyographic (EMG) and kinematic data from one adult male Japanese macaque (age, 8 years, body weight, 8.0 kg) during the precision grip task. The experiments took place at the Department of Neurophysiology, National institute of Neuroscience, National Center of Neurology and Psychiatry. The animal was treated in strict compliance with the Animal Care and Use Committee of the National Institute of Neuroscience, and with the NIH Guide for the Care and Use of Laboratory Animals. The protocol was approved by the local ethics committee for primate research at National Institute of Neuroscience (Permit #: 2012-004). All studies were performed in accordance with the recommendations of the Weatherall report, "The use of non-human primates in research." The animal was housed in a cage (80 × 70 × 80 cm) individually in a large room for the care of macaque monkeys in the primate research facility of the National Institute of Neuroscience, along with several other monkeys permitting rich visual, olfactory and auditory interactions. Water was available *ad libitum*, and a standard commercially formulated non-human primate diet (AS, Oriental Yeast, Tokyo, Japan) was provided once daily (120 g/meal) and supplemented daily with fresh fruit. Some toys (such as balls, empty plastic bottle, etc.) were given to the monkey as part of the environmental enrichment approach. Regular care and monitoring, balanced nutrition and environmental enrichment were provided by the staffs of this center. All surgeries were performed using sevoflurane anesthesia (1.5–2.5% in 2:1 O_2:N_2O), and the monkey was artificially respired. Respiration rate was adjusted to keep end-tidal CO_2 within 30–35 mmHg.

The details of the precision grip task, experimental setup, surgical operation, and EMG recording procedure were similar to those described previously (Takei and Seki, 2008). Briefly, the macaque monkey has been trained to grip, hold, and release spring-loaded levers using the thumb and index finger. The monkey sat in a chair with its right and left elbow restrained, and the thumb and index finger were inserted to separate holes to access the levers. Therefore, the position of the hand and fingers were quite stationary during the precision grip task. The lever positions were displayed on a computer screen as cursors, and the macaque was required to grip, hold, and release the levers according to the movement of the target displayed on the screen (**Figure 3**). The reaction forces applied to the fingertips were measured by strain gauges attached to the pinch levers. For EMG recording, pairs of stainless steel wires (AS631, Cooner Wire) were chronically implanted subcutaneously in the following eight muscles: (1) 1DIO, (2) FDS2, (3) FDP2, (4) ADP, (5) ABPL, (6) EDC2, (7) ED2P, and (8) ABPB. The EMG signals were amplified and filtered using a multichannel differential amplifier (5–3000 Hz; SS-6110, Nihon Kohden, Japan) and digitized at 5 kHz. Simultaneously, signals from the strain gauges were digitized at 1 kHz. Offline, the EMG signals were high-pass filtered (cut-off = 30 Hz), rectified, and downsampled to 100 Hz. The signal was then low-pass filtered (cut-off = 2.5 Hz) to obtain a linear envelope. The signals from the strain gauges were low-pass filtered (cut-off = 10 Hz) and downsampled to 100 Hz.

Simultaneous to the EMG recording, we filmed the hand movements of the macaque during the precision grip task using five AVCHD video cameras with a resolution of 1920 × 1080 (iVIS HF S21, Canon, Tokyo, Japan). From the motion images, we extracted well-recorded precision grip sequences and manually digitized the following 12 positions frame-by-frame: (1) tip of the 1DP, (2) head of the 1PP, (3) head of the 1MC, (4) 1CMC joint, (5) tip of the 2DP, (6) head of the 2MP, (7) head of the 2DP, (8) head of the 2MC, (9) head of the 3MC, (10) head of the 4MC, (11) head of the 5MC, and (12) styloid process of the ulna. The positions of the third, fourth, and fifth fingers were not digitized as these fingers were deeply flexed such that the joint positions were not detected by the cameras. We calculated the 3D movements of the 12 digitized positions using WinAnalyze 3D motion analysis software (Mikromak, Berlin, Germany) and digitally low-pass filtered the data at 5 Hz. The standard error of the mean accompanying each of the measured positions in the calibration was about 1.4 mm. The change in position of each coordinate over time was approximated by a polynomial function.

To replicate the 3D musculoskeletal kinematics of the macaque hand during the precision grip task, the model was first scaled to the size of the filmed macaque hand based on the length of the index finger. The hand musculoskeletal model was then registered to the recorded motion data by means of a least squares approach, i.e., minimizing the sum of distances between each digitized coordinate and the corresponding point on the hand model. The error associated with the scaling of a generic model has been suggested to be relatively minor (Valente et al., 2014; Kainz et al., 2021).

Inverse Dynamic Analysis of Precision Grip

Using the inverse dynamic method, the net joint torques required to perform a given motion can be uniquely computed from the

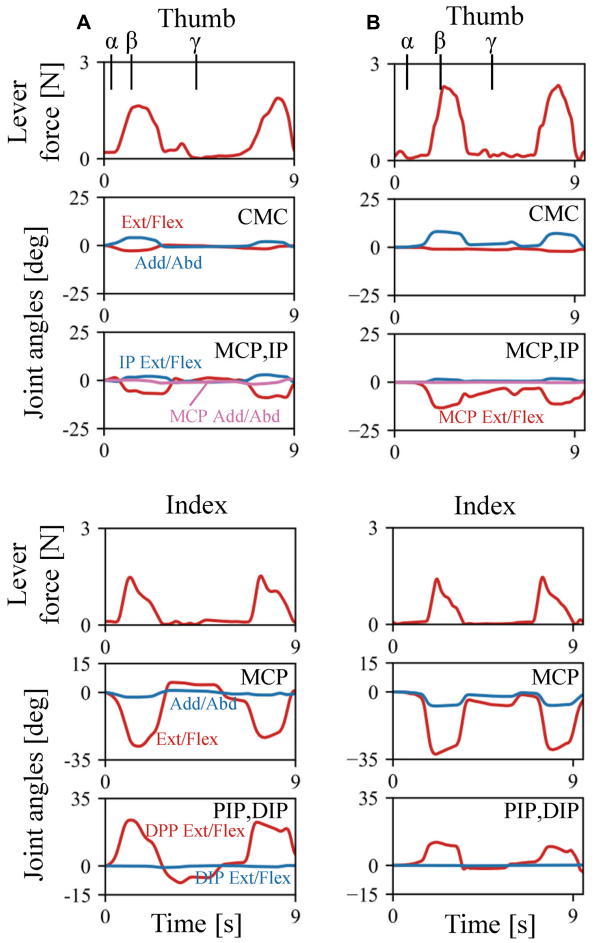

FIGURE 5 | Changes in lever forces and joint angles during the precision grip task in the Japanese macaque. **(A)** Trial 1. **(B)** Trial 2. Arrows α, β, and γ correspond to the moments at which the levers had just been gripped (α), the maximum forces were applied by the index finger (β), and the levers were released (γ), respectively.

measured kinematics and external forces, i.e., the lever forces in the present study. However, joint torques can be achieved by an infinitely large number of combinations of muscle forces, as the number of muscles spanning a joint far exceeds the DOF of the corresponding joint. In this study, we addressed the indeterminant redundancy problem of muscle recruitment using an optimization method (Tsirakos et al., 1997). We used the sum of the cubes of muscle stress, which are considered to be a proxy for muscle fatigue and hence a physiologically relevant measure, as an objective function (Crowninshield and Brand, 1981). Such calculation was conducted using Anybody Modeling System (AnyBody Technology, Aalborg, Denmark).

In the present study, the MCP and 1CMC joints were modeled as universal joints. In a universal joint, two components of the joint torque vector (flexion/extension and radial/ulnar deviation torques) should be simultaneously balanced by the sum of moments generated by the muscles spanning the joint. However, this was actually difficult because joint constraints due to passive elastic elements such as collateral and carpometacarpal ligaments and joint capsules were not imposed in the present model. Therefore, when conducting the inverse dynamic analysis, the rotational axes of the radio-ulnar deviation of the MCP joints and the radio-ulnar deviation and flexion/extension axes of the 1CMC joints were assumed to be instantaneously immobile in the present study, hence the respective torques were structurally balanced by reaction torques around each rotational axis.

To compare the predicted muscular force profiles with the shape and timing of the enveloped EMG signals, we calculated the cross-correlation r with zero time-lag (Blana et al., 2008; Michaud et al., 2021). The cross-correlation is a measure of the similarity between two waveforms, represented as a scalar between −1 and 1. If the two waveforms are identical, r is equal to 1. If the amplitude of the EMG signal was effectively zero, or the maximum force of the predicted muscular force was less than 0.3 N, we did not calculate the cross-correlation.

RESULTS

The musculoskeletal architecture of the macaque hand was well emulated by the computer model such that the 3D hand kinematics during precision grip were successfully reconstructed and visualized (**Figure 4**). The 3D hand musculoskeletal kinematics for two sequences of the precision grip task in the Japanese macaque were presented in **Figure 4**, and α, β, and γ correspond to the moment at which the lever had just been gripped (α), the moment at which the maximum force (blue line) had been applied by the index finger (β), and the moment at which the lever was released (γ). The mean matching bias of the markers (distance between each motion-captured marker and the corresponding marker on the model) averaged over time was 0.67 ± 0.03 and 0.47 ± 0.04 mm (mean ± SD) for the first and second sequences, respectively, indicating that the matching between the hand model and the digitized coordinates was reasonably high. We analyzed only two sequences because the hand and finger movements were quite stereotypical in the precision grip task (see section "Materials and Methods") and hence the variability of the movements was small in the present study. The peak force applied by the fingers was ∼1.5 N, and a comparatively larger force was applied by the thumb (∼2 N) during the precision grip task (**Figure 5**). It is also observed that the CMC, MCP, and IP joints of the thumb were mainly adducted, flexed, and extended, respectively, and the MCP and PIP joints of the index finger were mainly flexed and extended, respectively, when the lever was gripped (**Figure 5**).

The estimated muscular force patterns during the precision task were quite similar to the corresponding EMG patterns (**Figure 6**). Our inverse dynamic analysis estimated that the 1DIOr, 1DIOu, ADPt, FDS2, and FDP2 muscles would be activated when the levers were pinched, and that muscle activity would be negligible in the ABPL, EDC2, and ED2P muscles during the precision grip task. The cross-correlation values were generally greater than 0.6 for the 1DIOr, 1DIOu, FDS2, and FDP2 muscles. In these muscles, the peaks of

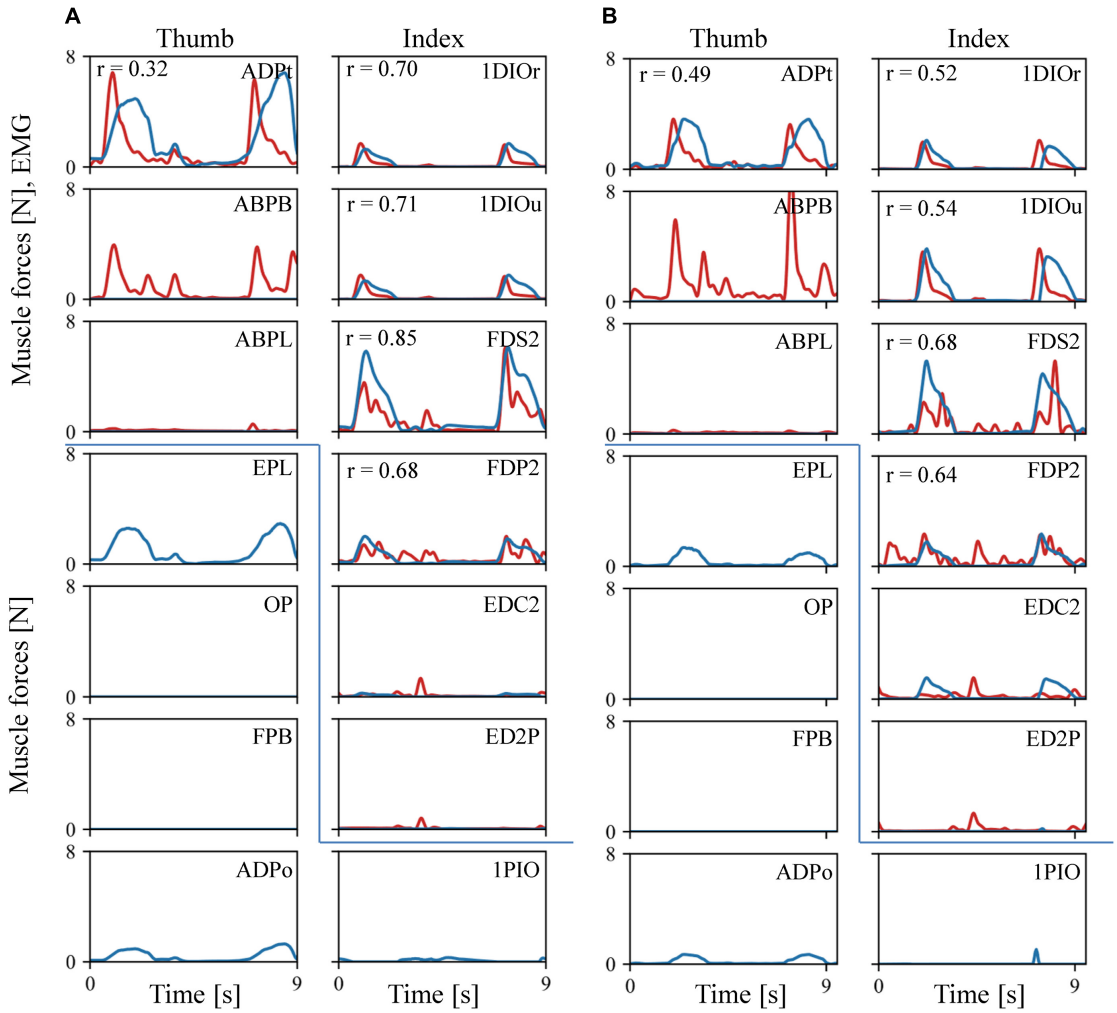

FIGURE 6 | Comparisons between the recorded EMG (red line) and the predicted muscle force patterns (blue line). **(A)** Trial 1. **(B)** Trial 2. As EMG amplitude is not directly comparable to the predicted muscular force, we scaled the EMG amplitude by the maximum force of the corresponding muscle. If the maximum force was less than 0.3N, or the amplitude of the EMG signal is effectively zero, the EMG amplitude was adjusted such that 100 mV was equal to 1 N.

the muscle forces correspond well to those of the EMG signals. Furthermore, the amplitudes of the EMG signal were effectively zero in the ABPL, EDC2, and ED2P muscles, muscle forces of which were estimated to be negligible. Therefore, the estimated muscular forces were generally in accordance with the EMG signals for six out of eight muscles. However, although the amplitude of the measured EMG signal was quite large in the ABPB muscle, the estimated muscular force pattern was zero in the present study. In addition, the cross-correlation values to be relatively low for the ADPt, indicating that the prediction was less accurate for these muscles.

Our model also predicted the force induced by muscles for which we did not obtain an EMG signal during the experiments (**Figure 6**). For example, the EPL and ADPo were predicted to be active when the levers were pinched, and no activity was predicted for the FPB or OP.

DISCUSSION

We used a newly constructed anatomically realistic musculoskeletal hand model to biomechanically analyze a precision grip task in the Japanese macaque using inverse dynamic calculations. Because of the structural complexity of the primate hand, this topic has challenged researchers in the field of biomechanics. As a result, few studies have succeeded in using the inverse dynamic approach to analyze hand movements even in humans (Grinyagin et al., 2005; Goislard de Monsabert et al., 2012; Wu et al., 2012). Additionally, to the best of our knowledge, no studies have compared calculated muscle force profiles with simultaneously recorded EMG data, as it is generally impractical to record EMG signals from multiple human hand muscles *in vivo*. Thus, the present study represents the first attempt to compare calculated force profiles of hand muscles with EMG signals recorded during a precision grip task with the intention

of evaluating the extent to which inverse dynamic analysis (based on an anatomically precise musculoskeletal model) can predict muscle activities during hand movements.

Our results demonstrate that optimized muscle forces calculated using the inverse dynamic approach are similar to those obtained by recording EMG signals during the precision grip task. One advantage of the inverse dynamic approach is that the muscle forces or activation levels can be estimated for all the muscles involved in the precision grip task. Placing wire electrodes in all of the hand muscles *via* a surgical intervention is generally difficult, even for non-human primates. However, if muscular force predictions based on the inverse dynamic approach are reasonably accurate, as in the present study, this technique may be applied to analyses of human precision grip capability.

We found that the 1DIO, ADPt, ADPo, and EPL were active during the precision grip task in the Japanese macaque. Although direct comparisons between macaques and humans are not possible owing to differences in hand anatomy and the kinematics of precision grip, our predicted muscle activation patterns were generally in agreement with EMG activity patterns recorded during the human precision grip task (Long et al., 1970; Cooney et al., 1985). However, we found the OP muscle to be inactive during precision grip, even though it is known to be active in humans (Long et al., 1970; Cooney et al., 1985) and also in macaques (Smith and Bourbonnais, 1981). This is possibly because the macaque used the ulnar side of the thumb, instead of the pulp, to push the lever during the precision grip task. Therefore, it is likely that the OP, which functions to oppose the thumb with the other fingers, was not activated during the precision grip task. Furthermore, we predicted that the EPL would be active during the hold phase. This is consistent with EMG recordings obtained during the precision grip task in humans (Cooney et al., 1985; Rufener and Hepp-Reymond, 1988) as well as macaques (Smith and Bourbonnais, 1981). In the precision grip task, activation of the extensor muscle is probably necessary for fine adjustments to the direction of fingertip force.

Despite our compelling results, our prediction of muscle activation was certainly not perfect. Particularly, the agreement between the force and EMG patterns was not sufficient for the ABPB and ADPt muscles. This discrepancy may be attributable to inaccuracies in the mechanical modeling of the hand musculoskeletal system. Although we attempted to construct the model to be anatomically realistic, the hand of a CT-scanned and dissected macaque is not identical to that of a motion-captured macaque. In addition, the present study assumed that the fingertip forces were horizontal and parallel to the direction of the lever movements as each fingertip force were measured by a uniaxial transducer, but there might have been vertical and mediolateral force components that possibly affected the prediction of the muscle forces. Furthermore, we did not consider the influence of passive elastic elements around the joints or certain muscle properties, such as force-length and force-velocity relationships. This is owing to the fact that such joint and muscle properties of the hand in the macaque have not been quantitatively investigated, but such simplifications may have affected the accuracy of our muscle force predictions. Further improvements to the accuracy of the model are necessary for improved muscle force prediction in the precision grip task. Conversely, the discrepancy could have arisen from the measurement of the EMG signals. For instance, EMG data generated using fine wires that are implanted within muscles can represent only a fraction of all active motor units in the target muscle (Basmajian and De Luca, 1985).

Of the existing limitations of this study, the muscle redundancy problem is the most vital (Tsirakos et al., 1997). In the present study, the sum of the cubes of muscle stress was chosen as an objective function for solving the redundancy problem of muscle recruitment. However, the way in which the central nervous system solves this redundancy problem remains unclear. Indeed, our computational technique would be improved by incorporating more biologically feasible hypotheses about this issue. For example, muscle synergies (i.e., co-activation of muscles by a single neural signal) may facilitate the control of redundant degrees-of-freedom in the musculoskeletal system. Spinal interneurons could form the structural basis for functional muscle synergies (for a review, see Bizzi et al., 2008). The ability to incorporate neuronal constraints related to muscle synergies into our inverse dynamic analysis could increase the accuracy of muscle force estimations. This, in turn, could lead to new hypotheses about how the nervous system solves the redundancy problem of muscle recruitment (Moritani and Ogihara, 2019). Therefore, the present model-based analysis of neurophysiological data may serve as a viable framework for understanding how the central nervous system deals with muscle recruitment redundancy, one of the central unresolved issues in the fields of neuroscience and biomechanics. Forward dynamic simulation of the precision grip based on the present hand model can also be used for the same purpose and should also be investigated in future studies (Gustus et al., 2012; Moritani and Ogihara, 2019).

DATA AVAILABILITY STATEMENT

The raw data supporting the conclusions of this article are available by the authors upon reasonable request.

ETHICS STATEMENT

The animal study was reviewed and approved by the local ethics committee for primate research at National Institute of Neuroscience (Permit #: 2012-004).

AUTHOR CONTRIBUTIONS

NO and KS conceived and designed the study. TS and NO constructed the musculoskeletal model and drafted the manuscript. TS, NO, TT, and KS performed the experiment and

data analysis. All authors edited and approved the manuscript prior to submission.

FUNDING

This study was supported by Grant-in-Aid for Scientific Research (Nos. 21700437, 22656063, 23700482, and 19H01092) and Grant-in-Aid for Scientific Research on Innovative Areas "Hyper-adaptability for overcoming body-brain dysfunction: Integrated empirical and system theoretical approaches" (No. 19H05724) from the Japan Society for the Promotion of Science.

ACKNOWLEDGMENTS

We thank T. Kikuchi (TERRABYTE Co. Ltd.) and C. Sasaki (National Institute of Neurosciences) for technical assistance.

REFERENCES

Alstermark, B., Pettersson, L., Nishimura, Y., Yoshino-Saito, K., Tsuboi, F., Takahashi, M., et al. (2011). Motor command for precision grip in the macaque monkey can be mediated by spinal interneurons. *J. Neurophysiol.* 106, 122–126.

Basmajian, J. V., and De Luca, C. J. (1985). *Muscles Alive*, 5th Edn. Baltimore, MD: Williams and Wilkins.

Bennett, K. M., and Lemon, R. N. (1996). Corticomotoneuronal contribution to the fractionation of muscle activity during precision grip in the monkey. *J. Neurophysiol.* 75, 1826–1842.

Bizzi, E., Cheung, V. C. K., d'Avella, A., Saltiel, P., and Tresch, M. (2008). Combining modules for movement. *Brain Res. Rev.* 57, 125–133.

Blana, D., Hincapie, J. G., Chadwick, E. K., and Kirsch, R. F. (2008). A musculoskeletal model of the upper extremity for use in the development of neuroprosthetic systems. *J. Biomech.* 41, 1714–1721. doi: 10.1016/j.jbiomech.2008.03.001

Chan, S. S., and Moran, D. W. (2006). Computational model of a primate arm: from hand position to joint angles, joint torques and muscle forces. *J. Neural Eng.* 3, 327–337. doi: 10.1088/1741-2560/3/4/010

Chao, E. Y. S., An, K. N., Cooney, W. P., and Linscheid, R. L. (1989). *Biomechanics of the Hand, A Basic Research Study*. Singapore: World Scientific, 191.

Cheng, E. J., and Loeb, G. E. (2008). On the use of musculoskeletal models to interpret motor control strategies from performance data. *J. Neural Eng.* 5, 232–253. doi: 10.1088/1741-2560/5/2/014

Cooney, W. P. III, An, K. N., Daube, J. R., and Askew, L. J. (1985). Electromyographic analysis of the thumb: a study of isometric forces in pinch and grasp. *J. Hand Surg. Am.* 10, 202–210. doi: 10.1016/s0363-5023(85)80106-4

Crowninshield, R. D., and Brand, R. A. (1981). A physiologically based criterion of muscle force prediction in locomotion. *J. Biomech.* 14, 793–801. doi: 10.1016/0021-9290(81)90035-x

Damsgaard, M., Rasmussen, J., Christensen, S. T., Surma, E., and de Zee, M. (2006). Analysis of musculoskeletal systems in the anybody modeling system. *Simul. Model. Pract. Ther.* 14, 1100–1111.

Delp, S. L., Loan, J. P., Hoy, M. G., Zajac, F. E., Topp, E. L., and Rosen, J. M. (1990). An interactive graphics-based model of the lower extremity to study orthopaedic surgical procedures. *IEEE Trans. Biomed. Eng.* 37, 757–867. doi: 10.1109/10.102791

Erdemir, A., McLean, S., Herzog, W., and van den Bogert, A. J. (2007). Model-based estimation of muscle forces exerted during movements. *Clin. Biomech.* 22, 131–154. doi: 10.1016/j.clinbiomech.2006.09.005

Garcia-Elias, M., An, K. N., Berglund, L., Linscheid, R. L., Cooney, W. P., and Chao, E. Y. (1991). Extensor mechanism of the fingers: I. A quantitative geometric study. *J. Hand Surg. Am.* 16, 1130–1140. doi: 10.1016/s0363-5023(10)80079-6

Goislard de Monsabert, B., Rossi, J., Berton, E., and Vigouroux, L. (2012). Quantification of hand and forearm muscle forces during a maximal power grip task. *Med. Sci. Sports Exerc.* 44, 1906–1916. doi: 10.1249/MSS.0b013e31825d9612

Grinyagin, I. V., Biryukova, E. V., and Maier, M. A. (2005). Kinematic and dynamic synergies of human precision-grip movements. *J. Neurophysiol.* 94, 2284–2294.

Gustus, A., Stillfried, G., Visser, J., Jörntell, H., and van der Smagt, P. (2012). Human hand modelling: kinematics, dynamics, applications. *Biol. Cybern.* 106, 741–755.

Jindrich, D. L., Courtine, G., Liu, J. J., McKay, H. L., Moseanko, R., Bernot, T. J., et al. (2011). Unconstrained three-dimensional reaching in rhesus monkeys. *Exp. Brain Res.* 209, 35–50.

Kainz, H., Wesseling, M., and Jonkers, I. (2021). Generic scaled versus subject-specific models for the calculation of musculoskeletal loading in cerebral palsy gait: Effect of personalized musculoskeletal geometry outweighs the effect of personalized neural control. *Clin. Biomech.* 87:105402. doi: 10.1016/j.clinbiomech.2021.105402

Lee, J. H., Asakawa, D. S., Dennerlein, J. T., and Jindrich, D. L. (2015). Finger muscle attachments for an OpenSim upper-extremity model. *PLoS One* 10:e012712. doi: 10.1371/journal.pone.0121712

Lemay, M. A., and Crago, P. E. (1996). A dynamic model for simulating movements of the elbow, forearm, and wrist. *J. Biomech.* 29, 1319–1330. doi: 10.1016/0021-9290(96)00026-7

Long, C. II, Conrad, P. W., Hall, E. A., and Furler, S. L. (1970). Intrinsic-extrinsic muscle control of the hand in power grip and precision handling. An electromyographic study. *J. Bone Joint Surg. Am.* 52, 853–867.

Maier, M. A., Bennett, K. M., Hepp-Reymond, M. C., and Lemon, R. N. (1993). Contribution of the monkey corticomotoneuronal system to the control of force in precision grip. *J. Neurophysiol.* 69, 772–785. doi: 10.1152/jn.1993.69.3.772

Matsuura, Y., Ogihara, N., and Nakatsukasa, M. (2010). A method for quantifying articular surface morphology of metacarpals using quadric surface approximation. *Int. J. Primatol.* 31, 263–274. doi: 10.1007/s10764-010-9397-3

Michaud, F., Lamas, M., Lugrís, U., and Cuadrado, J. (2021). A fair and EMG-validated comparison of recruitment criteria, musculotendon models and muscle coordination strategies, for the inverse-dynamics based optimization of muscle forces during gait. *J. NeuroEng. Rehabil.* 18:17. doi: 10.1186/s12984-021-00806-6

Mirakhorlo, M., Van Beek, N., Wesseling, M., Maas, H., Veeger, H. E. J., and Jonkers, I. (2018). A musculoskeletal model of the hand and wrist: model definition and evaluation. *Comput. Method Biomech. Biomed. Eng.* 21, 548–557. doi: 10.1080/10255842.2018.1490952

Moritani, Y., and Ogihara, N. (2019). A hypothetical neural network model for generation of human precision grip. *Neural Netw.* 110, 213–224. doi: 10.1016/j.neunet.2018.12.001

Muir, R. B., and Lemon, R. N. (1983). Corticospinal neurons with a special role in precision grip. *Brain Res.* 261, 312–316.

Ogihara, N., and Oishi, M. (2012). Muscle dimensions in the Japanese macaque hand. *Primates* 53, 391–396. doi: 10.1007/s10329-012-0309-3

Ogihara, N., Makishima, H., Aoi, S., Sugimoto, Y., Tsuchiya, K., and Nakatuskasa, M. (2009). Development of an anatomically based whole-body musculoskeletal model of the Japanese macaque (*Macaca fuscata*). *Am. J. Phys. Anthropol.* 139, 323–338. doi: 10.1002/ajpa.20986

Oya, T., Takei, T., and Seki, K. (2020). Distinct sensorimotor feedback loops for dynamic and static control of primate precision grip. *Commun. Biol.* 3:156. doi: 10.1038/s42003-020-0861-0

Rufener, E. A., and Hepp-Reymond, M. C. (1988). Muscle coactivation patterns in the precision grip. *Adv. Biosci.* 70, 169–172.

Sachdeva, P., Sueda, S., Bradley, S., Fain, M., and Pai, D. K. (2015). Biomechanical simulation and control of hands and tendinous systems. *ACM Trans. Graph* 34:42.

Sancho-Bru, J. L., Perez-Gonzalez, A., Vergara-Monedero, M., and Giurintano, D. (2001). A 3-D dynamic model of human finger for studying free movements. *J. Biomech.* 34, 1491–1500. doi: 10.1016/s0021-9290(01)00106-3

Schieber, M. H., and Rivlis, G. (2005). A spectrum from pure post-spike effects to synchrony effects in spike-triggered averages of electromyographic activity during skilled finger movements. *J. Neurophysiol.* 94, 3325–3341. doi: 10.1152/jn.00007.2005

Smith, A. M., and Bourbonnais, D. (1981). Neuronal activity in cerebellar cortex related to control of prehensile force. *J. Neurophysiol.* 45, 286–303. doi: 10.1152/jn.1981.45.2.286

Spector, S. A., Gardiner, P. F., Zernicke, R. F., Roy, R. R., and Edgerton, V. R. (1980). Muscle architecture and force-velocity characteristics of cat soleus and medial gastrocnemius: implications for motor control. *J. Neurophysiol.* 44, 951–960. doi: 10.1152/jn.1980.44.5.951

Takei, T., and Seki, K. (2008). Spinomuscular coherence in monkeys performing a precision grip task. *J. Neurophysiol.* 99, 2012–2020. doi: 10.1152/jn.01181.2007

Takei, T., and Seki, K. (2010). Spinal interneurons facilitate coactivation of hand muscles during a precision grip task in monkeys. *J. Neurosci.* 30, 17041–17050. doi: 10.1523/JNEUROSCI.4297-10.2010

Takei, T., and Seki, K. (2013). Spinal premotor interneurons mediate dynamic and static motor commands for precision grip in monkeys. *J. Neurosci.* 33, 8850–8860. doi: 10.1523/JNEUROSCI.4032-12.2013

Takei, T., Confais, J., Tomatsu, S., Oya, T., and Seki, K. (2017). Neural basis for hand muscle synergies in the primate spinal cord. *Proc. Natl. Acad. Sci. U.S.A.* 114, 8643–8648. doi: 10.1073/pnas.1704328114

Tsirakos, D., Baltzopoulos, V., and Bartlett, R. (1997). Inverse optimization: functional and physiological considerations related to the force-sharing problem. *Crit. Rev. Biomed. Eng.* 25, 371–407. doi: 10.1615/critrevbiomedeng.v25.i4-5.20

Tubiana, R. (1981). "Architecture and function of the hand," in *The Hand*, ed. R. Tubiana (Philadelphia, PA: Saunders), 19–93.

Valente, G., Pitto, L., Testi, D., Seth, A., Delp, S. L., Stagni, R., et al. (2014). Are subject-specific musculoskeletal models robust to the uncertainties in parameter identification? *PLoS One* 9:e112625. doi: 10.1371/journal.pone.0112625

Wannier, T. M., Maier, M. A., and Hepp-Reymond, M. C. (1991). Contrasting properties of monkey somatosensory and motor cortex neurons activated during the control of force in precision grip. *J. Neurophysiol.* 65, 572–589. doi: 10.1152/jn.1991.65.3.572

Wu, J. Z., Sinsel, E. W., Glekler, D. S., Wimer, B. M., Zhao, K. D., An, K. N., et al. (2012). Inverse dynamic analysis of the biomechanics of the thumb while pipetting: a case study. *Med. Eng. Phys.* 34, 693–701. doi: 10.1016/j.medengphy.2011.09.012

Conflict of Interest: The reviewer SS declared a shared affiliation with one of the authors NO at the time of review.

The authors declare that the research was conducted in the absence of any commercial or financial relationships that could be construed as a potential conflict of interest.

Publisher's Note: All claims expressed in this article are solely those of the authors and do not necessarily represent those of their affiliated organizations, or those of the publisher, the editors and the reviewers. Any product that may be evaluated in this article, or claim that may be made by its manufacturer, is not guaranteed or endorsed by the publisher.

Copyright © 2021 Saito, Ogihara, Takei and Seki. This is an open-access article distributed under the terms of the Creative Commons Attribution License (CC BY). The use, distribution or reproduction in other forums is permitted, provided the original author(s) and the copyright owner(s) are credited and that the original publication in this journal is cited, in accordance with accepted academic practice. No use, distribution or reproduction is permitted which does not comply with these terms.

frontiers in Human Neuroscience

ORIGINAL RESEARCH
published: 04 January 2022
doi: 10.3389/fnhum.2021.784292

Individual Optimal Attentional Strategy in Motor Learning Tasks Characterized by Steady-State Somatosensory and Visual Evoked Potentials

Takeshi Sakurada[1], Masataka Yoshida[2] and Kiyoshi Nagai[1]*

[1] Department of Robotics, College of Science and Engineering, Ritsumeikan University, Shiga, Japan, [2] Major in Advanced Mechanical Engineering and Robotics, Graduate School of Science and Engineering, Ritsumeikan University, Shiga, Japan

OPEN ACCESS

Edited by:
Jun Izawa,
University of Tsukuba, Japan

Reviewed by:
Tetsunari Inamura,
National Institute of Informatics, Japan
Yuichi Kobayashi,
Shizuoka University, Japan

****Correspondence:***
Takeshi Sakurada
sakurada@fc.ritsumei.ac.jp

Specialty section:
This article was submitted to Motor Neuroscience, a section of the journal Frontiers in Human Neuroscience

Received: *27 September 2021*
Accepted: *01 December 2021*
Published: *04 January 2022*

Citation:
Sakurada T, Yoshida M and Nagai K (2022) Individual Optimal Attentional Strategy in Motor Learning Tasks Characterized by Steady-State Somatosensory and Visual Evoked Potentials. Front. Hum. Neurosci. 15:784292. doi: 10.3389/fnhum.2021.784292

Focus of attention is one of the most influential factors facilitating motor performance. Previous evidence supports that the external focus (EF) strategy, which directs attention to movement outcomes, is associated with better motor performance than the internal focus (IF) strategy, which directs attention to body movements. However, recent studies have reported that the EF strategy is not effective for some individuals. Furthermore, neuroimaging studies have demonstrated that the frontal and parietal areas characterize individual optimal attentional strategies for motor tasks. However, whether the sensory cortices are also functionally related to individual optimal attentional strategy remains unclear. Therefore, the present study examined whether an individual's sensory processing ability would reflect the optimal attentional strategy. To address this point, we explored the relationship between responses in the early sensory cortex and individuals' optimal attentional strategy by recording steady-state somatosensory evoked potentials (SSSEP) and steady-state visual evoked potentials (SSVEP). Twenty-six healthy young participants first performed a motor learning task with reaching movements under IF and EF conditions. Of the total sample, 12 individuals showed higher after-effects under the IF condition than the EF condition (IF-dominant group), whereas the remaining individuals showed the opposite trend (EF-dominant group). Subsequently, we measured SSSEP from bilateral primary somatosensory cortices while presenting vibrotactile stimuli and measured SSVEP from bilateral primary visual cortices while presenting checkerboard visual stimuli. The degree of increasing SSSEP response when the individuals in the IF-dominant group directed attention to vibrotactile stimuli was significantly more potent than those in the EF-dominant individuals. By contrast, the individuals in the EF-dominant group showed a significantly larger SSVEP increase while they directed attention to visual stimuli compared with the IF-dominant

individuals. Furthermore, a significant correlation was observed such that individuals with more robust IF dominance showed more pronounced SSSEP attention modulation. These results suggest that the early sensory areas have crucial brain dynamics to characterize an individual's optimal attentional strategy during motor tasks. The response characteristics may reflect the individual sensory processing ability, such as control of priority to the sensory inputs. Considering individual cognitive traits based on the suitable attentional strategy could enhance adaptability in motor tasks.

Keywords: focus of attention, motor learning, individual differences, steady-state somatosensory evoked potentials, steady-state visual evoked potentials, sensory cortex

INTRODUCTION

The focus of attention is one of the most influential motor performance factors (Wulf et al., 2010). Previous studies investigated the effects of two distinct attentional strategies for motor learning: internal focus (IF) and external focus (EF). In the IF strategy, performers direct their attention to body movements, whereas performers direct their attention to movement outcomes in the EF strategy. Most previous studies on motor learning have found that the EF strategy improves motor performance compared to the IF strategy in many types of motor tasks such as basketball free-throw shooting (Zachry et al., 2005), volleyball serves (Wulf et al., 2002), golf pitch shots (Wulf and Su, 2007), and dart-throwing (Lohse et al., 2010; Wulf, 2013). The advantage of the EF strategy has been explained by the constrained-action hypothesis (Wulf et al., 2001); when individuals try to control their body movements actively, the attentional strategy corresponding to the IF strategy disrupts automatic processes for motor control. However, the disruption can be avoided when the attention is directed farther away from the body. This hypothesis is also supported by empirical findings such as facilitating high-frequency movement adjustments (McNevin et al., 2003) and efficient electromyography (EMG) activities during motor tasks (Zachry et al., 2005). For instance, when basketball players were asked to perform free throws under either the EF condition (directing their attention to the rim of the basket) or the IF condition (directing their attention to wrist flexion), the EF strategy was associated with not only an improvement in shooting accuracy but also a reduction in EMG activity in the biceps and triceps muscles. These findings suggest that the EF strategy enhanced fine and automatic motor control by reducing "noise" in the motor system associated with muscle activities (Zachry et al., 2005).

Although many previous studies have shown the advantage of the EF strategy, individual factors can weaken the advantage (Perkins-Ceccato et al., 2003; Emanuel et al., 2008). For instance, high-skilled golfers (mean handicap: 4) performed better under the EF than the IF condition. However, low-skill golfers (mean handicap: 26) showed better performance under the IF strategy than the EF strategy during the pitch shot task (Perkins-Ceccato et al., 2003). Furthermore, our recent studies on healthy and stroke populations demonstrated that the optimal attentional strategy for motor tasks depends on individual sensory modality dominance for cognitive function such as motor imagery (Sakurada et al., 2016a, 2017, 2019a). Specifically, the participants with visual imagery dominance showed better motor performance under the EF condition (EF-dominant). In contrast, participants with kinesthetic imagery dominance showed higher motor performance under the IF condition (IF-dominant). These findings suggest that the EF strategy did not always lead to better motor performance and it is necessary to identify the individual optimal attentional strategy to obtain the maximum motor performance.

The neural basis has also been examined along with the accumulation of behavioral evidence regarding the focus of attention (mainly supporting EF strategy's advantages). Some neuroimaging studies reported distinct neural activity patterns under different attentional conditions. For example, during a hitting-key task, the EF strategy in which participants directed their attention to keys rather than the IF strategy directing attention to finger movement induced greater activity in the primary somatosensory and motor cortices (Zentgraf et al., 2009). Another study reported that neural activation in the left lateral premotor cortex, left primary somatosensory cortex, and intraparietal lobule was induced by switching attentional strategy between IF and EF during a finger movement task (Zimmermann et al., 2012). These studies suggest that the cognitive attentional strategy can affect neural activities in motor- and sensory-related areas.

On the other hand, the differences in the brain dynamics between IF-dominant individuals and EF-dominant individuals have not been fully understood. Regarding this point, we recently demonstrated that the neural dynamics in the frontal and parietal areas, which are important regions for attentional control (Corbetta and Shulman, 2002; Dosenbach et al., 2008; Hu et al., 2013; Jerde and Curtis, 2013; Kehrer et al., 2015) are involved in determining an individual's optimal attentional strategy. Specifically, during a visuomotor learning task, the right dorsolateral prefrontal and right somatosensory association cortices showed lower activity under the individual optimal attentional strategy. These findings suggest that the optimal attentional strategy can facilitate efficient neural processing in the frontoparietal network to accelerate its motor learning effect (Sakurada et al., 2019b). Furthermore, individuals including healthy young, healthy elderly, and acute stroke individuals with an IF dominance showed higher left prefrontal activity than those with EF-dominant under the IF condition during a simple cyclic hand movement task (Sakurada et al., 2019a). These results suggest that the prefrontal dynamics reflect an individual's ability to process internal body information, characterizing

optimal attentional strategy. Taken together, although the frontal and parietal areas are one of the crucial regions for individual optimal attentional strategy, the involvements of other areas remain unclear.

Here, although the IF and EF strategies are traditionally defined as the difference in the attentional target (i.e., body movement or movement outcome), an alternative interpretation of this definition based on the difference in the targeted sensory modality may help clarify the difference in brain characteristics between the IF- and EF-dominant individuals. Specifically, since the IF is a strategy that focuses attention on body movements, internal body information such as tactile or somatosensory information is processed preferentially. On the other hand, since the movement outcomes targeted during the EF mainly exist in the external environment, it can be assumed that the sensory modality to be processed preferentially is visual information. Indeed, the framework represents the brain's various cognitive and motor functions based on the paired sensory modalities between internal and external body information. Examples of these kinds of modalities would be kinesthetic and visual motor imagery (Solodkin et al., 2004; Guillot et al., 2009; Hétu et al., 2013), tactile and visual working memory (Savini et al., 2012; Luck and Vogel, 2013), intrinsic muscle and extrinsic visual coordinates for motor representation (Swinnen, 2002; Sakurada et al., 2016b), and internal self-paced closed skill and externally paced open-skill sports (Di Russo et al., 2010). Interestingly, we recently demonstrated the correlation between the individual optimal attentional strategy (IF or EF strategy) and their modality dominance of motor imagery (kinesthetic or visual motor imagery) (Sakurada et al., 2016a, 2017, 2019a). Therefore, we can extend the framework to the focus of attention, and the difference between IF and EF strategies can be alternatively interpreted as the difference in the sensory modality processed during each strategy. Regarding the individual differences in the optimal attentional strategy, we can interpret that IF- and EF-dominant individuals are good at processing tactile/somatosensory and visual sensory information, respectively.

If the targeted sensory modality defines the difference between IF and EF strategies, it is expected that the responses in the sensory area will be different between the IF- and EF-dominant individuals. Since the responses of the sensory areas changes due to the top-down projection from the frontoparietal networks involved in attention control (Valenza et al., 2004; Corbetta et al., 2005; Vuilleumier et al., 2008), it is highly possible that individual differences in the optimal attentional strategy also influence the sensory area's responses. In this study, in order to examine the relationship between individual optimal attentional strategy and the characteristics of the sensory areas, we focused on the oscillatory electroencephalogram (EEG) responses in the sensory areas; steady-state somatosensory evoked potentials (SSSEP) and the steady-state visual evoked potentials (SSVEP). SSSEP can be observed in the primary somatosensory cortex when individuals receive vibrotactile stimuli at a constant frequency. By contrast, SSVEP can be observed in the primary visual cortex during receiving flickering visual stimuli. Furthermore, both SSSEP and SSVEP amplitudes are enhanced by the attention and reflect top-down facilitation of early sensory processing (Giabbiconi et al., 2004, 2007; Kim et al., 2007; Kashiwase et al., 2012), so the SSSEP/SSVEP is one of the brain signal suitable for quantifying the individual attention ability to sensory inputs. Based on these characteristics of SSSEP and SSVEP, we hypothesized that individuals with IF-dominant show strong attentional modulation of SSSEP, and conversely, those with EF-dominant have a strong SSVEP attentional modulation. To test our hypothesis, this study examined whether neural activities in the somatosensory and visual areas reflect an individual optimal attentional strategy for motor learning tasks. We first classified participants into IF- and EF-dominant individuals by comparing motor learning effects under the IF and EF conditions. Subsequently, based on this classification, we assessed differences in neural activity in the sensory areas between individuals with IF- and EF-dominant by recording SSSEP and SSVEP.

MATERIALS AND METHODS

Participants

Twenty-six healthy participants (mean age ± SD, 22.4 ± 1.0 years; 3 females, 23 males) were recruited from the students at Ritsumeikan University. All participants were right-handed as assessed by the Edinburgh Handedness Inventory (laterality 91.9 ± 12.6) (Oldfield, 1971). This study was conducted in accordance with the Declaration of Helsinki and approved by the Institutional Review Board at Ritsumeikan University. All participants provided written informed consent before participation. In addition, each participant completed the following experimental protocol in a single day, including a motor learning task aiming to evaluate the individual optimal attentional strategy and EEG recording task to compare SSSEP and SSVEP responses.

Motor Learning Task for Evaluating the Individual Optimal Attentional Strategy

Experimental Setup

Each participant was seated on a chair and asked to hold a digitizing pen on a drawing tablet (Intuos4 PTK-1240/K0, Wacom, Japan) with their right hand. As shown in **Figure 1A**, an LCD monitor (size: 31.0 cm × 41.0 cm) for visual stimulus presentation was vertically placed 30 cm from a participant's face. Because a cloth and small rack hid the participants' right hand, they could not directly see their right hand during the experimental tasks. Furthermore, their head position was fixed by a chin rest. All visual stimuli on the monitor were programmed in MATLAB (MathWorks, Inc., Natick, MA, United States) using the Cogent Toolbox (University College London, London, United Kingdom). The position of the digitizing pen tip was recorded using the Cogent Toolbox with sampling at 60 Hz. The monitor displayed a hand cursor (filled black circle in **Figure 1**) as real-time visual feedback reflecting the participant's hand movement. For instance, when a participant moved their hand to diagonally forward left direction on the tablet, the hand cursor synchronously moved to the upper left direction on the monitor. The participants were instructed to move their hands with their shoulder and elbow joints and not to move their

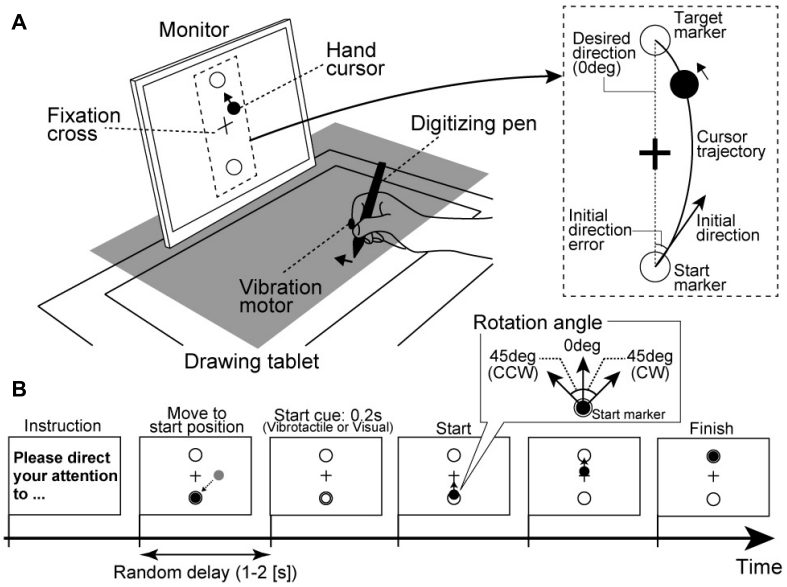

FIGURE 1 | Experimental setup in the motor learning task. **(A)** A rack to hide a participant's right hand is illustrated as a gray square. The participants control the hand cursor while looking at the fixation cross on the front monitor. **(B)** Trial procedure. Regarding the start cue, most trials presented sensory stimuli relevant to the attention target as the consistent trials (i.e., vibrotactile stimuli under the IF condition or visual stimuli under the EF condition) in order to properly guide the participants' attention.

fingers to control the hand cursor. The monitor also displayed a fixation cross at the center and two markers as start and target positions for reaching movements (open circles in **Figure 1**). The distance between the start and target markers on the monitor was 12 cm. The hand cursor moved 1.0 cm on the monitor for a 1.0-cm hand movement, so the drawing tablet's desired amplitude of the reaching movement was 12 cm. A vibration motor presenting vibrotactile stimuli was attached to the index fingertip of the right hand.

Procedure

Regarding experimental conditions, we introduced IF and EF conditions. Under the IF condition, participants were instructed to direct their attention to their hand movements itself covertly. By contrast, participants were instructed to direct their attention to the hand cursor movements on the monitor under the EF condition. Furthermore, as the standard instruction among both conditions, they were asked to fixate the fixation cross on the monitor during the reaching movements.

Regarding the procedure of each trial, before starting a trial, the monitor displayed experimental instructions to remind participants of the attentional strategy (IF or EF) to be used during the reaching movements. The participants firstly needed to move the hand cursor to the start marker position. Then, after a random delay period (1–2 s), the sensory stimulus was briefly presented (0.2 s) as a movement start cue. Specifically, vibrotactile stimulus from vibration motor (tactile start cue) or a color flickering of the hand cursor (visual start cue) was presented. The participants were instructed to start a reaching movement as quickly as possible in reaction to a start cue. They were also instructed to control the hand cursor straight from the start marker to the target marker. Each trial ended 1 s after the hand cursor reached the target marker (**Figure 1B**).

Here, we defined the trial type according to the movement start cue in each attention condition. For example, under the IF condition requiring attention to hand movements, trials with the tactile start cue were defined as consistent trials (i.e., both attention target and start cue stimulus target were related to participants' hands). In contrast, those with the visual start cue were defined as inconsistent trials (i.e., attention target was participants' hand movement, and start cue stimulus target was hand cursor). By contrast, under the EF condition, trials with a visual start cue and with tactile start cue were defined as consistent trials (i.e., both attention target and start cue stimulus target were hand cursor) and inconsistent trials (i.e., attention target was hand cursor and start cue stimulus target was related to participants' hand), respectively. The consistent trials had the role of guiding the participants' attention to the instructed target (hand movement or hand cursor) under each condition.

The reaching task consisted of two sessions, and the IF and EF conditions were randomly assigned for each participant's 1st and 2nd sessions. Each session had three phases: baseline, learning, and wash-out. In the baseline phase, the participants firstly performed ten consistent trials without visuomotor rotation (i.e., the hand cursor moved contingently according to the participant's hand movement; visuomotor rotation angle = 0°). Then, the participants performed 40 trials (35 consistent trials and five inconsistent trials, the inconsistent trials were randomly inserted among the consistent trials) as the learning phase. In the learning phase, the hand cursor movement was rotated by 45° from the origin (start marker position) in either clockwise (CW) or counterclockwise (CCW) direction relative to the

participant's actual hand movement. The CW and CCW settings were randomly assigned to the IF and EF conditions. Half of the participants performed the reaching movements under the IF condition with the CW rotation and the EF condition with the CCW rotation. The other participants performed the reaching movements under the IF condition with the CCW rotation and the EF condition with the CW rotation. In addition, participants were required to correctly modify their hand movements to control the hand cursor in a straight trajectory. Finally, the participants performed ten consistent trials without visuomotor rotation as the wash-out phase. The baseline, learning, and wash-out phase trials were successively run without interruption, and participants were not informed in advance about the CW/CCW disturbance.

Analysis

Reaction Time

To confirm whether the participants correctly directed their attention to the hand movement itself (IF condition) or to the hand cursor (EF condition), we analyzed the RT to the tactile and visual start cues in the learning phase. Although the tactile start cue did not directly reflect the hand movement itself, which is the attention target of the IF condition, the vibrotactile stimulus was effective in leading the participant's attention to the hand motor state. In other words, if participants correctly apply the IF strategy, it is expected that the responses to the tactile start cue presented to the body part performing the reaching movement will be shortened. While, since the visual start cue matched the attention target of the EF condition (i.e., hand cursor as a movement outcome) if participants correctly apply the EF strategy, the response to the visual start cue will be directly shortened. Our previous studies have also confirmed the effectiveness of linking such simple sensory inputs (vibrotactile and visual stimuli) with the IF and EF strategies (Sakurada et al., 2016a, 2019a,b). Therefore, in each trial, we defined the RT as the delay from the start cue presentation to the instant where tangential hand velocity exceeded 50 mm/s. We excluded RTs faster than 150 ms or slower than 1,500 ms (Ratcliff, 1993; Hultsch et al., 2002). The participants were considered to correctly direct their attention when the mean RT satisfied one of the following two equations.

$$\left(RT_{IF}^{T} < RT_{EF}^{T}\right) \cap \left(RT_{EF}^{V} < RT_{IF}^{V}\right) \quad (1)$$

$$\left(RT_{IF}^{T} < RT_{IF}^{V}\right) \cap \left(RT_{EF}^{V} < RT_{EF}^{T}\right) \quad (2)$$

Here, the superscripts T and V denote the modality of the start cue (T, Tactile; V, Visual), and the subscripts IF and EF denotes the attention condition. Thus, eqs. 1, 2 represent the situation where RT is faster in consistent trials than inconsistent trials.

Motor Performance and Attention Dominance

In each trial, the movement initiation was detected when the tangential hand velocity exceeded 50 mm/s, and the movement end was defined as when tangential hand velocity fell to 50 mm/s after the tangential peak velocity. Then, we calculated the initial direction error as the motor performance index. The initial direction was the direction of the initial hand velocity vector, connecting the start marker position and the hand cursor position on 100 ms after the movement initiation. Thus, initial direction error was defined as the angular difference between the directions of the visual target marker and the initial direction (**Figure 1A**, right panel). Note that in each participant, we defined the initial direction error in the visuomotor rotational direction in the learning phase as the positive direction. For instance, in a participant, when CW rotation was set for the IF condition, deviation to the right is a positive initial direction error. Similarly, when CCW rotation was set for the EF condition, deviation to the left is a positive value. To evaluate the degree of visuomotor learning under the IF and EF conditions, we focused on the after-effect, movement errors generated by unexpectedly removing the displacement of the visual hand cursor position after the learning phase (i.e., sudden removal of the visuomotor rotation in this task), indicating the learning a new transformation from the visual input to motor output in the brain (Krakauer, 2009). The after-effect in each condition was calculated based on the mean absolute initial direction error among the first to third trials of the wash-out phase. Additionally, the individual attentional strategy was determined by a difference value of the after-effect sizes between the IF and EF conditions. Specifically, we subtracted the after-effect under the IF condition from that under the EF condition. Because the size of the after-effect reflects the degree of learning effect for visuomotor rotation in the current motor task (i.e., large after-effect indicates strong motor learning effect), we defined the IF-dominant group as participants who showed larger after-effect under the IF condition than the EF condition (i.e., the difference of the after-effect is a negative value), and the EF-dominant group as participants who showed a larger after-effect under the EF condition than the IF condition (difference of the after-effect is a positive value), respectively.

Statistical Analysis

RTs were assessed by two-way repeated-measures analysis of variance (ANOVA) with "condition" (IF or EF) and "trial type" (consistent or inconsistent) as within-subject factors. In addition, to evaluate the degree of motor learning, a two-way ANOVA was applied to the after-effect size with "group" (IF- or EF-dominant) as a between-subjects factor and "condition" (IF or EF) as a within-subject factor. We used a significance threshold of $p < 0.05$ (two-tailed) for all tests.

Steady-State Somatosensory Evoked Potentials and Steady-State Visual Evoked Potentials Recording

Experimental Setup

Each participant was seated on a chair in a dimly lit room, and a chin rest fixed the participants' head position. The distance from the monitor to participants' eyes was 30 cm. When recording SSSEPs, we prepared a self-build vibrotactile device. First, sine waves were output from Arduino, and then the amplified sine waves generated vibration of diaphragms on the device (vibration amplitude was about 2 mm). Because the most effective frequency range of vibrotactile stimulus for

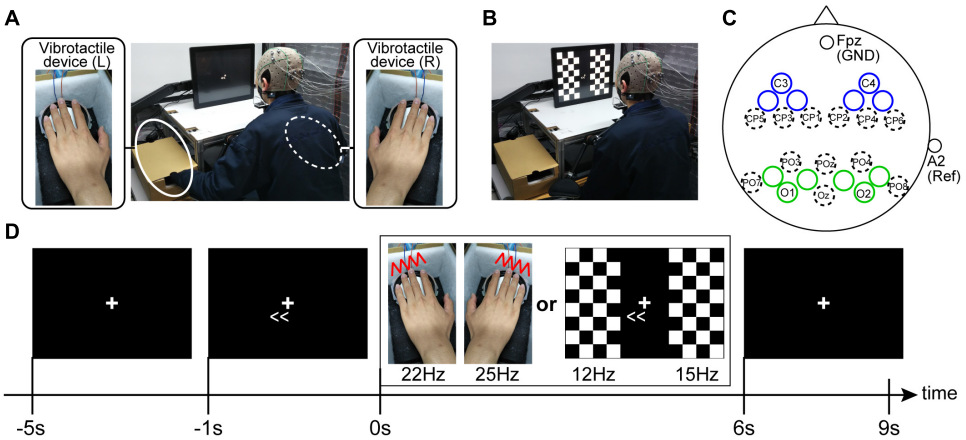

FIGURE 2 | Experimental setup for the SSSEP recordings **(A)** and the SSVEP recordings **(B)**. During the SSVEP recording, the participants were instructed to put their hands on ones' knees. **(C)** EEG electrode setup. Electrodes were placed in each bilateral sensory areas (blue and green circles indicate the electrode positions for SSSEP and SSVEP recording, respectively). The unlabeled blue and green circles are the recording electrode positions located at the midpoint of the electrode positions defined by the 10-10 extension coordinate system. **(D)** Trial procedure. The participants were instructed to sustain their attention in the indicated direction (left or right) during the stimulus presentation.

SSSEP is approximately 20–30 Hz (Tobimatsu et al., 1999; Ahn et al., 2016), we applied 22-Hz and 25-Hz vibrotactile stimuli for the left and right fingertips (index, middle, ring, and little fingers), respectively. In order to have constant contact pressure among the fingertips, bilateral fingertips were fixed on the rigid edge of the device (**Figure 2A**). When recording SSVEPs, the same LCD monitor used in the motor learning task (size: 31.0 cm × 41.0 cm, refresh rate: 60 Hz) showed pattern reversal stimuli with checkerboards. The checkerboard stimuli on the monitor were controlled by MATLAB using the Cogent Toolbox with 60 Hz. The left and right checkerboards were composed of 8 vertical × 4 horizontal squares (each size: 3.8 cm × 3.8 cm), respectively, and the white and black colors in each checkerboard stimuli were reversed at a specified frequency. The visual angles from the fixation cross to the center of the bilateral checkerboard stimuli were ±20°. Because the most effective frequency range of visual stimulus for SSVEP is approximately 10–20 Hz (Pastor et al., 2003), we applied 12-Hz and 15-Hz pattern reversal stimuli for the left and right visual fields, respectively (**Figure 2B**).

Electroencephalogram Data Acquisition

Electroencephalogram signals were detected by placing twenty Ag/AgCl active electrodes mounted in an elastic cap, according to the 10-5 EEG coordinate system. Specifically, for recording SSSEP, we used the EEG signals from the electrodes around the left and right primary somatosensory cortexes (blue circles in **Figure 2C**). By contrast, for recording SSVEP, we used the EEG signals from the electrodes around the left and right primary visual cortexes (green circles in **Figure 2C**). The ground was located at Fpz, and the reference was the right earlobe. The EEG signals were recorded with an OpenBCI Cyton+Daisy Biosensing Boards (OpenBCI, United States) with a sampling frequency of 1 kHz. Circuit impedance was kept below 20 kΩ for all electrodes. Furthermore, to check horizontal eye movements during the EEG recordings, two disposable electrodes were attached to the bilateral tails of the eyes, and the OpenBCI system also recorded electrooculography (EOG) signals.

Procedure

The EEG recording task consisted of four sessions. SSSEP and SSVEP recordings were assigned to the first two sessions in random order, and then these recordings were assigned again in reversed order in the last two sessions to reduce the order effect in each participant.

Each session had ten trials. A fixation cross was continually displayed in the center of the monitor during the trials and the participants were instructed to gaze at it. Furthermore, the participants were instructed to push a footswitch by their foot when they were ready to start a trial in each trial. Four seconds after pushing the footswitch, an arrow indicating the direction of attention (leftward or rightward) was displayed on the monitor, and the participants were asked to direct their attention to the indicated direction covertly. Then, the sensory stimuli (vibrotactile stimuli in the SSSEP recording sessions or checkerboard stimuli in the SSVEP recording sessions) were presented for 6 s from 1 s after the appearance of the arrow. Finally, after an interval of 3 s, a trial returns to the waiting phase to start the subsequent trial (**Figure 2D**). Regarding the attention direction, each session had five trials presented with a right-directional arrow (i.e., right-attention condition) and five with a left-directional arrow (i.e., left-attention condition). The order of the left- and the right-attention conditions were randomized in each session.

Analysis

Data processing was performed offline using custom-written MATLAB scripts. In the SSVEP recordings, the visual angles from the fixation cross to the edges of the left and right checkerboard stimuli (i.e., right edge of the left checkerboard and left edge of

the right checkerboard) were five degrees. Thus, eye movement with five degrees or more means that a participant directly saw the visual stimulus at the central visual field. To eliminate this scenario, the trial was excluded from the analysis when eye movement was detected from EOG signals, specifically when an EOG voltage change corresponding to eye movement of 5° or more. To eliminate the influence of eye movements, the exclusion criterion was also applied to the SSSEP recordings. After excluding the trials with eye movement, the EEG signals for 5 s (i.e., from 1 to 6 s after stimulus onset) were filtered with a two-order 5–55 Hz bandpass filter in each trial. Then, to evaluate the SSSEP and SSVEP responses under the left- and right-attention conditions, we calculated frequency spectrum density by a fast Fourier transform applying to the filtered EEG signals. Here, when the participants directed their attention to either the left or right sensory stimuli, an increase in the SSSEP/SSVEP response can be observed on the contralateral hemisphere (Giabbiconi et al., 2007; Kim et al., 2007; Bardouille et al., 2010; Kashiwase et al., 2012). Conversely, a decreasing or no change of SSSEP/SSVEP response can be observed on the ipsilateral hemisphere. Based on the attention modulation characteristics of SSSEP/SSVEP, we defined the "modulation index (*MI*)" representing the degree of SSSEP/SSVEP response change depending on the participant's covert attention by the eqs. (3–6):

$$MI^{L}_{S1} = \left(PP^{AttR}_{25Hz} - PP^{AttL}_{25Hz}\right) - \left(PP^{AttR}_{22Hz} - PP^{AttL}_{22Hz}\right) \quad (3)$$

$$MI^{R}_{S1} = \left(PP^{AttL}_{22Hz} - PP^{AttR}_{22Hz}\right) - \left(PP^{AttL}_{25Hz} - PP^{AttR}_{25Hz}\right) \quad (4)$$

$$MI^{L}_{V1} = \left(PP^{AttR}_{15Hz} - PP^{AttL}_{15Hz}\right) - \left(PP^{AttR}_{12Hz} - PP^{AttL}_{12Hz}\right) \quad (5)$$

$$MI^{R}_{V1} = \left(PP^{AttL}_{12Hz} - PP^{AttR}_{12Hz}\right) - \left(PP^{AttL}_{15Hz} - PP^{AttR}_{15Hz}\right) \quad (6)$$

Here, the superscripts L and R on the left-hand side denote the hemisphere (left hemisphere: L, right hemisphere: R), and the subscripts S1 and V1 on the left-hand side denote the targeted sensory area (primary somatosensory cortex: S1, primary visual cortex: V1). Thus, for instance, eq. (3) represents the MI in the left primary somatosensory cortex. PP is spectrum peak power at stimulus frequency in the left- or right-attention conditions. The superscripts AttL and AttR on the right-hand side denote the trial condition (AttL, left-attention condition; AttR, right-attention condition), and the subscripts on the right-hand side denote the targeted frequency to calculate the spectrum peak power. Therefore, MI is an index that summed the increase in the SSSEP/SSVEP response elicited by attention-directed stimuli and the amount of decrease in the SSSEP/SSVEP response elicited by non-attention stimuli in each sensory area. Note that, eqs. (3, 4), and eqs. (5, 6) are equivalent. After calculating the MI for each EEG electrode, the mean MI values among the three electrodes for each sensory area were used as the representative value.

Statistical Analysis

In order to clarify the relationship between the individual optimal attentional strategy observed in the first motor learning task and the attention modulation in SSSEP/SSVEP response, we compared the MI between IF- and EF-dominant groups by Wilcoxon rank-sum tests. In addition, Pearson's correlation coefficients were calculated for the inter-subject variability of the degree of attention dominance and MI. We used a significance threshold of $p < 0.05$ (two-tailed) for all tests.

RESULTS

Motor Learning Task

Reaction Time

We excluded trials in which RT did not meet our criterion (<150 or >1,500 ms). In total, 0.5% of consistent trials and 0.1% of inconsistent trials were excluded under the IF condition, and 0.3% of consistent trials and 1.2% of inconsistent trials were excluded under the EF condition.

Comparison of RTs revealed a significant main effect of trial type [$F(1,25) = 108.92$, $p = 1.34 \times 10^{-10}$, $\eta_p{}^2 = 0.81$], but the main effect of the condition [$F(1,25) = 0.25$, $p = 0.62$, $\eta_p{}^2 = 0.01$] and the two-way interaction [$F(1,25) = 0.65$, $p = 0.43$, $\eta_p{}^2 = 0.025$] did not reach statistical significance. These statistical results revealed that RTs for consistent trials were significantly faster than those for inconsistent trials [IF condition: 385.5 ± 53.7 SD ms (consistent trials) vs. 503.7 ± 90.4 SD ms (inconsistent trials). EF condition: 375.4 ± 60.4 SD ms (consistent trial) vs. 505.8 ± 108.6 SD ms (inconsistent trials)] and suggests that all participants correctly directed their attention according to experimental instructions.

Optimal Attentional Strategy

By comparing the size of the after-effect between the IF and EF conditions, we classified the participants into the IF-dominant group ($n = 12$) or EF-dominant group ($n = 14$). **Figures 3A,B** show the initial direction error changes as the consistent trials progressed (IF-dominant group, **Figure 3A**; EF-dominant group, **Figure 3B**). The hand cursor did not deviate from the desired straight trajectory in the baseline phase without visuomotor rotation (1st–10th trials). However, when the hand cursor movement was rotated during the learning phase (11th–45th trials), the initial direction error markedly increased and gradually decreased. At the end of the learning phase, initial direction error reached a plateau indicating that the participants in both groups successfully adapted to the visuomotor rotation. Finally, when the visuomotor rotation was removed in the wash-out phase (46th–55th trials), the participants showed large initial direction errors in the opposite direction (i.e., after-effect). The after-effects in each dominant group are shown in **Figure 3C**. Analysis of after-effect size revealed a significant two-way interaction of group × condition [Group: $F(1,24) = 0.023$, $p = 0.88$, $\eta_p{}^2 = 0.001$, Condition: $F(1,24) = 2.25$, $p = 0.15$, $\eta_p{}^2 = 0.086$, Interaction: $F(1,24) = 25.34$, $p = 0.000038$, $\eta_p{}^2 = 0.51$]. Post-hoc analysis with Bonferroni correction for the group × condition interaction revealed that the IF-dominant group showed significantly larger after-effect under the IF condition [$p = 0.00017$, simple main effect test] and the EF-dominant group showed significantly larger after-effect under the EF condition [$p = 0.016$, simple main effect test].

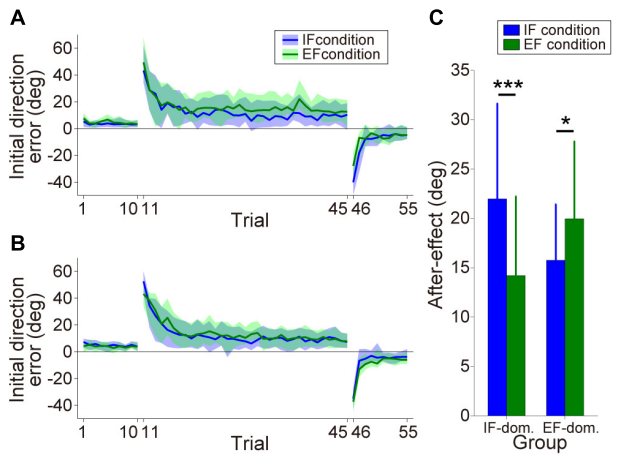

FIGURE 3 | Motor performance in the motor learning task. **(A,B)** Initial direction error transitions in the IF-dominant group **(A)** and EF-dominant group **(B)**, respectively. Blue and green lines indicate the mean initial direction errors under IF and EF conditions, respectively (note: only the consistent trials are plotted). The lighter colored regions around the mean lines denote the standard deviation. **(C)** After-effect sizes in each dominant group. Blue and green bars indicate after-effects under IF and EF conditions, respectively. Error bars denote the standard deviation. $^{*}p < 0.05$, $^{***}p < 0.001$.

Steady-State Somatosensory Evoked Potentials and Steady-State Visual Evoked Potentials Responses

Trials excluded based on EOG data comprised 3.2% of all trials.

Figures 4, **5** show the mean spectrum power of SSSEP from the primary somatosensory cortex and SSVEP from the primary visual cortex, respectively. The spectrum peaks at the stimulation frequencies indicate the induced SSSEPs and SSVEPs. First, we focus on the change in the peak power by comparing the left- and right-attention conditions in SSSEP recording (**Figure 4**). As a typical trend, the response from the left hemisphere in the IF-dominant group, the intensity at 25 Hz, was more substantial under the right-attention condition than under the left-attention condition. Conversely, the response intensity at 22 Hz was weaker when they directed attention to the right stimuli. On the other hand, no clear attention modulation was detected in the EF-dominant group, even in the left hemisphere. Regarding the right hemisphere, both IF- and EF-dominant groups did not show marked attention modulation.

Next, during the SSVEP recording, the tendency of attention modulation was reversed between both groups (**Figure 5**). Specifically, the responses from the left hemisphere tended to strengthen the 15 Hz spectrum peak and weaken the 12 Hz spectrum peak under the right-attention condition only in the EF-dominant group. Furthermore, as in the case of SSSEP recording, no marked attention modulation was observed in the right hemisphere in both groups.

Wilcoxon rank-sum tests for the mean MI among three electrodes in each sensory area revealed that the degree of SSSEP attention modulation in the left primary somatosensory cortex was significantly stronger in the IF-dominant group than in the EF-dominant group (IF-dominant group, 31.1 ± 34.3 SD; EF-dominant group, −19.1 ± 39.0 SD; $p = 0.001$). By contrast, the EF-dominant group showed a significantly stronger SSVEP attention modulation in the left visual cortex than the IF-dominant group (IF-dominant group, −46.0 ± 157.4 SD; EF-dominant group, 136.7 ± 285.7 SD; $p = 0.048$). No significant group difference was observed in the right hemisphere (SSSEP: IF-dominant group, 10.1 ± 33.7 SD; EF-dominant group, −4.3 ± 44.1 SD; $p = 0.52$. SSVEP: IF-dominant group, −21.7 ± 201.3 SD; EF-dominant group, 43.0 ± 95.7 SD; $p = 0.40$). **Figure 6** shows the individual attention dominance quantified in the first motor learning task and MI in the second EEG recording task. Again, there was a significant correlation between the two indices in SSSEP responses; individuals with more robust IF dominance had larger SSSEP attention modulation in the left hemisphere ($r = -0.55$, $p = 0.003$).

DISCUSSION

Consistent with our previous studies (Sakurada et al., 2016a, 2017, 2019a,b), the EF strategy did not always improve motor performance in about half of the participants. These results support our previous evidence that individual optimal strategy can facilitate motor learning effect. Furthermore, in this study, we demonstrated the involvement of sensory areas in the individual optimal attentional strategy. As expected, individuals with IF-dominant and those with EF-dominant had distinct neural dynamics to the sensory inputs. Therefore, these findings imply that we can alternatively interpret the difference between IF and EF strategies based on the attended sensory modality (i.e., tactile vs. visual) instead of the traditional definition based on the difference of the attention target (i.e., body movement vs. movement outcome). Here, we discuss the relationship between attention control and sensory processing.

Individual Differences in Optimal Attentional Strategy Based on Sensory Processing

Individual sensory modality dependency in the early sensory areas characterizes optimal attentional strategy during motor tasks. Specifically, the current findings indicated that higher abilities to directing attention to tactile and visual sensory inputs lead to the IF- and EF dominance, respectively. Regarding the attention modulations in SSSEP and SSVEP, we observed both increases at the attended stimulus-response and a decrease at the unattended stimulus-response in the current results. When the IF-dominant individuals received multi-frequency vibrotactile stimuli or the EF-dominant individuals received multi-frequency visual stimuli, suggesting that the individual superior cognitive ability to both enhancement and suppression is the basis of the optimal attentional strategy during motor tasks. The relationship between the attention process and responses in the sensory areas observed in this study can fit the findings of a previous study that the early sensory areas are enhanced by the attention process (Poghosyan and Ioannides, 2008). Furthermore, from the viewpoint of attention, directing attention to a specific sensory

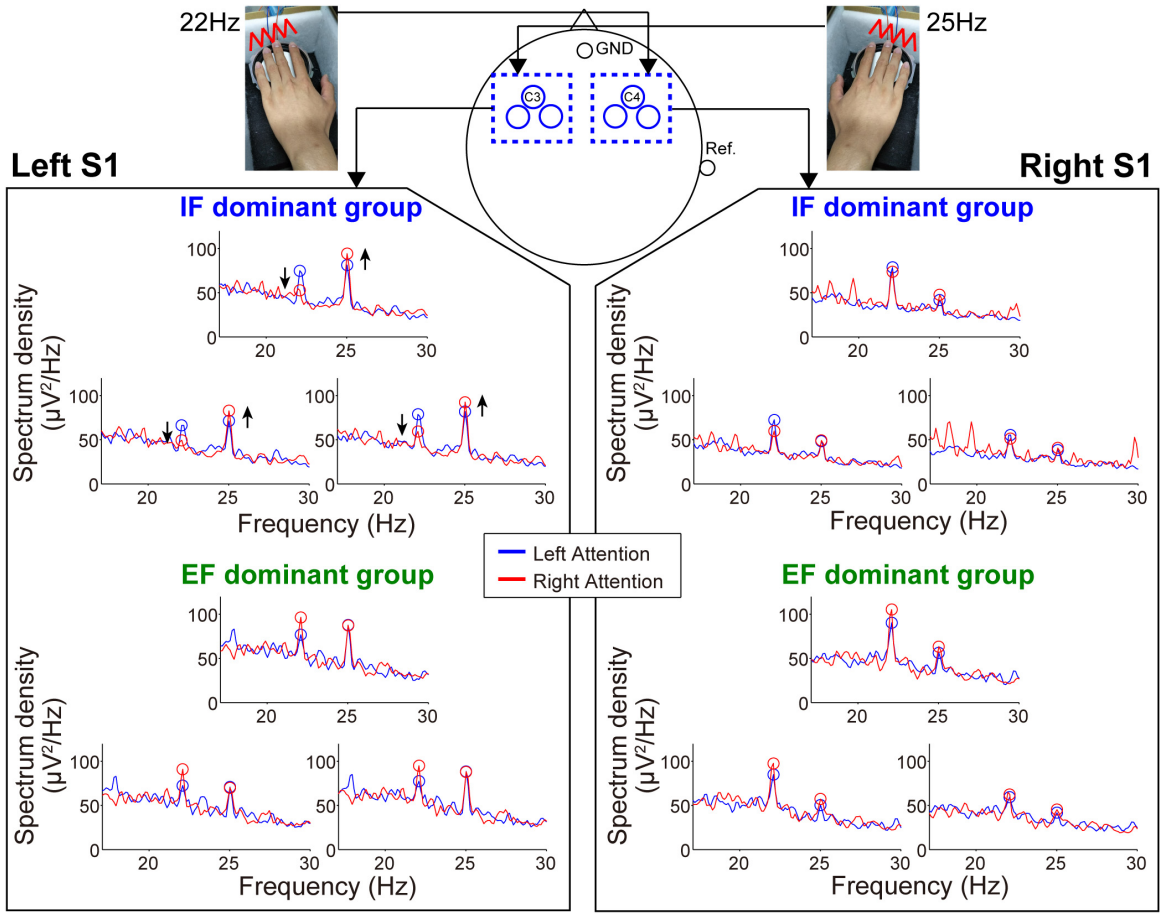

FIGURE 4 | Frequency spectrum in the SSSEP recording session. The vibrotactile stimuli presented to the fingertips mainly induced the SSSEP responses in the primary somatosensory area on the contralateral hemisphere. Blue and red lines indicate the spectrum under the left- and right-attention conditions, respectively. Bule and red circles indicate the peak points at stimulus frequencies. Attention modulation was strongly observed in the IF-dominant group as shown by the arrows in the spectrum of the left hemisphere.

stimulus modality controls the priority for the sensory inputs and contributes to facilitating perceptual sensitivity to the attended sensory information (Rahnev et al., 2011; Itthipuripat et al., 2014). Such attention processes have a crucial role in efficiently processing vast amounts of sensory inputs.

On the other hand, it is also important to suppress unnecessary (i.e., irrelevant) stimuli in tasks to perform sensory processing efficiently. It is well known that the sensory gating system contributes to filtering out irrelevant stimuli from the external environment in the brain. For instance, when paired-pulse stimuli with short inter-stimulus intervals are presented, a sensory gating phenomenon is observed; a specific oscillation response to the second stimulus is strongly reduced relative to that elicited by the first stimulus (Wiesman et al., 2017; Wiesman and Wilson, 2020). Such suppression process to sensory inputs also contributes to optimizing the neural resources available for behaviorally relevant neural computations (Cromwell et al., 2008). Furthermore, this filtering for suppressing sensory inputs is influenced by attention (Ishii et al., 2019; Wiesman and Wilson, 2020), and oscillation in the alpha band is considered to be important for the attentional suppression mechanism (Foxe and Snyder, 2011). Thus, attention to a proper sensory modality for individuals may enhance the motor learning effect by the combination of selecting the task-relevant sensory signals and suppressing the task-irrelevant sensory signals (Pestilli et al., 2011).

Although it is desired that SSSEP and SSVEP can characterize individual optimal attentional strategy, the task-dependency on the effectiveness of the current approach is unclear. In other words, we currently applied a lab-based visuomotor task based on simple upper limb movement with a low degree of freedom, but many previous studies investigating the focus of attention used various kinds of practical motor tasks with a high degree of freedom, such as basketball free-throw shooting (Zachry et al., 2005), golf pitch shots (Wulf and Su, 2007), and dart-throwing (Lohse et al., 2010; Wulf, 2013). It is essential to clarify whether the SSSEP- and SSVEP-based approach is also useful for other practical motor tasks as a test bed to characterize the individual cognitive trait. Following this point, in our preliminary results, we confirmed that the individual optimal attentional strategy in a simple visuomotor task is also an effective attentional strategy for improving another practical motor task with a high degree

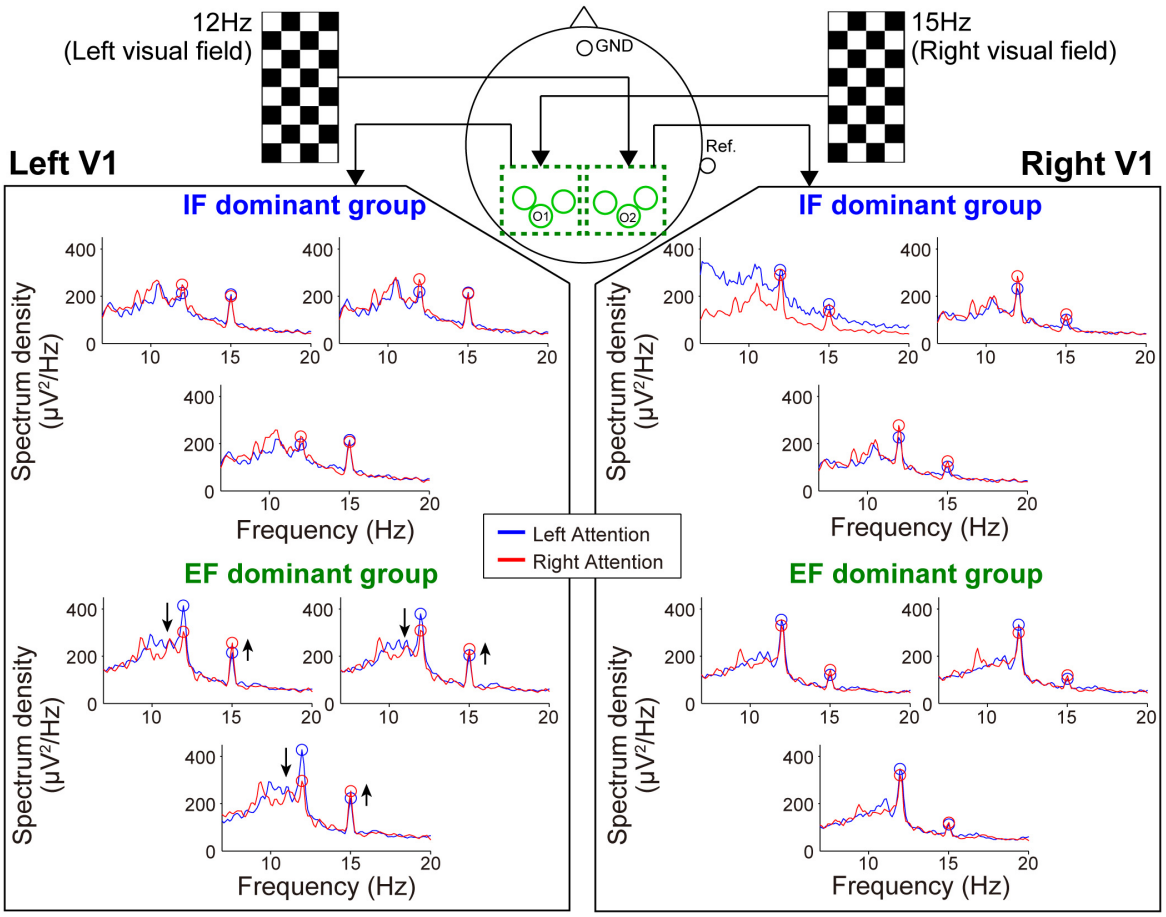

FIGURE 5 | Frequency spectrum in the SSVEP recording session. Attention modulation was strongly observed in the EF-dominant group as shown by the arrows in the spectrum of the left hemisphere.

of freedom (data not shown). Therefore, the current SSSEP- and SSVEP-based evaluations may be widely effective without task-dependency.

Large Variation in Ability to Direct Attention to Internal Body Information

Individual cognitive ability to process tactile or somatosensory information rather than visual information is a more important brain characteristic that forms the optimal attentional strategy during motor tasks. This finding is consistent with our previous reports (Sakurada et al., 2017, 2019a). In our daily life, since we actively direct attention to visual targets frequently, it is assumed that everyone can direct attention to the external space. On the other hand, the experience of actively and voluntarily directing attention to one's internal body sensory information will widely vary among individuals. For instance, individual sports experience has a significant influence. Specifically, since the internal body information has a crucial role in sports such as gymnastics or swimming, which strongly requires closed skills, individuals with such closed skill sports experience tend to have an IF-dominant (Sakurada et al., 2016a). Thus, it is interpreted that sports experience is one of the influential factors that increased individual differences in the attention ability to internal body information and formed individual dynamics in the somatosensory area. Furthermore, regarding the type of attention function evaluated in this study, the cognitive process reflected by SSVEP can be regarded as spatial attention to the external space. On the other hand, we can assume that the individual attention evaluated by SSSEP is the body-specific attention directed to near own body part(s) (Reed et al., 2006, 2010; Aizu et al., 2018). That is, the current findings might imply that the ability of body-specific attention rather than spatial attention to the external space has a large variance among individuals.

Sensory Stimulus Frequency for Quantifying Individual Attention Ability

The current study demonstrated that SSSEP and SSVEP are useful brain signals to evaluate individual attention ability based on sensory modality dependency. In this study, we applied the effective frequency band with the strongest response in SSSEP and SSVEP (Tobimatsu et al., 1999; Pastor et al., 2003; Ahn et al., 2016). However, given the relationship between brain function and neural oscillations, a more useful frequency band may quantify individual attention ability. Indeed, attention is

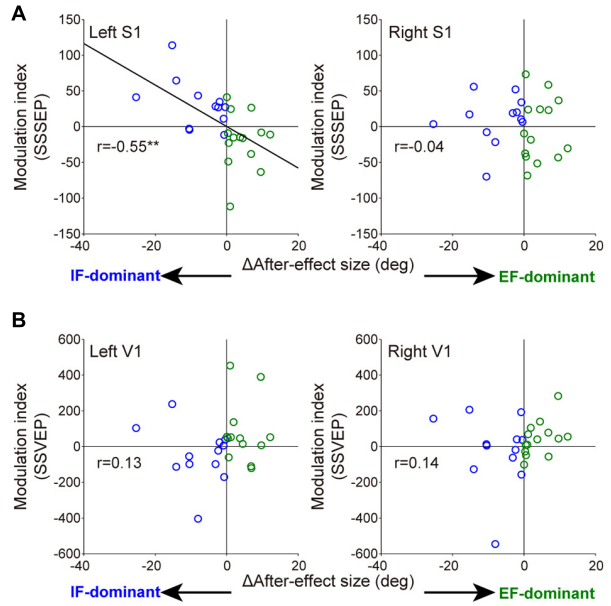

FIGURE 6 | Relationships between individual optimal attentional strategy and the attention modulation observed in SSSEP **(A)** and SSVEP **(B)**. The horizontal axis indicates the individual attention dominance calculated by the difference of after-effect size. Positive and negative values indicate IF- and EF-dominant, respectively. Modulation index (MI) on the longitudinal axis is averaged value among three electrodes in each sensory area. Blue and green circles indicate the individuals with IF dominance and those with EF dominance, respectively. Significant correlation was found in the left somatosensory cortex (right S1: $r = -0.04$, $p = 0.83$. left V1: $r = 0.13$, $p = 0.54$. right V1: $r = 0.14$, $p = 0.51$). $^{**}p < 0.01$.

associated with various ranges of neural oscillations, such as alpha and gamma bands. For instance, when directing one's attention to the left or right visual field, alpha band power in the ipsilateral posterior parietal cortex increases (Thut et al., 2006; Rihs et al., 2007). Thus, the increased alpha oscillations relate to an inhibitory attentional mechanism to task-irrelevant information in the unattended visual field.

On the other hand, directing attention to the somatosensory stimulus resulted in an increased gamma-band in the primary somatosensory cortex (Dockstader et al., 2010), attention to the right median nerve caused the gamma-band synchronization (Gobbelé et al., 2002). Taken together, because many previous studies reported that alpha band oscillations correlate negatively with attention and performance (i.e., inhibition/suppression of sensory processing) and gamma-band oscillation correlate positively with attention and performance (i.e., facilitation of sensory processing), it may be reasonable to use higher-frequency stimuli when assessing an individual's ability to direct attention to specific sensory inputs. To verify the frequency dependence can promote the development of individual difference evaluation methods.

Laterality of Attention Modulation

Although the current results suggest that the left hemisphere has neural dynamics that reflect individual optimal attentional strategy, we need to interpret this laterality carefully. First, hand dominance can influence attention modulation in the left hemisphere. Since all the participants in this study were right-handed, it is considered that they were more sensitive to the tactile or somatosensory stimuli on the right hand or to the visual stimuli in the right visual field where the right hand is present. The attentional bias to the right body or the right external space may have caused strong SSSEP and SSVEP attention modulation in the left hemisphere. Furthermore, the frequency of visual stimuli can induce laterality. Especially regarding SSVEP attention modulation, the peak of SSVEP amplitude in occipital regions was observed at 15 Hz (Pastor et al., 2003). These strong response characteristics may elicit large attention modulation in the left hemisphere processing 15 Hz-visual stimuli in this study. Note that, attention function itself exhibits lateralization (superior in the right hemisphere) (Corbetta et al., 2000; Müri et al., 2002; Shulman et al., 2010), it is also possible that such functional laterality may be an influential factor. Further investigations are required to clarify this point. For instance, we may prove this point by collecting data on left-handed participants or exploring the frequency characteristics of SSSEP and SSVEP other than the frequency adopted in this study. If the individual's dominant hand affects the laterality of attention modulation, the laterality suggests a functional aspect of attention control (i.e., intrinsic factor), whereas if there is a stimulation frequency dependency, it would simply suggest that the frequency characteristics of SSSEP and SSVEP responses lead to the laterality (i.e., extrinsic factor).

In addition to the neurophysiological factors, the influence of the experimental setup cannot be excluded. For example, previous studies reported that SSSEP and SSVEP and their attention modulation could also be observed in the frontal area where activities from the sensory area are projected (Herrmann, 2001; Giabbiconi et al., 2007; Adler et al., 2009; Pang and Mueller, 2014). Therefore, when the SSSEP or SSVEP is measured with the reference on the frontal area, the attention modulation component observed in the sensory area might be attenuated. Therefore, the reference electrode was placed on the right earlobe where the cortical signal was not measured to avoid this concern in the current study. However, under the current electrode montage, since the reference electrode was located near the right hemisphere, it might be challenging to detect the attention modulation of SSSEP and SSVEP in the right hemisphere. Therefore, as a better experimental setup, we need to adopt a different montage with the reference electrodes placed on the bilateral ear lobes in the future.

CONCLUSION

We demonstrated that individual differences in optimal attentional strategy during motor tasks reflect individual characteristics of sensory processing in the early sensory areas. Specifically, individuals with IF-dominant had a high ability to direct their attention to body movements and implicitly direct attention to internal body information, such as tactile or

somatosensory inputs related to body movements. By contrast, individuals with EF-dominant had a high ability to direct their attention to external body information such as visual inputs. These findings indicated that the dynamics of wide neural circuits, including the frontoparietal network responsible for attention control and the sensory areas, have an essential role in characterizing individual optimal attentional strategy. Thus, identifying individual differences in cognitive function depending on sensory modality will contribute to developing tailor-made protocols that maximize motor learning effects and adaptability.

DATA AVAILABILITY STATEMENT

The raw data supporting the conclusions of this article will be made available by the authors, without undue reservation.

ETHICS STATEMENT

The studies involving human participants were reviewed and approved by the Institutional Review Board at Ritsumeikan University. The participants provided their written informed consent to participate in this study.

AUTHOR CONTRIBUTIONS

TS conceived and designed the experiment, developed the experimental system, wrote the draft of the manuscript, and supervised the study. MY performed the participant experiments. TS and MY analyzed the data. All authors contributed to the discussion of the results and read and approved the final manuscript.

FUNDING

This research was supported by the Japan Society for the Promotion of Science (JSPS) KAKENHI (19K11400).

ACKNOWLEDGMENTS

The authors would like to thank all individuals who participated in this study.

REFERENCES

Adler, J., Giabbiconi, C. M., and Müller, M. M. (2009). Shift of attention to the body location of distracters is mediated by perceptual load in sustained somatosensory attention. *Biol. Psychol.* 81, 77–85. doi: 10.1016/j.biopsycho.2009.02.001

Ahn, S., Kim, K., and Jun, S. C. (2016). Steady-state somatosensory evoked potential for brain-computer interface-present and future. *Front. Hum. Neurosci.* 9:716. doi: 10.3389/fnhum.2015.00716

Aizu, N., Oouchida, Y., and Izumi, S.-I. (2018). Time-dependent decline of body-specific attention to the paretic limb in chronic stroke patients. *Neurology* 91, e751–e758. doi: 10.1212/WNL.0000000000006030

Bardouille, T., Picton, T. W., and Ross, B. (2010). Attention modulates beta oscillations during prolonged tactile stimulation. *Eur. J. Neurosci.* 31, 761–769. doi: 10.1111/j.1460-9568.2010.07094.x

Corbetta, M., Kincade, J., Ollinger, J., McAvoy, M., and Shulman, G. (2000). Voluntary orienting is dissociated from target detection in human posterior parietal cortex. *Nat. Neurosci.* 3, 292–297. doi: 10.1038/73009

Corbetta, M., Kincade, M. J., Lewis, C., Snyder, A. Z., and Sapir, A. (2005). Neural basis and recovery of spatial attention deficits in spatial neglect. *Nat. Neurosci.* 8, 1603–1610. doi: 10.1038/nn1574

Corbetta, M., and Shulman, G. L. (2002). Control of goal-directed and stimulus-driven attention in the brain. *Nat. Rev. Neurosci.* 3, 201–215. doi: 10.1038/nrn755

Cromwell, H., Mears, R., Wan, L., and Boutros, N. (2008). Sensory gating: a translational effort from basic to clinical science. *Clin. EEG Neurosci.* 39, 69–72. doi: 10.1177/155005940803900209

Di Russo, F., Bultrini, A., Brunelli, S., Delussu, A. S., Polidori, L., Taddei, F., et al. (2010). Benefits of sports participation for executive function in disabled athletes. *J. Neurotrauma* 27, 2309–2319. doi: 10.1089/neu.2010.1501

Dockstader, C., Cheyne, D., and Tannock, R. (2010). Cortical dynamics of selective attention to somatosensory events. *Neuroimage* 49, 1777–1785. doi: 10.1016/j.neuroimage.2009.09.035

Dosenbach, N. U. F., Fair, D. A., Cohen, A. L., Schlaggar, B. L., and Petersen, S. E. (2008). A dual-networks architecture of top-down control. *Trends Cogn. Sci.* 12, 99–105. doi: 10.1016/j.tics.2008.01.001

Emanuel, M., Jarus, T., and Bart, O. (2008). Effect of focus of attention and age on motor acquisition, retention, and transfer: a randomized trial. *Phys. Ther.* 88, 251–260. doi: 10.2522/ptj.20060174

Foxe, J., and Snyder, A. (2011). The role of alpha-band brain oscillations as a sensory suppression mechanism during selective attention. *Front. Psychol.* 2:154. doi: 10.3389/FPSYG.2011.00154

Giabbiconi, C. M., Dancer, C., Zopf, R., Gruber, T., and Müller, M. M. (2004). Selective spatial attention to left or right hand flutter sensation modulates the steady-state somatosensory evoked potential. *Cogn. Brain Res.* 20, 58–66. doi: 10.1016/j.cogbrainres.2004.01.004

Giabbiconi, C. M., Trujillo-Barreto, N. J., Gruber, T., and Müller, M. M. (2007). Sustained spatial attention to vibration is mediated in primary somatosensory cortex. *Neuroimage* 35, 255–262. doi: 10.1016/j.neuroimage.2006.11.022

Gobbelé, R., Waberski, T. D., Schmitz, S., Sturm, W., and Buchner, H. (2002). Spatial direction of attention enhances right hemispheric event-related gamma-band synchronization in humans. *Neurosci. Lett.* 327, 57–60. doi: 10.1016/S0304-3940(02)00384-1

Guillot, A., Collet, C., Nguyen, V. A., Malouin, F., Richards, C., and Doyon, J. (2009). Brain activity during visual versus kinesthetic imagery: an fMRI study. *Hum. Brain Mapp.* 30, 2157–2172. doi: 10.1002/hbm.20658

Herrmann, C. S. (2001). Human EEG responses to 1-100 Hz flicker: resonance phenomena in visual cortex and their potential correlation to cognitive phenomena. *Exp. Brain Res.* 137, 346–353. doi: 10.1007/s002210100682

Hétu, S., Grégoire, M., Saimpont, A., Coll, M. P., Eugène, F., Michon, P. E., et al. (2013). The neural network of motor imagery: an ALE meta-analysis. *Neurosci. Biobehav. Rev.* 37, 930–949. doi: 10.1016/j.neubiorev.2013.03.017

Hu, P., Fan, J., Xu, P., Zhou, S., Zhang, L., Tian, Y., et al. (2013). Attention network impairments in patients with focal frontal or parietal lesions. *Neurosci. Lett.* 534, 177–181. doi: 10.1016/j.neulet.2012.12.038

Hultsch, D. F., MacDonald, S. W. S., and Dixon, R. A. (2002). Variability in reaction time performance of younger and older adults. *Journals Gerontol. Ser. B Psychol. Sci. Soc. Sci.* 57, 101–115. doi: 10.1093/geronb/57.2.P101

Ishii, D., Takeda, K., Yamamoto, S., Noguchi, A., Ishibashi, K., Tanamachi, K., et al. (2019). Effect of visuospatial attention on the sensorimotor gating system. *Front. Behav. Neurosci.* 13:1. doi: 10.3389/FNBEH.2019.00001

Itthipuripat, S., Ester, E. F., Deering, S., and Serences, J. T. (2014). Sensory gain outperforms efficient readout mechanisms in predicting attention-related improvements in behavior. *J. Neurosci.* 34, 13384–13398. doi: 10.1523/JNEUROSCI.2277-14.2014

Jerde, T. A., and Curtis, C. E. (2013). Maps of space in human frontoparietal cortex. *J. Physiol. Paris* 107, 510–516. doi: 10.1016/j.jphysparis.2013.04.002

Kashiwase, Y., Matsumiya, K., Kuriki, I., and Shioiri, S. (2012). Time courses of attentional modulation in neural amplification and synchronization measured with steady-state visual-evoked potentials. *J. Cogn. Neurosci.* 24, 1779–1793. doi: 10.1162/jocn_a_00212

Kehrer, S., Kraft, A., Koch, S. P., Kathmann, N., Irlbacher, K., and Brandt, S. A. (2015). Timing of spatial priming within the fronto-parietal attention network: a TMS study. *Neuropsychologia* 74, 30–36. doi: 10.1016/j.neuropsychologia.2014.11.017

Kim, Y. J., Grabowecky, M., Paller, K. A., Muthu, K., and Suzuki, S. (2007). Attention induces synchronization-based response gain in steady-state visual evoked potentials. *Nat. Neurosci.* 10, 117–125. doi: 10.1038/nn1821

Krakauer, J. W. (2009). Motor learning and consolidation: the case of visuomotor rotation. *Adv. Exp. Med. Biol.* 629, 405–421. doi: 10.1007/978-0-387-77064-2_21

Lohse, K. R., Sherwood, D. E., and Healy, A. F. (2010). How changing the focus of attention affects performance, kinematics, and electromyography in dart throwing. *Hum. Mov. Sci.* 29, 542–555. doi: 10.1016/j.humov.2010.05.001

Luck, S. J., and Vogel, E. K. (2013). Visual working memory capacity: from psychophysics and neurobiology to individual differences. *Trends Cogn. Sci.* 17, 391–400. doi: 10.1016/j.tics.2013.06.006

McNevin, N. H., Shea, C. H., and Wulf, G. (2003). Increasing the distance of an external focus of attention enhances learning. *Psychol. Res.* 67, 22–29. doi: 10.1007/s00426-002-0093-6

Müri, R. M., Bühler, R., Heinemann, D., Mosimann, U. P., Felblinger, J., Schlaepfer, T. E., et al. (2002). Hemispheric asymmetry in visuospatial attention assessed with transcranial magnetic stimulation. *Exp. Brain Res.* 143, 426–430. doi: 10.1007/s00221-002-1009-9

Oldfield, R. C. (1971). The assessment and analysis of handedness: the Edinburgh inventory. *Neuropsychologia* 9, 97–113. doi: 10.1016/0028-3932(71)90067-4

Pang, C. Y., and Mueller, M. M. (2014). Test-retest reliability of concurrently recorded steady-state and somatosensory evoked potentials in somatosensory sustained spatial attention. *Biol. Psychol.* 100, 86–96. doi: 10.1016/j.biopsycho.2014.05.009

Pastor, M. A., Artieda, J., Arbizu, J., Valencia, M., and Masdeu, J. C. (2003). Human cerebral activation during steady-state visual-evoked responses. *J. Neurosci.* 23, 11621–11627. doi: 10.1523/JNEUROSCI.23-37-11621.2003

Perkins-Ceccato, N., Passmore, S. R., and Lee, T. D. (2003). Effects of focus of attention depend on golfers' skill. *J. Sports Sci.* 21, 593–600. doi: 10.1080/0264041031000101980

Pestilli, F., Carrasco, M., Heeger, D., and Gardner, J. (2011). Attentional enhancement via selection and pooling of early sensory responses in human visual cortex. *Neuron* 72, 832–846. doi: 10.1016/J.NEURON.2011.09.025

Poghosyan, V., and Ioannides, A. (2008). Attention modulates earliest responses in the primary auditory and visual cortices. *Neuron* 58, 802–813. doi: 10.1016/J.NEURON.2008.04.013

Rahnev, D., Maniscalco, B., Graves, T., Huang, E., de Lange, F. P., and Lau, H. (2011). Attention induces conservative subjective biases in visual perception. *Nat. Neurosci.* 14, 1513–1515. doi: 10.1038/nn.2948

Ratcliff, R. (1993). Methods for dealing with reaction time outliers. *Psychol. Bull.* 114, 510–532. doi: 10.1037/0033-2909.114.3.510

Reed, C., Betz, R., Garza, J., and Roberts, R. (2010). Grab it! Biased attention in functional hand and tool space. *Atten. Percept. Psychophys.* 72, 236–245. doi: 10.3758/APP.72.1.236

Reed, C., Grubb, J., and Steele, C. (2006). Hands up: attentional prioritization of space near the hand. *J. Exp. Psychol. Hum. Percept. Perform.* 32, 166–177. doi: 10.1037/0096-1523.32.1.166

Rihs, T., Michel, C., and Thut, G. (2007). Mechanisms of selective inhibition in visual spatial attention are indexed by alpha-band EEG synchronization. *Eur. J. Neurosci.* 25, 603–610. doi: 10.1111/J.1460-9568.2007.05278.X

Sakurada, T., Hirai, M., and Watanabe, E. (2016a). Optimization of a motor learning attention-directing strategy based on an individual's motor imagery ability. *Exp. Brain Res.* 234, 301–311. doi: 10.1007/s00221-015-4464-9

Sakurada, T., Ito, K., and Gomi, H. (2016b). Bimanual motor coordination controlled by cooperative interactions in intrinsic and extrinsic coordinates. *Eur. J. Neurosci.* 43, 120–130. doi: 10.1111/ejn.13123

Sakurada, T., Goto, A., Tetsuka, M., Nakajima, T., Morita, M., Yamamoto, S. I., et al. (2019a). Prefrontal activity predicts individual differences in optimal attentional strategy for preventing motor performance decline: a functional near-infrared spectroscopy study. *Neurophotonics* 6:025012. doi: 10.1117/1.NPh.6.2.025012

Sakurada, T., Hirai, M., and Watanabe, E. (2019b). Individual optimal attentional strategy during implicit motor learning boosts frontoparietal neural processing efficiency: a functional near-infrared spectroscopy study. *Brain Behav.* 9:e01183. doi: 10.1002/brb3.1183

Sakurada, T., Nakajima, T., Morita, M., Hirai, M., and Watanabe, E. (2017). Improved motor performance in patients with acute stroke using the optimal individual attentional strategy. *Sci. Rep.* 7:40592. doi: 10.1038/srep40592

Savini, N., Brunetti, M., Babiloni, C., and Ferretti, A. (2012). Working memory of somatosensory stimuli: an fMRI study. *Int. J. Psychophysiol.* 86, 220–228. doi: 10.1016/j.ijpsycho.2012.09.007

Shulman, G. L., Pope, D. L. W., Astafiev, S. V., McAvoy, M. P., Snyder, A. Z., and Corbetta, M. (2010). Right hemisphere dominance during spatial selective attention and target detection occurs outside the dorsal frontoparietal network. *J. Neurosci.* 30, 3640–3651. doi: 10.1523/JNEUROSCI.4085-09.2010

Solodkin, A., Hlustik, P., Chen, E. E., and Small, S. L. (2004). Fine modulation in network activation during motor execution and motor imagery. *Cereb. Cortex* 14, 1246–1255. doi: 10.1093/cercor/bhh086

Swinnen, S. P. (2002). Intermanual coordination: from behavioural principles to neural-network interactions. *Nat. Rev. Neurosci.* 3, 348–359. doi: 10.1038/nrn807

Thut, G., Nietzel, A., Brandt, S., and Pascual-Leone, A. (2006). Alpha-band electroencephalographic activity over occipital cortex indexes visuospatial attention bias and predicts visual target detection. *J. Neurosci.* 26, 9494–9502. doi: 10.1523/JNEUROSCI.0875-06.2006

Tobimatsu, S., Zhang, Y. M., and Kato, M. (1999). Steady-state vibration somatosensory evoked potentials: physiological characteristics and tuning function. *Clin. Neurophysiol.* 110, 1953–1958. doi: 10.1016/s1388-2457(99)00146-7

Valenza, N., Seghier, M., Schwartz, S., Lazeyras, F., and Vuilleumier, P. (2004). Tactile awareness and limb position in neglect: functional magnetic resonance imaging. *Ann. Neurol.* 55, 139–143. doi: 10.1002/ANA.10854

Vuilleumier, P., Schwartz, S., Verdon, V., Maravita, A., Hutton, C., Husain, M., et al. (2008). Abnormal attentional modulation of retinotopic cortex in parietal patients with spatial neglect. *Curr. Biol.* 18, 1525–1529. doi: 10.1016/J.CUB.2008.08.072

Wiesman, A., Heinrichs-Graham, E., Coolidge, N., Gehringer, J., Kurz, M., and Wilson, T. (2017). Oscillatory dynamics and functional connectivity during gating of primary somatosensory responses. *J. Physiol.* 595, 1365–1375. doi: 10.1113/JP273192

Wiesman, A. I., and Wilson, T. W. (2020). Attention modulates the gating of primary somatosensory oscillations. *Neuroimage* 211:116610. doi: 10.1016/j.neuroimage.2020.116610

Wulf, G. (2013). Attentional focus and motor learning: a review of 15 years. *Int. Rev. Sport Exerc. Psychol.* 6, 77–104. doi: 10.1080/1750984X.2012.723728

Wulf, G., McConnel, N., Gärtner, M., and Schwarz, A. (2002). Enhancing the learning of sport skills through external-focus feedback. *J. Mot. Behav.* 34, 171–182. doi: 10.1080/00222890209601939

Wulf, G., McNevin, N., and Shea, C. H. (2001). The automaticity of complex motor skill learning as a function of attentional focus. *Q. J. Exp. Psychol. A* 54, 1143–1154. doi: 10.1080/02724980143000118

Wulf, G., Shea, C., and Lewthwaite, R. (2010). Motor skill learning and performance: a review of influential factors. *Med. Educ.* 44, 75–84. doi: 10.1111/j.1365-2923.2009.03421.x

Wulf, G., and Su, J. (2007). An external focus of attention enhances golf shot accuracy in beginners and experts. *Res. Q. Exerc. Sport* 78, 384–389. doi: 10.1080/02701367.2007.10599436

Zachry, T., Wulf, G., Mercer, J., and Bezodis, N. (2005). Increased movement accuracy and reduced EMG activity as the result of adopting an external focus of attention. *Brain Res. Bull.* 67, 304–309. doi: 10.1016/j.brainresbull.2005.06.035

Zentgraf, K., Lorey, B., Bischoff, M., Zimmermann, K., Stark, R., and Munzert, J. (2009). Neural correlates of attentional focusing during finger movements: a fMRI study. *J. Mot. Behav.* 41, 535–541. doi: 10.3200/35-08-091

Zimmermann, K. M., Bischoff, M., Lorey, B., Stark, R., Munzert, J., and Zentgraf, K. (2012). Neural correlates of switching attentional focus during finger movements: an fMRI study. *Front. Psychol.* 3:555. doi: 10.3389/fpsyg.2012.00555

Conflict of Interest: The authors declare that the research was conducted in the absence of any commercial or financial relationships that could be construed as a potential conflict of interest.

Publisher's Note: All claims expressed in this article are solely those of the authors and do not necessarily represent those of their affiliated organizations, or those of the publisher, the editors and the reviewers. Any product that may be evaluated in this article, or claim that may be made by its manufacturer, is not guaranteed or endorsed by the publisher.

Copyright © 2022 Sakurada, Yoshida and Nagai. This is an open-access article distributed under the terms of the Creative Commons Attribution License (CC BY). The use, distribution or reproduction in other forums is permitted, provided the original author(s) and the copyright owner(s) are credited and that the original publication in this journal is cited, in accordance with accepted academic practice. No use, distribution or reproduction is permitted which does not comply with these terms.

frontiers in Human Neuroscience

ORIGINAL RESEARCH
published: 04 January 2022
doi: 10.3389/fnhum.2021.762223

Effect of Walking Adaptability on an Uneven Surface by a Stepping Pattern on Walking Activity After Stroke

Yusuke Sekiguchi[1]*, *Keita Honda*[1] and *Shin-Ichi Izumi*[1,2]

[1] Department of Physical Medicine and Rehabilitation, Graduate School of Medicine, Tohoku University, Sendai, Japan, [2] Department of Physical Medicine and Rehabilitation, Graduate School of Biomedical Engineering, Tohoku University, Sendai, Japan

Real-world walking activity is important for poststroke patients because it leads to their participation in the community and physical activity. Walking activity may be related to adaptability to different surface conditions of the ground. The purpose of this study was to clarify whether walking adaptability on an uneven surface by step is related to daily walking activity in patients after stroke. We involved 14 patients who had hemiparesis after stroke (age: 59.4 ± 8.9 years; post-onset duration: 70.7 ± 53.5 months) and 12 healthy controls (age: 59.5 ± 14.2 years). The poststroke patients were categorized as least limited community ambulators or unlimited ambulators. For the uneven surface, the study used an artificial grass surface (7 m long, 2-cm leaf length). The subjects repeated even surface walking and the uneven surface walking trials at least two times at a comfortable speed. We collected spatiotemporal and kinematic gait parameters on both the even and uneven surfaces using a three-dimensional motion analysis system. After we measured gait, the subjects wore an accelerometer around the waist for at least 4 days. We measured the number of steps per day using the accelerometer to evaluate walking activity. Differences in gait parameters between the even and uneven surfaces were calculated to determine how the subjects adapted to an uneven surface while walking. We examined the association between the difference in parameter measurements between the two surface properties and walking activity (number of steps per day). Walking activity significantly and positively correlated with the difference in paretic step length under the conditions of different surface properties in the poststroke patients ($r = 0.65$, $p = 0.012$) and step width in the healthy controls ($r = 0.68$, $p = 0.015$). The strategy of increasing the paretic step length, but not step width, on an uneven surface may lead to a larger base of support, which maintains stability during gait on an uneven surface in poststroke patients, resulting in an increased walking activity. Therefore, in poststroke patients, an increase in paretic step length during gait on an uneven surface might be more essential for improving walking activity.

Keywords: walking adaptability, walking activity, compensatory movement, stroke, uneven surface

OPEN ACCESS

Edited by:
Tomohiko Takei,
Tamagawa University, Japan

Reviewed by:
Kiyotaka Kamibayashi,
Doshisha University, Japan
Olivier Darbin,
University of South Alabama, United States

***Correspondence:**
Yusuke Sekiguchi
yusuke.sekiguchi.b2@tohoku.ac.jp

Specialty section:
This article was submitted to Motor Neuroscience, a section of the journal Frontiers in Human Neuroscience

Received: *21 August 2021*
Accepted: *16 November 2021*
Published: *04 January 2022*

Citation:
Sekiguchi Y, Honda K and Izumi S-I (2022) Effect of Walking Adaptability on an Uneven Surface by a Stepping Pattern on Walking Activity After Stroke. Front. Hum. Neurosci. 15:762223. doi: 10.3389/fnhum.2021.762223

INTRODUCTION

Real-world walking activity is important for poststroke patients because it leads to their participation in the community and physical activity, decreasing their risks of mental illness, hypertension, hyperlipidemia, and diabetes (Ivey et al., 2005; Hafer-Macko, 2008; Barclay et al., 2015; Saunders et al., 2016). It is often measured as the number of steps per day by using an activity monitor. A systematic review demonstrated that the walking activity (ranging from 1,389 to 7,379 steps/day) in poststroke patients was lower than that (ranging from 6,294 to 14,730 steps/day) in age-matched healthy controls (English et al., 2014). Kono et al. (2015) demonstrated that the attainment of approximately > 6,000 steps/day may reduce the risk of new vascular events in poststroke patients. Therefore, the lack of real-world walking activity is a serious problem in patients with hemiparesis.

The factors associated with decreased physical activity, including walking activity, after stroke were age, sex, physical function (6-min walk test distance, comfortable gait speed, Berg balance scale, and cardiorespiratory fitness), depression, fatigue, self-efficacy, and quality of life (Thilarajah et al., 2018). Especially, the 6-min walk test was better able to discriminate real-world walking activity among home, limited community, and full community ambulators (Fulk et al., 2017). However, in a previous study, following training, changes in specific clinical walking measures, including 6-min walk test distance, explained up to 33% of the changes in walking activity, although those in gait biomechanics explained up to 86% of the variance in altered walking activity, with specific associations with kinematic parameters at hip joints in both lower limbs (Ardestani et al., 2019). Biomechanical assessment (i.e., lower limb kinematics during gait) may be more available than clinical walking measures for detecting changes in walking activity.

Walking adaptability is an essential requisite for achieving independent and safe community walking (Balasubramanian et al., 2014). A situation that requires walking adaptability in a real-life environment is walking on uneven surfaces that are neither flat or firm (Balasubramanian et al., 2014). Healthy controls decreased their step length and increased the height of their toe clearance and step time and width when walking on uneven surfaces (i.e., railroad ballast and artificial grass) (Allet et al., 2009; Menant et al., 2009; Wade et al., 2010). The shorter and slower steps were represented as a cautious gait pattern to decrease the risk of slipping (Wade et al., 2010). In patients with incomplete spinal injury, the step length decreased and the step time increased during walking on uneven surfaces (i.e., artificial grass, soft, and pebble surfaces), but the step length symmetry did not change, as in the healthy controls (Promkeaw et al., 2019). In contrast, adapting to uneven surfaces may be difficult for patients after the onset of cerebral injury because of the damaged supraspinal motor pathways (i.e., motor cortex, cerebral white matter, and/or internal capsule) that are critical for walking adaptability. Additionally, the motor modules, which organize muscle activities in the lower limbs during gait, were merged by the impaired nervous system due to stroke (Clark et al., 2010; Brough et al., 2018). The fewer motor modules resulted in more asymmetry propulsion [i.e., lower propulsion on the paretic side (PS) than on the non-PS] during gait in patients after stroke (Clark et al., 2010). Similarly, the merged plantarflexor motor module increased whole-body angular momentum at the frontal plane during gait in patients, representing decreased balance control (Brough et al., 2018). Therefore, it may be difficult to adapt to the uneven surface by merging plantarflexor modules due to the instability of patients with an impaired nervous system as in stroke. However, patients with cerebral palsy also adapted to uneven surfaces (i.e., polyurethane) with decreased gait speed and cadence, increased toe clearance, and increased knee and hip flexion and pelvic anterior tilt, similar to the healthy controls (Böhm et al., 2014). Although a previous study investigated walking on uneven surfaces in poststroke patients, the study only clarified increased physiological cost index and decreased walking speed during walking on uneven surfaces (i.e., placing small strips of wood) (Burridge et al., 2007). Therefore, unlike patients with an incomplete spinal injury and cerebral palsy, how stroke patients adapt to an uneven surface by stepping on the PS during gait remains unclear. Clarifying how poststroke patients adapt to uneven surfaces by step and whether the adaptability to uneven surfaces by stepping on the PS is related to walking activity may be important for understanding the mechanism of the lack of real-world walking activity.

The purpose of this study was to examine stepping patterns during gait on uneven surfaces in poststroke patients and their relationship with real-world walking activity. As compensatory movements such as pelvic hiking and circumduction were used even when walking on level ground (Kerrigan et al., 2000), they may be applied even more owing to the need to take appropriate steps when walking on uneven surfaces. The compensatory movements contributed to energy cost during gait in poststroke patients, which was related to participation in the community (Chen et al., 2005; Stoquart et al., 2012; Franceschini et al., 2013). Postural orientation and dynamic equilibrium, which need balance control, use visual, vestibular, and somatosensory (cutaneous and proprioceptive) sensory information (Horak and Macpherson, 1996). The multiple sensory input is integrated and provides a coherent interpretation of the postural orientation and dynamic equilibrium. The information was available for comparison with an internal body model that maintains balance (Horak and Macpherson, 1996). The pathological dysfunction in the sensory-motor circuitry contributes to the loss of balance function (Darbin et al., 2016; Kuramatsu et al., 2021). However, the compensatory mechanism for somatosensory conditions by visual information completes sit-to-stand in patients after stroke (Kuramatsu et al., 2020). Like sit-to-stand, patients after stroke would be able to adapt gait function on an uneven surface. We hypothesized that the adaptability to uneven surfaces by shorter step length and time with compensatory movement is related to increased real-world walking activity in poststroke patients.

MATERIALS AND METHODS

Subjects

In total, 14 poststroke patients (11 men and 3 women) and 12 healthy controls (8 men and 4 women) of comparable ages and anthropometric characteristics participated in this study (**Table 1**). The inclusion criteria for poststroke patients were (1) ability to walk without a cane on artificial grass with an approximately 2-cm leaf length over a distance of at least 7 m; (2) a gait speed of > 60 cm/s during walking on an even surface based on the result of a previous study that at the slowest walking speeds (30–50 cm/s), the waist-positioned accelerometer recorded 0 step for approximately 48% of the walking trials; (3) the ability to follow verbal commands; and (4) a poststroke duration of at least a year. The inclusion criterion for controls was subjects without neurological lesions. All the participants were excluded if they had (1) unstable medical conditions, (2) major orthopedic surgery or an actual orthopedic condition interfering with locomotion, and (3) higher brain dysfunction, which skewed the measurements. The nine patients and four healthy controls were treated with blood pressure medication. The participants provided their written and informed consent prior to the start of the experimental session. This study was approved by our institutional review board.

Gait Assessment

In this study, artificial grass was used during walking in an uneven surface condition. Artificial grass is portable and useful instrumentation to assess walking on uneven surfaces in hospitals. Moreover, the use of artificial grass when walking can change the gait spatiotemporal parameters in patients with incomplete spinal injuries and healthy controls compared with when artificial grass is not used (i.e., even surfaces) (Promkeaw et al., 2019). This study applied the following two surface conditions: even surface in the laboratory and artificial grass surface of 7 m long and 1 m wide, with an approximately 2-cm leaf length for uneven surfaces (**Figure 1**). Even surface walking was completed first by all the participants. The leaf length used in this study was shorter than that in the previous study (Promkeaw et al., 2019). Although the patients with spinal cord injury in the previous study were allowed to use their customary walking devices (Promkeaw et al., 2019), the poststroke patients in this study were not allowed to be assisted by anyone and to use a cane during walking because their gait parameters were compared with those of the healthy controls, who did not use canes. All of the participants walked over the two surfaces with shoes and orthoses, which they usually wore, at a self-selected speed for more than two trials over each surface. The participants were allowed to rest between the trials, if required. Before the measurement, the participants familiarized themselves with walking over the two surfaces. Forty markers were attached to 13 segments composed of the head, torso, upper arms, forearms, pelvis, thighs, shanks, and feet based on the anthropometric data reported by Okada (Okada et al., 1996; **Table 2**). Whole-body motion data were collected at 120 Hz by using an 8-camera motion analysis system (MAC 3D, Motion Analysis Corporation, Santa Rosa, CA, United States). The three-dimensional coordinates were smoothed using a bidirectional fourth-order Butterworth lowpass filter with a cutoff frequency of 6 Hz. We detected the gait event (i.e., heel strike and toe off) using the horizontal sacral-heel distance (French et al., 2020). Spatiotemporal parameters were calculated according to the representative method (Butler et al., 2006). The kinematic data for each joint in the lower extremities were calculated using a joint coordinate system (Robertson et al., 2013). The representative parameters of joint angle in the lower limb in the sagittal plane during gait were determined based on the findings of a previous study (Benedetti et al., 1998). The representative parameters related to compensatory strategies in the paretic swing phase were calculated as the segment angle in the global coordination system (Kerrigan et al., 2000). Leg circumduction is the maximum thigh abduction angle in the paretic swing phase. In addition, the magnitude of the symmetry of step length and swing time was calculated as the ratio of the left values to the right values, with the larger value in the numerator (irrespective of the PS) (Patterson et al., 2010). These parameters were calculated using the customized MATLAB software (Mathworks Inc., Natick, MA, United States). The results were the average of more than five strides in successful trials.

TABLE 1 | [a]Values are means ± standard deviations. [b]Anterior cerebral artery, ACA; Middle cerebral artery, MCA. [c]The number of subjects who had lacunar infarct lesions (i.e., corona radiata, internal capsule, and both corona radiata and internal capsule) was 3, 2, and 1.

Characteristic	Patients	Controls
N	14	12
Gender (Male/Female)	11/3	8/4
Age (years)[a]	59.3 ± 8.9	59.5 ± 14.6
Height (cm)[a]	169 ± 5.56	163.1 ± 9.15
Weight (kg)[a]	68.1 ± 8.64	62.6 ± 11.49
Diagnosis (Hemorrhage/Infarct)	6/8	
Type of Hemorrhage		
Putamen/Thalamus/Subparietal lobe	4/1/1	
Vascular territory of Infarct		
ACA infarct[b]/MCA infarct[b]/lucnarinfarct[c]	1/1/6	
Paretic side (Left/Right)	4/10	
Time since stroke (months)[a]	70.7 ± 53.5	
SIAS motor function (0/1/2/3/4/5)		
Ankle joint	0/0/0/3/9/2	
Knee joint	0/0/1/8/5/0	
Hip joint	2/1/1/5/5/0	

Walking Activity

After the gait assessment, the subjects wore the ActiGraph (AG) accelerometer (GT9X Link, ActiGraph LLC, Pensacola, FL, United States) around the waist at the height of the iliac crest on the right side in the healthy controls and on the non-PS in the poststroke patients, which was held in place by an elastic belt. The AG accelerometer recorded the three axes of acceleration at 30 Hz by using a proprietary algorithm to calculate step counts

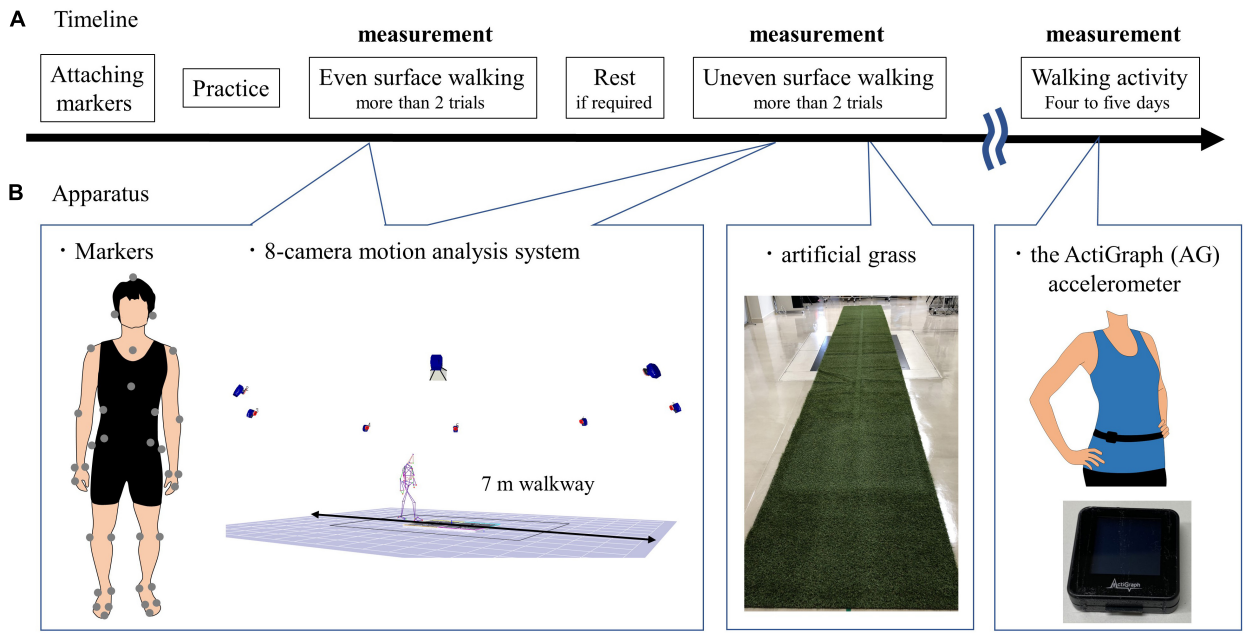

FIGURE 1 | Experimental paradigm. **(A)** Timeline. Even surface walking was completed first by all the participants; uneven surface walking was second after attaching markers. The participants were allowed to rest between the trials if required. After the gait assessment, the subjects wore the ActiGraph (AG) accelerometer (GT9X Link, ActiGraph LLC, Pensacola, FL, United States) around the waist at the height of the iliac crest on the right side in healthy controls and on the non-PS in poststroke patients; the device was held in place by an elastic belt. The AG accelerometer was worn for at least 4 days and at most 5 days. **(B)** Apparatus. Forty markers were attached to 13 segments; a 7 m gait on the even surface and uneven surface was measured using an 8-camera motion analysis system (MAC 3D, Motion Analysis Corporation, Santa Rosa, CA, United States). The artificial grass surface is 7 m long and 1 m wide, with an approximately 2 cm leaf length for uneven surfaces. The size of the AG accelerometer is 35 mm × 35 mm × 10 mm, and its weight is 14 g.

with a low-frequency extension (LFE) filter. We used the number of steps per day to evaluate walking activity. The participants were asked to wear the device while awake and to take it off before swimming or bathing. In this study, the AG accelerometer was worn for 14 ± 3 h on a single day by the healthy controls and for 13 ± 3 h for at least 4 days and at most 5 days.

TABLE 2 | Placement of markers on the body.

Segment	Placement of markers
Head	Top of head and both ears, and the spinous process of the 7th cervical vertebrae
Trunk	Spinous process of the 7th cervical vertebrae, spinous process of the 10th thoracic vertebrae, jugular notch where the clavicles meet the sternum, xiphoid process of the sternum, and the position in the middle of the right scapula
Upper arm	Both acromions and both lateral epicondyles of elbow
Forearm	Both lateral epicondyles of the elbow and both styloid processes of the ulna and radius
Pelvis	Both anterior superior iliac spines and both posterior superior iliac spines
Thigh	Both greater trochanters and both lateral and medial epicondyles of knee
Shank	Both lateral epicondyles of knee and both lateral and medial malleolus
Foot	Both the first and fifth metatarsal heads, both lateral and medial malleolus, and both calcaneus

Some subjects felt uncomfortable when they wore the AG accelerometer at the ankle for a day; thus, in this study, the subjects wore the AG accelerometer at the waist. However, a previous study demonstrated that the AG accelerometer produced the most accurate step count in poststroke patients when worn at the non-paretic ankle without LFE but not when worn at the waist (Campos et al., 2018). Therefore, before measurement of the number of steps per day, we evaluated its validity using the AG accelerometer. The subjects with AG walked at their self-selected comfortable pace for 1 min on a 30-m walkway on an even surface two times. The number of walking steps taken within 1 min was recorded using the AG accelerometer and counted by the physical therapist. Agreement in the number of 1-min walking steps calculated using the AG condition and the number of the steps counted by the physical therapist was determined using the Shrout-Fleiss intraclass correlation coefficient [ICC (3,1)] and served as the gold standard. The ICC (3,1) in the healthy controls and patients were 0.48 ($p = 0.047$) and 0.88 ($p < 0.001$). Moreover, the total number of steps counted using the AG accelerometer for 1 min was compared with that counted by the physical therapist, using paired *t*-tests for the data of both groups. Our results showed no significant differences in any of the parameters between the two groups.

The walking activity of 5,000–7,499 steps/day was categorized as least limited community ambulation, and

walking activity ≥7,500 was categorized as unlimited community ambulation (Fulk et al., 2017).

Statistical Analysis

Anthropometric characteristics and walking activity (number of steps/day) were compared between the patients and the healthy controls using unpaired Student's *t*-tests. Paretic and non-paretic sides in patients and the left side [LS] in healthy controls were compared to examine the effects of the groups and surfaces on gait-related parameters; also, the conditions between the even and uneven surfaces were compared using two-way analysis of variance followed by the Bonferroni *post hoc* test. Moreover, differences in gait parameters between the even and artificial grass surfaces were calculated to determine how the subjects adapted to the artificial grass surface while walking. We examined the association between the differences in surface and walking activity (number of steps per day) using the Pearson product-moment and Spearman's rank correlation coefficients if the parameter was non-normally distributed. A *p*-value of 0.05 was set as the criterion for statistical significance. Partial beta squared ($_p^2$) and Cohen's *d* were calculated as estimates of the effect size. The statistical analyses were performed using a statistical software package (SPSS version 24; IBM Corp., Armonk, NY, United States).

RESULTS

No significant differences in body height and weight were found between the patients and the healthy controls (**Table 1**). Gait speed, spatiotemporal and kinematic parameters during gait, and the number of steps per day for the patients and controls are presented in **Tables 3**, **4**. In addition, **Tables 5**, **6** showed the correlations between the number of steps per day and the difference in spatiotemporal and kinematic parameters under the conditions of different surface properties.

Walking Activity

The number of steps per day of the poststroke patients (10,118.0 ± 4,550.2 steps/day) was significantly less than that of the healthy controls (15,376.6 ± 5,440.1 steps/day; $p = 0.013$, $d = 1.06$). All the healthy controls and 78.6% of the poststroke patients were categorized as unlimited ambulators. In addition, 21.4% of the poststroke patients were categorized as least limited community ambulators.

Spatiotemporal Parameters

Gait speed on the even surface in the patients with hemiparesis and healthy controls was faster than 0.71 m/s. There were three patients with a shorter step length on the PS than step length on the non-PS when walking on the even surface. When walking on the uneven surface, in addition to the three patients, one patient had a longer step length on the non-PS.

Significant effects for group factor on gait speed [$F_{(1,24)} = 27.02$, $p < 0.001$, $\eta_p^2 = 0.53$], gait cycle time [$F_{(1,24)} = 15.38$, $p = 0.001$, $\eta_p^2 = 0.39$], stance [$F_{(2,37)} = 10.45$, $p < 0.001$, $\eta_p^2 = 0.36$] and swing times [$F_{(2,37)} = 7.99$, $p = 0.001$, $\eta_p^2 = 0.30$], step [$F_{(2,37)} = 11.46$, $p < 0.001$, $\eta_p^2 = 0.38$], and stride length [$F_{(1,24)} = 15.57$, $p = 0.001$, $\eta_p^2 = 0.39$] were observed. Gait speed, gait cycle time, and stride length in the patients were slower (0.95 ± 0.19 m/s vs. 1.37 ± 0.21 m/s), longer (1.21 ± 0.15 s vs. 1.03 ± 0.07 s), and shorter (1.13 ± 0.14 m vs. 1.38 ± 0.19 m) than those in the healthy controls. The stance times on the PS ($p = 0.019$, $d = 1.49$) and non-PS ($p < 0.001$, $d = 1.74$) were significantly longer than that on the LS in the healthy controls, although the step lengths on the PS ($p = 0.012$, $d = 1.13$) and non-PS ($p < 0.001$, $d = 1.96$) were shorter. Swing time on the PS was longer than that on the non-PS ($p = 0.034$, $d = 0.91$) and LS ($p = 0.001$, $d = 1.42$).

Significant effects for surface factor on gait speed [$F_{(1,24)} = 6.83$, $p = 0.015$, $\eta_p^2 = 0.22$], gait cycle time [$F_{(1,24)} = 15.38$, $p = 0.005$, $\eta_p^2 = 0.28$], stance [$F_{(1,37)} = 13.24$, $p = 0.001$, $\eta_p^2 = 0.26$] and swing times [$F_{(1,37)} = 12.45$, $p = 0.001$, $\eta_p^2 = 0.25$], and step width [$F_{(1,24)} = 16.50$, $p < 0.001$,

TABLE 3 | The mean and standard deviation of spatiotemporal data in patients after stroke and healthy controls.

	Paretic side		Non-paretic side		Left side in healthy controls		Two-way ANOVA *P*-value		
	Even	Uneven	Even	Uneven	Even	Uneven	Subjects	Surface	Interaction
Gait speed (m/s)	0.94 ± 0.20[c]	0.97 ± 0.19[cd]			1.35 ± 0.20	1.38 ± 0.22[d]	0.000	0.015	0.947
Gait cycle time (s)	1.23 ± 0.15[c]	1.20 ± 0.14[cd]			1.03 ± 0.06[a]	1.02 ± 0.14[ad]	0.001	0.005	0.204
Stance time (s)	0.66 ± 0.09[c]	0.64 ± 0.08[cd]	0.71 ± 0.12[c]	0.69 ± 0.11[cd]	0.55 ± 0.04[ab]	0.55 ± 0.05[abd]	<0.001	0.001	0.414
Swing time (s)	0.57 ± 0.07[bc]	0.56 ± 0.08[bcd]	0.51 ± 0.05[a]	0.50 ± 0.05[ad]	0.48 ± 0.03[a]	0.48 ± 0.04[ad]	0.001	0.001	0.503
Step length (m)	0.57 ± 0.08	0.56 ± 0.08	0.51 ± 0.06	0.52 ± 0.06	0.65 ± 0.07	0.65 ± 0.09	<0.001	0.149	0.237
Stride length (m)	1.12 ± 0.15[c]	1.13 ± 0.14[c]			1.38 ± 0.18[a]	1.39 ± 0.20[a]	0.001	0.369	0.846
Step width (m)	0.15 ± 0.04	0.16 ± 0.04[d]			0.13 ± 0.03	0.15 ± 0.03[d]	0.284	0.000	0.345
Stance time symmetry	1.09 ± 0.06[c]	1.08 ± 0.07[c]			1.03 ± 0.02[a]	1.02 ± 0.0.02[a]	0.003	0.589	0.996
Swing time symmetry	1.11 ± 0.09[c]	1.11 ± 0.10[c]			1.03 ± 0.03[a]	1.03 ± 0.02[a]	0.004	0.661	0.9.34

[a] *Significantly different from the paretic side at $p < 0.05$.*
[b] *Significantly different from non-paretic side at $p < 0.05$.*
[c] *Significantly different from healthy controls at $p < 0.05$.*
[d] *Significantly different from even surface at $p < 0.05$.*

TABLE 4 | The mean and standard deviation of angles in lower limb in patients after stroke and healthy controls.

	Paretic side		Non-paretic side		Left side in healthy controls		Two-way ANOVA *P*-value		
	Even	Uneven	Even	Uneven	Even	Uneven	Subjects	Surface	Interaction
Ankle plantarflexion in early stance	5.4 ± 5.7	5.4 ± 5.9	3.9 ± 4.0	3.5 ± 3.7	3.2 ± 2.9	2.9 ± 2.9	0.374	0.301	0.679
Ankle dorsiflexion in stance	−11.4 ± 8.2	−11.0 ± 9.2	−17.4 ± 5.7	−16.7 ± 6.0	−13.9 ± 7.0	−14.7 ± 6.4	0.110	0.834	0.279
Ankle plantarflexion at toe-off	−3.1 ± 8.5	−2.6 ± 8.8	−4.3 ± 8.1	−4.1 ± 7.9	−4.1 ± 7.5	−4.2 ± 7.7	0.885	0.476	0.629
Ankle dorsiflexion in swing	−4.8 ± 7.3	−4.4 ± 8.2	−8.5 ± 5.1	−8.1 ± 4.9	−6.8 ± 5.2	−7.1 ± 4.8	0.270	0.666	0.547
Knee flexion in early stance	−10.7 ± 8.7	−10.8 ± 9.3	−12.2 ± 8.0	−12.7 ± 7.9	−5.8 ± 4.1	−7.1 ± 3.7	0.123	0.052	0.274
Knee extension in stance	−1.7 ± 9.8	−1.8 ± 10.2	−2.1 ± 6.5	−1.8 ± 6.3	−3.3 ± 6.2	−4.6 ± 3.6	0.728	0.458	0.355
Knee flexion at toe-off	−25.1 ± 7.0[b]	−24.4 ± 7.6[b]	−31.2 ± 5.6[a]	−30.7 ± 5.3[a]	−24.0 ± 7.6	−25.2 ± 3.7	0.012	0.954	0.399
Knee flexion in swing	−46.2 ± 12.8[bc]	−48.4 ± 12.5[bcd]	−66.1 ± 5.1[a]	−67.5 ± 5.5[ad]	−61.0 ± 13.1[a]	−65.8 ± 2.4[ad]	<0.001	0.011	0.404
Hip flexion at foot contact	−29.0 ± 4.2[b]	−29.5 ± 4.5[bd]	−35.1 ± 6.5[a]	−36.0 ± 6.7[ad]	−32.3 ± 6.8	−34.0 ± 5.0[d]	0.015	0.042	0.537
Hip extension in stance	−0.2 ± 5.4[bc]	−0.1 ± 5.8[bc]	5.8 ± 4.6[a]	6.3 ± 3.8[a]	5.0 ± 5.0[a]	6.3 ± 3.4[a]	0.004	0.319	0.182
Hip flexion at foot off	−4.6 ± 6.1[bc]	−4.4 ± 6.3[bc]	1.6 ± 4.4[a]	1.4 ± 4.9[a]	2.9 ± 5.7[a]	4.4 ± 3.7[a]	0.001	0.245	0.246
Hip flexion during swing	−35.0 ± 2.7[b]	−36.3 ± 2.4[bd]	−40.0 ± 5.5[a]	−41.4 ± 5.7[ad]	−36.7 ± 5.6	−39.0 ± 4.6[d]	0.018	0.000	0.392
Maximum toe clearance (cm)	11.6 ± 2.4	12.4 ± 2.4[d]			13.3 ± 1.8	14.0 ± 1.6[d]	0.057	0.000	0.679
Compensatory movements (degrees)									
Thorax anterior tilt in the sagittal plane	−4.5 ± 2.5	−5.5 ± 2.7[d]			−4.8 ± 2.5	−5.7 ± 2.4[d]	0.797	0.000	0.831
Pelvic anterior tilt in the sagittal plane	−9.1 ± 4.0	−9.7 ± 4.4[d]			−10.8 ± 3.4	−11.1 ± 4.0[d]	0.338	0.018	0.428
Circumduction of lower limb	2.1 ± 4.5	2.0 ± 5.0			0.8 ± 2.4	1.2 ± 2.4	0.020	0.263	0.096

[a] *Significantly different from paretic side at $p < 0.05$.*
[b] *Significantly different from non-paretic side at $p < 0.05$.*
[c] *Significantly different from healthy controls at $p < 0.05$.*
[d] *Significantly different from even surface at $p < 0.05$.*

$\eta_p^2 = 0.41$] were observed but not on stride and step length. The temporal parameters on the artificial grass surface were smaller than those on the even surface, although gait speed was faster on the artificial grass surface (1.13 ± 0.29 m/s vs. 1.16 ± 0.29 m/s). The step width on the artificial grass surface was larger than that on the even surface (0.14 ± 0.04 m vs. 0.15 ± 0.03 m).

Significant interactions were found between the group and the surface in terms of step length symmetry [$F_{(1,24)} = 5.44$, $p = 0.028$, $\eta_p^2 = 0.19$]. In the poststroke patients, gait on the artificial grass surface showed significantly greater symmetry in step length ($p = 0.013$, $d = 0.24$) but not in the healthy controls (**Figure 2**).

Kinematic Parameters

Significant effects for group factor on knee flexion at foot off [$F_{(2,37)} = 4.97$, $p = 0.012$, $\eta_p^2 = 0.21$], maximum knee flexion during swing [$F_{(2,37)} = 18.46$, $p < 0.001$, $\eta_p^2 = 0.50$], hip flexion at initial contact [$F_{(2,37)} = 4.70$, $p = 0.015$, $\eta_p^2 = 0.20$], maximum hip extension in stance [$F_{(2,37)} = 6.58$, $p = 0.004$, $\eta_p^2 = 0.26$], hip flexion at foot off [$F_{(2,37)} = 9.06$, $p = 0.001$, $\eta_p^2 = 0.33$], and maximum hip flexion during swing [$F_{(2,37)} = 4.52$, $p = 0.018$, $\eta_p^2 = 0.20$] were observed. Knee flexion at foot off was highest on the non-PS, and hip flexion at foot off was highest on the PS. The maximum knee flexion angles during swing and hip extension in stance were lowest on the PS. Hip flexion at initial contact ($p = 0.013$, $d = 1.15$) and during swing ($p = 0.014$, $d = 1.18$) on the PS was significantly lower than that on non-PS.

TABLE 5 | The correlations between walking activity and surface difference in spatiotemporal parameters.

	Correlation	
	Paretic side	Left side in healthy controls
Gait speed (m/s)	0.49	−0.04
Gait cycle time (s)	−0.13	−0.32
Stance time (s)	−0.04	−0.24
Swing time (s)	−0.10	−0.42
Step length (m)	0.65[a]	0.02
Stride length (m)	0.48	0.07
Step width (m)	−0.06	0.68[a]
Symmetry step length	0.03	0.46
Symmetry stance time	−0.11	0.53
Symmetry swing time	0.02	0.55

[a] *$p < 0.05$.*

TABLE 6 | The correlations between walking activity and surface difference in kinematic parameters.

	Correlation		
	Paretic side	**Non-paretic side**	**Left side in healthy controls**
Peak angle			
Ankle plantarflexion in early stance	0.24	0.18	−0.18
Ankle dorsiflexion in stance	0.10	0.28	−0.03
Ankle plantarflexion at toe-off	0.11	0.68[b]	−0.21
Ankle dorsiflexion in swing	0.16	0.58[a]	0.03
Knee flexion in early stance	0.31	0.20	0.78[b]
Knee extension in stance	0.31	0.59[a]	0.28
Knee flexion at toe-off	0.24	0.24	−0.00
Knee flexion in swing	−0.11	−0.31	−0.40
Hip flexion at foot contact	−0.69[b]	−0.09	0.45
Hip extension in stance	0.25	0.35	−0.10
Hip flexion at foot off	0.32	0.18	−0.08
Hip flexion during swing	−0.45	−0.14	0.20
Compensatory movements during swing (degrees)			
Pelvic elevation on the PS in the frontal plane	−0.07		−0.71[b]
Thorax anterior tilt in the sagittal plane	−0.13		0.05
Pelvic anterior tilt in the sagittal plane	−0.33		0.35
Circumduction	0.43		0.38

[a]$p < 0.05$; [b]$p < 0.01$.

Significant effects for surface factor on maximum knee [$F_{(1,37)} = 7.20$, $p = 0.011$, $\eta_p^2 = 0.16$] and hip flexion [$F_{(1,37)} = 28.14$, $p < 0.001$, $\eta_p^2 = 0.43$], and thoracic [$F_{(1,24)} = 45.60$, $p = 0.001$, $\eta_p^2 = 0.66$] and pelvic anterior tilts [$F_{(1,24)} = 6.43$, $p = 0.018$, $\eta_p^2 = 0.21$] in the sagittal plane during swing phase, hip flexion at initial contact [$F_{(1,37)} = 4.42$, $p = 0.042$, $\eta_p^2 = 0.11$], and maximum toe clearance [$F_{(1,24)} = 29.66$, $p < 0.001$, $\eta_p^2 = 0.55$] were observed. All the angles on the artificial grass surface in the patients and healthy controls were larger than those on the even surface.

A significant interaction was observed in terms of pelvic tilt in the frontal plane during swing [$F_{(1,24)} = 12.63$, $p = 0.002$, $\eta_p^2 = 0.35$]. The maximum pelvic elevation on PS in the frontal plane during a swing in the poststroke patients increased as compared with that in the healthy controls on both the even ($p < 0.001$, $d = 1.74$) and artificial grass surfaces ($p = 0.003$, $d = 1.28$). In the poststroke patients, decreased maximum pelvic elevation on the PS during swing ($p = 0.055$, $d = 0.11$) was observed during gait on the artificial grass surface as compared with the even surface, but the increased maximum pelvic elevation was observed in the healthy controls ($p = 0.007$, $d = 0.31$) (**Figure 3**).

Relationship Between Walking Activity and Difference in Gait-Related Parameters

In the patients with hemiparesis, the difference in step length on the PS significantly and positively correlated with the number of steps per day ($r = 0.65$, $p = 0.012$; **Figure 4**). The difference in maximum knee extension in the stance phase ($r = 0.59$, $p = 0.026$; **Figure 4**) and ankle plantarflexion at foot off on the non-PS ($r = 0.68$, $p = 0.008$) were also significantly and positively associated with the number of steps per day, but the maximum ankle dorsiflexion during swing was negatively associated ($r = -0.58$, $p = 0.029$). However, no significant relationship was found between the difference in compensatory movements during the swing and the number of steps per day.

In the healthy controls, the difference in step width significantly and positively correlated with the numbers of steps per day ($r = 0.68$, $p = 0.015$). The difference in the maximum knee extension at initial contact was also associated with the number of steps per day ($r = 0.76$, $p = 0.004$).

DISCUSSION

Our findings showed a more symmetrical step length pattern and decreased pelvic hiking (i.e., pelvic elevation on PS in the frontal plane) in the swing phase, which indicates reduced compensatory movement, during walking on the artificial grass surface in the community ambulators after stroke. In addition, the changes in paretic step length, non-paretic knee extension, and ankle plantarflexion in the stance phase, and paretic hip flexion at initial contact were related to walking activity in the community ambulators after stroke. Contrary to our hypothesis, the walking adaptability to the artificial grass surface by increasing the paretic step length with compensation movement by the non-paretic lower limb during gait may increase walking activity in the community ambulators after stroke.

Both the poststroke patients and healthy controls adjusted with reduced gait cycle and swing times (i.e., step time) on both sides and increased gait speed but without changing the step length when walking on the artificial grass surface. The present results on step length and gait speed were contrary to our hypothesis. In the previous study on the lateralization of stroke in the chronic phase, right hemisphere damage was related to a slower walk and more asymmetry in single stance time (Chen et al., 2014). Guye et al. (2003) found a more extensive and stronger connected network in the dominant left hemisphere, carrying out the processing of sensory-motor data. This fact means that the extensive and strong connected network in the dominant left hemisphere may easily compensate for one damaged network component. Ten out of fourteen patients in this study had left hemisphere damage. Therefore, the patients who participated may change the parameter regarding rhythm with a change from an even surface to a short leaf grass surface during gait. In this study, unlike the previous study, the artificial grass surface did not cause a considerable cautious gait pattern (i.e., reduced gait speed, cadence, and step

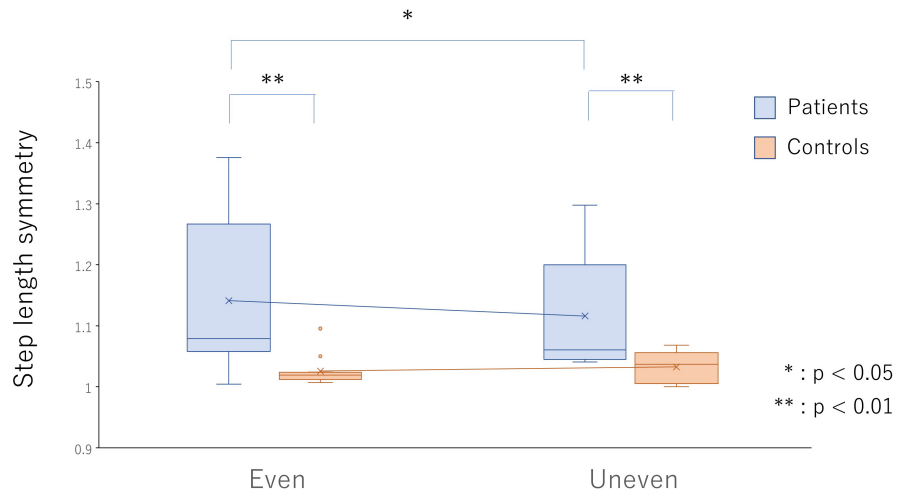

FIGURE 2 | Step length symmetry on the even surface (bars on the left side) and uneven surface (bars on the right side) in the poststroke patients (light blue bars) and the healthy controls (light red bars). *$p < 0.05$ and **$p < 0.01$ indicate statistical significance.

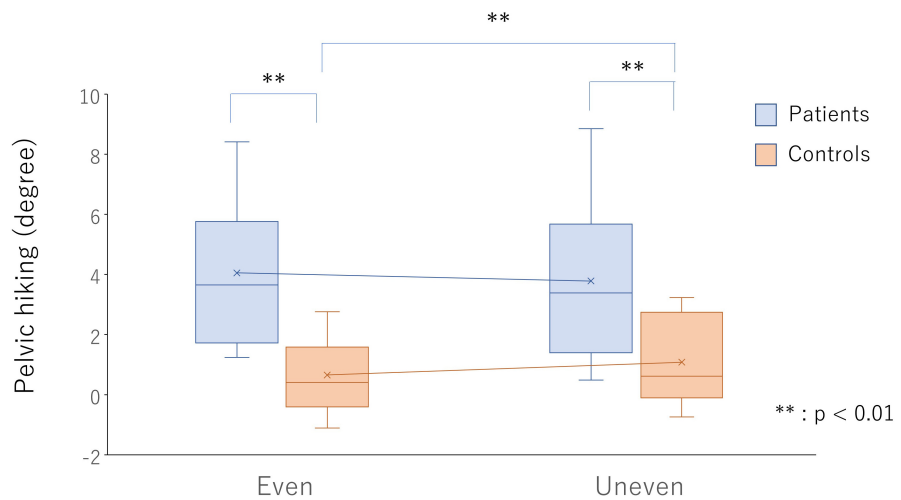

FIGURE 3 | Pelvic hiking on the even surface (bars on the left side) and uneven surface (bars on the right side) in the poststroke patients (light blue bars) and healthy controls (light red bars). ** $p < 0.01$ indicate statistical significance.

length) (Paysant et al., 2006; Menant et al., 2009; Promkeaw et al., 2019). Paysant et al. (2006) showed that the gait spatiotemporal parameters differed between an asphalt surface and grass surface with a leaf length of 12–20 cm in the healthy controls and amputees but not in the grass surface with a leaf length < 2–4 cm, which is similar to the length of the artificial grass used in this study. When standing on foam, information from both joint and cutaneous mechanoreceptors of the sole is less reliable, increasing body movement (Chiang and Wu, 1997; Fransson et al., 2007). To decrease tripping and slipping, gait on foam resulted in increased step length, width, and time compared with walking on a level surface (Maclellan and Patla, 2006). The short leaf grass, unlike foam, might produce sufficient information from both joint and cutaneous mechanoreceptors of the sole because short leaf grass is not soft like foam. Therefore, this study shows that with the short leaf length, gait stability on the artificial grass may be easier to maintain and may not need a shorter step length. Hsiao et al. (2016) demonstrated that the poststroke patients increased forward propulsion on the non-PS as the primary mechanism to increase gait speed. Considering the findings of the previous study, increased gait speed in the condition of an artificial grass surface may be attributed to the slip-resistant surface (i.e., artificial grass with short leaf has high friction property) on which subjects could generate propulsion. Moreover, the mean gait speed of the patients in this study (0.94 m/s) was faster than that of the patients categorized as a high-functioning group who can increase hip flexion power and ankle plantarflexion power on the PS to increase gait speed and reduce stride time (Jonkers et al., 2009; Sekiguchi et al., 2012). Therefore, the poststroke patients with high function in this study

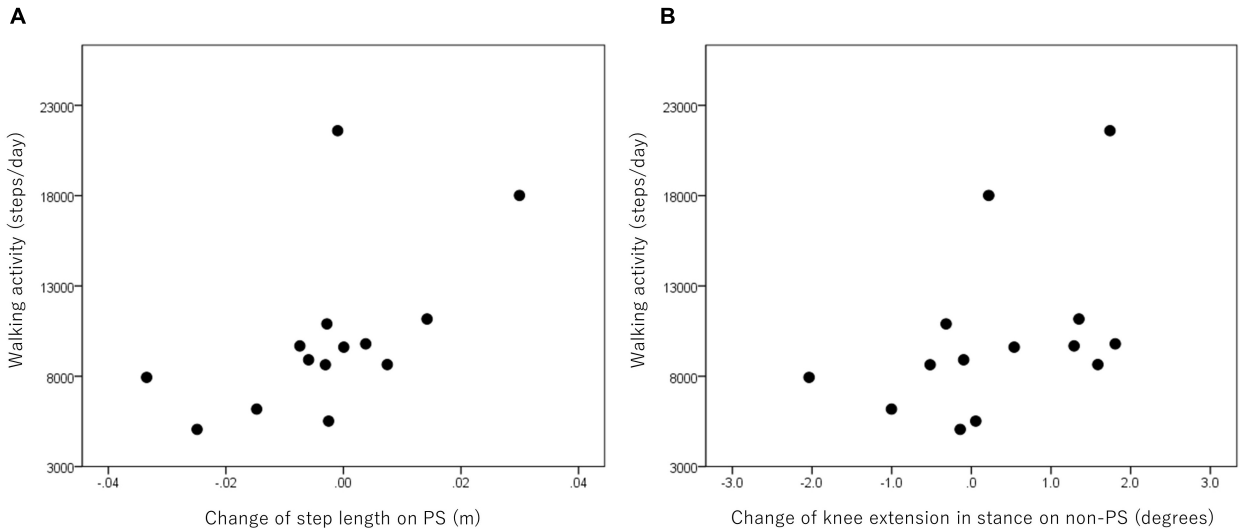

FIGURE 4 | Relationship between walking activity and changes in step length on the paretic side (PS) **(A)** and knee extension in stance on the non-PS **(B)** in the poststroke patients.

may be able to decrease step time and increase gait speed during gait on the artificial grass with a short leaf length compared with the healthy controls.

Only the poststroke community ambulators adapted gait on the artificial grass surface by increasing their symmetrical step length. A previous study that examined interlimb cutaneous reflexes demonstrated that in poststroke patients, the somatosensory network related to interlimb coordination between the legs and the arms was preserved, which indicates that the patients may have the ability to increase step length symmetry (Zehr and Loadman, 2012). The unevenness of the artificial grass might provide more somatosensory information from the plantar region than the evenness of the even surface in the patients who can increase their step length symmetry. Moreover, step length asymmetry was associated with propulsion asymmetry in the poststroke patients (Roelker et al., 2019). The slip-resistant surface of the artificial grass with a short leaf length might make propulsion easier to control. Therefore, the patients can increase their step length symmetry when walking on the artificial grass with a short leaf length. As a result, increased step length symmetry, which was related to balance measures (i.e., Berg balance scale), might increase stability when walking on the artificial grass in the poststroke patients (Lewek et al., 2014).

There were two types of strategies for the paretic step length for an uneven surface in this study. Five patients had a longer paretic step length on the uneven surface than on the even surface. Four of the five patients with a longer paretic step length had a longer non-paretic step length on the uneven surface than on the even surface. However, the other patient had a shorter non-paretic step length on the uneven surface. In the results, three of the five patients with a longer paretic step length on the uneven surface increased step length symmetry. In contrast, nine patients had a shorter paretic step length on the uneven surface than the even surface. Four of the nine patients with the shorter paretic step length had a shorter non-paretic step length on the uneven surface than on the even surface. However, five patients had a longer non-paretic step length on the uneven surface. Additionally, all five patients had a longer paretic step length than non-paretic step length on the even surface. Therefore, the patients with a shorter paretic step length on the uneven surface may maintain or increase the step length symmetry. In fact, seven of the nine patients with a shorter step length on the uneven surface increased step length symmetry. In summary, most patients with a longer paretic step length did not follow the strategy of non-paretic steps that would result in step length asymmetry similar to the patients with a shorter paretic step. Consequently, most patients after stroke with a longer paretic step length and more walking activity, but not all, may not have less step length symmetry on the uneven surface.

The hip and knee flexion angles during a swing on the artificial grass surface increased as compared with those on the even surface in the poststroke patients and healthy controls, consistent with the previous study in patients with multiple sclerosis and cerebral palsy (Böhm et al., 2014; van den Berg et al., 2017). When considered in conjunction with the present results showing increased toe clearance, the increase in hip and knee flexion angles during swing may lead to an increase in foot clearance on the artificial grass surface in both groups. Artificial grass surface was not used in the previous studies that examined toe clearance on the uneven surface (Böhm et al., 2014; van den Berg et al., 2017). In addition to walking on the other uneven surfaces, walking on artificial grass with a short leaf length may be necessary to increase the height of toe clearance as compared with that on the even surface. In line with the previous findings in patients with cerebral palsy (Böhm et al., 2014), greater anterior tilt angles of the pelvic and thorax were found in poststroke patients during the swing phase when walking on an artificial grass surface. The present findings show that decreased pelvic

hiking during gait on the artificial grass surface was found only in the poststroke patient. Increased pelvic and thoracic anterior tilt angles and decreased pelvic hiking may lower the height of the center of mass during gait in poststroke patients, as shown in previous studies (Chen et al., 2005; Saha et al., 2008). During gait on the artificial grass with a short leaf length, control of the trunk posture and increase in toe clearance may be necessary for maintaining dynamic stability, but the changes in the gait spatiotemporal parameters such as caution gait (i.e., short step length and slow gait speed) may not be necessary because maintaining gait on artificial grass with a short leaf length is an easier task.

The change in paretic step length, but not step width, from the even surface to the artificial grass was related to walking activity in the poststroke patients. The walking activity of the healthy controls was related to the increase in the step width when walking on the artificial grass. Like the healthy controls, the patients may have difficulty controlling their step width because of deficit of control in the frontal plane by the hip and ankle joints (Kim and Eng, 2004; Neckel et al., 2008; Sánchez et al., 2018; Hsiao et al., 2020). The healthy controls with increased walking activity increased their step width on the artificial grass, which increased the base of support like in cautious gait (McAndrew Young and Dingwell, 2012). Although maintaining gait on the artificial grass with a short leaf length is an easier task, high community walking activity may require adaptation on the artificial grass with a short leaf length not only by increasing step length on the PS in the poststroke patient but also by increasing the step width in the healthy controls to increase the base of support and maintain stability control. In addition, the walking activity of the poststroke patients correlated with the changes in the maximum knee extension in the stance phase and ankle plantarflexion at foot off on the non-PS and that of the step length on the PS. Consistent with the kinematic changes in the responders of walking activity after training (Ardestani et al., 2019), the kinematic change in the lower limb on the non-PS was associated with walking activity in patients. The poststroke patients with increased walking activity may also need the compensatory movement of the leg on the non-PS to increase their step length on the PS, like responders of walking activity after training.

This study has several limitations. First, the least limited and unlimited community ambulators participated in the study but not most limited and household ambulators. Therefore, the question of whether walking adaptability to the artificial grass surface was related to walking activity in most limited and household ambulators after stroke remains unclear. Second, kinetic data were not collected. Future studies should clarify whether power generated at the knee and hip joints during gait on the artificial grass surface is more needed on the non-PS than on the even surface and the energy cost during gait on the artificial grass surface in poststroke patients (Farris et al., 2015). Third, this study used only one kind of uneven surface (i.e., an artificial grass). Previous studies on gait on uneven surfaces used surfaces different from artificial grass. Several surfaces (i.e., foam, sand, railroad ballast, artificial grass, and artificial pebble surface) caused differences in the results of the step parameters (Maclellan and Patla, 2006; Wade et al., 2010; van den Berg et al., 2017; Promkeaw et al., 2019). Therefore, our findings are restricted to poststroke patients categorized as least limited and unlimited community ambulators and walking on short leaf artificial grass. Fourth, the intraclass correlation coefficient between the number of steps calculated from the accelerometer and the number of steps counted by the therapist was low in the healthy controls. In the healthy controls, the difference between the number of steps counted by the therapist and the number of steps calculated from the accelerometer was extremely larger than other subjects (i.e., the maximum difference in the healthy control: 43 steps vs. the other healthy controls: 5 steps). The result demonstrated the limitation of measuring the step count with an accelerometer. One factor that prevented AG from accurately detecting steps could be using an LFE filter in the healthy controls, as shown in a previous study (Campos et al., 2018). However, there is no difference in the main result between the data in all healthy controls and that excluding the healthy control No. 3 [i.e., also in the eleven healthy controls excluding No. 3, the difference in step width significantly and positively correlated with the numbers of steps per day ($r = 0.69$, $p = 0.015$)].

DATA AVAILABILITY STATEMENT

The raw data supporting the conclusion of this article will be made available by the authors, without undue reservation.

ETHICS STATEMENT

The studies involving human participants were reviewed and approved by The Research Ethics Committees at Tohoku University Graduate School of Medicine. The patients/participants provided their written informed consent to participate in this study.

AUTHOR CONTRIBUTIONS

YS and KH conceived and designed the experiments and collected and analyzed the data. YS wrote the manuscript. YS, KH, and S-II revised the manuscript critically. All authors read and approved the final manuscript.

FUNDING

This work was supported by JSPS KAKENHI Grant-in-Aid for Young Scientists (18K17665) and NEC corporation (J160001522).

ACKNOWLEDGMENTS

The authors would like to thank the staff at the Department of Physical Medicine and Rehabilitation at Tohoku University for their advice and help.

REFERENCES

Allet, L., Armand, S., De Bie, R. A., Pataky, Z., Aminian, K., Herrmann, F. R., et al. (2009). Gait alterations of diabetic patients while walking on different surfaces. *Gait Posture* 29, 488–493. doi: 10.1016/j.gaitpost.2008.11.012

Ardestani, M. M., Henderson, C. E., and Hornby, T. G. (2019). Improved walking function in laboratory does not guarantee increased community walking in stroke survivors: potential role of gait biomechanics. *J. Biomech.* 91, 151–159. doi: 10.1016/j.jbiomech.2019.05.011

Balasubramanian, C. K., Clark, D. J., and Fox, E. J. (2014). Walking adaptability after a stroke and its assessment in clinical settings. *Stroke Res. Treat.* 2014:591013. doi: 10.1155/2014/591013

Barclay, R. E., Stevenson, T. J., Poluha, W., Ripat, J., Nett, C., and Srikesavan, C. S. (2015). Interventions for improving community ambulation in individuals with stroke. *Cochrane Database Syst. Rev.* 2015:Cd010200. doi: 10.1002/14651858.CD010200.pub2

Benedetti, M. G., Catani, F., Leardini, A., Pignotti, E., and Giannini, S. (1998). Data management in gait analysis for clinical applications. *Clin. Biomech. (Bristol, Avon)* 13, 204–215.

Böhm, H., Hösl, M., Schwameder, H., and Döderlein, L. (2014). Stiff-knee gait in cerebral palsy: how do patients adapt to uneven ground? *Gait Posture* 39, 1028–1033. doi: 10.1016/j.gaitpost.2014.01.001

Brough, L. G., Kautz, S. A., Bowden, M. G., Gregory, C. M., and Neptune, R. R. (2018). Merged plantarflexor muscle activity is predictive of poor walking performance in post-stroke hemiparetic subjects. *J. Biomech.* 82, 361–367. doi: 10.1016/j.jbiomech.2018.11.011

Burridge, J. H., Elessi, K., Pickering, R. M., and Taylor, P. N. (2007). Walking on an uneven surface: the effect of common peroneal stimulation on gait parameters and relationship between perceived and measured benefits in a sample of participants with a drop-foot. *Neuromodulation* 10, 59–67. doi: 10.1111/j.1525-1403.2007.00088.x

Butler, E., Druizin, M., Sullivan, E., Rose, J., and Gamble, J. (2006). *Human Walking*, 3rd Edn. Philadelphia, MD: Lippincott, Williams and Wilkins, 131–147.

Campos, C., DePaul, V. G., Knorr, S., Wong, J. S., Mansfield, A., and Patterson, K. K. (2018). Validity of the ActiGraph activity monitor for individuals who walk slowly post-stroke. *Top Stroke Rehabil.* 25, 295–304. doi: 10.1080/10749357.2018.1446487

Chen, G., Patten, C., Kothari, D. H., and Zajac, F. E. (2005). Gait differences between individuals with post-stroke hemiparesis and non-disabled controls at matched speeds. *Gait Posture* 22, 51–56. doi: 10.1016/j.gaitpost.2004.06.009

Chen, I. H., Novak, V., and Manor, B. (2014). Infarct hemisphere and noninfarcted brain volumes affect locomotor performance following stroke. *Neurology* 82, 828–834. doi: 10.1212/wnl.0000000000000186

Chiang, J.-H., and Wu, G. (1997). The influence of foam surfaces on biomechanical variables contributing to postural control. *Gait Posture* 5, 239–245. doi: 10.1016/S0966-6362(96)01091-0

Clark, D. J., Ting, L. H., Zajac, F. E., Neptune, R. R., and Kautz, S. A. (2010). Merging of healthy motor modules predicts reduced locomotor performance and muscle coordination complexity post-stroke. *J. Neurophysiol.* 103, 844–857. doi: 10.1152/jn.00825.2009

Darbin, O., Gubler, C., Naritoku, D., Dees, D., Martino, A., and Adams, E. (2016). Parkinsonian balance deficits quantified using a game industry board and a specific battery of four paradigms. *Front. Hum. Neurosci.* 10:431. doi: 10.3389/fnhum.2016.00431

English, C., Manns, P. J., Tucak, C., and Bernhardt, J. (2014). Physical activity and sedentary behaviors in people with stroke living in the community: a systematic review. *Phys. Ther.* 94, 185–196. doi: 10.2522/ptj.20130175

Farris, D. J., Hampton, A., Lewek, M. D., and Sawicki, G. S. (2015). Revisiting the mechanics and energetics of walking in individuals with chronic hemiparesis following stroke: from individual limbs to lower limb joints. *J. Neuroeng. Rehabil.* 12:24. doi: 10.1186/s12984-015-0012-x

Franceschini, M., Rampello, A., Agosti, M., Massucci, M., Bovolenta, F., and Sale, P. (2013). Walking performance: correlation between energy cost of walking and walking participation. new statistical approach concerning outcome measurement. *PLoS One* 8:e56669. doi: 10.1371/journal.pone.0056669

Fransson, P. A., Gomez, S., Patel, M., and Johansson, L. (2007). Changes in multi-segmented body movements and EMG activity while standing on firm and foam support surfaces. *Eur. J. Appl. Physiol.* 101, 81–89. doi: 10.1007/s00421-007-0476-x

French, M. A., Koller, C., and Arch, E. S. (2020). Comparison of three kinematic gait event detection methods during overground and treadmill walking for individuals post stroke. *J. Biomech.* 99:109481. doi: 10.1016/j.jbiomech.2019.109481

Fulk, G. D., He, Y., Boyne, P., and Dunning, K. (2017). Predicting home and community walking activity poststroke. *Stroke* 48, 406–411. doi: 10.1161/STROKEAHA.116.015309

Guye, M., Parker, G. J., Symms, M., Boulby, P., Wheeler-Kingshott, C. A., Salek-Haddadi, A., et al. (2003). Combined functional MRI and tractography to demonstrate the connectivity of the human primary motor cortex in vivo. *Neuroimage* 19, 1349–1360. doi: 10.1016/s1053-8119(03)00165-4

Hafer-Macko, C. E. (2008). Skeletal muscle changes after hemiparetic stroke and potential beneficial effects of exercise intervention strategies. *J. Rehabil. Res. Dev.* 45, 261–272. doi: 10.1682/jrrd.2007.02.0040

Horak, F., and Macpherson, J. (1996). "Postural orientation and equilibrium," in *Handbook of Physiology./Exercise: Regulation and Integration of Multiple Systems*, eds J. Shepard and L. Rowell (New York, NY: American Physiological Society).

Hsiao, H., Awad, L. N., Palmer, J. A., Higginson, J. S., and Binder-Macleod, S. A. (2016). Contribution of paretic and nonparetic limb peak propulsive forces to changes in walking speed in individuals poststroke. *Neurorehabil. Neural Repair* 30, 743–752. doi: 10.1177/1545968315624780

Hsiao, H. Y., Gray, V. L., Borrelli, J., and Rogers, M. W. (2020). Biomechanical control of paretic lower limb during imposed weight transfer in individuals post-stroke. *J. Neuroeng. Rehabil.* 17:140. doi: 10.1186/s12984-020-00768-1

Ivey, F. M., Macko, R. F., Ryan, A. S., and Hafer-Macko, C. E. (2005). Cardiovascular health and fitness after stroke. *Topics Stroke Rehabil.* 12, 1–16. doi: 10.1310/geeu-yruy-vj72-lear

Jonkers, I., Delp, S., and Patten, C. (2009). Capacity to increase walking speed is limited by impaired hip and ankle power generation in lower functioning persons post-stroke. *Gait Posture* 29, 129–137.

Kerrigan, D. C., Frates, E. P., Rogan, S., and Riley, P. O. (2000). Hip hiking and circumduction: quantitative definitions. *Am. J. Phys. Med. Rehabil.* 79, 247–252.

Kim, C. M., and Eng, J. J. (2004). Magnitude and pattern of 3D kinematic and kinetic gait profiles in persons with stroke: relationship to walking speed. *Gait Posture* 20, 140–146. doi: 10.1016/j.gaitpost.2003.07.002

Kono, Y., Kawajiri, H., Kamisaka, K., Kamiya, K., Akao, K., Asai, C., et al. (2015). Predictive impact of daily physical activity on new vascular events in patients with mild ischemic stroke. *Int. J. Stroke* 10, 219–223. doi: 10.1111/ijs.12392

Kuramatsu, Y., Suzukamo, Y., and Izumi, S. I. (2021). Two types of sensorimotor strategies for whole-body movement in individuals with stroke: a pilot study. *Physiother. Theory Pract. [Online ahead of print]* 1–12. doi: 10.1080/09593985.2021.1962461

Kuramatsu, Y., Yamamoto, Y., and Izumi, S.-I. (2020). Sensorimotor strategies in individuals with poststroke hemiparesis when standing up without vision. *Motor Control* 24, 150–167. doi: 10.1123/mc.2018-0098

Lewek, M. D., Bradley, C. E., Wutzke, C. J., and Zinder, S. M. (2014). The relationship between spatiotemporal gait asymmetry and balance in individuals with chronic stroke. *J. Appl. Biomech.* 30, 31–36. doi: 10.1123/jab.2012-0208

Maclellan, M. J., and Patla, A. E. (2006). Adaptations of walking pattern on a compliant surface to regulate dynamic stability. *Exp. Brain Res.* 173, 521–530. doi: 10.1007/s00221-006-0399-5

McAndrew Young, P. M., and Dingwell, J. B. (2012). Voluntarily changing step length or step width affects dynamic stability of human walking. *Gait Posture* 35, 472–477. doi: 10.1016/j.gaitpost.2011.11.010

Menant, J. C., Steele, J. R., Menz, H. B., Munro, B. J., and Lord, S. R. (2009). Effects of walking surfaces and footwear on temporo-spatial gait parameters in young and older people. *Gait Posture* 29, 392–397. doi: 10.1016/j.gaitpost.2008.10.057

Neckel, N. D., Blonien, N., Nichols, D., and Hidler, J. (2008). Abnormal joint torque patterns exhibited by chronic stroke subjects while walking with a prescribed physiological gait pattern. *J. Neuroeng. Rehabil.* 5:19. doi: 10.1186/1743-0003-5-19

Okada, H., Ae, M., Fujii, N., and Morioka, Y. (1996). Body segment inertial properties of Japanese elderly. *Biomechanism* 13, 125–139.

Patterson, K. K., Gage, W. H., Brooks, D., Black, S. E., and McIlroy, W. E. (2010). Evaluation of gait symmetry after stroke: a comparison of current methods and

recommendations for standardization. *Gait Posture* 31, 241–246. doi: 10.1016/j.gaitpost.2009.10.014

Paysant, J., Beyaert, C., Datié, A. M., Martinet, N., and André, J. M. (2006). Influence of terrain on metabolic and temporal gait characteristics of unilateral transtibial amputees. *J. Rehabil. Res. Dev.* 43, 153–160.

Promkeaw, D., Arrayawichanon, P., Thaweewannakij, T., Mato, L., Amatachaya, P., and Amatachaya, S. (2019). Various surfaces challenge gait characteristics of ambulatory patients with spinal cord injury. *Spinal Cord* 57, 805–813. doi: 10.1038/s41393-019-0282-4

Robertson, G. E., Caldwell, G. E., Hamill, J., Kamen, G., and Whittlesey, S. (2013). *Research Methods in Biomechanics*. Champaign, IL: Human kinetics.

Roelker, S. A., Bowden, M. G., Kautz, S. A., and Neptune, R. R. (2019). Paretic propulsion as a measure of walking performance and functional motor recovery post-stroke: a review. *Gait Posture* 68, 6–14. doi: 10.1016/j.gaitpost.2018.10.027

Saha, D., Gard, S., and Fatone, S. (2008). The effect of trunk flexion on able-bodied gait. *Gait Posture* 27, 653–660. doi: 10.1016/j.gaitpost.2007.08.009

Sánchez, N., Acosta, A. M., López-Rosado, R., and Dewald, J. P. A. (2018). Neural constraints affect the ability to generate hip abduction torques when combined with hip extension or ankle plantarflexion in chronic hemiparetic stroke. *Front. Neurol.* 9:564. doi: 10.3389/fneur.2018.00564

Saunders, D. H., Sanderson, M., Hayes, S., Kilrane, M., Greig, C. A., Brazzelli, M., et al. (2016). Physical fitness training for stroke patients. *Cochrane Database Syst. Rev.* 3:Cd003316. doi: 10.1002/14651858.CD003316.pub6

Sekiguchi, Y., Muraki, T., Kuramatsu, Y., Furusawa, Y., and Izumi, S. (2012). The contribution of quasi-joint stiffness of the ankle joint to gait in patients with hemiparesis. *Clin. Biomech. (Bristol, Avon)* 27, 495–499. doi: 10.1016/j.clinbiomech.2011.12.005

Stoquart, G., Detrembleur, C., and Lejeune, T. M. (2012). The reasons why stroke patients expend so much energy to walk slowly. *Gait Posture* 36, 409–413. doi: 10.1016/j.gaitpost.2012.03.019

Thilarajah, S., Mentiplay, B. F., Bower, K. J., Tan, D., Pua, Y. H., Williams, G., et al. (2018). Factors associated with post-stroke physical activity: a systematic review and meta-analysis. *Arch. Phys. Med. Rehabil.* 99, 1876–1889. doi: 10.1016/j.apmr.2017.09.117

van den Berg, M. E. L., Barr, C. J., McLoughlin, J. V., and Crotty, M. (2017). Effect of walking on sand on gait kinematics in individuals with multiple sclerosis. *Mult. Scler. Relat. Disord.* 16, 15–21. doi: 10.1016/j.msard.2017.05.008

Wade, C., Redfern, M. S., Andres, R. O., and Breloff, S. P. (2010). Joint kinetics and muscle activity while walking on ballast. *Hum. Factors* 52, 560–573. doi: 10.1177/0018720810381996

Zehr, E. P., and Loadman, P. M. (2012). Persistence of locomotor-related interlimb reflex networks during walking after stroke. *Clin. Neurophysiol.* 123, 796–807. doi: 10.1016/j.clinph.2011.07.049

Conflict of Interest: The authors declare that the research was conducted in the absence of any commercial or financial relationships that could be construed as a potential conflict of interest.

Publisher's Note: All claims expressed in this article are solely those of the authors and do not necessarily represent those of their affiliated organizations, or those of the publisher, the editors and the reviewers. Any product that may be evaluated in this article, or claim that may be made by its manufacturer, is not guaranteed or endorsed by the publisher.

Copyright © 2022 Sekiguchi, Honda and Izumi. This is an open-access article distributed under the terms of the Creative Commons Attribution License (CC BY). The use, distribution or reproduction in other forums is permitted, provided the original author(s) and the copyright owner(s) are credited and that the original publication in this journal is cited, in accordance with accepted academic practice. No use, distribution or reproduction is permitted which does not comply with these terms.

frontiers in Human Neuroscience

ORIGINAL RESEARCH
published: 06 January 2022
doi: 10.3389/fnhum.2021.779920

Efficiency and Stability of Step-To Gait in Slow Walking

Kento Hirayama[1,2], Yohei Otaka[3], Taichi Kurayama[4], Toru Takahashi[1], Yutaka Tomita[5], Seigo Inoue[6], Kaoru Honaga[7], Kunitsugu Kondo[6] and Rieko Osu[1]*

[1]Faculty of Human Sciences, Waseda University, Saitama, Japan, [2]Hatsutomi Hoken Hospital, Chiba, Japan, [3]Department of Rehabilitation Medicine I, School of Medicine, Fujita Health University, Aichi, Japan, [4]Department of Physical Therapy, Faculty of Health Sciences, Uekusa Gakuen University, Chiba, Japan, [5]Faculty of Science and Technology, Keio University, Kanagawa, Japan, [6]Tokyo Bay Rehabilitation Hospital, Chiba, Japan, [7]Department of Rehabilitation Medicine, Juntendo University Graduate School of Medicine, Tokyo, Japan

As humans, we constantly change our movement strategies to adapt to changes in physical functions and the external environment. We have to walk very slowly in situations with a high risk of falling, such as walking on slippery ice, carrying an overflowing cup of water, or muscle weakness owing to aging or motor deficit. However, previous studies have shown that a normal gait pattern at low speeds results in reduced efficiency and stability in comparison with those at a normal speed. Another possible strategy is to change the gait pattern from normal to step-to gait, in which the other foot is aligned with the first swing foot. However, the efficiency and stability of the step-to gait pattern at low speeds have not been investigated yet. Therefore, in this study, we compared the efficiency and stability of the normal and step-to gait patterns at intermediate, low, and very low speeds. Eleven healthy participants were asked to walk with a normal gait and step-to gait on a treadmill at five different speeds (i.e., 10, 20, 30, 40, and 60 m/min), ranging from very low to normal walking speed. The efficiency parameters (percent recovery and walk ratio) and stability parameters (center of mass lateral displacement) were analyzed from the motion capture data and then compared for the two gait patterns. The results suggested that step-to gait had a more efficient gait pattern at very low speeds of 10–30 m/min, with a larger percent recovery, and was more stable at 10–60 m/min in comparison with a normal gait. However, the efficiency of the normal gait was better than that of the step-to gait pattern at 60 m/min. Therefore, step-to gait is effective in improving gait efficiency and stability when faced with situations that force us to walk slowly or hinder quick walking because of muscle weakness owing to aging or motor deficit along with a high risk of falling.

Keywords: gait pattern, adaptation, efficiency, stability, rehabilitation

OPEN ACCESS

Edited by:
Jun Izawa,
University of Tsukuba, Japan

Reviewed by:
Hideki Hida,
Nagoya City University, Japan
Mitsunari Abe,
Fukushima Medical University, Japan

****Correspondence:***
Kento Hirayama
kento.hirayama523@gmail.com

Specialty section:
This article was submitted to Motor Neuroscience, a section of the journal Frontiers in Human Neuroscience

Received: *20 September 2021*
Accepted: *14 December 2021*
Published: *06 January 2022*

Citation:
Hirayama K, Otaka Y, Kurayama T, Takahashi T, Tomita Y, Inoue S, Honaga K, Kondo K and Osu R (2022) Efficiency and Stability of Step-To Gait in Slow Walking. Front. Hum. Neurosci. 15:779920. doi: 10.3389/fnhum.2021.779920

INTRODUCTION

People change their walking speed depending on situations (Leroux et al., 2002); they walk slowly when external environments are unstable, such as on slippery ice, or when internal environments are deficient in walking quickly, for example, weakened muscle owing to aging or motor deficit. In such cases, they can walk slowly with a normal gait pattern, or they can change their gait

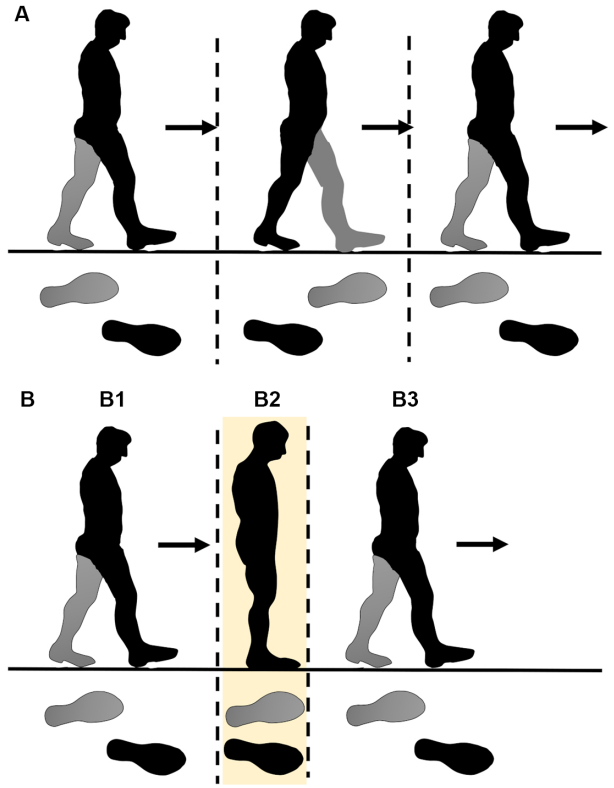

FIGURE 1 | Schematic presentation of the gait patterns in the study. In normal gait **(A)**, the participant stepped with both legs symmetrically. In the step-to gait pattern **(B)**, the participant places the preceding leg, which is pre-determined to be either the left or right leg, by themselves at a certain place **(B1)**, and then swings the other leg to the location where the preceding leg is located **(B2)**. Subsequently, the participants swing the same preceding leg again **(B3)**.

pattern to the step-to gait, in which the other foot is aligned with the first swing foot (**Figure 1**). For normal gait patterns, efficiency and stability have been reported to decrease at extremely low speeds (Cavagna et al., 1976; Bruijn et al., 2009; Murakami and Otaka, 2017; Best and Wu, 2020). However, no study has examined the characteristics of the step-to gait at significantly low speeds. If the step-to gait is stabler and more efficient than the normal gait at an extremely low speed, it can be recommended in situations where slow walking is necessary.

Cavagna et al. analyzed the percent recovery when healthy participants walked at various speeds with a normal gait pattern. The percent recovery is a measure of the gait efficiency, which is expressed as the rate of exchange of the potential and kinetic energies during walkingand can be estimated using the trajectory of the center of mass (CoM) measured by motion capture. They reported that the walking efficiency was maximum at intermediate walking speeds (66–116 m/min), which are the preferred walking speeds of healthy people, and showed an inverted U-shaped curve relative to the walking speed. In particular, walking efficiencies were found to be the highest at intermediate walking speeds and decreased as the walking speed decreased or increased (Cavagna et al., 1976).

The walk ratio, which is the ratio of the step length to cadence (step rate), is another important measure of human gait, and it is invariant across different speeds for a normal gait pattern (Sekiya, 1996). Zarrugh et al. (1974) reported that humans select a constant walk ratio across a wide range of speeds from all possible walk ratios because it is optimal in terms of energy consumption. However, Murakami et al. reported that this walk ratio was constant when the walking speed was moderate or fast but gradually increased when the speed was less than approximately 62 m/min. Therefore, they suggested that the efficiency is not optimized in a slow or normal gait (Murakami and Otaka, 2017).

Regarding the gait stability of normal gait, Best et al. analyzed the margin of stability of slow to very slow normal gait (6, 18, 30, and 36 m/min) using the lateral movement of the CoM and center of pressure of the trunk from open data measured on the treadmill. They reported that the margin of stability decreased with a decrease in speed, concluding that the lateral stability of normal gait decreased at low speeds, especially at extremely low speeds (Best and Wu, 2020).

In this study, we investigated the efficiency and stability of the step-to gait at five different speeds (i.e., 10 m/min, 20 m/min, 30 m/min, 40 m/min, and 60 m/min), ranging from very slow to the normal speed of a normal gait. We measured the percent recovery, walk ratio, and CoM lateral displacement in healthy participants during a treadmill walk.

The rest of the article is organized as follows. In sections "Materials and Methods", we analyze the parameters (efficiency and stability) from motion capture data, and then compare the two gait patterns in detail. Section "Results" presents the results of the study. The percent recovery, walk ratio, and CoM lateral displacement in healthy participants during treadmill gait are presented. Finally, the discussion and conclusion are presented in section "Discussion".

MATERIALS AND METHODS

Participants

Eleven healthy adults participated in this study: five males {mean [standard deviation (SD)] age: 22.6 (0.5) years; mean weight: 61.8 (9.6) kg; and mean height: 170.0 (4.7) cm} and six females [mean (SD) age: 22.7 (0.5) years; mean weight: 50.3 (3.9) kg; and mean height: 161.5 (6.5) cm]. The number of participants was determined based on similar previous studies related to gait analysis of healthy participants (Brown and Mueller, 1998; Orendurff et al., 2004; Best and Wu, 2020). The participants did not have any neurological or orthopedic diseases. The study protocol was approved by the Ethics Committee of Tokyo Bay Rehabilitation Hospital (No. 53-3). All participants provided written informed consent before participating in the study.

Tasks

The participants were instructed to walk on a treadmill (TRD-210, SAKAI Medical Co., Ltd., Tokyo, Japan) following two types of walking patterns, that is, step-to gait pattern and normal gait pattern, at five speed conditions (10, 20, 30, 40, and 60 m/min). All the participants first walked at all speed conditions with a

normal gait pattern, and after taking a short break, they walked at all speed conditions with the step-to gait pattern. This setup was implemented to exclude the aftereffect of step-to gait on normal gait. The ordering of the speed condition was randomly determined for each participant to remove order bias. In each condition, participants were asked to walk 40 steps after their gait stabilized. In the step-to gait pattern condition, the participants were instructed to walk by placing the preceding leg at a certain place and swinging the other leg to the location where the preceding leg was located (**Figure 1**). Before the experiments, the participants selected the preceding leg that they preferred to swing first and adequately practiced the gait pattern. Thereafter, the preceding leg was not changed for any participant throughout the experiment.

Motion Analysis

Measurements

The movements of both sides of the calcaneus and the spinous process of the third lumbar vertebra (**Figure 2**) were recorded at 100 Hz using a motion capture system (NDI OPTOTRAK, Waterloo, Ontario, Canada). After the motion data were low-pass filtered at 20 Hz using Butterworth fourth-order zero-lag filters, the efficiency and stability parameters were calculated using the data of 40 steps recorded after the gait stabilized during each task. Each step was determined using the vertical and lateral movements of both sides of the calcaneus. The movement of the third lumbar vertebra was recorded as the CoM movement (Meichtry et al., 2007; Kurayama et al., 2013). MATLAB R2013a (MathWorks Inc., Natick, MA, USA) was used for the motion analyses.

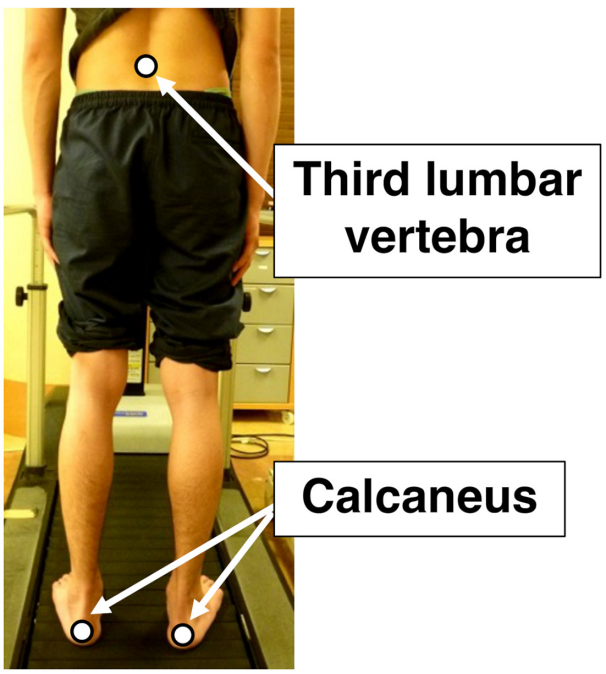

FIGURE 2 | Positions of optical marker for the motion capture system. The white dots represent the positions of the optical markers. They are the third lumbar vertebra and the bilateral calcaneus. The movements of the markers were recorded from the backsides of the participants using the motion capture system.

Parameters of Gait Efficiency

The percent recovery and walking ratio were calculated as the parameters of gait efficiency. Percent recovery is the rate of exchange of the potential and kinetic energies, focusing on the motion of the CoM during the walk (Cavagna et al., 1976). The larger the percent recovery, the less muscle activity is required during walking, and hence, the more efficient the gait. The percent recovery is approximately 65% at the intermediate walking speed of healthy people; thus, the remaining 35% depends mainly on the workload produced by muscle activity. We computed the percent recovery from the change in mechanical energy during each gait test using the CoM displacement data and the following formula (Cavagna et al., 1976).

$$\%\text{Recovery} = \left\{1 - \frac{Wt}{Wp + Wk}\right\} \times 100$$

Here, Wt is the increase in total mechanical energy, Wp is the increase in potential energy, and Wk is the increase in kinetic energy. The walk ratio was calculated by dividing the mean step length (m) by the cadence (steps/min). Each step was detected from each heel contact, which was the lowest point of motion data for each calcaneus.

Parameters of Gait Stability

The CoM lateral displacement was calculated as the parameter of gait stability. The CoM lateral displacement has been reported to be a useful parameter for evaluating the gait stability (Iida and Yamamuro, 1987; Shinoda et al., 2008). For the CoM lateral displacement, we calculated the difference between the maximum and minimum values of the lateral motion of the third lumbar vertebra in each gait cycle and then averaged them over 20 gait cycles. Furthermore, we calculated the CoM lateral displacement during the single-leg stance-phase: the preceding leg and following leg in the step-to gait, and the averaged values with left and right legs in the normal gait.

Statistical Analysis

For all parameters, the effects of the pattern of GAIT (normal and step-to gait pattern), SPEED (five-speed conditions), and their interaction (GAIT×SPEED) were investigated using a two-way analysis of variance (ANOVA) with repeated measures. Furthermore, two-way ANOVAs were conducted for the CoM lateral displacement during the single-leg stance-phase in the step-to gait and that of the stance-phases with both left and right legs in the normal gait. When a statistically significant interaction was found, a paired t-test between gait patterns for each speed condition was performed as a *post hoc* analysis for GAIT; when a statistically significant main effect of SPEED was found, multiple comparisons with Shaffer correction were performed for SPEED between speed conditions for each gait pattern. Before each statistical analysis, the normality of

the data was confirmed using the Shapiro-Wilk test. The spherical assumption was tested using Mauchly's sphericity test, and the degrees of freedom were adjusted using the Greenhouse-Geisser method when the spherical assumption was rejected. In addition, we investigated the correlation between percent recovery and CoM vertical displacement using Spearman's rank correlation coefficient to check the positive relationship between the CoM vertical displacement and percent recovery, similar to a previous study on normal gait (Wurdeman et al., 2017). Statistical analyses were performed using R (version 3.6.1.). The statistical significance was set at $P < 0.05$.

RESULTS

Percent Recovery

A significant interaction (GAIT×SPEED) was observed in percent recovery ($F_{(1.78, 17.8)} = 20.9$, $P < 0.01$, partial $\eta^2 = 0.68$; **Figure 3**). Significant main effects were observed in both GAIT ($F_{(1, 10)} = 11.3$, $P < 0.01$, partial $\eta^2 = 0.53$) and SPEED ($F_{(1.91, 19.1)} = 44.6$, $P < 0.01$, partial $\eta^2 = 0.82$). The tests of the simple main effect of the gait patterns revealed that the percent recovery was significantly larger for the step-to gait pattern than for the normal gait at 10 m/min, 20 m/min, and 30 m/min ($P < 0.01$), while it was significantly smaller for the step-to gait pattern than for the normal gait at 60 m/min ($P = 0.012$). The percent recovery was smaller at slower conditions than faster ones for both gait patterns, except at 60 m/min for the step-to gait pattern. The test of the simple main effect of the speeds showed simple main effects for normal ($P < 0.01$) and step-to gait ($P < 0.01$). For the normal gait pattern, multiple comparisons showed a significant difference between all speed conditions ($P < 0.01$). For the step-to gait pattern, multiple comparisons showed significant differences between 10 m/min and 20 m/min, 30 m/min and 40 m/min (*adj* $P < 0.01$), and 40 m/min and 60 m/min conditions (*adj* $P = 0.019$).

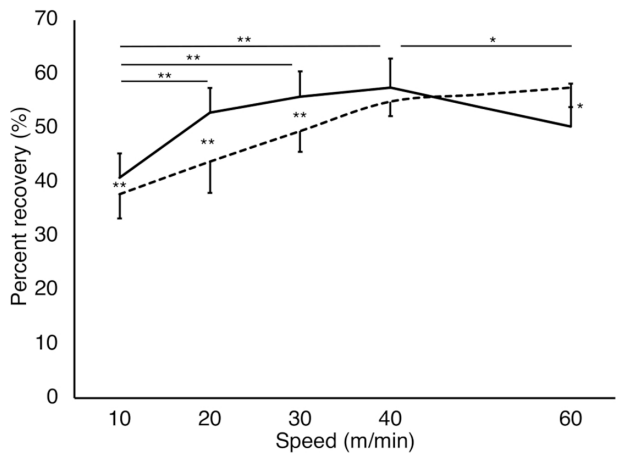

FIGURE 3 | Percent recovery of each gait pattern at each speed condition. The solid and dashed lines represent the step-to gait and normal gait patterns, respectively. The vertical and horizontal axes represent the percent recovery (%) and gait speeds (m/min), respectively. A large percent recovery indicates a more efficient gait with less muscle activity. There were significant differences in normal gait for all speed conditions ($P < 0.05$; not shown in the figure). Significant differences were found in the step-to gait pattern between speed conditions as well as between the gait patterns, which are presented in the figure. The larger the value, the higher the mechanical energy exchange efficiency. $^{**}P < 0.01$, $^{*}P < 0.05$. Error bars: Standard deviation.

Walk Ratio

A significant interaction (GAIT×SPEED) was observed for the walk ratio ($F_{(1.6, 16.2)} = 19.6$, $P < 0.01$, partial $\eta^2 = 0.66$; **Figure 4**). Significant main effects were observed in both GAIT ($F_{(1, 10)} = 136.1$, $P < 0.01$, partial $\eta^2 = 0.93$) and SPEED ($F_{(1.19, 11.9)} = 16.9$, $P < 0.01$, partial $\eta^2 = 0.62$). The simple main effect of the gait patterns revealed that the walk ratio for the step-to gait pattern was significantly smaller than that for the normal gait at all speed conditions ($P < 0.01$). A test of the simple main effect of the speeds showed simple main effects for the normal ($P < 0.01$) and step-to gait patterns ($P = 0.026$). Multiple comparisons between speed conditions of the normal gait pattern showed a significantly larger walk ratio at 10 m/min in comparison with the other speed conditions (*adj* $P < 0.01$). The walk ratio for the step-to gait pattern showed no statistically significant differences between all speed conditions.

CoM Lateral Displacement

A significant interaction (GAIT×SPEED) was observed in the CoM lateral displacement ($F_{(4, 40)} = 5.58$, $P < 0.01$, partial $\eta^2 = 0.35$; **Figure 5**). Significant main effects were observed in both GAIT ($F_{(1, 10)} = 63.4$, $P < 0.01$, partial $\eta^2 = 0.86$) and SPEED ($F_{(4, 40)} = 54.2$, $P < 0.01$, partial $\eta^2 = 0.84$). A test of the simple main effect of the gait patterns revealed that the CoM lateral displacements were significantly smaller for

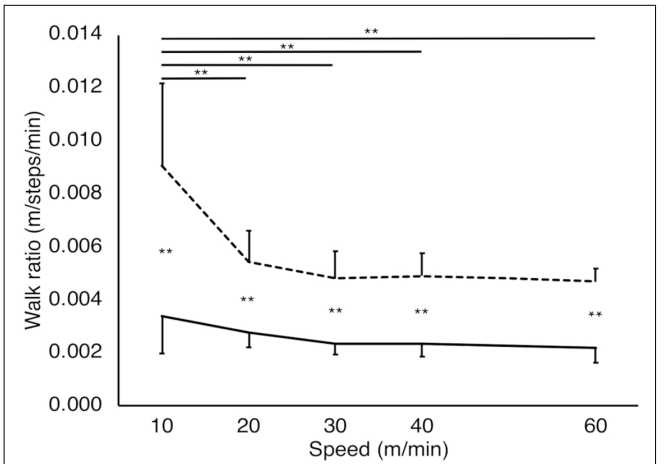

FIGURE 4 | Walk ratio of each gait pattern at each speed condition. The solid and dashed lines represent step-to gait and normal gait patterns, respectively. The vertical and horizontal axes represent the walk ratio (m/steps/min) and gait speeds (m/min), respectively. The walk ratio in the normal gait pattern was significantly larger at 10 m/min than the other speed conditions ($P < 0.01$). The walk ratio for the step-to gait pattern was significantly smaller than that for normal gait at all speed conditions. $^{**}P < 0.01$. Error bars: Standard deviation.

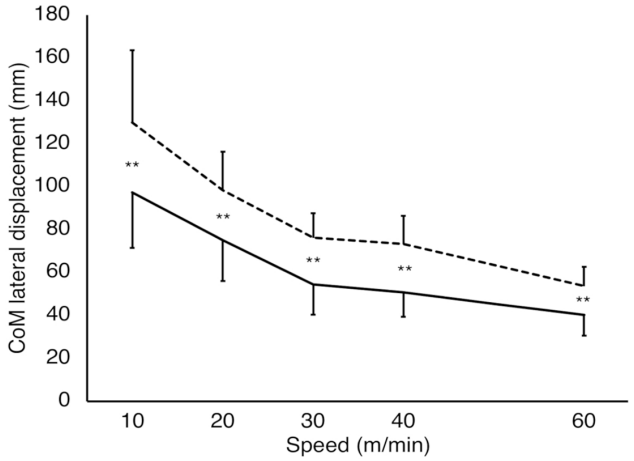

FIGURE 5 | CoM lateral displacement of each gait pattern at each speed condition. The solid and dashed lines represent the step-to gait and normal gait patterns, respectively. The vertical and horizontal axes represent the CoM lateral displacement (mm) and gait speeds (m/min). The larger the CoM lateral displacement, the larger the gait instability. There were significant differences between all speed conditions, except those at 30 and 40 m/min in each gait pattern ($P < 0.01$; not shown in the figure). The CoM lateral displacement for the step-to gait pattern was significantly smaller than that for normal gait at all speed conditions ($P < 0.01$), which are shown in the figure. $^{**}P < 0.01$. Error bars: Standard deviation.

the step-to gait pattern than for the normal gait at all speed conditions ($P < 0.01$). A test of the simple main effect of the speeds showed simple main effects in both normal ($P < 0.01$) and step-to gait patterns ($P < 0.01$). Multiple comparisons between each pair of speed conditions showed that the CoM lateral displacements were significantly larger for the low-speed conditions than for fast ones, except for those between 30 m/min and 40 m/min conditions in both gait patterns (*adj* $P < 0.01$). To investigate why the CoM lateral displacement of the step-to gait was significantly smaller than that of the normal gait, we compared the CoM lateral displacement during the stance-phase of the following leg as well as the preceding leg in the step-to gait with that during the single-leg stance-phase in the normal gait. For the CoM lateral displacement of the following-leg during the stance-phase (**Supplementary Figure 1A**), the two-way ANOVA showed a significant interaction (GAIT×SPEED; $F_{(1.77, 17.72)} = 10.89$, $P < 0.01$, partial $\eta^2 = 0.52$). The significant main effects were observed in both factors of GAIT ($F_{(1, 10)} = 139.51$, $P < 0.01$, partial $\eta^2 = 0.93$) and SPEED ($F_{(1.83, 18.3)} = 15.42$, $P < 0.01$, partial $\eta^2 = 0.61$). The significant simple main effects of GAIT were observed at 10 m/min ($P < 0.05$), 20 m/min, 30 m/min, 40 m/min, and 60 m/min ($P < 0.01$). Therefore, these results showed that the CoM lateral displacement of the following-leg during the stance-phase was significantly smaller than that during the single-leg stance-phase in the normal gait for all speed conditions. For the CoM lateral displacement of the preceding-leg during the stance-phase (**Supplementary Figure 1B**), the two-way ANOVA did not show a significant interaction (GAIT×SPEED; $P = 0.06$). The significant main effects were observed in both factors of GAIT ($F_{(1, 10)} = 12.75$, $P < 0.01$, partial $\eta^2 = 0.56$) and SPEED ($F_{(1.4, 13.9)} = 6.23$, $P < 0.05$, partial $\eta^2 = 0.38$).

CoM Vertical Displacement

A significant interaction (GAIT×SPEED) was observed in the CoMvertical displacement ($F_{(4, 40)} = 7.50$, $P < 0.01$, partial $\eta^2 = 0.43$; **Figure 6A**). The significant main effects were observed in both GAIT ($F_{(1, 10)} = 127.00$, $P < 0.01$, partial $\eta^2 = 0.93$) and SPEED ($F_{(4, 40)} = 74.16$, $P < 0.01$, partial $\eta^2 = 0.88$). The tests of the simple main effect of the gait patterns revealed that the CoM vertical displacements were significantly larger for the step-to gait pattern than for the normal gait at all speed conditions ($P < 0.01$). The tests of the simple main effect of the speeds showed significant simple main effects in both normal ($P < 0.01$) and step-to gait patterns ($P < 0.01$). Multiple comparisons between each pair of speed conditions showed that the CoM vertical displacements were significantly smaller for the low-speed conditions than for thefast ones (*adj* $P < 0.01$), except those between 20 m/min and 30 m/min as well as 30 m/min and 40 m/min in the step-to gait pattern. In the normal gait pattern, the CoM vertical displacements were significantly smaller for the low-speed conditions than for fast ones (*adj* $P < 0.01$), except those between 10 m/min and 20 m/min. Furthermore, a significant positive correlation was observed between the percent recovery and CoM vertical displacement using Spearman's rank correlation coefficient ($\rho = 0.721$, $P = 0.024$; **Figure 6B**).

DISCUSSION

This is the first study to investigate the efficiency and stability of the step-to gait relative to speeds and then compare them with those of normal gait. We used the percent recovery and walk ratio as parameters of gait efficiency, and CoM lateral displacement as a parameter of gait stability. The results suggest that the step-to gait is more stable at speeds between 10 m/min and 60 m/min and more efficient than normal gait at slow or very slow speeds of 10–30 m/min. Therefore, the results demonstrate the advantage of using step-to gait over normal gait when a slow or very slow walk is required, in terms of efficiency and stability.

Percent recovery is a measure of gait efficiency and is the exchange rate between the potential energy and kinetic energy (Cavagna et al., 1976). A large percent recovery indicates a more efficient gait with less muscle activity. In the speed range of 10–30 m/min, the percent recovery of the step-to gait was significantly larger than that of the normal gait, suggesting that step-to gait is an efficient gait pattern in slow or very slow walking. In healthy individuals with a normal gait, the percent recovery is maximal at intermediate walking speed (4 km/h to 7 km/h) and shows an inverse U-shaped relationship with speed variation (Cavagna et al., 1976). The percent recovery of the present results for the normal gait was maximal at 60 m/min, which is similar to the previous findings of Cavagna et al. (1976). Cappozzo et al. (1976) reported that the extension of the lower limbs during the stance phase of the gait cycle is important for accelerating the CoM using potential energy. As suggested by Wurdeman et al. (2017), we found a positive correlation between

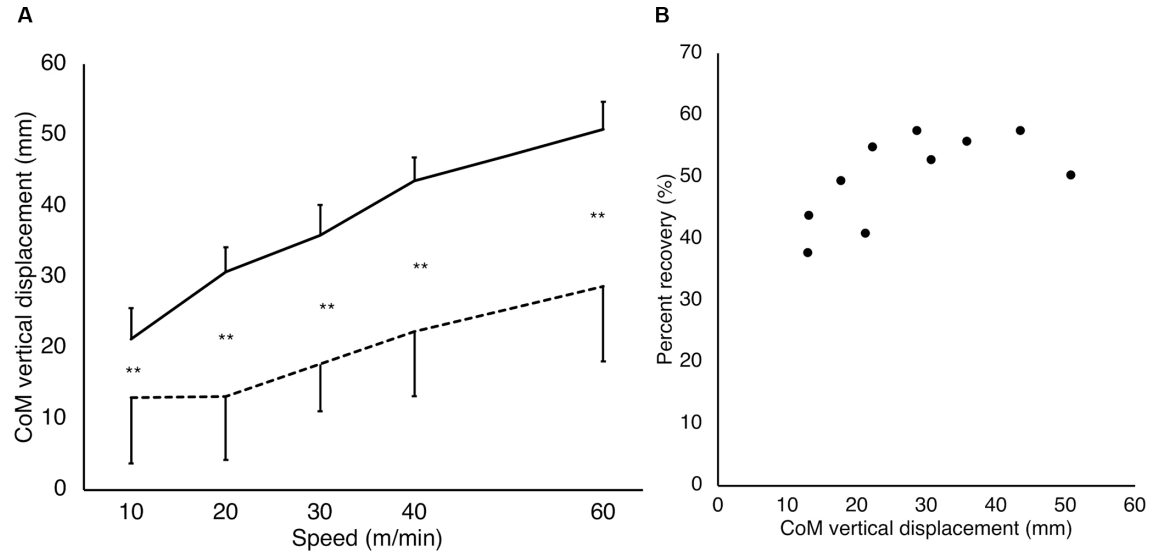

FIGURE 6 | CoM vertical displacement and correlation between the CoM vertical displacement and percent recovery. For the CoM vertical displacement **(A)**, the solid and dashed lines represent the step-to gait and normal gait patterns, respectively. The vertical and horizontal axes represent the CoM vertical displacement (mm) and gait speeds (m/min), respectively. There were significant differences among all speed conditions, except those between 20 m/min and 30 m/min as well as 30 m/min and 40 m/min in the step-to gait pattern ($P < 0.01$; not shown in the figure). In the normal gait pattern, there were significant differences among all speed conditions, except those between 10 m/min and 20 m/min ($P < 0.01$; not shown in the figure). Significant differences were observed between the patterns, which are presented in the figure. $^{**}P < 0.01$. Error bars: Standard deviation. For the correlation between the percent recovery and CoM vertical displacement **(B)**, the dots represent the averaged data of all participants in each condition with step-to gait and normal gait. The vertical and horizontal axes represent the percent recovery (%) and CoM vertical displacement (mm), respectively. A significant positive correlation was observed between the percent recovery and CoM vertical displacement using Spearman's rank correlation coefficient ($\rho = 0.721$, $P = 0.024$).

CoM vertical displacement and energy efficiency expressed as percent recovery (**Figure 6B**). In the present study, the CoM vertical displacement was significantly larger in the step-to gait than in the normal gait (**Figure 6A**). Thus, it is possible that in the step-to gait it was easier to extend the joints of the lower limbs and trunk and to raise the CoM than in the normal gait, as well as of the energy exchange rate of the CoM.

Many studies have shown that the walk ratio is unchanged among people walking at a wide range of walking speeds (Sekiya and Nagasaki, 1998). The walk ratio is optimal in terms of efficiency and attentional demands for a particular speed (Donelan et al., 2001; Legrand et al., 2021). However, in the present study, the walk ratio increased significantly at a very low speed of 10 m/min for the normal gait in comparison with other speeds of 20 m/min, 30 m/min, 40 m/min, and 60 m/min, while it remained constant in all speed conditions for the step-to gait. The observed increase in the walk ratio in slow normal gait was similar to the results of Murakami et al (Murakami and Otaka, 2017). Murakami et al. reported that in the normal gait of healthy participants, the walk ratio is consistent across the speed range of preferred to fast walking of 60–120 m/min; however, it increases with decreasing gait speed of 10–60 m/min. They argued that the coordination and automaticity of gait are disrupted during low-speed walking. Our results demonstrate that the step-to gait maintained a constant walk ratio even when the speed decreased, suggesting that the step-to gait is more coordinated and efficient than the normal gait at low speeds.

CoM lateral displacement is an important measure for evaluating gait balance and predicting falls (Tesio and Rota, 2019). The CoM lateral displacement of the step-to gait was significantly lower than that of the normal gait at all speeds, suggesting that the step-to gait is more advantageous in lateral stability than the normal gait. We speculate that the CoM lateral displacement was smaller in step-to gait than in normal gait because the CoM lateral displacement is smaller in step-to gait at the preceding leg's stance phase following its stance phase with both legs aligned than at the stance phase in normal gait (**Supplementary Figure 1**). The CoM lateral displacement is the largest at the swing phase in normal gait (Perry and Burnfield, 1992). Furthermore, the lateral displacement of the CoM increased with decreasing speed for both gait patterns. The increase in CoM displacement with decreasing speed was similar to that in a previous study of normal gait (Orendurff et al., 2004).The results of the present study suggest that the CoM is easily maintained at the center of the body in the step-to gait pattern, and the risk of lateral fall for it is low compared with the normal gait.

This study has several limitations. In this experiment, the participants walked on the treadmill; thus, the findings of this study should be interpreted with caution because there are some differences between treadmill and ground walking (Alton et al., 1998). We estimated the efficiency using the CoM trajectory, but measurement of metabolic efficiency by exhaled gas is preferable for a more accurate evaluation of gait efficiency. Despite these limitations, the parameters of the present study can represent the

efficiency and stability of gait; thus, the findings of this study are valuable in providing a new approach and hints for future research on gait with the step-to gait pattern.

The results of this study provide evidence that the step-to gait is advantageous, especially in terms of efficiency, for slow walking in an external environment with a high risk of falling (e.g., on slippery ice) or a physical function with a high risk of falling (e.g., aging). Furthermore, the results of this study prove the benefits of teaching step-to gait to patients who have gait disorders and walk at low speed during rehabilitation.In the future, we should investigate whether the characteristics of step-to gait in the elderly and patients with neurological and orthopedic diseases are similar to those of step-to gait in healthy participants in this study.

DATA AVAILABILITY STATEMENT

The raw data supporting the conclusions of this article will be provided by the authors, without undue reservation.

ETHICS STATEMENT

The studies involving human participants were reviewed and approved by Tokyo Bay Rehabilitation Hospital. The participants provided their written informed consent to participate in this study. Written informed consent was obtained from the individual(s) for the publication of any potentially identifiable images or data included in this article.

AUTHOR CONTRIBUTIONS

KHi, YO, TK, and RO designed the experiments and prepared the manuscript. KHi, TK, and YT collected and analyzed the data. TT, SI, KHo, and KK provided important suggestions for data analysis and the manuscript. All authors contributed to the article and approved the submitted version.

FUNDING

This research was supported by the Japan Society for the Promotion of Science Grants-in-Aid for Scientific Research (No. 20H05482, No. JP19K11393, and No. 21K20293).

ACKNOWLEDGMENTS

We would like to thank all individuals who participated in this study.

SUPPLEMENTARY MATERIALS

The Supplementary Material for this article can be found online at: https://www.frontiersin.org/articles/10.3389/fnhum.2021.779920/full#supplementary-material.

REFERENCES

Alton, F., Baldey, L., Caplan, S., and Morrissey, M. C. (1998). A kinematic comparison of overground and treadmill walking. *Clin. Biomech. (Bristol, Avon)* 13, 434–440. doi: 10.1016/s0268-0033(98)00012-6

Best, A. N., and Wu, A. R. (2020). Upper body and ankle strategies compensate for reduced lateral stability at very slow walking speeds. *Proc. Biol. Sci.* 287:20201685. doi: 10.1098/rspb.2020.1685

Brown, H. E., and Mueller, M. J. (1998). A "step-to" gait decreases pressures on the forefoot. *J. Orthop. Sports Phys. Ther.* 28, 139–145. doi: 10.2519/jospt.1998.28.3.139

Bruijn, S. M., van Dieën, J. H., Meijer, O. G., and Beek, P. J. (2009). Is slow walking more stable? *J. Biomech.* 42, 1506–1512. doi: 10.1016/j.jbiomech.2009.03.047

Cappozzo, A., Figura, F., and Marchetti, M. (1976). The interplay of muscular and external forces in human ambulation. *J. Biomech.* 9, 35–43. doi: 10.1016/0021-9290(76)90137-8

Cavagna, G. A., Thys, H., and Zamboni, A. (1976). The sources of external work in level walking and running. *J. Physiol.* 262, 639–657. doi: 10.1113/jphysiol.1976.sp011613

Donelan, J. M., Kram, R., and Kuo, A. D. (2001). Mechanical and metabolic determinants of the preferred step width in human walking. *Proc. Biol. Sci.* 268, 1985–1992. doi: 10.1098/rspb.2001.1761

Iida, H., and Yamamuro, T. (1987). Kinetic analysis of the center of gravity of the human body in normal and pathological gaits. *J. Biomech.* 20, 987–995. doi: 10.1016/0021-9290(87)90328-9

Kurayama, T., Tadokoro, Y., Fujimoto, S., Komiya, Z., Yoshida, S., Chakraborty, S., et al. (2013). A comparison of the movement characteristics between the kneeling gait and the normal gait in healthy adults. *Gait Posture* 37, 402–407. doi: 10.1016/j.gaitpost.2012.08.009

Legrand, T., Younesian, H., Gélinas-Trudel, C., Barthod, C. V., Campeau-Lecours, A., and Turcot, K. (2021). Influence of the overground walking speed control modality: Modification to the walk ratio and spatio-temporal parameters of gait. *Gait Posture* 83, 256–261. doi: 10.1016/j.gaitpost.2020.10.029

Leroux, A., Fung, J., and Barbeau, H. (2002). Postural adaptation to walking on inclined surfaces: I. Normal strategies. *Gait Posture* 15, 64–74. doi: 10.1016/s0966-6362(01)00181-3

Meichtry, A., Romkes, J., Gobelet, C., Brunner, R., and Müller, R. (2007). Criterion validity of 3D trunk accelerations to assess external work and power in able-bodied gait. *Gait Posture* 25, 25–32. doi: 10.1016/j.gaitpost.2005.12.016

Murakami, R., and Otaka, Y. (2017). Estimated lower speed boundary at which the walk ratio constancy is broken in healthy adults. *J. Phys. Ther. Sci.* 29, 722–725. doi: 10.1589/jpts.29.722

Orendurff, M. S., Segal, A. D., Klute, G. K., Berge, J. S., Rohr, E. S., and Kadel, N. J. (2004). The effect of walking speed on center of mass displacement. *J. Rehabil. Res. Dev.* 41, 829–834. doi: 10.1682/jrrd.2003.10.0150

Perry, J., and Burnfield, J. (1992). *Gait Analysis Normal and Pathological Function.* New Jersey: SLACK Incorporated.

Sekiya, N. (1996). The invariant relationship between step length and step rate during free walking. *J. Hum. Mov. Stud.* 30, 241–257.

Sekiya, N., and Nagasaki, H. (1998). Reproducibility of the walking patterns of normal young adults: test-retest reliability of the walk ratio (step-length/step-rate). *Gait Posture* 7, 225–227. doi: 10.1016/s0966-6362(98)00009-5

Shinoda, H., Sato, H., and Suzuki, Y. (2008). Evaluation of gait stability based on variability of medio-lateral motion of the center of mass. *Rigakuryoho Kagaku* 23, 55–60. doi: 10.1589/RIKA.23.55

Tesio, L., and Rota, V. (2019). The motion of body center of mass during walking: a review oriented to clinical applications. *Front. Neurol.* 10:999. doi: 10.3389/fneur.2019.00999

Wurdeman, S. R., Raffalt, P. C., and Stergiou, N. (2017). Reduced vertical displacement of the center of mass is not accompanied by reduced oxygen uptake during walking. *Sci. Rep.* 7:17182. doi: 10.1038/s41598-017-17532-6

Zarrugh, M. Y., Todd, F. N., and Ralston, H. J. (1974). Optimization of energy expenditure during level walking. *Eur. J. Appl. Physiol. Occup. Physiol.* 33, 293–306. doi: 10.1007/BF00430237

Conflict of Interest: The authors declare that the research was conducted in the absence of any commercial or financial relationships that could be construed as a potential conflict of interest.

Publisher's Note: All claims expressed in this article are solely those of the authors and do not necessarily represent those of their affiliated organizations, or those of the publisher, the editors and the reviewers. Any product that may be evaluated in this article, or claim that may be made by its manufacturer, is not guaranteed or endorsed by the publisher.

Copyright © 2022 Hirayama, Otaka, Kurayama, Takahashi, Tomita, Inoue, Honaga, Kondo and Osu. This is an open-access article distributed under the terms of the Creative Commons Attribution License (CC BY). The use, distribution or reproduction in other forums is permitted, provided the original author(s) and the copyright owner(s) are credited and that the original publication in this journal is cited, in accordance with accepted academic practice. No use, distribution or reproduction is permitted which does not comply with these terms.

frontiers in Systems Neuroscience

ORIGINAL RESEARCH
published: 10 January 2022
doi: 10.3389/fnsys.2021.804263

Model-Based Analyses for the Causal Relationship Between Post-stroke Impairments and Functional Brain Connectivity Regarding the Effects of Kinesthetic Illusion Therapy Combined With Conventional Exercise

*Yu Miyawaki[1,2,3], Masaki Yoneta[1], Megumi Okawada[1], Michiyuki Kawakami[1], Meigen Liu[1] and Fuminari Kaneko[1]**

[1]Department of Rehabilitation Medicine, Keio University School of Medicine, Tokyo, Japan, [2]Neurorehabilitation Research Center, Kio University, Nara, Japan, [3]Research Fellow of Japan Society for the Promotion of Science, Tokyo, Japan

Aims: Therapy with kinesthetic illusion of segmental body part induced by visual stimulation (KINVIS) may allow the treatment of severe upper limb motor deficits in post-stroke patients. Herein, we investigated: (1) whether the effects of KINVIS therapy with therapeutic exercise (TherEx) on motor functions were induced through improved spasticity, (2) the relationship between resting-state functional connectivity (rs-FC) and motor functions before therapy, and (3) the baseline characteristics of rs-FC in patients with the possibility of improving their motor functions.

Methods: Using data from a previous clinical trial, three path analyses in structural equation modeling were performed: (1) a mediation model in which the indirect effects of the KINVIS therapy with TherEx on motor functions through spasticity were drawn, (2) a multiple regression model with pre-test data in which spurious correlations between rs-FC and motor functions were controlled, and (3) a multiple regression model with motor function score improvements between pre- and post-test in which the pre-test rs-FC associated with motor function improvements was explored.

Results: The mediation model illustrated that although KINVIS therapy with TherEx did not directly improve motor function, it improved spasticity, which led to ameliorated motor functions. The multiple regression model with pre-test data suggested that rs-FC

OPEN ACCESS

Edited by:
Jun Izawa,
University of Tsukuba, Japan

Reviewed by:
Soha Saleh,
Kessler Foundation, United States
Rieko Osu,
Waseda University, Japan

***Correspondence:**
Fuminari Kaneko
f-kaneko@keio.jp

Received: *29 October 2021*
Accepted: *15 December 2021*
Published: *10 January 2022*

Citation:
Miyawaki Y, Yoneta M, Okawada M, Kawakami M, Liu M and Kaneko F (2022) Model-Based Analyses for the Causal Relationship Between Post-stroke Impairments and Functional Brain Connectivity Regarding the Effects of Kinesthetic Illusion Therapy Combined With Conventional Exercise. Front. Syst. Neurosci. 15:804263. doi: 10.3389/fnsys.2021.804263

Abbreviations: aIPS, Inferior parietal sulcus in the affected hemisphere; ARAT, Action Research Arm Test; ARAT-F, finger-related ARAT score; ARAT-FD, degree of ARAT-F score improvements from the pre-test to the post-test; ARAT-S, shoulder-related ARAT score; ARAT-SD, degree of ARAT-S score improvements from the pre-test to the post-test; aSMG, supramarginal gyrus in the affected hemisphere; FMA, Fugl-Meyer Assessment; FMA-D, degree of FMA score improvements from the pre-test to the post-test; KINVIS, kinesthetic illusion of segmental body part induced by visual stimulation; MAS, modified Ashworth Scale; rs-FC, resting-state functional connectivity; TherEx, therapeutic exercise; uIPL, inferior parietal lobule in the unaffected hemisphere; uIPS, inferior parietal sulcus in the unaffected hemisphere; uPMd, dorsal premotor cortex in the unaffected hemisphere.

of bilateral parietal regions is associated with finger motor functions, and that rs-FC of unaffected parietal and premotor areas is involved in shoulder/elbow motor functions. Moreover, the multiple regression model with motor function score improvements suggested that the weaker the rs-FC of bilateral parietal regions or that of the supramarginal gyrus in an affected hemisphere and the cerebellar vermis, the greater the improvement in finger motor function.

Conclusion: The effects of KINVIS therapy with TherEx on upper limb motor function may be mediated by spasticity. The rs-FC, especially that of bilateral parietal regions, might reflect potentials to improve post-stroke impairments in using KINVIS therapy with TherEx.

Keywords: clinical trial, functional connectivity, kinesthetic illusion therapy, spasticity, stroke

INTRODUCTION

Spasticity is frequently represented as the main symptom of motor deficits accompanied by paralysis, especially in the chronic phase in patients after stroke. The disorganization of afferent signals from peripheries or compensational signals from the brain to the peripheries is thought to cause spasticity. Motor deficits of the upper limb can impair patients' daily lives after stroke, and solving this problem is important in rehabilitation medicine. We have encountered an event in which spasticity masks potential motor functions as if the cause of spasticity exists in a different system from motor paralysis. In fact, some patients' motor accuracies improve immediately after the target muscle's spasm is suppressed by therapy for spasticity, such as reinforced stretching, for a muscle that can interfere with accurate movement.

Spasticity disturbs the skilled and gross motor performance of the upper limbs (Pundik et al., 2019). For these motor deficits, studies have proposed some effective therapies, such as constraint-induced movement therapy (Wolf et al., 2006), mental practice (Page et al., 2007), or robot therapy (Klamroth-Marganska et al., 2014), which can have moderate effects (Pollock et al., 2014). However, these therapies require patients to perform voluntary movements or motor imagery, and severe cases with strong difficulties in such performances are often excluded. Therefore, an effective therapy for severe cases is required, for which a novel therapy utilizing kinesthetic illusion of segmental body part induced by visual stimulation (KINVIS) was proposed (Kaneko et al., 2016a, 2019; Aoyama et al., 2020; Okawada et al., 2020).

KINVIS is defined as the psychological phenomenon in which a resting person feels as if his/her own body part is moving or feels the desire to move a body part while watching a movie of that body part moving (Kaneko et al., 2007). We previously demonstrated that primary motor cortex excitability is enhanced during/after KINVIS (Kaneko et al., 2007, 2016b; Aoyama et al., 2012), as shown in the motor imagery of hand or finger movements without performing a voluntary movement (Kaneko et al., 2003, 2014; Yahagi et al., 1996). Moreover, previous studies revealed that motor-related areas, such as the premotor, superior, or inferior parietal cortex, were activated when experiencing KINVIS more than observing a similar movement (Kaneko et al., 2015; Shibata and Kaneko, 2019). These psychological experiences and neurological effects may contribute to recovering post-stroke motor deficits. For example, mirror therapy (Altschuler et al., 1999) that can induce kinesthetic illusions such as KINVIS has a moderate effect on motor deficits (Dohle et al., 2009; Pollock et al., 2014). In terms of interhemispheric inhibition (Murase et al., 2004; Nowak et al., 2009), it is noteworthy that KINVIS requires no voluntary movements even in a non-paralyzed upper limb. Since the KINVIS paradigm enables a person to passively experience finger or hand movements as a kinesthetic illusion, it has the potential to work as a treatment for severe cases.

Based on these findings, the KINVIS therapy was proposed and a clinical trial was conducted for 10 days (Kaneko et al., 2019). In this trial, 11 patients with a severe paretic upper limb in the chronic phase underwent KINVIS therapy and conventional therapeutic exercise (TherEx). The KINVIS therapy comprised a combination of KINVIS and neuromuscular electrical stimulation (NMES). Participants observed prerecorded finger flexion and extension movements of a virtual upper limb displayed on a monitor parallel to and above their own actual limbs. When participants observed the movements, electrical stimulations on the finger extensor muscles were combined to provide proprioception matched with the visual movements. This therapy was undertaken for 20 min, after which TherEx was performed for 60 min. Before and after this 10-day intervention, upper limb motor functions, spasticity, and resting-state brain functional connectivity (rs-FC) were assessed (i.e., pre- and post-tests). This clinical trial produced two main findings.

First, a previous study (Kaneko et al., 2019) had demonstrated significant improvements in the Fugl-Meyer Assessment (FMA), Action Research Arm Test (ARAT), and modified Ashworth Scale (MAS) scores after the interventions (see **Supplementary Table 1**). Interestingly, the improvement of the MAS score reached a minimum of clinically important differences (i.e., reduction of one or more; Barros Galvão et al., 2014). Given that this trial included only patients in the chronic phase, the natural recovery after stroke may not sufficiently explain these improvements. Although this clinical

trial was undertaken only for 10 days, other therapies, such as mirror or robot therapy, require longer-term interventions (e.g., >6 weeks; Page et al., 2007; Dohle et al., 2009; Klamroth-Marganska et al., 2014). According to these facts, the effects of the KINVIS therapy with TherEx might have been observed by bringing out the masked potential functions of paretic upper limbs rather than directly recovering their motor deficits. Patients with severe motor deficits in the chronic phase often have severe spasticity, which can disturb the motor performance. In this trial, all patients had a MAS score of ≥2 (i.e., severe spasticity; Kaneko et al., 2019). Considering that significant improvements in the MAS scores were observed in this trial, the improvements in motor functions might have been induced through improvements in spasticity.

As the other finding, the previous clinical trial demonstrated significant correlations between rs-FC and FMA/ARAT scores (Kaneko et al., 2019). These motor function scores were correlated with the rs-FC between the inferior parietal sulcus in the affected (aIPS) and unaffected (uIPS) hemispheres, between the supramarginal gyrus in the affected hemisphere (aSMG) and the cerebellar vermis, and between the inferior parietal lobule in the unaffected hemisphere (uIPL) and dorsal premotor cortex in the unaffected hemisphere (uPMd). Although the causal relationships of these correlations remain unclear, these rs-FC can help capture characteristics in severe cases who participated in the previous trial (Kaneko et al., 2019). However, the previous study analyzed these correlations independently but did not consider spurious correlations. Because some regions composed of these rs-FC were similar to each other (i.e., parietal regions), the influences of their spurious correlations should be investigated. This investigation may contribute to exploring the characteristics of patients with the possibility of improved motor functions using KINVIS therapy with TherEx.

Taken together, although the KINVIS therapy may allow us to treat severe cases, further analyses of the data from the previous clinical trial (Kaneko et al., 2019) can help unravel the effects of its therapy. These analyses may lead to a hypothesis that should be examined in large-scale future clinical trials. Before proceeding to an ensuing trial, therefore, we sought to address the unresolved issues by performing path analyses in structural equation modeling with data from the previous clinical trial (Kaneko et al., 2019), i.e., reuse of data. First, we conducted a path analysis comprising the mediation model to investigate whether the improvements in upper limb motor functions after KINVIS therapy with TherEx were induced through improvements in spasticity. Second, we performed a path analysis comprising the multiple regression model to investigate the relationship among the three rs-FC (i.e., aIPS-uIPS, aSMG-Vermis, and uIPL-uPMd) and motor functions before intervention and without spurious correlations among them. Finally, we conducted a path analysis comprising the multiple regression model to investigate the baseline characteristics of rs-FC in patients with the possibility of improving their motor functions. This study is expected to help develop a novel treatment for patients with severe motor deficits.

METHODS

Previous Clinical Trial

Participants

We utilized the data from a previous clinical trial (Kaneko et al., 2019) of KINVIS therapy with TherEx, because we aimed to investigate improvements in motor functions and correlations with rs-FC observed in this trial, with 11 patients registered (seven men and four women; five right hemiparesis and six left hemiparesis; mean age = 54.7 years, SD = 10.8). The patients had a unilateral stroke without cortical involvement, the ability to flex the paretic fingers voluntarily without extension, time from stroke onset of >4 months, and the ability to walk independently with or without assistance. Moreover, the patients had not received other special rehabilitations or treatments for paretic upper limbs, such as transcranial magnetic stimulation, repetitive facilitative exercise, or botulinum toxin injection within 3 months. In summary, the patients had severe hemiparesis of the upper limbs in the chronic phase.

Interventions

The patients participated in the clinical trial, with assessments undertaken before and after this 10-day intervention (pre- and post-tests), comprising KINVIS therapy and conventional TherEx. In KINVIS, patients underwent a combination therapy of KINVIS and neuromuscular electrical stimulation (**Figure 1**). Electrical stimulation was combined to provide proprioception matched with visual finger movements and was applied at an intensity higher than the finger extensor muscles' motor threshold (motor threshold = 1.0–1.2 times higher; frequency = 20 Hz; pulse width = 50 μs) when watching a finger-extension phase movie. In one intervention (1 day), patients underwent KINVIS therapy for 20 min and TherEx for 60 min post KINVIS therapy.

MRI Data Acquisition and Preprocessing

All magnetic resonance imaging data (MRI) were obtained using a 1.5-T MRI scanner with a head coil (Optima 450w, GE Healthcare, Chicago, IL, USA). Resting-state functional MRI (fMRI) was performed to measure rs-FC. For this scanning session, a gradient-echo echo-planar sequence was used (3.75 × 3.75 × 3.5 voxels; echo time = 40 ms; repetition time = 2,500 ms, flip angle = 85), in order to collect BOLD contrast data of 244 slices. Moreover, a T1-weighted MRI scan was acquired. T1-weighted structural images were acquired as an anatomical reference (0.4688 × 0.4688 × 1.4 mm voxels; echo time = 3.076 ms; repetition time = 8.368 ms; flip angle = 12). MRI data acquisition was performed before and after the intervention.

All data preprocessing were carried out using CONN toolbox (Whitfield-Gabrieli and Nieto-Castanon, 2012) implemented on MATLAB (Mathworks Inc., Natick, MA, USA). CONN is a conjunction in Statistical Parametric Mapping 12 (SPM12; Well-come Department of Imaging Neuroscience, London, UK); therefore, the following preprocessing pipeline is SPM12 compliant. Image preprocessing consisted of the following: (1) reducing the signal for the first four slices for

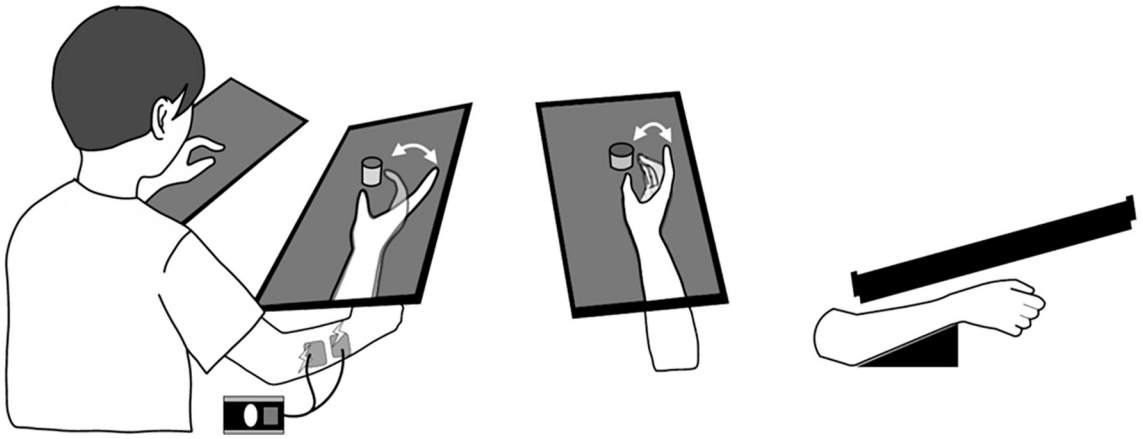

FIGURE 1 | KINVIS therapy setup. When participants observed the movie of prerecorded finger flexion and extension movements, the electrical stimulation on the finger extensor muscles was combined to provide proprioception matched with visual finger movements. The virtual upper limb on the monitor was set parallel to and above an actual limb.

magnetization equilibrium effects and adaptation of the subjects to the circumstances; (2) flipping of all structural/functional data of right-hand affected patients using non-rigid reflection along the x-axis, in order to align the affected hemisphere on the left side; (3) functional realignment and unwarping; (4) slice-timing correction applied to the images; (5) creating binary masks in gray matter, white matter, and cerebrospinal fluid images using structural segmentation; (6) denoising using outlier detection thresholded 97th percentile in normative samples of framewise displacement; (7) normalization to the EPI image template conforming to the Montreal Neurological Institute (MNI) space (2 mm iso voxels); (8) spatial smoothing with an isotropic Gaussian kernel of 7-mm full width at half maximum; and (9) band-pass filtering with a setting of 0.01–0.08 Hz.

After the data preprocessing, regions of interest, which were defined as spherical seed regions with a radius of 6 mm, were created in the MNI space on the affected and unaffected hemispheres (also see Kaneko et al., 2019 for more detailed methods).

Outcome Measures

In the present study, we adopted the data of the FMA, ARAT, MAS, and rs-FC (aIPS-uIPS, aSMG-Vermis, and uIPL-uPMd) for analyses using the FMA and ARAT scores as the main outcomes for upper limb motor function. The MAS score was analyzed to investigate the influence of spasticity and consisted of a total score of the 2nd to 5th fingers and wrist flexor muscles. The MAS is an ordinal scale with scores of 0, 1, 1+, 2, 3, and 4. For analyses using the MAS score, scores of 1+, 2, 3, and 4 were transformed to 2, 3, 4, and 5, respectively (transformed scores: 0, 1, 2, 3, 4, and 5). As the outcomes of brain activities, we focused on z-scores of the aIPS-uIPS, aSMG-Vermis, and uIPL-uPMd rs-FC (see "Introduction" section). These z-scores were calculated for each of the pre- and post-tests.

Statistics

Since all participants had the same FMA scores in the wrist (0 for all) and hand (1 for all) subscales, variances in the FMA scores reflected the shoulder, elbow, and forearm gross motor functions (scores of the shoulder/elbow/forearm subscales). We analyzed three variables using the ARAT scores: total, finger-related (ARAT-F), and shoulder-related (ARAT-S) scores. The ARAT-F refers to the total score of the grasp, grip, and pinch subscales, mainly reflecting the hand and finger skilled motor functions. The ARAT-S score refers to the gross movement subscale score, mainly reflecting the upper limb gross motor functions (especially the shoulder). Using these variables, we performed three main investigations. First, conducting a path analysis comprising the mediation model, we investigated the relationship between the effects of the KINVIS therapy with TherEx on upper limb motor function and spasticity. Second, performing a path analysis comprising the multiple regression model, we investigated the relationship among the three rs-FC (i.e., aIPS-uIPS, aSMG-Vermis, and uIPL-uPMd) and motor function prior to intervention and without spurious correlations among them. Finally, conducting path analysis comprising the multiple regression model, we investigated baseline characteristics of rs-FC in patients who can potentially improve their motor functions.

Correlation Analyses and t-Tests

Before the main analyses, we explored the characteristics of upper limb motor functions (FMA and ARAT scores). These investigations contributed to constituting the mediation model, wherein paths were provided to variables representing motor function improvements after KINVIS therapy with TherEx. Using paired t-tests, significant differences were previously reported in the FMA and ARAT total scores between the pre- and post-tests (Kaneko et al., 2019; **Figures 2**, **3**). Based on these results, we conducted correlation analyses to investigate the relationship between the pre-test motor function scores and

score improvements from the pre-test to the post-test (FMA-D or ARAT-D). Regarding the ARAT-F or ARAT-S scores, we conducted the same analyses as above (i.e., paired t-tests and correlation analyses). The analyses were conducted using R software (version 4.0.2).

Path Analysis Comprising the Mediation Model

After the above analyses, we conducted one of the main investigations, investigating whether improvements in upper limb motor functions after KINVIS therapy with TherEx were induced through spasticity improved by therapy. A path analysis (mediation model) in structural equation modeling was conducted with KINVIS therapy (dummy variable: 0 or 1) as an independent variable; MAS as a mediation variable; FMA, ARAT-F, and ARAT-S scores as dependent variables. This analysis utilized the pre- and post-tests scores. Based on the t-tests and correlation analysis results, we drew paths from the KINVIS to the MAS, FMA, and ARAT-F and from the MAS to the FMA, ARAT-F, and ARAT-S. We evaluated whether this model fit the data by a chi-square test and other model fit indices, such as the root mean square error of approximation (RMSEA), comparative fit index (CFI), or Tucker-Lewis index (TLI). If these indices showed a good fit, we accepted the model and proceeded to interpret the path coefficients. Path coefficients were estimated by the robust weighted least squares, suitable for analyzing the model including an ordinal variable (Muthén, 1984). These analyses were conducted using M-plus (version 8.5).

Path Analyses Comprising the Multiple Regression Models

Next, we investigated the relationship between the three rs-FC (i.e., z-scores of the aIPS-uIPS, aSMG-Vermis, and uIPL-uPMd) and upper limb motor functions. We analyzed the pre-test scores of their variables to determine the characteristics of patients with severe post-stroke impairments. Significant correlations between their rs-FC and motor functions (i.e., FMA or ARAT) have been previously reported (Kaneko et al., 2019). To control the rs-FC influences other than the one of interest among them, we conducted a path analysis (multiple regression model) with z-scores of the pre-test aIPS-uIPS, aSMG-Vermis, and uIPL-uPMd as independent variables and the pre-test FMA, ARAT-F, and ARAT-S scores as dependent variables. We drew paths from three independent variables (i.e., three rs-FC) for all three dependent variables.

Finally, we investigated whether pre-test rs-FC scores were associated with the degree of motor function improvements after intervention (i.e., explored the improvement potential in terms of rs-FC). We analyzed pre-test rs-FC scores as independent variables and the difference in motor function scores between pre- and post-tests as dependent variables. In this analysis, variables with significant differences in motor function scores between the pre- and post-tests were adopted as dependent variables (i.e., FMA-D and ARAT-FD, see "Results" section). We drew paths from three independent variables (three rs-FC) for all dependent variables.

These models were saturated, which completely fit the data. Path coefficients were estimated by the robust maximum likelihood, which allowed an accurate estimation regardless of multivariate normal distribution (Yuan and Bentler, 2000). These analyses were conducted using M-plus (version 8.5).

RESULTS

Upper Limb Motor Function Characteristics

Correlation analysis revealed no significant correlation between FMA-D and pre-test FMA (r = 0.37, p = 0.27; **Figure 2**), whereas a significant positive correlation was observed between the ARAT-D and pre-test ARAT scores (r = 0.87, $p < 0.001$; **Figure 3**). This result indicates that the higher the pre-test scores, the greater the improvements after the interventions.

A paired t-test revealed a significant difference between the pre- and post-test ARAT-F scores (t = 2.36, df = 10, p = 0.040, Hedges'g (Hedges, 1981) = 0.52; **Figure 4**). Correlation analysis revealed a significant positive correlation between the ARAT-FD and pre-test ARAT-F scores (r = 0.88, $p < 0.001$), consistent with those of the total ARAT scores. A paired t-test revealed similar pre- and post-test ARAT-S scores (t = 1.61, df = 10, p = 0.14, g = 0.26; **Figure 4**). Correlation analysis revealed similar ARAT-SD and pre-test ARAT-S scores (r = −0.094, p = 0.78). These results are summarized in **Supplementary Table 1**.

Effects of KINVIS Therapy With TherEx Mediated by Spasticity

Based on the above results, in structural equation modeling, we drew paths from the KINVIS to the MAS, FMA, and ARAT-F, but not to the ARAT-S (**Figure 5**); no significant improvement in the ARAT-S score after KINVIS therapy with TherEx was observed (**Figure 4**). To investigate spasticity influences, we drew paths from the MAS to the FMA, ARAT-F, and ARAT-S. This model fit the data very well; a chi-square test of model fit was not significant (χ^2 = 1.03, df = 1, p = 0.31; other model fit indices: RMSEA = 0.037, CFI = 0.99, TLI = 0.98). A path analysis revealed significant standardized path coefficients (β) from the KINVIS to the MAS (β = −0.52, p = 0.003) from the MAS to the FMA, β = −0.45, p = 0.013, ARAT-S, β = −0.53, $p < 0.001$, and ARAT-F, β = −0.52, p = 0.014, and non-significant standardized coefficients from the KINVIS to the FMA, β = 0.092, p = 0.72, and ARAT-F, β = −0.019, p = 0.95. Regarding the indirect KINVIS effects on the FMA and ARAT-F (product of KINVIS to the MAS and MAS to FMA/ARAT-F path coefficients), a bootstrap method (resampling = 2000) revealed bias-corrected 95% confidence intervals in the FMA (0.045, 0.53) and ARAT-F (0.029, 0.61). This model indicated that the KINVIS decreased the MAS score, indirectly improving the FMA and ARAT scores. **Supplementary Table 2** presents details of these results.

Relationship Between the rs-FC and Motor Function Before Intervention

Before a path analysis (multiple regression model), the variance inflation factors of the independent variables within the standard range (2.12, 1.02, and 2.11 in aIPS-uIPS, aSMG-Vermis, and uIPL-uPMd, respectively) were confirmed. A path analysis was

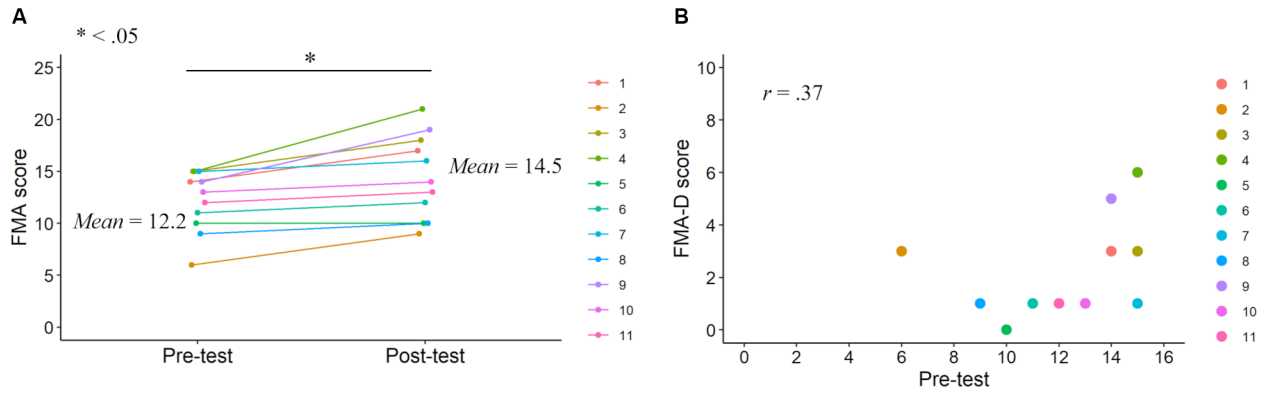

FIGURE 2 | FMA scores in the pre- and post-tests. FMA score improvements after the KINVIS therapy with TherEx reported by Kaneko et al. (2019) and their individual differences **(A)**. The relationship between the FMA-D (degree of the improvements from the pre- to post-tests) and pre-test scores **(B)**.

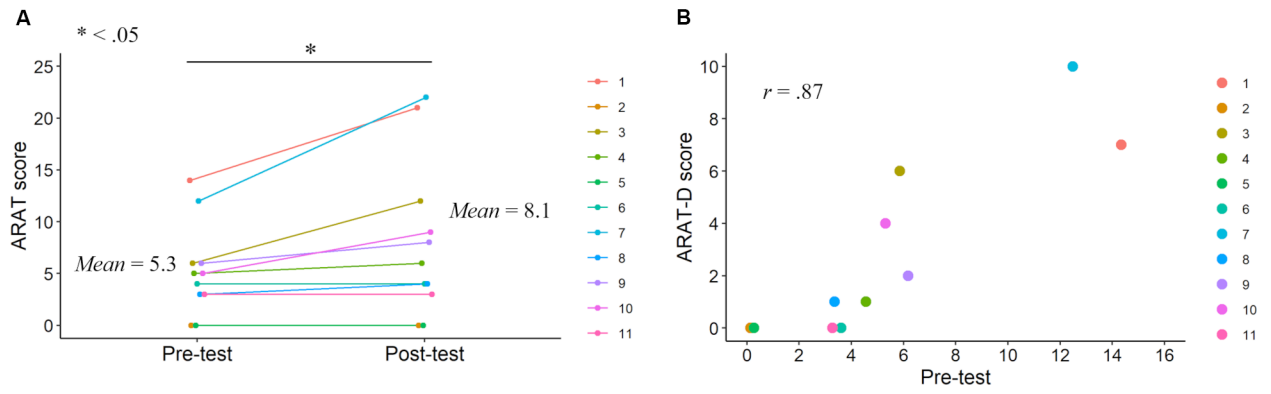

FIGURE 3 | ARAT scores in the pre- and post-tests. ARAT score improvements after the KINVIS therapy with TherEx reported by Kaneko et al. (2019) and their individual differences **(A)**. The relationship between the ARAT-D (degree of the improvements from the pre- to post-tests) and pre-test scores **(B)**.

conducted with z-scores of the pre-test aIPS-uIPS, aSMG-Vermis, and uIPL-uPMd as independent variables, and the pre-test FMA, ARAT-F, and ARAT-S scores as dependent variables. This analysis revealed significant standardized path coefficients (β) from the aIPS-uIPS to the ARAT-F, $\beta = -0.49$, $p = 0.024$, and from the uIPL-uPMd to the FMA, $\beta = -0.94$, $p < 0.001$, and ARAT-S, $\beta = -0.67$, $p = 0.006$ (**Figure 6**). **Supplementary Table 3** lists the details of these results.

Relationship Between the rs-FC and Motor Function Improvements

Path analysis was conducted using z-scores of the pre-test aIPS-uIPS, aSMG-Vermis, and uIPL-uPMd as independent variables, and the FMA-D and ARAT-FD scores (i.e., score improvements between the pre-test to the post-test) as dependent variables; the ARAT-SD score was not used in this analysis because no significant difference in score was observed between the pre- and post-tests (**Figure 4**). This analysis revealed significant standardized path coefficients (β) from the aIPS-uIPS to the ARAT-FD, $\beta = -0.50$, $p = 0.014$, and from the aSMG-Vermis to the ARAT-FD, $\beta = 0.38$, $p = 0.019$ (**Figure 7**). **Supplementary Table 4** lists the details of these results.

DISCUSSION

We aimed to investigate the complex relationships among KINVIS therapy with TherEx, spasticity, upper limb motor functions, and rs-FC (i.e., aIPS-uIPS, aSMG-Vermis, or uIPL-uPMd) observed previously (Kaneko et al., 2019). To achieve this, we conducted two main investigations by performing path analyses in structural equation modeling with data from the previous clinical trial (Kaneko et al., 2019). First, we investigated whether the effects of KINVIS therapy with TherEx on motor function improvements were induced through improved spasticity. Second, the relationships among the three rs-FC and motor functions before the interventions were analyzed without spurious correlations between their variables. Consequently, we provide three main findings with a hypothesis for future, large-scale, clinical trials.

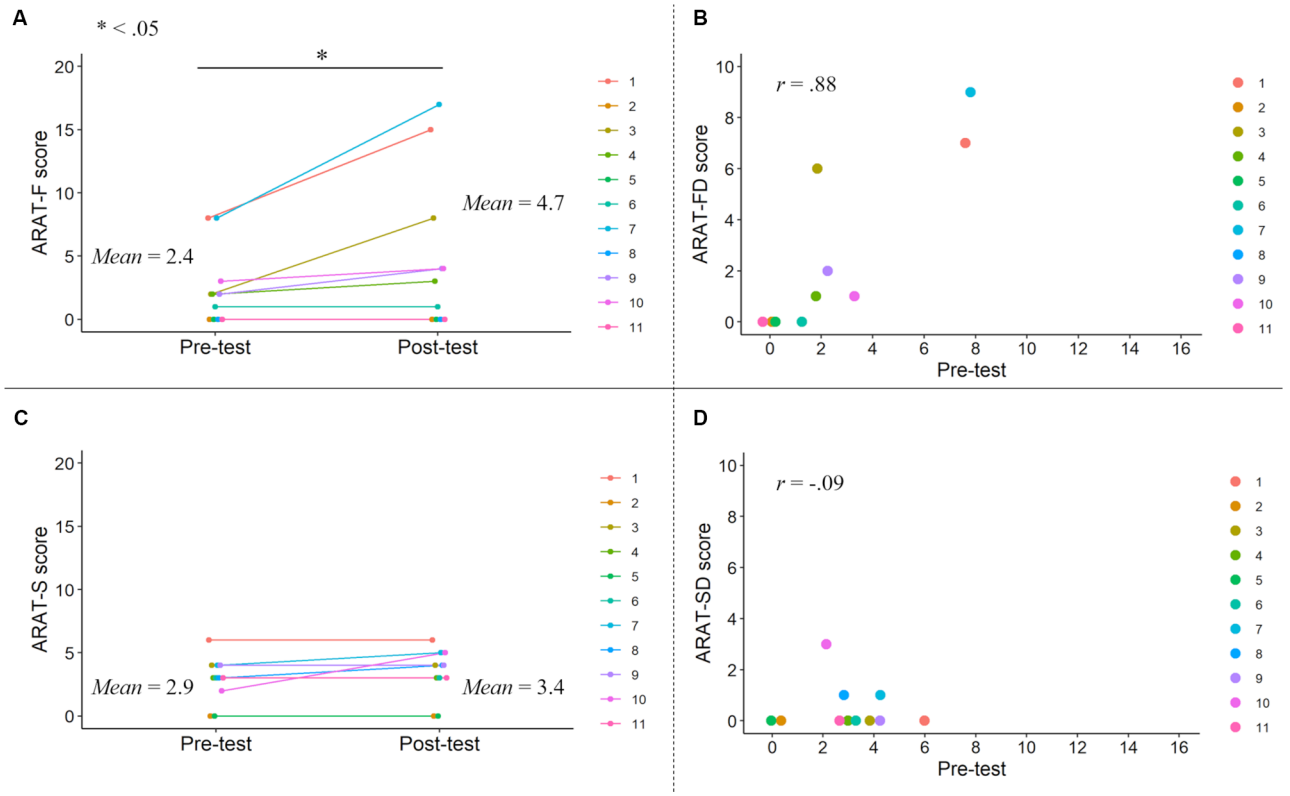

FIGURE 4 | ARAT-F and ARAT-S scores in the pre- and post-tests. ARAT-F score improvements after the KINVIS therapy with TherEx and their individual differences **(A)**. The relationship between the ARAT-FD (degree of the improvements from the pre- to post-tests) and ARAT-F pre-test scores **(B)**. The changes of the ARAT-S scores after the KINVIS therapy with TherEx in individuals **(C)**. The relationship between the ARAT-SD (degree of the improvements from the pre- to post-tests) and ARAT-S pre-test scores **(D)**. The ARAT-F score referred to the total score of the grasp, grip, and pinch subscales. The ARAT-S score referred to the score of the gross movement subscale.

Effects of KINVIS Therapy With TherEx Mediated by Spasticity

In the present study, we demonstrated that KINVIS therapy with TherEx decreased the MAS score that improved the FMA, ARAT-F, and ARAT-S scores (indirect effect of the KINVIS therapy with TherEx). Interestingly, in this mediation model, no significant direct effects from KINVIS to FMA and ARAT-F were observed, although the paired t-tests revealed significant improvements in the FMA and ARAT scores. These results, therefore, suggest that the effects of KINVIS therapy with TherEx on upper limb motor functions were mediated by spasticity. Considering that the patients underwent KINVIS therapy with TherEx for just 10 days, these interventions induced their potential spasticity-masked motor functions. In severe cases, motor function recovery can be smaller than in moderate or mild ones (Vliet et al., 2020). Besides, spasticity can disturb therapeutic exercises for severe cases, e.g., by obscuring motor learning (Subramanian et al., 2018). If the KINVIS therapy improved spasticity, its therapy likely facilitated the effects of TherEx post KINVIS. These combined effects may explain the improvements in motor function in severe cases observed in the previous clinical trial (Kaneko et al., 2019).

How did the KINVIS therapy with TherEx enable improvement of spasticity? To dissect this mechanism, evidence regarding mirror therapy, to treat paretic upper limb in post-stroke patients (Pérez-Cruzado et al., 2017), may help. Mirror therapy causes kinesthetic illusions such as KINVIS; however, few studies have reported significant improvements in spasticity after mirror therapy (Yavuzer et al., 2008; Samuelkamaleshkumar et al., 2014; Pérez-Cruzado et al., 2017). This difference in the effect on spasticity may be due to differences in neurological reactions or maneuvers between the KINVIS and mirror therapies. A systematic review on neuroimaging reported brain regions activated by mirror therapy, such as the superior parietal and fusiform regions (Deconinck et al., 2015). These two regions were consistent with those activated in experiencing KINVIS (Kaneko et al., 2015) and therefore possibly associated with kinesthetic illusions. The KINVIS experiences can activate premotor regions including the supplementary motor area and basal ganglia (Kaneko et al., 2015), not seen in mirror therapy, with little evidence that its therapy activates the mirror neuron system (Deconinck et al., 2015), although KINVIS can be interpreted to be driven by the contralateral hemispherical mirror neuron system. These

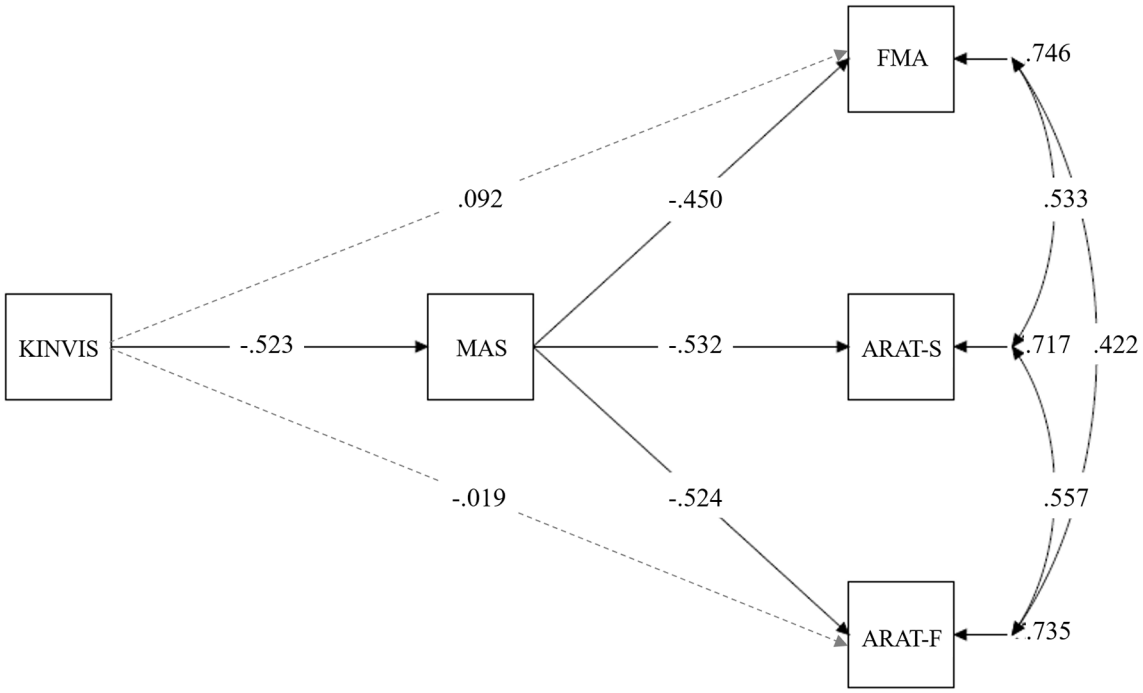

FIGURE 5 | Mediation model in the KINVIS, MAS, FMA, ARAT-F, and ARAT-S. The KINVIS referred to the kinesthetic illusion therapy with TherEx, which was transformed to the dummy variable in this model: before (0) and after (1) the interventions. The ARAT-F referred to the total score of the grasp, grip, and pinch subscales. The ARAT-S referred to the score of the gross movement subscale. Solid lines show paths with significant standardized coefficients, and broken lines show paths with nonsignificant standardized coefficients.

neurological differences in inducing kinesthetic illusions may be related to the different effects of KINVIS and mirror therapies on spasticity.

The activation of the premotor area, supplementary motor area, and/or network between the association motor and parietal areas may contribute to the effects of KINVIS therapy on spasticity. However, since the previous clinical study (Kaneko et al., 2019) did not measure brain activity during KINVIS, this possibility should be investigated further. KINVIS requires no voluntary movements, even in a non-paralyzed upper limb. In mirror illusion, however, proprioceptive input from non-paralyzed hand movements can affect the kinesthetic illusion (Chancel et al., 2016). Although the non-paralyzed hand movements may reinforce abnormal interhemispheric inhibition (Murase et al., 2004; Nowak et al., 2009), this issue is excluded in KINVIS. Whether these differences explain the mechanism of the effect on spasticity remains unclear; however, these may characterize the clinical effects of KINVIS. This clinical effect is noteworthy and highlights the necessity to explore its mechanism. Recent animal studies highlight the importance of ipsilateral premotor/supplementary-cortico-reticulospinal tract hyperexcitability from the unaffected motor cortex as a result of disinhibition after stroke (Li et al., 2019). Li et al. (2019) suggested a theoretical account that disinhibition after stroke in the premotor area and the supplementary area may cause spasticity and related movement impairments. The enhanced excitability of motor associated areas in the affected hemisphere and lower activity in the unaffected side are possibly remarkable points in managing spasticity. Further study to approach this pathophysiological account may be needed.

Our results also exhibited significant correlations among the FMA and ARAT residual variances, indicating other factors related to variances in the FMA and ARAT scores unexplained by the variables included in this model. This is unsurprising because upper limb motor functions are affected not only by spasticity but also by many factors, such as lesion sites. Regarding the changes in their scores, the present study suggests the importance of considering the pre-intervention motor function scores (at least the ARAT), since a significant correlation between the degree of improvement and pre-test ARAT score was observed. Although the results revealed no significant correlation in the FMA, such correlation could emerge by including patients with moderate or mild motor deficits (**Figure 2**). Brain activities, including rs-FC, may be associated with KINVIS therapy effects (Kaneko et al., 2015), although our patient sample size was too small to analyze a complex model including their variables. The indirect effect observed in our study, however, can contribute to future model construction, allowing us to explore the KINVIS effect mechanisms.

Relationship Between the rs-FC and Motor Functions Before the Intervention

We demonstrated significant coefficients from the aIPS-uIPS to the ARAT-F and from the uIPL-uPMd to the FMA and

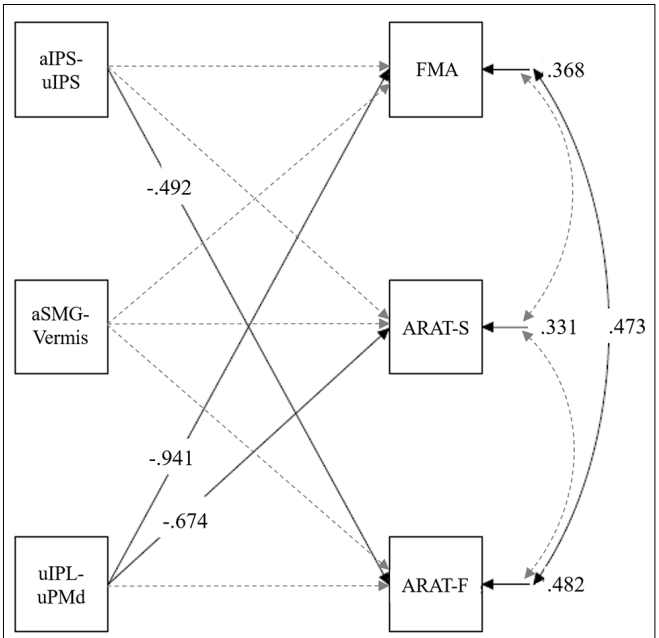

FIGURE 6 | Multiple regression model in pre-test rs-FC and upper limb motor functions. The ARAT-F referred to the total score of the grasp, grip, and pinch subscales. The ARAT-S referred to the score of the gross movement subscale. Solid lines show paths with significant standardized coefficients, and broken lines show nonsignificant paths. Only significant coefficients were shown for clarity (**Supplementary Table 3** shows all path coefficients). aIPS-uIPL: rs-FC between the inferior parietal sulcus in the affected and unaffected hemispheres. aSMG-Vermis: rs-FC between the supramarginal gyrus in the affected hemisphere and the cerebellar vermis. uIPL-uPMd: rs-FC between the inferior parietal lobule in the unaffected hemisphere and dorsal premotor cortex in the unaffected hemisphere.

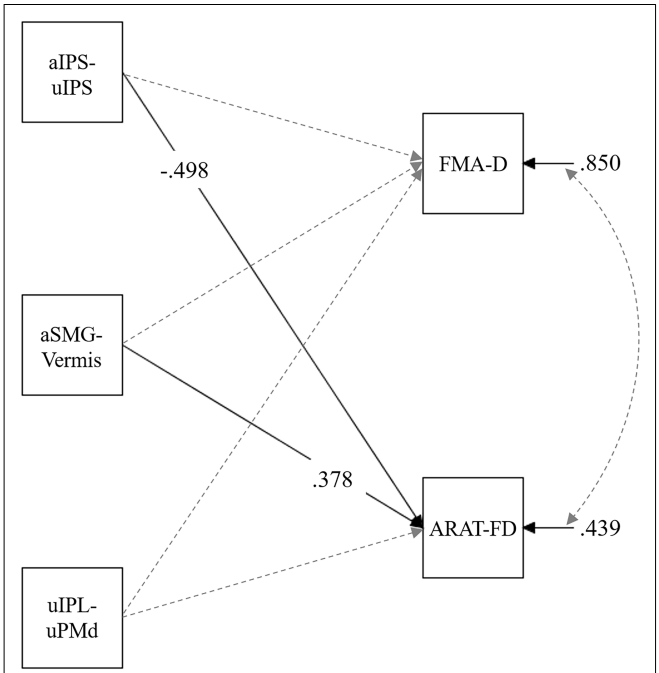

FIGURE 7 | Multiple regression model in pre-test rs-FC and score improvements of upper limb motor function between the pre- and post-test. The FMA-D referred to the degree of improvement between the pre- and post-test in the FMA score. The ARAT-FD referred to the degree of improvement between the pre- and post-test regarding the total score for grasp, grip, and pinch subscales. Solid lines show paths with significant standardized coefficients, and broken lines show nonsignificant paths. Only significant coefficients are shown for clarity (**Supplementary Table 4** shows all path coefficients). aIPS-uIPL: rs-FC between the inferior parietal sulcus in the affected and unaffected hemispheres. aSMG-Vermis: rs-FC between the supramarginal gyrus in the affected hemisphere and the cerebellar vermis. uIPL-uPMd: rs-FC between the inferior parietal lobule in the unaffected hemisphere and dorsal premotor cortex in the unaffected hemisphere.

ARAT-S. The former indicates that the rs-FC of aIPS-uIPS may be associated with skilled motor functions of the hands and fingers. Some studies reported that the motor imagery of hand or finger movements activated the parietal areas (Parsons et al., 1995; Stephan et al., 1995). Other evidence indicated that their activities during the motor imagery were similar to those just before performing finger movements, suggesting that their activities are involved in motor preparations (Hanakawa et al., 2003, 2008). According to these findings, the functional connectivity between aIPS and uIPS might play an important role in performing hand and finger movements. In fact, patients with damage in these regions can have difficulties in performing hand and finger movements and recognizing self-body and movements, even though the lesions do not extend to the corticospinal tract (apraxia; Appenzeller and Hanson, 1966). However, the present study illustrated that the stronger the rs-FC of aIPS-uIPS, the weaker the finger motor functions (i.e., negative correlation). This might be due to the strong rs-FC between parietal regions related to motor performances (when motor imageries and preparations are unnecessary) and/or that parietal regions should interact with ipsilateral occipital or frontal regions, but the connectivity in our study did not do so (connectivity between contralateral IPSs). If so, our results suggest a deviation of this functional connectivity from a normal one. This deviation could disturb the hand and finger motor performances.

The other significant coefficients (i.e., from the uIPL-uPMd to the FMA and ARAT-S) indicate that the rs-FC of uIPL-uPMd may be associated with the gross motor functions of the shoulders and elbows. In their gross movements, such as reaching, the motor intentions can arise from the projection through the superior longitudinal fasciculus II and III from the inferior parietal to premotor cortices (Graziano et al., 1994; Rizzolatti et al., 1998). Moreover, gross movements require proximal or trunk muscles to be controlled. Some studies have suggested that the premotor region has bilateral projections to the reticular formation (i.e., cortico-reticular pathway; Matsuyama and Drew, 1997; Kably and Drew, 1998; Yeo et al., 2012). These pathways might bilaterally project to proximal or trunk muscles and may be involved in the posture control required prior to limb movements (Matsuyama and Drew, 1997; Kably and Drew, 1998). It should be noted that the premotor cortex may also have an ipsilateral projection to proximal or trunk muscles. Our study revealed negative correlations

between rs-FC of uIPL-uPMd (i.e., uninvolved hemisphere) and motor functions of the paretic upper limb. Given that patients often compensate for motor functions on paretic limbs by the brain functions in the uninvolved hemisphere post stroke, these correlations might reflect compensatory brain activities due to severe motor deficits. Considering that the motor impairments of the patients were within a chronic phase, the rs-FC, aIPS-uIPS or uIPL-uPMd, may represent one of the post-stroke adaptations in the brain. To further investigate this possibility, a longitudinal study would be required.

Relationship Between the rs-FC and Motor Function Improvements

In terms of rs-FC, we explored the baseline characteristics of patients with the potential to improve their motor functions. Regarding the relationship between the pre-test rs-FC and motor function improvements, significant negative coefficients from the aIPS-uIPS to the ARAT-FD and positive coefficients from the aSMG-Vermis to the ARAT-FD were observed. The former indicates that the weaker rs-FC of aIPS-uIPS before the intervention, the greater the finger motor function improvements, suggesting that the patients with weak rs-FC of aIPS-uIPS have the potential to improve their motor functions. This result is consistent with the pre-test data analysis (see **Figure 6**), suggesting that the strength of this rs-FC may indicate a deviation from a normal one.

For the latter (positive coefficients from the aSMG-Vermis to the ARAT-FD), it should be noted that rs-FC of the aSMG-Vermis was negative (i.e., the aSMG was negatively correlated with the vermis) although rs-FC of aIPS-uIPS and uIPL-uPMd were positive (Kaneko et al., 2019). Therefore, the positive coefficients from the aSMG-Vermis to the ARAT-FD indicate that the weaker negative rs-FC of aSMG-Vermis before the interventions, the greater the finger motor function improvements. The vermis is known to receive somatosensory inputs from the spinal cord and is related to controlling the anti-gravity muscles of the trunk and legs (Lisberger and Thach, 2013). On the other hand, parietal regions including the SMG can be associated with finger motor functions through motor awareness (Desmurget et al., 2009) or multisensory integration (Quinn et al., 2014). Considering the negative functional connectivity between these regions, the activity of the vermis in a resting state could inhibit that of the SMG, thereby disturbing voluntary finger movements. If so, it is likely that the decline of this negative functional connectivity can contribute to improvements of finger motor functions, as shown by the positive coefficients from the aSMG-Vermis to the ARAT-FD. This may also be a topic of interest for future investigation.

Limitations

Since we utilized the sample data of a previous clinical trial (Kaneko et al., 2019), our study had similar limitations to that of the previous trial. For example, the previous study had no control group and therefore could not determine which of the two treatments (the KINVIS therapy and TherEx) was effective in reducing spasticity (also see Discussion in Kaneko et al., 2019). Moreover, since KINVIS therapy is composed of KINVIS and NMES, there is a possibility that the reduction of spasticity observed in the previous clinical trial (Kaneko et al., 2019) resulted from NMES itself. However, a meta-analysis on the effects of NMES indicated that NMES combined with other interventions can provide a significant effect on spasticity but not NMES alone, suggesting that combining NMES with other interventions can be a treatment option that provides improvements in spasticity (Stein et al., 2015). Moreover, this study showed that the use of NMES for 30 min five times per week for 3–4 weeks was effective, whereas KINVIS therapy was undertaken for 20 min per day for 10 days. Considering these findings, it seems that the reduction of spasticity observed in the previous clinical trial (Kaneko et al., 2019) resulted in NMES and KINVIS with TherEx. The improvement of motor functions through reducing spasticity may have been caused by the effect of this combination. This possibility should be further investigated by future clinical trials with a control group.

Conversely, the previous sample allowed us to benefit from its clinical characteristics; this sample consisted of patients with severe motor deficits in the chronic phase. For example, our study indicates that in such cases, the fact that the pre-test FMA and ARAT-S scores (gross motor functions of shoulders and elbows) did not predict their improvements, but rather spasticity, might be critical. We acknowledge the importance of using new samples. However, it is also true that conducting a clinical trial is very costly, especially in severe cases. For new studies, the use of previous sample data can be reasonable in some cases (e.g., clinical trials or meta-analysis studies).

Second, the models investigated in this study did not comprehensively include variables due to the small sample size. A complex and comprehensive model including latent variables needs a large sample size for its analysis (Bentler and Chou, 1987). Therefore, we adopted simple models and focused on path coefficients. To identify the relationship among KINVIS therapy, motor functions, and rs-FC, a further study comparing multiple models from the perspective of model fit indices and theory is needed.

CONCLUSIONS

In summary, our study provides three main findings. First, the effects of KINVIS therapy with TherEx on upper limb motor function can be mediated by spasticity. Second, the results suggest that rs-FC of aIPS-uIPS is associated with the skilled motor functions of the hands and fingers, and that rs-FC of uIPL-uPMd is involved in the gross motor functions of the shoulders and elbows. Finally, weaker rs-FC of aIPS-uIPS or aSMG-Vermis might reflect potentials to improve post-stroke impairments in using KINVIS therapy

with TherEx. These findings help construct hypothetical models examined in large-scale future clinical trials and underscore the necessity to examine the integrated model in which brain activities account for the indirect effect of KINVIS therapy with TherEx.

DATA AVAILABILITY STATEMENT

The original contributions presented in the study are included in the article/**Supplementary Material**, further inquiries can be directed to the corresponding author.

ETHICS STATEMENT

The studies involving human participants were reviewed and approved by Shonan Keiiku Hospital Ethics Committee. The patients/participants provided their written informed consent to participate in this study.

AUTHOR CONTRIBUTIONS

FK and ML received funding. FK managed the project and resources, supervision, conceptualization, partial writing—review and editing. YM and MY analyzed clinical and fMRI data. YM and all other authors wrote the article. All authors contributed to the article and approved the submitted version.

FUNDING

This work was supported by the Japan Agency for Medical Research and Development (AMED; Grant Numbers JP18he0402255 and JP21he2302006). FK received funds from the Japan Society for the Promotion of Science (JSPS) KAKENHI (Grant Number JP19H01088).

ACKNOWLEDGMENTS

We would like to express our gratitude to Dr. Norihiro Suzuki and the Radiology Department of Shonan Keiiku Hospital for their academic support and encouragement.

SUPPLEMENTARY MATERIALS

The Supplementary Material for this article can be found online at: https://www.frontiersin.org/articles/10.3389/fnsys.2021.804263/full#supplementary-material.

REFERENCES

Altschuler, E. L., Wisdom, S. B., Stone, L., Foster, C., Galasko, D., Llewellyn, D. M., et al. (1999). Rehabilitation of hemiparesis after stroke with a mirror. *Lancet* 353, 2035–2036. doi: 10.1016/s0140-6736(99)00920-4

Aoyama, T., Kanazawa, A., Kohno, Y., Watanabe, S., Tomita, K., Kimura, T., et al. (2020). Feasibility case study for treating a patient with sensory ataxia following a stroke with kinesthetic illusion induced by visual stimulation. *Prog. Rehabil. Med.* 5:20200025. doi: 10.2490/prm.20200025

Aoyama, T., Kaneko, F., Hayami, T., and Shibata, E. (2012). The effects of kinesthetic illusory sensation induced by a visual stimulus on the corticomotor excitability of the leg muscles. *Neurosci. Lett.* 514, 106–109. doi: 10.1016/j.neulet.2012.02.069

Appenzeller, O., and Hanson, J. C. (1966). Parietal ataxia. *Arch. Neurol.* 15, 264–269. doi: 10.1001/archneur.1966.00470150042007

Barros Galvão, S. C., Borba Costa dos Santos, R., Borba dos Santos, P., Cabral, M. E., and Monte-Silva, K. (2014). Efficacy of coupling repetitive transcranial magnetic stimulation and physical therapy to reduce upper-limb spasticity in patients with stroke: a randomized controlled trial. *Arch. Phys. Med. Rehabil.* 95, 222–229. doi: 10.1016/j.apmr.2013.10.023

Bentler, P. M., and Chou, C. P. (1987). Practical issues in structural modeling. *Sociol. Methods Res.* 16, 78–117. doi: 10.1177/0049124187016001004

Chancel, M., Brun, C., Kavounoudias, A., and Guerraz, M. (2016). The kinaesthetic mirror illusion: how much does the mirror matter?. *Exp. Brain Res.* 234, 1459–1468. doi: 10.1007/s00221-015-4549-5

Deconinck, F. J. A., Smorenburg, A. R. P., Benham, A., Ledebt, A., Feltham, M. G., and Savelsbergh, G. J. P. (2015). Reflections on mirror therapy: a systematic review of the effect of mirror visual feedback on the brain. *Neurorehabil. Neural Repair.* 29, 349–361. doi: 10.1177/1545968314546134

Desmurget, M., Reilly, K. T., Richard, N., Szathmari, A., Mottolese, C., and Sirigu, A. (2009). Movement intention after parietal cortex stimulation in humans. *Science* 324, 811–813. doi: 10.1126/science.1169896

Dohle, C., Püllen, J., Nakaten, A., Küst, J., Rietz, C., and Karbe, H. (2009). Mirror therapy promotes recovery from severe hemiparesis: a randomized controlled trial. *Neurorehabil. Neural Repair* 23, 209–217. doi: 10.1177/1545968308324786

Graziano, M. S., Yap, G. S., and Gross, C. G. (1994). Coding of visual space by premotor neurons. *Science* 266, 1054–1057. doi: 10.1126/science.7973661

Hanakawa, T., Dimyan, M. A., and Hallett, M. (2008). Motor planning, imagery and execution in the distributed motor network: a time-course study with functional MRI. *Cereb. Cortex.* 18, 2775–2788. doi: 10.1093/cercor/bhn036

Hanakawa, T., Immisch, I., Toma, K., Dimyan, M. A., Van Gelderen, P., and Hallett, M. (2003). Functional properties of brain areas associated with motor execution and imagery. *J. Neurophysiol.* 89, 989–1002. doi: 10.1152/jn.00132.2002

Hedges, L. V. (1981). Distribution theory for Glass's estimator of effect size and related estimators. *J. Educ. Stat.* 6, 107–128. doi: 10.3102/10769986006002107

Kably, B., and Drew, T. (1998). Corticoreticular pathways in the cat. I. Projection patterns and collaterization. *J. Neurophysiol.* 80, 389–405. doi: 10.1152/jn.1998.80.1.389

Kaneko, F., Blanchard, C., Lebar, N., Nazarian, B., Kavounoudias, A., and Romaiguère, P. (2015). Brain regions associated to a kinesthetic illusion evoked by watching a video of one's own moving hand. *PLoS One* 10:e0131970. doi: 10.1371/journal.pone.0131970

Kaneko, F., Hayami, T., Aoyama, T., and Kizuka, T. (2014). Motor imagery and electrical stimulation reproduce corticospinal excitability at levels similar to voluntary muscle contraction. *J. Neuroeng. Rehabil.* 11:94. doi: 10.1186/1743-0003-11-94

Kaneko, F., Inada, T., Matsuda, N., Shibata, E., and Koyama, S. (2016a). Acute effect of visually induced kinesthetic illusion in patients with stroke: a preliminary report. *Int. J. Neurorehabil.* 3, 1–6. doi: 10.4172/2376-0281.1000212

Kaneko, F., Shibata, E., Hayami, T., Nagahata, K., and Aoyama, T. (2016b). The association of motor imagery and kinesthetic illusion prolongs the effect of transcranial direct current stimulation on corticospinal tract excitability. *J. Neuroeng. Rehabil.* 13:36. doi: 10.1186/s12984-016-0143-8

Kaneko, F., Murakami, T., Onari, K., Kurumadani, H., and Kawaguchi, K. (2003). Decreased cortical excitability during motor imagery after disuse of an upper limb in humans. *Clin. Neurophysiol.* 114, 2397–2403. doi: 10.1016/s1388-2457(03)00245-1

Kaneko, F., Shindo, K., Yoneta, M., Okawada, M., Akaboshi, K., and Liu, M. (2019). A case series clinical trial of a novel approach using augmented reality that inspires self-body cognition in patients with stroke: effects on motor function and resting-state brain functional connectivity. *Front. Sys. Neurosci.* 13:76. doi: 10.3389/fnsys.2019.00076

Kaneko, F., Yasojima, T., and Kizuka, T. (2007). Kinesthetic illusory feeling induced by a finger movement movie effects on corticomotor excitability. *Neuroscience* 149, 976–984. doi: 10.1016/j.neuroscience.2007.07.028

Klamroth-Marganska, V., Blanco, J., Campen, K., Curt, A., Dietz, V., Ettlin, T., et al. (2014). Three-dimensional, task-specific robot therapy of the arm after stroke: a multicentre, parallel-group randomised trial. *Lancet Neurol.* 13, 159–166. doi: 10.1016/S1474-4422(13)70305-3

Li, S., Chen, Y. T., Francisco, G. E., Zhou, P., and Rymer, W. Z. (2019). A unifying pathophysiological account for post-stroke spasticity and disordered motor control. *Front. Neurol.* 10:468. doi: 10.3389/fneur.2019.00468

Lisberger, S. G., and Thach, W. T. (2013). "The cerebellum," in *Principles of Neural Science*, eds E. R. Kandel, J. D. Koester, S. H. Mack, and S. A. Siegelbaum (New York: McGraw-Hill), 960–981.

Matsuyama, K., and Drew, T. (1997). Organization of the projections from the pericruciate cortex to the pontomedullary brainstem of the cat: a study using the anterograde tracer Phaseolus vulgaris-leucoagglutinin. *J. Comp. Neurol.* 389, 617–641. doi: 10.1002/(sici)1096-9861(19971229)389:4<617::aid-cne6>3.0.co;2-3

Murase, N., Duque, J., Mazzocchio, R., and Cohen, L. G. (2004). Influence of interhemispheric interactions on motor function in chronic stroke. *Ann. Neurol.* 55, 400–409. doi: 10.1002/ana.10848

Muthén, B. (1984). A general structural equation model with dichotomous, ordered categorical and continuous latent variable indicators. *Psychometrika* 49, 115–132. doi: 10.1007/BF02294210

Nowak, D. A., Grefkes, C., Ameli, M., and Fink, G. R. (2009). Interhemispheric competition after stroke: brain stimulation to enhance recovery of function of the affected hand. *Neurorehabil. Neural Repair* 23, 641–656. doi: 10.1177/1545968309336661

Okawada, M., Kaneko, F., Shindo, K., Yoneta, M., Sakai, K., Okuyama, K., et al. (2020). Kinesthetic illusion induced by visual stimulation influences sensorimotor event-related desynchronization in stroke patients with severe upper-limb paralysis: a pilot study. *Restor. Neurol. Neurosci.* 38, 455–465. doi: 10.3233/RNN-201030

Page, S. J., Levine, P., and Leonard, A. (2007). Mental practice in chronic stroke. *Stroke* 38, 1293–1297. doi: 10.1161/01.STR.0000260205.67348.2b

Parsons, L. M., Fox, P. T., Downs, J. H., Glass, T., Hirsch, T. B., Martin, C. C., et al. (1995). Use of implicit motor imagery for visual shape discrimination as revealed by PET. *Nature* 375, 54–58. doi: 10.1038/375054a0

Pérez-Cruzado, D., Merchán-Baeza, J. A., González-Sánchez, M., and Cuesta-Vargas, A. I. (2017). Systematic review of mirror therapy compared with conventional rehabilitation in upper extremity function in stroke survivors. *Aust. Occup. Ther. J.* 64, 91–112. doi: 10.1111/1440-1630.12342

Pollock, A., Farmer, S. E., Brady, M. C., Langhorne, P., Mead, G. E., Mehrholz, J., et al. (2014). Interventions for improving upper limb function after stroke. *Cochrane Database Syst. Rev.* 2014:CD010820. doi: 10.1002/14651858.CD010820.pub2

Pundik, S., McCabe, J., Skelly, M., Tatsuoka, C., and Daly, J. J. (2019). Association of spasticity and motor dysfunction in chronic stroke. *Ann. Phys. Rehabil. Med.* 62, 397–402. doi: 10.1016/j.rehab.2018.07.006

Quinn, B. T., Carlson, C., Doyle, W., Cash, S. S., Devinsky, O., Spence, C., et al. (2014). Intracranial cortical responses during visual-tactile integration in humans. *J. Neurosci.* 34, 171–181. doi: 10.1523/JNEUROSCI.0532-13.2014

Rizzolatti, G., Luppino, G., and Matelli, M. (1998). The organization of the cortical motor system: new concepts. *Electroencephalogr. Clin. Neurophysiol.* 106, 283–296. doi: 10.1016/s0013-4694(98)00022-4

Samuelkamaleshkumar, S., Reethajanetsureka, S., Pauljebaraj, P., Benshamir, B., Padankatti, S. M., and David, J. A. (2014). Mirror therapy enhances motor performance in the paretic upper limb after stroke: a pilot randomized controlled trial. *Arch. Phys. Med. Rehabil.* 95, 2000–2005. doi: 10.1016/j.apmr.2014.06.020

Shibata, E., and Kaneko, F. (2019). Event-related desynchronization possibly discriminates the kinesthetic illusion induced by visual stimulation from movement observation. *Exp. Brain Res.* 237, 3233–3240. doi: 10.1007/s00221-019-05665-1

Stein, C., Fritsch, C. G., Robinson, C., Sbruzzi, G., and Plentz, R. D. M. (2015). Effects of electrical stimulation in spastic muscles after stroke: systematic review and meta-analysis of randomized controlled trials. *Stroke* 46, 2197–2205. doi: 10.1161/STROKEAHA.115.009633

Stephan, K. M., Fink, G. R., Passingham, R. E., Silbersweig, D., Ceballos-Baumann, A. O., Frith, C. D., et al. (1995). Functional anatomy of the mental representation of upper extremity movements in healthy subjects. *J. Neurophysiol.* 73, 373–386. doi: 10.1152/jn.1995.73.1.373

Subramanian, S. K., Feldman, A. G., and Levin, M. F. (2018). Spasticity may obscure motor learning ability after stroke. *J. Neurophysiol.* 119, 5–20. doi: 10.1152/jn.00362.2017

Vliet, R. van der., Selles, R. W., Andrinopoulou, E. R., Nijland, R., Ribbers, G. M., Frens, M. A., et al. (2020). Predicting upper limb motor impairment recovery after stroke: a mixture model. *Ann. Neurol.* 87, 383–393. doi: 10.1002/ana.25679

Whitfield-Gabrieli, S., and Nieto-Castanon, A. (2012). Conn: a functional connectivity toolbox for correlated and anticorrelated brain networks. *Brain Connect.* 2, 125–141. doi: 10.1089/brain.2012.0073

Wolf, S. L., Winstein, C. J., Miller, J. P., Taub, E., Uswatte, G., Morris, D., et al. (2006). Effect of constraint-induced movement therapy on upper extremity function 3 to 9 months after stroke: the EXCITE randomized clinical trial. *JAMA* 296, 2095–2104. doi: 10.1001/jama.296.17.2095

Yahagi, S., Shimura, K., and Kasai, T. (1996). An increase in cortical excitability with no change in spinal excitability during motor imagery. *Percept. Mot. Skills* 83, 288–290. doi: 10.2466/pms.1996.83.1.288

Yavuzer, G., Selles, R., Sezer, N., Sütbeyaz, S., Bussmann, J. B., Köseoğlu, F., et al. (2008). Mirror therapy improves hand function in subacute stroke: a randomized controlled trial. *Arch. Phys. Med. Rehabil.* 89, 393–398. doi: 10.1016/j.apmr.2007.08.162

Yeo, S. S., Chang, M. C., Kwon, Y. H., Jung, Y. J., and Jang, S. H. (2012). Corticoreticular pathway in the human brain: diffusion tensor tractography study. *Neurosci. Lett.* 508, 9–12. doi: 10.1016/j.neulet.2011.11.030

Yuan, K. H., and Bentler, P. M. (2000). Three likelihood-based methods for mean and covariance structure analysis with nonnormal missing data. *Sociol. Methodol.* 30, 165–200. doi: 10.1111/0081-1750.00078

Conflict of Interest: FK and MK are the founding scientists of the startup company INTEP Inc. for the social implementation of university research results. ML is currently an advisor of Connect Inc. These companies do not have any relationship with the device or setup used in the present study. FK received license fees from Inter Reha Co., Ltd.

The remaining authors declare that the research was conducted in the absence of any commercial or financial relationships that could be construed as a potential conflict of interest.

Publisher's Note: All claims expressed in this article are solely those of the authors and do not necessarily represent those of their affiliated organizations, or those of the publisher, the editors and the reviewers. Any product that may be evaluated in this article, or claim that may be made by its manufacturer, is not guaranteed or endorsed by the publisher.

Copyright © 2022 Miyawaki, Yoneta, Okawada, Kawakami, Liu and Kaneko. This is an open-access article distributed under the terms of the Creative Commons Attribution License (CC BY). The use, distribution or reproduction in other forums is permitted, provided the original author(s) and the copyright owner(s) are credited and that the original publication in this journal is cited, in accordance with accepted academic practice. No use, distribution or reproduction is permitted which does not comply with these terms.

frontiers in Systems Neuroscience

REVIEW
published: 10 January 2022
doi: 10.3389/fnsys.2021.806544

Excitatory-Inhibitory Homeostasis and Diaschisis: Tying the Local and Global Scales in the Post-stroke Cortex

Francisco Páscoa dos Santos[1,2,3] *and Paul F. M. J. Verschure*[2,4]*

[1] *Eodyne Systems SL, Barcelona, Spain,* [2] *Laboratory of Synthetic, Perceptive, Emotive and Cognitive Systems (SPECS), Institute for Bioengineering of Catalonia (IBEC), Barcelona, Spain,* [3] *Department of Information and Communications Technologies (DTIC), Universitat Pompeu Fabra (UPF), Barcelona, Spain,* [4] *Catalan Institution for Research and Advanced Studies (ICREA), Barcelona, Spain*

Maintaining a balance between excitatory and inhibitory activity is an essential feature of neural networks of the neocortex. In the face of perturbations in the levels of excitation to cortical neurons, synapses adjust to maintain excitatory-inhibitory (EI) balance. In this review, we summarize research on this EI homeostasis in the neocortex, using stroke as our case study, and in particular the loss of excitation to distant cortical regions after focal lesions. Widespread changes following a localized lesion, a phenomenon known as diaschisis, are not only related to excitability, but also observed with respect to functional connectivity. Here, we highlight the main findings regarding the evolution of excitability and functional cortical networks during the process of post-stroke recovery, and how both are related to functional recovery. We show that cortical reorganization at a global scale can be explained from the perspective of EI homeostasis. Indeed, recovery of functional networks is paralleled by increases in excitability across the cortex. These adaptive changes likely result from plasticity mechanisms such as synaptic scaling and are linked to EI homeostasis, providing a possible target for future therapeutic strategies in the process of rehabilitation. In addition, we address the difficulty of simultaneously studying these multiscale processes by presenting recent advances in large-scale modeling of the human cortex in the contexts of stroke and EI homeostasis, suggesting computational modeling as a powerful tool to tie the meso- and macro-scale processes of recovery in stroke patients.

Keywords: stroke, diaschisis, cortical reorganization, functional networks, excitability, homeostatic plasticity, Excitatory-inhibitory balance

OPEN ACCESS

Edited by:
Jun Ota,
The University of Tokyo, Japan

Reviewed by:
Yutaka Oouchida,
Osaka Kyoiku University, Japan
Tetsuya Hasegawa,
The University of Tokyo, Japan

***Correspondence:**
Paul F. M. J. Verschure
paul.verschure@specs-lab.com

Received: *31 October 2021*
Accepted: *29 November 2021*
Published: *10 January 2022*

Citation:
Páscoa dos Santos F and Verschure PFMJ (2022) Excitatory-Inhibitory Homeostasis and Diaschisis: Tying the Local and Global Scales in the Post-stroke Cortex. Front. Syst. Neurosci. 15:806544. doi: 10.3389/fnsys.2021.806544

STROKE AND DIASCHISIS

In stroke, disruptions in blood flow in the central nervous system lead to focal lesions in the brain or spinal cord, causing it to be one of the most burdening disorders in economically advantaged countries (Campbell and Khatri, 2020). As a result of such lesions, patients experience a broad range of symptoms, with deficits in motor (e.g., hemiparesis), sensory (e.g., hemianopia) and higher-order cognitive processes (e.g., aphasia, hemispatial neglect) (Musuka et al., 2015;

Campbell and Khatri, 2020), even leading to neuropsychiatric deficits such as depression (Towfighi et al., 2017) and dementia (Leys et al., 2005). While some of the effects of stroke can be directly attributed to loss of function of lesioned areas (Siegel et al., 2016), its effects extend beyond the lesioned area involving multiple areas across the cortex, a phenomenon known as diaschisis. The term diaschisis, coined by von Monakow (1914), first pertained to a remote loss in excitability following focal lesion impacting the function of brain areas distant to the lesion. Since, then the topic of diaschisis was further elaborated in the following century (Feeney and Baron, 1986), mainly focusing on changes in excitability affecting the local excitatory-inhibitory (EI) balance of distant cortical networks. However, the measurable effects of stroke are not limited to the mesoscale of disruptions in EI balance, extending into large-scale cortical dynamics, such as functional interactions between distant regions. Therefore, extensions to the concept of diaschisis have been proposed in recent years, suggesting remote disruptions in functional connectivity as a relevant aspect of the process (Campo et al., 2012; Carrera and Tononi, 2014). With this recent expansion, attempting to bridge these two types of diaschisis emerging on different spatial scales is, therefore, a relevant issue, not only to better understand possible common physiological causes, but also to inform therapeutical strategies, thus improving post-stroke recovery. That said, in this review, we summarize the main findings related to diaschisis, both regarding functional connectivity (FC) and excitability, and link long-term changes in excitability to cortical plasticity mechanisms related to EI homeostasis, suggesting that the effects of these local processes extend beyond the scale of local EI balance regulation, into large-scale network dynamics. In addition, we summarize the recent advances in computational modeling of stroke, proposing modeling as a framework for the study of the concurrent evolution of FC and excitability in the post-stroke brain.

DIASCHISIS AND FUNCTIONAL CONNECTIVITY

A number of studies have elaborated on remote changes in functional connectivity, either at rest or task-related, following a stroke. FC quantifies the interaction or coupling between two chosen areas in the brain and is usually computed as the temporal correlation between their neural activity, although different methods (e.g., spectral coherence, transfer entropy) can be used depending on the nature of the signals (Friston, 2011). While studies on task-related FC have been performed on stroke patients (Gerloff et al., 2006; Westlake and Nagarajan, 2011), the use of resting state FC has some advantages, even though it does not provide specific information about the connectivity and activation of particular networks in the brain when subjects are engaged in behaviors of interest (Carter et al., 2012). Shortly, resting-state protocols have no requirements regarding patient function, thus allowing network analysis of patients with stronger impairments. Also, due to their unspecific nature, they allow a more global analysis of changes in connectivity, without the need for *a priori* assumptions about regions of interest. With that in mind, this section will focus on studies regarding resting-state FC changes in the post-stroke brain and how they relate to recovery (Carter et al., 2012).

Some of the first studies regarding changes in FC after stroke focused on changes in the connectivity strength between particular brain regions. Initial studies (He et al., 2007) showed an acute disruption in interhemispheric connectivity of the posterior intraparietal sulcus, part of the dorsal attention network, in patients with structural lesions involving the ventral attention network. The deficit correlated with spatial neglect and was normalized after 6 months, fitting the requirements of diaschisis (Carrera and Tononi, 2014). These findings were further confirmed in patients with an array of lesions in different regions (Carter et al., 2009; Baldassarre et al., 2014), showing an additional correlation between disrupted interhemispheric connectivity of the somatomotor network and motor. The authors emphasize these decreases in interhemispheric connectivity as predictive of behavioral deficit, as opposed to changes in intrahemispheric connectivity, which were less related to patient performance. However, a later study on post-stroke changes in the connectivity of the motor cortex (Park et al., 2011) showed that behavioral deficits could be explained not only by decreased interhemispheric connectivity but also by increases in its intrahemispheric counterpart. While research has focused on the motor and, to some extent, attention networks, changes are not confined to those particular systems. Indeed, it has been shown that, even in subcortical stroke patients, changes in connectivity are experienced at a brain-wide level, with a generalized increase in internal FC in a range of areas, from the visual to the dorsal attention networks (Wang et al., 2014). At the same time, decreases were found more particularly in the anterior default-mode and ventral attention networks. In this case, since measurements were taken more than 6 months after stroke onset, it is likely that these changes were not related to a direct effect of focal lesions, but instead the consequence of cortical reorganization. When looking at global metrics of functional connectivity and its changes, the biomarkers of inter and intrahemispheric connectivity are evident again. In the longitudinal study of Siegel et al. (2016), it becomes clear again that a general decrease in interhemispheric connectivity is observed during the subacute period in stroke patients, being gradually corrected across time. Importantly, a similar but opposite variation was detected for intrahemispheric connectivity, constituting, together with decreased interhemispheric connectivity, a strong biomarker of impairment (**Figure 1A**). Not only that, but the magnitudes of both changes correlated with each other, showing that they co-evolve and might be equally important in the process of recovery. While the authors indicate that visual and motor impairments were better predicted by lesion site, the two biomarkers provided a strong predictor of the recovery of higher-order functions, such as memory and language, which is not unexpected since these more integrative functions are thought to engage larger and more distributed networks (Goldman-Rakic, 1988; Mesulam, 1990). In a further paper regarding the low dimensionality of behavioral deficits in stroke patients, the authors hypothesized a matching low dimensionality in

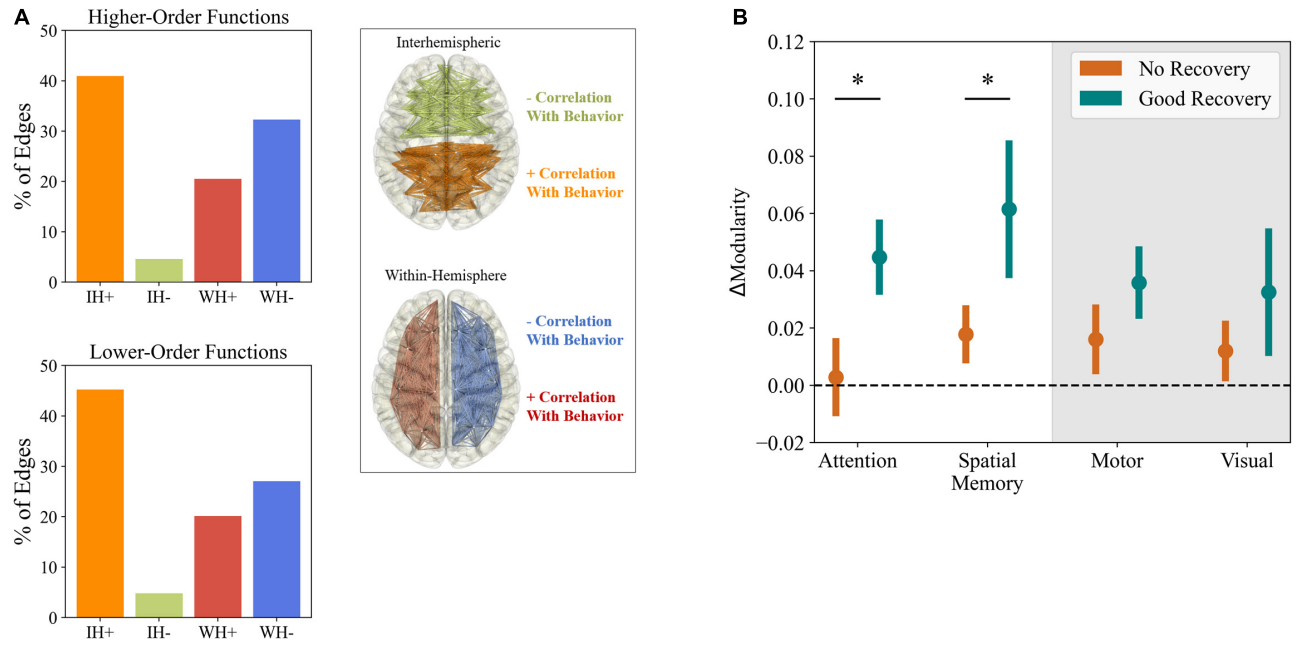

FIGURE 1 | Post-stroke changes in functional connectivity. **(A)** Predictive value of disruptions in functional connections for different behavioral deficits. The bar charts represent the percentage of connections, from the top 200 predicting behavior, belonging to each of the four groups described in the right (e.g., a percentage of 30% of IH+ means that increases in interhemispheric connectivity represent 30% of the 200 FC changes that best predict behavior). Notably, the strongest predictors of performance were increased interhemispheric connectivity and decreased intrahemispheric connectivity, both for higher (e.g., attention and working memory) and lower-order functions (e.g., motor and visual). Adapted from Siegel et al. (2016). **(B)** Correlation between changes in modularity and functional recovery. Patients with good behavioral recovery in higher-order functions, from attention to language, showed significantly higher changes in modularity than patients with poor recovery. The same pattern was not observed for motor and visual functions. ΔModularity represents the slope of a logarithmic fit to modularity at 2 weeks, 3 months, and 1 year. Adapted from Siegel et al. (2018). * Represents $p < 0.05$, from one-tailed unpaired *t*-test, after correction for multiple comparisons.

FC abnormalities, considering the two biomarkers of inter and intrahemispheric connectivity to be the strongest correlates of stroke-related deficits (Corbetta et al., 2018). However, as in less global metrics of functional connectivity, further research casts doubt into the role of intrahemispheric connectivity in stroke. A study using magneto encephalography (MEG) derived alpha-band connectivity (Westlake et al., 2012) showed increased intrahemispheric connectivity in the lesioned hemisphere, which was associated with better motor recovery, thus contradicting previous results (Siegel et al., 2016). Nonetheless, connectivity in the alpha band (8–12 Hz) may be reflective of different neurological processes that functional magnetic resonance imaging (fMRI) resting-state FC, which instead relies on much slower signals, in the order of 0.1 Hz (Cabral et al., 2011; Magri et al., 2012).

The study of post-stroke FC is, however, not limited to changes in the magnitude of connectivity between regions, and several examples can be found where more complex graph properties of functional networks have been related to stroke deficits and progression. One of the first examples is the work of Achard et al. (2006). By looking at the effects of progressive removal of nodes in an fMRI-derived FC graph, they showed that human functional networks were characterized by a small-world topology (Bassett and Bullmore, 2006) and were more resilient to progressive node removal than equivalent random and scale-free networks regarding the preservation of graph properties. While not particularly targeted at stroke, the work of Achard et al. (2006) already hinted at some of the later measured effects of local lesions in the graph properties of human FC. Indeed, in a subsequent study (Sporns et al., 2007), by analyzing data from cat and macaque cortical networks, it was found that removing structural connector hubs (nodes that connect different modules in the cortical network) leads to an increase in the small-world index of functional networks. This was explained by an increased path-length and clustering coefficient, indicative of segregation between areas in the analyzed cortical networks (Rubinov and Sporns, 2010). Further research has then confirmed the stronger effects of lesioning connector hubs, as opposed to lesions in sub-network hubs, by measuring the integrity of functional network organization (Gratton et al., 2012). One of the most common effects of stroke in human functional networks is an increase in segregation between areas in the brain (Sporns et al., 2007). This effect is evident not only by changes in metrics of segregation such as clustering coefficients, but also in measures of integration, as quantified by decreased local (Philips et al., 2017) and global (Philips et al., 2017; Zhang et al., 2017) efficiency or increased shorter path lengths (Zhang et al., 2017) in stroke patients. Interestingly, it might be the case that the effects on the graph properties of FC are more complex and involve changes in segregation and integration that are network specific. In that regard, measurements of modularity provide useful insights. Modularity measures the balance between the

degree of integration within and segregation between functional networks (Siegel et al., 2016). In a longitudinal study of stroke patients (Siegel et al., 2018), it was found that modularity was significantly reduced in the acute period, being partially recovered after 3 and 12 months. As in previous results (Siegel et al., 2016), these FC changes were more correlated to higher-order functions such as memory and language, pointing toward the importance of global network integrity for their performance and justifying a particular vulnerability of more integrated functions to widespread damage, as opposed to sensory functions which engage more peripheral areas of cortical functional networks (**Figure 1B**). Further studies expanded on the use of modularity as a post-stroke biomarker and researchers were able to explain its reduction by connecting it to lesions in connector hubs, as opposed to provincial hubs (Gratton et al., 2012) and, more recently, to structural disconnection, representing damage to white matter tracts connecting regions (Griffis et al., 2019). That considered, the evidence seems to indicate that decreasing segregation in functional networks to pre-lesion levels would be beneficial for patient recovery. Indeed, Wang et al. (2010), when looking at longitudinal fMRI from the motor execution network of stroke patients, found a negative correlation between clustering coefficients and recovery of motor function. In addition, a positive correlation with recovery was found for betweenness centrality, which quantifies the importance of individual nodes in the flow of information in the network.

While most of the discussed changes pertain to cortico-cortical networks, given the scope of this review, the effects of stroke in functional connectivity do extend to the realm of cortico-subcortical interactions. An example of such is the aforementioned effect of subcortical lesions, which have been shown to impact cortical connectivity in a widespread manner (Wang et al., 2010, 2014; Siegel et al., 2016; Zhang et al., 2017), although not as strongly as cortical lesions (Philips et al., 2017). Another example is the effect of stroke in cortico-subcortical connectivity, leading to longitudinal changes in connectivity between cerebellum, thalamus and motor areas (Wang et al., 2010), which were found to correlate with motor recovery (Park et al., 2011). That said, although cortico-subcortical interactions might be of relevance, since a significant number of lesions are experienced in subcortical regions (Corbetta et al., 2018), we focus on cortical networks, not only because they are equally impacted by subcortical lesions, but also due to the fact that the further discussed EI homeostasis mechanisms mostly play out in the cortex (Turrigiano, 2011). Therefore, while EI homeostasis may contribute to the recovery of connectivity between cortical regions after a stroke, its role regarding subcortical regions is not so clear.

In the face of the evidence toward widespread reorganization of cortical functional networks in the post-stroke cortex and its importance for the functional recovery of patients, underlying essential cognitive and motor adaptation, a fundamental question is then: how are these processes orchestrated globally through the cortex, given the localized nature of lesions? To answer that question, we propose that the fundamental tendency of neocortical networks to balance excitation and inhibition is a key participant in this effect. Since long-range projections in the human cortex are almost exclusively excitatory (Felleman and Van Essen, 1991; Tremblay et al., 2016), stroke lesions lead to an acute loss of excitation to distant areas, as encompassed by the original definition of diaschisis (von Monakow, 1914). Therefore, we hypothesize that this disruption will trigger the action of slow homeostatic plasticity mechanisms that adjust local synaptic weights to maintain balance, leading to changes in excitability and dynamics that in turn propagate throughout the brain. These widespread adaptations would then impact functional interactions between areas, participating in the recovery of the FC biomarkers mentioned in this section and in the appearance of new functional connections. Therefore, in the following sections, we summarize the findings regarding longitudinal and long-lasting changes in excitability in the post-stroke cortex. In addition, we highlight relevant findings showing EI balance as a fundamental property of cortical networks and the homeostatic plasticity mechanisms that actively work toward maintaining this equilibrium, emphasizing the correspondence between these processes and post-stroke variations in excitability.

DIASCHISIS AND EXCITABILITY

Due to the relative triviality of the concept of EI balance, it is not unreasonable to believe that anomalies to its normal function can be associated with pathologies such as stroke. To that effect, a parallel can be drawn between stroke and sensory deprivation studies (Hengen et al., 2013; Ma et al., 2019). Since most long-range connections in the cortex are excitatory (Felleman and Van Essen, 1991; Tremblay et al., 2016), the focal lesions experienced during a stroke effectively lead to a loss of excitation to regions that receive afferent terminals from the lesioned area, as encompassed by the original definition of diaschisis (von Monakow, 1914). Therefore, it is not far-fetched to think that these regions would experience EI balance changes similar to those described in sensory deprivation studies.

In fact, there have been plenty of studies on changes in excitability experienced in the brain following a stroke (Murphy and Corbett, 2009; Carmichael, 2012). Neumann-Haefelin et al. (1995) first measured an increase in excitability in the peri-infarct cortex of rats, 7 days after induced ischemic lesion. In similar rodent studies, it was subsequently shown that hyper-excitability persisted in the cortex of ischemic rats for several months post-lesion (Luhmann et al., 1995), although other studies suggest it peaks in the first weeks post-lesion (Schiene et al., 1996). Furthermore, and while the initial study of Neumann-Haefelin et al. (1995) focused on perilesional areas (in the vicinity of an ischemic lesion), a subsequent study in rodents used a paired-pulse stimulation protocol to demonstrate that measurable changes extend to the contralesional cortex (Buchkremer-Ratzmann and Witte, 1997), indicating the presence of diaschisis. Later research in human stroke patients found a similar increase in cortical excitability of areas distant from the lesion, when compared to healthy controls (Butefisch, 2003). Importantly, such changes in excitability correlated positively with patient motor recovery, suggesting regulation of EI balance as a part

of the process of functional recovery (Butefisch, 2003). Given the evidence supporting changes in the excitability of the post-stroke cortex, it is essential to understand the specific plastic process underlying such changes (Murphy and Corbett, 2009; Carmichael, 2012). A first candidate would be the regulation of excitatory signaling in post-synaptic pyramidal neurons. Indeed, research has shown it to be a possibility, manifested through prolonged excitatory postsynaptic potentials (EPSPs) mediated by N-methyl-D-aspartate (NMDA) receptors (Luhmann et al., 1995). When looking at receptor density instead, researchers found a gradual upregulation of NMDA receptors across the cortex of rats, lasting at least until 30 days post-lesion (Qü et al., 1999). In opposition to the idea of widespread increased excitability, a later study found no significant differences in the densities of both inhibitory γ-aminobutyric acid (GABA) and excitatory glutamate receptors in the cortex, apart from the perilesional area (Jolkkonen et al., 2003). Nonetheless, the same study showed a positive correlation between the contralesional number of binding sites for α-amino-3-hydroxy-5-methyl-4-isoxazolepropionic acid (AMPA), a glutamatergic receptor, and motor recovery after 25 days, suggesting a role of distant changes in excitability to the recovery process. Furthermore, Neumann-Haefelin and Witte (2000) showed a decreased amplitude of EPSPs in both ipsi and contralesional cortex, which would seemingly contradict the previously mentioned reports. However, the same researchers found a simultaneous downregulation of inhibitory synaptic transmission, which might compensate for the decrease in EPSP amplitude. In fact, changes in inhibitory signaling across the cortex seem to be even more involved in the post-stroke regulation of excitability than changes in excitatory transmission. Decreased inhibitory post-synaptic potentials (IPSPs) have been observed in rodent models of stroke (Luhmann et al., 1995) and found to also extend to regions in the contralesional cortex (Buchkremer-Ratzmann and Witte, 1997). Decreased inhibition was further measured in the affected hemisphere of stroke patients (Blicher et al., 2009), suggesting that this is not a detrimental effect, but part of the process of recovery, in accordance with subsequent results showing a positive correlation between decreased inhibition in the cortex of stroke patients and improved performance (Huynh et al., 2016). Such downregulation of inhibition has been mainly tied to changes in the density of GABAergic receptors. This decrease has been found across the brain already in the first-week post-stroke (Qü et al., 1998), remaining for several weeks post-lesion (Schiene et al., 1996; Redecker et al., 2002). Later, researchers have measured the availability of GABAa receptors in the cortex of stroke patients and found a similar longitudinal decrease 3 months after stroke (Kim et al., 2014). More importantly, the magnitude of this decrease correlated with the recovery of motor function (**Figure 2**). Conversely, changes in the number and structure of inhibitory neurons are not so clearly understood. While earlier studies found no structural changes in at least parvalbumin-positive interneurons (Luhmann et al., 1995), later results indicated a decrease in the number of both parvalbumin and somatostatin positive interneurons, visible at 30 days post-lesion (Alia et al., 2016). Nonetheless, it is clear that decreased inhibitory signaling across the brain is not only an essential

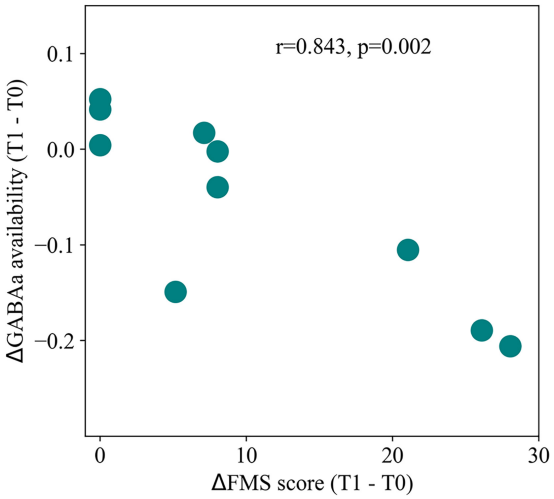

FIGURE 2 | Post-stroke changes in inhibitory signaling. Correlation between motor recovery, quantified through Fugl-Meyer scores (FMS), and changes in GABAa receptor availability in the contralesional cortex, measured with positron emission tomography. Decreases in receptor availability were strongly correlated with improved motor function, illustrating the importance of increasing excitability through plasticity of inhibitory synapses for functional recovery. T0 and T1 represent 1 and 3 months post-stroke, respectively. Adapted from Kim et al. (2014).

part of the observed changes in excitability following focal lesions, but also pivotal to the process of recovery. With all the evidence pointing toward the importance of the regulation of cortical excitability in stroke recovery, it is reasonable to assume that procedures aimed at manipulating the EI balance across the cortex can be applied to improve the behavioral outcomes of stroke patients. One of the possibilities is pharmacological manipulation. Some studies in this regard have focused on treatments that target, in particular, the increase in tonic inhibition in the acute period after stroke (Clarkson et al., 2010; Lake et al., 2015). While reducing tonic (or extrasynaptic) inhibition in the first days after stroke proved beneficial for recovery, it is also essential to focus on the potentiation of the processes previously mentioned in this section, which are more related to long-term changes in phasic inhibition. In that regard, it has been shown that reducing GABAa mediated transmission has prolonged effects, improving recovery up to 3 weeks after treatment (Alia et al., 2016). Pharmacological potentiation of AMPA receptors, in turn, has proved detrimental when applied at early stages, while a later application improved recovery, further supporting the delayed, long-term effect of these changes in excitability (Clarkson et al., 2011). Neuromodulation provides another option (Hummel and Cohen, 2006), and non-invasive techniques such as transcranial direct current (tDCS) and magnetic stimulation (TMS), aimed at increasing cortical excitability have been used to improve recovery in stroke patients (Blicher et al., 2009; Romero Lauro et al., 2014). An example of such techniques is theta burst stimulation (TBS) (Huang et al., 2005), based on the application of high frequency bursts of magnetic stimulation at intervals consistent with theta

frequencies (i.e., ∼200 ms). The application of TBS has proved beneficial for the clinical recovery of stroke patients (Ackerley et al., 2010), particularly by enhancing motor learning when paired with other rehabilitation procedures (Meehan et al., 2011). Not only that, but TBS is thought to potentiate cortical excitability (Huang et al., 2005) and, when applied to stroke rehabilitation, can be used to stimulate increases in excitability of the ipsilesional cortex that relate to clinical recovery (Di Lazzaro et al., 2008; Ackerley et al., 2010; Boddington et al., 2020), although the specific contribution of each particular area (e.g., somatosensory and motor cortices) to motor recovery is not yet fully understood (Meehan et al., 2011). Interestingly, recent results suggest that TBS further acts on functional connectivity, contributing to the recovery of important properties such as interhemispheric connectivity and global efficiency (Ding et al., 2021). Taking that into consideration, it is reasonable to believe that mesoscale excitability and large-scale connectivity are synergetic processes and can be simultaneously modulated by the same techniques, fitting the hypothesis that EI homeostasis is an underlying driver of cortical reorganization.

On another note, concerns may be raised regarding possible incompatibilities between the results on cortical reorganization, mostly derived from resting-state imaging data from humans, and the bulk of research on post-stroke changes in excitability, which is performed in rodents. The latter is addressed in some of the studies in human data mentioned previously (Butefisch, 2003; Blicher et al., 2009; Kim et al., 2014; Huynh et al., 2016), where results in humans generally follow the ones obtained in rodent studies. In addition, recent results have shown that, with respect to FC, the changes observed after a stroke are comparable across species (Hall et al., 2021), further supporting the translation of findings from rodents to humans. Having established the current knowledge on the longitudinal changes in excitability that contribute to recovery from stroke, it is essential to understand the phenomena underlying these changes. In the next sections, we then discuss the importance of EI balance in cortical networks, given their circuit organization, and how it is maintained at a neuronal level by synaptic plasticity mechanisms.

EXCITATORY-INHIBITORY BALANCE IN THE CORTEX

The cerebral cortex is the outer layer of neural tissue of the cerebrum of vertebrates, representing close to two-thirds of its volume. Cortical functions range from the integration of sensory information to higher cognitive functions such as attention, memory and consciousness (Kanwisher, 2010; Yeo and Eickhoff, 2016). The gross neuronal organization of cortical areas in the human brain is well known, comprising around 80% of excitatory neurons and 20% of inhibitory interneurons (Markram et al., 2004; Tremblay et al., 2016). Excitatory neurons are thought to be primarily responsible for coding and communicating messages across the cortex, since long-range cortical connections are almost exclusively excitatory (Felleman and Van Essen, 1991; Tremblay et al., 2016). In contrast, inhibitory interneurons form local and densely interconnected networks (Fino and Yuste, 2011; Tremblay et al., 2016). Altogether, these connectivity patterns lead to single pyramidal neurons in the cortex receiving thousands of excitatory and inhibitory inputs from other neurons. In fact, early studies attempting to define the canonical cortical microcircuit in a layer-specific manner (Douglas et al., 1989) already hinted at the fact that excitatory and inhibitory activity are not independent phenomena, but arise in a synergetic manner. At a relatively simplified level, the interplay between excitatory and inhibitory inputs unto pyramidal neurons and, in particular, their specific temporal patterns, causes postsynaptic neurons to fire action potentials when excitation surpasses inhibition sufficiently to reach the firing threshold. To add a level of complexity to the microcircuit organization of cortical networks, cortical areas connect to each other through long-rage excitatory white matter projections, the organization of which is far from random. Research shows that cortical networks organize in a small-world manner (Achard et al., 2006; Bassett and Bullmore, 2006), being highly clustered, while maintaining relatively short paths between their elements. In this architecture, a small number of highly interconnected areas serve as hubs of communication across the cortex, for which reason cortical connectivity is sometimes referred to as a rich-club (van den Heuvel and Sporns, 2011). In addition, tracing data from the macaque cortex (Markov et al., 2013), which gives information not only about strength, but also directionality of connectivity, suggests that the cortex organizes in a bow-tie manner, with a densely connected core sitting in the middle of the stream of information in the cortical hierarchy. In any case, it is relevant to consider that cortical areas receive varied levels of incoming excitation due to these differences in connectivity. While the initial canonical view of Douglas et al. (1989) states that most of the excitation received by pyramidal neurons is from local recurrent connections, the stipulated architectural differences in connectivity, and thus in incoming excitation, are still meaningful. Because the function of not only individual neurons, but also local neuronal networks in the cortex, is susceptible to imbalances in the excitatory and inhibitory inputs, it is then relevant to study how these inputs are balanced across the cortex. In their seminal 1996 work, van Vreeswijk and Sompolinsky (1996) demonstrated that a state of EI balance emerged spontaneously in artificial networks of coupled excitatory and inhibitory neurons, when connections were sparse and strong. Importantly, in such networks, the activity of individual neurons was dependent on random fluctuations in these inputs and consistent with the irregular activity empirically observed in cortical neurons. In the past 20 years, further modeling studies have stressed the importance of EI balance to realize specific computational principles of cortical networks. In particular, balanced networks of excitatory and inhibitory neurons ensure stochastic fluctuations in synaptic drive, which reproduce the irregular firing patterns observed *in vivo* and impact how neurons react to external noise, rendering them more sensitive to correlated input (Salinas and Sejnowski, 2000). In addition, it has been shown that appropriate EI balance at a neuronal level, in recurrent networks, simultaneously leads to increased robustness to input and output noise (Rubin et al., 2017). Furthermore, it has also been postulated that

a possible solution for the correct transmission of rate-coded information through layers in feedforward networks would be to have balanced feedback inhibition (Litvak et al., 2003), in accordance with the principles initially explored by van Vreeswijk and Sompolinsky (1996). Nonetheless, studies regarding the role of EI balance in cortical function have not been limited to the computational realm. Research in the auditory (Wehr and Zador, 2003; Froemke et al., 2007), barrel (Okun and Lampl, 2008), and visual (Mariño et al., 2005; Xue et al., 2014) cortices shows that the inhibitory input to pyramidal neurons tightly matches excitation and suggests that this property contributes not only to avoid runaway activity, but also to a sharper tuning of neurons to external stimuli. Critically, this state of balanced excitation and inhibition arises during neural development, in parallel to characteristics such as the aforementioned sensory co-tuning, in both the auditory (Dorrn et al., 2010) and visual cortices (Tao and Poo, 2005). In addition, the maintenance of EI balance is likely not limited to the sensory realm, being crucial for higher brain functions such as memory, by helping maintain stable activity and avoiding interference during learning of new memory traces (Vogels et al., 2011; Litwin-Kumar and Doiron, 2014). Furthermore, the maintenance of EI balance has been observed to occur across cortical states, such as sleep-wake cycles (Hengen et al., 2013) and quiescence vs. active locomotion (Zhou et al., 2014), although recent studies seem to indicate a more complex picture of differential points of balance being maintained in sleep and wake states (Bridi et al., 2020). Interestingly, in electrophysiological data from both human and monkey cortex, Dehghani et al. (2016) found a co-fluctuation of excitatory and inhibitory signals which is not only maintained through different stages of the sleep-wake cycle, but also present when looking at the detain a wide range of timescales. To further add to the importance of EI balance in cortical networks, a number of disorders such as epilepsy (Kullmann et al., 2012; Dehghani et al., 2016) schizophrenia (Kehrer et al., 2008; Kullmann et al., 2012), depression (Concerto et al., 2013; Page and Coutellier, 2019), anxiety (Page and Coutellier, 2019), chronic stress (Page and Coutellier, 2019), Alzheimer's disease (Vico Varela et al., 2019; Kazim et al., 2021), and autism spectrum disorders (Nelson and Valakh, 2015; Bruining et al., 2020), have been associated with alterations in cortical EI balance or excitability, supporting the idea that proper maintenance of this regime is crucial to ensure the correct function of the cortex.

All that considered, one should address the fact that the idea of a tight balance between excitation and inhibition seems to go against previous knowledge on the structure and function of cortical networks. Firstly, there is evidence that inhibitory interneurons form dense and largely unspecific networks on a local scale (Fino and Yuste, 2011; Packer and Yuste, 2011), which, at least, rules out the hypothesis that matching excitation and inhibition in individual neurons emerges from precise structural properties of connectivity. In addition, even though the blueprint of cortical microcircuitry is relatively stereotypical across the brain (Markram et al., 2004; Tremblay et al., 2016), local heterogeneities in the number of neurons and the relative proportion of excitatory and inhibitory synapses (Wang, 2020) add an extra layer of complexity to a tight maintenance of balanced activity. However, either by showing that excitatory and inhibitory postsynaptic currents (Xue et al., 2014) or conductances (Mariño et al., 2005) are matched in magnitude in individual neurons, or that there exists a precise stimulus co-tuning of excitatory and inhibitory synapses in individual pyramidal neurons (Wehr and Zador, 2003; Froemke et al., 2007), the corpus of research mentioned previously seems to point toward a tightly maintained EI balance, at the very least in sensory areas. Furthermore, the early study of Vreeswijk and Sompolinsky assumed the existence of a random, homogeneous, and sparse connectivity, leading to a natural emergence of EI balance (van Vreeswijk and Sompolinsky, 1996). However, due to phenomena such as the formation of neuronal assemblies through Hebbian plasticity (Denève and Machens, 2016; Mackwood et al., 2021), cortical networks are seldomly homogeneous, challenging the applicability of Vreeswijk and Sompolinsky's principles. Not only that, but the locally dense nature of inhibitory connectivity in the cortex (Fino and Yuste, 2011; Packer and Yuste, 2011) renders the assumption that balanced networks need to be sparse for EI balance to emerge unrealistic. Conveniently, these drawbacks have been addressed recently. Firstly, it was shown that the conclusions would still hold in networks with dense connectivity, as long as synaptic weights scale with the numbers of connections (Barral and Reyes, 2016). Then, in recurrent networks with introduced inhomogeneities in incoming connectivity, it was demonstrated physiologically relevant patterns of activity could be achieved as long as excitatory and inhibitory in-degrees were matched in individual neurons (Landau et al., 2016).

Considering all the evidence, the importance of having balanced excitatory and inhibitory inputs at a neuronal level seems clear. However, the influence of this balance spreads beyond the cellular scale into the realm of network activity patterns. In that regard, another aspect of the human neural function where EI balance is considered to play a fundamental part is the concept of criticality. Criticality, as a theory, was borrowed from physics and it pertains to an operating point in systems of interacting units on the verge of transitioning between states (Beggs and Timme, 2012). Importantly, criticality stipulates a dependence of the transition between phases on a control parameter, which is often related to EI balance. By analyzing trademarks of criticality such as the size and duration distribution of neural avalanches in resting-state activity, researchers have been able to detect it ubiquitously in the mammalian brain. From the first study of spike data in the rat somatosensory cortex *in vitro* by Beggs and Plenz (2003), signatures of criticality have been detected in cortical slices (Friedman et al., 2012) and cultures (Pasquale et al., 2008), *in vivo* data from the cortex of rats (Ma et al., 2019), cats (Hahn et al., 2017), and monkeys (Petermann et al., 2009; Hahn et al., 2017) and oscillatory data from human subjects (Poil et al., 2008; Bruining et al., 2020). This constant presence of criticality in brain systems suggests some degree of functional advantage. Indeed, the maintenance of activity near the critical transition point has been speculated to optimize crucial functional characteristics of neural networks such as dynamic range (Shew et al., 2009), information capacity

and transmission (Shew et al., 2011) and computational power (Beggs, 2008).

PLASTICITY MECHANISMS FOR EXCITATORY-INHIBITORY HOMEOSTASIS

Considering the evidence that EI balance is a pivotal characteristic of normal cortical activity, it is natural to question how it is maintained in the face of varying external inputs, changing behavioral states and different levels of incoming excitation due to the structural patterns of cortical connectivity (Bassett and Bullmore, 2006; van den Heuvel and Sporns, 2011; Markov et al., 2013). The logical assumption would then be that cortical neurons are equipped with plasticity mechanisms capable of maintaining a balance between excitatory and inhibitory incoming activity (Sprekeler, 2017). Indeed, homeostasis of EI balance has been a topic of study in the past years. Turrigiano et al. (1998) demonstrated that pyramidal neurons scale the amplitudes of excitatory postsynaptic currents when grown in cultures where either excitatory or inhibitory signaling was altered. This type of plasticity, likely occurring postsynaptically, was dubbed synaptic scaling. Operating at long timescales (hours to days in rodents) (Turrigiano, 2011), synaptic scaling facilitates the homeostatic maintenance of stable firing rates in pyramidal neurons without disrupting the fluctuations occurring in faster timescales essential for encoding and communicating information across the brain. In general, sensory deprivation studies have been the most common procedure to assess firing rate homeostasis *in vivo*. Commonly performed in rodents, sensory deprivation aims at disrupting the normal levels of excitation arriving at the primary visual cortex by interrupting connectivity from the retina. This is achieved mainly by suturing one of the eyelids (Maffei et al., 2004; Maffei and Turrigiano, 2008; Hengen et al., 2013; Ma et al., 2019), although retinal lesion (Keck et al., 2013) or inhibition of optic nerve firing (Maffei et al., 2004) have been applied to the same purpose. In all of the mentioned studies, neuronal firing rates in sensory cortices showed a decrease in activity, which was subsequently restored to baseline levels within a timescale of days (**Figure 3A**). A recent study further elucidated on these processes by showing that cortical networks *in vivo* depart from criticality after sensory deprivation and likely return to it through synaptic scaling, suggesting criticality as a possible homeostatic target in cortical networks, in parallel with stable firing rates (**Figure 3B**; Ma et al., 2019). The relevance of this work lies mainly in the fact that it provides a well-defined activity target regime for firing rate homeostasis, which goes toward the problem of conceptualizing and defining an optimal baseline firing rate that should be maintained to ensure proper cortical function.

While Turrigiano et al. (1998) and Turrigiano (2011) first hypothesized that synaptic scaling manifests mainly through postsynaptic changes in excitatory synapses, further research suggests that EI homeostasis may involve the regulation of inhibitory synapses unto pyramidal neurons or even their intrinsic excitability (Desai et al., 1999; Maffei and Turrigiano, 2008). However, the latter is not always observed (Maffei et al., 2004) and is thought to only come into play when scaling of synapses fails to compensate for perturbations (Turrigiano, 2011). As for inhibitory plasticity, the main arguments in favor of it being one of the main drivers of EI balance homeostasis lie in the fact that, in pyramidal neurons of developing sensory systems, the tuning curves of inhibitory postsynaptic currents evolve to match their excitatory counterparts closely (Dorrn et al., 2010) and change accordingly when the tuning of excitatory connections is altered (Wehr and Zador, 2003; Froemke et al., 2007). In addition, reducing excitability in layer II/III pyramidal neurons did not lead to changes in excitatory synapses, but to decreased inhibition from fast-spiking interneurons instead

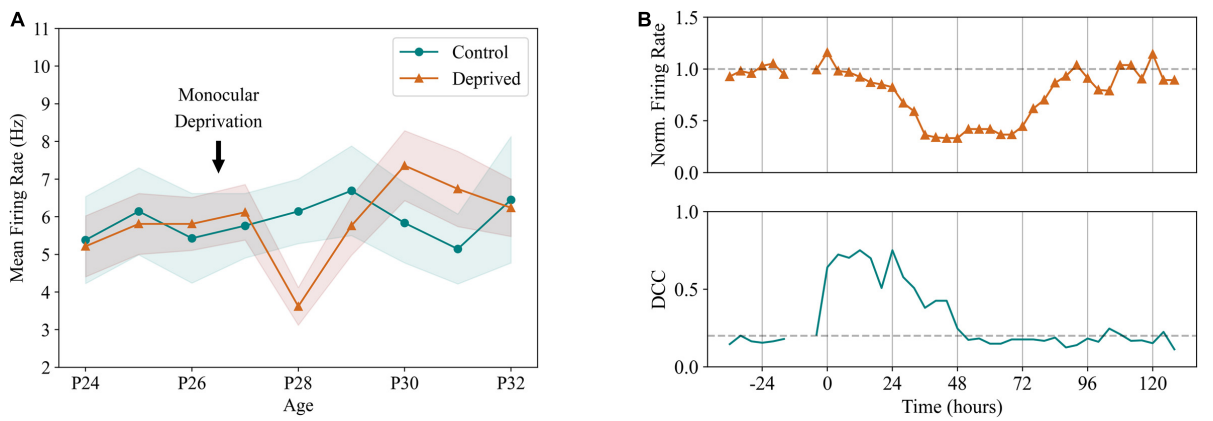

FIGURE 3 | Firing rate homeostasis in the cortex. **(A)** Homeostatic regulation of pyramidal neuron firing rates in a sensory deprivation protocol. In this experiment, unilateral deprivation of visual input was performed in rodents through lid suture, late at P26. Firing rates of the visual cortex in the deprived hemisphere show a significant reduction in the second day following suture, being recovered to pre-deprivation levels after 72 h, an effect not visible in the unaffected hemisphere. Adapted from Hengen et al. (2013). **(B)** After monocular deprivation, dynamics of the affected hemisphere show an immediate departure from criticality, quantified by increased distance from criticality coefficients (DCC). Criticality was recovered after 48 h through homeostatic plasticity, preceding the recovery of excitatory firing rates and indicating criticality as a setpoint for cortical dynamics. Adapted from Ma et al. (2019).

(Xue et al., 2014). More importantly, this effect was dependent on the activity of the postsynaptic target, fitting the characteristics of synaptic scaling. Studies in hippocampal pyramidal neurons seem to indicate an additional dependence of synaptic scaling of inhibitory synapses on presynaptic activity, as opposed to their excitatory counterparts, which only depend on post-synaptic activity (Turrigiano, 2011). Therefore, the pre and post-synaptic dependence of inhibitory synaptic scaling renders it more sensitive to changes in network activity, as opposed to excitatory synapses, which are thought to be scaled only accordingly to post-synaptic activity, in a cell-autonomous process. This, again, stresses the importance of inhibitory plasticity in the maintenance of EI balance at a network level. Accordingly, Vogels et al. (2011) derived a homeostatic inhibitory plasticity rule dependent on both pre and postsynaptic activity, aimed at maintaining postsynaptic firing at a defined target rate. In their study, this plasticity mechanism was sufficient to replicate a range of phenomena such as co-tuning of excitatory and inhibitory synapses, sparse responses and a return of balance and co-tuning after perturbation. In recurrent neural networks, a similar rule rendered dynamics robust to small perturbations, while still allowing for the formation and rearrangement of neural assemblies with sufficiently strong inputs (Litwin-Kumar and Doiron, 2014). Recently, a comparable form of synaptic plasticity was analytically derived in a recurrent neural network model (Mackwood et al., 2021), which simultaneously posed the hypothesis of similar processes happening in excitatory synapses unto inhibitory neurons. In fact, while most of the attention has been devoted to pyramidal neurons, studies have shown that changes in fast-spiking interneurons may also contribute to the maintenance of EI balance, either through regulation of intrinsic excitability or of incoming excitatory synapses (Kullmann et al., 2012).

All considered, it can be said that EI balance seems to be crucial to the function of cortical networks, that there are mechanisms in place to actively maintain this balance and that anomalies in the equilibrium are associated with a series of pathologies affecting a broad range of functions. That said, future studies should further focus on the hypothesis of criticality as a homeostatic target for cortical dynamics and how individual neurons capture departures from this regime and translate them into changes in synaptic dynamics or intrinsic excitability. In addition, attention should be devoted to the possibility of synaptic scaling mechanisms in cortical inhibitory interneurons playing an important role in regulating cortical dynamics, synergizing with similar processes in their excitatory counterparts.

TYING EXCITATORY-INHIBITORY HOMEOSTASIS AND FUNCTIONAL REORGANIZATION IN STROKE RECOVERY

The longer timescale of post-stroke changes in excitability and the occurrence of processes such as the up or downregulation of glutamatergic and GABAergic receptors (Luhmann et al., 1995; Qü et al., 1998, 1999; Neumann-Haefelin and Witte, 2000; Kim et al., 2014) suggests a connection between stroke and the homeostatic mechanisms of synaptic scaling (Turrigiano, 2011). Indeed, this possibility has been suggested before (Murphy and Corbett, 2009; Platz, 2021) and the current knowledge on EI homeostasis seems to fit the hypothesis that the general increase in excitability experienced in the post-stroke cortex might be a homeostatic response to a sudden loss of excitation from lesioned areas. A further possible connection to cortical reorganization can be made, given that FC has been previously tied to local excitability in both stroke patients (Volz et al., 2015) and healthy subjects (Nettekoven et al., 2015), offering a possible framework to tie the meso (local EI balance) and macro (global changes in network dynamics) scales of diaschisis. That said, we hypothesize that EI homeostasis, manifesting at a local level in cortical networks through mechanisms like synaptic scaling, is one of the main drivers of the process of recovery from diaschisis in the cortex of stroke patients. More importantly, the role of EI homeostasis is likely not limited to the adaptation of cortical regions to the loss of excitability experienced after a lesion in distant areas, but it may also be an important player in the process of cortical reorganization and recovery of FC properties relevant for recovery (Wang et al., 2010; Siegel et al., 2016, 2018; Griffis et al., 2019). This approach brings forward many interesting possibilities for exploration. First, an important concern that is rarely addressed by studies in excitability and stroke recovery is the putative side effects of compensatory changes in local EI balance. It is evident that proper EI balance is critical for the correct function of cortical networks (Beggs, 2008; Vogels et al., 2011; Xue et al., 2014; Rubin et al., 2017) and imbalances have been associated with several neural pathologies, some of which associated with stroke. A particular case is epilepsy (Kullmann et al., 2012; Dehghani et al., 2016) and, in a study with a rodent stroke model, it was demonstrated that, even though homeostatic reduction of tonic inhibition in the motor cortex proved to be beneficial to the recovery of motor function, it also raised the risk of suffering from epileptic seizures (Jaenisch et al., 2016). Such findings raise a concern about possible side effects coming from the recovery of cortical function, which is of particular importance, in this case, given that epilepsy is a common side-effect of stroke (Feyissa et al., 2019). While no similar studies have been performed in relation to the slow changes in phasic inhibition, it should not be out of the question that they might increase the propensity for the development of late-onset side effects related to EI balance, such as depression (Towfighi et al., 2017) in a patient-specific manner. That said, emphasis should be placed on relating recovery of FC and function to the appearance of side-effects of stroke that can be associated with EI imbalances, such as depression (Concerto et al., 2013; Towfighi et al., 2017; Page and Coutellier, 2019), fatigue (Kuppuswamy et al., 2015), chronic pain (Klit et al., 2011; Ratté and Prescott, 2016), and epilepsy (Feyissa et al., 2019).

Another particular direction of research is to investigate how targeted stimulation of particular areas in the brain might be used to tackle specific post-stroke deficits and how this effect ties to the regulation of local excitability through neuromodulation.

While approaches such as tDCS have been traditionally applied to modulate excitability, our hypothesis suggests that such neuromodulatory therapies may also be applied to stimulate cortical reorganization and the recovery of FC properties to healthy levels. Indeed, connectivity can also be modulated with neurostimulation techniques usually targeted at regulation of excitability (Grefkes and Fink, 2012). TBS has been shown to modulate both excitability (Ackerley et al., 2010; Boddington et al., 2020) and connectivity (Ding et al., 2021) in stroke patients and healthy controls (Nettekoven et al., 2014), although results in the latter showed that, even though both processes happen simultaneously, a correlation between them could not be found.

While it is well established that neuromodulation can be used to improve functional recovery in stroke patients (Blicher et al., 2009; Romero Lauro et al., 2014), we suggest that a deeper understanding of its effects not only in excitability, but also FC, is essential to unlocking the full potential of these rehabilitation procedures. In addition, the use of adaptive systems, such as the Rehabilitation Gaming System (RGS) (Cameirão et al., 2010), has been shown to engage widespread areas across the human cortex (Prochnow et al., 2013) and stimulate cortical reorganization of motor networks (Ballester et al., 2017), being a further potentiator of FC recovery. That said, we suggest an additional focus for future research on the synergy between the use of such adaptive rehabilitation procedures and neuromodulation techniques, in order to better potentiate beneficial changes in both excitability and connectivity.

Finally, it should not be out of the question that stroke is accompanied by impairments in EI homeostasis in the cortex. Data shows that the extent of changes in excitability correlates with recovery (Murphy and Corbett, 2009; Kim et al., 2014), suggesting that such impairments are likely to happen and impact the adaptive ability of the post-stroke brain. In this context, understanding the link between global changes in FC and local excitability would be a valuable contribution, by allowing the inference of localized disrupted homeostasis from global connectivity metrics extracted from non-invasive techniques such as fMRI. With this information, neuromodulation therapies could then be applied in a more targeted manner to areas with particularly impaired EI balance in a patient-specific manner. Again, we stress that the benefits of such individualized therapies would not be limited to excitability, likely extend toward a better recovery of functional connectivity.

That considered, it is first and foremost essential to address the relationship between post-stroke changes in excitability and cortical reorganization (summarized in **Figure 4**), scanning for putative causal relations between both phenomena, possible impairments in EI homeostatic mechanisms such as synaptic scaling (Turrigiano, 2011) and their further suitability as a target for post-stroke rehabilitation procedures addressing excitability and connectivity concurrently. However, studying both aspects of cortical function simultaneously and with the needed level of detail might be a difficult endeavor when analyzing human imaging or electrophysiological data. This is due to the different scales of both processes, which would require the use of different imaging or recording modalities or advanced techniques of inferring excitability from techniques such as fMRI. This is where large-scale computational modeling becomes a useful framework for studying the evolution of whole-brain dynamics after disruptive events. In the next section, the state of the art of large-scale modeling will be described, particularly in the topics of EI homeostasis and the evolution of cortical networks in reaction to stroke/localized lesions.

LARGE SCALE MODELING OF THE HUMAN CORTEX: EXCITATORY-INHIBITORY BALANCE AND STROKE

Computational modeling is a powerful tool for the exploration of neural dynamics, allowing for a more direct analysis and easier parameter manipulation than physiological studies. One can achieve this by applying mathematic concepts to the description of neural dynamics at different scales, from the molecular and synaptic level to the modeling of large-scale activity. The latter relies on the assumption that the activities of individual neurons are generally uncorrelated, meaning that the ensemble activity can be reduced to its mean and variance (Breakspear, 2017). This mean-field approach can be extremely useful in computational neuroscience, allowing for the modeling of large-scale dynamics at a higher level of abstraction, which is more computationally tractable. Since the model of interacting excitatory and inhibitory populations derived by Wilson and Cowan (1972), different mean-field models have been derived and applied in the study of large-scale dynamics of the cortex (see Breakspear, 2017 for a detailed review). While neural mass models can accurately describe, with some level of abstraction, the behavior of local cortical populations of interacting excitatory and inhibitory populations at a mesoscale, large-scale cortical dynamics require a further level of complexity. To bridge the gap between scales, one can look at the cortex as a network of connected local neural masses. In that regard, great progress is due to the advent of Connectomics, coined by Sporns et al. (2005) to describe the anatomical connections between regions in the human brain. While large scale connectivity has been a topic of exploration in primates already since the nineties (Felleman and Van Essen, 1991), human Connectomics have been a particular field of interest in the past 15 years, after the consolidation of the standard approach to human brain mapping by unraveling the structural core of the human cortex using diffusion spectrum imaging (Hagmann et al., 2007, 2008). This step allowed for the investigation of the graph properties of the human cortex, finding relations between structural connectivity (SC) and FC (Sporns, 2011; Thomas Yeo et al., 2011; Goñi et al., 2014). Honey et al. (2007) showed that simple mean-field models constrained by macaque SC data could reproduce features of empirically measured resting-state FC. Later, through a similar approach, the same researchers demonstrated, with a higher resolution human connectome, how SC shaped large-scale dynamics and can inform properties of FC (Honey et al., 2009). Since then, several whole-brain modeling studies have contributed to our knowledge about how model parameters influence large-scale dynamics

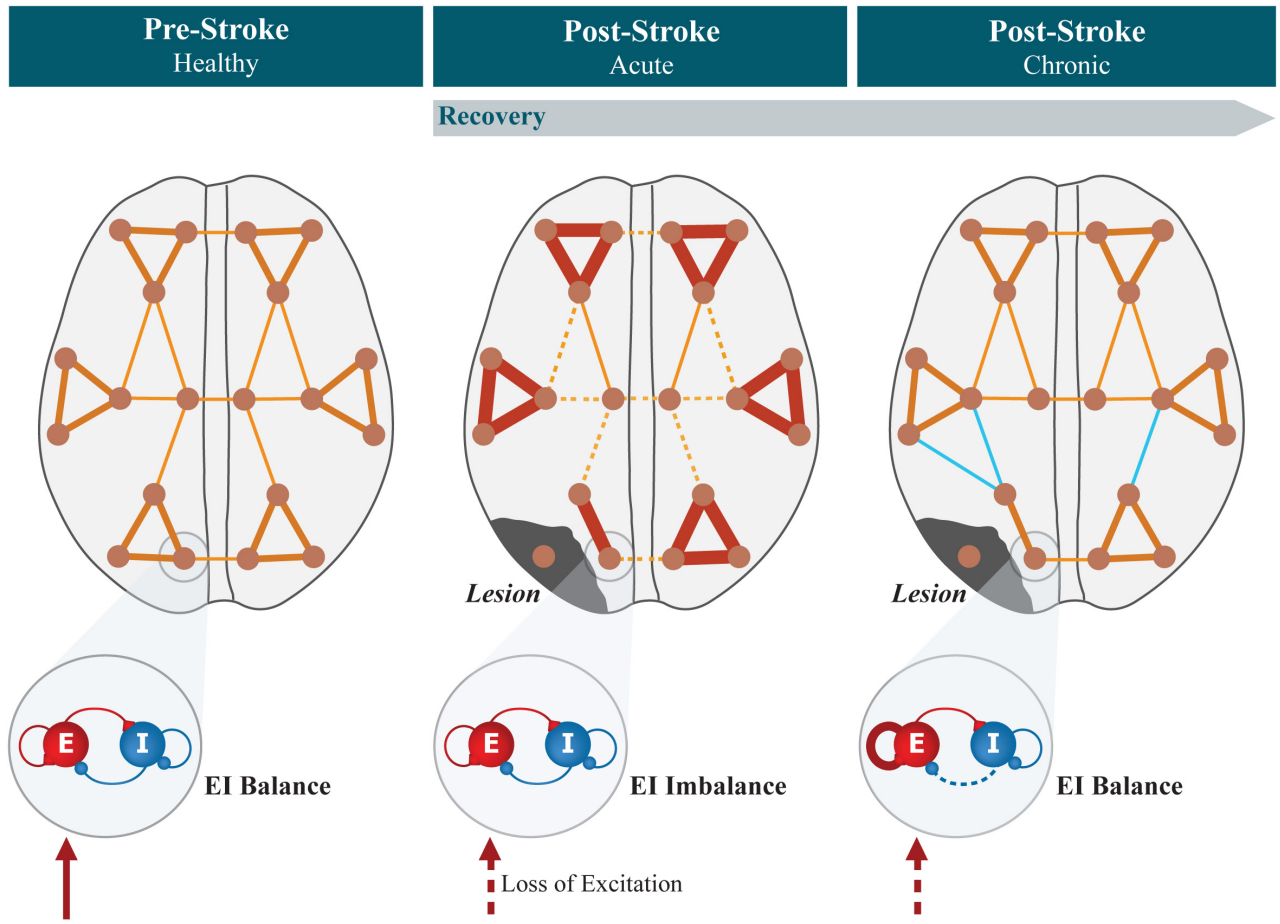

FIGURE 4 | Summary of the evolution of connectivity and local EI balance in cortical networks after stroke. In the healthy brain, functional networks show a modular structure, with strongly connected regions forming modules, connected by functional hubs. Excitatory and inhibitory synapses are regulated locally by EI homeostasis so that balance is maintained, accounting for the level of excitation received from external sources and keeping neuronal firing rates stable. Focal lesions experienced by stroke patients lead to neural tissue necrosis in confined areas. In the acute period after lesion, the modular organization of functional networks is disrupted, showing increased segregation between modules, together with decreased interhemispheric and increased intrahemispheric connectivity. Simultaneously, areas that previously received white matter projections from the lesioned region experience a sudden reduction in the levels of external excitation, causing a local imbalance in excitatory and inhibitory activity. During the process of recovery, synaptic plasticity compensates for the reduced excitation by increasing/decreasing the strength of excitatory/inhibitory synapses unto pyramidal neurons, increasing their excitability to restore local EI balance. Concurrently, functional connectivity changes toward pre-lesion levels, either through the recovery of healthy functional networks or *via* cortical reorganization and the formation of new functional pathways (represented in light blue).

(Deco et al., 2009), how clusters of regions in the human cortex synchronize and interact to form large-scale networks (Cabral et al., 2011) and how these interactions underlie certain cognitive functions and processes (Thomas Yeo et al., 2011).

Moreover, EI balance has also been in the scope of research in whole-brain modeling. The reliance of approaches such as the Wilson-Cowan model on interacting excitatory and inhibitory populations, with a relatively simple parameter space, provides a highly controllable and measurable framework to study the effects of EI balance manipulations. Deco et al. (2014) conducted one of the first large-scale modeling studies to investigate how changes in local EI dynamics impact global properties of cortical networks. By applying a regulatory mechanism on local feedback inhibition aimed at maintaining excitatory firing rates stable (similar to synaptic scaling; Turrigiano, 2011; Vogels et al., 2011) they demonstrated that models with self-maintained local EI balance better predicted empirical FC for a wider range of parameters and showed improved information capacity. Later, Hellyer et al. (2016) adapted the inhibitory mechanism proposed by Vogels et al. (2011) into a large-scale model of the human cortex. In this model, the parameters of local populations were such that, depending on the input levels, the dynamics experienced a Hopf bifurcation, transitioning from a state of irregular, noise-driven low activity, to an oscillatory one. When using this transition point as a homeostatic target for inhibitory plasticity, models achieved a better fit to empirical FC and maintained criticality across the cortex. Furthermore, it was shown that local inhibition strength was correlated with graph properties of the connectome, further emphasizing how local and global properties interact to shape cortical

activity. More importantly, by exploring the homeostatic firing rate target, the authors emphasize the importance of poising local activity near the critical Hopf bifurcation, stressing the relationship between EI balance, criticality and cortical function (Ma et al., 2019). Building on these foundations, further research demonstrated that the same homeostatic mechanisms rendered cortical networks more robust to changes in parameters such as transduction delays and global coupling strength (Abeysuriya et al., 2018). Interestingly, in a recent study, using an updated model of coupled excitatory and inhibitory populations with a term that quantifies the concentration of excitatory and inhibitory neurotransmitters at a local level, it was found that there are optimal concentrations of glutamate and GABA that maximize fit of simulated and empirical FC (Naskar et al., 2021). Not only that, but these suggested optimal concentrations also corresponded to a working point of activity where the brain is in a state of heightened metastability. Importantly, by changing the concentration of neurotransmitters to simulate epilepsy conditions, they could reproduce findings regarding the segregation and integration of FC graphs. In this case, epilepsy was used as a use case, but similar measures have been applied in stroke (Honey et al., 2007; Philips et al., 2017; Zhang et al., 2017; Siegel et al., 2018), which points toward the utility of applying such models to study brain pathologies in general. Furthermore, the regional heterogeneities in cortical microcircuitry (Wang, 2020) have also been brought to the field of computational modeling (Deco et al., 2021). By varying the excitability of networks nodes according to physiological constraints, it was shown that the system was able to reproduce phenomena like ignition dynamics and a hierarchy of intrinsic timescales (Wang, 2020), while maintaining the similarity between simulated and empirical resting-state FC. While this perspective might first seem at odds with the previous works of Hellyer et al. (2016) and Abeysuriya et al. (2018), which consider local cortical regions to regulate toward the same setpoint of criticality across the brain, the model in question also included a mechanism akin to synaptic scaling to maintain the firing rate of populations clamped at a physiologically realistic level, as in previous work (Deco et al., 2014). This model hints at the possibility of reconciling the maintenance of cortical activity at criticality (Ma et al., 2019), while simultaneously allowing for functional specialization (Mashour et al., 2020). Nonetheless, it did not capture particular aspects of ignition dynamics, such as higher-order areas (e.g., prefrontal cortex) maintaining self-sustained activity after stimulus termination (Mashour et al., 2020), which remain to be investigated. Therefore, further studies should elaborate on how homeostatic plasticity acts in the face of structural heterogeneities, the possibility of different local targets for EI balance and possible regulation through neurotransmitters. In addition, importance should be given to reconciling the hypothesis of criticality as an optimal working point across the cortex and the functional specialization of specific cortical areas, particularly higher-order ones.

Whole-brain modeling has also proved useful in a more applied context, in neurological disorders such as epilepsy (Jirsa et al., 2017), Alzheimer's (Stefanovski et al., 2019) and Parkinson's disease (Saenger et al., 2017), and respective exploration of therapeutical procedures (Deco and Kringelbach, 2014). This has also been the case for the effects of local lesions and stroke, in particular. While earlier studies had already assessed the effect of node removal when analyzing brain functional networks (Achard et al., 2006) and structural (Sporns et al., 2007; Gratton et al., 2012) networks, Honey and Sporns first modeled the effect of localized lesions in a whole-brain model of the macaque cortex (Honey and Sporns, 2008). In their study, lesions to structural hubs of the connectome lead to larger changes in system dynamics, spread beyond the vicinity of lesions, akin to the phenomenon of diaschisis (Carrera and Tononi, 2014). Subsequent studies in the human connectome (Alstott et al., 2009) further elaborated on which networks are more vulnerable to damage and how the graph properties of SC can help predict the effects of targeted lesions. In addition, further research has delved into how localized lesions affect network graph properties (Cabral et al., 2012; Joyce et al., 2013). Nonetheless, research in this field has not been confined to studies of the effect of lesions in networks obtained from healthy controls. In a subsequent modeling study (Falcon et al., 2016), large-scale models were constrained with DTI data from stroke patients and healthy volunteers to evaluate the fit to empirical FC by changing parameters such as global coupling, conduction delays and local EI coupling. The authors found that stroke patients had, among other features, reduced inhibitory to excitatory coupling compared to healthy controls, similarly to previous results (Kim et al., 2014) and in line with the hypothesis of synaptic scaling of inhibitory synapses (Turrigiano, 2011; Vogels et al., 2011; Hellyer et al., 2016; Abeysuriya et al., 2018). While the decreased inhibition did not correlate with motor performance, the coupling from excitatory to inhibitory neurons showed a negative correlation, which is still in line with the hypothesis of increased excitability. This latter effect is due to decreased excitation to interneurons, translating into weaker feedback inhibition. While evidence toward synaptic scaling of E to I synapses is not so clear (Kullmann et al., 2012), it might also occur as a mechanism of EI homeostasis (Turrigiano, 2011), having, therefore, a possible role in stroke recovery deserving further investigation. On another note, Adhikari et al. (2017) used an algorithm to adjust modeled structural connectivity to optimize the fitting between empirical and functional networks and found that changes in information capacity and integration, graph properties relevant in the context of stroke (Philips et al., 2017; Zhang et al., 2017; Siegel et al., 2018), are not a direct consequence of lesion volume. When looking at changes at a resting-state network level (Thomas Yeo et al., 2011), a generalized decrease in the level of integration and information capacity has been reported, with the latter being significantly correlated with impairments in network-specific functions (Adhikari et al., 2017).

A common shortcoming of the modeling studies on the effects of lesions mentioned above is that, while network activity is dynamic, the model parameters are either static or manipulated to improve fitting with empirical data. In contrast, cortical networks are plastic and undergo observable changes after focal lesions, particularly in the case of stroke, either in terms of connectivity (Wang et al., 2010, 2014; Siegel et al., 2018) or excitability (Kim et al., 2014; Huynh et al., 2016). The existence

of plasticity mechanisms for EI homeostasis and the parallel between stroke and sensory deprivation (Hengen et al., 2013; Ma et al., 2019) bring into light the importance of studying how plastic whole-brain networks react in the face of localized lesions. Studies tackling this particular challenge have been scarce and show limitations in their approach. Vattikonda et al. (2016) were the first to study how EI balance homeostasis may aid in post-stroke recovery, in a model where homeostatic plasticity of local inhibitory synapses was applied through a recursive process aimed at maintaining firing rates at a physiological level (**Figure 5A**). They found that, even though the immediate effects of lesions were strongly dependent on the strength and participation coefficient of lesioned nodes, EI homeostasis was able to return resting-state FC close to pre-lesion levels. Furthermore, the success of recovery was dependent on lesioned node strength, indicating that the level of recovery attained might depend on the properties of the lesioned area, albeit less strongly than the immediate effects of lesions (**Figure 5B**). In particular, these results showed a simultaneous recovery of functional connectivity and EI balance, although no particular correlation was established between the two. Despite the fact that the mathematical formulation of plasticity was, in this case, different from more physiologically grounded rules (Vogels et al., 2011), the working principle is quite similar to synaptic scaling and, particularly, to other implementations in whole-brain modeling (Hellyer et al., 2016; Abeysuriya et al., 2018). Later, a similar study was performed in conjunction with behavioral analysis of longitudinal data from stroke patients (Rocha et al., 2020). Homeostatic plasticity was implemented through a normalization of the weights of the structural connectivity matrix after a number of simulation timesteps, thus keeping the levels of incoming excitation to each

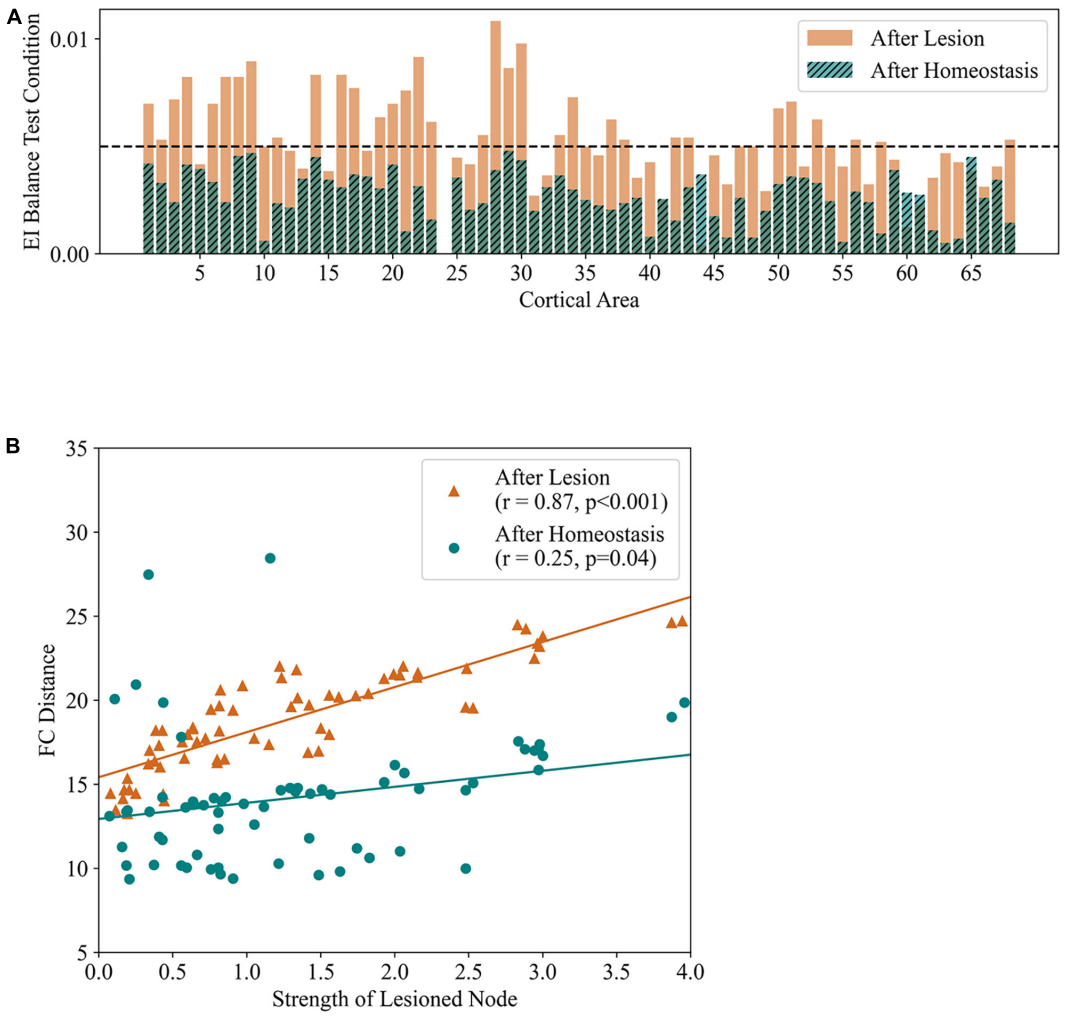

FIGURE 5 | EI homeostasis and recovery of FC cooccur in large-scale computational models of stroke. Results from the application of focal structural lesions in a large-scale model of the cortex with local EI homeostasis. **(A)** EI balance test condition measured immediately after lesion in the left precuneus and after homeostatic adaptation. Areas with values lower than 0.005 are considered balanced. It can be observed that EI balance is lost across the cortex immediately after lesion, being re-established by local homeostasis. **(B)** Correlation between the strength of lesioned nodes and differences in FC from baseline (FCD), immediately after lesion (black) and after restoring EI balance (black). Adapted from Vattikonda et al. (2016).

cortical region relatively constant across time. The authors found that dynamic properties of cortical networks, such as criticality, are altered after focal lesions and slowly recovered in parallel with behavior, pointing to a group of structural connections important for the recovery of criticality, mainly related to the default mode, attention and execution networks. While having the advantage of being a patient-specific study, its shortcomings lie in the used plasticity mechanism. Firstly, it was dependent on post-synaptic weights, and not on activity, while synaptic scaling of excitatory synapses shows dependence on postsynaptic activity instead (Ibata et al., 2008; Turrigiano, 2011). Secondly, plasticity was applied on the long-range structural excitatory connections, not accounting for the important role of inhibitory plasticity in EI homeostasis (Turrigiano, 2011; Vogels et al., 2011; Xue et al., 2014) and the fact that the excitatory connectivity of excitatory neurons is mostly received from local sources (Douglas et al., 1989; Hellwig, 2000). In other words, the most significant effect of excitatory synaptic scaling would be felt in local recurrent connections. Nonetheless, the study was not targeted in particular to the study of the role of local synaptic scaling in EI homeostasis, providing, still, useful insights into altered post-stroke dynamics and the evolution of large-scale structural connectivity.

Finally, a common shortcoming of all the mentioned models is the lack of a deeper investigation of the side-effects of the recovery of functional connectivity by homeostatic mechanisms, particularly regarding changes in the excitability of particular regions, which might be tied to known side effects of stroke, as already hinted about by previous research (Jaenisch et al., 2016). That said, further attention should be devoted to modeling how EI balance evolves after perturbations such as stroke lesions. Studies should consider the inclusion of physiologically grounded mechanisms related to synaptic scaling of local excitatory and inhibitory synapses, possibly in combination with the regulation of intrinsic excitability, their ability to recover pre-lesion properties and, more importantly, the local changes happening in parallel to this recovery of global function.

SUMMARY AND FUTURE DIRECTIONS

Stroke is one of the most burdening diseases today in economically advantaged countries, not only by being the second largest cause of mortality but through the range of side-effects felt by stroke patients and their impact in life post-stroke (Campbell and Khatri, 2020). Therefore, it is essential to understand the changes operated in the brain that are direct effects of stroke lesions and the neural mechanisms of recovery that can restore function. Excitatory-inhibitory balance is one of the characteristics of neural activity essential to maintain several relevant functions, from sensory to higher-order association cortices (Wehr and Zador, 2003; Vogels et al., 2011; Xue et al., 2014; Hellyer et al., 2016). Here, we reviewed some of the relevant findings regarding EI balance and how it is maintained by homeostatic mechanisms in the face of external perturbations. Plastic processes known as synaptic scaling, operating in slow timescales, are ubiquitous and shown to contribute greatly to the maintenance of balance in cortical networks (Turrigiano et al., 1998; Hengen et al., 2013; Ma et al., 2019). In the context of stroke, due to the sudden loss of excitation from lesioned areas to connected regions of the cortex, it is reasonable to expect that such homeostatic process would play an important role in recovery. Indeed, the longitudinal variation of excitability in the cortex (Huynh et al., 2016) and, in particular, changes in the availability of excitatory (Qü et al., 1999; Jolkkonen et al., 2003) and inhibitory receptors (Jolkkonen et al., 2003; Kim et al., 2014), often in areas distant from the lesion, seem to point in that direction. Therefore, future attention should be devoted to investigating possible impairments in mechanisms such as synaptic scaling in stroke patients that could prevent cortical areas from compensating for lesion related imbalances. The therapeutic value of neuromodulation techniques aimed at increasing excitability is already known. Procedures such as tDCS and TMS (Blicher et al., 2009; Romero Lauro et al., 2014) have been applied in the past years, particularly targeted at modulation of motor cortex excitability, and future studies should focus on extending such therapies to different areas in the brain that might experience greater changes in normal levels of incoming excitation, possibly even in a patient-specific manner. Critically, it is important to stress that particular changes in excitability that can aid in the functional recovery of stroke patients might also have side effects. Indeed, increases in motor cortex excitability that are beneficial for motor recovery concurrently raise the risk of developing epileptic seizures (Jaenisch et al., 2016), a common side effect of stroke (Feyissa et al., 2019). Further symptoms of stroke such as depression (Concerto et al., 2013; Towfighi et al., 2017; Page and Coutellier, 2019), chronic pain (Klit et al., 2011; Ratté and Prescott, 2016) and fatigue (Kuppuswamy et al., 2015) have also been related to changes in the excitability of particular brain areas. Therefore, it is not out of the question that, in the process of compensating for diaschisis, homeostatic plasticity mechanisms lead to changes that might increase the propensity of stroke patients to develop the mentioned pathologies.

Another important aspect that is strongly affected by stroke is cortical functional connectivity. Either through changes in the strength of connections between particular areas (He et al., 2007; Carter et al., 2009; Corbetta et al., 2018) or more complex changes in the graph organization of functional networks (Wang et al., 2014; Siegel et al., 2016), stroke can cause deep disruptions in the function of large-scale cortical networks, spreading beyond lesioned areas. These are particularly related to decreased homotopic interhemispheric connectivity (Corbetta et al., 2018), increased segregation of functional networks and decreased modularity (Siegel et al., 2018), and can be, to some extent, returned to pre-lesion levels by spontaneous recovery. Indeed, from the evidence presented in the clinical, experimental and modeling studies discussed so far, it seems likely that the recovery of FC properties during stroke recovery is, to a certain level, dependent on the regulation of excitability at a local level. Previous research indicates that neuromodulation methods that target excitability of particular brain areas also lead to changes in connectivity (Nettekoven et al., 2014, 2015; Volz et al., 2015), suggesting a possibility of simultaneously

manipulating cortical activity in both a local (excitability) and global (connectivity) scale. In consequence, given the unclear way both processes influence each other (Nettekoven et al., 2014), future studies must address the relationship between the maintenance of EI balance after stroke and the reorganization of functional networks, elucidating on a possible causal interaction between these two phenomena.

As previously mentioned, computational modeling can be of great use in this context by providing a more controllable and manipulable framework to study neurological disorders. More particularly, in the case of stroke, large-scale computational models of cortical activity would then allow the study of simultaneous changes in excitability and functional connectivity. More importantly, personalized stroke models could be applied to detect areas of particular impairment in a patient-specific manner, being further used to test the effects of therapies such as tDCS before they are applied in the clinical context. To address this, emphasis should be put on developing interactive modeling and visualization platforms (Arsiwalla et al., 2015) that allow the exploration of the dynamic evolution of cortical activity in stroke patients, aiding in the detection of specific impairments and targets for stimulation, including modeling in the pipeline of clinical decision making. Particular care should be given as well to the possibility of side effects arising from changes in excitability, which might be necessary to recover properties of FC networks, important for the performance of higher-order integrated functions such as memory, language and attention. Research should therefore focus on investigating the likelihood of developing impairments related to excitability in the process of restoring FC by correcting EI imbalances. Another approach would be to investigate the possibility of restoring FC without significant changes in excitability. However, in this case, particular areas of the cortex would require targeted manipulation. For example, while functional connectivity has been proved essential for associative functions (Goldman-Rakic, 1988; Mesulam, 1990), the recovery of visual and motor functions may not share such relation to the connectivity of visual and motor areas, being more dependent on the function these more peripheral cortices, which could suffer more if EI balance is not restored.

In conclusion, while connecting the local and global scales of diaschisis and stroke recovery is poised to be one of the main challenges in the future of stroke research, the study of EI balance and functional connectivity might be the direction to take toward a better understanding of these two aspects of cortical activity. Thus, shedding light into their interaction can be the key to understanding the range of side-effects of stroke and to designing and developing more efficient therapies, thus improving rehabilitation procedures for stroke patients. In addition, the localized nature of stroke lesions provides a framework to advance our understanding of cortical function, both at regional and network levels, clarifying how behavioral and cognitive functions emerge from the local and global properties of cortical activity.

AUTHOR CONTRIBUTIONS

FP and PFMJV contributed to the format and writing of the review and approved the final submitted version. FP contributed to the design and selection of the figures. Both authors contributed to the article and approved the submitted version.

FUNDING

This work was supported by the EU projects euSNN (MSCA-ITN-ETN H2020—ID 860563), Virtual Brain Cloud (H2020 ID 826421), ReHyb (H2020—ID 871767), and RGS@HOME (H2020—EIT Health—ID 19277).

ACKNOWLEDGMENTS

We thank Maria Carlos Oliveira for the invaluable help with the creation and design of **Figure 4**.

REFERENCES

Abeysuriya, R. G., Hadida, J., Sotiropoulos, S. N., Jbabdi, S., Becker, R., Hunt, B. A. E., et al. (2018). A biophysical model of dynamic balancing of excitation and inhibition in fast oscillatory large-scale networks. *PLoS Comput. Biol.* 14:e1006007. doi: 10.1371/journal.pcbi.1006007

Achard, S., Salvador, R., Whitcher, B., Suckling, J., and Bullmore, E. (2006). A resilient, low-frequency, small-world human brain functional network with highly connected association cortical hubs. *J. Neurosci.* 26, 63–72. doi: 10.1523/JNEUROSCI.3874-05.2006

Ackerley, S. J., Stinear, C. M., Barber, P. A., and Byblow, W. D. (2010). Combining theta burst stimulation with training after subcortical stroke. *Stroke* 41, 1568–1572. doi: 10.1161/STROKEAHA.110.583278

Adhikari, M. H., Hacker, C. D., Siegel, J. S., Griffa, A., Hagmann, P., Deco, G., et al. (2017). Decreased integration and information capacity in stroke measured by whole brain models of resting state activity. *Brain* 140, 1068–1085. doi: 10.1093/brain/awx021

Alia, C., Spalletti, C., Lai, S., Panarese, A., Micera, S., and Caleo, M. (2016). Reducing GABAA-mediated inhibition improves forelimb motor function after focal cortical stroke in mice. *Sci. Rep.* 6:37823. doi: 10.1038/srep37823

Alstott, J., Breakspear, M., Hagmann, P., Cammoun, L., and Sporns, O. (2009). Modeling the impact of lesions in the human brain. *PLoS Comput. Biol.* 5:e1000408. doi: 10.1371/journal.pcbi.1000408

Arsiwalla, X. D., Zucca, R., Betella, A., Martinez, E., Dalmazzo, D., Omedas, P., et al. (2015). Network dynamics with BrainX3: a large-scale simulation of the human brain network with real-time interaction. *Front. Neuroinform.* 9:2. doi: 10.3389/fninf.2015.00002

Baldassarre, A., Ramsey, L., Hacker, C. L., Callejas, A., Astafiev, S. V., Metcalf, N. V., et al. (2014). Large-scale changes in network interactions as a physiological signature of spatial neglect. *Brain* 137, 3267–3283. doi: 10.1093/brain/awu297

Ballester, B. R., Nirme, J., Camacho, I., Duarte, E., Rodríguez, S., Cuxart, A., et al. (2017). Domiciliary VR-based therapy for functional recovery and cortical reorganization: randomized controlled trial in participants at the chronic stage post stroke. *JMIR Serious Games* 5:e15. doi: 10.2196/games.6773

Barral, J., and Reyes, A. D. (2016). Synaptic scaling rule preserves excitatory–inhibitory balance and salient neuronal network dynamics. *Nat. Neurosci.* 19, 1690–1696. doi: 10.1038/nn.4415

Bassett, D. S., and Bullmore, E. (2006). Small-world brain networks. *Neuroscientist* 12, 512–523. doi: 10.1177/1073858406293182

Beggs, J. M. (2008). The criticality hypothesis: how local cortical networks might optimize information processing. *Philos. Trans. R. Soc. Math. Phys. Eng. Sci.* 366, 329–343. doi: 10.1098/rsta.2007.2092

Beggs, J. M., and Plenz, D. (2003). Neuronal avalanches in neocortical circuits. *J. Neurosci.* 23, 11167–11177. doi: 10.1523/JNEUROSCI.23-35-11167.2003

Beggs, J. M., and Timme, N. (2012). Being Critical of Criticality in the Brain. *Front. Physiol.* 3:163. doi: 10.3389/fphys.2012.00163

Blicher, J. U., Jakobsen, J., Andersen, G., and Nielsen, J. F. (2009). Cortical excitability in chronic stroke and modulation by training: a TMS study. *Neurorehabil. Neural Repair* 23, 486–493. doi: 10.1177/1545968308328730

Boddington, L. J., Gray, J. P., Schulz, J. M., and Reynolds, J. N. J. (2020). Low-intensity contralesional electrical theta burst stimulation modulates ipsilesional excitability and enhances stroke recovery. *Exp. Neurol.* 323:113071. doi: 10.1016/j.expneurol.2019.113071

Breakspear, M. (2017). Dynamic models of large-scale brain activity. *Nat. Neurosci.* 20, 340–352. doi: 10.1038/nn.4497

Bridi, M. C. D., Zong, F.-J., Min, X., Luo, N., Tran, T., Qiu, J., et al. (2020). Daily oscillation of the excitation-inhibition balance in visual cortical circuits. *Neuron* 105, 621–629.e4. doi: 10.1016/j.neuron.2019.11.011

Bruining, H., Hardstone, R., Juarez-Martinez, E. L., Sprengers, J., Avramiea, A.-E., Simpraga, S., et al. (2020). Measurement of excitation-inhibition ratio in autism spectrum disorder using critical brain dynamics. *Sci. Rep.* 10:9195. doi: 10.1038/s41598-020-65500-4

Buchkremer-Ratzmann, I., and Witte, O. W. (1997). Extended brain disinhibition following small photothrombotic lesions in rat frontal cortex. *Neuroreport* 8, 519–522. doi: 10.1097/00001756-199701200-00028

Butefisch, C. M. (2003). Remote changes in cortical excitability after stroke. *Brain* 126, 470–481. doi: 10.1093/brain/awg044

Cabral, J., Hugues, E., Kringelbach, M. L., and Deco, G. (2012). Modeling the outcome of structural disconnection on resting-state functional connectivity. *NeuroImage* 62, 1342–1353. doi: 10.1016/j.neuroimage.2012.06.007

Cabral, J., Hugues, E., Sporns, O., and Deco, G. (2011). Role of local network oscillations in resting-state functional connectivity. *NeuroImage* 57, 130–139. doi: 10.1016/j.neuroimage.2011.04.010

Cameirão, M. S., Badia, S. B., Oller, E. D., and Verschure, P. F. (2010). Neurorehabilitation using the virtual reality based rehabilitation gaming system: methodology, design, psychometrics, usability and validation. *J. NeuroEngineering Rehabil.* 7:48. doi: 10.1186/1743-0003-7-48

Campbell, B. C. V., and Khatri, P. (2020). Stroke. *Lancet* 396, 129–142. doi: 10.1016/S0140-6736(20)31179-X

Campo, P., Garrido, M. I., Moran, R. J., Maestu, F., Garcia-Morales, I., Gil-Nagel, A., et al. (2012). Remote effects of hippocampal sclerosis on effective connectivity during working memory encoding: a case of connectional diaschisis? *Cereb. Cortex* 22, 1225–1236. doi: 10.1093/cercor/bhr201

Carmichael, S. T. (2012). Brain excitability in stroke. *Arch. Neurol.* 69, 161–167. doi: 10.1001/archneurol.2011.1175

Carrera, E., and Tononi, G. (2014). Diaschisis: past, present, future. *Brain* 137, 2408–2422. doi: 10.1093/brain/awu101

Carter, A. R., Astafiev, S. V., Lang, C. E., Connor, L. T., Rengachary, J., Strube, M. J., et al. (2009). Resting state inter-hemispheric fMRI connectivity predicts performance after stroke. *Ann. Neurol.* 67, 365–375. doi: 10.1002/ana.21905

Carter, A. R., Shulman, G. L., and Corbetta, M. (2012). Why use a connectivity-based approach to study stroke and recovery of function? *NeuroImage* 62, 2271–2280. doi: 10.1016/j.neuroimage.2012.02.070

Clarkson, A. N., Huang, B. S., MacIsaac, S. E., Mody, I., and Carmichael, S. T. (2010). Reducing excessive GABA-mediated tonic inhibition promotes functional recovery after stroke. *Nature* 468, 305–309. doi: 10.1038/nature09511

Clarkson, A. N., Overman, J. J., Zhong, S., Mueller, R., Lynch, G., and Carmichael, S. T. (2011). AMPA receptor-induced local brain-derived neurotrophic factor signaling mediates motor recovery after stroke. *J. Neurosci.* 31, 3766–3775. doi: 10.1523/JNEUROSCI.5780-10.2011

Concerto, C., Lanza, G., Cantone, M., Pennisi, M., Giordano, D., Spampinato, C., et al. (2013). Different patterns of cortical excitability in major depression and vascular depression: a transcranial magnetic stimulation study. *BMC Psychiatry* 13:300. doi: 10.1186/1471-244X-13-300

Corbetta, M., Siegel, J. S., and Shulman, G. L. (2018). On the low dimensionality of behavioral deficits and alterations of brain network connectivity after focal injury. *Cortex J. Devoted Study Nerv. Syst. Behav.* 107, 229–237. doi: 10.1016/j.cortex.2017.12.017

Deco, G., Jirsa, V., McIntosh, A. R., Sporns, O., and Kotter, R. (2009). Key role of coupling, delay, and noise in resting brain fluctuations. *Proc. Natl. Acad. Sci. U.S.A.* 106, 10302–10307. doi: 10.1073/pnas.0901831106

Deco, G., and Kringelbach, M. L. (2014). Great expectations: using whole-brain computational connectomics for understanding neuropsychiatric disorders. *Neuron* 84, 892–905. doi: 10.1016/j.neuron.2014.08.034

Deco, G., Kringelbach, M. L., Arnatkeviciute, A., Oldham, S., Sabaroedin, K., Rogasch, N. C., et al. (2021). Dynamical consequences of regional heterogeneity in the brain's transcriptional landscape. *Sci. Adv.* 7:eabf4752. doi: 10.1126/sciadv.abf4752

Deco, G., Ponce-Alvarez, A., Hagmann, P., Romani, G. L., Mantini, D., and Corbetta, M. (2014). How local excitation-inhibition ratio impacts the whole brain dynamics. *J. Neurosci.* 34, 7886–7898. doi: 10.1523/JNEUROSCI.5068-13.2014

Dehghani, N., Peyrache, A., Telenczuk, B., Le Van Quyen, M., Halgren, E., Cash, S. S., et al. (2016). Dynamic balance of excitation and inhibition in human and monkey neocortex. *Sci. Rep.* 6:23176. doi: 10.1038/srep23176

Denève, S., and Machens, C. K. (2016). Efficient codes and balanced networks. *Nat. Neurosci.* 19, 375–382. doi: 10.1038/nn.4243

Desai, N. S., Rutherford, L. C., and Turrigiano, G. G. (1999). Plasticity in the intrinsic excitability of cortical pyramidal neurons. *Nat. Neurosci.* 2, 515–520. doi: 10.1038/9165

Di Lazzaro, V., Pilato, F., Dileone, M., Profice, P., Capone, F., Ranieri, F., et al. (2008). Modulating cortical excitability in acute stroke: a repetitive TMS study. *Clin. Neurophysiol.* 119, 715–723. doi: 10.1016/j.clinph.2007.11.049

Ding, Q., Zhang, S., Chen, S., Chen, J., Li, X., Chen, J., et al. (2021). The effects of intermittent theta burst stimulation on functional brain network following stroke: an electroencephalography study. *Front. Neurosci.* 15:1432. doi: 10.3389/fnins.2021.755709

Dorrn, A. L., Yuan, K., Barker, A. J., Schreiner, C. E., and Froemke, R. C. (2010). Developmental sensory experience balances cortical excitation and inhibition. *Nature* 465, 932–936. doi: 10.1038/nature09119

Douglas, R. J., Martin, K. A. C., and Whitteridge, D. (1989). A canonical microcircuit for neocortex. *Neural Comput.* 1, 480–488. doi: 10.1162/neco.1989.1.4.480

Falcon, M. I., Riley, J. D., Jirsa, V., McIntosh, A. R., Elinor Chen, E., and Solodkin, A. (2016). Functional mechanisms of recovery after chronic stroke: modeling with the virtual brain. *Eneuro* 3:ENEURO.0158-15.2016. doi: 10.1523/ENEURO.0158-15.2016

Feeney, D. M., and Baron, J. C. (1986). Diaschisis. *Stroke* 17, 817–830. doi: 10.1161/01.STR.17.5.817

Felleman, D. J., and Van Essen, D. C. (1991). Distributed hierarchical processing in the primate cerebral cortex. *Cereb. Cortex N.Y.* 1, 1–47. doi: 10.1093/cercor/1.1.1-a

Feyissa, A. M., Hasan, T. F., and Meschia, J. F. (2019). Stroke-related epilepsy. *Eur. J. Neurol.* 26:18.e3. doi: 10.1111/ene.13813

Fino, E., and Yuste, R. (2011). Dense inhibitory connectivity in neocortex. *Neuron* 69, 1188–1203. doi: 10.1016/j.neuron.2011.02.025

Friedman, N., Ito, S., Brinkman, B. A. W., Shimono, M., DeVille, R. E. L., Dahmen, K. A., et al. (2012). Universal critical dynamics in high resolution neuronal avalanche data. *Phys. Rev. Lett.* 108:208102. doi: 10.1103/PhysRevLett.108.208102

Friston, K. J. (2011). Functional and effective connectivity: a review. *Brain Connect* 1, 13–36. doi: 10.1089/brain.2011.0008

Froemke, R. C., Merzenich, M. M., and Schreiner, C. E. (2007). A synaptic memory trace for cortical receptive field plasticity. *Nature* 450, 425–429. doi: 10.1038/nature06289

Gerloff, C., Bushara, K., Sailer, A., Wassermann, E. M., Chen, R., Matsuoka, T., et al. (2006). Multimodal imaging of brain reorganization in motor areas of the contralesional hemisphere of well recovered patients after capsular stroke. *Brain J. Neurol.* 129, 791–808. doi: 10.1093/brain/awh713

Goldman-Rakic, P. S. (1988). Topography of cognition: parallel distributed networks in primate association cortex. *Annu. Rev. Neurosci.* 11, 137–156. doi: 10.1146/annurev.ne.11.030188.001033

Goñi, J., van den Heuvel, M. P., Avena-Koenigsberger, A., Mendizabal, N. V., de, Betzel, R. F., et al. (2014). Resting-brain functional connectivity predicted by

analytic measures of network communication. *Proc. Natl. Acad. Sci. U.S.A.* 111, 833–838. doi: 10.1073/pnas.1315529111

Gratton, C., Nomura, E. M., Pérez, F., and D'Esposito, M. (2012). Focal brain lesions to critical locations cause widespread disruption of the modular organization of the brain. *J. Cogn. Neurosci.* 24, 1275–1285. doi: 10.1162/jocn_a_00222

Grefkes, C., and Fink, G. R. (2012). Disruption of motor network connectivity post-stroke and its noninvasive neuromodulation. *Curr. Opin. Neurol.* 25, 670–675. doi: 10.1097/WCO.0b013e3283598473

Griffis, J. C., Metcalf, N. V., Corbetta, M., and Shulman, G. L. (2019). Structural disconnections explain brain network dysfunction after stroke. *Cell Rep.* 28, 2527–2540.e9. doi: 10.1016/j.celrep.2019.07.100

Hagmann, P., Cammoun, L., Gigandet, X., Meuli, R., Honey, C. J., Wedeen, V. J., et al. (2008). Mapping the structural core of human cerebral cortex. *PLoS Biol.* 6:e159. doi: 10.1371/journal.pbio.0060159

Hagmann, P., Kurant, M., Gigandet, X., Thiran, P., Wedeen, V. J., Meuli, R., et al. (2007). Mapping human whole-brain structural networks with diffusion MRI. *PLoS One* 2:e597. doi: 10.1371/journal.pone.0000597

Hahn, G., Ponce-Alvarez, A., Monier, C., Benvenuti, G., Kumar, A., Chavane, F., et al. (2017). Spontaneous cortical activity is transiently poised close to criticality. *PLoS Comput. Biol.* 13:e1005543. doi: 10.1371/journal.pcbi.1005543

Hall, G. R., Kaiser, M., and Farr, T. D. (2021). Functional connectivity change in response to stroke is comparable across species: from mouse to man. *Stroke* 52, 2961–2963. doi: 10.1161/STROKEAHA.121.034097

He, B. J., Snyder, A. Z., Vincent, J. L., Epstein, A., Shulman, G. L., and Corbetta, M. (2007). Breakdown of functional connectivity in frontoparietal networks underlies behavioral deficits in spatial neglect. *Neuron* 53, 905–918. doi: 10.1016/j.neuron.2007.02.013

Hellwig, B. (2000). A quantitative analysis of the local connectivity between pyramidal neurons in layers 2/3 of the rat visual cortex. *Biol. Cybern.* 82, 111–121. doi: 10.1007/PL00007964

Hellyer, P. J., Jachs, B., Clopath, C., and Leech, R. (2016). Local inhibitory plasticity tunes macroscopic brain dynamics and allows the emergence of functional brain networks. *NeuroImage* 124, 85–95. doi: 10.1016/j.neuroimage.2015.08.069

Hengen, K. B., Lambo, M. E., Van Hooser, S. D., Katz, D. B., and Turrigiano, G. G. (2013). Firing rate homeostasis in visual cortex of freely behaving rodents. *Neuron* 80, 335–342. doi: 10.1016/j.neuron.2013.08.038

Honey, C. J., Kötter, R., Breakspear, M., and Sporns, O. (2007). Network structure of cerebral cortex shapes functional connectivity on multiple time scales. *Proc. Natl. Acad. Sci. U.S.A.* 104, 10240–10245. doi: 10.1073/pnas.0701519104

Honey, C. J., and Sporns, O. (2008). Dynamical consequences of lesions in cortical networks. *Hum. Brain Mapp.* 29, 802–809. doi: 10.1002/hbm.20579

Honey, C. J., Sporns, O., Cammoun, L., Gigandet, X., Thiran, J. P., Meuli, R., et al. (2009). Predicting human resting-state functional connectivity from structural connectivity. *Proc. Natl. Acad. Sci U.S.A.* 106, 2035–2040. doi: 10.1073/pnas.0811168106

Huang, Y.-Z., Edwards, M. J., Rounis, E., Bhatia, K. P., and Rothwell, J. C. (2005). Theta burst stimulation of the human motor cortex. *Neuron* 45, 201–206. doi: 10.1016/j.neuron.2004.12.033

Hummel, F. C., and Cohen, L. G. (2006). Non-invasive brain stimulation: a new strategy to improve neurorehabilitation after stroke? *Lancet Neurol.* 5, 708–712. doi: 10.1016/S1474-4422(06)70525-7

Huynh, W., Vucic, S., Krishnan, A. V., Lin, C. S.-Y., and Kiernan, M. C. (2016). Exploring the evolution of cortical excitability following acute stroke. *Neurorehabil. Neural Repair* 30, 244–257. doi: 10.1177/1545968315593804

Ibata, K., Sun, Q., and Turrigiano, G. G. (2008). Rapid synaptic scaling induced by changes in postsynaptic firing. *Neuron* 57, 819–826. doi: 10.1016/j.neuron.2008.02.031

Jaenisch, N., Liebmann, L., Guenther, M., Hübner, C. A., Frahm, C., and Witte, O. W. (2016). Reduced tonic inhibition after stroke promotes motor performance and epileptic seizures. *Sci. Rep.* 6:26173. doi: 10.1038/srep26173

Jirsa, V. K., Proix, T., Perdikis, D., Woodman, M. M., Wang, H., Gonzalez-Martinez, J., et al. (2017). The virtual epileptic patient: individualized whole-brain models of epilepsy spread. *NeuroImage* 145, 377–388. doi: 10.1016/j.neuroimage.2016.04.049

Jolkkonen, J., Gallagher, N. P., Zilles, K., and Sivenius, J. (2003). Behavioral deficits and recovery following transient focal cerebral ischemia in rats: glutamatergic and GABAergic receptor densities. *Behav. Brain Res.* 138, 187–200. doi: 10.1016/S0166-4328(02)00241-3

Joyce, K. E., Hayasaka, S., and Laurienti, P. J. (2013). The human functional brain network demonstrates structural and dynamical resilience to targeted attack. *PLoS Comput. Biol.* 9:e1002885. doi: 10.1371/journal.pcbi.1002885

Kanwisher, N. (2010). Functional specificity in the human brain: a window into the functional architecture of the mind. *Proc. Natl. Acad. Sci. U.S.A.* 107, 11163–11170. doi: 10.1073/pnas.1005062107

Kazim, S. F., Seo, J. H., Bianchi, R., Larson, C. S., Sharma, A., Wong, R. K. S., et al. (2021). Neuronal network excitability in Alzheimer's disease: the puzzle of similar versus divergent roles of amyloid β and tau. *eNeuro* 8:ENEURO.0418-20.2020. doi: 10.1523/ENEURO.0418-20.2020

Keck, T., Keller, G. B., Jacobsen, R. I., Eysel, U. T., Bonhoeffer, T., and Hübener, M. (2013). Synaptic scaling and homeostatic plasticity in the mouse visual cortex *in vivo*. *Neuron* 80, 327–334. doi: 10.1016/j.neuron.2013.08.018

Kehrer, C., Maziashvili, N., Dugladze, T., and Gloveli, T. (2008). Altered excitatory-inhibitory balance in the NMDA-hypofunction model of schizophrenia. *Front. Mol. Neurosci.* 1:6. doi: 10.3389/neuro.02.006.2008

Kim, Y. K., Yang, E. J., Cho, K., Lim, J. Y., and Paik, N.-J. (2014). Functional recovery after ischemic stroke is associated with reduced GAB aergic inhibition in the cerebral cortex: A GABA PET study. *Neurorehabil. Neural Repair* 28, 576–583. doi: 10.1177/1545968313520411

Klit, H., Finnerup, N. B., Overvad, K., Andersen, G., and Jensen, T. S. (2011). Pain following stroke: a population-based follow-up study. *PLoS One* 6:e27607. doi: 10.1371/journal.pone.0027607

Kullmann, D. M., Moreau, A. W., Bakiri, Y., and Nicholson, E. (2012). Plasticity of Inhibition. *Neuron* 75, 951–962. doi: 10.1016/j.neuron.2012.07.030

Kuppuswamy, A., Clark, E. V., Turner, I. F., Rothwell, J. C., and Ward, N. S. (2015). Post-stroke fatigue: a deficit in corticomotor excitability? *Brain* 138, 136–148. doi: 10.1093/brain/awu306

Lake, E. M. R., Chaudhuri, J., Thomason, L., Janik, R., Ganguly, M., Brown, M., et al. (2015). The effects of delayed reduction of tonic inhibition on ischemic lesion and sensorimotor function. *J. Cereb. Blood Flow Metab.* 35, 1601–1609. doi: 10.1038/jcbfm.2015.86

Landau, I. D., Egger, R., Dercksen, V. J., Oberlaender, M., and Sompolinsky, H. (2016). The impact of structural heterogeneity on excitation-inhibition balance in cortical networks. *Neuron* 92, 1106–1121. doi: 10.1016/j.neuron.2016.10.027

Leys, D., Hénon, H., Mackowiak-Cordoliani, M.-A., and Pasquier, F. (2005). Poststroke dementia. *Lancet Neurol.* 4, 752–759. doi: 10.1016/S1474-4422(05)70221-0

Litvak, V., Sompolinsky, H., Segev, I., and Abeles, M. (2003). On the transmission of rate code in long feedforward networks with excitatory–inhibitory balance. *J. Neurosci.* 23, 3006–3015. doi: 10.1523/JNEUROSCI.23-07-03006.2003

Litwin-Kumar, A., and Doiron, B. (2014). Formation and maintenance of neuronal assemblies through synaptic plasticity. *Nat. Commun.* 5:5319. doi: 10.1038/ncomms6319

Luhmann, H. J., Mudrick-Donnon, L. A., Mittmann, T., and Heinemann, U. (1995). Ischaemia-induced long-term hyperexcitability in rat neocortex. *Eur. J. Neurosci.* 7, 180–191. doi: 10.1111/j.1460-9568.1995.tb01054.x

Ma, Z., Turrigiano, G. G., Wessel, R., and Hengen, K. B. (2019). Cortical circuit dynamics are homeostatically tuned to criticality *in vivo*. *Neuron* 104, 655–664e4. doi: 10.1016/j.neuron.2019.08.031

Mackwood, O., Naumann, L. B., and Sprekeler, H. (2021). Learning excitatory-inhibitory neuronal assemblies in recurrent networks. *eLife*. 10:e59715. doi: 10.7554/eLife.59715

Maffei, A., Nelson, S. B., and Turrigiano, G. G. (2004). Selective reconfiguration of layer 4 visual cortical circuitry by visual deprivation. *Nat. Neurosci.* 7, 1353–1359. doi: 10.1038/nn1351

Maffei, A., and Turrigiano, G. G. (2008). Multiple modes of network homeostasis in visual cortical layer 2/3. *J. Neurosci.* 28, 4377–4384. doi: 10.1523/JNEUROSCI.5298-07.2008

Magri, C., Schridde, U., Murayama, Y., Panzeri, S., and Logothetis, N. K. (2012). The amplitude and timing of the BOLD signal reflects the relationship between local field potential power at different frequencies. *J. Neurosci.* 32, 1395–1407. doi: 10.1523/JNEUROSCI.3985-11.2012

Mariño, J., Schummers, J., Lyon, D. C., Schwabe, L., Beck, O., Wiesing, P., et al. (2005). Invariant computations in local cortical networks with balanced excitation and inhibition. *Nat. Neurosci.* 8, 194–201. doi: 10.1038/nn1391

Markov, N. T., Ercsey-Ravasz, M., Van Essen, D. C., Knoblauch, K., Toroczkai, Z., and Kennedy, H. (2013). Cortical high-density counterstream architectures. *Science* 342:1238406. doi: 10.1126/science.1238406

Markram, H., Toledo-Rodriguez, M., Wang, Y., Gupta, A., Silberberg, G., and Wu, C. (2004). Interneurons of the neocortical inhibitory system. *Nat. Rev. Neurosci.* 5, 793–807. doi: 10.1038/nrn1519

Mashour, G. A., Roelfsema, P., Changeux, J.-P., and Dehaene, S. (2020). Conscious processing and the global neuronal workspace hypothesis. *Neuron* 105, 776–798. doi: 10.1016/j.neuron.2020.01.026

Meehan, S. K., Dao, E., Linsdell, M. A., and Boyd, L. A. (2011). Continuous theta burst stimulation over the contralesional sensory and motor cortex enhances motor learning post-stroke. *Neurosci. Lett.* 500, 26–30. doi: 10.1016/j.neulet.2011.05.237

Mesulam, M.-M. (1990). Large-scale neurocognitive networks and distributed processing for attention, language, and memory. *Ann. Neurol.* 28, 597–613. doi: 10.1002/ana.410280502

Murphy, T. H., and Corbett, D. (2009). Plasticity during stroke recovery: from synapse to behaviour. *Nat. Rev. Neurosci.* 10, 861–872. doi: 10.1038/nrn2735

Musuka, T. D., Wilton, S. B., Traboulsi, M., and Hill, M. D. (2015). Diagnosis and management of acute ischemic stroke: speed is critical. *CMAJ Can. Med. Assoc. J.* 187, 887–893. doi: 10.1503/cmaj.140355

Naskar, A., Vattikonda, A., Deco, G., Roy, D., and Banerjee, A. (2021). Multiscale dynamic mean field (MDMF) model relates resting-state brain dynamics with local cortical excitatory–inhibitory neurotransmitter homeostasis. *Netw. Neurosci.* 5, 757–782. doi: 10.1162/netn_a_00197

Nelson, S. B., and Valakh, V. (2015). Excitatory/inhibitory balance and circuit homeostasis in autism spectrum disorders. *Neuron* 87, 684–698. doi: 10.1016/j.neuron.2015.07.033

Nettekoven, C., Volz, L. J., Kutscha, M., Pool, E.-M., Rehme, A. K., Eickhoff, S. B., et al. (2014). Dose-dependent effects of theta burst rTMS on cortical excitability and resting-state connectivity of the human motor system. *J. Neurosci.* 34, 6849–6859. doi: 10.1523/JNEUROSCI.4993-13.2014

Nettekoven, C., Volz, L. J., Leimbach, M., Pool, E.-M., Rehme, A. K., Eickhoff, S. B., et al. (2015). Inter-individual variability in cortical excitability and motor network connectivity following multiple blocks of rTMS. *NeuroImage* 118, 209–218. doi: 10.1016/j.neuroimage.2015.06.004

Neumann-Haefelin, T., Hagemann, G., and Witte, O. W. (1995). Cellular correlates of neuronal hyperexcitability in the vicinity of photochemically induced cortical infarcts in rats *in vitro*. *Neurosci. Lett.* 193, 101–104. doi: 10.1016/0304-3940(95)11677-O

Neumann-Haefelin, T., and Witte, O. W. (2000). Periinfarct and remote excitability changes after transient middle cerebral artery occlusion. *J. Cereb. Blood Flow Metab.* 20, 45–52. doi: 10.1097/00004647-200001000-00008

Okun, M., and Lampl, I. (2008). Instantaneous correlation of excitation and inhibition during ongoing and sensory-evoked activities. *Nat. Neurosci.* 11, 535–537. doi: 10.1038/nn.2105

Packer, A. M., and Yuste, R. (2011). Dense, unspecific connectivity of neocortical parvalbumin-positive interneurons: a canonical microcircuit for inhibition? *J. Neurosci.* 31, 13260–13271. doi: 10.1523/JNEUROSCI.3131-11.2011

Page, C. E., and Coutellier, L. (2019). Prefrontal excitatory/inhibitory balance in stress and emotional disorders: evidence for over-inhibition. *Neurosci. Biobehav. Rev.* 105, 39–51. doi: 10.1016/j.neubiorev.2019.07.024

Park, C., Chang, W. H., Ohn, S. H., Kim, S. T., Bang, O. Y., Pascual-Leone, A., et al. (2011). Longitudinal changes of resting-state functional connectivity during motor recovery after stroke. *Stroke* 42, 1357–1362. doi: 10.1161/STROKEAHA.110.596155

Pasquale, V., Massobrio, P., Bologna, L. L., Chiappalone, M., and Martinoia, S. (2008). Self-organization and neuronal avalanches in networks of dissociated cortical neurons. *Neuroscience* 153, 1354–1369. doi: 10.1016/j.neuroscience.2008.03.050

Petermann, T., Thiagarajan, T. C., Lebedev, M. A., Nicolelis, M. A. L., Chialvo, D. R., and Plenz, D. (2009). Spontaneous cortical activity in awake monkeys composed of neuronal avalanches. *Proc. Natl. Acad. Sci. U.S.A.* 106, 15921–15926. doi: 10.1073/pnas.0904089106

Philips, G. R., Daly, J. J., and Príncipe, J. C. (2017). Topographical measures of functional connectivity as biomarkers for post-stroke motor recovery. *J. NeuroEngineering Rehabil.* 14:67. doi: 10.1186/s12984-017-0277-3

Platz, T. (ed.) (2021). *Clinical Pathways in Stroke Rehabilitation: Evidence-based Clinical Practice Recommendations*. Cham: Springer International Publishing.

Poil, S.-S., van Ooyen, A., and Linkenkaer-Hansen, K. (2008). Avalanche dynamics of human brain oscillations: relation to critical branching processes and temporal correlations. *Hum. Brain Mapp.* 29, 770–777. doi: 10.1002/hbm.20590

Prochnow, D., Bermúdez i Badia, S., Schmidt, J., Duff, A., Brunheim, S., Kleiser, R., et al. (2013). A functional magnetic resonance imaging study of visuomotor processing in a virtual reality-based paradigm: rehabilitation gaming system. *Eur. J. Neurosci.* 37, 1441–1447. doi: 10.1111/ejn.12157

Qü, M., Buchkremer-Ratzmann, I., Schiene, K., Schroeter, M., Witte, O. W., and Zilles, K. (1998). Bihemispheric reduction of GABAA receptor binding following focal cortical photothrombotic lesions in the rat brain. *Brain Res.* 813, 374–380. doi: 10.1016/S0006-8993(98)01063-4

Qü, M., Schiene, K., Witte, O. W., and Zilles, K. (1999). Widespread up-regulation of N-methyl-d-aspartate receptors after focal photothrombotic lesion in rat brain. *Neurosci. Lett.* 273, 77–80. doi: 10.1016/S0304-3940(99)00598-4

Ratté, S., and Prescott, S. A. (2016). Afferent hyperexcitability in neuropathic pain and the inconvenient truth about its degeneracy. *Curr. Opin. Neurobiol.* 36, 31–37. doi: 10.1016/j.conb.2015.08.007

Redecker, C., Wang, W., Fritschy, J.-M., and Witte, O. W. (2002). Widespread and long-lasting alterations in GABAA-receptor subtypes after focal cortical infarcts in rats: mediation by NMDA-dependent processes. *J. Cereb. Blood Flow Metab.* 22, 1463–1475. doi: 10.1097/01.WCB.0000034149.72481.BD

Rocha, R. P., Koçillari, L., Suweis, S., Grazia, M. D. F. D., de Schotten, M. T., Zorzi, M., et al. (2020). Recovery of neural dynamics criticality in personalized whole brain models of stroke. *bioRxiv* [Preprint]. doi: 10.1101/2020.12.17.423349 *bioRxiv, 2020.12.17.423349,

Romero Lauro, L. J., Rosanova, M., Mattavelli, G., Convento, S., Pisoni, A., Opitz, A., et al. (2014). TDCS increases cortical excitability: direct evidence from TMS–EEG. *Cortex* 58, 99–111. doi: 10.1016/j.cortex.2014.05.003

Rubin, R., Abbott, L. F., and Sompolinsky, H. (2017). Balanced excitation and inhibition are required for high-capacity, noise-robust neuronal selectivity. *Proc. Natl. Acad. Sci. U.S.A.* 114, E9366–E9375. doi: 10.1073/pnas.1705841114

Rubinov, M., and Sporns, O. (2010). Complex network measures of brain connectivity: Uses and interpretations. *NeuroImage* 52, 1059–1069. doi: 10.1016/j.neuroimage.2009.10.003

Saenger, V. M., Kahan, J., Foltynie, T., Friston, K., Aziz, T. Z., Green, A. L., et al. (2017). Uncovering the underlying mechanisms and whole-brain dynamics of deep brain stimulation for Parkinson's disease. *Sci. Rep.* 7:9882. doi: 10.1038/s41598-017-10003-y

Salinas, E., and Sejnowski, T. J. (2000). Impact of correlated synaptic input on output firing rate and variability in simple neuronal models. *J. Neurosci.* 20, 6193–6209. doi: 10.1523/JNEUROSCI.20-16-06193.2000

Schiene, K., Bruehl, C., Zilles, K., Qu, M., Hagemann, G., Kraemer, M., et al. (1996). Neuronal hyperexcitability and reduction of GABAA-receptor expression in the surround of cerebral photothrombosis. *J. Cereb. Blood Flow Metab.* 16, 906–914. doi: 10.1097/00004647-199609000-00014

Shew, W. L., Yang, H., Petermann, T., Roy, R., and Plenz, D. (2009). Neuronal avalanches imply maximum dynamic range in cortical networks at criticality. *J. Neurosci.* 29, 15595–15600. doi: 10.1523/JNEUROSCI.3864-09.2009

Shew, W. L., Yang, H., Yu, S., Roy, R., and Plenz, D. (2011). Information capacity and transmission are maximized in balanced cortical networks with neuronal avalanches. *J. Neurosci.* 31, 55–63. doi: 10.1523/JNEUROSCI.4637-10.2011

Siegel, J. S., Ramsey, L. E., Snyder, A. Z., Metcalf, N. V., Chacko, R. V., Weinberger, K., et al. (2016). Disruptions of network connectivity predict impairment in multiple behavioral domains after stroke. *Proc. Natl. Acad. Sci. U.S.A.* 113, E4367–E4376. doi: 10.1073/pnas.1521083113

Siegel, J. S., Seitzman, B. A., Ramsey, L. E., Ortega, M., Gordon, E. M., Dosenbach, N. U. F., et al. (2018). Re-emergence of modular brain networks in stroke recovery. *Cortex* 101, 44–59. doi: 10.1016/j.cortex.2017.12.019

Sporns, O. (2011). The human connectome: a complex network: the human connectome. *Ann. N.Y. Acad. Sci.* 1224, 109–125. doi: 10.1111/j.1749-6632.2010.05888.x

Sporns, O., Honey, C. J., and Kötter, R. (2007). Identification and classification of hubs in brain networks. *PLoS One* 2:e1049. doi: 10.1371/journal.pone.0001049

Sporns, O., Tononi, G., and Kötter, R. (2005). The human connectome: a structural description of the human brain. *PLoS Comput. Biol.* 1:e42. doi: 10.1371/journal.pcbi.0010042

Sprekeler, H. (2017). Functional consequences of inhibitory plasticity: homeostasis, the excitation-inhibition balance and beyond. *Curr. Opin. Neurobiol.* 43, 198–203. doi: 10.1016/j.conb.2017.03.014

Stefanovski, L., Triebkorn, P., Spiegler, A., Diaz-Cortes, M.-A., Solodkin, A., Jirsa, V., et al. (2019). Linking molecular pathways and large-scale computational modeling to assess candidate disease mechanisms and pharmacodynamics in Alzheimer's disease. *Front. Comput. Neurosci.* 13:54. doi: 10.3389/fncom.2019.00054

Tao, H. W., and Poo, M. (2005). Activity-dependent matching of excitatory and inhibitory inputs during refinement of visual receptive fields. *Neuron* 45, 829–836. doi: 10.1016/j.neuron.2005.01.046

Thomas Yeo, B. T., Krienen, F. M., Sepulcre, J., Sabuncu, M. R., Lashkari, D., Hollinshead, M., et al. (2011). The organization of the human cerebral cortex estimated by intrinsic functional connectivity. *J. Neurophysiol.* 106, 1125–1165. doi: 10.1152/jn.00338.2011

Towfighi, A., Ovbiagele, B., El Husseini, N., Hackett, M. L., Jorge, R. E., Kissela, B. M., et al. (2017). Poststroke depression: a scientific statement for healthcare professionals from the american heart association/american stroke association. *Stroke* 48, e30–e43. doi: 10.1161/STR.0000000000000113

Tremblay, R., Lee, S., and Rudy, B. (2016). GABAergic interneurons in the neocortex: from cellular properties to circuits. *Neuron* 91, 260–292. doi: 10.1016/j.neuron.2016.06.033

Turrigiano, G. G. (2011). Too many cooks? Intrinsic and synaptic homeostatic mechanisms in cortical circuit refinement. *Annu. Rev. Neurosci.* 34, 89–103. doi: 10.1146/annurev-neuro-060909-153238

Turrigiano, G. G., Leslie, K. R., Desai, N. S., Rutherford, L. C., and Nelson, S. B. (1998). Activity-dependent scaling of quantal amplitude in neocortical neurons. *Nature* 391, 892–896. doi: 10.1038/36103

van den Heuvel, M. P., and Sporns, O. (2011). Rich-club organization of the human connectome. *J. Neurosci.* 31, 15775–15786. doi: 10.1523/JNEUROSCI.3539-11.2011

van Vreeswijk, C., and Sompolinsky, H. (1996). Chaos in neuronal networks with balanced excitatory and inhibitory activity. *Science* 274, 1724–1726. doi: 10.1126/science.274.5293.1724

Vattikonda, A., Surampudi, B. R., Banerjee, A., Deco, G., and Roy, D. (2016). Does the regulation of local excitation–inhibition balance aid in recovery of functional connectivity? *Comput. Account. NeuroImage* 136, 57–67. doi: 10.1016/j.neuroimage.2016.05.002

Vico Varela, E., Etter, G., and Williams, S. (2019). Excitatory-inhibitory imbalance in Alzheimer's disease and therapeutic significance. *Neurobiol. Dis.* 127, 605–615. doi: 10.1016/j.nbd.2019.04.010

Vogels, T. P., Sprekeler, H., Zenke, F., Clopath, C., and Gerstner, W. (2011). Inhibitory plasticity balances excitation and inhibition in sensory pathways and memory networks. *Science* 334, 1569–1573. doi: 10.1126/science.1211095

Volz, L. J., Sarfeld, A.-S., Diekhoff, S., Rehme, A. K., Pool, E.-M., Eickhoff, S. B., et al. (2015). Motor cortex excitability and connectivity in chronic stroke: a multimodal model of functional reorganization. *Brain Struct. Funct.* 220, 1093–1107. doi: 10.1007/s00429-013-0702-8

von Monakow, C. (1914). *Die Lokalisation im Grosshirn und der Abbau der Funktion durch kortikale Herde*. Available online at: https://wellcomecollection.org/works/sv9frejr (accessed September 30, 2021).

Wang, C., Qin, W., Zhang, J., Tian, T., Li, Y., Meng, L., et al. (2014). Altered functional organization within and between resting-state networks in chronic subcortical infarction. *J. Cereb. Blood Flow Metab.* 34, 597–605. doi: 10.1038/jcbfm.2013.238

Wang, L., Yu, C., Chen, H., Qin, W., He, Y., Fan, F., et al. (2010). Dynamic functional reorganization of the motor execution network after stroke. *Brain* 133, 1224–1238. doi: 10.1093/brain/awq043

Wang, X. J. (2020). Macroscopic gradients of synaptic excitation and inhibition in the neocortex. *Nat. Rev. Neurosci.* 21, 169–178. doi: 10.1038/s41583-020-0262-x

Wehr, M., and Zador, A. M. (2003). Balanced inhibition underlies tuning and sharpens spike timing in auditory cortex. *Nature* 426, 442–446. doi: 10.1038/nature02116

Westlake, K., and Nagarajan, S. (2011). Functional connectivity in relation to motor performance and recovery after stroke. *Front. Syst. Neurosci.* 5:8. doi: 10.3389/fnsys.2011.00008

Westlake, K. P., Hinkley, L. B., Bucci, M., Guggisberg, A. G., Findlay, A. M., Byl, N., et al. (2012). Resting state alpha-band functional connectivity and recovery after stroke. *Exp. Neurol.* 237, 160–169. doi: 10.1016/j.expneurol.2012.06.020

Wilson, H. R., and Cowan, J. D. (1972). Excitatory and inhibitory interactions in localized populations of model neurons. *Biophys. J.* 12, 1–24.

Xue, M., Atallah, B. V., and Scanziani, M. (2014). Equalizing excitation–inhibition ratios across visual cortical neurons. *Nature* 511, 596–600. doi: 10.1038/nature13321

Yeo, B. T. T., and Eickhoff, S. B. (2016). A modern map of the human cerebral cortex. *Nature* 536, 152–154. doi: 10.1038/nature18914

Zhang, J., Zhang, Y., Wang, L., Sang, L., Yang, J., Yan, R., et al. (2017). Disrupted structural and functional connectivity networks in ischemic stroke patients. *Neuroscience* 364, 212–225. doi: 10.1016/j.neuroscience.2017.09.009

Zhou, M., Liang, F., Xiong, X. R., Li, L., Li, H., Xiao, Z., et al. (2014). Scaling down of balanced excitation and inhibition by active behavioral states in auditory cortex. *Nat. Neurosci.* 17, 841–850. doi: 10.1038/nn.3701

Conflict of Interest: FP is employed by company Eodyne Systems SL. PFMJV is founder and shareholder of Eodyne Systems S.L., which aims at bringing scientifically validated neurorehabilitation and education technology to society.

Publisher's Note: All claims expressed in this article are solely those of the authors and do not necessarily represent those of their affiliated organizations, or those of the publisher, the editors and the reviewers. Any product that may be evaluated in this article, or claim that may be made by its manufacturer, is not guaranteed or endorsed by the publisher.

Copyright © 2022 Páscoa dos Santos and Verschure. This is an open-access article distributed under the terms of the Creative Commons Attribution License (CC BY). The use, distribution or reproduction in other forums is permitted, provided the original author(s) and the copyright owner(s) are credited and that the original publication in this journal is cited, in accordance with accepted academic practice. No use, distribution or reproduction is permitted which does not comply with these terms.

frontiers in Systems Neuroscience

ORIGINAL RESEARCH
published: 18 January 2022
doi: 10.3389/fnsys.2021.792665

Preceding Postural Control in Forelimb Reaching Movements in Cats

*Mirai Takahashi[1], Toshi Nakajima[2] and Kaoru Takakusaki[1]**

[1] Department of Physiology, Division of Neuroscience, Asahikawa Medical University, Asahikawa, Japan, [2] Department of Integrative Neuroscience, Faculty of Medicine, The University of Toyama, Toyama, Japan

Postural control precedes the goal-directed movement to maintain body equilibrium during the action. Because the environment continuously changes due to one's activity, postural control requires a higher-order brain function that predicts the interaction between the body and the environment. Here, we tried to elucidate to what extent such a preceding postural control (PPC) predictively offered a posture that ensured the entire process of the goal-directed movement before starting the action. For this purpose, we employed three cats, which we trained to maintain a four-leg standing posture on force transducers to reach the target by either forelimb. Each cat performed the task under nine target locations in front with different directions and distances. As an index of posture, we employed the center of pressure (CVP) and examined CVP positions when the cat started postural alteration, began to lift its paw, and reached the target. After gazing at the target, each cat started PPC where postural alteration was accompanied by a 20–35 mm CVP shift to the opposite side of the forelimb to be lifted. Then, the cat lifted its paw at the predicted CVP position and reached the forelimb to the target with a CVP shift of only several mm. Moreover, each cat had an optimal target location where the relationship between the cat and target minimized the difference in the CVP positions between the predicted and the final. In this condition, more than 80% of the predicted CVP positions matched the final CVP positions, and the time requiring the reaching movement was the shortest. By contrast, the forelimb reaching movement required a greater CVP shift and longer time when the target was far from the cat. In addition, the time during forelimb reaching showed a negative correlation with the speed of the CVP shift during the PPC. These results suggest that the visuospatial information, such as the body-environment interaction, contributes to the motor programming of the PPC. We conclude that the PPC ensures postural stability throughout the action to optimize the subsequent goal-directed movements. Impairments in these processes may disturb postural stability during movements, resulting in falling.

Keywords: postural control, higher order brain function, forelimb reaching, anticipatory postural adjustments, optimization

OPEN ACCESS

Edited by:
Jun Izawa,
University of Tsukuba, Japan

Reviewed by:
Tetsuro Funato,
The University of Electro-Communications, Japan
Eros Quarta,
Sapienza University of Rome, Italy

****Correspondence:***
Kaoru Takakusaki
kusaki@asahikawa-med.ac.jp

Received: *11 October 2021*
Accepted: *02 December 2021*
Published: *18 January 2022*

Citation:
Takahashi M, Nakajima T and Takakusaki K (2022) Preceding Postural Control in Forelimb Reaching Movements in Cats. Front. Syst. Neurosci. 15:792665. doi: 10.3389/fnsys.2021.792665

INTRODUCTION

Posture means the static position of any part of the body, and movements are the transition from one posture to another (Brooks, 1986). To achieve the goal-directed movement, there is a need to prepare an appropriate posture before the onset of the purposeful action and to maintain body equilibrium during ongoing movement so that the subject stabilizes the body's center of mass until the end of the task (Horak, 2006). Because movements accompany continuous changes in one's body and environment, a series of the postural control requires higher-order brain function in order to predict these changes. Accordingly, dysfunction of the higher-order brain functions due to aging and neural disorders is suggested to elicit gait failure and falling because of impairment of these postural control processes (Snijders et al., 2007). Then, the critical question is how such a "predictive and preparatory posture control" is accomplished. Anticipatory postural adjustment (APA) is known as an example of posture control that precedes purposeful action. Indeed, plenty of studies have been shown that the APA is disturbed when various neural structures, such as the cerebellum (Timmann and Horak, 2001; Bruttini et al., 2015), basal ganglia (Jacobs et al., 2009b; Ng et al., 2013), and cerebral cortex and their adjacent areas are damaged (Delafontaine et al., 2019). However, it has not been well understood how APA guarantees the postural equilibrium during and at the end of the subsequent goal-directed movement. Moreover, there was no substantial evidence of how the above brain structures regulate the APA. Accordingly, we still cannot describe the relationship between the disturbances in APA and damages in any brain structures resulting in falling.

It has been shown that APA is triggered not only by whole body movement such as step initiation (McIlroy and Maki, 1999; Delafontaine et al., 2019), but also by focal body movements such as upper limb rising (Belen'kii et al., 1967) and handle pulling (Cordo and Nashner, 1982). It is also observed in quadrupeds, such as rodents (Yamaura et al., 2013) and cats (Schepens and Drew, 2003). Regardless of whether human beings or animals, the APA is often expressed by postural reaction that resists changes in the center of gravity accompanying the movements. Using kinemato-dynamic measurement procedures, Hugon et al. (1982) and Varghese et al. (2016) temporally separated APA, which was characterized by the inverse postural reaction, from purposeful action of the entire movement. Accordingly, most studies have focused on the mechanisms of generating such an inversive reaction as a parameter of the APA. However, there was a report showing that younger healthy subjects without the inversive reaction maintained postural equilibrium well in response to the gait initiation (Hyodo et al., 2012), indicating that the inversive postural reaction is not necessary for APA. Therefore, neuronal mechanisms that generate "preceding postural control (PPC)," other than the inversive reaction may exist so that stable posture is ensured from the onset to the end of movements. We hypothesize that the mechanisms require satisfying the following two conditions. The first condition is that the posture offered by the PPC before starting the goal-directed movement ensures postural stability during and until the end of the movement. Namely, there is a need to predict and provide appropriate postural control for the whole period of the action before its starting. The second is that the PPC alters depending on the relationship between the subject and one's surrounding circumstances.

The present study was designed to verify the above hypothesis using cat experiments. For this purpose, we trained three cats to perform the forelimb reaching movement task from a four-leg standing posture. Then, we evaluated postural changes in the whole movement by investigating the changes in spatiotemporal parameters of the center of vertical pressure (CVP), an index of the center of gravity. Here, we tried to elucidate the following three issues. The first issue was to examine to what extent the PPC predicted the CVP position at the end of the reaching movement. The second was to investigate whether and how the PPC was altered depending on the spatial relationship between the target and the cat. It was also essential to examine whether each cat had an optimal target position where the cat achieved the task with high performance. Third, we tried to identify which spatiotemporal parameters of the PPC related to the degree of the task performance.

We demonstrated the following characteristics of the PPC in the forelimb reaching task in the cat. First, the PPC largely achieved postural alteration of the entire movement. Specifically, while the CVP shift during the PPC was more than 20 mm, it was several millimeters during the forelimb reaching. Second, not only were CVP positions altered by changes in the target position, but there was also an optimal target-subject condition in each cat where the difference in the CVP positions between the predicted and the final was the minimum. In this condition, more than 80% of the expected CVP positions matched the final CVP positions, and the time during the forelimb reaching was the shortest. Third, the time during reaching showed a negative correlation with the speed of the CVP shift during the PPC. These results suggest that motor programs based on cognitive visuomotor processing achieve both voluntary movement and the PPC. The PPC, therefore, may ensure a stable posture of the subsequent purposeful movement and affect its performance. The spatiotemporal parameters of PPC can be an index of postural stability and also, a fall-risk marker for predicting falls due to higher-order brain dysfunction. In a series of studies, we will elucidate in animal experiments how damage to various brain structures modifies PPC. This study is the first and fundamental study for that purpose.

MATERIALS AND METHODS

Animals

The study was based on three adult female cats, which weighed from 2.2 to 2.4 kg. These cats were obtained from a laboratory animal supplier and bred at the animal facility of Asahikawa Medical University, where they were kept in individual cages under constant temperature and light-dark cycles. All the procedures of the present experiments were approved by the Animal Studies Committee of Asahikawa Medical University (approval number; R3-116) and were following the Guide for the Care and Use of Laboratory Animals (NIH Guide), revised 1996.

Experimental Setup

The cat maintained a standing posture in the platform and performed forelimb reaching movements to the target in front (**Figure 1**). The ground reactive force exerting in each foot was measured by force transducers (TEAC, with sampling rate of 10 kHz) placed beneath each foot. The length of a side of each transducer was 40 mm in which size was just enough to place each foot. Four transducers were placed on a horizontal plane so that the centers of them formed a rectangle with its antero-posterior and left-right edges spanning 180 mm and 100 mm, respectively. This setup allowed the cat naturally maintain its standing posture. A food pellet, which is the target, was put into a cylinder (30 mm diameter) fixed to the board in front, and the cat reached the target by either forelimb. In a standard condition, the target location was 240 mm in the distance from the forelimb force transducers with a height of 150 mm, mainly equal to the cats' shoulders. In addition, we investigated how the cat's postural control altered during the forelimb reaching task in response to changes in the target's spatial position, which we moved in the left-right and anterior-posterior directions with 50 and 20 mm, respectively. We detected the moment the forelimbs reached the touch sensor, which was fixed to the back of the board and attached to the feeding cylinder.

Recordings, Measurements, and Parameters

We trained the cats three times a week for 3 months or more until the cat steadily performed the reaching task. After that, the experiment was carried out three times a week. A fasting period of 0.5–1 day was set the day before the experiment, paying attention to the weight fluctuation and health of the cat. Each experimental session continued as long as the cat tackled the task. Changes in ground reactive force of all trials of the forelimb reaching task were recorded in LabChart software by PowerLab system (AD Instruments) and stored in the hard disk for later off-line analyses. In addition, we simultaneously recorded the dorsal and lateral views of the cat's movements by the Powerlab system at a rate of 30 frames/s (**Figure 1**).

Figure 2 shows an example of polygraphic recordings of a forelimb reaching movement, which was composed of three phases as "stabilizing posture," "PPC," and "reaching movement." In the first stabilizing posture phase, the cat kept stabilizing posture by attending to the food pellet as a target put into the cylinder. The second PPC phase corresponded from the onset of postural change (a dashed line with a filled circle) to either forelimb's paw lift (**Figure 2Aa**). When the ground reactive force became zero, we determined this moment as paw lift (a dashed line with a blue circle). Finally, we defined the period from the paw lift to the target reach as the reaching movement phase. The touch sensor signal (indicated by a dashed line with a red circle) indicated the end of the task. Then, the cat dropped the food pellet on the tray in front to get the reward. The cat, after that, again took stabilizing posture so that it started the subsequent trials. Thus, we changed target conditions every 30 trials. We further determined the period that required the PPC as "preceding postural control time (Pt)" and that to the forelimb reaching movement as

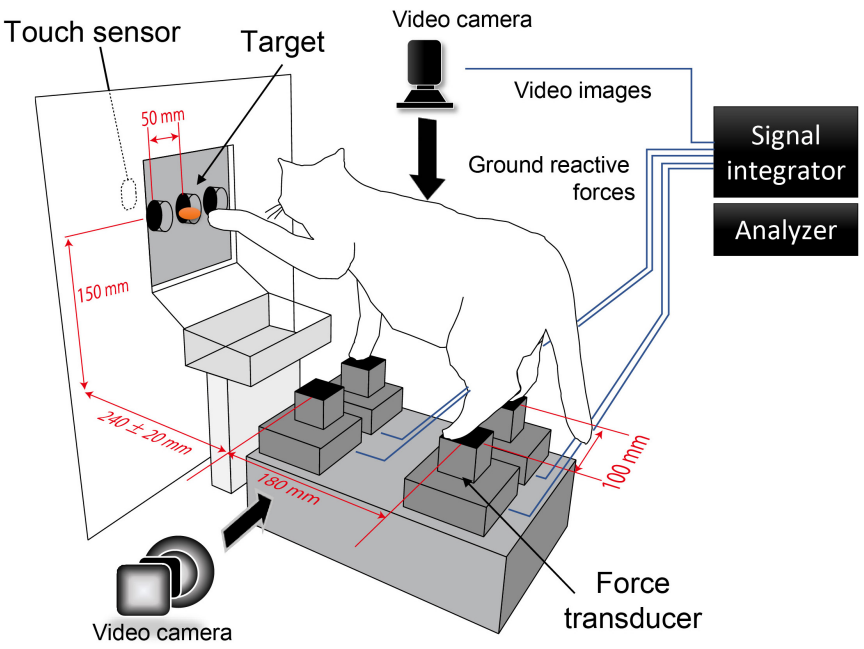

FIGURE 1 | Experimental setup. The cat maintained a standing posture in the platform and performed forelimb reaching movement to the target in front. The task was performed under the nine different target conditions (distance: 240 ± 20 mm, direction: center, left 50 mm, right 50 mm). The ground reactive force and the video from dorsal and lateral views were integrated and recorded by the signal integrator. The moment of target reaching was detected by the touch sensor installed behind the target.

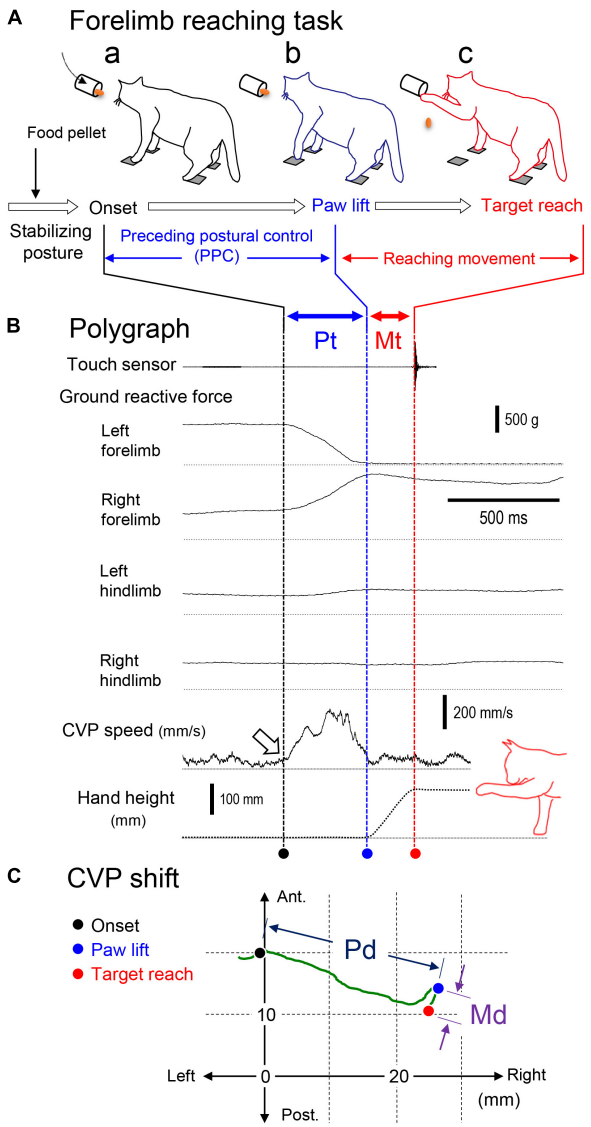

FIGURE 2 | Recordings, measurements, and parameters of the forelimb reaching task of the cat. **(A)** Illustrated cat figures of the forelimb reaching task at the onset of the preceding postural control **(a)**, paw lift **(b)**, and target reach **(c)**. The task was composed of three phases as "stabilizing posture," "preceding postural control (PPC)," and "reaching movement." **(B)** Polygraphic recordings of the task. Vertical lines and circles below the with different colors indicate the moment of onset (black), paw lift (blue), and target reach (red). The periods of time from the onset to paw lift and from the paw lift to target reach were determined as postural time (Pt) and movement time (Md), respectively. **(C)** The shift of the center of vertical pressure (CVP) in the above trial. Circles with different colors indicate positions of the CVP at onset (black), paw lift (blue), and target reach (red). The distance of the CVP between the onset and paw lift was determined as postural distance (Pd), and that between the paw lift and target reach was determined as movement distance (Md).

"movement time (Mt)." The center of vertical pressure (CVP), a parameter of the center of gravity, was calculated by the following equation from the ground reactive forces generated by each of four force transducers. We used changes in CVP positions associating with the forelimb reaching task as the index of posture change.

$$\mathbf{CVP} = (\mathbf{CVP}_{LR}, \mathbf{CVP}_{AP})$$

$$CVP_{LR} = \frac{F_{rFL} + F_{rHL} - F_{lFL} - F_{lHL}[\mathrm{kg \cdot m/s^2}]}{M_{cat}g[\mathrm{kg \cdot m/s^2}]} \times 50\,[\mathrm{mm}]$$

$$CVP_{AP} = \frac{F_{lFL} + F_{rFL} - F_{lHL} - F_{rHL}[\mathrm{kg \cdot m/s^2}]}{M_{cat}g[\mathrm{kg \cdot m/s^2}]} \times 90\,[\mathrm{mm}]$$

The distance between the centers of the force transducers were 100 mm for the left-right direction, and 180 mm for the antero-posterior direction. Therefore, the coordinates of the CVP positions were calculated by multiplying the distributions of the ground reaction force in the left-right and antero-posterior direction by 50 and 90 mm, respectively. CVP_{LR}, CVP at the left-right direction on the horizontal axis; CVP_{AP}, CVP at the anterior-posterior direction on the vertical axis; F_{rFL}, ground reactive force at the right forelimb; F_{rHL}, ground reactive force at the right hindlimb; F_{lFL}, ground reactive force at the left forelimb; F_{lHL}, ground reactive force at the left hindlimb; M_{cat}, body weight of the cat.

To characterize the postural control of the forelimb reaching task, we selected positions of CVP at the moments of the "onset" of postural changes, namely, "paw-lift" and "target-reach" (**Figure 2C**). Then, we calculated the distance between these CVP positions according to the coordinates. Moreover, we defined the difference in CVP positions between "onset (a filled circle)" and "paw-lift (a blue circle)" as "a CVP distance for preceding postural control (Pd)," and that between "paw-lift (a blue circle)" and "target-reach (a red circle)" as "a CVP distance for postural control associating with reaching movement (Md)." Similarly, we defined the periods requiring the preceding postural control and the forelimb reaching movement as preceding postural control time (Pt) and movement time (Mt), respectively. We also defined the mean speed of CVP shift during the PPC and forelimb movement as postural CVP speed (P-CVPs) and movement CVP speed (M-CVPs), respectively. The P-CVPs and M-CVPs were calculated by Pd/Pt and Md/Mt, respectively. As indicated by an open arrow in **Figure 2B**, the rapid increase in the CVP speed corresponded to the onset of the PPC.

Statistics

We employed R [R Core Team (2018). R: A language and environment for statistical computing. R Foundation for Statistical Computing, Vienna, Austria][1] for all statistical analyses. The mean value is expressed by mean ± standard deviation (SD). We judged the case where the p-value was less than 0.05 as significant. When conditions were with different target locations, we used the distance of the targets in the anterior-posterior direction (240 mm ± 20 mm) and left-right direction (50 mm left or right) as explanatory variables to

[1]https://www.R-project.org/

examine the statistical significance of each parameter. Student's *t*-test was used to compare the changes in each parameter under two specific conditions. In addition, Pearson's correlation coefficient was calculated to investigate the relationship between the parameters under the nine target conditions. Those whose absolute value of the correlation coefficient was more than 0.4 and were significant were judged to be correlated (Evans, 1996). We calculated the 95% confidence interval of the CVP distributions at each moment (Onset, Paw lift, and Target reach) and displayed it as a confidence ellipse.

RESULTS

Preceding Postural Control Began With a Decrease in the Load on the Forelimb to Be Lifted

As described in introduction, most studies so far focused on the inversive kinetic reaction, which is characterized by the transient load increase acting on the forelimb to be lifted, as is the APA. However, through the period of this study, we have encountered many trials without such a transient loading. One example of the forelimb reaching task in the same cat are shown in **Figure 3**. The trial in **Figure 3A** showed a transient increase in the ground reactive force exerting the left forelimb (indicated by an arrow), which preceded the onset of the PPC. The temporary load increase reflected the CVP shift from the first position (an open circle) to the left with a distance of approximately 10 mm. However, a trial in **Figure 3B** did not exhibit such an apparent transient loading. Whether the transient loading increase existed or not, the PPC, characterized by unloading the left forelimb and loading the right forelimb, started. The times required to the PPC (Pt) were 125 and 150 ms for trials (A) and (B), respectively. The changes in the loading of the forelimbs and those of the hindlimbs evoked a rapid increase in the shift of CVP speed during the PPC. For trial (A), the maximum speed of the CVP shift was 475 mm/s with a mean CVP speed (P-CVPs) of 217 mm/s. These were 503 and 156 mm/s for (B). During this period, CVP moved the position from a filled circle to a blue circle. For (A), the CVP moved to the right and anterior directions with 27 and 3 mm, respectively. For (B), it moved to 22 mm right and 8 mm posterior. Therefore, a CVP shift during PPC, which corresponded to the Pd, was calculated as 27.2 mm for (A) and 23.4 mm for (B). Then, the PPC was followed by forelimb movements. The Mt and Md were 140 ms and 5.2 mm, respectively, for (A). They were 155 ms and 2.8 mm for (B). The mean CVP movement speed (M-CVPs) was 37 mm/s for (A) and 18 mm/s for (B). Accordingly, the Md and M-CVPs were much smaller than Pd and P-CVPs, respectively. While we examined more than 2,500 trials in three cats, the trials that accompanied the transient loading before the PPC was less than 60%. It was observed to be 56.9% (338/594 trials) for Cat 1, 57.1% (432/756 trials) for Cat 2, and 26.8% (316/1227 trials) for Cat 3. These findings indicate that the presence of the inversive postural reaction is not essential for PPC. Therefore, we defined that the PPC began with a reduction of the load on the forelimb to be lifted regardless of the presence or absence of the inversive reaction. Then, we performed the subsequent analysis according to this definition.

Parameters of Center of Vertical Pressure During Forelimb Reaching Task

Next, we investigated whether the changes in spatiotemporal parameters associated with CVP shifts were common to all animals. Examples are shown in **Figure 4** where each cat achieved the forelimb reaching movement to the target at the mid-left location (an arrow in **Figure 4A**). Traces in **Figure 4B** showed CVP shift in 10 consecutive trials of the forelimb reaching task of Cat 1. Before starting PPC, each CVP (CVP_{onset}; filled circles) was distributed between 20 and 40 mm in the anterior-posterior coordinate and −20 and 8 mm in the left-right coordinate. When starting the PPC, CVP shifted 25–35 mm in the right-posterior direction to the position where paw lift would occur (CVP_{lift}; blue circles). Thus, the positions of the CVP_{lift} in 10 trials existed within the limited area surrounded by the coordinates of the 22–35 mm right and 15–33 mm anterior. Then, the cat started lifting the paw to extend the forelimb so that the CVP shifted to the position where the cat reached the target (CVP_{reach}; red circles). Despite dynamic limb movements in this process, CVP in any trial only moved within a few millimeters.

Using this procedure, we investigated the changes in CVP positions of the forelimb reaching the same target location in the three cats. Each graph in **Figure 4C** shows CVP_{onset} (black cross mark), CVP_{lift} (blue cross mark), and CVP_{reach} (red cross mark) together with translucent colored ellipses that indicate 95% areas of confidence for Cat 1 (left), Cat 2 (center), and Cat 3 (right). In each, these diamond marks with different colors indicate average positions of the CVP of all trials at each moment of interest. While the average positions of the CVP_{onset} (diamonds) in each cat primarily existed at 5–10 mm to the left, those were different in the anterior-posterior direction. They were approximately 32, 9, and 21 mm rostral to the reference point for the Cats 1, 2, and 3, respectively. Moreover, the size of the 95% areas of confidence for CVP_{onset} (light gray) differed among the animals. It was approximately 940 mm^2 for Cat 1, 1,200 mm^2 for Cat 2, and 2,100 mm^2 for Cat 3. Compared to the CVP_{onset}, the size of the areas consisting of the CVP_{lift} and CVP_{reach} were much smaller. For Cat 1, 2, and 3, the CVP_{lift} areas (faded blue) were approximately 210, 310, and 360 mm^2 and the CVP_{reach} areas (faded red) were about 190, 200, and 290 mm^2 in size, respectively. We further observed that the two areas considerably overlapped in each cat (**Figure 4C**). For example, when we counted the number of CVP_{lift} (blue cross mark) within areas of 95% confidence of CVP_{reach} (faded red), it was found to be 56 out of 69 (81%) for Cat 1, 59 out of 71 (83%) for Cat 2, and 93 out of 112 (83%) for Cat 3. We defined these percentages as the matching score of the CVP_{lift} and CVP_{reach}. That is, as shown in **Figure 4E**, they were 0.81, 0.83, and 0.83 in Cats 1, 2, and 3, respectively.

In **Figure 4D**, we compared spatiotemporal parameters of CVP shift in each cat during the PPC and during forelimb reaching in the upper and lower graphs, respectively. The mean

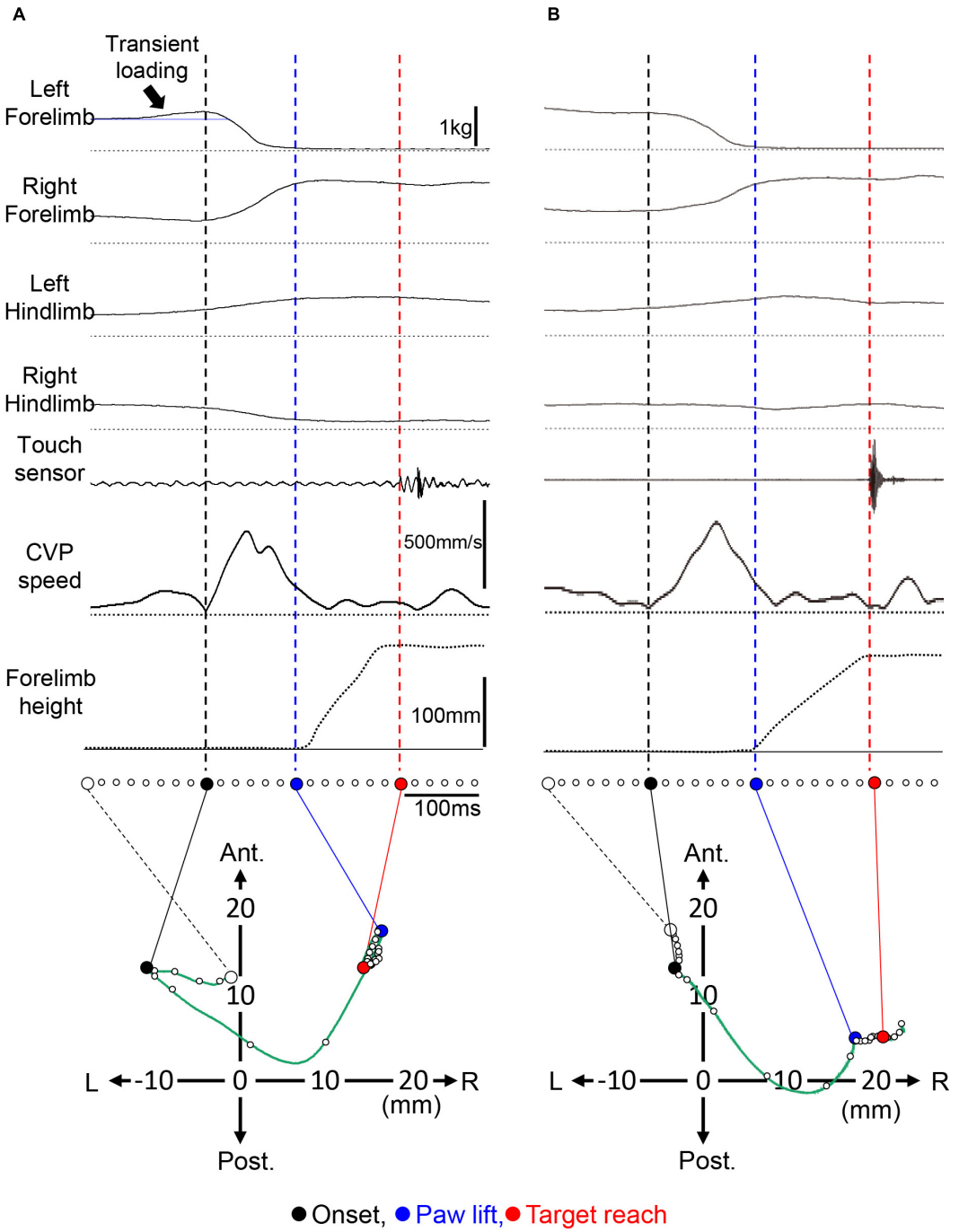

FIGURE 3 | Forelimb reaching movement with and without transient loading of the forelimb before PPC. **(A)** An example of the trial with a transient. An arrow indicates the transient loading. The presence of the loading was reflected by the CVP shift before the onset of the PPC from an open circle to a filled circle. An open circle in the CVP shift indicates the CVP position at the stabilizing posture of the cat before the onset of the transient loading. **(B)** A representative trial without the transient loading. The format is the same as panel **(A)**. L, left; R, right; Ant, anterior; Post, posterior.

distance of CVP shift in each cat was more than 25 mm during the PPC (Pd). However, it was less than 6 mm during forelimb movement (Md) (left in **Figure 4D**), indicating that postural change during forelimb reaching was more petite than during PPC. Concerning times requiring for the PPC (Pt) and forelimb movement (Mt), the former was longer than the latter in each cat (center in **Figure 4D**). Moreover, CVP speed during PPC (P-CVPs) was much faster than that during forelimb movement (M-CVPs) in each animal (right in **Figure 4D**). These common findings in the three cats suggest that the cat did not evoke significant postural change during the goal-directed movement, but had achieved appropriate postural alteration during PPC even

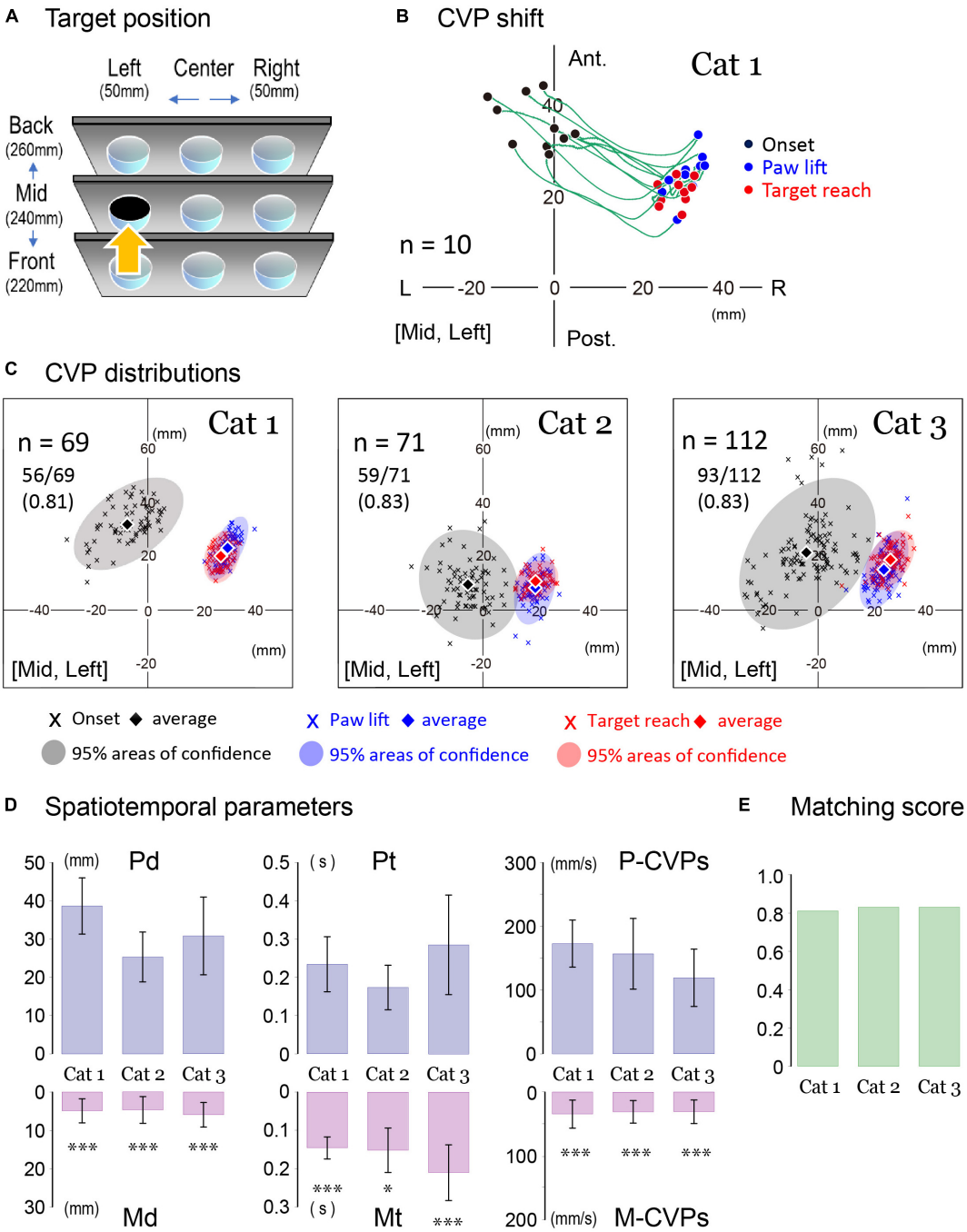

FIGURE 4 | Parameters of forelimb reaching task. **(A)** An arrow indicates a target location. **(B)** CVP shifts of ten consecutive trials of the left forelimb reaching movement in Cat 1. The CVP positions at the onset of PPC, paw lift, and target reach were indicated by black, blue, and red circles. The green lines are the trajectory of the CVP shift in each trial. **(C)** The distributions of CVP at each moment in three cats. Cross marks indicate CVP positions in each moment with different colors (onset: black, paw lift: blue, target reach: red). Translucent colored ellipses represent 95% areas of confidence. Diamonds indicate the average position of the CVP at each moment. **(D)** From left to right, comparisons were made between Pd and Md (left), Pt and Mt (center), and postural CVP speed (P-CVPs) and movement CVP speed (M-CVPs). These data were obtained from 69 trials in Cat 1, 71 trials in Cat 2, and 112 trials in Cat 3. The Pd was 38.6 ± 7.4 mm for Cat 1, 25.3 ± 6.5 mm for Cat 2, and 30.8 ± 10.2 mm for Cat 3. The Md was 4.9 ± 3.1 mm for Cat 1, 4.7 ± 3.5 mm for Cat 2, 5.9 ± 3.2 mm for Cat 3. The Pt was 0.234 ± 0.072 s for Cat 1, 0.173 ± 0.058 s for Cat 2, and 0.285 ± 0.130 s for Cat 3. The Mt was 0.146 ± 0.029 s for Cat 1, 0.152 ± 0.058 s for Cat 2, and 0.210 ± 0.073 s for Cat 3. P-CVPs and M-CVPs were 173 ± 37 mm/s and 34.5 ± 21.9 mm/s for Cat 1, 157 ± 55 mm/s and 30.9 ± 17.7 mm/s for Cat 2, 119 ± 45 and 30.7 ± 18.4 mm/s for Cat 3, respectively. In each cat, there was a significant difference between Pd and Md, Pt and Mt, and P-CVPs and M-CVPs for each cat. The bar plots show each spatiotemporal parameter in each cat. Box and bar indicate the Mean ± SD. Asterisk(s) indicate a significant difference. $^{*}p < 0.05$, $^{***}p < 0.001$. **(E)** Matching score of CVP at paw lift and CVP at target reach in three cats. L, left; R, right; Ant, anterior; Post, posterior.

before forelimb movement. In addition, because the matching score was more than 0.8 (**Figure 4E**), we postulate that the cat had already predicted to determine posture at the target reaching (CVP_{reach}) until lifting its forelimb (CVP_{lift}) with a much higher probability.

Changes in Spatiotemporal Parameters of the Center of Vertical Pressure Induced by Different Target Conditions

Next, we examined whether and how the difference in the target location altered the entire process of the forelimb reaching. Then, each cat performed the forelimb reaching movement to the nine targets placed at different locations in the rostrocaudal and left-right directions. Representative findings are shown in **Figures 5A,B**, where Cat 2 reached the target at "left-front" and "right-back" locations, respectively. Against the left-front target condition, the cat started the task with a PPC time (Pt) of less than 0.15 s and a CVP speed of 300–600 mm/s. Subsequently, the cat reached the target with a movement time (Mt) between 0.09 and 0.13 s (**Figure 5Ab**). Concerning the CVP position (**Figure 5Ac**), the CVP_{onset} of each trial (filled circles) was broadly distributed. During the PPC, they moved a distance of 20–30 mm in right or right-posterior directions to gather to the area of 15–25 mm right and ∼10 mm anterior to the coordinate to arrive at the CVP_{lift} positions (blue circles). Subsequently, each CVP moved approximately 3 mm, arriving at the positions of the CVP_{reach} (red circles). The distribution of the CVP_{onset}, CVP_{lift}, and CVP_{reach} of 99 trials in this condition are illustrated in **Figure 5Ad**. The average position of the CVP_{onset} was 8.6 mm left and 8.7 mm anterior to the coordinate (filled diamond). A gray colored circle corresponded to the area of 95% confidence with a radius of 20 mm centered on the point representing the average CVP_{onset} position. On the other hand, areas representing the distribution of the CVP_{lift} and CVP_{reach} were smaller than the area of the CVP_{onset}. The average position of the CVP_{lift} was 16.2 mm right with 2.6 mm anterior, and that of the CVP_{reach} was 15.5 mm right with 5.0 mm anterior. Because of their close positions, there was considerable overlap, or matching, between these two areas.

In the "right-back" target condition (**Figure 5Ba**), the cat required approximately 0.2 s for the PPC and 0.2 s for the subsequent forelimb movement (**Figure 5Bb**). The CVP speed during the PPC (P-CVPs) was less than 300 mm/s. Along with the PPC progress, the CVP of the five trials first moved to the right and then turned to the anterior direction so that the CVP arrived at the CVP_{lift} position (**Figure 5Bc**). The forelimb movement further took the CVP position 5–10 mm forward to achieve the movement, resulting in the separation of the CVP_{lift} and CVP_{reach} positions. **Figure 5Bd** shows distributions of each CVP position of 48 trials. The average positions were 2.8 mm left and 9.2 mm anterior for the CVP_{onset}, 19.6 mm right and 9.7 mm anterior for the CVP_{lift}, and 20.9 mm right and 19.7 mm anterior for the CVP_{reach}. Consequently, the average CVP_{onset} was approximately 6 mm to the right in the right-back condition compared to the left-front condition. Moreover, the average CVP_{lift} and CVP_{reach} positions in the latter condition were approximately 7 and 15 mm anterior to the former condition, respectively. Thus, in the latter condition, the distributions of CVP_{lift} (faded blue) and CVP_{reach} (faded red) had a slight overlap, or were less matching, which reflected the considerable difference of 10 mm between the average CVP positions at the lift (blue diamond) and reach (red diamond).

We compared parameters between the above two conditions during the PPC (**Figure 5C**) and forelimb movements (**Figure 5D**). The distance of the CVP shift during PPC (Pd) was longer ($p < 0.01$, *t*-test) in the left-front condition (26.6 ± 7.3 mm, $n = 99$) than in the right-back condition (22.8 ± 7.8 mm, $n = 48$, **Figure 5Ca**). On the other hand, there was no difference in the time required for PPC (Pt) between the two conditions (0.161 ± 0.068 s, $n = 99$ for left-front; 0.175 ± 0.062 s, $n = 48$ for right-back, **Figure 5Cb**). The speed in the CVP during the PPC (P-CVPs) was, accordingly, faster ($p < 0.001$, *t*-test) in the left-front condition (179 ± 59 mm/s, $n = 99$) than right-back condition (138 ± 45 mm/s, $n = 48$; **Figure 5Cc**). During forelimb movement, the former condition showed a shorter ($p < 0.001$, *t*-test) distance of the CVP shift (Md, 4.1 ± 2.8 mm, $n = 99$, **Figure 5Da**), a shorter ($p < 0.001$, *t*-test) period of the time (Mt, 0.118 ± 0.058s, $n = 99$, **Figure 5Db**), and faster ($p < 0.001$, *t*-test) speed in the CVP shift (M-CVPs, 41 ± 29 mm/s, $n = 99$, **Figure 5Dc**) than the latter condition (10.4 ± 4.3 mm, $n = 48$ for Md, 0.168 ± 058 s, for Mt, and 66 ± 29 mm/s, $n = 48$ for M-CVPs). The matching score, which was the number of CVP_{lift} relative to the number of CVP_{reach} in the red colored area, was 86% in the former condition. However, it was only 46% in the latter. Therefore, the difference in the target location altered spatiotemporal parameters relating to both the PPC and forelimb movement.

Presentation of the targets with different locations considerably altered forelimb reaching task parameters in Cat 2. Then, we tried to answer whether targets at different positions modified the parameters of the other two animals. It was further critical to elucidate what parameter changes were common to all three animals.

Changes in the Distribution of Center of Vertical Pressure Induced by Different Target Conditions

Figure 6 and **Table 1** showed that different target conditions altered CVP positions of interest in all three cats. Specifically, the CVP_{lift} (blue) and CVP_{reach} (red) moved forward in all cats by moving the center target from front to back (**Figures 6Aa–c**). Similarly, the CVP_{lift} (blue) and CVP_{reach} (red) moved to the right in all cats when positions of the target in the front row moved from left to right (**Figures 6Ba–c**). In addition, CVP_{onset} (black) also moved forward or to the right in Cats 1 (**Figures 6Aa,Ba**) and 2 (**Figures 6Ab,Bb**) in the above two conditions. However, the CVP_{onset} of Cat 3 (**Figures 6Ac,Bc**) did not move in either target condition.

The above findings suggest that changes in CVP_{lift} and CVP_{reach} in the three cats shifted depending on the target location alterations. The findings also support our hypothesis that CVP_{lift} can be offered in anticipation of CVP_{reach}. Moreover, the CVP_{onset} of Cats 1 and 2, but not Cat 3, changed depending on the

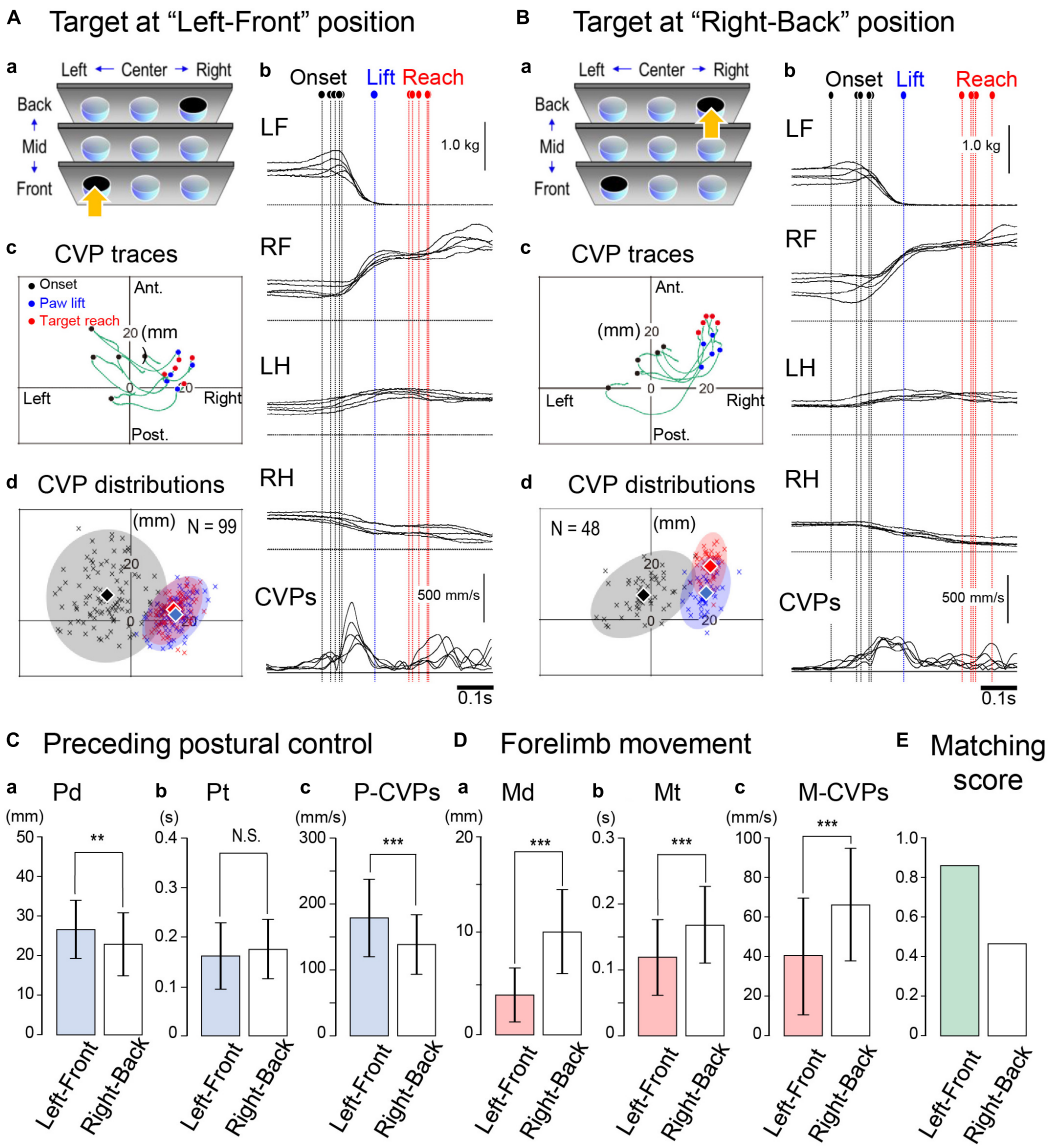

FIGURE 5 | Changes in spatiotemporal parameters of the CVP induced by different target conditions. **(A)** Forelimb reaching the target at the "left-front" location. **(a)** The arrow indicates the target location. **(b)** Polygraphic recordings of consecutive five trials, which were aligned at the paw lift. Colored dashed lines indicate the moments of onset (black), paw lift (blue), and target reach (red). **(c)** Traces of CVP shifts in the five trials. Each circle indicates the CVP position at each moment. **(d)** The CVP distribution of 99 trials in this target condition. Translucent colored ellipses represent 95% areas of confidence. The diamonds indicate the average position of the CVP at each moment. **(B)** Forelimb reaching the target at the "right-back" location. From panels **(a–d)**, data are presented in the same format as panel **(A)**. **(C)** Comparison of parameters relating to the PPC between the two conditions. Panels **(a–c)** are Pd, Pt, P-CVPs, respectively. **(D)** Comparison of parameters relating to the forelimb movement between the two conditions. Panels **(a–c)** are Md, Mt, and M-CVPs, respectively. **(E)** Comparison of matching scores between the two conditions. Box and bar indicate the Mean ± SD. Asterisk(s) indicate a significant difference. $^{**}p < 0.01$, $^{***}p < 0.001$.

target condition difference. Therefore, the difference in the target conditions may also affect waiting or stabilizing posture before starting the PPC.

Comparison of All Parameters That Altered Depending on the Difference in Target Conditions

Finally, we elucidated the optimal target location for each cat to achieve the task with the most stable posture. The optimal target location can be determined by investigating to what extent PPC offered the CVP_{lift} that matched the location of the CVP_{reach}. It is also critical to identify spatiotemporal parameters contributing to the optimal postural control common to all three cats. To clarify these issues, we visualized the changes in the parameters depending on the different target conditions using shades of colors, as shown in **Figure 7**.

Figure 7A shows the matching score. This was 0.62–0.91 for Cat 1, 0.46–0.86 for Cat 2, and 0.70–0.85 for Cat 3. When the

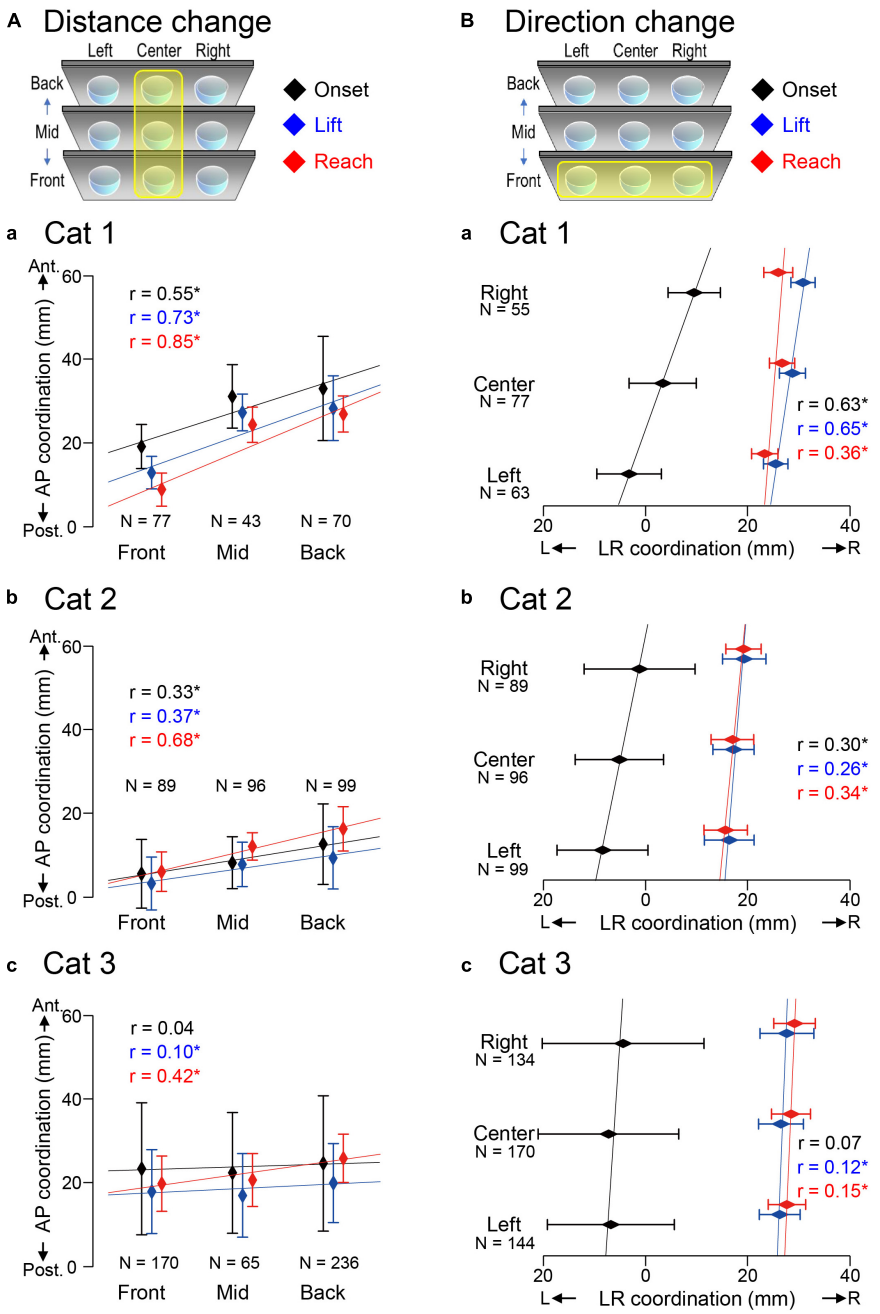

FIGURE 6 | Alterations of CVP induced by different target conditions. **(A)** Alterations in CVP on the anterior-posterior coordination depending on the different target distances. Each rhombus and bar indicate the Mean + SD of CVP, at the moment of onset (black), paw lift (blue) and target reach (red). Each regression line represents the target condition as the explanatory variable and CVP as the objective variable. "*r*" indicates the correlation coefficient. **(B)** Alterations in CVP on the Left-Right coordination depending on the different target directions. The format is the same as panel **(A)**. Asterisk indicate a statistical significance of $p < 0.05$.

target was at the left-front, the matching score of all cats was higher than 85%. On the other hand, the target location at the right-back reduced the matching in each cat. In **Figures 7B–G**, we set 1.0 for the mean value of each parameter under the reference target location at the mid-center. Then, each parameter under other eight target locations was expressed as a relative value against the reference condition. Changes in the target locations considerably altered each parameter. The Pd, which is the distance shift during PPC, changed in the range of 0.79–1.36 for Cat 1, 0.91–1.15 for Cat 2, and 1.00–1.48 for Cat 3 (**Figure 7B**). In Cat 1, the Pd was relatively small when targets were placed in the right, but it was rather large when the targets were placed in the left. While Pd in Cat 2 exhibited a small change with a relative value of less than 1.15 under any target locations, Cat 3 had a

TABLE 1 | Correlation coefficients between target conditions and center of vertical pressure (CVP) positions.

		Target conditions (explanatory variable)					
		Distance (Front - Mid - Back)			Direction (Left - Center - Right)		
Cat number		Cat1	Cat2	Cat3	Cat1	Cat2	Cat3
CVP							
CVP_{onset}	L⇔R	0.22*	0.05	0.14*	0.63*	0.30*	0.07
	A⇔P	0.55*	0.33*	0.04	0.05	−0.26*	−0.07
CVP_{lift}	L⇔R	0.60*	0.11	0.15*	0.65*	0.26*	0.12*
	A⇔P	0.73*	0.37*	0.10*	0.39*	0.07	0.02
CVP_{reach}	L⇔R	0.59*	0.30*	0.31*	0.36*	0.34*	0.15*
	A⇔P	0.85*	0.68*	0.42*	0.15*	0.42*	0.16*
							*$p < 0.05$
		Number of trials in each target condition					
		Front	Mid	Back	Left	Center	Right
Cat 1		77	43	70	63	77	55
Cat 2		96	98	75	99	96	89
Cat 3		170	65	236	144	170	134

rather large value of more than 1.20 for target locations other than the mid-center and mid-right. Moreover, target locations with the smallest and largest Pd were different in each cat. The Pt, which corresponded to the time requiring PPC, was in the ranges of 0.80–1.07 for cat 1, 0.81–1.00 for cat 2, and 0.89–1.14 for cat 3 (**Figure 7C**). While targets in the front row exhibited a relative value of less than 0.9 in all cats, target locations with the smallest and largest Pt differed among the three animals. The P-CVPs, a mean CVP speed during PPC, changed in the range of 0.91–1.38 for Cat 1, 0.96–1.31 for Cat 2, and 0.92–1.56 for Cat 3 (**Figure 7D**). When the target was placed at the mid-right, all three cats exhibited the smallest value. However, the target location with the largest value differed among the animal.

The relative value of Md, a distance of CVP shift during forelimb movement, changed in the range of 0.87–1.59 for Cat 1, 0.70–1.76 for Cat 2, and 0.85–1.55 for Cat 3. It was the minimum for all three cats when the target location was left-front (**Figure 7E**). In addition, the relative value became large for all cats when targets were located at the right. The relative value of Mt, a time requiring forelimb movement, changed in the range of 0.84–1.20 for Cat 1, 0.67–1.02 for Cat 2, and 0.72–1.06 for Cat 3. Notably, the relative value of Mt was the minimum for all three cats when the target location was at the left-front (**Figure 7F**). On the other hand, when the target locations were at the right, Mt was rather large in all cats. The relative value of the CVP speed during forelimb movement (M-CVPs) was 1.0–1.36 for Cat 1, 0.85–1.92 for Cat 2, and 1.0–1.74 for Cat 3 (**Figure 7G**). Like the Md and Mt, while M-CVP was relatively large when the target locations were at the right, no target locations exhibited either the smallest or largest value common to the three cats. Altogether, common to all three animals, the matching score was higher in the left-front target, where the Mt and Md was the minimum, indicating that this target location was the most preferred and the optimal for each cat's forelimb reaching movement task.

Since the forelimb reaching movement is triggered following the PPC, it is reasonable to assume that the PPC-related parameters determine the parameters of the forelimb reaching movement. We then examined the relationship between the PPC-related parameters and the movement-related parameters. Results are show in **Figure 8**. Between spatial parameters, such as Pd and Md, there was significant negative correlations between in Cats 1 ($r = -0.70$, $p = 0.035$) and 2 ($r = -0.67$, $p = 0.050$), but not in Cat 3 ($r = 0.44$, $p = 0.241$; **Figure 8A**). Between temporal parameters Pt and Mt, Cat 1 had a significant correlation ($r = -0.67$, $p = 0.051$), but Cat 2 ($r = 0.68$, $p = 0.046$) and Cat 3 ($r = 0.69$, $p = 0.039$) exhibited positive correlations (**Figure 8B**). Between P-CVPs and M-CVPs, parameters of CVP movement speed, no correlation was found in Cats 1 ($r = -0.28$, $p = 0.467$) and Cat 2 ($r = -0.07$, $p = 0.852$). However, Cat 3 showed a positive correlation ($r = 0.78$, $p = 0.014$; **Figure 8C**). Accordingly, no parameters in the same dimension existed common to all animals between the two postural control processes in the forelimb reaching task. Therefore, as shown in **Table 2**, we further made correlation analyses between all above parameters (**Figure 8D**). Eventually, we found it exists that only a combination of P-CVPs and Mt had a strong negative correlation in the 3 animals ($r = -0.67$, $p = 0.048$ for Cat 1, $r = -0.98$, $p < 0.001$ for Cat 2, $r = -0.68$, $p = 0.043$ for Cat 3).

DISCUSSION

Experiment Design and Its Limitation

Many studies reported on the mechanisms of APA. Before the onset of the goal-directed actions, the APA had a role in canceling the postural sway of whole body and local body parts caused by the movements (Massion, 1992). The APA was observed just before the initiation of bipedal gait in humans

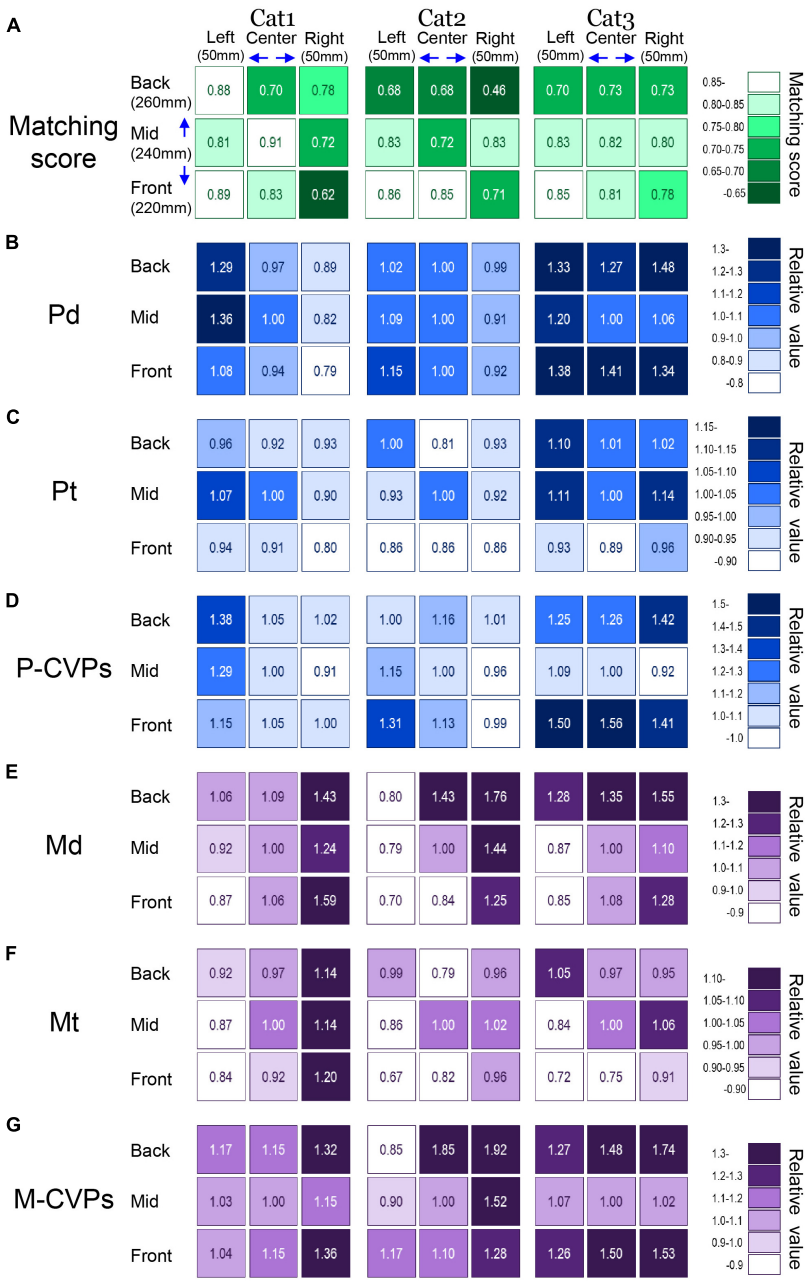

FIGURE 7 | Comparison of all parameters that altered depending on the difference in target conditions. **(A)** Matching scores in each target condition of three cats. Panels **(B–G)** show the relative value of each spatiotemporal parameter when the mean value in the standard target condition (Mid-Center) is 1.0. See text for detailed explanations.

(Boisset and Do, 2008), the lifting up of either forelimb of cats (Gahéry et al., 1980; Birjukova et al., 1989), and the initiation of the forelimb reaching of the cat (Alstermark and Wessberg, 1985). Schepens and Drew (2003) measured the ground reactive force exerting on the cat extremities together with electromyograms (EMGs) of four legs so that they determined the APA. As a result, the transient load increase that occurred immediately before lifting the paw of the forelimb facilitated the movement of the CVP to the contralateral side, and the authors considered this as the APA in the cat forelimb reaching movement. A transient load increase in the forelimb to reach the target was also observed (**Figures 3A**, **5**) in this study. At the beginning, we focused on the mechanism of generating this inversive postural reaction. However, the magnitude and time of this reaction differed from trial to trial in any cat, even when the target location was changed. Consequently, we detected the apparent inversive reaction in less than 60% of trials.

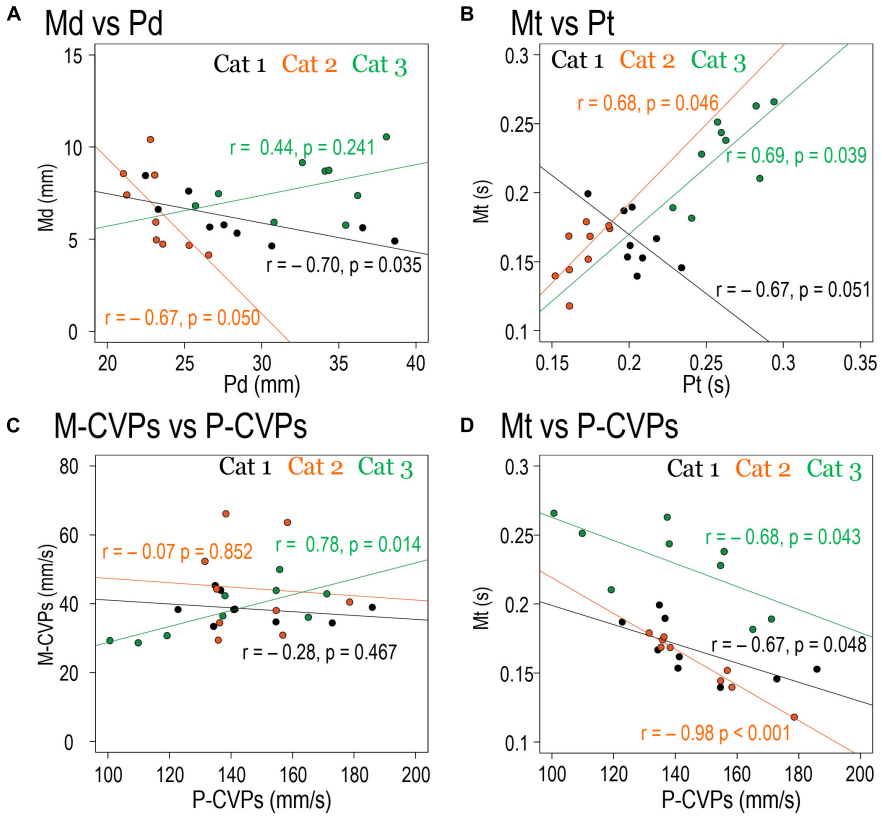

FIGURE 8 | The Relationships between parameters. Each scatters plot shows the correlation between the mean values of each spatiotemporal parameter under nine target conditions of three cats. **(A)** Relationships between Pd and Md. **(B)** Relationships between Pt and Mt. **(C)** Relationships between P-CVPs and M-CVPs. **(D)** Relationships between P-CVPs and Mt.

TABLE 2 | Correlation coefficients between parameters of posture and movement.

	Parameters of movement								
	Md			**Mt**			**M-CVPs**		
Cat number	**Cat1**	**Cat2**	**Cat3**	**Cat1**	**Cat2**	**Cat3**	**Cat1**	**Cat2**	**Cat3**
Parameters of posture									
Pd	−0.70*	−0.67	0.44	−0.77*	−0.73*	−0.50	−0.56	−0.40	0.86*
Pt	−0.76*	−0.16	0.05	−0.67	0.68*	0.69*	−0.77*	−0.46	−0.50
P-CVPs	−0.50	−0.48	0.22	−0.67*	−0.98*	−0.68*	−0.28	−0.07	0.78*

*$p < 0.05$.

Lower incidence of this inversive reaction in this study is possibly due to the difference between the experimental design of this study and those of Schepens and Drew (2003). They simultaneously measured the ground reactive force in three directions and EMGs of extremities. They judged the APA by the start of the transient increase in the ground reactive force together with an elevation of EMGs of the triceps brachii muscles. On the other hand, we judged postural change only from the CVP shift calculated from the ground reactive force generated in the vertical direction. Therefore, we cannot negate the possibility of the low detection accuracy of the transient reaction. Another possibility would be the difference in the task setting. Schepens and Drew (2003) used the reaction time task. Canadian cats needed to wait until a go-signal was generated. Such a "ready and go" conditioning might have frequently generated the inversive reactions. On the other hand, we did not use such conditioning. That is, when the cat stabilized one's posture, the food was thrown into the targeting tube so that the cat spontaneously started the task at one's timing without waiting. We might test this possibility if we employ the "ready and go" conditioning that they employed. Nonetheless, between trials with and without the transient load increase, we did not detect any difference in changes in ground reactive force other than the transient load increase. Therefore, we defined the postural change from the decrease in the forelimb's

ground reactive force to the moment when the cat lifted its paw as the PPC in this study. In addition, we distinguished it from the APA, which accompanied the transient load increase of the lifting forelimb. We believe, however, that the APA and PPC share common neuronal mechanisms. On the other hand, we should also mention that we did not elucidate on to what extent the cat's forelimb accurately reached the target. However, considering that the cylinder containing the target was a diameter of 30 mm in which the size was just enough to fit the hand, the analysis accuracy of the reaching movement itself could be sufficiently guaranteed in the trial when the cat reached the target.

Many previous studies, such as Schepens and Drew (2003), used six-axis force transducers. On the other hand, we used one-axis force transducers in this study to elucidate the detailed changes of parameters that depended on the target conditions. To evaluate how the PPC is achieved by means of momentum exerting in each foot will be the subject of our future study. However, it is still meaningful that such a simple recording system is able to evaluate postural changes, especially for human studies on postural control.

What Parameters Determined the Optimality of the Preceding Postural Control?

As an index of postural control, CVP or center of pressure (COP) has been employed for many studies. For example, in humans, CVP was used to elucidate the postural control when standing at rest (Winter et al., 1996; Gage et al., 2004) and to examine biomechanics at start walking (Jian et al., 1993; Halliday et al., 1998). In addition, Maki et al. (1994) and Quijoux et al. (2020) examined the relationship between CVP agitation and falls in the human standing posture. Benvenuti (2001) proposed several indexes for CVP to elucidate standing posture. Moreover, Kapteyn et al. (1983) pointed out that both the averages of CVP speed and root mean square were valuable indicators of postural stability. Rocchi et al. (2002) used these indexes to quantitatively evaluate the therapeutic effects of deep brain stimulation and L-DOPA on postural sway in Parkinson's disease patients. In rodents, both movements and distributions of the CVP were also used to examine postural stability (Hutchinson et al., 2007; Funato et al., 2017). In the cat, some studies have focused on the changes in postural synergy during forelimb movements (Gahéry et al., 1980; Birjukova et al., 1989; Schepens and Drew, 2003). However, no studies have quantitatively evaluated the changes in the CVP depending on the target-subject relationship. This study demonstrated that the different target conditions altered the CVP_{onset}, CVP_{lift}, and CVP_{reach}, indicating that the PPC changed the CVP_{lift} position depending on the subject-target relationship using feed-forward mechanisms, or motor programs, based on prediction. In human studies, Day and his collaborators demonstrated that the center of mass (COM) before the onset of the step already had information on the acceleration and speed of the first step (Lyon and Day, 1997; Bancroft and Day, 2016). Yiou et al. (2016) also showed that the pre-step activity altered depending on the final position and distance of the foot. Together with our findings, these results are consistent with the description by Mille et al. (2012) that "the anticipatory nature of the postural step coordination appears to involve a role for motor prediction."

We observed that Md, the difference between CVP_{reach} and CVP_{lift}, altered depending on the target's location. For example, while Md was the smallest when the target was in the left-front (**Figure 5A**), it was large if targets were far to the right (**Figure 5B**). In the former condition, the distributions of CVP_{lift} and CVP_{reach} overlapped in more than 80% of trials. Accordingly, as mentioned earlier, the cat possibly predicted the posture of the end of the task before starting the action, and Md can be the "prediction difference." When Md was large, cats were required to simultaneously perform both goal-directed forelimb reaching movement and accompanying postural control. Considering that both of these processes require visuomotor processing of the higher-order brain function, the reaching task under the latter condition requires higher cortical activity than the former. Therefore, we corroborate that the change in Md associated with the target location difference can be a candidate parameter that may contribute to anticipating the visuomotor processing capability.

When the target was left-front, not only Md but Mt (the time required for reaching movement) was the minimum in all cats. Suppose this result applies to Fitts' law (speed-accuracy trade-off, Fitts, 1954), the smaller the Mt, the higher the performance of the reaching movement, suggesting that the goal-directed action became to be more optimized. Therefore, the fact that Mt became the minimum together with Md at the left-front target location indicates that this target location corresponded to the optimal target-subject relationship. Consequently, we further postulate that the functional role of the PPC can be to ensure the stability of the posture during the entire period of the goal-directed movement by adjusting Md and Mt so that it can optimize the action. This postulation fits well with the consideration by Do et al. (1992) and Boisset and Do (2008), who described how "postural control is programmed in relation not only to the focal movement parameters *per se* but more generally to task movement parameters."

Then, which of the PPC parameters determined postural control during the forelimb reaching movement? We examined the correlation between parameters of the PPC and those during reaching movement in three cats (**Table 2**). Only the Mt and P-CVPs combination showed a negative correlation in the three cats (**Figure 8D**). This finding indicates that reaching movement required time to perform under the target condition where the speed of the CVP shift during PPC was slow. Moreover, Birjukova et al. (1989) found, in the cat forelimb reaching task, that speed of COP shift on the base-of-support during postural control before the onset of forelimb movement reduced after removal of the sensorimotor cortex. Their findings, together with the present results, suggest that P-CVPs can be not only the determinant of the Mt but also the indicator reflecting the cortical function of integrating target-subject interaction.

Furthermore, these animal studies' findings are significant to understanding pathophysiological mechanisms of postural disturbances in neurological disorders. Namely, patients with Parkinson's disease and cerebrovascular disorders showed the

reduced speed in COP shift that occurred before the onset of arm-hand reaching movements in upright standing posture (Porter et al., 2016; Portnoy et al., 2017). More specifically, damages in APA during gait initiation in stroke patients is characterized by atypical patterns (Rajachandrakumar et al., 2017), longer duration (Hesse et al., 1997; Sousa et al., 2015), lower velocity (Gama et al., 2019), and lower amplitude (Melzer et al., 2010; Sharma et al., 2015). Accordingly, there is a need to elucidate whether the above parameters can be beneficial to judge the stability of postural control of patients with neurological disorders and can be the predicting maker of falling. For this, studies combined with biological research, biomechanics, and control theory should be required (Johansson et al., 2009; Pettersson et al., 2012; Kaminishi et al., 2020, 2021).

Commonalities and Differences in the Preceding Postural Control in Each Animal

There is a need to mention the commonalities and differences in each cat. To identify the postural control mechanism common to all cats, we examined how PPC altered by changing the target conditions (nine conditions). As a result, we found that the speed of the PPC had an inverse correlation with Mt in all cats, as shown in **Figure 8D**. On the other hand, there was a positive correlation between Mt and Pt in Cats 2 and 3, but Cat 1 exhibited a negative correlation between the two parameters (**Figure 8B**). However, there is a possibility that the obtained correlation was spurious since we only used nine conditions (nine measurement points) for statistical analyses. Therefore, we employed regression analysis to see if the correlation was significant so that we overcame the drawback of having few measurement points.

The following commonalities existed in each cat. Regarding CVP, there was a substantial overlap in the distribution of CVP_{lift} and CVP_{reach}. Such an overlap, a matching score, was much higher when the target was at the left-front position. However, as the target moved to the right or backward, the distribution of CVP_{lift} and CVP_{reach} also changed, suggesting that each cat performed PPC based on the spatial relationship between oneself and the target. Therefore, the cortical visuomotor process may contribute to both the forelimb reaching movement and the PPC. Furthermore, each cat exhibited a negative correlation between the postural CVP speed and the forelimb movement time (Mt), indicating that the PPC coded the temporal parameter of the purposeful movement in addition to the posture at the end of the movement. Based on these considerations, we postulate that the common motor program can produce both the PPC and goal-directed movements based on cortical visuomotor processes.

On the other hand, the following were not common to each cat. First, the inversive response before the onset of PPC was 50–60% for Cat 1 and 2 but 26% for Cat 3. Second, the CVP_{onset} of Cat 1 and 2 moved depending on the target conditions, but not the case in Cat 3. These differences may be due to the tasks used in this study. As mentioned earlier, if we employed the reaction time task as used by Schepens and Drew (2003), the inversive reaction might occur in all cats. Moreover, if the inverse reaction further requires the cat's attention against the target, CVP_{onset} in each animal may also alter depending on the change in the target position. An alternative interpretation would be that the inversive reaction depends on the age of the subject. When we made this study, Cats 1, 2, and 3 were 6, 5, and 1 year old, respectively. As described in the "Introduction" section, the younger subject did not often exhibit inversive reactions when starting the step (Hyodo et al., 2012). Therefore, we cannot disregard the possibility that the incidence of the inversive response is lower in younger cats than in elder cats. In addition, while there was a positive correlation between Mt and Pt in Cats 2 and 3, Cat 1 exhibited a negative correlation between the two parameters (**Figure 8B**). This indicates that the PPC may have coded even the time required for forelimb reaching with different strategies in each cat.

Possible Neuronal Mechanisms of the Preceding Postural Control

Because PPC precedes goal-directed movements, descending pathways other than the lateral corticospinal tract may be involved in the PPC. For example, in the cat, Yakovenko and Drew (2009) demonstrated that pyramidal neurons in the motor-related cortical areas exhibited higher activity before starting the forelimb reaching movement. Mori et al. (2003) observed that injection of muscimol, a GABAergic agonist, into monkeys' supplementary motor area (SMA) made it difficult to maintain posture during bipedal locomotion on the treadmill. Moreover, a muscimol injection into the dorsal premotor area (PMd) disturbed sensory-guided locomotion. In a clinical study, Jacobs et al. (2009a) reported that transcranial magnetic stimulation (TMS) to SMA altered APA in healthy individuals and patients with Parkinson's disease. Therefore, the motor-related cortical areas such as SMA and PM, which generate motor programs, may play a crucial role in the PPC and APA. Because abundant fibers exist projecting from these motor areas to the pontomedullary reticular formation (Keizer and Kuypers, 1989; Matsuyama and Drew, 1997), the PPC or APA is possibly mediated by the cortico-reticular projection and the reticulospinal tract. In addition, the motor-related cortical areas may send a program of forelimb reaching to the primary motor cortex (M1), which evokes goal-directed movements via activation of the lateral corticospinal tract. Evidence showed that the damages in the cerebellum (Timmann and Horak, 2001; Bruttini et al., 2015) and the basal ganglia (Jacobs et al., 2009b; Ng et al., 2013) also disturbed the APA, indicating that the motor loop between the motor-related cortical areas with the cerebellum and basal ganglia are involved in both the motor programming and execution of the PPC.

In this study, the cat PPC predicted and provided the posture at the end of forelimb reaching movement even under the condition of different target locations. This result suggests that the cat recognized the relationship between the target and oneself in space and reflected this in the motor program of both the PPC and forelimb reaching movement. The cognitive information required to generate this motor program is produced in the parietal association area. This area is considered to integrate sensory information necessary for the maintenance of upright

posture (Bisdorff et al., 1996; Peterka, 2002; Barbieri et al., 2008) and to produce spatial cognitive information and internal models of the self-body (Andersen, 1997; Andersen and Buneo, 2002). This cognitive information is possibly sent to the motor-related areas such as SMA via the abundant projection from this region (Luppino et al., 1993). Furthermore, we recently observed that microinjection of muscimol into the parietal cortex of the cat altered both the forelimb reaching movement and the PPC (Takahashi et al., 2019a,b). In other words, the parietal association area may play a significant role in postural control, and dysfunction of this area may disturb postural control, resulting in falling.

CONCLUSION

We demonstrated that the postural control that preceded the forelimb reaching movement of the cat predicted the posture at the end of the movement and provided it before starting the movement. We also showed that optimization of the subject-target relationship achieved the preceding postural control that induced high-performance forelimb reaching movement. We conclude, therefore, that the motor program generated based on the cognitive visuomotor processes may accomplish the PPC in addition to the goal-directed movement.

AUTHOR NOTE

This manuscript was also published in the Ph.D. thesis of author MT.

DATA AVAILABILITY STATEMENT

The raw data supporting the conclusions of this article will be made available by the authors, without undue reservation.

ETHICS STATEMENT

The animal study was reviewed and approved by Animal Studies Committee of Asahikawa Medical University.

AUTHOR CONTRIBUTIONS

MT and KT conceived and designed the experiment. MT and TN acquired and analyzed the data. MT, TN, and KT drafted and revised the manuscript and gave final approval to the submitted version.

FUNDING

This research was supported by KAKENHI grant numbers JP26120004, 19H05726, 19K06934, and 21K15607.

ACKNOWLEDGMENTS

We would particularly like to thank T. Drew for the insightful comments and suggestions. We would like to thank R. Chiba and T. Noguchi for useful discussions. We also thank S. Miyagishi for technical support.

REFERENCES

Alstermark, B., and Wessberg, J. (1985). Timing of postural adjustment in relation to forelimb target-reaching in cats. *Acta Physiol. Scand.* 125, 337–340. doi: 10.1111/j.1748-1716.1985.tb07724.x

Andersen, R. A. (1997). Multimodal integration for the representation of space in the posterior parietal cortex. *Philos. Trans. R. Soc. London Ser. B Biol. Sci.* 352, 1421–1428. doi: 10.1098/rstb.1997.0128

Andersen, R. A., and Buneo, C. A. (2002). Intentional maps in posterior parietal cortex. *Annu. Rev. Neurosci.* 25, 189–220. doi: 10.1146/annurev.neuro.25.112701.142922

Bancroft, M. J., and Day, B. L. (2016). The throw-and-catch model of human gait: evidence from coupling of pre-step postural activity and step location. *Front. Hum. Neurosci.* 10:635. doi: 10.3389/fnhum.2016.00635

Barbieri, G., Gissot, A.-S., Fouque, F., Casillas, J.-M., Pozzo, T., and Pérennou, D. (2008). Does proprioception contribute to the sense of verticality? *Exp. Brain Res.* 185, 545–552. doi: 10.1007/s00221-007-1177-8

Belen'kii, V. E., Gurfinkel', V. S., and Pal'tsev, E. I. (1967). Control elements of voluntary movements. *Biophysics* 12, 135–141.

Benvenuti, F. (2001). Physiology of human balance. *Adv. Neurol.* 87, 41–51.

Birjukova, E. V., Dufossé, M., Frolov, A. A., Ioffé, M. E., and Massion, J. (1989). Role of the sensorimotor cortex in postural adjustments accompanying a conditioned paw lift in the standing cat. *Exp. Brain Res.* 78, 588–596. doi: 10.1007/BF00230246

Bisdorff, A. R., Wolsley, C. J., Anastasopoulos, D., Bronstein, A. M., and Gresty, M. A. (1996). The perception of body vertically (subjective postural vertical) in peripheral and central vestibular disorders. *Brain .J. Neurol.* 119, 1523–1534. doi: 10.1093/brain/119.5.1523

Boisset, S., and Do, M.-C. (2008). Posture, dynamic stability, and voluntary movement. *Neurophys. Clin. Clin. Neurophysiol.* 38, 345–362. doi: 10.1016/j.neucli.2008.10.001

Brooks, V. B. (1986). *The Neural Basis of Motor Control*. New York, NY: Oxford Press.

Bruttini, C., Esposti, R., Bolzoni, F., Vanotti, A., Mariotti, C., and Cavallari, P. (2015). Temporal disruption of upper-limb anticipatory postural adjustments in cerebellar ataxic patients. *Exp. Brain Res.* 233, 197–203. doi: 10.1007/s00221-014-4103-x

Cordo, P. J., and Nashner, L. M. (1982). Properties of postural adjustments associated with rapid arm movements. *J. Neurophysiol.* 47, 287–302. doi: 10.1152/jn.1982.47.2.287

Delafontaine, A., Vialleron, T., Hussein, T., Yiou, E., Honeine, J.-L., and Colnaghi, S. (2019). Anticipatory postural adjustments during gait initiation in stroke patients. *Front. Neurol.* 10:352. doi: 10.3389/fneur.2019.00352

Do, M. C., Nouillot, P., and Bouisset, S. (1992). Is balance or posture at the end of a voluntary movement programmed? *Neurosci. Lett.* 130, 9–11. doi: 10.1016/0304-3940(91)90215-f

Evans, J. D. (1996). *Straightforward Statistics for the Behavioral Sciences*. Pacific Grove, CA: Thomson Brooks/Cole Publishing Co.

Fitts, P. M. (1954). The information capacity of the human motor system in controlling the amplitude of movement. *J. Exp. Psychol.* 47, 381–391. doi: 10.1037/h0055392

Funato, T., Sato, Y., Fujiki, S., Sato, Y., Aoi, S., Tsuchiya, K., et al. (2017). Postural control during quiet bipedal standing in rats. *PLoS One* 12:e0189248. doi: 10.1371/journal.pone.0189248

Gage, W. H., Winter, D. A., Frank, J. S., and Adkin, A. L. (2004). Kinematic and kinetic validity of the inverted pendulum model in quiet standing. *Gait Posture* 19, 124–132. doi: 10.1016/S0966-6362(03)00037-7

Gahéry, Y., Ioffe, M., Massion, J., and Polit, A. (1980). "The postural support of movement in cat and dog," in *The Warsaw Colloquium on Instrumental Conditioning and Brain Research*, eds B. Żernicki and K. Zieliński (Dordrecht: Springer Netherlands), 284–298. doi: 10.1007/978-94-009-8225-3_21

Gama, G. L., Celestino, M. L., Barela, J. A., and Barela, A. M. F. (2019). Gait initiation and partial body weight unloading for functional improvement in post-stroke individuals. *Gait & Posture* 68, 305–310. doi: 10.1016/j.gaitpost.2018.12.008

Halliday, S. E., Winter, D. A., Frank, J. S., Patla, A. E., and Prince, F. (1998). The initiation of gait in young, elderly, and Parkinson's disease subjects. *Gait Posture* 8, 8–14. doi: 10.1016/S0966-6362(98)00020-4

Hesse, S., Reiter, F., Jahnke, M., Dawson, M., Sarkodie-Gyan, T., and Mauritz, K.-H. (1997). Asymmetry of gait initiation in hemiparetic stroke subjects. *Arch. Phys. Med. Rehabili.* 78, 719–724. doi: 10.1016/S0003-9993(97)90079-4

Horak, F. B. (2006). Postural orientation and equilibrium: what do we need to know about neural control of balance to prevent falls? *Age Ageing* 35, ii7–ii11. doi: 10.1093/ageing/afl077

Hugon, M., Massion, J., and Wiesendanger, M. (1982). Anticipatory postural changes induced by active unloading and comparison with passive unloading in man. *Pflugers Arch.* 393, 292–296. doi: 10.1007/BF00581412

Hutchinson, D., Ho, V., Dodd, M., Dawson, H. N., Zumwalt, A. C., Schmitt, D., et al. (2007). Quantitative measurement of postural sway in mouse models of human neurodegenerative disease. *Neuroscience* 148, 825–832. doi: 10.1016/j.neuroscience.2007.07.025

Hyodo, M., Saito, M., Ushiba, J., Tomita, Y., Minami, M., and Masakado, Y. (2012). Anticipatory postural adjustments contribute to age-related changes in compensatory steps associated with unilateral perturbations. *Gait Posture* 36, 625–630. doi: 10.1016/j.gaitpost.2012.06.018

Jacobs, J. V., Nutt, J. G., Carlson-Kuhta, P., Stephens, M., and Horak, F. B. (2009b). Knee trembling during freezing of gait represents multiple anticipatory postural adjustments. *Exp. Neurol.* 215, 334–341. doi: 10.1016/j.expneurol.2008.10.019

Jacobs, J. V., Lou, J. S., Kraakevik, J. A., and Horak, F. B. (2009a). The supplementary motor area contributes to the timing of the anticipatory postural adjustment during step initiation in participants with and without Parkinson's disease. *Neuroscience* 164, 877–885. doi: 10.1016/j.neuroscience.2009.08.002

Jian, Y., Winter, D., Ishac, M., and Gilchrist, L. (1993). Trajectory of the body COG and COP during initiation and termination of gait. *Gait Posture* 1, 9–22. doi: 10.1016/0966-6362(93)90038-3

Johansson, R., Fransson, P.-A., and Magnusson, M. (2009). Optimal coordination and control of posture and movements. *J. Physiol. Paris* 103, 159–177. doi: 10.1016/j.jphysparis.2009.08.013

Kaminishi, K., Chiba, R., Takakusaki, K., and Ota, J. (2020). Investigation of the effect of tonus on the change in postural control strategy using musculoskeletal simulation. *Gait Posture* 76, 298–304. doi: 10.1016/j.gaitpost.2019.12.015

Kaminishi, K., Chiba, R., Takakusaki, K., and Ota, J. (2021). Increase in muscle tone promotes the use of ankle strategies during perturbed stance. *Gait Posture* 90, 67–72. doi: 10.1016/j.gaitpost.2021.08.003

Kapteyn, T. S., Bles, W., Njiokiktjien, C. J., Kodde, L., Massen, C. H., and Mol, J. M. (1983). Standardization in platform stabilometry being a part of posturography. *Agressologie* 24, 321–326. doi: 10.1007/s10874-011-9211-4

Keizer, K., and Kuypers, H. G. J. M. (1989). Distribution of corticospinal neurons with collaterals to the lower brain stem reticular formation in monkey (*Macaca fascicularis*). *Exp. Brain Res.* 74, 311–318. doi: 10.1007/BF00248864

Luppino, G., Matelli, M., Camarda, R., and Rizzolatti, G. (1993). Corticocortical connections of area F3 (SMA-proper) and area F6 (pre-SMA) in the macaque monkey. *J. Comp. Neurol.* 338, 114–140. doi: 10.1002/cne.903380109

Lyon, I. N., and Day, B. L. (1997). Control of frontal plane body motion in human stepping. *Exp. Brain Res.* 115, 345–356. doi: 10.1007/PL00005703

Maki, B. E., Holliday, P. J., and Topper, A. K. (1994). A prospective study of postural balance and risk of falling in an ambulatory and independent elderly population. *J. Gerontol.* 49, M72–M84. doi: 10.1093/geronj/49.2.m72

Massion, J. (1992). Movement, posture and equilibrium: Interaction and coordination. *Prog. Neurobiol.* 38, 35–56. doi: 10.1016/0301-0082(92)90034-C

Matsuyama, K., and Drew, T. (1997). Organization of the projections from the pericruciate cortex to the pontomedullary brainstem of the cat: a study using the anterograde tracer Phaseolus vulgaris-leucoagglutinin. *J. Comp. Neurol.* 389, 617–641. doi: 10.1002/(sici)1096-9861(19971229)389:4<617::aid-cne6>3.0.co;2-3

McIlroy, W. E., and Maki, B. E. (1999). The control of lateral stability during rapid stepping reactions evoked by antero-posterior perturbation: does anticipatory control play a role? *Gait Posture* 9, 190–198. doi: 10.1016/S0966-6362(99)00013-2

Melzer, I., Goldring, M., Melzer, Y., Green, E., and Tzedek, I. (2010). Voluntary stepping behavior under single- and dual-task conditions in chronic stroke survivors: a comparison between the involved and uninvolved legs. *J. Electromyogr. Kinesiol.* 20, 1082–1087. doi: 10.1016/j.jelekin.2010.07.001

Mille, M.-L., Creath, R. A., Prettyman, M. G., Johnson Hilliard, M., Martinez, K. M., MacKinnon, C. D., et al. (2012). Posture and locomotion coupling: a target for rehabilitation interventions in persons with Parkinson's disease. *Parkinson's Dis.* 2012, 1–10. doi: 10.1155/2012/754186

Mori, F., Nakajima, K., Tachibana, A., Nambu, A., and Mori, S. (2003). Cortical mechanisms for the control of bipedal locomotion in Japanese monkeys: II. local inactivation of the supplementary motor area (SMA). *Neurosci. Res.* 46:S157.

Ng, T. H. B., Sowman, P. F., Brock, J., and Johnson, B. W. (2013). Neuromagnetic brain activity associated with anticipatory postural adjustments for bimanual load lifting. *NeuroImage* 66, 343–352. doi: 10.1016/j.neuroimage.2012.10.042

Peterka, R. J. (2002). Sensorimotor integration in human postural control. *J. Neurophysiol.* 88, 1097–1118. doi: 10.1152/jn.2002.88.3.1097

Pettersson, R., Bartonek, Å, and Gutierrez-Farewik, E. M. (2012). Posture strategies generated by constrained optimization. *J. Biomechanics* 45, 461–468. doi: 10.1016/j.jbiomech.2011.11.053

Porter, S., Dalton, C., and Nantel, J. (2016). Postural instability in the ML direction in individuals with Parkinson's disease before, during and when recovering from a forward reach. *J. Alzheimers Dis. Parkinsonism* 6:267. doi: 10.4172/2161-0460.1000267

Portnoy, S., Reif, S., Mendelboim, T., and Rand, D. (2017). Postural control of individuals with chronic stroke compared to healthy participants: timed-up-and-go, functional reach test and center of pressure movement. *Eur. J. Phys. Rehabil. Med.* 53, 685–693. doi: 10.23736/S1973-9087.17.04522-1

Quijoux, F., Vienne-Jumeau, A., Bertin-Hugault, F., Zawieja, P., Lefèvre, M., Vidal, P.-P., et al. (2020). Center of pressure displacement characteristics differentiate fall risk in older people: a systematic review with meta-analysis. *Ageing Res. Rev.* 62:101117. doi: 10.1016/j.arr.2020.101117

R Core Team (2018). *R: A Language and Environment for Statistical Computing*. Vienna, Austria: R Foundation for Statistical Computing.

Rajachandrakumar, R., Fraser, J. E., Schinkel-Ivy, A., Inness, E. L., Biasin, L., Brunton, K., et al. (2017). Atypical anticipatory postural adjustments during gait initiation among individuals with sub-acute stroke. *Gait Posture* 52, 325–331. doi: 10.1016/j.gaitpost.2016.12.020

Rocchi, L., Chiari, L., and Horak, F. B. (2002). Effects of deep brain stimulation and levodopa on postural sway in Parkinson's disease. *J. Neurol. Neurosurgery Psychiatry* 73, 267–274. doi: 10.1136/jnnp.73.3.267

Schepens, B., and Drew, T. (2003). Strategies for the integration of posture and movement during reaching in the cat. *J. Neurophysiol.* 90, 3066–3086. doi: 10.1152/jn.00339.2003

Sharma, S., McMorland, A. J. C., and Stinear, J. W. (2015). Stance limb ground reaction forces in high functioning stroke and healthy subjects during gait initiation. *Clin. Biomech.* 30, 689–695. doi: 10.1016/j.clinbiomech.2015.05.004

Snijders, A. H., van de Warrenburg, B. P., Giladi, N., and Bloem, B. R. (2007). Neurological gait disorders in elderly people: clinical approach and classification. *Lancet Neurol.* 6, 63–74. doi: 10.1016/S1474-4422(06)70678-0

Sousa, A. S., Silva, A., and Santos, R. (2015). Reliability of two methods for identifying the postural phase of gait initiation in healthy and poststroke subjects. *J. Appl. Biomech.* 31, 349–356. doi: 10.1123/jab.2014-0222

Takahashi, M., Nakajima, T., Miyagishi, S., Chiba, R., Obara, K., and Takakusaki, K. (2019a). "Roles of the parietal cortex in postural adjustments that accompany forelimb reaching in the cat," in *Proceeding of the Conference presentation The 42nd Annual Meeting of the Japan Neuroscience Society, Niigata, Japan*.

Takahashi, M., Nakajima, T., Miyagishi, S., Obara, K., Chiba, R., Drew, T., et al. (2019b). "Role of parietal cortex involved in postural control during forelimb reaching in the cat," in *Proceeding of the Conference presentation The 29th*

Annual Meeting of the Society for the Neural Control of Movement, Toyama, Japan.

Timmann, D., and Horak, F. (2001). Perturbed step initiation in cerebellar subjects: 2. modification of anticipatory postural adjustments. *Exp. Brain Res.* 141, 110–120. doi: 10.1007/s002210100858

Varghese, J. P., Merino, D. M., Beyer, K. B., and McIlroy, W. E. (2016). Cortical control of anticipatory postural adjustments prior to stepping. *Neuroscience* 313, 99–109. doi: 10.1016/j.neuroscience.2015.11.032

Winter, D. A., Prince, F., Frank, J. S., Powell, C., and Zabjek, K. F. (1996). Unified theory regarding A/P and M/L balance in quiet stance. *J. Neurophysiol.* 75, 2334–2343. doi: 10.1152/jn.1996.75.6.2334

Yakovenko, S., and Drew, T. (2009). A motor cortical contribution to the anticipatory postural adjustments that precede reaching in the cat. *J. Neurophysiol.* 102, 853–874. doi: 10.1152/jn.00042.2009

Yamaura, H., Hirai, H., and Yanagihara, D. (2013). Postural dysfunction in a transgenic mouse model of spinocerebellar ataxia type 3. *Neuroscience* 243, 126–135. doi: 10.1016/j.neuroscience.2013.03.044

Yiou, E., Artico, R., Teyssedre, C. A., Labaune, O., and Fourcade, P. (2016). Anticipatory postural control of stability during gait initiation over obstacles of different height and distance made under reaction-time and self-initiated instructions. *Front. Hum. Neurosci.* 10:449. doi: 10.3389/fnhum.2016.00449

Conflict of Interest: The authors declare that the research was conducted in the absence of any commercial or financial relationships that could be construed as a potential conflict of interest.

Publisher's Note: All claims expressed in this article are solely those of the authors and do not necessarily represent those of their affiliated organizations, or those of the publisher, the editors and the reviewers. Any product that may be evaluated in this article, or claim that may be made by its manufacturer, is not guaranteed or endorsed by the publisher.

Copyright © 2022 Takahashi, Nakajima and Takakusaki. This is an open-access article distributed under the terms of the Creative Commons Attribution License (CC BY). The use, distribution or reproduction in other forums is permitted, provided the original author(s) and the copyright owner(s) are credited and that the original publication in this journal is cited, in accordance with accepted academic practice. No use, distribution or reproduction is permitted which does not comply with these terms.

frontiers in Systems Neuroscience

ORIGINAL RESEARCH
published: 20 January 2022
doi: 10.3389/fnsys.2021.802148

Decreased Tactile Sensitivity Induced by Disownership: An Observational Study Utilizing the Rubber Hand Illusion

Kota Ataka[1,2], Tamami Sudo[1,3], Ryoji Otaki[1,4], Eizaburo Suzuki[1,5] and Shin-Ichi Izumi[1,6]**

[1] Department of Physical Medicine and Rehabilitation, Tohoku University Graduate School of Medicine, Sendai, Japan, [2] Department of Rehabilitation, Tohoku University Hospital, Sendai, Japan, [3] Department of Computer and Information Sciences, Graduate School of Engineering, Tokyo University of Agriculture and Technology, Tokyo, Japan, [4] Department of Rehabilitation, Yamagata Saisei Hospital, Yamagata, Japan, [5] Department of Physical Therapy, Yamagata Prefectural University of Health Sciences, Yamagata, Japan, [6] Department of Physical Medicine and Rehabilitation, Tohoku University Graduate School of Biomedical Engineering, Sendai, Japan

The sense of body ownership, the feeling that one's own body belongs to oneself, is generated from the integration of visual, tactile, and proprioceptive information. However, long-term non-use of parts of the body due to physical dysfunction caused by trauma or illness may disturb multisensory integration, resulting in a decreased sense of body ownership. The rubber hand illusion (RHI) is an experimental method of manipulating the sense of ownership (SoO). In this illusion, subjects feel as if the rubber hand in front of them were their own hand. The RHI elicits the disownership phenomenon; not only does the rubber hand feels like one's own hand, but one's own hand does not feel like one's own hand. The decrease of ownership of one's own body induced by the bodily illusion is accompanied by neurophysiological changes, such as attenuation of somatosensory evoked potential and decreases in skin temperature. If the loss of the SoO is associated with decreased neurophysiological function, the dysfunction of patients complaining of the loss of ownership can be exacerbated; appropriate rehabilitation prescriptions are urgently required. The present study attempted to induce a sense of disownership of subjects' own hands using the RHI and investigated whether the tactile sensitivity threshold was altered by disownership. *Via* questionnaire, subjects reported a decrease of ownership after the RHI manipulation; at the same time, tactile sensitivity thresholds were shown to increase in tactile evaluation using the Semmes-Weinstein monofilaments test. The tactile detection rate changes before and after the RHI were negatively correlated with the disownership-score changes. These results show that subjects' sense of disownership, that their own hands did not belong to them, led to decreases in tactile sensitivity. The study findings also suggest that manipulating of illusory ownership can be a tool for estimating the degree of exacerbation of sensory impairment in patients. Consideration of new interventions that optimize the sense of body ownership may contribute to new rehabilitation strategies for post-stroke sensory impairment.

Keywords: body ownership, disownership, multisensory integration, rubber hand illusion, tactile sensitivity, sensory impairment, rehabilitation

OPEN ACCESS

Edited by:
Jun Izawa,
University of Tsukuba, Japan

Reviewed by:
Carlotta Fossataro,
University of Turin, Italy
Tomohisa Asai,
Advanced Telecommunications Research Institute International (ATR), Japan

***Correspondence:**
Tamami Sudo
t-sudo@go.tuat.ac.jp
Shin-Ichi Izumi
izumis@med.tohoku.ac.jp

Received: *26 October 2021*
Accepted: *22 December 2021*
Published: *20 January 2022*

Citation:
Ataka K, Sudo T, Otaki R, Suzuki E and Izumi S-I (2022) Decreased Tactile Sensitivity Induced by Disownership: An Observational Study Utilizing the Rubber Hand Illusion.
Front. Syst. Neurosci. 15:802148.
doi: 10.3389/fnsys.2021.802148

INTRODUCTION

Sense of ownership (SoO) is the feeling that parts of the body, or the entire body, belong to oneself (Gallagher, 2000). This subjective experience is generated from multisensory integration of visual, proprioceptive, and somatosensory information through comparisons between the visually perceived body and the anatomical model of the bodily self (Gallagher, 2000; Jeannerod, 2003; Ehrsson et al., 2004; Tsakiris, 2010). When one's own hand is observed in the appropriate position, as part of one's body, and can be moved according to one's own will, the hand can be clearly recognized as part of one's own body. This conscious experience is crucial to the proper perception of information from the surroundings and to the corresponding adaptive movement.

The sense of body ownership can be altered selectively by stroke-induced brain damage, interfering with multisensory integration. Patients' complaints like that I feel that this hand that I am now observing is not my own are occasionally reported in clinical cases. According to an observational study of stroke patients using the Visual Analog Scale (VAS) to investigate body disownership after brain damage, body disownership was also detected in cases with no obvious agnosia. Moreover, in patients with more severe impairment of motor and sensory function, more reduction in body ownership has been detected (Ronchi et al., 2020). In more serious cases, asomatognosia (unawareness of or ignoring parts or sides of the body), and somatoparaphrenia (a syndrome that includes unawareness of ownership of body parts, delusional misidentification, and anthropomorphism) due to stroke are known to cause symptoms such as loss of body ownership and attribution of the limb to another person (Feinberg and Venneri, 2014; Romano and Maravita, 2019).

The principal sources of these complaints from stroke patients include not only the primary factor, such as damage to the areas responsible for motor and sensory function, but also secondary factors, such as decreased frequency of use. Use-dependent plasticity is the brain's ability to adapt to various changes in the surrounding environment (Nudo and Milliken, 1996; Nudo et al., 1996a,b). When use of the body part corresponding to impairment is drastically reduced, less of the cortical area is afforded to the corresponding body part over time (Liepert et al., 1995); motor training involving frequent use of a specific part of the body increases cortical representation and improves motor function accordingly (Nudo et al., 2001). Therefore, in stroke rehabilitation it is important to provide training to increase the frequency of use of paretic limbs, such as Constraint-Induced (CI) movement therapy (Liepert et al., 2000; Taub et al., 2002). Stroke patients often learn to use their intact limbs to perform compensatory actions for paretic limbs, a phenomenon called "learned nonuse" that further reduces the frequency of use of the paretic limb (Taub et al., 2006). Learned nonuse is due primarily to somatosensory deafferentation, according to a lesion study disrupting the dorsal horn of the spinal cord corresponding to a monkey's unilateral forelimbs (Taub, 1980). Moreover, a study examining the factors associated with the frequency of paretic limb use in stroke patients revealed that both motor and sensory functions, especially tactile sensation, determine the contribution of paretic limbs to ADL (Tashiro et al., 2021). Thus, improvement of sensory deficits in stroke rehabilitation is important to prevent reduced frequency of paretic limb use.

Psychophysical experiments using bodily illusion have been widely used in recent years to elucidate the mechanism of the occurrence of a sense of body ownership. Among the experiments utilizing bodily illusion, the rubber hand illusion (RHI), first reported by Botvinick and Cohen (1998), is the most typical paradigm. Since then, many experimental studies applying this illusion have revealed that changes in the sense of body ownership have a significant effect on motor, sensory, and physiological functions. With motor function, physiological evidence has been provided to show that the amplitude of the motor-evoked potential recorded from the real hand is significantly reduced with respect to baseline during the RHI experience (Della Gatta et al., 2016). Other studies measuring somatosensory evoked potentials (SEPs) for visuo-tactile stimulation in bodily illusions have shown that experimentally induced illusory body ownership modulates activity in the primary somatosensory cortex as well as in the temporo-parietal cortex and frontal cortex, and simultaneously attenuates somatosensory precision in order to resolve conflicting multisensory input (Dieguez et al., 2009; Aspell et al., 2012; Zeller et al., 2015). In addition, taking ownership of artificial body parts *via* RHI has been demonstrated to cause physiological changes, such as reduced skin temperature of the real hand (Moseley et al., 2008; Salomon et al., 2013), and decreased tactile detection (Zopf et al., 2011; Rossi Sebastiano et al., 2021).

A significant amount of neurological evidence has been obtained through studying illusory ownership of the virtual body. However, it remains unclear whether the attribution of ownership to the virtual body is complementary to the disownership of the actual body. In a study with a psychometric approach to the RHI, subjects reported feeling that their own hands had been replaced with rubber hands, rather than that a new third hand had been added (Longo et al., 2008). A study focusing on disownership during the RHI supported the claim that the conscious experience of disownership can be induced by illusion (Lane et al., 2017). Thus, several studies support the claim that the decrease of ownership of the actual body is caused by the attribution of ownership to the virtual body. From these findings, the manipulation of body ownership by the bodily illusion is understood to reproduce a condition similar to that of a patient who complains of decrease of body ownership due to brain damage.

In the present study, we hypothesized that the introspection on decreased body ownership in stroke patients has analogical properties to the decrease in body ownership caused by the bodily illusion. Observing changes in subjects' ownership of their own hands during studies utilizing the RHI leads to an understanding of the relationship between the patient's decrease of body ownership and the change of sensory function

in clinical practice. To examine the effect of disownership on tactile sensation, this study investigated healthy subjects' perceived changes in the ownership of their real hands due to the RHI as well as changes in the tactile pressure detection rate before and after the illusory manipulation. Clarifying the relationship between changes in ownership and tactile sensation can potentially contribute to the development of new rehabilitation strategies that improve sensory impairment by optimizing perceptions of body ownership of patients with post-stroke sensory impairment.

MATERIALS AND METHODS

Participants

Twenty-six healthy adults (16 male, 25 right-handed, mean age = 29.4 ± 4.6 years) were recruited by posting notices within the Tohoku University campus and at Tohoku University Hospital and by publishing the recruitment information on the Miyagi Occupational Therapists' Association website. Handedness was assessed by way of the Edinburgh Handedness Inventory (Oldfield, 1971). All participants self-reported being healthy with normal or normally corrected vision, normal sense of touch, and no history of neurological or psychiatric disorders. The purpose and methods of the study were fully explained to the participants in writing and orally before the study was conducted. After confirming their understanding of the study, participants consented to participate in the study willingly. This study was conducted with the approval of the Ethics Committee of Tohoku University School of Medicine (registration number: 2020-1-47).

Procedure

The series of experiments consisted of three components: the RHI, questionnaire and tactile evaluation. Each operation was carried out in the order shown in **Figure 1**. The details of each operation are described below.

The Rubber Hand Illusion

The study's RHI manipulation procedure was based on the method of Botvinick and Cohen (1998) with some modifications (see **Figure 2**). Each subject was seated in a chair with a backrest, with the chair placed in front of a desk in a quiet room. The subject was instructed to place his or her left hand in a supinated position in a wooden box (450 mm × 900 mm × 100 mm), handmade for this study and placed on the desk. The subject's left hand was hidden in the box. In place of the subject's hand, a rubber hand (an adult cosmetic prosthesis) was placed in the same supinated position adjusted to the center of the subject's sitting position approximately 15 cm to the right of the subject's hand.

The experimenter stroked the subject's palm and the palm of the rubber hand with two identical cosmetic brushes for 120 s, excluding the thumb, which was the test site of the subsequent tactile evaluation. The frequency of the brush stroking was set to 1 Hz and controlled by a metronome. This part of the experiment consisted of two conditions: the first in which the rubber hand and the subject's hand were stroked simultaneously, wherein the illusion generally occurs (synchronous condition), and the second in which the rubber hand and the subject's hand were stroked at different times, wherein the illusion generally does not occur (asynchronous condition). The order of the experimental conditions was counterbalanced among the subjects.

Questionnaire

To evaluate changes in the subjective sense of body ownership, subjects were asked to rate the following two statements, items modified from a questionnaire used by Lane et al. (2017).

Q1. "I feel as if the rubber hand is my hand."

Q2. "I feel as if the real left hand is no longer mine."

Question 1 queried the amount of illusory body ownership of the rubber hand (ownership score). Question 2 queried the amount of ownership decrease of the real hand due to the illusion (disownership score). Responses were collected verbally on a 7-point numerical rating scale and ranged from "−3" (very strongly disagree) to "+3" (very strongly agree). Pre-evaluation in the observation phase of the rubber hand before the synchronous or asynchronous stimulation was defined as the baseline to derive the amount of change of subjective evaluation, and to investigate the correlation with the amount of change of other indicators. Thus, a total of four measurements were conducted before and after the illusion-induced operation in the synchronous and asynchronous conditions.

Tactile Evaluation

The tactile pressure evaluation was conducted immediately after the questionnaire on body ownership; the evaluation was conducted four times, as with the questionnaire measurements. A modified version of the method from Bell-Krotoski et al. (1993) was used for the evaluation. A Semmes-Weinstein monofilament (SWMT, SOT-DM20A, Sakai Medical Co., Ltd., Japan) was used for the tactile evaluation (see **Figure 3A**). Preliminary experiments with constant methods have shown that most healthy subjects have a sensory threshold between filaments No. 2.36 (0.02 g) and No. 2.44 (0.04 g). Thus, in this study those two filament types were selected from the kit (see **Figure 3B**). The experimenter held the monofilament lightly, lowered the tip of the filament vertically toward the subject's thumb surface for 1–1.5 s, and released it for 1–1.5 s (see **Figures 3C,D**). The subjects were asked to respond "yes" when they felt pressure. The stimulation with each filament was performed 15 times, for a total of 30 instances. The order of stimuli and the order of interstimulus intervals were randomized.

Statistical Analysis

The Shapiro–Wilk test was used to examine the distribution of all datasets. As the results of the questionnaire and of the tactile pressure sensation assessment were datasets that were not normally distributed, the Wilcoxon signed-rank test was used to analyze the difference between the means of the two datasets before and after the intervention. Spearman's rank correlation coefficient was then used to examine the relationship between

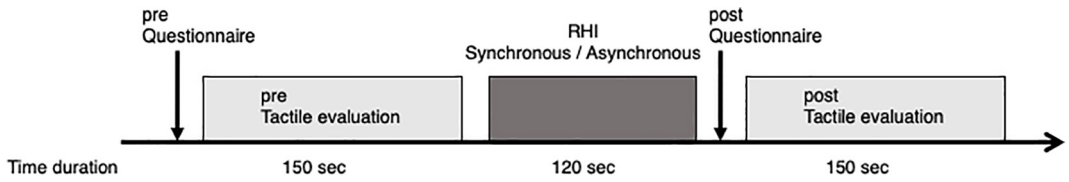

FIGURE 1 | Schematic representation of the series of experimental operations. The experiment was conducted based on the A–B or B–A experimental design, composed of synchronous and asynchronous conditions. Each condition was composed of a series of operations consisting of a questionnaire, tactile evaluation, and RHI. The baseline (denoted as pre) of illusion rating questionnaires and tactile evaluation was performed prior to the start of the 120 s of visuo-tactile stimulation. Immediately following the visuo-tactile stimulation, illusion rating questionnaires and tactile evaluation was performed again (denoted as post).

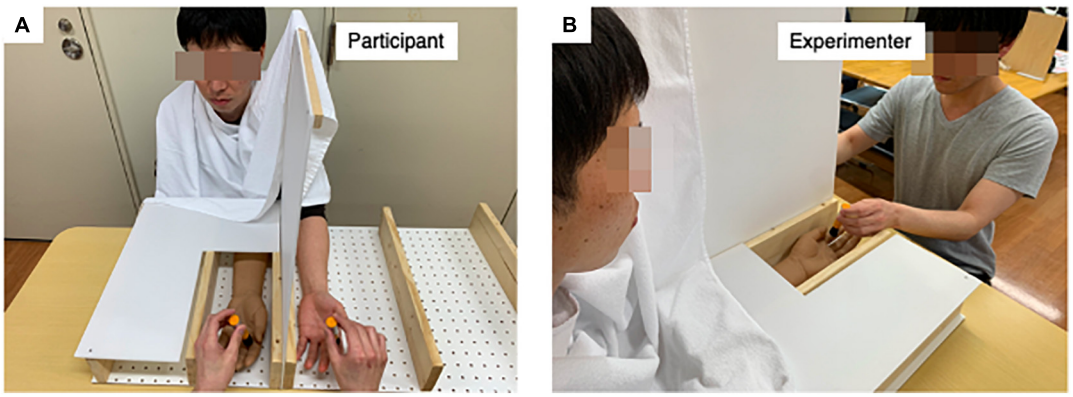

FIGURE 2 | Settings of the rubber hand illusion (RHI). **(A)** Settings of the RHI from the experimenter's viewpoint. The RHI box is a (450 mm long × 900 mm wide × 100 mm high) made of wood and plastic materials. **(B)** Presentation of the RHI stimuli from the subjects' viewpoint.

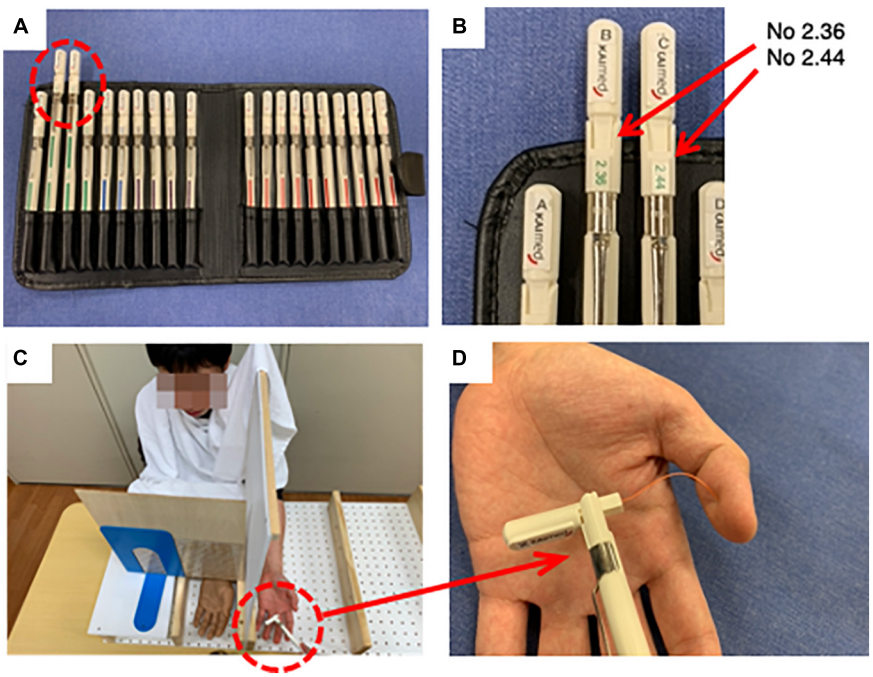

FIGURE 3 | Settings of the tactile evaluation. **(A)** The Semmes-Weinstein monofilament (SWMT, SOT-DM20A, Sakai Medical Co., Ltd., Japan). **(B)** Two types of filaments used in this experiment, No. 2.36 (0.02 g) and No. 2.44 (0.04 g). **(C)** Settings of the tactile evaluation. **(D)** Detection site in tactile evaluation.

the amount of change in the decrease of body ownership score and the amount of change in the justification rate of tactile pressure sensation.

RESULTS

One of the participants who was recruited reported numbness in the arm during the experiment and ceased their participation. Therefore, data for 25 participants were obtained and analyzed.

Ownership and Disownership Questionnaire Scores

The SoO scores (ownership score) from Q1 are shown in **Figure 4A**. In the synchronous condition, the median before the illusory manipulation was −3 (the interquartile range was between −3 and −2), and the median after the illusory manipulation was 0 (the interquartile range was between−3 and 1.5). In the asynchronous condition, the median before the illusory manipulation was −3 (the interquartile range was between −3 and −1.5), and the median after the illusory manipulation was −3 (the interquartile range was between −3 and −1). The ownership score for the synchronous condition changed significantly from pre-evaluation as the baseline (Wilcoxon signed-rank test, $p < 0.0005$), while in the asynchronous condition no significant change was revealed.

The decrease of ownership scores (disownership score) from Q2 are shown in **Figure 4B**. In the synchronous condition, the median before the illusory manipulation was −3 (the interquartile range was between −3 and −1.5), and the median after illusory manipulation was 0 (the interquartile range was between −2 and 2). In the asynchronous condition, the median before the illusory manipulation was −3 (the interquartile range was between −3 and −1), and the median after the illusory manipulation was −3 (the interquartile range was between −3 and −0.5). The disownership score for the synchronous condition changed significantly from pre-evaluation as the baseline (Wilcoxon signed-rank test, $p < 0.0005$), while in the asynchronous condition no significant change was revealed.

Both the ownership score and the disownership score was significantly higher in the synchronous condition after the illusory manipulation (post-sync) than in the asynchronous condition (post-async) (Wilcoxon signed-rank test, $p < 0.0005$). From these results, the RHI induction by the visuo-tactile stimulation has confirmed.

Tactile Evaluation

The detection rate of the No. 2.36 filament in the tactile evaluation is shown in **Figure 5A**. No. 2.36 filament was thinner and harder to detect than the other one, so the detection rate was low overall both pre and post evaluations. The detection rate in the synchronous condition was 31.7 ± 4.5% before the illusion manipulation and 14.9 ± 3.5% after the illusion manipulation. While the detection rate in the asynchronous condition was 30.1 ± 4.0% before the illusion manipulation and 31.5 ± 4.7% after the illusion manipulation. In the synchronous condition, the detection rate of the No. 2.36 filament was significantly lower after the illusion operation than before the illusion operation (Wilcoxon signed-rank test, $p = 0.002$).

The detection rate of the No. 2.44 filament is shown in **Figure 5B**. The detection rate in the synchronous condition was 88.8 ± 1.6% before the illusion manipulation and 48.8 ± 5.5% after the illusion manipulation. The detection rate in the asynchronous condition was 89.1 ± 2.1% before the illusion manipulation and 82.4 ± 2.9% after the illusion manipulation. The detection rate of the No. 2.44 filament was significantly lower after the illusion operation than before the illusion operation under both synchronous ($p < 0.0005$) and asynchronous conditions ($p = 0.030$).

Relationship Between the Amount of Change in the Body-Disownership Score and the Amount of Change in the Filament-Detection Rate

To clarify the relationship between the decrease of the SoO and tactile detection ability, the correlation between subjective rating changes and detection-rate changes was investigated. The correlation between the amount of change in each score (ownership/disownership-score, detection-rate changes) is shown in **Table 1**. The subjective rating changes are indicated by subtracting the score measured before the illusion operation (pre-evaluation) from the score measured after the illusion operation (post-evaluation). The detection-rate changes are obtained by calculating the difference in the percentage of detection accuracy shown in **Figure 5**. Significant correlations were found between all pairs. A particularly important point was the correlations between the amount of change in the detection rate and the disownership score (see **Figure 6**). The amount of change in the detection rate of the No. 2.36 filament before and after the illusion showed a significant negative correlation with the amount of change in the disownership score ($\rho = -0.478$, $p < 0.0005$; **Figure 6A**). The amount of change in the detection rate of the No. 2.44 filament before and after the illusion also showed a particularly strong and significant negative correlation ($\rho = -0.713$, $p < 0.0005$; **Figure 6B**).

DISCUSSION

In this study that synchronized visuo-tactile stimuli, subjects experienced feeling as if a rubber hand was part of their own body, while at the same time declaring a decrease of ownership toward their actual hand. There was a high correlation between the subjective ratings of Q1 and Q2. This correlation indicates deductively that embodiment of the rubber hand and disembodiment of the self-hand are complementary phenomena. In comparisons before and after presentation of the illusion stimulus, subjects' filament-detection rates were significantly decreased after the illusion. Correlations were found between the disownership data obtained from the questionnaire and filament-detection rate changes; the greater the change in disownership, the greater the decrease in the filament-detection rate. These study results revealed that subjects' tactile pressure thresholds

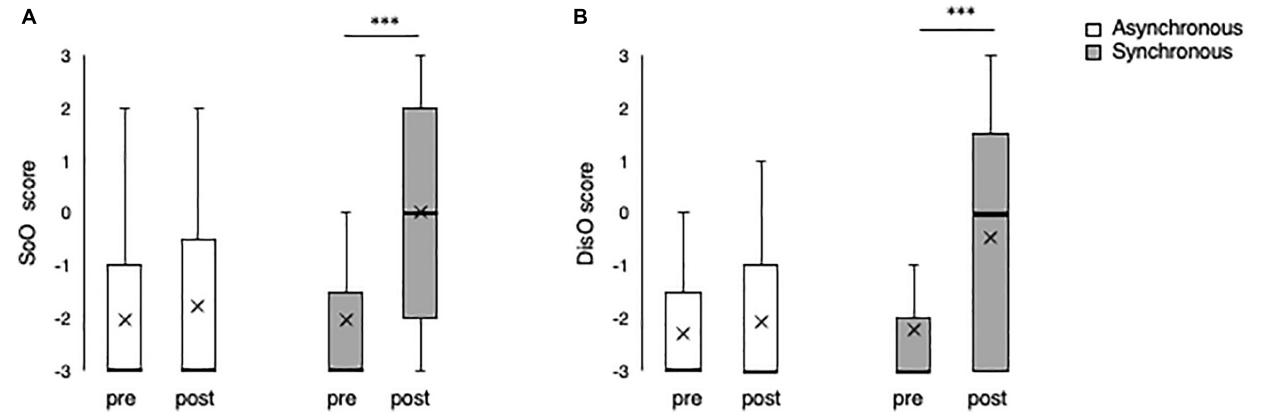

FIGURE 4 | Ownership and disownership scores before and after the RHI. **(A)** Ownership score (SoO) from Question 1 in synchronous and asynchronous conditions. **(B)** Disownership scores (DisO) from Question 2 in synchronous and asynchronous conditions. Pre indicates results before the illusion operation, and post indicates results after the illusion operation. In the box-plots, the thick horizontal bars indicate the median, and the cross marks indicate the average values. ***$p < 0.0005$; error bars ± 1 SD.

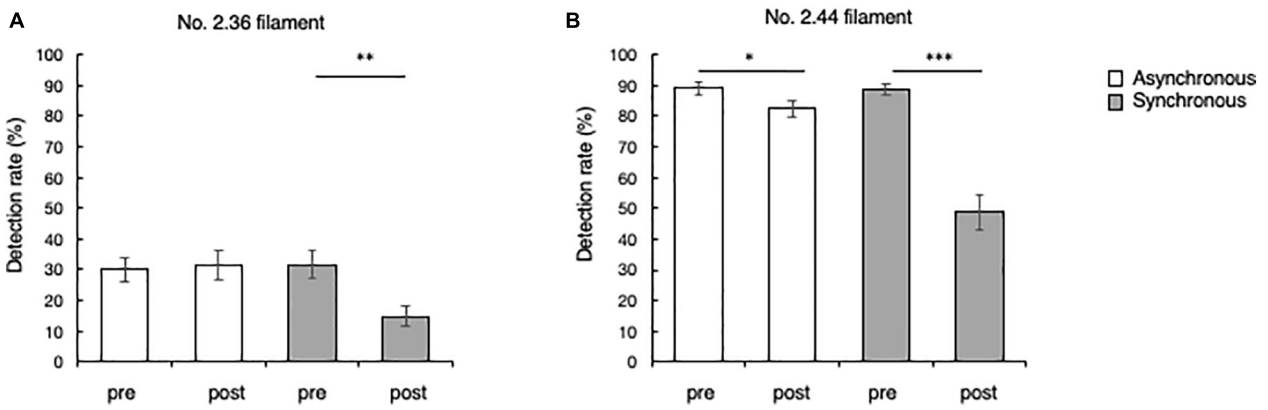

FIGURE 5 | Tactile sensitivity before and after the RHI. **(A)** The detection rates of the No. 2.36 filament in the synchronous and asynchronous conditions. **(B)** The detection rates of the No. 2.44 filament in the synchronous and asynchronous conditions. Pre indicates results before the illusion operation, and post indicates results after the illusion operation. *$p < 0.05$; **$p < 0.005$; ***$p < 0.0005$; error bars ± 1 SE.

increased when they felt a decrease of their sense of body ownership, induced by the illusion's stimuli.

Decreased Tactile Sensitivity Due to Feelings of Disownership Under the Illusion

Tactile information ascends primarily from the spinal thalamic tract and is detected when it reaches the primary somatosensory cortex (S1). From there, the information is further transmitted to higher association areas, such as the parietal and temporal lobes, resulting in more complex cognition, including renewal of body representation (Iwamura, 1998; Kandel et al., 2014). A previous study assessing evoked potential during the RHI showed a relative attenuation of somatosensory evoked responses in frontal electrodes corresponding to cortical sources in the higher sources of the parietal lobe in the attribution of ownership of an artificial hand (Zeller et al., 2015). This relative attenuation may reflect a decrease in the precision of somatosensory detection. Another SEP study on the full body illusion induced by applying visuo-tactile stimuli to other parts of the body demonstrated two distinct brain activity modulations. The activation around the time of the first parietal component of tibial nerve SEPs (P40) was enhanced during the illusion; the later activation, originating in higher somatosensory regions in the parietal cortex, had greater amplitude and longer duration in the non-illusion condition (Aspell et al., 2012). This study also suggested that the parietal lobe plays a significant role in the detection of visuo-tactile conflicts from each modality and modulating activity in the frontal network. These findings suggest the following three effects associated with disownership of one's own body under the illusion, (1) multisensory integration effects (the sense of detecting tactile stimuli with the virtual body), (2) attentional modulation effects (the shift of spatial attention from the self-body to the virtual body) (Ortigue et al., 2006), and (3) functional deafferentation in the physical body. In the RHI stimulation in

TABLE 1 | Correlation coefficients between all the amount of changes.

	2	3	4
1. Change in SoO	0.857***	−0.657***	−0.719***
2. Change in DisO		**−0.478*** **	**−0.713*** **
3. Change in No. 2.36 detection			0.578***
4. Change in No. 2.44 detection			

****$p < 0.0005$, SoO, ownership score; DisO, disownership score. The values shown in bold are also mentioned in scatterplots (**Figure 6**).*

the present study, these three effects may have been induced in terms of the subjects' hands. As a result, illusory ownership is likely to have made it difficult for the subjects' actual hands to detect tactile stimuli under the illusion, and the detection rate for the tactile stimuli decreased.

Another recent psychophysical experiment has shown the opposite effect of suppressing tactile detection and promoting visual detection after the RHI (Rossi Sebastiano et al., 2021). This effect is considered to reflect the trade-off between downregulation of the somatosensory system during the RHI and increase of the connectivity between visual regions and the premotor cortex. Indeed, the functional connectivity to resolve the multisensory conflicts caused by RHI has been observed using neuroimaging (fMRI), electrophysiological (EEG) and near-infrared spectroscopy (NIRS) measurement data (Limanowski and Blankenburg, 2015; Arizono et al., 2016; Zeller et al., 2016). According to the predictive coding theory, in self-body identification by multisensory integration, the spatio-temporal mismatches between visual, tactile, and proprioceptive information associated with the bodily illusion produce a bottom-up effect on the parietal lobe, inducing a change in ownership. The updated information on integrated body representation in the parietal lobe provides a top-down inhibition of prediction errors on sensory processing in the frontoparietal network (Tsakiris and Haggard, 2005; Costantini and Haggard, 2007; Apps and Tsakiris, 2014). It is surmised that the visuo-tactile stimuli in the present experiment provided a top-down inhibitory effect on sensory processing similar to the effect in previous studies, and that this inhibition was one of the causes of decreased sensory detection.

Relationship Between the Tactile Sensitivity and Intensity of Illusory Ownership

In the tactile-pressure evaluation test conducted before and after the visuo-tactile stimulation in this study, the filament-detection rate was significantly lower after stimulation than before stimulation under all conditions (except for the detection of the thin filament, No. 2.36, under asynchronous conditions due to the poor detection rate both before and after stimulation). In addition, negative correlations were observed between the amount of change in the filament-detection rate and the change in the disownership score, collected *via* the questionnaire, in all conditions regardless of the filament applied (No. 2.36 or No. 2.44). These correlations indicate that the tactile-pressure threshold increased relatively as feelings of ownership of their real hand decreased significantly because of the RHI, resulting in difficulty detecting the tactile stimuli.

In a previous study investigating changes in tactile-detection performance after the presentation of illusion stimuli, the detection of vibration after synchronous conditions was significantly lower than detection after asynchronous conditions

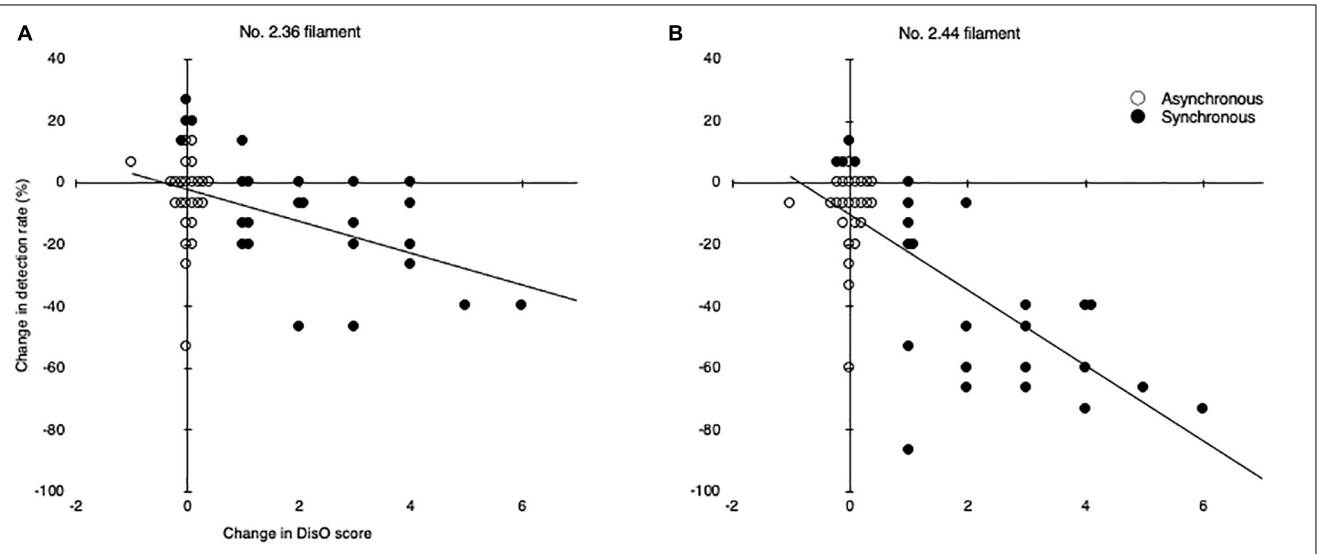

FIGURE 6 | Scatterplots of disownership-score changes and detection-rate changes. **(A)** The relationship between disownership-score (DisO) changes and detection-rate changes for the No. 2.36 filament in all conditions. **(B)** The relationship between disownership-score (DisO) changes and detection-rate changes for the No. 2.44 filament in all conditions. Data from 25 subjects are plotted. Closed circles indicate plots under the synchronous condition. Open circles indicate plots under the asynchronous condition. Trend-lines show significant negative correlations for both No. 2.36 filaments ($\rho = -0.478$, $p < 0.0005$) and No. 2.44 filaments ($\rho = -0.713$, $p < 0.0005$).

(Zopf et al., 2011). Although this study found that observing one's own body is a major reason for decreased tactile detection, the study did not consider the standalone effect of changes in body ownership, excluding visual information. The present evaluation shielded the contact area during the clinical examination and removed the suppressing effect of the detection of tactile stimuli by visual information. Note that the detection threshold was specified in more detail by measuring the tactile-detection rate before and after offering the illusion stimuli using two types of filaments. The disownership caused by the illusion-inducing stimuli attenuated the accuracy of tactile detection even without observing the corresponding body parts. This is a novel finding that differs from findings of previous studies.

Physiological changes induced by illusory body ownership include less activation of motor-evoked potential of the corresponding body part (Della Gatta et al., 2016), an attenuation in SEPs for subsequent sensory input (Zeller et al., 2015), modulation of tactile and visual detectability (Zopf et al., 2011; Rossi Sebastiano et al., 2021), and delays in temporal order judgments with decreased skin temperature (Moseley et al., 2008; Salomon et al., 2013). All of this evidence was obtained by comparing illusion and non-illusion conditions. The evidence did not explain the relationship between the intensity of the illusion and the physiological changes; the relationship between the susceptibility to illusion and the intensity of illusory body ownership also remains unclear. Thus, subjective evaluation using the conventional questionnaire can detect the occurrence of illusions but cannot make a quantitative evaluation of the intensity of illusory ownership. Study results show that there were significant changes in the sensory detection rate and negative correlations with the disownership changes, indicating the existence of subtle changes in the SoO that were indiscernible using the 7-point scaled questionnaire and conventional methodology. The amount of change in the filament-detection rate, a quantitative index of physiological evaluation, reflected changes in the disownership of subjects' own bodies according to the intensity of the illusion.

In the study's experimental environment, the rubber hand was placed next to the subject's own hand in a homologous orientation, which is generally prone to be under the illusion. Therefore, most subjects reported a change in ownership through the illusion manipulation of their non-dominant hands. The detection rate of thick (No. 2.44) filaments was significantly reduced in the study, even under asynchronous conditions. A previous study reported that visual information from a first-person perspective enabled the provision of illusory ownership even under asynchronous visuo-tactile stimulation (Maselli and Slater, 2013). The current study's results indicate that the asynchronous visuo-tactile stimuli also induced illusory ownership, though not as much as under the synchronous conditions. The evaluation of tactile sensitivity in this study also revealed a slight change in illusory ownership under asynchronous conditions.

Clinical Applications

The present study demonstrated that illusion-induced stimulation in healthy adults leads to a decrease in sensory detection as well as to a decrease in the SoO of the subjects' own hands. In clinical cases, many stroke patients declaring disownership showed severe sensory and motor deficits (Ronchi et al., 2020), indicating that the reduced frequency of use for the affected limb, as well as the brain damage in areas involved in sensory and motor function, might be the causes of the decrease of ownership. This study's experimentally generated situation in illusory ownership may be useful in understanding the pathological condition of patients with sensory and motor deficits.

A previous study using RHI with healthy subjects reported that the illusion had a greater effect on the non-dominant than on the dominant hand (Dempsey-Jones and Kritikos, 2019). Another study that included a group of healthy subjects who prevented left-hand movements by using a cast for 1 week also showed stronger illusory effects on the immobilized hand and weaker illusory effects on the non-immobilized hand (Burin et al., 2017). Expansion of the subject group of hemiplegic patients also showed that patients displayed stronger illusory effects on their paretic hand than the intact hand (Burin et al., 2015). These findings indicate that body parts used infrequently in daily life are generally vulnerable to manipulation in body ownership. Specifically, hemiplegic patients with somatosensory disorders have relatively decreased use frequency of their paretic limbs in daily life, leading those patients to experience further decrease of the SoO of their paretic limbs and, thus, leading to further nonuse.

Results of the present study revealed that the sense of disownership induced by the RHI is an inhibiting factor for sensory detection. Based on this finding, optimizing the SoO of limbs with sensory impairment and decreasing the occurrence of learned nonuse may contribute to the normalization of sensory function. These trials are expected to lead to innovations in rehabilitation strategies.

Limitations

First, the ownership and disownership scores in this study were obtained from questionnaires completed by healthy subjects only; similar results describing changes in the SoO due to illness or trauma are not guaranteed. The causal relationship between the loss of the sense of body ownership and sensory dysfunction in clinical cases remains unclear. Future studies will require the same questionnaire evaluations from clinical patients. Second, the tactile pressure evaluation's examination region was limited to part of the left thumb; therefore, changes in sensory function throughout the entire hand or in other body parts are unknown. Future investigations that examine if the same physiological change extends to the whole body are necessary and should utilize other experimental set-ups, such as full body illusion.

CONCLUSION

A sense of disownership invoked by inducing the RHI in healthy subjects led to an increase in those subjects'

tactile-pressure thresholds. This result suggests that decrease of body ownership is an important factor in changing the function of tactile sensation. Interventions that alter the sense of body ownership may contribute to the rehabilitation of sensory impairment after stroke.

DATA AVAILABILITY STATEMENT

The raw data supporting the conclusions of this article will be made available by the authors, without undue reservation.

ETHICS STATEMENT

The studies involving human participants were reviewed and approved by the Ethics Committee of Tohoku University School of Medicine (registration number: 2020-1-47). The patients/participants provided their written informed consent to participate in this study.

AUTHOR CONTRIBUTIONS

KA, TS, and S-II conceived and designed the experiment. KA developed the experimental system, conducted the experiment, and statistical analysis. TS, RO, and ES provided critical review of the experimental procedure and data analysis. KA and TS wrote the draft of the manuscript. All authors contributed to the discussion of the results and approved the final manuscript.

FUNDING

This research was supported by the Japan Society for the Promotion of Science Grants-in-Aid for Scientific Research (JSPS KAKENHI) (Grant number JP20H05456).

ACKNOWLEDGMENTS

The authors would like to thank all individuals who participated in this study.

REFERENCES

Apps, M. A. J., and Tsakiris, M. (2014). The free-energy self: a predictive coding account of self-recognition. *Neurosci. Biobehav. Rev.* 41, 85–97. doi: 10.1016/j.neubiorev.2013.01.029

Arizono, N., Ohmura, Y., Yano, S., and Kondo, T. (2016). Functional connectivity analysis of nirs data under rubber hand illusion to find a biomarker of sense of ownership. *Neural Plast.* 2016, 1–9. doi: 10.1155/2016/6726238

Aspell, J. E., Palluel, E., and Blanke, O. (2012). Early and late activity in somatosensory cortex reflects changes in bodily self-consciousness: an evoked potential study. *Neuroscience* 216, 110–122. doi: 10.1016/j.neuroscience.2012.04.039

Bell-Krotoski, J., Weinstein, S., and Weinstein, C. (1993). Testing sensibility, including touch-pressure, two-point discrimination, point localization, and vibration. *J. Hand Ther.* 6, 114–123. doi: 10.1016/s0894-1130(12)80292-4

Botvinick, M., and Cohen, J. (1998). Rubber hands 'feel' touch that eyes see. *Nature* 391:756. doi: 10.1038/35784

Burin, D., Garbarini, F., Bruno, V., Fossataro, C., Destefanis, C., Berti, A., et al. (2017). Movements and body ownership:evidence from the rubber hand illusion after mechanical limb immobilization. *Neuropsychologia* 107, 41–47. doi: 10.1016/j.neuropsychologia.2017.11.004

Burin, D., Livelli, A., Garbarini, F., Fossataro, C., Folegatti, A., Gindri, P., et al. (2015). Are movements necessary for the sense of body ownership? evidence from the rubber hand illusion in pure hemiplegic patients. *PLoS One* 10:e0117155. doi: 10.1371/journal.pone.0117155

Costantini, M., and Haggard, P. (2007). The rubber hand illusion: Sensitivity and reference frame for body ownership. *Conscious. Cogn.* 16, 229–240. doi: 10.1016/j.concog.2007.01.001

Della Gatta, F., Garbarini, F., Puglisi, G., Leonetti, A., Berti, A., and Borroni, P. (2016). Decreased motor cortex excitability mirrors own hand disembodiment during the rubber hand illusion. *Elife* 5:e14972. doi: 10.7554/eLife.14972

Dempsey-Jones, H., and Kritikos, A. (2019). Handedness modulates proprioceptive drift in the rubber hand illusion. *Exp. Brain Res.* 237, 351–361. doi: 10.1007/s00221-018-5391-3

Dieguez, S., Mercier, M. R., Newby, N., and Blanke, O. (2009). Feeling numbness for someone else's finger. *Curr. Biol.* 19, R1108–R1109. doi: 10.1016/j.cub.2009.10.055

Ehrsson, H. H., Spence, C., and Passingham, R. E. (2004). That's my hand! Activity in premotor cortex reflects feeling of ownership of a limb. *Science* 305, 875–877. doi: 10.1126/science.1097011

Feinberg, T. E., and Venneri, A. (2014). Somatoparaphrenia: evolving theories and concepts. *Cortex* 61, 74–80. doi: 10.1016/j.cortex.2014.07.004

Gallagher, I. (2000). Philosophical conceptions of the self: Implications for cognitive science. *Trends Cogn. Sci.* 4, 14–21. doi: 10.1016/s1364-6613(99)01417-5

Iwamura, Y. (1998). Hierarchical somatosensory processing. *Curr. Opin. Neurobiol.* 8, 522–528. doi: 10.1016/s0959-4388(98)80041-x

Jeannerod, M. (2003). The mechanism of self-recognition in humans. *Behav. Brain Res.* 142, 1–15. doi: 10.1016/s0166-4328(02)00384-4

Kandel, E. R., Schwartz, J. H., Jessell, T. M., Siegelbaum, S. A., and Hudspeth, A. J. (2014). *Principles of Neural Science*, 5th Edn. New York, NY: McGraw-Hill Education, 491–522.

Lane, T., Yeh, S. L., Tseng, P., and Chang, A. Y. (2017). Timing disownership experiences in the rubber hand illusion. *Cogn. Res. Princ. Implic.* 2:4. doi: 10.1186/s41235-016-0041-4

Liepert, J., Bauder, H., Wolfgang, H. R., Miltner, W. H., Taub, E., and Weiller, C. (2000). Treatment-induced cortical reorganization after stroke in humans. *Stroke* 31, 1210–1216. doi: 10.1161/01.str.31.6.1210

Liepert, J., Tegenthoff, M., and Malin, J. P. (1995). Changes of cortical motor area size during immobilization. *Electroencephalogr. Clin. Neurophysiol.* 97, 382–386. doi: 10.1016/0924-980x(95)00194-p

Limanowski, J., and Blankenburg, F. (2015). Network activity underlying the illusory self-attribution of a dummy arm. *Hum. Brain Mapp.* 36, 2284–2304. doi: 10.1002/hbm.22770

Longo, M. R., Schüür, F., Kammers, M. P., Tsakiris, M., and Haggard, P. (2008). What is embodiment? A psychometric approach. *Cognition* 107, 978–998. doi: 10.1016/j.cognition.2007.12.004

Maselli, A., and Slater, M. (2013). The building blocks of the full body ownership illusion. *Front. Hum. Neurosci.* 7:83. doi: 10.3389/fnhum.2013.00083

Moseley, G. L., Olthof, N., Venema, A., Don, S., Wijers, M., Gallace, A., et al. (2008). Psychologically induced Cooling of a specific body part caused by the illusory ownership of an artificial counterpart. *Proc. Natl Acad. Sci. U.S.A.* 105, 13169–13173. doi: 10.1073/pnas.0803768105

Nudo, R. J., and Milliken, G. W. (1996). Reorganization of movement representations in primary motor cortex following focal ischemic infarcts in adult squirrel monkeys. *J. Neurophysiol.* 75, 2144–2149. doi: 10.1152/jn.1996.75.5.2144

Nudo, R. J., Milliken, G. W., Jenkins, W. M., and Merzenich, M. M. (1996a). Use-dependent alterations of movement representations in primary motor cortex of

adult squirrel monkeys. *J. Neurosci.* 16, 785–807. doi: 10.1523/JNEUROSCI.16-02-00785.1996

Nudo, R. J., Wise, B. M., SiFuentes, F., and Milliken, G. W. (1996b). Neural substrates for the effects of rehabilitative training on motor recovery after ischemic infarct. *Science* 272, 1791–1794. doi: 10.1126/science.272.5269.1791

Nudo, R. J., Plautz, E. J., and Frost, S. B. (2001). Role of adaptive plasticity in recovery of function after damage to motor cortex. *Muscle Nerve* 24, 1000–1019. doi: 10.1002/mus.1104

Oldfield, R. C. (1971). The assessment and analysis of handedness: the edinburgh inventory. *Neuropsychologia* 9, 97–113. doi: 10.1016/0028-3932(71)90067-4

Ortigue, S., Mégevand, P., Perren, F., Landis, T., and Blanke, O. (2006). Double dissociation between representational personal and extrapersonal neglect. *Neurology* 66, 1414–1417. doi: 10.1212/01.wnl.0000210440.49932.e7

Romano, D., and Maravita, A. (2019). The dynamic nature of the sense of ownership after brain injury. Clues from asomatognosia and somatoparaphrenia. *Neuropsychologia* 132:107119. doi: 10.1016/j.neuropsychologia.2019.107119

Ronchi, R., Bassolino, M., Viceic, D., Bellmann, A., Vuadens, P., Blanke, O., et al. (2020). Disownership of body parts as revealed by a visual scale evaluation. An observational study. *Neuropsychologia* 138:107337. doi: 10.1016/j.neuropsychologia.2020.107337

Rossi Sebastiano, A., Bruno, V., Ronga, I., Fossataro, C., Galigani, M., Neppi-Mondona, M., et al. (2021). Diametrical modulation of tactile and visual perceptual thresholds during the rubber hand illusion: a predictive coding account . *Psychol. Res.* doi: 10.1007/s00426-021-01608-0

Salomon, R., Lim, M., Pfeiffer, C., Gassert, R., and Blanke, O. (2013). Full body illusion is associated with widespread skin temperature reduction. *Front. Behav. Neurosci.* 7:65. doi: 10.3389/fnbeh.2013.00065

Tashiro, S., Kuroki, M., Okuyama, K., Oshima, O., Ogura, M., Hijikata, N., et al. (2021). Factors related to daily use of the paretic upper limb in patients with chronic hemiparetic stroke-A retrospective cross-sectional study. *PLoS One* 16:e0247998. doi: 10.1371/journal.pone.0247998

Taub, E. (1980). "Somatosensory deafferentation research with monkeys: implications for rehabilitation medicine," in *Behavioral Psychology in Rehabilitation Medicine: Clinical Applications*, ed. L. P. Ince (New York, NY: Williams & Wilkins), 371–401.

Taub, E., Uswatte, G., and Elbert, T. (2002). New treatments in neurorehabilitation founded on basic research. *Nat. Rev. Neurosci.* 3, 228–236. doi: 10.1038/nrn754

Taub, E., Uswatte, G., Mark, V. W., and Morris, D. M. M. (2006). The learned nonuse phenomenon: Implications for rehabilitation. *Eura. Medicophys.* 42, 241–256.

Tsakiris, M. (2010). My body in the brain: a neurocognitive model of body-ownership. *Neuropsychologia* 48, 703–712. doi: 10.1016/j.neuropsychologia.2009.09.034

Tsakiris, M., and Haggard, P. (2005). The rubber hand illusion revisited: visuotactile integration and self-attribution. *J. Exp. Psychol. Hum. Percept. Perform.* 31, 80–91. doi: 10.1037/0096-1523.31.1.80

Zeller, D., Litvak, V., Friston, K. J., and Classen, J. (2015). Sensory processing and the rubber hand illusion–an evoked potentials study. *J. Cogn. Neurosci.* 27, 573–582. doi: 10.1162/jocn_a_00705

Zeller, D., Litvak, V., Friston, K. J., and Classen, J. (2016). Dynamic causal modeling of touch-evoked potentials in the rubber hand illusion. *Neuroimage* 138, 266–273. doi: 10.1016/j.neuroimage.2016.05.065

Zopf, R., Harris, J. A., and Williams, M. A. (2011). The influence of body-ownership cues on tactile sensitivity. *Cogn. Neurosci.* 2, 147–154. doi: 10.1080/17588928.2011.578208

Conflict of Interest: The authors declare that the research was conducted in the absence of any commercial or financial relationships that could be construed as a potential conflict of interest.

Publisher's Note: All claims expressed in this article are solely those of the authors and do not necessarily represent those of their affiliated organizations, or those of the publisher, the editors and the reviewers. Any product that may be evaluated in this article, or claim that may be made by its manufacturer, is not guaranteed or endorsed by the publisher.

Copyright © 2022 Ataka, Sudo, Otaki, Suzuki and Izumi. This is an open-access article distributed under the terms of the Creative Commons Attribution License (CC BY). The use, distribution or reproduction in other forums is permitted, provided the original author(s) and the copyright owner(s) are credited and that the original publication in this journal is cited, in accordance with accepted academic practice. No use, distribution or reproduction is permitted which does not comply with these terms.

frontiers in Systems Neuroscience

ORIGINAL RESEARCH
published: 25 January 2022
doi: 10.3389/fnsys.2021.805746

Body-Specific Attention to the Hands and Feet in Healthy Adults

Naoki Aizu[1], Ryoji Otaki[2], Kazuhiro Nishii[1,3], Takumi Kito[1], Runhong Yao[4], Kenya Uemura[5], Shin-ichi Izumi[2,6] and Kouji Yamada[1,3]*

[1]School of Health Sciences, Faculty of Rehabilitation, Fujita Health University, Toyoake, Japan, [2]Department of Physical Medicine and Rehabilitation, Tohoku University Graduate School of Medicine, Sendai, Japan, [3]Graduate School of Health Sciences, Fujita Health University, Toyoake, Japan, [4]Department of Physical Therapy, School of Health Sciences, Japan University of Health Sciences, Satte, Japan, [5]Department of Rehabilitation, Hachinohe City Hospital, Hachinohe, Japan, [6]Department of Physical Medicine and Rehabilitation, Tohoku University Graduate School of Biomedical Engineering, Sendai, Japan

To execute the intended movement, the brain directs attention, called body-specific attention, to the body to obtain information useful for movement. Body-specific attention to the hands has been examined but not to the feet. We aimed to confirm the existence of body-specific attention to the hands and feet, and examine its relation to motor and sensory functions from a behavioral perspective. The study included two groups of 27 right-handed and right-footed healthy adults, respectively. Visual detection tasks were used to measure body-specific attention. We measured reaction times to visual stimuli on or off the self-body and calculated the index of body-specific attention score to subtract the reaction time on self-body from that off one. Participants were classified into low and high attention groups based on each left and right body-specific attention index. For motor functions, Experiment 1 comprised handgrip strength and ball-rotation tasks for the hands, and Experiment 2 comprised toe grip strength involved in postural control for the feet. For sensory functions, the tactile thresholds of the hands and feet were measured. The results showed that, in both hands, the reaction time to visual stimuli on the hand was significantly lesser than that offhand. In the foot, this facilitation effect was observed in the right foot but not the left, which showed the correlation between body-specific attention and the normalized toe gripping force, suggesting that body-specific attention affected postural control. In the hand, the number of rotations of the ball was higher in the high than in the low attention group, regardless of the elaboration exercise difficulty or the left or right hand. However, this relation was not observed in the handgripping task. Thus, body-specific attention to the hand is an important component of elaborate movements. The tactile threshold was higher in the high than in the low attention group, regardless of the side in hand and foot. The results suggested that more body-specific attention is directed to the limbs with lower tactile abilities, supporting the sensory information reaching the brain. Therefore, we suggested that body-specific attention regulates the sensory information to help motor control.

Keywords: body-specific attention, hand, foot, healthy adults, motor control, sensory function

OPEN ACCESS

Edited by:
Jun Ota,
The University of Tokyo, Japan

Reviewed by:
Wen Wen,
The University of Tokyo, Japan
Eiichi Naito,
National Institute of Information and Communications Technology (Japan), Japan

****Correspondence:***
Naoki Aizu
naoki.aizu@fujita-hu.ac.jp

Received: *30 October 2021*
Accepted: *23 December 2021*
Published: *25 January 2022*

Citation:
Aizu N, Otaki R, Nishii K, Kito T, Yao R, Uemura K, Izumi S-i and Yamada K (2022) Body-Specific Attention to the Hands and Feet in Healthy Adults. Front. Syst. Neurosci. 15:805746. doi: 10.3389/fnsys.2021.805746

INTRODUCTION

To execute the intended movement, the brain generates a motor program based on various sensory information from the body. At that time, the brain directs attention to one's own body and regulates the amount of information from the effectors to help with motor control. Recent research has shown that visual detection tasks can objectively measure attentional function. Specifically, responses to the visual stimuli on the body are faster than responses to the visual stimuli farther away from the body (Whiteley et al., 2004, 2008; Kao and Goodale, 2009) in the personal space, indicating that attention is potentially directed to the body (Aizu et al., 2018). This facilitation of response is observed not only in the personal space but also in the peripersonal space, near the body. Considering the peripersonal space, previous reports have demonstrated that healthy adults can detect visual targets more quickly when the targets are presented near the hand than when they are presented farther away (Reed et al., 2006, 2010; Dufour and Touzalin, 2008). This body facilitation effect, which enables faster detection of a target either on or nearer to the body, also occurs in situations involving proprioceptive information without hand visual information (Reed et al., 2006) and passive movement of the hand (Whiteley et al., 2008). This facilitation of response is based on the distance from the body (Hari and Jousmäki, 1996), suggesting that the response is faster on the body than near the body. This dominance of visual stimulus detection on the self-body was interpreted to be a result of latent attention towards the self-body, which is called body-specific attention (Aizu et al., 2018). Thus, it is important to understand the characteristics of this body-specific attention because sensory information from the extremities is useful for motor control.

Body-specific attention adapts to the activity status of the body. In patients with hemiparesis after a stroke, a time-dependent decline in body-specific attention to the paretic hand indicated that such decline was caused by patients learning to avoid using the paretic limb by considering the paretic limb useless for daily tasks rather than such decline being caused by brain damage (Aizu et al., 2018). Another study showed that detection improves for targets presented with the rake as a tool, after training with the rake in hand (Kao and Goodale, 2009; Reed et al., 2010). This finding provides strong support for the idea that this effect can be modulated by training, such that new objects, such as tools, can be incorporated into the body representation in the brain; that is, the brain recognizes tools as a part of the body. This affects the processing of visual stimuli (Kao and Goodale, 2009). Therefore, the facilitation either on or near the body is well documented in the context of body representations in the brain. Since peripersonal space in the foot reportedly facilitates the response (Schicke et al., 2009; Stettler and Thomas, 2017; Stone et al., 2018), it can be inferred that the personal space also facilitates the response in the foot, thereby indicating body-specific attention to the foot. However, Body-specific attention to the hands has been examined but not to the feet.

Owing to the different roles limbs play in human behavior (for example, hands are used for manipulating objects and feet are a means of postural control and transportation, and functional role of dominant and non-dominant in hand and foot), body-specific attention towards the hands and feet may be different. Considering the functional roles of the left and right feet, evidence indicates that the dominant foot produces a more propulsive force while the non-dominant foot provides preferential support during gait (Sadeghi et al., 1997). In addition, it is behaviorally unclear which functions are related to the body-specific attention to the hands and which to the feet. In the motor function of the hand, since body-specific attention plays an important role in motor control, we measured the ball rotation task as an elaborate movement requiring more control, and in contrast, we measured the simple handgrip task as maximal force exertion. In the motor function of the foot, since toe grasping force as foot motor function is an important factor for postural control (Kobayashi et al., 1999; Menz et al., 2005; Hashimoto and Sakuraba, 2014), we measured the grasping force; moreover, we measured the standing long jump task. In sensory function, many studies discussed that the tactile sensation is closely related to motor control. Previous reports have demonstrated that the precision grip of the hand and postural responses of the lower limb are impaired when sensory input from the hand (Johansson and Westling, 1984, 1987) or foot (Magnusson et al., 1990; Perry et al., 2000) is temporarily blocked in healthy participants. Recent reports in amputees have also demonstrated that generating tactile feedback through a prosthetic hand and foot can improve control with the prosthesis (Hebert et al., 2014; Valle et al., 2018; Petrini et al., 2019). Therefore, these findings indicated that sensory-motor integration plays an important role in motor control. In sensory function, we measured the tactile threshold of the hand and foot. We hypothesized that if body-specific attention exists, body-specific attention would be related to ball rotation tasks as elaborate movements in the hands, to toe grasping task in the feet in motor function, and body-specific attention would be related to the tactile threshold in sensory function. The purpose of this study is to confirm the existence of body-specific attention to the hands and feet and to examine how body-specific attention to the hands and feet is related to motor and sensory functions from a behavioral perspective.

METHODS

We performed a cross-sectional study using prospectively collected data from the Fujita Health University, Japan. Fifty-four healthy young adults participated in the experiment. Two groups of 27 individuals participated independently in two different experiments: Experiment 1 (mean age ± SD, 20.9 ± 0.5 years; 15 male, all with a right dominant hand) and Experiment 2 (mean age ± SD, 20.8 ± 0.7 years; 17 male, all with a right dominant foot; Oldfield, 1971; Chapman et al., 1987). Body-specific attention to the hands was measured in Experiment 1 and body-specific attention to the feet was measured in Experiment 2 by using a visual detection task. All the participants performed our visual detection task for the first time. We also assessed motor function using hand grip strength and a ball-rotation

task in Experiment 1, and using toe grip strength and standing long jump tasks in Experiment 2. In addition, we assessed sensory function as the tactile threshold of the back of the hand in Experiment 1 and the sole of the foot in Experiment 2.

Standard Protocol Approvals, Registrations, and Participants' Consent

The Fujita Health University Ethics Committee approved this research (HM19-382), which was conducted in compliance with the ethical standards of the Declaration of Helsinki. Prior to our experiment, all participants agreed to participate in our experiment and provided written informed consent.

Experimental Procedure

In order to quantitatively measure body-specific attention to the hands and feet, a visual detection experiment was used for detecting light emitting diode (LED) lighting on either the surface of the self-body parts or surfaces far from the body parts (**Figure 1**). This experiment was designed to measure body-specific attention to detect a visual target near the body and has previously been tested in healthy adults (Whiteley et al., 2004, 2008; Reed et al., 2006, 2010; Kao and Goodale, 2009; Aizu et al., 2018). This task can measure body-specific attention as a body facilitation effect, which enables faster detection of a target on the body compared to a target far from the body.

The participants sat in a chair in front of a rack in a quiet room (**Figures 1A,B**). They were required to respond as quickly as possible to the glow of a blue LED that appeared on either the self-body parts or opposite to them. After the green LED fixation appeared, the target LED randomly appeared for 800–1,600 ms (**Figures 1C,D**). The participants were required to push the button only when a blue LED appeared, and gazed at the green LED as the fixation point. A blue LED representing a "go" visual target appeared in 80% of the trials. In the rest of the trials, a red LED representing a "no-go" target, that required no response, appeared. Reaction time (RT) was considered to be the time between the onset of glowing of the LED and the reaction of the participants (pushing the button). The response button was located at the same distance from each target LED. To equalize the visual information in the visual detection task, a white cloth or board covered the patients' arms or legs (**Figures 1E,F**). In one condition, the participant performed 80 trials. Before the experiment, the participants performed 60 trials as a training session for the visual detection task. In order to eliminate the effects of delayed reactions owing to inattention during the task and accelerated reactions owing to anticipation of the appearance of the visual target, the obtained reaction time data that exceeded two standard deviations (SD) above and below the mean reaction time were excluded from the results as outliers.

Conditions in Experiment 1

Body-specific attention to the left and right hands was measured according to previous methods (Aizu et al., 2018). To minimize differences in appearance between the self-hand and a dummy hand, both hands were covered with white cotton gloves (**Figure 1E**).

In the Hand-L condition, participants placed their hands in the left space; in contrast, a dummy hand was placed in the right space. In the Hand-R condition, the participants placed their hands in the right space; in contrast, a dummy hand was placed in the left space. In the control condition, the self-hand was placed on the abdomen, and two dummy hands were placed on the rack. The participants pushed a button with the index finger as soon as the target LED appeared. The participants were separately exposed to the tests in a counterbalanced manner.

The target LED was located 18 cm from the midsagittal plane. The distance between the green LED and target LED was 28 cm, and the distance between the target LED and the participants was 28 cm. The dummy hand was placed 36 cm away from the hand on the rack.

Conditions in Experiment 2

To measure body-specific attention to the left and right foot, the conditions were defined as the Foot-L, Foot R, and Control conditions (**Figure 1F**). In the Foot-L condition, the participant placed their left foot on the foot stand (knee extension position), and the right foot was placed on the ground. The left foot was positioned such that the target LED was located at the center of the left ankle. In the Foot-R condition, the participant placed their right foot on the foot stand (knee extension position), with the right foot positioned where the target LED on the right side was presented. The left foot was placed on the ground. In the control condition, the left and right feet were both on the ground, and participants responded to the target LED to confirm the attentional bias between the left and right spaces. The participants pushed a button with their right index finger as soon as the target LED appeared. The participants were separately exposed to the tests in a counterbalanced manner.

At the beginning of each trial, the target LED was located 21 cm from the midsagittal plane, the distance between the green LED and the target LED was 32 cm, and the distance between the target LED and the participants was approximately 65 cm, depending on the length of their lower extremities.

Motor Assessment

In Experiment 1 relating to the hands, we conducted a ball-rotation task and a handgrip task for motor function measurements. In the ball-rotation task, they rotated two balls using either their left or right hand to assess the elaborate movement. The two balls were rotated on the palmar surface for 20 s. The measurements were recorded using a video camera, and the number of rotations of the balls were counted. The balls were spherical, 4 cm in diameter, and weighed 75 g. To confirm whether the ball rotation task was an elaborate movement for the participants, two tasks with different difficulty levels were performed: the easy task was clockwise rotation with the right hand and counterclockwise rotation with the left hand, while the hard task required the right hand to rotate the ball counterclockwise and the left hand to rotate it clockwise. Participants performed a handgripping task to assess the maximal force exertion in the left and right hands.

In Experiment 2, we conducted a toe grip strength task and a standing long jump task. In relation to the feet, the participants

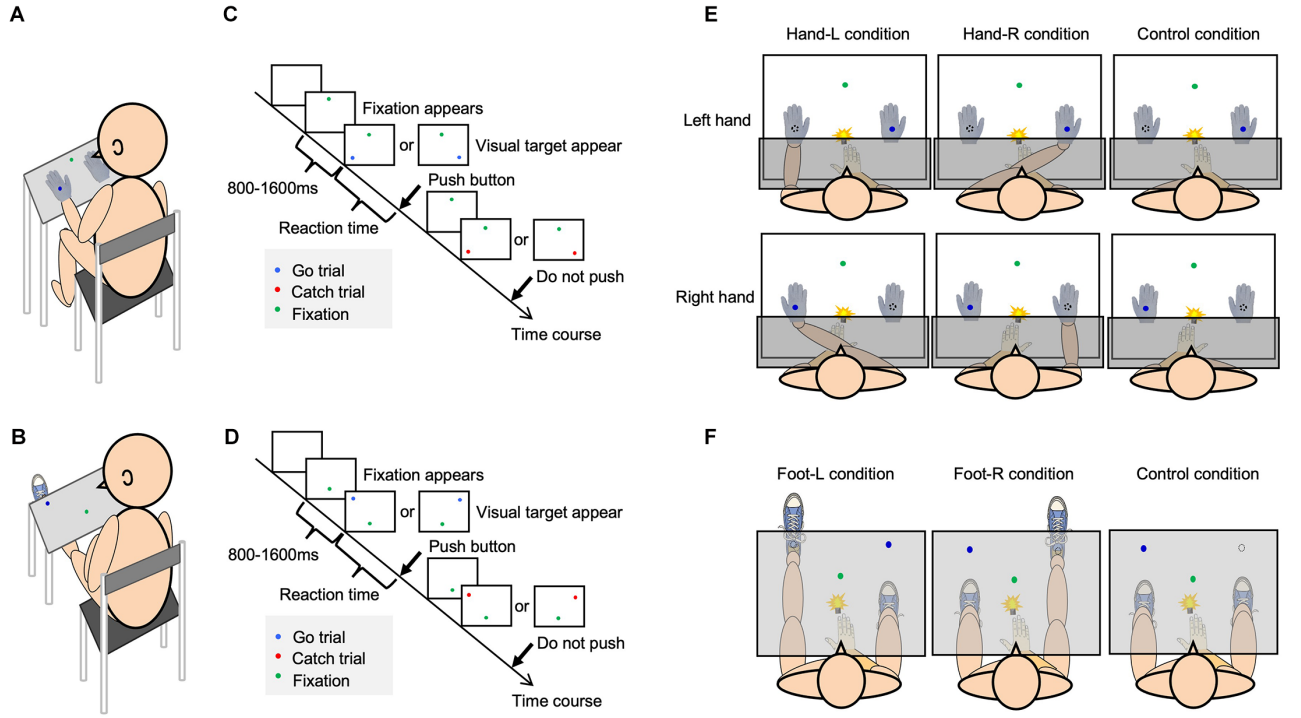

FIGURE 1 | Experimental setup and the visual detection task. Each figure shows the experimental setup [**(A)** hand; **(B)** foot], procedure of visual detection task [**(C)** hand; **(D)** foot], and each condition [**(E)** hand; **(F)** foot].

performed the toe gripping task (Toe grip dynamometer, Takei Scientific Instruments) to assess the maximum force exerted in the left and right feet. In the standing long jump task, they jumped as far as they could from a standing position and the distance was measured. All motor assessments were performed thrice, and the average of the three assessments was calculated. In addition, for each task, the trial order of the left and right, and the difficulty level were counterbalanced for each participant.

Sensory Assessment

We measured the tactile threshold using Semmes–Weinstein monofilaments (Sakai Medical) of different thicknesses. We measured the tactile thresholds of the dorsum of the hand (second metacarpal metaphyseal part) in Experiment 1 and the sole of the foot (ball of the big toe) in Experiment 2. The staircase method was used for the measurement, and the average value of seven change points was calculated as the tactile threshold. The left and right trial orders were counterbalanced and conducted for each participant.

Statistical Analyses

The measured data were checked for normality using the Shapiro–Wilk test before the usage of statistical methods. To confirm body-specific attention to the hand in Experiment 1, we performed a three-way analysis of variance (ANOVA; hand, hand position, target LED position) with repeated measures and multiple comparisons, as a *post hoc* test with the Bonferroni correction. If there was an interaction effect between the two factors (hand position and visual target position), the response to visual stimuli on the hand was significantly faster than that to stimuli on the fake hand. To confirm body-specific attention to the foot in Experiment 2, we performed a two-way analysis of variance (ANOVA; foot position, target LED position) with repeated measures and multiple comparisons, as a *post hoc* test with the Bonferroni correction. If there was an interaction effect between the two factors (foot position and target LED position), the response to visual stimuli on the foot was significantly faster than that to stimuli off the foot. In the control condition, we used two-way ANOVA with repeated measures and paired t-tests to compare the response times of both sides in Experiments 1 and 2, respectively.

The index of body-specific attention was calculated by subtracting the RT for the target-on-self-body parts from that for the target-off-self-body parts. Furthermore, to examine what attention to the hand and foot affected participant-specific factors, we classified the participants into low and high attention groups based on the index of body-specific attention to each left and right hand and foot. In the comparison between the two groups, the results of the motor and sensory assessment were compared by using the three-way and two-way ANOVA.

To avoid the effect of body size on the maximal force exertion in the hand and foot, the measured values were divided by body weight and normalized. In addition, the score of the standing long jump was normalized according to the body height.

Statistical significance was set at $p < 0.05$. Regarding the software for analysis, we used SPSS version 26.

RESULTS

We confirmed the existence of body-specific attention to the hands and feet in Experiments 1 and 2. In the visual detection task, the three-way ANOVA with repeated measures showed a statistically significant interaction term in Experiment 1 (Two factors: hand position, visual target position $F_{(1,25)} = 32.609$, $p < 0.001$, $\eta_p^2 = 0.538$; **Figure 2**). In the multiple comparisons with the Bonferroni correction, the RT on the hand was shorter than that off the hand in the hand-L ($p = 0.011$) and hand-R conditions ($p = 0.008$). RT was facilitated when the hand position and the visual target position were spatially congruent than when incongruent, regardless of the hand. The ANOVA of healthy adults showed that there was no main effect for the factors (hand: $F_{1,25} = 2.184$, $p = 0.152$, $\eta_p^2 = 0.050$ hand position: $F_{1,25} = 0.771$, $p = 0.388$, $\eta_p^2 = 0.010$, visual target position $F_{1,25} = 0.001$, $p = 0.983$, $\eta_p^2 = 0.008$) and no interaction effect (hand × hand position × visual target position: $F_{1,25} = 0.005$, $p = 0.942$, $\eta_p^2 = 0.007$). In the control condition, the two-way ANOVA with repeated measures showed that there was no main effect for the factors (hand: $F_{1,26} = 2.326$, $p = 0.139$, $\eta_p^2 = 0.082$, visual target position: $F_{1,26} = 0.150$, $p = 0.701$, $\eta_p^2 = 0.006$) and no interaction ($F_{1,26} = 0.003$, $p = 0.957$, $\eta_p^2 = 0.001$). In other words, there was no difference in the RT for the left and right sides in Experiment 1. For Experiment 2, a two-way ANOVA with repeated measures showed a statistically significant interaction term (two factors: foot position, visual target position, $F_{1,26} = 4.936$, $p = 0.035$, $\eta_p^2 = 0.160$; **Figure 3**). In the multiple comparisons with the Bonferroni correction, the RT on the foot was shorter than that off the foot in the foot-R conditions ($p = 0.026$), while in the foot L conditions, there was no significance ($p = 0.306$). In addition, the ANOVA for healthy adults showed that there was no main effect for the factors (foot position $F_{1,26} = 1.544$, $p = 0.225$, $\eta_p^2 = 0.056$, visual target position $F_{1,26} = 0.745$, $p = 0.398$, $\eta_p^2 = 0.028$). In the control condition, there was no difference in the RT between the left and right sides in Experiment 2 (paired t-test, df = 26 $t = 1.674$, $p = 0.106$). In the right foot, RT was facilitated when the foot position and the visual target position was spatially congruent than when incongruent. The average incorrect responses in Experiment 1 were 0.44 times in the "no-go" target (16 trials) and 0.40 in Experiment 2, showing no difference in the incorrect response times between Experiments 1 and 2.

To examine the functions of body-specific attention in healthy adults, we compared the results of the motor and sensory assessments by classifying participants into low and high attention groups based on the index of body-specific attention. For the hand, in ball rotation task, three-way ANOVA demonstrated a statistically significant main effect for the factors (task: $F_{1,50} = 81.139$, $p < 0.001$, $\eta_p^2 = 0.448$, groups: $F_{1,50} = 7.593$, $p = 0.007$, $\eta_p^2 = 0.071$; **Figure 4**). Moreover, there was no main effect for the factors (hand: $F_{1,50} = 0.764$, $p = 0.384$, $\eta_p^2 = 0.008$) and no interaction effect (hand × task × groups: $F_{1,50} = 0.337$, $p = 0.563$, $\eta_p^2 = 0.003$). Thus, the number of rotations of the ball was higher in the high attention group (left hand in easy task: Mean = 10.7, SD = 2.6, $N = 13$, left hand in hard task: Mean = 6.8, SD = 2.9, $N = 13$, right hand in easy task: Mean = 10.5, SD = 2.1, $N = 13$, right hand in hard task: Mean = 6.3, SD = 1.9, $N = 13$) than that in the low attention group (left hand in easy task: Mean = 9.5, SD = 3.1, $N = 14$, left hand in hard task: Mean = 5.4, SD = 2.3, $N = 14$, right hand in easy task: Mean = 9.7, SD = 2.7, $N = 14$, right hand in hard task: Mean = 6.2, SD = 2.8, $N = 14$), regardless of the difficulty of the elaboration exercise or the left or right hand. In addition, our results confirmed that the level of difficulty was distinguished between the hard and the easy task. In the normalized gripping force of gripping task, two-way ANOVA demonstrated that there was no main effect (hand: $F_{1,50} = 0.835$, $p = 0.365$, $\eta_p^2 = 0.016$, groups: $F_{1,50} = 3.331$, $p = 0.075$, $\eta_p^2 = 0.062$) and no interaction (hand × groups: $F_{1,50} = 0.285$, $p = 0.596$, $\eta_p^2 = 0.006$). In the tactile sensation of the hand, the tactile threshold in the high attention group (left hand:

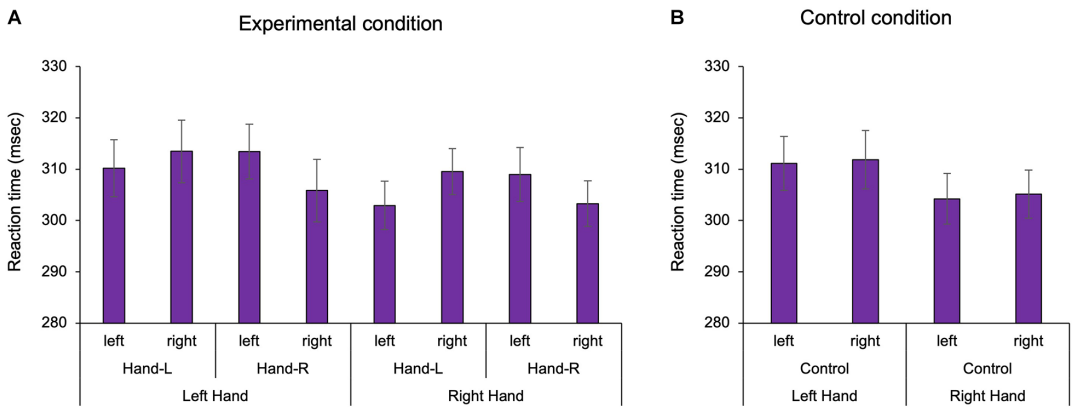

FIGURE 2 | The reaction time of the hand in Experiment 1. In the experimental condition, the existence of the hand facilitated the reaction time in the left and right hands, regardless of hand position. In the control condition, there was no difference in the reaction time between the left and right sides. Hand-L: The participant placed their hand in the left space. Hand-R: The participant placed their hand in the right space. **(A)** Experimental condition; **(B)** Control condition, Mean ± Standard error.

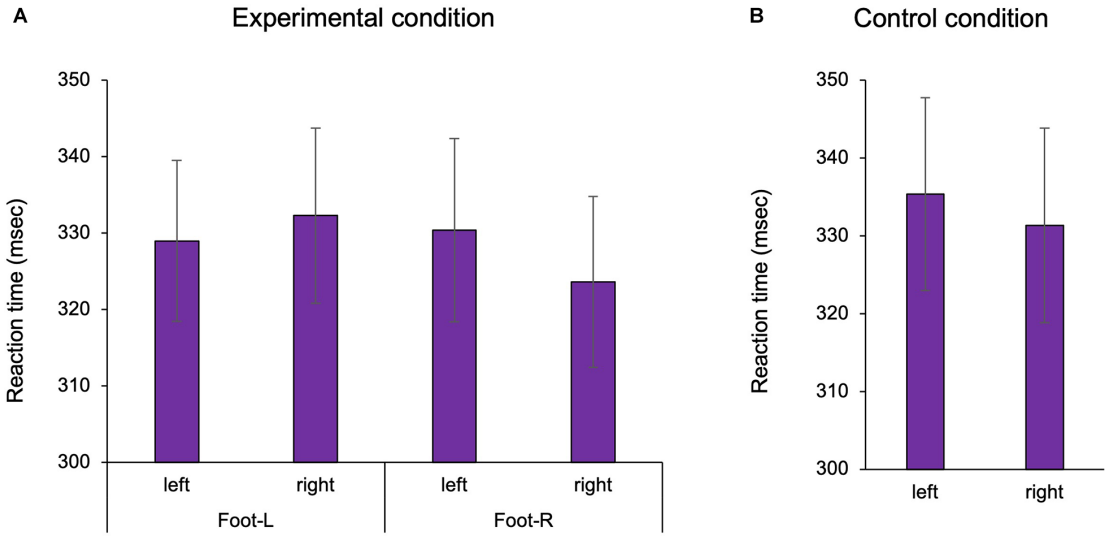

FIGURE 3 | The reaction time of the foot in Experiment 2. In the experimental condition, the presence of the foot facilitated the reaction time. In the control condition, there was no difference in the reaction time between the left and right sides. Foot-L: The left foot was positioned under the left target LED. Foot-R: The right foot was positioned under the right target LED. **(A)** Experimental condition; **(B)** Control condition, Mean ± Standard error. LED, light emitting diode.

Mean = 0.193, SD = 0.109, N = 13, right hand: Mean = 0.288, SD = 0.179, N = 13) was higher than that in low attention group (left hand: Mean = 0.136, SD = 0.102, N = 14, right hand: Mean = 0.166, SD = 0.111, N = 14), regardless of the left or right hand (**Figure 5**). Two-way ANOVA showed a statistically significant main effect for the factor (groups: $F_{1,50}$ = 6.466, p = 0.014, η_p^2 = 0.115). Moreover, there was no main effect (hand: $F_{1,50}$ = 3.172, p = 0.081, η_p^2 = 0.060) and interaction (hand × groups: $F_{1,50}$ = 0.853, p = 0.360, η_p^2 = 0.017).

In experiment 2, in tactile sensation of the foot, the tactile threshold in the high attention group (left foot: Mean = 0.758, SD = 0.698, N = 13, right foot: Mean = 0.409, SD = 0.439, N = 13) was higher than that in the low attention group (left foot: Mean = 0.211, SD = 0.142, N = 14, right hand: Mean = 0.337, SD = 0.258, N = 14), regardless of the left or right foot (**Figure 5**). Two-way ANOVA showed a statistically significant main effect for the factor (groups: $F_{1,50}$ = 6.968, p = 0.011, η_p^2 = 0.122) and interaction (foot × groups: $F_{1,50}$ = 4.103, p = 0.048, η_p^2 = 0.076). Moreover, there was no main effect (foot: $F_{1,50}$ = 0.900, p = 0.347, η_p^2 = 0.018). In multiple comparisons with the Bonferroni correction, the tactile threshold of the high attention group in left foot was higher than that of the low attention group in the left foot (p = 0.002) and that of the high attention group in the right foot (p = 0.044). In normalized distance of the long jump task, two-way ANOVA showed that there was no main effect (foot: $F_{1,50}$ = 0.001, p = 0.995, η_p^2 = 0.001, groups: $F_{1,50}$ = 1.701, p = 0.198, η_p^2 = 0.033) and no interaction (hand × groups: $F_{1,50}$ = 0.033, p = 0.856, η_p^2 = 0.001). In the normalized toe gripping force of the foot gripping task, two-way ANOVA showed that there was interaction (foot × groups: $F_{1,50}$ = 4.609, p = 0.037, η_p^2 = 0.084), but no main effect (foot: $F_{1,50}$ = 0.559, p = 0.458, η_p^2 = 0.011, groups: $F_{1,50}$ = 0.125, p = 0.725, η_p^2 = 0.003). In the multiple comparisons with the Bonferroni correction, the normalized toe gripping force of the high attention group in the left foot tend to be lower than that of the low attention group in the left foot (p = 0.083) and that of the high attention group in the right foot (p = 0.050). In the left foot, no facilitation of the reaction time was observed when the foot position and the visual target position were spatially congruent; however, there was a relationship between body-specific attention and the normalized toe gripping force. Therefore, a correlation analysis between body-specific attention and normalized toe gripping force was conducted. In the correlation analysis, there was a correlation between body-specific attention of the left foot and the normalized toe gripping force of the left foot (Pearson, r = −0.476, p = 0.012; **Figure 6**).

DISCUSSION

In healthy adults, we confirmed the existence of body-specific attention to the hands and feet. In Experiment 1, the number of rotations of the ball was higher in the high attention group than that in the low attention group, regardless of the difficulty of the elaboration exercise or the left or right hand. However, this relation was not observed in the gripping task. These findings indicated that body-specific attention of the hand is an important factor in the motor control as elaborate movement. In the tactile sensation of the hand and foot, the tactile threshold in the high attention group was higher than that in the low attention group, regardless of the left or right. The results suggested that more body-specific attention is directed to the limbs with lower tactile abilities, supporting the sensory information reaching the brain. In Experiment 2, in the visual detection task, the facilitation effect of the reaction time was observed in the right foot but not in the left foot. In the left non-dominant foot, which plays an important role in postural control, there was a

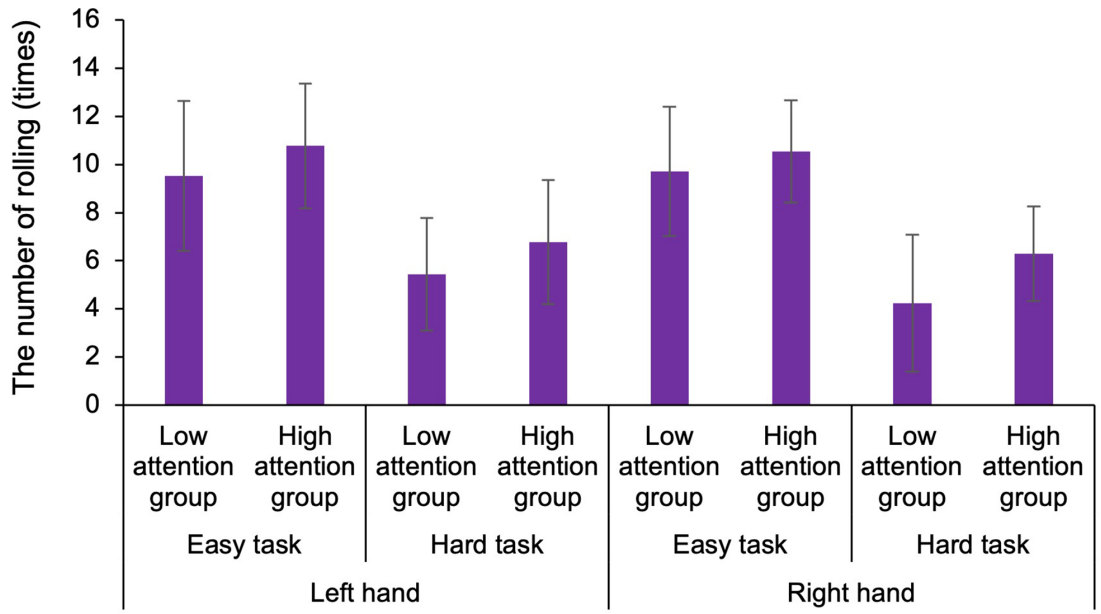

FIGURE 4 | Comparison of the number of rotations of the ball for different difficulty tasks in the low and high attention groups. The number of rotations of the ball was higher in the high attention group than that in the low attention group, regardless of the difficulty of the elaboration exercise or the left or right hand. The level of difficulty was distinguished between the hard and easy tasks.

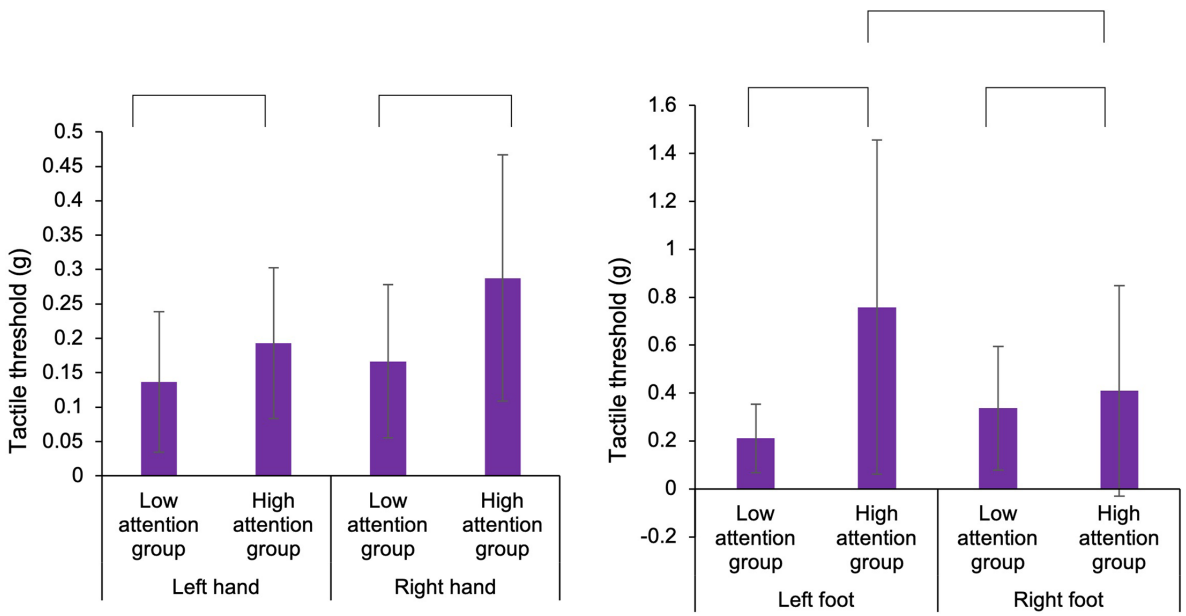

FIGURE 5 | Comparison of the tactile threshold of the hands and feet in the low and high attention groups. In the hands and feet, the tactile threshold in the high attention group was higher than that in the low attention group. In the foot, in the high attention group, the tactile threshold in the left foot was higher than that in the right foot.

correlation between body-specific attention of the left foot and the normalized toe gripping force of the left foot, indicating that body-specific attention was affected by the toe grip strength in the left foot. In the right dominant foot, on the other hand, there was no relationship between the body-specific attention and other motor functions. Thus, body-specific attention to the feet demonstrated differences between the left and right sides, suggesting that body-specific attention varied based on the functional role of the left and right foot. Considering that body-specific attention adapts to the state of the body (Aizu et al., 2018), we indicated that body-specific attention to the hands and feet plays an important role in motor control. Therefore,

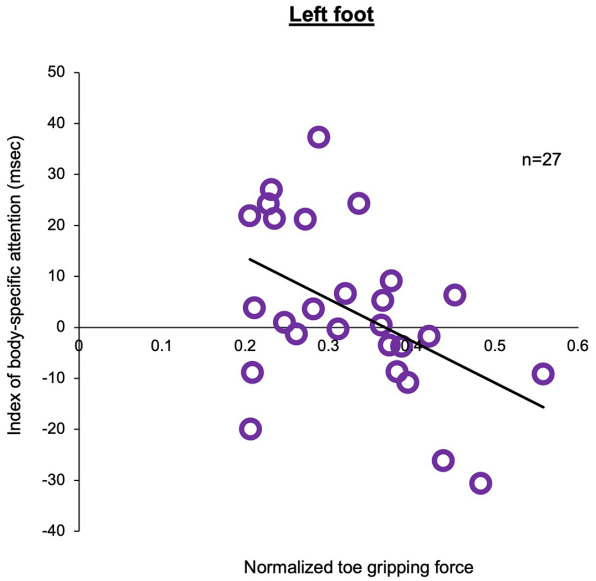

FIGURE 6 | Correlation between the index of body-specific attention to the foot and normalized toe gripping force in the left foot.The higher the value of the normalized toe gripping force, the stronger the toe gripping force against body weight. There was a negative correlation between the index of body-specific attention to the foot and normalized toe gripping force (Pearson, $n = 27$, $r = -0.476$, $p = 0.012$).

we suggested that body-specific attention regulates the sensory information to help motor control.

Our results indicate that body-specific attention supports elaborate movements. Previous reports have shown that spatial selective attention to the body facilitates somatosensory information processing (García-Larrea et al., 1991; Schubert et al., 2008). The response in the primary somatosensory cortex is generally gated during simple movement of the corresponding body part (Nakata et al., 2003; Wasaka et al., 2003), but elaborate movements such as ball rotation showed an enhancement of sensorimotor integration in the somatosensory cortex compared to other simple tasks such as grasping (Wasaka et al., 2017). In our results, for the left and right hand, the number of ball rotations was high in the high attention group. This result was also observed in the easy and difficult ball-rotation tasks. In addition, there was no relationship between the scores for body-specific attention and handgrip strength. Interestingly, our data showed that tactile thresholds were higher in the high attention group. Therefore, for participants who could not discriminate between small amounts of tactile stimuli, adaptive changes were suggested to increase sensory input to the brain by directing attention to their own hand. Past reports showed that elaborate movements are impaired when sensory input from the hand is temporarily blocked in healthy adults (Johansson and Westling, 1984, 1987). These findings suggest that body-specific attention facilitates sensory information processing during elaborate movement and facilitates motor control.

In Experiment 2, the visual stimulus detection task showed the presence of body-specific attention in the right foot but not in the left foot. Similar to our results, in the peripersonal space of the foot, the facilitation effect was observed only in the right foot and not in the left foot (Stettler and Thomas, 2017). Importantly, in the left foot, our correlation results showed that weak toe grip strength resulted in a higher score of body-specific attention to the foot. A previous study reported that toe plantar flexor muscle strength was one of the predictors of balance ability in older adults (Menz et al., 2005). This study revealed that weak toe flexor muscle strength indicates poor balance ability. In addition, preliminary evidence suggests that "grasping" exercises to strengthen toe muscles result in improved standing balance in older adults (Kobayashi et al., 1999). Moreover, in young adults, training the foot flexor strength improves movement performance (Hashimoto and Sakuraba, 2014) and gait ability (Fukuda and Kobayashi, 2008). These findings indicate that toe grasping force is an important factor in postural control. In addition, the participants in this study were all right-footed according to the dominant foot test (Chapman et al., 1987), indicating that the right foot was the dominant foot. In the functional role of the left and right feet, there is evidence suggesting that the dominant foot generates more propulsion during walking, while the non-dominant foot preferentially provides support (Sadeghi et al., 1997). Martelli et al. (2013) suggested that the non-dominant foot may be better suited for maintaining stability in response to perturbations. These findings indicate that the left foot has a higher postural control ability to support and maintain the body than the right foot (dominant foot). This could explain our results, which demonstrated a strong relationship between toe grip strength and body-specific attention only in the left foot. Considering that body-specific attention adapts to the activity status of the body (Aizu et al., 2018), in the left foot, we suggested that body-specific attention would be adaptively altered by the toe grip strength. Therefore, there is an adaptive change that increases the body-specific attention when toe grip strength is weak, and this adaptive change presumably occurs to help postural control.

Our data demonstrated that the tactile threshold was higher in the high attention group in both feet. Importantly, previous reports have shown impaired postural responses when sensory input is blocked on the foot in healthy persons (Magnusson et al., 1990; Perry et al., 2000). Given that the facilitates sensory information processing by attention (García-Larrea et al., 1991; Schubert et al., 2008), we suggested that when the function of sensory discrimination of the feet is low, body-specific attention may increase the sensory input to the brain. Therefore, these findings suggested that body-specific attention facilitates sensory information processing during postural control in the foot. However, body-specific attention to the right foot did not relate toe gripping task and standing long jump task in this study. Further investigation of the relationship between body-specific attention to the foot and postural control is warranted.

We have several hypotheses regarding the neural basis of body-specific attention. First, recent studies related to body representation in the brain have focused on the frontoparietal network (Naito et al., 2007; Takeuchi et al., 2016), and we hypothesize that body-specific attention reflecting body representation in the brain is related to this network. This network includes brain regions related to the body in the

brain, including body consciousness, which includes a sense of ownership and a sense of agency (Ehrsson et al., 2004; Naito et al., 2007; Gentile et al., 2013; Ohata et al., 2020). This frontoparietal network represents the self-body in the brain and contributes to the realization of efficient motor control and body cognition in humans. Furthermore, this frontoparietal network has also been previously known as the attentional network, which plays an important role in understanding the positional relationship between the body and the environment (Buschman and Miller, 2007; Cona and Scarpazza, 2019). These findings suggest that the neural basis of body-specific attention is most likely a frontoparietal network for attention and body representations in the brain. Next, because body-specific attention is measured based on the effect of nearby-hands (Reed et al., 2010; Tseng et al., 2012), it is likely that the posterior parietal cortex (PPC), which is the brain's region of peripersonal spatial representation, is the most important part of the frontoparietal network (Moseley et al., 2012). The PPC is a region of multisensory integration, which includes vision and somatosensory perception, and is classically known as a region involved in body schema and body image. Although most studies related to self-body have been conducted on the upper limbs, the results of studies on the lower limbs suggest a similar neural basis. Contrarily, studies on healthy subjects and amputees have demonstrated that somatotopy occurs in the sensorimotor cortex before input to the parietal association cortex (Lotze et al., 2001; Simões et al., 2012). In the hierarchy of perceptual representation, the body part is reproduced clearly, and at a higher level of propositional representation, the body part is modified *via* top-down awareness of the environment and contextual thoughts, and the integrated self-body representation is used to carry out daily activities (Cona and Scarpazza, 2019). We believe that the neural basis of body-specific attention involves the frontoparietal network, with the parietal lobe being a particularly important region.

There are limitations to this study as well. First, the difference in motor and sensory functions in healthy adults is very small compared to that in patients with motor or sensory dysfunction and top athletes or skilled performers in music. By measuring body-specific attention in these participants, future studies will be able to clarify the characteristics of body-specific attention. In addition, interventions on body-specific attention may be able to improve motor performance. Second, our results could not clearly demonstrate the relationship between body-specific attention and motor control of the foot. It is necessary to investigate body-specific attention and motor function, especially postural control, taking into account functional differences between the left and right in the foot.

In summary, this study showed the presence of body-specific attention to the feet and hands. In addition, body-specific attention was shown to be closely related to motor and sensory functions. Furthermore, it was shown that body-specific attention is adaptively altered to obtain the sensory information necessary for motor control. Given these adaptive changes in body-specific attention, further research is needed to clarify the role of body-specific attention in improving motor function.

DATA AVAILABILITY STATEMENT

The datasets presented in this study can be found in online repositories. The names of the repository/repositories and accession number(s) can be found below: https://doi.org/10.5061/dryad.9ghx3ffjc.

ETHICS STATEMENT

The studies involving human participants were reviewed and approved by The Fujita Health University ethics committee in Fujita Health University (HM19-382). The patients/participants provided their written informed consent to participate in this study.

AUTHOR CONTRIBUTIONS

NA conceived the study concept and design and wrote the manuscript. NA, TK, RY, and KN collected data. NA, RO, and KU analyzed and interpreted the data. S-iI and KY supervised the study. All authors reviewed the manuscript. All authors contributed to the article and approved the submitted version.

FUNDING

This work was partially supported by JSPS KAKENHI, Grant-in-Aid for Scientific Research on Innovative Areas (Grant Number: 20H05456) and Grant-in-Aid for Young Scientists (Grant Number: 19K19826).

REFERENCES

Aizu, N., Oouchida, Y., and Izumi, S. I. (2018). Time-dependent decline of body-specific attention to the paretic limb in chronic stroke patients. *Neurology* 91, e751–e758. doi: 10.1212/WNL.0000000000006030

Buschman, T. J., and Miller, E. K. (2007). Top-down versus bottom-up control of attention in the prefrontal and posterior parietal cortices. *Science* 315, 1860–1862. doi: 10.1126/science.1138071

Chapman, J. P., Chapman, L. J., and Allen, J. J. (1987). The measurement of foot preference. *Neuropsychologia* 25, 579–584. doi: 10.1016/0028-3932(87)0082-0

Cona, G., and Scarpazza, C. (2019). Where is the "where" in the brain? A meta-analysis of neuroimaging studies on spatial cognition. *Hum. Brain Mapp.* 40, 1867–1886. doi: 10.1002/hbm.24496

Dufour, A., and Touzalin, P. (2008). Improved visual sensitivity in the perihand space. *Exp. Brain Res.* 190, 91–98. doi: 10.1007/s00221-008-1453-2

Ehrsson, H. H., Spence, C., and Passingham, R. E. (2004). That's my hand! Activity in premotor cortex reflects feeling of ownership of a limb. *Science* 305, 875–877. doi: 10.1126/science.1097011

Fukuda, I., and Kobayashi, R. (2008). The effect of the toes-grip training in healthy young adults. *Phys. Ther. Jpn.* 35, 261–266. doi: 10.15063/rigaku.KJ00005028753

García-Larrea, L., Bastuji, H., and Mauguière, F. (1991). Mapping study of somatosensory evoked potentials during selective spatial attention. *Electroencephalogr. Clin. Neurophysiol.* 80, 201–214. doi: 10.1016/0168-5597(91)90122-e

Gentile, G., Guterstam, A., Brozzoli, C., and Ehrsson, H. H. (2013). Disintegration of multisensory signals from the real hand reduces default limb self-attribution:

an fMRI study. *J. Neurosci.* 33, 13350–13366. doi: 10.1523/JNEUROSCI.1363-13.2013

Hari, R., and Jousmäki, V. (1996). Preference of personal to extrapersonal space in a visuomotor task. *J. Cogn. Neurosci.* 8, 305–307. doi: 10.1162/jocn.1996.8.3.305

Hashimoto, T., and Sakuraba, K. (2014). Strength training for the intrinsic flexor muscles of the foot: effects on muscle strength, the foot arch and dynamic parameters before and after the training. *J. Phys. Ther. Sci.* 26, 373–376. doi: 10.1589/jpts.26.373

Hebert, J. S., Olson, J. L., Morhart, M. J., Dawson, M. R., Marasco, P. D., Kuiken, T. A., et al. (2014). Novel targeted sensory reinnervation technique to restore functional hand sensation after transhumeral amputation. *IEEE Trans. Neural Syst. Rehabil. Eng.* 22, 765–773. doi: 10.1109/TNSRE.2013.2294907

Johansson, R. S., and Westling, G. (1984). Roles of glabrous skin receptors and sensorimotor memory in automatic control of precision grip when lifting rougher or more slippery objects. *Exp. Brain Res.* 56, 550–564. doi: 10.1007/BF00237997

Johansson, R. S., and Westling, G. (1987). Signals in tactile afferents from the fingers eliciting adaptive motor responses during precision grip. *Exp. Brain Res.* 66, 141–154. doi: 10.1007/BF00236210

Kao, K. L., and Goodale, M. A. (2009). Enhanced detection of visual targets on the hand familiar tools. *Neuropsychologia* 47, 2454–2463. doi: 10.1016/j.neuropsychologia.2009.04.016

Kobayashi, R., Hosoda, M., Minematsu, A., Sasaki, H., Maejima, H., Tanaka, S., et al. (1999). Effects of toe grasp training for the aged on spontaneous postural sway. *J. Phys. Ther. Sci.* 11, 31–34. doi: 10.1589/JPTS.11.31

Lotze, M., Flor, H., Grodd, W., Larbig, W., and Birbaumer, N. (2001). Phantom movements and pain. An fMRI study in upper limb amputees. *Brain* 124, 2268–2277. doi: 10.1093/brain/124.11.2268

Magnusson, M., Enbom, H., Johansson, R., and Pyykkö, I. (1990). Significance of pressor input from the human feet in anterior-posterior postural control. The effect of hypothermia on vibration-induced body-sway. *Acta Otolaryngol.* 110, 182–188. doi: 10.3109/00016489009122535

Martelli, D., Monaco, V., Bassi Luciani, L., and Micera, S. (2013). Angular momentum during unexpected multidirectional perturbations delivered while walking. *IEEE Trans. Biomed. Eng.* 60, 1785–1795. doi: 10.1109/TBME.2013.2241434

Menz, H. B., Morris, M. E., and Lord, S. R. (2005). Foot and ankle characteristics associated with impaired balance and functional ability in older people. *J. Gerontol. A. Biol. Sci. Med. Sci.* 60, 1546–1552. doi: 10.1093/gerona/60.12.1546

Moseley, G. L., Gallace, A., and Spence, C. (2012). Bodily illusions in health and disease: physiological and clinical perspectives and the concept of a cortical 'body matrix'. *Neurosci. Biobehav. Rev.* 36, 34–46. doi: 10.1016/j.neubiorev.2011.03.013

Naito, E., Nakashima, T., Kito, T., Aramaki, Y., Okada, T., and Sadato, N. (2007). Human limb-specific and non-limb-specific brain representations during kinesthetic illusory movements of the upper and lower extremities. *Eur. J. Neurosci.* 25, 3476–3487. doi: 10.1111/j.1460-9568.2007.05587.x

Nakata, H., Inui, K., Wasaka, T., Nishihira, Y., and Kakigi, R. (2003). Mechanisms of differences in gating effects on short-and long-latency somatosensory evoked potentials relating to movement. *Brain Topogr.* 15, 211–222. doi: 10.1023/a:1023908707851

Ohata, R., Asai, T., Kadota, H., Shigemasu, H., Ogawa, K., and Imamizu, H. (2020). Sense of agency beyond sensorimotor process: decoding self-other action attribution in the human brain. *Cereb. Cortex* 30, 4076–4091. doi: 10.1093/cercor/bhaa028

Oldfield, R. C. (1971). The assessment and analysis of handedness: the Edinburgh inventory. *Neuropsychologia* 9, 97–113. doi: 10.1016/0028-3932(71)90067-4

Perry, S. D., Mcilroy, W. E., and Maki, B. E. (2000). The role of plantar cutaneous mechanoreceptors in the control of compensatory stepping reactions evoked by unpredictable, multi-directional perturbation. *Brain Res.* 877, 401–406. doi: 10.1016/s0006-8993(00)02712-8

Petrini, F. M., Bumbasirevic, M., Valle, G., Ilic, V., Mijović, P., ŠCvanŠcara, P., et al. (2019). Sensory feedback restoration in leg amputees improves walking speed, metabolic cost and phantom pain. *Nat. Med.* 25, 1356–1363. doi: 10.1038/s41591-019-0567-3

Reed, C. L., Betz, R., Garza, J. P., and Roberts, R. J., Jr. (2010). Grab it! Biased attention in functional hand tool space. *Atten. Percept. Psychophys.* 72, 236–245. doi: 10.3758/APP.72.1.236

Reed, C. L., Grubb, J. D., and Steele, C. (2006). Hands up: attentional prioritization of space near the hand. *J. Exp. Psychol. Hum. Percept. Perform.* 32, 166–177. doi: 10.1037/0096-1523.32.1.166

Sadeghi, H., Allard, P., and Duhaime, M. (1997). Functional gait asymmetry in able-bodied subjects. *Hum. Mov. Sci.* 16, 243–258. doi: 10.1016/S0167-9457(96)00054-1

Schicke, T., Bauer, F., and Röder, B. (2009). Interactions of different body parts in peripersonal space: how vision of the foot influences tactile perception at the hand. *Exp. Brain Res.* 192, 703–715. doi: 10.1007/s00221-008-1587-2

Schubert, R., Ritter, P., Wüstenberg, T., Preuschhof, C., Curio, G., Sommer, W., et al. (2008). Spatial attention related SEP amplitude modulations covary with BOLD signal in S1--a simultaneous EEG--fMRI study. *Cereb. Cortex* 18, 2686–2700. doi: 10.1093/cercor/bhn029

Simões, E. L., Bramati, I., Rodrigues, E., Franzoi, A., Moll, J., Lent, R., et al. (2012). Functional expansion of sensorimotor representation and structural reorganization of callosal connections in lower limb amputees. *J. Neurosci.* 32, 3211–3220. doi: 10.1523/JNEUROSCI.4592-11.2012

Stettler, B. A., and Thomas, L. E. (2017). Visual processing is biased in peripersonal foot space. *Atten. Percept. Psychophys.* 79, 298–305. doi: 10.3758/s13414-016-1225-1

Stone, K. D., Kandula, M., Keizer, A., and Dijkerman, H. C. (2018). Peripersonal space boundaries around the lower limbs. *Exp. Brain Res.* 236, 161–173. doi: 10.1007/s00221-017-5115-0

Takeuchi, N., Izumi, S. I., Ota, J., and Ueda, J. (2016). Neural plasticity on body representations: advancing translational rehabilitation. *Neural Plast.* 2016:9737569. doi: 10.1155/2016/9737569

Tseng, P., Bridgeman, B., and Juan, C. H. (2012). Take the matter into your own hands: a brief review of the effect of nearby-hands on visual processing. *Vis. Res.* 72, 74–77. doi: 10.1016/j.visres.2012.09.005

Valle, G., Mazzoni, A., Iberite, F., D'anna, E., Strauss, I., Granata, G., et al. (2018). Biomimetic intraneural sensory feedback enhances sensation naturalness, tactile sensitivity and manual dexterity in a bidirectional prosthesis. *Neuron* 100, 37–45.e7. doi: 10.1016/j.neuron.2018.08.033

Wasaka, T., Hoshiyama, M., Nakata, H., Nishihira, Y., and Kakigi, R. (2003). Gating of somatosensory evoked magnetic fields during the preparatory period of self-initiated finger movement. *Neuroimage* 20, 1830–1838. doi: 10.1016/s1053-8119(03)00442-7

Wasaka, T., Kida, T., and Kakigi, R. (2017). Facilitation of information processing in the primary somatosensory area in the ball rotation task. *Sci. Rep.* 7:15507. doi: 10.1038/s41598-017-15775-x

Whiteley, L., Kennett, S., Taylor-Clarke, M., and Haggard, P. (2004). Facilitated processing of visual stimuli associated with the body. *Perception* 33, 307–314. doi: 10.1068/p5053

Whiteley, L., Spence, C., and Haggard, P. (2008). Visual processing and the bodily self. *Acta Psychol. (Amst)* 127, 129–136. doi: 10.1016/j.actpsy.2007.03.005

Conflict of Interest: The authors declare that the research was conducted in the absence of any commercial or financial relationships that could be construed as a potential conflict of interest.

Publisher's Note: All claims expressed in this article are solely those of the authors and do not necessarily represent those of their affiliated organizations, or those of the publisher, the editors and the reviewers. Any product that may be evaluated in this article, or claim that may be made by its manufacturer, is not guaranteed or endorsed by the publisher.

Copyright © 2022 Aizu, Otaki, Nishii, Kito, Yao, Uemura, Izumi and Yamada. This is an open-access article distributed under the terms of the Creative Commons Attribution License (CC BY). The use, distribution or reproduction in other forums is permitted, provided the original author(s) and the copyright owner(s) are credited and that the original publication in this journal is cited, in accordance with accepted academic practice. No use, distribution or reproduction is permitted which does not comply with these terms.

frontiers in Computational Neuroscience

ORIGINAL RESEARCH
published: 04 February 2022
doi: 10.3389/fncom.2021.784592

Reinforcement Learning Model With Dynamic State Space Tested on Target Search Tasks for Monkeys: Self-Determination of Previous States Based on Experience Saturation and Decision Uniqueness

Tokio Katakura[1], *Mikihiro Yoshida*[1], *Haruki Hisano*[2], *Hajime Mushiake*[1] *and Kazuhiro Sakamoto*[1,2]*

[1] Department of Physiology, Tohoku University School of Medicine, Sendai, Japan, [2] Department of Neuroscience, Faculty of Medicine, Tohoku Medical and Pharmaceutical University, Sendai, Japan

The real world is essentially an indefinite environment in which the probability space, i. e., what can happen, cannot be specified in advance. Conventional reinforcement learning models that learn under uncertain conditions are given the state space as prior knowledge. Here, we developed a reinforcement learning model with a dynamic state space and tested it on a two-target search task previously used for monkeys. In the task, two out of four neighboring spots were alternately correct, and the valid pair was switched after consecutive correct trials in the exploitation phase. The agent was required to find a new pair during the exploration phase, but it could not obtain the maximum reward by referring only to the single previous one trial; it needed to select an action based on the two previous trials. To adapt to this task structure without prior knowledge, the model expanded its state space so that it referred to more than one trial as the previous state, based on two explicit criteria for appropriateness of state expansion: experience saturation and decision uniqueness of action selection. The model not only performed comparably to the ideal model given prior knowledge of the task structure, but also performed well on a task that was not envisioned when the models were developed. Moreover, it learned how to search rationally without falling into the exploration–exploitation trade-off. For constructing a learning model that can adapt to an indefinite environment, the method of expanding the state space based on experience saturation and decision uniqueness of action selection used by our model is promising.

Keywords: reinforcement learning, dynamic state space, target search task, experience saturation, decision uniqueness, exploration-exploitation trade-off, indefinite environment

OPEN ACCESS

Edited by:
Jun Ota,
The University of Tokyo, Japan

Reviewed by:
Tetsuro Funato,
The University of Electro-Communications, Japan
Shiro Yano,
Tokyo University of Agriculture and Technology, Japan

***Correspondence:**
Kazuhiro Sakamoto
sakamoto@tohoku-mpu.ac.jp

Received: *28 September 2021*
Accepted: *29 December 2021*
Published: *04 February 2022*

Citation:
Katakura T, Yoshida M, Hisano H, Mushiake H and Sakamoto K (2022) Reinforcement Learning Model With Dynamic State Space Tested on Target Search Tasks for Monkeys: Self-Determination of Previous States Based on Experience Saturation and Decision Uniqueness. Front. Comput. Neurosci. 15:784592. doi: 10.3389/fncom.2021.784592

INTRODUCTION

Uncertainty is classified into two types. The first is where the state or probability space of the situation or environment is defined and fixed, as in the case of rolling a die. We cannot predict which roll will emerge, but we do know that a number from 1 to 6 will appear; thus, it is possible to utilize this prior knowledge. The other is the case where even the probability or state space of

the environment is neither given nor hypothesized in advance. An environment with the latter type of uncertainty is defined as an indefinite environment, and adaptation to such an ever-changing indefinite environment is a critical issue for living systems (Shimizu, 1993).

Learning is a primary ability of animals, allowing them to adapt to their environment. Reinforcement learning is a form of learning in which the agent learns to take a certain action in an uncertain environment, or without being explicitly informed of the correct answer. Instead, the agent learns a policy based on the state at the previous time-step to maximize the cumulative reward (Sutton and Barto, 1998). In particular, reinforcement learning models employing partially observable Markov decision process (POMDP) methods represent the most popular approach to coping with situations in which the current state is uncertain (Jaakkola et al., 1995; Thrun et al., 2005) and remain a thriving research area that attracts many researchers (e.g., Ahmadi et al., 2020; Bhattacharya et al., 2020; Bouton et al., 2020; Xie et al., 2020; Maliah and Shani, 2021). In particular, some recent POMDP models can learn policies from multiple past states or generate an infinite number of distributions within the probability or feature space, which has greatly improved the adaptability of machine learning to complex environments (Doshi-Velez, 2009; Doshi-Velez et al., 2015; Hausknecht and Stone, 2015; Azizzadenesheli et al., 2016; Igl et al., 2018). However, the current state of the environment functions as prior knowledge in reinforcement learning models. Even in the abovementioned advanced POMDP models, possible environmental states are generated within a given probability or feature space (**Figures 1A,B**). Therefore, these architectures may not achieve high learning performance in any unknown environment.

Infinite hidden Markov models (iHMMs) enable learning based on the arbitrary length of previous states without prior knowledge, even about the probability space (Beal et al., 2002; Teh et al., 2006; Mochihashi and Sumita, 2007; Mochihashi et al., 2009; Pfau et al., 2010; Doshi-Velez et al., 2015). This approach, by using Dirichlet process hierarchically, can dynamically generate states referring to arbitrary length of previous states, and is applied to, for example, inference of words within sentences (Mochihashi and Sumita, 2007; Mochihashi et al., 2009). However, this approach does not include explicit criteria for determining the appropriateness of state generation and its termination, raising concerns about whether it learns both dynamically and reproducibly.

With respect to our own experience, the state space is not uniquely and unilaterally provided to us in an indefinite environment; instead it is subjectively determined through our interaction with that environment. And even under such circumstances, we aim to ensure that the desired results are achieved. When we cannot obtain our desired outcomes, we will not blindly roll a die; instead, we seek an causal attribution (Heider, 1958; Kelley, 1967, 1973). That is, we will attempt to change our view of the situation we face or the state of the environment and make a deterministic or unique decision based on sufficient experience. This view is supported by findings in humans and animals: children prefer deterministic decisions, that is, infer unobserved causes whenever observed causes appear to act only stochastically (Schulz and Sommerville, 2006); when a rodent is presented an ambiguous conditional stimulus (CS) that is followed by an unconditional stimulus (US) in one context but not in another, the contextual information is recruited by the animal to determine the situation uniquely (Fanselow, 1990).

Here, we propose a reinforcement learning model with a dynamic state space that performs well in a two-target search task that was previously used in a physiological experiment with non-human primates (Kawaguchi et al., 2013, 2015; **Figure 2**, see also **Supplementary Figure 1**). Briefly, subjects were required to gaze at one light spot from among four identical stimuli. If the correct spot (designated by green in **Figure 1**) was selected, a reward was delivered. After training, the subjects learned to saccade alternately to two targets in a valid pair, and received a reward for several correct trials in a row (the exploitation phase). If the valid pair was changed without instruction, they started searching for a new valid pair after making errors (the exploration phase). In this task, by simply hypothesizing that the previous state is the previous trial, the agent cannot maximize the total reward. To do so, the agent must consider the two previous trials together as the previous state. Thus, this task can address the issue of how the two previous trials together can come to be regarded as the previous state without prior knowledge of the task structure. Our proposed model is given no prior knowledge of the task structure other than the action of gazing at one of the four spots. Instead, it starts learning using the immediately preceding trial as the starting state, and expands and contracts the state space in the direction of previous trials based on the criteria of experience saturation and the decision uniqueness of the action selection (**Figure 1C**). The model performed comparably to the optimal model, in which prior knowledge of the task structure was available. We consider the dynamic learning mechanism proposed in this study to be a crucial component for systems to adapt to indefinite environments.

METHODS

The Reinforcement Learning Model

We developed a reinforcement learning model with a dynamic state space. The basic structure of the model was grounded in the conventional reinforcement learning (Rescorla and Solomon, 1967) as follows. The action value function, $Q(S_N = s_i, A_N = a_j)$ for the pair of a particular state, s_i, and an action, a_j, at the Nth trial were updated by the following equation:

$$Q\left(S_{N+1}, A_{N+1}\right) \leftarrow Q\left(S_N, A_N\right) + \alpha\delta\left(S_N, A_N\right), \tag{1}$$

where α is the learning rate, set to 0.1 in the range that showed desirable results revealed by the parameter search (see **Figure 7**). δ is the reward prediction error, given by

$$\delta(S_N, A_N) \equiv r - Q(S_N, A_N), \tag{2}$$

where r is the reward delivered for A_N taken at S_N in the Nth trial. If the correct spot was selected, a reward $r = 1$ was delivered, otherwise $r = 0$ was given. In the following, we will refer to whether a reward has been obtained or not as (reward) outcome.

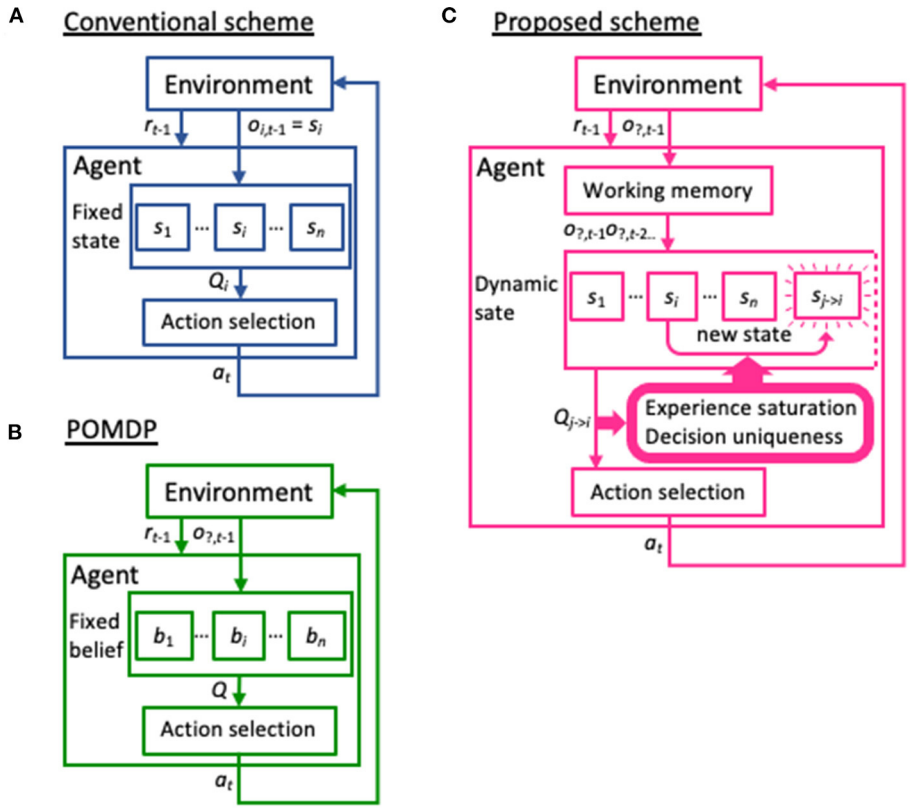

FIGURE 1 | Differences in the basic schemes between previous models and the model presented in the current study. **(A)** In the conventional reinforcement learning scheme, observed variables and state variables are not distinguished. That is, the current state s_i is set based on the observation of the environment $o_{i,t-1}$ at the time $t-1$ and has a corresponding Q-table Q_i, which provides an action a_t. **(B)** In the partially observable Markov decision process (POMDP) model, the environment provides only a partial observation $o_{?,t-1}$ to identify the current state. The agent has a set of beliefs or stochastic distribution for the possible states $\{b_i\}$, and renews them through actions a and their reward outcomes r. Note that similar to the conventional scheme, the possible states are provided to the POMDP model in advance, in the form of beliefs. **(C)** Our dynamic state scheme also hypothesizes that the agent receives only partial information from the environment. However, unlike POMDP, these observations are temporarily stored in working memory and serve to generate a new state not prepared a priori, based on the two criteria experience saturation and decision uniqueness.

A_N was selected according to the stochastic function, $P^{\pi}(A_N = a_j|S_N = s_i)$, under $S_N = s_i$. A policy, π, i.e., P^{π} is the softmax function, defined by

$$P^{\pi}\left(a_j|s_i\right) \equiv \frac{\exp(\beta Q\left(s_i,\ a_j\right))}{\sum_k^4 \exp(\beta Q\left(s_i,\ a_k\right))}, \tag{3}$$

where the parameter β, termed the inverse-temperature, was set to 7 in the range that provided desirable results revealed by the parameter search (see **Figure 8**). For action selection, the state that refers to the longest history of recent trials among generated states was used.

Expanding and Contacting the State Space

Our model was designed to avoid the need for stochastic decisions as much as possible. Specifically, when the model did not have a value function for a particular action that required a much larger value compared with others following extensive experience with the state, it expanded the range of the state backward in time. We illustrate the algorithm of this expansion in **Figure 3A**.

The initial state space of the model calculation was set as a particular combination of the four possible actions, namely gazing at the right-up (RU), left-up (LU), left-down (LD), or right-down (RD) spot, and the outcome (correct or error) from one trial. The initial Q-value for each action was set to 0.5. The model monitored the stochastic mean policy for each state s_i, given by

$$P^{\pi}_{mean,N_{update,s_i}}(\boldsymbol{a}|s_i) \equiv \frac{1}{N_{update,s_i}} \sum_{l=1}^{N_{update,s_i}} P^{\pi}_{l}(\boldsymbol{a}|s_i) \tag{4}$$

where $N_{update,si}$ is the number of times that the Q-values for the state s_i were updated. Then, it calculated the information gain or the Kullback-Leibler divergence (KLD) obtained by updating the stochastic policy (step 1 in **Figure 3A**):

$$Update_KLD_{s_i}$$
$$\left(P^{\pi}_{mean,N_{update,s_i}}(\boldsymbol{a}|s_i)||P^{\pi}_{mean,N_{update,s_i}-1}(\boldsymbol{a}|s_i)\right)$$

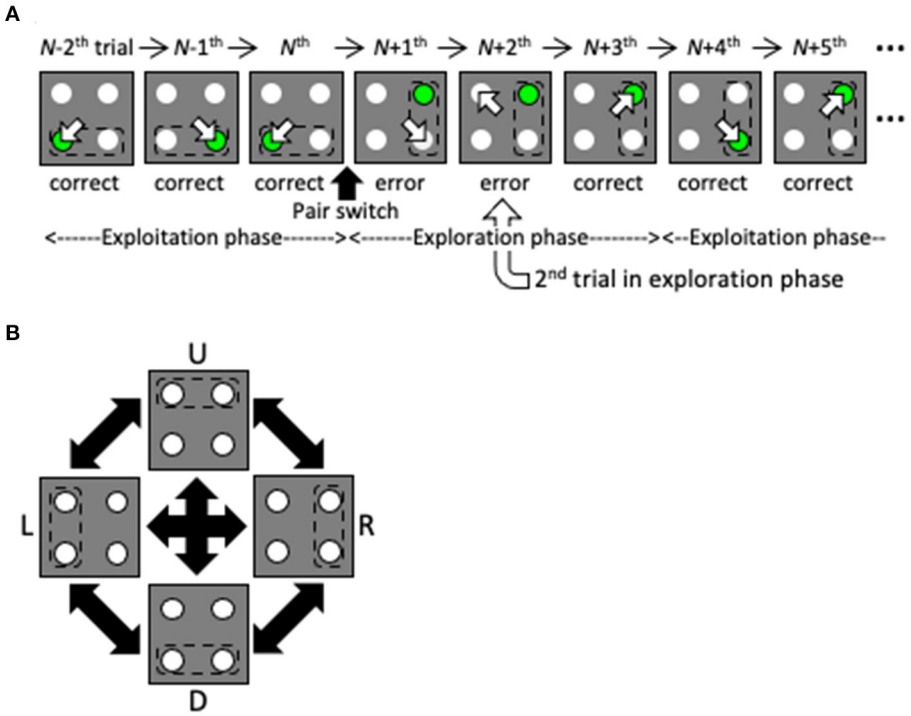

FIGURE 2 | Overview of the two-target search task. **(A)** Schematic of several trials before and after a valid pair change. The pair change triggers the transition from the exploitation phase to the exploration phase. Dashed lines, empty arrows and green spots denote valid pairs, gazes and correct targets, respectively. Note that the subjects were not instructed to move their eyes by the green spot before gaze shift. **(B)** Valid pairs are randomly altered after a series of correct trials.

$$\equiv \sum_{j}^{4} P^{\pi}_{mean,N_{update,s_i}}\left(a_j|s_i\right)\log\frac{P^{\pi}_{mean,N_{update,s_i}}\left(a_j|s_i\right)}{P^{\pi}_{mean,N_{update,s_i}-1}\left(a_j|s_i\right)}. \quad (5)$$

We referred to this as the Update_KLD. $N_{update,si}$ - 1 indicates the number of trials since the model last encountered state s_i and calculated the mean $P(\boldsymbol{a}|s_i)$. We used the Cesàro average to test whether the decision uniqueness would be improved by promoting state expansion when the number of trials experienced in the state of interest becomes large.

Next, the model judged whether the Update_KLD of the state s_i fell below the criterion for experience saturation, ζ (step 2),

$$Update_KLD_{s_i} < \zeta \quad (6)$$

indicating that information can no longer be gained by updating. The value of ζ was determined to be 10^{-6} in the range that showed desirable results revealed by the parameter search (see **Figure 5**). When the Update_KLD$_{si}$ was $< \zeta$, the distribution of $P^{\pi}_{mean,N_{update,s_i}}(\boldsymbol{a}|s_i)$ was compared with $P^{\pi}_{ideal}(\boldsymbol{a}|s)$. $P^{\pi}_{ideal}(\boldsymbol{a}|s)$ is the action selection probability that only one action will be selected and was obtained as follows. First, the ideal policy, $Q_{ideal}(\boldsymbol{a}|s_i)$, was obtained by setting the largest value within $Q(\boldsymbol{a}|s_i)$ to 1 and the other values to zero. For example, if the $Q(\boldsymbol{a}|s_i)$ were, {0.1, 0.4, 0.2, 0.1}, the $Q_{ideal}(\boldsymbol{a}|s_i)$, would be set to {0, 1, 0, 0}. Thereafter, the $P^{\pi}_{ideal}(\mathbf{a}|s)$ was calculated from $Q_{ideal}(\boldsymbol{a}|s_i)$ using the softmax function in Equation (3). For comparison, another KLD was calculated, as described below (step 3):

$$D_KLD_{s_i}\left(P^{\pi}_{mean,N_{update,s_i}}(\boldsymbol{a}|s_i)||P^{\pi}_{ideal}(\boldsymbol{a}|s)\right)$$
$$\equiv \sum_{j} P^{\pi}_{mean,N_{update,s}}\left(a_j|s_i\right)\log\frac{P^{\pi}_{mean,N_{update,s}}\left(a_j|s_i\right)}{P^{\pi}_{ideal}\left(a_j|s\right)} \quad (7)$$

We called this the Decision-uniqueness KLD (D_KLD). When the D_KLD was below the criterion for a preference for deterministic action selection, η (step 4),

$$D_KLD_{s_i} < \eta \quad (8)$$

the agent had uniquely selected an action for state s_i, and the Q-table was not expanded any further. η was set to 3, the median of the range between values of > 1 and < 5, which produced fair performance revealed by the parameter search (see **Figure 6**). When the D_KLD did not meet the criterion, it was also compared to the parent D_KLD (step 5), defined as the D_KLD of the parent state from which the current state s_i had been expanded (e.g., **Figure 3B**). In step 6, when the D_KLD is judged to be less than its corresponding Parent D_KLD, as in Equation (9),

$$D_KLD_{s_i} < Parent\ D_KLD_{s_i} + bias \quad (9)$$

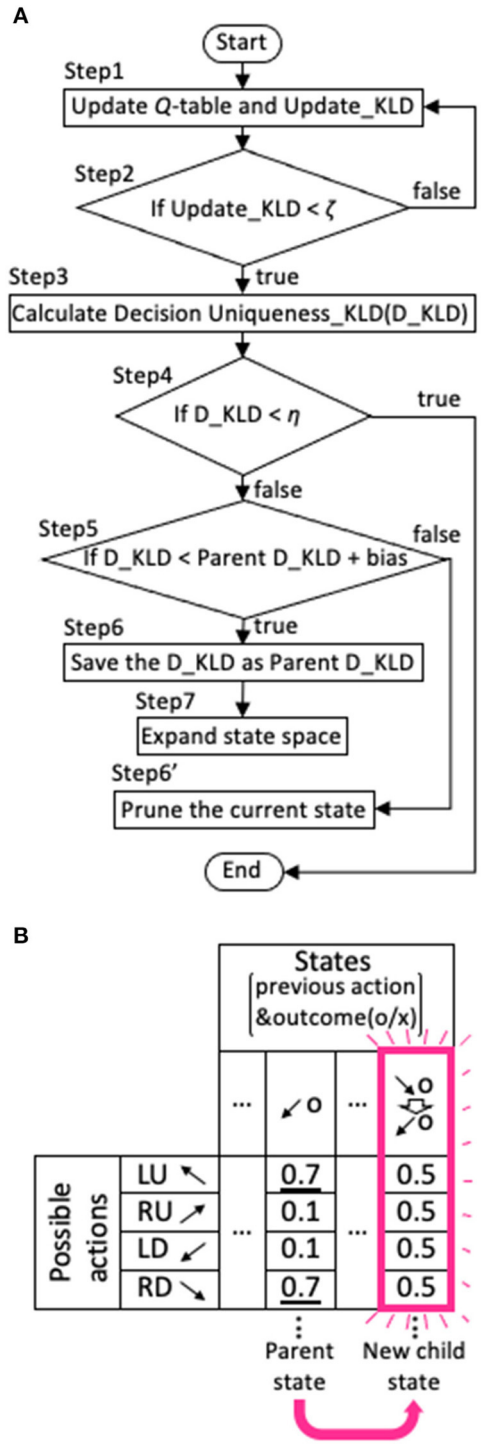

FIGURE 3 | Expansion and contraction of the state space. **(A)** Flowchart of the expansion and contraction process. **(B)** An example of state expansion derived from a parent state in Q-table. The direction of the arrow represents the target that the agent looked at, and o and x represent the correct answer and error, respectively. The example in the figure shows that a new state is generated from the state that the agent looked at LD and was rewarded one trial ago, to the state that it looked at LD and was rewarded one trial ago after it looked at RD and was rewarded two trials ago. The numbers in the Q-table represent Q-values. The initial Q-value for each action is set to 0.5.

the D_KLD value is saved as the parent D_KLD, and the state is expanded as depicted in the Q-table of **Figure 3B** (step 7). That is, the new state (child state) is the combination of the parent state and the state of one more previous trial to which the parent state refers. In the schematic example in **Figure 3B**, a new state is generated from the state that the agent looked at LD and was rewarded one trial ago, to the state that it looked at LD and was rewarded one trial ago after it looked at RD and was rewarded two trials ago. The initial Q-value for each action is set to 0.5. On the other hand, if Equation (9) does not hold, the current state being processed (see flowchart in **Figure 3A**) is pruned (step 6'). When the current state consists of only the previous one trial, it is not erased because there is no parent state with which it could be compared. The bias is set to be −1 in all calculation except in the case shown in **Figure 9**.

Models Used for Comparison

In the Results section, we compare our dynamic state model with three models with state spaces of fixed sizes. The first model was called the fixed 4-state model, the state space of which consisted of four elements. In other words, this model selected the next action based on the previous four possible actions, ignoring their reward outcomes. We called the second model the fixed 8-state model, which had a state space comprising eight elements, that is, the combination of four actions and their outcomes (i.e., correct or error) from the previous trial. In any case, since the action selection in these two models was based only on the previous one trial, they did not show good performance in the two-target search task. By contrast, as the best model for the two-target search task (because it assumed that the task structure was known and made decisions based on the actions and reward outcomes of the last two trials), the "fixed 8by8-state model" was used to evaluate the performance of our dynamic state model.

For further comparison, we also created a simple POMDP model (Thrun et al., 2005). The model referred only to the action of the previous one trial and its reward outcome (eight total cases). Instead, to estimate the current valid pair, the belief for each target pair (i.e., right [R], left [L], up [U], and down [D] pairs; **Figure 2B**) was calculated. Specifically, the value of the belief, b_k, about the pair k inferred from the previous gaze (e.g., the R pair and U pair in the case of RU) was increased or decreased depending on the reward outcome, while normalizing the total of the beliefs to 1. Because the above-mentioned eight cases existed for each of the four possible pairs, the Q-table consisted of 32 total rows. Then, the composite Q-value was obtained as

$$\sum_{k}^{4} b_k Q_k(s_i, a_j) \tag{10}$$

the sum of the 4 rows within the Q-table corresponding to the previous state s_i, weighted by the relevant belief b_k. The next action was selected by substituting the composite Q-value into the softmax function (3). The Q-value for the selected action a_j and each belief b_k was updated using the reward prediction error δ_k, as in Equation (2), multiplied by the learning rate and belief, $\alpha b_k \delta_k (s_i, a_j)$.

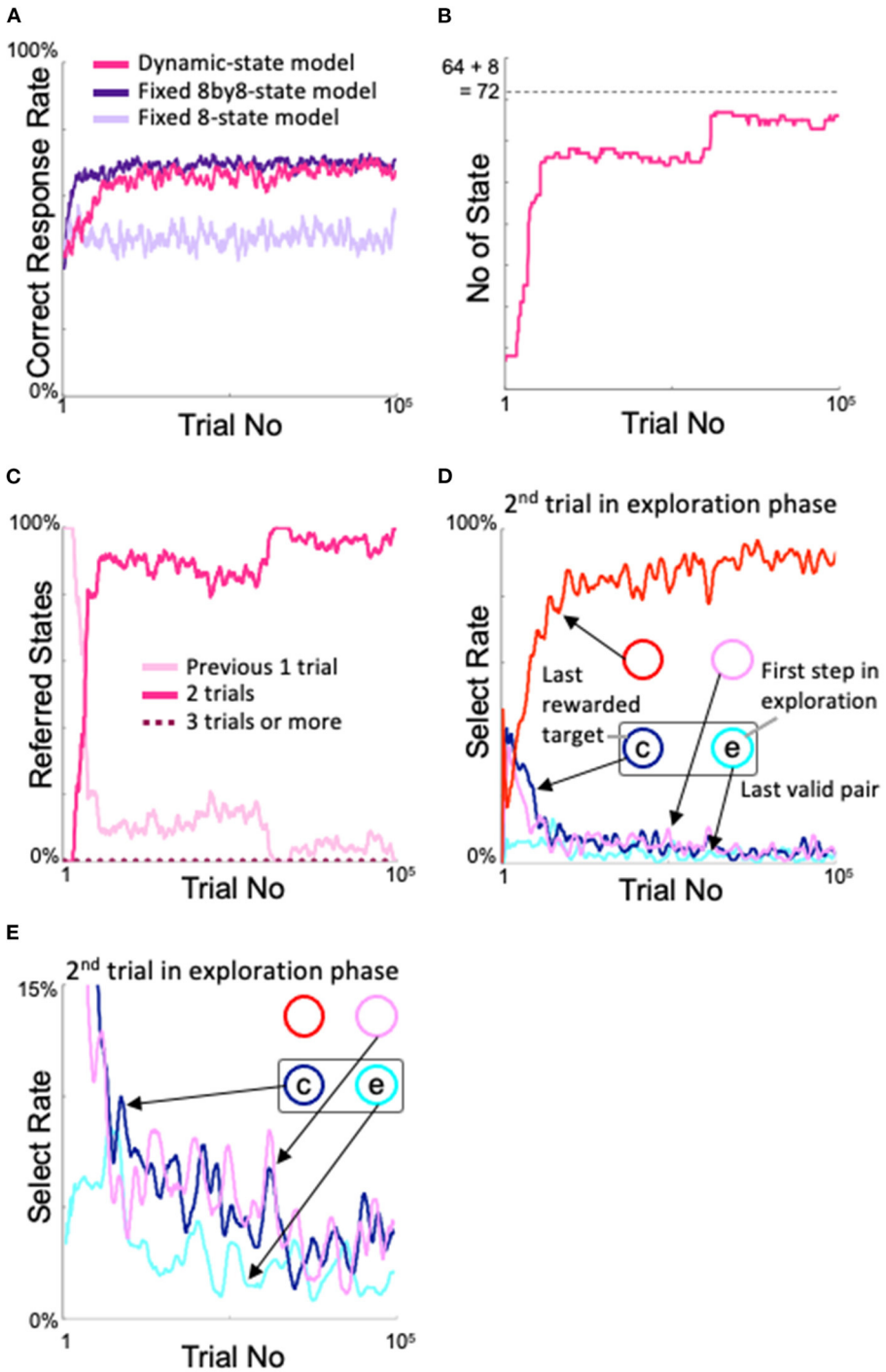

FIGURE 4 | Changes in the proposed model with learning. **(A)** Time course of the correct response rate and comparison with fixed state models. **(B)** Increase in the number of states. **(C)** Changes in the states referred to in each action selection. **(D)** Analysis of the model's behavior during the second trial of the exploration phase. "c" and "e" denote correct and error response, respectively. **(E)** Enlarged view of the 0–15% area of the select rate in **(D)**.

We also compared the proposed model with iHMMs, which hierarchically use a Dirichlet process as models to dynamically generate states based on history without prior knowledge (**Supplementary Figure 2A**). The model starts from the base state, which has no defining conditions, and probabilistically generates new states (**Supplementary Figure 2B**). As in the proposed model, states other than the base state consist of combinations of previous actions and their reward outcomes.

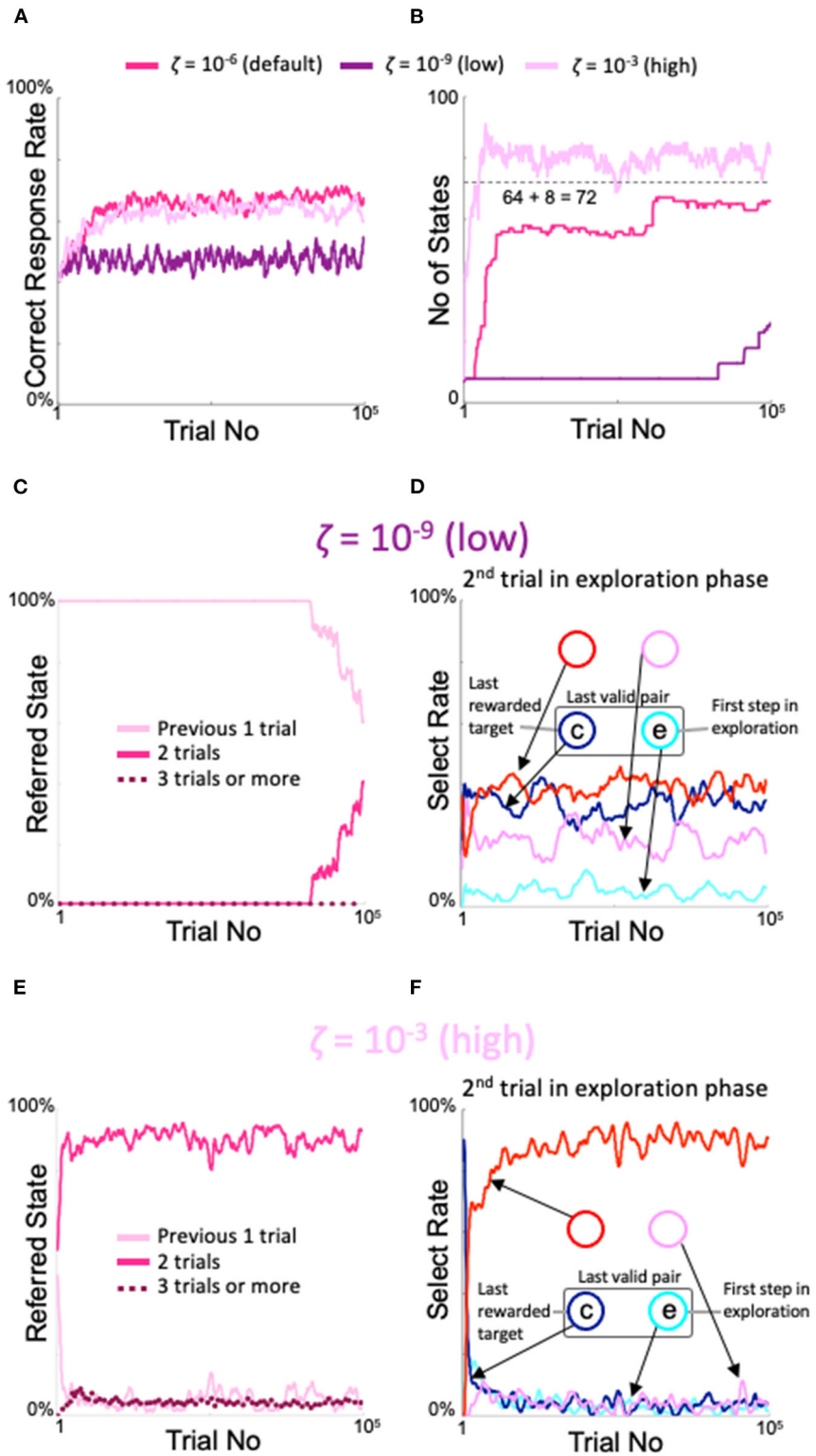

FIGURE 5 | Effects of threshold modulation of experience saturation. Formats are identical to **Figure 4**. **(A)** Correct response rates. **(B)** Corresponding number of states. **(C,D)** States referred to in each action selection **(C)** and analysis of the model's behavior in the second trial of the exploration phase **(D)** at a low value of $\zeta = 10^{-9}$. **(E,F)** Same plots as **(C,D)** for a high value of $\zeta = 10^{-3}$.

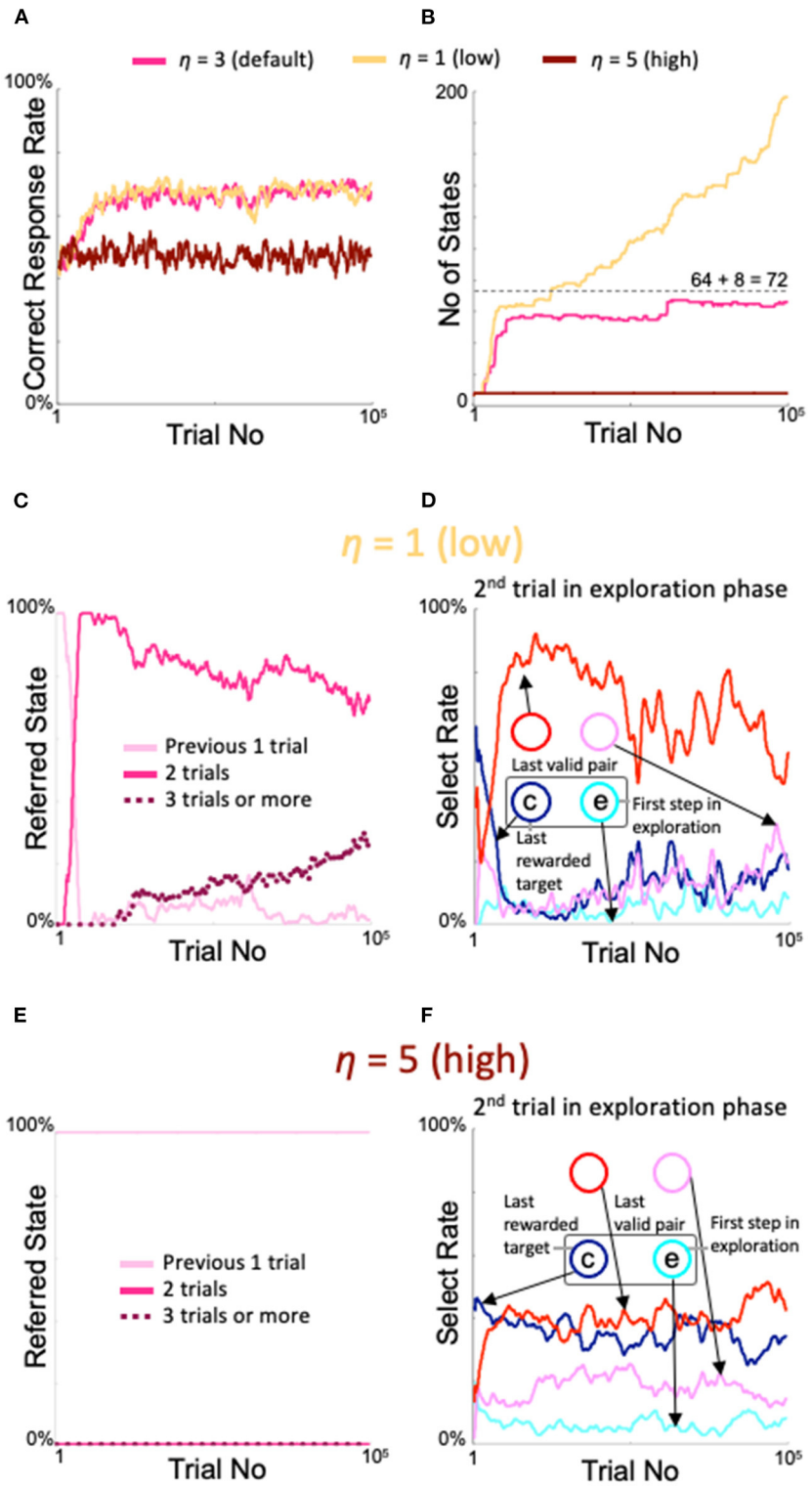

FIGURE 6 | Effects of threshold modulation of the degree of decision uniqueness. Formats are identical to **Figure 5**. **(A)** Percentage of correct answers. **(B)** Changes in number of states. **(C,D)** States referred to in each action selection **(C)** and the model's behavior in the second trial of the exploration phase **(D)** at a low value of $\eta = 1$. **(E,F)** Same plots as **(C,D)** for a high value of $\eta = 5$.

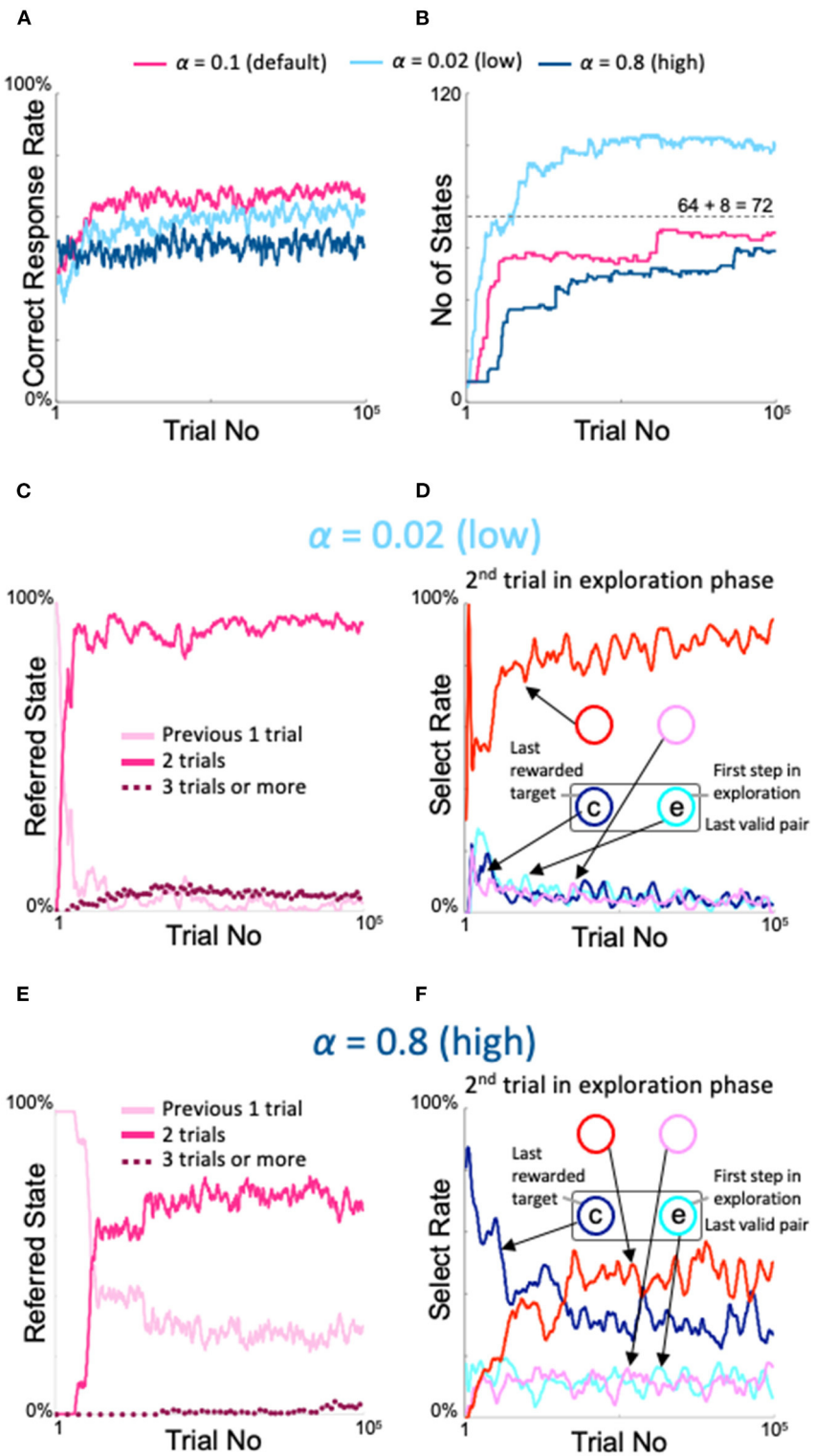

FIGURE 7 | Effects of modulation of learning rate. Formats are identical to **Figures 5**, **6**. **(A)** Percentage of correct answers. **(B)** Changes in number of states. **(C,D)** States referred to in each action selection **(C)** and the model's behavior in the second trial of the exploration phase **(D)** at a low value of $\alpha = 0.02$. **(E,F)** Same plots as **(C,D)** for a high value of $\alpha = 0.8$.

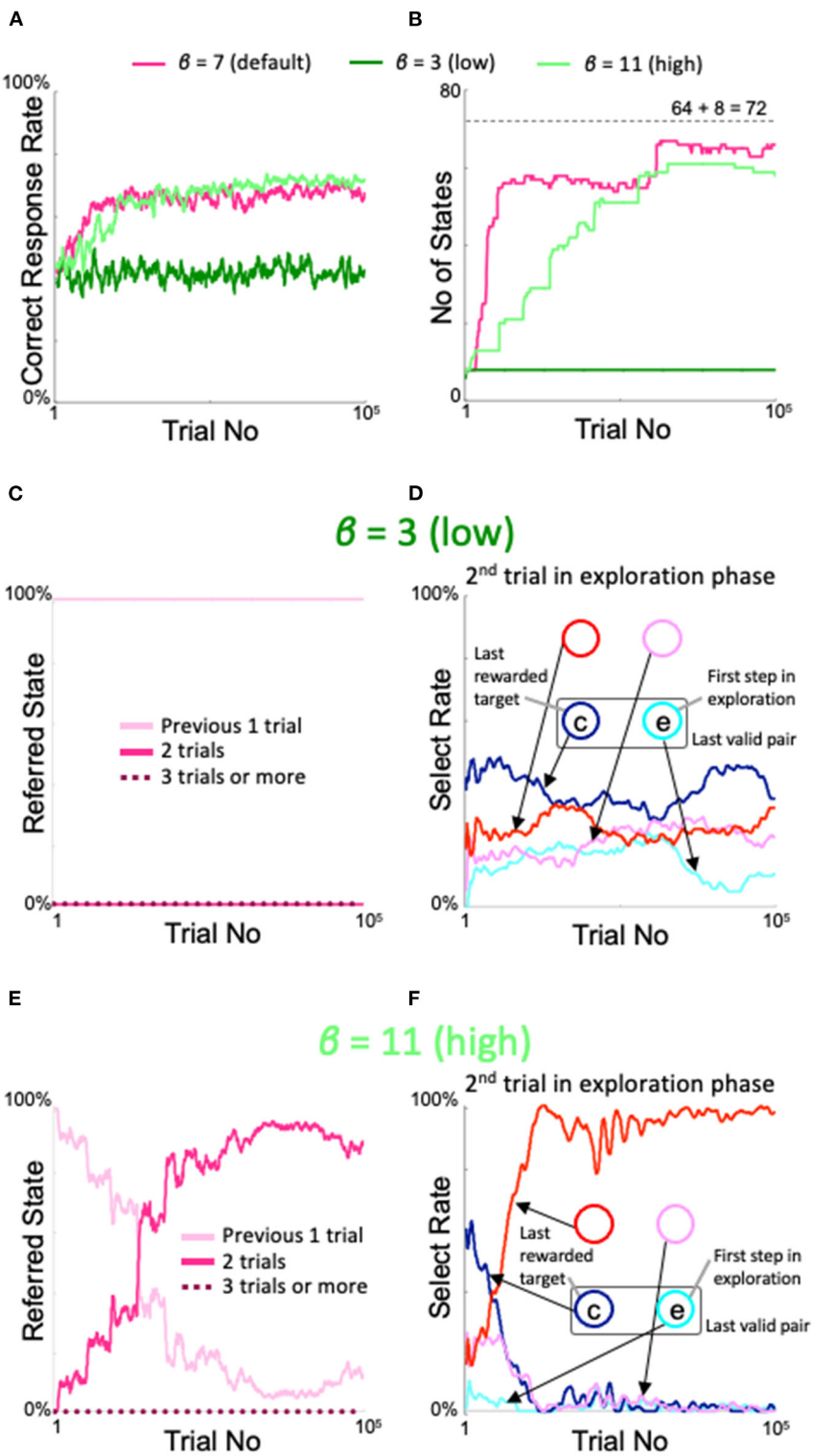

FIGURE 8 | Effects of modulation of inverse temperature in the softmax function used for action selection. Formats are identical to **Figures 5**–**7**. **(A)** Percentage of correct answers. **(B)** Changes in number of states. **(C,D)** States referred to in each action selection **(C)** and the model's behavior in the second trial of the exploration phase **(D)** at a low value of $\beta = 3$. **(E,F)** Same plots as **(C,D)** for a high value of $\beta = 11$.

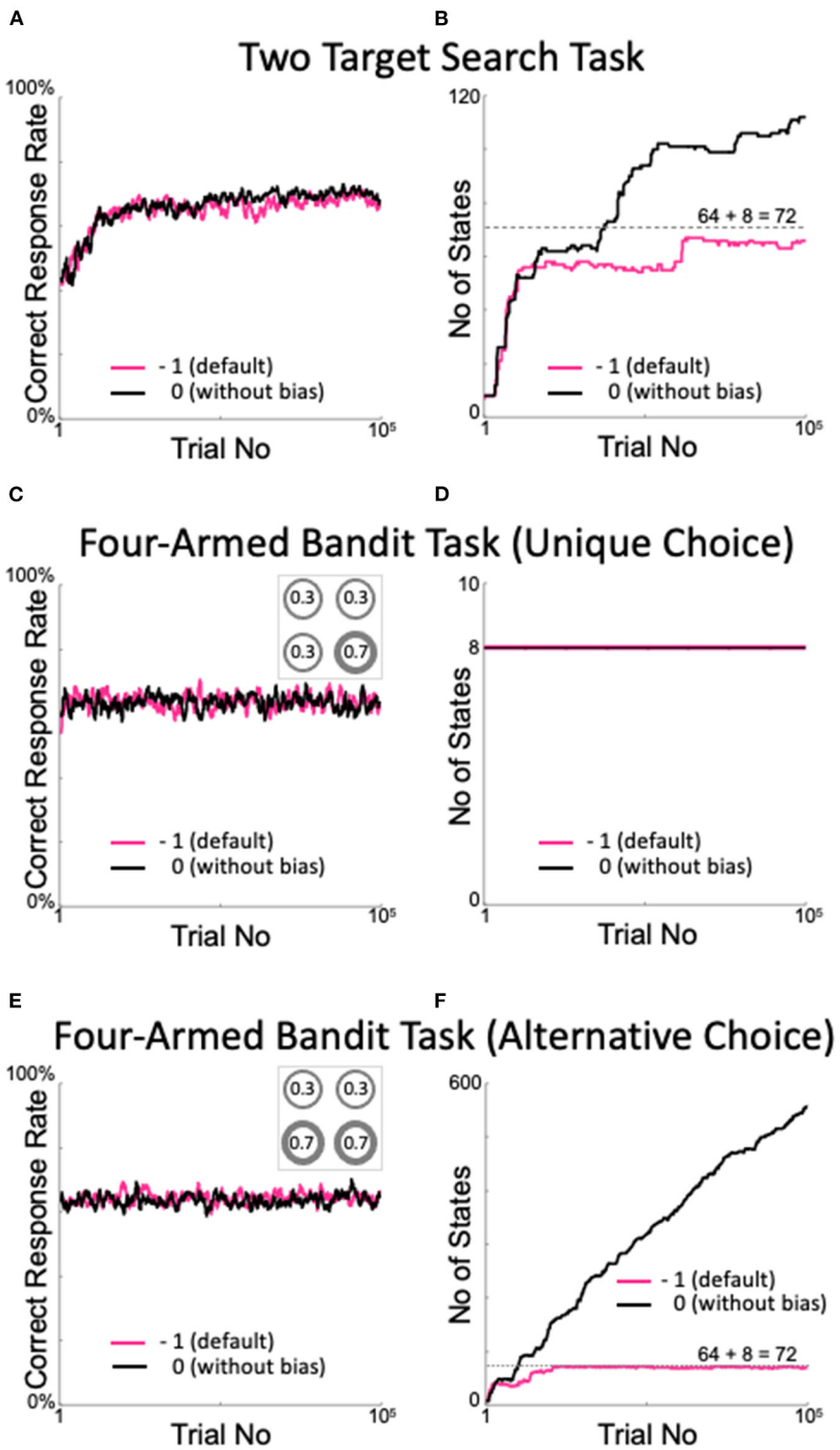

FIGURE 9 | Effects of the presence or absence of the parent–child comparison bias. **(A,B)** Percentage of correct answers **(A)**, and changes in the number of states **(B)** in the two-target search task. **(C,D)** The same plots for the four-armed bandit task. The number in each circle in the inset of C represents the reward probability for each target. **(E,F)** The same plots for the alternative version of the four-armed bandit task. This version includes the two targets with the highest reward probabilities, as shown in the inset in **(E)**.

Nodes consisting of an action and its result of one previous trial are generated directly below the base state. Below these nodes are nodes that refer to the information of the last two trials. As the tree further branches downward, the number of trials to be referred to increases. The Chinese restaurant process was used to implement the Dirichlet process (**Supplementary Figures 2C,D**) (Teh et al., 2006). Tables (filled tables in **Supplementary Figures 2C,D**) were prepared for each of the four possible actions, at each of which guests were seated (represented by the people with filled heads in **Supplementary Figures 2C,D**). If the executed action is correct, a new guest will be seated at the table. In a state s_i, each action a_j is selected with the following probability, where g_j is the number of guests seated at the corresponding table:

$$P\left(a_j|s_i\right) = \frac{g_j}{\sum_k^4 g_k + \lambda} \tag{11}$$

The new state (child state), which considers one more previous trial, is generated from the current state (parent state) with the following probability:

$$\frac{\lambda}{\sum_k^4 g_k + \lambda} \tag{12}$$

where λ is the concentration parameter. In the Dirichlet process version (**Supplementary Figure 2C**), the initial child state has one unique guest (presented by a person with a brank head in **Supplementary Figure 2C**) in each action table, i.e., there is a uniform distribution. On the other hand, in the hierarchical Dirichlet process (**Supplementary Figure 2D**), the initial value of the child state is given by the distribution of the parent state. The latter is more popular, however, the former method was also used for a fairness of comparison, because in the proposed model, the child state does not inherit the *Q*-value of the parent state for evaluating the amount of learning (see **Figure 13**). In contrast to the proposed model, these two iHMMs are vulnerable to the parameter λ. After preliminary calculations, we selected 0.2 as the λ value, where the Dirichlet process version performed closest to the proposed model (see **Figure 12**). Similar to the proposed model, the end of the tree, i.e., the state referring to a large number of trials, was preferentially used for action selection. If the selected action was incorrect, the guest was removed from the table, and the state including a guestless table was pruned. However, state pruning was not observed in the simulation.

Supplementary Explanation of the Two-Target Search Task

In the two-target search task that the animals actually performed, each trial consisted of a sequence of events of 500 ms in duration, including a fixation period. However, for simplicity, in the present study, one time step of calculation was set to one trial (i.e., a combination of events in which the agent takes an action and obtains its reward outcome). When an incorrect spot was chosen, the same trial was repeated until the correct target was found. The valid pair was switched pseudo-randomly. The number of consecutive correct trials required before the valid-pair switch was set to seven, as in our previous physiological experiments involving monkeys.

RESULTS

Performance of the Proposed Model

In **Figure 4A**, we show the changes in percentage of correct responses from the start of learning of the models. The fixed 8by8-state model is the ideal learner for the two-target search task, i.e., with $8\times8 = 64$ states, so it quickly learned the current pair and obtained a high correct response rate, with the upper limit close to the theoretical value. On the other hand, the fixed 8-state model has only eight states, which are the combination of the gaze action and its reward outcome on the previous trial. In the two-target search task, even if the correct answer is obtained by looking at one target, two targets might be correct in the next trial. In this sense, the fixed 8-state model is not an ideal learner for the two-target search task. In fact, the correct response rate was not as good as the fixed 8by8-state model. Our proposed dynamic state model exhibited a slower increase in the correct response rate than the fixed 8by8-state model, but its performance was comparable to that of the ideal model after approximately 20,000 trials.

The state was expanded based on experience saturation and action decision uniqueness. The number of states of the dynamic state model showed a change corresponding to the change in the correct response rate (**Figure 4B**). At the very beginning of the learning process, the dynamic state model had the same eight states as the fixed 8-state model, but the number of states began to increase rapidly around the 3,000th trial; by the time the correct response rate was comparable to that of the fixed 8by8-state model, the number of states had almost stopped increasing. Microscopically, there were also many places where the number of states slightly decreased, which indicates that the model was appropriately pruning unnecessary states. The fact that the final number of states did not exceed $8 + 8^2 = 72$ (dashed line in **Figure 4B**), which means that the model refers to less than three trials, indicates that the model appropriately expands and contracts the number of states. **Figure 4C** shows the number of former trials that the model referenced for action selection. The fact that it did not refer to more than two trials indicates that the number of states is not expanded more than necessary.

The increase in performance with learning of the dynamic state model is thought to correspond to an increase in sophisticated searching for novel target pairs during the exploration phase. To examine this, we analyzed where the model looked during the second trial of the exploratory phase (see **Figure 2A**). **Figure 4D** shows that, in the second trial of the exploration phase, as the correct response rate increased, the model had a high probability of looking at the diagonal side of the incorrect gaze during the first trial of the exploration phase ("e" in **Figures 4D,E**); below, this will be referred to as the diagonal spot in the second trial of the exploration phase. This choice of diagonal gaze is reasonable; a valid pair always comprised two neighboring spots, so if the agent correctly answered two trials ago and incorrectly one trial ago, then the probability was high

that the other neighboring spot of the correct target two trials ago ("c" in **Figures 4D,E**), i.e., the diagonal side of the spot that was incorrect one trial ago, was the correct answer. The behavior of this model was also in good agreement with the behavioral results from our monkey experiments (Figure 3 of Kawaguchi et al., 2015). This sophisticated behavior during the exploration phase means that the model did not stick rigidly to the most recent valid pair, nor did it suddenly "roll a die." In other words, in the dynamic state model (and the ideal model, i.e., the fixed 8by8-state model), and in monkeys that perform the two-target search task, exploration and exploitation are not in a trade-off relationship; rather, the models and monkeys learned how to search.

Looking back at **Figure 4B**, we can see a step-like increase in the number of states after the 60,000th trial, although the correct rate did not considerably differ (**Figure 4A**). This corresponded to a decrease in access to the state that considers only the previous trial (**Figure 4C**). In more detail, during this period, access to the "correct answer two trials ago → incorrect answer one trial ago" state increased instead of the "incorrect answer one trial ago" state. This step-like increase was reflected in a slight increase in the diagonal gaze in the second trial in the exploration period (**Figure 4D**) due to further refinement of the exploration behavior. **Figure 4E** shows an enlargement of the lower part of **Figure 4D**. Notably, the probability of gazing at spots other than the diagonal spot decreased further in the second trial of the exploration period after approximately 60,000 trials, although variation was observed in each line.

Determination of the Ranges of Meta-Parameters for Desirable Model Performance

Our dynamic state–space model showed good performance in a sufficiently wide range for each of the ζ, η, α, and β meta-parameters. Below, we will show how the model behaves beyond and below the default range.

When the criterion for experience saturation ζ was set lower than the default value of 10^{-6}, the increase in the correct rate was delayed. When ζ was 10^{-9}, the rate of correct answers was similar to the rate of correct answers for the fixed 8-state model (dark purple line in **Figure 5A**). Similarly, the number of states stayed at eight for an extended period and finally began to increase after 80,000 trials (dark purple line in **Figure 5B**). Notably, this corresponded to the persistence of the period in which the model referred only to the previous one trial (**Figure 5C**). In the second trial of the exploration period, the rate of gazing at the spot diagonally opposite the spot gazed at during the first trial was also low (red line in **Figure 5D**). In contrast, when ζ was set higher than the default value, the number of trials referenced exceeded two, while the correct rate did not substantially change. When ζ was set to 10^{-3}, the rate of correct responses was only slightly lower than when ζ was set to the default value, and the gaze pattern in the second exploratory trial was similar to the default gaze pattern (**Figure 5F**). However, the number of states that increased faster than the default was limited but exceeded $8 + 8^2 = 72$ (light purple line in **Figure 5B**); indeed, the results of the last three trials were referenced with a small but distinct probability (dotted line in **Figure 5E**).

The excessive expansion and de-expansion of the number of states observed above was also obtained by varying the threshold for the degree of decision uniqueness. When η was set to 1, which was smaller than the default value, the correct response rate was similar to the correct response rate with the default value (yellow line in **Figure 6A**); however, the number of states increased rapidly over the 100,000 trials (yellow line in **Figure 6B**) and the rate of referring to the results of the last three trials continued to increase (dotted line in **Figure 6C**). Associated with the increase in this rate, the rate of diagonal gaze in the second trial of the exploration phase deteriorated (red line in **Figure 6D**). In contrast, when η was set to 5, a larger value than the default, the percentage of correct responses (brown line in **Figure 6A**), number of states (brown line in **Figure 6B**), number of immediate trials referenced (pink line in **Figure 6E**), and behavior during the second trial of the exploration period (**Figure 6F**) were all identical to the findings in the fixed 8-state model.

We also examined the effects of changing the learning rate α, a conventional meta-parameter for reinforcement learning. When α was set to the lowest possible value (0.02), the correct response rate was slightly lower than the rate observed with the default value (light blue line in **Figure 7A**), the number of states was limited but exceeded $8 + 8^2 = 72$ (light blue line in **Figure 7B**), the last three trials were referenced at a low but nearly constant rate (dotted line in **Figure 7C**), and the diagonal spot was gazed at frequently in the second trial of the exploration period (red line in **Figure 7D**). However, the highest value ($\alpha = 0.8$) showed a peculiar property not described above. In particular, the correct response rate was higher than in the fixed 8-state model but lower than in the dynamic state–space model (dark blue line in **Figure 7A**). The number of states also increased, although it was lower than in the dynamic state–space model (dark blue line in **Figure 7B**). Importantly, the rate at which only the previous trial was referenced did not substantially decrease (pink line in **Figure 7E**), although the last three trials were rarely but sometimes referenced (dotted line in **Figure 7E**). Therefore, the diagonal gaze rate did not increase enough in the second trial of the exploration period (red line in **Figure 7F**).

The effects of varying the inverse temperature β in the softmax function for action selection were as follows. When β was lowered from the default value to 3, the correct response rate (dark green line in **Figure 8A**), number of states (dark green line in **Figure 8B**), number of immediate trials referenced (pink line in **Figure 8C**), and the behavior during the second trial of the exploration period (**Figure 8D**) all exhibited the same properties as observed in the fixed 8-state model. However, when the inverse temperature was increased to 11, i.e., beyond the range of desirable results, the increases in the correct response rate (light green line in **Figure 8A**), number of states (light green line in **Figure 8B**), rate referencing the last two trials (red line in **Figure 8E**), and rate of diagonal gaze during the second trial of the exploration period (red line in **Figure 8F**) were not bad, but delayed compared with the default case.

In the calculations of the present model, a relatively strict criterion was set for state expansion. That is, we used a bias when comparing the D_KLD values of the parent and child states (Equation 9). If the degree of decision uniqueness of the child state was not significantly improved over that of the parent state, the child state was pruned. However, when learning the two-target search task, the percentage of correct responses in the absence of a bias (black line in **Figure 9A**) was comparable to the high percentage in the presence of a bias (red line in **Figure 9A**). As expected, in the absence of a bias, the number of generated states increased, although not constantly (black line in **Figure 9B**). These results indicate that the default values of the four above-discussed meta-parameters have high validity.

To check the generality and applicability of the default values of the meta-parameters, we ran a four-armed bandit task and examined model performance. In the bandit task, four targets used in the two-target search task were assigned distinct reward probabilities (**Figure 9C** inset). When the optimal target selection was uniquely determined, i.e., when there was a single target with the largest reward probability (**Figure 9C** inset), the model quickly learned the behavior that yielded the largest correct response rate, regardless of the presence or absence of a bias (**Figure 9C**). In this case, the number of states remained minimal (determined as 8, depending on the model configuration; **Figure 9D**). The model learned to select only the target with the maximum reward probability and thus did not expand the number of states. The performance indicates that our model, and the values of the meta-parameters used therein, are generally and broadly applicable.

When there were multiple targets with the maximum reward probability (in this case, two: **Figure 9E** inset), the correct response rate was high (70%) in the presence or absence of a bias (**Figure 9E**), while the change in the number of states differed greatly between cases with and without a bias (**Figure 9F**). In the presence of a bias, the number of states did not exceed 72, and fewer than three trials were referred to. This result is generally plausible. In the bandit task, where there is no history of reward probabilities, referencing up to two trials does not improve the uniqueness of the action decision over the parent state, where only the last trial is referenced. After the eight states referring to the previous trial (which are not pruned according to our model) are saturated with experience, the states referring to the previous two trials are repeatedly generated and pruned. The behavior of the model without a bias is also reasonable. In the absence of a bias, child states are not pruned if their decision uniqueness is nearly equal to but slightly less than that of their parent state. Therefore, the model refers back to increasingly larger numbers of trials in search of a state that can deterministically select its action. The question of whether it is better to have bias is addressed in the Discussion section.

Adaptability to an Unexpected Behavioral Task

We examined the adaptability of the model to unexpected situations and found that our proposed dynamic state model adapted to unexpected changes in the task requirements. We trained the fixed 8by8-state model, which is an ideal model for the two-target search task, and also the dynamic state model to perform a three-target search task that has not been attempted in monkeys (**Figure 10**). In this task, three of the four spots were the correct targets in a clockwise or counterclockwise order; the valid three-spot set was switched after seven consecutive correct trials, as in the two-target search task. Although there was no significant difference between the two models until after 100,000 trials (**Figure 10A**), **Figure 10B** shows that the dynamic state model steadily increased its number of states. As the number of trials increased, the fixed 8by8-state model showed no increase in the correct rate, while the dynamic state model demonstrated a steady increase (**Figure 10C**) due to the increase in the number of states (**Figure 10D**). Although the rate of increase in the number of states slowed compared with the rate during the first 100,000 trials, the increase continued after the millionth trial (data not shown).

We also created a simple POMDP model that was intended to perform well in the two-target search task. The model inferred which pair was currently the valid pair, although it only referred to the previous trial. As expected, the model performed in a manner comparable with the dynamic state model for the two-target search task (**Figure 11A**). However, in the three-target search task, the POMDP model showed lower performance than did the dynamic state model throughout the first 100,000 trials (**Figure 11B**); unlike the dynamic state model, the POMDP model did not show any improvement after nearly one million training trials (**Figure 11C**).

Furthermore, we compared our models with other iHMMs that also generate arbitrary numbers of states without prior knowledge of the two-target search task (**Supplementary Figure 2**). **Figure 12** shows the time dependences of the correct response rate (**Figures 12A,D,H**), number of states (**Figures 12B,E,I**), and cumulative pair switching counts (**Figures 12C,F,J**) when the proposed model, Dirichlet version of the iHMM, and hierarchical Dirichlet version of the iHMM were trained five times each on the two-target search task. The proposed model showed stable and good performance in the two-target search task. The change in correct response rate was almost ideal (over approximately 20,000 trials) in all five calculations (**Figure 12A**). Correspondingly, the number of states increased rapidly but did not exceed $8 + 8^2 = 72$, which corresponds to the case of referring up to two trials (**Figure 12B**). The model exhibited smooth pair switching, and after 100,000 trials, achieved over 7,000 pair switches with good reproducibility (**Figure 12C**).

The Dirichlet model also exhibited ideal trends in correct response rates (**Figure 12D**). However, in some cases, performance declined rapidly during the learning process, once every few calculations (pale red area in **Figure 12D**, indicated by a bold arrow). In many cases, the number of states continuously increased. Consequently, 600–800 states that are unnecessary to perform the two-target search task were generated (**Figure 12E**). In contrast, in some cases, the model

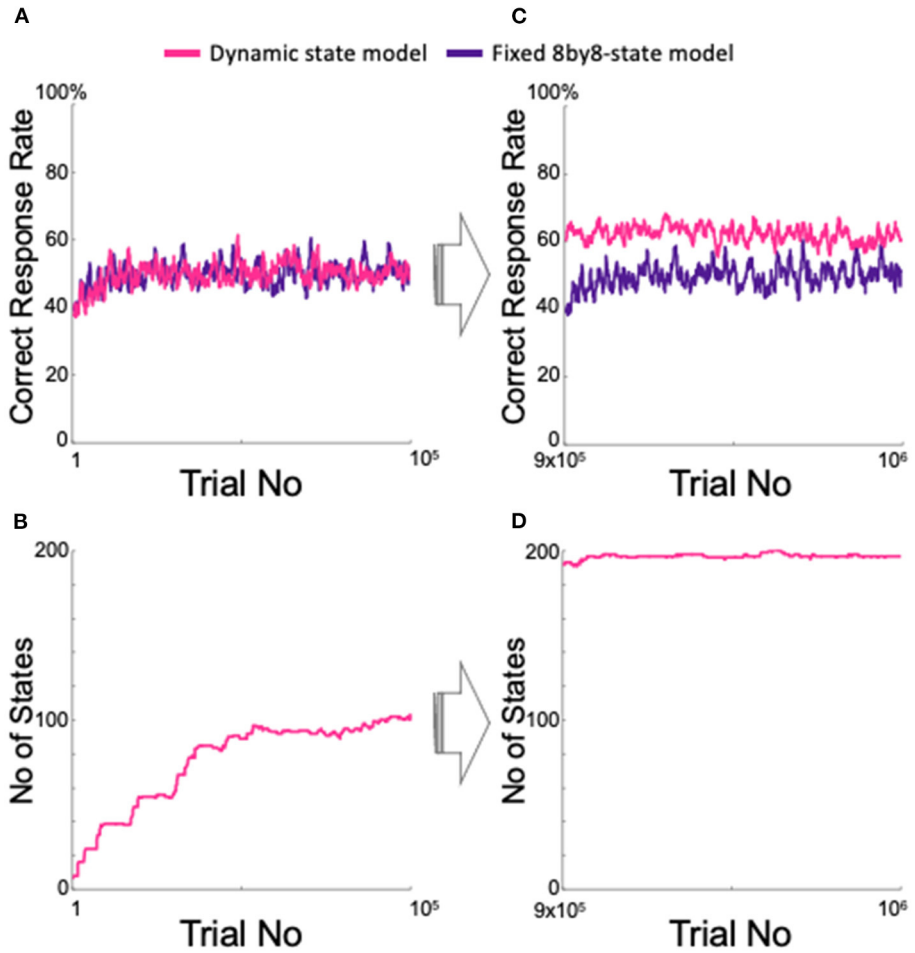

FIGURE 10 | Changes in the proposed model as it learned a three-target search task and comparison with the fixed 8by8-state model. **(A)** Correct response rate for the first 10^5 trials. **(B)** Increase in the corresponding number of the states. **(C)** Correct response rate for the 9×10^5th trial to the 10^6th trial. **(D)** Corresponding number of states.

failed to increase the number of states (shown by the pale red area in **Figure 12E**, also indicated by a bold arrow). This calculation example achieved very little pair switching (**Figure 12F** pale red line with a filled arrow). In the other examples, the model steadily increased the cumulative count of pair switches, but did not show the same reproducibility as the proposed method (**Figure 12F**). In the example calculation of poor performance shown in **Figures 12D–F** as pale red lines, sharp variation existed in the number of reference trials (**Figure 12G**).

The Dirichlet model was compared with the proposed model, which used a neutral initial *Q*-value of 0.5 (see **Figure 3B**) when a new state was generated. For fairness of comparison, a neutral distribution was used in the Dirichlet model (see Method and **Supplementary Figure 2C**) as the initial value when a new state was generated. In contrast, the hierarchical Dirichlet models, which is more common than the Dirichlet model, inherit the parent distribution when a new state is generated, as schematized in **Supplementary Figure 2D**. **Figures 12H–K** show the results of the hierarchical Dirichlet model. The model exhibited a generally slower increase in the correct response rate than the above two models, but the rate became high near 100,000 trials (**Figure 12H**). We also encountered a calculation case where the correct rate deteriorated rapidly (**Figure 12H**, pale blue line indicated by a blank arrow). As expected, the increase in number of states was, in general, much smaller than that of the Dirichlet model (**Figure 12I**), because new states inherit the experienced distribution of their parents; consequently, the probability of generating a new state was low. Also, as in the Dirichlet model, the increase in the number of states was significantly smaller in the calculations that showed poor performance than in the other calculations (pale blue line in **Figure 12I** indicated by open arrows). Overall, the cumulative count of

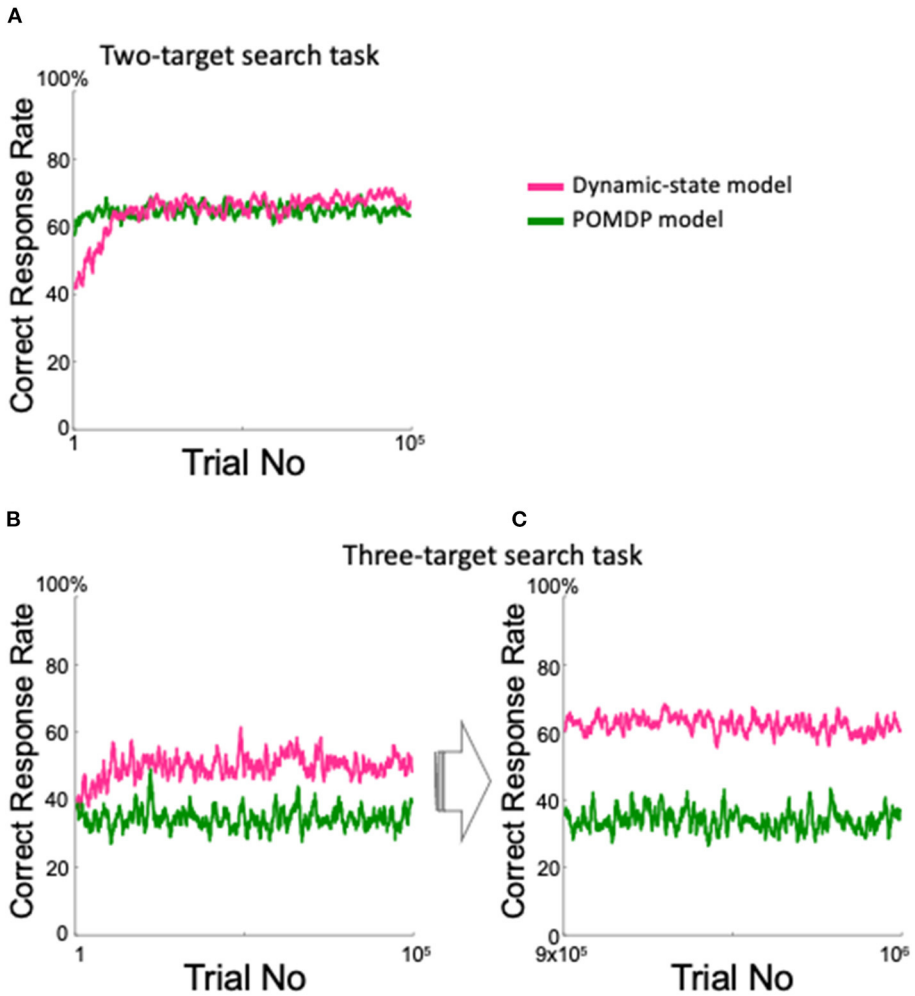

FIGURE 11 | Comparison between the proposed model and the POMDP model. **(A)** Correct response rate in the two-target search task. **(B,C)** Correct response rates in the three-target search task for the first 10^5 trials **(B)** and for the 9×10^5th to the 10^6th trials **(C)**.

pair switches decreased significantly (**Figure 12J**), whereas the example defective calculations also exhibited almost no pair switches (pale blue line in **Figure 12J**). The example denoted by the pale blue line of **Figure 12I** had fewer than 72 states, but this does not mean that only the last two trials were referred to. **Figure 12K** shows the time evolution of the referred state exhibited by the defective calculation example denoted by the pale blue lines in **Figures 12H–J**. The model frequently took states that refer to more than two trials (dotted line in **Figure 12K**), which implies that a large number of states referred to more than two trials and an insufficient number of states referred to the optimal two trials on the two-target search task. Moreover, **Figure 12K** shows that the states referring to one, two, and three or more trials were rapidly switched during training, which differs from the stable behavior of the proposed model (**Figure 4C**). In conclusion, the Dirichlet and hierarchical Dirichlet models show not bad but unstable performance, in contrast to our proposed model.

Exploration–Exploitation Trade-Off

The balance or trade-off between exploration and exploitation is recognized as a major challenge in reinforcement learning (Sutton and Barto, 1998). To maximize the total reward amount when executing a task, agents should neither rely very rigidly on their prior successful experiences (exploitation) nor select actions in an excessively arbitrary manner (exploration). The two-target search task includes exploration and exploitation phases. Therefore, our task is suitable for studying the exploration–exploitation trade-off problem by examining the relationship between the amount of learning in the model and the perseverative tendency with respect to the previously valid pair.

To examine this trade-off problem, we obtained the correlation between the total amount of learning at the time of a valid-pair switch and the number of consecutive trials for which the action adhered to the most recent valid pair (**Figure 13**). The correlations were calculated from the 50,000th to the 100,000th trial, when the correct response rate was considered sufficiently

stable based on **Figure 4A**. The initial value of Q for each state was set to 0.5, so the total learning was defined as the sum of the absolute values of the differences from 0.5 within the Q table. For example, if the model has four states, {0.1, 0.7, 0.2, 0.6}{0.1, 0.7, 0.2, 0.6}{0.1, 0.7, 0.2, 0.6}{0.1, 0.7, 0.2, 0.6}, the total amount of learning is $(|0.1 - 0.5| + |0.7 - 0.5| + |0.2 - 0.5| + |0.6 - 0.5|) \times 4 = 4$. In the fixed 4-state model, the state is based only on what was seen in the previous trial, i.e., the result is not considered (**Figure 13A**). This model naturally had a low rate of correct answers (data not shown) and, as a result, the number of pair-switching trials was as low as 904 in this calculation example. The number of trials with perseveration was also high (up to 20), and a stronger correlation between the total amount of learning and this number ($r = 0.19$) was observed than in the models shown in **Figures 13B,C**. This indicates that, in the fixed 4-state model, a high total amount of learning was associated with more difficulty in switching to exploratory behavior. In other words, there was a trade-off between exploration and exploitation.

However, in the fixed 8-state model (**Figure 4A**), in which the choice of action was based not only on the action of the previous trial but also on the result thereof, as well as the number of trials with perseveration, the correlation between the total amount of learning and this number was also greatly reduced ($r = 0.0021$; **Figure 13B**). However, the number of valid-pair switches did not significantly increase ($n = 973$), because this model required a large number of trials to obtain a deterministic behavioral decision.

The dynamic state also allowed the model to avoid the exploration–exploitation trade-off. In our proposed model, although the total amount of learning increased with the number of states, the number of trials with perseveration decreased further, and the number of valid-pair switches increased dramatically ($n = 3{,}916$). Concerning the correlation between the total amount of learning and the number of trials with perseveration, a small, or even negative, value was found ($r = -0.025$; **Figure 13C**). These results indicate that by including the results of the action in the state, the models learned how to take an action when they made a mistake—they learned how to explore.

DISCUSSION

In this study, we developed a reinforcement learning model with a dynamic state space and tested its ability to execute a two-target search task in which the exploration and exploitation phases alternated. To obtain a high score in this task, it is necessary to select an action according to the actions and reward outcomes of the two previous trials. The proposed model was able to dynamically and reproducibly expand and contract the state space based on two explicit criteria for the appropriateness of state expansion: experience saturation (ζ) and a preference for deterministic action or decision uniqueness (η). Thus, it demonstrated high performance, comparable with the performance of an ideal model with a fixed state space specific to the task, although it did not have a state space suitable for the task in advance. In addition, regardless of a behavioral task structure that was not assumed a priori, the proposed model exhibited an improvement in performance that could not be achieved with the fixed state model described above. Furthermore, by learning how to explore during the exploration phase, the proposed model did not exhibit a trade-off between exploration and exploitation.

Validity of the Proposed Model

As shown in the behavioral analysis in Kawaguchi et al. (2015), monkeys were smart enough to learn to switch their behavior reflecting their own previous actions and their results (Shima and Tanji, 1998), rather than to learn by trial and error which spots to look at each time the correct target is changed. Therefore, it was necessary for the foundation of the proposed model, or the main models for comparison to highlight the characteristics of the proposed model (specifically, the Fixed 8by8-state model and the Fixed 8-state model), to have the actions taken by the subject and their results as the states. It may not be the usual manner in the field of reinforcement learning to define the state space the same as the action space. The state space usually corresponds to perceptual information, which in the case of **Figure 2A** would be the single state of presentation of the four white spots. However, it is obvious that the performance of a model using such a single state that learns to shift its gaze by trial and error is far less than that of monkeys, and discussions based on such a model are not fruitful. Furthermore, even if the action space into the state space were to be incorporated, the majority of RL researchers would use four states, that is, states based on the definition of "seeing one light spot among four identical stimuli" in the case of the two-target search task, rather than using eight states that the main models in this study based on. In fact, because we understand this point, we also showed calculations in **Figure 13A** for the model including the fixed four states. However, there is not much to be gained by using that model as the main comparison for the proposed model, for the same reason as mentioned above.

The dynamic state model performed as expected. Analysis of the state space dynamics (shown in **Figures 4B,C**) revealed that the model appropriately handles state space, which it readily expands or contracts. The performance in the multi-armed bandit task (**Figures 9C–F**) also indicates that the model did not extend states if their decision uniqueness is not better than that of their parent states. The dynamic state model is also robust. The model meta-parameters (α, β, ζ, and η) have a sufficiently wide range to enable the model to perform well (**Figures 5–8**). Even without the bias of parent–child comparison, the model still produces a high correct rate (**Figure 9A**) and a slightly high, but limited, number of states (**Figure 9B**) in the two-target search task, while it shows high correct rates (**Figures 9C,E**) and the expected numbers of states (**Figures 9D,F**) in the multi-armed bandit tasks.

The proposed model has an intrinsically greater ability to adapt to an indefinite environment, compared with the POMDP model requiring prior assumption at least for the probability space. Indeed, in the two-target search task, the POMDP model showed a high correct rate by estimating the current valid pair given as prior knowledge, although it only referred to the previous trial (**Figure 11A**). However, in the three-target search

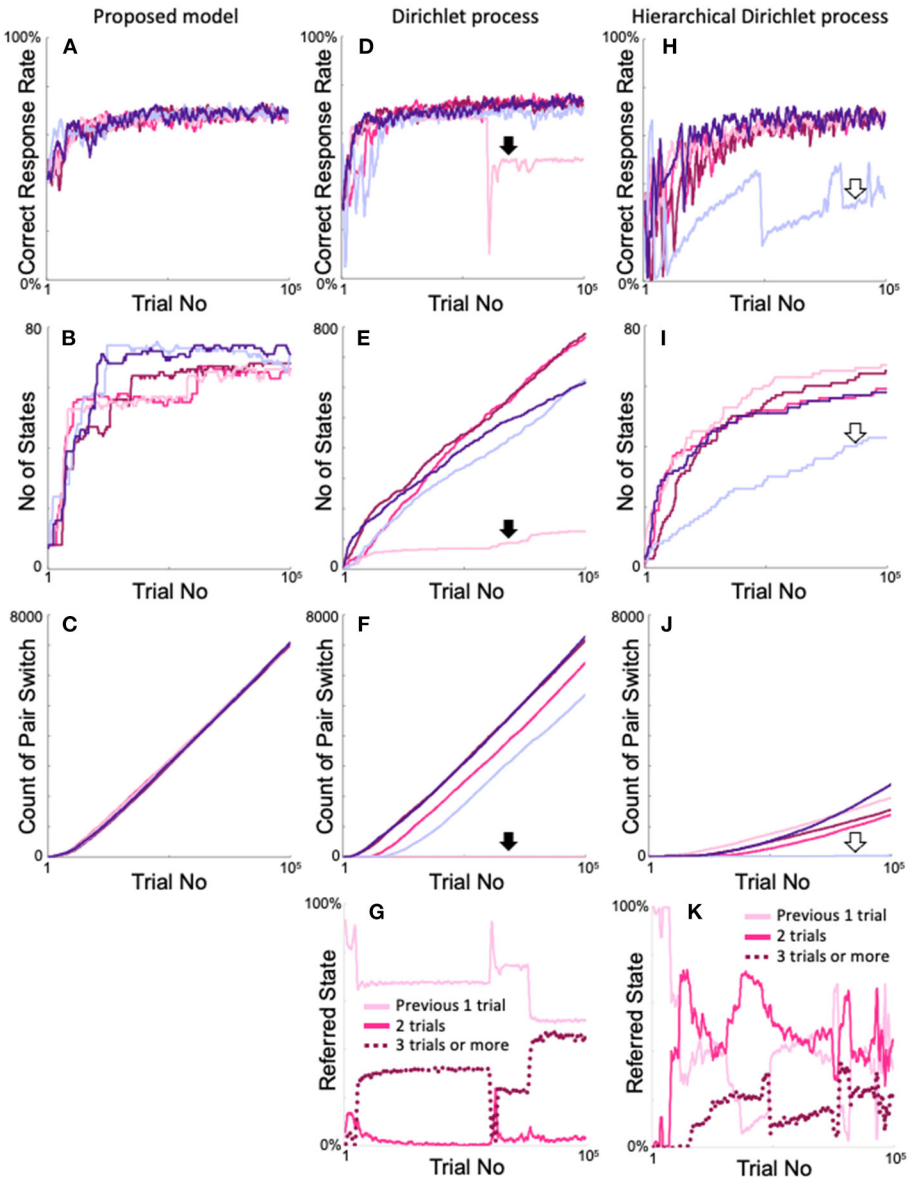

FIGURE 12 | Comparison of the proposed model and the iHMMs in terms of the reproducibility of two-target search task learning. **(A–C)** Time courses of the correct response rate **(A)**, increase in number of states **(B)**, and increase in the cumulative number of target pair-switches **(C)** exhibited by the proposed model. **(D–F)** Identical plots of the Dirichlet process version of the iHMM (see **Supplementary Figure 2C**). **(G)** Changes in states with each action selection in the calculation example indicated by the filled arrows in **(D–F)**. **(H–J)** Identical plots of the hierarchical Dirichlet process version of the iHMM (see **Supplementary Figure 2D**). **(K)** Plot identical to G for the calculation example indicated by the blank arrows in **(H–J)**. The same color in the simulations of each model denotes the same calculation.

task, where prior knowledge of the valid pair was irrelevant, our dynamic state model performed much better than did the POMDP model (**Figures 11B,C**).

The iHMMs illustrated in **Figure 12** are probably the closest to the proposed model, as they do not require the assumption of prior knowledge of the environment. These models follow the Dirichlet process and dynamically expand the state according to the history of each action taken in the state. However, unlike the proposed model, there is no explicit criterion for determining the appropriateness of state expansion; therefore, the state is not always easily expanded when it should be, and may be easily expanded when it should not be. As a result, the number of recent trials referred to in the action decision is unstable (**Figures 12G,K**), resulting in less reproducibility of the correct response rates (**Figures 12D,H**), a higher number of states (**Figure 12E**), and a low reproducibility in the cumulative number of pair-switches (**Figures 12F,J**) in the two-target search task compared with the proposed model. Decision uniqueness provides the purpose of state expansion, and experience saturation determines the timing of state expansion. These two

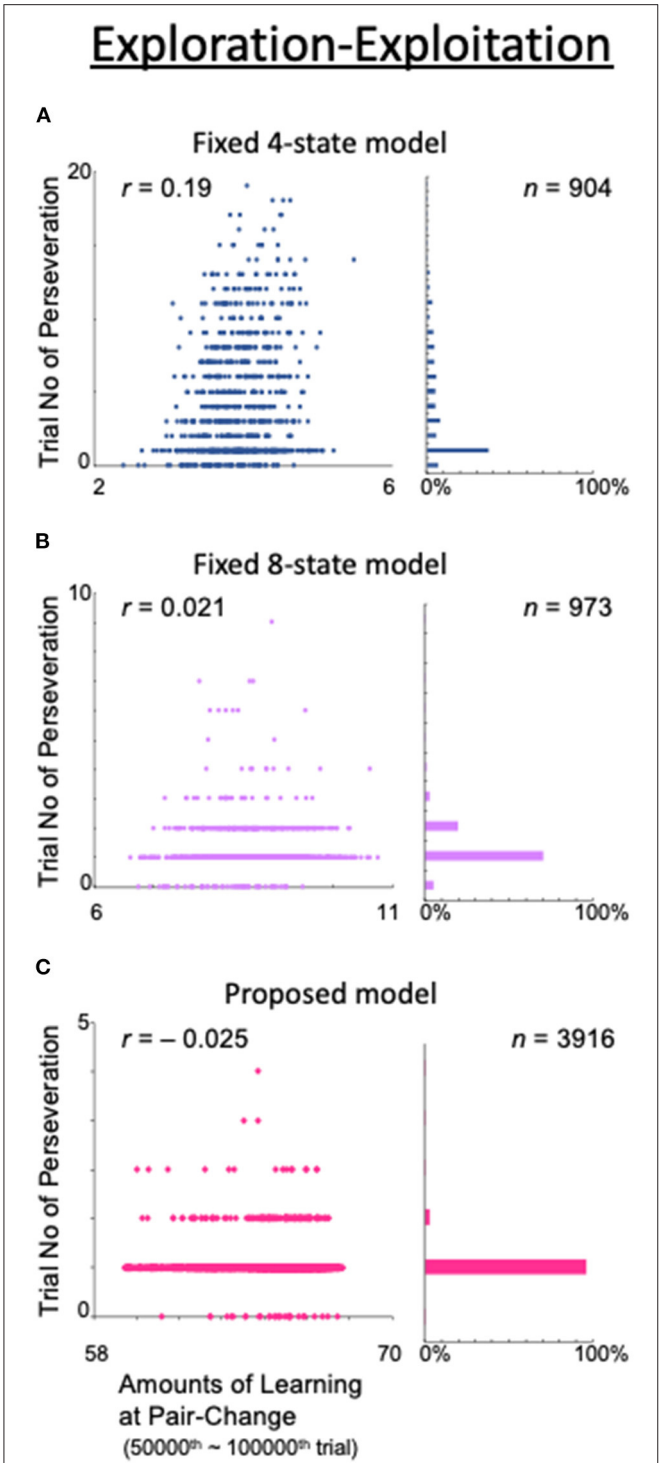

FIGURE 13 | Analysis of the exploration–exploitation trade-off problem. (Left column) Amount of learning at the end of the last exploitation phase (abscissa) and the number of consecutive trials during which the model exhibited an action that persisted from the previous valid pair (ordinate). (Right column) Histograms of trials with perseveration as a percentage of the total number of trials. **(A)** Fixed 4-state model. **(B)** Fixed 8-state model. **(C)** Proposed model.

criteria regulate the appropriateness of state expansion, resulting in flexible and stable model performance.

Decision uniqueness is related to an orientation toward causal determination or causal attribution (Heider, 1958; Kelley, 1967, 1973). To our knowledge, no published models consider experience saturation and a preference for deterministic action or decision uniqueness in reinforcement learning, although it is quite reasonable to assume them. For example, doctors clearly require sufficient study and experience to be able to properly diagnose patients; doctors would never roll the dice, despite encountering a patient who is difficult to diagnose. Each doctor would consult his or her colleagues and study relevant literature to make a specific, unique decision. The validity of decision uniqueness is supported by behavioral studies: this orientation has also been found in children (Schulz and Sommerville, 2006); Rodents recruit contextual information from the environment to uniquely determine the meaning of ambiguous CS (Fanselow, 1990). Furthermore, experience saturation is related to boredom, which is the counterpart to curiosity. In non-human primates, extensive experience with a task can lead to boredom (Harlow, 1950), as often observed by researchers who train monkeys to execute behavioral tasks. While it may be undesirable for artificial intelligence to exhibit "boredom," this phenomenon is very common in humans. The drive toward state–space expansion based on these two criteria is an expression of curiosity; it reflects a tendency to deepen one's understanding of the environment.

Implications of the Model's Behavior

Figure 4B shows a step-like increase in the number of states at approximately 60,000 trials. This corresponds to an increase in the diagonal gaze rate and a decrease in other gaze rates in the second trial of the exploration period (**Figures 4D,E**). However, these changes were slight, as were changes in the correct response rate (**Figure 4A**). The contrast between this small change and the rapid increase in the number of states is intriguing. This contrast may indicate that learning is not solely determined by environmental factors through correct and incorrect answers; it also reflects a process of refinement and maturation within the model. This observation may mean that, for example, each professional athlete appears to have a much higher level of knowledge and experience of the game, compared with amateurs; however, behind the slight differences in skill that determine who wins and loses lie large differences between players in terms of knowledge and experience.

The behavior of the model in response to outlier values of the meta-parameters is also important to note (**Figures 5–8**). When the criterion for experience saturation ζ is too low, the model tries to obtain more information from the existing state and thus does not expand the state space (dark purple line in **Figure 5B**). Conversely, when ζ was too high, the model easily gained what it considered sufficient information, the number of states generated was somewhat higher than the minimal required number (i.e., 72), though there was no uncontrollable increase in it (light purple line in **Figure 5B**). These findings indicate that

neither insatiable learners nor learners who become too easily bored are ideal.

Somewhat similarly, if η was too low, even a Q-table with a sufficient preference for a single action was not regarded as deterministic and the state space was over-expanded to refer to the last three trials (yellow line in **Figure 6B**), though the correct rate itself was almost ideal. By contrast, if η was too high, the unique action selection was compromised, resulting in only eight states being retained, and thus referring to only the previous trial (brown line in **Figure 6B**). These observations may indicate that if learners try to decide things in an excessively strict manner, they may become mired in the tiny details of the situation; if learners are excessively irresponsible, they will not achieve a correct understanding of the environment.

The behavior of the model with outliers in the inverse temperature β of the softmax function can be understood in a manner similar to the case of η (**Figure 8**). If β was insufficient, the model chose actions randomly (i.e., in an irresponsible manner), which did not improve its understanding of the environment. Conversely, if β was excessive, the model persisted in certain actions, which limited the speed of its environmental understanding. Notably, the situation differed for the learning rate α (**Figure 7**). In particular, when the learning rate was high, the model learned the new valid pair quickly after pair switching, which did not lead to a good understanding of the task structure. This suggests that quick learners do not understand things deeply.

The bias in the parent–child comparison with a value of -1 suppresses the explosion in the number of states. Indeed, in the absence of a bias, the number of states is limited but more than the minimum required number (72) in the two-target search task, although there is no difference in the correct rates. In this sense, a bias is beneficial to the two-target search task. Given the change in number of states in the alternative version of the four-armed bandit task (**Figure 9F**), we consider whether it is preferable to have a bias. In the presence of a bias, increasing the number of states referring to the last two trials does not improve decision uniqueness; therefore, those states are pruned. However, this cannot handle the case where an action can be uniquely determined only after the last three or more trials have been considered. In contrast, in the absence of a bias, state expansion does not stop while the state is comparable to its parent state in terms of decision uniqueness. Therefore, when the task is essentially stochastic, as in this bandit task, it is not possible to stop state expansion. An intermediate method between the two is needed, which should be addressed in the future.

Relationship of the Proposed Model to Related Works

The hierarchical Dirichlet model, which is compared with the proposed model in **Figures 12H–K**, is useful for language recognition problems, such as word estimation in sentences and word segmentation in Chinese and Japanese (Mochihashi and Sumita, 2007; Mochihashi et al., 2009). This model shows unstable performance in the two-target search task compared with the proposed model, although it often exhibits good performance. However, the rapid expansion of the state in the hierarchical Dirichlet model seems to be useful in problems such as language recognition, where the number of samples must be small, unlike the two-target search task where tens of thousands of trials can be sampled. The two criteria for the appropriateness of state expansion used in the proposed model are somewhat strict; if similar but more relaxed criteria are incorporated into the iHMM for language recognition processing, the model performance may improve.

As a learning architecture using KLDs, the free-energy principle has recently attracted considerable attention (Friston, 2009, 2010; Friston et al., 2009). This principle infers hidden variables in the environment such that free energy is minimized; specifically, predictions are maximized while allowing learners to actively work on the environment. KLD is used to maximize predictions; therefore, the computation aims to make no better predictions. This corresponds to the calculation of experience saturation in our model. It also may include active perceptual behavior (e.g., moving the eyes) to maximize prediction, which is consistent with our own behavior. However, this method is similar to the POMDP method in that it includes estimation of uncertain states, and the possible states are provided as prior knowledge. Thus, we cannot conclude that this principle is inherently equipped with the ability to adapt to indefinite environments.

Our proposed model attempted to extract complex temporal structures in the environment by using dynamic state space, similar to the reconstruction of dynamical systems in the field of non-linear dynamics. In particular, embedding is regarded as a method for identifying the underlying dynamics from time series data (e.g., Takens, 1981; Sauer et al., 1991; Ikeguchi and Aihara, 1995). For example, a chaotic dynamical system requires at least three dimensions. To reconstruct the trajectory of the chaotic system from the time series, two time intercepts (two-dimensional reconstruction map) are insufficient; three time intercepts (three-dimensional reconstruction map) are necessary. By applying the proposed model, we may be able to build a model that can learn to automatically reconstruct the non-linear dynamical system behind the time series data, just as our model could learn the task structure behind the three-target search task.

Future Directions

The model proposed in this study showed a higher correct response rate in the three-target search task than the fixed 8by8-state model, which is an ideal model for the two-target search task (**Figure 10**). However, the difference between the two models did not become clear until approximately 1 million trials had elapsed. It took about 3 months (∼100,000 trials) for the monkeys to master the two-target search task, including understanding of the events in a single trial, and the three-target search task is clearly more difficult than this task. However, in our experience, the three-target search task is easier than the path-planning and shape manipulation tasks that we had used in our previous experiments, which required more than 10 months of training (Mushiake et al., 2001; Sakamoto et al.,

2008, 2015, 2020a,b). The reason why the model took so long to learn the three-target search task was because the optimal model for the three-target search task had to make a decision based on a combination of three trials, i.e., as many as $8^3 = 512$ states. In other words, the model faced the curse-of-dimensionality problem, where convergence slows as the number of states increases. To overcome this, the model will need the ability to generalize or abstract its experiences, such as "target three of the four points in order." In fact, monkeys have much greater generalization ability, compared with our model, so they are expected to be able to learn the difficult tasks mentioned above. This generalization ability may correspond to the abstract representation of sequential actions by neuronal activities in the prefrontal cortex of monkeys (Shima et al., 2007; Sakamoto et al., 2020a).

In this paper, we dealt with a model in which one trial corresponds to one time step, but in the two-target search task that the animals actually performed, one trial included a sequence of events (Kawaguchi et al., 2013, 2015). It is not easy to build a model that can learn that more realistic latter situation, because we are faced with the problem of how to deal with one previous state. That is, it is unclear what constitutes one previous computation time increment; it could be one previous task event or one complete previous trial.

Einstein described his skepticism about quantum mechanics as follows: "Der Alte würfelt nicht (the old man does not roll the dice)." This expression seems to imply his desire for a deterministic understanding of the principles of the universe. Currently, artificial intelligence (AI), including reinforcement learning, is developing rapidly, and humans are delegating various decisions to AI. However, we do not want AI to roll the dice when we entrust it with important decisions. Instead, we want AI to constantly deepen its knowledge and experience, and to make deterministic decisions. The model proposed in this study did not exhibit a trade-off between exploration and exploitation (**Figure 13**). We hope that this model can serve as one of the foundations of AI that constantly deepens knowledge and experience, thus permitting deterministic decisions in complex and difficult environments.

DATA AVAILABILITY STATEMENT

The raw data supporting the conclusions of this article will be made available by the authors, without undue reservation.

AUTHOR CONTRIBUTIONS

TK, HM, and KS designed research. TK, MY, HH, and KS performed research and analyzed data. KS wrote the first draft of the paper and edited the paper. All authors contributed to the article and approved the submitted version.

FUNDING

This work was supported by JSPS KAKENHI Grant Number JP16H06276 (Platform of Advanced Animal Model Support), 17K07060, 20K07726 (Kiban C), MEXT KAKENHI Grant Number 15H05879 (Non-linear Neuro-oscillology), 26120703 (Prediction and Decision Making), 20H05478 (Hyper–Adaptability) and Japan Agency for Medical Research and Development (AMED) under Grant Number JP18dm0207051.

ACKNOWLEDGMENTS

We thank Prof. Y. Matsuzaka and Dr. Y. Nishimura of Tohoku Medical and Pharmaceutical University for advice and suggestions.

SUPPLEMENTARY MATERIAL

The Supplementary Material for this article can be found online at: https://www.frontiersin.org/articles/10.3389/fncom.2021.784592/full#supplementary-material

Supplementary Figure 1 | The event sequence of one trial of the two target search task. Note that the actions in one trial and the results to them are defined as one time step, and the learning including the task sequence was not in this paper.

Supplementary Figure 2 | The infinite hidden Markov models (iHMMs) compared to our proposed model. **(A)** Overview of the iHMM scheme. While the iHMM is similar to the proposed model (**Figure 1C**), it lacks a process to evaluate the appropriateness of state expansion. **(B)** Schematic tree showing how iHMMs expand the states. They start with a base state referring to no previous trials; each tree node stage corresponds to the reference trial number. Each state is the combination of the actions taken and their reward outcomes, as in the proposed model. **(C)** Schematic of the Dirichlet process version of the iHMM. The model was implemented using the Chinese restaurant process. Each filled circle (table) represents a possible action. If the action is rewarded, a new guest (a person with a filled head) sits at the table for that action. If an empty table is chosen, a new state is generated. In this case, a new state starts with the initial condition, in which each filled table has an "intrinsic guest" (a person with an empty head). **(D)** Schematic for the hierarchical similar Dirichlet process version. The newly generated child state inherits the distribution of the parent state. The *P*s in **(C,D)** represent the probabilities that each action is taken.

REFERENCES

Ahmadi, M., Jansen, N., Wu, B., and Topcu, U. (2020). Control Theory Meets POMDPs: A Hybrid Systems Approach. *IEEE Trans. Automat. Contr.* 66, 5191–5204. doi: 10.1109/TAC.2020.3035755

Azizzadenesheli, K., Lazaric, A., and Anandkumar, A. (2016). Reinforcement learning of pomdps using spectral methods. *JMLR: Workshop Conf. Proc.* 49, 1–64.

Beal, M. J., Ghahramani, Z., and Rasmussen, C. (2002). The infinite hidden Markov model. *Adv. Neural Inform. Proc. Syst.* 14, 577–584.

Bhattacharya, S., Badyal, S., Wheeler, T., Gil, S., and Bertsekas, D. (2020). Reinforcement learning for pomdp: partitioned rollout and policy iteration with application to autonomous sequential repair problems. *IEEE Robot. Autom. Lett.* 5, 3967–3974. doi: 10.1109/LRA.2020.2978451

Bouton, M., Tumova, J., and Kochenderfer, M. J. (2020). Point-based methods for model checking in partially observable Markov decision processes. *Proc. AAAI Conf. Artif. Intell.* 34, 10061–10068. doi: 10.1609/aaai.v34i06.6563

Doshi-Velez, F. (2009). The infinite partially observable Markov decision process. *Adv. Neural Inform. Proc. Syst.* 21, 477–485.

Doshi-Velez, F., Pfau, D., Wood, F., and Roy, N. (2015). Bayesian nonparametric methods for partially-observable reinforcement learning. *IEEE Trans. Pattern Anal. Mach. Intell.* 37, 394–407. doi: 10.1109/TPAMI.2013.191

Fanselow, M. S. (1990). Factors governing one trial contextual conditioning. *Anim. Learn. Behav.* 18, 264–270. doi: 10.3758/BF03205285

Friston, K. (2009). The free-energy principle: a rough guide to the brain? *Trends. Cogn. Sci.* 13, 293–301. doi: 10.1016/j.tics.2009.04.005

Friston, K. (2010). The free-energy principle: a unified brain theory? *Nat. Rev. Neurosci.* 11, 127–138. doi: 10.1038/nrn2787

Friston, K., Daunizeau, J., and Kiebel, S. J. (2009). Reinforcement learning or active inference? *PLoS ONE* 4, e6421. doi: 10.1371/journal.pone.0006421

Harlow, H. F. (1950). Learning and satiation of response in intrinsically motivated complex puzzle performance by monkeys. *J. Comp. Physiol. Psychol.* 43, 289–294. doi: 10.1037/h0058114

Hausknecht, M., and Stone, P. (2015). "Deep recurrent q-learning for partially observable MDPs," in *2015 AAAI Fall Symposium Series* (Arlington, VA), 29–37.

Heider, F. (1958). *The Psychology of Interpersonal Relations*. New York, NY: Wiley.

Igl, M., Zintgraf, L., Le, T. A., Wood, F., and Whiteson, S. (2018). Deep variational reinforcement learning for POMDPs. *Proc. 35th Intl. Conf. Machine Learn. Proc. Mach. Learn. Res*. 80, 2117–2126.

Ikeguchi, T., and Aihara, K. (1995). Prediction of chaotic time series with noise. *IEICE Trans. Fund. Electr. Commun. Comput. Sci. E*78-A, 1291–1298.

Jaakkola, T., Singh, S. P., and Jordan, M. I. (1995). Reinforcement learning algorithm for partially observable Markov decision problems. *Adv. Neural Inf. Process. Syst.* 7, 345–352.

Kawaguchi, N., Sakamoto, K., Furusawa, Y., Saito, N., Tanji, J., and Mushiake, H. (2013). Dynamic information processing in the frontal association areas of monkeys during hypothesis testing behavior. *Adv. Cogn. Neurodynam.* 4, 691–698. doi: 10.1007/978-94-007-4792-0_92

Kawaguchi, N., Sakamoto, K., Saito, N., Furusawa, Y., Tanji, J., Aoki, M., et al. (2015). Surprise signals in the eye field: rectified prediction errors drive exploration–exploitation transitions. *J. Neurophysiol.* 113, 1001–1014. doi: 10.1152/jn.00128.2014

Kelley, H. H. (1967). Attribution theory in social psychology. *Nebr. Symp. Motiv.* 15, 192–238.

Kelley, H. H. (1973). The processes of causal attribution. *Am. Psychol.* 28, 107–128. doi: 10.1037/h0034225

Maliah, S., and Shani, G. (2021). Using POMDPs for learning cost sensitive decision trees. *Artif. Intell.* 292, 103400. doi: 10.1016/j.artint.2020.103400

Mochihashi, D., and Sumita, E. (2007). The infinite Markov model. *Adv. Neural Inform. Proc. Syst.* 20, 1017–1024.

Mochihashi, D., Tamada, T., and Ueda, N. (2009). "Bayesian unsupervised word segmentation with nested Pitman-Yor language modeling," in *Proc. 47th Ann. Meeting ACL 4th IJCNLP AFNLP* (Singapore), 100–108.

Mushiake, H., Saito, N., Sakamoto, K., Sato, Y., and Tanji, J. (2001). Visually based path planning by Japanese monkeys. *Cogn. Brain Res.* 11, 165–169. doi: 10.1016/S0926-6410(00)00067-7

Pfau, D., Bartlett, N., and Wood, F. (2010). Probabilistic deterministic infinite automata. *Adv. Neural Inform. Proc. Syst.* 23, 1930–1938.

Rescorla, R. A., and Solomon, R. L. (1967). Two-process learning theory: relationships between Pavlovian conditioning and instrumental learning. *Psychol. Rev.* 74, 151–182. doi: 10.1037/h0024475

Sakamoto, K., Kawaguchi, N., and Mushiake, H. (2020b). Differences in task-phase-dependent time-frequency patterns of local field potentials in the dorsal and ventral regions of the monkey lateral prefrontal cortex. *Neurosci. Res.* 156, 41–49. doi: 10.1016/j.neures.2019.12.016

Sakamoto, K., Kawaguchi, N., Yagi, K., and Mushiake, H. (2015). Spatiotemporal patterns of current source density in the prefrontal cortex of a behaving monkey. *Neural Netw.* 62, 67–72. doi: 10.1016/j.neunet.2014.06.009

Sakamoto, K., Mushiake, H., Saito, N., Aihara, K., Yano, M., and Tanji, J. (2008). Discharge synchrony during the transition of behavioral goal representations encoded by discharge rates of prefrontal neurons. *Cereb. Cortex* 18, 2036–2045. doi: 10.1093/cercor/bhm234

Sakamoto, K., Saito, N., Yoshida, S., and Mushiake, H. (2020a). Dynamic axis-tuned cells in the monkey lateral prefrontal cortex during a path-planning task. *J. Neurosci.* 40, 203–219. doi: 10.1523/JNEUROSCI.2526-18.2019

Sauer, T., Yorke, J. A., and Casdagli, M. (1991). Embedology. *J. Stat. Phys.* 65, 579–616. doi: 10.1007/BF01053745

Schulz, L. E., and Sommerville, J. (2006). God does not play dice: causal determinism and preschoolers' causal inferences. *Child Dev.* 77, 427–442. doi: 10.1111/j.1467-8624.2006.00880.x

Shima, K., Isoda, M., Mushiake, H., and Tanji, J. (2007). Categorization of behavioural sequences in the prefrontal cortex. *Nature* 445, 315–318. doi: 10.1038/nature05470

Shima, K., and Tanji, J. (1998). Role for cingulate motor area cells in voluntary movement selection based on reward. *Science* 282, 1335–1338. doi: 10.1126/science.282.5392.1335

Shimizu, H. (1993). Biological autonomy: the self-creation of constraints. *Appl. Math. Comput.* 56, 177–201. doi: 10.1016/0096-3003(93)90122-U

Sutton, R. S., and Barto, A. G. (1998). *Reinforcement Learning: An Introduction*. Cambridge, MA: MIT Press.

Takens, F. (1981). Detecting strange attractors in turbulence. *Lect. Notes Math.* 898, 366–381. doi: 10.1007/BFb0091924

Teh, Y. W., Jordan, M. I., Beal, M. J., and Blei, D. M. (2006). Hierarchical Dirichlet processes. *J. Am. Statist. Assoc.* 101, 1566–1581. doi: 10.1198/016214506000000302

Thrun, S., Burgard, W., and Fox, D. (2005). *Probabilistic Robotics*. Cambridge, MA: MIT Press.

Xie, Y., Dibangoye, J., and Buffet, O. (2020). Optimally solving two-agent decentralized POMDPs under one-sided information sharing. *Proc. 37th Intl. Conf. Mach. Learn. Proc. Mach. Learn. Res*. 119, 10473–10482.

Conflict of Interest: The authors declare that the research was conducted in the absence of any commercial or financial relationships that could be construed as a potential conflict of interest.

Publisher's Note: All claims expressed in this article are solely those of the authors and do not necessarily represent those of their affiliated organizations, or those of the publisher, the editors and the reviewers. Any product that may be evaluated in this article, or claim that may be made by its manufacturer, is not guaranteed or endorsed by the publisher.

Copyright © 2022 Katakura, Yoshida, Hisano, Mushiake and Sakamoto. This is an open-access article distributed under the terms of the Creative Commons Attribution License (CC BY). The use, distribution or reproduction in other forums is permitted, provided the original author(s) and the copyright owner(s) are credited and that the original publication in this journal is cited, in accordance with accepted academic practice. No use, distribution or reproduction is permitted which does not comply with these terms.

frontiers in Human Neuroscience

ORIGINAL RESEARCH
published: 09 February 2022
doi: 10.3389/fnhum.2021.787487

"Tricking the Brain" Using Immersive Virtual Reality: Modifying the Self-Perception Over Embodied Avatar Influences Motor Cortical Excitability and Action Initiation

Karin A. Buetler[1†], Joaquin Penalver-Andres[1,2†], Özhan Özen[1], Luca Ferriroli[1], René M. Müri[3,4], Dario Cazzoli[3,4,5] and Laura Marchal-Crespo[1,6]*

[1] Motor Learning and Neurorehabilitation Laboratory, ARTORG Center for Biomedical Engineering Research, University of Bern, Bern, Switzerland, [2] Psychosomatic Medicine, Department of Neurology, University Hospital of Bern (Inselspital), Bern, Switzerland, [3] Gerontechnology and Rehabilitation Group, ARTORG Center for Biomedical Engineering Research, University of Bern, Bern, Switzerland, [4] Department of Neurology, University Neurorehabilitation, University Hospital of Bern (Inselspital), University of Bern, Bern, Switzerland, [5] Neurocenter, Luzerner Kantonsspital, Lucerne, Switzerland, [6] Department of Cognitive Robotics, Delft University of Technology, Delft, Netherlands

OPEN ACCESS

Edited by:
Jun Izawa,
University of Tsukuba, Japan

Reviewed by:
Takeshi Sakurada,
Ritsumeikan University, Japan
Yasuharu Koike,
Tokyo Institute of Technology, Japan

***Correspondence:**
Karin A. Buetler
Karin.buetler@unibe.ch

[†] These authors share first authorship

Specialty section:
This article was submitted to Motor Neuroscience, a section of the journal Frontiers in Human Neuroscience

Received: *30 September 2021*
Accepted: *13 December 2021*
Published: *09 February 2022*

Citation:
Buetler KA, Penalver-Andres J, Özen Ö, Ferriroli L, Müri RM, Cazzoli D and Marchal-Crespo L (2022) "Tricking the Brain" Using Immersive Virtual Reality: Modifying the Self-Perception Over Embodied Avatar Influences Motor Cortical Excitability and Action Initiation. Front. Hum. Neurosci. 15:787487. doi: 10.3389/fnhum.2021.787487

To offer engaging neurorehabilitation training to neurologic patients, motor tasks are often visualized in virtual reality (VR). Recently introduced head-mounted displays (HMDs) allow to realistically mimic the body of the user from a first-person perspective (i.e., avatar) in a highly immersive VR environment. In this immersive environment, users may embody avatars with different body characteristics. Importantly, body characteristics impact how people perform actions. Therefore, alternating body perceptions using immersive VR may be a powerful tool to promote motor activity in neurologic patients. However, the ability of the brain to adapt motor commands based on a perceived modified reality has not yet been fully explored. To fill this gap, we "tricked the brain" using immersive VR and investigated if multisensory feedback modulating the physical properties of an embodied avatar influences motor brain networks and control. Ten healthy participants were immersed in a virtual environment using an HMD, where they saw an avatar from first-person perspective. We slowly transformed the surface of the avatar (i.e., the "skin material") from human to stone. We enforced this visual change by repetitively touching the real arm of the participant and the arm of the avatar with a (virtual) hammer, while progressively replacing the sound of the hammer against skin with stone hitting sound via loudspeaker. We applied single-pulse transcranial magnetic simulation (TMS) to evaluate changes in motor cortical excitability associated with the illusion. Further, to investigate if the "stone illusion" affected motor control, participants performed a reaching task with the human and stone avatar. Questionnaires assessed the subjectively reported strength of embodiment and illusion. Our results show that participants experienced the "stone arm illusion." Particularly, they rated their arm as heavier, colder, stiffer, and more insensitive when immersed with the stone than human avatar, without the illusion affecting their experienced feeling of body ownership. Further,

the reported illusion strength was associated with enhanced motor cortical excitability and faster movement initiations, indicating that participants may have physically mirrored and compensated for the embodied body characteristics of the stone avatar. Together, immersive VR has the potential to influence motor brain networks by subtly modifying the perception of reality, opening new perspectives for the motor recovery of patients.

Keywords: embodiment, body illusion, self-perception, motor cortex, motor evoked potentials (MEPs), motor control, immersive virtual reality (IVR)

INTRODUCTION

Stroke represents a leading cause of long-term disability in adults worldwide, with one-third of chronic stroke patients requiring assistance during activities of daily living (Feigin et al., 2014). Intensive and costly neurorehabilitation interventions are an integral part of the therapy following stroke, aiming at regaining (part of) the motor functionality of patients. Within this context, robotic neurorehabilitation has been receiving increasing interest to provide more cost-effective therapy (Lum et al., 2012). Robotic-assisted interventions allow for repetitive, high-intensity, and task-specific training, lowering costs and personal limitations (e.g., fatigue) and optimizing the potential of motor recovery of patients (Marchal-Crespo and Reinkensmeyer, 2009).

To increase the engagement of patients during training, motor tasks are often visualized in virtual reality (VR), allowing the simulation of various real and imaginary activities of daily living (Lee et al., 2003; Perez-Marcos et al., 2018). VR further offers the possibility to individualize the virtual environment to the needs of the patients, and to provide standardized and safe training (Rose et al., 2005; Marchal-Crespo and Reinkensmeyer, 2008). A large body of research has demonstrated the efficacy of VR therapy in (robotic) stroke rehabilitation (Adamovich et al., 2004; Deutsch et al., 2004; Jang et al., 2005). However, in standard clinical VR settings, computer screens are used to display the virtual training environment. Here, the patient interacts with the virtual elements using an abstract virtual representation (e.g., a cursor). While this symbolic interaction provides useful visual guidance, it strongly deviates from interactions required in the real world and, therefore, may limit the transfer of acquired skills into activities of daily living (de Mello Monteiro et al., 2014; Bezerra et al., 2018).

Recently emerging head-mounted displays (HMDs) provide highly immersive virtual training environments. In this immersive virtual environment, the user interacts with a virtual self-representation perceived from first-person perspective (i.e., an avatar), realistically mimicking the body of the user. Previous work has suggested that immersive virtual reality, compared with screens, may further promote motor training because they enhance embodiment over the avatar (Wenk et al., 2021) i.e., the body of the avatar is –at least partially– processed like the own (virtual) body (Kilteni et al., 2012a). In the immersive virtual training environment, the user may experience the feeling of body ownership over the avatar. Body ownership –one out of the three components of embodiment together with agency [i.e., the feeling of initiating and being in control of the own actions; (e.g., David et al., 2008; Braun et al., 2018)] and location [i.e., the experienced location of the body in space; (e.g., Blanke, 2012)]– is the cognition that a body and/or its parts belong to oneself (Blanke, 2012). Body ownership results from the integration and interpretation of multimodal sensory information in the brain, importantly, visual, somatosensory, and proprioceptive signals (Botvinick and Cohen, 1998; Maravita et al., 2003; Ehrsson, 2004). Neuroimaging studies have shown that body ownership relies on frontal premotor, somatosensory, temporoparietal junction, and insular brain regions (Botvinick and Cohen, 1998; Maravita et al., 2003; Ehrsson, 2004; Tsakiris, 2010).

Even though our body and its physical features and capabilities (e.g., the size of body parts and/or the color or material of the skin) usually do not change –and one could assume that the perception of the own body is stable–a vast amount of research has shown that bodily self-perceptions are continuously updated in the brain in response to sensory signals related to the body characteristics (de Vignemont, 2010; Serino and Haggard, 2010; Tsakiris, 2010, 2017; Longo and Haggard, 2011; Blanke et al., 2015). Consequently, multisensory feedback can be used to modulate the self-perception of the body, as for example, in the well-known "rubber hand illusion" paradigm, first introduced by Botvinick and Cohen (1998). Here, an experimenter simultaneously strokes the hidden real hand of a participant and a rubber hand placed in front of the participant. The simultaneously felt stroking on the real hand and the visual perception of the rubber hand being stroked has been shown to reliably induce the feeling of body ownership over the rubber hand in the participant. The rubber hand illusion has also been demonstrated by providing auditory instead of visual feedback. In the "marble hand illusion," Senna et al. (2014) touched the (hidden) hand of the participant with a hammer that was coupled with stone-hitting sound. This led participants to experience their own hand to be more stone-like than in the control condition (e.g., they rated their own hand as stiffer, heavier, harder, unnatural, and less sensitive). Various variations of the rubber hand illusion paradigm have shown that body ownership can be experimentally induced in a part of a body or an entire body other than one's own in healthy young (Ehrsson, 2004; Tsakiris and Haggard, 2005; Tsakiris et al., 2006; Lloyd, 2007; Haans et al., 2008; Kammers et al., 2009; van der Hoort et al., 2011; Kalckert and Ehrsson, 2012; Lopez et al., 2012; Pozeg et al., 2014; Crea et al., 2015; Flögel et al., 2016; Wen et al., 2016; Burin et al., 2017; Riemer et al., 2019; Matsumoto et al., 2020), elderly (Burin and Kawashima, 2021), and neurologic patients (Zeller et al., 2011; Lenggenhager et al., 2012; Burin et al., 2015; Wawrzyniak et al., 2018). The demonstrated flexibility of the brain is indeed crucial to preserve a stable body image while the

perceptual characteristics of the body constantly vary in everyday life. For example, the skin color may change depending on light, and the size and shape of body parts are influenced by posture and distance. Therefore, to save resources, the brain is trained to accept deviations resulting from a mismatch between sensory signals [such as the proprioceptive incongruency between the location of the real hand and the rubber hand in the case of the rubber hand illusion paradigm; (Knoblich, 2006; Makin et al., 2008; Tsakiris, 2010)].

Numerous studies have shown that immersive VR is an especially powerful tool to alternate body perceptions. The rubber hand illusion has, for example, been replicated numerous times in VR –in the so-called "virtual hand illusion"– where congruent (e.g., haptic or tactile) feedback is provided to the real hand of the participant together with visual feedback in VR [i.e., on the hand of the avatar seen by the participant; (Slater, 2008; Perez-Marcos et al., 2009; Sanchez-Vives et al., 2010; Pyasik et al., 2020; Jeong and Kim, 2021; Kanayama et al., 2021)]. Further, the high visuo-motor or visuo-proprioceptive synchrony –i.e., the high spatial and temporal correlation between the performed movement and the visually perceived feedback on the display– in immersive VR has also been shown to induce strong embodiment over the avatar, without the need of additional tactile stimulation (Sanchez-Vives et al., 2010; Carey et al., 2019; Odermatt et al., 2021). Notably, immersive VR, together with additional sensory feedback, can be used to induce embodiment over "unrealistic" avatars (Kilteni et al., 2012b; Preston and Newport, 2012). For example, Kilteni et al. (2012b) induced a "very long arm illusion" by visually elongating a virtual arm and simultaneously providing haptic feedback to the real hand of the participant which was visually reproduced in the VR (namely, the touching of a grass surface).

Importantly, body perceptions impact how people interact with the environment. When we perform actions, it is critical to keep track of, for example, the size and shape of the different body parts (Head and Holmes, 1911; Holmes and Spence, 2004; Maravita and Iriki, 2004). In a series of experiments, Tajadura-Jiménez et al. (2012, 2015b, 2016) used real-time auditory feedback to induce illusionary ownership over elongated arms (e.g., by providing sounds that implied to originate from a greater distance when participants tapped their hand on a surface). Crucially, the authors showed that the illusion of having a longer arm also influenced the real arm movements of participants, similarly to what would be expected if the illusionary body characteristics were real (Tajadura-Jiménez et al., 2016). Further, in another study by Kilteni et al. (2013), the authors showed that participants who embodied dark-skinned avatars using immersive VR improved their drumming patterns compared to light-skinned avatars, therefore, not only showing that participants expected people with darker skin color to be better at drumming than people with lighter skin color, but also that they embodied the darker-skinned avatar.

The finding that motor actions are influenced by manipulating the self-perception of the own body using immersive VR may have important applications for neurorehabilitation. The flexibility of the brain regarding embodiment could be exploited to induce the feeling of body ownership over avatars with different body characteristics, modulating underlying motor brain networks and performance and optimizing recovery. For example, embodying a virtual stone arm may increase the physical engagement during training, similarly to lifting an empty bottle that is believed to be full. However, the ability of the brain to adapt motor commands based on a perceived modified reality has not yet been fully explored. Evidence suggests that the embodiment over an artificial limb may go in line with the disembodiment of the own limb (for a review see Golaszewski et al., 2021). Previous neurophysiological studies using non-invasive brain stimulation techniques (transcranial magnetic and direct current stimulation) and electroencephalography (EEG) have evidenced attenuated activity in motor (della Gatta et al., 2016; Fossataro et al., 2018) and somatosensory (Tajadura-Jiménez et al., 2012; Zeller et al., 2015; Hornburger et al., 2019; Isayama et al., 2019; Sakamoto and Ifuku, 2021) brain areas, along with enhanced error tolerance (Raz et al., 2020) during the experience of illusionary body ownership. However, most studies on the neural correlates underlying embodiment investigated illusionary body ownership over a rubber hand (Botvinick and Cohen, 1998; Ehrsson, 2004; Tsakiris and Haggard, 2005; Haans et al., 2008). Importantly, in the rubber hand illusion paradigm, the hand of the participant is not located at the same place as the rubber hand. To overcome this proprioceptive mismatch and to embody the rubber hand, the brain may be forced to disembody the own hand, lowering neural activity in the corresponding brain areas. Further, the experience of illusionary body ownership is commonly associated with congruent multisensory feedback (for example, applied to the participants real hand and a rubber hand), while the control condition (i.e., low body ownership) is associated with incongruent feedback, previously shown to introduce confounding congruency effects (Rao and Kayser, 2017; Odermatt et al., 2021). Yet, immersive VR allows for congruent multisensory feedback with high visuo-proprioceptive congruency –i.e, the motor actions are spatially and temporally highly correlated with the visual feedback perceived through the HMD– and therefore, disembodiment of the own limb may not be necessary, allowing for a more naturalistic embodiment. This is in line with previous work showing that body illusions based on unimodal sensory feedback and without proprioceptive mismatch enhance activity in motor brain networks: visual kinesthetic illusions, in which the illusory feeling of motion of a static body part is induced by mechanically vibrating the tendon muscle of a physically constrained joint, have been associated with an increase in motor cortical excitability (for a review see Dilena et al., 2019). Therefore, in this study, we aimed at "tricking the brain" in a naturalistic fashion using immersive VR and investigate if multisensory feedback modulating the physical properties of an embodied avatar influences motor brain networks and control. To allow for a more naturalistic embodiment, we decided to change the skin material rather than the limb size or shape (e.g., elongated arm), to not introduce a proprioceptive mismatch during the illusion which could be associated with reduced motor activity.

Ten healthy participants were immersed in VR with an HMD, where they saw an avatar from a first-person perspective. We applied multisensory feedback (i.e., auditory, tactile, and

visual) to induce a "stone arm illusion," inspired by the work of the marble hand illusion by Senna et al. (2014). We slowly transformed the surface of the avatar (i.e., the "skin material") from human to stone. We enforced this visual change by repetitively touching the arm of the participant and the real arm of the avatar with a (virtual) hammer, while progressively replacing the sound of a hammer against skin with the sound of a hammer against stone provided via a speaker. To study changes in motor brain networks associated with the illusion, we applied single-pulse transcranial magnetic stimulation (TMS) over the primary motor cortex. Applying TMS through the scalp over the primary motor cortex elicits action potentials in motor neurons of the brain, which can be captured as motor evoked potentials (MEPs) with electromyographic recordings on the corresponding muscles (Rothwell, 1997; Wolf et al., 2005; Groppa et al., 2012). Amplitude and latency of the MEPs are influenced by the cortical excitability of the motor system and corticospinal tract and can therefore be used as an index of physiological state changes in the primary motor area (Barker et al., 1985; Rothwell et al., 1987a,b; Bestmann, 2012; Bestmann and Krakauer, 2015; Rossini et al., 2015; Schmidt and Brandt, 2021). Further, to investigate if the "stone illusion" affected action execution, participants performed a reaching task visualized in VR with the human and stone avatar, i.e., they had to reach as fast and accurately as possible from a resting hand position on a table to appearing spheres above the table. Finally, we used questionnaires to assess the subjectively reported strength of the embodiment and illusion.

We expected that the immersive, highly congruent multisensory feedback in VR would induce strong body ownership over the avatar across both the human and stone conditions. In addition, we expected higher subjectively rated "stone feeling" in the stone versus human avatar condition, indicating the presence of a "stone arm illusion." We further hypothesized that the stone arm illusion or the subjectively experienced stone feeling would be associated with enhanced motor cortical excitability, reflecting an adaptation of motor brain processes to the altered body image. Further, we hypothesized that the stone arm illusion or stronger subjectively experienced stone feeling would enforce accelerated movement patterns and/or motor overshooting in the reaching movements, due to an overestimation of the weight of the real arm. Finally, to better understand the nature of the stone arm illusion, we were further interested in exploring the relationship between the stone feeling and embodiment components (as stronger subjectively experienced stone feeling may hamper agency but not body ownership), and between the reaching movements and cortical excitability in the human and stone condition.

MATERIALS AND METHODS

Participants

We recruited 10 healthy participants [five female; age (M ± SD) = 29.4 ± 6.5 years] from the campus of the University of Bern, Switzerland. All participants reported to be right-handed when asked to indicate their dominant hand and to have normal or corrected-to-normal vision. None of them had a psychiatric or neurological clinical history. Participants were naïve to the hypotheses of the experiment. The study was approved by the local ethics committee and all participants gave written informed consent.

Experimental Setup

Material

An overview of the experimental setup can be seen in **Figure 1**. A head-mounted display (HTC Vive, HTC, Taiwan and Valve, United States), two trackers, and one controller (HTC Vive, Taiwan and Valve, United States) were employed in the VR setup. Two trackers were attached on the right upper arm and wrist of the participant with Velcro® straps to record the motion kinematic data and visually animate the avatar in the VE. The controller was operated by the experimenter to animate a virtual hammer. The kinematic data of the trackers were continuously collected at a sampling rate of ∼50 Hz in the Unity game engine and stored for offline analysis (version 2018.3.0f2; Unity Technologies, United States).

A 4-button response box (The Black Box ToolKit Ltd., United Kingdom) placed on a table was used by the participants to answer the questionnaires in VR. A loudspeaker located on the right side of the same table provided the auditory feedback. The data obtained via response box were collected in the Unity game engine and stored for offline analysis.

A Magstim 200 Mono Pulse stimulator (Magstim Ltd., United Kingdom) and a figure-of-eight coil were used to apply TMS pulses through the scalp of the head of the participant over the primary motor area (**Figure 1A**). A TMS navigation system (Localite GmbH, Germany) was employed for the co-registration of the position and orientation of the coil with the head of the participant. Electromyographic recordings in the shape of MEPs elicited by the TMS pulses were obtained using the Dantec Keypoint G4 Workstation (Natus Medical Incorporated, United States) from the right hand of the participant in a belly-tendon montage by means of Ag/AgCl surface tab electrodes with a diameter of 5 mm (Medtronic Ltd., United Kingdom). The active electrode was placed over the belly of the first dorsal interosseous (FDI) muscle, the reference electrode over the proximal interphalangeal joint of the index finger (tendon), and the ground electrode over the abductor digiti minimi (**Figure 1B**). The electromyographic raw signal was amplified, recorded with a sampling rate of 48 kHz, and stored for offline analysis using Keypoint.Net Software (version 2.31; Natus Medical Incorporated, United States).

Virtual Environment and Avatar

The virtual environment was built in Unity game engine (version 2018.3.0f2; Unity Technologies, United States) and consisted of a virtual living room. A male and a female avatar were designed in MakeHuman (open source software version 1.1.1)[1]. Participants saw the gender-matched avatar from a first-person perspective sitting on a chair in front of a table, i.e., they could see the upper body (arms, shoulder) and parts of the legs of the avatar (**Figures 1C,D**). The right arm of the avatar was animated using

[1]http://www.makehumancommunity.org

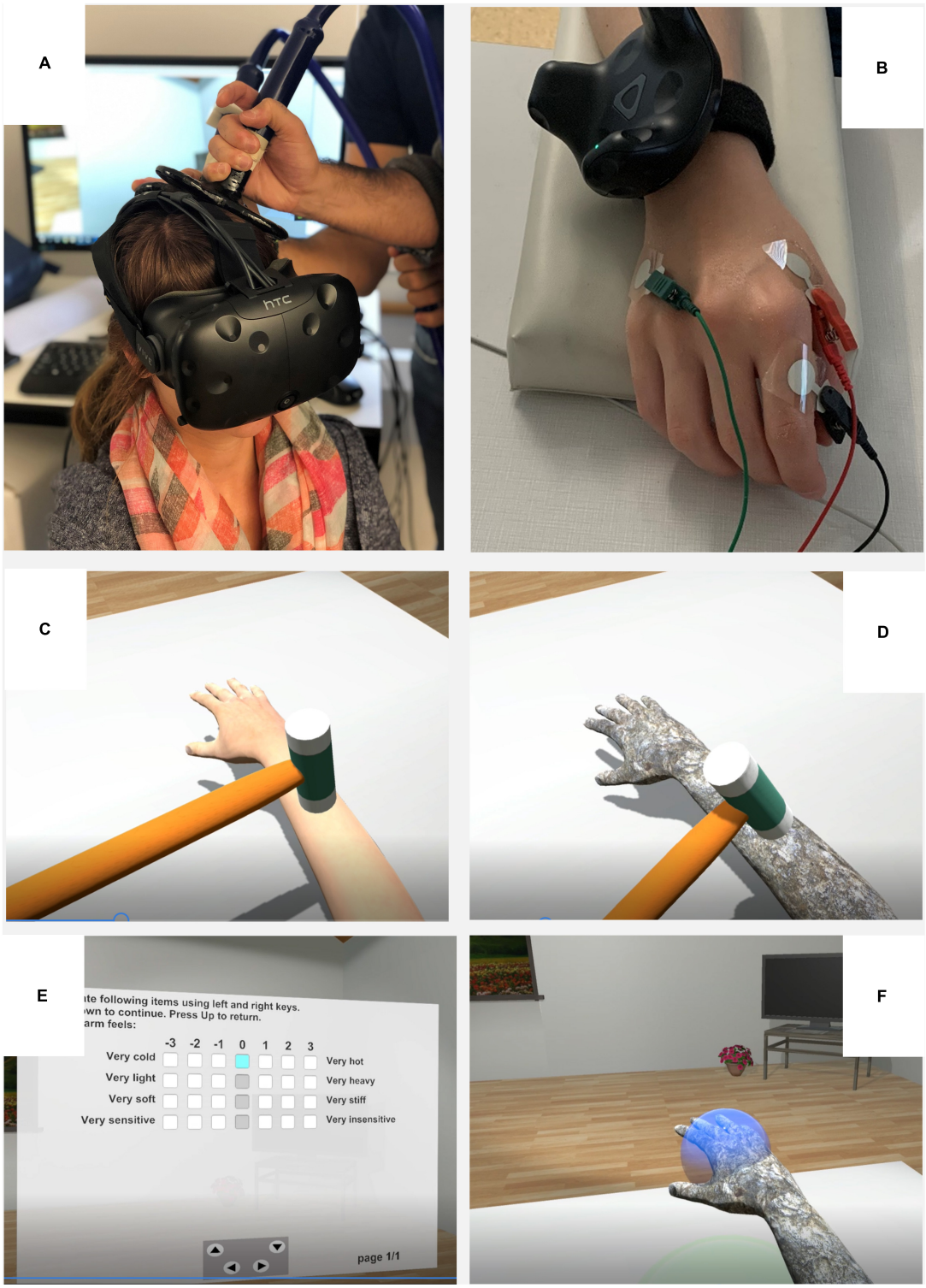

FIGURE 1 | Experimental setup and virtual environment. **(A)** Participant wearing the head-mounted display (HMD) and receiving transcranial magnetic simulation (TMS) over the primary motor cortex. **(B)** Electromyographic recordings in the shape of MEPs elicited by the TMS pulses were obtained from the first dorsal interosseous (FDI) muscle of the right hand of the participant placed on an armrest and with the tracker around wrist and upper arm. **(C)** The first-person perspective point of view of the participant in the VR during the multisensory feedback in the human and **(D)** stone condition. **(E)** The first-person perspective of the participant during the questionnaires, and **(F)** the motor task.

the position of the trackers of HTC Vive placed on the right upper arm and wrist of participants. The left arm of the avatar was rendered to be located under the virtual table (i.e., the left hand of the avatar was neither animated nor visible in VR). A controller operated by the experimenter was employed to animate a virtual hammer.

Experimental Procedure

The whole experiment was completed in a single session with a total duration of approximately 60–70 min. Participants were seated comfortably at a table with their right hand placed on a soft armrest in a predefined position in front of them, matching the hand of the avatar on the virtual table in VR.

The experiment consisted of five phases, i.e., a baseline phase (phase 0) and four experimental phases (phases 1–4; **Figure 2A**). Task instructions were presented outside VR before the start of the experiment. The baseline phase was performed outside VR to assess the motor hotspot for the TMS application on the head of the participant [see section "Motor Hotspot Definition (Phase 0)"]. Then, participants were immersed in VR with their right hand placed on the armrest and the left hand on the response box (to fill in the questionnaires). Before starting the experiment, participants could visually explore the virtual environment. In each experimental phase, participants performed three measurement blocks, i.e., a questionnaire block [see section "Questionnaire Blocks (Phases 1–4)"], an MEP evaluation block [see section "Motor Evoked Potential Evaluation Blocks (Phases 1–4)"], and a motor task block [see section "Motor Task Blocks (Phases 1–4)"], while continuously being immersed in VR. The phases or blocks were manually initiated by the experimenter. Phases 1 and 4 were performed with the avatar animated with human skin while phases 2 and 3 were performed with the avatar animated with a stone surface (**Figure 2B**).

The first experimental phase performed with a human-skinned avatar (i.e., first human avatar condition) started with the questionnaire block (QT1). Then, participants underwent the first MEP evaluation block (MEP1) and finished with a motor task block (MT1). After phase 1, participants received the multisensory feedback for approximately 50 s during which we induced the "stone arm illusion" [see section "Experimental Conditions (Phases 1–4)"]. After the skin transformation was finished, phases 2 and 3 (i.e., first and second stone arm conditions) started with alternating multisensory feedback and measurement blocks. First, participants answered the questionnaires (QT2), followed by the MEP evaluation (MEP2), another questionnaire (QT3), and a motor task block (MT2). Then, participants received another MEP evaluation block (MEP3), followed by a motor task block (MT3). Between each experimental block in phases 2 and 3, participants received multisensory feedback for 15 s, i.e., they felt/saw a hammer touching their real/the arm of the avatar triggering a stone sound from the speaker. The order of phases 2 and 3 was selected to prioritize the TMS evaluation and questionnaire ratings over the motor task, in case the reaching movements would break the illusion. After phases 2 and 3, we transformed the avatar back to a human skin surface by applying the multisensory feedback for around 50 s [see section "Experimental Conditions (Phases 1–4)"]. Finally, the fourth phase started (i.e., second human avatar condition), where participants first received the MEP evaluation (MEP4), then performed the motor task (MT4) and finished by filling in the questionnaires (QT4) for the last time. Finally, participants were taken out of the immersive VR and debriefed about the study aim.

Motor Hotspot Definition (Phase 0)

Before the experimental phases in the VR environment, we determined the location of the "motor hotspot," i.e., the stimulation site on the head of the participant reliably producing high amplitude TMS-induced MEPs recorded from the FDI muscle of the right hand of the participant. Participants were asked to relax the muscles in arm and hand. Complete muscle relaxation was monitored via audiovisual feedback. Then, single-pulse TMS was applied by a blinded experimenter (i.e., naïve to the experimental conditions) over the primary motor cortex. Stimulation intensity started at 10% and was slowly increased in increments of 2–5%. The region over the skull where the stimulation induced reliable MEPs of the first dorsal interosseous muscle activation across 10 consecutive trials was defined as the "motor hotspot." Mean stimulation intensity across all participants was 49% (SD = 6.5; range 40–57%). The coil position of the hotspot was marked directly on the scalp to ensure accurate coil repositioning. Since efficiency (i.e., the stimulus intensity required to bring corticospinal neurons to firing threshold) and type (i.e., direct axonal versus indirect trans-synaptic) of TMS stimulation are highly influenced by the orientation of the neural element within the induced electric field (Bonato et al., 2006; Thut et al., 2011), we co-registered the M1 hotspot location on the participants head with the TMS coil using a neuronavigation system (Localite GmbH, Germany). The whole baseline procedure took around 10–15 min.

Experimental Conditions (Phases 1–4)

The two experimental conditions represent the embodiment of a human arm/hand avatar and a stone avatar, respectively, which we modulated using congruent multisensory feedback. After the experimental phase 1 (resp., after phase 3), we induced a "stone arm illusion" (resp. "human arm illusion") by gradually transforming the surface of the avatar (i.e., the "skin material") from human to stone (resp., from stone to human; **Figure 2B**). We enforced this visual change by gently and repetitively touching at ∼1 Hz the real forearm of the participant with an HTC Vive controller while touching the forearm of the avatar in the VR with a virtual hammer animated using the position and orientation of the controller. We progressively replaced the sound of a hammer against skin displayed from the loudspeaker on the table with the sound of a hammer against stone (resp., vice versa; see "**Supplementary Material**" for an exemplar video). The stone hitting sound was generated by recording the sound of a real hammer hitting a real stone. The human skin hitting sound was generated by recording the sound of a real hammer hitting a real arm. Of note, the tactile feedback (i.e., the touch with the controller on the forearm of the participant) did not

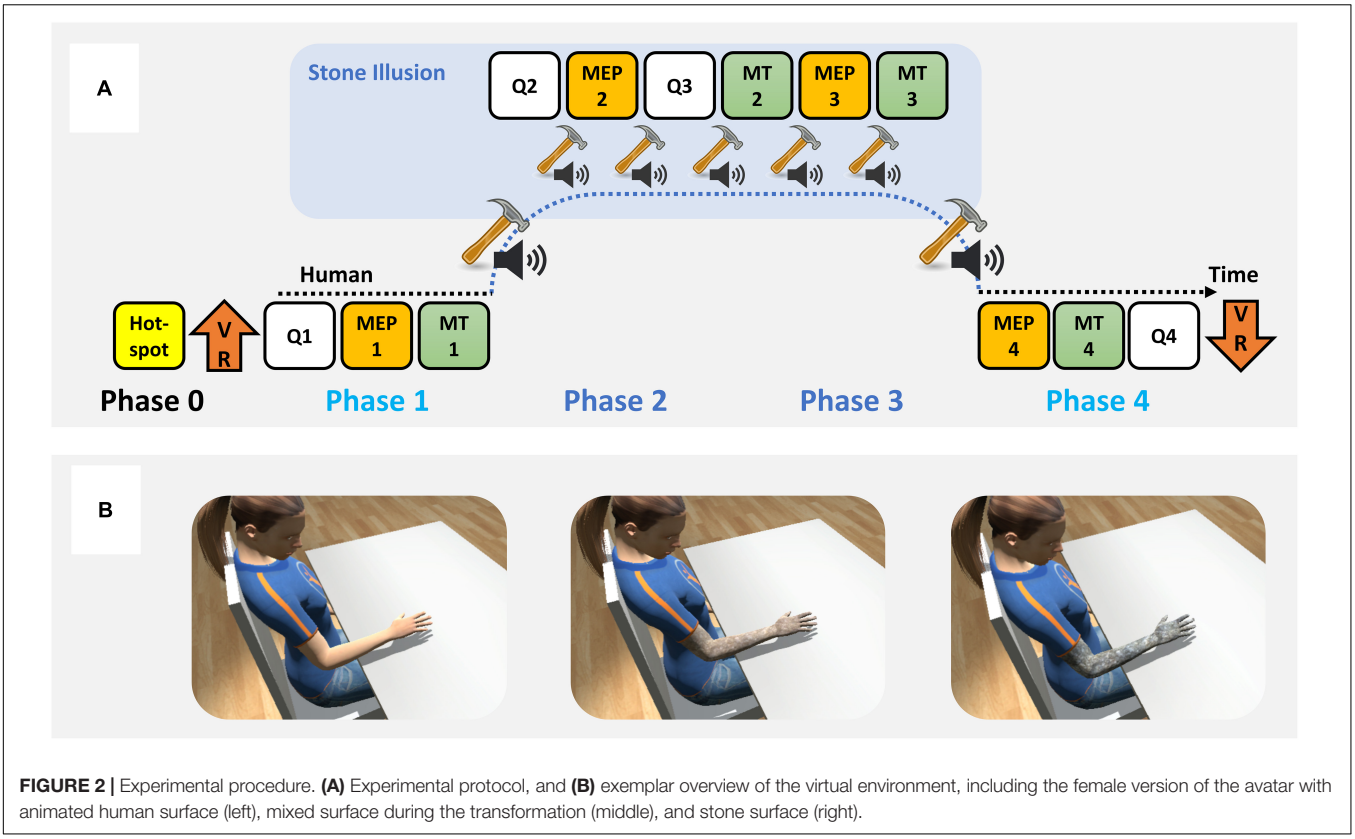

FIGURE 2 | Experimental procedure. **(A)** Experimental protocol, and **(B)** exemplar overview of the virtual environment, including the female version of the avatar with animated human surface (left), mixed surface during the transformation (middle), and stone surface (right).

change across transformation. The transformation lasted for approximately 50 s.

Questionnaire Blocks (Phases 1–4)

Participants filled in two questionnaires to assess the subjectively reported embodiment and the perceptual correlates of the stone arm illusion (i.e., stone feeling). Questionnaires were presented in VR to keep them standardized and to facilitate immersion and answered by the participants with the left hand on the response box (**Figure 1E**).

The stone feeling questionnaire consisted of four items on a 7-point Likert scale, indicating how cold/hot, light/heavy, soft/stiff, and sensitive/insensitive participants rated their right arm (see **Table 1**). The questionnaire was adapted from the study by Senna et al. (2014). The embodiment questionnaire consisted of eight items adapted from established questionnaires (Longo et al., 2008; Bassolino et al., 2018) that were rated on a 7-point Likert scale from −3 (strongly disagree) to 3 (strongly agree). The three main components of embodiment (body ownership, agency, and location) and disownership were assessed. In addition, control items unrelated to the body illusion were included to validate the specificity of potential illusion effects (**Table 2**). Participants took around 1–3 min to fill in the questionnaires.

Motor Evoked Potential Evaluation Blocks (Phases 1–4)

During the MEP evaluation blocks, participants received single-pulse TMS over the left primary motor cortex, i.e., contralateral to the electromyographic leads at the marked optimal site [i.e., motor hotspot, see section "Motor Hotspot Definition (Phase 0)"] for first dorsal interosseous muscle activation of the right hand. The consistent coil orientation across MEP blocks was verified using a neuronavigation system (Localite GmbH, Germany). A total of 20 ± 2 TMS pulses were applied, and the corresponding MEPs recorded in each block with an inter-pulse interval of approx. 3 s. The total duration of an MEP evaluation block was around 2 min.

Motor Task Blocks (Phases 1–4)

Participants were asked to perform a motor task consisting of reaching as fast and accurately as possible with their right arm or hand placed on the armrest located on the table to vertically appearing blue spheres (**Figure 1F**). The resting initial position was indicated with a green sphere in the virtual environment. After reaching to a blue sphere, participants were asked to bring back their hands to the rest position (green sphere) until a next blue sphere appeared. One block consisted of four trials/blue spheres, i.e., two blue spheres placed 32 cm and two blue spheres placed 36 cm above the table (i.e., 20 and 24 cm above the resting position/armrest, respectively). The two different reaching distances were selected to minimize the possibility of potential movement anticipation strategies of participants. All blue spheres were placed above the initial position of the hand resting on the table (i.e., the vertical projection over the green sphere). The order of the spheres was randomized to minimize anticipation. One motor task block lasted for around 1 min.

TABLE 1 | Stone feeling questionnaire.

Item	Dimension	"My right arm feels"							
			−3	−2	−1	0	1	2	3	
I1	Coldness	very cold								very hot
I2	Heaviness	very light								very heavy
I3	Stiffness	very soft								very stiff
I4	Insensitivity	very sensitive								very insensitive

Adapted from Senna et al. (2014).

TABLE 2 | Embodiment questionnaire.

Items	
Body ownership	
Q1	It seemed like the virtual arm was my arm
Q2	It seemed like the virtual arm was part of my body
Location	
Q3	It seemed like my arm was in the location where the virtual arm was
Agency	
Q4	It seemed like I was in control of the virtual arm
Disownership	
Q5	It seemed like the experience on my real arm was less vivid than normal
Q6	It seemed like my real arm had disappeared
Control items	
Q7	It seemed like I had more than two arms
Q8	It seemed as if my real arm was becoming virtual

Q1–4, Q6–8 (Longo et al., 2008); Q5 (Bassolino et al., 2018).

Metrics and Data Processing

Stone Feeling

To quantify the subjectively experienced stone feeling, the mean of the coldness (of note, this item was reversed for the analyses, so that positive values reflect coldness), heaviness, stiffness, and insensitivity item ratings for the human and stone condition were calculated for each participant.

Embodiment

To quantify the subjectively experienced level of embodiment over the avatar, the mean of the body ownership (Q1–Q2), agency (Q4), location (Q3), disownership (Q5–Q6), and control items (Q7–Q8) were calculated for each participant and condition (i.e., human, stone).

Cortical Excitability

Cortical excitability was quantified using the peak-to-peak amplitude from the TMS-induced MEPs (Di Lazzaro and Rothwell, 2014; Schulz et al., 2014; Bestmann and Krakauer, 2015; Rossini et al., 2015; Smith et al., 2019; Ammann et al., 2020). The peak-to-peak MEP amplitude (mV) was calculated as the voltage difference between the maximum positive and maximum negative peak in the electromyographic potential occurring 15–80 ms after TMS pulse onset and averaged across participants and conditions (i.e., human and stone).

Kinematic Variables

Due to the uneven sampling rate in Unity (∼50 Hz), data were linearly interpolated every 15 ms (= 66.67 Hz). We calculated the maximum speed (m/s), the time to the maximum speed (s), the maximum acceleration (m/s^2), and path length (m) of the reaching movements. We selected these kinematic variables based on previously used ones in literature to quantify motor performance (Shishov et al., 2017; Basalp et al., 2021). Since we expected that the real sensory feedback during the motor task may break the stone illusion (i.e., due to visuo-motor or visuo-proprioceptive synchrony), we calculated the kinematic variables for both, the first 150 ms after movement onset (a period in which the cerebellum is assumed to not have received updated sensory feedback; Miall et al. (2007); and therefore, reflecting feedforward kinematics associated with movement initiation) and from movement onset until the visual outer border of the sphere was crossed (defined by a collider in Unity). Further, the time (s) from movement onset until the visual outer boarder of the sphere was reached (defined by a collider in Unity) was computed. Finally, motor overshooting (m) was quantified by calculating the highest point reached by the center of the hand in the upward movement after movement onset minus the height of the center of the blue sphere. Movement onset was defined as the time point when 2% of the maximum velocity after the presentation of the sphere was reached. Each kinematic variable was averaged per participant and condition (i.e., human, stone).

Data Analysis

The data of both human arm (phases 1 and 4) and stone arm (phases 2 and 3) conditions were averaged for each participant to account for the time factor, which may be associated with intra-subject habituation or fatigue effects across experimental phases.

To investigate whether the stone feeling and the embodiment questionnaires, MEP amplitudes, and the kinematic variables differentiated between the human and stone condition, parametric (paired t-tests) and non-parametric (Wilcoxon Signed-Rank tests) pairwise comparisons were performed when applicable.

Further, Pearson product-moment or Spearman's rank correlation analyses (depending on the statistical distribution of the datasets) were conducted to study the relationship between (1) stone feeling items and MEP amplitudes, (2) stone feeling items and kinematic variables, (3) stone feeling items and embodiment components, and (4) kinematic variables and MEP

TABLE 3 | Descriptive statistics and results of the pairwise comparisons.

Variables	Human condition	Stone condition	t/z	*p* value
Stone illusion				
Coldness	0.0 (1.08)	0.75 (1.12)	2.5 (t)	0.02*
Heaviness	0 (−1 to 0)	1 (0–1)	2.10 (z)	0.036*
Stiffness	−0.1 (1.12)	0.75 (1.37)	2.99 (t)	0.016*
Insensitivity	0 (−0.25 to 0)	0 (0–1)	−2.44 (z)	0.02*
Embodiment				
Body ownership	4.78 (1.16)	4.35 (1.42)	−1.56 (t)	0.22
Agency	6 (5–6.25)	5.5 (5–7)	−1.26 (z)	0.26
Location	5.9 (0.94)	5.4 (1.53)	−1.81 (t)	0.22
Disembodiment	3.48 (1.78)	3.85 (1.16)	1.58 (t)	0.22
Control	3.38 (0.72)	3.2 (0.8)	−0.82 (t)	0.42
Cortical excitability				
MEP Amplitude (*mV*)	0.95 (0.81–1.82)	1.03 (0.83–1.87)	−0.04 (z)	0.49
Feedforward kinematics (movement initiation)				
Max speed (*m/s*)	1.14 (0.44)	1.3 (0.44)	−1.53 (t)	0.14
Time to max speed (*s*)	0.12 (0.11–0.14)	0.14 (0.13–0.14)	−2.28 (z)	0.048*
Max acceleration (m/s^2)	12.93 (6.83)	14.31 (7.11)	−1.18 (t)	0.16
Path length (*m*)	0.1 (0.04)	0.11 (0.04)	−0.76 (t)	0.23
Movement until sphere				
Max speed (*m/s*)	1.11 (0.98–1.78)	1.17 (1–1.97)	−2.82 (z)	0.09
Time to max speed (*s*)	0.15 (0.14–0.19)	0.15 (0.14–0.17)	−0.20 (z)	0.84
Max acceleration (m/s^2)	11.25 (8.2–20.34)	11.55 (8.55–21.38)	−1.01 (z)	0.62
Path length (*m*)	0.19 (0.05)	0.2 (0.07)	−0.46 (t)	0.84
Motor overshooting				
Height above sphere (*m*)	0.05 (0.01)	0.05 (0.02)	0.40 (t)	0.48

Mean (standard deviation) or median (25% quantile–75% quantile) range are reported.
**Indicates significance at the 0.05 level.*

amplitudes. Correlation analyses were performed separately for the human and stone condition.

Assumptions for parametric testing were checked using normality tests (Kolmogorov–Smirnov, $p > 0.05$). Outlier trials (more than ± 2.5 SDs from the mean of the participant) were excluded from the analyses. All *p* values were corrected for multiple hypothesis testing using Tukey–Kramer and Bonferroni–Holm, respectively (between conditions comparisons) and the Benjamini-Hochberg false discovery rate (correlation analyses). Statistical analyses were performed with *R* v. 4.1.1 and the significance threshold was set at $\alpha < 0.05$. If not otherwise stated, two-sided hypothesis testing was applied (and we indicate one-sided testing in the case there was a clear directed *a priori* hypothesis).

RESULTS

A summary of the results with the statistics is represented in **Table 3**.

Between Conditions Differences

Stone Illusion

Pairwise comparisons showed significant (one-sided) stone illusion effects. Subjects rated their right arm to be colder, heavier, stiffer, and more insensitive in the stone versus human condition (**Figure 3A**).

Embodiment

Pairwise comparisons did not show significant differences in the subjectively reported embodiment components (i.e., body ownership, agency, and location), disembodiment, and control items between the human and stone condition (**Figure 3B**).

Cortical Excitability

The pairwise comparison did not reveal a significant (one-sided) modulation of the MEP amplitude between the human and stone condition (**Figure 3C**).

Kinematic Variables

We found a significant (one-sided) effect of the illusion on the time until the maximum speed in the feedforward kinematics, which was higher in the stone than in the human condition (**Figure 3D**). None of the other kinematic variables showed significant differences between the human versus stone avatar condition in the pairwise comparisons.

Correlation Analyses

Stone Feeling and Motor Evoked Potentials

Correlation analyses revealed a significant relationship between the subjectively reported stone feeling with the MEP amplitude

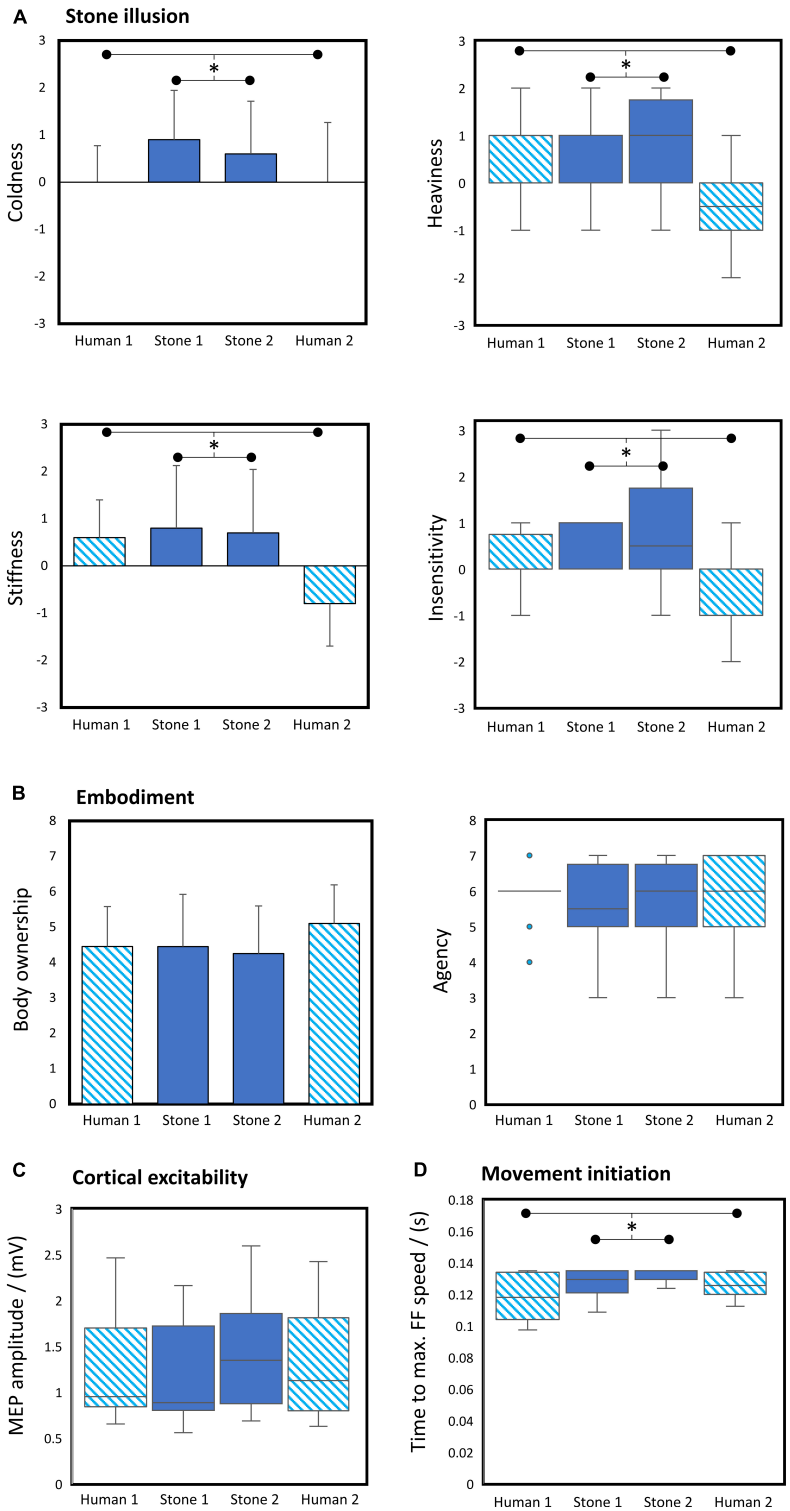

FIGURE 3 | Between conditions differences. **(A)** Rated stone feeling, **(B)** subjectively experienced embodiment, **(C)** cortical excitability assessed via motor evoked potential (MEP) amplitudes, and **(D)** time to the maximum speed in the feedforward kinematics reflecting movement initiation across phases. H1, first human condition; S1, first stone condition; S2, second stone condition; H2, second human condition. Bar plots: Error bars represent standard deviation. Boxplots: Whiskers show the data ranging 1.5 times inter-quartile range above the upper or below lower quartiles, boxed horizontal solid lines show the median and box vertical boundaries show the inter-quartile range. *$p < 0.05$ for pairwise comparisons between human (mean H1 + H2) and stone (mean S1 + S2) condition.

in the stone but not the human condition (**Figure 4A**). The stronger the rated coldness [$r_s(18) = 0.44$, p (one-sided) = 0.03] and stiffness [$r_s(18) = 0.53$, p (one-sided) = 0.02], the higher was the cortical excitability. We further found a trend for an association between the rated heaviness with the MEP amplitude [$r_s(18) = 0.40$, p (one-sided) = 0.08]. The MEP amplitudes were not associated with the insensitivity item of the stone feeling [$r_s(18) = 0.08$, p (one-sided) = 0.5].

Stone Feeling and Embodiment

A significant negative correlation between the stone feeling and agency (but not body ownership) was observed in the human and stone conditions. In the stone condition, coldness ratings were associated with reduced agency [$r_s(18) = -0.56$, $p = 0.02$]. In the human condition, insensitivity was associated with reduced agency [$r_s(18) = -0.55$, $p = 0.02$], while there was a trend for the heaviness [$r_s(18) = -0.41$, $p = 0.08$].

Stone Feeling and Kinematic Variables

We also found significant positive correlations between the stone feeling items with kinematic variables in the stone but not human condition. The higher the rated coldness [$r_p(18) = 0.57$, p (one-sided) = 0.02] and stiffness [$r_p(18) = 0.44$, p (one-sided) = 0.03] of the arm of the subject, the longer were the performed paths within the 150 ms after movement onset in the stone condition (**Figure 4B**). Further, the coldness item was associated with longer paths in the movements until the sphere in the stone condition [$r_p(18) = 0.55$, $p = 0.04$; **Figure 4C**].

Kinematic Variables and Motor Evoked Potentials

Finally, we found a significant correlation between the feedforward kinematics (i.e., within the 150 ms after movement onset) and MEP amplitudes in the stone but not the human condition. The higher the cortical excitability, the longer were the performed paths [$r_s(18) = 0.72$, $p = 0.03$; **Figure 4D**]. For the movements until the sphere, we found significant associations between the kinematics and the MEP amplitude for the stone condition. More precisely, higher cortical excitability was associated with longer paths [$r_s(18) = 0.51$, $p = 0.03$] and higher maximum acceleration [$r_s(18) = 0.48$, $p = 0.03$]. Further, we found a trend for an association between the motor overshooting and the MEP amplitudes in the stone condition [$r_s(18) = 0.43$, $p = 0.06$].

No further correlation analyses reached significance. A summary of the correlation analyses is represented in **Table 4**.

DISCUSSION

We "tricked the brain" using immersive VR to investigate if multisensory feedback modulating the physical properties of an embodied avatar influences motor brain networks and control. Ten healthy participants were immersed in a virtual environment using an HMD, where they saw an avatar from first-person perspective. We slowly transformed the visual appearance of the human-skinned avatar to an avatar with a stone surface. To enforce the "stone arm illusion," we simultaneously applied auditory and tactile feedback during the visual transformation, i.e., participants saw and felt a (virtual) hammer touching their real arm or the arm of the avatar, triggering a progressively changing human to stone hitting sound from a loudspeaker. Participants filled in questionnaires to report their level of embodiment and experienced stone feeling, had single-pulse TMS applied over the primary motor cortex, and performed an arm reaching task to study how the "stone arm illusion" affected motor cortical excitability and action execution.

The Strength of Subjectively Experienced "Stone Arm Illusion" Is Associated With Enhanced Motor Cortical Excitability

In line with our expectation, our participants indeed experienced the "stone arm illusion." They rated their arm as colder, heavier, stiffer, and more insensitive when we enforced illusionary ownership over a stone versus human avatar using multisensory feedback in immersive VR. The adaptation of the participants to the stone illusion is further visible in the aftereffects found after the transformation back to the human avatar. Participants rated their own arm as less heavy, stiff, and insensitive after the illusion compared with the baseline (i.e., first human block). The stone illusion is a result of both the relatively enhanced stone feeling during the immersion with the stone compared with the human avatar and the relatively lowered stone ratings below baseline after the transformation back to the human avatar. Importantly, the stone illusion did not impact the experienced level of embodiment. Participants reported high body ownership and agency over the avatar, independently of the condition. Our results are in line with a vast amount of research that used multisensory feedback with (Slater, 2008; Perez-Marcos et al., 2009; Kilteni et al., 2012b, 2016; Pyasik et al., 2020; Tambone et al., 2021) and without immersive VR (Botvinick and Cohen, 1998; Ehrsson, 2004; Petkova and Ehrsson, 2008; van der Hoort et al., 2011; Burin et al., 2017) to induce various body illusions. These findings established the view that body perceptions are continuously updated in the brain in response to sensory signals related to the body (Blanke, 2012; Tsakiris, 2017). A certain flexibility of the brain regarding body perception is indeed crucial to maintain a stable body image despite that body characteristics constantly change in response to external influences such as light, temperature, and posture.

We further showed that the strength of the reported stone feeling was associated with enhanced cortical excitability, i.e., with an increased amplitude of the TMS-induced motor evoked potentials in the stone but not human avatar condition. More precisely, the subjectively rated coldness and stiffness of the own arms of the participants in the stone condition were associated with enhanced motor excitability, while we found a tendency for the rated heaviness to be associated with the MEP amplitudes. This finding may indicate that participants physically mirrored the embodied body characteristics of the stone avatar. Participants may have enhanced the muscle tension or activity in their own arm, (unconsciously) mimicking the stiffness of the stone avatar with increasing illusion strength. Cortical excitability is generally thought to reflect the responsiveness of the brain to

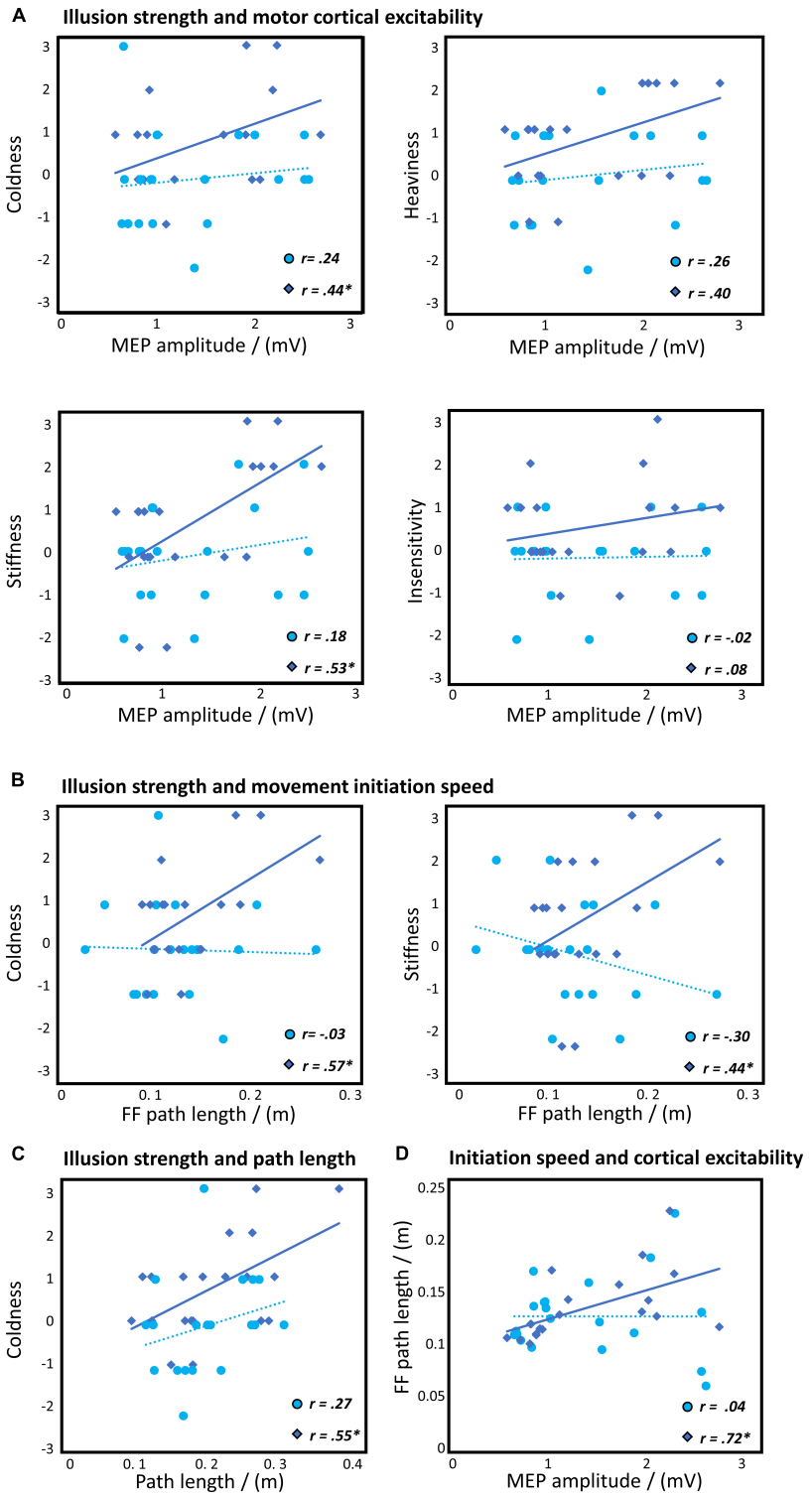

FIGURE 4 | Results of the correlation analyses for the human (in lighter blue/circles) and stone (in darker blue/diamonds) condition. **(A)** Stone illusion strength and MEP amplitude reflecting cortical excitability. **(B)** Stone illusion strength and feedforward (FF) path length reflecting the average speed in the movement initiation. **(C)** Stone illusion strength and path length for the movement until the sphere. **(D)** Average speed in the feedforward kinematics and cortical excitability. Of note, due to few very similar values across human and stone conditions, the number of individually visible plots (i.e., circles and diamonds) may be lower than the number of measurement points (i.e., 20). *$p < 0.05$.

TABLE 4 | Significant correlations ($p < 0.05$) between measures for human (H) and stone (S) condition.

Variables		Cortical excitability	Stone feeling			
		MEP amplitude (*mV*)	**Coldness**	**Heaviness**	**Stiffness**	**Insensitivity**
Cortical excitability	MEP amplitude (*mV*)	–	S+		S+	
Embodiment	Body ownership	–				
	Agency	–	S–			H–
Feedforward kinematics (movement initiation)	Max. speed (*m/s*)					
	Time to max. speed (*s*)					
	Max. acceleration (m/s^2)					
	Path length (*m*)	S+	S+		S+	
Movement until sphere	Max. speed (*m/s*)					
	Time to max. speed (*s*)					
	Max. acceleration (m/s^2)	S+				
	Path length (*m*)	S+	S+			
Overshooting	Height above sphere (*m*)					

The plus and minus signs indicate if the correlation is positive or negative.

exogenous and/or endogenous signals (Rosanova et al., 2011). In the case of the primary motor cortex, excitability is linked with a decreased motor threshold and modulated, for example, during action preparation and/or execution (Starr et al., 1988; Bestmann, 2012; Bestmann and Krakauer, 2015). In line with our conclusion, previous studies have shown that muscle contractions enhance primary motor cortical excitability (Arányi et al., 1998; Yahagi et al., 2003; Perez and Cohen, 2008; Perez et al., 2012). However, since our experimental setup was already crowded, we did not add electromyographic recordings during the experiment to objectivate our conclusion on the enhanced muscle tone. Alternatively, the embodied "stone feeling" may have increased the perceived difficulty to control the arm, as task difficulty has previously also been shown to enhance motor cortical excitability (Pearce and Kidgell, 2009; Watanabe et al., 2018).

Importantly, the subjectively experienced illusion strength was only correlated with the MEP amplitude in the stone but not the human avatar condition. The stone avatar condition was further temporally embedded between the human avatar condition, minimizing the possibility that the neurophysiological effects were impacted by confounding factors related to the duration of the experiment, such as room temperature or fatigue (which could be equally expected for the human and stone condition). Since the average cortical excitability did not differentiate between human and stone condition (i.e., in the between conditions analyses), our findings suggests that the MEP amplitudes are crucially modulated during the presence of the stone illusion depending on the subjectively experienced illusion strength.

In line with this conclusion, we found a negative association between subjectively reported stone feeling, namely, the rated coldness, with reported agency, indicating that participants were feeling less in control over their arm, the stronger they experienced the stone illusion. Importantly, the "stone feeling" did not affect the experienced level of body ownership over the avatar. The correlation between the reported stone feeling with the reported embodiment was only present for agency, but not for body ownership and location – the two other embodiment components (Kilteni et al., 2012a). Therefore, the strength of the stone illusion impacted how well participants think they can control their arm, but they kept experiencing the virtual stone arm as their own arm. However, analyses showed a similar pattern for the human avatar condition. Agency (but not body ownership) was also negatively associated with the reported stone feeling in the human avatar condition. Therefore, carry-over effects may have influenced the results, i.e., stone feeling may have persisted in the human condition, hampering the feeling of agency when immersed with the human avatar. Alternatively, other inter-subject variables, such as fatigue or body temperature, which could have also been captured with the questionnaire, may contribute to the reduced reported agency.

To the best of our knowledge, we are the first to show modulated motor brain processing associated with altered body perceptions using immersive VR. Our findings on neurophysiological effects extend previous studies reporting, for example, affective (Tajadura-Jiménez et al., 2015a), (social) cognitive (D'Angelo et al., 2019; Burin and Kawashima, 2021; Clausen et al., 2021; Tambone et al., 2021), and motor (Kilteni et al., 2013; Tajadura-Jiménez et al., 2015a, 2016) effects of body illusions.

Interestingly, the found enhancement in excitability associated with the strength of the illusionary self-perception suggests a more "complete" body illusion using immersive VR compared with classical paradigms, notably, the rubber hand illusion. Non-invasive brain stimulation studies showed that the activity in motor (della Gatta et al., 2016; Fossataro et al., 2018) and somatosensory (Zeller et al., 2015; Hornburger et al., 2019; Isayama et al., 2019) brain areas was attenuated during the experience of illusionary ownership over a rubber hand (i.e., during the synchronous but not asynchronous multisensory stimulation). These findings have previously been discussed as an indication for the disembodiment of the real hand necessary to embody a rubber hand (for a review see Golaszewski et al., 2021). The use of immersive VR with highly congruent visuo-motor

and proprioceptive feedback –compared with the rubber hand illusion, no proprioceptive mismatch is present– may allow to induce highly realistic illusions, without the necessity for the user/brain to disembody the own limbs. As a consequence, the highly realistic visuo-proprioceptive synchrony experienced in immersive VR illusions may influence brain networks similarly as could be expected from modifying real body characteristics (Tajadura-Jiménez et al., 2016).

Together, immersive VR may be an especially powerful tool to realistically modify the perception of the bodily self and influence associated brain networks. Our results show that participants embodied the stone avatar in immersive VR and that the reported illusion strength was associated with the motor cortical excitability, indicative of a physical mirroring of the embodied body characteristics of the stone arm.

The "Stone Arm Illusion" Influences Movement Initiation in a Reaching Task

We further predicted that the modulated body perception associated with the stone arm illusion using immersive VR would impact motor actions, as body characteristics such as shape and weight critically influence interactions with the environment (Head and Holmes, 1911; Maravita and Iriki, 2004). Our participants performed a simple goal-oriented motor task visualized in the virtual environment, i.e., they had to reach as fast and accurately as possible with their hand from a resting position to vertically appearing spheres. Since we expected that the reaching movement may break the illusion, in addition to the whole movement until the sphere, we analyzed feedforward kinematics within 150 ms after movement onset, in which the cerebellum would not have received updated sensory (e.g., proprioceptive) feedback (Miall et al., 2007).

We found that participants in the stone condition were marginally slower in reaching the maximum speed within the first 150 ms of the movement than when they were in the human condition. Since the maximum speed/path length in the feedforward movement did not differ across conditions, this result indicates an, on average, slightly slower movement initiation when the motor task was performed with the stone versus human avatar. This finding is contrary to what we expected. We predicted that, if the stone illusion worked, participants would overestimate the weight of their real arm, as reflected in enhanced acceleration patterns and motor overshooting, similar to lifting an empty bottle of water that is expected to be full.

However, our correlation analyses suggest that the movement initiation may critically depend on the subjectively experienced illusion strength. The reported stone feeling, namely, the experienced coldness and stiffness, was associated with longer paths within the first 150 ms after movement onset, indicating on average faster movements (average speed defined as the path length over the 150 ms time window). Therefore, participants with stronger illusion effects may have not only stronger physically mirrored (see section "The Strength of Subjectively Experienced 'Stone Arm Illusion' Is Associated With Enhanced Motor Cortical Excitability") but also compensated for the embodied body characteristics of the stone avatar. Stronger experienced illusions might have led participants to put more physical engagement into the task to compensate for the additional (illusionary) weight of the stone arm, resulting in faster feedforward movements or initiations than participants with weaker experienced illusions. In contrast, weak illusion effects during the stone avatar condition could have hampered movement initiation. Participants with relatively weak illusion effects likely experienced an enhanced sensory mismatch in the stone condition than participants with stronger illusion effects. Incongruency of information in virtual environments has previously shown to hamper reaction times and motor performance, independently of the experienced body ownership over the avatar (Odermatt et al., 2021). The facilitated versus hampered feedforward movement depending on the illusion strength could explain why, across the whole group, marginal overall slowed movement initiations were found in the stone versus human avatar condition. Apart from this marginal effect on the movement initiation, the kinematic variables were not influenced by the human versus stone conditions when considering the whole group, suggesting that the physical compensation reflected in the movement initiation may be critically modulated by the subjectively experienced illusion strength.

Our conclusion on a physical compensation of the embodied stone characteristics in the motor task may be further supported by the association between the cortical excitability with faster movement initiation in the stone, but not human condition. The higher the cortical excitability associated with the subjectively reported stiffness and coldness, the faster were the reaching movements 150 ms after movement onset on average (namely, reflected in longer performed paths). It is possible that the previously discussed potential physical mirroring and/or compensation of the embodied body characteristics of the stone avatar "chronically" activated and increased the cortical excitability in motor brain areas, boosting movement initiation. Previous research has shown that the motor cortical excitability is correlated with the force (Baud-Bovy et al., 2008; Perez and Cohen, 2009; Barthélemy et al., 2012) and speed of performed movements (Uehara et al., 2011). However, it needs to be pointed out that the assessment of the cortical excitability was temporally separated from the motor task. Even though literature points toward short-term influences of motor actions on cortical excitability within the range of milliseconds to seconds (Chen et al., 1998; Chen and Hallett, 1999), the exact time course of corticospinal excitability is yet poorly understood.

Our results suggest stronger illusion effects on feedforward kinematics than on the "whole" movement, contrasting previous studies reporting relatively long-lasting motor effects. However, in these studies, the motor task was part of the multisensory feedback to induce the illusion. Tajadura-Jiménez et al. (2012, 2015b, 2016), for example, instructed blindfolded participants to tap with their hand on a surface, eliciting sound implying a longer arm (e.g., the provision of lighter sound to simulate increased distance). The authors showed that the illusion of having a longer arm slowed and prolonged the real arm movements of participants. The same authors also found alternated gait patterns when participants had the illusion of owning a lighter versus heavier body modulated with different sounds provided

with each footstep (Tajadura-Jiménez et al., 2015a). In both studies, the movements were directly coupled with the real-time auditory feedback modulating the body characteristics. Kilteni et al. (2013), in one of the few studies that used immersive VR to create illusions, showed that participants who embodied dark-skinned avatars exhibited more variable and faster drumming movements compared with embodied light-skinned avatars. Even though, here, no additional sensory enforcement was induced during the motor task, participants were continuously performing the movements. Conversely, in our experiment, the reaching movements were performed between resting periods without the audio-tactile feedback used to enforce the stone arm illusion. Therefore, the (sudden) proprioceptive feedback linked with the movement in the motor task may have more likely disrupted or lowered the illusion effects compared with the setups used in previous studies.

Together, we replicate and extend previous findings with our "stone arm illusion." We show that a modulated self-perception using multisensory feedback in immersive VR impacts motor control, and may crucially depend on the subjectively experienced illusion strength. Participants with higher reported illusion strength performed, on average, faster reaching movements, indicating that they may have physically compensated for the embodied body characteristics of the stone avatar. In contrast, the incongruent multisensory information associated with weaker experienced illusion effects may have hampered movement initiation.

Clinical Implications

Our finding that motor brain activity can be influenced based on a perceived modified reality may have important applications for neurorehabilitation. The use of immersive virtual training environments may help to subtly "trick the brain" and change the self-perception of neurologic patients, enhancing the engagement of motor brain networks during motor training. Besides, future studies may investigate to what extent motor brain networks can be activated via the mere immersion into VR environments, without actual motor execution, especially in neurologic patients.

Further, the embodiment of avatars with different body characteristics may offer a playful possibility to implicitly increase the (physical) engagement during training, optimizing motor recovery. However, our results show that the effects of body illusions highly depend on the subjectively experienced illusion strength, and do not necessarily follow from the experimental manipulation of multisensory information. Our findings may be of special relevance for clinical settings considering previous work suggesting that the strength of body illusions in neurologic patients depends on their motor impairment. Using the rubber hand illusion paradigm, Burin et al. (2015) showed that hemiplegic patients reported stronger illusion effects for their impaired hand and weaker effects for the unimpaired hand than healthy controls. The chronic absence of movements may enhance the flexibility of the brain with regard to body ownership for the paralyzed limb, while the healthy limb may be more strictly embodied (Burin et al., 2015). Future studies are needed to investigate how to enforce and optimize body illusions and their behavioral and neural benefits in patients.

Study Limitations

Similar to previous studies, we did not find consistent illusion effects across different kinematic parameters (Tajadura-Jiménez et al., 2016). As previously highlighted by Tajadura-Jiménez et al. (2016), the small sample size limits the findings and conclusions of the present study. A further reason for the lack of stronger effects found in the kinematic variables may be the experimental setup. The soft armrest on which participants placed their arm during the experiment was slightly sticky and, therefore, noticeable for the participants during the motor task. This may have reduced the immersion in VR, enhancing the attention on the sensory feedback associated with the movement and mitigating illusion effects. In addition, the motor task consisted of only four trials per block (i.e., eight trials per condition) to lower the risk of the performed movements to break the illusion, therefore, conclusions drawn from the movement performance should be treated with caution.

Further, the questionnaire used to assess the stone feeling may have assessed confounds such as inter-subject variability in physical or mental fatigue, motivation, or perceived body temperature. This could also explain why not all stone feeling items showed consistent effects with the experimental manipulation. Future studies may implement additional questionnaires or sensors (e.g., temperature, skin conductance) to objectivate or control for inter-subject confounds.

Moreover, even though we aimed at balancing our two conditions as much as possible to control for intra-subject confounds, for example, related to the duration of the experiment, some differences remained. Participants experienced more audio-tactile feedback during the stone than human condition, to enforce the stone arm illusion between the measurement blocks. The tactile feedback may have increased the awareness of the own arm, in turn, influencing motor brain networks. For example, attention has shown to modulate motor cortical excitability (Conte et al., 2007). Further, the third block was the only block where the MEP evaluation was performed directly after the motor task, and carry-over effects could have impacted our cortical excitability results. However, analysis excluding the third block did not significantly change our findings. This is consistent with findings showing short-lasting effects of movements on cortical excitability (Chen et al., 1998; Chen and Hallett, 1999). In addition, learning effects may confound our results despite our balanced design. Indeed, learning effects were present in most kinematic performance variables. For example, participants showed more accurate (as reflected in shorter path lengths in the movements until the sphere) and faster reaching movements at the end compared with the beginning of the experiment. However, learning may have not occurred linearly across blocks, and therefore, differently affected the performance in the human condition (consisting of the first and last experimental blocks) and the stone condition (consisting of the two embedded experimental blocks). Averaging the blocks of each condition might have, therefore, not fully accounted for learning effects.

Finally, correlation analyses do not reveal the directionality of an association. For example, it is possible that participants with

enhanced cortical excitability were more "prone" to experience body illusions and/or to perform faster movements. Similarly, better performance in VR may have enforced the embodiment of the stone avatar (Grechuta et al., 2017, 2019). Future studies are needed to disentangle the directionality and causality of the relationship between VR illusions effects and behavior or neural correlates.

CONCLUSION

The goal of this study was to "trick the brain" using immersive VR and to investigate how modulated physical properties of an embodied avatar influence motor brain networks and action execution. Our results show that participants indeed experienced the "stone arm illusion." The reported illusion strength was associated with enhanced motor cortical excitability and faster movements, indicating that participants may have physically mirrored and compensated for the embodied body characteristics of the stone avatar. Together, alternating the perception of the own body and associated motor brain networks in a subtle way using immersive VR may have important applications for neurorehabilitation and boost the motor recovery of neurologic patients.

DATA AVAILABILITY STATEMENT

The dataset presented in this study can be found online in the following repository: doi: 10.5281/zenodo.5522866.

ETHICS STATEMENT

The studies involving human participants were reviewed and approved by the Ethics Committee of the Canton of Bern (KEK). The patients/participants provided their written informed consent to participate in this study.

AUTHOR CONTRIBUTIONS

KB, JP-A, and LM-C designed the study. JP-A set up the experiment. KB, JP-A, and DC tested all subjects. KB and JP-A analyzed the data. ÖÖ contributed to the analysis of kinematic data. KB and LM-C wrote the manuscript. All authors edited and revised the manuscript and approved the submitted version.

FUNDING

This work was supported by the Swiss National Science Foundation through the grant PP00P2 163800, Swiss National Center of Competence in Research (NCCR Robotics), and UniBE ID Grant.

ACKNOWLEDGMENTS

We would like to thank all members of the Motor Learning and Neurorehabilitation Laboratory and the Eyelab for their kind support during this project. A special thanks goes to our participants.

SUPPLEMENTARY MATERIAL

The Supplementary Material for this article can be found online at: https://www.frontiersin.org/articles/10.3389/fnhum.2021.787487/full#supplementary-material

REFERENCES

Adamovich, S. V., Merians, A. S., Boian, R., Tremaine, M., Burdea, G. S., Recce, M., et al. (2004). A virtual reality based exercise system for hand rehabilitation post-stroke: transfer to function. *Conf. Proc. IEEE Eng. Med. Biol. Soc.* 7, 4936–4939. doi: 10.1109/IEMBS.2004.1404364

Ammann, C., Guida, P., Caballero-Insaurriaga, J., Pineda-Pardo, J. A., Oliviero, A., and Foffani, G. (2020). A framework to assess the impact of number of trials on the amplitude of motor evoked potentials. *Sci. Rep.* 10:21422. doi: 10.1038/s41598-020-77383-6

Arányi, Z., Mathis, J., Hess, C. W., and Rösler, K. M. (1998). Task-dependent facilitation of motor evoked potentials during dynamic and steady muscle contractions. *Muscle Nerve* 21, 1309–1316.

Barker, A. T., Jalinous, R., and Freeston, I. L. (1985). Non-invasive magnetic stimulation of human motor cortex. *Lancet* 325, 1106–1107. doi: 10.1016/S0140-6736(85)92413-4

Barthélemy, D., Alain, S., Grey, M. J., Nielsen, J. B., and Bouyer, L. J. (2012). Rapid changes in corticospinal excitability during force field adaptation of human walking. *Exper. Brain Res.* 217, 99–115. doi: 10.1007/s00221-011-2977-4

Basalp, E., Wolf, P., and Marchal-Crespo, L. (2021). Haptic training: which types facilitate (re)learning of which motor task and for whom answers by a review. *IEEE Trans. Haptics* 14, 722–739. doi: 10.1109/TOH.2021.3104518

Bassolino, M., Franza, M., Bello Ruiz, J., Pinardi, M., Schmidlin, T., Stephan, M. A., et al. (2018). Non-invasive brain stimulation of motor cortex induces embodiment when integrated with virtual reality feedback. *Eur. J. Neurosci.* 47, 790–799. doi: 10.1111/ejn.13871

Baud-Bovy, G., Prattichizzo, D., and Rossi, S. (2008). Contact forces evoked by transcranial magnetic stimulation of the motor cortex in a multi-finger grasp. *Brain Res. Bull.* 75, 723–736. doi: 10.1016/j.brainresbull.2008.01.005

Bestmann, S. (2012). "Functional modulation of primary motor cortex during action selection," in *Cortical Connectivity*, eds R. Chen and J. C. Rothwell (Berlin: Springer), 183–205. doi: 10.1007/978-3-662-45797-9_10

Bestmann, S., and Krakauer, J. W. (2015). The uses and interpretations of the motor-evoked potential for understanding behaviour. *Exper. Brain Res.* 233, 679–689. doi: 10.1007/s00221-014-4183-7

Bezerra, ÍM. P., Crocetta, T. B., Massetti, T., Silva, T. D., da Guarnieri, R., de Meira, C. M., et al. (2018). Functional performance comparison between real and virtual tasks in older adults: a cross-sectional study. *Medicine* 97:e9612. doi: 10.1097/MD.0000000000009612

Blanke, O. (2012). Multisensory brain mechanisms of bodily self-consciousness. *Nat. Rev. Neurosci.* 13, 556–571. doi: 10.1038/nrn3292

Blanke, O., Slater, M., and Serino, A. (2015). Behavioral, neural, and computational principles of bodily self-consciousness. *Neuron* 88, 145–166. doi: 10.1016/j.neuron.2015.09.029

Bonato, C., Miniussi, C., and Rossini, P. M. (2006). Transcranial magnetic stimulation and cortical evoked potentials: a TMS/EEG co-registration study. *Clin. Neurophysiol.* 117, 1699–1707. doi: 10.1016/j.clinph.2006.05.006

Botvinick, M., and Cohen, J. (1998). Rubber hands 'feel' touch that eyes see. *Nature* 391, 756–756. doi: 10.1038/35784

Braun, N., Debener, S., Spychala, N., Bongartz, E., Sörös, P., Müller, H. H. O., et al. (2018). The senses of agency and ownership: a review. *Front. Psychol.* 9:535. doi: 10.3389/fpsyg.2018.00535

Burin, D., and Kawashima, R. (2021). Repeated exposure to illusory sense of body ownership and agency over a moving virtual body improves executive functioning and increases prefrontal cortex activity in the elderly. *Front. Hum. Neurosci.* 15:674326. doi: 10.3389/fnhum.2021.674326

Burin, D., Livelli, A., Garbarini, F., Fossataro, C., Folegatti, A., Gindri, P., et al. (2015). Are movements necessary for the sense of body ownership? evidence from the rubber hand illusion in pure Hemiplegic patients. *PLoS One* 10:e0117155. doi: 10.1371/journal.pone.0117155

Burin, D., Pyasik, M., Salatino, A., and Pia, L. (2017). That's my hand! therefore, that's my willed action: how body ownership acts upon conscious awareness of willed actions. *Cognition* 166, 164–173. doi: 10.1016/j.cognition.2017.05.035

Carey, M., Crucianelli, L., Preston, C., and Fotopoulou, A. (2019). The effect of visual capture towards subjective embodiment within the full body illusion. *Sci. Rep.* 9:2889. doi: 10.1038/s41598-019-39168-4

Chen, R., and Hallett, M. (1999). The time course of changes in motor cortex excitability associated with voluntary movement. *J. Can. Des Sci. Neurol.* 26, 163–169. doi: 10.1017/S0317167100000196

Chen, R., Yaseen, Z., Cohen, L. G., and Hallett, M. (1998). Time course of corticospinal excitability in reaction time and self-paced movements. *Ann. Neurol.* 44, 317–325. doi: 10.1002/ana.410440306

Clausen, S., Tajadura-Jiménez, A., Janssen, C. P., and Bianchi-Berthouze, N. (2021). Action sounds informing own body perception influence gender identity and social cognition. *Front. Hum. Neurosci.* 15:688170. doi: 10.3389/fnhum.2021.688170

Conte, A., Gilio, F., Iezzi, E., Frasca, V., Inghilleri, M., and Berardelli, A. (2007). Attention influences the excitability of cortical motor areas in healthy humans. *Exper. Brain Res.* 182, 109–117. doi: 10.1007/s00221-007-0975-3

Crea, S., D'Alonzo, M., Vitiello, N., and Cipriani, C. (2015). The rubber foot illusion. *J. Neuroeng. Rehabil.* 12:77. doi: 10.1186/s12984-015-0069-6

D'Angelo, M., di Pellegrino, G., and Frassinetti, F. (2019). The illusion of having a tall or short body differently modulates interpersonal and peripersonal space. *Behav. Brain Res.* 375:112146. doi: 10.1016/j.bbr.2019.112146

David, N., Newen, A., and Vogeley, K. (2008). The "sense of agency" and its underlying cognitive and neural mechanisms. *Conscious. Cogn.* 17, 523–534. doi: 10.1016/j.concog.2008.03.004

de Mello Monteiro, C. B., Massetti, T., da Silva, T. D., van der Kamp, J., de Abreu, L. C., Leone, C., et al. (2014). Transfer of motor learning from virtual to natural environments in individuals with cerebral palsy. *Res. Dev. Disabil.* 35, 2430–2437. doi: 10.1016/j.ridd.2014.06.006

de Vignemont, F. (2010). Body schema and body image—Pros and cons. *Neuropsychologia* 48, 669–680. doi: 10.1016/j.neuropsychologia.2009.09.022

della Gatta, F., Garbarini, F., Puglisi, G., Leonetti, A., Berti, A., and Borroni, P. (2016). Decreased motor cortex excitability mirrors own hand disembodiment during the rubber hand illusion. *eLife* 5:e14972. doi: 10.7554/eLife.14972

Deutsch, J. E., Merians, A. S., Adamovich, S., Poizner, H., and Burdea, G. C. (2004). Development and application of virtual reality technology to improve hand use and gait of individuals post-stroke. *Restor. Neurol. Neurosci.* 22, 371–386.

Di Lazzaro, V., and Rothwell, J. C. (2014). Corticospinal activity evoked and modulated by non-invasive stimulation of the intact human motor cortex. *J. Physiol.* 592, 4115–4128. doi: 10.1113/jphysiol.2014.274316

Dilena, A., Todd, G., Berryman, C., Rio, E., and Stanton, T. R. (2019). What is the effect of bodily illusions on corticomotoneuronal excitability? A systematic review. *PLoS One* 14:e0219754. doi: 10.1371/journal.pone.0219754

Ehrsson, H. H. (2004). That's My Hand! activity in premotor cortex reflects feeling of ownership of a limb. *Science* 305, 875–877. doi: 10.1126/science.1097011

Feigin, V. L., Forouzanfar, M. H., Krishnamurthi, R., Mensah, G. A., Connor, M., Bennett, D. A., et al. (2014). Global and regional burden of stroke during 1990-2010: findings from the global burden of disease study 2010. *Lancet* 383, 245–254. doi: 10.1016/s0140-6736(13)61953-4

Flögel, M., Kalveram, K. T., Christ, O., and Vogt, J. (2016). Application of the rubber hand illusion paradigm: comparison between upper and lower limbs. *Psychol. Res.* 80, 298–306. doi: 10.1007/s00426-015-0650-4

Fossataro, C., Bruno, V., Giurgola, S., Bolognini, N., and Garbarini, F. (2018). Losing my hand. Body ownership attenuation after virtual lesion of the primary motor cortex. *Eur. J. Neurosci.* 48, 2272–2287. doi: 10.1111/ejn.14116

Golaszewski, S., Frey, V., Thomschewski, A., Sebastianelli, L., Versace, V., Saltuari, L., et al. (2021). Neural mechanisms underlying the Rubber Hand Illusion: a systematic review of related neurophysiological studies. *Brain Behav.* 11:e02124. doi: 10.1002/brb3.2124

Grechuta, K., Guga, J., Maffei, G., Rubio Ballester, B., and Verschure, P. F. M. J. (2017). Visuotactile integration modulates motor performance in a perceptual decision-making task. *Sci. Rep.* 7:3333. doi: 10.1038/s41598-017-03488-0

Grechuta, K., Ulysse, L., Rubio Ballester, B., and Verschure, P. F. M. J. (2019). Self beyond the body: action-driven and task-relevant purely distal cues modulate performance and body ownership. *Front. Hum. Neurosci.* 13:91. doi: 10.3389/fnhum.2019.00091

Groppa, S., Oliviero, A., Eisen, A., Quartarone, A., Cohen, L. G., Mall, V., et al. (2012). A practical guide to diagnostic transcranial magnetic stimulation: report of an IFCN committee. *Clin. Neurophysiol.* 123, 858–882. doi: 10.1016/j.clinph.2012.01.010

Haans, A., IJsselsteijn, W. A., and de Kort, Y. A. W. (2008). The effect of similarities in skin texture and hand shape on perceived ownership of a fake limb. *Body Image* 5, 389–394. doi: 10.1016/j.bodyim.2008.04.003

Head, H., and Holmes, G. (1911). Sensory disturbances from cerebral lesions. *Brain* 34, 102–254. doi: 10.1093/brain/34.2-3.102

Holmes, N. P., and Spence, C. (2004). The body schema and multisensory representation(s) of peripersonal space. *Cogn. Process.* 5, 94–105. doi: 10.1007/s10339-004-0013-3

Hornburger, H., Nguemeni, C., Odorfer, T., and Zeller, D. (2019). Modulation of the rubber hand illusion by transcranial direct current stimulation over the contralateral somatosensory cortex. *Neuropsychologia* 131, 353–359. doi: 10.1016/j.neuropsychologia.2019.05.008

Isayama, R., Vesia, M., Jegatheeswaran, G., Elahi, B., Gunraj, C. A., Cardinali, L., et al. (2019). Rubber hand illusion modulates the influences of somatosensory and parietal inputs to the motor cortex. *J. Neurophysiol.* 121, 563–573. doi: 10.1152/jn.00345.2018

Jang, S. H., You, S. H., Hallett, M., Cho, Y. W., Park, C.-M., Cho, S.-H., et al. (2005). Cortical reorganization and associated functional motor recovery after virtual reality in patients with chronic stroke: an experimenter-blind preliminary study. *Archiv. Phys. Med. Rehabil.* 86, 2218–2223. doi: 10.1016/j.apmr.2005.04.015

Jeong, H., and Kim, J. (2021). Development of a guidance system for motor imagery enhancement using the virtual hand illusion. *Sensors* 21:2197. doi: 10.3390/s21062197

Kalckert, A., and Ehrsson, H. H. (2012). Moving a rubber hand that feels like your own: a dissociation of ownership and agency. *Front. Hum. Neurosci.* 6:40. doi: 10.3389/fnhum.2012.00040

Kammers, M. P. M., de Vignemont, F., Verhagen, L., and Dijkerman, H. C. (2009). The rubber hand illusion in action. *Neuropsychologia* 47, 204–211. doi: 10.1016/j.neuropsychologia.2008.07.028

Kanayama, N., Hara, M., and Kimura, K. (2021). Virtual reality alters cortical oscillations related to visuo-tactile integration during rubber hand illusion. *Sci. Rep.* 11:1436. doi: 10.1038/s41598-020-80807-y

Kilteni, K., Bergstrom, I., and Slater, M. (2013). Drumming in immersive virtual reality: the body shapes the way we play. *IEEE Trans. Vis. Comput. Graph.* 19, 597–605. doi: 10.1109/TVCG.2013.29

Kilteni, K., Grau-Sánchez, J., Veciana De Las Heras, M., Rodríguez-Fornells, A., and Slater, M. (2016). Decreased corticospinal excitability after the illusion of missing part of the arm. *Front. Hum. Neurosci.* 10:145. doi: 10.3389/fnhum.2016.00145

Kilteni, K., Groten, R., and Slater, M. (2012a). The sense of embodiment in virtual reality. *Presence Teleoperat. Virtual Environ.* 21, 373–387. doi: 10.1162/PRES_a_00124

Kilteni, K., Normand, J.-M., Sanchez-Vives, M. V., and Slater, M. (2012b). Extending body space in immersive virtual reality: a very long arm illusion. *PLoS One* 7:e40867. doi: 10.1371/journal.pone.0040867

Knoblich, G. (ed.) (2006). *Human Body Perception From the Inside Out*. Oxford: Oxford University Press.

Lenggenhager, B., Pazzaglia, M., Scivoletto, G., Molinari, M., and Aglioti, S. M. (2012). The sense of the body in individuals with spinal cord injury. *PLoS One* 7:e50757. doi: 10.1371/journal.pone.0050757

Lee, J. H., Ku, J., Cho, W., Hahn, W. Y., Kim, I. Y., Lee, S.-M., et al. (2003). A virtual reality system for the assessment and rehabilitation of the activities of daily living. *Cyberpsychol. Behav.* 6, 383–388. doi: 10.1089/109493103322278763

Lloyd, D. M. (2007). Spatial limits on referred touch to an alien limb may reflect boundaries of visuo-tactile peripersonal space surrounding the hand. *Brain Cogn.* 64, 104–109. doi: 10.1016/j.bandc.2006.09.013

Longo, M. R., and Haggard, P. (2011). Weber's illusion and body shape: anisotropy of tactile size perception on the hand. *J. Exper. Psychol.* 37, 720–726. doi: 10.1037/a0021921

Longo, M. R., Schüür, F., Kammers, M. P. M., Tsakiris, M., and Haggard, P. (2008). What is embodiment? A psychometric approach. *Cognition* 107, 978–998. doi: 10.1016/j.cognition.2007.12.004

Lopez, C., Bieri, C. P., Preuss, N., and Mast, F. W. (2012). Tactile and vestibular mechanisms underlying ownership for body parts: a non-visual variant of the rubber hand illusion. *Neurosci. Lett.* 511, 120–124. doi: 10.1016/j.neulet.2012.01.055

Lum, P. S., Godfrey, S. B., Brokaw, E. B., Holley, R. J., and Nichols, D. (2012). Robotic approaches for rehabilitation of hand function after stroke. *Am. J. Phys. Med. Rehabil.* 91, S242–S254. doi: 10.1097/PHM.0b013e31826bcedb

Makin, T. R., Holmes, N. P., and Ehrsson, H. H. (2008). On the other hand: dummy hands and peripersonal space. *Behav. Brain Res.* 191, 1–10. doi: 10.1016/j.bbr.2008.02.041

Maravita, A., and Iriki, A. (2004). Tools for the body (schema). *Trends Cogn. Sci.* 8, 79–86. doi: 10.1016/j.tics.2003.12.008

Maravita, A., Spence, C., and Driver, J. (2003). Multisensory integration and the body schema: close to hand and within reach. *Curr. Biol.* 13, R531–R539. doi: 10.1016/S0960-9822(03)00449-4

Marchal-Crespo, L., and Reinkensmeyer, D. J. (2008). Haptic guidance can enhance motor learning of a steering task. *J. Motor Behav.* 40, 545–556. doi: 10.3200/JMBR.40.6.545-557

Marchal-Crespo, L., and Reinkensmeyer, D. J. (2009). Review of control strategies for robotic movement training after neurologic injury. *J. Neuroeng. Rehabil.* 6:20. doi: 10.1186/1743-0003-6-20

Matsumoto, N., Nakai, R., Ino, T., and Mitani, A. (2020). Brain activity associated with the rubber foot illusion. *Neurosci. Lett.* 721:134820. doi: 10.1016/j.neulet.2020.134820

Miall, R. C., Christensen, L. O. D., Cain, O., and Stanley, J. (2007). Disruption of state estimation in the human lateral cerebellum. *PLoS Biol.* 5:e316. doi: 10.1371/journal.pbio.0050316

Odermatt, I. A., Buetler, K. A., Wenk, N., Özen, Ö, Penalver-Andres, J., Nef, T., et al. (2021). Congruency of information rather than body ownership enhances motor performance in highly embodied virtual reality. *Front. Neurosci.* 15:678909. doi: 10.3389/fnins.2021.678909

Pearce, A. J., and Kidgell, D. J. (2009). Corticomotor excitability during precision motor tasks. *J. Sci. Med. Sport* 12, 280–283. doi: 10.1016/j.jsams.2007.12.005

Perez, M. A., and Cohen, L. G. (2008). Mechanisms underlying functional changes in the primary motor cortex ipsilateral to an active hand. *J. Neurosci.* 28, 5631–5640. doi: 10.1523/JNEUROSCI.0093-08.2008

Perez, M. A., and Cohen, L. G. (2009). Scaling of motor cortical excitability during unimanual force generation. *Cortex* 45, 1065–1071. doi: 10.1016/j.cortex.2008.12.006

Perez, M. A., Soteropoulos, D. S., and Baker, S. N. (2012). Corticomuscular coherence during bilateral isometric arm voluntary activity in healthy humans. *J. Neurophysiol.* 107, 2154–2162. doi: 10.1152/jn.00722.2011

Perez-Marcos, D., Bieler-Aeschlimann, M., and Serino, A. (2018). Virtual reality as a vehicle to empower motor-cognitive neurorehabilitation. *Front. Psychol.* 9:2120. doi: 10.3389/fpsyg.2018.02120

Perez-Marcos, D., Slater, M., and Sanchez-Vives, M. V. (2009). Inducing a virtual hand ownership illusion through a brain-computer interface. *Neuroreport* 20, 589–594. doi: 10.1097/WNR.0b013e32832a0a2a

Petkova, V. I., and Ehrsson, H. H. (2008). If I were you: perceptual illusion of body swapping. *PLoS One* 3:e3832. doi: 10.1371/journal.pone.0003832

Pozeg, P., Rognini, G., Salomon, R., and Blanke, O. (2014). Crossing the hands increases illusory self-touch. *PLoS One* 9:e94008. doi: 10.1371/journal.pone.0094008

Preston, C., and Newport, R. (2012). How long is your arm? Using multisensory illusions to modify body image from the third person perspective. *Perception* 41, 247–249. doi: 10.1068/p7103

Pyasik, M., Tieri, G., and Pia, L. (2020). Visual appearance of the virtual hand affects embodiment in the virtual hand illusion. *Sci. Rep.* 10:5412. doi: 10.1038/s41598-020-62394-0

Rao, I. S., and Kayser, C. (2017). Neurophysiological correlates of the rubber hand illusion in late evoked and alpha/beta band activity. *Front. Hum. Neurosci.* 11:377. doi: 10.3389/fnhum.2017.00377

Raz, G., Gurevitch, G., Vaknin, T., Aazamy, A., Gefen, I., Grunstein, S., et al. (2020). Electroencephalographic evidence for the involvement of mirror-neuron and error-monitoring related processes in virtual body ownership. *Neuroimage* 207:116351. doi: 10.1016/j.neuroimage.2019.116351

Riemer, M., Trojan, J., Beauchamp, M., and Fuchs, X. (2019). The rubber hand universe: on the impact of methodological differences in the rubber hand illusion. *Neurosci. Biobehav. Rev.* 104, 268–280. doi: 10.1016/j.neubiorev.2019.07.008

Rosanova, M., Casarotto, S., Pigorini, A., Canali, P., Casali, A. G., and Massimini, M. (2011). "Combining transcranial magnetic stimulation with electroencephalography to study human cortical excitability and effective connectivity," in *Neuronal Network Analysis*, Vol. 67, eds T. Fellin and M. Halassa (Totowa, NJ: Humana Press), 435–457. doi: 10.1007/7657_2011_15

Rose, F. D., Brooks, B. M., and Rizzo, A. A. (2005). Virtual reality in brain damage rehabilitation: review. *Cyberpsychol. Behav.* 8, 241–262. doi: 10.1089/cpb.2005.8.241

Rossini, P. M., Burke, D., Chen, R., Cohen, L. G., Daskalakis, Z., Di Iorio, R., et al. (2015). Non-invasive electrical and magnetic stimulation of the brain, spinal cord, roots and peripheral nerves: basic principles and procedures for routine clinical and research application. An updated report from an I.F.C.N. Committee. *Clin. Neurophysiol.* 126, 1071–1107. doi: 10.1016/j.clinph.2015.02.001

Rothwell, J. C. (1997). Techniques and mechanisms of action of transcranial stimulation of the human motor cortex. *J. Neurosci. Methods* 74, 113–122. doi: 10.1016/S0165-0270(97)02242-5

Rothwell, J. C., Day, B. L., Thompson, P. D., Dick, J. P., and Marsden, C. D. (1987a). Some experiences of techniques for stimulation of the human cerebral motor cortex through the scalp. *Neurosurgery* 20, 156–163. doi: 10.1097/00006123-198701000-00032

Rothwell, J. C., Thompson, P. D., Day, B. L., Dick, J. P. R., Kachi, T., Cowan, J. M. A., et al. (1987b). Motor cortex stimulation in intact man: 1. General characteristics of EMG responses in different muscles. *Brain* 110, 1173–1190. doi: 10.1093/brain/110.5.1173

Sakamoto, M., and Ifuku, H. (2021). Attenuation of sensory processing in the primary somatosensory cortex during rubber hand illusion. *Sci. Rep.* 11:7329. doi: 10.1038/s41598-021-86828-5

Sanchez-Vives, M. V., Spanlang, B., Frisoli, A., Bergamasco, M., and Slater, M. (2010). Virtual hand illusion induced by visuomotor correlations. *PLoS One* 5:e10381. doi: 10.1371/journal.pone.0010381

Schmidt, S. H., and Brandt, S. A. (2021). "Motor threshold, motor evoked potential, central motor conduction time," in *The Oxford Handbook of Transcranial Stimulation*, 2nd Edn, eds E. M. Wassermann, A. V. Peterchev, U. Ziemann, S. H. Lisanby, H. R. Siebner, and V. Walsh (Oxford: Oxford University Press), doi: 10.1093/oxfordhb/9780198832256.013.11

Schulz, H., Übelacker, T., Keil, J., Müller, N., and Weisz, N. (2014). Now I am Ready—Now I am not: the influence of Pre-TMS oscillations and corticomuscular coherence on motor-evoked potentials. *Cereb. Cortex* 24, 1708–1719. doi: 10.1093/cercor/bht024

Senna, I., Maravita, A., Bolognini, N., and Parise, C. V. (2014). The marble-hand illusion. *PLoS One* 9:e91688. doi: 10.1371/journal.pone.0091688

Serino, A., and Haggard, P. (2010). Touch and the body. *Neurosci. Biobehav. Rev.* 34, 224–236. doi: 10.1016/j.neubiorev.2009.04.004

Shishov, N., Melzer, I., and Bar-Haim, S. (2017). Parameters and measures in assessment of motor learning in neurorehabilitation; a systematic review of the literature. *Front. Hum. Neurosci.* 11:82. doi: 10.3389/fnhum.2017.00082

Slater, M. (2008). Towards a digital body: the virtual arm illusion. *Front. Hum. Neurosci.* 2:6. doi: 10.3389/neuro.09.006.2008

Smith, V., Maslovat, D., and Carlsen, A. N. (2019). StartReact effects are dependent on engagement of startle reflex circuits: support for a subcortically mediated initiation pathway. *J. Neurophysiol.* 122, 2541–2547. doi: 10.1152/jn.00505.2019

Starr, A., Caramia, M., Zarola, F., and Rossini, P. M. (1988). Enhancement of motor cortical excitability in humans by non-invasive electrical stimulation appears

prior to voluntary movement. *Electroencephalogr. Clin. Neurophysiol.* 70, 26–32. doi: 10.1016/0013-4694(88)90191-5

Tajadura-Jiménez, A., Basia, M., Deroy, O., Fairhurst, M., Marquardt, N., and Bianchi-Berthouze, N. (2015a). "As light as your footsteps: altering walking sounds to change perceived body weight, emotional state and gait," in *Proceedings of the 33rd Annual ACM Conference on Human Factors in Computing Systems*, eds B. Begole, J. Kim, W. Woo, and K. Inkpen (Seoul: Association for Computing Machinery), 2943–2952. doi: 10.1145/2702123.2702374

Tajadura-Jiménez, A., Tsakiris, M., Marquardt, T., and Bianchi-Berthouze, N. (2015b). Action sounds update the mental representation of arm dimension: contributions of kinaesthesia and agency. *Front. Psychol.* 6:689. doi: 10.3389/fpsyg.2015.00689

Tajadura-Jiménez, A., Marquardt, T., Swapp, D., Kitagawa, N., and Bianchi-Berthouze, N. (2016). Action sounds modulate arm reaching movements. *Front. Psychol.* 7:1391. doi: 10.3389/fpsyg.2016.01391

Tajadura-Jiménez, A., Väljamäe, A., Toshima, I., Kimura, T., Tsakiris, M., and Kitagawa, N. (2012). Action sounds recalibrate perceived tactile distance. *Curr. Biol.* 22, R516–R517. doi: 10.1016/j.cub.2012.04.028

Tambone, R., Poggio, G., Pyasik, M., Burin, D., Dal Monte, O., Schintu, S., et al. (2021). Changing your body changes your eating attitudes: embodiment of a slim virtual avatar induces avoidance of high-calorie food. *Heliyon* 7:e07515. doi: 10.1016/j.heliyon.2021.e07515

Thut, G., Veniero, D., Romei, V., Miniussi, C., Schyns, P., and Gross, J. (2011). Rhythmic TMS causes local entrainment of natural oscillatory signatures. *Curr. Biol.* 21, 1176–1185. doi: 10.1016/j.cub.2011.05.049

Tsakiris, M. (2010). My body in the brain: a neurocognitive model of body-ownership. *Neuropsychologia* 48, 703–712. doi: 10.1016/j.neuropsychologia.2009.09.034

Tsakiris, M. (2017). The multisensory basis of the self: from body to identity to others. *Q. J. Exper. Psychol.* 70, 597–609. doi: 10.1080/17470218.2016.1181768

Tsakiris, M., and Haggard, P. (2005). The rubber hand illusion revisited: visuotactile integration and self-attribution. *J. Exper. Psychol. Hum. Percept. Perform.* 31, 80–91. doi: 10.1037/0096-1523.31.1.80

Tsakiris, M., Prabhu, G., and Haggard, P. (2006). Having a body versus moving your body: how agency structures body-ownership. *Conscious. Cogn.* 15, 423–432. doi: 10.1016/j.concog.2005.09.004

Uehara, K., Higashi, T., Tanabe, S., and Sugawara, K. (2011). Alterations in human motor cortex during dual motor task by transcranial magnetic stimulation study. *Exper. Brain Res.* 208, 277–286. doi: 10.1007/s00221-010-2478-x

van der Hoort, B., Guterstam, A., and Ehrsson, H. H. (2011). Being barbie: the size of One's own body determines the perceived size of the world. *PLoS One* 6:e20195. doi: 10.1371/journal.pone.0020195

Watanabe, H., Mizuguchi, N., Mayfield, D. L., and Yoshitake, Y. (2018). Corticospinal excitability during actual and imaginary motor tasks of varied difficulty. *Neuroscience* 391, 81–90. doi: 10.1016/j.neuroscience.2018.08.011

Wawrzyniak, M., Klingbeil, J., Zeller, D., Saur, D., and Classen, J. (2018). The neuronal network involved in self-attribution of an artificial hand: a lesion network-symptom-mapping study. *Neuroimage* 166, 317–324. doi: 10.1016/j.neuroimage.2017.11.011

Wen, W., Muramatsu, K., Hamasaki, S., An, Q., Yamakawa, H., Tamura, Y., et al. (2016). Goal-directed movement enhances body representation updating. *Front. Hum. Neurosci.* 10:329. doi: 10.3389/fnhum.2016.00329

Wenk, N., Penalver-Andres, J., Buetler, K. A., Nef, T., Müri, R. M., and Marchal-Crespo, L. (2021). Effect of immersive visualization technologies on cognitive load, motivation, usability, and embodiment. *Virtual Real.* doi: 10.1007/s10055-021-00565-8

Wolf, S. L., Butler, A. J., Alberts, J. L., and Kim, M. W. (2005). Contemporary linkages between EMG, kinetics and stroke rehabilitation. *J. Electromyogr. Kinesiol.* 15, 229–239. doi: 10.1016/j.jelekin.2005.01.002

Yahagi, S., Ni, Z., Takahashi, M., Takeda, Y., Tsuji, T., and Kasai, T. (2003). Excitability changes of motor evoked potentials dependent on muscle properties and contraction modes. *Motor Control* 7, 328–345.

Zeller, D., Gross, C., Bartsch, A., Johansen-Berg, H., and Classen, J. (2011). Ventral premotor cortex may be required for dynamic changes in the feeling of limb ownership: a lesion study. *J. Neurosci.* 31, 4852–4857. doi: 10.1523/JNEUROSCI.5154-10.2011

Zeller, D., Litvak, V., Friston, K. J., and Classen, J. (2015). Sensory processing and the rubber hand illusion—an evoked potentials study. *J. Cogn. Neurosci.* 27, 573–582. doi: 10.1162/jocn_a_00705

Conflict of Interest: The authors declare that the research was conducted in the absence of any commercial or financial relationships that could be construed as a potential conflict of interest.

Publisher's Note: All claims expressed in this article are solely those of the authors and do not necessarily represent those of their affiliated organizations, or those of the publisher, the editors and the reviewers. Any product that may be evaluated in this article, or claim that may be made by its manufacturer, is not guaranteed or endorsed by the publisher.

Copyright © 2022 Buetler, Penalver-Andres, Özen, Ferriroli, Müri, Cazzoli and Marchal-Crespo. This is an open-access article distributed under the terms of the Creative Commons Attribution License (CC BY). The use, distribution or reproduction in other forums is permitted, provided the original author(s) and the copyright owner(s) are credited and that the original publication in this journal is cited, in accordance with accepted academic practice. No use, distribution or reproduction is permitted which does not comply with these terms.

frontiers in Systems Neuroscience

ORIGINAL RESEARCH
published: 10 February 2022
doi: 10.3389/fnsys.2022.774475

Individual Sensory Modality Dominance as an Influential Factor in the Prefrontal Neurofeedback Training for Spatial Processing: A Functional Near-Infrared Spectroscopy Study

Takeshi Sakurada[1,2,3], Mayuko Matsumoto[2,4] and Shin-ichiroh Yamamoto[4]*

[1] Department of Robotics, College of Science and Engineering, Ritsumeikan University, Shiga, Japan, [2] Functional Brain Science Laboratory, Center for Development of Advanced Medical Technology, Jichi Medical University, Tochigi, Japan, [3] Department of Neurosurgery, Jichi Medical University, Tochigi, Japan, [4] Graduate School of Systems Engineering and Science, Shibaura Institute of Technology, Saitama, Japan

Neurofeedback is a neuromodulation technique used to improve brain function by self-regulating brain activity. However, the efficacy of neurofeedback training varies widely between individuals, and some participants fail to self-regulate brain activity. To overcome intersubject variation in neurofeedback training efficacy, it is critical to identify the factors that influence this type of neuromodulation. In this study, we considered that individual differences in cognitive ability may influence neurofeedback training efficacy and aimed to clarify the effect of individual working memory (WM) abilities, as characterized by sensory modality dominance, on neurofeedback training efficacy in healthy young adults. In particular, we focused on the abilities of individuals to retain internal (tactile or somatosensory) or external (visual) body information in their WM. Forty participants performed functional near-infrared spectroscopy-based neurofeedback training aimed at producing efficient and lower-level activity in the bilateral dorsolateral prefrontal cortex and frontopolar cortex. We carried out a randomized, sham-controlled, double-blind study that compared WM ability before and after neurofeedback training. Individual WM ability was quantified using a target searching task that required the participants to retain spatial information presented as vibrotactile or visual stimuli. Participants who received feedback information based on their own prefrontal activity showed gradually decreasing activity in the right prefrontal area during the neurofeedback training and demonstrated superior WM ability during the target searching task with vibrotactile stimuli compared with the participants who performed dummy neurofeedback training. In comparison, left prefrontal activity was not influenced by the neurofeedback training. Furthermore, the efficacy of neurofeedback training (i.e., lower right prefrontal activity and better searching task performance) was

OPEN ACCESS

Edited by:
Tomohiko Takei, Tamagawa University, Japan

Reviewed by:
Nan Liang, Kyoto University, Japan
Hiroyuki Hamada, The University of Tokyo, Japan

***Correspondence:**
Takeshi Sakurada
sakurada@fc.ritsumei.ac.jp

Received: *12 September 2021*
Accepted: *07 January 2022*
Published: *10 February 2022*

Citation:
Sakurada T, Matsumoto M and Yamamoto S (2022) Individual Sensory Modality Dominance as an Influential Factor in the Prefrontal Neurofeedback Training for Spatial Processing: A Functional Near-Infrared Spectroscopy Study. Front. Syst. Neurosci. 16:774475. doi: 10.3389/fnsys.2022.774475

higher in participants who exhibited tactile dominance rather than visual dominance in their WM. These findings indicate that sensory modality dominance in WM may be an influential neurophysiological factor in determining the efficacy of neurofeedback training. These results may be useful in the development of neurofeedback training protocols tailored to individual needs.

Keywords: neurofeedback, functional near-infrared spectroscopy, working memory, prefrontal cortex, individual differences, sensory modality

INTRODUCTION

Neurofeedback is a neuromodulation technique that aims to self-regulate brain activity patterns to improve specific functions (Ehlis et al., 2018; Xiang et al., 2018; Jeunet et al., 2019). In healthy individuals, theta electroencephalography (EEG) power increases during neurofeedback training have been shown to assist in improving motor sequential learning (Rozengurt et al., 2016), and high sensorimotor rhythm power has been associated with better motor performance in a sporting task (Cheng et al., 2015). Moreover, neurofeedback training has been noted as a useful protocol for improving cognitive functions such as attention (Wang and Hsieh, 2013), working memory (WM) (Escolano et al., 2011) and mental rotation (Hanslmayr et al., 2005). In clinical fields, neuromodulation by neurofeedback has been used successfully to alter brain activity in a wide range of disorders, such as attention deficit hyperactivity disorder (Leins et al., 2007) and Parkinson's disease (Subramanian et al., 2011).

Although EEG and fMRI are the imaging techniques most commonly used for neurofeedback training, the use of functional near-infrared spectroscopy (fNIRS) has increased over the last 10 years (Ehlis et al., 2018; Kohl et al., 2020). fNIRS recording has several advantages. For example, if the probes are in close contact with the head, we can measure brain activity, regardless of posture or any slight body movement. Furthermore, fNIRS is resistant to electrical noise, an especially useful feature when conducting neuroimaging experiments. For instance, using fNIRS-based neurofeedback, self-regulation of the right dorsolateral prefrontal cortex (DLPFC) has been shown to contribute to improved emotional regulation (Yu et al., 2021), and postural stability has been found to be affected by greater supplementary motor area activity (Fujimoto et al., 2017). Moreover, neurofeedback of the premotor area during a rehabilitation protocol requiring motor imagery of a paretic hand's movements enhanced the recovery of finger motor function in patients with hemiplegic stroke. Specifically, the motor imagery-related premotor activity changes during neurofeedback training significantly correlated with functional recovery (Mihara et al., 2013). Altogether, these reports demonstrate that fNIRS-based neurofeedback might constitute an effective approach to neuromodulation. However, it is worth noting that acquiring higher brain activity does not always correlate with improvement in a specific brain function. Lower (i.e., efficient) brain activity can also lead to high brain function performance (Jansma et al., 2001; Ramsey et al., 2004; Koike et al., 2013). Therefore, the direction of self-regulation of brain activity must be appropriately determined in neurofeedback training.

Although various types of neurofeedback training have been reported to be useful for brain functional training, the efficacy of neurofeedback training varies widely among individuals, and a certain population obtains no benefit from neurofeedback training and fails to self-regulate brain activity patterns (Alkoby et al., 2018; Diaz Hernandez et al., 2018; Kadosh and Staunton, 2019). A recent review pointed out that participants who failed to self-regulate during neurofeedback training represented about 50% of the population (Alkoby et al., 2018). For instance, a neurofeedback training protocol that aimed to improve WM ability by increasing upper alpha power indicated that three of nine participants failed to control their alpha power after several training sessions (Escolano et al., 2011). Moreover, during neurofeedback training to modulate sensorimotor rhythm, approximately half of the participants did not learn to regulate their own brain activities even after numerous training sessions (Weber et al., 2011).

To overcome these individual differences in the efficacy of neurofeedback training, we need to identify the predictor (influential factor) of the neuromodulation. Although the factors influencing neurofeedback training are not fully understood, the issue has been discussed recently, and several factors have been pointed out (Alkoby et al., 2018; Diaz Hernandez et al., 2018; Kadosh and Staunton, 2019). First, the effect of psychological factors such as mental strategy, motivation, and mood has been discussed frequently. The most successful mental strategies during neurofeedback training were found to be related to positive thoughts such as those of friends, love, or family (Nan et al., 2012). Another study demonstrated that the psychological effects depended on the targeted EEG component. Specifically, individuals with no specific mental strategy showed improvements from neurofeedback training for sensorimotor rhythm, and the efficacy of neurofeedback training for gamma power did not vary among individuals, regardless of their mental strategies (Kober et al., 2013). The authors pointed out the disadvantage of overloading cognitive resource data from the use of a specific mental strategy during neurofeedback training. Second, in addition to psychological factors, neurophysiological factors also influence the ability to regulate brain activity using neurofeedback. For instance, alpha powers in the eyes-closed and eyes-open resting state before neurofeedback training were significantly correlated with successful EEG learning (Wan et al., 2014). Another study found that an individual's ability to modulate sensorimotor rhythm in early neurofeedback training sessions predicted later neurofeedback training efficacy (Weber et al., 2011). Thus, even if the psychological state is similar among trainees, different

functional brain characteristics might affect the efficacy of neurofeedback training.

Regarding these neurophysiological factors, we should consider the possibility that individual differences in the qualitative characteristics of cognitive function determine neurofeedback training efficacy. We recently reported a wide variation in the sensory modalities that individuals are good at processing; hereafter, we refer to these individual differences as modality dominance. Specifically, individual cognitive abilities in motor imagery or attention control can be characterized by the modality dominance, and this can lead to better processing of internal body information such as tactile or somatosensory stimuli or external body information such as visual stimuli (Sakurada et al., 2016, 2017, 2019a,b). In these studies, individuals with visual motor imagery dominance showed better motor performance when using an external focus attentional strategy, which required that the participant's attention was focused on a body movement outcome. Conversely, individuals with kinesthetic motor imagery dominance demonstrated better motor performance when using an internal focus attentional strategy, which required that the participant's attention was focused on the body movement itself. Furthermore, individual WM ability that relates to spatial information processing (Robertson et al., 2001) can be characterized by modality dominance. When participants were required to retain spatial information, they could be grouped into those who were good at retaining vibrotactile-based or visual-based spatial information (Matsumoto et al., 2020). These findings indicate that modality dominance is one of the important parameters in characterizing the qualitative aspects of cognitive function, but whether distinct qualitative differences in cognitive function among individuals affects neurofeedback training efficacy remains unclear.

This study aimed to examine whether modality dominance in WM influences the efficacy of neurofeedback training. Based on our previous findings regarding the neural basis of individual differences in WM modality dominance (Matsumoto et al., 2020), the neurofeedback protocol used in this study provided feedback of the bilateral DLPFC and frontopolar cortex (FPC), which are also critical for WM (Owen et al., 2005; Pleger et al., 2006; Slotnick and Moo, 2006; Kaas et al., 2007; Giglia et al., 2014). We hypothesized that the individual modality dominance in WM is one of the influential factors in neurofeedback training. Specifically, we predicted that the degree of neuromodulation in the prefrontal area and cognitive performance after neurofeedback training would highlight differences between individuals exhibiting tactile- versus visual dominance.

MATERIALS AND METHODS

Participants

Forty healthy participants (mean age ±SD, 22.4 ± 3.2 years; 19 males, 21 females) were recruited from the student population at Jichi Medical University. All participants were right-handed as assessed by the Edinburgh Handedness Inventory (laterality 96.4 ± 8.9) (Oldfield, 1971). This study was conducted in accordance with the Declaration of Helsinki and approved by the Institutional Review Board at Jichi Medical University. All participants provided written informed consent prior to participation. Each participant completed the following experimental protocol in 1 day, including the fNIRS-based neurofeedback training task that aimed to regulate bilateral prefrontal activities and a behavioral task that was used to evaluate WM ability before and after neurofeedback training.

Regulation of the Prefrontal Activity by Functional Near-Infrared Spectroscopy-Based Neurofeedback Training

Experimental Setup

Each participant sat on a chair facing an LCD monitor (size: H30.5 × W37.7 cm) that presented the visual stimulus and was asked to hold a computer mouse in their right hand. All visual stimuli presented on the monitor were programmed in MATLAB (MathWorks, Inc., Natick, MA, United States). During the fNIRS-based neurofeedback training task, the right hand was hidden by a small rack (**Figure 1A**). A multichannel fNIRS system (ETG-7100, Hitachi Medical Corporation, Kashiwa, Japan) with probes arranged to cover the prefrontal area was used to measure prefrontal activity. All of the fNIRS channel inputs were sampled at 10 Hz. A 3 × 9 multichannel probe holder contained eight laser sources that emitted at 695 and 830 nm and seven detecting probes that were alternately arranged with an interprobe distance of 3 cm. The midpoint between an emitter/detector pair was defined as the location of a recording channel (the probe set initially had 22 recording channels). Importantly, fNIRS signals reflect changes in hemoglobin that originate in cortical tissue due to brain activation and skin blood flow. To eliminate the impact of skin blood flow on the fNIRS signals, we set eight additional short detecting probes at an interprobe distance of 1.5 cm and applied multidistance independent component analysis (ICA) to the fNIRS analysis (Hirosaka et al., 2004; Morren et al., 2004; Akgül et al., 2006; Kohno et al., 2007; Funane et al., 2014). Signals from recording channels with a 1.5 cm interprobe distance primarily included skin blood flow signals in shallow tissues. Based on these signals, we discriminated between the effects of cortical tissue and skin blood flow on the fNIRS signals. As it was possible to apply multidistance ICA only to the recording channels around the short detecting probes, the number of available recording channels was reduced to 15 after applying multidistance ICA as shown in **Figure 1B**. All results presented in this study were recorded after multidistance ICA processing from the fNIRS system (i.e., the effects of skin blood flow have been removed based on fNIRS signals from the 1.5-cm interprobe channels). The probe holder was placed on the scalp with the lowest-row center emitter located at the participant's Fpz position according to the standard international 10–20 system (**Figure 1B**). To spatially register fNIRS maps onto the Montreal Neurological Institute coordinate space, we individually measured scalp landmarks and all fNIRS recording channel positions using a 3D magnetic space digitizer (FASTRAK, Polhemus, United States). We then used the position

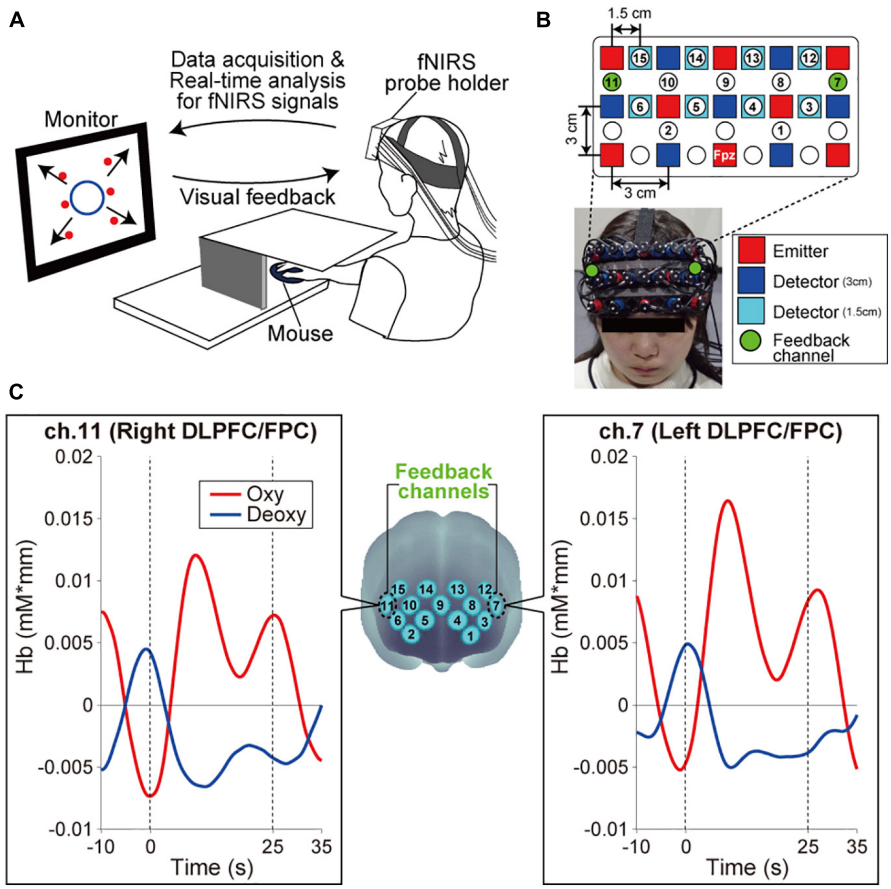

FIGURE 1 | Experimental setup. **(A)** Neurofeedback training set up. The monitor presented visual feedback on the status of participants' bilateral prefrontal cortex in real-time. Furthermore, the six red circles on the monitor indicated the visual stimuli that participants were required to remember. Specifically, in each task block, the all-red circles were sequentially presented individually in random order at the predetermined fixed positions {with the center of the monitor as the origin, the coordinates of the six circles were [*x*(cm), *y*(cm)] = (–10, 8), (10, 8), (–10, 0), (10, 0), (–10, –8), and (10, –8)}. The appearance order changed with every task block. The participants were required to remember the spatial appearance order of six visual stimuli on the monitor. **(B)** Configuration of the fNIRS probe. Probes were placed over the prefrontal area. The channels, numbered 1–15, indicated the channels that output fNIRS signals that have been removed based on multidistance ICA. Ch.7 and ch.11 conveyed signals from the left and right DLPFC/FPC, respectively, as neurofeedback. **(C)** Spatial registration of the fNIRS maps onto MNI coordinate space. The left and right panels show typical profiles of oxy-Hb and deoxy-Hb in the feedback channels. Time zero indicates the onset of the task block. After starting the task block, the oxy-Hb signal showed a stronger response than the deoxy-Hb signal.

data from all of the participants' recording channels to estimate spatial profiling without MRI (Singh et al., 2005). The estimated spatial profiling of each recording channel is shown in **Table 1**.

Procedure

The neurofeedback training task consisted of eight sessions, each comprising seven alternating 15-s rest and 25-s task blocks with an additional rest block inserted at the end of each session (i.e., 15 blocks per session).

During the task blocks, the monitor reported neurofeedback information as a circle in which the diameter reflected the online prefrontal activities in channels 7 and 11, corresponding mainly to the bilateral DLPFC and FPC. Although we measured oxygenated and deoxygenated hemoglobin (oxy- and deoxy-Hb), we used the oxy-Hb signals to calculate the neurofeedback information because of their greater sensitivity to changes in cerebral blood flow and higher signal-to-noise ratio than deoxy-Hb signals (Toronov et al., 2001; Strangman et al., 2002). As shown in **Figure 1C**, we also confirmed that the oxy-Hb signal change was stronger than that of deoxy-Hb in this study. Thus, the circle diameter was determined based on the oxy-Hb signals of ch.7 and ch.11. Furthermore, as the fNIRS signals are relative values, we should avoid using the values directly. Instead, the online oxy-Hb signals during the task blocks in each feedback channel were normalized to the mean and standard deviation during the 10 s prior to each task block (i.e., z-scoring). We then averaged *z*-score values between channels 7 and 11. The circle size increased when the averaged *z*-score among the two channels decreased. The circle was the largest (diameter: 45 cm) when the brain activity in the task block was below the average activity level for 10 s before starting the task block. Under this neurofeedback setting, participants were instructed to make the circle on the monitor as large as possible. In other words, the current neurofeedback training protocol aimed to acquire more

TABLE 1 | Spatial profiling of each recording channel.

Ch.	Localization	Brodmann area	Probability
1	Left FPC	10	1
2	Right FPC	10	1
3	Left FPC	10	0.96
	Left DLPFC	46	0.04
4	Left FPC	10	1
5	Right FPC	10	1
6	Right FPC	10	0.99
	Right DLPFC	46	0.01
7	Left DLPFC	46	0.82
	Left FPC	10	0.18
8	Left FPC	10	0.84
	Left DLPFC	9	0.16
9	Right FPC	10	0.86
	Right DLPFC	9	0.14
10	Right FPC	10	0.80
	Right DLPFC	9	0.20
11	Right DLPFC	46	0.77
	Right FPC	10	0.23
12	Left DLPFC	9	0.70
	Left DLPFC	46	0.24
	Left FPC	10	0.05
	Left includes FEF	8	0.01
13	Left DLPFC	9	0.82
	Left includes FEF	8	0.18
14	Right DLPFC	9	0.81
	Right includes FEF	8	0.19
15	Right DLPFC	9	0.84
	Right DLPFC	46	0.06
	Right FPC	10	0.05
	Right includes FEF	8	0.05

FPC, frontopolar cortex; DLPFC, dorsolateral prefrontal cortex; FEF, frontal eye fields.

efficient (i.e., lower) activities in the bilateral DLPFC/FPC during spatial WM processing. Regarding task instructions related to brain activity, we only explained that the circle enlarged in response to cognitive brain activity for properly holding the target spatial information. We did not explicitly instruct the desired brain activity change (i.e., whether the participants should increase or decrease brain activity). This neurofeedback setting was based on the previous reports that decreasing prefrontal activity is associated with familiarity or a higher skill level during cognitive tasks (Jansma et al., 2001; Ramsey et al., 2004; Koike et al., 2013).

To drive spatial WM processing in the prefrontal area, we set up a cognitive-motor task during the task blocks. For the cognitive-motor task, the monitor sequentially showed six small visual stimuli. Each visual stimulus shown was a red circle with a diameter of 1 cm. The six visual stimuli were sequentially and individually presented in random order at predetermined fixed positions (top-left, top-right, middle-left, middle-right, bottom-left, or bottom-right on the monitor). A series of visual stimuli was presented just after the start of each task block, and the order was different for every task block. The participants were given information on the six visual stimuli (number, position, and randomness of appearance order). They were then instructed to remember the sequential patterns (spatial appearance order) of the six stimuli and to verbally answer the order of the visual stimuli in the rest block immediately after each task block. The participants were also required to press the computer mouse button at about 1 Hz with their index fingers. We utilized this cognitive-motor task during the task blocks, because the effect of cognitive processing cannot be assessed when a task is too easy for participants (Landers et al., 2005; Wulf et al., 2007, 2009) and individual differences in cognitive ability may not appear when the task is of insufficient difficulty (Sakurada et al., 2017).

We randomly assigned the participants to Real or Sham groups (each group contained 20 participants), but the group assignment for each participant was not provided to the experimental operator or the participant. The circle diameter for the Real group was determined in real-time based on each participant's own oxy-Hb signals in ch.7 and ch.11. Conversely, the circle size for the Sham group was based on the prerecorded oxy-Hb signals of another person and was unrelated to the participant's own cortical activation.

Functional Near-Infrared Spectroscopy Offline Analysis

Preprocessing

After applying the multidistance ICA, to remove baseline drift, the individual time course data from the oxy-Hb signals from each channel were high-pass filtered using a cut-off frequency of 0.0125 Hz. Next, to remove blocks containing motion-related artifacts, we applied an artifact detection algorithm based on HOMER2 software [MGH-Martinos Center for Biomedical Imaging (NITRC, 2021: Homer2: Tool/Resource Info)]. As no blocks containing artifacts were detected, we analyzed the entire oxy-Hb time course data obtained from this study.

General Linear Model Analysis

General linear model analysis (Friston et al., 1994a,b) can be used to detect task-related hemodynamic changes in the cortex from fNIRS data (Schroeter et al., 2004; Plichta et al., 2007). To identify neuromodulation in the prefrontal regions related to the WM processing of spatial information, we used GLM analysis with least-squares estimation of the oxy-Hb signals. For the preprocessed oxy-Hb signals, a Gaussian function with a peak time of 6 s and full width half maximum of 5.4 s was used as a hemodynamic response function to better mimic brain signals. The resulting beta values at each recording channel estimated by the GLM analysis were then used in the group analysis to evaluate the degree of neuromodulation during the neurofeedback training.

As described previously, the participants were instructed to enlarge the circle size on the monitor. This means that the participants needed to reduce the average activity of the neurofeedback channels (7 and 11). However, it should be noted that there were some potential patterns of brain activity in which participants were considered to have achieved the neurofeedback training goal. Specifically, the participants could enlarge the circle size not only by a simultaneous decreasing of both the left and

right neurofeedback channel activities but also by a large decrease of either the left or right activity. Therefore, as channels 7 and 11 might show different activity changes during the neurofeedback training, we independently analyzed the activity changes in each channel, rather than the average activity between the two.

Statistical Analysis

The beta values from all of the recording channels were analyzed by three-way repeated-measures analysis of variance (ANOVA) with session (1st or 8th session) and feedback channel (ch.7 or ch.11) as within-subject factors and neurofeedback training group (Real or Sham group) as a between-subject factor. Regarding the effect size, we applied a partial eta squared, which is robust for the number of factors. To evaluate the degree of neural activity change in the feedback channels, the beta values in the first session were compared with those in the eighth session by a *post hoc* test (simple-simple main effect test).

Target Searching Task for Evaluating Spatial Working Memory Ability

Experimental Setup

Based on our previous study (Matsumoto et al., 2020), we applied a target searching task to quantify individual WM modality dominance during spatial processing. The participants performed this searching task in a booth different from that used in the neurofeedback training task. Each participant was seated on a chair and asked to hold a digitizing-pen on a drawing tablet (Intuos4 PTK-1240/K0, Wacom, Japan) with their right hand. An LCD monitor (size: H30.5 × W37.7 cm) used to present the visual stimulus was placed horizontally at 16.5 cm above the tablet. As their right hand was hidden by a cloth and the monitor, the participants could not see it directly during the experimental tasks. Visual stimuli such as task instructions presented on the monitor were programmed in MATLAB using the Cogent Toolbox (University College London, London, United Kingdom). The Cogent Toolbox also recorded the position of the digitizing-pen tip with sampling at 60 Hz. A vibration motor presenting a vibrotactile stimulus was attached to the tip of the index finger on the right hand.

Procedure

The searching task required participants to find six targets appearing somewhere in the search area by moving the digitizing-pen on the drawing tablet (search area: H30.5 × W37.7 cm). The targets were located randomly and appeared individually in a predetermined, sequential order. Note that the target locations and appearance orders in this searching task were unrelated to those of the red visual stimuli presented during the neurofeedback training task. We introduced two experimental conditions, a tactile condition and a visual condition, that differed in the sensory modality of the stimulus cues presenting the target locations and orders of appearance. Under the tactile condition, when the tip of the digitizing-pen came into a target area on the tablet (diameter: 10 cm), a vibrotactile stimulus was presented to the right index finger from the vibration motor to indicate the target location. Conversely, under the visual condition, a circular visual cursor was presented on the monitor just above the corresponding digitizing-pen position to indicate the target location. Regarding the target settings, we had prepared different target locations and their appearance orders between the tactile and visual conditions and among the participants. However, the six predetermined target locations and their appearance orders within each participant were fixed throughout the trials under each condition.

In each trial, the participants were first required to move the digitizing-pen to the center of the search area on the tablet. Then, the background color of the monitor changed as a start cue for the participants to begin searching for the first target. When the digitizing-pen entered a target area, the vibrotactile or visual stimulus was presented, and the sensory stimuli continued until the tip of the digitizing-pen moved out of the target area. If the digitizing-pen remained in the target area for 0.7 s, a beep signal informed the participant of successful target detection. Then, the participants immediately began searching for the next target. Finally, each trial finished when the participant found all six targets. Participants were also instructed to find all six targets as quickly as possible. Therefore, they had to retain spatial information, namely, the target locations and orders of appearance, in the repeated trials. We expected that participants would gradually show efficient searching as a learning effect if they could retain the spatial information of the target under each condition.

Before the neurofeedback training task, the participants performed alternating the tactile and visual conditions a total of 20 trials as successive trials, so 10 trials were performed in each condition (the Pre-WM task). The first trial was randomly assigned as the tactile or visual condition for each participant. As described previously, the target locations for each participant differed between the tactile and visual conditions. Therefore, we can expect no transfer of spatial information from the tactile condition to the visual condition and vice versa. Furthermore, to align the task difficulty between the two conditions, the total distance between all targets (i.e., the sum of the straight-line distances connecting the six targets) was the same for both conditions. The participants were required to hold the two patterns of target spatial information from both conditions simultaneously, so we set the number of trials needed to properly retain the information. In a preliminary experiment, we estimated the number of trials required for the searching cost to finally reach the plateau. After the neurofeedback training task, the participants performed alternating both conditions a total of 20 trials again (the Post-WM task), and the target locations in the Post-WM task were the same as those in the Pre-WM task. Thus, the participants can refer to the target spatial information held during the Pre-WM task to improve searching performance during the Post-WM task. If the current neurofeedback training has a positive effect on individual WM ability, the participants in the Real group would show higher searching performance during the Post-WM task than those in the Sham group.

Analysis

To evaluate individual WM ability, we applied the same index as that in our previous study (Matsumoto et al., 2020). Specifically, we calculated the searching cost based on searching time (Time)

and normalized the movement distance (Dis) in each trial. The searching time was the duration taken to find all of the targets, and the normalized movement distance was the distance moved by the right hand divided by the shortest distance connecting the six targets with a straight line. We defined the "searching cost" using Eq. (1):

$$SearchingCost_i = \sqrt{Time_i^2 + (Dis_i - 1)^2} \quad (1)$$

Where subscript i denotes the trial number (1–10 in each condition). The searching cost in each trial indicates the distance from the (0, 1) coordinate on a Time–Dis plane. We can deduce that the searching cost reflects the individual WM ability because retaining spatial information for hidden targets can optimize the searching movement path on the drawing tablet (i.e., participants can search for the targets in a shorter distance and a shorter searching time). In this scenario, lower searching costs indicate a higher WM ability to efficiently retain the target locations and order of appearance. Note that the first trial in the Pre-WM task was excluded from the statistical analysis, because the participants did not know the target locations during the first trial and needed to search randomly for them without relying on their WM. Thus, the searching costs in the 2nd to 10th trials in the Pre-WM task and the 1st to 10th trials in the Post-WM task were assumed to reflect the individual WM ability.

Furthermore, to characterize the modality dominance in the WM as a qualitative aspect of cognition in individuals, we compared the searching costs between the tactile and visual conditions at the 10th trial in the Pre-WM task. We subtracted the searching cost under the tactile condition from that under the visual condition as an index of modality dominance. Therefore, positive and negative values indicated tactile-dominant (TD) and visual-dominant (VD) individuals, respectively.

Statistical Analysis

The searching costs in the Pre- and Post-WM tasks were analyzed by three-way repeated-measures ANOVA with trial (2nd or 10th trial for the Pre-WM task and 1st or 10th trial for the Post-WM task) and condition (tactile or visual condition) as within-subject factors and neurofeedback training group (Real or Sham group) as a between-subject factor.

Then, to clarify the relationship between individual learning ability and the efficacy of neurofeedback training, we calculated the Pearson correlation coefficients (r) between the amount of decrease in searching cost from the 2nd to the 10th trial and the beta value change. Specifically, we focused on the effect of the performance improvement in the Pre-WM task on the beta value change and the effect of the beta value change on the performance improvement in the Post-WM task.

Furthermore, to evaluate the influence of individual modality dominance in WM on the efficacy of neurofeedback training, we calculated the Pearson correlation coefficient (r) between the beta value change and searching cost in the final trial under the Post-WM task. Then, we compared the beta value change and searching cost in the Post-WM task between TD and VD individuals in the Real group using Wilcoxon rank sum tests. If the individual modality dominance affected the efficacy of the neurofeedback training, the TD and VD individuals were expected to be distributed as distinct clusters on the plane of the beta value change and searching cost. Therefore, we estimated the decision boundary between TD and VD individuals by linear discriminant analysis based on the beta value change and searching cost. We then compared discriminant function values calculated by linear discriminant analysis between TD and VD individuals using a Wilcoxon rank sum test.

RESULTS

Neurofeedback Training Task

Prefrontal Activity

The prefrontal activity patterns in the feedback channels [left prefrontal area (ch.7) and right prefrontal area (ch.11)] and the beta value transitions as estimated by GLM analysis for the oxy-Hb signals are shown in **Figure 2**. With respect to the beta values of the oxy-Hb signals, we found a marked group-difference in the ch.11 activity patterns. The three-way ANOVA revealed significant interactions for group × session [$F(1,38) = 7.40$, $p = 0.0098$, $\eta_p^2 = 0.16$] and group × channel [$F(1,38) = 4.82$, $p = 0.034$, $\eta_p^2 = 0.11$] and a marginally significant interaction for group × session × channel [$F(1,38) = 3.13$, $p = 0.085$, $\eta_p^2 = 0.076$]. *Post hoc* tests on the Real group revealed that the beta value in ch.11 decreased, which was consistent with the neurofeedback training aims [$p = 0.057$, simple-simple main effect test (1st vs. 8th)], and these decreasing trends were focal and limited to the right hemisphere [ch.14: $p = 0.0027$, ch.15: $p = 0.029$; simple-simple main effect test (1st vs. 8th)]. However, there was no notable beta value change in ch.7 [$p = 0.73$; simple-simple main effect test (1st vs. 8th)]. With respect to the Sham group, individuals showed an increasing trend only in the right feedback channel (ch.11: $p = 0.031$, ch.7: $p = 0.13$; simple-simple main effect). The increasing trends in the Sham group were identified in the broad areas including the left and right hemispheres (ch.3, 5, 6, 11, 12, and 14). The beta value transitions for all of the recording channels are shown in **Supplementary Figure 1**, and all of the statistical values from the three-way ANOVA of the beta values are shown in **Supplementary Table 1**.

On the other hand, regarding the beta value of the deoxy-Hb signals, no significant changes were observed compared to the oxy-Hb, as was expected. In both channels, the beta values tended to increase slightly in the Real group and decrease slightly in the Sham group [average beta values: Real group –0.0027 (ch.7, 1st session), –0.0014 (ch.7, 8th session), –0.0024 (ch.11, 1st session), –0.0010 (ch.11, 8th session); Sham group 9.7×10^{-5} (ch.7, 1st session), –0.00055 (ch.7, 8th session), -2.8×10^{-6} (ch.11, 1st session), –0.0035 (ch.11, 8th session)]. All statistical values calculated from the three-way ANOVA of the beta values are shown in **Supplementary Table 2**.

Cognitive Performance

With respect to the appearance order of the six visual stimuli, all participants exceeded the correct answer rate of 80% (mean ± SD: 96.9 ± 3.9, range: 83.3–100%). No significant correlation was

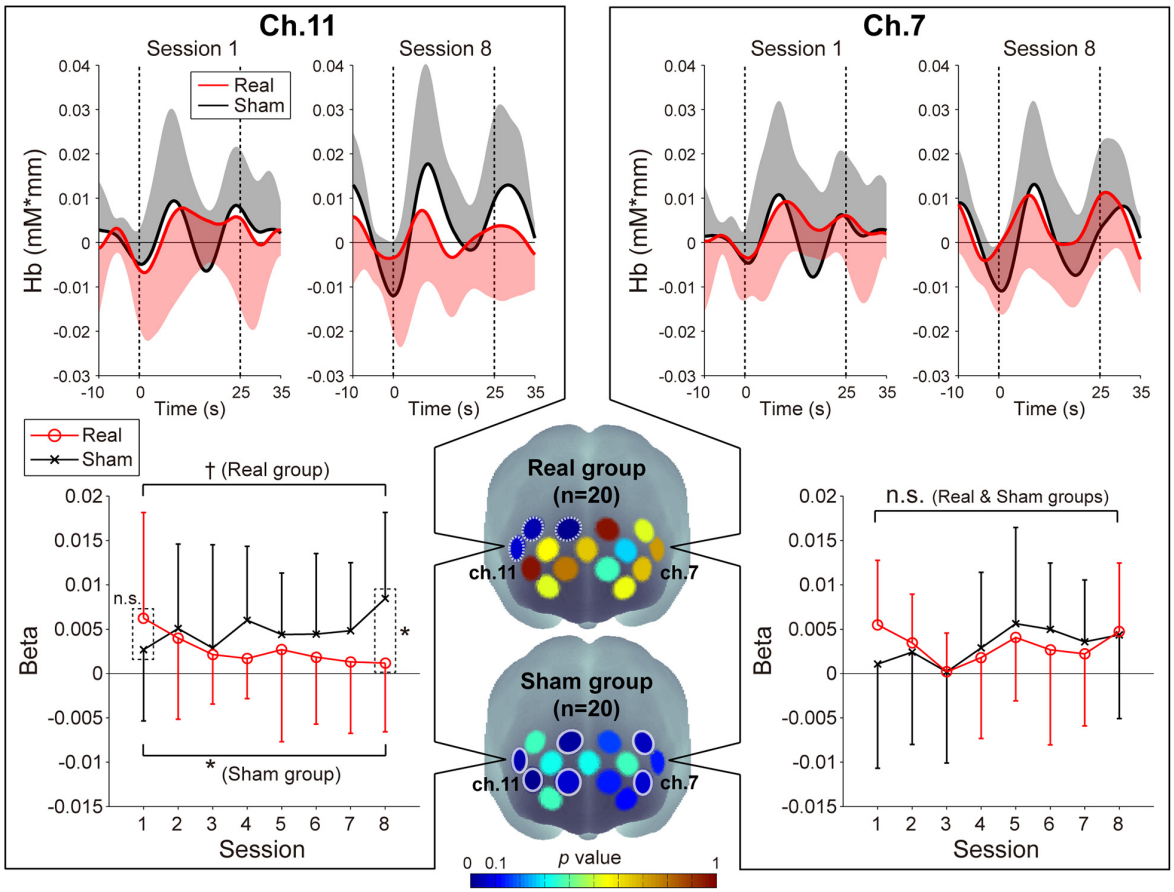

FIGURE 2 | Neuromodulations of the prefrontal cortex activity during the neurofeedback training task. Upper panels: The temporal profiles of the oxy-Hb signals in ch.11 (left panels) and ch.7 (right panels). The red and black lines represent the time courses of the oxy-Hb signals in the Real and Sham groups, respectively. The lighter colored regions around the time course lines denote the standard deviation. The upper or lower directional standard deviation regions are shown for the profiles of the Real and Sham groups, respectively. In ch.11, compared to the first session, the oxy-Hb signal in the final session tended to decrease in the Real group and increase in the Sham group. Lower panels: Beta value transitions in ch.11 (left panels) and ch.7 (right panels). In the first session of ch.11, although there was no significant difference in the beta value between the Real and Sham groups, the Real group showed significantly lower activity than the Sham group at the final session. In contrast, in ch.7, no significant beta value change was observed in both groups. Middle lower 3D brain illustrations: Spatial configurations of the *p*-values from the simple-simple main effect test comparing the beta value in the first session and that in the last session. In the Real group, activities focally decreased in the right hemisphere, including the feedback channel (white dotted circles), while in the Sham group, large activity increases were observed in the bilateral broad region (white solid circles). Error bars denote the standard deviation. $^{\dagger}p < 0.1$, $^{*}p < 0.05$.

observed between the individual differences in cognitive ability for the current cognitive-motor task and the amount of oxy-Hb beta value change from the 1st to the 8th session (ch.7: $r = 0.14$, $p = 0.39$, ch.11: $r = 0.22$, $p = 0.16$).

Target Searching Task

Searching Cost

In the Pre-WM task, all of the participants gradually reduced the searching cost over successive trials. In the Post-WM task involving the same target locations as the Pre-WM task, low searching costs were shown from the first trial, and the participants were able to search more efficiently during repeated trials (**Figure 3A**).

Here, we focused on the difference in searching costs between the Real and Sham groups (**Figure 3B**). In the Pre-WM task, a three-way ANOVA of the searching cost showed only a significant main effect of trial [$F(1,38) = 101.93$, $p = 2.62 \times 10^{-12}$, $\eta_p^2 = 0.73$]. The other factors did not reach the level of statistical significance ($Fs < 2.16$, $ps > 0.15$). These statistical results for the Pre-WM task indicated the baseline WM performance before neurofeedback training was not different between the Real and Sham groups. Next, three-way ANOVA for the Post-WM task revealed a significant main effect of trial [$F(1,38) = 50.36$, $p = 1.82 \times 10^{-8}$, $\eta_p^2 = 0.57$] and a significant two-way interaction of condition × group [$F(1,38) = 13.43$, $p = 7.52 \times 10^{-4}$, $\eta_p^2 = 0.26$]. The other factors did not reach the level of statistical significance ($Fs < 3.27$, $ps > 0.79$). Note that the simple main effect test for the condition × group interaction found that the Real group exhibited significantly lower searching costs than the Sham group under the tactile condition (Tactile condition: $p = 0.0017$, Visual condition: $p = 0.69$). All statistical values

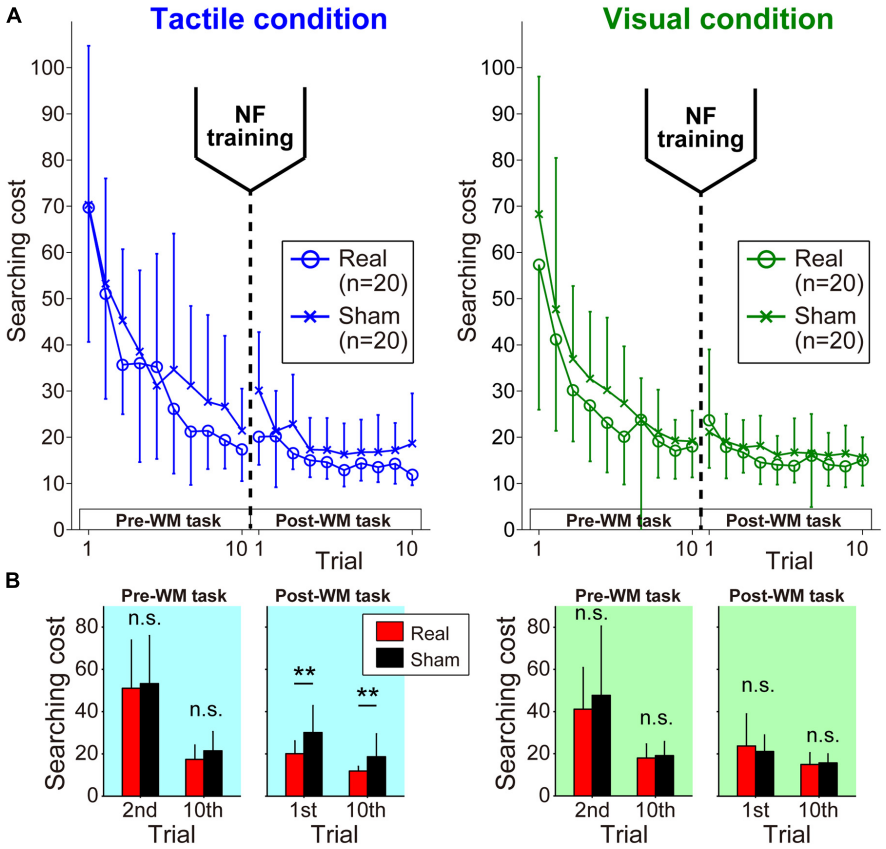

FIGURE 3 | Learning curves during pre- and post-WM tasks. **(A)** In each task phase, the participants successfully reduced the searching cost. **(B)** The Real group showed significantly better performance in the Post-WM task only under the tactile condition. Error bars denote the standard deviation. $^{**}p < 0.01$.

of the three-way ANOVA for the searching cost are shown in **Supplementary Tables 3, 4**.

Individual Modality Dominance in Working Memory

Based on differences in the searching cost between the tactile and visual conditions at the 10th trial in the Pre-WM task (i.e., modality dominance in WM), we labeled the 40 participants as TD or VD individuals. Consistent with our previous study (Matsumoto et al., 2020), we also confirmed that the modality dominance in WM ability varied widely among individuals. Specifically, 10 of the participants in the Real group were labeled as TD-individuals and 10 as VD individuals, respectively, whereas eight members of the Sham group were labeled as TD-individuals and 12 as VD individuals, respectively.

Modality Dominance Dependency in Neurofeedback Training Efficacy

Regarding the tactile condition with significant group difference in the target searching task, neither group showed a significant correlation between the amount of behavioral performance improvement observed in the Pre-WM task (i.e., the amount of decrease in searching cost) and the beta value change (Real group: $r = -0.01$, $p = 0.96$; Sham group: r = 0.29, $p = 0.22$). Similarly, no significant correlation was found between the beta value change and the amount of behavioral performance improvement observed in the Post-WM task (Real group: $r = -0.32$, $p = 0.16$; Sham group: $r = -0.13$, $p = 0.56$).

We then examined whether the neurofeedback training efficacy differed between TD and VD individuals. **Figure 4A** shows the distribution of the beta value changes in ch.11 during neurofeedback training and WM performance under the tactile condition following the neurofeedback training for the 20 individuals in the Real group. Although there was no significant correlation between the intersubject variance of beta value changes and that of searching costs for the entire cohort ($r = -0.14$, $p = 0.55$), the clusters of TD- and VD individuals seemed to be dissociated. Indeed, the TD-individuals showed significantly greater self-regulation of neural activity than the VD individuals ($p = 0.0073$), and the mean searching cost for TD-individuals was lower than that for VD individuals ($p = 0.064$). Based on the distribution of the Real group, the decision function was estimated as $f = -246.4 * \Delta\beta - 1.1 * SC + 12.3$ (*SC* denotes "searching cost"), and the estimated decision boundary revealed that the TD-individuals were located in the lower left of the scatter plot compared with the VD individuals. Thus, as shown in **Figure 4A**, when located in the lower left of the plane, the decision function shows a larger value. A larger decision function value indicates higher neurofeedback training efficacy, reflecting

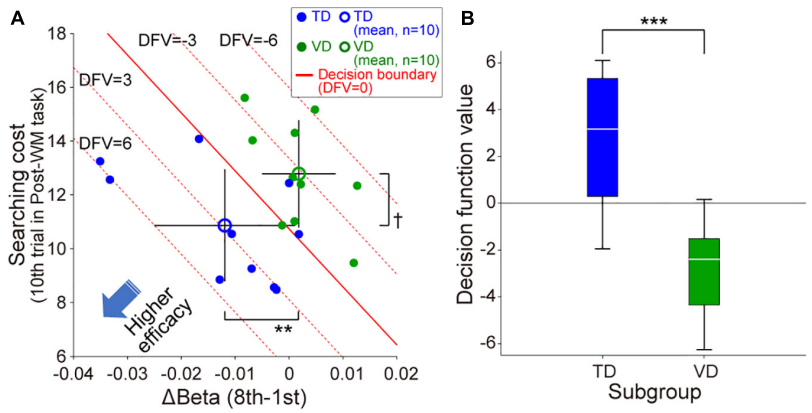

FIGURE 4 | Individual modality dominance dependency of neurofeedback training efficacy in the Real group. **(A)** Scatter plot of the individual neurofeedback training efficacy based on the beta value change in ch.11 and WM task performance in the Post-WM task. TD-individuals are relatively distributed in the lower left of the scatter plot compared with the VD individuals. The red solid line indicates the decision boundary estimated by linear discriminant analysis [i.e., the decision function value (DFV) is zero on this decision boundary]. The red dotted lines represent other DFVs (6, 3, –3, and –6, respectively). Error bars of the mean values denote the standard deviation. **(B)** The decision function values for the TD-individuals were significantly higher than those for the VD individuals. $^{\dagger}p < 0.1$, $^{**}p < 0.01$, $^{***}p < 0.001$.

greater decreases in right prefrontal activities and better WM performance after neurofeedback training. Based on the decision function value, the neurofeedback training of the TD-individuals was more effective than that of the VD individuals ($p = 0.00058$, **Figure 4B**). Note that we also confirmed that the Sham group had relatively lower decision function values than the Real group (-10.4 ± 13.1 SD).

DISCUSSION

The neurofeedback training provided in this study succeeded in lowering neural activity in the right prefrontal area. Moreover, this efficient prefrontal activity facilitated the WM ability to retain internal body information. With respect to the influence of modality dominance on the efficacy of neurofeedback training, the individuals exhibiting tactile dominance showed higher levels of neuromodulation and greater WM performance compared with the individuals with visual dominance. In this study, we focused on the importance of considering individual differences in cognitive function when applying neurofeedback training.

Effectiveness of Functional Near-Infrared Spectroscopy-Based Neurofeedback Training for Working Memory

The fNIRS-based neurofeedback training used in this study is a useful approach to improving self-regulation of the prefrontal area and facilitating WM performance. In particular, lower prefrontal activity contributed to the ability to retain sensory information. The current level of training efficacy is reasonable given the relationship between lower prefrontal activity and higher cognitive skill (Jansma et al., 2001; Ramsey et al., 2004; Koike et al., 2013). Previously, lower levels of activity in the prefrontal and posterior parietal lobes were shown to be associated with an individual optimal attentional strategy, and this led to a higher motor learning effect (Sakurada et al., 2019b), implying that lower prefrontal activity increases the cognitive resource margin due to higher cognitive processing efficiency. As a result, efficient prefrontal activity may lead to improvements in cognitive or motor performance. Although no direct evidence has supported this interpretation, the lower oxy-Hb signals during the current neurofeedback training may provide a hint of the idea of the promoting cognitive margin. Conversely, a number of previous neurofeedback training strategies have been aimed at increasing the prefrontal activity of the target brain area(s) (Wang and Hsieh, 2013; Hsueh et al., 2016). Several studies have reported that increasing prefrontal activity is an effective approach to improving WM ability in the elderly and in patients with stroke (van Asselen et al., 2006; Jones et al., 2015; Stephens and Berryhill, 2016). These previous studies have demonstrated that increasing neural activity by neurofeedback training is also an effective approach to improving specific brain functions. Increasing activity may improve cognitive performance by maximizing active cognitive resources rather than promoting efficiency in cognitive processing within constant resources. The reason for such a discrepancy that both an increase and a decrease of prefrontal activity can contribute to improving WM ability is unclear. However, age and medical history (especially cerebrovascular disease) may be influential factors for the neuromodulation effect. Therefore, in applying neurofeedback training, it is necessary to make an appropriate choice about increasing or decreasing activity according to the target brain function or training population.

The efficacy of the neurofeedback training presented in this study was limited; the prefrontal neuromodulation contributed to the maintenance of vibrotactile rather than visual information. These results might be due to individual differences in cognitive function as characterized by the ability to process internal body information (Sakurada et al., 2017, 2019a; Matsumoto et al., 2020). Specifically, while most participants have a certain

cognitive ability to process visual stimuli, some individuals are less good at processing internal body information such as vibrotactile stimuli. Thus, a greater margin of improvement observed in participants for the tactile condition than for the visual condition might have resulted in significantly better training efficacy for the tactile condition. In addition, note that the protocol included only a short-term training period (i.e., only 1 day), which may have been the reason for the lack of training efficacy seen for the visual stimulation. In a number of previous studies, the neurofeedback training was longer in duration than in the present protocol (Wang and Hsieh, 2013; Hsueh et al., 2016), and longer neurofeedback training might provide greater benefits even for the visual condition. Further investigation is needed on this point.

Modality Dominance Dependency in Neurofeedback Training Efficacy

Sensory modality dominance in cognitive function is an influential factor in determining the efficacy of neurofeedback training. As in our previous study (Matsumoto et al., 2020), we found large intersubject variability in the modality dominance of WM and demonstrated the relationship between the individual modality dominance and degree of neuromodulation and behavioral performance. Furthermore, as no significant correlation was found between the amount of behavioral performance improvement in the target searching task and the neurofeedback training efficacy, the current findings imply that the individual differences in the amount of neuromodulation during neurofeedback training are not affected by the learning ability. In other words, the sensory modality dominance is a more crucial factor than the individual learning ability, as the individual brain characteristics determine the neurofeedback training efficacy. When not only neurophysiological factors such as alpha power or sensorimotor rhythm (Weber et al., 2011; Wan et al., 2014) but also modality dominance are used to characterize the cognitive traits of an individual, it is possible to predict neurofeedback training efficacy more accurately. Note that we confirmed that 75% of participants in the Real group showed the same sensory modality dominance between Pre- and Post-WM tasks (i.e., tactile or visual dominance was maintained), and the other few participants showed different dominance (tactile changed to visual in one participant and visual changed to tactile in four participants). Therefore, although we found relatively more participants who had a change from visual to tactile, the current neurofeedback training would have no effect on reversing the sensory processing ability between tactile and visual modalities to a specific direction.

With regard to the acquisition of "low prefrontal activity," which is the purpose of the current neurofeedback training as a successful training efficacy for the self-regulation of brain activity, 90% of individuals with tactile dominance showed decreased prefrontal activity during training sessions. This rate of success was higher than that seen in previous studies (Alkoby et al., 2018). Conversely, the success rate for the neuromodulation of VD individuals was only 30% in terms of the purpose of decreasing prefrontal activity in the current neurofeedback training. Thus, using the statistical approach of comparing Real and Sham groups, which did not consider individual modality dominance, might result in inaccurate predictions of neurofeedback training efficacy for the entire Real group. However, predicting training efficacy based on individual differences in brain function can contribute to optimizing individual training protocols and improving the training success rate.

Role of the Right Prefrontal Cortex

The efficiency of prefrontal cortex activity was shown to facilitate the WM ability to hold internal body information. Specifically, significant changes in activity were observed during neurofeedback training in the right hemisphere, which corresponds to the DLPFC (Brodmann area 46 and 9) and FPC (Brodmann area 10). The bilateral DLPFC and FPC have been widely recognized as critical structures for WM (Owen et al., 2005). For instance, increasing activity in the right DLPFC with transcranial direct current stimulation led to improved accuracy in memorizing visuospatial locations (Giglia et al., 2014). In addition, the DLPFC and FPC are associated with visual spatial memory (Slotnick and Moo, 2006). Moreover, the left DLPFC and FPC play an important role in processing internal body information such as tactile or somatosensory stimuli. Activity in the left DLPFC correlates with accuracy in discriminating two successive somatosensory stimuli (Pleger et al., 2006). Furthermore, the left FPC is associated with WM representations of haptic information and the integration of spatial and motor components (Kaas et al., 2007). Note that the neurofeedback training protocol used in this study required participants to retain spatial information; therefore, the participants succeeded in self-regulating neural activity in the right prefrontal area that was related to spatial memory. However, we presumed that the modulation of activity in the left DLPFC/FPC failed because the neurofeedback training was based on visual information (i.e., the participants were required to retain spatial information based on visual stimuli). If the neurofeedback training task had required the participants to retain spatial information based on tactile information such as a vibrotactile stimulus, the left DLPFC might also have been successfully modulated. Taken together, the findings suggested that the improvement in the WM ability to hold spatial information with efficient activity levels in the right DLPFC/FPC promoted a behavioral outcome under the tactile condition.

The brain networks between DLPFC and other areas are also important approaches in interpreting the neurofeedback training efficacy. For instance, the prefrontal cortex and posterior parietal cortex are the crucial neural bases for spatial cognition. Persistent activities in these areas reflect not only the maintenance of a WM representation but also the maintenance of a motor intention (Jerde and Curtis, 2013). Furthermore, it has been reported that bilateral primary somatosensory cortices are involved in tactile WM and that DLPFC contributes to bridging the somatosensory cortices from both sides for goal-directed action generation (Zhao et al., 2017). In other words, for the processing WM function, DLPFC forms the frontoparietal network and a network connected with sensory areas. Therefore, the acquisition of efficient prefrontal activity may promote

processing in these other connected areas with the prefrontal cortex, leading to a higher adaptive capacity.

Conclusion

We demonstrate that lowering the activity in the right prefrontal cortex using fNIRS-based neurofeedback training (i.e., improving the efficiency of activity) can facilitate the ability of the WM to retain spatial information. Moreover, individual differences in the sensory modality dominance of the WM, in particular, the ability to hold internal body information, which varies widely among individuals, is an important and newly identified neurophysiological factor that can determine the efficacy of neurofeedback training. Therefore, a customized approach to developing neurofeedback training protocols that are suited to the brain dynamics of the individual will provide more effective neuromodulation methods. Specifically, when applying neurofeedback training to stroke patients with large individual differences in cognitive function, considering the individual sensory modality dominance will provide a tailor-made neurorehabilitation protocol with higher cognitive or motor training effects.

DATA AVAILABILITY STATEMENT

The raw data supporting the conclusions of this article will be made available by the authors, without undue reservation.

ETHICS STATEMENT

The studies involving human participants were reviewed and approved by the Institutional Review Board at Jichi Medical University. The participants provided their written informed consent to participate in this study. Written informed consent was obtained from the individual(s) for the publication of any identifiable images or data included in this article.

AUTHOR CONTRIBUTIONS

TS conceived and designed the experiment, developed the experimental system, wrote the draft of the manuscript, and supervised the study. MM performed the participant experiments. TS and MM analyzed the data. All authors contributed to the discussion of the results, and read and approved the final manuscript.

FUNDING

This research was supported by the Japan Society for the Promotion of Science (JSPS) KAKENHI (15K16366 and 17K13096) and Pfizer Health Research Foundation.

ACKNOWLEDGMENTS

We thank M. Hirai and M. Tetsuka at Jichi Medical University for their help and encouragement.

SUPPLEMENTARY MATERIAL

The Supplementary Material for this article can be found online at: https://www.frontiersin.org/articles/10.3389/fnsys.2022.774475/full#supplementary-material

REFERENCES

Akgül, C. B., Akin, A., and Sankur, B. (2006). Extraction of cognitive activity-related waveforms from functional near-infrared spectroscopy signals. *Med. Biol. Eng. Comput.* 44, 945–958. doi: 10.1007/s11517-006-0116-3

Alkoby, O., Abu-Rmileh, A., Shriki, O., and Todder, D. (2018). Can we predict who will respond to neurofeedback? A review of the inefficacy problem and existing predictors for successful EEG neurofeedback learning. *Neuroscience* 378, 155–164. doi: 10.1016/j.neuroscience.2016.12.050

Cheng, M. Y., Huang, C. J., Chang, Y. K., Koester, D., Schack, T., and Hung, T. M. (2015). Sensorimotor rhythm neurofeedback enhances golf putting performance. *J. Sport Exerc. Psychol.* 37, 626–636. doi: 10.1123/jsep.2015-0166

Diaz Hernandez, L., Rieger, K., and Koenig, T. (2018). Low motivational incongruence predicts successful EEG resting-state neurofeedback performance in healthy adults. *Neuroscience* 378, 146–154. doi: 10.1016/j.neuroscience.2016.12.005

Ehlis, A. C., Barth, B., Hudak, J., Storchak, H., Weber, L., Kimmig, A. C. S., et al. (2018). Near-infrared spectroscopy as a new tool for neurofeedback training: applications in psychiatry and methodological considerations. *Jpn. Psychol. Res.* 60, 225–241. doi: 10.1111/jpr.12225

Escolano, C., Aguilar, M., and Minguez, J. (2011). "EEG-based upper alpha neurofeedback training improves working memory performance," in *Proceedings of the IEEE Engineering in Medicine and Biology Society* (Piscataway, NJ: Institute of Electrical and Electronics Engineers), 2327–2330. doi: 10.1109/IEMBS.2011.6090651

Friston, K. J., Holmes, A. P., Worsley, K. J., Poline, J. P. B., Frith, C. D., and Frackowiak, R. S. J. (1994a). Statistical parametric maps in functional imaging: a general linear approach. *Hum. Brain Mapp.* 2, 189–210. doi: 10.1002/hbm.460020402

Friston, K. J., Jezzard, P., and Turner, R. (1994b). Analysis of functional MRI time-series. *Hum. Brain Mapp.* 1, 153–171. doi: 10.1002/hbm.460010207

Fujimoto, H., Mihara, M., Hattori, N., Hatakenaka, M., Yagura, H., Kawano, T., et al. (2017). Neurofeedback-induced facilitation of the supplementary motor area affects postural stability. *Neurophotonics* 4:045003. doi: 10.1117/1.NPH.4.4.045003

Funane, T., Atsumori, H., Katura, T., Obata, A. N., Sato, H., Tanikawa, Y., et al. (2014). Quantitative evaluation of deep and shallow tissue layers' contribution to fNIRS signal using multi-distance optodes and independent component analysis. *Neuroimage* 85, 150–165. doi: 10.1016/j.neuroimage.2013.02.026

Giglia, G., Brighina, F., Rizzo, S., Puma, A., Indovino, S., Maccora, S., et al. (2014). Anodal transcranial direct current stimulation of the right dorsolateral prefrontal cortex enhances memory-guided responses in a visuospatial working memory task. *Funct. Neurol.* 29, 189–193. doi: 10.11138/FNeur/2014.29.3.189

Hanslmayr, S., Sauseng, P., Doppelmayr, M., Schabus, M., and Klimesch, W. (2005). Increasing individual upper alpha power by neurofeedback improves cognitive performance in human subjects. *Appl. Psychophysiol. Biofeedback* 30, 1–10. doi: 10.1007/s10484-005-2169-8

Hirosaka, R., Katura, T., Kawaguchi, H., Tanaka, N., and Iwamoto, M. (2004). Noisy time-delayed decorrelation and its application to extraction of neural activity from single optical recordings in guinea pigs. *Phys. D Nonlinear Phenom.* 194, 320–332. doi: 10.1016/J.PHYSD.2004.03.005

Hsueh, J.-J., Chen, T.-S., Chen, J.-J., and Shaw, F.-Z. (2016). Neurofeedback training of EEG alpha rhythm enhances episodic and working memory. *Hum. Brain Mapp.* 37, 2662–2675. doi: 10.1002/hbm.23201

Jansma, J. M., Ramsey, N. F., Slagter, H. A., and Kahn, R. S. (2001). Functional anatomical correlates of controlled and automatic processing. *J. Cogn. Neurosci.* 13, 730–743. doi: 10.1162/08989290152541403

Jerde, T. A., and Curtis, C. E. (2013). Maps of space in human frontoparietal cortex. *J. Physiol. Paris* 107, 510–516. doi: 10.1016/j.jphysparis.2013.04.002

Jeunet, C., Glize, B., McGonigal, A., Batail, J. M., and Micoulaud-Franchi, J. A. (2019). Using EEG-based brain computer interface and neurofeedback targeting sensorimotor rhythms to improve motor skills: theoretical background, applications and prospects. *Clin. Neurophysiol.* 49, 125–136. doi: 10.1016/j.neucli.2018.10.068

Jones, K. T., Stephens, J. A., Alam, M., Bikson, M., and Berryhill, M. E. (2015). Longitudinal neurostimulation in older adults improves working memory. *PLoS One* 10:e0121904. doi: 10.1371/journal.pone.0121904

Kaas, A. L., Van Mier, H., and Goebel, R. (2007). The neural correlates of human working memory for haptically explored object orientations. *Cereb. Cortex* 17, 1637–1649. doi: 10.1093/cercor/bhl074

Kadosh, K. C., and Staunton, G. (2019). A systematic review of the psychological factors that influence neurofeedback learning outcomes. *Neuroimage* 185, 545–555. doi: 10.1016/j.neuroimage.2018.10.021

Kober, S. E., Witte, M., Ninaus, M., Neuper, C., and Wood, G. (2013). Learning to modulate one's own brain activity: the effect of spontaneous mental strategies. *Front. Hum. Neurosci.* 7:695. doi: 10.3389/fnhum.2013.00695

Kohl, S. H., Mehler, D. M. A., Lührs, M., Thibault, R. T., Konrad, K., and Sorger, B. (2020). The potential of functional near-infrared spectroscopy-based neurofeedback-A systematic review and recommendations for best practice. *Front. Neurosci.* 14:594. doi: 10.3389/FNINS.2020.00594

Kohno, S., Miyai, I., Seiyama, A., Oda, I., Ishikawa, A., Tsuneishi, S., et al. (2007). Removal of the skin blood flow artifact in functional near-infrared spectroscopic imaging data through independent component analysis. *J. Biomed. Opt.* 12:062111. doi: 10.1117/1.2814249

Koike, S., Takizawa, R., Nishimura, Y., Kinou, M., Kawasaki, S., and Kasai, K. (2013). Reduced but broader prefrontal activity in patients with schizophrenia during n-back working memory tasks: a multi-channel near-infrared spectroscopy study. *J. Psychiatr. Res.* 47, 1240–1246. doi: 10.1016/j.jpsychires.2013.05.009

Landers, M., Wulf, G., Wallmann, H., and Guadagnoli, M. (2005). An external focus of attention attenuates balance impairment in patients with Parkinson's disease who have a fall history. *Physiotherapy* 91, 152–158. doi: 10.1016/j.physio.2004.11.010

Leins, U., Goth, G., Hinterberger, T., Klinger, C., Rumpf, N., and Strehl, U. (2007). Neurofeedback for children with ADHD: a comparison of SCP and Theta/Beta protocols. *Appl. Psychophysiol. Biofeedback* 32, 73–88. doi: 10.1007/s10484-007-9031-0

Matsumoto, M., Sakurada, T., and Yamamoto, S. (2020). Distinct bilateral prefrontal activity patterns associated with the qualitative aspect of working memory characterized by individual sensory modality dominance. *PLoS One* 15:e0238235. doi: 10.1371/journal.pone.0238235

Mihara, M., Hattori, N., Hatakenaka, M., Yagura, H., Kawano, T., Hino, T., et al. (2013). Near-infrared spectroscopy-mediated neurofeedback enhances efficacy of motor imagery-based training in poststroke victims: a pilot study. *Stroke* 44, 1091–1098. doi: 10.1161/STROKEAHA.111.674507

Morren, G., Wolf, U., Lemmerling, P., Wolf, M., Choi, J. H., Gratton, E., et al. (2004). Detection of fast neuronal signals in the motor cortex from functional near infrared spectroscopy measurements using independent component analysis. *Med. Biol. Eng. Comput.* 42, 92–99. doi: 10.1007/bf02351016

Nan, W., Rodrigues, J. P., Ma, J., Qu, X., Wan, F., Mak, P. I., et al. (2012). Individual alpha neurofeedback training effect on short term memory. *Int. J. Psychophysiol.* 86, 83–87. doi: 10.1016/j.ijpsycho.2012.07.182

NITRC (2021). *Homer2: Tool/Resource Info*. Available online at: https://www.nitrc.org/projects/homer2/ (accessed August 1, 2021).

Oldfield, R. C. (1971). The assessment and analysis of handedness: the Edinburgh inventory. *Neuropsychologia* 9, 97–113. doi: 10.1016/0028-3932(71)90067-4

Owen, A. M., McMillan, K. M., Laird, A. R., and Bullmore, E. (2005). N-back working memory paradigm: a meta-analysis of normative functional neuroimaging studies. *Hum. Brain Mapp.* 25, 46–59. doi: 10.1002/hbm.20131

Pleger, B., Ruff, C. C., Blankenburg, F., Bestmann, S., Wiech, K., Stephan, K. E., et al. (2006). Neural coding of tactile decisions in the human prefrontal cortex. *J. Neurosci.* 26, 12596–12601. doi: 10.1523/JNEUROSCI.4275-06.2006

Plichta, M. M., Heinzel, S., Ehlis, A. C., Pauli, P., and Fallgatter, A. J. (2007). Model-based analysis of rapid event-related functional near-infrared spectroscopy (NIRS) data: A parametric validation study. *Neuroimage* 35, 625–634. doi: 10.1016/j.neuroimage.2006.11.028

Ramsey, N. F., Jansma, J. M., Jager, G., Van Raalten, T., and Kahn, R. S. (2004). Neurophysiological factors in human information processing capacity. *Brain* 127, 517–525. doi: 10.1093/brain/awh060

Robertson, E. M., Tormos, J. M., Maeda, F., and Pascual-Leone, A. (2001). The role of the dorsolateral prefrontal cortex during sequence learning is specific for spatial information. *Cereb. Cortex* 11, 628–635. doi: 10.1093/cercor/11.7.628

Rozengurt, R., Barnea, A., Uchida, S., and Levy, D. A. (2016). Theta EEG neurofeedback benefits early consolidation of motor sequence learning. *Psychophysiology* 53, 965–973. doi: 10.1111/psyp.12656

Sakurada, T., Goto, A., Tetsuka, M., Nakajima, T., Morita, M., Yamamoto, S. I., et al. (2019a). Prefrontal activity predicts individual differences in optimal attentional strategy for preventing motor performance decline: a functional near-infrared spectroscopy study. *Neurophotonics* 6:025012. doi: 10.1117/1.NPh.6.2.025012

Sakurada, T., Hirai, M., and Watanabe, E. (2016). Optimization of a motor learning attention-directing strategy based on an individual's motor imagery ability. *Exp. Brain Res.* 234, 301–311. doi: 10.1007/s00221-015-4464-9

Sakurada, T., Hirai, M., and Watanabe, E. (2019b). Individual optimal attentional strategy during implicit motor learning boosts frontoparietal neural processing efficiency: A functional near-infrared spectroscopy study. *Brain Behav.* 9:e01183. doi: 10.1002/brb3.1183

Sakurada, T., Nakajima, T., Morita, M., Hirai, M., and Watanabe, E. (2017). Improved motor performance in patients with acute stroke using the optimal individual attentional strategy. *Sci. Rep.* 7:40592. doi: 10.1038/srep40592

Schroeter, M. L., Bücheler, M. M., Müller, K., Uludağ, K., Obrig, H., Lohmann, G., et al. (2004). Towards a standard analysis for functional near-infrared imaging. *Neuroimage* 21, 283–290. doi: 10.1016/j.neuroimage.2003.09.054

Singh, A. K., Okamoto, M., Dan, H., Jurcak, V., and Dan, I. (2005). Spatial registration of multichannel multi-subject fNIRS data to MNI space without MRI. *Neuroimage* 27, 842–851. doi: 10.1016/j.neuroimage.2005.05.019

Slotnick, S. D., and Moo, L. R. (2006). Prefrontal cortex hemispheric specialization for categorical and coordinate visual spatial memory. *Neuropsychologia* 44, 1560–1568. doi: 10.1016/j.neuropsychologia.2006.01.018

Stephens, J. A., and Berryhill, M. E. (2016). Older adults improve on everyday tasks after working memory training and neurostimulation. *Brain Stimul.* 9, 553–559. doi: 10.1016/j.brs.2016.04.001

Strangman, G., Culver, J. P., Thompson, J. H., and Boas, D. A. (2002). A quantitative comparison of simultaneous BOLD fMRI and NIRS recordings during functional brain activation. *Neuroimage* 17, 719–731. doi: 10.1016/S1053-8119(02)91227-9

Subramanian, L., Hindle, J. V., Johnston, S., Roberts, M. V., Husain, M., Goebe, R., et al. (2011). Real-time functional magnetic resonance imaging neurofeedback for treatment of Parkinson's disease. *J. Neurosci.* 31, 16309–16317. doi: 10.1523/JNEUROSCI.3498-11.2011

Toronov, V., Webb, A., Choi, J. H., Wolf, M., Michalos, A., Gratton, E., et al. (2001). Investigation of human brain hemodynamics by simultaneous near-infrared spectroscopy and functional magnetic resonance imaging. *Med. Phys.* 28, 521–527. doi: 10.1118/1.1354627

van Asselen, M., Kessels, R. P. C., Neggers, S. F. W., Kappelle, L. J., Frijns, C. J. M., and Postma, A. (2006). Brain areas involved in spatial working memory. *Neuropsychologia* 44, 1185–1194. doi: 10.1016/j.neuropsychologia.2005.10.005

Wan, F., Nan, W., Vai, M. I., and Rosa, A. (2014). Resting alpha activity predicts learning ability in alpha neurofeedback. *Front. Hum. Neurosci.* 8:500. doi: 10.3389/fnhum.2014.00500

Wang, J. R., and Hsieh, S. (2013). Neurofeedback training improves attention and working memory performance. *Clin. Neurophysiol.* 124, 2406–2420. doi: 10.1016/j.clinph.2013.05.020

Weber, E., Köberl, A., Frank, S., and Doppelmayr, M. (2011). Predicting successful learning of SMR neurofeedback in healthy participants: methodological considerations. *Appl. Psychophysiol. Biofeedback* 36, 37–45. doi: 10.1007/s10484-010-9142-x

Wulf, G., Landers, M., Lewthwaite, R., and Töllner, T. (2009). External focus instructions reduce postural instability in individuals with Parkinson disease. *Phys. Ther.* 89, 162–168. doi: 10.2522/ptj.20080045

Wulf, G., Töllner, T., and Shea, C. H. (2007). Attentional focus effects as a function of task difficulty. *Res. Q. Exerc. Sport* 78, 257–264. doi: 10.5641/193250307X13082490461183

Xiang, M. Q., Hou, X. H., Liao, B. G., Liao, J. W., and Hu, M. (2018). The effect of neurofeedback training for sport performance in athletes: a meta-analysis. *Psychol. Sport Exerc.* 36, 114–122. doi: 10.1016/J.PSYCHSPORT.2018.02.004

Yu, L., Long, Q., Tang, Y., Yin, S., Chen, Z., Zhu, C., et al. (2021). Improving emotion regulation through real-time neurofeedback training on the right dorsolateral prefrontal cortex: evidence from behavioral and brain network analyses. *Front. Hum. Neurosci.* 15:620342. doi: 10.3389/FNHUM.2021.620342

Zhao, D., Zhou, Y.-D., Bodner, M., and Ku, Y. (2017). The causal role of the prefrontal cortex and somatosensory cortex in tactile working memory. *Cereb. Cortex* 28, 3468–3477. doi: 10.1093/cercor/bhx213

Conflict of Interest: The authors declare that the research was conducted in the absence of any commercial or financial relationships that could be construed as a potential conflict of interest.

Publisher's Note: All claims expressed in this article are solely those of the authors and do not necessarily represent those of their affiliated organizations, or those of the publisher, the editors and the reviewers. Any product that may be evaluated in this article, or claim that may be made by its manufacturer, is not guaranteed or endorsed by the publisher.

Copyright © 2022 Sakurada, Matsumoto and Yamamoto. This is an open-access article distributed under the terms of the Creative Commons Attribution License (CC BY). The use, distribution or reproduction in other forums is permitted, provided the original author(s) and the copyright owner(s) are credited and that the original publication in this journal is cited, in accordance with accepted academic practice. No use, distribution or reproduction is permitted which does not comply with these terms.

frontiers in Human Neuroscience

ORIGINAL RESEARCH
published: 18 February 2022
doi: 10.3389/fnhum.2022.788729

Neuroimaging Examination of Driving Mode Switching Corresponding to Changes in the Driving Environment

Ryu Ohata[1], Kenji Ogawa[2] and Hiroshi Imamizu[1,3,4]**

[1] Department of Psychology, Graduate School of Humanities and Sociology, The University of Tokyo, Tokyo, Japan,
[2] Department of Psychology, Graduate School of Humanities and Human Sciences, Hokkaido University, Sapporo, Japan,
[3] Cognitive Mechanisms Laboratories, Advanced Telecommunications Research Institute International (ATR), Kyoto, Japan,
[4] Research Into Artifacts, Center for Engineering, The University of Tokyo, Tokyo, Japan

Car driving is supported by perceptual, cognitive, and motor skills trained through continuous daily practice. One of the skills that characterize experienced drivers is to detect changes in the driving environment and then flexibly switch their driving modes in response to the changes. Previous functional neuroimaging studies on motor control investigated the mechanisms underlying behaviors adaptive to changes in control properties or parameters of experimental devices such as a computer mouse or a joystick. The switching of multiple internal models mainly engages adaptive behaviors and underlies the interplay between the cerebellum and frontoparietal network (FPN) regions as the neural process. However, it remains unclear whether the neural mechanisms identified in previous motor control studies also underlie practical driving behaviors. In the current study, we measure functional magnetic resonance imaging (fMRI) activities while participants control a realistic driving simulator inside the MRI scanner. Here, the accelerator sensitivity of a virtual car is abruptly changed, requiring participants to respond to this change flexibly to maintain stable driving. We first compare brain activities before and after the sensitivity change. As a result, sensorimotor areas, including the left cerebellum, increase their activities after the sensitivity change. Moreover, after the change, activity significantly increases in the inferior parietal lobe (IPL) and dorsolateral prefrontal cortex (DLPFC), parts of the FPN regions. By contrast, the posterior cingulate cortex, a part of the default mode network, deactivates after the sensitivity change. Our results suggest that the neural bases found in previous experimental studies can serve as the foundation of adaptive driving behaviors. At the same time, this study also highlights the unique contribution of non-motor regions to addressing the high cognitive demands of driving.

Keywords: car driving, motor control, internal model, frontoparietal network, default mode network, salience network

OPEN ACCESS

Edited by:
Belén Rubio Ballester, Institute for Bioengineering of Catalonia (IBEC), Spain

Reviewed by:
Otto Lappi, University of Helsinki, Finland
Isao Nambu, Nagaoka University of Technology, Japan

****Correspondence:***
Ryu Ohata
ryu.oohata@gmail.com
Hiroshi Imamizu
imamizu@gmail.com

Specialty section:
This article was submitted to Motor Neuroscience, a section of the journal Frontiers in Human Neuroscience

Received: *03 October 2021*
Accepted: *31 January 2022*
Published: *18 February 2022*

Citation:
Ohata R, Ogawa K and Imamizu H (2022) Neuroimaging Examination of Driving Mode Switching Corresponding to Changes in the Driving Environment. Front. Hum. Neurosci. 16:788729. doi: 10.3389/fnhum.2022.788729

INTRODUCTION

A car is one of the most advanced devices humans operate in daily life. Accordingly, people need to accumulate a certain amount of driving experience to acquire practical driving skill. One of the skills that characterize experienced drivers is the ability to rapidly detect changes in the driving environment and then flexibly switch the driving mode in response to those changes. For example,

experienced drivers can maintain their car's movement at a constant speed regardless of running uphill or downhill, and they can keep their driving stable after their car suddenly encounters a slippery road surface. Such adaptive driving behaviors are supported by sophisticated computation in the brain. Knowledge of human motor control, which has been extensively studied in the fields of psychology and neuroscience, could play an important role in understanding the neural mechanism underlying adaptive driving behaviors (Lappi, 2015). However, a limited number of studies have investigated the neural basis for driving from the perspective of human motor control.

A neural system that may support flexible switching of driving modes is internal models, which mimick the input–output properties of our body or controlled devices (Wolpert et al., 1995; Wolpert and Kawato, 1998; Kawato, 1999). The brain maintains not a single but multiple internal models employed for different environments or properties of control devices. Previous neuroimaging studies suggest that the motor-related regions, especially in the cerebellum, maintain multiple internal models in a modular manner (Imamizu et al., 2003; Krakauer et al., 2004; Girgenrath et al., 2008). Imamizu et al. (2003) demonstrated that different control properties (velocity vs. rotation control of a computer mouse) were organized with spatially segregated patterns in the cerebellum. The neural mechanism that allows flexible switching of multiple internal models has also been studied (Imamizu et al., 2004; Imamizu and Kawato, 2008). The frontoparietal network (FPN) regions play a key role in internal model switching through interacting with the cerebellar cortex. The roles of the FPN regions are different; the superior parietal lobe (SPL) is involved in switching depending on predictive contextual information, while the dorsolateral prefrontal cortex (DLPFC) and inferior parietal lobe (IPL) contribute to switching driven by sensorimotor feedback (Imamizu and Kawato, 2008). Thus, the acquisition and switching of multiple internal models is fundamental to adaptive motor control. The previous literature on human motor control provides clues to understanding the neural mechanisms involved in flexible switching of driving modes in response to changes in the driving environment. However, previous findings were based on well-controlled experimental paradigms using a computer mouse or a joystick. It remains unknown whether the neural bases found in previous motor control studies also support the skills needed for practical car driving.

In the current study, we investigated the brain regions recruited in car driving using functional magnetic resonance imaging (fMRI). Participants drove a virtual car on a simulated circuit course by controlling custom-made devices, which had a relationship between device control and car behavior (i.e., input-output relationship in driving) similar to that in actual driving, inside the MRI scanner (**Figure 1A**). We defined the ratio of acceleration relative to a stepping-in amount of the accelerator pedal as accelerator sensitivity and abruptly changed this sensitivity at the mid-point of a straight section of the course in order to introduce unpredictable changes in the driving environment into the experimental task. Participants were required to respond to the change quickly while maintaining stable driving. We explored activation/deactivation in response to the change in the level of accelerator sensitivity. We also performed multivoxel pattern analysis (MVPA) to examine the cerebellar activity patterns involved in switching of driving modes in response to different levels of accelerator sensitivity.

MATERIALS AND METHODS

Participants

Twenty-five healthy volunteers (three females) with a mean age of 21.9 years (19–33) participated in our experiment. We recruited volunteers who had obtained a driving license. The mean licensed period was 2.7 years (0.4–15). The mean hours of driving per week was 4.42 (0.25–21) across the participants. We collected data of 10 participants from the University of Tokyo and 15 participants from Hokkaido University. We excluded the data of five participants from analysis due to large head motion during the fMRI scan (for details, see below: *Preprocessing of MRI data*). We eventually analyzed the data of 20 participants (two females) with a mean age of 22.2 years (19–33), a mean licensed period of 2.9 years (0.8–15), and mean driving hours of 4.8 (0.5–21). Written informed consent was obtained from all volunteers in accordance with the latest version of the Declaration of Helsinki. The experimental protocol was approved by the ethics committee at the University of Tokyo.

Experimental Task

Participants drove a virtual car using a driving simulator (CarSim, Virtual Mechanics, Japan) by controlling a custom-made MRI-compatible control device (Leading-Edge Research and Development Accelerator, Inc., Japan; **Figure 1A**). They manipulated two levers serving as brake and accelerator pedals with their left hand while controlling a knob serving as a steering wheel with their right hand. This custom-made device required participants to coordinate different effectors to operate their virtual car, as with actual car driving. Furthermore, the input-output relationship in this virtual car driving was similar to that in actual driving. We customized program codes with MATLAB and Simulink (Mathworks, United States) to set up the ratio of acceleration/deceleration to a stepping-in amount of the brake and accelerator pedals and that of steering angle to the degree of turning the knob.

A virtual car ran on a circuit course consisting of 1,000-m straight sections and 150-m radius curves (**Figure 1B**). Participants were instructed to drive their car while following a preceding car during the task. They were required to keep their car at a 25-m distance from the preceding car as precisely as possible through the straight sections. We incorporated this task to control the timing of changes in accelerator sensitivity and participant driving behavior. Note that participants learned how to keep the target distance during the 5-day practice session before the fMRI experiment (for details, see below). Although following the preceding car was required, they were not required to attend to the distance between the two cars while driving through the curves. At the start of each run, the participant's car was placed at the beginning of a curve (star in **Figure 1B**). The preceding car ran at 40 km/h for the first 400 m of the straight

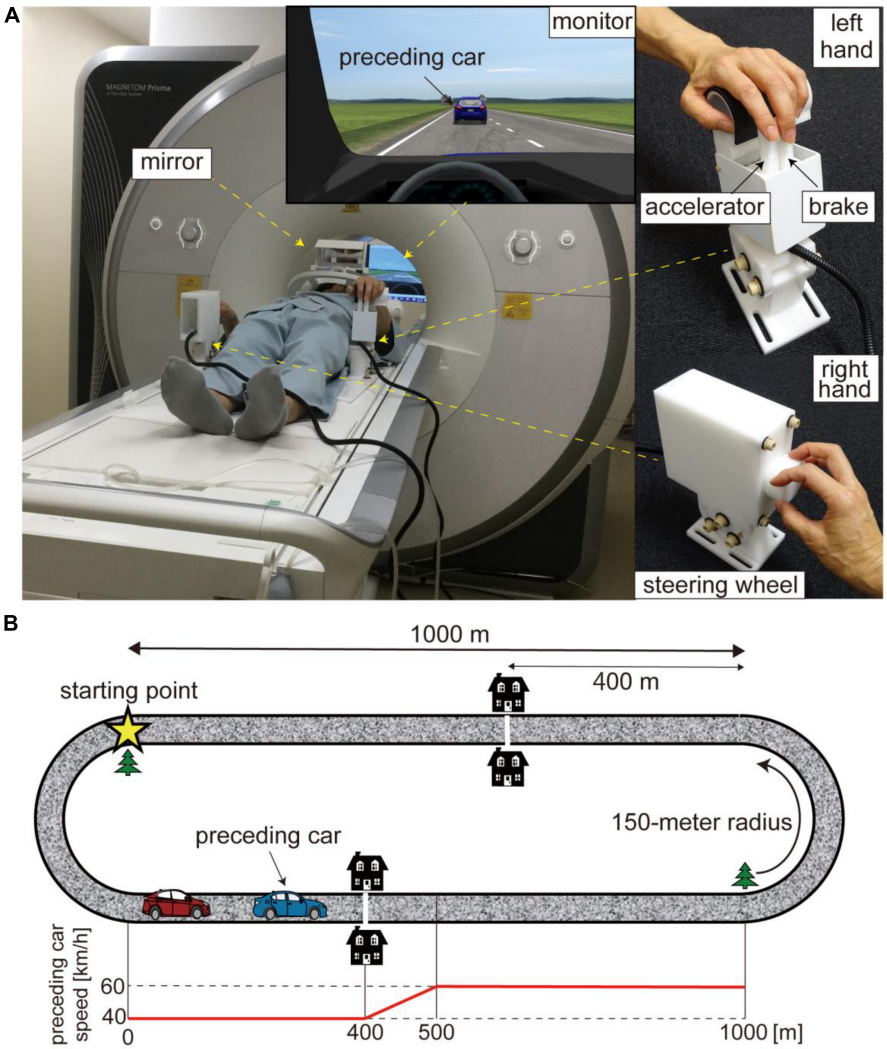

FIGURE 1 | (A) Experimental setup. Participants drove a virtual car while lying on the bed of an MRI scanner. The virtual car was controlled with MRI-compatible customized devices. The two levers manipulated with the index and middle fingers of the left hand served as brake and accelerator pedals (upper right) while the knob controlled with the right hand functioned as a steering wheel (lower right). Participants viewed a monitor via a mirror. **(B)** Driving course. The driving circuit consisted of 1,000-m straight sections and 150-m radius curves. The star denotes the starting point. The preceding car runs at 40 km/h for the first 400 m of the straight section and accelerates from 40 to 60 km/h for the next 100 m. The white line and two houses were displayed to inform participants of the acceleration point of the preceding car. The bottom panel shows the trajectory of the preceding car's speed. The trajectory is aligned to the beginning of the straight section (0 m).

section and accelerated from 40 to 60 km/h for the next 100 m. A white line across the road and two houses were located in the display 400 m from the beginning of the straight section to inform participants of the timing of the acceleration. Then, the preceding car ran on the remaining 500-m straight section at 60 km/h (speed trajectory of preceding car is shown in the bottom panel of **Figure 1B**, see also **Supplementary Movie 1**). We positioned a tree as a landmark of the end of the straight section. The preceding car decelerated from 60 to 40 km/h while going around a curve. We defined the drive through a straight section as one trial. Participants were asked to drive their car four laps in a run, that is, a run consisted of eight trials.

We defined "accelerator sensitivity" as the ratio of the acceleration of a virtual car to the stepping-in amount of an accelerator pedal. We established two levels of accelerator sensitivity (high and low sensitivity), and they abruptly changed from one to the other in the middle of driving on the straight section. Specifically, they changed when the participant's car crossed the 500-m point from the beginning of the straight section. The high-sensitivity level was three times more sensitive than the low-sensitivity level. This means that a car at high sensitivity produced three times greater acceleration than one at low sensitivity with the same amount of stepping pressure on the accelerator pedal. The level of accelerator sensitivity changed in half of the trials, while not in the remainder of the trials. Participants were informed of the initial accelerator sensitivity at the beginning of each run to reduce the difficulty of driving through the first curve.

Experiment Schedule

We asked each participant to conduct a 5-day practice, held outside an MRI scanner, and a 2-day MRI session. Note that the practice and MRI sessions were not always conducted on consecutive days. One participant conducted MRI experiments for 3 days due to his limited schedule. In the practice session, participants drove their car with either low or high sensitivity during an entire run (i.e., without changes in accelerator sensitivity). They practiced driving a car with the two levels of sensitivity in eight runs each throughout the 5-day practice (i.e., 16 runs in total). We instructed them to keep a 25-m distance from the preceding car while driving. A white line was displayed 25 m behind the preceding car as guidance of the target distance in the first eight runs of the practice session. In addition to the 16-run practice, participants conducted the same task as the MRI experiment, in which the accelerator sensitivity changed in the middle of driving on a straight section, for two runs at the end of the practice session. The MRI session consisted of five runs per day, and thus we conducted 10 runs over 2 days. Note that three participants (out of 20) performed nine runs in total due to their limited schedule during the MRI scanning.

Magnetic Resonance Imaging Data Acquisition

A 3 Tesla Magnetom Prisma scanner (Siemens, Germany) with a 64-channel head coil was used to acquire T2*-weighted echo-planar images (EPI). We acquired 435 volumes in each run with a gradient echo EPI sequence under the following scanning parameters: repetition time (TR), 2,000 ms; echo time (TE), 30 ms; flip angle (FA), 80°; field of view (FOV), 192 × 192 mm; matrix, 64 × 64; 32 axial slices; and thickness, 4 mm with a 1-mm gap. T1-weighted (T1w) magnetization-prepared rapid acquisition gradient-echo (MP-RAGE) fine-structural images were obtained with 1 × 1 × 1-mm resolution with a gradient echo sequence [repetition time, 2,250 ms; echo time, 2.98 ms; inversion time (TI), 900 ms; flip angle, 9°; FOV, 256 × 256; 192 axial slices; and slice thickness, 1 mm without gap]. Although we collected MRI data at both the University of Tokyo and Hokkaido University, the scanners (i.e., 3 Tesla Magnetom Prisma, Siemens), number of channels in a coil, and imaging parameters were identical to each other.

Preprocessing of Magnetic Resonance Imaging Data

We performed preprocessing of the MRI data using the pipeline provided by fMRIPrep version 20.2.0 (Esteban et al., 2019). The preprocessing steps included slice-timing correction, motion correction, segmentation of T1-weighted structural images, coregistration, and normalization to Montreal Neurological Institute (MNI) space (for more details on the pipeline).[1] The first five volumes of each run were discarded. We next applied spatial smoothing to the data with a 6-mm full-width at half-maximum (FWHM) Gaussian kernel using SPM 12 (Wellcome Trust Centre for Neuroimaging, London, UCL) on MATLAB. Spatial smoothing was not applied to the data for MVPA, since this might blur the fine-grained information contained in multivoxel activity (Mur et al., 2009).

We calculated frame-wise displacement (FD) based on the six realign parameters as an index of the amount of head motion for each run in each participant (Power et al., 2012). We excluded the runs in which the number of frames with FD > 0.5 mm was over 5% of all frames in a run from further analysis. As a result, the number of runs of five participants' data became less than five; thus, we excluded these five participants from data analysis.

General Linear Model Analysis

We used a general linear model (GLM) analysis to explore activations or deactivations in brain regions after changing the level of accelerator sensitivity. One run included four conditions involving the sensitivity change: (1) change from low to high sensitivity, (2) change from high to low, (3) no change from low sensitivity, and (4) no change from high sensitivity. The following three periods of straight-section driving in each of the four conditions were modeled as separate 12-boxcar regressors that were convolved with a canonical hemodynamic response function: (1) a baseline period (period between the timings when the participant's car passed the 100-m point of the straight section and when the preceding car passed the 400-m point), (2) an acceleration period (period between the timings when the preceding car passed the 400-m point of the straight section and when the participant's car passed the 500-m point), (3) a target period (period between the timings when the participant's car passed the 500-m point of the straight section and when the preceding car passed the 1,000-m point). Note that we excluded the period for the first 100-m driving on the straight section from the baseline period to avoid contamination of the baseline period by the effect of curve driving. The six realign parameters were modeled as a regressor of no interest. We removed low-frequency noise using a high-pass filter with a cut-off period of 128 s. Serial correlations among scans were estimated with an autoregressive model implemented in SPM12.

To explore regions that were activated after the change in the level of accelerator sensitivity, we generated a contrast image using a fixed-effects model. We first generated contrasts of the target vs. baseline period in both the change and no-change conditions. We then subtracted the contrast in the no-change from that in the change condition:

$$\left(Target_c - Baseline_c\right) - \left(Target_n - Baseline_n\right). \quad (1)$$

Here, $Target_c$ and $Baseline_c$ represent the target and baseline periods, respectively, of the change condition. $Target_n$ and $Baseline_n$ represent the target and baseline periods, respectively, of the no-change condition. Next, we explored regions that were deactivated after the sensitivity change by subtracting the contrasts in the opposite direction:

$$\left(Target_n - Baseline_n\right) - \left(Target_c - Baseline_c\right). \quad (2)$$

We also generated contrasts of the acceleration vs. baseline period using trials in both change and no-change conditions together in order to investigate brain regions that were

[1] http://fmriprep.readthedocs.io/en/latest/workflows.html

activated or deactivated in response to acceleration of the preceding car. The contrast images of all participants were taken into the second-level group analysis using a random-effects model of a one-sample *t*-test. We adopted statistical inference with a threshold of $p < 0.05$ [family-wise error (FWE) corrected at cluster level with a cluster-forming threshold of $p < 0.001$]. The anatomical localization was determined according to the automated anatomical labeling (AAL) atlas (Tzourio-Mazoyer et al., 2002).

Multi-Voxel Pattern Analysis

We performed MVPA to classify whether participants were driving the car with either high or low accelerator sensitivity from the fMRI voxel patterns (Haynes and Rees, 2005; Kamitani and Tong, 2005; Norman et al., 2006). We modeled the target period of each of the eight trials as a separate boxcar regressor that was convolved with a canonical hemodynamic response function. The GLM also included the six realign parameters as a regressor of no interest. As a result, eight independently estimated parameters (β-values) per run were yielded for each voxel. We used the parameter estimates within a region of interest (ROI) as the input of a classifier. We used the linear support vector machine (SVM) implemented in LIBSVM[2] with default parameters (a fixed regularization parameter C = 1). Because it has been suggested that the cerebellum is involved in internal models (Shadmehr and Holcomb, 1997; Wolpert et al., 1998; Imamizu et al., 2000; Shadmehr and Krakauer, 2008; Cerminara et al., 2009; Stein, 2009), we targeted the anterior and posterior cerebellum as ROIs, which were anatomically defined with the AAL atlas and split into the left and right sides.

The SVM classifier was trained using the data in the no-change conditions (**Figure 2**, left). We first aimed to examine whether the cerebellar activity exhibited distinct patterns that corresponded to the low- and high-sensitivity levels. We thus applied the trained classifier to the data in the no-change conditions ("test 1" in **Figure 2**, right) and obtained a classification accuracy. Next, we aimed to examine whether the cerebellum switched its activity patterns according to the change in the level of accelerator sensitivity. Here, we applied the classifier trained with the data in the no-change condition to the data in the change conditions ("test 2" in **Figure 2**, right). Here, we allocated high- or low-sensitivity labels to the test data according to sensitivity levels after the sensitivity change (darker colored car in the bottom-right area of **Figure 2**). We expected classification accuracy to be significantly higher than chance level if voxel patterns were switched in response to the sensitivity change. In contrast, we expected classification accuracy to be significantly lower than chance if voxel patterns were unaffected by the change. We performed a leave-one-run-out cross-validation in both "test 1" and "test 2" procedures to estimate classification accuracies as a way to prevent the differences among runs from becoming a confounding factor.

We statistically tested decoding accuracies by calculating z-scores using the following permutation procedure (Langfelder et al., 2011; Shibata et al., 2016; Ohata et al., 2020). We first randomly permuted the correspondence between the fMRI activity and the condition labels (i.e., high vs. low sensitivity) of the training dataset and then applied the classifier trained using the permuted data to the test dataset. We generated 1,000 surrogate classification accuracies by repeating the procedure 1,000 times. We calculated the *z*-scores of the original (without permutation) classification accuracies based on the empirical distribution of the 1,000 surrogate data for each participant separately. We tested the statistical significance of the *z*-scores using a two-sided *t*-test with a threshold of $p < 0.05$.

[2]http://www.csie.ntu.edu.tw/~cjlin/libsvm/

RESULTS

Behavioral Results

Figure 3A shows time courses of the inter-vehicle distance (distance between the preceding and participant's driving cars) for one participant as an example. The time courses were aligned at the possible timing of change in accelerator sensitivity (0 s: timing of passing the 500-m point of the straight section, see **Figure 1B**). His car speeded up after the change in the level of accelerator sensitivity from low to high, resulting in the shortened inter-vehicle distance (**Figure 3A**, left). By contrast, his car slowed down due to the sensitivity change from high to low, resulting in the lengthened distance (**Figure 3A**, right). Once the inter-vehicle distance reached the maximum or minimum, the distance gradually returned to the target distance (25 m). Next, we subtracted the inter-vehicle distance in the no-change condition from that in the change condition at every sampling point. **Figure 3B** shows the difference averaged across participants. The difference in the inter-vehicle distance became largest at 9.6 s (averaged across participants, SD: 4.5 s) after the accelerator sensitivity changed from low to high and at 12.0 s (SD: 6.0) after the sensitivity changed from high to low. Note that the reported mean peak timing is not the same as the peak timing seen in **Figure 3B**; this was because the averaged value was strongly affected by the data of some participants with large values.

General Linear Model Results

We explored the brain regions in which the activities responded to the change in the level of accelerator sensitivity according to the contrast of activity represented in Equation (1). **Figure 4A** shows the regions activated after the sensitivity change (see **Table 1**). We first found significant activation in the left cerebellum, cerebellar lobule VI. We also found activation in the bilateral supramarginal gyrus and right middle frontal gyrus, which are portions of the IPL and DLPFC, respectively. The bilateral anterior insula (AI) and the thalamus, which are the components of the salience network (SN, Seeley et al., 2007; Menon and Uddin, 2010; Seeley, 2019), also activated after the sensitivity change. Next, we explored the deactivations in response to the sensitivity change (**Figure 4B** and **Table 1**) according to the contrast represented in Eq. (2). The posterior cingulate cortex (PCC), which is a component of the default mode network (DMN, Raichle et al., 2001; Buckner et al., 2008), and a part of the right cerebellum (VIIA CrusI) were

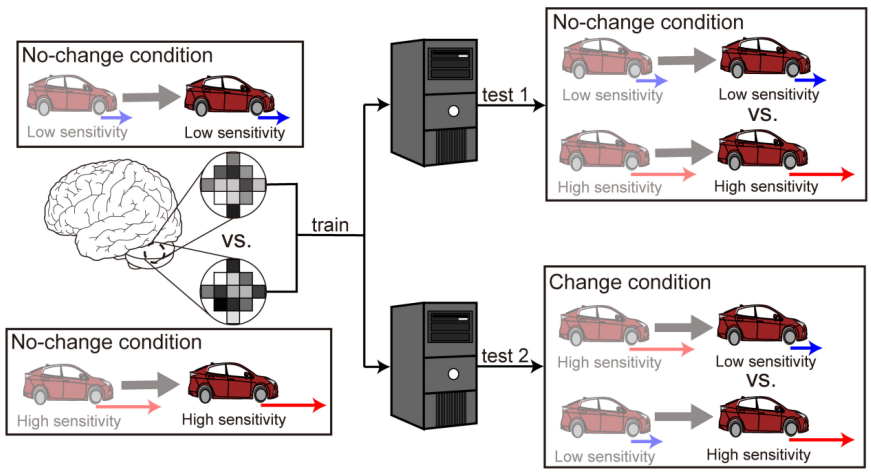

FIGURE 2 | Multivoxel pattern analysis procedure. First, a classifier was trained to discriminate high from low sensitivity using the fMRI data in the no-change conditions. The trained classifier was applied separately to the data in the no-change conditions (denoted as "test 1") and the data in the change conditions (denoted as "test 2"). The anterior and posterior parts of the cerebellum split into the left and right sides are selected as ROIs.

significantly deactivated in response to the change in the level of accelerator sensitivity.

Next, we investigated brain regions activated by the acceleration of the preceding car. We generated the contrast between the acceleration and baseline periods from the data in both change and no-change conditions together. We found that some activated regions overlapped those found in **Figure 4** (**Supplementary Figure 1**). We were concerned that the activities involved in the preceding car's acceleration were, for some reason, different between the change and no-change conditions and affected the activations in response to the change in sensitivity (i.e., **Figure 4**). To assess this concern, we generated the contrasts (acceleration vs. baseline periods) from the data in the change and no-change conditions separately. We compared the two contrasts but found no region showing a significant difference in the contrasts. Therefore, the activations/deactivations shown in **Figure 4** were very unlikely involved in the preceding car acceleration prior to the change in acceleration sensitivity. Finally, we compared the activation related to the accelerator sensitivity changes with those related to the preceding car's acceleration. We found significantly larger activations in the sensorimotor regions, including the left primary motor area and supplementary motor area, and in the bilateral IPL in response to the preceding car's acceleration than in response to the accelerator sensitivity changes (**Supplementary Figure 2**).

Multivoxel Pattern Analysis Results

We first examined whether the cerebellar activity distinguished the two levels of accelerator sensitivity (high vs. low sensitivity) while participants were driving their car. We performed the classification analysis using the data only in the no-change condition ("test 1" in **Figure 2**). As a result, we did not find any significant above-chance classification accuracy in any cerebellar ROI: 50.6% (SD: 12.9%) in the left anterior cerebellum [$t(19) = -0.29$, $p = 0.77$], 48.9% (13.2%) in the right anterior cerebellum [$t(19) = -0.31$, $p = 0.77$], 48.7% (11.5%) in the left posterior cerebellum [$t(19) = -0.50$, $p = 0.62$], and 52.5% (12.0%) in the right posterior cerebellum [$t(19) = 0.99$, $p = 0.33$]. We next applied the classifier trained using the data in the no-change condition to those in the change condition ("test 2" in **Figure 2**). The accuracy in no ROI was significantly higher than the chance level: 48.9% (7.02%) in the left anterior cerebellum [$t(19) = -0.74$, $p = 0.47$], 51.8% (7.03%) in the right anterior cerebellum [$t(19) = -0.97$, $p = 0.34$], 47.8% (8.76%) in the left posterior cerebellum [$t(19) = -1.26$, $p = 0.22$], and 51.5% (8.92%) in the right posterior cerebellum [$t(19) = 0.83$, $p = 0.42$]. Accordingly, contrary to our expectation, the cerebellum did not maintain distinct activity patterns corresponding to the two levels of accelerator sensitivity or switch patterns in response to the sensitivity change.

DISCUSSION

The current fMRI study investigated the neural bases supporting driving behaviors to flexibly switch driving modes in response to changes in the driving environment. We first found the activities in the sensorimotor area, including the cerebellum, the FPN, and SN regions, that increase in response to abrupt changes in the accelerator sensitivity of a virtual car (**Figure 4A**). By contrast, we found deactivation in the PCC, a component of the DMN, after the change (**Figure 4B**). The GLM results suggest that the sensorimotor system is engaged in adaptive behaviors for car driving. Our results also highlight the role of the large-scale networks related to saliency, attention, and cognition in adaptive driving behaviors.

Drivers are required to construct and switch multiple driving modes in response to changes in driving environments. Internal models may be the key mechanism underlying such adaptive driving behavior. Previous studies, in which participants controlled a computer mouse or joystick, demonstrated the

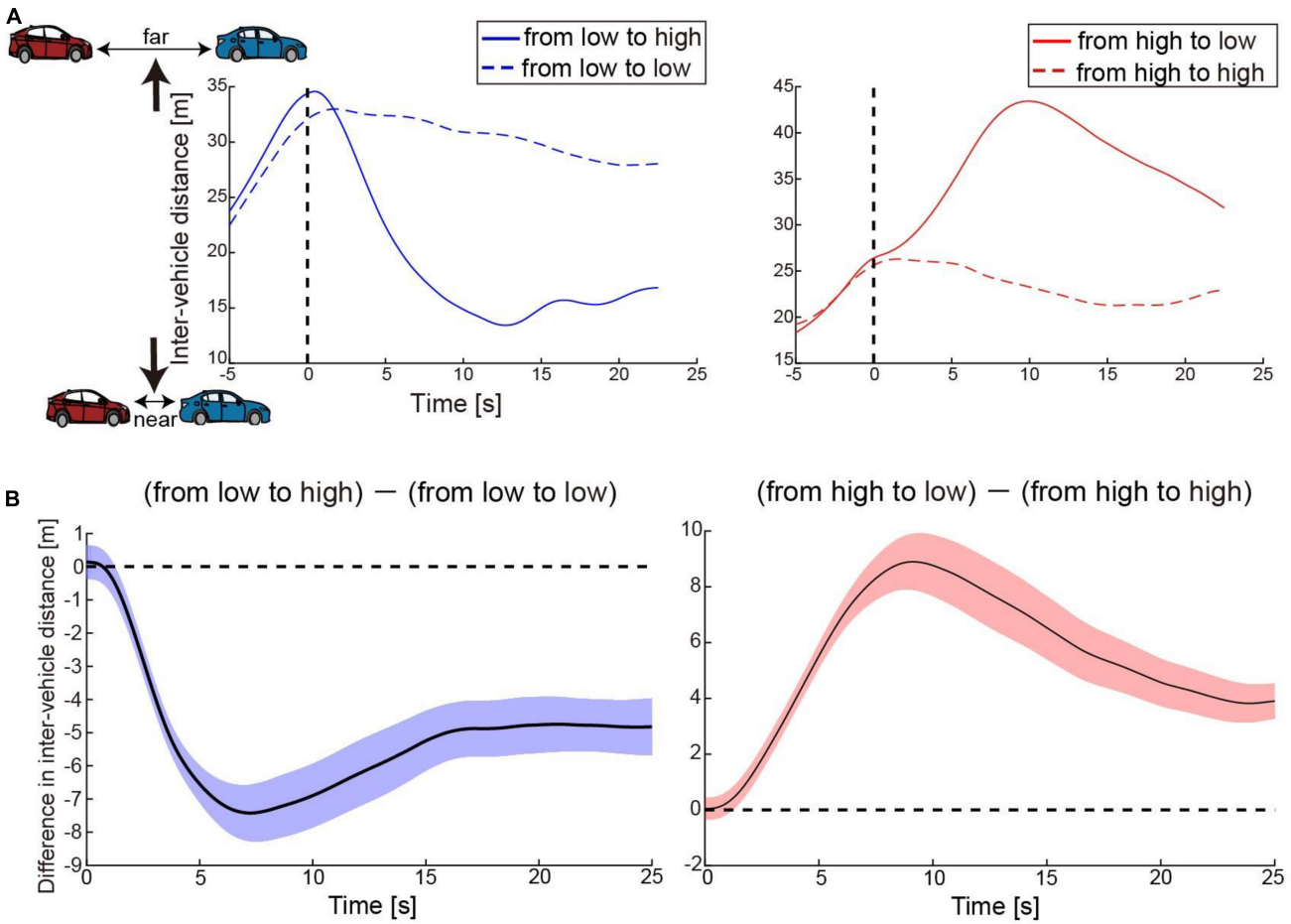

FIGURE 3 | Behavior results. **(A)** Time courses of inter-vehicle distance for one participant as an example. The solid blue and red lines denote time courses of the distance in the conditions when accelerator sensitivity changed from low to high and from high to low, respectively. By contrast, the dotted blue and red lines indicate time courses of the distance in the conditions where the sensitivity remained low or high, respectively. The distance was averaged across trials in each condition. The vertical dotted line denotes the timing at which his car passed the 500-m point of the straight section. In the change conditions, the level of accelerator sensitivity changed at this timing. **(B)** Time courses of difference in inter-vehicle distance between change and no-change conditions. The values were averaged across participants at every moment. Colored shaded areas indicate 95% confidence intervals.

cerebellar activity that reflects the acquisition of internal models (Imamizu et al., 2000, 2003; Seidler and Noll, 2008; Kim et al., 2015). The current driving study also reveals that the activity in the left cerebellar lobule VI significantly increases after the change in the level of accelerator sensitivity (**Figure 4A**). Importantly, the activated area found in our study largely overlaps that involved in velocity control, not positional control, of a cursor manipulated with a computer mouse (Imamizu et al., 2003). This finding suggests the possibility that internal models for the same control property are allocated to the activity in the same cerebellar region regardless of the type of control device.

We also found activation in the DLPFC, IPL, and insula (**Figure 4A**), all of which were reported to be associated with internal model switching (Imamizu et al., 2004). It has been suggested that the DLPFC and IPL contribute to internal model switching driven by the error between predicted and actual sensorimotor feedback (postdictive switching, Imamizu and Kawato, 2008). Forward internal models predict sensorimotor feedback from the efference copy of a motor command and are influential in the comparison between predicted and actual feedback (Wolpert et al., 1995; Miall and Wolpert, 1996; Blakemore et al., 2000). In our task, the level of accelerator sensitivity randomly changed in a trial-by-trial manner so that internal models could not be switched in advance of the sensitivity change (i.e., predictive switching). Thus, the model optimized for the environment before the sensitivity change addressed the new environment, resulting in a large prediction error. Our results suggest that such prediction error functioned as a signal of the change in the driving environment and prompted the brain to switch internal models postdictively.

Although the GLM results suggest the possibility of internal model switching, the MVPA results show neither distinction nor switching of cerebellar activity patterns during car driving. One possible reason for this unexpected result is that internal model switching is not necessarily an optimal strategy for every participant to address changes in the driving environment.

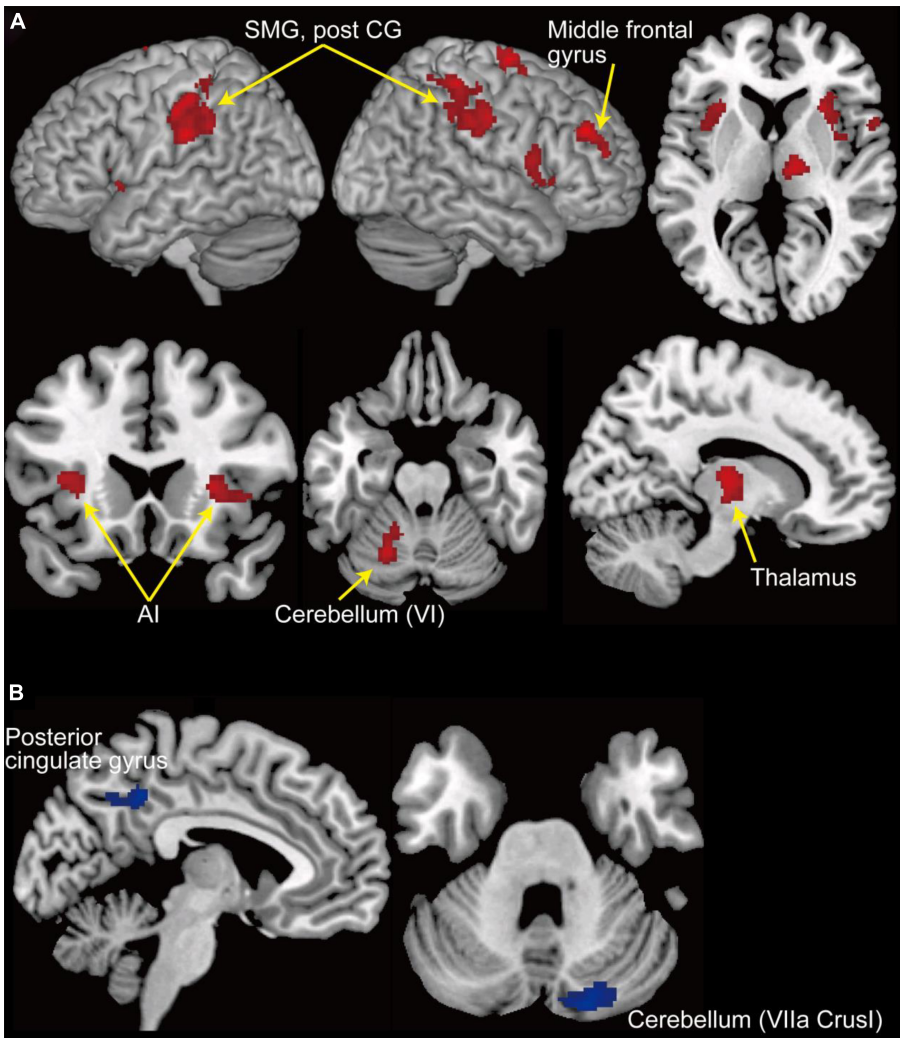

FIGURE 4 | GLM results. **(A)** Clusters of activation (in red) that significantly increased after change in the level of accelerator sensitivity. **(B)** Clusters of activation (in blue) that significantly decreased after change in the level of accelerator sensitivity. A threshold at $p < 0.05$ (FWE-corrected at cluster level with a cluster-forming threshold of $p < 0.001$) was set for statistical testing. AI, anterior insula; Post CG, post central gyrus; SMG, supramarginal gyrus.

Driving engages executive cognitive functions, such as attentional control, cognitive inhibition, and cognitive flexibility (Navarro et al., 2018). Some participants might dominantly exert cognitive strategies in which such executive functions are employed rather than internal model switching. The driving simulator used in this study did not provide a perfectly realistic driving experience. The difference between real and simulated driving experiences might encourage participants to develop cognitive strategies uniquely optimal to the simulated environment. We found a large variance in the classification accuracies across participants, which might imply individual differences in their strategies. Another possible reason is the difficulty of controlling participant driving behavior in the driving simulator. We could control participant driving behavior to some extent by requiring them to follow the preceding car at a constant distance. However, there was no measure to monitor whether and when participants switched their driving modes. Hence, it might be possible to use the trials in which participants could not switch their driving modes, or the switching timing was much delayed, for MVPA.

We also found deactivation in the PCC in response to the change in the level of accelerator sensitivity (**Figure 4B**). The PCC is a part of the DMN, a set of coordinated brain regions that shows more activation at rest than during cognitive demand tasks (Raichle et al., 2001; Buckner et al., 2008). The DMN regions respond to non-stimulus induced or internally oriented thoughts such as mind-wandering (Andrews-Hanna et al., 2010; Raichle, 2015), and thus the activation could interfere with task performance (Eichele et al., 2008; Hinds et al., 2013). The change in the driving environment possibly required participants to switch their cognitive modes of car-driving in addition to internal model switching. The deactivation in the PCC encouraged them to switch such cognitive modes quickly. The activities in the DMN regions are typically anticorrelated to those in the FPN regions (Fox et al., 2005, 2009). Previous studies suggest the

TABLE 1 | Summary of GLM results.

Brain region	Side	Cluster size	*t*-value at peak	MNI coordinates(Peak voxel)		
				x	y	z
Activate						
1. Thalamus	Right	282	6.53	16	−16	12
2. Supramarginal gyrus	Left	647	6.06	−66	−26	28
3. Superior frontal gyrus	Right	208	6.05	24	−4	72
4. Middle frontal gyrus	Right	156	6.00	36	40	32
5. Postcentral gyrus	Right	624	5.91	38	−34	58
6. Cerebellum (VI)	Left	190	5.46	−20	−60	−22
7. Insula	Right	290	5.14	28	20	6
8. Insula	Left	204	4.94	−30	16	12
9. Opercular part of inferior frontal gyrus	Right	144	4.71	54	10	14
Deactivate						
1. Cerebellum (VIIa Crus1)	Right	252	6.21	16	−84	−34
2. Posterior cingulate gyrus	Left	158	5.00	−2	−44	42

A threshold at $p < 0.05$ (FWE-corrected at cluster level with a cluster-forming threshold of $p < 0.001$) was set for statistical testing.

crucial role of the SN in switching this balance between the FPN and DMN (Sridharan et al., 2008; Menon and Uddin, 2010; Uddin, 2015). Importantly, the current study found significant activation in the bilateral AI and thalamus, parts of the SN (**Figure 4A**). Our results imply the involvement of the large-scale networks (FPN, DMN, and SN) and their switching mechanism in adaptive driving behavior, which was a possible candidate of unique neural features for car driving.

Previous neuroimaging studies have identified multiple brain regions involved in different aspects of car driving using driving simulators or video games (Walter et al., 2001; Calhoun et al., 2002; Uchiyama et al., 2003; Horikawa et al., 2005; Spiers and Maguire, 2007; Okamoto et al., 2020; see also review and meta-analysis studies in Lappi, 2015; Navarro et al., 2018). The neural correlates of driving reported in the previous literature overlap those found in the current study. Calhoun et al. (2002), having identified functional co-activation patterns using independent component analysis, related the cerebellar and occipital activation to complex visuomotor integration during driving. This study also found that the activation in the DMN regions decreased during driving and was negatively correlated with driving speed, suggesting an association with the vigilance function during driving. In addition, Spiers and Maguire (2007) suggested that the activations in the cerebellum, posterior parietal cortex, and SN regions were associated with unprepared actions such as swerving and avoiding collisions. These regions were considered necessary for responding to abrupt events. Thus, the brain regions found in the current study reflected the suggestions from previous findings. Meanwhile, our study aimed at more specific functions for driving (i.e., switching of multiple driving modes) than those examined in previous studies in order to elucidate the detailed role of each region from the perspective of adaptive motor control.

Although we obtained findings suggesting that adaptive driving behaviors were involved in internal model switching, it is still open to debate whether the brain allocates different internal models to different parameters with the same type of control property (e.g., different angles in rotation control or different gains in velocity control). Hence, there remains the possibility that the brain achieved switching of driving mode without changing internal models in the current experimental setting. One possible scenario could be the brain using a single internal model for controlling a virtual car and adjusting the control parameters of the internal model in response to changes in the driving environment. Consequently, as a limitation of this study, we cannot deny the possibility that the internal models are not switched.

As mentioned above, our driving simulator cannot represent a perfectly realistic driving experience. In particular, the device used in this study required participants to control steering and acceleration/deceleration using different effectors from those used in actual driving (i.e., steering control by turning a steering knob with the right hand vs. by manipulating a steering wheel with both hands; acceleration/brake control by pushing two pedals with the left index finger vs. by stepping on two pedals with the right foot). We assume that the skill targeted in the current study, that is, flexibly switching different driving modes in response to changes in the driving environment, is supported by higher-order motor/cognitive functions that can be generalized regardless of the effectors used. However, we still cannot deny the possibility that the target skill is dependent on control devices. Therefore, it might also be possible that we observed brain activities that were unique to the current setup. The best approach to overcoming this limitation is to develop a device that can measure brain activity, with comparable precision to an fMRI scanner, in a real car. Because the current technology cannot offer such devices, we translated driving behaviors into possible naturalistic behaviors inside an fMRI scanner while minimizing head movements (realistic steering handle and acceleration and brake pedals manipulated in the MRI environment;

Kim et al., 2020; Okamoto et al., 2020). In our simulator, the accelerator and brake pedals were replaced by hand levers while the steering wheel was replaced by a knob dial. Such substitutions are common in the controllers of remote-control cars. Future studies are needed to improve both the driving simulator and neuroimaging devices in order to measure brain activities in more realistic driving experiences than that of the current study.

The current study targeted adaptive driving behaviors determined by sensorimotor feedback (i.e., switching of driving modes in response to changes in the driving environment postdictively). However, experienced drivers also possess the skill of anticipating future changes and preparing for possible responses to environmental changes. Unfortunately, our experimental design did not allow us to investigate such predictive aspects of driving skills. To further probe comprehensive driving skills, we need future studies on predictive switching of driving modes by introducing into experimental tasks various environmental changes that participants can anticipate in advance (e.g., an uphill incline that decelerates car speed).

In sum, this study searched for the neural substrates that support flexibly switching of different driving modes in car driving. Our findings demonstrate that the neural bases found in previous motor control studies, especially the cerebellum involving internal models and the DLPFC, IPL, and insula for switching of different internal models, are also fundamental to the adaptive behaviors of switching driving modes. Furthermore, this study also highlighted the involvement of the large-scale brain network in addressing cognitive demands for driving, suggesting a possible neural process unique to car driving.

DATA AVAILABILITY STATEMENT

The raw data supporting the conclusions of this article will be made available by the authors, without undue reservation.

ETHICS STATEMENT

The studies involving human participants were reviewed and approved by The University of Tokyo. The patients/participants provided their written informed consent to participate in this study.

AUTHOR CONTRIBUTIONS

RO and HI designed the study and wrote the manuscript. RO and KO collected the data. RO analyzed the data. KO reviewed and approved the final version of the manuscript. All authors contributed to the article and approved the submitted version.

FUNDING

This study was supported by a TOYOTA Joint Research Grant. HI was partially supported by JSPS KAKENHI (Grant Nos. 19H05725 and 21H03780).

ACKNOWLEDGMENTS

We are grateful to Terumasa Endo, Satoshi Inoue, and Takeshi Hamaguchi (TOYOTA Motor Corporation) for their help in the experimental setup and insightful discussions about the results. We also thank Shuhei Nishida and Yusuke Haruki for their assistance in collecting the data.

SUPPLEMENTARY MATERIAL

The Supplementary Material for this article can be found online at: https://www.frontiersin.org/articles/10.3389/fnhum.2022.788729/full#supplementary-material

REFERENCES

Andrews-Hanna, J. R., Reidler, J. S., Huang, C., and Buckner, R. L. (2010). Evidence for the default network's role in spontaneous cognition. *J. Neurophysiol.* 104, 322–335. doi: 10.1152/jn.00830.2009

Blakemore, S. J., Wolpert, D., and Frith, C. (2000). Why can't you tickle yourself? *Neuroreport* 11, R11–R16. doi: 10.1097/00001756-200008030-00002

Buckner, R. L., Andrews-Hanna, J. R., and Schacter, D. L. (2008). The brain's default network: anatomy, function, and relevance to disease. *Ann. N. Y. Acad. Sci.* 1124, 1–38. doi: 10.1196/annals.1440.011

Calhoun, V. D., Pekar, J. J., McGinty, V. B., Adali, T., Watson, T. D., and Pearlson, G. D. (2002). Different activation dynamics in multiple neural systems during simulated driving. *Hum. Brain Mapp.* 16, 158–167. doi: 10.1002/hbm.10032

Cerminara, N. L., Apps, R., and Marple-Horvat, D. E. (2009). An internal model of a moving visual target in the lateral cerebellum. *J. Physiol.* 587, 429–442. doi: 10.1113/jphysiol.2008.163337

Eichele, T., Debener, S., Calhoun, V. D., Specht, K., Engel, A. K., Hugdahl, K., et al. (2008). Prediction of human errors by maladaptive changes in event-related brain networks. *Proc. Natl. Acad. Sci. U.S.A.* 105, 6173–6178. doi: 10.1073/pnas.0708965105

Esteban, O., Markiewicz, C. J., Blair, R. W., Moodie, C. A., Isik, A. I., Erramuzpe, A., et al. (2019). fMRIPrep: a robust preprocessing pipeline for functional MRI. *Nat. Methods* 16, 111–116. doi: 10.1038/s41592-018-0235-4

Fox, M. D., Snyder, A. Z., Vincent, J. L., Corbetta, M., Van Essen, D. C., and Raichle, M. E. (2005). The human brain is intrinsically organized into dynamic, anticorrelated functional networks. *Proc. Natl. Acad. Sci. U.S.A.* 102, 9673–9678. doi: 10.1073/pnas.0504136102

Fox, M. D., Zhang, D., Snyder, A. Z., and Raichle, M. E. (2009). The global signal and observed anticorrelated resting state brain networks. *J. Neurophysiol.* 101, 3270–3283. doi: 10.1152/jn.90777.2008

Girgenrath, M., Bock, O., and Seitz, R. J. (2008). An fMRI study of brain activation in a visual adaptation task: activation limited to sensory guidance. *Exp. Brain Res.* 184, 561–569. doi: 10.1007/s00221-007-1124-8

Haynes, J. D., and Rees, G. (2005). Predicting the orientation of invisible stimuli from activity in human primary visual cortex. *Nat. Neurosci.* 8, 686–691. doi: 10.1038/nn1445

Hinds, O., Thompson, T. W., Ghosh, S., Yoo, J. J., Whitfield-Gabrieli, S., Triantafyllou, C., et al. (2013). Roles of default-mode network and supplementary motor area in human vigilance performance: evidence from real-time fMRI. *J. Neurophysiol.* 109, 1250–1258. doi: 10.1152/jn.00533.2011

Horikawa, E., Okamura, N., Tashiro, M., Sakurada, Y., Maruyama, M., Arai, H., et al. (2005). The neural correlates of driving performance identified using

positron emission tomography. *Brain Cogn.* 58, 166–171. doi: 10.1016/j.bandc.2004.10.002

Imamizu, H., and Kawato, M. (2008). Neural correlates of predictive and postdictive switching mechanisms for internal models. *J. Neurosci.* 28, 10751–10765. doi: 10.1523/JNEUROSCI.1106-08.2008

Imamizu, H., Kuroda, T., Miyauchi, S., Yoshioka, T., and Kawato, M. (2003). Modular organization of internal models of tools in the human cerebellum. *Proc. Natl. Acad. Sci. U.S.A.* 100, 5461–5466. doi: 10.1073/pnas.0835746100

Imamizu, H., Kuroda, T., Yoshioka, T., and Kawato, M. (2004). Functional magnetic resonance imaging examination of two modular architectures for switching multiple internal models. *J. Neurosci.* 24, 1173–1181. doi: 10.1523/JNEUROSCI.4011-03.2004

Imamizu, H., Miyauchi, S., Tamada, T., Sasaki, Y., Takino, R., Putz, B., et al. (2000). Human cerebellar activity reflecting an acquired internal model of a new tool. *Nature* 403, 192–195. doi: 10.1038/35003194

Kamitani, Y., and Tong, F. (2005). Decoding the visual and subjective contents of the human brain. *Nat. Neurosci.* 8, 679–685. doi: 10.1038/nn1444

Kawato, M. (1999). Internal models for motor control and trajectory planning. *Curr. Opin. Neurobiol.* 9, 718–727. doi: 10.1016/s0959-4388(99)00028-8

Kim, H. S., Mun, K. R., Choi, M. H., and Chung, S. C. (2020). Development of an fMRI-compatible driving simulator with simultaneous measurement of physiological and kinematic signals: the multi-biosignal measurement system for driving (MMSD). *Technol. Health Care* 28, 335–345. doi: 10.3233/THC-209034

Kim, S., Ogawa, K., Lv, J., Schweighofer, N., and Imamizu, H. (2015). Neural substrates related to motor memory with multiple timescales in sensorimotor adaptation. *PLoS Biol.* 13:e1002312. doi: 10.1371/journal.pbio.1002312

Krakauer, J. W., Ghilardi, M. F., Mentis, M., Barnes, A., Veytsman, M., Eidelberg, D., et al. (2004). Differential cortical and subcortical activations in learning rotations and gains for reaching: a PET study. *J. Neurophysiol.* 91, 924–933. doi: 10.1152/jn.00675.2003

Langfelder, P., Luo, R., Oldham, M. C., and Horvath, S. (2011). Is my network module preserved and reproducible? *PLoS Comput. Biol.* 7:e1001057. doi: 10.1371/journal.pcbi.1001057

Lappi, O. (2015). The racer's brain–how domain expertise is reflected in the neural substrates of driving. *Front. Hum. Neurosci.* 9:635. doi: 10.3389/fnhum.2015.00635

Menon, V., and Uddin, L. Q. (2010). Saliency, switching, attention and control: a network model of insula function. *Brain Struct. Funct.* 214, 655–667. doi: 10.1007/s00429-010-0262-0

Miall, R. C., and Wolpert, D. M. (1996). Forward models for physiological motor control. *Neural Netw.* 9, 1265–1279. doi: 10.1016/S0893-6080(96)00035-4

Mur, M., Bandettini, P. A., and Kriegeskorte, N. (2009). Revealing representational content with pattern-information fMRI–an introductory guide. *Soc. Cogn. Affect. Neurosci.* 4, 101–109. doi: 10.1093/scan/nsn044

Navarro, J., Reynaud, E., and Osiurak, F. (2018). Neuroergonomics of car driving: a critical meta-analysis of neuroimaging data on the human brain behind the wheel. *Neurosci. Biobehav. Rev.* 95, 464–479. doi: 10.1016/j.neubiorev.2018.10.016

Norman, K. A., Polyn, S. M., Detre, G. J., and Haxby, J. V. (2006). Beyond mind-reading: multi-voxel pattern analysis of fMRI data. *Trends Cogn. Sci.* 10, 424–430. doi: 10.1016/j.tics.2006.07.005

Ohata, R., Asai, T., Kadota, H., Shigemasu, H., Ogawa, K., and Imamizu, H. (2020). Sense of agency beyond sensorimotor process: decoding self-other action attribution in the human brain. *Cereb. Cortex* 30, 4076–4091. doi: 10.1093/cercor/bhaa028

Okamoto, Y., Sasaoka, T., Sadato, N., Fukunaga, M., Yamamoto, T., Soh, Z., et al. (2020). Is human brain activity during driving operations modulated by the viscoelastic characteristics of a steering wheel?: An fMRI study. *IEEE Access* 8, 215073–215090. doi: 10.1109/access.2020.3040231

Power, J. D., Barnes, K. A., Snyder, A. Z., Schlaggar, B. L., and Petersen, S. E. (2012). Spurious but systematic correlations in functional connectivity MRI networks arise from subject motion. *Neuroimage* 59, 2142–2154. doi: 10.1016/j.neuroimage.2011.10.018

Raichle, M. E. (2015). The brain's default mode network. *Annu. Rev. Neurosci.* 38, 433–447. doi: 10.1146/annurev-neuro-071013-014030

Raichle, M. E., MacLeod, A. M., Snyder, A. Z., Powers, W. J., Gusnard, D. A., and Shulman, G. L. (2001). A default mode of brain function. *Proc. Natl. Acad. Sci. U.S.A.* 98, 676–682. doi: 10.1073/pnas.98.2.676

Seeley, W. W. (2019). The salience network: a neural system for perceiving and responding to homeostatic demands. *J. Neurosci.* 39, 9878–9882. doi: 10.1523/jneurosci.1138-17.2019

Seeley, W. W., Menon, V., Schatzberg, A. F., Keller, J., Glover, G. H., Kenna, H., et al. (2007). Dissociable intrinsic connectivity networks for salience processing and executive control. *J. Neurosci.* 27, 2349–2356. doi: 10.1523/JNEUROSCI.5587-06.2007

Seidler, R. D., and Noll, D. C. (2008). Neuroanatomical correlates of motor acquisition and motor transfer. *J. Neurophysiol.* 99, 1836–1845. doi: 10.1152/jn.01187.2007

Shadmehr, R., and Holcomb, H. H. (1997). Neural correlates of motor memory consolidation. *Science* 277, 821–825. doi: 10.1126/science.277.5327.821

Shadmehr, R., and Krakauer, J. W. (2008). A computational neuroanatomy for motor control. *Exp. Brain Res.* 185, 359–381. doi: 10.1007/s00221-008-1280-5

Shibata, K., Watanabe, T., Kawato, M., and Sasaki, Y. (2016). Differential activation patterns in the same brain region led to opposite emotional states. *PLoS Biol.* 14:e1002546. doi: 10.1371/journal.pbio.1002546

Spiers, H. J., and Maguire, E. A. (2007). Neural substrates of driving behaviour. *Neuroimage* 36, 245–255. doi: 10.1016/j.neuroimage.2007.02.032

Sridharan, D., Levitin, D. J., and Menon, V. (2008). A critical role for the right fronto-insular cortex in switching between central-executive and default-mode networks. *Proc. Natl. Acad. Sci. U.S.A.* 105, 12569–12574. doi: 10.1073/pnas.0800005105

Stein, J. (2009). Cerebellar forward models to control movement. *J. Physiol.* 587, 299–299. doi: 10.1113/jphysiol.2008.167627

Tzourio-Mazoyer, N., Landeau, B., Papathanassiou, D., Crivello, F., Etard, O., Delcroix, N., et al. (2002). Automated anatomical labeling of activations in SPM using a macroscopic anatomical parcellation of the MNI MRI single-subject brain. *Neuroimage* 15, 273–289. doi: 10.1006/nimg.2001.0978

Uchiyama, Y., Ebe, K., Kozato, A., Okada, T., and Sadato, N. (2003). The neural substrates of driving at a safe distance: a functional MRI study. *Neurosci. Lett.* 352, 199–202. doi: 10.1016/j.neulet.2003.08.072

Uddin, L. Q. (2015). Salience processing and insular cortical function and dysfunction. *Nat. Rev. Neurosci.* 16, 55–61. doi: 10.1038/nrn3857

Walter, H., Vetter, S. C., Grothe, J., Wunderlich, A. P., Hahn, S., and Spitzer, M. (2001). The neural correlates of driving. *Neuroreport* 12, 1763–1767. doi: 10.1097/00001756-200106130-00049

Wolpert, D. M., Ghahramani, Z., and Jordan, M. I. (1995). An internal model for sensorimotor integration. *Science* 269, 1880–1882. doi: 10.1126/science.7569931

Wolpert, D. M., and Kawato, M. (1998). Multiple paired forward and inverse models for motor control. *Neural Netw.* 11, 1317–1329. doi: 10.1016/s0893-6080(98)00066-5

Wolpert, D. M., Miall, R. C., and Kawato, M. (1998). Internal models in the cerebellum. *Trends Cogn. Sci.* 2, 338–347. doi: 10.1016/S1364-6613(98)01221-2

Conflict of Interest: The authors declare that this study received funding from TOYOTA. The funder had the following involvement in the study: discussions about the experimental setup and the results.

Publisher's Note: All claims expressed in this article are solely those of the authors and do not necessarily represent those of their affiliated organizations, or those of the publisher, the editors and the reviewers. Any product that may be evaluated in this article, or claim that may be made by its manufacturer, is not guaranteed or endorsed by the publisher.

Copyright © 2022 Ohata, Ogawa and Imamizu. This is an open-access article distributed under the terms of the Creative Commons Attribution License (CC BY). The use, distribution or reproduction in other forums is permitted, provided the original author(s) and the copyright owner(s) are credited and that the original publication in this journal is cited, in accordance with accepted academic practice. No use, distribution or reproduction is permitted which does not comply with these terms.

frontiers in Systems Neuroscience

ORIGINAL RESEARCH
published: 22 February 2022
doi: 10.3389/fnsys.2021.806257

Relationship Between Body-Specific Attention to a Paretic Limb and Real-World Arm Use in Stroke Patients: A Longitudinal Study

*Ryoji Otaki[1,2], Yutaka Oouchida[1,3], Naoki Aizu[1,4], Tamami Sudo[1,5], Hiroshi Sasahara[2], Yuki Saito[6], Sunao Takemura[6] and Shin-Ichi Izumi[1,7]**

[1]Department of Physical Medicine and Rehabilitation, Tohoku University Graduate School of Medicine, Sendai, Japan, [2]Department of Rehabilitation, Yamagata Saisei Hospital, Yamagata, Japan, [3]Department of Education, Osaka Kyoiku University, Osaka, Japan, [4]Faculty of Rehabilitation, School of Health Sciences, Fujita Health University, Toyoake, Japan, [5]Department of Computer and Information Sciences, Tokyo University of Agriculture and Technology, Tokyo, Japan, [6]Department of Neurosurgery, Yamagata Saisei Hospital, Yamagata, Japan, [7]Department of Physical Medicine and Rehabilitation, Tohoku University Graduate School of Biomedical Engineering, Sendai, Japan

Learned nonuse is a major problem in upper limb (UL) rehabilitation after stroke. Among the various factors that contribute to learned nonuse, recent studies have focused on body representation of the paretic limb in the brain. We previously developed a method to measure body-specific attention, as a marker of body representation of the paretic limb and revealed a decline in body-specific attention to the paretic limb in chronic stroke patients by a cross-sectional study. However, longitudinal changes in body-specific attention and paretic arm use in daily life (real-world arm use) from the onset to the chronic phase, and their relationship, remain unknown. Here, in a longitudinal, prospective, observational study, we sought to elucidate the longitudinal changes in body-specific attention to the paretic limb and real-world arm use, and their relationship, by using accelerometers and psychophysical methods, respectively, in 25 patients with subacute stroke. Measurements were taken at baseline (T_{BL}), 2 weeks (T_{2w}), 1 month (T_{1M}), 2 months (T_{2M}), and 6 months (T_{6M}) after enrollment. UL function was measured using the Fugl-Meyer Assessment (FMA) and Action Research Arm Test (ARAT). Real-world arm use was measured using accelerometers on both wrists. Body-specific attention was measured using a visual detection task. The UL function and real-world arm use improved up to T_{6M}. Longitudinal changes in body-specific attention were most remarkable at T_{1M}. Changes in body-specific attention up to T_{1M} correlated positively with changes in real-world arm use up to T_{6M}, and from T_{1M} to T_{6M}, and the latter more strongly correlated with changes in real-world arm use. Changes in real-world arm use up to T_{2M} correlated positively with changes in FMA up to T_{2M} and T_{6M}. No correlation was found between body-specific attention and FMA scores. Thus, these results suggest that improved body-specific attention to the paretic limb during the early phase contributes to increasing long-term real-world arm use and that increased real-world use is associated with the recovery of UL function. Our results may contribute

OPEN ACCESS

Edited by:
Jun Ota,
The University of Tokyo, Japan

Reviewed by:
Hiroshi Imamizu,
The University of Tokyo, Japan
Anna Danielsson,
University of Gothenburg, Sweden
Kohei Kaminishi,
The University of Tokyo, Japan

***Correspondence:**
Shin-Ichi Izumi
izumis@med.tohoku.ac.jp

Received: *31 October 2021*
Accepted: *21 December 2021*
Published: *22 February 2022*

Citation:
Otaki R, Oouchida Y, Aizu N, Sudo T, Sasahara H, Saito Y, Takemura S and Izumi S-I (2022) Relationship Between Body-Specific Attention to a Paretic Limb and Real-World Arm Use in Stroke Patients: A Longitudinal Study. Front. Syst. Neurosci. 15:806257. doi: 10.3389/fnsys.2021.806257

to the development of rehabilitation strategies to enhance adaptive changes in body representation in the brain and increase real-world arm use after stroke.

Keywords: accelerometer, body representation, body-specific attention, learned nonuse, recovery, rehabilitation, stroke, upper limb

INTRODUCTION

The most common disability after stroke is upper limb (UL) paralysis, which occurs contralateral to a unilateral hemispheric injury. More than 80% of stroke patients experience this condition in the acute phase, and more than 40% of these patients have a residual disability in the chronic phase (Gresham et al., 1995). With the recent developments in acute stroke treatment, it has been reported that the percentage of patients with UL motor impairment within 72 h after stroke onset has decreased; however, 48% of stroke patients still had UL motor impairment (Alt Murphy et al., 2011; Persson et al., 2012). UL paralysis affects activities of daily living and reduces the quality of life (Nichols-Larsen et al., 2005). Many stroke patients with UL paralysis will stop using their paretic hand to avoid failure or inconvenience. Once the patient becomes accustomed to using the non-paretic hand, attempts to use the paretic hand are further reduced, resulting in learned nonuse, which is a major clinical problem (Taub et al., 2002). Learned nonuse leads to progressively smaller cortical areas representing the paretic limbs of the brain due to use-dependent neuroplasticity. These secondary changes in the neural system can worsen the motor impairment of the paretic limb. This negative cycle caused by learned nonuse prevents the recovery of the paretic limb after a stroke. For these reasons, in recent rehabilitation medicine, active use of the paretic limb is recommended to overcome and prevent learned nonuse (Morris et al., 2006).

Since the concept of learned nonuse was proposed, the importance of using the paretic hand in daily life (real-world arm use) as well as in function has been emphasized in the rehabilitation of stroke patients (Hebert et al., 2016; Winstein et al., 2016; Kelly et al., 2018). Accelerometers have been widely used as a method to measure real-world arm use objectively (Uswatte et al., 2000, 2005a). Early studies using accelerometers focused on stroke patients in the chronic phase (Uswatte et al., 2000, 2005a), but later cross-sectional studies investigated the acute phase (Gebruers et al., 2008) and the subacute phase (Thrane et al., 2011; Alt Murphy et al., 2019) of stroke. These studies using accelerometers from the acute to the chronic phase after stroke have been conducted and established an objective method to measure real-world arm use after stroke (Noorkoiv et al., 2014). Using accelerometers, several studies have reported factors associated with paretic hand use in patients with stroke. Although it has been thought that improvements in UL function translate directly to increased arm use in daily life, evidence from recent research, in which daily life arm use was evaluated using accelerometry, did not support this notion (Rand and Eng, 2012, 2015; Waddell et al., 2017). Instead, these studies indicated that, while UL function and arm use in daily life are related, they are distinctly different constructs. Specifically, it has been recognized that there is a disparity between UL function and real-world arm use (Rand and Eng, 2012). Despite improvements in UL function with inpatient rehabilitation after stroke, the use of the paretic hand did not improve significantly, and the use ratio of the paretic hand to the non-paretic hand was only 25%. Furthermore, when the effect of whether the paretic hand was dominant in real-world arm use was examined, no significant effect was found (Rand and Eng, 2012). In addition, this discrepancy between improved UL function and increased real-world arm use is known to occur even after hospital discharge (Rand and Eng, 2015; Doman et al., 2016). A comparison of paretic hand use at discharge to home and 12 months post-stroke showed that, despite significant improvement in UL function, there was no significant improvement in the use of the paretic hand in daily life. The use ratio of the paretic hand to the non-paretic hand at 12 months after stroke was 35%, which was very limited (Rand and Eng, 2015). These findings suggest that there is a discrepancy between improvement in UL function and real-world arm use and that factors other than function may also influence real-world arm use. Other studies have examined the impact of individual factors, including psychosocial factors and function, on real-world arm use. Observations up to 12 weeks after onset showed that real-world arm use increased, but that psychosocial factors (belief and confidence in UL performance, and motivation for UL use) had no effect on real-world arm use (Waddell et al., 2019a). A study of the psychosocial factors up to 6 months post-onset found that beliefs, confidence, and motivation regarding UL use remained high up to 6 months post-stroke, there was no correlation between psychosocial factors and clinical outcomes (Waddell et al., 2019b). Although these studies on real-world arm use have examined functional and psychosocial factors, the factors that influence the recovery of real-world arm use remain unclear.

In recent years, among the various factors that contribute to learned nonuse, many studies have focused on body consciousness, including body representation in the brain (Aymerich-Franch and Ganesh, 2016; Naito et al., 2016; Oouchida et al., 2016; Matamala-Gomez et al., 2020). Body consciousness is the consciousness of one's own body, which has been discussed in philosophy and phenomenology. When body consciousness changes after a stroke, stroke patients relate the consciousness that "I feel as if it is not my hand" about the paretic limb. This body consciousness is broadly classified by Gallagher into "sense of body ownership" and "sense of agency" (Gallagher, 2000). In the hierarchy of body consciousness, sensorimotor representation is the lowest level. Sensorimotor representation is the body consciousness that is integrated

by sensory and predictive information. This is the body representation in the brain that has been studied in the fields of psychology and medicine in recent years. Human movements are planned and executed based on this body representation in the brain.

In stroke patients, in addition to the paralysis caused by the brain injury, maladaptive changes in body representation of the paretic limb in the brain may prevent the use of the paretic limb in daily life. If the brain does not recognize the paretic hand as "my hand," it may be difficult to use the paretic hand spontaneously in daily life. Body consciousness, including body representation of the limb in the brain, could not be observed externally. Thus, a method, using a visual detection task, has been developed to measure the amount of body-specific attention, i.e., attention specifically directed at the body (Aizu et al., 2018). In the above method, based on the body facilitation effect of visual detection of the self (Hari and Jousmäki, 1996; Whiteley et al., 2004, 2008; Reed et al., 2006, 2010; Tseng et al., 2012), the difference between the reaction time to a visual target outside the body and the reaction time to visual target on the body is defined as body-specific attention. This facilitation effect has been reported to occur even when the hand is not visible (Reed et al., 2006), and by attributing the hand to oneself (Whiteley et al., 2008). These studies support the idea that body representations in the brain facilitate the detection of visual information. In chronic stroke patients, it has been reported that, the more severe the hemiparesis and the longer the duration of the stroke, the lower is the body-specific attention (the facilitation effect did not occur in the paretic hand; Aizu et al., 2018). The results suggested that maladaptive changes in the body representation of the paretic hand in the brain occurred due to learned nonuse in chronic stroke patients. However, although the relationship between body-specific attention and UL function in cross-sectional studies of chronic stroke patients has been clarified, the longitudinal changes in body-specific attention and real-world arm use from stroke onset to the chronic phase, and the relationship between them, are unclear.

We hypothesized that improvements in body-specific attention to the paretic hand may facilitate real-world arm use. Since the previous study made it possible to measure learned nonuse from the aspect of body representation quantitatively, it may be possible to clarify how learned nonuse of the paretic limb progresses after the onset of stroke from the perspective of body representation in the brain and behavior of stroke patients, by using a visual detection task and accelerometer.

Therefore, this study aimed to elucidate the longitudinal changes in body-specific attention to the paretic limb and real-world arm use, and the relationship between them, by using accelerometers and psychophysical methods, respectively, in subacute stroke patients. This is expected to clarify the adaptive mechanisms underlying UL recovery after stroke from the perspective of behavior and body representation of the paretic limb in the brain.

MATERIALS AND METHODS

Study Design

This was a longitudinal, prospective, observational cohort study involving patients with hemiparesis after stroke.

Participants

This study collected data from the Yamagata Saisei Hospital, Japan. The inclusion criteria were: (1) first-ever stroke; (2) unilateral supratentorial lesions; (3) presence of UL motor deficits; (4) general condition was stable after 2 weeks from stroke onset; (5) age between 20 and 80 years. Patients with (1) multiple strokes; (2) aphasia; (3) apraxia; (4) attentional bias to the left or right visual field, which can be found in unilateral spatial neglect (USN); (5) hemianopia; or (6) serious uncontrolled medical conditions were excluded. From 2018 to 2020, 25 patients were recruited consecutively from the inpatients of Yamagata Saisei Hospital.

Thus, the subjects were 25 patients with subacute stroke whose general condition was stable after 2 weeks from stroke onset [mean age ± standard deviations (SD), 60.8 ± 12.8 years; 18 male; 13 right hemiparesis; 25 right-handed (**Table 1**)]. The measurement time points were baseline (within 1 week of study enrollment, T_{BL}), 2 weeks (T_{2w}: T_{BL}+ 2 weeks), 1 month (T_{1M}: T_{BL}+ 1 month), 2 months (T_{2M}: T_{BL}+ 2 months) and 6 months (T_{6M}: T_{BL}+ 6 months) after the baseline measurement. For rehabilitation during the study period, the usual occupational and physical therapies were performed according to the general condition (early mobilization, activities of daily living training, and self-management guidance). The content and amount of UL exercises were controlled using a standardized UL program graded repetitive arm supplementary program (GRASP) for 1 h per day (Harris et al., 2009, 2010; Murdolo et al., 2017; Simpson et al., 2017).

Standard Protocol Approvals, Registrations, and Patient Consents

The Tohoku University and Yamagata Saisei Hospital ethics committee approved this study (ID 2017-1-1076, ID348), which was conducted according to the ethical standards of the Declaration of Helsinki. Prior to our experiment, all participants agreed to participate in our experiment and provided written informed consent.

Real-World Arm Use Measurement

Real-world arm use was measured using wrist-worn accelerometers (ActiGraph Link, GT9X, Actigraph Corp, Pensacola, FL). These wireless devices are small (35 mm × 35 mm × 10 mm, 14 g), have a solid-state accelerometer with a dynamic range of ±8 G gravity units, and can collect data locally. Wrist-worn accelerometers have an established validity and reliability for measuring the activity of the paretic limb in stroke patients (Uswatte et al., 2005b, 2006). Many methods of measuring paretic limb activity (equipment, measurement time) in stroke patients have been reported (Uswatte et al., 2005a; Noorkoiv et al., 2014; Hayward et al., 2016), and the measurement and data analysis methods used in

TABLE 1 | Clinical characteristics of stroke patients.

ID	Age (years)	Sex	Diagnosis	Lesion location	Duration (days)	Paresis side	Handedness	FMA-UE motor	FMA-UE sensory
S1	71	M	I	L Thalamus	53	R	R	14	6
S2	69	M	H	R Thalamus	40	L	R	41	6
S3	80	M	H	R Putamen	25	L	R	45	6
S4	59	F	H	L Thalamus	32	R	R	47	0
S5	61	M	I	L ICA	35	R	R	42	12
S6	35	M	I	R Putamen, Corona radiata	30	L	R	22	12
S7	66	M	I	L Corona radiata	36	R	R	38	10
S8	76	M	I	L Corona radiata	31	R	R	34	12
S9	71	M	H	R Putamen	19	L	R	53	10
S10	22	F	I	R ICA	60	L	R	15	8
S11	53	F	H	R Putamen	89	L	R	14	2
S12	49	M	I	R MCA	45	L	R	15	6
S13	58	M	I	R Putamen, Corona radiata	20	L	R	39	10
S14	73	F	I	R Corona radiata	31	L	R	19	12
S15	71	F	H	L Thalamus	39	R	R	20	0
S16	61	M	I	L Putamen, Corona radiata	42	R	R	33	10
S17	58	M	H	R Thalamus	56	L	R	28	7
S18	53	M	I	L Posterior limb of internal capsule	25	R	R	38	12
S19	66	M	I	R MCA	15	L	R	48	10
S20	72	F	I	L Posterior limb of internal capsule	20	R	R	53	10
S21	66	M	I	R Internal capsule, Corona radiata	18	L	R	21	10
S22	47	M	H	L Putamen	29	R	R	32	9
S23	58	M	H	L Putamen	25	R	R	14	10
S24	63	M	I	R Putamen, Corona radiata	39	L	R	37	12
S25	62	F	H	L Putamen	63	R	R	21	10
Mean	60.8	F: 7	I: 15	L: 12	36.7	R: 13	R: 25	31.3	8.5
SD	12.8	M: 18	H: 10	R: 13	17.1	L: 12	L: 0	12.8	3.5

H, hemorrhage; I, infarction; ICA, internal carotid artery; MCA, middle cerebral artery; FMA, Fugl–Meyer assessment.

this study were performed as previously reported (Uswatte et al., 2006; Taub et al., 2013).

Accelerometers were attached to both wrists. The accelerometer was attached to the distal forearm using a wristwatch-type belt (Actigraph, Pensacola, FL). In order to obtain accurate data, the accelerometer was initially attached by an occupational therapist who confirmed the appropriate belt length and position according to the circumference of the patient's distal forearm (to avoid loosening). Over the 3-day measurement period (Van Der Pas et al., 2011; Franck et al., 2019), patients wore the accelerometers from waking until sleep, and were only removed from both wrists during bathing. Patients and caregivers were instructed to comply with the wearing method and wearing time described above, and all precautions were documented and given to them. In addition, to prevent inappropriate wearing and loss of data, ward nurses attached and removed the accelerometers during hospitalization, and family members assisted the patient in wearing and removing the accelerometers after discharge, except for patients who lived alone (caregivers always checked the accelerometers even for patients who could remove them by themselves). As a safety consideration, the presence of skin problems in the belt area was checked daily, and the presence of pain or discomfort was assessed daily. Data analysis was performed excluding the time when the accelerometer was not attached, such as sleeping and bathing, from the 72-h measurement period. Data were sampled and recorded along three axes (X, Y, and Z axes) at 60 Hz. The obtained data were band-pass filtered between 0.25 Hz and 2.5 Hz, and activity counts (acceleration unit set by Actigraph Corp) for each axis were collected in 60-s epochs, using ActiLife 6 software (Actigraph Corp). Activity counts were combined across the three axes to create a single-vector magnitude value ($\sqrt{x^2 + y^2 + z^2}$) for each second of the data. The amount of use of the paretic hand in daily life was defined as real-world arm use (ratio of paretic to non-paretic vector magnitude value). A ratio close to 1.0 means that the paretic hand is used to the same extent as the non-paretic hand, and a ratio close to 0 indicates that the paretic hand is used markedly less frequently than the non-paretic hand (Uswatte et al., 2006; Taub et al., 2013; Gebruers et al., 2014; Hayward et al., 2016).

Body-Specific Attention to the Paretic Hand

As an index reflecting the body representation of the paretic hand in the brain, we measured the body-specific attention of the paretic hand in a visual detection task (Aizu et al., 2018). Since the brain monitors the location of its own body parts by body representations in the brain, it is assumed that attention is more strongly directed to body space than to out-of-body space. Previous studies have reported a body-related "facilitation effect" that allows healthy subjects to detect a visual target faster when the target is presented near the hand than when it is presented far away (Hari and Jousmäki, 1996; Whiteley et al., 2004, 2008; Reed et al., 2006, 2010; Tseng et al., 2012). Such a facilitation effect has been used in psychophysical experiments as a reflection of body representations in the brain (Whiteley et al., 2008). For example, it has been shown that there is no

facilitation effect in conditions where no attribution is given to the hand, but there is a facilitation effect in conditions where attribution is given to the hand by passive movement of the hand (Whiteley et al., 2008). This indicates that the facilitation effect occurs only when the brain recognizes the hand as part of its own body, suggesting that body representation in the brain facilitates the detection of visual information. It was also shown that the facilitation effect occurred even in the condition of only proprioceptive information where the hand could not be visually confirmed (Reed et al., 2006). Furthermore, in a study on the facilitation effects of tools, it was reported that training with a rake in hand facilitated the detection of targets presented on the rake (Kao and Goodale, 2009). This result suggests that the tool is incorporated as the body representation in the brain, i.e., the brain has come to recognize the tool as a part of its own body. This result strongly supports the idea that the body facilitation effect reflects the body representation in the brain. In addition, a recent study by Aizu reported that healthy subjects responded more quickly to visual targets on their own hand using a visual detection task designed to measure body facilitation effects (Aizu et al., 2018). This facilitative effect of visual detection on one's own body has been interpreted as a result of latent attention to one's own body and is referred to as body-specific attention (Aizu et al., 2018). Body-specific attention, which is the attention potentially directed to one's own body, may reflect body representations in the brain.

In the present study, we measured the body-specific attention to the paretic hand in a visual detection task as an index reflecting the body representation of the paretic limb in the brain (Aizu et al., 2018).

Experimental Setup and the Visual Detection Task

The visual detection task was created in the programming software MATLAB (version 2017b, MathWorks, Natick, MA, USA) using a Macintosh personal computer (Mac Book Pro, Apple Inc., Cupertino, CA, USA). In the visual detection task, a fixation point was first presented in the center of the screen, and then the button (USB numeric keypad, SANWA SUPPLY NT-9UH2BK, Okayama, Japan) was pressed as soon as possible when the blue visual target (Go trial) appeared in either the left or right position (**Figures 1A–C**). In this case, the button was not pressed when the red visual target (Catch trial) appeared (**Figure 1C**). The time between the presentation of the visual target and pressing of the button was recorded as the reaction time. To exclude the effect of anticipation of the appearance of the visual target on the reaction time, the time from the fixation point to the presentation of the visual target was varied randomly between 800 and 1,600 ms, and the visual target was presented randomly in either the left or right position. In addition, blue or red visual targets were randomly presented at a ratio of 4:1.

The subjects sat in a chair in front of a desk in a quiet room. A personal computer on which the visual detection task was created was connected to a projector (EB-S12H, Epson, Suwa, Japan) set up above the desk such that a fixation point and visual target could be projected onto the desk (**Figure 1A**). Responsive buttons were placed at the center of the desk (**Figure 1B**). The visual target had a visual angle of 1.7°, 28 cm away from the subject, with 36 cm between the visual targets. The distance between the projected visual targets and the fixation point was 28 cm. To ensure that the reaction time results were not affected by eye movements, subjects were instructed to gaze at the fixation

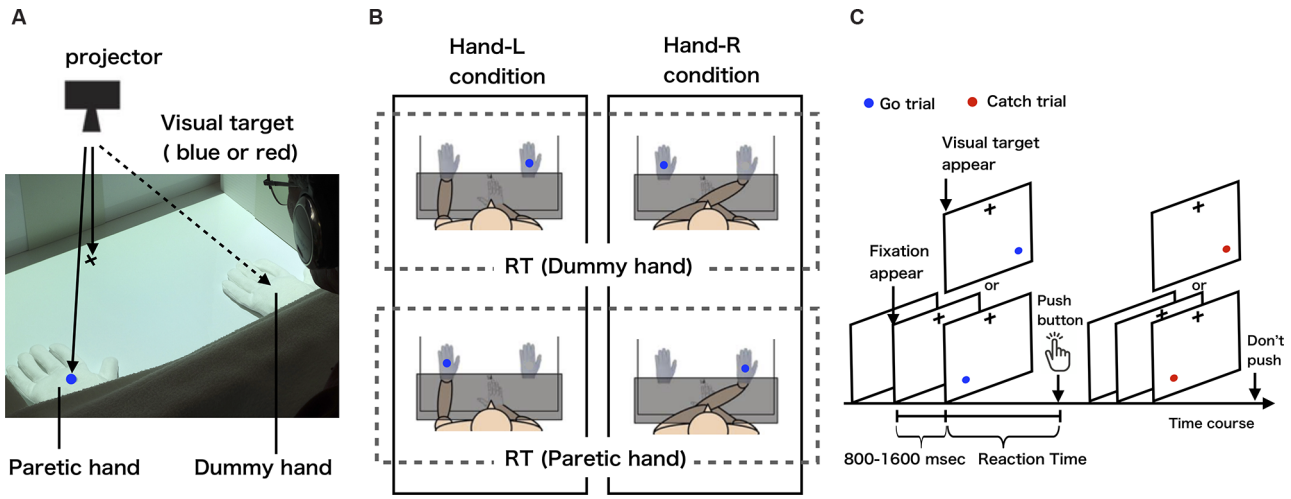

FIGURE 1 | (A) The measurement of body-specific attention to the paretic hand. **(B)** Experimental conditions and definition of body-specific attention (each condition is circled by a solid line; dummy or paretic hand reaction time is circled by a dotted-line). These schematic views show the hand-L and hand-R conditions for patients with left hemiparesis. The patients placed their paretic hand either on the left side (hand-L) or right side (hand-R). In both conditions, the dummy hand was placed on the opposite side of the midline to the paretic hand. For patients with right hemiparesis, the paretic hand was placed to the left of the midline in the hand-L condition and to the right of the midline in the hand-R condition. We defined the amount of body-specific attention directed to the paretic hand as the average reaction time for when the visual target was presented on the dummy hand minus the average reaction time for when the visual target was presented on the paretic hand (body-specific attention = dummy hand − paretic hand). **(C)** Visual detection task. After the presentation of a fixation point, the visual target appeared randomly from 800 to 1,600 ms, on one of the two hands (paretic or dummy hand). Participants pushed the button only when a blue-filled circle appeared.

point throughout the task. Considering the effects of fatigue during the experiment, the number of visual targets presented in a single condition was set to 80. In order to control the visual information given to the subject during the experiment, the two hands in which the visual target was presented were a paretic hand wearing white cotton gloves and a dummy hand made of white cotton gloves (**Figures 1A,B**). In addition, a whiteboard was used to hide the subject's forearm and button-pressing hand from the subject's view during the task, thus controlling the visual information given to the subject.

Experimental Condition

To measure the body-specific attention directed at the paretic hand quantitatively, we set up two experimental conditions and one control condition. In the experimental condition, in order to exclude the effect of hand position in space, we set the hand-L condition, in which the paretic hand was placed in the left position and the dummy hand in the right position (**Figure 1B** left), and the hand-R condition, in which the paretic hand was placed in the right position and the dummy hand in the left position (**Figure 1B** right), at the two locations at which the visual target was presented on the desk. In the control condition, the dummy hand was placed at both locations where the visual target was presented on the desk (the paretic hand was on the abdomen), in order to check for attentional bias in space. Button pressing was performed with the index finger on the non-paretic side. For example, when a left hemiplegic patient performed the experimental condition (hand-L condition), the paretic hand was wearing a white cotton glove, the paretic hand was placed in the space on the left side, and the button was pressed with the right, non-paretic hand (**Figures 1A,B**). The experiment was counterbalanced for each subject so that the order of task execution did not affect the results. To familiarize the subjects with the visual detection task, we presented 60 visual targets and had participants perform the task as practice trials. In the practice trials, the subject's paretic hand or dummy hand was not placed on the desk, but the visual target was presented directly on the desk and the subject responded. The subjects were asked to perform the task without any instructions that could direct their attention intentionally.

Experimental Data Analysis

The average reaction time of paretic and dummy hands was calculated for each condition to ascertain the amount of body-specific attention to the paretic hand (**Figure 1B**). To remove the effects of delayed reactions due to inattention during the task and accelerated reactions due to anticipation of the visual target appearing, the obtained reaction time data exceeding two SD above and below the mean reaction time were excluded from the results as outliers.

Based on the results obtained under the experimental conditions, we defined the amount of body-specific attention directed to the paretic hand as the average reaction time for when the visual target on the dummy hand was presented minus the average reaction time for when the visual target on the paretic hand was presented (body-specific attention = dummy hand − paretic hand). A positive value of body-specific attention means that the reaction time to the presentation of the visual target on the paretic hand was shorter than the reaction time to the presentation of the visual target on the dummy hand.

Additional Study Assessments

The Fugl-Meyer Assessment (FMA) was used to evaluate clinical UL function. The FMA is a stroke-specific rating scale based on the recovery process of hemiplegia after stroke. The FMA upper extremity motor (FMA-UE motor) consists of 33 items, each of which is scored on a scale of 0–2 (0 = generally corresponding to no function, 1 = partial function, 2 = perfect function), with the highest score being 66 (Fugl-Meyer et al., 1975). The Action Research Arm Test (ARAT) was used to measure UL capacity. The ARAT is a valid and reliable measure of UL capacity in adults with paresis. It is a 19-item assessment of grasp, grip, pinch, and gross motor function. Individual items were scored using a 0–3 ordinal scale (0 = can perform no part of the test, 1 = performs test partially, 2 = completes test but takes abnormally long time or has great difficulty, 3 = performs test normally). Individual item scores are summed, and the final score ranges from 0 to 57, with higher scores indicating better motor function (Lyle, 1981; Van der Lee et al., 2001).

The FMA-UE sensory score was measured as a sensory function assessment. FMA-UE sensory consists of six items: light touch (forearm, palm) and proprioception (shoulder, elbow, wrist, thumb IP), and each item is scored on a 3-point scale from 0 to 2 (light touch score 0 = anesthesia; 1 = hypoesthesia or dysesthesia; 2 = normal, proprioception score 0 = less than 3/4 of the answers correct or absence; 1 = 3/4 of the answers correct or considerable difference; 2 = correct 100% or no difference). The maximum score is 12 points (Fugl-Meyer et al., 1975).

Statistical Analysis

To examine longitudinal changes in UL function, real-world arm use and body-specific attention were analyzed using repeated measures analysis of variance (ANOVA) and multiple comparisons were adjusted with the Bonferroni correction. To examine longitudinal changes in sensory function (FMA-UE sensory) was analyzed using Friedman test and multiple comparisons were adjusted with the Bonferroni correction. For comparison between two groups of stroke patients in this study and healthy older people in a previous study that used cross-sectional data, at each time point of body-specific attention, we used the Welch's two-sample *t*-test (data of healthy older people were taken from a previous study by Aizu et al. (2018).

To investigate the correlation between the amount of change in real-world arm use and the amount of change in body-specific attention during the UL recovery process, Pearson's product-moment correlation coefficient or Spearman's rank correlation coefficient tests were performed, after assessing the normality of data distribution by using the Shapiro–Wilk test. This correlation analysis also focused on the amount of change in each index over different time periods in order to clarify the hypothesis that increased body-specific attention would promote real-world arm use. Specifically, we examined the relationship

between the amount of change in body-specific attention in the early phase and the amount of change in real-world arm use until the chronic phase, because plastic changes in the brain, including body representations, change significantly in the early phase after stroke onset, but behavioral changes, such as arm use, may require a longer time. To examine the patient-specific factors affecting changes in body-specific attention, as well as changes in real-world arm use, characteristics at enrollment, such as age, duration since onset, FMA-UE sensory, and FMA-UE motor were investigated using Pearson's product-moment correlation coefficient or Spearman's rank correlation coefficient test, after assessing data normality by the Shapiro–Wilk test. Based on the principle of use-dependent plasticity of the brain, we also examined the relationship between the amount of change in real-world arm use and the amount of change in UL function. It was considered that if real-world arm use improved in the early phase, UL function would recover in the long term, but conversely, if real-world arm use decreased in the early phase, functional recovery in the long term would be poor. Therefore, we focused on such periods to conduct a correlation analysis between arm use and UL function. Although our main interest was in the analysis of longitudinal data, correlations in cross-sectional data were also analyzed using the same procedure, in order to examine the relationship between indices at each time point. The statistical significance level was set at 5%. Statistical analyses were performed using SPSS, version 27.0 J (SPSS Japan Inc., Tokyo, Japan).

RESULTS

There were no participant dropouts during the 6-month study period. All outcomes were measured in five assessment sessions for all patients.

UL Function (FMA-UE Motor) and Ability to Manipulate Objects (ARAT)

Figure 2 shows the longitudinal changes in UL function and the ability to manipulate objects. One-way repeated measures ANOVA on FMA-UE motor demonstrated that there was a significant improvement in FMA-UE motor across the 6-month study period ($F = 91.39$, $p < 0.01$). Compared to the FMA-UE motor at T_{BL}, FMA-UE motor was significantly increased at T_{2w} ($p < 0.01$), T_{1M} ($p < 0.01$), T_{2M} ($p < 0.01$), and T_{6M} ($p < 0.01$). Compared to the FMA-UE motor at T_{2w}, FMA-UE motor was significantly increased at T_{1M} ($p < 0.01$), T_{2M} ($p < 0.01$), and T_{6M} ($p < 0.01$). Compared to the FMA-UE motor at T_{1M}, FMA-UE motor was significantly increased at T_{2M} ($p < 0.01$) and T_{6M} ($p < 0.01$), but there was no significant difference between T_{2M} and T_{6M} ($p = 0.095$). Similarly, there was a significant improvement in ARAT across the 6-month study period (repeated-measures ANOVA, $F = 61.82$, $p < 0.01$). Compared to the ARAT at T_{BL}, ARAT was significantly increased at the T_{2w} ($p < 0.01$), T_{1M} ($p < 0.01$), T_{2M} ($p < 0.01$), and T_{6M} ($p < 0.01$). Compared to the ARAT at T_{2w}, ARAT was significantly increased at T_{1M} ($p < 0.01$), T_{2M} ($p < 0.01$), and T_{6M} ($p < 0.01$). Compared to the ARAT at T_{1M}, ARAT was significantly increased at T_{2M} ($p = 0.01$) and T_{6M} ($p < 0.01$), but there was no significant difference between T_{2M} and T_{6M} ($p = 0.61$).

Sensory Function (FMA-UE Sensory)

The Friedman test on FMA-UE sensory demonstrated that there was a significant improvement in FMA-UE sensory during the 6-month study period ($p < 0.001$). Compared to the FMA-UE sensory at T_{BL}, FMA-UE sensory was significantly increased at T_{1M} ($p = 0.019$), T_{2M} ($p = 0.013$), and T_{6M} ($p < 0.01$). Compared to the FMA-UE sensory at T_{2w}, FMA-UE sensory was significantly increased at T_{6M} ($p < 0.05$), but there were no significant differences between the other periods.

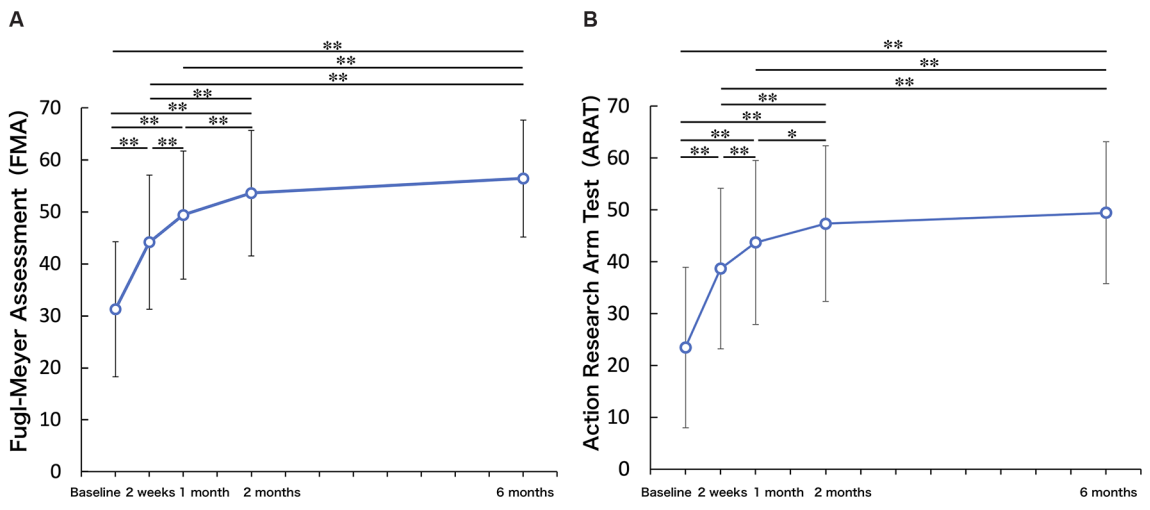

FIGURE 2 | Upper limb function. **(A)** Fugl-Meyer Assessment (FMA). **(B)** Action Research Arm Test (ARAT). Upper limb function and ability to manipulate objects improved up to 2 months and were maintained up to 6 months (One-factor repeated-measures analysis of variance (ANOVA), multiple comparison procedure: Bonferroni correction. $^{*}p < 0.05$, $^{**}p < 0.01$).

Real-World Arm Use

Figure 3A presents the change in real-world arm use. There was a significant improvement in real-world arm use across the 6 months after baseline (repeated-measures ANOVA, $F = 9.35$, $p < 0.01$). Compared to the real-world arm use at T_{BL}, real-world arm use was significantly increased at T_{2w} ($p < 0.01$), T_{1M} ($p < 0.01$), T_{2M} ($p < 0.05$), and T_{6M} ($p < 0.05$). Compared to the real-world arm use at T_{2w}, real-world arm use was significantly increased at T_{6M} ($p < 0.05$), while there was no significant difference at T_{1M} ($p = 0.28$) and T_{2M} ($p = 1.00$). There was also no significant difference between T_{1M} and T_{6M}.

Body-Specific Attention to the Paretic Hand

Body-specific attention to the paretic limb did not change significantly over the 6 months after baseline (repeated-measures ANOVA, $F = 1.30$, $p = 0.28$, **Figure 3B**). Compared with the previously published data on a healthy adult group (Aizu et al., 2018), stroke participants showed significantly lower body-specific attention to the paretic hand at T_{2w} ($p < 0.05$, t value = 2.20, 95% CI 0.9–20.1). There was a high degree of variability in body-specific attention across participants. The mean value of body-specific attention to the paretic limb peaked at T_{1M} (approaching the mean value of healthy adults), and then declined slightly between T_{1M} and T_{6M}, but remained within the range of the values of healthy adults at T_{6M} (no significant difference compared to healthy older adults).

The average incorrect response was 0.45 times in the catch trials (16 trials), and the average response of exclusions due to the patient's exceeding the 2SD was 1.42 times in all trials (80 trials).

Correlation Between Body-Specific Attention and Real-World Arm Use

Correlation Analysis of Longitudinal Data

To show alterations in the relationship between the amount of change in body-specific attention and the amount of change in real-world arm use over time visually, **Figure 4** presents individual plots from the study participants. There was a significant, moderate, positive relationship between the amount of change in body-specific attention from T_{BL} to T_{1M}, and in the amount of change in real-world arm use from the T_{BL} to T_{6M} ($r = 0.491$, $p = 0.013$, **Figures 4A**, **5**). This relationship increased between the amount of change in body-specific attention from T_{BL} to T_{1M} and the amount of change in the real-world arm use from T_{1M} to T_{6M} ($r = 0.649$, $p < 0.01$, **Figures 4B**, **5**), indicating that long-term recovery of real-world arm use was associated with body-specific attention to the paretic limb in the early phase after stroke. Moreover, there was a significant, moderately positive relationship between the amount of change in body-specific attention from T_{BL} to T_{2w} (the period of least longitudinal change in body-specific attention) and the amount of change in real-world arm use from T_{BL} to T_{2M} ($r = 0.42$, $p = 0.035$).

In addition, correlations between the amount of change in body-specific attention and individual factors and clinical outcomes were confirmed. There were no correlations with age at enrollment, duration after stroke onset, UL function (FMA-UE motor), sensory impairment (FMA-UE sensory), and ability to manipulate objects (ARAT).

Regarding the association between the amount of change in real-world arm use and other individual factors, in the short-term, there was a significant positive correlation between the amount of change in real-world arm use from T_{BL} to T_{2M} and the amount of change in FMA-UE motor from T_{BL} to T_{2M} ($r = 0.40$, $p = 0.048$, **Figure 5**). Furthermore, in the long-term, there was a

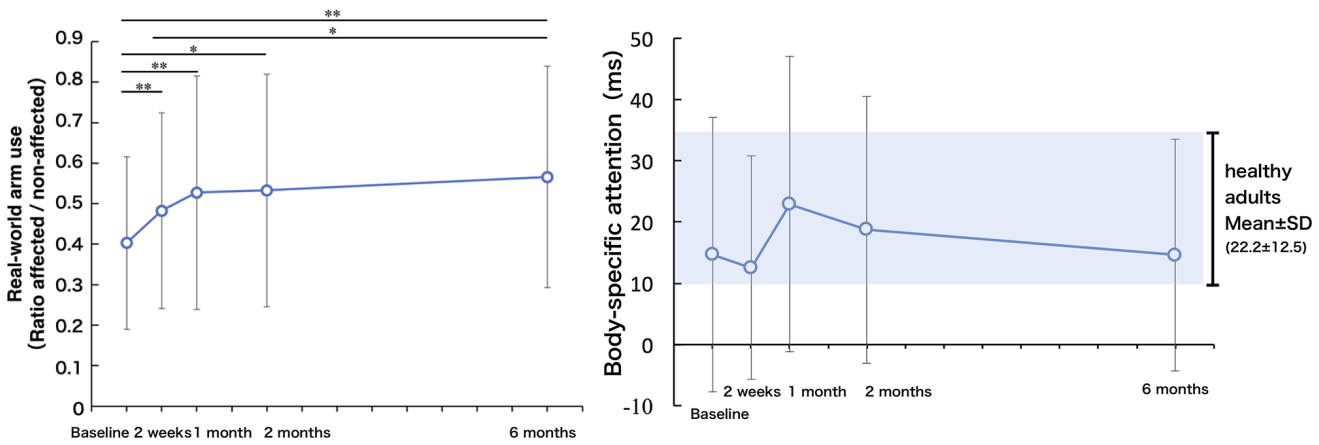

FIGURE 3 | (A) Real-world arm use (use ratio). The real-world arm use increased up to 1 month and improved slowly up to 6 months (one-factor repeated-measures ANOVA, multiple comparison procedure: Bonferroni correction. $^*p < 0.05$, $^{**}p < 0.01$). **(B)** Body-specific attention: longitudinal changes in body-specific attention were highly individual and not significant, but based on mean values, the body-specific attention was maximum at 1 month. The gray area represents the mean ± SD of the index of body facilitation effect in healthy controls.

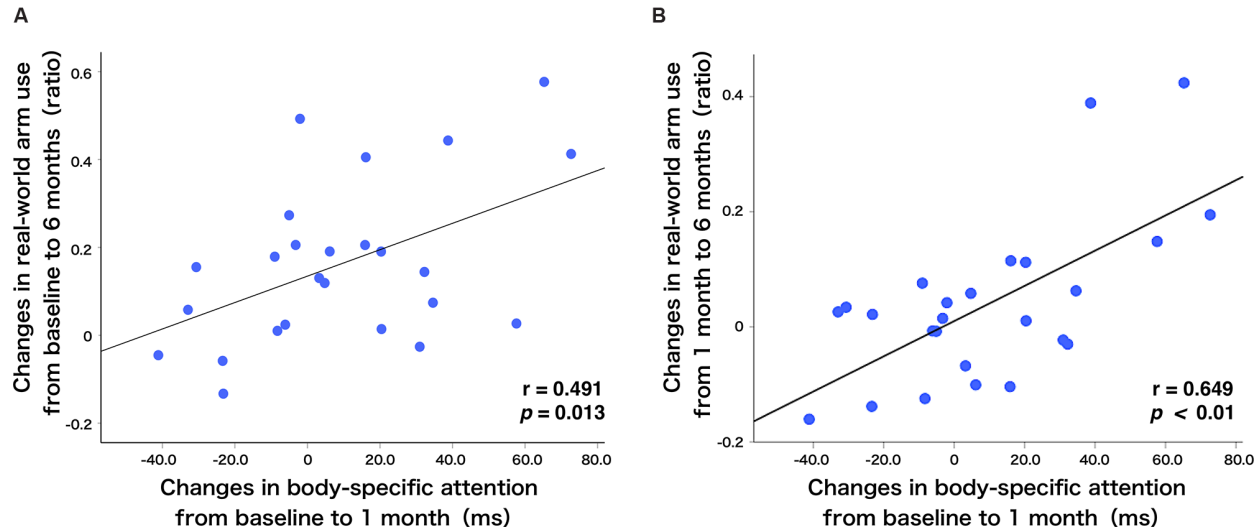

FIGURE 4 | Relationship between real-world arm use and body-specific attention. **(A)** There was a positive correlation between the changes in body-specific attention from baseline to 1 month and the changes in the real-world arm use from baseline to 6 months ($r = 0.491$, $p = 0.013$). **(B)** Additionally, there was a positive correlation between the changes in body-specific attention from baseline to 1 month and the changes in the real-world arm use from 1 month to 6 months ($r = 0.649$, $p < 0.01$). The blue dots represent individual patients.

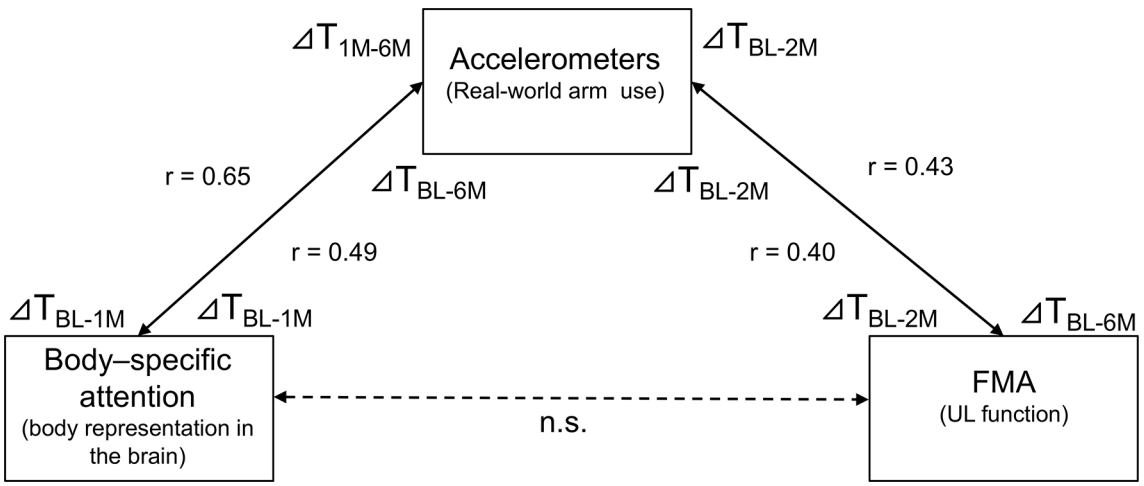

FIGURE 5 | Relationship between changes in body-specific attention, real-world arm use, and UL function as revealed by correlation analysis using longitudinal data. There was a significant positive correlation between the amount of change in body-specific attention from baseline to 1 month and the change in real-world arm usage from baseline to 6 months ($r = 0.491$, $p = 0.013$). Moreover, there was a significant positive correlation between the amount of change in body-specific attention from baseline to 1 month and the change in real-world arm use from 1 month to 6 months ($r = 0.649$, $p < 0.01$). The amount of change in real-world arm use from baseline to 2 months had a significant positive correlation with the amount of change in UL function over the same period ($r = 0.40$, $p = 0.048$). In addition, the amount of change in real-world arm use from baseline to 2 months had a significant positive correlation with the amount of change in UL function from baseline to 6 months ($r = 0.43$, $p = 0.034$). On the other hand, there was no correlation between body-specific attention and UL function. T: Time of measurement, BL: baseline, M: month, (ex. $\Delta T_{BL\text{-}6M}$: during the measurement period from baseline to 6 months).

moderately significant positive correlation between the amount of change in real-world arm use from T_{BL} to T_{2M} and the amount of change in FMA-UE motor from T_{BL} to T_{6M} ($r = 0.43$, $p = 0.034$, **Figure 5**). The amount of change in real-world arm use during the early phase showed results associated with short- and long-term changes in UL function. No correlations were found with age at enrollment, duration since onset, sensory impairment (FMA-UE sensory), and ability to manipulate objects (ARAT).

Correlation Analysis of Cross-sectional Data

In the cross-sectional correlation analyses, there were no correlations between body-specific attention and other factors at each time point from T_{BL} to T_{6M}. Although there was a strong positive correlation between real-world arm use and FMA-UE motor at each time point from T_{BL} to T_{6M}, the relationship gradually weakened with time after onset (T_{BL} $r = 0.78$, $p < 0.001$; T_{2w} $r = 0.68$, $p < 0.001$; T_{1M} $r = 0.65$, $p < 0.001$; T_{2M} $r = 0.59$,

$p = 0.002$; T_{6M} $r = 0.59$, $p = 0.002$). In addition, there was positive correlation between real-world arm use and ARAT at each time point from T_{BL} to T_{6M} (T_{BL} $r = 0.59$, $p = 0.002$; T_{2w} $r = 0.65$, $p = 0.001$; T_{1M} $r = 0.61$, $p = 0.001$; T_{2M} $r = 0.54$, $p = 0.005$; T_{6M} $r = 0.55$, $p = 0.005$).

DISCUSSION

In this study, we elucidated the longitudinal changes in body-specific attention to the paretic limb and real-world arm use in 25 stroke patients with hemiparesis, using psychophysical methods and accelerometers, respectively. The relationship between body-specific attention to the paretic limb and real-world arm use was also examined. To the best of our knowledge, no previous study had examined the longitudinal changes in body-specific attention to the paretic limb and real-world arm use in stroke patients, or the relationship between them. Our results showed that UL function and real-world arm use improved significantly across the 6-month study period. The longitudinal change in body-specific attention to the paretic hand was greatest at 1 month, although there were large individual differences. Our study also showed that, in patients in whom body-specific attention to the paretic hand increased up to 1 month, the real-world arm use increased up to 6 months. In addition, an increase in real-world arm use was associated with the recovery of UL function. Thus, our data suggested that increased body-specific attention to the paretic hand in the early phase after stroke was associated with long-term recovery of real-world arm use. These findings provide new insights into the relationship between real-world arm use and body representation in the brain, which may facilitate the use of the paretic hand, leading to long-term UL recovery after stroke.

Longitudinal Changes of Real-World Arm Use

One of the new findings in this study was that real-world arm use increased in the early phase after stroke and continued to improve over 6 months. This result was in contrast to previous studies that showed no improvement in daily use of the paretic arm, despite improved UL function, in subacute (Rand and Eng, 2012) and chronic stroke patients (Rand and Eng, 2015; Waddell et al., 2017), and supports recent studies that have shown improvement in arm use in the early phase (first 3 months) after onset (Waddell et al., 2019a). Additionally, our results confirmed the long-term recovery process up to 6 months. The present study also showed that UL function and the ability to manipulate objects during the process of recovery from UL paralysis after stroke improved significantly up to 2 months, and the improvement was maintained up to 6 months. These longitudinal data support previous reports on the motor recovery process in post-stroke UL paralysis (Duncan et al., 2000).

Participants had a mean FMA-UE motor of 31.3 at enrollment, which is a relatively severe score that would classify them as moderately paralyzed according to the FMA-UE motor severity classification (Severe: 0–28; Moderate: 29–42; Mild: 43–66; Woytowicz et al., 2017). The real-world arm use ratio at 6 months was 56.5%, which is a high score considering the previously reported 35% use ratio at 12 months after stroke (Rand and Eng, 2015). In most previous observational studies using accelerometers, the content and amount of UL rehabilitation after stroke were not controlled. Such differences in the rehabilitation provided may have affected the amount of use of the paretic hand. In the present study, by using a standardized program for the content and amount of UL rehabilitation after stroke (Harris et al., 2009, 2010; Murdolo et al., 2017; Simpson et al., 2017), the variation in arm use due to different rehabilitation methods was minimized and certain enhancing effects on arm use were achieved as compared to previous studies. Previous clinical trials of this program have reported improvements in UL function (Chedoke Arm and Hand Activity Inventory, ARAT, grip strength) and use of the arm in daily life (Harris et al., 2009). However, those previous studies used the Motor Activity Log (MAL), a patient-reported assessment for arm use, and it was unclear whether real-world arm use measured objectively also improved (Harris et al., 2009). In the present study, we demonstrated for the first time the process of long-term recovery of real-world arm use over 6 months, as observed with accelerometers, using a program that standardizes the content and amount of UL rehabilitation after stroke.

Longitudinal Changes of Body-Specific Attention

Body-specific attention showed a different recovery process from that of recovery of UL function and real-world arm use. Longitudinal changes in body-specific attention were highly individual and not significant, but based on mean values, they increased during the early post-stroke phase, up to 1 month, and decreased slowly up to 6 months. When compared with previous data of the body-specific attention for healthy older subjects (Aizu et al., 2018), body-specific attention in the present study was significantly lower at 2 weeks and did not differ from the values of healthy subjects at 1 month. Since body-specific attention is calculated based on the body facilitation effect of visual detection on the self-hand (Reed et al., 2006, 2010; Tseng et al., 2012), the fact that it was significantly lower than that of the healthy elderly subjects at the 2 weeks means that the paretic hand was not properly represented in the brain. In contrast, the fact that body-specific attention was not significantly different from that of the healthy elderly subjects at 1 month means that the paretic hand was properly represented in the brain as in the healthy elderly subjects. Previous fMRI studies examining brain representations of hand-related visual targets have reported greater activation in the intraparietal sulcus (IPS) and lateral occipital complex (LOC) when the visual target was presented near the hand compared to when it was presented farther away (Makin et al., 2007). Furthermore, comparisons between the real and dummy hand and different hand positions revealed that activity in the posterior IPS and LOC was more modulated by visual information of the hand, while activity in the anterior IPS was more modulated by proprioceptive information of the hand (Makin et al., 2007). The authors reported that cortical areas in the posterior IPS and LOC may represent the hand-centered space mainly visually, while the anterior IPS may represent

the space around the hand multisensory. It has been reported that such peripersonal spatial representation is represented by the posterior parietal cortex (PPC), which includes the IPS (Moseley et al., 2012). The PPC has a role in multisensory integration of vision and somatosensory perception and is classically considered to be a region involved in body schema and body image, which is appropriate for the representation of the self-body in the brain. The PPC is also involved in sensorimotor transformations and in directing attention to important information for motor planning to reach an object of interest based on body representations (Corbetta and Shulman, 2002; Sestieri et al., 2017). The results of these studies also suggest that measuring body-specific attention using a visual stimulus detection task may explain changes in body representations in the brain. Therefore, it is suggested that the increase in body-specific attention observed in the early phase reflects a process of adaptive changes in the body representation of the paretic hand in the brain.

Although body-specific attention at 6 months in stroke patients was not significantly different from that of healthy older people, the mean score was lower than that at 1 month after enrollment. Our previous cross-sectional study (Aizu et al., 2018) showed a negative correlation between body-specific attention and interval from stroke onset (7–192 months), suggesting that body-specific attention may gradually decrease during the stage that patients learn not to use the paretic hand, a phenomenon known as learned nonuse (Taub et al., 2002). The present longitudinal study supports such maladaptive changes of body-specific attention in chronic patients with stroke, suggested by the cross-sectional study.

Most patients have to adapt the body representations in the brain that have been constructed over a long period of time to a body that has changed significantly and suddenly due to stroke. While mildly paralyzed patients may adapt early, many paralyzed patients experience varying degrees of mismatch between their body and body representations in response to sudden changes in the body and nervous system. Similarly, a mismatch is known to occur in amputees with phantom limb pain, who do not have direct brain damage, but where the mismatch is caused by an inability to update the body representations previously built up in the brain in response to sudden physical changes (Flor et al., 1995; Ramachandran and Hirstein, 1998). Such mismatch between body representation and real body is also likely to occur in stroke patients, which might lead to maladaptive changes of body representation or a state known as learned nonuse. In addition, it has been reported that in stroke patients, early after the onset of stroke, the decrease in intracortical inhibition, or disinhibition (Liepert et al., 2000; Shimizu et al., 2002; Manganotti et al., 2008) and adaptive or compensatory reorganization of dynamic brain functions occur in the bilateral cerebral hemispheres (Marshall et al., 2000; Feydy et al., 2002; Ward et al., 2003; Tombari et al., 2004; Rehme et al., 2011b), which is considered to be one of the factors explaining the process of changes in body representation in the brain. Some animal studies (Calford and Tweedale, 1988, 2009) and neuroimaging studies in patients (Simões et al., 2012) suggested that plastic changes in brain sensory maps and body representations can occur either immediately (Calford and Tweedale, 2009) or slowly (Grüsser et al., 2001; Simões et al., 2012). Thus, longitudinal changes in body-specific attention were not significant, but based on mean values, the fast and large changes observed in the early phase up to 1 month and the slow and gradual changes observed up to 6 months in the present study may reflect the process of adaptive or maladaptive changes in the body representation of the paretic hand in the brain.

Body representations in the brain are formed and updated by sensory information from the body, and have a significant impact on motor control and body perception (Aymerich-Franch and Ganesh, 2016; Naito et al., 2016; Oouchida et al., 2016; Matamala-Gomez et al., 2020). Based on this principle, body-specific attention, which reflects body representations in the brain, is updated by sensory input during arm use, so it is conceivable that the more upper limbs are used, the higher the body-specific attention. Contrary to this relationship, it is important to clarify whether an increase in body-specific attention contributes to the promotion of arm use in order to develop rehabilitation that promotes the arm use. Symptoms characterized by reduced or complete lack of awareness and response to body or spatial stimuli contralateral to the brain lesion that occur after a stroke are known as USN (Buxbaum et al., 2004). In particular, neglect symptoms related to the body are referred to as body representation neglect, and deficits in attention to the body are recognized as body representation problems (Glocker et al., 2006; Cocchini et al., 2010). A previous report examining the relationship between attention to the paretic side and UL function after stroke showed that the more severe the USN, the lower the improvement in UL function (FMA), and reported on the possibility that the lack of attention to the paretic side space contributed to the nonuse of the paretic arm (Nijboer et al., 2014). Conversely, limb activation training (Robertson et al., 2010), which involves active paretic arm use in practice and daily life, has been reported to improve body-related deficits in spatial neglect in subacute stroke patients (Reinhart et al., 2012). It was concluded that the improvement in performance was probably due to activation of body representation in the brain by limb activation training (Reinhart et al., 2012). Furthermore, patients with motor neglect, a symptom of refusal to move the paretic arm, have both motor intention and attentional problems. However, it has been reported that when attention is directed to the paretic hand, motor performance improves (spatial errors during movement are improved; Punt et al., 2013). Based on these findings, it was known that attention to the paretic side space was interrelated with UL motor performance and arm use, and that increased attention to the paretic side space affected the paretic arm use. However, it is not clear whether increased body-specific attention would increase paretic arm use in stroke patients. The present study demonstrated positive correlation between increase in body-specific attention and increase in paretic arm use for the first time.

Correlation Between Body-Specific Attention and Real-World Arm Use

The most salient finding of this study was that there was a positive correlation between the amount of change in

body-specific attention during the early phase (longitudinal changes in body-specific attention were most remarkable up to 1 month) and the amount of long-term change in real-world arm use. These results were consistent with our hypothesis. Specifically, there was a positive correlation between the amount of change in body-specific attention (from baseline to 1 month) and the amount of change in real-world arm use (from baseline to 6 months) in this study. Furthermore, there was a stronger positive correlation between the amount of change in body-specific attention over the same period and the amount of change in real-world arm use (from 1 month to 6 months). Although short-term, there was also a positive correlation between the amount of change in body-specific attention at 2 weeks from baseline and the amount of change in real-world arm use at 2 months from baseline, supporting the idea that adaptive changes in body-specific attention are associated with increased real-world arm use. In contrast, cross-sectional correlation analysis showed no correlation between body-specific attention and real-world arm use in the subacute (baseline, 2 weeks, 1 month, 2 months) to early chronic post-stroke (6 months) stages in this study. These findings suggest that body-specific attention to the paretic hand would be an enhancing factor for arm use in hemiparetic patients.

Our results showed that changes in body-specific attention up to 1 month were associated with long-term changes in real-world arm use but changes in body-specific attention after 2 months were not associated with real-world arm use. In the early post-stroke period, previous fMRI and TMS studies have shown brain plastic changes, including activation of the contralesional hemisphere (Marshall et al., 2000; Feydy et al., 2002; Ward et al., 2003; Tombari et al., 2004; Rehme et al., 2011b), disinhibition of the ipsilesional hemisphere (Liepert et al., 2000; Manganotti et al., 2008), and disinhibition of the contralesional hemisphere (Shimizu et al., 2002; Manganotti et al., 2008). Furthermore, brain reorganization through dynamic changes in functional connectivity has been reported in both task and resting state fMRI studies (Grefkes et al., 2010; Grefkes and Fink, 2011; Park et al., 2011; Rehme et al., 2011a). In addition, long-term changes in brain activity reported in longitudinal studies have also revealed a process of convergence of bilateral hemispheric activity observed in the early post-onset period to the ipsilesional hemisphere between the acute and chronic periods (Marshall et al., 2000; Feydy et al., 2002; Ward et al., 2003; Tombari et al., 2004), as well as a process of asymmetry in intercortical functional connectivity that was maximal at 1 month but slowly reduced by 6 months (Park et al., 2011). These processes of brain disinhibition and long-term changes in brain activity and functional connectivity after stroke in previous studies are generally consistent with the process observed in the present study, in which body-specific attention, which reflects body representations in the brain, is maximal at 1 month and slowly decreases by 6 months.

Although the neural basis of body-specific attention is still unclear, there is evidence that body representation neglect (Glocker et al., 2006; Cocchini et al., 2010) and pusher phenomenon, which are impairments of body representations in the brain, often improve early after onset (Karnath et al., 2002; Danells et al., 2004). Such reports also support the possibility that reconstruction of body representations in the brain may occur early after stroke. In addition, it has been shown that reorganization of brain networks in the early post-stroke period promotes recovery of motor functions after stroke (Volz et al., 2016), which emphasizes the importance of brain reorganization in the early post-stroke period. Furthermore, it has been shown that the recovery of brain networks also correlates with the recovery of higher-order functions such as attention and language (Siegel et al., 2018), and it is possible that these brain networks are involved in the recovery of body-related attention. In the present study, we found an association between increased body-specific attention and improved long-term real-world arm use during a period of brain reorganization involving cortical disinhibition and dynamic changes in intracortical and intercortical functional connectivity. Therefore, it is suggested that the increase in body-specific attention (adaptive changes in body representations in the brain) during the period of abundant plasticity in the brain may have facilitated arm use based on appropriate body representations.

As expected from the principle of use-dependent brain plasticity reported in previous studies (Taub et al., 2002; Gauthier et al., 2008), early (from baseline to 2 months) changes in real-world arm use were correlated positively with changes in FMA-UE motor during the same period and also the longer period (from baseline to 6 months). Thus, it is concluded that real-world arm use is associated with long-term improvement in UL function.

In the present study, we showed that increased body-specific attention to the paretic hand in stroke patients, i.e., adaptive changes in body representation of the paretic hand in the brain, is associated with increased real-world arm use. Some studies have shown that improvement of paretic hand use contributes more to the improvement of quality of life (QOL) in stroke patients than UL function (Kelly et al., 2018). This underscores that understanding the relationship between body representations in the brain and real-world arm use has clinical significance for improving QOL in stroke patients.

Limitations

There are several limitations to this study. First, this study used GRASP to control the content and amount of upper extremity rehabilitation, and the results were obtained under the condition of 1 h of practice per day during hospitalization. Therefore, the results may not be the same for patients with poor UL practice. However, previous observational studies that focused on real-world arm use could not exclude the influence of differences in the content and amount of rehabilitation on the amount of real-world arm use. Thus, GRASP was suitable for this study because it could provide a standardized rehabilitation program according to the severity of paralysis, and a wide range of patients with severe to mild paralysis could be targeted. Second, only univariate analysis was available to analyze the association among arm use, body-specific attention, and UL function, as multivariate analysis was judged inappropriate due to the small sample size. Third, this was a single-center study. It is necessary to conduct a multicenter study in the future, with more case

accumulation. In addition, the above results were obtained only up to 6 months, and a study with a longer period of observation would be warranted because plastic changes in the brain have been reported even after 6 months (Tombari et al., 2004; Lin et al., 2018). Finally, further studies are also needed to discover ways to increase body-specific attention to the paretic limb in order to examine the effects of the increase in body-specific attention on real-world arm use and motor recovery after stroke.

CONCLUSION

In the recovery process of paretic UL, body-specific attention to the paretic hand was found to be related to real-world arm use in patients after stroke. The findings in this longitudinal study suggest adaptive changes in body representation of the paretic limb in the brain during the early phase contributes to increasing long-term real-world arm use and are associated with UL recovery through use-dependent plasticity. We believe that the results will contribute to the innovation of rehabilitation strategies to enhance adaptive changes in body representation in the brain and increase real-world arm use after stroke.

DATA AVAILABILITY STATEMENT

The raw data supporting the conclusions of this article will be made available by the authors, without undue reservation.

ETHICS STATEMENT

The studies involving human participants were reviewed and approved by The Tohoku University and Yamagata Saisei Hospital ethics committee. The patients/participants provided their written informed consent to participate in this study.

AUTHOR CONTRIBUTIONS

ST and YS recruited patients and were medically in charge of the patients. RO managed the quality of clinical rehabilitation and examinations; collected the clinical examination data and analyzed the clinical examination data. RO, YO, NA, TS, HS, and S-II conceived and designed the study. YO and S-II critically reviewed the manuscript. All authors contributed to the article and approved the submitted version.

FUNDING

This work was partially supported by JSPS KAKENHI, Grant-in-Aid for Scientific Research (Grant No. 20H05456).

ACKNOWLEDGMENTS

We thank the Rehabilitation Department of Yamagata Saisei Hospital for their assistance, and also thank all the participants for their dedication, time, and effort to this study.

REFERENCES

Aizu, N., Oouchida, Y., and Izumi, S. I. (2018). Time-dependent decline of body-specific attention to the paretic limb in chronic stroke patients. *Neurology* 91, e751–e758. doi: 10.1212/WNL.0000000000006030

Alt Murphy, M., Andersson, S., Danielsson, A., Wipenmyr, J., and Ohlsson, F. (2019). Comparison of accelerometer-based arm, leg and trunk activity at weekdays and weekends during subacute inpatient rehabilitation after stroke. *J. Rehabil. Med.* 51, 426–433. doi: 10.2340/16501977-2553

Alt Murphy, M., Persson, H. C., Danielsson, A., Broeren, J., Lundgren-Nilsson, Å., and Sunnerhagen, K. S. (2011). SALGOT - stroke arm longitudinal study at the university of gothenburg, prospective cohort study protocol. *BMC Neurol.* 11:56. doi: 10.1186/1471-2377-11-56

Aymerich-Franch, L., and Ganesh, G. (2016). The role of functionality in the body model for self-attribution. *Neurosci. Res.* 104, 31–37. doi: 10.1016/j.neures.2015.11.001

Buxbaum, L. J., Ferraro, M. K., Veramonti, T., Farne, A., Whyte, J., Ladavas, E., et al. (2004). Hemispatial neglect: subtypes, neuroanatomy, and disability. *Neurology* 62, 749–756. doi: 10.1212/01.wnl.0000113730.73031.f4

Calford, M. B., and Tweedale, R. (1988). Immediate and chronic changes in responses of somatosensory cortex in adult flying-fox after digit amputation. *Nature* 332, 446–448. doi: 10.1038/332446a0

Calford, M. B., and Tweedale, R. (2009). Immediate expansion of receptive fields of neurons in area 3b of macaque monkeys after digit denervation. *Somatosens. Mot. Res.* 8, 249–260. doi: 10.3109/08990229109144748

Cocchini, G., Beschin, N., and Jehkonen, M. (2010). The fluff test: a simple task to assess body representation neglect. *Neuropsychol. Rehabil.* 11, 17–31. doi: 10.1080/09602010042000132

Corbetta, M., and Shulman, G. L. (2002). Control of goal-directed and stimulus-driven attention in the brain. *Nat. Rev. Neurosci.* 3, 201–215. doi: 10.1038/nrn755

Danells, C. J., Black, S. E., Gladstone, D. J., and McIlroy, W. E. (2004). Poststroke "pushing". Natural history and relationship to motor and functional recovery. *Stroke* 35, 2873–2878. doi: 10.1161/01.STR.0000147724.83468.18

Doman, C. A., Waddell, K. J., Bailey, R. R., Moore, J. L., and Lang, C. E. (2016). Changes in upper-extremity functional capacity and daily performance during outpatient occupational therapy for people with stroke. *Am. J. Occup. Ther.* 70, 7003290040p1–7003290040p11. doi: 10.5014/ajot.2016.020891

Duncan, P. W., Min Lai, S., and Keighley, J. (2000). Defining post-stroke recovery: implications for design and interpretation of drug trials. *Neuropharmacology* 39, 835–841. doi: 10.1016/s0028-3908(00)00003-4

Feydy, A., Carlier, R., Roby-Brami, A., Bussel, B., Cazalis, F., Pierot, L., et al. (2002). Longitudinal study of motor recovery after stroke. *Stroke* 33, 1610–1617. doi: 10.1161/01.str.0000017100.68294.52

Flor, H., Elbert, T., Knecht, S., Wienbruch, C., Pantev, C., Birbaumers, N., et al. (1995). Phantom-limb pain as a perceptual correlate of cortical reorganization following arm amputation. *Nature* 375, 482–484. doi: 10.1038/375482a0

Franck, J. A., Smeets, R. J. E. M., and Seelen, H. A. M. (2019). Changes in actual arm-hand use in stroke patients during and after clinical rehabilitation involving a well-defined arm-hand rehabilitation program: a prospective cohort study. *PLoS One* 14:e0214651. doi: 10.1371/journal.pone.0214651

Fugl-Meyer, A. R., Jääskö, L., Leyman, I., and Olsson, S. (1975). The post-stroke hemiplegic patient. 1. a method for evaluation of physical performance. *Scand. J. Rehabil. Med.* 7, 13–31.

Gallagher, S. (2000). Philosophical conceptions of the self: implications for cognitive science. *Trends Cogn. Sci.* 4, 14–21. doi: 10.1016/s1364-6613(99)01417-5

Gauthier, L. V., Taub, E., Perkins, C., Ortmann, M., Mark, V. W., and Uswatte, G. (2008). Remodeling the brain: plastic structural brain changes produced by different motor therapies after stroke. *Stroke* 39, 1520–1525. doi: 10.1161/STROKEAHA.107.502229

Gebruers, N., Truijen, S., Engelborghs, S., and De Deyn, P. P. (2014). Prediction of upper limb recovery, general disability and rehabilitation status by activity measurements assessed by accelerometers or the fugl-meyer score

in acute stroke. *Am. J. Phys. Med. Rehabil.* 93, 245–252. doi: 10.1097/PHM.0000000000000045

Gebruers, N., Truijen, S., Engelborghs, S., and Deyn, P. P. D. (2008). Actigraphic measurement of motor deficits in acute ischemic stroke. *Cerebrovasc. Dis.* 26, 533–540. doi: 10.1159/000160210

Glocker, D., Bittl, P., and Kerkhoff, G. (2006). Construction and psychometric properties of a novel test for body representational neglect (Vest Test). *Restor. Neurol. Neurosci.* 24, 303–317. Available online at https://pubmed.ncbi.nlm.nih.gov/17119306/. Accessed October 17, 2021.

Gresham, G. E., Duncan, P. W., Stason, W. B., Adams, H. P., Adelman, A. M., Alexander, N. et al. (1995). "Post-stroke rehabilitation," in *Clinical Practice Guideline, No. 16*. Rockville, MD: U.S. Department of Health and Human Services. Public Health Service, Agency for Health Care Policy and Research.

Grefkes, C., and Fink, G. R. (2011). Reorganization of cerebral networks after stroke: new insights from neuroimaging with connectivity approaches. *Brain* 134, 1264–1276. doi: 10.1093/brain/awr033

Grefkes, C., Nowak, D. A., Wang, L. E., Dafotakis, M., Eickhoff, S. B., and Fink, G. R. (2010). Modulating cortical connectivity in stroke patients by rTMS assessed with fMRI and dynamic causal modeling. *Neuroimage* 50, 233–242. doi: 10.1016/j.neuroimage.2009.12.029

Grüsser, S. M., Winter, C., Mühlnickel, W., Denke, C., Karl, A., Villringer, K., et al. (2001). The relationship of perceptual phenomena and cortical reorganization in upper extremity amputees. *Neuroscience* 102, 263–272. doi: 10.1016/s0306-4522(00)00491-7

Hari, R., and Jousmäki, V. (1996). Preference of personal to extrapersonal space in a visuomotor task. *J. Cogn. Neurosci.* 8, 305–307. doi: 10.1162/jocn.1996.8.3.305

Harris, J. E., Eng, J. J., Miller, W. C., and Dawson, A. S. (2009). A self-administered graded repetitive arm supplementary program (GRASP) improves arm function during inpatient stroke rehabilitation: a multi-site randomized controlled trial. *Stroke* 40, 2123–2128. doi: 10.1161/STROKEAHA.108.544585

Harris, J. E., Eng, J. J., Miller, W. C., and Dawson, A. S. (2010). The role of caregiver involvement in upper-limb treatment in individuals with subacute stroke. *Phys. Ther.* 90, 1302–1310. doi: 10.2522/ptj.20090349

Hayward, K. S., Eng, J. J., Boyd, L. A., Lakhani, B., Bernhardt, J., and Lang, C. E. (2016). Exploring the role of accelerometers in the measurement of real world upper-limb use after stroke. *Brain Impair.* 17, 16–33. doi: 10.1017/BrImp.2015.21

Hebert, D., Lindsay, M. P., McIntyre, A., Kirton, A., Rumney, P. G., Bagg, S., et al. (2016). Canadian stroke best practice recommendations: Stroke rehabilitation practice guidelines, update 2015. *Int. J. Stroke* 11:1747493016643553. doi: 10.1177/1747493016643553

Kao, K. L. C., and Goodale, M. A. (2009). Enhanced detection of visual targets on the hand familiar tools. *Neuropsychologia* 47, 2454–2463. doi: 10.1016/j.neuropsychologia.2009.04.016

Karnath, H. O., Johannsen, L., Broetz, D., Ferber, S., and Dichgans, J. (2002). Prognosis of contraversive pushing. *J. Neurol.* 249, 1250–1253. doi: 10.1007/s00415-002-0824-z

Kelly, K. M., Borstad, A. L., Kline, D., and Gauthier, L. V. (2018). Improved quality of life following constraint-induced movement therapy is associated with gains in arm use, but not motor improvement. *Top. Stroke Rehabil.* 25, 467–474. doi: 10.1080/10749357.2018.1481605

Liepert, J., Storch, P., Fritsch, A., and Weiller, C. (2000). Motor cortex disinhibition in acute stroke. *Clin. Neurophysiol.* 111, 671–676. doi: 10.1016/s1388-2457(99)00312-0

Lin, L. Y., Ramsey, L., Metcalf, N. V., Rengachary, J., Shulman, G. L., Shimony, J. S., et al. (2018). Stronger prediction of motor recovery and outcome post-stroke by cortico-spinal tract integrity than functional connectivity. *PLoS One* 13:e0202504. doi: 10.1371/journal.pone.0202504

Lyle, R. (1981). A performance test for assessment of upper limb function in physical rehabilitation treatment and research. *Int. J. Rehabil. Res.* 4, 483–492. doi: 10.1097/00004356-198112000-00001

Makin, T. R., Holmes, N. P., and Zohary, E. (2007). Is that near my hand? multisensory representation of peripersonal space in human intraparietal sulcus. *J. Neurosci.* 27, 731–740. doi: 10.1523/JNEUROSCI.3653-06.2007

Manganotti, P., Acler, M., Zanette, G. P., Smania, N., and Fiaschi, A. (2008). Motor cortical disinhibition during early and late recovery after stroke. *Neurorehabil. Neural Repair* 22, 396–403. doi: 10.1177/1545968307313505

Marshall, R. S., Perera, G. M., Lazar, R. M., Krakauer, J. W., Constantine, R. C., and DeLaPaz, R. L. (2000). Evolution of cortical activation during recovery from corticospinal tract infarction. *Stroke* 31, 656–661. doi: 10.1161/01.str.31.3.656

Matamala-Gomez, M., Malighetti, C., Cipresso, P., Pedroli, E., Realdon, O., Mantovani, F., et al. (2020). Changing body representation through full body ownership illusions might foster motor rehabilitation outcome in patients with stroke. *Front. Psychol.* 11:1962. doi: 10.3389/fpsyg.2020.01962

Morris, D. M., Taub, E., and Mark, V. W. (2006). Constraint-induced movement therapy: characterizing the intervention protocol. *Eura. Medicophys.* 42, 257–268.

Moseley, G. L., Gallace, A., and Spence, C. (2012). Bodily illusions in health and disease: physiological and clinical perspectives and the concept of a cortical "body matrix". *Neurosci. Biobehav. Rev.* 36, 34–46. doi: 10.1016/j.neubiorev.2011.03.013

Murdolo, Y., Brown, T., Fielding, L., Elliott, S., and Castles, E. (2017). Stroke survivors' experiences of using the graded repetitive arm supplementary program (GRASP) in an australian acute hospital setting: a mixed-methods pilot study. *Aust. Occup. Ther. J.* 64, 305–313. doi: 10.1111/1440-1630.12363

Naito, E., Morita, T., and Amemiya, K. (2016). Body representations in the human brain revealed by kinesthetic illusions and their essential contributions to motor control and corporeal awareness. *Neurosci. Res.* 104, 16–30. doi: 10.1016/j.neures.2015.10.013

Nichols-Larsen, D. S., Clark, P. C., Zeringue, A., Greenspan, A., and Blanton, S. (2005). Factors influencing stroke survivors' quality of life during subacute recovery. *Stroke* 36, 1480–1484. doi: 10.1161/01.STR.0000170706.13595.4f

Nijboer, T. C. W., Kollen, B. J., and Kwakkel, G. (2014). The impact of recovery of visuo-spatial neglect on motor recovery of the upper paretic limb after stroke. *PLoS One* 9:e100584. doi: 10.1371/journal.pone.0100584

Noorkoiv, M., Rodgers, H., and Price, C. I. (2014). Accelerometer measurement of upper extremity movement after stroke: a systematic review of clinical studies. *J. Neuroeng. Rehabil.* 11:144. doi: 10.1186/1743-0003-11-144

Oouchida, Y., Sudo, T., Inamura, T., Tanaka, N., Ohki, Y., and Izumi, S.-I. (2016). Maladaptive change of body representation in the brain after damage to central or peripheral nervous system. *Neurosci. Res.* 104, 38–43. doi: 10.1016/j.neures.2015.12.015

Park, C. H., Chang, W. H., Ohn, S. H., Kim, S. T., Bang, O. Y., Pascual-Leone, A., et al. (2011). Longitudinal changes of resting-state functional connectivity during motor recovery after stroke. *Stroke* 42, 1357–1362. doi: 10.1161/STROKEAHA.110.596155

Persson, H. C., Parziali, M., Danielsson, A., and Sunnerhagen, K. S. (2012). Outcome and upper extremity function within 72 hours after first occasion of stroke in an unselected population at a stroke unit. a part of the SALGOT study. *BMC Neurol.* 12:162. doi: 10.1186/1471-2377-12-162

Punt, T. D., Riddoch, M. J., and Humphreys, G. W. (2013). Motor extinction: a deficit of attention or intention. *Front. Hum. Neurosci.* 7:644. doi: 10.3389/fnhum.2013.00644

Ramachandran, V. S., and Hirstein, W. (1998). The perception of phantom limbs. the D. O. hebb lecture. *Brain* 121, 1603–1630. doi: 10.1093/brain/121.9.1603

Rand, D., and Eng, J. J. (2012). Disparity between functional recovery and daily use of the upper and lower extremities during subacute stroke rehabilitation. *Neurorehabil. Neural Repair* 26, 76–84. doi: 10.1177/1545968311408918

Rand, D., and Eng, J. J. (2015). Predicting daily use of the affected upper extremity 1 year after stroke. *J. Stroke Cerebrovasc. Dis.* 24, 274–283. doi: 10.1016/j.jstrokecerebrovasdis.2014.07.039

Reed, C. L., Betz, R., Garza, J. P., and Roberts, R. J. (2010). Grab it! biased attention in functional hand tool space. *Attention, Perception, Psychophys.* 72, 236–245. doi: 10.3758/APP.72.1.236

Reed, C. L., Grubb, J. D., and Steele, C. (2006). Hands up: Attentional priorization of space near the hand. *J. Exp. Psychol. Hum. Percept. Perform.* 32, 166–177. doi: 10.1037/0096-1523.32.1.166

Rehme, A. K., Eickhoff, S. B., Wang, L. E., Fink, G. R., and Grefkes, C. (2011a). Dynamic causal modeling of cortical activity from the acute to the chronic stage after stroke. *Neuroimage* 55, 1147–1158. doi: 10.1016/j.neuroimage.2011.01.014

Rehme, A. K., Fink, G. R., von Cramon, D. Y., and Grefkes, C. (2011b). The role of the contralesional motor cortex for motor recovery in the early days after stroke assessed with longitudinal fMRI. *Cereb. Cortex* 21, 756–768. doi: 10.1093/cercor/bhq140

Reinhart, S., Schmidt, L., Kuhn, C., Rosenthal, A., Schenk, T., Keller, I., et al. (2012). Limb activation ameliorates body-related deficits in spatial neglect. *Front. Hum. Neurosci.* 6:188. doi: 10.3389/fnhum.2012.00188

Robertson, I. H., McMillan, T. M., MacLeod, E., Edgeworth, J., and Brock, D. (2010). Rehabilitation by limb activation training reduces left-sided motor impairment in unilateral neglect patients: a single-blind randomised control trial. *Neuropsychol. Rehabil.* 12, 439–454. doi: 10.1080/09602010244000228

Sestieri, C., Shulman, G. L., and Corbetta, M. (2017). The contribution of the human posterior parietal cortex to episodic memory. *Nat. Rev. Neurosci.* 18, 183–192. doi: 10.1038/nrn.2017.6

Shimizu, T., Hosaki, A., Hino, T., Sato, M., Komori, T., Hirai, S., et al. (2002). Motor cortical disinhibition in the unaffected hemisphere after unilateral cortical stroke. *Brain* 125, 1896–1907. doi: 10.1093/brain/awf183

Siegel, J. S., Seitzman, B. A., Ramsey, L. E., Ortega, M., Gordon, E. M., Dosenbach, N. U. F., et al. (2018). Re-emergence of modular brain networks in stroke recovery. *Cortex* 101, 44–59. doi: 10.1016/j.cortex.2017.12.019

Simões, E. L., Bramati, I., Rodrigues, E., Franzoi, A., Moll, J., Lent, R., et al. (2012). Functional expansion of sensorimotor representation and structural reorganization of callosal connections in lower limb amputees. *J. Neurosci.* 32, 3211–3220. doi: 10.1523/JNEUROSCI.4592-11.2012

Simpson, L. A., Eng, J. J., and Chan, M. (2017). H-GRASP: the feasibility of an upper limb home exercise program monitored by phone for individuals post stroke. *Disabil. Rehabil.* 39, 874–882. doi: 10.3109/09638288.2016.1162853

Taub, E., Uswatte, G., and Elbert, T. (2002). New treatments in neurorehabiliation founded on basic research. *Nat. Rev. Neurosci.* 3, 228–236. doi: 10.1038/nrn754

Taub, E., Uswatte, G., Bowman, M. H., Mark, V. W., Delgado, A., Bryson, C., et al. (2013). Constraint-induced movement therapy combined with conventional neurorehabilitation techniques in chronic stroke patients with plegic hands: a case series. *Arch. Phys. Med. Rehabil.* 94, 86–94. doi: 10.1016/j.apmr.2012.07.029

Thrane, G., Emaus, N., Askim, T., and Anke, A. (2011). Arm use in patients with subacute stroke monitored by accelerometry: association with motor impairment and influence on self-dependence. *J. Rehabil. Med.* 43, 299–304. doi: 10.2340/16501977-0676

Tombari, D., Loubinoux, I., Pariente, J., Gerdelat, A., Albucher, J. F., Tardy, J., et al. (2004). A longitudinal fMRI study: in recovering and then in clinically stable sub-cortical stroke patients. *Neuroimage* 23, 827–839. doi: 10.1016/j.neuroimage.2004.07.058

Tseng, P., Bridgeman, B., and Juan, C. H. (2012). Take the matter into your own hands: a brief review of the effect of nearby-hands on visual processing. *Vis. Res.* 72, 74–77. doi: 10.1016/j.visres.2012.09.005

Uswatte, G., Foo, W. L., Olmstead, H., Lopez, K., Holand, A., and Simms, L. B. (2005a). Ambulatory monitoring of arm movement using accelerometry: an objective measure of upper-extremity rehabilitation in persons with chronic stroke. *Arch. Phys. Med. Rehabil.* 86, 1498–1501. doi: 10.1016/j.apmr.2005.01.010

Uswatte, G., Giuliani, C., Winstein, C., Zeringue, A., Hobbs, L., and Wolf, S. L. (2006). Validity of accelerometry for monitoring real-world arm activity in patients with subacute stroke: evidence from the extremity constraint-induced therapy evaluation trial. *Arch. Phys. Med. Rehabil.* 87, 1340–1345. doi: 10.1016/j.apmr.2006.06.006

Uswatte, G., Miltner, W. H. R., Foo, B., Varma, M., Moran, S., and Taub, E. (2000). Objective measurement of functional upper-extremity movement using accelerometer recordings transformed with a threshold filter. *Stroke* 31, 662–667. doi: 10.1161/01.str.31.3.662

Uswatte, G., Taub, E., Morris, D., Vignolo, M., and McCulloch, K. (2005b). Reliability and validity of the upper-extremity motor activity log-14 for measuring real-world arm use. *Stroke* 36, 2493–2496. doi: 10.1161/01.STR.0000185928.90848.2e

Van der Lee, J. H., De Groot, V., Beckerman, H., Wagenaar, R. C., Lankhorst, G. J., and Bouter, L. M. (2001). The intra- and interrater reliability of the action research arm test: a practical test of upper extremity function in patients with stroke. *Arch. Phys. Med. Rehabil.* 82, 14–19. doi: 10.1053/apmr.2001.18668

Van Der Pas, S. C., Verbunt, J. A., Breukelaar, D. E., Van Woerden, R., and Seelen, H. A. (2011). Assessment of Arm activity using triaxial accelerometry in patients with a stroke. *Arch. Phys. Med. Rehabil.* 92, 1437–1442. doi: 10.1016/j.apmr.2011.02.021

Volz, L. J., Rehme, A. K., Michely, J., Nettekoven, C., Eickhoff, S. B., Fink, G. R., et al. (2016). Shaping early reorganization of neural networks promotes motor function after stroke. *Cereb. Cortex* 26, 2882–2894. doi: 10.1093/cercor/bhw034

Waddell, K. J., Strube, M. J., Bailey, R. R., Klaesner, J. W., Birkenmeier, R. L., Dromerick, A. W., et al. (2017). Does task-specific training improve upper limb performance in daily life poststroke. *Neurorehabil. Neural Repair* 31, 290–300. doi: 10.1177/1545968316680493

Waddell, K. J., Strube, M. J., Tabak, R. G., Haire-Joshu, D., and Lang, C. E. (2019a). Upper limb performance in daily life improves over the first 12 weeks poststroke. *Neurorehabil. Neural Repair* 33, 836–847. doi: 10.1177/1545968319868716

Waddell, K. J., Tabak, R. G., Strube, M. J., Haire-Joshu, D., and Lang, C. E. (2019b). Belief, confidence and motivation to use the paretic upper limb in daily life over the first 24 weeks after stroke. *J. Neurol. Phys. Ther.* 43, 197–203. doi: 10.1097/NPT.0000000000000287

Ward, N. S., Brown, M. M., Thompson, A. J., and Frackowiak, R. S. J. (2003). Neural correlates of motor recovery after stroke: a longitudinal fMRI study. *Brain* 126, 2476–2496. doi: 10.1093/brain/awg245

Whiteley, L., Kennett, S., Taylor-Clarke, M., and Haggard, P. (2004). Facilitated processing of visual stimuli associated with the body. *Perception* 33, 307–314. doi: 10.1068/p5053

Whiteley, L., Spence, C., and Haggard, P. (2008). Visual processing and the bodily self. *Acta Psychol. (Amst).* 127, 129–136. doi: 10.1016/j.actpsy.2007.03.005

Winstein, C. J., Stein, J., Arena, R., Bates, B., Cherney, L. R., Cramer, S. C., et al. (2016). Guidelines for adult stroke rehabilitation and recovery: a guideline for healthcare professionals from the american heart association/american stroke association. *Stroke* 47, e98–e169. doi: 10.1161/STR.0000000000000098

Woytowicz, E. J., Rietschel, J. C., Goodman, R. N., Conroy, S. S., Sorkin, J. D., Whitall, J., et al. (2017). Determining levels of upper extremity movement impairment by applying a cluster analysis to the fugl-meyer assessment of the upper extremity in chronic stroke. *Arch. Phys. Med. Rehabil.* 98, 456–462. doi: 10.1016/j.apmr.2016.06.023

Conflict of Interest: The authors declare that the research was conducted in the absence of any commercial or financial relationships that could be construed as a potential conflict of interest.

Publisher's Note: All claims expressed in this article are solely those of the authors and do not necessarily represent those of their affiliated organizations, or those of the publisher, the editors and the reviewers. Any product that may be evaluated in this article, or claim that may be made by its manufacturer, is not guaranteed or endorsed by the publisher.

Copyright © 2022 Otaki, Oouchida, Aizu, Sudo, Sasahara, Saito, Takemura and Izumi. This is an open-access article distributed under the terms of the Creative Commons Attribution License (CC BY). The use, distribution or reproduction in other forums is permitted, provided the original author(s) and the copyright owner(s) are credited and that the original publication in this journal is cited, in accordance with accepted academic practice. No use, distribution or reproduction is permitted which does not comply with these terms.

frontiers in Systems Neuroscience

METHODS
published: 25 February 2022
doi: 10.3389/fnsys.2022.786200

Real-Time Detection and Feedback of Canonical Electroencephalogram Microstates: Validating a Neurofeedback System as a Function of Delay

Tomohisa Asai[1], Takamasa Hamamoto[1,2], Shiho Kashihara[1] and Hiroshi Imamizu[1,3]*

[1] Cognitive Mechanisms Laboratories, Advanced Telecommunications Research Institute International (ATR), Kyoto, Japan, [2] Graduate School of Frontier Biosciences, Osaka University, Osaka, Japan, [3] Department of Psychology, Graduate School of Humanities and Sociology, The University of Tokyo, Tokyo, Japan

Recent neurotechnology has developed various methods for neurofeedback (NF), in which participants observe their own neural activity to be regulated in an ideal direction. EEG-microstates (EEGms) are spatially featured states that can be regulated through NF training, given that they have recently been indicated as biomarkers for some disorders. The current study was conducted to develop an EEG-NF system for detecting "canonical 4 EEGms" in real time. There are four representative EEG states, regardless of the number of channels, preprocessing procedures, or participants. Accordingly, our 10 Hz NF system was implemented to detect them (msA, B, C, and D) and audio-visually inform participants of its detection. To validate the real-time effect of this system on participants' performance, the NF was intentionally delayed for participants to prevent their cognitive control in learning. Our results suggest that the feedback effect was observed only under the no-delay condition. The number of Hits increased significantly from the baseline period and increased from the 1- or 20-s delay conditions. In addition, when the Hits were compared among the msABCD, each cognitive or perceptual function could be characterized, though the correspondence between each microstate and psychological ability might not be that simple. For example, msD should be generally task-positive and less affected by the inserted delay, whereas msC is more delay-sensitive. In this study, we developed and validated a new EEGms-NF system as a function of delay. Although the participants were naive to the inserted delay, the real-time NF successfully increased their Hit performance, even within a single-day experiment, although target specificity remains unclear. Future research should examine long-term training effects using this NF system.

Keywords: neurofeedback, delay, EEG microstates, control, sense of agency

OPEN ACCESS

Edited by:
Dietmar Plenz,
National Institute of Mental Health (NIH), United States

Reviewed by:
Frederic Von Wegner,
University of New South Wales, Australia
Anthony Zanesco,
University of Miami, United States

****Correspondence:***
Tomohisa Asai
asai@atr.jp

Received: *30 September 2021*
Accepted: *04 February 2022*
Published: *25 February 2022*

Citation:
Asai T, Hamamoto T, Kashihara S and Imamizu H (2022) Real-Time Detection and Feedback of Canonical Electroencephalogram Microstates: Validating a Neurofeedback System as a Function of Delay. Front. Syst. Neurosci. 16:786200. doi: 10.3389/fnsys.2022.786200

INTRODUCTION

Recent neurotechnology has developed various methods for neurofeedback (NF), in which participants observe their own neural activity to be regulated in an ideal direction. This neuromodulation through long-term training could improve participants' cognitive performance or even some clinical traits for people with mental disorders

(see for review, Watanabe et al., 2017; Lubianiker et al., 2019). These previous findings suggest our mental adaptability, where the NF system serves to assist our innate ability to learn new mental states. Since neural activity itself does not produce any sensory feedback within the brain, the system can "externalize" that activity to be controlled by the participants themselves. This strategy has been technically developed in terms of brain-computer-interface (BCI), where participants can control the externalized "sensory feedback" of their neural activity through training.

Regarding the implementation of the NF system, there are two options: spatial or temporal priority over the neural representations of the brain. The former is achieved by functional magnetic resonance imaging (fMRI)-NF, while the latter is mainly achieved by electroencephalogram (EEG)-NF. In terms of clinical application, resting-state functional connectivity (FC) in fMRI analysis can be a target of fMRI-NF (i.e., FC-NF), since FC is assumed to be a biomarker for some mental disorders (e.g., Yamada et al., 2017). More recently, however, resting-state EEG signals have also been actively used in line this this, taking advantage of its high temporal resolution to complement the disadvantages of fMRI, which has a resolution of only a few seconds, making it difficult to provide immediate feedback. One useful EEG measure in the context of NF is the EEG microstate. EEG-microstates (EEGms) are spatially featured expressions that can be regulated through NF training (Diaz Hernandez et al., 2016) since recent studies have also suggested EEGms as biomarkers (e.g., da Cruz et al., 2020; Murphy et al., 2020).

Accordingly, the current study was conducted to develop an EEG-NF system for detecting "canonical EEGms" in real time (see **Figure 1** for an overview). Once simple resting-state EEG data are collected from a sufficient participant population, group-level common EEG states can be obtained. Previous studies have repeatedly reported that there are only four representative EEG states, regardless of the number of channels, preprocess procedures, or participants (Khanna et al., 2015). Although the optimal number of canonical states remains debatable (Seitzman et al., 2017; Michel and Koenig, 2018), the four most agreed-upon spatial patterns are often called msA, B, C, and D (**Figure 2**). Therefore, in this study, our 10 Hz NF system was implemented to detect all four msABCD and audio-visually inform participants of its detection, unlike a previous NF system for a specific microstate (Diaz Hernandez et al., 2016).

The EEGms are observed as quasi-stable potentials lasting 60–120 ms that represent whole-brain network activity (Michel and Koenig, 2018). The suggested procedure for EEGms analysis consists of two main stages: *clustering* and *labeling*. At the clustering stage, the standard deviation (global field power: GFP) among all electrodes is first calculated for each recording session. The time points of the greatest strength in the neuroelectric field, namely GFP peaks, are well-reasoned to best represent periods of momentary stability in the voltage topography (Zanesco, 2020). Consequently, it is preferable to select GFP peak points to achieve a high signal-to-noise ratio. Every spatial pattern at the local maximum of each GFP time series is accumulated as the GFP peak dataset for a participant group as a whole. An unsupervised learning algorithm, such as K-means, conducts clustering of the GFP peak dataset into optimal classes. Finally, group-wise common topographies are obtained as templates (i.e., centroid) for each class (typically, msA, B, C, and D). After that, the labeling procedure calculates the similarity between the templates obtained and every time point (including the GFP peak points) of the participants and labels one of them (e.g., msA) for all data points in a so-called "winner-take-all" manner (see section "Discussion", Mishra et al., 2020). Since each topography should last for a while in a millisecond order, the original EEG data with multiple channels are now simply seen as a state transition pattern among four states, such as C, D, B, A, D, etc. As a result, the EEGms analysis typically reveals the frequency of the state ("occurrence"), the lasting of the state ("duration"), and transition patterns among the states ("transition probability") for each recording session or each participant. These depicted features of EEGms can be compared among participant groups as potential biomarkers (de Bock et al., 2020; Perrottelli et al., 2021).

The current study examined the real-time effect of the developed NF system, which has been implemented to detect canonical msABCD (group-wise common topographies) and audio-visually inform participants of its detection. The audio-visual NF, however, was intentionally delayed for participants to prevent their control in learning (i.e., hit the targeted state; see section "Materials and Methods"). We hypothesized that an inserted delay would affect participants' learning through the NF system due to their inability to utilize the feedback. Although EEG-NF is advantageous in terms of its temporal resolution in comparison with fMRI-NF, the real-time effect has not been examined well in the literature, especially for EEGms. Given that the EEGms might be assumed as basic components of consciousness, often referred to as "atoms of thoughts" (Koukkou and Lehmann, 1987; Lehmann, 1992; Lehmann et al., 1998; Changeux and Michel, 2006), and last for a short period of time, EEGms-NF should become less effective with a certain delay (e.g., over some hundreds of milliseconds). Aside from EEGms-NF, several studies have attempted to implement real-time EEG feedback (Zich et al., 2015; Pei et al., 2020). A recent study examined the effect of latency in visual NF that falls within the range of 300 to 1000 ms in terms of a parietal alpha rhythm (Belinskaya et al., 2020), and concluded that the delay is a crucial parameter that must be minimized to achieve the desired NF effect. This policy is also motivation to enhance the "sense of agency" for participants in their NF training: a feeling of "I am the origin of the sensory feedback" (Gallagher, 2000). In addition to many psychophysical studies that have demonstrated that the feedback delay clearly reduces both participants' sense of agency (Asai and Tanno, 2007; Asai, 2016) and their performance in motor control tasks (Tanaka et al., 2011), Evans et al. also suggested that an inserted delay resulted in a reduced sense of agency over the externalized feedback through a motor imagery-based BCI system (Evans et al., 2015).

The aim of the current study was to develop a closed-loop NF system and validate it as a function of the inserted delay. Participants were instructed to attempt to make more "Hits" with audio-visual feedback (see **Figures 3**, **4** for the definition of "Hits"). However, in some conditions (i.e., "sessions" in the current case) the additional delay was inserted between

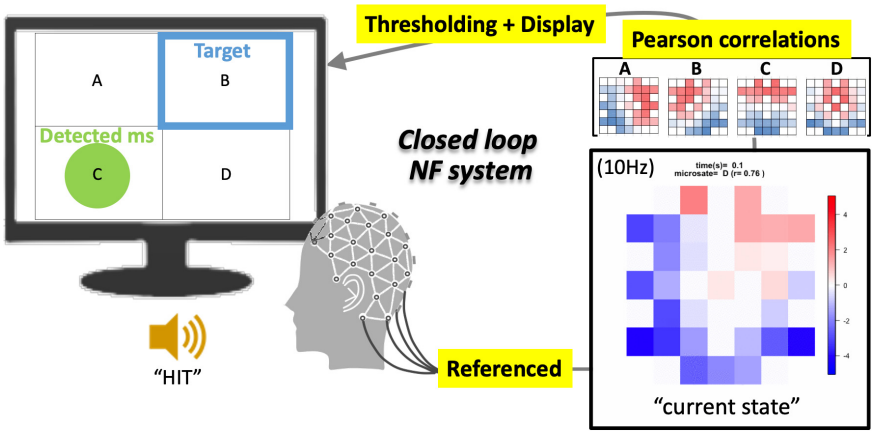

FIGURE 1 | Schematics of EEGms neurofeedback system. The referenced bipolar signals are processed every 100 ms (10 Hz) into an epoch-averaged spatial pattern. This current state is compared with four EEGms templates on the basis of spatial similarity (Pearson's correlation). When the largest value among the four absolute correlation coefficients is greater than 0.8 (for example) threshold, the display suggests a green circle in the corresponding area. The targeted state is suggested at the same time using a blue frame. If the green circle overlaps the blue frame, the participants receive a ringing sound as a reward.

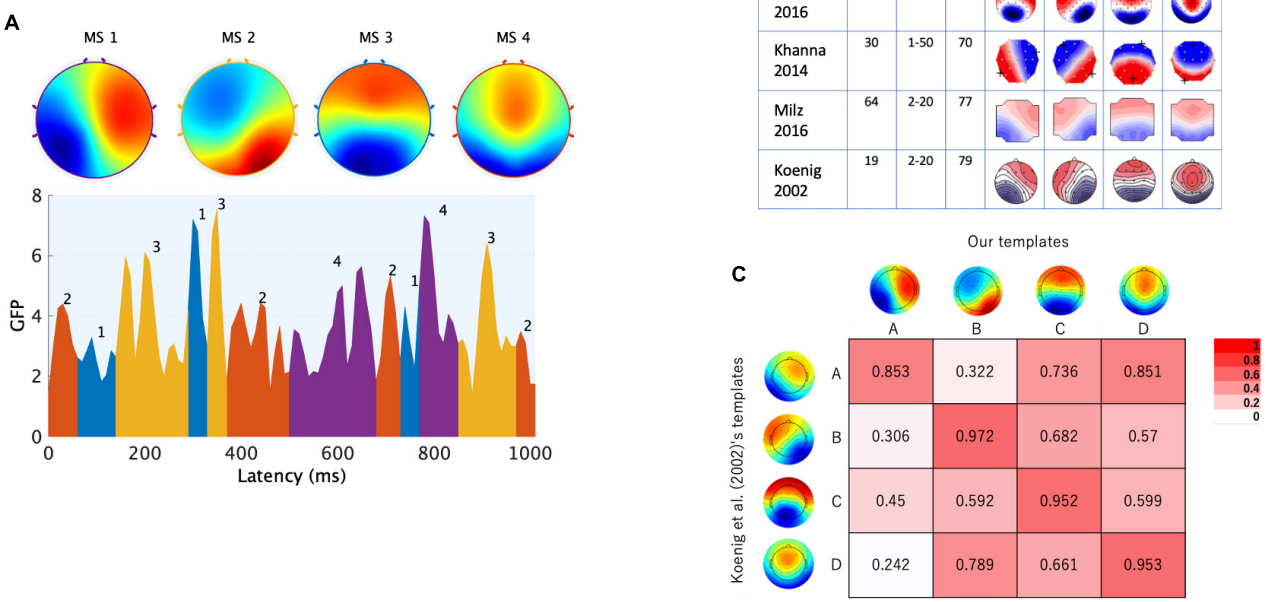

FIGURE 2 | Canonical EEGms templates as the targeted states in neurofeedback. The microstate maps obtained from external participants under the eyes-closed resting state are shown. **(A)** Four maps are identified through a typical microstate analysis (upper) based on the GFP (global field power) peak dataset (lower). The sequences of microstate classes were determined by back-fitting to the data with the highest topographical correlation (see text for details). **(B)** These canonical templates were spatially congruent with previous studies, regardless of the EEG measurement or analysis tools. **(C)** Polarity-ignored spatial similarity (Pearson's | r|) with normative templates in which both configurations were interpolated onto 67 × 67 grids.

participants' neural activity and its externalized feedback in a secret manner (**Figure 5** for experimental design). If real-time NF is effective for learning, participants' Hit performance should be increased from the baseline period and from delayed conditions. In particular, given that each EEGms could be a different cognitive unit, as previously discussed, the controllability of each microstate in the real-time NF situation and robustness of the controllability to a feedback delay may be different depending

on its cognitive responsibility. Therefore, we also compared the real-time effects of msA, B, C, and D in terms of each cognitive functionality.

MATERIALS AND METHODS

Participants

A total of 18 young naive participants (9 females, mean age = 26.3) were recruited from the local community and paid for their participation. All participants reported normal or corrected-to-normal vision and hearing. All participants provided written informed consent before the experiments were conducted. The experiment was conducted in accordance with the principles of the Declaration of Helsinki. The protocol of the present study was approved by the local ethics committee (reference number is 20–144 for the Ethics Committee of ATR).

Preparing for EEG-Microstates Templates

The templates used in our NF system to be matched with the participants' current state were prepared in our previous study as a set of independent group-wise common topography, where 31 healthy people (15 females) in their 20 to 60 s were recorded under the four resting-like eye-closed conditions (resting state, meditated state, respiration counting, and heartbeat counting). Although the details for that experiment will be published elsewhere, the canonical four templates (msA, B, C, and D) were obtained from all those data, as briefly described below.

The EEG signals were recorded from 32 silver-silver chloride electrodes attached to a saltwater sponge-based electro-cap (R-net, Brain Products GmbH, Germany) and were placed at Fp1, Fp2, Fz, F3, F4, F7, F8, F9, F10, FC1, FC2, FC5, FC6, Cz, C3, C4, T7, T8, CP1, CP2, CP5, CP6, Pz, P3, P4, P7, P8, P9, P10, Oz, O1, and O2, according to the extended international 10–20 Systems. The reference and ground electrodes were placed at FCz and Fpz, respectively. We maintained impedances under 50 k**Ω**. EEG signals were amplified with a bandpass of 0.016–250 Hz and digitized at a 500 Hz sampling rate using an EEG recorder (BrainAmp ExG, Brain Products GmbH, Germany). The preprocessing of the EEG data was conducted in MATLAB (R2019b, MathWorks, United States) using the EEGLAB toolbox (EEGLAB2019_0; Delorme and Makeig, 2004). First, the raw signals were down-sampled to 100 Hz and filtered using a finite impulse response filter with a high pass of 2 Hz and a low-pass filter of 20 Hz. Then, we conducted a visual inspection to detect artifacts, including sweat, muscle, movement, and electrode trouble, to be removed manually. Channels with severe artifacts during the entire recording period were spatially interpolated. Furthermore, independent component analysis (ICA) was conducted to remove components with artifacts.

Microstate analysis was further applied to this clean dataset in MATLAB R2019b using the MST plugin for EEGLAB (Poulsen et al., 2018). We calculated the GFP and accumulated topographic voltage maps at local maxima (peaks) in the GFP time series (1000 GFP peaks per session as a default setting) for all participants to be analyzed by the modified k-means clustering algorithm, which ignores the polarity of the voltage maps. GFP peaks were used to generate initial maps for clustering to maximize the topographic signal-to-noise ratio. We defined the number of microstates as four, given that previous studies reported them as the most common (Khanna et al., 2014, 2015), although recent studies have also argued for the possibility of more canonical templates (e.g., Wackermann et al., 1993; Seitzman et al., 2017; Michel and Koenig, 2018).

Developing EEG-Microstates-NF System

The EEGms-NF system was developed using OpenViBE (Renard et al., 2010) with embedded MATLAB code so that the same EEG cap and amplifier work with our templates (**Figure 1**). The input EEG signals (500 Hz) were first referenced and then bandpass-filtered (FIR, 2–20 Hz). After this minimum online denoising, our system implemented time-epoching, template-matching, thresholding, and displaying at 10 Hz. The epoching module in OpenViBE determines the time window that averages the online EEG signals as the "current" EEG topology that consists of a 32-dimensional vector, as a result. Since the typical duration of each microstate has been reported to be approximately 100 ms (Khanna et al., 2015; 60–120 ms, Koenig et al., 2002; Michel and Koenig, 2018), our 10 Hz system depicts a 100-ms–averaged topology for every process (i.e., for sequential 100-ms blocks without an overlap). This means that the only temporally stable microstate (duration of approximately 100 ms) should be detected for the following process. In this sense, a polarity reversal (e.g., A + to A−) should self-cancel the topography and should not be detected by the neurofeedback system at this stage.

Because our four prepared templates are also 32D vectors, the template matching was simply applied by calculating the spatial similarity (Pearson's correlation in our case) between two 32D vectors for each template (i.e., the current vs. each template). As a result, the system output includes four time-series of correlation coefficients that range from −1.0 to + 1.0 in the definition. For the following, however, the absolute r value was used because the polarity is not of interest regarding EEGms (see above for definition of microstate). At this stage, we can define the threshold parameter for the absolute r values (see **Figure 3A** for our 10-Hz system). If the system is processed at 100 Hz (**Figure 3B** shows as an offline processing for comparison), we observe positive–negative fluctuation regardless of the template (**Figure 3B**) when we define positive-negative templates as anterior-posterior contrasts. Since our template A may not be optimal (see **Figure 2C** diagonals), spatial or temporal correlations between template A and B in the current case could be exceptional. For participants to learn to effectively "hit the target" by controlling their own neural state, audio-visual feedback should be appropriate in terms of its frequency (**Figure 4**). If the threshold is too low (e.g., $r_{thr} = 0.1$), participants receive feedback too often to learn (i.e., it is annoying, **Figure 4B**). Therefore, our pilot tests for the participants from our research group determined the threshold as approximately 0.8 and further individually adjusted (see below) in an explorative manner to reduce the frequency of feedback (**Figure 4A**). This also means

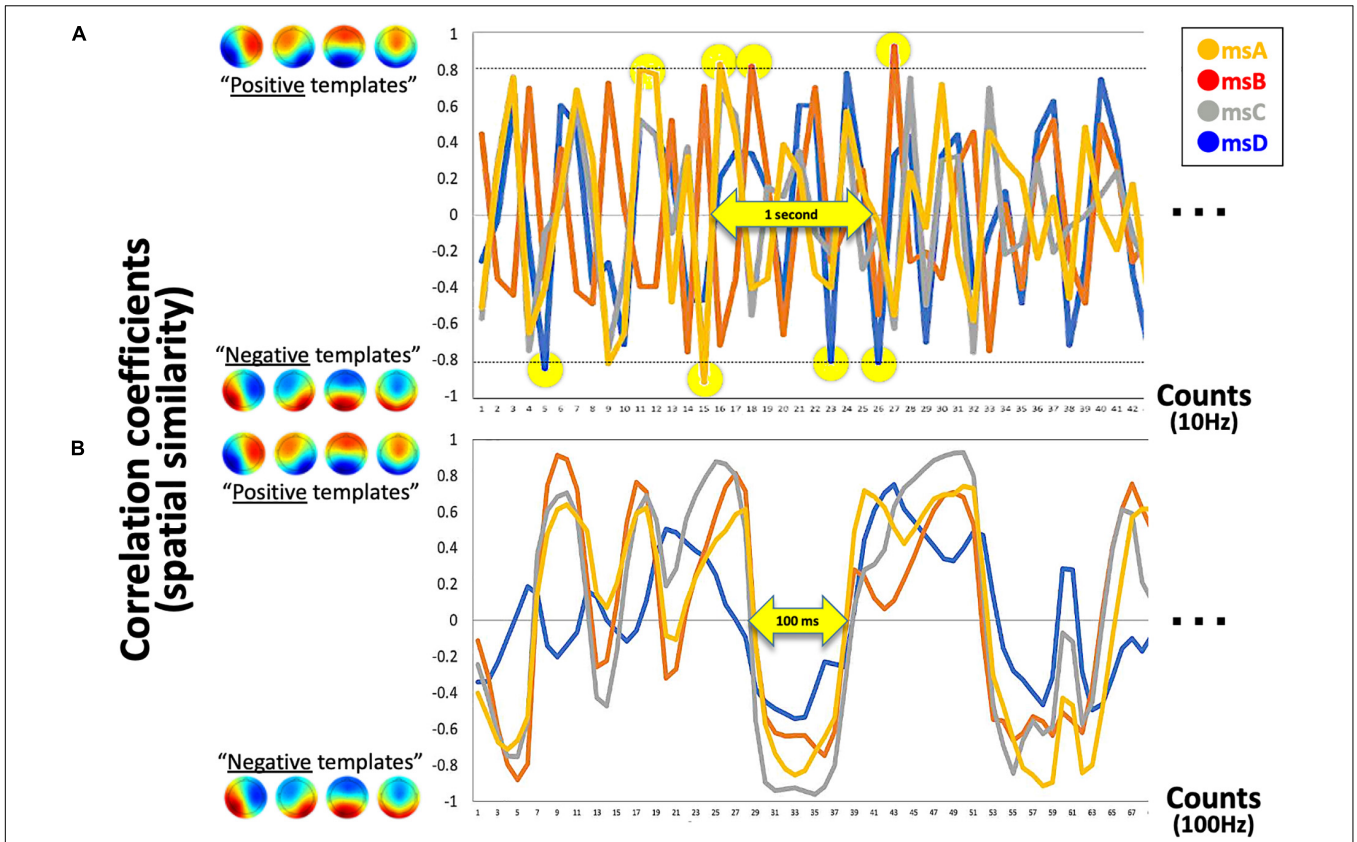

FIGURE 3 | Detected canonical msABCD templates. **(A)** The exemplified time series of four correlation coefficients with template msABCD at 10 Hz is shown. The yellow circle indicates the detected canonical microstates in real-time (when r_{thr} = 0.8). **(B)** If the system is processed at 100 Hz (for comparison), a continuous state-transition dynamic can be observed. In this sense, our time-averaged 10-Hz system detects only spatio-temporally robust microstates.

that only the spatially robust microstate (topology near the templates) should be detected for the following process.

Finally, when the current topology passed the above-mentioned criteria for a spatio-temporally robust microstate, a display for participants indicated its detection (**Figure 1**) where participants always saw four frames with labels (A, B, C, or D). Only when that state was detected, a green circle appeared within the corresponding frame (the highest-r label is selected so that only one green circle was shown at a certain moment). At the same time, a blue frame was presented among four possible states as the target. When participants' EEGms detected by the system hit the target (a green circle appears within a blue frame), a reward sound was played. Therefore, in short, participants were instructed to "generate more sounds" whereas the blue target randomly moved every 20 s. There were five target conditions (no target, A, B, C, and D) within a session of 5 min (20 s × 5 conditions × 3 repetitions) (**Figure 5A**).

Behavior of the System Developed

In summary, the developed system was implemented to detect "four canonical microstates" in terms of the duration and spatial pattern, where those definitions (e.g., threshold) were parameterized. The current setting (time window = 100 ms and spatial similarity $>0.8 \sim 0.7$) was intended to detect only spatio-temporally robust states, so that participants received roughly 1–3 instances of visual feedbacks per 1 s by default (mean ± SD: 2.7 ± 0.7 times/s) (**Figure 4A**) because EEGms transition should be an innate neural dynamic. Accordingly, only minimal online denoising was required, because potentially noisy states (e.g., eye blink, head motion, and other possible artifacts) must be ignored in the definition. We also confirmed that such intentionally added noise does not respond to our system regardless of msA, B, C, or D in preceding pilot tests. This indicates that participants could not use physical strategies; instead, they were encouraged to try only mental strategies to "make sounds".

A previous study implemented the EEGms-NF system (Diaz Hernandez et al., 2016) in which the temporally weighted contribution of msD during the recent 1 s was fed back auditorily to participants. This policy was based on a typical microstate analysis, since each data point was assigned to msA, B, C, or D without polarity (often followed by temporal smoothing to ignore rapid transitions), whose templates were depicted individually. The current NF system, however, has a different approach to promote its real-time status on the basis of our simpler definition of the "state." We need only a recent 100-ms data if the state lasts approximately that duration. This means, in turn, that a polarity reversal and a rapid mixture among

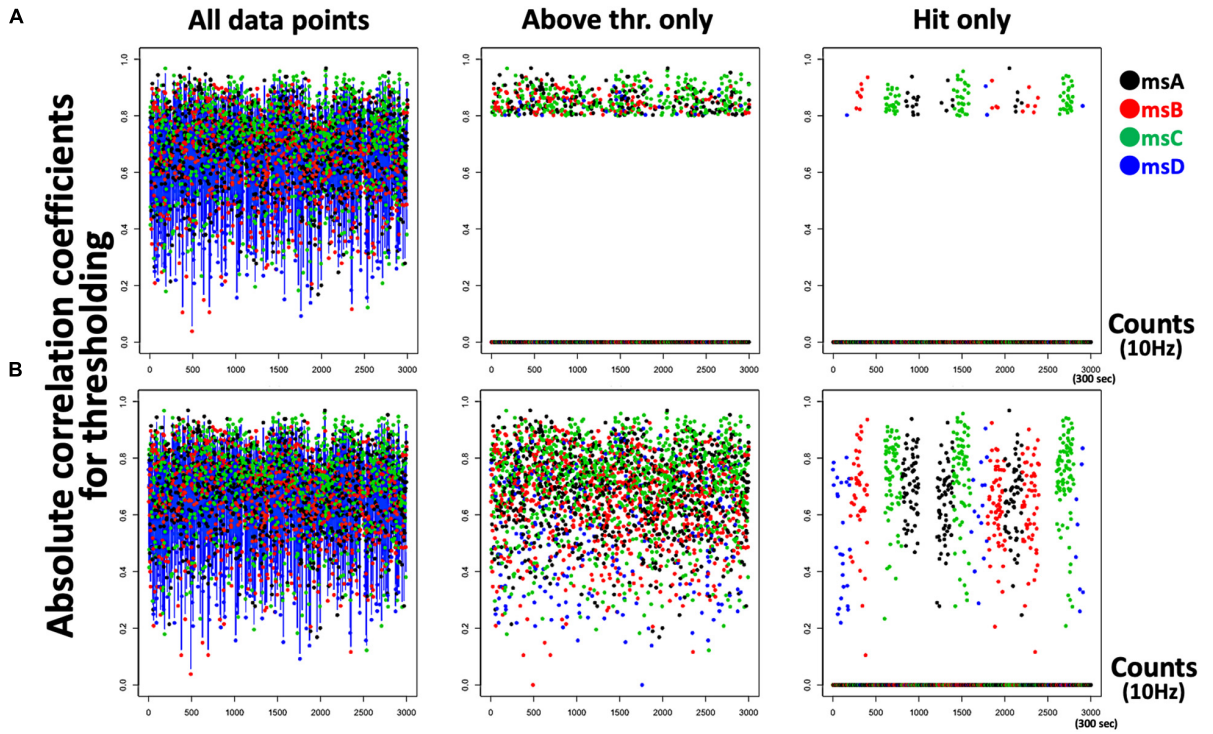

FIGURE 4 | Outputs of the neurofeedback system. **(A)** A typical scatter plot of a 5-min session (left) showing visually informed (circle feedback) data points only (middle) and auditory-informed "Hits" only (right). **(B)** If the threshold is lowered (e.g., r_{thr} = 0.1 for comparison), participants receive too much feedback (visual for the middle panel and auditory for the right panel) to learn.

msABCD should self-cancel the topography and should not be detected by the neurofeedback system. Therefore, our current system is conservative where only spatio ($r > 0.8$ approximately)-temporally (100 ms approximately) stable states should be detected at every 10 Hz epoching process. Other possibilities, including mistiming, polarity reversal, mixture among msABCD, and intrinsic/extrinsic noisy states, were ignored. In addition, our audio-visual feedback achieves supervised learning for participants who are aware of their current state independent of the target state (group-wise common topography). The difference between them can serve as a prediction error to be minimized through learning. Real-time feedback would contribute to the calculation of prediction errors with a valid temporal correspondence between the current state and the target. Therefore, we hypothesized that participants could learn to make more Hits through real-time feedback of the system, compared with delay-inserted conditions, as shown below.

Inserting Delay for System Validation

For that purpose, we additionally inserted an audio-visual delaying hardware (SS-FBDL82, SPORTS SENSING Co., LTD., JAPAN) between the NF system and both the monitor and speaker (**Figure 5B**). The inserted delay parameters were 0, 1 s, or 20 s and were manipulated session-wise in a manner blinded to the participants. They repeated six sessions in total (three conditions × two repetitions in random order). Accordingly, participants had three delay conditions as a between-session factor and five target conditions as a within-session factor. Previous studies have suggested that approximately a 1-s delay or epoching may be long enough to disturb or reduce the effect of EEG-NF (Mulholland et al., 1979; Belinskaya et al., 2020). Furthermore, a 20-s delay was intended to make a total discrepancy between the current and target state since the target moves every 20 s (for example, participants see the target msA then try to make an msA state of their own, but the presented visual feedback was for the previous target condition other than msA). If the functionality of the targeted microstate was not perceptual, but more cognitive, a 1-s or even 20-s delay might be acceptable, but in that case (especially for a 20-s delay), this is not likely a pure EEG-NF effect, but should include a task general effect similar to the results of a cognitive workload (see section "Discussion").

Participants first received instructions regarding EEG measurement and the necessity to remain immobile during experiments and about microstates in terms of controlling their occurrence. They were then instructed to make more Hits (a green circle within a blue frame) by changing their conscious states in an explorative manner for which success was also indicated by auditory ringing feedback. First, a 1-min practice session was conducted using the same system without additional delay, where the experimenters visually checked the response of the system (i.e., audio-visual feedback) to determine individual thresholds among 0.8, 0.75, and 0.7, to absorb potential individual differences. Because the system responsiveness could

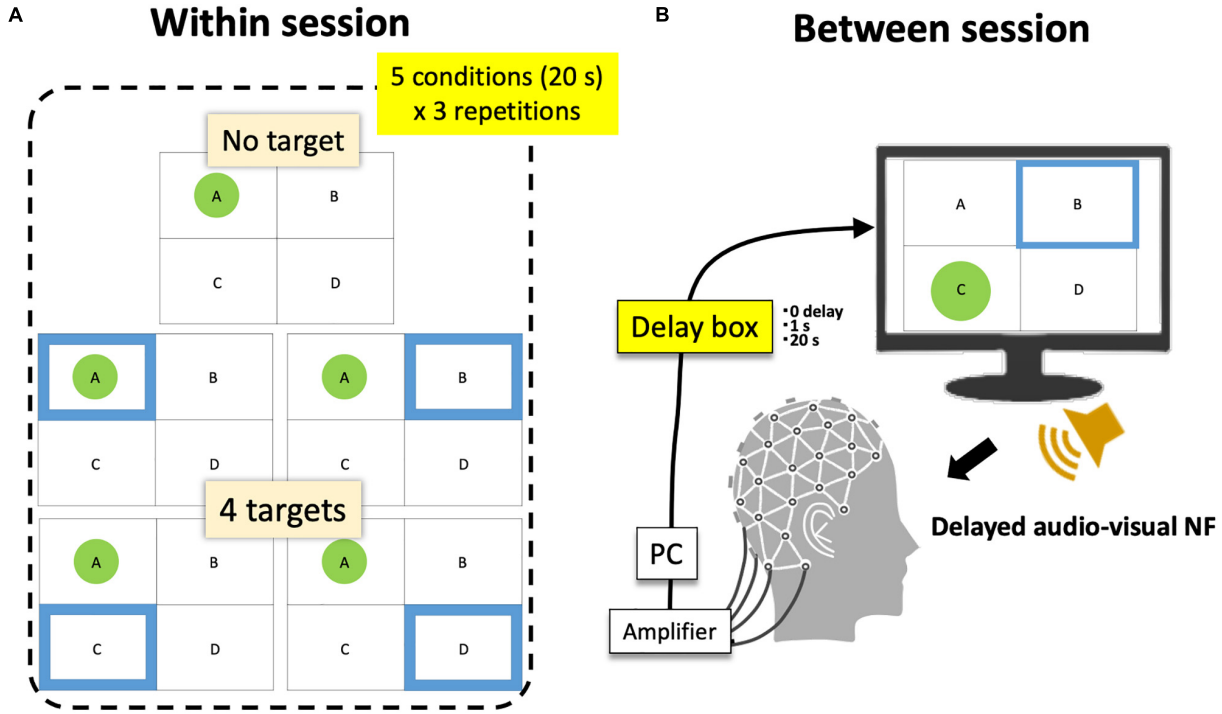

FIGURE 5 | Within- and between-session conditions. **(A)** A session consists of five within-session target conditions × 3 repetitions. **(B)** Participants completed 6 sessions (3 between-session delay conditions × 2 repetitions). The order of conditions was randomized.

be affected by several factors [a cap condition with potentially bad channels or fit of the cap to the participant's head (S, M, or L size) as well as individual differences in participants' innate states in terms of the similarity with the canonical templates]. Six participants for each threshold were determined as a result. Since this was a simple manipulation to roughly equalize feedback frequency among participants, the effect of the threshold would not be examined (see also Discussion for further update of the procedure). After the practice session, the participants repeated six sessions with or without delay insertion, as mentioned above. Participants were also required to answer a question regarding subjective controllability of their own neural state toward each EEGms (A, B, C, or D) as well as their sleepiness using a 5-point Likert scale after each session. This was expected to be a proxy measure for evaluating participants' sense of agency over the EEGms-NF. The total time for the current experiment per subject was 2 h.

RESULTS

The templates we obtained are shown in **Figure 2**, where the labels of maps were named according to previously established studies (i.e., typically msA, B, C and D; Lehmann et al., 1987; Koenig et al., 2002; Khanna et al., 2014, 2015; Diaz Hernandez et al., 2016; Milz et al., 2016; Michel and Koenig, 2018). The topography showing a left posterior to right anterior orientation was determined as msA, the right posterior-left anterior orientation was msB, the anterior-posterior orientation was msC, and the fronto-central extreme location was msD. The spatial configurations of these four maps were highly similar to those previously described and frequently cited in EEG microstate research (Koenig et al., 2002) (**Figure 2B**). Comparing each two maps with the corresponding label assignment (Brodbeck et al., 2012), we achieved high spatial correlation coefficients (0.85–0.97, **Figure 2C**). Furthermore, we calculated the global explained variance (GEV) of the templates. The GEV is one of the parameters that can be used to evaluate whether this set of maps is reasonable as a canonical template. It provides a metric of how well the selected template maps account for the variance of the entire dataset (Poulsen et al., 2018). The higher the GEV, the better the explanation of the entire dataset. As a result, our template of four cluster maps explained 75% of the variance. Referring to previous studies (**Figure 2B**), the GEV was 71% in Diaz Hernandez et al. (2016), who recorded and preprocessed EEG signals with the same number of electrodes and filter settings as ours, 70% in Khanna et al. (2014) (they used a wider bandpass filter than ours), and 77% in Milz et al. (2016) (they used a larger number of electrodes than ours). Therefore, we obtained canonical microstates that were congruent with previous observations. These templates were used in our NF system to be matched with participants' EEG states in real time.

Questionnaire and Raw Hit Scores

Participants' raw reports about their subjective controllability over EEGms based on their Hit performance are summarized

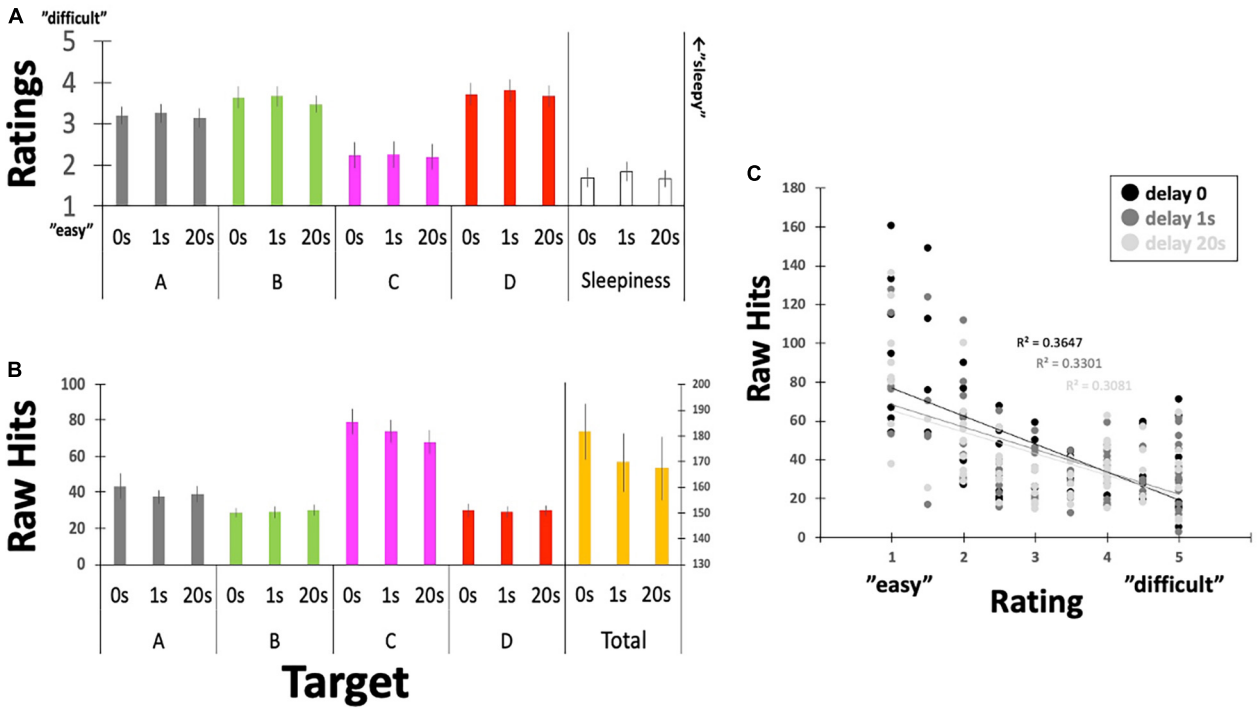

FIGURE 6 | Questionnaire ratings for controllability and the raw number of Hits. **(A)** Participants reported their subjective feelings regarding "controllability" over the targeted EEGms and their sleepiness on the five-point Likert scale. **(B)** Participants' raw Hits performance for each EEGms target. **(C)** A plot between the number of raw Hits and the Likert rating, including the delay conditions. Error bars indicate ± SE.

TABLE 1 | Descriptive statistics for participants' raw Hits and ratings.

(A) Raw hits					(B) Ratings				
Descriptive statistics	**Mean**	**Std. deviation**	**Minimum**	**Maximum**	**Descriptive statistics**	**Mean**	**Std. deviation**	**Minimum**	**Maximum**
Total_0s	181.6	46.96	111	281	A_0s	3.194	0.957	1	5
Total_1s	169.6	49.74	93.5	268.5	B_0s	3.639	1.148	2	5
Total_20s	167.3	54.13	89.5	266	C_0s	2.222	1.396	1	5
msA_0s	43.39	31.25	17	160.5	D_0s	3.722	1.166	1.5	5
msA_1s	37.42	16.72	17	81	Sleep_0s	1.694	1.002	1	3.5
msA_20s	39.08	18.79	17	99.5	A_1s	3.25	1.018	1	5
msB_0s	28.81	11.68	15.5	61.5	B_1s	3.667	1.098	1.5	5
msB_1s	29	14.39	9	56.5	C_1s	2.25	1.364	1	5
msB_20s	30.17	12.65	9.5	56	D_1s	3.806	1.202	1.5	5
msC_0s	79.17	30.64	39	149	Sleep_1s	1.833	1.043	1	4
msC_1s	73.89	27.68	42.5	127.5	A_20s	3.139	1.026	1	5
msC_20s	67.89	29.08	37.5	136	B_20s	3.472	0.899	2	5
msD_0s	29.97	15.29	5	64	C_20s	2.194	1.33	1	5
msD_1s	29.14	13.87	2.5	54.5	D_20s	3.667	1.125	1.5	5
msD_20s	30	12.56	8	60.5	Sleep_20s	1.667	0.874	1	4

in **Figure 6** and **Table 1**. The current results are congruent with some previous studies in terms of the statistical features of the four EEGms. For example, msC is reportedly the most dominant at default, especially in young, healthy participants (Tomescu et al., 2018). In line with this, the current participants' raw number of Hits for msC was higher than that for msA, B, or D, regardless of the inserted delay (**Figure 6B**). The two-way ANOVA (4-target within conditions × 3-delay within condition) revealed significant main effects of the target and an interaction [$F(3,51) = 24.2$, $p < 0.0001$, and $F(6,102) = 2.36$, $p = 0.0355$], while the main effect of delay missed significance [$F(2,34) = 24.2$, $p = 0.0501$]. Multiple comparisons with Ryan's method for the main effect of the target indicated that msC was significantly increased compared to msA, B, or D, respectively (ps < 0.05).

Regarding the interaction, the simple main effect of delay on msC was significant [$F(2,136) = 7.90$, $p = 0.0006$]. The main effect of delay on the total Hits was significant [one-way ANOVA, $F(2,34) = 3.36$, $p = 0.0466$]. Accordingly, participants' subjective feelings about the difficulty in controllability were also reduced for msC (**Figure 6A**). The two-way ANOVA (4-target within conditions × 3-delay within condition) revealed a significant main effect of target [$F(3,51) = 7.93$, $p = 0.0002$], while that of delay or the interactions were not significant [$F(2,34) = 0.49$, $p = 0.6189$, and $F(6,102) = 0.09$, $p = 0.9969$, respectively]. Multiple comparisons with Ryan's method indicated that msC was significantly reduced from msA, B, or D (ps < 0.05). In addition, sleepiness reports did not differ among 3-delay conditions [one-way ANOVA, $F(2,34) = 0.69$, $p = 0.5072$].

This outcome-dependent relationship between NF or BCI performance and perceived agency has been examined previously (Evans et al., 2015; Caspar et al., 2021). In particular, when the desired outcome is achieved, participants feel agency even if that outcome is not achieved by their own neural activity (Evans et al., 2015). Similarly, in the current study, it seems that agency ratings might have simply been reflected on the actual number of Hits by receiving or counting the sounds (e.g., for msC). **Figure 6C** clearly depicts the negative correlation between them with collapsing four target conditions, regardless of the inserted delay. However, regarding the effect of delay, there was no difference in ratings for either controllability or sleepiness, although Hit performance could be modulated by the inserted delay (see below for details). This suggests, in turn, that participants were not aware of the inserted delay, unlike many behavioral studies, when even short-time delays are easily detectable (Asai and Tanno, 2007). In such a situation, participants' perceived agency is correlated with the detection of delay, which makes it difficult to eliminate the possibility that the reduced agency also affects participants' motivation to learn. In this sense, no difference in their rating for the inserted delay (as a manipulation check) should be an important controlling result, especially in the current study.

The Relative Hits as a Function of Delay

To further examine the effect of delay on participants' Hit performance, the raw scores were individually standardized based on the baseline period (no-target condition, see **Figure 5A**) because raw Hits by default have individual differences and also depend on the system threshold (r_{thr} = 0.8, 0.75, or 0.7) that were not strictly determined individually in the current study. **Figure 7** indicates the relative Hits score, the relative magnification in comparison to the individual no-target condition without delay, as a function of the inserted delay. Our results clearly suggest that the real-time effect was observed only under the no-delay condition in the total score (**Figure 7A**). The relative Hits significantly increased from the 1- or 20-s delay conditions. A one-way ANOVA revealed that the main effect of delay was significant [$F(2,34) = 4.86$, $p = 0.0139$] with a difference between delay-0 and -1, and delay-0 and -20 revealed by a *post hoc* multiple comparisons using Ryan's method (ps < 0.05). Furthermore, the two-way ANOVA (4-target within conditions × 3-delay within condition) revealed that the main effect of the target was significant [$F(3,51) = 3.94$, $p = 0.0128$], while that of delay and interactions were not [$F(2,34) = 1.05$, $p = 0.3601$, and $F(6,102) = 1.04$, $p = 0.4032$,

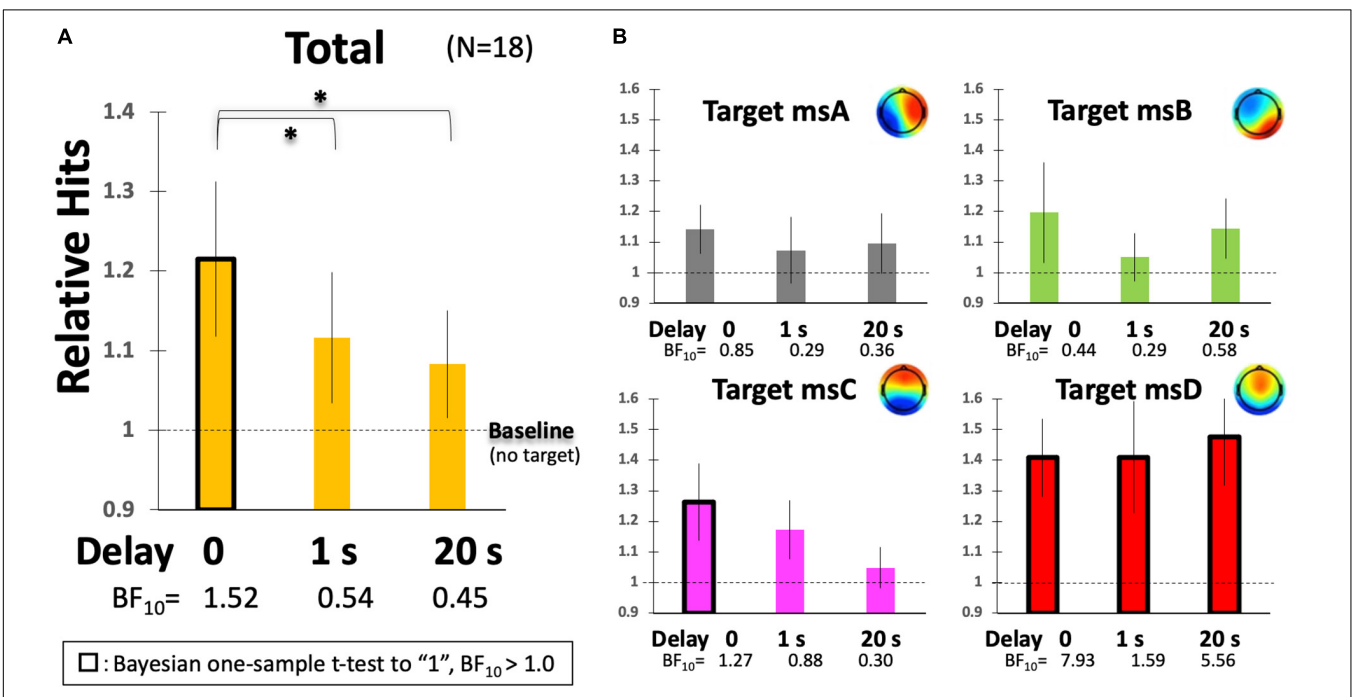

FIGURE 7 | Participants' Hit performance as a function of delay. **(A)** The relative magnification of total Hits in comparison to the individual baseline (no-target condition). **(B)** The same indices are calculated, respectively, for msA, B, C, and D. Error bars indicate ± 1 SE. *$p<0.05$ in ANOVA.

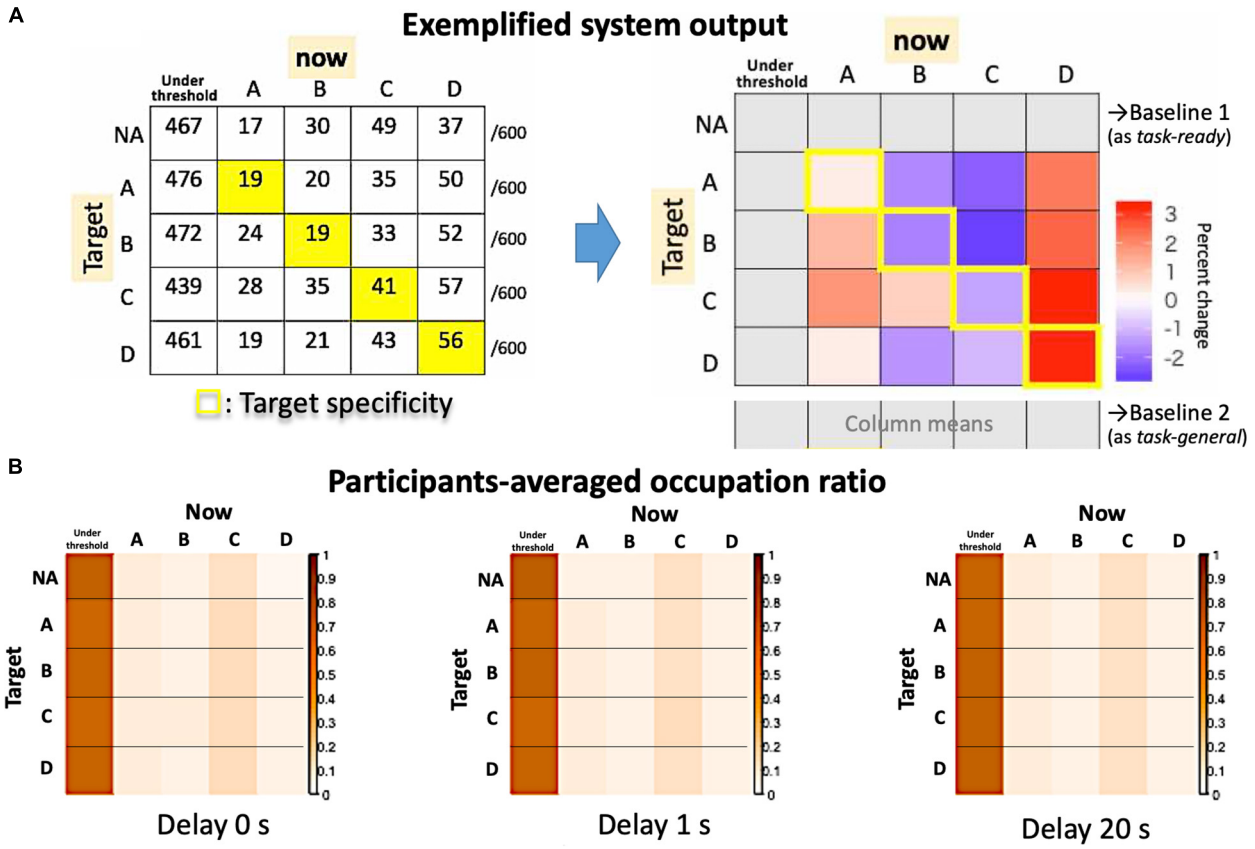

FIGURE 8 | System outputs as an asymmetrical matrix. **(A)** The raw counts for an exemplified session (left) and the summarized matrix for the target specificity are shown in contrast to possible baselines (right). **(B)** Actual participants' averages as occupation ratios for each delay condition.

respectively]. The relative Hit for msD was significantly increased from msA, B, and D, regardless of the delay, according to a multiple comparisons using Ryan's method (ps < 0.05), suggesting a potential difference in the functionality of msABCD in terms of the responsiveness of our NF system with the inserted delay (**Figure 7B**).

For the individual EEGms, the increase from the baseline was the significant contrast of interest. For that purpose, we applied a Bayesian one-sample *t*-test to the baseline to avoid repetition of multiple tests (e.g., multiple Student's *t*-tests). When we took a two-sided alternative hypothesis (H1:$\delta \neq 1$, since the relative Hits could be lower than 1) against the null hypothesis (H0:$\delta = 1$), a Bayesian one-sample *t*-test with JASP (JASP Team, 2019) revealed weak but interpretable evidence ($BF_{10} > 1$) under the no-delay condition for the total, msC, and msD (as well as under the delay-1 or -20 condition for msD). For example, $BF_{10} = 1.52$ for total score without delay, indicates that the data are approximately 1.5 times more likely to occur under H1 than under H0, suggesting at least weak evidence in favor of H1 (a Bayes factor between 1 and 3 is considered weak evidence, but this range might be common in behavioral sciences). A confirmatory non-parametric *t*-test with Wilcoxon signed-rank suggested the same results, where the five conditions with black-framed bars in **Figure 7** were significantly different from the baseline (ps < 0.05). Accordingly, when the Hits were compared among the msABCD, each cognitive function could be characterized. The total result is congruent solely with the msC, in which only the no-delay condition increased significantly above the baseline. Although a similar trend was detected for msA and msB, the difference was not significant. The msD is especially interesting, given that even a 20-s delay elevated the relative Hit performance compared with baseline (no-target specified), suggesting its general task-positive functionality. This in turn indicates the necessity of using a task-general baseline (see below); a previous study suggested the importance of using multiple baselines for assessing a training effect (Alkoby et al., 2018).

Target Specificities for Each Delay Condition

The output of the system is summarized in **Figure 8**, in which a 4 × 4 (originally 5 × 5) matrix compares the Hits (diagonal components) and Misses (non-diagonals). For the group average, we assume that the "no-target" condition serves as a "task-ready" state rather than a resting state (**Figure 8B**), since the occupation ratio is almost that same as other "target" conditions regardless of the delay. Indeed, participants could observe their own EEG states as visual feedback even during the no-target

period. Therefore, the individual baseline is needed to examine a small effect from real-time feedback on learning (i.e., the effect of a delay) within a single-day experiment. Since the definition of the baseline might change the results, the "task-general" baseline was also used for comparison with target conditions (**Figure 8A**, right).

Figure 8 shows the target specificity analyzed with two possible baselines: the no-target period ("task-ready") under the no-delay condition (similar to **Figure 7**) and the session average (the column means for "task-general") for each delay condition (see **Figure 8A**, right). According to **Figures 9A,B**, the values are generally reduced with a delay regardless of being a Hit or Miss. A Hit for msC is the most sensitive to a delay, while msA exhibits the same tendency as msC in **Figure 9A** but msB shows the opposite in **Figure 9B**. The increase in msD evident in **Figure 9A** almost disappears in **Figure 9B**. A three-way ANOVA (4 targets × 4 currents × 3 delay conditions) applied to the "task-general" baseline (**Figure 9C**) shows that the effects of the delay and the target were significant [$F(2,34) = 10.19$, $p = 0.0003$; $F(3,51) = 5.501$, $p = 0.0024$, respectively]; the interaction between them was also significant [$F(6,102) = 2.643$, $p = 0.02$]. Accordingly, the target specificity (i.e., the three-way interaction or an interaction between the target and the detected state) was not specifically confirmed, although the main effect of a delay indicates a real-time effect from feedback, which was our initial purpose.

Although the target specificity is still unclear, that effect can be predicted to be learnable by participants through long-term training using this feedback system in a future study. This is related to their functional responsibility. Previous studies have suggested that the functionality of msA and msB are perceptual (auditory for msA and visual for msB); therefore, they might be passive and less controllable (oriented for sensory inflow, which is mainly audio–visual for humans), while msC and msD are cognitive (saliency or default mode for msC and attentive or executive for msD); therefore, they are active and more controllable (oriented for motor outflow with switching from internal to external awareness); below we discuss this functional difference in terms of delay sensitivity in our EEGms-NF system.

DISCUSSION

In the current study, we developed a new EEGms-NF system and validated it by examining the decline in participants' performance as a function of delay. Although participants were presumably totally naive about the inserted delay as the result of the agency questionnaire also implies (**Figure 6A**), the real-time NF successfully increased their Hit performance in total (**Figure 7A**), even within a single-day experiment. This suggests that by using our NF system, participants could implicitly learn through a supervised manner how to control their own neural state, spatially represented in EEG channels, immediately during each no-delay session. Contrastingly, participants' subjective agency was not modulated (i.e., reduced) even by a 20-s–delay, unlike many behavioral studies, given that they should not have been aware of the inserted delay. This indicates that we do not have an internal model of our own neural state (EEG state in our case) by default. Without this type of externalizing BCI system, it is difficult for us to estimate our own neural state or to compare the actual and desired states in forward modeling. This should be an essential factor why we do not feel a sense of control over BCI interactions in real time, where only outcome-dependent agency may be elicited (Evans et al., 2015). However, the current study further indicates that the use of an NF system that implements real-time sensory feedback like ours in long-term training for some months (such as daily motor behaviors), for example, an internal model over that system with subjective online agency can be developed. If the NF system represents our neural dynamics in nature, controlling or internalizing the system would mean that we could regulate our own neural state through the developed internal model (possibly even without the NF system). The EEGms, in this sense, are candidates for representing natural dynamics in the brain. Therefore, developing a BCI-based NF system in terms of online agency (or internal model) should be an important framework for future studies. For that purpose, our results suggest that minimizing feedback delays could be a worthwhile implementation for improving task learning (Belinskaya et al., 2020) such as motor learning (Tanaka et al., 2011).

In comparison with the preceding EEGms-NF system (Diaz Hernandez et al., 2016), there are several points to be discussed here. First, the templates in the system as the desired target state are group-wise topographies in our case, while in the previous study they were individually defined. This difference could be expected to result in different training outcomes. In our case, the spatial pattern itself was the target for participants' learning, given that the individual EEGms must be slightly different from the group-wise EEGms (the "canonical" EEGms). We may observe the changes for individual EEGms moving toward group-wise EEGms through long-term training in future studies. However, individually defined templates should be easier for participants to induce, because they exhibit these patterns by default in nature, although the canonical EEGms are reportedly common across participants. Another difference in the implementation is sensory feedback. For supervised learning, participants were visually aware of their current and targeted state simultaneously. In addition to the visual feedback used in the previous study, the auditory feedback was provided to indicate Hits (successes in minimizing a prediction error) and to reward participants, as well. This audio-visual BCI monitors and externalizes whole-brain mass neural activity as EEGms to be regulated (Diaz Hernandez et al., 2016). This implementation enables us to treat four targets simultaneously (see **Figure 1**). In addition, the optimal frequency of NF is an important factor for participants' learning so that the definition of EEGms has been further parameterized in terms of its duration and topographical robustness. Therefore, the difference to note is our definition of the state. Our system detects only spatio-temporally robust EEGms (approximately 100 ms for duration and $r_{thr} = 0.8$ for spatial similarity) so that strict online denoising was not necessary, which is always a nuisance in the "winner-take-all" definition of EEGms. Both noisy states and spatio-temporally less-robust states are ignored in our system.

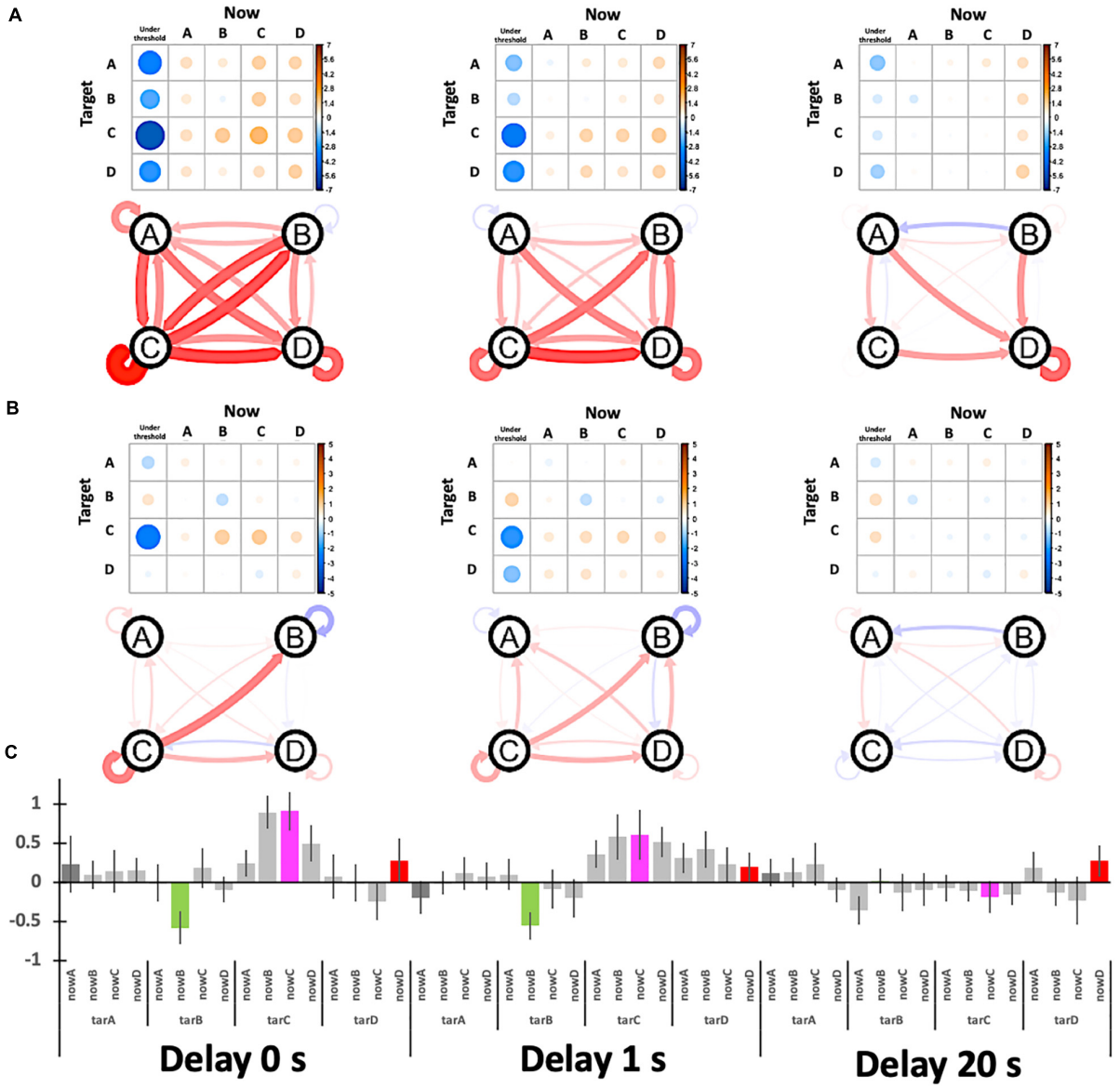

FIGURE 9 | Participants' relative performance for target specificity. **(A)** The baseline is the no-target period ("task-ready") under the no-delay condition. **(B)** The baseline is the session average (the column-means for "task-general") for each delay condition. The graphs show the relative Hits (self-recursive arrows for target specificity) and Misses (other arrows) where the nodes (A, B, C, and D) indicate the target. **(C)** The bar plot summarizes **(B)** with ± 1 S.E. error bars.

This largely helped the real-time implementation. However, if a polarity reversal or rapid transition is observed during the 100 ms (e.g., msA followed by msC and msD), the system ignores that state (i.e., as a mixture of A, C, and D, see **Figure 3B**). This is contrasted to a conventional offline EEG microstate analysis that has been implemented to handle this with polarity-ignored labeling (msABCD) and final temporal smoothing among labels (Poulsen et al., 2018). Recently, this classical approach of microstate labeling ("winner-take-all") has been controversial (e.g., Shaw et al., 2019; Mishra et al., 2020). Some previous studies have intentionally introduced "unlabeled" states for this reason (e.g., Zanesco et al., 2021). In this sense, the current system was not developed to be matched with the classical labels, and there should be non-small differences between them depending on the analysis parameters, especially temporal smoothing of labels. Accordingly, our conservative system was not designed to detect every robust state but to not falsely detect them. We can imagine that 1-ms or 10-ms–averaged state is less reliable for learning and needs further temporal smoothing during a certain period. In this sense, we may update to a 100-Hz system using overlapping 100-ms blocks in a future study.

Regarding the potential differences among the four EEGms in responsible cognitive functionality, our results suggest some

results congruent with previous studies as well as some new findings, especially in terms of neural controllability. First, for msD, the most frequently examined among the four EEGms, was reportedly increased through NF training for 10 days (Diaz Hernandez et al., 2016). Although that study was the first attempt to modify EEGms, msD is a specific target for future clinical application, since msD may be a biomarker for schizophrenia. Therefore, a link between schizophrenic symptomatology and the function of msD has often been discussed. Previous studies indicate that msD is functionally related to attentional control or central executive function that the frontoparietal network underpins. Simultaneous EEG-fMRI recordings suggest a link where the fluctuation of msD (time-series of spatial correlation to msD template) explains BOLD signals in the right-lateralized dorsal and ventral areas of the frontoparietal cortex (Britz et al., 2010). More recently, a simple mental arithmetic calculation increased participants' duration of msD (Seitzman et al., 2017; Bréchet et al., 2019). If msD is responsible for this attentive cognitive load in general, our results are consistent with this. Even during 20-s–delay NF sessions (participants were not aware of this), participants tried to make more Hits so that the msD was increased compared to baseline. However, msC has often been discussed in contrast to msD as some previous studies indicate that the increased msD coincides with the decreased msC (e.g., Seitzman et al., 2017; Bréchet et al., 2019). Indeed, simultaneous recordings suggested that msC is neurally related to the default mode or saliency network, which is the functionally opposite network to the frontoparietal network (Britz et al., 2010; as a review, Seitzman et al., 2017; Michel and Koenig, 2018). In the current study, msC was the most delay-sensitive and controllable in real time. In this sense, saliency-related cognitive function may be a candidate for msC.

In contrast to the msC-D axis for controllable cognitive states, msA and B have been discussed as more perceptual functionalities. Simultaneous recordings suggest that msA is neurally related to the auditory region, while msB is related to the visual region (Britz et al., 2010). Recent studies also indicate msA for auditory perception as well as msB for visual perception, depending on the stimuli of modality or perceptual experiences (e.g., Cai et al., 2018; Bréchet et al., 2019; D'Croz-Baron et al., 2021). On the other hand, our results suggest that msA or B did not increase, even with real-time NF. These results indicate that the functionality of msA and B (or msA-B axis) is more perceptual; therefore, it might be passive and difficult to control intentionally. Although a more comprehensive understanding of four canonical EEGms is needed, since previous findings were given in a relatively sporadic matter, our results discriminated between msC-D and msA-B in terms of real-time controllability with NF. Our experiment did not examine each functionality directly and we do not assume that cognitive functionality has a 1:1 correspondence to each microstate, rather, microstate "dynamics" could be responsible to our cognition and perception (Michel and Koenig, 2018; Ruggeri et al., 2019, 2020). However, the result is interpretable in line with or extending the existing understanding of EEGms where the functionality of msA and B are perceptual (auditory for msA and visual for msB), and therefore, may be less controllable, while msC and D are cognitive (saliency or default mode for msC and attentive or executive for msD), and therefore, more controllable.

This study has some limitations for future applications. The current study was conducted within a single day for each participant. Accordingly, the effects of long-term training using the system are unknown, especially for the target specificity. Even within a session, the total Hit performance (and msC and msD) increased above the "task-ready" baseline (**Figure 9A**), suggesting that long-term training is predicted. If msC or msD is a candidate biomarker for some diseases (for example, schizophrenia), our system is clinically applicable for future studies as it is (without the inserted delay, of course). Although msA and msB appear more difficult to control according to the current results, they are still useful for examining the effect of long-term training, since a non-significant tendency for increasing was observed (**Figures 7**, **9**). Another possible future approach would be to manipulate a parameter of threshold (spatial correlation r) individually, as well as msABCD, respectively. The former serves to absorb individual differences in an EEG cap condition, head fitness with a cap, and innate similarity with canonical templates. The latter serves to equalize the feedback frequency among msABCD because msC might occur more often innately. Examining thresholds could improve the balance between discriminability and detectability among msA, B, C, and D (**Figures 3A,B**). For this purpose, pre-training recording is required to determine the optimal thresholds and objective procedure. Whether this parameter should be changed daily through long-term training should also be considered. Even in this case, our system has already parameterized the threshold value. This should prove helpful, especially for specific participants with disorders who might have a reduced msD, for example, the system with a regular parameter should be less responsive to them than to healthy participants. Finally, the definition of a state as a canonical EEGms and the number of microstates are controversial (Michel and Koenig, 2018; Tarailis et al., 2021). Further studies should address this issue, since the current study used traditional definitions. Because our system was developed to make the template easily replaceable, new state definitions can be readily applied for participant learning (e.g., a 7-EEGms model).

In conclusion, the aim of the current study was to develop a closed-loop NF system and validate it as a function of the inserted delay. If real-time NF is effective for learning, the participants' Hit performance should increase above baseline and from delayed conditions. Our results suggest that this is the case, although the target specificity is still unclear. Future studies can examine long-term training with this NF system, even for a specific population.

DATA AVAILABILITY STATEMENT

The raw data supporting the conclusions of this article will be made available by the authors, without undue reservation.

ETHICS STATEMENT

The studies involving human participants were reviewed and approved by the Ethics Committee of ATR (reference number is 20–144). The patients/participants provided their written informed consent to participate in this study.

AUTHOR CONTRIBUTIONS

TA mainly designed the experiments, analyzed the data, and wrote the manuscript. TH and SK partially analyzed the data and wrote the manuscript. TA, TH, SK, and HI discussed the results and reviewed the manuscript. All authors approved the final version of the manuscript for submission.

FUNDING

This study was mainly supported by "Research and development of technology for enhancing functional recovery of elderly and disabled people based on non-invasive brain imaging and robotic assistive devices (16824707)", the Commissioned Research of National Institute of Information and Communications Technology (NICT), JAPAN. HI was also partially supported by JSPS KAKENHI (grant 19H05725).

ACKNOWLEDGMENTS

We would like to thank Chizuru Homma, Yuki Inoue, Yoshiko Umemoto, Masaru Nishioka, and Ayako Tsukamoto for their experimental support.

REFERENCES

Alkoby, O., Abu-Rmileh, A., Shriki, O., and Todder, D. (2018). Can we predict who will respond to neurofeedback? A review of the inefficacy problem and existing predictors for successful EEG neurofeedback learning. *Neuroscience* 378, 155–164. doi: 10.1016/j.neuroscience.2016.12.050

Asai, T. (2016). Agency elicits body-ownership: proprioceptive drift toward a synchronously acting external proxy. *Exp. Brain Res.* 234, 1163–1174. doi: 10.1007/s00221-015-4231-y

Asai, T., and Tanno, Y. (2007). The relationship between the sense of self-agency and schizotypal personality traits. *J. Mot. Behav.* 39, 162–168. doi: 10.3200/JMBR.39.3.162-168

Belinskaya, A., Smetanin, N., Lebedev, M. A., and Ossadtchi, A. (2020). Short-delay neurofeedback facilitates training of the parietal alpha rhythm. *J. Neural Eng.* 17:abc8d7. doi: 10.1088/1741-2552/abc8d7

Bréchet, L., Brunet, D., Birot, G., Gruetter, R., Michel, C. M., and Jorge, J. (2019). Capturing the spatiotemporal dynamics of self-generated, task-initiated thoughts with EEG and fMRI. *Neuroimage* 194, 82–92. doi: 10.1016/j.neuroimage.2019.03.029

Britz, J., Van De Ville, D., and Michel, C. M. (2010). BOLD correlates of EEG topography reveal rapid resting-state network dynamics. *Neuroimage* 52, 1162–1170. doi: 10.1016/j.neuroimage.2010.02.052

Brodbeck, V., Kuhn, A., von Wegner, F., Morzelewski, A., Tagliazucchi, E., Borisov, S., et al. (2012). EEG microstates of wakefulness and NREM sleep. *Neuroimage* 62, 2129–2139. doi: 10.1016/j.neuroimage.2012.05.060

Cai, Y., Huang, D., Chen, Y., Yang, H., Wang, C. D., Zhao, F., et al. (2018). Deviant dynamics of resting state electroencephalogram microstate in patients with subjective tinnitus. *Front. Behav. Neurosci.* 12:122. doi: 10.3389/fnbeh.2018.00122

Caspar, E. A., De Beir, A., Lauwers, G., Cleeremans, A., and Vanderborght, B. (2021). How using brain-machine interfaces influences the human sense of agency. *PLoS One* 16:e0245191. doi: 10.1371/journal.pone.0245191

Changeux, J. P., and Michel, C. M. (2006). "Mechanisms of neural integration at the brain-scale level: the neuronal workspace and microstate models in Microcircuits," in *The Interface Between Neurons And Global Brain Function*, eds S. Grillner and A. M. Graybiel (Cambridge, MA: MIT Press), 347–370.

D'Croz-Baron, D. F., Bréchet, L., Baker, M., and Karp, T. (2021). Auditory and visual tasks influence the temporal dynamics of EEG microstates during post-encoding rest. *Brain Topogr.* 34, 19–28. doi: 10.1007/s10548-020-00802-4

da Cruz, J. R., Favrod, O., Roinishvili, M., Chkonia, E., Brand, A., Mohr, C., et al. (2020). EEG microstates are a candidate endophenotype for schizophrenia. *Nat. Commun.* 11:3089. doi: 10.1038/s41467-020-16914-1

de Bock, R., Mackintosh, A. J., Maier, F., Borgwardt, S., Riecher-Rössler, A., and Andreou, C. (2020). EEG microstates as biomarker for psychosis in ultra-high-risk patients. *Transl. Psychiatry* 10:300. doi: 10.1038/s41398-020-00963-7

Delorme, A., and Makeig, S. (2004). EEGLAB: an open source toolbox for analysis of single-trial EEG dynamics including independent component analysis. *J. Neurosci. Methods* 134, 9–21. doi: 10.1016/j.jneumeth.2003.10.009

Diaz Hernandez, L., Rieger, K., Baenninger, A., Brandeis, D., and Koenig, T. (2016). Towards using microstate-neurofeedback for the treatment of psychotic symptoms in schizophrenia. A feasibility study in healthy participants. *Brain Topogr.* 29, 308–321. doi: 10.1007/s10548-015-0460-4

Evans, N., Gale, S., Schurger, A., and Blanke, O. (2015). Visual feedback dominates the sense of agency for brain-machine actions. *PLoS One* 10:e0130019. doi: 10.1371/journal.pone.0130019

Gallagher, I. (2000). Philosophical conceptions of the self: implications for cognitive science. *Trends Cogn. Sci.* 4, 14–21. doi: 10.1016/s1364-6613(99)01417-5

JASP Team (2019). *JASP (Version 0.14)[Computer software]*.

Khanna, A., Pascual-Leone, A., and Farzan, F. (2014). Reliability of resting-state microstate features in electroencephalography. *PLoS One* 9:e114163. doi: 10.1371/journal.pone.0114163

Khanna, A., Pascual-Leone, A., Michel, C. M., and Farzan, F. (2015). Microstates in resting-state EEG: current status and future directions. *Neurosci. Biobehav. Rev.* 49, 105–113. doi: 10.1016/j.neubiorev.2014.12.010

Koenig, T., Prichep, L., Lehmann, D., Sosa, P. V., Braeker, E., Kleinlogel, H., et al. (2002). Millisecond by millisecond, year by year: normative EEG microstates and developmental stages. *Neuroimage* 16, 41–48. doi: 10.1006/nimg.2002.1070

Koukkou, M., and Lehmann, D. (1987). An information-processing perspective of psychophysiological measurements. *J. Psychophysiol.* 1, 109–112.

Lehmann, D. (1992). "Brain," in *Electric Fields And Brain Functional States. Springer Proceedings In Physics*. Berlin Heidelberg: Springer, 235–248. doi: 10.1007/978-3-642-84781-3_12

Lehmann, D., Ozaki, H., and Pal, I. (1987). EEG alpha map series: brain micro-states by space-oriented adaptive segmentation. EEG Alpha Map Series. . *Electroencephalogr. Clin. Neurophysiol.* 67, 271–288. doi: 10.1016/0013-4694(87)90025-3

Lehmann, D., Strik, W. K., Henggeler, B., Koenig, T., and Koukkou, M. (1998). Brain electric microstates and momentary conscious mind states as building blocks of spontaneous thinking: i. Visual imagery and abstract thoughts. *Int. J. Psychophysiol.* 29, 1–11. doi: 10.1016/s0167-8760(97)00098-6

Lubianiker, N., Goldway, N., Fruchtman-Steinbok, T., Paret, C., Keynan, J. N., Singer, N., et al. (2019). Process-based framework for precise neuromodulation. *Nat. Hum. Behav.* 3, 436–445. doi: 10.1038/s41562-019-0573-y

Michel, C. M., and Koenig, T. (2018). EEG microstates as a tool for studying the temporal dynamics of whole-brain neuronal networks: a review. *Neuroimage* 180, 577–593. doi: 10.1016/j.neuroimage.2017.11.062

Milz, P., Pascual-Marqui, R. D., Lehmann, D., and Faber, P. L. (2016). Modalities of thinking: state and trait effects on cross-frequency functional independent brain networks. *Brain Topogr.* 29, 477–490. doi: 10.1007/s10548-016-0469-3

Mishra, A., Englitz, B., and Cohen, M. X. (2020). EEG microstates as a continuous phenomenon. *Neuroimage* 208:116454. doi: 10.1016/j.neuroimage.2019.116454

Mulholland, T., Boudrot, R., and Davidson, A. (1979). Feedback delay and amplitude threshold and control of the occipital EEG. *Biofeedback Self Regul.* 4, 93–102. doi: 10.1007/BF01007104

Murphy, M., Whitton, A. E., Deccy, S., Ironside, M. L., Rutherford, A., Beltzer, M., et al. (2020). Abnormalities in electroencephalographic microstates are state and trait markers of major depressive disorder. *Neuropsychopharmacology* 45, 2030–2037. doi: 10.1038/s41386-020-0749-1

Pei, G., Guo, G., Chen, D., Yang, R., Shi, Z., Wang, S., et al. (2020). BrainKilter: a real-time EEG analysis platform for neurofeedback design and training. *IEEE Access* 8, 57661–57673. doi: 10.1109/ACCESS.2020.2967903

Perrottelli, A., Giordano, G. M., Brando, F., Giuliani, L., and Mucci, A. (2021). EEG-based measures in at-risk mental state and early stages of schizophrenia: a systematic review. *Front. Psychiatry* 12:653642. doi: 10.3389/fpsyt.2021.653642

Poulsen, A. T., Pedroni, A., Langer, N., and Hansen, L. K. (2018). Microstate EEGLAB toolbox: an introductory guide. *bioRxiv* [Preprint]. doi: 10.1101/289850

Renard, Y., Lotte, F., Gibert, G., Congedo, M., Maby, E., Delannoy, V., et al. (2010). OpenViBE: an open-source software platform to design, test and use brain–computer interfaces in real and virtual environments. *Presence* 19, 35–53. doi: 10.1162/pres.19.1.35

Ruggeri, P., Meziane, H. B., Koenig, T., and Brandner, C. (2019). A fine-grained time course investigation of brain dynamics during conflict monitoring. *Sci. Rep.* 9:3667. doi: 10.1038/s41598-019-40277-3

Ruggeri, P., Nguyen, N., Pegna, A. J., and Brandner, C. (2020). Interindividual differences in brain dynamics of early visual processes: impact on score accuracy in the mental rotation task. *Psychophysiology* 57:e13658. doi: 10.1111/psyp.13658

Seitzman, B. A., Abell, M., Bartley, S. C., Erickson, M. A., Bolbecker, A. R., and Hetrick, W. P. (2017). Cognitive manipulation of brain electric microstates. *Neuroimage* 146, 533–543. doi: 10.1016/j.neuroimage.2016.10.002

Shaw, S. B., Dhindsa, K., Reilly, J. P., and Becker, S. (2019). Capturing the forest but missing the trees: microstates inadequate for characterizing shorter-scale EEG dynamics. *Neural Comput.* 31, 2177–2211. doi: 10.1162/neco_a_01229

Tanaka, H., Homma, K., and Imamizu, H. (2011). Physical delay but not subjective delay determines learning rate in prism adaptation. *Exp. Brain Res.* 208, 257–268. doi: 10.1007/s00221-010-2476-z

Tarailis, P., Šimkutė, D., Koenig, T., and Griškova-Bulanova, I. (2021). Relationship between spatiotemporal dynamics of the brain at rest and self-reported spontaneous thoughts: an EEG microstate approach. *J. Pers. Med.* 11:1216. doi: 10.3390/jpm11111216

Tomescu, M. I., Rihs, T. A., Rochas, V., Hardmeier, M., Britz, J., Allali, G., et al. (2018). From swing to cane: sex differences of EEG resting-state temporal patterns during maturation and aging. *Dev. Cogn. Neurosci.* 31, 58–66. doi: 10.1016/j.dcn.2018.04.011

Wackermann, J., Lehmann, D., Michel, C. M., and Strik, W. K. (1993). Adaptive segmentation of spontaneous EEG map series into spatially defined microstates. *Int. J. Psychophysiol.* 14, 269–283. doi: 10.1016/0167-8760(93)90041-m

Watanabe, T., Sasaki, Y., Shibata, K., and Kawato, M. (2017). Advances in fMRI real-time neurofeedback. *Trends Cogn. Sci.* 21, 997–1010. doi: 10.1016/j.tics.2017.09.010

Yamada, T., Hashimoto, R. I., Yahata, N., Ichikawa, N., Yoshihara, Y., Okamoto, Y., et al. (2017). Resting-state functional connectivity-based biomarkers and functional MRI-based neurofeedback for psychiatric disorders: a challenge for developing theranostic biomarkers. *Int. J. Neuropsychopharmacol.* 20, 769–781. doi: 10.1093/ijnp/pyx059

Zanesco, A. P. (2020). EEG electric field topography is stable during moments of high field strength. *Brain Topogr.* 33, 450–460. doi: 10.1007/s10548-020-00780-7

Zanesco, A. P., Skwara, A. C., King, B. G., Powers, C., Wineberg, K., and Saron, C. D. (2021). Meditation training modulates brain electric microstates and felt states of awareness. *Hum. Brain Mapp.* 42, 3228–3252. doi: 10.1002/hbm.25430

Zich, C., Debener, S., Kranczioch, C., Bleichner, M. G., Gutberlet, I., and De Vos, M. (2015). Real-time EEG feedback during simultaneous EEG–fMRI identifies the cortical signature of motor imagery. *Neuroimage* 114, 438–447. doi: 10.1016/j.neuroimage.2015.04.020

Conflict of Interest: The authors declare that the research was conducted in the absence of any commercial or financial relationships that could be construed as a potential conflict of interest.

Publisher's Note: All claims expressed in this article are solely those of the authors and do not necessarily represent those of their affiliated organizations, or those of the publisher, the editors and the reviewers. Any product that may be evaluated in this article, or claim that may be made by its manufacturer, is not guaranteed or endorsed by the publisher.

Copyright © 2022 Asai, Hamamoto, Kashihara and Imamizu. This is an open-access article distributed under the terms of the Creative Commons Attribution License (CC BY). The use, distribution or reproduction in other forums is permitted, provided the original author(s) and the copyright owner(s) are credited and that the original publication in this journal is cited, in accordance with accepted academic practice. No use, distribution or reproduction is permitted which does not comply with these terms.

frontiers in Computational Neuroscience

ORIGINAL RESEARCH
published: 25 February 2022
doi: 10.3389/fncom.2022.785099

A Neural Controller Model Considering the Vestibulospinal Tract in Human Postural Control

Yuichiro Omura[1], Kohei Kaminishi[2], Ryosuke Chiba[3], Kaoru Takakusaki[3] and Jun Ota[2]*

[1] Department of Precision Engineering, School of Engineering, The University of Tokyo, Tokyo, Japan, [2] Research Into Artifacts, Center for Engineering, School of Engineering, The University of Tokyo, Tokyo, Japan, [3] Division on Neuroscience, Department of Physiology, Asahikawa Medical University, Asahikawa, Japan

Humans are able to control their posture in their daily lives. It is important to understand how this is achieved in order to understand the mechanisms that lead to impaired postural control in various diseases. The descending tracts play an important role in controlling posture, particularly the reticulospinal and the vestibulospinal tracts (VST), and there is evidence that the latter is impaired in various diseases. However, the contribution of the VST to human postural control remains unclear, despite extensive research using neuroscientific methods. One reason for this is that the neuroscientific approach limits our understanding of the relationship between an array of sensory information and the muscle outputs. This limitation can be addressed by carrying out studies using computational models, where it is possible to make and validate hypotheses about postural control. However, previous computational models have not considered the VST. In this study, we present a neural controller model that mimics the VST, which was constructed on the basis of physiological data. The computational model is composed of a musculoskeletal model and a neural controller model. The musculoskeletal model had 18 degrees of freedom and 94 muscles, including those of the neck related to the function of the VST. We used an optimization method to adjust the control parameters for different conditions of muscle tone and with/without the VST. We examined the postural sway for each condition. The validity of the neural controller model was evaluated by comparing the modeled postural control with (1) experimental results in human subjects, and (2) the results of a previous study that used a computational model. It was found that the pattern of results was similar for both. This therefore validated the neural controller model, and we could present the neural controller model that mimics the VST.

Keywords: postural control, forward dynamics simulation, neural controller model, musculoskeletal model, vestibulospinal tract

OPEN ACCESS

Edited by:
Arpan Banerjee, National Brain Research Centre (NBRC), India

Reviewed by:
Shinya Aoi, Kyoto University, Japan
Vittorio B. Lippi, University of Freiburg Medical Center, Germany
Supriya Ray, Allahabad University, India

****Correspondence:***
Yuichiro Omura
omura@race.t.u-tokyo.ac.jp

Received: *28 September 2021*
Accepted: *31 January 2022*
Published: *25 February 2022*

Citation:
Omura Y, Kaminishi K, Chiba R, Takakusaki K and Ota J (2022) A Neural Controller Model Considering the Vestibulospinal Tract in Human Postural Control. Front. Comput. Neurosci. 16:785099. doi: 10.3389/fncom.2022.785099

1. INTRODUCTION

Postural control is essential for maintaining a stable standing posture, and thus it is a particularly important human motor function. Understanding human postural control is important in order to understand the disease mechanisms that lead to an impaired posture. This could lead to more effective rehabilitation strategies.

The basic neural mechanisms involved in standing upright are located in the brainstem and the spinal cord. The descending pathways from the brainstem to the spinal cord are responsible for the automatic processes that are involved in postural control (Takakusaki et al., 2017). Among these descending pathways, the reticulospinal tract (RST) and the vestibulospinal tract (VST) are particularly important for controlling posture (Takakusaki, 2017). The RST regulates muscle tone, the constant muscular tension that enables a standing posture to be maintained (Takakusaki et al., 1994, 2016). The RST both excites and inhibits muscles throughout the body (Magoun and Rhines, 1946; Rhines and Magoun, 1946). In contrast, the VST maintains the body and head in an upright position (Roberts, 1973; Schor, 1974; Takakusaki et al., 2017). It works by exciting the extensor muscles and inhibiting the flexor muscles, unlike the RST (Grillner et al., 1970; McCall et al., 2017).

It can be seen that both the VST and the RST are involved in maintaining an upright posture in humans. However, it has been suggested that damage to the VST underlies the impaired postural control seen in diseases such as Parkinson's disease and stroke (Miller et al., 2014; Lazzaro et al., 2018). This would suggest that the VST in particular plays an important role in controlling posture. Although neuroscientific methods have yielded a large amount of physiological data concerning the VST (Grillner et al., 1970; Roberts, 1973; Schor, 1974; McCall et al., 2017; Takakusaki et al., 2017), the exact contribution of the VST to postural control remains unclear. One reason for this is that the neuroscientific approach precisely verify input-output relationships under carefully controlled conditions. This can then limit our understanding of what happens when there is a wide array of sensory information and muscle outputs. To address this issue, computational models have been used to make and validate hypotheses about postural control.

Previous studies that modeled postural control have adopted an inverted pendulum model with 1∼3 degrees of freedom (DOF) as a model of the human body (Kuo, 1995; Morasso et al., 1999; van der Kooij et al., 1999; Peterka, 2002; Peterka and Loughlin, 2004; Maurer and Peterka, 2005; Masani et al., 2006; Bottaro et al., 2008; Asai et al., 2009; Mahboobin et al., 2009). Neural controllers have been modeled with feedback (FB) control (Peterka, 2002; Mergner et al., 2003; Peterka and Loughlin, 2004; Mahboobin et al., 2009), as well as with both feedforward (FF) and FB control (Kuo, 1995; Morasso et al., 1999; van der Kooij et al., 1999). Neural controller models have also been developed that can compensate for the time delays involved in receiving sensory information (van der Kooij et al., 1999; Masani et al., 2006). For instance, a model developed by van der Kooij et al. integrates multisensory inputs and estimates posture using a Kalman filter, and was shown to maintain a standing posture with a time delay of 100 ms (van der Kooij et al., 1999). In another study, Masani et al. showed it was possible to compensate for a time delay by using FB control with sufficiently large FB gains (Masani et al., 2006). Intermittent control models have also been developed that use the mechanical properties of an inverted pendulum for intermittent control (Bottaro et al., 2008; Asai et al., 2009). Asai et al. compared a continuous FB controller with an intermittent controller. They showed that the intermittent controller was more robust than the continuous FB controller, because the model of the human body was stable with a smaller gain and with a larger parameter space (Asai et al., 2009).

A problem with the inverted pendulum model is that it simplifies the human anatomical structure to such an extent that it is difficult to see how it corresponds to the actual human skeleton and muscles. In addition, the inverted pendulum model controls the joint torque, which is the sum of the forces exerted by the muscles, rather than the activity of many muscles.

Computational modeling studies have also been conducted using musculoskeletal models, which have more DOF than the inverted pendulum model (Jiang et al., 2016; Kaminishi et al., 2019, 2020; Koelewijn and Ijspeert, 2020). These models better represent the human anatomical structure, and they include muscle control. Jiang et al. developed a musculoskeletal simulator that models human postural control. This was composed of a musculoskeletal model, with seven DOF and 70 muscles, and a neural controller model (Jiang et al., 2016) with proprioceptive FB control (from muscle length and lengthening velocity) and FF control from the RST. The simulator was able to maintain a standing posture with a time delay of up to 120 ms by modeling the muscle tone regulation mechanism. By introducing visual and vestibular FB control, it was possible to verify the relationship between sensory information and muscle tone (Jiang et al., 2017). The simulator has since been improved by Kaminishi et al. to investigate postural control when there is some disturbance (Kaminishi et al., 2019, 2020).

It can be seen that many studies have investigated postural control using computational models. As previously stated, human postural control is achieved by generating muscle output from sensory information *via* the descending tract. Furthermore, the relationship between descending tracts and postural control disorders in various diseases [Parkinson's disease (Lazzaro et al., 2018), stroke (Miller et al., 2014)] have been shown. Therefore, although the model considering both RST and VST is essential to examine postural control of these diseases, none of the studies using the inverted pendulum models considered the descending tracts. Besides, previous studies using the musculoskeletal model have only examined the importance of RST during the standing posture of healthy subjects.

This study aims to present a neural controller model that mimics the VST.

An overview of the method is given as follows. For this purpose, we constructed a neural controller mimicking the VST based on a previous model (Jiang et al., 2016). Furthermore, we constructed a musculoskeletal model having neck DOFs and muscles, which are needed to represent the VST. The validity of the model was evaluated by comparing the postural control seen in the model with (1) experimental results in human subjects using evaluation indices of postural sway (the velocity and the power spectral density (PSD) of postural sway), and (2) the results of a previous computational model, which showed that the effect of noise becomes smaller when muscle tone is greater (Kaminishi et al., 2020). The details are described in the next section.

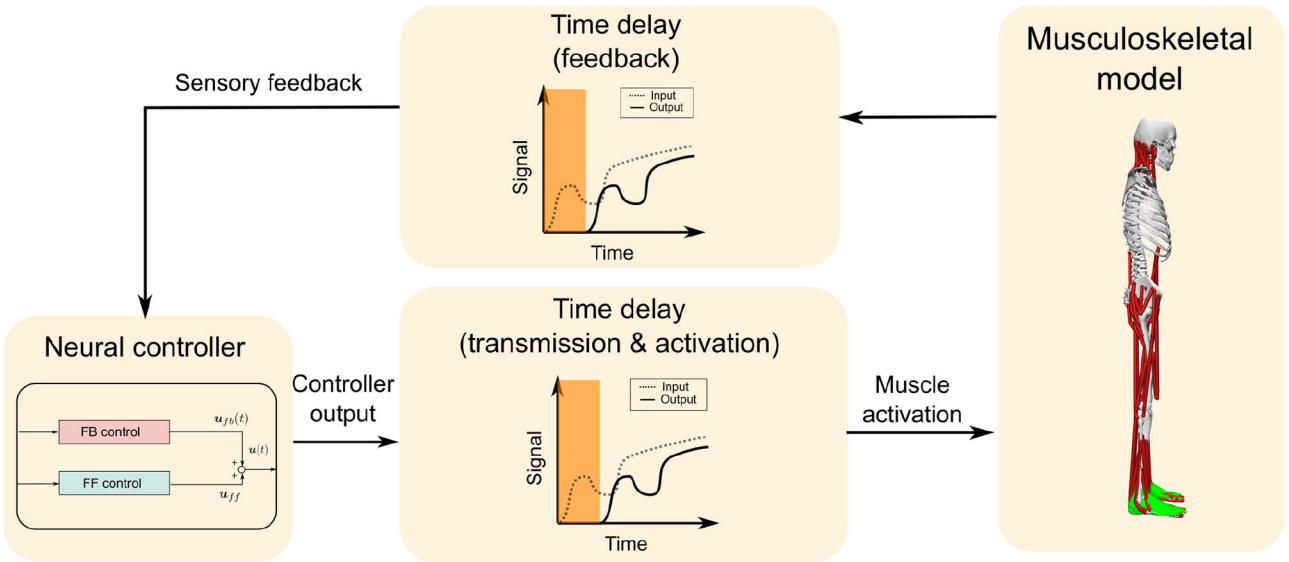

FIGURE 1 | Overall design of the computational model. The computational model is composed of a musculoskeletal model and a neural controller model, which includes feedforward (FF) and feedback (FB) control. A time delay is added to the FB from the musculoskeletal model to the neural controller model, and also to the muscle activation output from the neural controller model to the musculoskeletal model, which totals 120 ms.

2. METHODS

2.1. Basic Design

2.1.1. Task

This study focused on postural control when standing still because most people spend considerable time in this position. The task was to maintain an upright standing posture for 5,000 ms using the musculoskeletal model. This posture was chosen on the basis of a previous study (Kaminishi et al., 2019). As this model has many DOF and muscles, it is suitable for representing the function of the VST, which sends different signals to each muscle type and maintains the body in a vertical position. It was assumed that we could evaluate postural control by assessing the maintenance of a standing posture for 5,000 ms because we focused on static upright position.

2.1.2. Assumption

We assumed the following:

1. Sensory information is only obtained from the vestibular and proprioceptive systems.
2. The contraction and relaxation of muscles with the same function (flexion and extension) in each joint are consistent with each other.
3. The control of each muscle is bilaterally symmetrical.

Concerning assumption 1, we considered the maintenance of an upright standing position when the eyes are closed. For this reason, the sensory information in the neural controller model was defined as vestibular and proprioceptive, excluding vision.

Concerning assumption 2, because the task was to maintain a static upright position, no postural change, such as taking a step, should occur; therefore, each joint movement was expected to be small. With such small joint movements, if the body falls forwards, the soleus and gastrocnemius muscles, which are the extensors of the ankle joint, would both contract. For this reason, we made assumption 2.

Concerning assumption 3, human muscles are bilaterally symmetrical, and because the task was to maintain a bilaterally symmetrical upright posture, we made assumption 3.

2.2. Computational Model

The computational model was composed of a musculoskeletal model that represents the human body and a neural controller model that controls it, as shown in **Figure 1**. The computational model was constructed and simulations were performed in OpenSim 4.0 SimTK.org (Delp et al., 2007; Seth et al., 2018) (**Supplementary Materials Data Sheet 1**).

2.2.1. Musculoskeletal Model

The musculoskeletal model had 18 DOF and 94 muscles, including those of the neck related to the function of the VST (**Figure 2**). This model was based on the musculoskeletal model from a previous study, with four DOF (pitch, roll) added to the neck and 24 additional muscles to control these movements. The previous study had considered the upper part of the body to be a single rigid unit (Jiang et al., 2016, 2017; Kaminishi et al., 2019, 2020), and therefore these additional DOFs and muscles were necessary because our model included the vestibular sense, which is greatly influenced by head movements.

The center of rotation of the joint DOF and the skeletal and muscular parameters were based on the models developed by Vasavada et al. (1998), Thelen (2013), and Cazzola et al. (2017). The musculoskeletal model proposed by Cazzola et al. had 78 muscles in the neck. If we added all these muscles to the model, it becomes difficult to generate proper motion in the neck. The reason is that the calculation time to adjust

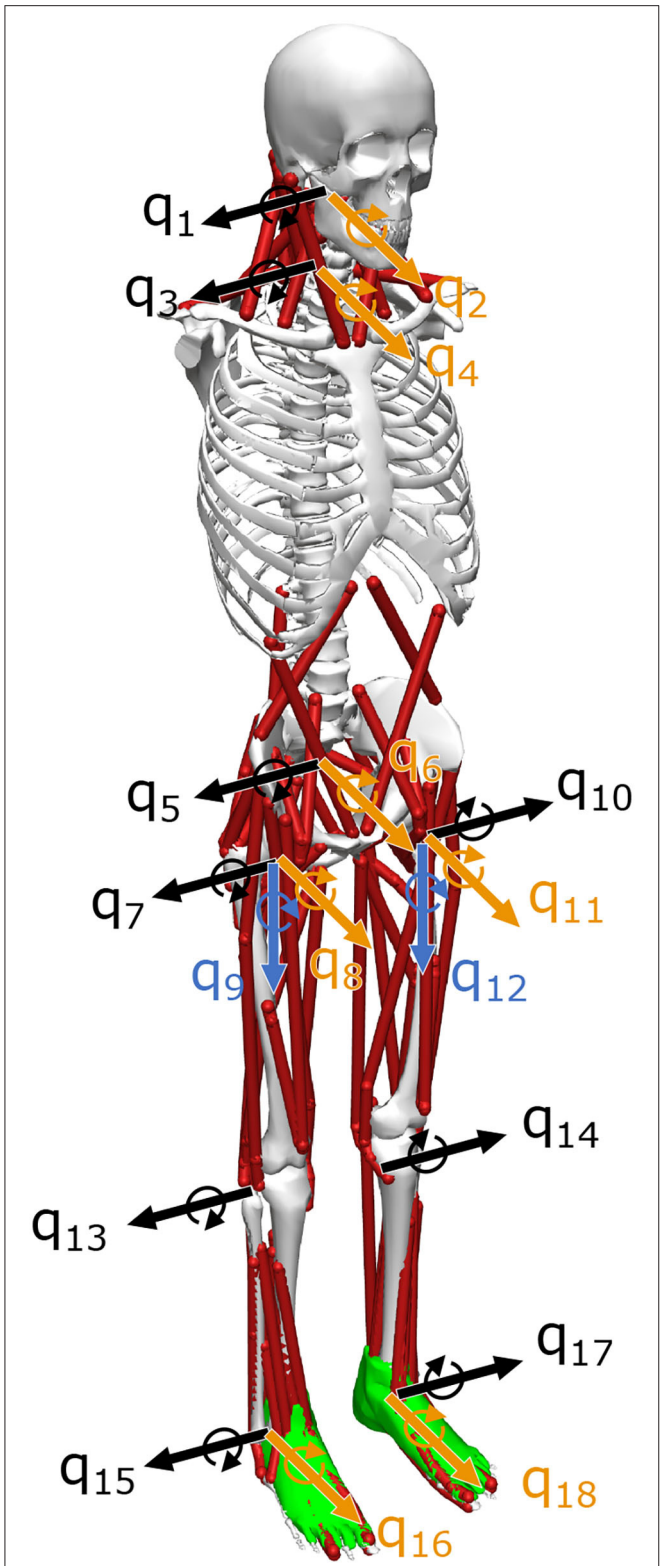

FIGURE 2 | Musculoskeletal model. The musculoskeletal model has 94 muscles and 18 degrees of freedom (DOF). q_1–q_{18} represent the DOF, where black is the sagittal plane, yellow is the frontal plane, and blue is the horizontal plane. The model is based on one developed in a previous study, but q_1–q_4 degrees of freedom have been added to the neck (Kaminishi et al., 2019).

control parameters increases exponentially as the number of muscles increases. The calculation to adjust control parameters is described in Section 2.2.3.2. Therefore, we added 24 neck muscles (see **Supplementary Materials Table 3**) to our model to reduce calculation time to adjust control parameters. The criteria were as follows. We excluded those muscles with a lower maximum isometric muscle force and a shorter length. However, to avoid large differences in the muscle force that can be exerted, the maximum isometric muscle force of the excluded muscles was added to that of the included muscles, which have the same function. The muscle model used was the Hill-type model (Millard et al., 2013).

2.2.2. Neural Controller Model

In this study, we considered both the VST and the RST. The neural controller model mimicked the VST, based on physiological data, and also included the RST proposed by Jiang et al. The proposed model is shown in **Figure 3**. It is composed of FF control, FB control, and time delays. The inputs are the initial values of the proprioceptive and vestibular information and also the values at $t - \tau_{fb}$ (time delays). The proprioceptive information is taken from the muscle lengths and the muscle lengthening velocities. The vestibular information is taken from the head acceleration, head angular acceleration, head velocity, head angular velocity, head position, and head angle. The outputs are the constant values for FF control (muscle tone, $\boldsymbol{u}_{ff}$), which are determined through the RST, and the muscle activity of feedback control ($\boldsymbol{u}_{fb}$) that will correct the difference between the current posture and the target posture, which is determined using FB control. The summation of these outputs gives the resulting output from the neural controller ($\boldsymbol{u}$). The $\boldsymbol{u}$ is converted into muscle activity $\boldsymbol{a}$ which involves a time delay and output to the musculoskeletal model. Forward dynamics simulations are performed with this muscle activity $\boldsymbol{a}$.

2.2.2.1. FF Control

The FF control is based on previous studies. It models the muscle tone regulation carried out by the RST (Jiang et al., 2016). It is known that the RST controls muscle tone for the whole body, which involves constant muscular activity (Takakusaki et al., 2017). A certain amount of muscle tone is needed to maintain a posture and resist gravity.

The output from the FF control was therefore defined as muscle tone ($\boldsymbol{u}_{ff}$) in this study. It had a constant value because it involves continuous muscular activity that is not affected by time delays. The muscle tone could be set for each muscle, and various magnitudes of muscle tone could be set, even for the same posture. It was therefore possible to select multiple muscle tones for the same upright posture and to compare them. For this we used $\|\boldsymbol{u}_{ff}\|^2$, expressed in the following Equation (1), as the evaluation index of whole-body muscle tone to represent the muscle tone, which is a vector of 94 dimensions, with a scalar value (Jiang et al., 2016).

$$\|\boldsymbol{u}_{ff}\|^2 = \sum_{i=1}^{n} u_{ff,i}^2 \tag{1}$$

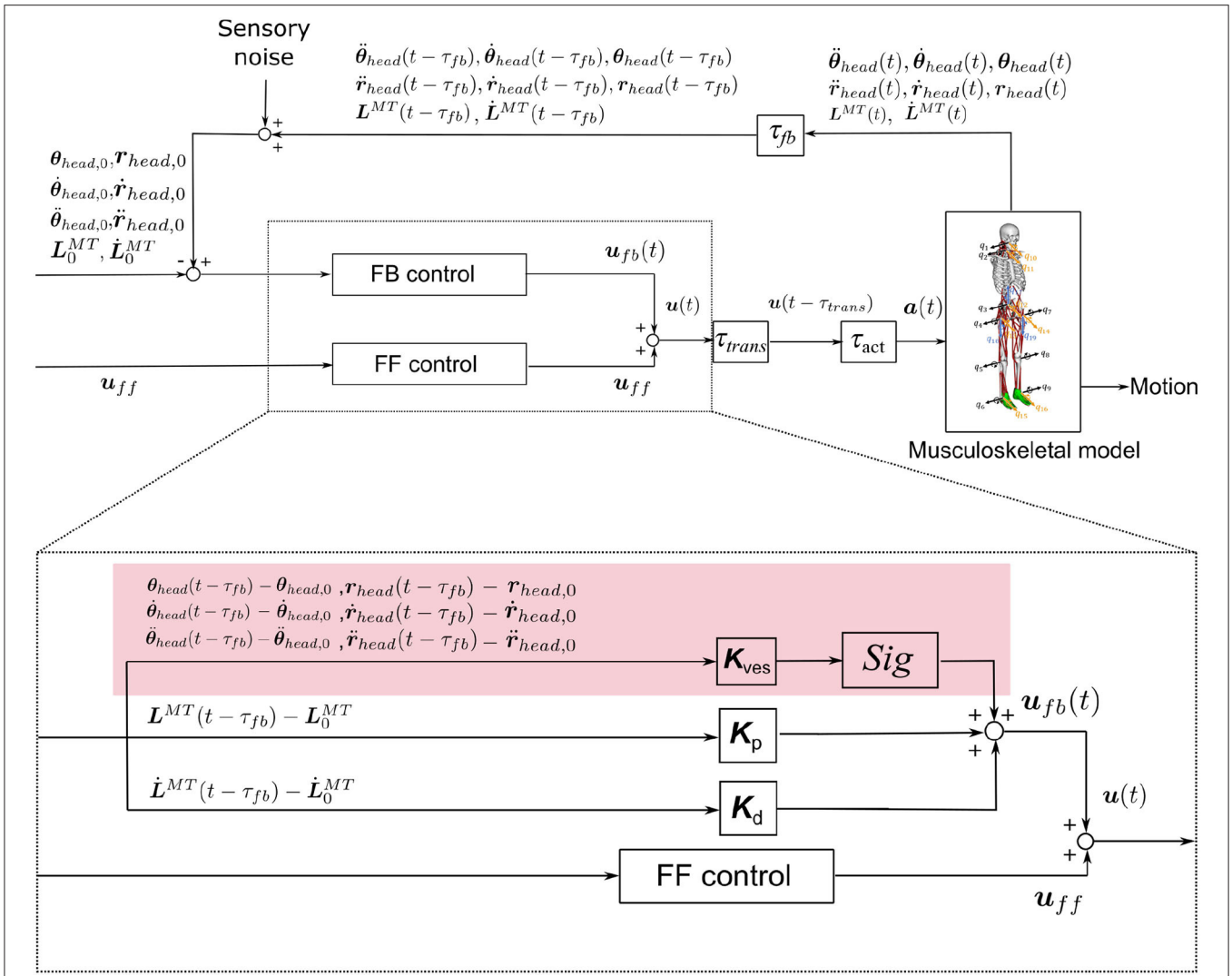

FIGURE 3 | Neural controller model. The red area represents a control system that mimics the VST. $\boldsymbol{K}_p$, $\boldsymbol{K}_d$ are the FB gains. $\boldsymbol{L}^{MT}(t-\tau_{fb})$, $\dot{\boldsymbol{L}}^{MT}(t-\tau_{fb})$ are the muscle length and the lengthening velocity, including the time delay associated with FB. $\boldsymbol{K}_{ves}$ is the FB gain for the vestibular sensory information. τ_{fb}, τ_{trans}, and τ_{act} are time delays associated with FB, neurotransmission, and muscle activation/deactivation, respectively. $\ddot{r}_{x,head}$, $\ddot{r}_{y,head}$, and $\ddot{r}_{z,head}$ represent the translational acceleration of the head in the x, y, and z axes. $\ddot{\theta}_{x,head}$, $\ddot{\theta}_{y,head}$, and $\ddot{\theta}_{z,head}$ represent the angular acceleration of the head in the x, y, and z axes. $\dot{r}_{x,head}$, $\dot{r}_{y,head}$, and $\dot{r}_{z,head}$ represent the translational velocities of the head in the x, y, and z axes. $\dot{\theta}_{x,head}$, $\dot{\theta}_{y,head}$, and $\dot{\theta}_{z,head}$ represent the head angular velocities in the x, y, and z axes. $r_{x,head}$, $r_{y,head}$, and $r_{z,head}$ represent the head positions in the x, y, and z axes. $\theta_{x,head}$, $\theta_{y,head}$, and $\theta_{z,head}$ represent the head angles in the x, y, and z axes. *Sig* is a variable that changes the positive or negative value of the output. It is set to 1 if the output muscle is an extensor, and −1 if it is a flexor.

$u_{ff,i}$ is the FF control output to the ith muscle. The n is the total number of muscles, which is $n = 94$ in this study. Similarly, we used $\|\boldsymbol{u}_{fb}\|^2$, expressed in the following Equation (2), as the evaluation index of muscle activity of feedback control.

$$\|\boldsymbol{u}_{fb}\|^2 = \sum_{i=1}^{n} u_{fb,i}^2 \tag{2}$$

2.2.2.2. FB Control

FB control was included in the neural controller model to enable the difference between the target and the current posture to be corrected. It is known that humans use such FB control to maintain a standing posture. The target posture was set by specifying each joint angle. We adopted the upright standing position as our target posture, as in the previous study (Kaminishi et al., 2019). The initial posture was set to be the same as the target posture.

The FB control used vestibular sensory information, mimicking the VST, as described in Section 2.2.2.2.1, and also proprioceptive sensory information, as described in a previous study (Jiang et al., 2016).

2.2.2.2.1. Physiology of the VST. The VST can be divided into the lateral VST and the medial VST. The medial VST mainly connects to the cervical region (Perlmutter et al., 1998; McCall et al., 2017), and it has both excitatory and inhibitory effects on the cervical

motoneurons (Wilson et al., 1970; Carleton and Carpenter, 1983; Takakusaki, 2017). It is involved in coordinating eye and neck movements (Takakusaki, 2017). The lateral VST extends along the entire spinal cord (Nyberg-Hansen and Mascitti, 1964), and it has an excitatory effect on extensor muscles and an inhibitory effect on flexor muscles (Grillner et al., 1970; McCall et al., 2017). It is involved in maintaining the head in a stable vertical position and in keeping the body vertical by using the vestibular sense (Roberts, 1973; Schor, 1974; Takakusaki et al., 2017). Because of the assumptions described in Section 2.1.2, only the lateral VST was included in the neural controller model; the medial VST was not included because it uses visual information.

2.2.2.2.2. Vestibular FB Control Mimicking the VST. We included FB control using vestibular information, which mimics the physiology of the VST, as described in Section 2.2.2.2.1. The vestibular information consisted of the head translational acceleration, head angular acceleration, head translational velocity, head angular velocity, head position, and head angle. This information is thought to be obtained in the vestibular organs and the vestibular nuclei. The following Equation (3)∼(9) was used to express the output ($u_{fb,ves,i}$) of FB control for the ith muscle using vestibular information.

$$u_{fb,ves,i} = sig\boldsymbol{K}_{ves,i}\boldsymbol{e}_{ves} \tag{3}$$

$$sig = \begin{cases} -1, & \text{Flexor muscles} \\ 1, & \text{Extensor muscles} \end{cases} \tag{4}$$

$$\boldsymbol{K}_{ves,i} = \begin{bmatrix} K_{1,ves,i} & K_{2.ves,i} & \cdots & K_{18,ves,i} \end{bmatrix} \tag{5}$$

$$\boldsymbol{e}_{ves} = \begin{bmatrix} \ddot{\boldsymbol{r}}_{head} \\ \ddot{\boldsymbol{\theta}}_{head} \\ \dot{\boldsymbol{r}}_{head} \\ \dot{\boldsymbol{\theta}}_{head} \\ \boldsymbol{r}_{head} \\ \boldsymbol{\theta}_{head} \end{bmatrix} \tag{6}$$

$$\boldsymbol{r}_{head} = \begin{bmatrix} |r_{x,head} - r_{x,head,0}| \\ r_{y,head} \\ |r_{z,head} - r_{z,head,0}| \end{bmatrix} \tag{7}$$

$$r_{head,y} = \begin{cases} |r_{y,head} - r_{y,head,0}|, & (r_{y,head} - r_{y,head,0} < 0) \\ 0, & (r_{y,head} - r_{y,head,0} \geq 0) \end{cases} \tag{8}$$

$$\boldsymbol{\theta}_{head} = \begin{bmatrix} |\theta_{x,head} - \theta_{x,head,0}| \\ |\theta_{y,head} - \theta_{y,head,0}| \\ |\theta_{z,head} - \theta_{z,head,0}| \end{bmatrix} \tag{9}$$

$K_{1,ves,i} \sim K_{18,ves,i}$ is the FB gain in the ith muscle based on vestibular information. $\ddot{r}_{x,head}$, $\ddot{r}_{y,head}$, $\ddot{r}_{z,head}$, $\ddot{\theta}_{x,head}$, $\ddot{\theta}_{y,head}$, $\ddot{\theta}_{z,head}$, $\dot{r}_{x,head}$, $\dot{r}_{y,head}$, $\dot{r}_{z,head}$, $\dot{\theta}_{x,head}$, $\dot{\theta}_{y,head}$, $\dot{\theta}_{z,head}$, $r_{x,head}$, $r_{y,head}$, $r_{z,head}$, $\theta_{x,head}$, $\theta_{y,head}$, and $\theta_{z,head}$ are the head translational acceleration, head angular acceleration, head translational velocity, head angular velocity, head position, and head angle for the x, y, and z axes, respectively. The subscript 0 for each variable represents the initial value. sig is -1 if the ith muscle is a flexor and 1 if it is an extensor. This causes the vestibular FB control to send inhibitory signals to flexor muscles and excitatory signals to extensor muscles (Equation 4). The VST keeps the body vertical, causing the head to move in the positive direction of the y-axis. This is expressed in the Equation (8). $\boldsymbol{K}_{ves} \neq O$ is defined as the presence of the VST. $\boldsymbol{K}_{ves} = O$ is defined as the absence of the VST.

2.2.2.2.3. Proprioceptive FB Control. We included proprioceptive FB control, as in previous studies. The proprioceptive information was defined as the muscle-tendon's length and lengthening velocity. We considered that this information is obtained by converting the information from the muscle spindle and Golgi tendon organs. This is because the previous study has inferred that the length of the tendon is obtained from the Golgi tendon organ using a model (Kistemaker et al., 2013). The output ($u_{fb,prop,i}$) of the proprioceptive FB control for the ith muscle is expressed in the following Equation (10) (Jiang et al., 2016):

$$u_{fb,prop,i}(t) = K_{p,i}\frac{L_i^{MT}(t-\tau_{fb}) - L_{i,0}^{MT}}{L_{i,0}^{MT}} + K_{d,i}\frac{\dot{L}_i^{MT}(t-\tau_{fb}) - \dot{L}_{i,0}^{MT}}{V_{i,max}} \tag{10}$$

$K_{p,i}$, $K_{d,i}$ are the FB gains for the ith muscle based on the muscle length and the muscle lengthening velocity, respectively. $L_i^{MT}(t-\tau_{fb})$, $\dot{L}_i^{MT}(t-\tau_{fb})$ are the length and the lengthening velocity of the ith muscle, respectively, following the time delay that is associated with FB. $L_{i,0}^{MT}$ and $\dot{L}_{i,0}^{MT}$ are the initial values of the length and the lengthening velocity of the ith muscle, respectively. $V_{i,max}$ is the maximum lengthening velocity of the ith muscle.

2.2.2.3. Time Delays

There are various time delays in the human nervous system. We included three major time delays in our model (τ_{fb}, τ_{trans}, $\tau_{act,\ deact}$) (Jiang et al., 2016). τ_{fb} denotes the time delay for receiving sensory information from the sensory receptors. τ_{trans} denotes the time delay for sending signals to the muscles from the neural controller. τ_{act}, τ_{deact} represents the time delay for either activating or deactivating the muscles. We set $\tau_{fb} = 40$ ms, $\tau_{trans} = 40$ ms, $\tau_{act} = 10$ ms, $\tau_{deact} = 40$ ms, in accordance with previous studies (Zajac, 1989; Winters, 1995; Masani et al., 2006).

2.2.2.4. Sensory Noise

There is a certain amount of error in sensory information due to noise. This limits the ability to accurately detect the exact amount of body movement. In our model, we represented the noise in sensory information from the sensory receptors.

In previous studies, Gaussian noise added to the sensory information (van der Kooij et al., 2001; Peterka and Loughlin, 2004; Maurer and Peterka, 2005; Mahboobin et al., 2009). We also add Gaussian noise as sensory noise to each sensory information based on the previous studies. Let y be the sensory information

used as feedback information by the neural controller model. y is given in the following Equation (11).

$$y = x + k_{noise}\mu X \tag{11}$$

x is the true value of the sensory information. k_{noise} is a coefficient to change the magnitude of the noise. μ is the average of the absolute values for each sensory signal (x). We ran simulations in which the musculoskeletal model maintained an upright posture for 5,000 ms under the condition of k_{noise}=0, and the average value of the sensory information of the standing results was used as μ. The noise level is determined by k_{noise} with μ as the standard noise level for each sensory signal. X is a computational random variable that follows a Gaussian distribution with a mean of zero and a standard deviation of one. We created X by using a random number generator. As it is difficult to measure the magnitude of human sensory noise (k_{noise}) experimentally, the magnitude of the noise was set to $k_{noise} = 0.01$ in this study. The neural controller model generated muscle activity using y. Forward dynamics simulations were performed using this muscle activity. Deterministic differential equations were solved by the Runge-Kutta method using this muscle activity and the musculoskeletal model's state (Thelen et al., 2003).

2.2.3. Control Parameter Adjustments

There were two control parameters in the neural controller model: the muscle tone ($\boldsymbol{u}_{ff}$) and FB gains ($\boldsymbol{K}_p$, $\boldsymbol{K}_d$, $\boldsymbol{K}_{ves}$). If these parameters are not adjusted, the musculoskeletal model cannot remain standing. Adjustments were therefore made, as described below.

The assumptions described in Section 2.1.2 meant that the FB gains of muscles belonging to the same functional group had the same value, and they were bilaterally symmetrical (note that muscle tone is independent of displacement; therefore, muscle tone can have a different value for each muscle). The muscles were divided into 14 groups according to the joint, whether they function in flexion or extension, and with reference to the moment arm generated by each muscle at the joint (Kaminishi et al., 2019) (Lumbar extensor, Lumbar flexor, Hip extensor, Hip flexor, Knee extensor, Knee flexor, Ankle extensor, Ankle flexor, Subtalar evertor, Subtalar invertor, Biarticular, Neck extensor, Neck flexor, Biarticular for neck). The parameters that could be adjusted were $\boldsymbol{u}_{ff}$: 94 dimensions, $\boldsymbol{K}_p$: 14 dimensions, $\boldsymbol{K}_d$: 14 dimensions, and $\boldsymbol{K}_{ves}$: 14 × 18 dimensions because there are 94 muscles in the musculoskeletal model.

The muscle tone was not affected by time delay. In contrast, the FB gain was affected by the time delay. This was therefore adjusted with the time delay using an optimization method after calculating the muscle tone to efficiently adjust the control parameters (**Figure 4**). Previous studies using a similar model have shown that the muscle activity is closest to that of healthy subjects when the muscle tone is low (Jiang et al., 2016). On the basis of this, we calculated several muscle tone values and selected muscle tones including low muscle tone at regular intervals from calculated candidates. For each of these, we adjusted the FB gain to enable the musculoskeletal model to remain standing.

2.2.3.1. Muscle Tone Calculation

Muscle tone is the continuous contraction of muscles that allows humans to remain standing. It therefore has a constant value that is independent of time delay. In our study, the muscle tone was calculated using the method described below. We set $\tau_{fb} = \tau_{trans} = 0$ ms (no time delay condition), $k_{noise} = 0$ (no noise condition), $\boldsymbol{u}_{ff} = \boldsymbol{0}$, and various FB gains (based on Equations 14 ∼ 16), and we ran the simulation to determine whether the musculoskeletal model could maintain a standing posture. If this was achieved, the muscle tone was calculated from the average muscle activity (Equation 12), using a method developed by Jiang et al. (2016).

$$u_{ff,i} = \frac{\int_{t1}^{t2} a_i(t)dt}{t_2 - t_1} \tag{12}$$

$u_{ff,i}$ is the FF control output of the ith muscle. t_1, t_2 are set as t_1 = 3,000 ms, t_2 = 5,000 ms, in accordance with previous studies (Jiang et al., 2016). a_i is the muscle activity of the ith muscle. Similarly, the target joint angle was updated using the following Equation (13).

$$q_{i,target} = \frac{\int_{t1}^{t2} q_i(t)dt}{t_2 - t_1} \tag{13}$$

$q_{i,target}$ is the target joint angle of the ith joint. t_1, t_2 are set as t_1 = 3,000 ms, t_2 = 5,000 ms. q_i is the joint angle of the ith joint.

By giving various FB gains as initial values, various muscle tones can be calculated. Thus, different FB gains were given to each muscle group by changing k_p, k_d, and $\boldsymbol{k}_{ves}$, which are represented by the Equations (14) and (15), respectively. Depending on the combination of FB gains given, the musculoskeletal model may not be able to maintain a standing posture. We therefore calculated the muscle tones by giving various FB gains in the specified range. We were able to calculate various muscle tone candidates of multiple sizes because there were several FB gains that could maintain the standing position (see the upper side and the right side in **Figure 4**).

$$[K_{p,i}, K_{d,i}] = \begin{cases} [0.50k_p, 0.23k_d], & \text{Lumbar extensor} \\ [0.48k_p, 0.11k_d], & \text{Lumbar flexor} \\ [0.45k_p, 0.05k_d], & \text{Hip extensor} \\ [0.50k_p, 0.16k_d], & \text{Hip flexor} \\ [0.33k_p, 0.05k_d], & \text{Knee extensor} \\ [0.28k_p, 0.23k_d], & \text{Knee flexor} \\ [0.17k_p, 0.06k_d], & \text{Ankle extensor} \\ [0.30k_p, 0.27k_d], & \text{Ankle flexor} \\ [0.50k_p, 0.11k_d], & \text{Subtalar evertor} \\ [0.50k_p, 0.05k_d], & \text{Subtalar inventor} \\ [0.39k_p, 0.05k_d], & \text{Biarticular} \\ [0.17k_p, 0.06k_d], & \text{Neck extensor} \\ [0.17k_p, 0.27k_d], & \text{Neck flexor} \\ [0.17k_p, 0.06k_d], & \text{Neck biarticular} \end{cases} \tag{14}$$

$$\boldsymbol{K}_{ves,i} = 0.01\boldsymbol{k}_{ves} \tag{15}$$

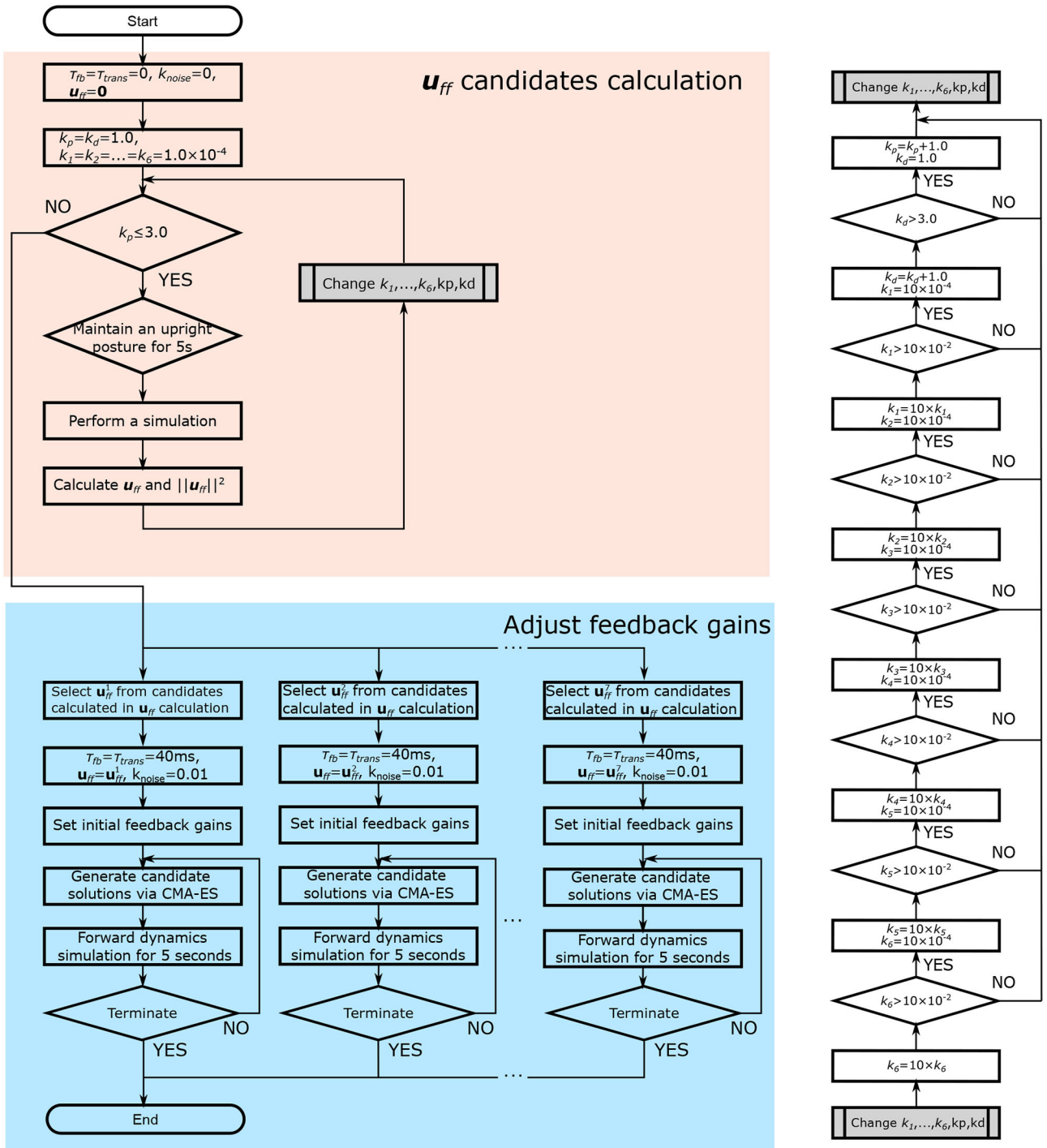

FIGURE 4 | Flowchart of the parameter adjustment. First, muscle tone values ($\boldsymbol{u}_{ff}$) are calculated (shown in red). Muscle tones are selected, and the FB gain is adjusted using an optimization method (the Covariance Matrix Adaptation Evolution Strategy) (shown in blue). In the figure, τ_{fb} and τ_{trans} denote the time delay due to FB and neurotransmission, respectively. k_{noise} denotes the magnitude of the noise. k_p and k_d denote the FB gain for the proprioceptive information. $k_{1,\ldots,6}$ denote the FB gain for the vestibular sense.

$$\boldsymbol{k}_{ves} = \left[k_1\boldsymbol{e}_3 \;\; k_2\boldsymbol{e}_3 \;\; k_3\boldsymbol{e}_3 \;\; k_4\boldsymbol{e}_3 \;\; k_5\boldsymbol{e}_3 \;\; k_6\boldsymbol{e}_3\right] \tag{16}$$

$\boldsymbol{e}_3$ is a row vector of the third order with all of the elements being 1. The FB gains are empirically given in the range of 1.0 to 3.0 for k_p and k_d, and in the range of 1.0×10^{-4} to 1.0×10^{-2} for $k_1 \sim k_6$. The coefficients were determined referring to the value in a previous study (Kaminishi et al., 2019).

In this study, seven muscle tones were selected from the candidates so that the evaluation index of muscle tone, $\|\boldsymbol{u}_{ff}\|^2$, was closest to values from 1.5 to 4.5 with an increment of 0.5. If the musculoskeletal model could not maintain a standing posture with selected uff in adjustment of feedback gains, the next closest uff was chosen. The reason for this was to compare postural control for a range of muscle tones including $\|\boldsymbol{u}_{ff}\|^2 = 2.0$, which was found, in a previous study, to be the closest to the muscle activity while standing still (Jiang et al., 2016), because there were too many calculated muscle tone candidates to perform the simulation with all of them.

2.2.3.2. Adjustment of Feedback Gains

The musculoskeletal model cannot maintain the standing position using muscle tone alone when there are time delays. In real life, humans are thought to remain standing by using FB gains to adjust the muscle tone. The FB gains were therefore adapted so that the standing position could be maintained, even with time delays, using the optimization method.

The algorithm used for the adjustment was the Covariance Matrix Adaptation Evolution Strategy (CMA-ES) which is one of the evolution strategies (Hansen et al., 2003). This was chosen as it can be used for optimization with multimodality, thus making it suitable for tuning the FB gains in this study. In CMA-ES, forward dynamics simulations for 5,000 ms with time delays and noise are repeated to search for the FB gain that minimizes the objective function J, which is shown in the following Equations (17)∼(20):

$$J = w_{fail}J_{fail} + w_{pos}J_{pos} \tag{17}$$

$$J_{fail} = \frac{1}{T_{fail}}(T_{simu} - T_{fail}) \tag{18}$$

$$T_{fail} = \begin{cases} T_{stop}, & (h_{COM} < 0.7m) \\ T_{simu}, & (h_{COM} \geq 0.7m) \end{cases} \tag{19}$$

$$J_{pos} = \sum_{j=1}^{15} \int_0^{T_{fail}} |\theta_j(t) - \theta_j(0)| dt \tag{20}$$

w_{fail} is the weight of J_{fail}, which evaluates the fall of the musculoskeletal model. w_{pos} is the weight of J_{pos}, which evaluates the posture of the musculoskeletal model. w_{fail} and w_{pos} are set at 10,000 and 1, respectively, in accordance with previous studies (Kaminishi et al., 2019). The algorithm prioritizes the search for FB gains that do not cause the musculoskeletal model to fall. When this has been obtained, the algorithm then searches for the FB gain that minimizes J_{pos}. In Equation (19), T_{simu} is the simulation time, which is 5,000 ms in this study. T_{stop} is the time at which the musculoskeletal model falls. Falling was defined as when the h_{COM} (the height of the center of mass (COM) of the musculoskeletal model) was below 0.7 m, or when the COM was out of the base of support (BOS). The threshold value of h_{COM} was set at 0.7 m because falling would be expected to occur at this point. For comparison, the h_{COM} of the musculoskeletal model is 0.72 m when the hip joint is rotated by 90 degrees; however, such a large joint flexion was not expected to occur because the upright standing position was maintained. When the COM is not within the BOS when standing upright, humans try to remain standing by stepping. We therefore regarded forward and backward deviations from the BOS as a fall because we focused on forward and backward swaying. $\theta_j(t)$ is the joint angle of the jth joint at time t. J_{pos} is the time-integrated value of the change in the joint angle from the initial position.

These parameters were not adjusted to fit the experimental data because we adjusted them using the optimization method with an objective function that evaluates the fall and posture of the musculoskeletal model.

2.3. Evaluation

This section describes how the validity of the neural controller model was evaluated. Simulations were run to determine whether the musculoskeletal model would remain standing for 5,000 ms, using the adjusted control parameters described in Section 2.2.3. This included various conditions of muscle tone and with the VST either present or absent. The evaluation index was calculated from the simulation. To consider the effect of noise, we performed ten simulations for each condition. The noise was changed in each simulation because the random seed was changed. The following three evaluation indices were used for the validity assessment:

- The center of pressure (COP) velocity
- The slope of the PSD of COP
- The correlation coefficient between the standard deviation of the COP velocity and the muscle tone

These evaluation indices were chosen on the basis of findings reported in previous studies. For instance, it has been found that patients with vestibular disorders have a significantly greater COP velocity compared with healthy subjects (Talebi et al., 2016; Sprenger et al., 2017). Furthermore, differences have been found for the slope of the PSD of COP between patients with vestibular disorders and healthy subjects. Specifically, the slope β_1 in the ∼1 Hz region has been found to be larger in the positive direction, and the slope β_2 in the 1∼5 Hz region has been found to be larger in the negative direction for patients (Aoki et al., 2014). The increase in β_1 in the positive direction indicates that the power tends to be lower at lower frequencies and higher at higher frequencies in the ∼1 Hz region, resulting in finer fluctuations. The increase in β_2 in the negative direction indicates that the power tends to be higher at lower frequencies and lower at higher frequencies in the 1∼5 Hz region. In other words, this indicates that the postural sway contains more low-frequency components in the 1∼5 Hz region. In another study, computational models showed that the effect of sensory noise decreases as the muscle tone increases (Kaminishi et al., 2020). This means that the variation (standard deviation) in COP velocity due to noise should decrease as the muscle tone increases. These previous studies led us focus on the three evaluation indices listed above.

In our model, the conditions with and without the VST represented healthy subjects and patients with vestibular disorders, respectively. The COP velocity was calculated in the

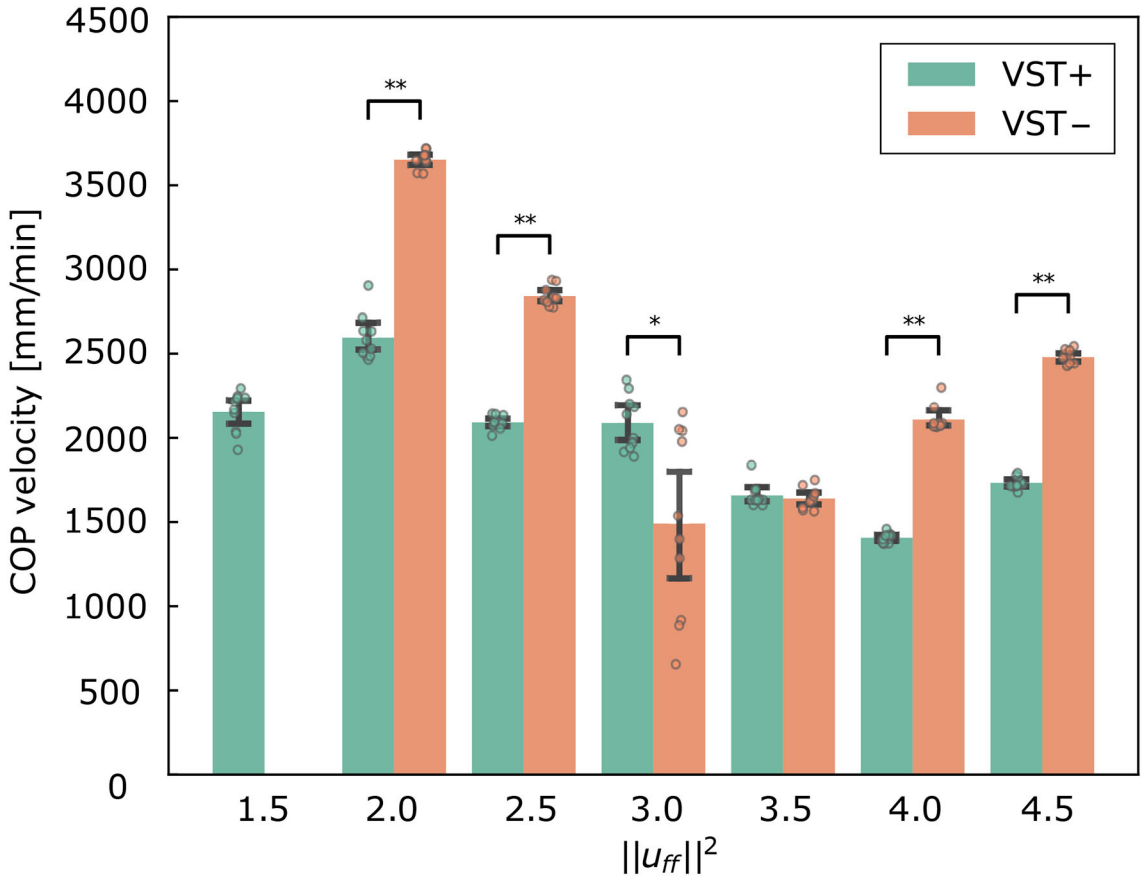

FIGURE 5 | Center of pressure (COP) velocity in the forward and backward directions for each condition. Mean ± S.D. are plotted on the graph. VST ± denotes the presence or absence of the vestibulospinal tract (VST). For VST-, the value is 0 where the muscle tone $\|\boldsymbol{u}_{ff}\|^2 = 1.5$ could not been calculated. *$P < 0.050$. **$P < 0.010$.

anterior-posterior direction (the average of 10 trials), because the VST was considered to play a large role in this direction. The COP velocity in each condition were compared between the conditions with and without the VST using *t*-test. $P < 0.0083$ was considered statistically significant with a Bonferroni correction. The PSD of COP was calculated and then β_1 and β_2 were determined. Because the sampling frequency of the simulation was not constant, the Lomb-Scargle method was used to calculate the PSD of COP. This was then normalized to sum to 1. The slopes in the ∼1 Hz area (β_1) and the 1∼5 Hz area (β_2) were calculated using linear regression in log-log plot (Aoki et al., 2014). The PSD was calculated for the trial with the median objective function calculated from Equation (17), where the effect of noise was considered to be intermediate among the ten trials.

3. RESULTS

Several muscle tone (FF output) candidates were calculated using the method described in Section 2.2.3.1. We could calculate 1,442 muscle tone candidates for the condition with the VST and 383 muscle tone candidates for the condition without the VST. Seven of these were selected in the vicinity of $\|\boldsymbol{u}_{ff}\|^2 = 1.5, 2.0, 2.5, 3.0, 3.5, 4.0, 4.5$, at even intervals. The exact values of these were $\|\boldsymbol{u}_{ff}\|^2 = 1.50, 1.93, 2.48, 3.00, 3.55, 3.95, 4.45$ for the condition with the VST, and $\|\boldsymbol{u}_{ff}\|^2 = 2.09, 2.56, 2.97, 3.56, 3.94, 4.51$ for the condition without the VST (**Supplementary Materials Table 1**, **Data Sheet 2**). For the former condition (with the VST), it was possible to calculate muscle tone values of approximately $\|\boldsymbol{u}_{ff}\|^2 = 1.5$, whereas this was not the case for the latter condition (without the VST); here, a muscle tone below $\|\boldsymbol{u}_{ff}\|^2 = 1.97$ could not be calculated. In other words, without the VST, the musculoskeletal model could not maintain a muscle tone lower than $\|\boldsymbol{u}_{ff}\|^2 = 1.97$, even without a time delay. The FB gain was adjusted using the method described in Section 2.2.3.2 for each selected muscle tone (**Supplementary Materials Table 2**). Using the optimization method, it was possible to determine the FB gain that would enable the musculoskeletal model to remain standing for 5,000 ms. This was the case for all of the selected muscle tones.

Figure 5 shows the COP velocities with and without the VST for each muscle tone (**Supplementary Materials Data Sheet 3**). The COP velocities were found to be significantly lower with the

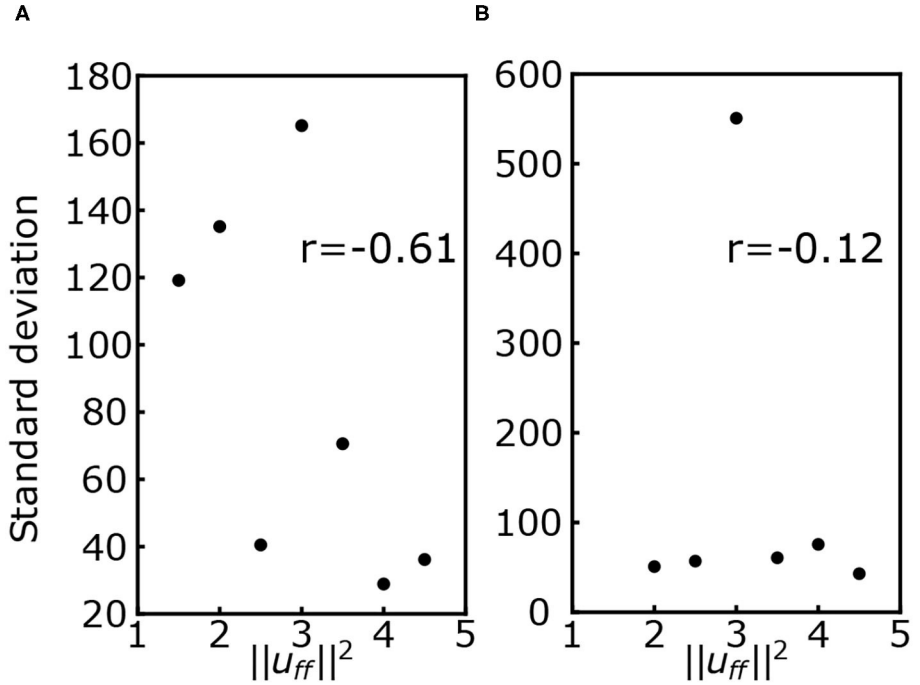

FIGURE 6 | (A) Standard deviation of the center of pressure (COP) velocity for each muscle tone with the VST. **(B)** Standard deviation of the COP velocity for each muscle tone without the VST. r denotes the correlation coefficient.

VST for all of the muscle tones except $\|\boldsymbol{u}_{ff}\|^2 = 3.0, 3.5$ ($P < 0.0010$). The COP velocities were significantly lower without the VST for $\|\boldsymbol{u}_{ff}\|^2 = 3.0$ ($P = 0.0076$), and were not different for $\|\boldsymbol{u}_{ff}\|^2 = 3.5$. The lowest COP velocity was for $\|\boldsymbol{u}_{ff}\|^2 = 3.0$ without the VST and for $\|\boldsymbol{u}_{ff}\|^2 = 4.0$ with the VST.

Figure 6 shows the standard deviation of the COP velocity for each muscle tone in conditions with and without the VST. The correlation coefficient between $\|\boldsymbol{u}_{ff}\|^2$ and the standard deviation of the COP velocity was $r = -0.61$ for the condition with the VST, and $r = -0.12$ for the condition without the VST.

Figure 7 shows the PSD and the slopes β_1, β_2. **Figure 8** shows the slopes β_1, β_2. For $\|\boldsymbol{u}_{ff}\|^2 = 1.5 \sim 2.5$, β_1 was larger in the negative direction, and β_2 was larger in the positive direction with the VST. For $\|\boldsymbol{u}_{ff}\|^2 = 3.0 \sim 4.5$, β_1 tended to be larger in the negative direction, and β_2 tended to be larger in the positive direction without the VST.

Figure 9 shows the muscle tone for each muscle at the selected $\|\boldsymbol{u}_{ff}\|^2$.

Figure 10 shows $\|\boldsymbol{u}_{fb}\|^2$ for each condition. The value of $\|\boldsymbol{u}_{fb}\|^2$ was significantly lower in the condition with the VST than in the condition without the VST for $\|\boldsymbol{u}_{fb}\|^2 = 1.5 \sim 3.0$ ($P < 0.0010$). The value of $\|\boldsymbol{u}_{fb}\|^2$ was significantly higher in the condition with the VST than in the condition without the VST for $\|\boldsymbol{u}_{fb}\|^2 = 3.5 \sim 4.5$, except for $\|\boldsymbol{u}_{fb}\|^2 = 4.0$ ($P < 0.0010$). For $\|\boldsymbol{u}_{fb}\|^2 = 4.0$, the value of $\|\boldsymbol{u}_{fb}\|^2$ was significantly lower in the condition with the VST than in the condition without the VST ($P < 0.0010$).

Table 1 shows the means of the joint angle during simulation and target value of joint angle in a sagittal plane corresponding to the swaying in the anterior-posterior direction (q_1, q_3, q_5, q_7, q_{13}, q_{15} in **Figure 2**). The data of all joint angles are included in the **Supplementary Materials Table 4**.

4. DISCUSSION

4.1. Validation of the Neural Controller Model

4.1.1. COP Velocity

Figure 5 shows that the COP velocities were significantly larger without the VST for all of the selected muscle tones, with the exception of $\|\boldsymbol{u}_{ff}\|^2 = 3.0, 3.5$. This result is consistent with experimental results in human subjects (Talebi et al., 2016; Sprenger et al., 2017).

The results for $\|\boldsymbol{u}_{ff}\|^2 = 1.5, 2.0$ show that, with the VST, the musculoskeletal model could maintain a standing posture with a lower muscle tone and a lower COP velocity than without the VST. This indicates that the VST enabled the musculoskeletal model to maintain a standing posture when the muscle tone was low. In line with this, a previous study reported that muscle tone increases when sensory information is inhibited during standing (Chiba et al., 2013). It is consistent with this study that the presence or absence of the VST caused a difference in muscle tone to remain standing.

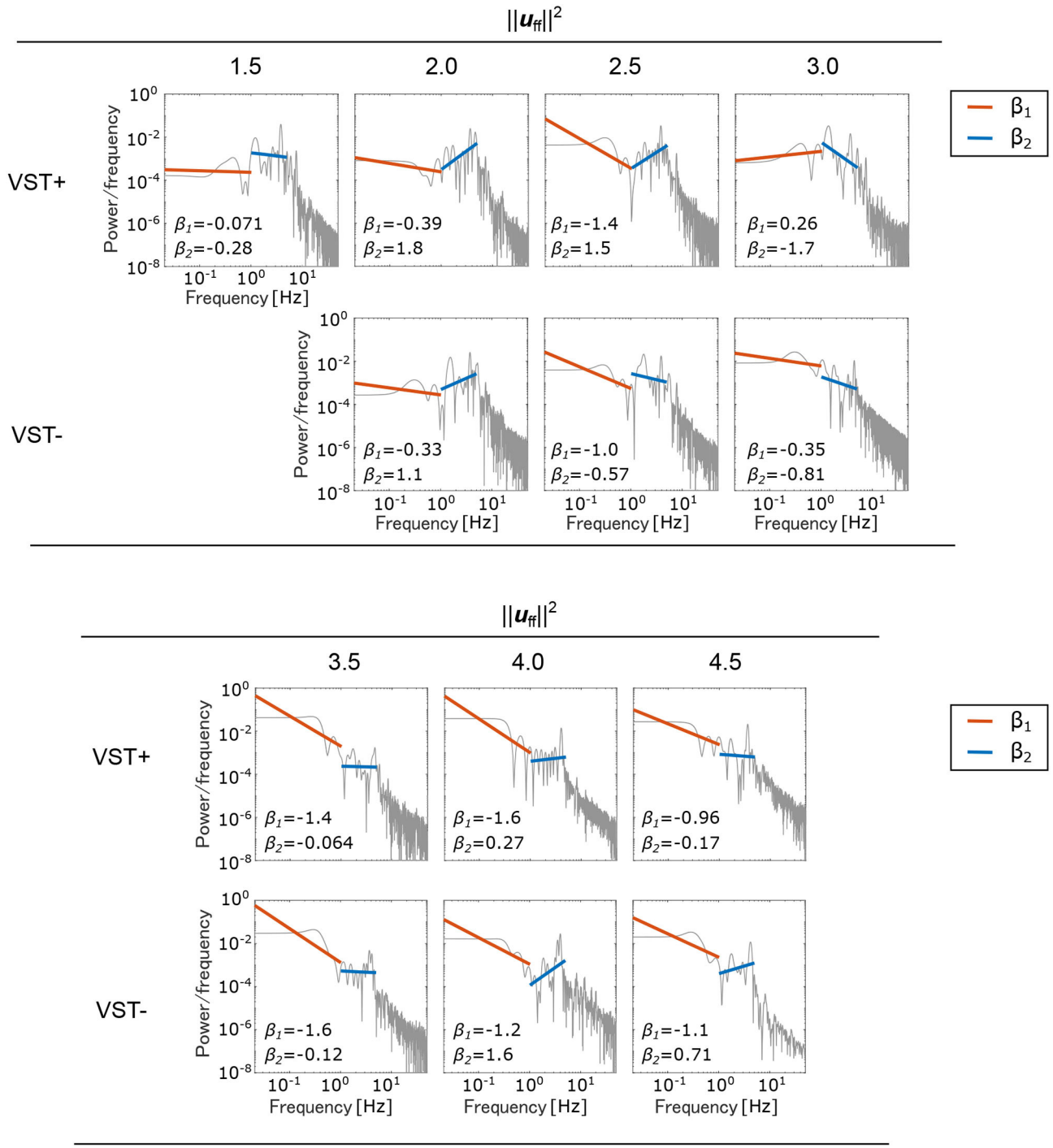

FIGURE 7 | Power spectral density (PSD) of the center of pressure (COP). A separate log-log plot is shown for each condition. The PSDs for the seven selected muscle tones are shown; VST ± denotes the presence or absence of the VST. For VST-, a muscle tone could not be calculated where $\|u_{ff}\|^2 = 1.5$; the corresponding field is therefore blank. The PSDs were normalized to sum to 1. The slope β_1 in the low-frequency region (∼1 Hz) and the slope β_2 in the high-frequency region (1∼5 Hz) are both shown on the graphs.

Concerning the relationship between the COP velocity and the muscle tone, it could be seen that the COP velocity decreased as the muscle tone increased. The COP velocity was lowest at $\|u_{ff}\|^2 = 4.0$ in the condition with the VST, and at $\|u_{ff}\|^2 = 3.0$ in the condition without the VST. Above these values, the COP velocity increased as the muscle tone

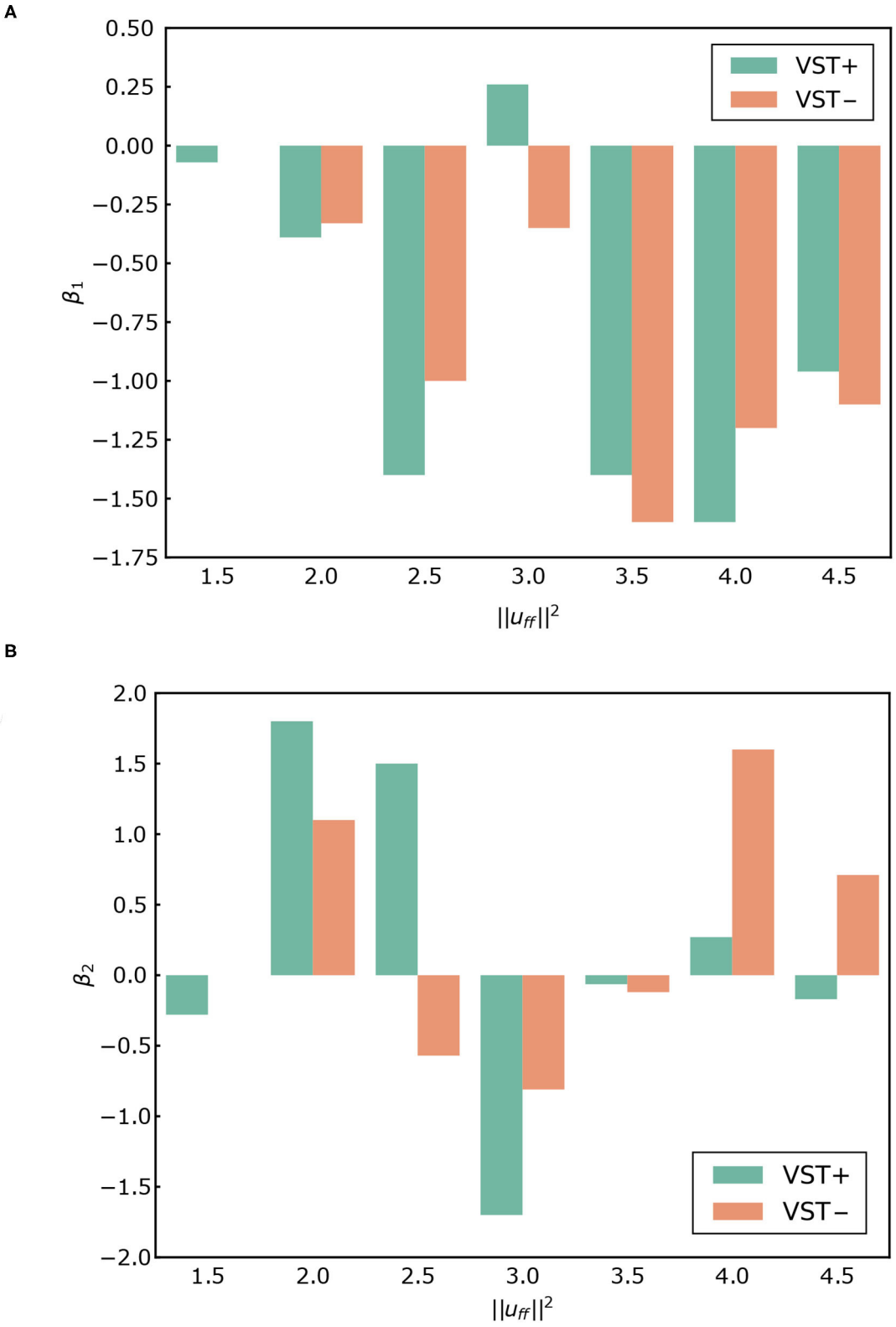

FIGURE 8 | (A) β_1 for each condition. **(B)** β_2 for each condition. VST ± denotes the presence or absence of the vestibulospinal tract (VST). For VST-, the value is 0 where the muscle tone $\|\boldsymbol{u}_{ff}\|^2 = 1.5$ could not been calculated.

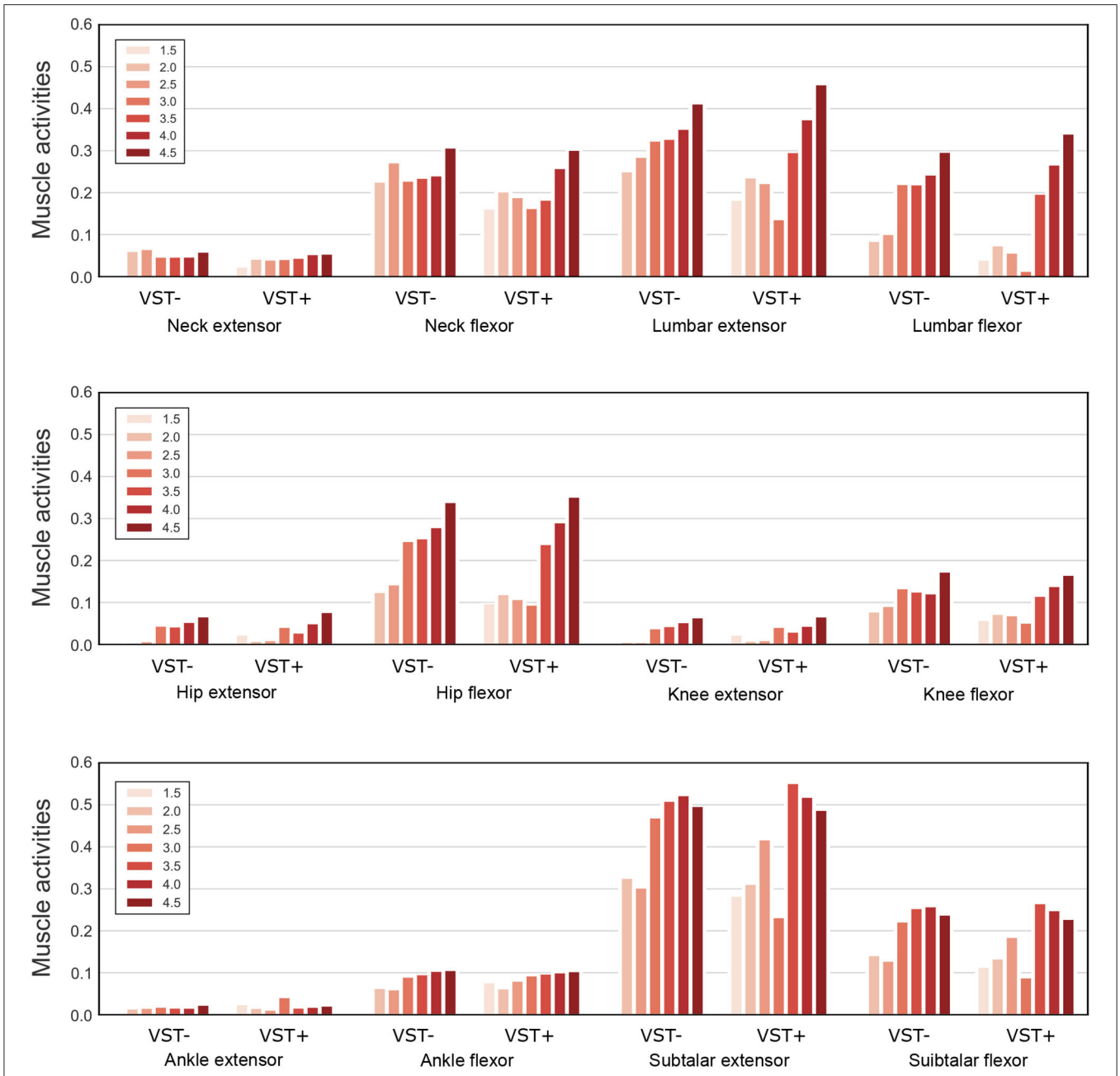

FIGURE 9 | Muscle tone of the extensor and flexor muscles at each joint. Muscle tones for seven values of $\|\boldsymbol{u}_{ff}\|^2$ are plotted on the graph. For VST-, the value is 0 where the muscle tone $\|\boldsymbol{u}_{ff}\|^2 = 1.5$ could not been calculated. VST ± denotes the presence or absence of the VST.

increased. It is conceivable that when the muscle tone is less than $\|\boldsymbol{u}_{ff}\|^2 = 3.0, 4.0$, the muscle stiffness increases as the muscle tone increases. This would decrease the magnitude of the postural sway and thus reduce the COP velocity. However, when the muscle tone is greater than $\|\boldsymbol{u}_{ff}\|^2 = 3.0, 4.0$, the increased stiffness could cause an increase in high frequency oscillations, which would then increase the COP velocity. In line with this, **Figure 7** shows that the power of frequencies approximately 3∼5 Hz is greater for muscle tones above $\|\boldsymbol{u}_{ff}\|^2 = 3.0$.

Figure 5 shows that the COP velocities were significantly smaller without the VST for $\|\boldsymbol{u}_{ff}\|^2 = 3.0$ and not different between with and without the VST for $\|\boldsymbol{u}_{ff}\|^2 = 3.5$. Several feedback gains were larger in the condition without the VST at $\|\boldsymbol{u}_{ff}\|^2 = 3.0$. The large feedback gains reduce the displacement. However they are usually not selected by the optimization method because the musculoskeletal model may become unstable depending on the noise with large feedback gains. It is considered that the large feedback gains were selected at $\|\boldsymbol{u}_{ff}\|^2 = 3.0$ because $\|\boldsymbol{u}_{ff}\|^2 = 3.0$ was the value that allowed the model to

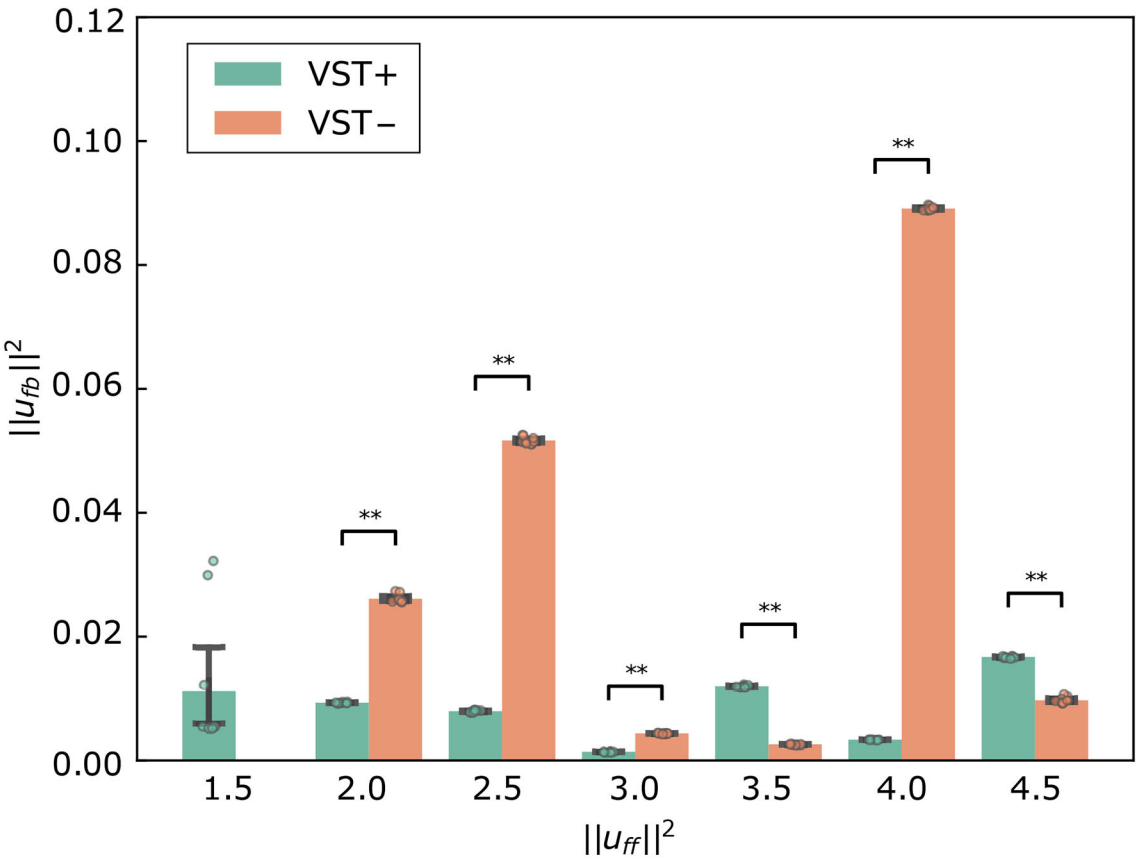

FIGURE 10 | $\|\boldsymbol{u}_{fb}\|^2$ for each condition. Mean ± S.D. are plotted on the graph. VST ± denotes the presence or absence of the vestibulospinal tract (VST). For VST-, the value is 0 where the muscle tone $\|\boldsymbol{u}_{ff}\|^2 = 1.5$ could not been calculated. $^{**}P < 0.010$.

maintain a stable standing posture. COP velocity was therefore very small for some noises. We think that the musculoskeletal model was unstable with the possibility of falling due to the large feedback gains at $\|\boldsymbol{u}_{ff}\|^2 = 3.0$ when the number of trials and the noise increased. Regarding $\|\boldsymbol{u}_{ff}\|^2 = 3.5$, the COP velocity was not different between the conditions with and without the VST. Additionally, the muscle tone at which the smallest COP velocity was achieved was different for each condition, due to the difference in the controller. Considering this, when COP velocity was compared between different muscle tones, there was a difference between the condition without the VST at $\|\boldsymbol{u}_{ff}\|^2 = 3.5$ and the condition with the VST at $\|\boldsymbol{u}_{ff}\|^2 = 4.0$. We therefore concluded that the musculoskeletal model can maintain a more stable standing posture in the condition with the VST.

4.1.2. Slope of the PSD of COP

It has previously been reported that the slope of the PSD of COP in the ∼1 Hz region, β_1, is larger in the positive direction in patients with vestibular disorders than in healthy subjects. The mean of β_1 was reported to be -1.22 for healthy subjects and -1.02 for patients with vestibular disorders (Aoki et al., 2014). In our study, the value of β_1 was larger in the positive direction in the condition without the VST than in the condition with the VST for $\|\boldsymbol{u}_{ff}\|^2 = 1.5 \sim 2.5$, as shown in **Figures 7**, **8**. This indicates that the amplitude of the higher frequency components increases in the ∼1 Hz region when there is no VST, i.e., the postural sway becomes finer. This difference between the presence and absence of the VST is consistent with the studies on patients with vestibular disorders. It was noted that the β_1 at $\|\boldsymbol{u}_{ff}\|^2 = 2.5$ was closest to that found in a study comparing patients with healthy controls. This implies that humans may maintain a standing posture using a muscle tone of approximately $\|\boldsymbol{u}_{ff}\|^2 = 2.5$. This would be in line with previous findings (Jiang et al., 2016).

In contrast to this, β_1 was found to be larger in the negative direction in the condition without the VST for the higher muscle tones ($\|\boldsymbol{u}_{ff}\|^2 = 3.0 \sim 4.5$), with the exception of $\|\boldsymbol{u}_{ff}\|^2 = 4.0$. This result is not consistent with the experimental results obtained in human subjects. This may be because the muscle tone is higher than that found in healthy individuals ($\|\boldsymbol{u}_{ff}\|^2 = 2.0$). Such an increase in muscle tone would increase the stiffness, which would reduce the amount of FB control needed to maintain an upright posture. In this way, the effect of the VST would not be apparent.

It has previously been reported that the slope β_2 in the 1∼5 Hz region is larger in the negative direction in patients

TABLE 1 | Joint angle.

Conditions	$\|u_{ff}\|^2$	Source	Joint (°)					
			q_1	q_3	q_5	q_7	q_{13}	q_{15}
VST+	1.5	Mean	2.9 ± 0.088	−0.14 ± 0.13	−11 ± 0.095	−5.8 ± 0.062	2.0 ± 0.011	2.1 ± 0.053
		Target	2.8	0.053	−11	−5.9	1.9	2.1
	2.0	Mean	2.3 ± 0.26	−0.25 ± 0.16	−11 ± 0.069	−5.9 ± 0.073	2.0 ± 0.011	2.4 ± 0.046
		Target	1.8	0.0081	−11	5.8	1.7	2.3
	2.5	Mean	2.2 ± 0.19	−0.21 ± 0.20	−12 ± 0.13	−5.9 ± 0.069	2.0 ± 0.011	2.3 ± 0.035
		Target	1.8	−0.017	−11	−5.8	1.9	2.2
	3.0	Mean	10 ± 0.11	0.71 ± 0.31	−11 ± 0.17	−5.9 ± 0.10	2.1 ± 0.011	1.9 ± 0.053
		Target	9.7	0.92	−11	−6.0	2.0	1.8
	3.5	Mean	2.8 ± 0.84	0.61 ± 0.69	−12 ± 0.31	−5.4 ± 0.098	1.9 ± 0.025	2.2 ± 0.092
		Target	1.4	0.045	−11	−5.5	1.5	2.2
	4.0	Mean	2.5 ± 0.22	0.085 ± 0.16	−11 ± 0.081	−5.4 ± 0.044	1.8 ± 0.033	2.1 ± 0.048
		Target	2.1	0.11	−11	−5.4	1.5	2.2
	4.5	Mean	3.8 ± 0.29	0.0055 ± 0.21	−11 ± 0.15	−5.4 ± 0.051	1.9 ± 0.031	2.1 ± 0.050
		Target	2.6	0.18	−11	−5.4	1.5	2.1
VST-	2.0	Mean	3.1 ± 0.21	−0.35 ± 0.16	−12 ± 0.12	−5.9 ± 0.10	2.0 ± 0.016	2.4 ± 0.058
		Target	1.8	−0.032	−11	−5.7	1.7	2.3
	2.5	Mean	3.8 ± 0.44	−0.48 ± 0.29	−11 ± 0.20	−5.9 ± 0.12	1.9 ± 0.017	2.5 ± 0.067
		Target	2.0	0.021	−11	−5.8	1.7	2.3
	3.0	Mean	2.0 ± 0.65	−0.19 ± 0.97	−12 ± 0.12	−5.4 ± 0.059	1.9 ± 0.017	2.3 ± 0.030
		Target	1.4	0.020	−11	−5.4	1.6	2.2
	3.5	Mean	1.9 ± 0.36	−2.6 ± 0.65	−11 ± 0.13	−5.4 ± 0.10	1.9 ± 0.032	2.1 ± 0.077
		Target	1.9	0.081	−11	−5.4	1.6	2.2
	4.0	Mean	2.5 ± 0.29	−1.7 ± 0.21	−11 ± 0.089	−5.3 ± 0.056	1.9 ± 0.020	2.0 ± 0.050
		Target	2.0	0.13	−11	−5.3	1.7	2.1
	4.5	Mean	2.9 ± 0.24	0.058 ± 0.25	−12 ± 0.14	−5.3 ± 0.060	1.9 ± 0.046	2.2 ± 0.084
		Target	2.3	0.18	−11	−5.4	1.5	2.2

*The means of joint angle during simulation and target value of joint angle in sagittal plane corresponding to the swaying in the anterior-posterior direction (q_1, q_3, q_5, q_7, q_{13}, q_{15} in **Figure 2**) for each conditions. The lower limbs are partially omitted due to symmetry. VST ± denotes the presence or absence of the vestibulospinal tract.*

with vestibular disorders compared with that of healthy controls (Aoki et al., 2014). In our study, β_2 increased in the negative direction in the condition without the VST at low muscle tones ($\|\boldsymbol{u}_{ff}\|^2 = 1.5 \sim 2.5$), as shown in **Figures 7**, **8**. This is consistent with the patients' results in that, for both, the power of the lower frequencies tends to increase, and the power of the higher frequencies tends to decrease in the 1∼5 Hz region. However, in the patient study, β_2 was negative, whereas in the computational model, β_2 was found to be positive for many of the conditions. This may be due to the high sampling frequency in the computational model (approximately 1,000 Hz in this study). In one previous study, the PSD of COP was compared for conditions with intermittent control and continuous control using an inverted pendulum model. It was found that the high-frequency component increased when there was continuous control, whereas the low-frequency component increased when there was intermittent control (Asai et al., 2009). Although it is difficult to investigate the time intervals for control in humans, the sampling frequency is considered to have a significant effect on the PSD of COP. In our study, β_1 at $\|\boldsymbol{u}_{ff}\|^2 = 2.5$ was close to the results found in humans. However, by controlling at a lower sampling frequency, it is possible to obtain β_1 and β_2 values that are closer to those found in humans, even when the muscle tone is lower.

For the higher muscle tones ($\|\boldsymbol{u}_{ff}\|^2 = 3.0 \sim 4.5$), β_2 was found to be larger in the positive direction without the VST, with the exception of $\|\boldsymbol{u}_{ff}\|^2 = 3.5$. This is not in line with the results found in patients, and may be due to the fact that the muscle tones are higher than those found in healthy individuals, as considered for β_1. It is possible that the effect of the VST was not apparent at these higher muscle tones because of the increase in stiffness.

4.1.3. Correlation Between the Standard Deviation of the COP Velocity and the Muscle Tone

A previous study using a musculoskeletal model found that the effect of noise decreases as the muscle tone increases (Kaminishi et al., 2020). In line with this, we found a negative correlation between the muscle tone and the standard deviation of the COP velocity for the condition with the VST, as shown in **Figure 6A**. This result indicates that the effect of noise becomes smaller as the muscle tone increases. It is possible that this is due to an increase in joint stiffness at the higher muscle tones, which would lead to a smaller effect of noise. This would be consistent with the previous computational model.

For the condition without the VST, we found that there was no correlation between the muscle tone and the standard deviation of the COP velocity, as shown in **Figure 6B**. This may relate to the fact that with the VST, FB information is obtained from both vestibular and proprioceptive senses, with an effect of noise added to both. In contrast, without the VST, only proprioceptive information is used, and thus the effect of the noise is smaller. Because greater muscle tone is associated with smaller effect of noise, the muscle tone here may have been sufficiently large for the magnitude of given noise without the VST. As a result, the standard deviation of the COP velocity would be smaller without the VST than with the VST, and no correlation would be observed.

4.2. Muscle Tones at Which the Musculoskeletal Model Can Remain Standing

For the condition with the VST, we were able to obtain a muscle tone corresponding to $\|\boldsymbol{u}_{\boldsymbol{ff}}\|^2 = 1.5$; without the VST, this was not achieved. In other words, the musculoskeletal model could not remain standing without the VST at a muscle tone equivalent to $\|\boldsymbol{u}_{\boldsymbol{ff}}\|^2 = 1.5$, even without time delays. This indicates that the muscle tone at which the musculoskeletal model can remain standing depends on whether the VST is functioning. This result is consistent with previous studies (Chiba et al., 2013).

4.3. Change of Muscle Activity of FB Control by the VST

The comparison of $\boldsymbol{u}_{\boldsymbol{fb}}$ may not be appropriate as an evaluation index of the controller because $\boldsymbol{u}_{\boldsymbol{fb}}$ is affected by small oscillations that do not affect the stability; however a certain trend can be observed. The value of $\|\boldsymbol{u}_{\boldsymbol{fb}}\|^2$ was significantly lower in the condition with the VST than in the condition without the VST for $\|\boldsymbol{u}_{\boldsymbol{ff}}\|^2 = 1.5 \sim 3.0$, as shown in **Figure 10**. This indicates that the VST enables the musculoskeletal model to maintain a standing posture with low $\boldsymbol{u}_{\boldsymbol{fb}}$ for low muscle tone. The value of $\|\boldsymbol{u}_{\boldsymbol{fb}}\|^2$ was significantly higher in the condition with the VST than in the condition without the VST for $\|\boldsymbol{u}_{\boldsymbol{ff}}\|^2 = 3.5 \sim 4.5$. In the presence of sufficiently large muscle tone to stabilize, the condition with the VST is expected to have a greater $\boldsymbol{u}_{\boldsymbol{fb}}$ than the condition without the VST because of the difference in muscle activity between flexors and extensors.

At $\|\boldsymbol{u}_{\boldsymbol{ff}}\|^2 = 1.5$, the vestibular feedback gains were large. These gains may have been larger to maintain a standing posture with lower muscle tone. It is considered that the variation was large at $\|\boldsymbol{u}_{\boldsymbol{ff}}\|^2 = 1.5$ because of these large vestibular feedback gains. The value of $\|\boldsymbol{u}_{\boldsymbol{fb}}\|^2$ was significantly large at $\|\boldsymbol{u}_{\boldsymbol{ff}}\|^2 = 4.0$ without the VST because of a small oscillation of the neck, as mentioned above. With high muscle tone, oscillations occur depending on the patterns of muscle tone.

4.4. Effects of Sensory Noise

In this study, the magnitude of the noise was set at $k_{noise} = 0.01$ in Equation (11). The musculoskeletal model could remain standing at all of the selected muscle tones with a time delay, regardless of the VST, and this suggests that there was not enough noise to cause a fall. In line with this, it is known that there is noise in human sensory information, but this does not cause healthy people to fall. We therefore concluded that the magnitude of the noise in this study was not excessive.

In our study, we found that the standard deviation of the COP velocity was higher at $\|\boldsymbol{u}_{\boldsymbol{ff}}\|^2 = 3.0$ with the VST (**Figures 5**, **6**). This result indicates that the effect of noise increases at this muscle tone. The reason for this can be determined by examining (**Figure 9**). This shows that the muscle tone of the ankle extensors increased, while the muscle tone of the lumbar, knee, and hip joint muscles decreased at $\|\boldsymbol{u}_{\boldsymbol{ff}}\|^2 = 3.0$ compared with the other muscle tones. The increased muscle tone in the ankle extensors would lead to a reduced COP velocity. However, the stiffness of each joint would have decreased because of a reduced co-contraction magnitude. As a result, the effect of noise would have increased.

In addition, we found that the standard deviation of the COP velocity was larger at $\|\boldsymbol{u}_{\boldsymbol{ff}}\|^2 = 3.0$ without the VST than that at other $\|\boldsymbol{u}_{\boldsymbol{ff}}\|^2$ values (**Figures 5**, **6**). As mentioned in Section 4.1.1, several feedback gains were larger in the condition without the VST at $\|\boldsymbol{u}_{\boldsymbol{ff}}\|^2 = 3.0$ than at other $\|\boldsymbol{u}_{\boldsymbol{ff}}\|^2$ values. Noise may reverse the number sign of sensory information. This can lead to an increase or decrease in muscle activity that is contrary to what is needed. The large feedback gains magnify this effect. The condition without the VST at $\|\boldsymbol{u}_{\boldsymbol{ff}}\|^2 = 3.0$ would therefore have large variation.

4.5. Strength of Proposed Model

We proposed a neural controller model and a musculoskeletal model. Regarding the neural controller model, we proposed a model that mimics the VST. We believe that this neural controller model can be used to validate posture control focusing on the VST. By varying model parameters, it would be possible to simulate the prediction of symptoms and make detailed proposals for rehabilitation. Moreover, since both the RST and VST were modeled, it would be possible to examine the effects and interactions of each the descending tract on postural control when disease or injury impair these descending pathways.

Alternatively, regarding the musculoskeletal model, we proposed a model having additional degrees of freedom and neck muscles to the model from the previous study. Although the proposed model increased computational cost, we could model the function of the VST. Furthermore, **Table 1** shows that the model could maintain a posture close to the target posture with a difference of fewer than about three degrees. This result suggests that the proposed musculoskeletal model which added the neck joints and muscles could represent the stable motion of the neck during static standing. We concluded that this musculoskeletal model is therefore enough to simulate static standing. Using the proposed multi-degree of freedom musculoskeletal model, it is possible to investigate individual muscle activities and coordinated movements of polyarticular muscles, compared to previous models with fewer degrees of freedom, such as the inverted pendulum model. Additionally, the proposed model,

including the neck, can express the abnormal posture seen in Parkinson's disease.

4.6. Limitations

The proposed musculoskeletal model does not include arms. Instead, their mass was added to the torso. However, it is known that the arms contribute to postural stability, especially in difficult standing positions, such as tandem standing (standing with one leg in front of the other) and standing on one leg. It has previously been found that a difficult standing position is more stable when the arms are free, while a normal standing position is more stable when the arms are fixed (Objero et al., 2019). If we were to add arms to our musculoskeletal model, we would be able to examine their effect on postural control under various conditions.

Muscles of the musculoskeletal model did not consider short-range stiffness. Muscle short-range stiffness is a muscle property that increases muscle force in muscle fiber stretch. This property is essential in the stability of a body with perturbations (De Groote et al., 2017). This property was not considered in this study because we focused on static standing positions. However, it should be considered when dynamic posture control is focused on in the future.

In this study, FB information was obtained only from the vestibular system and proprioception because we assumed that the eyes were closed. We considered the maintenance of an upright position with closed eyes to focus on the vestibular system. In fact, many tests of standing posture control are conducted with closed eyes. Visual information is crucial when postural control is difficult, such as during external disturbances or when standing on foam. It is therefore necessary in the case of evaluating difficult postural control conditions. Hence, we hope to be able to add visual feedback to this model in the future.

The proposed neural controller model did not consider estimations through the cerebellum. The reason for this was because we believed that the cerebellum's contributions of estimation and learning were smaller during static and stable standing than dynamic and challenging standing (Foerster et al., 2017). However, it has been reported that the cerebellum is more active in the static standing than in the supine position (Ouchi et al., 1999), thus we may need to consider the cerebellum in the future.

The proposed neural controller also did not consider stretch reflex control and cognitive effects. However, we consider that the model was enough because we could validate this model concerning the focused phenomenon (the effect of the VST on static standing). A limitation of modeling studies is that it is difficult to create a model that includes all elements. This is because the more elements are included, the more difficult it becomes to correspond each element to the results. There is also a limit to the number of parameters. The computational cost is high even in this research. The simulation took about 100 h for each condition using 30 threads (Intel Xeon, 36 cores, 2.60 GHz) and simulations for 13 conditions took about 1,300 h in total. As the number of parameters is increased, the computational cost increases exponentially. Therefore, we aim to construct a model that can explain the phenomenon with as few elements as possible.

5. CONCLUSIONS AND FUTURE PERSPECTIVES

This study presents a neural controller model that mimics the VST, which was constructed on the basis of physiological findings. The model's validity was evaluated by reproducing human postural control using adjusted parameters. The results were compared with findings from human subjects and previous computational models, and revealed similar trends for both. The study involved adjusting various parameters using the objective function which evaluates whether the musculoskeletal model can remains standing. In other words, the parameters are not adjusted to match the experimental results in humans. Nevertheless, as in the experiments in human subjects, there was a significant difference in COP velocity of the proposed model. In addition, the slope of the PSD of COP in the ∼1 Hz region was larger in the positive direction in the condition without the VST than in the condition with the VST and the slope of the PSD of COP in the 1∼5 Hz region was larger in the negative direction in the condition without the VST than in the condition with the VST. These results were also consistent with those of human experiments. We therefore conclude that the validity of the neural controller model was confirmed, and could present the neural controller that mimics the VST. Our future work will focus on disorders of the descending tract and how these affect patients' motor control. We will use our computational model to better understand the mechanisms involved and to improve our understanding of postural control disorders, such as Parkinson's disease.

DATA AVAILABILITY STATEMENT

The original contributions presented in the study are included in the article/**Supplementary Material**, further inquiries can be directed to the corresponding author.

AUTHOR CONTRIBUTIONS

YO performed the simulations, analyzed the data, and wrote the manuscript. KK helped to perform the simulations. KK, RC, KT, and JO provided a review of the research methods. JO supervised the study. All authors designed the study, discussed the results, and reviewed the article. All authors contributed to the article and approved the submitted version.

FUNDING

This work was supported by JSPS KAKENHI, Grant-in-Aid for Scientific Research on Innovative Areas Hyper-adaptability for

overcoming body-brain dysfunction: Integrated empirical and system theoretical approaches (Grant Numbers 19H05722 and 19H05730), and the Mohammed bin Salman Center for Future Science and Technology for Saudi-Japan Vision 2030 at the University of Tokyo (MbSC2030).

SUPPLEMENTARY MATERIAL

The Supplementary Material for this article can be found online at: https://www.frontiersin.org/articles/10.3389/fncom.2022.785099/full#supplementary-material

REFERENCES

Aoki, M., Tokita, T., Kuze, B., Mizuta, K., and Ito, Y. (2014). A characteristic pattern in the postural sway of unilateral vestibular impaired patients. *Gait Post*. 40, 435–440. doi: 10.1016/j.gaitpost.2014.05.013

Asai, Y., Tasaka, Y., Nomura, K., Nomura, T., Casadio, M., and Morasso, P. (2009). Correction: A model of postural control in quiet standing: robust compensation of Delay-Induced instability using intermittent activation of feedback control. *PLoS ONE* 4, e6169. doi: 10.1371/journal.pone.0006169

Bottaro, A., Yasutake, Y., Nomura, T., Casadio, M., and Morasso, P. (2008). Bounded stability of the quiet standing posture: an intermittent control model. *Hum. Mov. Sci*. 27, 473–495. doi: 10.1016/j.humov.2007.11.005

Carleton, S. C., and Carpenter, M. B. (1983). Afferent and efferent connections of the medial, inferior and lateral vestibular nuclei in the cat and monkey. *Brain Res*. 278, 29–51. doi: 10.1016/0006-8993(83)90223-8

Cazzola, D., Holsgrove, T. P., Preatoni, E., Gill, H. S., and Trewartha, G. (2017). Cervical spine injuries: a whole-body musculoskeletal model for the analysis of spinal loading. *PLoS ONE* 12, e0169329. doi: 10.1371/journal.pone.0169329

Chiba, R., Ogawa, H., Takakusaki, K., Asama, H., and Ota J. (2013). "Muscle activities changing model by difference in sensory inputs on human posture control," in *Intelligent Autonomous Systems 12: Advances in Intelligent Systems and Computing, Vol. 194*, eds S. Lee, H. Cho, K. J. Yoon, and J. Lee (Berlin: Springer). doi: 10.1007/978-3-642-33932-5_44

De Groote, F., Allen, J. L., and Ting, L. H. (2017). Contribution of muscle short-range stiffness to initial changes in joint kinetics and kinematics during perturbations to standing balance: a simulation study. *J. Biomech*. 55, 71–77. doi: 10.1016/j.jbiomech.2017.02.008

Delp, S. L., Anderson, F. C., Arnold, A. S., Loan, P., Habib, A., John, C. T., et al. (2007). OpenSim: open-source software to create and analyze dynamic simulations of movement. *IEEE Trans. Biomed. Eng*. 54, 1940–1950. doi: 10.1109/TBME.2007.901024

Foerster, Á., Melo, L., Mello, M., Castro, R., Shirahige, L., Rocha, S., et al. (2017). Cerebellar transcranial direct current stimulation (ctDCS) impairs balance control in healthy individuals. *Cerebellum* 16, 872–875. doi: 10.1007/s12311-017-0863-8

Grillner, S., Hongo, T., and Lund, S. (1970). The vestibulospinal tract. Effects on alpha-motoneurones in the lumbosacral spinal cord in the cat. *Exp. Brain Res*. 10, 94–120. doi: 10.1007/BF00340521

Hansen, N., Müller, S. D., and Koumoutsakos, P. (2003). Reducing the time complexity of the derandomized evolution strategy with covariance matrix adaptation (CMA-ES). *Evol. Comput*. 11, 1–18. doi: 10.1162/106365603321828970

Jiang, P., Chiba, R., Takakusaki, K., and Ota, J. (2016). Generation of the human biped stance by a neural controller able to compensate neurological time delay. *PLoS ONE* 11, e0163212. doi: 10.1371/journal.pone.0163212

Jiang, P., Chiba, R., Takakusaki, K., and Ota, J. (2017). A postural control model incorporating multisensory inputs for maintaining a musculoskeletal model in a stance posture. *Adv. Robot*. 31, 55–67. doi: 10.1080/01691864.2016.1266095

Kaminishi, K., Chiba, R., Takakusaki, K., and Ota, J. (2020). Investigation of the effect of tonus on the change in postural control strategy using musculoskeletal simulation. *Gait Post*. 76, 298–304. doi: 10.1016/j.gaitpost.2019.12.015

Kaminishi, K., Jiang, P., Chiba, R., Takakusaki, K., and Ota, J. (2019). Postural control of a musculoskeletal model against multidirectional support surface translations. *PLoS ONE* 14, e0212613. doi: 10.1371/journal.pone.0212613

Kistemaker, D. A., Van Soest, A. J. K., Wong, J. D., Kurtzer, I., and Gribble, P. L. (2013). Control of position and movement is simplified by combined muscle spindle and golgi tendon organ feedback. *J. Neurophysiol*. 109, 1126–1139. doi: 10.1152/jn.00751.2012

Koelewijn, A. D., and Ijspeert, A. J. (2020). Exploring the contribution of proprioceptive reflexes to balance control in perturbed standing. *Front. Bioeng. Biotechnol*. 8:866. doi: 10.3389/fbioe.2020.00866

Kuo, A. D. (1995). An optimal control model for analyzing human postural balance. *IEEE Trans. Biomed. Eng*. 42, 87–101. doi: 10.1109/10.362914

Lazzaro, G. D., Schirinzi, T., Giambrone, M. P., Mauro, R. D., Palmieri, M. G., Rocchi, C., et al. (2018). Pisa syndrome in Parkinson's disease: evidence for bilateral vestibulospinal dysfunction. *Parkinsons Dis*. 2018, 8673486. doi: 10.1155/2018/8673486

Magoun, H. W., and Rhines, R. (1946). An inhibitory mechanism in the bulbar reticular formation. *J. Neurophysiol*. 9, 165–171. doi: 10.1152/jn.1946.9.3.165

Mahboobin, A., Loughlin, P., Atkeson, C., and Redfern, M. (2009). A mechanism for sensory re-weighting in postural control. *Med. Biol. Eng. Comput*. 47, 921–929. doi: 10.1007/s11517-009-0477-5

Masani, K., Vette, A. H., and Popovic, M. R. (2006). Controlling balance during quiet standing: proportional and derivative controller generates preceding motor command to body sway position observed in experiments. *Gait Post*. 23, 164–172. doi: 10.1016/j.gaitpost.2005.01.006

Maurer, C., and Peterka, R. J. (2005). A new interpretation of spontaneous sway measures based on a simple model of human postural control. *J. Neurophysiol*. 93, 189–200. doi: 10.1152/jn.00221.2004

McCall, A. A., Miller, D. M., and Yates, B. J. (2017). Descending influences on vestibulospinal and vestibulosympathetic reflexes. *Front. Neurol*. 8, 112. doi: 10.3389/fneur.2017.00112

Mergner, T., Maurer, C., and Peterka, R. J. (2003). "A multisensory posture control model of human upright stance," in Neural Control of Space Coding and Action Production, Vol. 142, eds C. Prablanc, D, Pélisson, and Y. Rossetti (Elsevier). p. 189–201.

Millard, M., Uchida, T., Seth, A., and Delp, S. L. (2013). Flexing computational muscle: modeling and simulation of musculotendon dynamics. *J. Biomech. Eng*. 135, 021005. doi: 10.1115/1.4023390

Miller, D. M., Klein, C. S., Suresh, N. L., and Rymer, W. Z. (2014). Asymmetries in vestibular evoked myogenic potentials in chronic stroke survivors with spastic hypertonia: evidence for a vestibulospinal role. *Clin. Neurophysiol*. 125, 2070–2078. doi: 10.1016/j.clinph.2014.01.035

Morasso, P. G., Baratto, L., Capra, R., and Spada, G. (1999). Internal models in the control of posture. *Neural Netw*. 12, 1173–1180. doi: 10.1016/S0893-6080(99)00058-1

Nyberg-Hansen, R., and Mascitti, T. A. (1964). Sites and mode of termination of fibers of the vestibulospinal tract in the cat. An experimental study with silver impregnation methods. *J. Comp. Neurol*. 122, 369–387. doi: 10.1002/cne.901220307

Objero, C. N., Wdowski, M. M., and Hill, M. W. (2019). Can arm movements improve postural stability during challenging standing balance tasks? *Gait Post*. 74, 71–75. doi: 10.1016/j.gaitpost.2019.08.010

Ouchi, Y., Okada, H., Yoshikawa, E., Nobezawa, S., and Futatsubashi, M. (1999). Brain activation during maintenance of standing postures in humans. *Brain* 122 (Pt 2), 329–338. doi: 10.1093/brain/122.2.329

Perlmutter, S. I., Iwamoto, Y., Baker, J. F., and Peterson, B. W. (1998). Interdependence of spatial properties and projection patterns of medial vestibulospinal tract neurons in the cat. *J. Neurophysiol*. 79, 270–284. doi: 10.1152/jn.1998.79.1.270

Peterka, R. J. (2002). Sensorimotor integration in human postural control. *J. Neurophysiol*. 88, 1097–1118. doi: 10.1152/jn.2002.88.3.1097

Peterka, R. J., and Loughlin, P. J. (2004). Dynamic regulation of sensorimotor integration in human postural control. *J. Neurophysiol*. 91, 410–423. doi: 10.1152/jn.00516.2003

Rhines, R., and Magoun, H. W. (1946). Brain stem facilitation of cortical motor response. *J. Neurophysiol*. 9, 219–229. doi: 10.1152/jn.1946.9.3.219

Roberts, T. D. M. (1973). Biological sciences: reflex balance. *Nature* 244, 156–158. doi: 10.1038/244156a0

Schor, R. H. (1974). Responses of cat vestibular neurons to sinusoidal roll tilt. *Exp. Brain Res*. 20, 347–362. doi: 10.1007/BF00237380

Seth, A., Hicks, J. L., Uchida, T. K., Habib, A., Dembia, C. L., Dunne, J. J., et al. (2018). OpenSim: simulating musculoskeletal dynamics and neuromuscular control to study human and animal movement. *PLoS Comput. Biol*. 14, e1006223. doi: 10.1371/journal.pcbi.1006223

Sprenger, A., Wojak, J. F., Jandl, N. M., and Helmchen, C. (2017). Postural control in bilateral vestibular failure: Its relation to visual, proprioceptive, vestibular, and cognitive input. *Front. Neurol*. 8, 444. doi: 10.3389/fneur.2017.00444

Takakusaki, K. (2017). Functional neuroanatomy for posture and gait control. *Mov. Disord*. 10, 1–17. doi: 10.14802/jmd.16062

Takakusaki, K., Chiba, R., Nozu, T., and Okumura, T. (2016). Brainstem control of locomotion and muscle tone with special reference to the role of the mesopontine tegmentum and medullary reticulospinal systems. *J. Neural Transm*. 123, 695–729. doi: 10.1007/s00702-015-1475-4

Takakusaki, K., Shimoda, N., Matsuyama, K., and Mori, S. (1994). Discharge properties of medullary reticulospinal neurons during postural changes induced by intrapontine injections of carbachol, atropine and serotonin, and their functional linkages to hindlimb motoneurons in cats. *Exp. Brain Res*. 99, 361–374. doi: 10.1007/BF00228973

Takakusaki, K., Takahashi, M., Obara, K., and Chiba, R. (2017). Neural substrates involved in the control of posture. *Adv. Robot*. 31, 2–23. doi: 10.1080/01691864.2016.1252690

Talebi, H., Karimi, M. T., Abtahi, S. H. R., and Fereshtenejad, N. (2016). Static balance in patients with vestibular impairments: a preliminary study. *Scientifica* 2016, 6539858. doi: 10.1155/2016/6539858

Thelen, D. G. (2013). *Gait 2392 and 2354 Models - OpenSim Documentation - Global Site*. Available online at: https://simtk-confluence.stanford.edu:8443/display/OpenSim/Gait+2392+and+2354+Models (accessed August 3, 2021).

Thelen, D. G., Anderson, F. C., and Delp, S. L. (2003). Generating dynamic simulations of movement using computed muscle control. *J. Biomech*. 36, 321–328. doi: 10.1016/S0021-9290(02)00432-3

van der Kooij, H., Jacobs, R., Koopman, B., and Grootenboer, H. (1999). A multisensory integration model of human stance control. *Biol. Cybern*. 80, 299–308. doi: 10.1007/s004220050527

van der Kooij, H., Jacobs, R., Koopman, B., and Van Der Helm, F. (2001). An adaptive model of sensory integration in a dynamic environment applied to human stance control. *Biol. Cybern*. 84, 103–115. doi: 10.1007/s004220000196

Vasavada, A. N., Li, S., and Delp, S. L. (1998). Influence of muscle morphometry and moment arms on the moment-generating capacity of human neck muscles. *Spine* 23, 412–422. doi: 10.1097/00007632-199802150-00002

Wilson, V. J., Yoshida, M., and Schor, R. H. (1970). Supraspinal monosynaptic excitation and inhibition of thoracic back motoneurons. *Exp. Brain Res*. 11, 282–295. doi: 10.1007/BF01474387

Winters, J. M. (1995). An improved muscle-reflex actuator for use in large-scale neuromusculoskeletal models. *Ann. Biomed. Eng*. 23, 359–374. doi: 10.1007/BF02584437

Zajac, F. E. (1989). Muscle and tendon: properties, models, scaling, and application to biomechanics and motor control. *Crit Rev. Biomed. Eng*. 17, 359–411.

Conflict of Interest: The authors declare that the research was conducted in the absence of any commercial or financial relationships that could be construed as a potential conflict of interest.

Publisher's Note: All claims expressed in this article are solely those of the authors and do not necessarily represent those of their affiliated organizations, or those of the publisher, the editors and the reviewers. Any product that may be evaluated in this article, or claim that may be made by its manufacturer, is not guaranteed or endorsed by the publisher.

Copyright © 2022 Omura, Kaminishi, Chiba, Takakusaki and Ota. This is an open-access article distributed under the terms of the Creative Commons Attribution License (CC BY). The use, distribution or reproduction in other forums is permitted, provided the original author(s) and the copyright owner(s) are credited and that the original publication in this journal is cited, in accordance with accepted academic practice. No use, distribution or reproduction is permitted which does not comply with these terms.

frontiers in Systems Neuroscience

ORIGINAL RESEARCH
published: 14 March 2022
doi: 10.3389/fnsys.2022.785143

Clarify Sit-to-Stand Muscle Synergy and Tension Changes in Subacute Stroke Rehabilitation by Musculoskeletal Modeling

Ruoxi Wang[1], Qi An[2], Ningjia Yang[3], Hiroki Kogami[1], Kazunori Yoshida[1], Hiroshi Yamakawa[1], Hiroyuki Hamada[1], Shingo Shimoda[3], Hiroshi R. Yamasaki[4], Moeka Yokoyama[3], Fady Alnajjar[3,5], Noriaki Hattori[6], Kouji Takahashi[7], Takanori Fujii[7], Hironori Otomune[7], Ichiro Miyai[7], Atsushi Yamashita[1] and Hajime Asama[1]*

[1] Department of Precision Engineering, The University of Tokyo, Tokyo, Japan, [2] Department of Information Science and Electrical Engineering, Kyushu University, Fukuoka, Japan, [3] RIKEN Center for Brain Science, Aichi, Japan, [4] Department of Physical Therapy, Saitama Prefectural University, Saitama, Japan, [5] College of Information Technology, United Arab Emirates University, Al Ain, United Arab Emirates, [6] Department of Rehabilitation, University of Toyama, Toyama, Japan, [7] Morinomiya Hospital, Osaka, Japan

Post-stroke patients exhibit distinct muscle activation electromyography (EMG) features in sit-to-stand (STS) due to motor deficiency. Muscle activation amplitude, related to muscle tension and muscle synergy activation levels, is one of the defining EMG features that reflects post-stroke motor functioning and motor impairment. Although some qualitative findings are available, it is not clear if and how muscle activation amplitude-related biomechanical attributes may quantitatively reflect during subacute stroke rehabilitation. To better enable a longitudinal investigation into a patient's muscle activation changes during rehabilitation or an inter-subject comparison, EMG normalization is usually applied. However, current normalization methods using maximum voluntary contraction (MVC) or within-task peak/mean EMG may not be feasible when MVC cannot be obtained from stroke survivors due to motor paralysis and the subject of comparison is EMG amplitude. Here, focusing on the paretic side, we first propose a novel, joint torque-based normalization method that incorporates musculoskeletal modeling, forward dynamics simulation, and mathematical optimization. Next, upon method validation, we apply it to quantify changes in muscle tension and muscle synergy activation levels in STS motor control units for patients in subacute stroke rehabilitation. The novel method was validated against MVC-normalized EMG data from eight healthy participants, and it retained muscle activation amplitude differences for inter- and intra-subject comparisons. The proposed joint torque-based method was also compared with the common static optimization based on squared muscle activation and showed higher simulation accuracy overall. Serial STS measurements were conducted with four post-stroke patients during their subacute rehabilitation stay (137 ± 22 days) in the hospital. Quantitative results of patients suggest that maximum muscle tension and activation level of muscle synergy temporal patterns may reflect the effectiveness of subacute stroke rehabilitation. A quality comparison between muscle synergies computed with

OPEN ACCESS

Edited by:
Belén Rubio Ballester, Institute for Bioengineering of Catalonia (IBEC), Spain

Reviewed by:
Zimi Sawacha, University of Padua, Italy
Alessandro Scano, National Research Council (CNR), Italy

***Correspondence:**
Qi An
anqi@ait.kyushu-u.ac.jp

Received: *28 September 2021*
Accepted: *15 February 2022*
Published: *14 March 2022*

Citation:
Wang R, An Q, Yang N, Kogami H, Yoshida K, Yamakawa H, Hamada H, Shimoda S, Yamasaki HR, Yokoyama M, Alnajjar F, Hattori N, Takahashi K, Fujii T, Otomune H, Miyai I, Yamashita A and Asama H (2022) Clarify Sit-to-Stand Muscle Synergy and Tension Changes in Subacute Stroke Rehabilitation by Musculoskeletal Modeling. Front. Syst. Neurosci. 16:785143. doi: 10.3389/fnsys.2022.785143

the conventional within-task peak/mean EMG normalization and our proposed method showed that the conventional was prone to activation amplitude overestimation and underestimation. The contributed method and findings help recapitulate and understand the post-stroke motor recovery process, which may facilitate developing more effective rehabilitation strategies for future stroke survivors.

Keywords: muscle tension, muscle synergy, sit-to-stand (STS), stroke, subacute rehabilitation, EMG normalization, musculoskeletal modeling

1. INTRODUCTION

Virtually every country in the world is experiencing a shift in the age distribution of its population toward older ages (United Nations, 2019). The prevalence of age-related chronic diseases such as stroke is anticipated to increase steeply as the global population rapidly ages (James et al., 2018). Stroke has been the worldwide leading cause of disability and mortality (World Health Organization, 2019). Post-stroke patients suffer from significant motor deficiency and diminished independence in performing fundamental sit-to-stand (STS) movement (Cheng et al., 1998), which is the starting point of daily life and a reflection on one's quality of life. When transferring body momentum upwards from a sitting position, post-stroke patients are susceptible to falls, a well-known source of high injury severity and mortality (Cheng et al., 1998; Sterling et al., 2001). Repetitive and facilitated rehabilitation training on STS in addition to usual care can improve the patient's motor abilities (de Sousa et al., 2019).

At present, stroke rehabilitation demands evidence-based treatment strategies tailored to the needs of individual post-stroke patients (Hatem et al., 2016). Many studies investigated post-stroke STS muscle activities in hopes of discovering suitable rehabilitation strategies. It was found that patients exhibit distinctive muscle activation, such as delayed activation in tibialis anterior (Silva et al., 2013), premature activation in soleus (Cheng et al., 2004), prolonged duration of muscle activities (Chou et al., 2003), postponed activation peak timing of muscle synergy temporal patterns for hip raise (Yang et al., 2019), as well as diminished muscle strength (Jones, 2017).

Muscle activation amplitude and activation timing are two defining features regarding muscle activities. Muscle activity, detected by surface electromyography (EMG) devices placed on the skin and displayed in electromyogram, is a collective electrical signal acquired from activated muscle tissues (Raez et al., 2006). As a function of time, EMG signal is described by its amplitude and duration, reflecting both peripheral and central properties of the neuromuscular system (Farina et al., 2004). Depending on the muscle type, both muscle activation amplitude and activation timing may vary as mobility restores over time, and hence studies on both activation amplitude and timing are indispensable to an ampler understanding of whether and how the process of motor ability restoration would reflect in these biomechanical attributes.

Abnormal muscle activation timing features, such as delayed activation peak time and prolonged duration, may suggest that patients alter neural control strategies in executing movements. On the other hand, muscle activation amplitude is related to the magnitude of muscle tension and the maximum ability to produce muscle force (Vigotsky et al., 2018). As both muscle activation and muscle force depend on the number of active motor units, EMG amplitude can be applied to estimate muscle tension (Farina et al., 2004; Farina, 2006). EMG amplitude is also a valid measure to help interpret the contribution of muscle strength, facilitate diagnoses, and direct treatment strategies (Edgerton et al., 1996). Diminished amplitude of muscle activation patterns is an indicative factor of loss of independence and mobility impairment (Cheng et al., 2004; Lomaglio and Eng, 2005; Jones, 2017). However, isolated usage of EMG amplitude to explain the underlying neuromotor adaptation mechanism and infer outcomes in sports and rehabilitation medicine is prone to misinterpretations and should be avoided (Farina, 2006; Enoka and Duchateau, 2015; Del Vecchio et al., 2017; Vigotsky et al., 2018), although the popularity of its practice in research design has been surging since 1950 (Vigotsky et al., 2018). As a scaling factor, EMG amplitude alone does not account for muscle architectural properties or muscle contraction dynamics, such as muscle fiber length, physiological cross-sectional area, pennation angle, muscle contraction velocity, and passively generated muscle tension (Zajac, 1989; Hicks et al., 2015). When combined with musculoskeletal models integrated with these parameters, EMG data can facilitate estimating muscle tension, which is an informative and important factor often investigated in biomechanics research (Staudenmann et al., 2010; Hicks et al., 2015). To answer the question of whether and how muscle strength may change following neuromotor recovery in stroke rehabilitation, we avoid isolated interpretation of EMG data in this study by employing musculoskeletal modeling, in which discrete muscle is represented by the well-established Hill-type muscle model (Zajac, 1989) to capture necessary muscle properties and muscle-tendon dynamics (Staudenmann et al., 2010; Hicks et al., 2015; Vigotsky et al., 2018).

While EMG-informed analysis of muscle tension production using neuromusculoskeletal modeling is important for biomechanics questions (Hicks et al., 2015), muscle synergy analysis has been another useful way to study the complex mechanism underlying human movement. First proposed by Bernstein, muscle synergy hypothesis suggests that the human central nervous system controls modules of muscles in synergies to solve muscle redundancy and accomplish motor tasks (Bernstein, 1967). Although the ambiguity concerning whether muscle synergy can truly represent the neural strategy of motor control still remains (Tresch and Jarc,

2009; Kutch and Valero-Cuevas, 2012; Hirashima and Oya, 2015), numerous studies have implemented muscle synergy to infer motor deficiency in population with neurological disorders (Clark et al., 2010; Roh et al., 2013; Steele et al., 2015; Ellis et al., 2017; Mileti et al., 2020). Including our group's previous works, activation timing features of post-stroke muscle synergy were examined to simplify the complex control and coordinative recruitment of muscles, understand and translate indicative synergy time changes into more effective rehabilitation interventions for future stroke survivors (Yang et al., 2017, 2019; Kogami et al., 2018, 2021). It has been demonstrated that musculoskeletal modeling and simulation enhance muscle synergy analysis, which helps answer experimental questions in biomechanics and rehabilitation research (Steele et al., 2013; Hicks et al., 2015; Vigotsky et al., 2018).

Previous studies utilizing STS muscle activation features to indicate motor impairment and predict chances of motor recovery in the subacute stage focused on characteristics of activation timing, but they did not address activation amplitude (Prudente et al., 2013; Silva et al., 2013; Yang et al., 2019). Although Cheng et al. (2004) reported qualitative findings, such as post-stroke patients who tend to fall in STS have no or merely low-amplitude activation in tibialis anterior, it was not clear how activation amplitude respecting this fundamental movement would quantitatively reflect in stroke rehabilitation. The subacute stroke rehabilitation period (one to six months after stroke onset), wherein the most prominent recovery took place (Langhorne et al., 2011; Hatem et al., 2016), deserves more attention for studies on the patient's motor recovery progress. To better enable a longitudinal investigation into the patient's muscle activation changes during rehabilitation or an inter-subject comparisons, EMG normalization is usually applied (Besomi et al., 2020). Interpretations based on non-normalized EMG should be avoided if possible, and misinterpreted conclusions are often made if EMG data are not properly normalized before comparisons (Farina et al., 2004; Besomi et al., 2020). In our case, prior to studying the patient's muscle activation amplitude differences before and after rehabilitation, EMG normalization is necessary because EMG signal may be influenced by factors such as different skin conditions and electrode positions between measurement days (Besomi et al., 2020).

The most commonly used normalization technique by studies on muscle activation amplitude and muscle strength is normalization to the maximum voluntary contraction (MVC) (Raez et al., 2006; Besomi et al., 2020). MVC normalization may suit most non-disabled people, but it may be inapplicable to subacute stroke survivors who are unable to undertake MVC measurements or voluntarily activate muscles due to motor paralysis after the life-threatening cerebrovascular accident (Besomi et al., 2020). In that case, prior studies with post-stroke patients accomplished normalization without utilizing MVC by adopting the in-task peak/mean EMG amplitude for normalization (Besomi et al., 2020), such as using within-trial peak EMG (Yang et al., 2019; Kogami et al., 2021), within-subject peak EMG across trials (Clark et al., 2010; Prudente et al., 2013), and peak EMG of the ensemble average (Cheng et al., 2004). Normalization utilizing the peak or mean EMG amplitude facilitates the examination and interpretation of EMG timing features, including peak timing, on/off timing of activities, and periods of inactivity, but it does not enable EMG amplitude comparisons (Cheng et al., 2004; Prudente et al., 2013; Yang et al., 2019; Besomi et al., 2020). Essentially, the method scales a large distribution of EMG data, taking the peak or mean EMG derived from trials as 100%, and removes the inherent differences in maximum EMG amplitude (Besomi et al., 2020). Despite the current consensus for experimental design involving EMG, there may be no normalization method available in some cases when participants have difficulties or cannot voluntarily activate a muscle (Besomi et al., 2020). Therefore, we aim to propose a novel normalization method that not only retains EMG amplitude differences for comparisons but also suits subacute stroke patients whose MVC cannot be obtained, in order to study the changes in muscle activation amplitude during recovery.

As analyses of muscle tension and muscle synergy can be complemented by musculoskeletal modeling and simulation (Steele et al., 2013; Hicks et al., 2015; Vigotsky et al., 2018), we sought to determine normalized muscle activation utilizing an originally proposed musculoskeletal model informed with experimental EMG and kinematics of post-stroke patients. Inverse dynamics is a common approach to calculating joint torques and muscle activation. However, simulated muscle activation often shows poor conformity to measured EMG (Hicks et al., 2015; Shuman et al., 2019). Forward dynamics, on the other hand, was widely used for muscle activation simulation in prior studies of human movement (Neptune et al., 2009; An et al., 2014, 2015; Hicks et al., 2015; Mehrabi et al., 2019). Muscle activation can be determined *via* optimization while accounting for co-contraction and muscle redundancy (Kutch and Valero-Cuevas, 2012; An et al., 2014, 2015; Trinler et al., 2018). However, assessments of simulated muscle activation against experimental EMG data have largely been qualitative rather than quantitative (Shuman et al., 2019). Nevertheless, various optimization algorithms have been proposed, including more customized ones often accompanied by highly personalized model design (Liu et al., 2008; Walter et al., 2014) and the commonly used static optimization (SO) by minimizing the squared error of muscle activation (An et al., 2014, 2015; Shuman et al., 2019; Wang et al., 2022).

For medical diagnosis and treatment, the most applicable and clinically relevant information is about the longitudinal outcome investigated serially by kinematic and kinetic measurements in conjunction with clinical assessments (Kwakkel et al., 2017; Vigotsky et al., 2018; Awad et al., 2020). EMG-informed conclusions made by researchers can easily become unsubstantiated due to the complexity of EMG data itself and insufficient longitudinal investigations (Vigotsky et al., 2018). Therefore, we aim to identify and quantify longitudinal changes in both muscle tension and muscle synergy to unravel the underlying biomechanical and neuromotor rehabilitation process within the post-stroke subacute period when patients are subjected to a greater likelihood of recovery. Due to the limitation of conventional EMG normalization methods, we propose a musculoskeletal model to determine normalized muscle

activation through a combination of inverse dynamics joint torque calculation, EMG-informed forward dynamics simulation of joint torque and muscle activation, and an optimization algorithm to define muscle activation amplitude. Due to the multiple scopes of this research, we first evaluate muscle activation estimation results by the proposed normalization against results by traditional MVC normalization; next, we show the accuracy improvement of the proposed joint torque-based algorithm for musculoskeletal simulation compared to that of the most common SO based on squared muscle activation; finally, following a quality comparison between muscle synergies computed with our proposed method and the conventional peak EMG normalization in previous studies, we demonstrate the methodological impact on synergy structures and longitudinal changes in muscle tension and muscle synergy during subacute stroke rehabilitation to address our ultimate goal to provide new perspectives and independent reference data for future research on stroke rehabilitation. We also believe that modeling to recapitulate the process of functional recovery after motor dysfunctions is a promising approach to understanding hyper-adaptability in humans, the mechanism of adaptation to changes in the nervous and musculoskeletal systems (Eberle et al., 2021).

2. METHODS

2.1. Musculoskeletal Modeling

The proposed approach realizes the biomechanical phenomenon of joint torques being generated by active and passive tension forces coactivated in skeletal muscles and the correlation between muscle activation and joint torques (Lomaglio and Eng, 2005; Vena et al., 2015; Jones, 2017). It was suggested that larger joint torques are reflected by muscles in greater activation. In this section, we present a novel method to normalize and scale a distribution of muscle activation signals based on joint torques; specifically, compute virtually normalized muscle activation using musculoskeletal models constructed based on the human body's anatomical, kinematic, and dynamic characteristics. First, joint torques are calculated from pre-defined and measured body kinematics in a four-link skeletal model by inverse dynamics principles (Section 2.1.1). Next, a musculoskeletal model incorporating the Hill-type muscle model (Zajac, 1989) is built for forward dynamics simulation and mapping of joint torques, in which muscle-tendon dynamics, anthropometry, and muscle activation are integrated besides body kinematics (Section 2.1.2). Lastly, muscle activation amplitude is determined by mathematical optimization to overcome muscle redundancy problems (Section 2.1.3).

2.1.1. Skeletal Model and Inverse Dynamics

A four-link skeletal model was constructed to represent the entire human body in the sagittal plane with four segments and four joints to calculate joint torques from measured body kinematics (An et al., 2015). As in **Figure 1A**, each link specifies a segment of the human body as shank, thigh, pelvis, and HAT (head, arm, and truck). The four nodes connecting each segment indicate joints of the ankle, knee, hip, and lumbar. Definitions of joint angles and joint torques are shown in **Figure 1B**, where $\theta_{k=1,2,3,4}$ and $\tau_{k=1,2,3,4}$ symbolize joint angles and joint torques formed at the ankle, knee, hip, and lumbar, respectively.

Torques generated at each joint can be calculated given body kinematics and external forces using the following equation of motion (An et al., 2015):

$$\mathbf{I}(\Theta,\dot{\Theta})\ddot{\Theta}+\mathbf{H}(\Theta,\dot{\Theta})+\mathbf{g}(\Theta)+\Psi(\Theta,\dot{\Theta})=\mathbf{T}_{\text{jnt}}+\Phi(\Theta,\dot{\Theta}), \quad (1)$$

where Θ is a vector representing joint angles $\theta_{k=1,2,3,4}$ calculated from measured joint positions at the ankle, knee, hip, and lumbar. Matrices $\mathbf{I}(\Theta,\dot{\Theta})$, $\mathbf{H}(\Theta,\dot{\Theta})$, $\mathbf{g}(\Theta)$ indicate the moment of inertia of a segment, non-linear forces, and gravitational force, respectively. $\Phi(\Theta,\dot{\Theta})$ is a matrix of reaction forces at the feet and hip. $\Psi(\Theta,\dot{\Theta})$ is a matrix denoting the endured viscous resistance forces at each joint. Its magnitude is contingent on the type of joint at which the forces are received. Specified in Equation (2), resistance force $\Psi(\Theta,\dot{\Theta})$ is determined by joint angular velocity $\dot{\theta_k}$ at the ankle, knee, and hip joints ($k=1,2,3$) (Davy and Audu, 1987); whereas $\Psi(\Theta,\dot{\Theta})$ is defined by the range of joint angle at the lumbar joint ($k=4$) (Christophy et al., 2012).

$$\Psi(\Theta,\dot{\Theta})=\begin{cases} d_k\dot{\theta_k} & k=1,2,3 \\ d_k^{\text{ext}}\theta_k & k=4,\theta_k>0.0314 \\ d_k^{\text{flex}}\theta_k & k=4,\theta_k<-0.0314. \end{cases} \quad (2)$$

Lastly, $\mathbf{T}_{\text{jnt}}$ is the only unknown variable in Equation (1), denoting torques generated at each joint during STS. Given body kinematics and existing anatomical knowledge, joint torque $\mathbf{T}_{\text{jnt}}$ can be calculated following the inverse dynamics principle.

2.1.2. Forward Dynamics Simulation

While joint torques are calculated given body kinematics with the four-link skeletal model and inverse dynamics, joint torques are also simulated by forward dynamics (An et al., 2015). The proposed musculoskeletal model comprising 11 uniarticular and bi-articular muscles essential for rendering the human body STS movement by forward dynamics is shown in **Figure 2**. In this model, joint torques are supposed to be generated by net forces in contracted and passively activated muscles. The Hill-type muscle model is applied to describe individual muscle force production in two elements: contractile element (CE) and parallel element (PE) (Zajac, 1989). Names of the 11 modeled muscles are Tibialis Anterior (TA), Soleus (SOL), Gastrocnemius (GAS), Rectus Femoris (RF), Vastus Lateralis (VAS), Biceps Femoris Long Head (BFL), Biceps Femoris Short Head (BFS), Gluteus Maximus (GMAX), Rectus Abdominis (RA), Erector Spinae (ES), and Iliopsoas (IL).

The simulated joint torque $\boldsymbol{\tau}_{\text{jnt}}$ is represented by a vector of torques $\tau_{k=1,2,3,4}$ around the ankle, knee, hip, and lumbar joints, as in Equation (3). Torque τ_k at individual joints is a net quantity of torques generated by each associated muscle exerting tension F_i about the joint center at an equivalent distance of the anatomical muscle moment arm r_{ki}, as in Equation (4). r_{ki} designates the moment arm of the ith muscle ($i=1,...,11$) attached to the kth joint ($k=1,2,3,4$). According to the Hill-type muscle model, muscle tension F_i is a combination of the actively generated force F_i^{CE} by the contractile element (CE) and

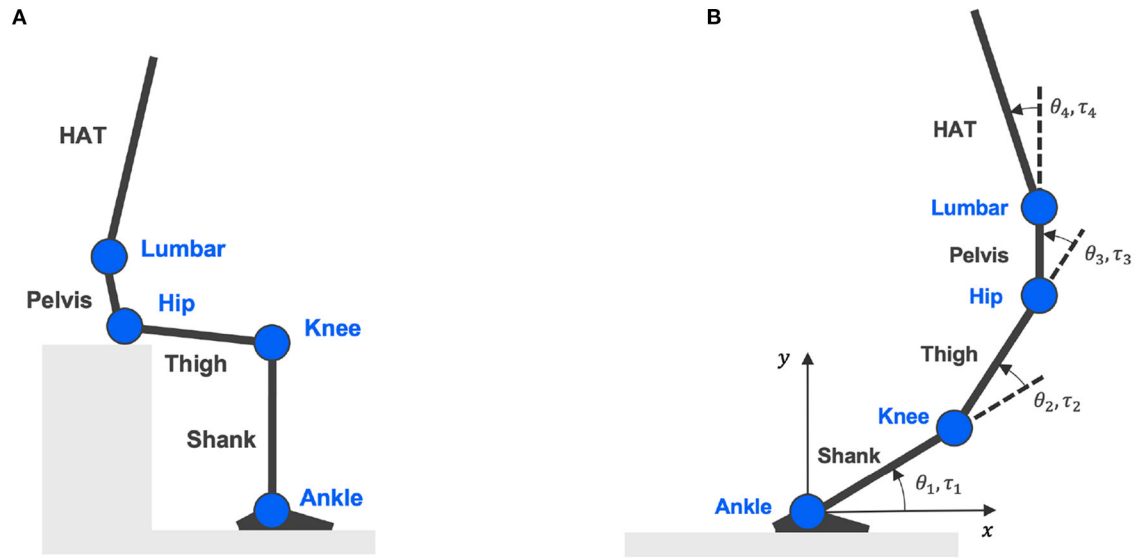

FIGURE 1 | Four-link skeletal model. **(A)** Is the skeletal model representing body segments of shank, thigh, pelvis, and HAT (head, arm, and truck); connected by four joints: ankle, knee, hip, and lumbar. **(B)** Shows the definitions of joint angles and joint torques.

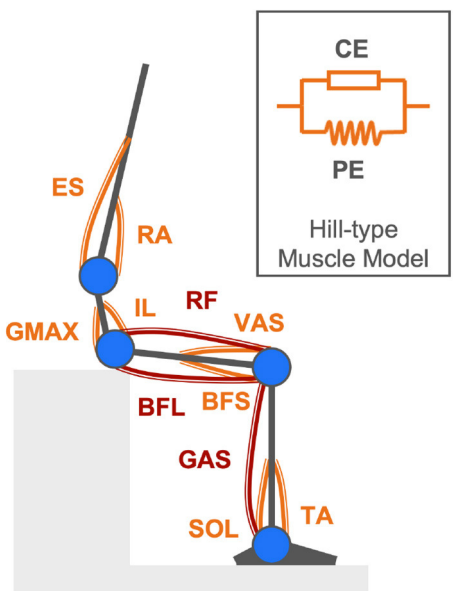

FIGURE 2 | Musculoskeletal model comprising eight uniarticular muscles (orange components) and three bi-articular muscles (maroon components) described by the Hill-type muscle model for rendering the human body STS movement in forward dynamics simulation.

a passive force F_i^{PE} contributed by the parallel element (PE), as in Equation (5).

$$\boldsymbol{\tau}_{\mathrm{jnt}} = \left[\tau_1 \;\; \tau_2 \;\; \tau_3 \;\; \tau_4\right]^{\mathrm{T}}, \tag{3}$$

$$\tau_k = \sum_{k=1}^{4} \sum_{i=1}^{11} r_{ki} F_i, \tag{4}$$

$$F_i = F_i^{\mathrm{CE}} + F_i^{\mathrm{PE}}. \tag{5}$$

The actively generated contraction force F_i^{CE} in the ith muscle is determined by the ith muscle's isometric maximum muscle force $F_i^{\max}$, force-length relationship f_{fl}, force-velocity relationship f_{fv}, and normalized muscle activation $\hat{m}_i$, as in Equation (6). The normalized muscle activation $\hat{m}_i$ is unknown and will be solved following computations detailed in the next Section 2.1.3. The two time-varying dynamic muscular properties of force-length relationship f_{fl} and force-velocity relationship f_{fv} are defined in Equations (7), (8), respectively (Hatze, 1977; Ogihara and Yamazaki, 2001), where f_{fl} is a function of the normalized ith muscle length to its optimal muscle length, denoted by $\hat{l}_i$, and f_{fv} is a function of the normalized ith muscle contraction velocity to the maximum muscle contraction velocity, denoted by $\hat{v}_i$.

$$F_i^{\mathrm{CE}} = F_i^{\max} f_{\mathrm{fl}} f_{\mathrm{fv}} \hat{m}_i, \tag{6}$$

$$f_{\mathrm{fl}} = \exp(-(\hat{l}_i - 1)^2), \tag{7}$$

$$f_{\mathrm{fv}} = 1 + \tanh(3\hat{v}_i). \tag{8}$$

Additionally, the passive force F_i^{PE} in Equation (5) by the parallel element (PE) is produced when a muscle stretches and exceeds its optimal muscle fiber length. Once generated, this passive force

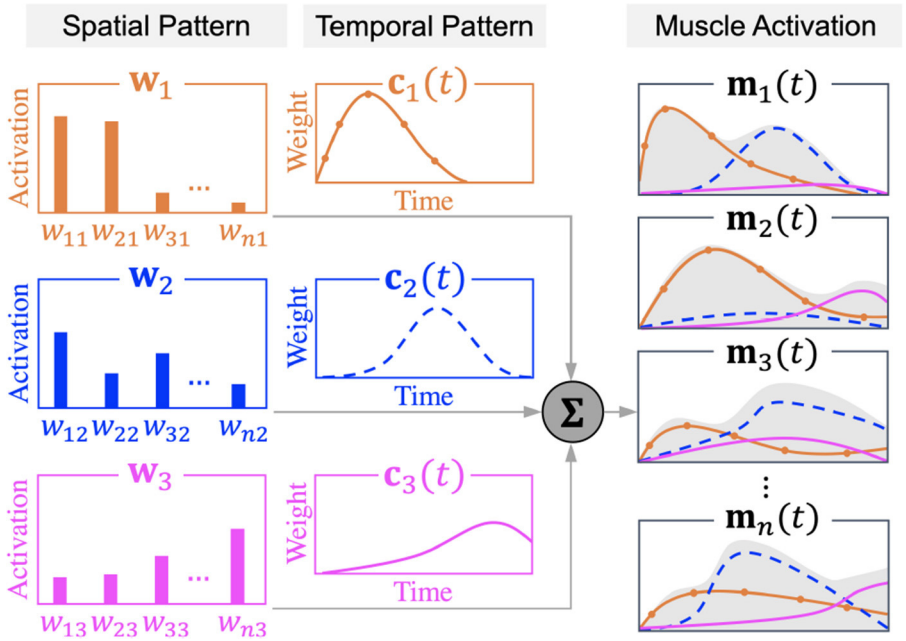

FIGURE 3 | Muscle synergy model.

is related to the normalized muscle length $\hat{l}_i$ and the isometric maximum muscle force $F_i^{\max}$, as in Equation (9).

$$F_i^{\mathrm{PE}} = \begin{cases} 0 & \hat{l}_i < 1.0 \\ F_i^{\max} \frac{e^{10(\hat{l}-1)}}{e^5} & 1.0 \leq \hat{l}_i \leq 1.5 \\ F_i^{\max} & 1.5 < \hat{l}_i. \end{cases} \tag{9}$$

2.1.3. Muscle Activation Calculation

The proposed musculoskeletal model incorporates several biarticular muscles, which induces the muscle redundancy problem as there are more muscles than mechanical degrees of freedom (Kutch and Valero-Cuevas, 2011). In forward dynamics simulation, the computation of torques produced by 11 types of muscles at four joint positions are governed by Equation (4); subsequently, creating an underdetermined system of equations with 11 unknowns and four equations. The underdetermined system of equations is solved by optimization with additional constraints. The goal is to enable the proposed musculoskeletal model to simulate movements that resemble the actual STS movements performed in reality.

All the unknown muscle activation $\hat{m}_i$ from Equation (6) is determined by finding the optimal activation that can simulate joint torques equivalent to the torques calculated by inverse dynamics from body kinematics to replicate the observed STS movement. Optimization is implemented under the constraint that the simulated muscle activation $\hat{m}_i$ and the measured muscle activation preserve a perfect positive correlation throughout the motion progress; meanwhile, subjected to an objective function defined as to minimize the errors between the extrema of simulated joint torques $\boldsymbol{\tau}_{\mathrm{jnt}}$ and joint torques $\mathbf{T}_{\mathrm{jnt}}$ calculated from body kinematics, as in Equation (10).

$$Z = ||\mathbf{T}_{\mathrm{jnt}}^{\max} - \boldsymbol{\tau}_{\mathrm{jnt}}^{\max}||^2 + ||\mathbf{T}_{\mathrm{jnt}}^{\min} - \boldsymbol{\tau}_{\mathrm{jnt}}^{\min}||^2. \tag{10}$$

2.2. Muscle Synergy Model

Muscle synergy theory modularizes the complex control of individual muscles into a limited number of synchronized muscle activation to explain each different type of human body movement (Ivanenko et al., 2004; Clark et al., 2010). Human STS movement can be explained by four synergies for healthy subjects and post-stroke patients (Yang et al., 2017), with each synergy corresponding to the phase of lumbar flexion, hip raise, body extension, and posture control in STS (Schenkman et al., 1990). By analyzing muscle synergy patterns, post-stroke STS accomplished by the redundant human body can be easily understood from the perspective of muscle coordination in motor control units. The time-dependent muscle activation is expressed as a linear summation of spatiotemporal patterns as in Equation (11), where matrices **M**, **W**, and **C** indicate muscle activation, spatial pattern, and temporal pattern, respectively.

$$\mathbf{M} = \mathbf{WC}. \tag{11}$$

The $n \times t_{\max}$ matrix **M** of muscle activation comprises time-varying muscle activation vectors $\mathbf{m}_{i(i=1,2,\ldots,n)}$ which represent muscle activation in n different muscles at time $1 < t < t_{\max}$.

The $n \times N$ matrix **W** denotes muscle synergy spatial patterns in which relative activation levels of muscles are defined. Each column in the **W** matrix refers to one of the N different numbers of synergies $\mathbf{w}_{j(j=1,2,\ldots,N)}$. Vector $\mathbf{w}_{j(j=1,2,\ldots,N)}$ represents

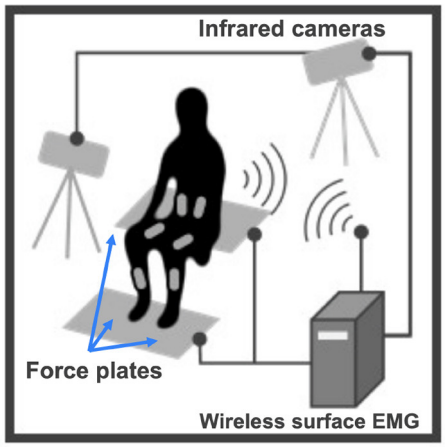

FIGURE 4 | STS measurement experiment setup.

the relative activation level of the ith muscle ($i = 1, 2, ..., n$) in the jth muscle synergy ($j = 1, 2, ..., N$).

The time-dependent $N \times t_{\max}$ matrix $\mathbf{C}$ of temporal patterns defines the weighting coefficient of each of the N different muscle synergies in a vector $\mathbf{c}_{j(j=1,2,...,N)}$. Vector $\mathbf{c}_{j(j=1,2,...,N)}$ is a time-varying scaling factor of the corresponding spatial pattern $\mathbf{w}_{j(j=1,2,...,N)}$ at time $1 < t < t_{\max}$.

Figure 3 shows the schematic design of a muscle synergy model that exemplifies the case of n muscles' activation expressed as the linear summation of spatial patterns ($\mathbf{w}_{1,2,3}$) and temporal patterns ($\mathbf{c}_{1,2,3}$) of three muscle synergies. Activation in each of the n muscles is depicted by the gray area under the curve.

For the extraction of muscle synergy patterns $\mathbf{W}$ and $\mathbf{C}$ from muscle activation $\mathbf{M}$, non-negative matrix factorization (NNMF) was used (Lee and Seung, 1999). Muscle synergies were extracted from each trial of each subject (Ivanenko et al., 2005; Oliveira et al., 2014; Yang et al., 2017; Kogami et al., 2021).

2.3. Measurement Experiment

2.3.1. Subjects

Eight healthy male adults (age 23.8 ± 2.6) and four post-stroke patients (age 55.0 ± 4.8) participated in a series of measurement experiments.

Each healthy participant performed 15 trials of STS movement by standing up at a self-paced speed from a seat adjusted to the height of the person's knee. Measurements of maximum voluntary contraction (MVC) were conducted with healthy participants to obtain ground truth data for the validation and assessment of the proposed method.

Post-stroke patients were invited to serial STS measurements during their subacute rehabilitation stay (137 ± 22 days) in the hospital in order to compare and investigate individual patient's biomechanical changes at different times in the subacute stage. Two patients finished two measurements, and the other two each finished three and four measurements. On each measurement day, the patient was asked to do ten STS trials without assistance at a self-paced speed from a seat adjusted to the height of the knee. Patients' improvements in Fugl-Meyer Assessment (FMA) clinical score of the lower limb motor recovery over their inpatient subacute rehabilitation were +13, +8, +3, and 0 points, respectively.

All the healthy and patient participants were asked to remain their feet still at a comfortable position throughout measurement trials.

Informed consent was obtained from healthy participants and patients before the experiment, which was approved, respectively, by the Institute Review Board of The University of Tokyo and the Institute Review Board of Morinomiya Hospital, Osaka, Japan.

2.3.2. Measurements

STS experiment setup is shown in **Figure 4**. An optical motion capture system (Motion Analysis Corp.), including 14 infrared cameras, was used to record body kinematics at 100 Hz. Body kinematics data, such as joint positions, were used to calculate joint angles in SIMM (Musculographics, Inc.). Three separate force plates (TechGihan Corp.) were set under the hip and each foot to measure the reaction forces at 2,000 Hz. The seat-off moment was marked when the vertical force recorded under the hip dropped below 10 N. Reaction force data were low-pass filtered at 20 Hz. Wireless surface Electromyography (EMG) sensors (Cometa Corp.) were directly placed on the participant's skin to record muscle activity. Surface EMG sensors were placed at ten types of uniarticular and biarticular muscles in the upper trunk and lower limbs to obtain muscle activation signals at 1,000 Hz for healthy subjects and 2,000 Hz for post-stroke patients. Each recorded muscle contributes to accomplishing STS movement by either flexion or extension at one or two joints of the ankle, knee, hip, and lumbar. Measured muscles are the same ones considered in the proposed musculoskeletal model (TA, SOL, GAS, RF, VAS, BFL, BFS, GMAX, RA, ES), except for Iliopsoas (IL), since IL is an inner hip flexion muscle and its activation cannot be measured with surface EMG sensors. Surface EMG electrodes locations were determined by the point on a line between two anatomical landmarks of individual muscles, according to the European SENIAM recommendations (Hermens et al., 2000; Blanc and Dimanico, 2010). Muscle activation signals were band-pass filtered with a zero-lag fourth-order Butterworth filter of 40–400 Hz and rectified with a fourth-order low-pass Butterworth filter at 4 Hz (Clark et al., 2010; Gizzi et al., 2011). All EMG data were recorded continuously throughout measurement trials with the participant. Each STS trial was extracted from the entire process according to the seat-off time such that one STS trial is a discrete 3-second interval, with one second before the seat-off moment and two seconds elapsed after seat-off.

Additionally, in the MVC activation measurement with healthy subjects, an experimenter applied resistive forces by hand in different directions to the participant's joints at the ankle, knee, hip, and lumbar while the participant voluntarily exerted a maximum force by muscle contraction to push or pull against the applied force. EMG signals were recorded for the same types of muscles (TA, SOL, GAS, RF, VAS, BFL, BFS, GMAX, RA, and ES). EMG signals collected in the MVC measurement were processed in the same way as those collected from STS

TABLE 1 | Muscle activation simulation results evaluated against measured MVC-normalized EMG from healthy subjects.

	Pearson's *r*			RMSE		
Muscle name	**SO**	**Proposed**	**Improvement**	**SO**	**Proposed**	**Improvement**
TA	0.669	1.00	49.5%	0.0691	0.0617	10.7%
GAS	0.469	1.00	113%	0.0253	0.0167	33.9%
SOL	0.604	1.00	65.6%	0.0335	0.0313	6.46%
RF	0.924	1.00	8.20%	0.0657	0.0274	58.3%
VAS	0.849	1.00	17.8%	0.0581	0.0266	54.2%
BFL	0.826	1.00	21.0%	0.0500	0.0266	46.7%
BFS	0.964	1.00	3.80%	0.0617	0.0226	63.4%
GMAX	0.982	1.00	1.90%	0.0698	0.0551	21.0%
RA	0.782	1.00	28.0%	0.1005	0.0865	14.0%
ES	0.778	1.00	28.5%	0.0279	0.0241	13.8%

With reference to MVC-normalized EMG, an inter-method simulation accuracy comparison was done between the proposed joint torque-based algorithm and SO based on muscle activation. Muscle activation profile conformity and peak amplitude agreement are evaluated and compared by Pearson's correlation ($-1 \leqslant r \leqslant 1$) and root-mean-square error (RMSE), respectively, between the proposed and SO algorithms. Within-muscle simulation accuracy improvements by the proposed algorithm are reported as percentages.

measurements. For each type of muscle, the MVC activation, to which all the EMG data of healthy subjects were normalized, was determined by the maximum muscle activation value during the participant's measurement.

3. RESULTS

3.1. Muscle Activation Estimation Accuracy

Simulation results were evaluated against the measured muscle activation data from eight healthy subjects to validate the proposed method. All courses of computation were done in MathWorks MATLAB (2021). Two factors were evaluated between the simulated and measured muscle activation, namely, Pearson's correlation coefficient (Pearson's r) and root-mean-square error (*RMSE*). **Table 1** shows within-muscle Pearson's r of the ensemble average across subjects to demonstrate the quality of conformity between simulation and the observed MVC-normalized muscle activation (Cheung et al., 2005; Staudenmann et al., 2010; Laine et al., 2021). All muscles (TA, SOL, GAS, RF, VAS, BFL, BFS, GMAX, RA, and ES) achieved a Pearson's $r = 1$ (Mukaka, 2012) throughout the motion progress due to the constrained optimization conditions. *RMSE* informs the within-muscle amplitude error between the peak values in simulation and the observed reference. **Table 1** also compares the simulation performance of our proposed joint torque-based algorithm with that of the commonly used SO algorithm based on squared muscle activation (An et al., 2014, 2015; Shuman et al., 2019; Wang et al., 2022). Both enhancements in correlation and reduction of amplitude error are reported as a percentage quantity, showing the better performance of the proposed method. Due to the constrained correlation ($r = 1$) between simulated muscle activation and measured EMG, the onset and offset timing in simulations and experiments also aligned perfectly. Additionally, the percentage relative error (%*RE*) (Kat and Els, 2012) between the simulated and calculated joint torque maxima in motion progress was 8.9 ± 5.9%. The knee joint, especially, scored the highest accuracy with a minimal %*RE* of 0.36 ± 0.83%. Since the activation of Iliopsoas (IL), an inner hip flexor, could not be measured using surface EMG sensors in the experiment, its simulation accuracy was not verified. Therefore, barring IL muscle, all the other muscles of post-stroke cases will be scrutinized for activation changes over the subacute rehabilitation period. The reconstruction quality with four synergies obtained using trial-by-trial extraction of muscle synergy was 94.2 ± 3.4%, overall satisfied the threshold of 90% (Cheung et al., 2005).

TABLE 2 | Compare muscle tension results from post-stroke cases: changes in maximum muscle tension over the subacute rehabilitation period of four patients with +13, +8, +3, and +0 points in the Fugl-Meyer Assessment (FMA) of motor recovery.

	Max muscle tension percentage change [%]			
Muscle name	**Case: FMA +13**	**Case: FMA +8**	**Case: FMA +3**	**Case: FMA +0**
TA	892*	1.66*	−50.6*	−0.402
GAS	62.6*	−58.6*	−1.30	−5.32*
SOL	12.6*	−17.3*	31.8*	−33.6*
RF	111*	−0.272	215*	49.0*
VAS	19.1*	−2.29	0.0553	−2.00
BFL	−11.5*	−2.89*	102*	4.59*
BFS	592*	−2.60*	−35.1*	−49.3*
GMAX	−27.0*	−3.80	−58.7*	19.9*
RA	113*	57.9*	131*	−31.2*
ES	90.2*	1.30	−7.41*	−7.04*

**Change with statistical significance, $p < 0.001$.*

3.2. Post-stroke Muscle Activation Amplitude-Related Features

As muscle activation amplitude is related to the magnitude of muscle tension and the level of muscle synergy, this study examined activation amplitude-related features for post-stroke

TABLE 3 | Temporal synergy patterns progression in subacute rehabilitation.

	Peak change in temporal patterns [%]		
	Case: FMA +13	**Case: FMA +3**	**Case: FMA +0**
Synergy 1	88.3*	61.0*	−15.9*
Synergy 2	152*	−38.8*	9.27
Synergy 3	134*	46.2	15.9
Synergy 4	65.0*	35.5*	−4.01

Results of three subacute stroke patients with +13, +3, and +0 points in the Fugl-Meyer Assessment (FMA) of motor recovery.
**Change with statistical significance, $p < 0.05$.*

patients, including maximum muscle tension and peak level of muscle synergy. The following Sections 3.2.1 and 3.2.2 show results pertaining to the progression of patients' muscle tension and muscle synergy during the subacute rehabilitation period. Courses of computation were completed in MathWorks MATLAB (2021). Statistical significance of changes between different measurement days was decided by the Wilcoxon rank-sum test for patients with two times of measurements (Rosner et al., 2006) and by the Kruskal–Wallis test (one-way analysis of variance on ranks) for patients who completed three or more times of measurements (McDonald, 2014).

3.2.1. Maximum Muscle Tension

After patients' STS muscle activation amplitude values were determined and virtually normalized based on joint torques by the proposed method, tension force generated in each muscle was calculated by Equations (5), (6). Regarding the intra-subject changes on the paretic side among four patients, significant increases ($p < 0.001$) to various extents were found in maximum muscle tension and peak muscle activation amplitude. RF and VAS are the only two muscles that did not show any significant peak tension reduction after rehabilitation in all patients. RF is a biarticular muscle acting as a knee extensor and hip flexor, whereas VAS is a uniarticular muscle acting as a knee extensor.

As in **Table 2**, the number of muscles that yielded significant increases in maximum tension was the greatest for the patient with the greatest motor recovery among the four. The patient with +13 points in FMA was detected to have eight muscles (TA, GAS, SOL, RF, VAS, BFS, RA, and ES) experiencing tension increases, comparing to two, four, and three muscles demonstrating tension increase in the other three patients with +8, +3, and +0 in FMA, respectively. Likewise, the number of muscles showing significant tension decreases after rehabilitation was the least in the most improved patient (FMA +13), with only two muscles (BFL and GMAX).

As for the patients with more than two measurements, it was noted that the greatest peak muscle tension did not necessarily disclose on the last measurement day.

3.2.2. Muscle Synergy Progression

With normalized muscle activation, muscle synergy spatial and temporal patterns were determined by NNMF, and the amplitude of synergy patterns became appropriate for comparisons. For all patients, their spatial patterns appeared similar over the subacute rehabilitation. The dominant muscles with the highest relative activation in spatial patterns in each muscle synergy were in line with the ones found by Yang et al. (2017). The peak level of patients' temporal patterns, however, exhibited some variations in rehabilitation. Summarized in **Table 3**, the patient with the greatest improvement in motor recovery (FMA +13) showed significant peak level increases ($p < 0.05$) in temporal patterns of all four muscle synergies; respectively, by 88.3, 152, 134, and 65.0%. In comparison, the other patients had fewer temporal patterns revealing peak level increases. The patient with no improvement in FMA only had an amplitude decrease in the temporal pattern of Synergy 1 (body flexion) by 15.9% after 154 days, while the patient's other temporal patterns of Synergy 2 (hip raise), Synergy 3 (body extension), and Synergy 4 (posture control) were found with no significant amplitude changes over time.

For the patient with the greatest improvement in FMA of motor recovery, both amplitude and timing of temporal patterns showed distinctive changes throughout the subacute rehabilitation. **Figure 5** shows the representative subject's normalized muscle synergy spatial patterns and their progression over 144 days of inpatient rehabilitation. Spatial patterns calculated with the conventional within-subject peak EMG normalization are also presented, noted as pseudo-normalized for comparison. Similarly, temporal patterns obtained by the proposed method and by the conventional within-subject peak EMG normalization can both be found in **Figure 6**.

4. DISCUSSION

This study proposed a novel method to calculate muscle activation and normalize it based on joint torques. Upon validating the method with eight healthy young subjects, we applied the proposed approach with four subacute stroke patients to investigate their muscle activation amplitude-related biomechanical features such as muscle tension and muscle synergy level. Like in most cases, uncertainties and limitations of generic-scaled musculoskeletal modeling remained in this study, especially in analyses with post-stroke patients (Hicks et al., 2015; Kainz et al., 2021). Nevertheless, quantitative results found may hint that maximum muscle tension and activation level of muscle synergy temporal patterns could reflect the effectiveness of subacute stroke rehabilitation.

4.1. Method Validation

The proposed EMG-informed generic-scaled musculoskeletal model that estimates muscle tension in the Hill-type muscle model was compared to the existing approach of previous relevant studies as recommended by Hicks et al. (2015) to validate its performance. With reference to the MVC-normalized experimental muscle activation as a virtual ground truth, we compared simulation accuracy of the proposed joint torque-based method with the commonly used SO based on squared muscle activation. Shown in **Table 1**, the proposed method performed better across muscle types and estimated STS muscle activation more accurately; overall, with enhanced

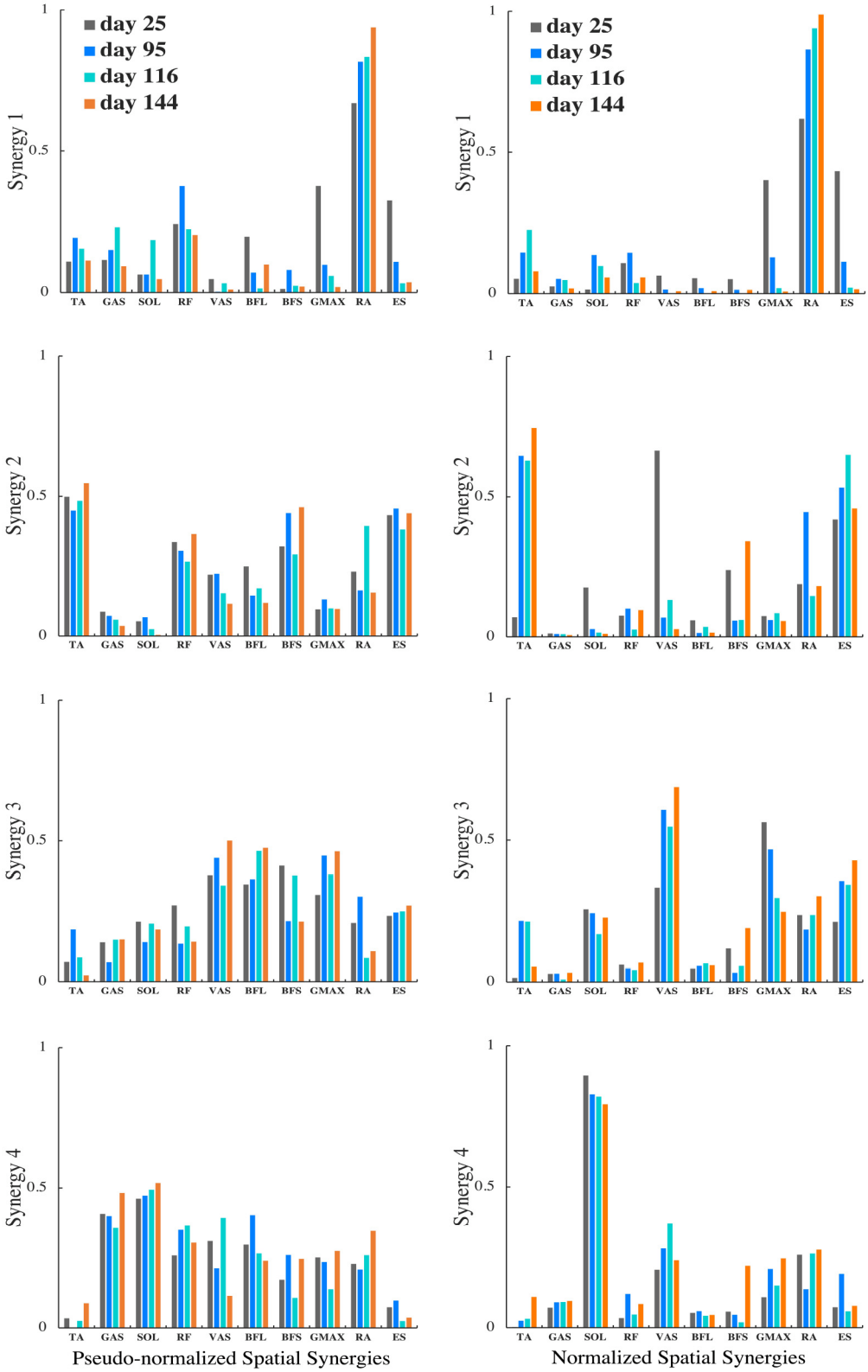

FIGURE 5 | Muscle synergy spatial patterns of the representative patient with +13 points of improvement in FMA score on the 25th, 95th, 116th, and 144th day after initial stroke onset. The left column shows spatial patterns of each synergy normalized by within-subject peak EMG, noted as pseudo-normalized for comparison. The right column shows spatial patterns of each synergy normalized by proposed method. Vertical axis indicates relative muscle activation levels ranging from 0 to 1. Horizontal axis presents muscle names.

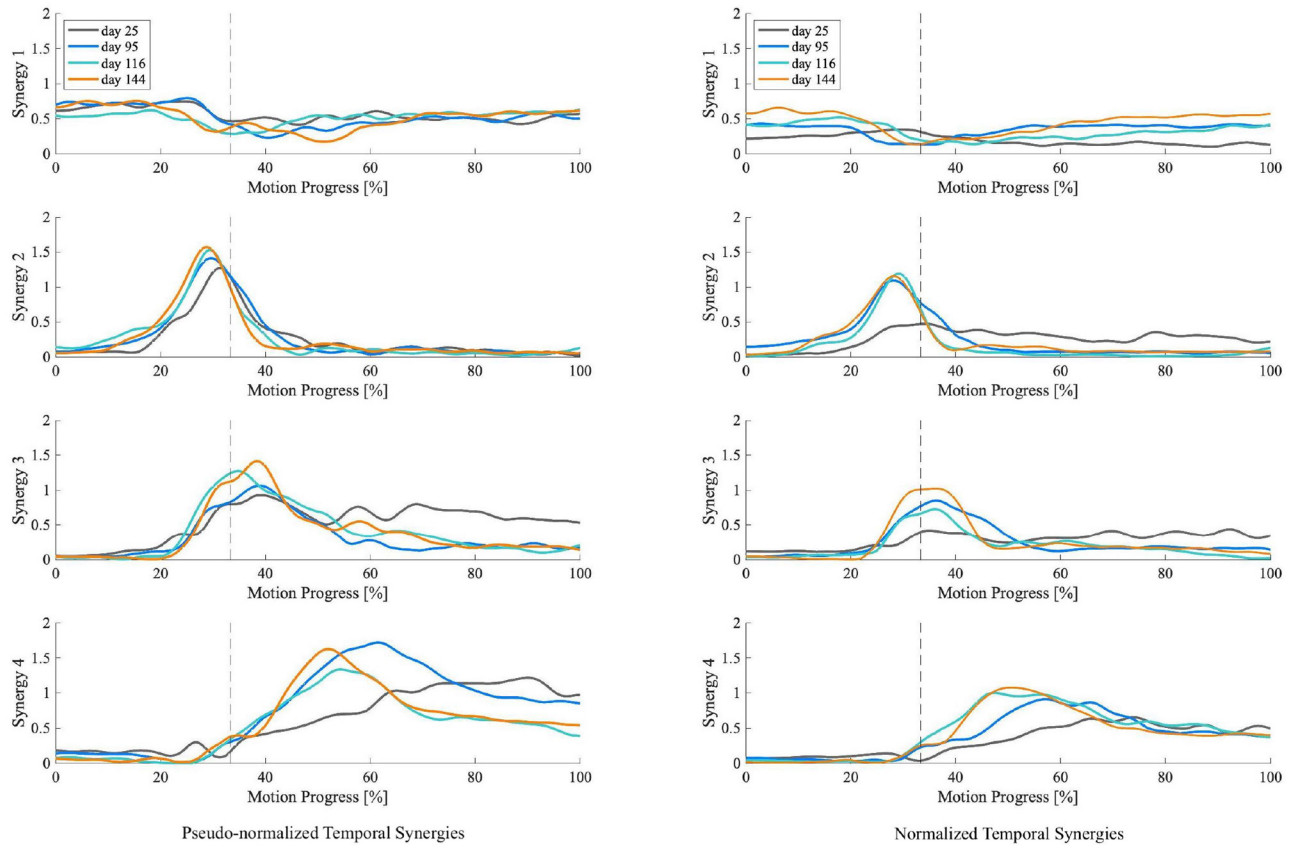

FIGURE 6 | Muscle synergy temporal patterns of the representative patient with +13 points of improvement in FMA score on the 25th, 95th, 116th, and 144th day after initial stroke onset. The left column shows temporal patterns of each synergy normalized by within-subject peak EMG, noted as pseudo-normalized for comparison. The right column shows temporal patterns of each synergy normalized by proposed method. Vertical axis indicates the weighting coefficients. Horizontal axis is STS motion progress expressed in percentage. Dotted vertical lines represent the seat-off time.

muscle activation profile conformity (greater Pearson's *r*) and reduced error in muscle activation peak amplitude (smaller *RMSE*). Moreover, in contrast to conventional within-subject peak normalization (Cheng et al., 2004; Silva et al., 2013; Yang et al., 2019), the normalized peak muscle activation in different muscles and subjects were no longer an indiscriminate value of 100%. Muscle activation profiles estimated in forward dynamics simulation and EMG curves measured in experiments are similar, and their critical onset and offset timings also perfectly agree (Hicks et al., 2015).

In this study, anthropometry parameters were carefully retrieved from past studies based on muscle-tendon data derived from human cadavers and MRI-based measurements of multiple subjects (Riener and Fuhr, 1998; Ward et al., 2009; Arnold et al., 2010). Muscle tension estimated by the Hill-type muscle model may be sensitive to parameters such as force-length relationship and isometric maximum muscle force (Scovil and Ronsky, 2006). Muscle moment arms and muscle geometry may also vary between different individuals, especially when pathological conditions are involved (Scheys et al., 2008; Kainz et al., 2021). These parameters, to which estimated muscle tension may be sensitive, were generalized between healthy and post-stroke groups in this study.

However, in our model, muscle tension was generated throughout the STS trial to meet the goal by producing the same amount of joint torques calculated from kinematics. Scovil and Ronsky (2006) found that muscle forces generated to track a specified trajectory or meet movement goals were less sensitive to muscle model parameters. Moreover, using EMG data collected from patients with neurological disorders to estimate muscle forces in the Hill-type model can overcome the limitation imposed by models assuming an identical neuromuscular control strategy between individuals (Lloyd and Besier, 2003; Hoang et al., 2018). Therefore, our generalized parameters may have less impact on simulations in the healthy group with which the model was initially validated. Meantime, we suggest that current muscle tension results of the neurologically impaired stroke group may be interpreted with caution due to the modeling limitation and our current small size of patients. Nevertheless, the current method demonstrated its ability to estimate muscle activation with markedly reduced errors between MVC-normalized EMG and perfectly aligned

on/off timings with measured EMG from both healthy and post-stroke subjects.

To investigate the impact of normalization on muscle synergy analysis, we compared synergy progression results (over 144 days) normalized by the proposed method and those by the conventional peak EMG normalization utilized in previous studies (Cheng et al., 2004; Clark et al., 2010; Prudente et al., 2013; Yang et al., 2017, 2019; Kogami et al., 2018, 2021). As in **Figure 5**, in comparison, when muscle activation was normalized to within-subject peak activation (noted as pseudo-normalized in figures) prior to NNMF, spatial activation in dominant muscles in synergies are underestimated (e.g., RA in Synergy 1, TA in Synergy 2, VAS and ES in Synergy 3, SOL in Synergy 4), whereas the subordinate muscle contributors are prone to overestimation. In **Figure 6**, we presented the corresponding temporal pattern progression (over 144 days) normalized by the proposed method in tandem with that by the traditional peak EMG normalization. With the pseudo-normalized temporal patterns, differences in peak levels of temporal synergy are more subtle. The less evident amplitude changes in temporal and spatial patterns may be the consequence of the fact that within-subject peak EMG normalization indiscriminately scales peak activation in different muscles to 100%, which removes inherent peak activation differences and induces amplitude overestimation or underestimation. Conversely, peak timings of temporal synergy are very similar with both methods, which is favorable, as the peak EMG normalization has been broadly applied by past studies on synergy timing. It demonstrates that the proposed method can be useful for clarifying activation levels, as well as synergy timing features. The synergy activation timing agreement can be attributed to the perfect covariation and high conformity of our simulated muscle activation with experimental EMG. Lastly, we compared muscle synergy reconstruction quality by the proposed joint torque-based normalization with that by the within-subject peak EMG normalization reported previously in studies that had similar experimental design; on average, around 94% by the proposed and around 88% by peak EMG (Yang et al., 2017; Kogami et al., 2021).

4.2. Rehabilitation of Muscle Tension

Although the model's sensitivity and uncertainty may be affected by muscle geometry and pathology, muscle tension changes with regard to patients' sensorimotor functioning (i.e., FMA scores) found in this study can still provide new perspectives in answering if and how activation amplitude-related features would reflect in subacute stroke rehabilitation. Our results can be a reference for future studies on muscle tension with subacute stroke patients and help expand the pool of available independent data (Hicks et al., 2015).

Shown in **Table 2**, the difference between patients in the number of muscles yielding increased muscle tension after rehabilitation may indicate a correlation between the degree of mobility restoration and the capacity of muscle force production in lower limbs of subacute stroke patients. A similar difference in the number of muscles showing significant activation amplitude increases was also found between the sampled patients with various degrees of motor recovery. As past studies found that chronic stroke patients showed significant gains in isometric muscle strength and assessment scores of motor performance in upper limb muscles after receiving rehabilitation training (Lum et al., 2002), findings of this study may imply that the likelihood of seeing muscle activation increases on the paretic side is higher for subacute stroke patients with notable improvement in lower limb FMA. The greater number of muscles demonstrating diminished activation amplitude and tension in less-improved patients could suggest that patients who do not really recover in subacute rehabilitation may develop altered muscle activation strategies in accomplishing STS. One hypothesis may be that patients who improve poorly in the subacute stage tend to shun the usage or reliance of their paretic side; instead, they consciously or subconsciously rely more on the non-paretic side for training, which eventually resulting in motor compensation from the more capable side rather than true motor recovery on the paretic side.

The most improved patient (FMA +13) showed some exclusive progress with peak muscle tension, which other less-improved patients did not experience, such as increased tension in the ankle plantar-flexor and knee flexor GAS, knee extensor VAS, and lumbar extensor ES. On top of that, the most improved patient, who also happened to be the only one showing significant increases in ankle joint torque after rehabilitation, gained a phenomenal growth of peak muscle tension in the ankle dorsiflexor TA by 892%. Similar drastic changes were found with the patient's muscle activation amplitude as well. Besides, a small yet significant increase in TA's tension was also found with the second best-improved case (FMA +8). According to qualitative findings in the past, post-stroke patients with a greater burden on motor function and a higher chance to collapse in STS exhibited no or a merely perceptible low-amplitude activity in their TA muscles (Cheng et al., 2004). In this study, as patients with relatively higher FMA score improvements significantly enlarged both activation and tension in their TA muscles, it may suggest an important contributing factor to their outstanding rehabilitation, after which time their enhanced TA muscles mitigated the risk of collapsing.

As for the case of FMA +0, suggesting little to no recovery in terms of motor functioning, balance, sensation, and joint functioning after rehabilitation (Fugl-Meyer et al., 1975), the patient revealed significant increases in hip joint torque and the hip extensor GMAX's peak tension and activation amplitude after rehabilitation, which was something not observed in other patients with some degree of motor recovery. It could hint that patients with more restored motor ability do not employ their hips in STS the same way as those with less motor recovery. Furthermore, this patient showed a peak tension decrease in the lumbar flexor RA, whereas the other patients with FMA improvement returned with considerable tension increases in RA. The distinguished improvement in RA may indicate a better upper body momentum generation in STS with the better-improved cases. These hypotheses may be affirmed with a larger pool of subacute stroke patients in future studies.

This study also confirmed that increased muscle tension does not necessarily correspond to increased muscle activation amplitude and vice versa (Vigotsky et al., 2018), as EMG analysis

does not encompass muscle geometry or muscle contraction dynamics. For future rehabilitation evaluation, we also suggest avoiding isolated usage of EMG data and encourage analyses of both EMG and muscle tension to study neuromotor recovery.

4.3. Rehabilitation of Muscle Synergy

Muscle synergy spatial patterns of the sampled post-stroke patients remained rather similar over subacute rehabilitation. Dominant muscles found with the highest relative activation in spatial patterns in each muscle synergy concurred with previous findings by Yang et al. (2017). In Synergy 1, corresponding to the initial lumbar flexion phase, the spatial activation of lumbar flexor RA dominated in upper body momentum generation. In Synergy 2, the ankle dorsiflexor TA was primarily activated to dorsiflex the ankle to the maximum position while moving the center of mass forward until the hip was raised from the seat. Synergy 3, responding for the body extension phase, was predominantly led by the knee extensor VAS and lumbar extensor ES. Both acted in extending the whole body during the upward momentum transition until the body reached the full upright position. For the last Synergy 4, the ankle planter-flexor SOL's spatial activation surpassed other muscles,' showing distinguished activation in stabilizing the body posture.

For the patient with the greatest motor recovery (FMA +13), both amplitude and timing of the patient's muscle synergy temporal patterns showed distinctive changes over the subacute rehabilitation. As shown in **Figure 6**, the patient's temporal pattern of normalized Synergy 2 exhibited a significant increase in peak amplitude on the second measurement day (95 days after stroke onset). After that, the amplitude escalation plateaued out. No apparent amplitude differences were found in the temporal pattern of normalized Synergy 2 between day 95, day 116, and day 144 after the stroke onset. Similarly, the peak time also seemed to advance toward an earlier time in the motion progress. This reduced lag in peak times, together with the increased peak amplitude in normalized Synergy 2 (for hip raise), may explain the patient's motor recovery since former studies have found that the peak time of Synergy 2 delayed significantly after stroke onset when compared to that of healthy controls (Yang et al., 2017, 2019). These former studies thereby insisted on teaching the patients the right time to raise their hips. According to the results, this study advocates such rehabilitation strategies targeted on unlearning incorrect ways of hip lifting. Additionally, the same patient (FMA +13) was the only one who showed significant amplitude increases in normalized Synergy 3. As in **Figure 6**, the peak level of temporal patterns in normalized Synergy 3 expanded more gradually, eventually reaching the highest peak amplitude by the last measurement day (144 days after stroke onset). It may suggest that apart from the timing features regarding Synergy 3 (Yang et al., 2019), growth in peak amplitude of Synergy 3 (body extension) may also be a distinctive feature indicating a better improvement in motor functioning.

For Synergy 4, besides the patient without any FMA improvement, the others exhibited significant peak amplitude increases. For instance, as in **Figure 6**, a continuously heightened peak amplitude in the temporal pattern of normalized Synergy 4 can be observed throughout the four measurements between day 25 and day 144 after stroke onset. A similar advancement of peak timing observed in Synergy 2 can also be seen in Synergy 4. The lessened delay in peak time and the increased peak amplitude in normalized Synergy 4 (for posture control) may be indicators of improvement in motor functioning, which may be used to discern motor recovery.

4.4. Limitations and Future Works

First, due to the generalized anthropometry in modeling different post-stroke participants, muscle tension estimated in the Hill-type muscle model may be sensitive to the change of some muscle geometry parameters. Both subject-specific musculoskeletal geometry and different neuromuscular control strategies have an impact on simulation results (Kainz et al., 2021). Although this study accounted for each participant's unique muscle activation when estimating muscle tension, it may be worth exploring further the impact of parameters, such as muscle fiber length and physiological cross-sectional area, on simulation results involving complex pathology (Redl et al., 2007). Second, the healthy and stroke groups are not age-matched in this study. Since anthropometry may not only change with pathology but also vary by age (Hicks et al., 2015), a future validation study with age-matched healthy participants may be necessary. Lastly, we followed the subacute rehabilitation of four inpatient stroke survivors on an average span of 4.5 months, and the number of patient participants is small. Current results may be indicative, but a larger pool of subacute patients is needed in order to draw stronger relevance between the observed biomechanical consequences and rehabilitation effectiveness (Yang et al., 2019). Recruiting more subacute stroke participants will also enable a future study to explain the current perplexing results found with less-improved patients, who may have experienced motor compensation instead of motor recovery.

5. CONCLUSION

This study proposed a novel method to compute post-stroke muscle activation based on joint torques. Upon validating the EMG-informed generic-scaled musculoskeletal model with eight healthy subjects, we applied it to investigate features related to muscle activation amplitude such as muscle tension and muscle synergy levels for four and three subacute stroke patients, respectively, during 137 $\pm$ 22 days of rehabilitation. In contrast to conventional EMG normalization methods, this joint torque-based normalization does not require MVC measurements or overestimate peak muscle activation in different muscles by indiscriminately scaling its peak to 100%, and hence activation amplitude comparisons can be made. Compared to the common SO algorithm based on squared muscle activation, our proposed algorithm based on joint torques produced results that were much closer to the MVC-normalized activation (virtual ground truth in this study). The contributed method and quantitative findings with patients of this study help enhance the understanding of post-stroke motor recovery mechanism and hyper-adaptability in humans with neurological disorders. It should also assist in the development of more effective rehabilitation strategies for future stroke survivors.

DATA AVAILABILITY STATEMENT

The original contributions presented in the study are included in the article/supplementary material, further inquiries can be directed to the corresponding author/s.

ETHICS STATEMENT

The studies involving human participants were reviewed and approved by Institute Review Board of The University of Tokyo and the Institute Review Board of Morinomiya Hospital, Osaka, Japan. The patients/participants provided their written informed consent to participate in this study.

AUTHOR CONTRIBUTIONS

RW, QA, IM, and HA conceived the study. AY and HA supervised the research project. QA, HRY, AY, and HA developed the musculoskeletal model. QA, FA, and SS developed the measurement system. RW, QA, NY, HK, KY, HY, SS, HRY, MY, NH, KT, TF, and HO performed the measurement experiment and collected the data. NY and SS organized the database. RW, QA, and HH processed and analyzed the data. HH, SS, NH, IM, AY, and HA contributed critical review of the experiment procedure, physical therapy, patient rehabilitation, and method implementation. RW and QA wrote the manuscript. All authors read, revised, and approved the submitted manuscript.

FUNDING

This research was supported by JSPS KAKENHI Grant Numbers 19H05729, 19K22799, and 18H01405.

ACKNOWLEDGMENTS

The authors gratefully acknowledge the assistance of the staff at the Morinomiya Hospital and all the participants in helping with the experiments over the years.

REFERENCES

An, Q., Ishikawa, Y., Aoi, S., Funato, T., Oka, H., Yamakawa, H., et al. (2015). "Analysis of muscle synergy contribution on human standing-up motion using a neuro musculoskeletal model," in *2015 IEEE Int. Conf. Robot. Autom. (ICRA).* (Seattle, WA), 5885–5890.

An, Q., Ishikawa, Y., Funato, T., Aoi, S., Oka, H., Yamakawa, H., Yamashita, A., and Asama, H. (2014). "Generation of human standing-up motion with muscle synergies using forward dynamic simulation," in *2014 IEEE Int. Conf. Robot. Autom. (ICRA).* (Hong Kong), 730–735.

Arnold, E. M., Ward, S. R., Lieber, R. L., and Delp, S. L. (2010). A model of the lower limb for analysis of human movement. *Ann. Biomed. Eng.* 38, 269–279. doi: 10.1007/s10439-009-9852-5

Awad, L. N., Lewek, M. D., Kesar, T. M., Franz, J. R., and Bowden, M. G. (2020). These legs were made for propulsion: advancing the diagnosis and treatment of post-stroke propulsion deficits. *J. NeuroEng. Rehabil.* 17, 139. doi: 10.1186/s12984-020-00747-6

Bernstein, N. A. (1967). *The Co-Ordination and Regulation of Movements.* Oxford: Pergamon Press.

Besomi, M., Hodges, P. W., Clancy, E. A., Van Dieën, J., Hug, F., Lowery, M., et a. (2020). Consensus for experimental design in electromyography (CEDE) project: Amplitude normalization matrix. *J. Electromyogr. Kinesiol.* 53, 102438. doi: 10.1016/j.jelekin.2020.102438

Blanc, Y., and Dimanico, U. (2010). Electrode placement in surface electromyography (sEMG) minimal crosstalk area (MCA). *Open Rehabil. J.* 3, 110–126. doi: 10.2174/1874943701003010110

Cheng, P.-T., Chen, C.-L., Wang, C.-M., and Hong, W.-H. (2004). Leg muscle activation patterns of sit-to-stand movement in stroke patients. *Am. J. Phys. Med. Rehabil.* 83, 10–16. doi: 10.1097/01.PHM.0000104665.34557.56

Cheng, P.-T., Liaw, M.-Y., Wong, M.-K., Tang, F.-T., Lee, M.-Y., and Lin, P.-S. (1998). The sit-to-stand movement in stroke patients and its correlation with falling. *Arch. Phys. Med. Rehabil.* 79, 1043–1046. doi: 10.1016/s0003-9993(98)90168-x

Cheung, V. C. K., d'Avella, A., Tresch, M. C., and Bizzi, E. (2005). Central and sensory contributions to the activation and organization of muscle synergies during natural motor behaviors. *J. Neurosci.* 25, 6419–6434. doi: 10.1523/JNEUROSCI.4904-04.2005

Chou, S.-W., Wong, A. M. K., Leong, C.-P., Hong, W.-S., Tang, F.-T., and Lin, T.-H. (2003). Postural control during sit-to stand and gait in stroke patients. *Am. J. Phys. Med. Rehabil.* 82, 42–47. doi: 10.1097/00002060-200301000-00007

Christophy, M., Senan, N. A. F., Lotz, J. C., and O'Reilly, O. M. (2012). A musculoskeletal model for the lumbar spine. *Biomech. Model Mechanobiol.* 11, 19–34. doi: 10.1007/s10237-011-0290-6

Clark, D. J., Ting, L. H., Zajac, F. E., Neptune, R. R., and Kautz, S. A. (2010). Merging of healthy motor modules predicts reduced locomotor performance and muscle coordination complexity post-stroke. *J. Neurophysiol.* 103, 844–857. doi: 10.1152/jn.00825.2009

Davy, D. T., and Audu, M. L. (1987). A dynamic optimization technique for predicting muscle forces in the swing phase of gait. *J. Biomech.* 20, 187–201. doi: 10.1016/0021-9290(87)90310-1

de Sousa, D. G., Harvey, L. A., Dorsch, S., Varettas, B., Jamieson, S., Murphy, A., et al. (2019). Two weeks of intensive sit-to-stand training in addition to usual care improves sit-to-stand ability in people who are unable to stand up independently after stroke: a randomised trial. *J. Physiother.* 65, 152–158. doi: 10.1016/j.jphys.2019.05.007

Del Vecchio, A., Negro, F., Felici, F., and Farina, D. (2017). Associations between motor unit action potential parameters and surface EMG features. *J. Appl. Physiol. (1985).* 123, 835–843. doi: 10.1152/japplphysiol.00482.2017

Eberle, H., Hayashi, Y., Kurazume, R., Takei, T., and An, Q. (2021). Modeling of hyper-adaptability: from motor coordination to rehabilitation. *Adv. Robot.* 35, 802–817. doi: 10.1080/01691864.2021

Edgerton, V. R., Wolf, S. L., Levendowski, D. J., and Roy, R. R. (1996). Theoretical basis for patterning emg amplitudes to assess muscle dysfunction. *Med. Sci. Sports Exerc.* 28, 744–751. doi: 10.1097/00005768-199606000-00013

Ellis, M. D., Schut, I., and Dewald, J. P. A. (2017). Flexion synergy overshadows flexor spasticity during reaching in chronic moderate to severe hemiparetic stroke. *Clin. Neurophysiol.* 128, 1308–1314. doi: 10.1016/j.clinph.2017.04.028

Enoka, R. M., and Duchateau, J. (2015). Inappropriate interpretation of surface EMG signals and muscle fiber characteristics impedes understanding of the control of neuromuscular function. *J. Appl. Physiol. (1985).* 119, 1516–1518. doi: 10.1152/japplphysiol.00280.2015

Farina, D. (2006). Interpretation of the surface electromyogram in dynamic contractions. *Exerc. Sport. Sci. Rev.* 34, 121–127. doi: 10.1249/00003677-200607000-00006

Farina, D., Merletti, R., and Enoka, R. M. (2004). The extraction of neural strategies from the surface emg. *J. Appl. Physiol. (1985).* 96, 1486–1495. doi: 10.1152/japplphysiol.01070.2003

Fugl-Meyer, A. R., Jääskö, L., Leyman, I., Olsson, S., and Steglind, S. (1975). The post-stroke hemiplegic patient. 1. a method for evaluation of physical performance. *Scand. J. Rehabil. Med.* 7, 13–31.

Gizzi, L., Nielsen, J. F., Felici, F., Ivanenko, Y. P., and Farina, D. (2011). Impulses of activation but not motor modules are preserved in the locomotion of subacute stroke patients. *J. Neurophysiol.* 106, 202–210. doi: 10.1152/jn.00727.2010

Hatem, S. M., Saussez, G., della Faille, M., Prist, V., Zhang, X., Dispa, D., et al. (2016). Rehabilitation of motor function after stroke: a multiple systematic review focused on techniques to stimulate upper extremity recovery. *Front. Hum. Neurosci.* 10, 442. doi: 10.3389/fnhum.2016.00442

Hatze, H. (1977). A myocybernetic control model of skeletal muscle. *Biol. Cybern.* 25, 103–119.

Hermens, H. J., Freriks, B., Disselhorst-Klug, C., and Rao, G. (2000). Development of recommendations for SEMG sensors and sensor placement procedures. *J. Electromyogr. Kinesiol.* 10, 361–374. doi: 10.1016/s1050-6411(00)00027-4

Hicks, J. L., Uchida, T. K., Seth, A., Rajagopal, A., and Delp, S. L. (2015). Is my model good enough? best practices for verification and validation of musculoskeletal models and simulations of movement. *J. Biomech. Eng.* 137, 020905. doi: 10.1115/1.4029304

Hirashima, M., and Oya, T. (2015). How does the brain solve muscle redundancy? filling the gap between optimization and muscle synergy hypotheses. *Neurosci. Res.* 104, 80–87. doi: 10.1016/j.neures.2015.12.008

Hoang, H. X., Pizzolato, C., Diamond, L. E., and Lloyd, D. G. (2018). Subject-specific calibration of neuromuscular parameters enables neuromusculoskeletal models to estimate physiologically plausible hip joint contact forces in healthy adults. *J. Biomech.* 80, 111–120. doi: 10.1016/j.jbiomech.2018.08.023

Ivanenko, Y. P., Cappellini, G., Dominici, N., Poppele, R. E., and Lacquaniti, F. (2005). Coordination of locomotion with voluntary movements in humans. *J. Neurosci.* 25, 7238–7253. doi: 10.1523/JNEUROSCI.1327-05.2005

Ivanenko, Y. P., Poppele, R. E., and Lacquaniti, F. (2004). Five basic muscle activation patterns account for muscle activity during human locomotion. *J. Physiol.* 556, 267–282. doi: 10.1113/jphysiol.2003.057174

James, S. L., Abate, D., Abate, K. H., Abay, S. M., Abbafati, C., Abbasi, H., and et al. (2018). Global, regional, and national incidence, prevalence, and years lived with disability for 354 diseases and injuries for 195 countries and territories, 1990–2017: a systematic analysis for the Global Burden of Disease Study 2017. *Lancet.* 392, 1789–1858. doi: 10.1016/S0140-6736(18)32279-7

Jones, T. A. (2017). Motor compensation and its effects on neural reorganization after stroke. *Nat. Rev. Neurosci.* 18, 267–280. doi: 10.1038/nrn.2017.26

Kainz, H., Wesseling, M., and Jonkers, I. (2021). Generic scaled versus subject-specific models for the calculation of musculoskeletal loading in cerebral palsy gait: Effect of personalized musculoskeletal geometry outweighs the effect of personalized neural control. *Clin. Biomech. (Bristol, Avon)* 87, 105402. doi: 10.1016/j.clinbiomech.2021.105402

Kat, C.-J., and Els, P. S. (2012). Validation metric based on relative error. *Math. Comput. Model.. Dyn. Syst.* 18, 487–520. doi: 10.1080/13873954.2012.663392

Kogami, H., An, Q., Yang, N., Wang, R., Yoshida, K., Hamada, H., et al. (2021). Analysis of muscle synergy and kinematics in sit-to-stand motion of hemiplegic patients in subacute period. *Adv. Robot.* 35, 867–877. doi: 10.1080/01691864.2021.1928547

Kogami, H., An, Q., Yang, N., Yamakawa, H., Tamura, Y., Yamashita, A., et al. (2018). Effect of physical therapy on muscle synergy structure during standing-up motion of hemiplegic patients. *IEEE Robot. Autom. Lett.* 3, 2229–2236. doi: 10.1109/LRA.2018.2811050

Kutch, J. J., and Valero-Cuevas, F. J. (2011). Muscle redundancy does not imply robustness to muscle dysfunction. *J. Biomech.* 44, 1264–1270. doi: 10.1016/j.jbiomech.2011.02.014

Kutch, J. J., and Valero-Cuevas, F. J. (2012). Challenges and new approaches to proving the existence of muscle synergies of neural origin. *PLoS Comput. Biol.* 8, e1002434. doi: 10.1371/journal.pcbi.1002434

Kwakkel, G., Lannin, N. A., Borschmann, K., English, C., Ali, M., Churilov, L., et al. (2017). Standardized measurement of sensorimotor recovery in stroke trials: Consensus-based core recommendations from the stroke recovery and rehabilitation roundtable. *Neurorehabil. Neural Repair.* 31, 784–792. doi: 10.1177/1545968317732662

Laine, C. M., Cohn, B. A., and Valero-Cuevas, F. J. (2021). Temporal control of muscle synergies is linked with alpha-band neural drive. *J Physiol.* 599, 3385–3402. doi: 10.1113/JP281232

Langhorne, P., Bernhardt, J., and Kwakkel, G. (2011). Stroke rehabilitation. *Lancet.* 377, 1693–1702. doi: 10.1016/S0140-6736(11)60325-5

Lee, D. D., and Seung, H. S. (1999). Learning the parts of objects by non-negative matrix factorization. *Nature.* 401, 788–791. doi: 10.1038/44565

Liu, M. Q., Anderson, F. C., Schwartz, M. H., and Delp, S. L. (2008). Muscle contributions to support and progression over a range of walking speeds. *J. Biomech.* 41, 3243–3252. doi: 10.1016/j.jbiomech.2008.07.031

Lloyd, D. G., and Besier, T. F. (2003). An EMG-driven musculoskeletal model to estimate muscle forces and knee joint moments *in vivo*. *J. Biomech.* 36, 765–776. doi: 10.1016/s0021-9290(03)00010-1

Lomaglio, M. J., and Eng, J. J. (2005). Muscle strength and weight-bearing symmetry relate to sit-to-stand performance in individuals with stroke. *Gait Posture.* 22, 126–131. doi: 10.1016/j.gaitpost.2004.08.002

Lum, P. S., Burgar, C. G., Shor, P. C., Majmundar, M., and der Loos, M. V. (2002). Robot-assisted movement training compared with conventional therapy techniques for the rehabilitation of upper-limb motor function after stroke. *Arch. Phys. Med. Rehabil.* 83, 952–959. doi: 10.1053/apmr.2001.33101

MATLAB, 2021. version 9.10.0.1602886 (2021), Natick, Massachusetts: The MathWorks Inc.

McDonald, J. H. (2014). *Handbook of biological statistics (3rd ed.)*. Baltimore, MD: Sparky House Publishing.

Mehrabi, N., Schwartz, M. H., and Steele, K. M. (2019). Can altered muscle synergies control unimpaired gait? *J. Biomech.* 90, 84–91. doi: 10.1016/j.jbiomech.2019.04.038

Mileti, I., Zampogna, A., Santuz, A., Asci, F., Del Prete, Z., Arampatzis, A., et al. (2020). Muscle synergies in Parkinson's disease. *Sensors (Basel).* 20, 3209. doi: 10.3390/s20113209

Mukaka, M. (2012). A guide to appropriate use of correlation coefficient in medical research. *Malawi Med. J.* 24, 69–71.

Neptune, R. R., Clark, D. J., and Kautz, S. A. (2009). Modular control of human walking: a simulation study. *J. Biomech.* 42, 1282–1287. doi: 10.1016/j.jbiomech.2009.03.009

Ogihara, N., and Yamazaki, N. (2001). Generation of human bipedal locomotion by a bio-mimetic neuro-musculo-skeletal model. *Biol. Cybern.* 84, 1–11. doi: 10.1007/PL00007977

Oliveira, A. S., Gizzi, L., Farina, D., and Kersting, U. G. (2014). Motor modules of human locomotion: influence of EMG averaging, concatenation, and number of step cycles. *Front. Hum. Neurosci.* 8, 335. doi: 10.3389/fnhum.2014.00335

Prudente, C., Rodrigues-de-Paula, F., and Faria, C. (2013). Lower limb muscle activation during the sit-to-stand task in subjects who have had a stroke. *Am. J. Phys. Med. Rehabil.* 92, 666–675. doi: 10.1097/PHM.0b013e318282c87a

Raez, M. M. I., Hussain, M. S., and Mohd-Yasin, F. (2006). Techniques of emg signal analysis: detection, processing, classification and applications. *Biol. Proced. Online.* 8, 11–35. doi: 10.1251/bpo115

Redl, C., Gfoehler, M., and Pandy, M. G. (2007). Sensitivity of muscle force estimates to variations in muscle-tendon properties. *Hum. Mov. Sci.* 26, 306–319. doi: 10.1016/j.humov.2007.01.008

Riener, R., and Fuhr, T. (1998). Patient-driven control of FES-supported standing up: a simulation study. *IEEE Trans. Neural Syst. Rehabil. Eng.* 6, 113–124. doi: 10.1109/86.681177

Roh, J., Rymer, W. Z., Perreault, E. J., Yoo, S. B., and Beer, R. F. (2013). Alterations in upper limb muscle synergy structure in chronic stroke survivors. *J. Neurophysiol.* 109, 768–781. doi: 10.1152/jn.00670.2012

Rosner, B., Glynn, R. J., and Lee, M.-L. T. (2006). The wilcoxon signed rank test for paired comparisons of clustered data. *Biometrics.* 62, 185–192. doi: 10.1111/j.1541-0420.2005.00389.x

Schenkman, M., Berger, R. A., Riley, P. O., Mann, R. W., and Hodge, W. A. (1990). Whole-body movements during rising to standing from sitting. *Phys. Ther.* 70, 638–648. doi: 10.1093/ptj/70.10.638

Scheys, L., Campenhout, A. V., Spaepen, A., Suetens, P., and Jonkers, I. (2008). Personalized MR-based musculoskeletal models compared to rescaled generic models in the presence of increased femoral anteversion: effect on hip moment arm lengths. *Gait Posture* 28, 358–365. doi: 10.1016/j.gaitpost.2008

Scovil, C. Y., and Ronsky, J. L. (2006). Sensitivity of a Hill-based muscle model to perturbations in model parameters. *J. Biomech.* 39, 2055–2063. doi: 10.1016/j.jbiomech.2005.06.005

Shuman, B. R., Goudriaan, M., Desloovere, K., Schwartz, M. H., and Steele, K. M. (2019). Muscle synergy constraints do not improve estimates of muscle activity from static optimization during gait for unimpaired children or

children with cerebral palsy. *Front. Neurorobot.* 13, 102. doi: 10.3389/fnbot.2019.00102

Silva, A., Sousa, A. S. P., Pinheiro, R., Ferraz, J., Tavares, J. M. R. S., Santos, R., et al. (2013). Activation timing of soleus and tibialis anterior muscles during sit-to-stand and stand-to-sit in post-stroke vs. healthy subjects. *Somatosens Mot Res.* 30, 48–55. doi: 10.3109/08990220.2012.754755

Staudenmann, D., Roeleveld, K., Stegeman, D. F., and van Dieën, J. H. (2010). Methodological aspects of SEMG recordings for force estimation–a tutorial and review. *J. Electromyogr. Kinesiol.* 20, 375–387. doi: 10.1016/j.jelekin.2009.08.005

Steele, K. M., Rozumalski, A., and Schwartz, M. H. (2015). Muscle synergies and complexity of neuromuscular control during gait in cerebral palsy. *Dev. Med. Child Neurol.* 57, 1176–1182. doi: 10.1111/dmcn.12826

Steele, K. M., Tresch, M. C., and Perreault, E. J. (2013). The number and choice of muscles impact the results of muscle synergy analyses. *Front. Comput. Neurosci.* 7, 105. doi: 10.3389/fncom.2013.00105

Sterling, D. A., O'Connor, J. A., and Bonadies, J. (2001). Geriatric falls: injury severity is high and disproportionate to mechanism. *J. Trauma.* 50, 116–119. doi: 10.1097/00005373-200101000-00021

Tresch, M. C., and Jarc, A. (2009). The case for and against muscle synergies. *Curr. Opin. Neurobiol.* 19, 601–607. doi: 10.1016/j.conb.2009.09.002

Trinler, U., Hollands, K., Jones, R., and Baker, R. (2018). A systematic review of approaches to modelling lower limb muscle forces during gait: Applicability to clinical gait analyses. *Gait Posture.* 61, 353–361. doi: 10.1016/j.gaitpost.2018.02.005

United Nations (2019). *World population ageing 2019.* Technical Report ST/ESA/SER.A/444, Department of Economic and Social Affairs, Population Division, United Nation, New York, NY.

Vena, D., Novak, A. C., King, E. C., Dutta, T., and Fernie, G. R. (2015). The evaluation of vertical pole configuration and location on assisting the sit-to-stand movement in older adults with mobility limitations. *Assist. Technol.* 27, 208–218. doi: 10.1080/10400435.2015.1030514

Vigotsky, A. D., Halperin, I., Lehman, G. J., Trajano, G. S., and Vieira, T. M. (2018). Interpreting signal amplitudes in surface electromyography studies in sport and rehabilitation sciences. *Front.. Physiol.* 8, 985. doi: 10.3389/fphys.2017.00985

Walter, J. P., Kinney, A. L., Banks, S. A., D'Lima, D. D., Besier, T. F., Lloyd, D. G., et al. (2014). Muscle synergies may improve optimization prediction of knee contact forces during walking. *J. Biomech. Eng.* 136, 021031. doi: 10.1115/1.4026428

Wang, R., An, Q., Yang, N., Kogami, H., Yoshida, K., Hamada, H., et al. (2022). 11Muscle tension analysis in stroke patient sit-to-stand motion by joint torque-based normalization," in *Converging Clinical and Engineering Research on Neurorehabilitation IV. ICNR 2020. Biosystems & Biorobotics*, Vol. 28, eds D. Torricelli, M. Akay, and J. Pons (Cham: Springer), 809–813.

Ward, S. R., Eng, C. M., Smallwood, L. H., and Lieber, R. L. (2009). Are current measurements of lower extremity muscle architecture accurate? *Clin. Orthop. Relat. Res.* 467, 1074–1082. doi: 10.1007/s11999-008-0594-8

World Health Organization (2019). *Global Health Estimates: Life Expectancy and Leading Causes of Death and Disability*. Geneva: World Health Organization, www.who.int/data/gho/data/themes/mortality-and-global-health-estimates (Retrieved August 2021.

Yang, N., An, Q., Kogami, H., Yamakawa, H., Tamura, Y., Takahashi, K., et al. (2019). Temporal features of muscle synergies in sit-to-stand motion reflect the motor impairment of post-stroke patients. *IEEE Trans. Neural Syst. Rehabil. Eng.* 27, 2118–2127. doi: 10.1109/TNSRE.2019.2939193

Yang, N., An, Q., Yamakawa, H., Tamura, Y., Yamashita, A., Takahashi, K., et al. (2017). "Clarification of muscle synergy structure during standing-up motion of healthy young, elderly and post-stroke patients," in *IEEE Int. Conf. Rehabil. Robot.* (London), 19–24.

Zajac, F. E. (1989). Muscle and tendon: properties, models, scaling, and application to biomechanics and motor control. *Crit. Rev. Biomed. Eng.* 17, 359–411.

Conflict of Interest: The authors declare that the research was conducted in the absence of any commercial or financial relationships that could be construed as a potential conflict of interest.

Publisher's Note: All claims expressed in this article are solely those of the authors and do not necessarily represent those of their affiliated organizations, or those of the publisher, the editors and the reviewers. Any product that may be evaluated in this article, or claim that may be made by its manufacturer, is not guaranteed or endorsed by the publisher.

Copyright © 2022 Wang, An, Yang, Kogami, Yoshida, Yamakawa, Hamada, Shimoda, Yamasaki, Yokoyama, Alnajjar, Hattori, Takahashi, Fujii, Otomune, Miyai, Yamashita and Asama. This is an open-access article distributed under the terms of the Creative Commons Attribution License (CC BY). The use, distribution or reproduction in other forums is permitted, provided the original author(s) and the copyright owner(s) are credited and that the original publication in this journal is cited, in accordance with accepted academic practice. No use, distribution or reproduction is permitted which does not comply with these terms.

frontiers in Systems Neuroscience

ORIGINAL RESEARCH
published: 16 March 2022
doi: 10.3389/fnsys.2022.800628

Neural Network Models for Spinal Implementation of Muscle Synergies

*Yunqing Song[1], Masaya Hirashima[2,3] and Tomohiko Takei[1,4,5]**

[1] Graduate School of Medicine, Kyoto University, Kyoto, Japan, [2] Center for Information and Neural Networks (CiNet), Advanced ICT Research Institute, National Institute of Information and Communications Technology (NICT), Suita, Japan, [3] Graduate School of Frontier Biosciences, Osaka University, Suita, Japan, [4] The Hakubi Center for Advanced Research, Kyoto University, Kyoto, Japan, [5] Brain Science Institute, Tamagawa University, Machida, Japan

Muscle synergies have been proposed as functional modules to simplify the complexity of body motor control; however, their neural implementation is still unclear. Converging evidence suggests that output projections of the spinal premotor interneurons (PreM-INs) underlie the formation of muscle synergies, but they exhibit a substantial variation across neurons and exclude standard models assuming a small number of unitary "modules" in the spinal cord. Here we compared neural network models for muscle synergies to seek a biologically plausible model that reconciles previous clinical and electrophysiological findings. We examined three neural network models: one with random connections (non-synergy model), one with a small number of spinal synergies (simple synergy model), and one with a large number of spinal neurons representing muscle synergies with a certain variation (population synergy model). We found that the simple and population synergy models emulate the robustness of muscle synergies against cortical stroke observed in human stroke patients. Furthermore, the size of the spinal variation of the population synergy matched well with the variation in spinal PreM-INs recorded in monkeys. These results suggest that a spinal population with moderate variation is a biologically plausible model for the neural implementation of muscle synergies.

Keywords: muscle synergies, optimization, spinal interneurons, neural manifold, redundancy

OPEN ACCESS

Edited by:
Stefano Panzeri,
University of Trento, Italy

Reviewed by:
Andrea d'Avella,
University of Messina, Italy
Simon Giszter,
Drexel University, United States

****Correspondence:***
Tomohiko Takei
takei@lab.tamagawa.ac.jp

Received: *23 October 2021*
Accepted: *23 February 2022*
Published: *16 March 2022*

Citation:
Song Y, Hirashima M and Takei T (2022) Neural Network Models for Spinal Implementation of Muscle Synergies. Front. Syst. Neurosci. 16:800628. doi: 10.3389/fnsys.2022.800628

INTRODUCTION

Our body is remarkably complex, yet we display a highly stable motor performance. For example, to reach for a coffee cup on a desk, there are an infinite number of patterns of muscle activity involved in extending the arm because multiple muscles span the same joint. Nevertheless, we show a highly stereotyped movement trajectory and agonist-antagonist muscle activity patterns (Morasso, 1981). Understanding how the central nervous system (CNS) coordinates the redundant musculoskeletal system is a central question of motor control.

Muscle synergies have been proposed as a solution to control redundant systems by coordinating a number of muscles with a smaller number of control modules, which are called muscle synergies (Tresch et al., 1999; Bizzi et al., 2002; d'Avella et al., 2003). This hypothesis is phenomenologically supported by experimental observations that a linear combination of basic patterns of muscle activity successfully reconstructs muscle activity during a wide range of behaviors, including reflex movements (Tresch et al., 1999; Cheung et al., 2005), postural tasks (Torres-Oviedo et al., 2006;

Ting and McKay, 2007), locomotion (Ivanenko et al., 2004; Krouchev et al., 2006; Dominici et al., 2011), reaching, and grasping (d'Avella et al., 2006; Overduin et al., 2008; Takei et al., 2017). However, there is still a heated debate regarding whether these experimental observations reflect a physiological basis of low-dimensional control in the CNS or an epiphenomenon based on task constraints and/or biomechanics (Tresch and Jarc, 2009; Kutch and Valero-Cuevas, 2012; Lillicrap and Scott, 2013; Hirashima and Oya, 2016).

Hirashima and Oya (2016) demonstrated that a neural network model that did not explicitly assume muscle synergies in the model could produce a synergy-like low-dimensional structure in muscle activity when the network was optimized to produce different combinations of elbow and shoulder torques while minimizing motor effort and motor error (Hirashima and Oya, 2016). This clearly shows that the mere fact that muscle synergies can be extracted from muscle activity is not enough to separate the presence or absence of underlying neural modules in the control system. Therefore, to examine the existence of muscle synergies, it is essential to identify the neural implementation of muscle synergies in the nervous system and develop a biologically plausible model.

Accumulating evidence from physiological and anatomical studies suggests that spinal premotor interneurons (PreM-INs) to motoneuron pools are the neural basis of muscle synergies in frogs (Kargo and Giszter, 2000, 2008; Hart and Giszter, 2010; Kargo et al., 2010), rodents (Levine et al., 2014), and primates (Takei and Seki, 2010, 2013; Takei et al., 2017). For the hindlimb control in frogs, it has been established that neural circuits for muscle synergies are implemented in the spinal cord (Kargo and Giszter, 2000, 2008; Kargo et al., 2010). Furthermore, output projections of PreM-INs identified by spike-triggered averaging showed a significant correlation with output patterns of extracted muscle synergies during wiping reflexes (Hart and Giszter, 2010). For the upper limb control in primates, our previous study demonstrated that cervical spinal PreM-INs have a divergent projection to multiple hand and arm motoneurons (Takei and Seki, 2010, 2013) and their spatial distribution corresponds to the spatial weight of muscle synergies extracted from muscle activity (Takei et al., 2017). These results suggest the contribution of spinal PreM-INs to the generation of muscle synergies. However, while the output projection of each PreM-IN corresponded to the muscle synergies, they also showed a substantial variation in the projection patterns across PreM-INs. Moreover, their temporal activation patterns were heterogeneous and were not clustered as muscle synergies at the individual neuron level. This finding clearly contradicts the assumption that each muscle synergy can be modeled as a unitary "module," where single or population neurons are synchronously activated by common inputs and act as fixed units. Such unitary modules are implicitly or explicitly assumed when applying linear decomposition methods such as non-negative matrix factorization (NNMF). Therefore, the development of neural models to explain how muscle synergies are implemented with divergent spinal PreM-INs has been awaited to reconcile physiological findings.

Here, we created neural network models for muscle synergies and compared their performance to explain a known experimental phenomenon: the robustness of muscle synergies for cortical stroke (Cheung et al., 2009, 2012). In experiment 1, we examined the existence of muscle synergies by comparing two neural network models: one with random connections from the cortical layer to the muscle layer (non-synergy model) and the other with a small number of spinal synergies in the middle (simple synergy model). Then, in experiment 2, we sought a more biologically plausible model for muscle synergies by allowing a certain level of variation in spinal neurons that constitute muscle synergies (population synergy model). Our results demonstrate that (1) the simple and population synergy models emulate the robustness against cortical stroke that was observed in human stroke patients, and that (2) the population synergy model has a similar performance to the simple synergy model when the spinal variation was moderate, as in the variations of spinal PreM-IN recorded in non-human primates in our previous study (Takei et al., 2017). These results suggest that the population synergy model with a moderate spinal variation is a biologically plausible model for neural implementation of muscle synergy to achieve robust motor control.

MATERIALS AND METHODS

Neural Network Models

We compared three types of neural network models for neural implementation of muscle synergy: (1) non-synergy model, (2) simple synergy model, and (3) population synergy model.

Non-synergy Model

The non-synergy model was the same as the neural network model in previous studies (Hirashima and Nozaki, 2012; Hirashima and Oya, 2016). Briefly, a feedforward neural network was used to convert the desired torque (input layer) into the actual torque (output layer) through an intermediate layer composed of 1,000 cortical neurons and eight muscles (**Figure 1A**). Each cortical neuron received the desired torque vector (τ) from the input layer with synaptic weights (W). Then, the cortical neurons projected to the muscles with innervation weights (Z). The innervation weights from each cortical neuron to muscles were established so that Z_i (i = 1–1,000) were uniformly distributed on the surface of a sphere in an 8-dimensional space, with a radius of 0.002 (=2/n). The eight muscles included two shoulder flexors (outer and inner shoulder flexors: SFo and SFi, respectively), two shoulder extensors (outer and inner shoulder extensors: SEo and SEi, respectively), an elbow flexor and extensor (EF and EE, respectively), and a biarticular flexor and extensor (BiF and BiE, respectively). The mechanical effects of the muscles (mechanical direction vectors, MD vectors) were in line with those of the previous model (M) (Hirashima and Nozaki, 2012; Hirashima and Oya, 2016). Muscle activity (a) was constrained to be non-negative by replacing negative muscle activity with zero, which made the model non-linear ($a \geq 0$). The total output of the network (T) was expressed as the vector sum of the mechanical output of all muscles. The

synaptic weight from the input layer to the cortical neurons was initially selected from a standard normal distribution with a zero mean and unitary standard deviation. Then, it was modified by the error feedback-with-decay algorithm (Hirashima and Nozaki, 2012; Hirashima and Oya, 2016) (see section "Training Procedure").

Simple Synergy Model

In the simple synergy model, we added a spinal synergy layer between the cortical and muscle layers (**Figure 1B**). Other than the addition of the spinal synergy layer, the simple synergy model was identical to the non-synergy model. The cortical output to the spinal synergies (X) was similarly defined as the non-synergy model (Z), but the target number was different. To define the spinal synergies, we extracted muscle synergies from muscle activations produced by the optimized non-synergy model. After optimizing the non-synergy model in the learning simulation of 40,000 trials, we applied a non-negative matrix factorization (NNMF) to the muscle activation patterns during the last 100 trials of the training session. To determine the number of muscle synergies, we performed a four-fold cross validation of NNMF for the different numbers of muscle synergies (1–7), and plotted the averaged variance accounted for (VAF) as a function of the number of muscle synergies (**Figure 1E**). VAF was calculated as VAF = 1 – SSE/SST, where SSE is the sum of the squares of residual errors, and SST is the sum of the square differences between each data point and the overall mean. Similar to Hirashima and Oya (2016), we successfully extracted four muscle synergies from their non-synergy network model based on the criterion that the VAF exceeds 0.90 (Hirashima and Oya, 2016). To maintain consistency in the muscle synergy extraction, we set the number of synergies to four for the following NNMF analyses. The synergy weights (Sy1–4) of the non-synergy model were used to define the output of the four spinal synergies (V) in the simple synergy model. In this regard, the synergies explicitly defined in the simple synergy model were identical to the muscle synergies that were originally extracted from the non-synergy model, which are referred to as original synergies. This procedure is particularly critical when testing the robustness of muscle synergies because the previous study demonstrated that different synergies could be extracted when NNMF is executed from different initial values (Hirashima and Oya, 2016). By applying the muscle synergies extracted from the non-synergy model to the other model, we controlled the initial synergy structure of both models to be the same.

Population Synergy Model

In experiment 2, we further tested another synergy model, in which there were 100 spinal neurons (n = 100). Initially, each group of 25 spinal neurons was provided one of the synergy weights (Sy1–4) for their outputs (V). Then, by adding a different proportion of Gaussian noise to the synergy weights (V), we systematically created population synergy models with different spinal variation levels. The output weights of each spinal neuron (V_i, i = 1–100) was obtained by mixing the original synergy weights (Sy_k, k = 1–4) with Gaussian noise (ω), which was normalized to the norm to be unitary, with a certain proportion (ρ):

$$V_i = (1-\rho)\mathrm{Sy} + \rho\omega$$

By changing the proportion of noise (ρ) from 0 to 1, we systematically investigated the synergy models which had different spinal variations, replicating a variation of the spinal PreM-INs recorded in monkeys performing a precision grip task (Takei et al., 2017). The silhouette value was calculated to evaluate the clustering of the spinal neurons with regard to their similarity to the original synergies (Sy1–4) (Rousseeuw, 1987).

Isometric Torque Production Task

We trained each network to perform isometric torque production tasks using a two-joint system (shoulder and elbow) (Herter et al., 2007). The target torque combination was chosen from eight possible torque combinations [shoulder flexion (SF), shoulder and elbow flexion (SF + EF), elbow flexion (EF), shoulder extension and elbow flexion (SE + EF), shoulder extension (SE), shoulder and elbow extension (SE + EE), elbow extension (EE), and shoulder flexion and elbow extension (SF + EE)] with the norm of 1 Nm.

Training Procedure

The synaptic weight from the input layer to the cortical neurons (W) was modified using the error feedback-with-decay algorithm (Hirashima and Nozaki, 2012; Hirashima and Oya, 2016):

$$\Delta W_{ij} = -\alpha \frac{\partial J_e}{\partial W_{ij}} - \beta W_{ij}$$

where, α is the learning rate (α = 20) and J_e is the error cost, as calculated by the error vector ($e = T - \tau$) between the output torque and the desired torque: $J_e = 1/2e^T e$. The second term indicates that the changes in synaptic weight due to synaptic memory decay in each step are proportional to the current synaptic weight W_{ij}. The decay rate β was set to 1.0×10^{-4}, which is much smaller than the learning rate (α = 20). By randomly presenting one of the eight target torque combinations in 40,000 trials and modifying the synaptic weight (W) after each trial, the network was trained to produce the appropriate output torque. The step-by-step update of W for the non-synergy model can be written as:

$$\begin{aligned} W(t+1) &= W(t) + \Delta W(t) \\ &= W(t) + \left(-\alpha \frac{\partial J_e}{\partial W(t)} - \beta W(t)\right) \\ &= W(t) - \alpha Z^T M^T (MZW(t) - I)\,\tau(t)\,\tau(t)^T \\ &\quad -\beta W(t) \qquad (1) \end{aligned}$$

This update procedure has been mathematically proven to reach an optimal solution for linear models (Hirashima and Nozaki, 2012). To incorporate the non-linearity of our model, where muscle activity is constrained to be non-negative ($a \geq 0$), we modified M by replacing the MD vector with $[0,0]^T$ if the

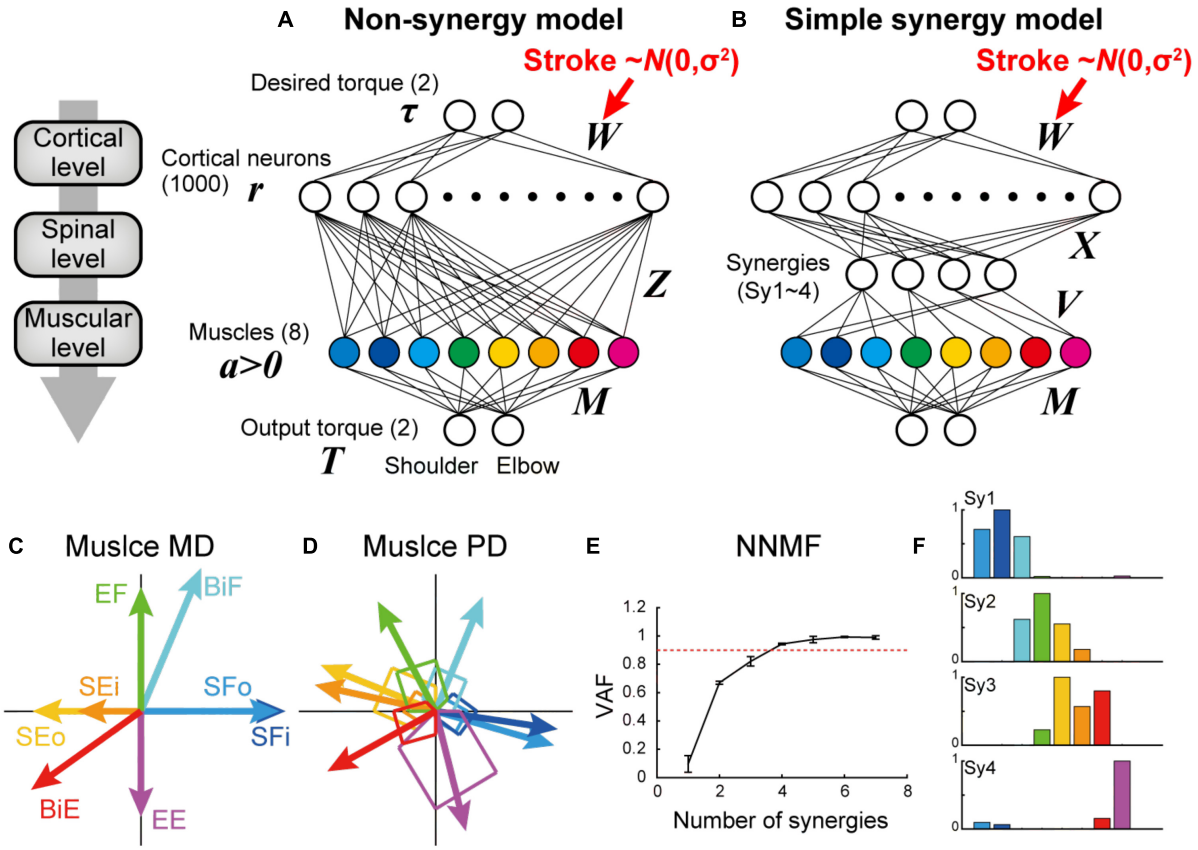

FIGURE 1 | Non-synergy and simple synergy models for shoulder and elbow torque task. **(A,B)** Neural network model without (non-synergy model, **A**) or with a synergy layer (simple synergy model, **B**). Cortical stroke was modeled as an addition of Gaussian noise to *W*. **(C)** Mechanical direction (MD) for the eight muscle groups. **(D)** Preferred direction (PD) after optimization with the non-synergy model shown in panel **(A)**. **(E)** Cross-validation procedures of non-negative matrix factorization (NNMF) to select the number of muscle synergies. NNMF was applied to the muscle activations of the last 100 trials in the learning simulation with the non-synergy model shown in panel **(A)**. Error bars: standard deviation. **(F)** Muscle synergies extracted from the non-synergy model. Note that these synergy weights (Sy1–4) were used to define the output of four synergies (*V*) in the simple synergy model shown in panel **(B)**.

muscle activity generated at each step $[a = ZW(t)\tau(t)]$ was negative ($a < 0$). With the modified MD vector, $\tilde{M}$, the update equation [Eq. (1)] can be rewritten as:

$$W(t+1) = W(t) - \alpha Z^T \tilde{M}^T \left(\tilde{M}ZW(t) - I\right) \tau(t) \tau(t)^T - \beta W(t) \quad (2)$$

This procedure eliminates the effect of negative muscle activity by disabling the mechanical output of the muscles. Our previous numerical simulation demonstrated that our training procedure can make the non-linear system reach a solution qualitatively similar to the optimal solution derived by the linear model. This was demonstrated by the fact that the synaptic weight matrix (W) is aligned orthogonally to the mechanical property matrix (M) of the muscle, which is an essential property of the optimal solution (i.e., pseudo-inverse of M) (Hirashima and Nozaki, 2012). For the synergy model (simple or population synergy model), Z in Eq. (1) and (2) is replaced with VX.

Stroke Model

To simulate the situation of cortical stroke, we added Gaussian noise ($\sim N[0, \sigma^2]$) to the cortical synaptic weights (Stroke, **Figures 1A,B**, **6A,B**), since previous human imaging studies showed that the long-scale entropy of MEG signal increased in perilesional tissues in stroke patients (Kielar et al., 2016). We systematically changed the stroke size (σ) from 0 to 10 standard deviations (SD) of the original synaptic weights (W). We sampled 200 different stroke cases for each stroke size (σ = 0–10) and evaluated their task performance.

Evaluation of Task Performance and Muscle Synergies

To evaluate the stroke effect on task performance and muscle synergies, we used 96 target torque combinations (32 uniformly distributed torque directions × 3 amplitudes [0.5, 1, and 2 Nm]) instead of the eight trained torque combinations. We quantified two types of performance errors, directional error and amplitude error, as a function of stroke size. The directional error was defined as the angle between the target torque vector and the

torque vector output by the model. The amplitude error was defined as the difference between the amplitude of the target torque and the model output. Both errors were calculated for each stroke size, and the absolute values were averaged across the 200 stroke cases.

To evaluate the consistency of muscle activation patterns, we quantified the shift in the preferred direction (ΔPD). PD was defined as the direction in which the muscle is maximally active and it was calculated by the summation of the target torque vectors weighted by muscle activity. ΔPD was defined as the absolute shift in PD from no stroke cases ($\sigma = 0$).

To evaluate the robustness of muscle synergies in cortical stroke, we quantified two different measures: VAF by the original muscle synergies and similarity of muscle synergies to the original muscle synergies. For these evaluations, we used muscle activations during the same 96 target torque combinations. To evaluate the VAF by the original muscle synergies (Sy1–4), we applied NNMF for muscle activation without updating the synergy weights (Sy1–4). We then calculated the VAF between the observed and reconstructed muscle activity. This measure indicates how much variance in muscle activity can be explained by the original muscle synergies (Sy1–4). Note that the synergy weights (V) for the simple and population synergy models were derived from the original muscle synergies extracted from the non-synergy model (see section "Neural Network Models"). Therefore, we expect that the VAF by the original muscle synergies will be the same for all synergy models under the intact ($\sigma = 0$). and no spinal variation ($\rho = 0$) conditions. We also compared the similarity of muscle synergies extracted in each stroke case with the original muscle synergies. We applied NNMF to muscle activity to extract muscle synergies for each stroke case. For this extraction, we did not use n-fold cross validation, and the number of muscle synergies was fixed at four to allow for a consistent comparison. Then, we calculated the dot product between the extracted synergies and the original synergies. We used the max dot product to determine the similarity of each muscle synergy and averaged the values across the four synergies. This measurement represents the consistency of the muscle synergies between different stroke conditions.

Statistical Analyses

To test the significance of the effect of different neural network models on performance measures (directional error, amplitude error, ΔPD, VAF by the original synergies, and similarity with the original synergies), we used the bootstrap method. For the two groups of parameter samples ($n = 200$), we first calculated the original difference in the mean of two populations (Δmean). Then, we pooled the two populations, resampled two populations of the same size with replacement, and calculated the Δmean. This process was repeated 1,000 times to obtain a baseline distribution of the Δmean. We set the significance limits of this distribution to 0.23 (= 2.5/number of stroke conditions) and 99.77 (= 100 – 2.5/number of stroke conditions) percentile that matched a significance level of $p < 0.05$, with Bonferroni's correction. All simulations and analytical procedures were performed using MATLAB (MathWorks, RRID:SCR_001622).

RESULTS

Non-synergy and Simple Synergy Models Have Comparable Training Ability

In experiment 1, to test the existence of muscle synergies in the nervous system, we compared the task performance of the neural network model with and without muscle synergies (simple synergy vs. non-synergy models). In the non-synergy model, cortical neurons had random direct connections to the muscles (Z). Cortical activation patterns (W) were optimized to achieve the model to output the desired shoulder and elbow torques while minimizing the sum of squares of cortical activity (**Figure 1A**). As Hirashima and Oya (2016) demonstrated previously, the non-synergy model reproduced a shift in the preferred direction of muscles (**Figure 1D**) relative to their mechanical directions (**Figure 1C**), and the muscle activation patterns were successfully reconstructed with a linear combination of four muscle synergies (VAF $\geq$ 0.9, **Figures 1E,F**). We refer to the synergies extracted from the non-synergy model as the original synergies (Sy1–4, **Figure 1F**). In the simple synergy model, we added four spinal synergies between the cortical and muscle layers (**Figure 1B**). We set the output weight of the synergies (V) to be the same as the synergy weights extracted from the non-synergy model (Sy1–4, **Figure 1F**). Other than the addition of the synergy layer, the simple synergy model was the same as the non-synergy model.

First, we compared the learning performance of the non-synergy and simple synergy models. Both models were trained to produce eight combinations of shoulder and elbow torques while minimizing the sum of squared cortical activity (i.e., minimizing error cost and motor cost). **Figure 2A** shows the trial-dependent changes in the error magnitude averaged across the eight target conditions. After a 40,000-trial training, we found that learning converged in both models, and they reached similar residual errors (**Figure 2C**). However, during the training, the learning speeds differed. At the initial phase of the training (**Figure 2A**, left), the learning curve was steeper in the simple synergy model than in the non-synergy model, and the learning rate, fitted by an exponential curve, was higher in the simple synergy model (**Figure 2B**, $p < 0.05$, bootstrap test, $n = 1{,}000$). This indicates that learning progressed faster in the simple synergy model than in the non-synergy model. This result is consistent with the previous study, which examined the learning performance of similar network models (Hagio and Kouzaki, 2018). Furthermore, we also tested trial-dependent changes in the sum of squared cortical neural activity (**Figure 2D**). We found that after training, cortical activity was less for the simple synergy model than for the non-synergy model (**Figure 2E**). **Figure 3A** compares the distribution of activity size of cortical neurons in both models. This shows that the distribution is narrower in the simple synergy model than in the non-synergy model, and that the activity size is generally reduced rather than changed in a specific group of neurons. Interestingly, despite the prominent difference in cortical activity, the sum of squared muscle activity was the same for both models

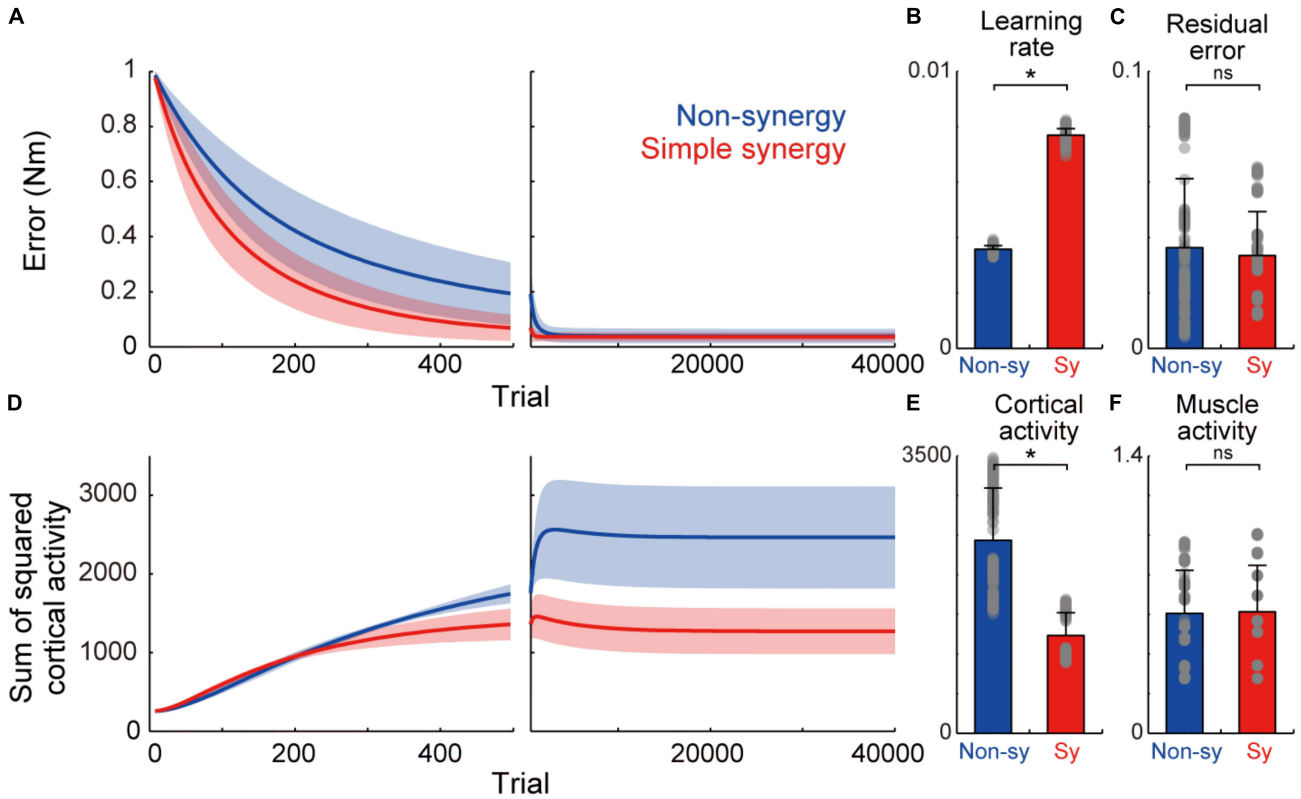

FIGURE 2 | Learning performance of non-synergy and simple synergy models. **(A)** Trial-dependent changes in the error magnitude for non-synergy (blue) and simple synergy model (red). Line and shade, mean and standard deviation across the simulations (n = 200). Trials of each set of eight targets were averaged for presentation purpose. **(B)** Averaged learning speed calculated by fitting of an exponential curve. Gray dots, each simulation. Error bar, standard deviation. **(C)** The same format but for residual error at the end of the training. **(D)** The same format but for the sum of squared cortical neural activity. **(E,F)** The same format but for the sum of squared activity of cortical neurons **(E)** and muscle activity **(F)** at the end of training. *$p < 0.05$; ns, non-significant; bootstrap test, n = 1,000.

(**Figure 2F**). These results indicate that the simple synergy model showed faster convergence of learning and smaller neural activity, although both models exhibited similar task performance.

Simple Synergy Model Exhibits a Higher Robustness Against Cortical Stroke Than Non-synergy Model

We compared the robustness of non-synergy and simple synergy models against cortical stroke. To simulate the situation of cortical stroke, we added random noise to the cortical connections (W) of different sizes (σ = 0–10 SD). We tested 200 different stroke cases for each stroke size. **Figure 4** shows three examples of torque output by the non-synergy model (**Figure 4A**) and simple synergy model (**Figure 4B**) in no-stroke and in two different sizes of stroke (σ = 1 and 2 SD). Both models showed increasing instability as the stroke size increased. However, systematic differences exist in the distribution of the errors. While the errors of the non-synergy model were distributed almost evenly in all directions (i.e., circular shape), the errors of the simple synergy model were distributed more ovally, and the main axis was along the target direction. For example, for the shoulder flexion target (the rightmost target) with σ = 2SD, the error was distributed horizontally in the simple synergy model (**Figure 4B**); however, it was distributed evenly in the non-synergy model (**Figure 4A**). To examine the details of the task performance, we evaluated two types of errors: directional error and amplitude error. The directional error is the angle between the target torque vector and the torque vector output by the model, while the amplitude error is the difference between the amplitude of the target torque and the output of the model. **Figures 4C,D** show an increase in the directional and amplitude errors as a function of stroke size. The figures show that whereas the amplitude error of both the non-synergy and simple synergy models increased in a similar manner, the simple synergy model produced a smaller size of directional error ($p < 0.05$, bootstrap test, n = 1,000) although the effect size was relatively small (Cohen's d was ranged from 0.15 to 0.94). This result suggests that the simple synergy model retains the ability to coordinate muscle activity even when cortical activity is disturbed, and robustly generates joint torques in the correct direction.

Next, we compared the robustness of muscle activation patterns between non-synergy and simple synergy models. **Figures 5A,B** illustrate muscle activation for each target direction with non-synergy and simple synergy models in no-stroke and two different sizes of stroke cases (σ = 3 and 6 SD). While muscle

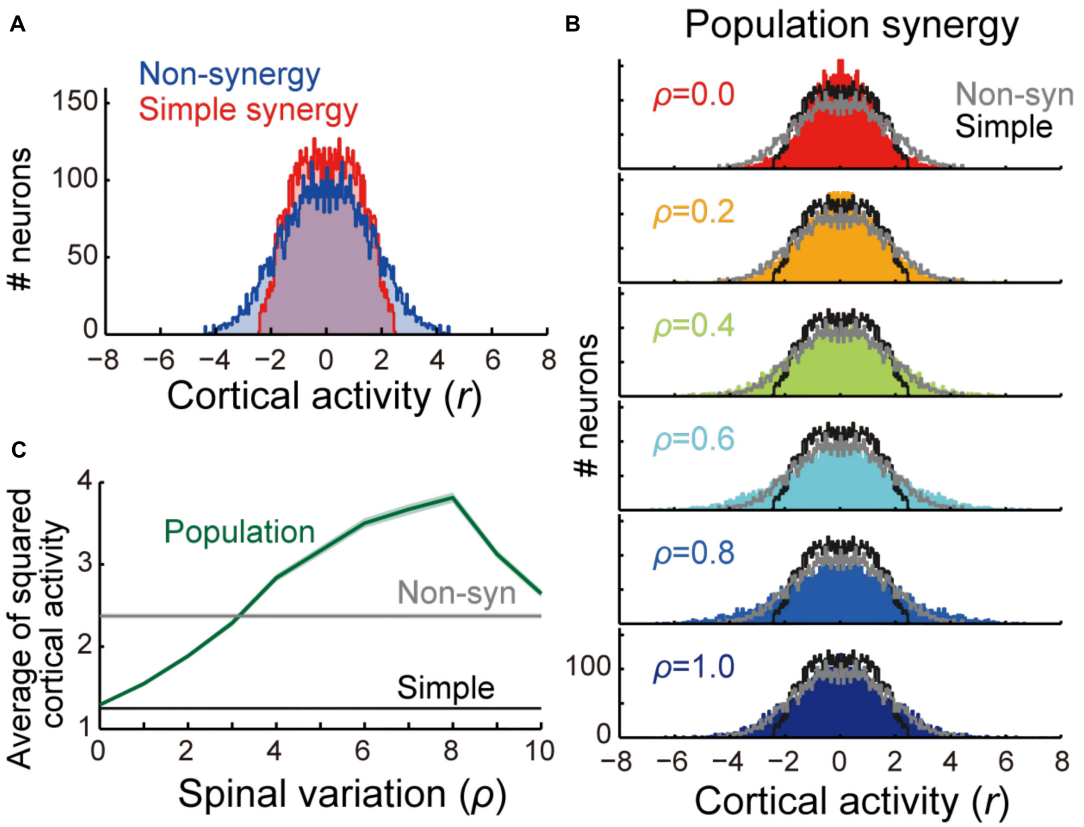

FIGURE 3 | Comparison of cortical activity between models. **(A)** Distribution of cortical activity of non-synergy (blue) and simple synergy model (red). Activity of cortical neurons (n = 1,000) was pooled for 8 target locations (n = 8,000). **(B)** Comparison of cortical activity between population synergy model with different spinal variation (ρ) with non-synergy (gray) and simple synergy (black) models. **(C)** Mean squared cortical activity of population synergy model (blue) with different spinal variation (ρ) in comparison with non-synergy (gray) and simple synergy (black) models. Line and shade, mean and standard error of mean across pooled neurons (n = 8,000).

activation of the non-synergy model was severely disturbed by stroke, the simple synergy model expressed more consistent muscle activation. The shift in PD (ΔPD) was quantified as the absolute difference of the PD from no-stroke cases (σ = 0). **Figure 5C** shows that ΔPD was significantly smaller for the simple synergy model than for the non-synergy model ($p < 0.05$, bootstrap test, n = 1,000). This result indicates that the simple synergy model is more robust for cortical stroke to generate consistent muscle activation.

We further compared the robustness of muscle synergies between non-synergy and simple synergy models. To quantify the robustness of muscle synergies, we compared two measures: (1) how much variance of affected muscle activity can be accounted for by original synergies (VAF by original synergies) and (2) how similar the synergies extracted from the affected muscle activity was to the original synergies (similarity with original synergies). **Figures 5D,E** demonstrate that while both measures steeply decrease in the non-synergy model, they remain high in the simple synergy model (≥0.90, **Figure 5D**, red dotted line), even when the stroke size increased to 10 SD. The difference in the effect of stroke size on each model was significant for both measures ($p < 0.05$, bootstrap test, n = 1,000). These results indicate that the simple synergy model more robustly generates consistent muscle synergies under stroke conditions.

Population Synergy Model With a Moderate Spinal Variation Exhibits a Comparable Robustness to Simple Synergy Model

We examined how the synergies could be organized in the spinal layer. The simplest model is that in which each synergy is represented by a single neuron or unitary "module" (simple synergy model, **Figures 1B**, **6A**). However, our previous physiological study showed that a muscle field of individual spinal PreM-INs did not completely match muscle synergies but showed substantial variation in spatial and temporal activation patterns (Takei et al., 2017). Therefore, a more plausible model can be developed in such a way that a synergy is represented by a population of neurons with some variation (population synergy model, **Figure 6B**). To test this scenario, in experiment 2, we compared the robustness of these synergy models against the introduction of cortical stroke. First, we systematically changed the size of the variation of synergies by changing the proportion

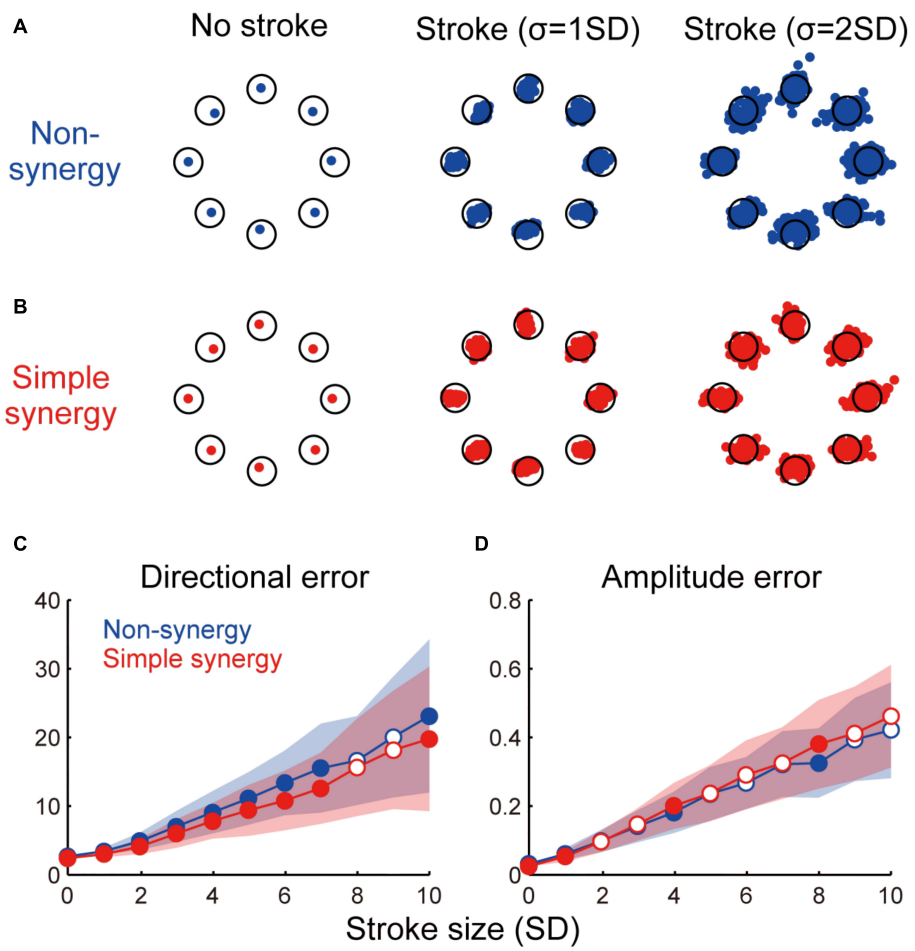

FIGURE 4 | Effect of cortical stroke on task performance. **(A,B)** Examples of torque output by non-synergy model **(A)** and simple synergy model **(B)** in no stroke and two different sizes of stroke (σ = 1 and 2 SD). Each dot indicates one stroke case. Only 100 examples are plotted for visualization purpose. Open circle, target torque combination. **(C,D)** Size of directional error **(C)** and amplitude error **(D)** as a function of stroke size (σ = 1–10SD). Line and shade, mean and standard deviation across 200 stroke cases. Open and filled circles indicate significant and non-significant differences between two models ($p < 0.05$, bootstrap test, $n = 1{,}000$).

(ρ) of Gaussian noise to the synergy weights (V). We found that spatial clustering of the output weights of each spinal neuron based on the similarity to the original muscle synergies decreased as the variation level ρ increased (**Figure 6C**). The level of clustering was evaluated using silhouette values (0.93, 0.81, and 0.56 for $\rho = 0.2$, 0.3, and 0.4, respectively) (Rousseeuw, 1987). Importantly, our previous electrophysiological study demonstrated that the similarity of output projection of spinal PreM-INs to extracted muscle synergies showed a spatial clustering and their silhouette values ranged from 0.79 to 0.87 (Figure 2A of Takei et al., 2017). This silhouette value was comparable to that of the population synergy model, with $\rho = 0.3$. After network training procedures, all population synergy models showed a similar level of task performance, with residual errors ranging from 0.017 to 0.083, comparable to the performance of the non-synergy and the simple synergy models (**Figure 2C**, 95% interval: 0.006 – 0.083 and 0.012 – 0.064, respectively). The amount of cortical activity generally increased as spinal variability increased, and it exceeded the non-synergy model when spinal variability was greater than 0.3 which was the physiologically observed level ($\rho > 0.3$, **Figures 3B,C**).

Then, we compared the robustness of task performance and muscle synergies in cortical stroke between the simple and population synergy models. **Figures 7A–E** shows the change in task performance, ΔPD, and muscle synergies as an effect of cortical stroke. As a reference, we also plot the results of the non-synergy model (**Figures 7A–E**, gray rectangles). In general, results of the population synergy models spanned from the results of the simple synergy model to those of the non-synergy model. For example, the directional error of the population synergy model was similar to the simple synergy model when the spinal variation was smaller (ρ = 0.0–0.2, **Figures 7A–E**, red lines), while it was similar to the non-synergy model when the variation was larger (ρ = 0.8–1.0, blue lines). This gradual change was observed for directional error, ΔPD, and two muscle synergy measures ($p < 0.05$, bootstrap test, n = 1,000), but not for the amplitude error (**Figure 7B**). Critically, the robustness of the population synergy models remained almost at the same

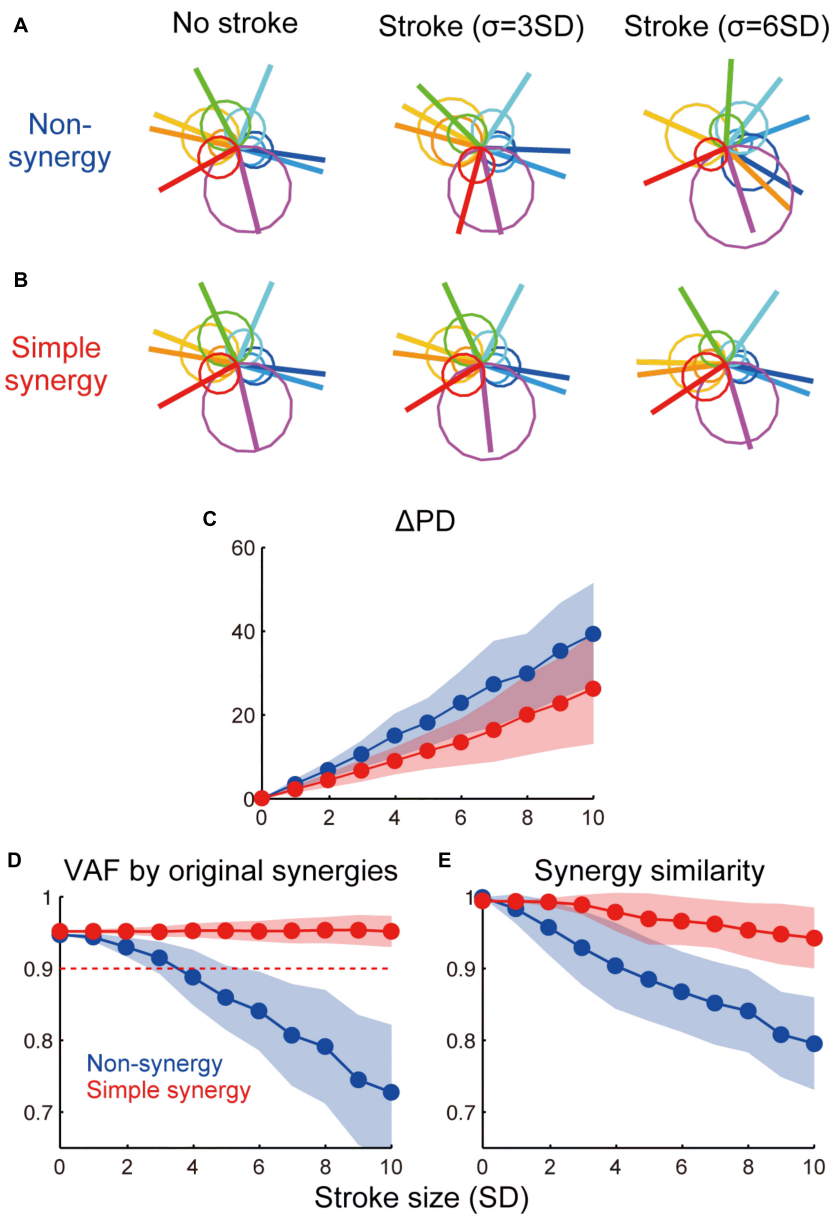

FIGURE 5 | Effect of cortical stroke on muscle synergies. **(A,B)** Examples of muscle activation with non-synergy model **(A)** and simple synergy model **(B)** in no-stroke and two different sizes of stroke cases (σ = 3 and 6 SD). Circles indicate muscle activation for each torque direction and lines indicate a PD of muscles. **(C)** Averaged shift of PD (ΔPD) from no stroke (σ = 0) condition. **(D)** VAF by original muscle synergies extracted from non-synergy model and used for simple synergy model **(Figure 1F)**. **(E)** Similarity of muscle synergies extracted in each stroke case to the original muscle synergies. The format is the same as **Figures 4C,D**.

level as the simple synergy model until the spinal variation level was increased to 0.3 (**Figures 7C–E**, red-yellow), and then these measures steeply decreased when the variation increased further (green-blue). These results indicate that the population synergy model with moderate variation exhibited robustness against cortical stroke comparable to that of the simple muscle synergy model. These results suggest that the muscle synergies are not necessarily implemented as unitary "modules," but they can be implemented as the population of spinal neurons with a moderate variation.

DISCUSSION

In this study, we compared different neural network models with a focus on their robustness to cortical stroke. In experiment 1, we compared two types of neural network models: one with random connections (non-synergy model) and the other with a smaller number of spinal synergies (simple synergy model). After optimization, we found that both models achieved comparable task performance and similar muscle synergies, confirming the prediction of a previous study (Hirashima and Oya, 2016).

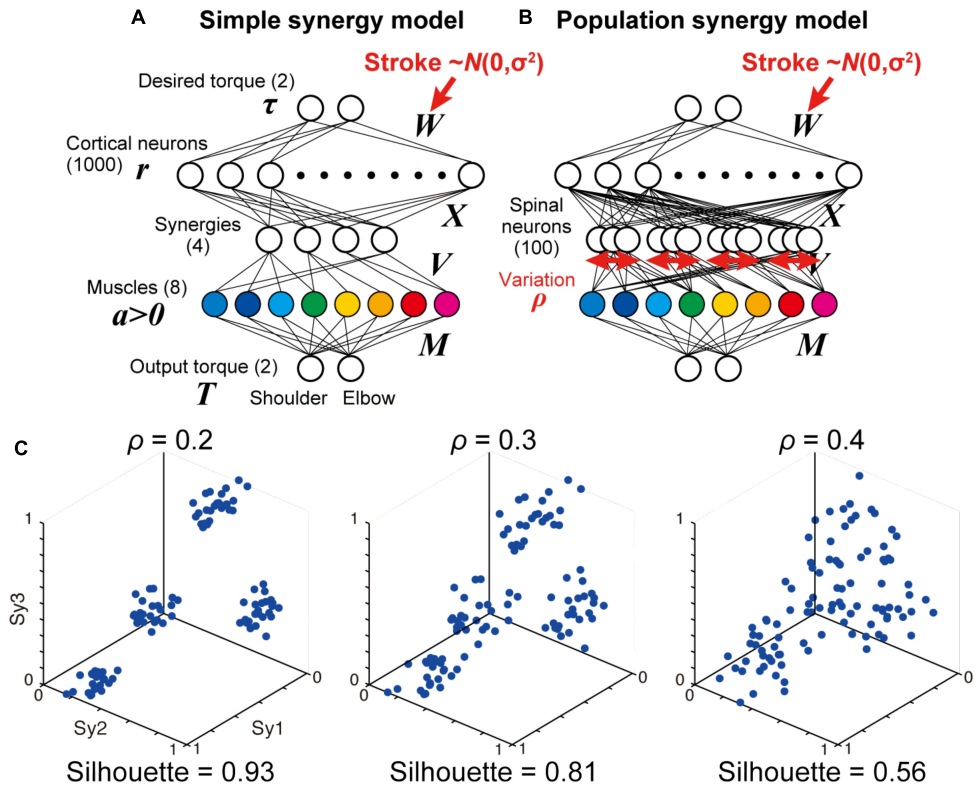

FIGURE 6 | Simple and population models for muscle synergies. **(A,B)** Neural network models with simple synergies **(A**, same as **Figure 1B)** and population synergies with some variations **(B)**. **(C)** Spatial similarity of output weights of each synergy (*V*) with the original muscle synergies with different spinal variation levels (ρ = 0.2, 0.3, 0.4).

Interestingly, despite the similar task performance after the training, the simple synergy model had higher learning rates, consistent with previous findings (Hagio and Kouzaki, 2018), and smaller cortical activity (**Figures 2A–F**). This indicates that although the output performances were similar, the simple synergy model achieved more efficient muscle control with less neural activity cost than the non-synergy model.

Then, we tested the robustness of the model performance against cortical stroke, which was modeled as the addition of noise to the cortical layer. The results demonstrated that the simple synergy model exhibited (1) smaller directional error in torque production and (2) higher consistency of muscle synergies with the original muscle synergies. This robustness of muscle synergies was consistent with observations in human stroke patients (Cheung et al., 2009, 2012). compared muscle synergies extracted from the unaffected and affected arms of stroke patients with moderate-to-severe unilateral ischemic lesions in the frontal motor areas (Cheung et al., 2009). Their results demonstrated that most of the patients showed muscle synergies that were strikingly similar between the unaffected and affected arms despite differences in motor performance between the arms. The similarity evaluated by a dot product between muscle synergies from the arms ranged from 0.80 to 0.95 with an average of 0.90. Our results showed that the similarity of muscle synergies with the original synergies was maintained at >0.90, even with a severe stroke in the simple synergy model (**Figure 5D**, red dotted line). The consistency of our results with previous findings suggests that the existence of a synergy layer is an essential factor in explaining the robustness of muscle synergies in stroke conditions.

We further explored a biologically plausible model for the neural implementation of muscle synergies. Our previous study demonstrated that spinal PreM-INs have divergent output projections to multiple hand and arm motoneurons (Takei and Seki, 2010, 2013) and their spatial distribution corresponds to the spatial weight of muscle synergies (Takei et al., 2017). However, although the output projection of PreM-INs corresponded to muscle synergies as a population, there was a substantial variation in the projection patterns across individual PreM-INs. Moreover, their temporal activation patterns were heterogeneous and were not clustered as muscle synergies at the individual neuron level. From these observations, we hypothesized that each muscle synergy is not represented by a unitary "module," in which single or population neurons are synchronously activated by common inputs, but by a population of PreM-INs that have variable output projections and are activated independently (Takei et al., 2017). Consistent with this hypothesis, the present results demonstrated that the population synergy models with a spinal variation exhibited comparable robustness of muscle synergies with the simple synergy model against cortical stroke

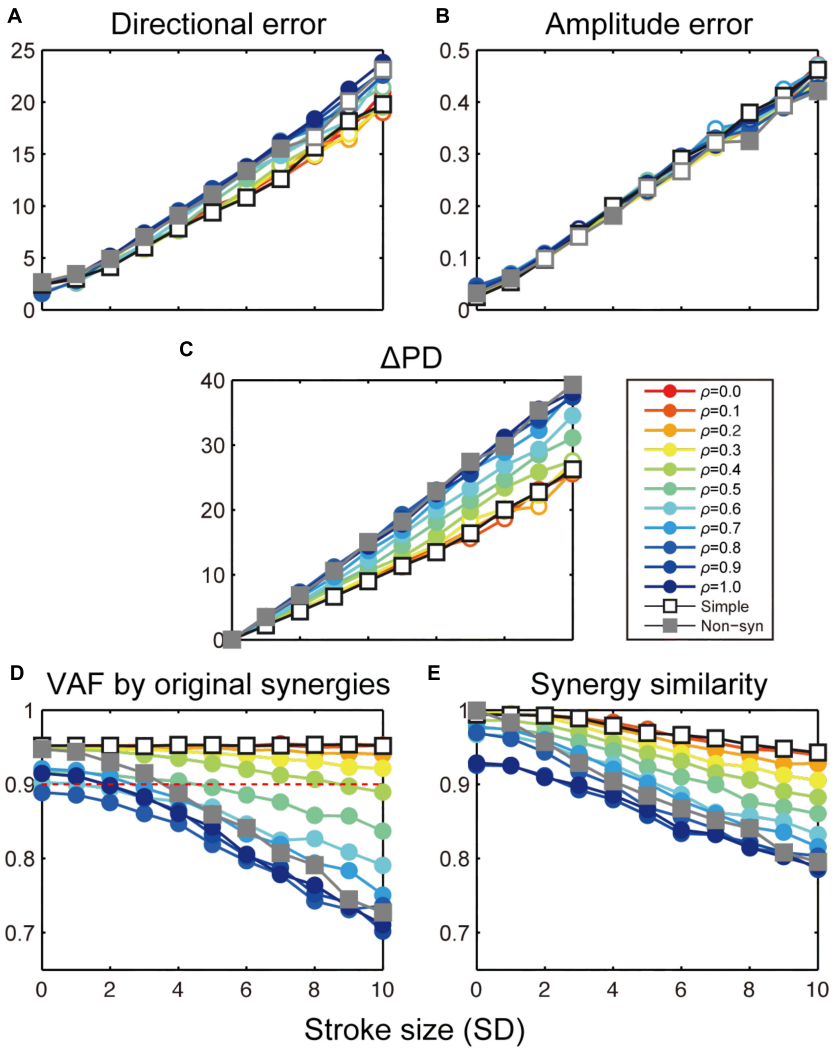

FIGURE 7 | Stroke effects on task performance and muscle synergies with simple and population synergy models. Change in directional error **(A)**, amplitude error **(B)**, shift of PD **(C)**, VAF by the original synergies **(D)**, and similarity with the original synergies **(E)** as a function of the size of cortical stroke (SD). Open and filled circles indicate a significant and non-significant difference from the simple synergy model (open square, $p < 0.05$, bootstrap test, $n = 1{,}000$).

(Cheung et al., 2009, 2012). The similarity of muscle synergy to the original synergies remained high (>0.90, **Figure 7D**, red dotted line) even when the spinal variation level was increased up to $\rho \leq 0.3$ (**Figures 7D,E**, red-yellow). Importantly, the variation of spinal PreM-INs reported in our previous study (Takei et al., 2017) corresponded to $\rho = 0.3$, according to the silhouette value calculated from the cluster analysis for spinal PreM-INs (**Figure 2A**; Takei et al., 2017). This variation level was within the range where the present models preserved the robustness of muscle synergies against cortical stroke. These findings suggest that the population of spinal neurons with a moderate variation is a biologically plausible model for the neural implementation of muscle synergies. Note that previous studies on muscle synergy modeling also utilize a variation or noise addition, but their purpose was to test the robustness and degradation of the model performance (Kargo et al., 2010; Ausborn et al., 2019), which corresponds to cortical stroke in the present study. On the other hand, we added a spinal variation to change the synergy structure so that each spinal neuron has different output projections and receives input from cortical neurons independently, which allows spinal neurons to be activated asynchronously. This is qualitatively different from the conventional "module" models, which assume that the population of neurons in the same module are synchronously activated by common input. Our finding showed that the population synergy model with a moderate spinal variation showed high robustness and similarity to the monkey physiological data.

This finding has several implications for the low-dimensional control of the limb and muscles. First, muscle synergies do not necessarily reflect the reduction of the degrees of freedom (DOFs) by a smaller number of unitary modules. Previously, muscle synergy has often been modeled as a unitary module, where single

or population neurons are synchronously activated by common inputs and act as fixed units, and has been interpreted as a simplified strategy for motor control. However, the spinal PreM-IN showed substantial variation between neurons to contradict such a simple view of modular control (Takei et al., 2017). One possible explanation for the variation of spinal PreM-INs is that these spinal PreM-INs represent another muscle synergy that was not recruited in the task tested (a precision grip task). Indeed, for the control of primate dexterous hand movements, it is suggested that the higher-order control is working with the lower-order control which is usually detected as synergies (Santello et al., 1998; Yan et al., 2020). It is of interest to further examine how the spinal variability identified here can contribute to the higher-order control for dexterous hand movements. Another explanation is that the muscle synergies are represented by a population of PreM-INs with a certain variability of input and output connections. The present simulation results demonstrated that the population of spinal neurons which have a moderate variation has an ability to robustly control muscle activity to achieve motor coordination in task space. Despite the apparent higher dimensionality of the population synergy model, to achieve the motor coordination in task space the variability of spinal neurons will necessarily be averaged in the output or may effectively be in a null space of the output-potent dimension. To exploit the variations in the population synergy, more selective or sparse recruitment of subsets the population synergy layer may be required and then added amplifications of this output may be needed in a real spinal system. It is noteworthy that a similar constraint of neural variability to task space has been identified as neural manifolds in the population activity of motor cortices (Kaufman et al., 2014; Elsayed et al., 2016; Gallego et al., 2017). It is of interest to investigate how the cortical manifold and spinal synergy space interact and are hierarchically organized to regulate the dimensionality of motor control.

Our model of spinal population with a moderate variation in muscle synergy also provides implications for motor learning and development of motor coordination. Previous studies have demonstrated that motor tasks compatible with the original muscle synergy are learned faster than tasks incompatible with muscle synergies (Berger et al., 2013). Interestingly, the results also showed that although the learning rate was slow during the incompatible task, learning progressed to explore new synergies. During this exploration process, the variation in spinal neurons may be involved in changing the muscle coordination patterns. It is also interesting to understand how muscle synergies are obtained during development. In the sensory system, it is known that the synaptic connection in primary sensory cortices increases after birth till it reaches a maximum, then prunes and decreases as neural selectivity increases (Huttenlocher et al., 1982). In contrast, in the motor system it has been suggested that muscle synergy is generally conserved from early development to adulthood in a variety of motor animals (Dominici et al., 2011; Giszter, 2015; Yang et al., 2019) and that many aspects of afferent controls and premotor patterning may be independent of early stage functional activity (Haverkamp, 1986; Mendelson and Frank, 1991). However, at the same time, these studies also demonstrated that there are some modifications of muscle synergies over the course of development, including increased inter-subject variability (Yang et al., 2019) and recruitment of additional synergies (Dominici et al., 2011). It would be of interest to investigate how the variation of spinal PreM-INs shown in this study relates to these developmental and learning modifications of muscle synergies.

In conclusion, our network simulation showed that muscle synergies could be implemented as a population of PreM-INs with a moderate variation rather than unitary "modules." This view provides new insight into understanding the mechanism and functional relevance of how the CNS controls the redundant motor system.

DATA AVAILABILITY STATEMENT

The raw data supporting the conclusions of this article will be made available by the authors, without undue reservation.

AUTHOR CONTRIBUTIONS

TT designed the study. YS and TT carried out the experiments and analyzed the data. YS, MH, and TT wrote the manuscript. All authors contributed to the article and approved the submitted version.

FUNDING

This work was supported by Grants-in-Aid (19H03975, 19H05311, and 21H00309) from the Ministry of Education, Culture, Sports, Science and Technology of Japan (MEXT), Fusion Oriented Research for Disruptive Science and Technology (FOREST) program of Japan Science and Technology Agency (JST), Uehara Memorial Foundation, Naito Foundation, and Takeda Science Foundation (TT).

ACKNOWLEDGMENTS

We would like to thank Dr. Tadashi Isa for his support in setting up our laboratory.

REFERENCES

Ausborn, J., Shevtsova, N. A., Caggiano, V., Danner, S. M., and Rybak, I. A. (2019). Computational modeling of brainstem circuits controlling locomotor frequency and gait. *Elife* 8:e43587. doi: 10.7554/eLife.43587

Berger, D. J., Gentner, R., Edmunds, T., Pai, D. K., and d'Avella, A. (2013). Differences in adaptation rates after virtual surgeries provide direct evidence for modularity. *J. Neurosci.* 33, 12384–12394. doi: 10.1523/JNEUROSCI.0122-13.2013

Bizzi, E., d'Avella, A., Saltiel, P., and Tresch, M. (2002). Modular organization of spinal motor systems. *Neuroscientist* 8, 437–442. doi: 10.1177/107385802236969

Cheung, V. C., Piron, L., Agostini, M., Silvoni, S., Turolla, A., and Bizzi, E. (2009). Stability of muscle synergies for voluntary actions after cortical stroke

in humans. *Proc. Natl. Acad. Sci. U.S.A.* 106, 19563–19568. doi: 10.1073/pnas.0910114106

Cheung, V. C., Turolla, A., Agostini, M., Silvoni, S., Bennis, C., Kasi, P., et al. (2012). Muscle synergy patterns as physiological markers of motor cortical damage. *Proc. Natl. Acad. Sci. U.S.A.* 109, 14652–14656. doi: 10.1073/pnas.1212056109

Cheung, V. C. K., d'Avella, A., Tresch, M. C., and Bizzi, E. (2005). Central and sensory contributions to the activation and organization of muscle synergies during natural motor behaviors. *J. Neurosci.* 25, 6419–6434. doi: 10.1523/JNEUROSCI.4904-04.2005

d'Avella, A., Portone, A., Fernandez, L., and Lacquaniti, F. (2006). Control of fast-reaching movements by muscle synergy combinations. *J. Neurosci.* 26, 7791–7810. doi: 10.1523/JNEUROSCI.0830-06.2006

d'Avella, A., Saltiel, P., and Bizzi, E. (2003). Combinations of muscle synergies in the construction of a natural motor behavior. *Nat. Neurosci.* 6, 300–308. doi: 10.1038/nn1010

Dominici, N., Ivanenko, Y. P., Cappellini, G., d'Avella, A., Mondì, V., Cicchese, M., et al. (2011). Locomotor primitives in newborn babies and their development. *Science* 334, 997–999. doi: 10.1126/science.1210617

Elsayed, G. F., Lara, A. H., Kaufman, M. T., Churchland, M. M., and Cunningham, J. P. (2016). Reorganization between preparatory and movement population responses in motor cortex. *Nat. Commun.* 7:13239. doi: 10.1038/ncomms13239

Gallego, J. A., Perich, M. G., Miller, L. E., and Solla, S. A. (2017). Neural Manifolds for the Control of Movement. *Neuron* 94, 978–984. doi: 10.1016/j.neuron.2017.05.025

Giszter, S. F. (2015). Motor primitives-new data and future questions. *Curr. Opin. Neurobiol.* 33, 156–165. doi: 10.1016/j.conb.2015.04.004

Hagio, S., and Kouzaki, M. (2018). Modularity speeds up motor learning by overcoming mechanical bias in musculoskeletal geometry. *J. R. Soc. Inter.* 15:20180249. doi: 10.1098/rsif.2018.0249

Hart, C. B., and Giszter, S. F. (2010). A neural basis for motor primitives in the spinal cord. *J. Neurosci.* 30, 1322–1336. doi: 10.1523/JNEUROSCI.5894-08.2010

Haverkamp, L. J. (1986). Anatomical and physiological development of the Xenopus embryonic motor system in the absence of neural activity. *J. Neurosci.* 6, 1338–1348. doi: 10.1523/JNEUROSCI.06-05-01338.1986

Herter, T. M., Kurtzer, I., Cabel, D. W., Haunts, K. A., and Scott, S. H. (2007). Characterization of torque-related activity in primary motor cortex during a multijoint postural task. *J. Neurophysiol.* 97, 2887–2899. doi: 10.1152/jn.00757.2006

Hirashima, M., and Nozaki, D. (2012). Learning with slight forgetting optimizes sensorimotor transformation in redundant motor systems. *PLoS Comput. Biol.* 8:e1002590. doi: 10.1371/journal.pcbi.1002590

Hirashima, M., and Oya, T. (2016). How does the brain solve muscle redundancy? Filling the gap between optimization and muscle synergy hypotheses. *Neurosci. Res.* 104, 80–87. doi: 10.1016/j.neures.2015.12.008

Huttenlocher, P. R., Courten, C. D., Garey, L. J., and Loos, H. V. D. (1982). Synaptogenesis in human visual cortex — evidence for synapse elimination during normal development. *Neurosci. Lett.* 33, 247–252. doi: 10.1016/0304-3940(82)90379-2

Ivanenko, Y. P., Poppele, R. E., and Lacquaniti, F. (2004). Five basic muscle activation patterns account for muscle activity during human locomotion. *J. Physiol.* 556, 267–282. doi: 10.1113/jphysiol.2003.057174

Kargo, W. J., and Giszter, S. F. (2000). Rapid correction of aimed movements by summation of force-field primitives. *J. Neurosci.* 20, 409–426. doi: 10.1523/JNEUROSCI.20-01-00409.2000

Kargo, W. J., and Giszter, S. F. (2008). Individual premotor drive pulses, not time-varying synergies, are the units of adjustment for limb trajectories constructed in spinal cord. *J. Neurosci.* 28, 2409–2425. doi: 10.1523/JNEUROSCI.3229-07.2008

Kargo, W. J., Ramakrishnan, A., Hart, C. B., Rome, L. C., and Giszter, S. F. (2010). A simple experimentally based model using proprioceptive regulation of motor primitives captures adjusted trajectory formation in spinal frogs. *J. Neurophysiol.* 103, 573–590. doi: 10.1152/jn.01054.2007

Kaufman, M. T., Churchland, M. M., Ryu, S. I., and Shenoy, K. V. (2014). Cortical activity in the null space: permitting preparation without movement. *Nat. Neurosci.* 17, 440–448.

Kielar, A., Deschamps, T., Chu, R. K., Jokel, R., Khatamian, Y. B., Chen, J. J., et al. (2016). Identifying Dysfunctional Cortex: Dissociable Effects of Stroke and Aging on Resting State Dynamics in MEG and fMRI. *Front. Aging Neurosci.* 8:22–32. doi: 10.3389/fnagi.2016.00040

Krouchev, N., Kalaska, J. F., and Drew, T. (2006). Sequential activation of muscle synergies during locomotion in the intact cat as revealed by cluster analysis and direct decomposition. *J. Neurophysiol.* 96, 1991–2010. doi: 10.1152/jn.00241.2006

Kutch, J. J., and Valero-Cuevas, F. J. (2012). Challenges and new approaches to proving the existence of muscle synergies of neural origin. *PLoS Comput. Biol.* 8:e1002434. doi: 10.1371/journal.pcbi.1002434

Levine, A. J., Hinckley, C. A., Hilde, K. L., Driscoll, S. P., Poon, T. H., Montgomery, J. M., et al. (2014). Identification of a cellular node for motor control pathways. *Nat. Neurosci.* 17, 586–593. doi: 10.1038/nn.3675

Lillicrap, T. P., and Scott, S. H. (2013). Preference distributions of primary motor cortex neurons reflect control solutions optimized for limb biomechanics. *Neuron* 77, 168–179. doi: 10.1016/j.neuron.2012.10.041

Mendelson, B., and Frank, E. (1991). Specific monosynaptic sensory-motor connections form in the absence of patterned neural activity and motoneuronal cell death. *J. Neurosci.* 11, 1390–1403. doi: 10.1523/JNEUROSCI.11-05-01390.1991

Morasso, P. (1981). Spatial control of arm movements. *Exp. Brain Res.* 42, 223–227.

Overduin, S. A., d'Avella, A., Roh, J., and Bizzi, E. (2008). Modulation of muscle synergy recruitment in primate grasping. *J. Neurosci.* 28, 880–892. doi: 10.1523/JNEUROSCI.2869-07.2008

Rousseeuw, P. J. (1987). Silhouettes: a graphical aid to the interpretation and validation of cluster analysis. *J. Comput. Appl. Math.* 20, 53–65.

Santello, M., Flanders, M., and Soechting, J. F. (1998). Postural hand synergies for tool use. *J. Neurosci.* 18, 10105–10115. doi: 10.1523/JNEUROSCI.18-23-10105.1998

Takei, T., Confais, J., Tomatsu, S., Oya, T., and Seki, K. (2017). Neural basis for hand muscle synergies in the primate spinal cord. *Proc. Natl. Acad. Sci. U.S.A.* 114, 8643–8648. doi: 10.1073/pnas.1704328114

Takei, T., and Seki, K. (2010). Spinal interneurons facilitate coactivation of hand muscles during a precision grip task in monkeys. *J. Neurosci.* 30, 17041–17050. doi: 10.1523/JNEUROSCI.4297-10.2010

Takei, T., and Seki, K. (2013). Synaptic and functional linkages between spinal premotor interneurons and hand-muscle activity during precision grip. *Front. Comput. Neurosci.* 7:40. doi: 10.3389/fncom.2013.00040

Ting, L. H., and McKay, J. L. (2007). Neuromechanics of muscle synergies for posture and movement. *Curr. Opin. Neurobiol.* 17, 622–628. doi: 10.1016/j.conb.2008.01.002

Torres-Oviedo, G., Macpherson, J. M., and Ting, L. H. (2006). Muscle synergy organization is robust across a variety of postural perturbations. *J. Neurophysiol.* 96, 1530–1546. doi: 10.1152/jn.00810.2005

Tresch, M. C., and Jarc, A. (2009). The case for and against muscle synergies. *Curr. Opin. Neurobiol.* 19, 601–607. doi: 10.1016/j.conb.2009.09.002

Tresch, M. C., Saltiel, P., and Bizzi, E. (1999). The construction of movement by the spinal cord. *Nat. Neurosci.* 2, 162–167. doi: 10.1038/5721

Yan, Y., Goodman, J. M., Moore, D. D., Solla, S. A., and Bensmaia, S. J. (2020). Unexpected complexity of everyday manual behaviors. *Nat. Commun.* 11:3564. doi: 10.1038/s41467-020-17404-0

Yang, Q., Logan, D., and Giszter, S. F. (2019). Motor primitives are determined in early development and are then robustly conserved into adulthood. *Proc. Natl. Acad. Sci. U.S.A.* 116:201821455. doi: 10.1073/pnas.1821455116

Conflict of Interest: The authors declare that the research was conducted in the absence of any commercial or financial relationships that could be construed as a potential conflict of interest.

Publisher's Note: All claims expressed in this article are solely those of the authors and do not necessarily represent those of their affiliated organizations, or those of the publisher, the editors and the reviewers. Any product that may be evaluated in this article, or claim that may be made by its manufacturer, is not guaranteed or endorsed by the publisher.

Copyright © 2022 Song, Hirashima and Takei. This is an open-access article distributed under the terms of the Creative Commons Attribution License (CC BY). The use, distribution or reproduction in other forums is permitted, provided the original author(s) and the copyright owner(s) are credited and that the original publication in this journal is cited, in accordance with accepted academic practice. No use, distribution or reproduction is permitted which does not comply with these terms.

frontiers | Frontiers in Systems Neuroscience

ORIGINAL RESEARCH
published: 12 April 2022
doi: 10.3389/fnsys.2022.780652

Hyper-Adaptation in the Human Brain: Functional and Structural Changes in the Foot Section of the Primary Motor Cortex in a Top Wheelchair Racing Paralympian

*Tomoyo Morita[1,2], Satoshi Hirose[1,3], Nodoka Kimura[1], Hiromasa Takemura[1,2,4,5], Minoru Asada[1,6,7] and Eiichi Naito[1,2]**

[1] Center for Information and Neural Networks (CiNet), Advanced ICT Research Institute, National Institute of Information and Communications Technology (NICT), Osaka, Japan, [2] Graduate School of Frontier Biosciences, Osaka University, Osaka, Japan, [3] Otemon Gakuin University, Faculty of Psychology, Osaka, Japan, [4] Division of Sensory and Cognitive Brain Mapping, Department of System Neuroscience, National Institute for Physiological Sciences, Okazaki, Japan, [5] Department of Physiological Sciences, School of Life Science, SOKENDAI (The Graduate University for Advanced Studies), Kanagawa, Japan, [6] Institute for Open and Transdisciplinary Research Initiatives, Osaka University, Osaka, Japan, [7] International Professional University of Technology in Osaka, Osaka, Japan*

The human brain has the capacity to drastically alter its somatotopic representations in response to congenital or acquired limb deficiencies and dysfunctions. The main purpose of the present study was to elucidate such extreme adaptability in the brain of an active top wheelchair racing Paralympian (participant P1) who has congenital paraplegia (dysfunction of bilateral lower limbs). Participant P1 has undergone long-term wheelchair racing training using bilateral upper limbs and has won a total of 19 medals in six consecutive summer Paralympic games as of 2021. We examined the functional and structural changes in the foot section of the primary motor cortex (M1) in participant P1 as compared to able-bodied control participants. We also examined the functional and structural changes in three other individuals (participants P2, P3, and P4) with acquired paraplegia, who also had long-term non-use period of the lower limbs and had undergone long-term training for wheelchair sports (but not top athletes at the level of participant P1). We measured brain activity in all the participants using functional magnetic resonance imaging (MRI) when bimanual wrist extension-flexion movement was performed, and the structural MRI images were collected. Compared to 37 control participants, participant P1 showed significantly greater activity in the M1 foot section during the bimanual task, and significant local GM expansion in this section. Significantly greater activity in the M1 foot section was also observed in participant P4, but not in P2 and P3, and the significant local GM expansion was observed in participant P2, but not in P3 and P4. Thus, functional or structural change was observed in an acquired paraplegic participant, but was not observed in all the paraplegic participants. The functional and structural changes typically observed in participant P1 may represent extreme adaptability of the human brain. We discuss the results in terms of a new idea of hyper-adaptation.

Keywords: hyper-adaptation, functional magnetic resonance imaging, hand movement, somatotopy, primary motor cortex, gray matter expansion, wheelchair sports, paraplegia

OPEN ACCESS

Edited by:
Jun Ota,
The University of Tokyo, Japan

Reviewed by:
Daan Wesselink,
Harvard Medical School, United States
Harriet Dempsey-Jones,
University College London, United Kingdom

****Correspondence:***
Eiichi Naito
eiichi.naito@nict.go.jp

Received: *21 September 2021*
Accepted: *18 March 2022*
Published: *12 April 2022*

Citation:
Morita T, Hirose S, Kimura N, Takemura H, Asada M and Naito E (2022) Hyper-Adaptation in the Human Brain: Functional and Structural Changes in the Foot Section of the Primary Motor Cortex in a Top Wheelchair Racing Paralympian. Front. Syst. Neurosci. 16:780652. doi: 10.3389/fnsys.2022.780652

INTRODUCTION

Somatotopy is a fundamental functional structure for sensorimotor processing in the brain and is rich in plasticity. Previous neuroimaging studies have shown that the human brain has the capacity to drastically change its somatotopic representations in response to congenital or acquired limb deficiencies and dysfunction (Flor et al., 1995, 2006; Bruehlmeier et al., 1998; Lotze et al., 1999, 2001; Mikulis et al., 2002; Stoeckel et al., 2009; Hahamy et al., 2017; Dempsey-Jones et al., 2019; Hahamy and Makin, 2019; Nakagawa et al., 2020).

The main purpose of the present study was to elucidate such higher adaptability in the brain of an active top, wheelchair racing Paralympian (participant P1), who had congenital paraplegia (dysfunction of bilateral lower limbs). Participant P1 had received long-term wheelchair racing training using bilateral upper limbs, since she was eight years old, and had won a total of 19 medals in six consecutive summer Paralympic games as of 2021. We examined the functional and structural changes in the foot section of the primary motor cortex (M1) in participant P1, as compared to able-bodied control participants.

We conducted functional and structural magnetic resonance imaging (MRI). In the functional MRI experiment, prompted by the previous reports that somatotopic representation of the primary sensorimotor cortices in persons with congenital deficiency of a limb (e.g., upper limbs) is involved in sensory-motor processing of the other body parts (e.g., lower limbs; Hahamy et al., 2017; Dempsey-Jones et al., 2019; Hahamy and Makin, 2019; Nakagawa et al., 2020), we tested our hypothesis that the M1 foot section of participant P1 was involved in sensory-motor processing of the hand, which is rarely seen in able-bodied persons (Morita et al., 2021a). In the present study, we were particularly interested in the M1 because this is the executive locus of voluntary limb movement. In the structural MRI experiment, we examined the change in volume of the gray matter (GM) in the foot section of M1 of participant P1. It is known that long-term intensive hand/finger training, for manipulating musical instruments, causes GM expansion in the M1 hand section (Gaser and Schlaug, 2003). If the M1 foot section of participant P1 had been used as the hand section through her long-term training for wheelchair racing, using the upper limbs, we may expect the GM expansion (increase in GM volume) in this section. In addition to these investigations, we also explored the change in white matter (WM) in the brain of participant P1. If the GM of the M1 foot section of participant P1 is expanding, we may also expect the development of the nerve fibers that connect between the M1 foot section and other regions of the brain, resulting in expansion of WM which contains such developed nerve fibers.

The secondary purpose of the present study was to test whether the functional and structural changes expected in participant P1 are specific to this participant or common to other paraplegic participants. We tried to recruit paraplegic participants who had a long-term non-use period of the lower limbs and long-term wheelchair sports training and obtained three participants. One participant had paraplegia at the age of one (P2), and the remaining two had paraplegia due to spinal cord injury at the ages of 17 (P3) and of 21 (P4), respectively. They were acquired paraplegic persons having leg non-use period of more than 30 years and long-term training for wheelchair sports (**Table 1**). But none of them were top athletes at the level of participant P1.

In both functional and structural MRI experiments, our region of interest (ROI) was the M1 foot section. It is known that the foot section of M1 is represented in the medial wall motor region, which is closely located in the hand region of the cingulate motor area (CMA) in monkeys (He et al., 1995) and humans (Ehrsson et al., 2003; Naito et al., 2007; Amiez and Petrides, 2014). In addition, the trunk section of M1 is known to be closely located to the M1 foot section (Naito et al., 2021). Therefore, we first defined the ROI in the foot section of M1 (M1 foot ROI) using the functional MRI data obtained when 37 able-bodied control participants performed a right foot, right hand, and trunk tasks.

TABLE 1 | Participants' information.

Participant	P1	P2	P3	P4
Age (in years)	30	61	54	52
Sex	F	M	M	M
Leg non-use period	30 years	60 years	37 years	31years
Neurological level	T12	Cannot be specified	T3	T8
Cause	*Spina bifida	Poliomyelitis	Spinal cord injury	Spinal cord injury
ASIA impairment scale	A	undefined	A	A
SCI	Complete	undefined	Complete	Complete
FIM	101/126	108/126	101/126	101/126
Wheelchair sports (years played) Training period (age), training days/week, training hours/day	Track racing and marathon (23) 8-14yo, 2/w, 8 h 15-17yo, 7/w, 1-8 h 18-30yo, 6/w, 2 h	Basketball (42) 17-22yo, 4-5/w, 3h 23-58yo, 1-2/w, 3h Table tennis (4) 15-18yo, 1/w, 2h	Table tennis (27) 28-54yo, 2-4w, 2.5-8h	Basketball (31) 22-35yo, 5/w, 3h 36-52yo, 1/w, 3h Marathon (9) 27-35yo, 2/w, 3h Fencing (9) 27-35yo, 2/w, 3h
Paralympics participation	2004, 2008, 2012, 2014, 2016, 2021	None	2016	None
Number of medals in Summer Paralympic games	19	0	0	0
Handedness score	60	7	100	90

**Congenital.*

ASIA, American Spinal Injury Association; SCI, Spinal Cord Injury; FIM, Functional Independence Measurement; T, thoracic; yo, years old; w, week; h, hours.

In the functional MRI experiment, we scanned the brain activity when the four paraplegic participants (P1, P2, P3, and P4), and the control participants performed bimanual wrist extension-flexion movements. We selected a bimanual task because moving both hands and arms simultaneously is essential movement for pedaling a wheelchair. We first directly compared the brain activity obtained from each paraplegic participant (P1, P2, P3, or P4) to that of the control participants to explore regions, in which a paraplegic participant shows significantly greater activity than the control participants, within the M1 foot ROI (contrast analysis; see below). Next, we tested if the activity obtained from the ROI and the number of activated voxels identified in the ROI were significantly greater in each paraplegic participant when compared with the control participants (ROI analysis; see below).

In the structural MRI experiment, we collected the structural MRI images from all the participants and performed voxel-based morphometry (VBM) analysis. We first explored regions, in which a paraplegic participant shows significant change in GM volume as compared to the control participants, within the M1 foot ROI (contrast analysis; see below). Next, we tested if the GM volume of the ROI in each paraplegic participant (P1, P2, P3, or P4) was significantly different from that of the control participants (ROI analysis; see below). Finally, we explored whether there was a significant change in WM volume in the whole brain space in each paraplegic participant as compared to the control participants.

MATERIALS AND METHODS

Participants

One participant with congenital paraplegic (participant P1) and three participants with acquired paraplegia (P2, P3, and P4) participated in this study. The details of the participants are summarized in **Table 1**. Participant P1 was an active, top, wheelchair racing Paralympian aged 30. She began racing at the age of eight and had long-term wheelchair racing training using the bilateral upper limbs since then. She has won a total of 19 medals in the six consecutive Summer Paralympic Games as of 2021. Participants P2, P3, and P4 were not top athletes at the level of participant P1, but they had more than 30 years of leg non-use period and long-term wheelchair sports training (**Table 1**). Participant P2 had paraplegia at the age of one and had 42 years of experience in wheelchair basketball and 4 years of experience in wheelchair table tennis. Participant P3 had paraplegia at the age of 17 and had 27 years of experience in wheelchair table tennis. He was a Paralympian in Río de Janeiro. Participant P4 had paraplegia at the age of 21, and had 31 years of experience in wheelchair basketball, 9 years of experience in wheelchair marathon, and 9 years of experience in wheelchair fencing. Participants P1, P3, and P4 had no somatic sensations (light touch and pin prick) from their lower limbs and had complete immobility. Participant P2 had complete immobility of his lower limbs; nonetheless, there were somatic sensations (light touch and pin prick). These were evaluated by a physiotherapist with more than 10 years of experience (NK, one of the authors). We confirmed the handedness of the participants using the Edinburgh Handedness Inventory (Oldfield, 1971), and participants P1, P3, and P4 were right-handers, and participant P2 was ambidextrous (**Table 1**).

Regarding the control participants, we recruited right-handed and -footed able-bodied adults (n = 37; 37.4 ± 10.9 [mean ± standard deviation] years old, range 25-59 years old, 25 female). They had experience in various sports since their school days, but none of them were athletes participating in a particular sport. We confirmed the handedness of the control participants using the Edinburgh Handedness Inventory (95.9 ± 7.6, Oldfield, 1971). Moreover, we determined the dominant operating foot using a question "which leg would you use to kick a ball" in the Inventory. This question is shown to be valid to determine the dominant operating foot (van Melick et al., 2017). Among the participants, 33 participants reported using their right leg and 4 used both legs. Based on self-reports, none of the participants had a history of neurological, psychiatric, or movement disorders.

The study protocol was approved by the Ethics Committee of the National Institute of Information and Communications Technology (NICT) and by the MRI Safety Committee of the Center for Information and Neural Networks (CiNet; no. 2003260010). We explained the details of the experiment to each participant before the experiment, after which they provided written informed consent. The study was conducted according to the principles and guidelines of the Declaration of Helsinki (1975).

General Procedure

We conducted both functional and structural MRI experiments. We first collected the functional data, and at the end of entire experiment, we collected the structural MRI data from all participants. In the functional MRI experiment, to define the foot section of M1, the 37 control participants performed right foot, right hand, and trunk tasks (**Figure 1A**), in addition to a main bimanual task (**Figure 2A**). The paraplegic participants performed the bimanual task. After the bimanual task, both the control and paraplegic participants also performed right-hand active and passive movement tasks, which we intend to report in a future paper.

Before the fMRI experiment, we explained the tasks to be performed in the scanner to every participant, and they experienced the tasks outside the MRI room to familiarize themselves with the tasks. Thereafter, the participants entered the room and were placed in the MRI scanner. Their heads were immobilized using sponge cushions and an adhesive tape, and their ears were plugged. The participant's body parts (chest, pelvis, and shin) of the participants were fixed to the MRI bed using Velcro to reduce their body movements during the task. When performing a task, the participants were asked to close their eyes, relax their entire body, refrain from producing unnecessary movements, and only think of the assigned task.

Each participant completed one experimental 160-s run for each task. The run comprised five task epochs, each lasting 15 s (**Figure 2B**). Considering each epoch, the participants continuously exerted cyclic movements for each task in synchronization with cyclic audio tones. The details of each task are described below. The task epochs were separated by 15-s baseline (rest) periods. Each run also included a 25-s

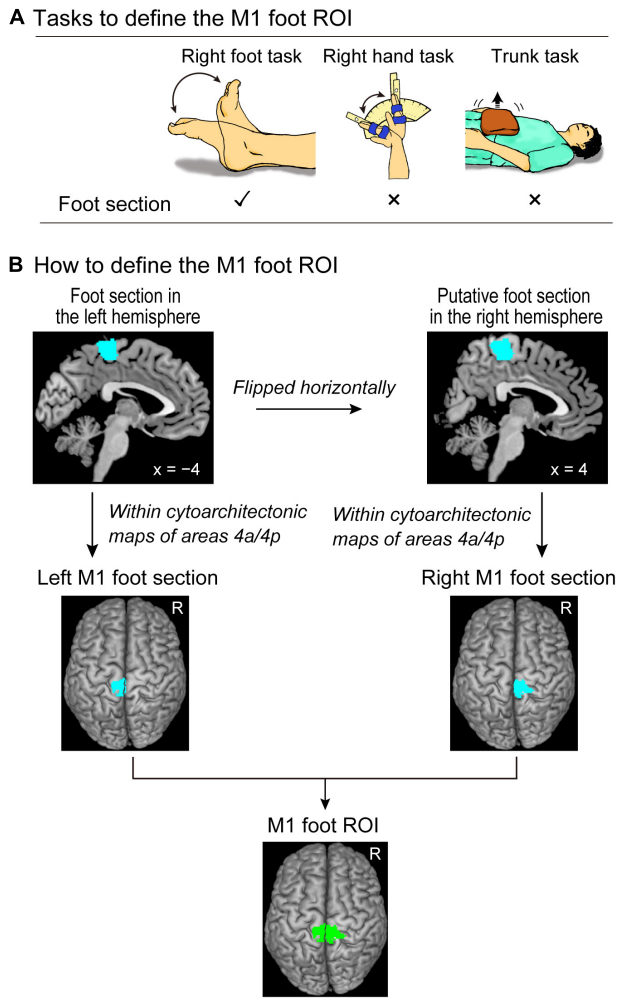

FIGURE 1 | Defining the M1 foot ROI. **(A)** Tasks to define the M1 foot ROI. We use the right foot, right hand, and trunk tasks to identify the brain regions that are activated during the right foot task, but not during the right hand and trunk tasks. **(B)** Procedures to define the M1 foot ROI (green section). Please see the text for details. M1, primary motor cortex; ROI, region-of-interest.

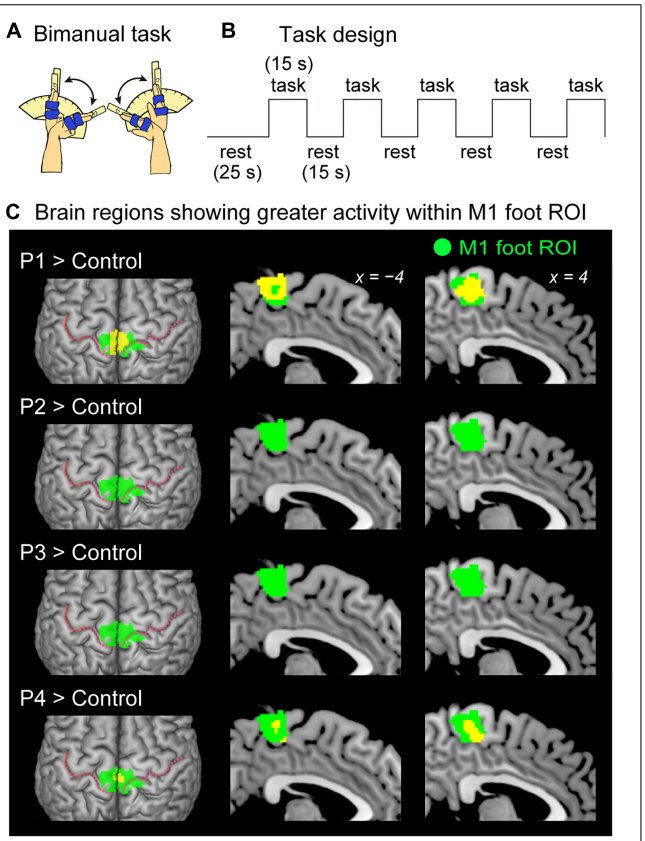

FIGURE 2 | Results from contrast analysis for functional data. **(A)** Bimanual task used in the present study. All of the participants continuously exert cyclic in-phase extension–flexion movements of their left and right wrists in synchronization with 1-Hz tones. **(B)** Task design of the bimanual task. Please see the text for details. **(C)** Results from one-to-many two-sample *t*-test. Significant clusters of voxels (yellow sections) showing greater activity within the M1 foot ROI when compared with the control participants are shown. Participants P1 and P4 showed a significant cluster (yellow sections) in the M1 foot ROI (green sections). Participant P2 and P3 had no significant cluster. These sections are superimposed on the MNI standard brain. The top view, and sagittal slices (x = −4 and 4) are shown in each row. In each top view panel, pink dotted lines indicate the central sulci. M1, primary motor cortex; ROI, region-of-interest; MNI, Montreal Neurological Institute.

baseline period before the start of the first epoch. During the experimental run, we provided the participants with auditory instructions that indicated the start of a task epoch (three, two, one, start). We also provided a 'stop' instruction generated by a computer to notify the participants of the end of each epoch. The participants heard the same cyclic audio tones; however, they did not generate any movement during the rest periods. All the auditory stimuli were provided through an MRI-compatible headphone. An experimenter who stood beside the scanner bed checked if the participants were performing each task properly by visual inspection throughout the run.

MRI Data Acquisition

Functional MRI images were acquired using T2*-weighted gradient echo-planar imaging (EPI) sequences with a 3.0-Tesla MRI scanner (MAGNETOM Trio Tim; Siemens, Germany) and 32-channel array coil. We used a multiband imaging technique (multiband factor = 3), which was used in our previous study (Amemiya et al., 2021). Each volume consisted of 48 slices (slice thickness = 3.0 mm) acquired in an interleaved manner, covering the entire brain. The time interval between the successive acquisitions from the same slice was 1000 ms. An echo time of 27 ms and a flip angle of 60° were used. The field of view was 192 × 192 mm, and the matrix size was 64 × 64 pixels. The voxel dimensions were 3 × 3 × 3 mm along the x-, y-, and z-axes, respectively. We collected 160 volumes for each experimental run.

Regarding the structural MRI image, a T1-weighted magnetization-prepared rapid gradient echo (MP-RAGE) image was acquired using the same scanner for each participant, which was used in the following voxel-based morphometry

(VBM) analysis. The imaging parameters were as follows: TR = 1900 ms, TE = 2.48 ms; FA = 9°, field of view = 256 × 256 mm^2, matrix size = 256 × 256 pixels, slice thickness = 1.0 mm; voxel size = 1 × 1 × 1 mm^3, and 208 contiguous transverse slices.

Tasks to Functionally Define the Foot Section of M1

We prepared the following three tasks (**Figure 1A**) to functionally define the foot section of M1 in the control participants.

Right Foot Task

The control participants performed alternating dorsi- and plantar-flexions of the right foot at a frequency of 1 Hz (left panel in **Figure 1A**). They were required to continuously perform these movements in synchronization with 1-Hz cyclic tones while relaxing their left foot. A supporter was placed under the right calf and the right leg was lifted off the bed to enable the participants to generate these movements without their right heel touching the bed. The participants were instructed to perform right foot movements within the range of their maximum dorsi- and plantar-flexion angles. These were measured outside the scanner (average range of motion across participants was approximately 68.6 ± 15.5°). This task was used to identify the brain regions that were associated with foot movement.

Right Hand Task

The control participants continuously exerted cyclic extension–flexion movements of their right wrist in synchronization with 1-Hz cyclic tones. We prepared a device to control the range of wrist motion (middle panel in **Figure 1A**), which was used in our previous study (Morita et al., 2021a). A movable hand-rest was mounted on the device (middle panel in **Figure 1A**), and the hand was fixed on the hand-rest that indicated the wrist angle. Two stoppers were fixed onto the device to control the range of the wrist motion across the task epochs and participants. They were positioned to prevent the wrist from extending beyond the straight (0°) position and flexing beyond 60°. The participants had to touch one of the stoppers (0° or 60°) alternately with the hand-rest in synchronization with the 1-Hz audio tones while making controlled and continuous wrist extension–flexion movements. An example of kinematic data when performing this task is shown in Morita et al. (2021a). This task was used to depict foot-specific M1 section distinctly from the CMA hand region. This is because the foot section of M1 and the CMA hand region are closely represented in the medial wall (see Introduction).

Trunk Task

The control participants pushed up a 4-kg weight placed on their abdomen (right panel in **Figure 1A**). They were asked to repeatedly perform a set of push-ups and immediate relaxation in synchronization with 0.8 Hz of tones, without moving their heads, and 0.8 Hz was chosen because in our pilot experiment, some participants reported that 1-Hz was too fast. They indicated that 0.8 Hz was comfortable to follow the movements. The participants were instructed to keep their breathing as normal as possible during the scanning. The weight was placed on their abdomen at the start of each task epoch started and removed when the epoch was completed. This task was used to identify the foot-specific M1 section, distinctly from the M1 trunk section, because the foot movement could potentially co-activated the M1 trunk section (Naito et al., 2021).

Bimanual Task (Main Task)

All the participants continuously exerted cyclic extension–flexion movements of their left and right wrists in synchronization with the 1-Hz tones (**Figure 2A**). The participants generated in-phase extension–flexion movements of both hands. The range of the wrist motion was between 0° and 60° as shown in the right-hand task (see above). To control the range of motion, the same device, used in the right hand task, was used for each of the left and right hands.

fMRI Data Preprocessing and Single-Subject Analysis

To eliminate the effects of unsteady magnetization during the tasks, the first ten EPI images in each fMRI run were discarded. The imaging data were analyzed using SPM 12 (Wellcome Centre for Human Neuroimaging, London, United Kingdom) implemented in MATLAB (MathWorks, Sherborn, MA, United States). The following preprocessing was done for each participant. SPM default parameters were used unless otherwise specified. First, all of the EPI images were aligned to the first EPI image of the first session with six degrees-of-freedom (translation and rotation about x-, y-, z-axes) rigid displacement. Through this realignment procedure, we obtained the data related to the position of the head that changed over time from the first frame and through the six parameters. All the participants had a maximum displacement of less than 1.5 mm in the x-, y-, or z-plane and less than 0.1° of angular rotation about each axis during each fMRI run. These values were comparable to those from our previous study (see Morita et al., 2019), and thus no data were excluded from the analysis. The T1-weighted structural image of each participant was co-registered to the mean image of all the realigned EPI images by using affine transformation. Finally, the structural image and the realigned EPI images were spatially normalized to the standard stereotactic Montreal Neurological Institute (MNI) space (Evans et al., 1994). Normalization parameters to align the structural image to MNI template brain were calculated using the SPM12 normalization algorithm. The same parameters were used to transform the realigned EPI images. The normalized EPI images were resliced to 2-mm isotropic resolution, and the successful alignment was visually checked. Finally, the normalized images were spatially smoothed using a Gaussian kernel with a full width at half maximum of 4 mm along the x-, y-, and z-axes.

Following the preprocessing, we used a general linear model (Friston et al., 1995; Worsley and Friston, 1995) to analyze the fMRI data. We prepared a design matrix for each participant. Considering this single-subject analysis, the design matrix contained a boxcar function for the task epoch in the run, which was convolved with a canonical hemodynamic response function. To correct the residual motion-related variance after the realignment, the six realignment parameters were also included in the design matrix as regressors of no interest. In

the analysis, we did not perform global mean scaling to avoid inducing Type I errors in the evaluation of negative blood oxygenation level-dependent (BOLD) responses (deactivation) (Aguirre et al., 1998). We generated an image showing the task-related activity in each task for each participant, which was used in the subsequent analyses. In this image, the effect of the cyclic tones was most likely eliminated because the participants heard the sound consistently during the task epochs and rest periods.

Defining the M1 Foot ROI

The procedure is summarized in **Figure 1B**. We performed a second-level group analysis (Holmes and Friston, 1998) using a one-sample t-test to identify the brain regions that were significantly activated during the right foot task in the control participants as a whole. Here, we depicted the regions exclusively activated during the right foot task. For this purpose, we identified the brain regions that were activated during the right foot task, but not during the right hand and trunk tasks for the group of the control participants. This was carried out using two exclusive masks of images showing the right hand and trunk task-related activities. As for a mask image of the right hand task-related activity, we generated a mask image by performing one-sample t-tests to depict the brain regions that were active during the right hand task using height threshold of $p < 0.05$ uncorrected. The same analysis was done to generate a mask image of trunk task-related activity. We used these two mask images (union of these two images) to exclude the regions in which activity increased during the right hand and/or trunk task. We used the family wise error rate (FWE)-corrected extent threshold ($p < 0.05$) in the entire brain for a voxel-cluster image generated at an uncorrected height threshold of $p < 0.005$. We found a significant cluster of active voxels in the left (contralateral) medial wall motor regions (foot section in the left hemisphere).

To define the M1 in the medial wall motor regions, we used the cytoarchitectonic maps for areas 4a and 4p implemented in the SPM Anatomy toolbox (Eickhoff et al., 2005). We defined the left M1 foot section (the foot section of the left M1) by depicting the overlapped region between the functional cluster in the left medial wall and the cytoarchitectonic maps for areas 4a and 4p. We checked the individual activity in the left M1 foot section during the right foot, hand, and trunk tasks (see **Supplementary Material** and **Supplementary Figure 1**). We also defined the right M1 foot section. We first flipped the cluster horizontally from the left medial wall to the right hemisphere. Thereafter, we defined the putative right M1 foot section by identifying the overlapped region between the flipped cluster in the right medial wall and the cytoarchitectonic maps for areas 4a and 4p. Finally, we defined the M1 foot ROI (845 voxels, voxel size = 2 mm × 2 mm × 2 mm) by combining the left and right M1 foot sections.

Functional Analysis of Bimanual Task

Contrast Analysis for Functional Data

First, we explored regions, in which a paraplegic participant showed significantly greater activity than the control participants during the bimanual task, within the M1 foot ROI. In this analysis, we directly compared the brain activity obtained from each paraplegic participant to that of the control participants (**Figure 2C**). This was a one-to-many two-sample t-test that was identical to Crawford and Howell t-test (Mühlau et al., 2009; Boucard et al., 2016), which is a modification of the regular independent two-sample t-test, allowing us to compare one sample with a group of multiple samples, where the within-group variance is estimated from the latter group by assuming the within-group variances in two groups are identical (Crawford and Howell, 1998). In this analysis, we included the age and sex of all participants as nuisance covariates (effect of no interest) because these factors could have an influence on the evaluation of present between-group difference. This approach has been widely used in a GLM analysis to evaluate the target factor by considering effects of the nuisance covariates (e.g., Luo et al., 2014; Morita et al., 2021a). We searched for significant clusters of voxels within the M1 foot ROI using a small volume correction (SVC; $p < 0.05$, FWE-corrected for a voxel-cluster image generated at an uncorrected height threshold of $p < 0.005$).

ROI Analysis for Functional Data

In addition to the above contrast analysis, we performed ROI analysis. We first tested if the activity obtained from the M1 foot ROI during the bimanual task was significantly greater in a paraplegic participant compared to the control participants (**Figure 3A**). We calculated mean activity of the voxels in the entire M1 foot ROI in each participant. Next, we tested if the number of activated voxels identified in the ROI was significantly greater in a paraplegic participant compared to the control participants. We counted the number of activated voxels (height threshold of $p < 0.005$ ($T > 2.61$)) in the M1 foot ROI for each participant (**Figures 3B,C**). In each ROI analysis, we performed the Crawford and Howell t-test with Bonferroni correction (Crawford and Howell, 1998; Crawford and Garthwaite, 2012) to compare the data obtained from each paraplegic participant with that of the control participants ($n = 37$). Given that this test was repeated for four paraplegic participants, we corrected the p-values based on the number of test repetitions ($n = 4$). We used the threshold of $p < 0.05$ with Bonferroni correction. Finally, prompted by our previous report that the M1 foot section in able-bodied persons are deactivated during hand movement (Morita et al., 2021a), we also checked for any significant decrease in activity (less than 0) in the entire M1 foot ROI during the bimanual task in the control participants as a whole by performing one-sample t-test (**Figure 3A**).

Gray Matter (GM) Volume Analysis

Contrast Analysis for GM Volume

A voxel-based morphometry (VBM) analysis was performed to examine the change in GM volume in the M1 foot ROI in each paraplegic participant, compared to the control participants. First, we visually inspected the anatomical images of all the participants and confirmed the absence of observable structural abnormalities and motion artifacts. Subsequently, the data were processed using Statistical Parametric Mapping (SPM12, Wellcome Centre for Human Neuroimaging). The following

steps were performed using the default settings in SPM12 as recommended by Ashburner (2010).

First, the anatomical image obtained from each participant was segmented into GM, WM, cerebrospinal fluid (CSF), and non-brain parts. Next, using Diffeomorphic Anatomical Registration Through Exponentiated Lie Algebra (DARTEL), we generated GM and WM DARTEL templates based on the anatomical images obtained from all the participants. Thereafter, we applied an affine transformation to the GM and WM DARTEL templates to align them with their tissue probability maps in the Montreal Neurological Institute (MNI) standard space. Subsequently, a segmented GM image from each participant was warped non-linearly to the GM DARTEL template in the MNI space (spatial normalization). The warped image was modulated by Jacobian determinants of the deformation field to preserve the relative GM volume, even after spatial normalization. The modulated image of each participant was smoothed with an 8-mm FWHM Gaussian kernel and resampled to a resolution of 1.5 mm × 1.5 mm × 1.5 mm voxel size. The methods described above were also used in our previous study (Morita et al., 2021b).

As in the contrast analysis for functional data, we performed one-to-many two-sample t-test by directly comparing the GM volume obtained from each paraplegic participant to that of the control participants (**Figure 4A**). This analysis has been repeatedly used in the VBM analysis (Mühlau et al., 2009; Scarpazza et al., 2013; Taubert et al., 2015). In this analysis, we included age, sex, and intracranial volume (sum of GM, WM, and CSF volumes) as nuisance covariates because these factors may have a significant effect on the results of a VBM analysis in general (Hu et al., 2011). To restrict the search volume within the GM, we used a GM mask image that was created from our present data using the SPM Masking Toolbox (Ridgway et al., 2009)[1]. Thus, the voxels outside the mask image were excluded from the analysis. We first searched for significant clusters of voxels showing GM expansion (= increase of GM volume) within the M1 foot ROI using SVC ($p < 0.05$ FWE-corrected for a voxel-cluster image generated at an uncorrected height threshold of $p < 0.005$ ($T > 2.73$)). In addition, prompted by the previous reports that the GM in the primary sensory-motor cortices often shrinks after spinal cord injury even after several years of injury (Crawley et al., 2004; Freund et al., 2013; Hou et al., 2014), we also checked for significant clusters of voxels showing GM atrophy (= reduction of GM volume) within the M1 foot ROI in each paraplegic participant compared to the control participants, using the same procedure described above.

ROI Analysis for GM Volume

In addition to the contrast analysis, we performed a ROI analysis. We tested if the GM volume of the ROI in a paraplegic participant was significantly different (increase or decrease) from the control participants (**Figure 4C**). We calculated the GM volume of the M1 foot ROI in each participant. According to Whitwell et al. (2001), the GM volume of the M1 foot ROI was divided by intracranial volume to adjust for the size of the head of each participant. Using this value, we performed the Crawford and Howell *t*-test with Bonferroni correction (see above) to determine if there was significant increase or decrease in the GM volume of the entire M1 foot ROI in a paraplegic participant (two-tailed) as compared to the control participants ($n = 37$). Given that this test was repeated for four paraplegic participants, we corrected the p-values based on the number of test repetitions ($n = 4$). We used the threshold of $p < 0.05$ with Bonferroni correction.

White Matter (WM) Volume Analysis

The procedure for conducting the analysis prior to spatial normalization was identical to that in the GM volume analysis. For spatial normalization, a segmented WM image from each participant was warped non-linearly to the WM DARTEL template in the MNI space. The warped image was modulated by Jacobian determinants of the deformation field to preserve the relative WM volume, even after spatial normalization. As in the GM analysis, the modulated image of each participant was smoothed with an 8-mm FWHM Gaussian kernel and resampled to a resolution of 1.5 mm × 1.5 mm × 1.5 mm voxel size.

As we used in the GM volume analysis, one-to-many two-sample t-test was performed by directly comparing the WM volume obtained from each paraplegic participant to that of the control participants (**Figure 5**). We also included age, sex, and the intracranial volume as the nuisance covariates in the analysis (see above). To restrict the search volume within the WM, we used a WM mask image that was created based on our present data using the SPM Masking Toolbox (Ridgway et al., 2009). Therefore, the voxels outside this mask were excluded from the analysis. We searched for significant clusters of voxels showing WM expansion (increase of WM volume) in each paraplegic participant when compared with the control participants. Because there was no specific anatomical hypothesis available for this analysis, we explored the brain regions showing WM expansion in the entire brain space. We used the FWE-corrected extent threshold of $p < 0.05$ in the entire brain for a voxel-cluster image generated at the uncorrected height threshold of $p < 0.005$. We also checked for the brain region showing WM atrophy (decrease of WM volume) in the entire brain, in each paraplegic participant, as compared to the control participants using the procedure as described above.

To visualize the individual WM volume in the significant cluster identified in participant P1, we calculated the WM volume of the cluster in each participant. As we did in the ROI analysis for GM volume, we calculated proportion of WM volume of the significant cluster to the intracranial volume in each participant (see above). This was done purely for visualization purposes. To avoid the circular evaluation issue raised by Kriegeskorte et al. (2009), no statistical evaluations were performed.

RESULTS

fMRI Results From the Bimanual Task

When the brain activity in each paraplegic participant was directly compared to that of the control participants, it was found that two of the paraplegic participants had a significant cluster of voxels showing greater activity within the M1 foot

[1] http://www0.cs.ucl.ac.uk/staff/g.ridgway/masking/

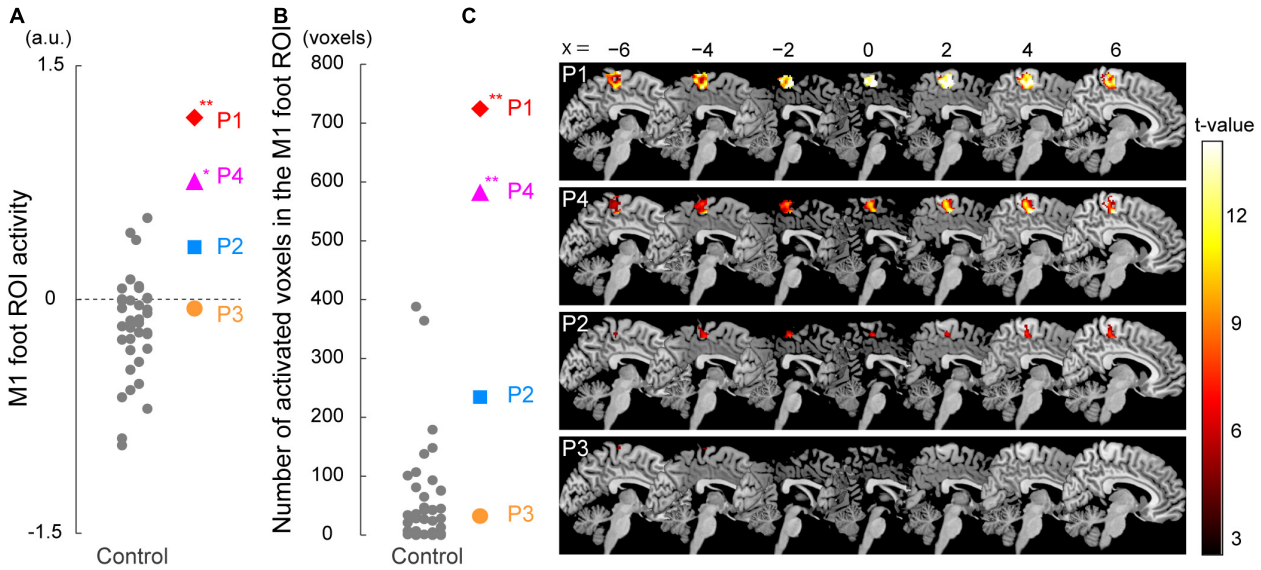

FIGURE 3 | Results from ROI analysis for functional data. **(A)** Individual M1 foot ROI activity during the bimanual task. A vertical axis indicates the mean value of the brain activity (parameter estimates) obtained from the ROI. Participants P1 and P4 showed significantly greater M1 foot ROI activity compared to the control participants. **(B)** The number of activated voxels having T-value greater than 2.61 (which corresponded to height threshold $p < 0.005$) within the M1 foot ROI in each participant. A vertical axis indicates the number of activated voxels. The number of activated voxels in participants P1 and P4, but not in P2 and P3, were significantly larger than those in the control participants. **(A,B)** Red diamonds, blue rectangles, orange circles, and pink triangles represent the data obtained from paraplegic participants P1, P2, P3, and P4, respectively. Gray dots represent the data obtained from the control participants. The plotted points for the control participants are horizontally jittered to avoid over-plotting. Asterisks indicate significant differences from the control data (** $p < 0.001$, * $p < 0.05$ with Bonferroni correction). **(C)** Voxels having T-value greater than 2.61 (height threshold $p < 0.005$) within the M1 foot ROI in each participant. Please note that participants are listed in order of greater number of activated voxels, from top to bottom. These voxels are superimposed on the sagittal slices (x = -6, −4, −2, 0, 2, 4, and 6) of the MNI standard brain. M1, primary motor cortex; ROI, region-of-interest; a.u., *arbitrary unit*.

ROI (**Figure 2C**). One was participant P1, who had a significant cluster (peak coordinates: x, y, and z = 8, −24, and 62; T = 10.15, 423 voxels) in the M1 foot ROI. The other was participant P4, who also showed a significant cluster (peak coordinates: x, y, and z = 2, -32, and 64; T = 7.35; 136 voxels). Importantly, the significant clusters identified in these participants were located in the pre-central region (**Figure 2C**), though the M1 foot ROI seemed to extend to the right post-central region. Participants P2 and P3 did not show any significant clusters. Participant P2 merely had a total of 30 voxels having T-value greater than 2.73 (which corresponded to height threshold $p < 0.005$) within the ROI (not shown in **Figure 2C**). Participant P3 had no such voxels in the ROI.

When we looked at the individual activity obtained from the M1 foot ROI, participants P1 and P4 showed an increase in activity beyond the range of distribution of the control data (**Figure 3A**). Indeed, when we performed the Crawford and Howell t-test, participants P1 and P4 showed significantly greater activity of the M1 foot ROI as compared to the control participants (P1; $t(36) = 4.06$, $p = 5.0 \times 10^{-4}$ after Bonferroni correction, P4; $t(36) = 2.82$, $p = 0.02$ after Bonferroni correction). Neither of the participants P2 and P3 showed significantly greater M1 foot ROI activity when compared to the control participants (P2; $t(36) = 1.53$, $p = 0.27$ after Bonferroni correction, P3; $t(36) = 0.33$, $p > 1$ after Bonferroni correction). On the other hand, activity of the entire M1 foot ROI decreased (less than 0) in 26 (about 70%) of the 37 control participants (**Figure 3A**). One-sample t-test revealed significant decrease in activity in the control participants as a whole ($t(36) = 3.14$, $p = 0.003$).

Next, when the number of activated voxels identified in the M1 foot ROI (845 voxels) were counted, 724, 234, 32, and 582 voxels were found in the participant P1, P2, P3, and P4, respectively (**Figures 3B,C**). Participants P1 and P4 showed greater number of activated voxels beyond the range of distribution of the control data (**Figure 3B**). The Crawford and Howell t-test showed that the numbers of the activated voxels in the participants P1 and P4 were significantly larger than those in the control participants (P1; $t(36) = 7.46$, $p = 1.7 \times 10^{-8}$ after Bonferroni correction, P4; $t(36) = 5.86$, $p = 2.1 \times 10^{-6}$ after Bonferroni correction). The number of the activated voxels in the participants P2 and P3 was not significantly different from those in the control participants (P2; $t(36) = 1.94$, $p = 0.12$ after Bonferroni correction, P3; $t(36) = -0.33$, $p > 1$ after Bonferroni correction). These results (the significant differences only in P1 and P4) were replicated when we counted the number of activated voxels using two different height thresholds of $p < 0.01$ ($T > 2.35$) and of $p < 0.001$ ($T > 3.15$) (not shown in **Figure 3B**).

Viewed collectively, the series of analyses consistently showed that the participants P1 and P4 had significantly greater activity in the M1 foot ROI during the bimanual task as compared to the control participants.

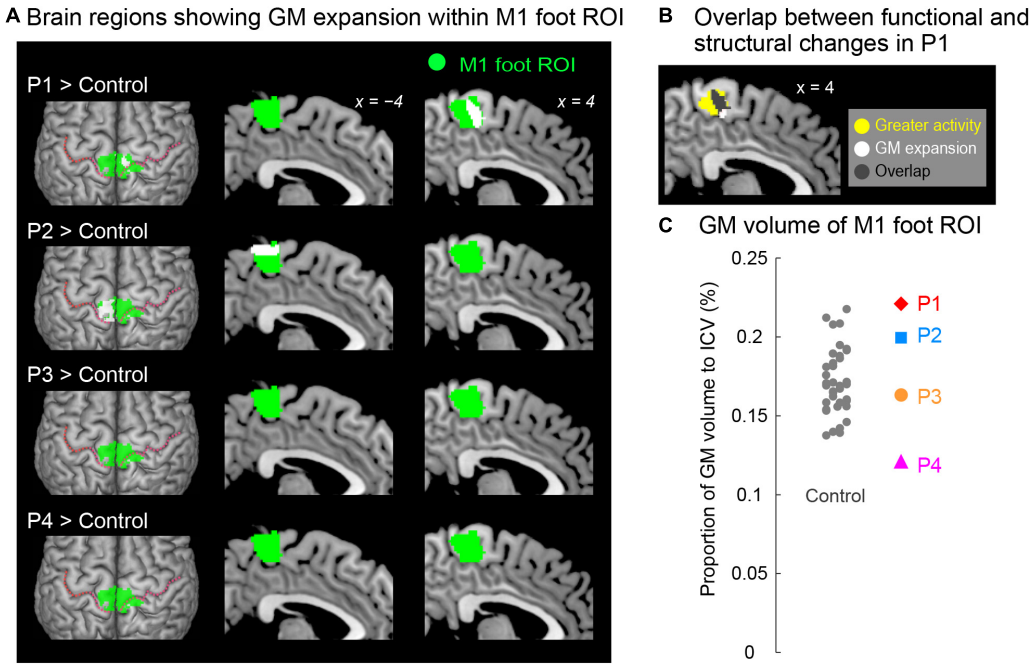

FIGURE 4 | (A) Results from contrast analysis for GM volume. Significant clusters of voxels (white sections) showing GM expansion within the M1 foot ROI when compared with the control participants are shown. Only participants P1 and P2 showed a significant cluster (white sections) in the M1 foot ROI (green sections). These sections are superimposed on the MNI standard brain. The top view, and sagittal slices (x = –4 and 4) are shown in each row. In each top view panel, pink dotted lines indicate the central sulci. **(B)** Overlap (gray section) between the M1 foot section in which participant P1 showed significant GM expansion (white and gray sections) and the region where she showed significantly greater activity during the bimanual task than the control participants (yellow and gray sections). **(C)** Individual GM volume in the M1 foot ROI. A vertical axis indicates the proportion of GM volume in the ROI to ICV. None of paraplegic participant showed significant difference from the control participants. A red diamond, blue rectangle, orange circle, and pink triangle represent the data obtained from paraplegic participants P1, P2, P3, and P4, respectively. Gray dots represent the data obtained from the control participants, and these are horizontally jittered to avoid over-plotting. GM, gray matter; M1, primary motor cortex; ROI, region-of-interest; ICV, intracranial volume; MNI, Montreal Neurological Institute.

Gray Matter (GM) Volume Change

When we explored the GM expansion (= increase in GM volume) in the M1 foot ROI in each paraplegic participant as compared to the control participants, two of the paraplegic participants (P1 and P2) showed a significant cluster of voxels showing GM expansion in the ROI (**Figure 4A**). As in the functional clusters (**Figure 2C**), the significant clusters identified in these participants were located in the pre-central region. In participant P1, the significant cluster of voxels showing GM expansion was observed in the right side of the M1 foot ROI (peak coordinates = 6, −23, 54; T = 4.82; 240 voxels; **Figure 4A**). Importantly, 75% of the expanded region (gray section in **Figure 4B**) overlapped with the region in which the participant showed a significant cluster of voxels showing greater activity during the bimanual task than the control participants (yellow and gray sections in **Figure 4B**). When we calculated the dice coefficient (range from 0 to 1, with 1 meaning complete overlap) to evaluate the spatial overlap, the value was 0.29. In participant P2, the significant cluster of voxels showing GM expansion was observed in the left side of the M1 foot ROI (peak coordinates = -15, −33, 69; T = 6.10; 395 voxels; **Figure 4A**). Neither of the participants P3 and P4 showed voxels having T-value greater than 2.73 (which corresponded to height threshold $p < 0.005$) in the ROI.

We also examined the GM atrophy (= decrease in GM volume) in the M1 foot ROI. None of the paraplegic participants showed any significant clusters of voxels showing a decrease of GM volume within the ROI, compared to the control participants. A non-significant cluster of voxels (103 voxels having T-value greater than 2.73) was found in participant P4 (not shown in **Figure 4A**), and none of the other participants (P1, P2 and P3) had such voxels in the ROI.

When we looked at the individual GM volume of the M1 foot ROI, none of paraplegic participants showed a significant increase or decrease in GM volume when compared with the control participants, though participant P4 showed a relatively lower value of GM volume (**Figure 4C**). Thus, even though a significant cluster of voxels showing GM expansion was found in participants P1 and P2 (**Figure 4A**), the expansion was most likely localized in a limited section of the M1 foot ROI, and the GM expansion was not observed throughout the M1 foot ROI.

White Matter (WM) Volume Change

Finally, when we explored the WM expansion (= increase of WM volume) in the entire brain, participant P1 showed significant clusters of voxels indicating WM expansion in the bilateral medial frontal regions (**Figure 5A**) and in the bilateral structures

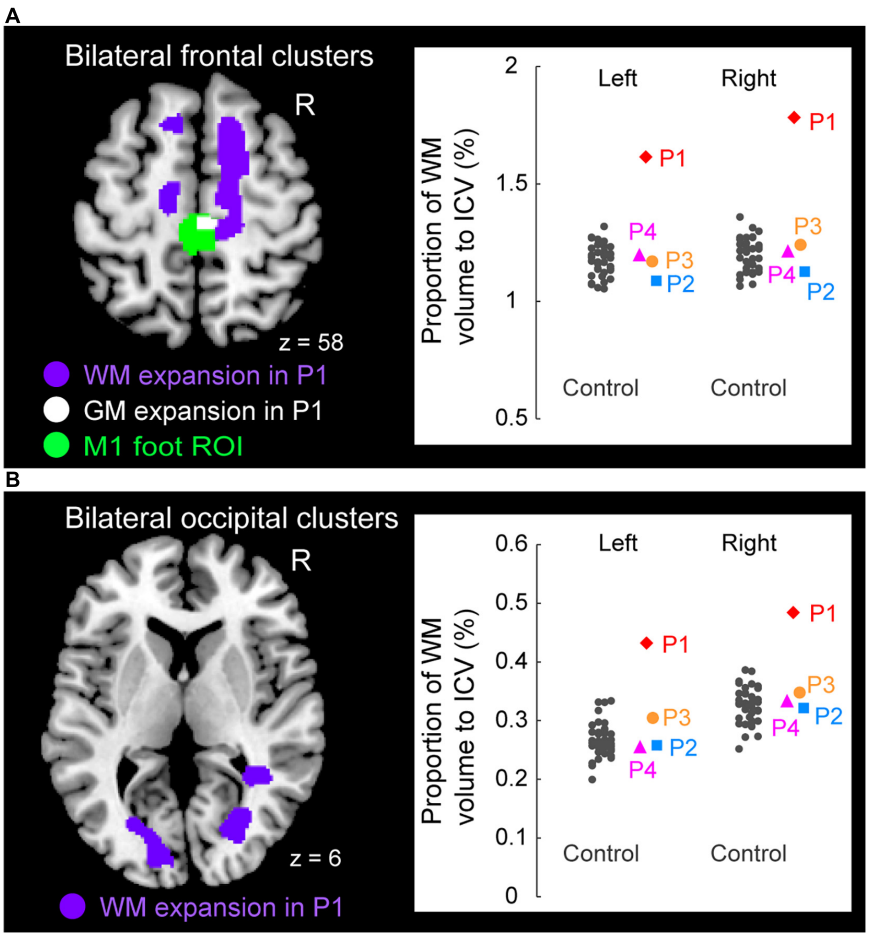

FIGURE 5 | Significant white matter (WM) expansion (purple sections) in participant P1 when compared with the control participants. Significant WM expansion was observed only in participant P1. The expansions were observed from the medial prefrontal cortices to the medial-wall motor regions **(A)** and in the structure along with the optic radiation **(B)** bilaterally. These sections are superimposed on the MNI standard brain. **(A)** The right medial frontal cluster seemed to connect to the right M1 foot section in which she showed GM expansion (white section) within the M1 foot ROI (green section). **(A,B)** The right panels in A and B show scatter plots of individual WM volumes obtained from the left and right medial frontal clusters **(A)** and from the left and right occipital clusters **(B)**, respectively. In each panel, a vertical axis represents the proportion of WM volume to ICV. A red diamond, blue rectangle, orange circle, and pink triangle represent the data obtained from paraplegic participants P1, P2, P3, and P4, respectively. Gray dots represent the data obtained from the control participants, and these are horizontally jittered to avoid over-plotting. GM, gray matter; WM, white matter; M1, primary motor cortex; ROI, region-of-interest; ICV, intracranial volume; MNI, Montreal Neurological Institute.

along the optic radiation (**Figure 5B**). Anatomical locations of these clusters are shown in **Table 2**. None of the other participants (P2, P3, and P4) exhibited significant WM expansion in any region of the brain. The right medial frontal cluster seemed to be connected to the right M1 foot section in which the GM expansion was observed (white section in **Figure 5A**). When we visually inspected the individual WM volume in the cluster identified in participant P1, the data obtained from participants P2, P3, and P4 were within the range of distribution of the control data, whereas participant P1 showed the largest value beyond the range of distribution of the control data in both frontal (right panel in **Figure 5A**) and occipital (right panel in **Figure 5B**) clusters of the bilateral hemispheres of the brain. Finally, none of the participants showed significant WM atrophy in any of the regions of the brain.

DISCUSSION

Compared to the 37 control participants, participant P1 had a significant cluster of voxels showing greater activity within the M1 foot ROI (**Figure 2C**) during the bimanual task, and a significant cluster of voxels showing GM expansion within the M1 foot ROI (**Figure 4A**). Thus, functional and structural changes were observed in participant P1 as expected. A significant cluster within the M1 foot ROI was also observed in participant P4, during the bimanual task, but not in P2 and P3 (**Figure 2C**). On the other hand, a significant cluster showing GM expansion within the ROI was observed in participant P2, but not in P3 and P4 (**Figure 4A**). Hence, the significant functional or structural change was not always observable in all the paraplegic participants, and only

TABLE 2 | Brain regions in which participant P1 showed significant WM expansion.

Cluster	Cluster size (voxels)	MNI coordinates			*P* value
		X	y	z	
Right medial frontal cluster	8662	10.5	13.5	55.5	8.03
		9	31.5	39	7.65
		9	22.5	54	6.86
Left medial frontal cluster	8581	−12	24	55.5	6.62
		−12	33	22.5	5.48
		−13.5	45	30	5.41
Left occipital cluster	2295	−9	−87	3	6.16
		−21	−87	18	5.20
		−22.5	−72	3	3.95
Right occipital cluster	2432	10.5	−85.5	27	4.05
		31.5	−46.5	7.5	3.95
		24	−72	6	3.94

participant P1 exhibited both functional and structural changes in the M1 foot ROI.

There are limitations to the current study. First, we could only recruit a limited number of paraplegic participants owing to the restrictions imposed by COVID-19 although we could recruit a relatively larger number of able-bodied control participants. The number of participants was too small to conclude the difference between congenital and acquired paraplegia, the effect of the type of wheelchair sport, or the effect of the duration of wheelchair sport training. In addition, there were differences in the age and sex among the paraplegic participants. And their ages were somewhat higher than those of the control participants, though neither participant's age was significantly different from the control group (P1; $p > 1$, P2; $p = 0.08$, P3; $p = 0.29$, P4; $p = 0.40$ after Bonferroni correction). As for the M1 foot ROI, we should have mapped the right M1 foot section by actually measuring brain activity during a left foot task. In addition, it should be borne in mind that the M1 foot section of paraplegic individuals could be different from that of the control participants in terms of its size and location. Finally, collecting more data per participant may have increased reliability of the data. Despite these limitations, this study has several implications, as discussed below.

Using M1 Foot Section for Sensory-Motor Processing of the Hand

As reported in our previous study (Morita et al., 2021a), we confirmed a significant decrease in activity of the M1 foot ROI during the bimanual task in the control participants as a whole (**Figure 3A**). Such activity decrease can be considered as cross-somatotopic inhibition (Zeharia et al., 2012; Morita et al., 2021a; Naito et al., 2021), in which the brain tries to suppress the occurrence of an unintended foot movement during hand movement. In contrast, in participant P1, we found significantly greater activity in the ROI (pre-central region) during the task when compared to the control participants (**Figure 2C**). In the ROI analysis, we also confirmed significantly greater activity (**Figure 3A**) and significantly greater number of activated voxels (**Figure 3B**) in the M1 foot ROI, when compared with the control participants. These lines of evidence strongly indicate that cross-somatotopic inhibition does not exist (disinhibited) in the brain of participant P1, and that the M1 foot section is likely utilized for sensory-motor processing of the hand as if the foot section were converted to the hand section. The exact functional role of the activity in the foot section of M1 could not be determined. However, considering the fact that the hand section of M1, in persons with congenitally compromised hand functions, has a direct output to the spinal motor neurons innervating the foot muscles (Stoeckel et al., 2009), we cannot deny the possibility that the M1 foot section in participant P1 may generate motor commands to control the hand muscles.

Significantly greater activity and number of activated voxels in the M1 foot ROI were also observed in participant P4, during the bimanual task, but not in P2 and P3 (**Figures 2C**, **3**). Hence, the results suggest that the use of M1 foot section for sensory-motor processing of the hand may occur even in an individual with acquired paraplegia; however, it does not always occur in all individuals with acquired paraplegia even though they have long-term non-use periods of the lower limbs and long-term wheelchair sports training.

It is known that human somatotopic representations have begun to develop from the fetal stage (Yamada et al., 2016; AboEllail et al., 2018; Dall'Orso et al., 2018), although clearly-distinct, adult-like somatotopic representations in the M1 appear to mature after 11-12 years old (Nebel et al., 2014). If we consider this evidence, we may speculate that in participant P1 with congenital paraplegia, the foot section had not developed as a foot section and developed as a section for other body parts (e.g., hand) since the fetal stage, and that in participant P2, the foot representation was still immature when he afflicted with paraplegia at the age of one.

In contrast, in the case of participant P4, the foot section would have developed as a normal foot section until being afflicted with paraplegia at the age of 21. Thus, the use of the M1 foot section for sensory-motor processing of the hand (**Figures 2C**, **3**) should be considered as reorganization of the already acquired foot representation after being affected by paraplegia, and this reorganization is likely due to long-term training of upper limbs through wheelchair sports training. On the other hand, participant P3, whose foot section would also have developed as normal foot section until being afflicted with paraplegia at the age of 17, did not use the M1 foot section for sensory-motor processing of the hand (**Figures 2C**, **3**). The difference between participants P3 and P4 implies the possibility that the content of wheelchair sports training (purposes of using the hands) could be an important factor to promote the use of the M1 foot section for sensory-motor processing of the hand.

From this perspective, we could point out that both participants P1 and P4 had long-term training for wheelchair track racing and marathon (**Table 1**) that are the sports in which the hands are used only for wheelchair mobility. The M1 foot section in an able-bodied individual is mainly used for mobility purposes (i.e., locomotion). Hence, it would be interesting to see if intensive training through the use of the hands for this purpose promotes the conversion of the M1 foot section into the hand section. However, these observations would be considered to be in the realm of speculation until they are verified by future studies.

In the case of individuals born without one hand, it has been reported that the cerebellar hand section for the missing hand, in addition to the hand section of the primary sensorimotor cortices, is involved in the sensory-motor processing of the foot (Hahamy et al., 2017; Hahamy and Makin, 2019). However, in the present study, none of our paraplegic participants showed a significant increase in the activity in the cerebellar foot section during the bimanual task (see **Supplementary Material** and **Supplementary Figure 2**). This suggests the possibility of a difference in the latent potential for the conversion of somatotopic representation between the hand and foot sections in the cerebellum. In addition, it is known that long-term training of the hand (Krings et al., 2000) or foot (Naito and Hirose, 2014) movement may facilitate efficient recruitment of the brain activity (show reduction of brain activity) in its corresponding somatotopic sections. However, contrary to these previous reports, none of our paraplegic participants efficiently recruited (showed less) activity in the hand sections of the multiple motor areas (the M1, CMA, and cerebellum) during the bimanual task (see **Supplementary Material** and **Figure 3**), although they had long-term training of the upper limbs during wheelchair sports training (**Table 1**). Further investigations are required to generalize these findings to a larger population of individuals with long-term wheelchair sports training.

Gray Matter Changes

As expected, the contrast analysis revealed significant GM expansion within the M1 foot ROI in participant P1 when compared with the control participants (**Figure 4A**). Such significant GM expansion was also observed in participant P2, but not in P3 and P4 (**Figure 4A**). Hence, similar to the above functional changes, the GM expansion within the M1 foot ROI may occur even in an individual with acquired paraplegia, but does not always occur in all individuals with acquired paraplegia even though they have long-term non-use period of the lower limbs and long-term wheelchair sports training.

Importantly, such GM expansion was localized in a limited portion of the M1 foot ROI (**Figure 4A**), and the expansion was not observed throughout the M1 foot ROI as shown in the ROI analysis (**Figure 4C**). In addition, we could point out that the GM expansion was observed in the right pre-central region in participant P1, while it was observed in the left region in participant P2, though we have no clear reasons for the difference. Although the exact physiological changes underlying GM expansion are still unknown, axon sprouting, dendritic branching synaptogenesis, neurogenesis, and changes in the glial number and morphology are suggested to be important contributors to GM expansion (Zatorre et al., 2012). Hence, our data suggest that these changes would have occurred in the localized pre-central regions of participants P1 and P2.

The finding that significant GM expansion was observed in participants P1 and P2 but not in P3 and P4 (**Figure 4A**) leads us to conjecture that GM expansion is likely to occur in persons who became paraplegic at a very early stage of development. From the developmental perspective, it should also be noted that neither of the participants P3 and P4, who became paraplegic as a result of spinal cord injury during adulthood, showed significant GM atrophy in the M1 foot ROI (**Figure 4C**). Despite GM atrophy is often reported in the primary sensory-motor cortices after spinal cord injury even after several years of injury (Crawley et al., 2004; Freund et al., 2013; Hou et al., 2014). It is possible that GM atrophy would have been observed if the brains of participants P3 and P4 were scanned immediately following their spinal cord injury. Therefore, there is a possibility that long-term wheelchair sports training might have contributed to improve the putative GM atrophy. In the case of participant P4, since his M1 foot section was involved in sensory-motor processing of the hand (**Figures 2C**, **3**), long-term training of the upper limbs through wheelchair sports training could have restored his putative GM atrophy. In the case of participant P3 who did not use the M1 foot section for sensory-motor processing of the hand (**Figures 2C**, **3**), long-term training of other body parts through wheelchair sports training could have restored the putative atrophy.

In participant P1, 75% of the GM-expanded region (gray section in **Figure 4B**) overlapped with the region in which the participant showed a significantly greater activity than the control participants (yellow and gray sections in **Figure 4B**) during the bimanual task. Such consistency between functional and structural changes were only observed in participant P1. Hence, in participant P1, the GM was expanded in the M1 foot section that was used for sensory-motor processing of the hand. If we consider that GM expansion is deeply associated with use-dependent plasticity (Gaser and Schlaug, 2003; Draganski et al., 2004), long-term training of the upper limbs through wheelchair racing training could be an important factor for the GM expansion. We may further speculate that participant P1 has used the M1 foot section for sensory-motor processing of the hand more frequently than the control participants have used this section for foot movements. In the case of participant P2 who did not use the M1 foot section for sensory-motor processing of the hand (**Figures 2C**, **3**), long-term training of other body parts through wheelchair sports training could have contributed the GM expansion (**Figure 4A**).

Finally, none of our paraplegic participants showed significant GM expansion in the hand sections of the M1, CMA, and cerebellum (see **Supplementary Material** and **Supplementary Figure 4**), suggesting that our paraplegic participants use these hand sections to the same degree as the control participants use them. Similarly, none of our paraplegic participants showed significant GM expansion in the cerebellar foot section (**Supplementary Figure 4**).

White Matter Changes

Only participant P1 showed significant WM expansion in the bilateral medial frontal regions and in the bilateral structures

along the optic radiation (**Figure 5**). Although the exact physiological changes underlying WM expansion are not fully understood, white matter changes are thought to be related to changes in the number of axons, axon diameter, the packing density of fibers, axon branching, axon trajectories and myelination (Zatorre et al., 2012). As with GM volume, use-dependent plasticity can also be an important factor for WM expansion (Scholz et al., 2009). Thus, the long-term wheelchair racing training must be associated with the WM expansion in this participant.

WM expansion in the bilateral structures along the optic radiation are most likely associated with visual functions, which implies the possibility of the intensive use of visual system by participant P1. On the other hand, the medial frontal regions are likely to contain nerve fibers that connect the medial prefrontal cortex and the medial wall motor regions, including the M1 foot sections (probably the superior branch of the superior longitudinal fasciculus; Parlatini et al., 2017). Indeed, the right medial frontal cluster seemed to connect to the right M1 foot section in which the participant showed GM expansion (white section in **Figure 5A**). Evidence has been accumulating to support the view that the medial prefrontal cortex is important for generating highly-motivated behaviors (Walton et al., 2003; Husain and Roiser, 2018; Nakamura et al., 2021). Without a higher level of motivation, one cannot participate in six consecutive Paralympic Games and win a total of 19 medals. Thus, the WM expansion in the bilateral medial frontal regions could be associated with the repetition of highly-motivated wheelchair pedaling during long-term wheelchair racing training.

Hyper-Adaptation

In the brain of participant P1, the M1 foot section was used for sensory-motor processing of the hand (**Figures 2C**, **3**), and this claim was further corroborated by the GM expansion in the foot section that was activated during the hand sensory-motor processing (**Figures 4A,B**). The M1 foot section is normally deactivated during the hand sensory-motor processing in able-bodied people (**Figure 3A**; Morita et al., 2021a). Hence, in this participant, the M1 foot section, which is normally suppressed during the hand sensory-motor processing, has drastically changed to become used for this sensory-motor processing other than its original function of foot motor control. We want to propose that such phenomenon (a brain region that is not normally involved in a certain information processing, but is rather suppressed during this information processing, in able-bodied persons, is chronically disinhibited and is regularly used during this information processing), could be better referred to hyper-adaptation. Because such adaptation may represent extreme adaptability of the human brain, which is rarely seen in typically developed individuals and should be distinct from normal adaptions as we often observe in force-field (e.g., Shadmehr and Mussa-Ivaldi, 1994) and visuo-motor (e.g., Imamizu et al., 2000) adaptations and so on.

The use of the foot section for the hand sensory-motor processing was also observed in participant P4 (**Figures 2C**, **3**), though no supportive evidence of significant GM expansion was observed in this participant. Thus, it was likely that hyper-adaptation might also occur in this participant. In participants P2 and P3, the activity in the M1 foot section during the bimanual task was comparable to that observed in the control participants (**Figures 2C**, **3**). However, this does not guarantee that hyper-adaptation does not occur in their brains because their M1 foot sections might be used for other sensory-motor processing rather than the hand, which was not directly assessed in the current work.

Based on the above definition, tactile processing in the visual cortex of some blind individuals (e.g., Sadato et al., 1996, 2002) could also be another example of hyper-adaptation because the human visual cortex is normally suppressed during sensory-motor processing in sighted people (cross-modal inhibition; Morita et al., 2019), but the visual cortex of some blind individuals has drastically changed to become involved in tactile processing other than its original function of visual processing. Hyper-adaptation may also occur when the brain manages to adapt to irreversible and severe injuries and diseases through long-term sensory, motor and cognitive trainings. Further researches will reveal what kind of adaptation should be termed hyper-adaptation, and neural mechanisms and psycho-behavioral factors that trigger and promote hyper-adaptation.

DATA AVAILABILITY STATEMENT

The original contributions presented in the study are included in the article/**Supplementary Material**, further inquiries can be directed to the corresponding author/s.

ETHICS STATEMENT

The studies involving human participants were reviewed and approved by the study was approved by the Ethics Committee of the National Institute of Information and Communications Technology and by the MRI Safety Committee of the Center for Information and Neural Networks (no. 2003260010). The patients/participants provided their written informed consent to participate in this study. Written informed consent was obtained from the individual(s) for the publication of any potentially identifiable images or data included in this article.

AUTHOR CONTRIBUTIONS

TM and EN: conceptualization. TM, SH, HT, and EN: methodology. TM, SH, NK, HT, MA, and EN: validation and writing – review and editing. TM and EN: formal analysis, writing – original draft preparation, and funding acquisition. TM, SH, NK, HT, and EN: investigation. TM: visualization. MA: supervision. EN: project administration. All authors contributed to the article and approved the submitted version.

FUNDING

This study was supported by JSPS KAKENHI Grant Number JP19H05723 to EN and by JSPS KAKENHI Grant Number

JP20H04492 to TM. The funding sources had no involvement in the study design; in the collection, analysis, and interpretation of data; in the writing of the report; and in the decision to submit the article for publication.

ACKNOWLEDGMENTS

We are grateful to Keiko Ueyama and CiNet MRI staff for their support during the study. We also thank the NHK Miracle Body staff, especially Yoriko Koizumi and Shiho Sakamoto for giving us the opportunity to investigate the brain of the top wheelchair racing Paralympian. We would like to thank Editage for the English language editing.

SUPPLEMENTARY MATERIAL

The Supplementary Material for this article can be found online at: https://www.frontiersin.org/articles/10.3389/fnsys.2022.780652/full#supplementary-material

REFERENCES

AboEllail, M. A. M., Kanenishi, K., Mori, N., Moguchi, J., Marumo, G., and Hata, T. (2018). Ultrasound study of fetal movements in singleton and twin pregnancies at 12-19 weeks. *J. Perinat. Med.* 46, 832–838. doi: 10.1515/jpm-2017-0158

Aguirre, G. K., Zarahn, E., and D'Esposito, M. (1998). The inferential impact of global signal covariates in functional neuroimaging analyses. *Neuroimage* 8, 302–306. doi: 10.1006/nimg.1998.0367

Amemiya, K., Morita, T., Hirose, S., Ikegami, T., Hirashima, M., and Naito, E. (2021). Neurological and behavioral features of locomotor imagery in the blind. *Brain Imaging Behav.* 15, 656–676. doi: 10.1007/s11682-020-00275-w

Amiez, C., and Petrides, M. (2014). Neuroimaging evidence of the anatomo-functional organization of the human cingulate motor areas. *Cereb. Cortex* 24, 563–578. doi: 10.1093/cercor/bhs329

Ashburner, J. (2010). *VBM Tutorial*. London: Wellcome Trust Centre for Neuroimaging.

Boucard, C. C., Rauschecker, J. P., Neufang, S., Berthele, A., Doll, A., Manoliu, A., et al. (2016). Visual imagery and functional connectivity in blindness: a single-case study. *Brain Struct. Funct.* 221, 2367–2374. doi: 10.1007/s00429-015-1010-2

Bruehlmeier, M., Dietz, V., Leenders, K. L., Roelcke, U., Missimer, J., and Curt, A. (1998). How does the human brain deal with a spinal cord injury? *Eur. J. Neurosci.* 10, 3918–3922. doi: 10.1046/j.1460-9568.1998.00454.x

Crawford, J. R., and Garthwaite, P. H. (2012). Single-case research in neuropsychology: a comparison of five forms of t-test for comparing a case to controls. *Cortex* 48, 1009–1016. doi: 10.1016/j.cortex.2011.06.021

Crawford, J. R., and Howell, D. C. (1998). Comparing an individual's test score against norms derived from small samples. *Clin. Neuropsychol.* 12, 482–486. doi: 10.1076/clin.12.4.482.7241

Crawley, A., Jurkiewicz, M., Yim, A., Heyn, S., Verrier, M., Fehlings, M., et al. (2004). Absence of localized grey matter volume changes in the motor cortex following spinal cord injury. *Brain Res.* 1028, 19–25. doi: 10.1016/j.brainres.2004.08.060

Dall'Orso, S., Steinweg, J., Allievi, A. G., Edwards, A. D., Burdet, E., and Arichi, T. (2018). Somatotopic mapping of the developing sensorimotor cortex in the preterm human brain. *Cereb. Cortex* 28, 2507–2515. doi: 10.1093/cercor/bhy050

Dempsey-Jones, H., Wesselink, D. B., Friedman, J., and Makin, T. R. (2019). Organized toe maps in extreme foot users. *Cell Rep.* 28, 2748–2756. doi: 10.1016/j.celrep.2019.08.027

Draganski, B., Gaser, C., Busch, V., Schuierer, G., Bogdahn, U., and May, A. (2004). Changes in grey matter induced by training. *Nature* 427, 311–312. doi: 10.1038/427311a

Ehrsson, H. H., Geyer, S., and Naito, E. (2003). Imagery of voluntary movement of fingers, toes, and tongue activates corresponding body-part–specific motor representations. *J. Neurophysiol.* 90, 3304–3316. doi: 10.1152/jn.01113.2002

Eickhoff, S. B., Stephan, K. E., Mohlberg, H., Grefkes, C., Fink, G. R., Amunts, K., et al. (2005). A new SPM toolbox for combining probabilistic cytoarchitectonic maps and functional imaging data. *Neuroimage* 25, 1325–1335. doi: 10.1016/j.neuroimage.2004.12.034

Evans, A. C., Kamber, M., Collins, D. L., and MacDonald, D. (1994). "An MRI-based probabilistic atlas of neuroanatomy," in *Magnetic Resonance Scanning and Epilepsy NATO ASI Series*, eds S. D. Shorvon, D. R. Fish, F. Andermann, G. M. Bydder, and H. Stefan (Boston, MA: Springer), 263–274. doi: 10.1007/978-1-4615-2546-2_48

Flor, H., Elbert, T., Knecht, S., Wienbruch, C., Pantev, C., Birbaumer, N., et al. (1995). Phantom-limb pain as a perceptual correlate of cortical reorganization following arm amputation. *Nature* 375, 482–484. doi: 10.1038/375482a0

Flor, H., Nikolajsen, L., and Staehelin Jensen, T. (2006). Phantom limb pain: a case of maladaptive CNS plasticity? *Nat. Rev. Neurol.* 7, 873–881. doi: 10.1038/nrn1991

Freund, P., Weiskopf, N., Ashburner, J., Wolf, K., Sutter, R., Altmann, D. R., et al. (2013). MRI investigation of the sensorimotor cortex and the corticospinal tract after acute spinal cord injury: a prospective longitudinal study. *Lancet Neurol.* 12, 873–881. doi: 10.1016/S1474-4422(13)70146-7

Friston, K. J., Holmes, A. P., Poline, J. B., Grasby, P. J., Williams, S. C., Frackowiak, R. S., et al. (1995). Analysis of fMRI time-series revisited. *Neuroimage* 2, 45–53. doi: 10.1006/nimg.1995.1007

Gaser, C., and Schlaug, G. (2003). Brain structures differ between musicians and non-musicians. *J. Neurosci.* 23, 9240–9245. doi: 10.1523/JNEUROSCI.23-27-09240.2003

Hahamy, A., Macdonald, S. N., van den Heiligenberg, F., Kieliba, P., Emir, U., Malach, R., et al. (2017). Representation of multiple body parts in the missing-hand territory of congenital one-handers. *Curr. Biol.* 27, 1350–1355. doi: 10.1016/j.cub.2017.03.053

Hahamy, A., and Makin, T. R. (2019). Remapping in cerebral and cerebellar cortices Is not restricted by somatotopy. *J. Neurosci.* 39, 9328–9342. doi: 10.1523/JNEUROSCI.2599-18.2019

He, S. Q., Dum, R. P., and Strick, P. L. (1995). Topographic organization of corticospinal projections from the frontal lobe: motor areas on the medial surface of the hemisphere. *J. Neurosci.* 15, 3284–3306. doi: 10.1523/JNEUROSCI.15-05-03284.1995

Holmes, A. P., and Friston, K. J. (1998). Generalisability, random effects and population inference. *Neuroimage* 7:S754. doi: 10.1016/j.neuroimage.2004.08.055

Hou, J., Yan, R., Xiang, Z., Zhang, H., Liu, J., Wu, Y., et al. (2014). Brain sensorimotor system atrophy during the early stage of spinal cord injury in humans. *Neuroscience* 266, 208–215. doi: 10.1016/j.neuroscience.2014.02.013

Hu, X., Erb, M., Ackermann, H., Martin, J. A., Grodd, W., and Reiterer, S. M. (2011). Voxel-based morphometry studies of personality: issue of statistical model specification–effect of nuisance covariates. *Neuroimage* 54, 1994–2005. doi: 10.1016/j.neuroimage.2010.10.024

Husain, M., and Roiser, J. P. (2018). Neuroscience of apathy and anhedonia: a transdiagnostic approach. *Nat. Rev. Neurol.* 19, 470–484. doi: 10.1038/s41583-018-0029-9

Imamizu, H., Miyauchi, S., Tamada, T., Sasaki, Y., Takino, R., PuÈtz, B., et al. (2000). Human cerebellar activity reflecting an acquired internal model of a new tool. *Nature* 403, 192–195. doi: 10.1038/35003194

Kriegeskorte, N., Simmons, W. K., Bellgowan, P. S., and Baker, C. I. (2009). Circular analysis in systems neuroscience: the dangers of double dipping. *Nat. Neurosci.* 12, 535–540. doi: 10.1038/nn.2303

Krings, T., Töpper, R., Foltys, H., Erberich, S., Sparing, R., Willmes, K., et al. (2000). Cortical activation patterns during complex motor tasks in piano players and control subjects. A functional magnetic resonance imaging study. *Neurosci. Lett.* 278, 189–193. doi: 10.1016/S0304-3940(99)00930-1

Lotze, M., Flor, H., Grodd, W., Larbig, W., and Birbaumer, N. (2001). Phantom movements and pain An fMRI study in upper limb amputees. *Brain* 124, 2268–2277. doi: 10.1093/brain/124.11.2268

Lotze, M., Laubis-Herrmann, U., Topka, H., Erb, M., and Grodd, W. (1999). Reorganization in the primary motor cortex after spinal cord injury - A functional Magnetic Resonance (fMRI) Study. *Restor. Neurol. Neurosci.* 14, 183–187.

Luo, C., Song, W., Chen, Q., Zheng, Z., Chen, K., Cao, B., et al. (2014). Reduced functional connectivity in early-stage drug-naive Parkinson's disease: a resting-state fMRI study. *Neurobiol. Aging* 35, 431–441. doi: 10.1016/j.neurobiolaging.2013.08.018

Mikulis, D. J., Jurkiewicz, M. T., Mcllroy, W. E., Staines, W. R., Rickards, L., Kalsi-Ryan, S., et al. (2002). Adaptation in the motor cortex following cervical spinal cord injury. *Neurology* 58, 794–801. doi: 10.1212/WNL.58.5.794

Morita, T., Asada, M., and Naito, E. (2019). Developmental changes in task-induced brain deactivation in humans revealed by a motor task. *Dev. Neurobiol.* 79, 536–558. doi: 10.1002/dneu.22701

Morita, T., Asada, M., and Naito, E. (2021a). Examination of the development and aging of brain deactivation using a unimanual motor task. *Adv. Robot.* 35, 842–857. doi: 10.1080/01691864.2021.1886168

Morita, T., Asada, M., and Naito, E. (2021b). Gray-matter expansion of social brain networks in individuals high in public self-consciousness. *Brain Sci.* 11:374. doi: 10.3390/brainsci11030374

Mühlau, M., Wohlschläger, A. M., Gaser, C., Valet, M., Weindl, A., Nunnemann, S., et al. (2009). Voxel-based morphometry in individual patients: a pilot study in early huntington disease. *Am. J. Neuroradiol.* 30, 539–543. doi: 10.3174/ajnr.A1390

Naito, E., and Hirose, S. (2014). Efficient foot motor control by Neymar's brain. *Front. Hum. Neurosci.* 8:594. doi: 10.3389/fnhum.2014.00594

Naito, E., Morita, T., Kimura, N., and Asada, M. (2021). Existence of interhemispheric inhibition between foot sections of human primary motor cortices: evidence from negative blood oxygenation-level dependent signal. *Brain Sci.* 11:1099. doi: 10.3390/brainsci11081099

Naito, E., Nakashima, T., Kito, T., Aramaki, Y., Okada, T., and Sadato, N. (2007). Human limb-specific and non-limb-specific brain representations during kinesthetic illusory movements of the upper and lower extremities. *Eur. J. Neurosci.* 25, 3476–3487. doi: 10.1111/j.1460-9568.2007.05587.x

Nakagawa, K., Takemi, M., Nakanishi, T., Sasaki, A., and Nakazawa, K. (2020). Cortical reorganization of lower-limb motor representations in an elite archery athlete with congenital amputation of both arms. *Neuroimage Clin.* 25:102144. doi: 10.1016/j.nicl.2019.102144

Nakamura, S., Kishimoto, Y., Sekino, M., Nakamura, M., and Tsutsui, K.-I. (2021). Depression-like state induced by low-frequency repetitive transcranial magnetic stimulation to ventral medial frontal cortex in monkeys. *bioRxiv* [Preprint]. [accessed on May 23, 2021] doi: 10.1101/2021.05.21.445094

Nebel, M. B., Joel, S. E., Muschelli, J., Barber, A. D., Caffo, B. S., Pekar, J. J., et al. (2014). Disruption of functional organization within the primary motor cortex in children with autism. *Hum. Brain Mapp.* 35, 567–580. doi: 10.1002/hbm.22188

Oldfield, R. C. (1971). The assessment and analysis of handedness: the Edinburgh inventory. *Neuropsychologia* 9, 97–113. doi: 10.1016/0028-3932(71)90067-4

Parlatini, V., Radua, J., Dell'Acqua, F., Leslie, A., Simmons, A., Murphy, D., et al. (2017). Functional segregation and integration within fronto-parietal networks. *Neuroimage* 146, 367–375. doi: 10.1016/j.neuroimage.2016.08.031

Ridgway, G. R., Omar, R., Ourselin, S., Hill, D. L. G., Warren, J. D., and Fox, N. C. (2009). Issues with threshold masking in voxel-based morphometry of atrophied brains. *Neuroimage* 44, 99–111. doi: 10.1016/j.neuroimage.2008.08.045

Sadato, N., Okada, T., Honda, M., and Yonekura, Y. (2002). Critical period for cross-modal plasticity in blind humans: a functional MRI study. *Neuroimage* 16, 389–400. doi: 10.1006/nimg.2002.1111

Sadato, N., Pascual-Leone, A., Grafman, J., Ibañez, V., Deiber, M. P., Dold, G., et al. (1996). Activation of the primary visual cortex by Braille reading in blind subjects. *Nature* 380, 526–528. doi: 10.1038/380526a0

Scarpazza, C., Sartori, G., De Simone, M. S., and Mechelli, A. (2013). When the single matters more than the group: very high false positive rates in single case Voxel Based Morphometry. *Neuroimage* 70, 175–188. doi: 10.1016/j.neuroimage.2012.12.045

Scholz, J., Klein, M. C., Behrens, T. E., and Johansen-Berg, H. (2009). Training induces changes in white-matter architecture. *Nat. Neurosci.* 12, 1370–1371. doi: 10.1038/nn.2412

Shadmehr, R., and Mussa-Ivaldi, F. A. (1994). Adaptive representation of dynamics during learning of a motor task. *J. Neurosci.* 14, 3208–3224. doi: 10.1523/JNEUROSCI.14-05-03208.1994

Stoeckel, M. C., Seitz, R. J., and Buetefisch, C. M. (2009). Congenitally altered motor experience alters somatotopic organization of human primary motor cortex. *PNAS* 106, 2395–2400. doi: 10.1073/pnas.0803733106

Taubert, M., Wenzel, U., Draganski, B., Kiebel, S. J., Ragert, P., Krug, J., et al. (2015). Investigating neuroanatomical features in top athletes at the single subject level. *PLoS One* 10:e0129508. doi: 10.1371/journal.pone.0129508

van Melick, N., Meddeler, B. M., Hoogeboom, T. J., Nijhuis-van der Sanden, M. W., and van Cingel, R. E. H. (2017). How to determine leg dominance: the agreement between self-reported and observed performance in healthy adults. *PLoS One* 12:e0189876. doi: 10.1371/journal.pone.0189876

Walton, M., Bannerman, D., and Rushworth, M. (2003). The role of rat medial frontal cortex in effort-based decision making. *J. Neurosci.* 22, 10996–11003. doi: 10.1523/JNEUROSCI.22-24-10996.2002

Whitwell, J. L., Crum, W. R., Watt, H. C., and Fox, N. C. (2001). Normalization of cerebral volumes by use of intracranial volume: implications for longitudinal quantitative MR imaging. *Am. J. Neuroradiol.* 22, 1483–1489.

Worsley, K. J., and Friston, K. J. (1995). Analysis of fMRI time-series revisited—again. *Neuroimage* 2, 173–181. doi: 10.1006/nimg.1995.1023

Yamada, Y., Kanazawa, H., Iwasaki, S., Tsukahara, Y., Iwata, O., Yamada, S., et al. (2016). An embodied brain model of the human foetus. *Sci. Rep.* 6;27893. doi: 10.1038/srep27893

Zatorre, R. J., Fields, R. D., and Johansen-Berg, H. (2012). Plasticity in gray and white: neuroimaging changes in brain structure during learning. *Nat. Neurosci.* 15, 528–536. doi: 10.1038/nn.3045

Zeharia, N., Hertz, U., Flash, T., and Amedi, A. (2012). Negative blood oxygenation level dependent homunculus and somatotopic information in primary motor cortex and supplementary motor area. *PNAS* 109, 18565–18570. doi: 10.1073/pnas.1119125109

Conflict of Interest: The authors declare that the research was conducted in the absence of any commercial or financial relationships that could be construed as a potential conflict of interest.

Publisher's Note: All claims expressed in this article are solely those of the authors and do not necessarily represent those of their affiliated organizations, or those of the publisher, the editors and the reviewers. Any product that may be evaluated in this article, or claim that may be made by its manufacturer, is not guaranteed or endorsed by the publisher.

Copyright © 2022 Morita, Hirose, Kimura, Takemura, Asada and Naito. This is an open-access article distributed under the terms of the Creative Commons Attribution License (CC BY). The use, distribution or reproduction in other forums is permitted, provided the original author(s) and the copyright owner(s) are credited and that the original publication in this journal is cited, in accordance with accepted academic practice. No use, distribution or reproduction is permitted which does not comply with these terms.

frontiers | Frontiers in Human Neuroscience

ORIGINAL RESEARCH
published: 12 May 2022
doi: 10.3389/fnhum.2022.842883

Stochastic Physiological Gaze-Evoked Nystagmus With Slow Centripetal Drift During Fixational Eye Movements at Small Gaze Eccentricities

*Makoto Ozawa, Yasuyuki Suzuki and Taishin Nomura**

Department of Mechanical Science and Bioengineering, Graduate School of Engineering Science, Osaka University, Osaka, Japan

Involuntary eye movement during gaze (GZ) fixation, referred to as fixational eye movement (FEM), consists of two types of components: a Brownian motion like component called drifts-tremor (DRT) and a ballistic component called microsaccade (MS) with a mean saccadic amplitude of about 0.3° and a mean inter-MS interval of about 0.5 s. During GZ fixation in healthy people in an eccentric position, typically with an eccentricity more than 30°, eyes exhibit oscillatory movements alternating between centripetal drift and centrifugal saccade with a mean saccadic amplitude of about 1° and a period in the range of 0.5–1.0 s, which has been known as the physiological gaze-evoked nystagmus (GEN). Here, we designed a simple experimental paradigm of GZ fixation on a target shifted horizontally from the front-facing position with fewer eccentricities. We found a clear tendency of centripetal DRT and centrifugal MS as in GEN, but with more stochasticity and with slower drift velocity compared to GEN, even during FEM at GZ positions with small eccentricities. Our results showed that the target shift-dependent balance between DRT and MS achieves the GZ bounded around each of the given targets. In other words, GZ relaxes slowly with the centripetal DRT toward the front-facing position during inter-MS intervals, as if there always exists a quasi-stable equilibrium posture in the front-facing position, and MS actions pull GZ intermittently back to the target position in the opposite direction to DRT.

Keywords: physiological gaze-evoked nystagmus, fixational eye movements, ocular drift, centripetal drift, microsaccade, inter-microsaccadic interval, small gaze eccentricity

OPEN ACCESS

Edited by:
Jun Izawa,
University of Tsukuba, Japan

Reviewed by:
Ziad M. Hafed,
University of Tübingen, Germany
Toru Ohira,
Nagoya University, Japan

****Correspondence:***
Taishin Nomura
taishin@bpe.es.osaka-u.ac.jp

Specialty section:
This article was submitted to Motor Neuroscience, a section of the journal Frontiers in Human Neuroscience

Received: *24 December 2021*
Accepted: *05 April 2022*
Published: *12 May 2022*

Citation:
Ozawa M, Suzuki Y and Nomura T (2022) Stochastic Physiological Gaze-Evoked Nystagmus With Slow Centripetal Drift During Fixational Eye Movements at Small Gaze Eccentricities. Front. Hum. Neurosci. 16:842883. doi: 10.3389/fnhum.2022.842883

INTRODUCTION

Human eyes always keep moving, even when one tries to fixate gaze (GZ) steadily. In this way, eyeball posture and the resultant GZ position fluctuate mostly involuntarily with small amplitudes during GZ fixation, referred to as fixational eye movement (FEM) (Ditchburn and Ginsborg, 1953; Rucci and Poletti, 2015), although recent studies report the voluntary aspects of FEM (Willeke et al., 2019). The corresponding time series of GZ position is referred to here as the GZ time series. It has been known that FEM contributes to visual perceptual constancy by counteracting

sensory adaptation (Martinez-Conde et al., 2004). The GZ time series during FEM is composed of two types of eye movements: the drifts-tremor (DRT) and the microsaccade (MS). DRT is a slowly migrating quasi-continuous eye movement, like a Brownian motion, whose spectral power is dominated at a low-frequency band below 40 Hz, with the remaining power widely distributed in the range less than 100 Hz (Findlay, 1971; Ezenman et al., 1985). On the other hand, MS is a ballistic eye movement with a mean saccadic amplitude of about 0.3° during FEM (Martinez-Conde et al., 2009), which occurs approximately two times per second with Poisson-point-process-like inter-MS intervals (Cunitz and Steinman, 1969; Engbert and Kliegl, 2004; Engbert and Mergenthaler, 2006; Otero-Millan et al., 2008).

When the GZ target is located at an eccentric position, typically with an eccentricity more than 30°, which forces one eyeball to rotate largely away from the nose and the other eyeball to rotate toward the nose, the GZ position, defined as the binocular eye position, exhibits oscillatory movements alternating between a centripetal drift toward the front-face position and a centrifugal saccade back to the fixation target position, with a mean saccadic amplitude of about 1° and the oscillation period in the range of 0.5–1.0 s. This phenomenon is known as the physiological gaze-evoked nystagmus (physiological GEN), also called end-point nystagmus (EPN). Recent studies suggested that healthy people commonly exhibit physiological GEN at wide horizontal angles of the fixation target, from −40° to 40° across the entire range that humans can GZ (Whyte et al., 2010; Bertolini et al., 2013). On the other hand, dysfunctions of the brainstem or cerebellum can cause GZ instability, leading to pathological GEN (Cannon and Robinson, 1987; Versino et al., 1996). In both pathological and physiological GEN, the incidence rate of GEN and the absolute velocity of centripetal drifts increases with increasing GZ angle, i.e., high GZ eccentricity (Eizenman et al., 1990; Büttner and Grundei, 1995; Leigh and Zee, 2015; Tarnutzer et al., 2015). These studies imply that pathological GEN and physiological GEN share common neural networks within the cerebellum and the brainstem that has an oculomotor velocity-to-position neural integrator with leakiness. For example, increasing the amount of alcohol intake that impairs cerebellar oculomotor functions makes centripetal drifts faster with increased GZ eccentricity (Romano et al., 2017).

The relationships between FEM and physiological GEN have not been clearly understood. Bertolini et al. (2013) reported a linear relationship between a horizontal centripetal drift velocity of and horizontal GZ eccentricity (GZ angle of the fixation target) in healthy people, in which the slope of the linear relationship was about 0.02 [°/s]/[°], i.e., the horizontal centripetal drift velocity increases by the amount of 0.02/s per 1 of increase in the horizontal GZ eccentricity, for small GZ eccentricities less than 20°, and the slope was altered to about 0.05 [°/s]/[°] for large GZ eccentricities in the range of 20° to 40°. Their estimates imply a centripetal drift velocity of 0.2°/s at a horizontal fixation point of 10°, which is non-negligibly large. To establish a GZ fixation with the error caused by such a non-negligible centripetal DRT velocity, the centrifugal MS must work for counterbalancing. However, because the fixation target used by Bertolini et al. was an LED that flashed briefly for 0.050 s every 2 s and moving between −40° and 40° synchronously with the flashing, the FEM data acquired for each fixation point was too short to characterize the relationships between centripetal DRT and centrifugal MS in FEM in healthy people.

The purpose of this study was to characterize centripetal DRT and centrifugal MS more accurately than previous studies as a function of the horizontal position with small GZ eccentricities, and to elucidate the counterbalanced coordination between centripetal DRT drift and centrifugal MS jumps. To this end, we measured FEM in young healthy participants to acquire the corresponding GZ time series for a small visual target presented in front of the face, and investigated how their characteristics change depending on the horizontal position of the target, particularly in the horizontal component of FEM. In the data analysis, we decomposed the GZ time series into DRT components and MS components to define the DRT time series consisting of DRT components only, as well as MS time series consisting of MS components only. Based on the DRT and MS time series, we investigated how they could be characterized differently depending on horizontal GZ position.

MATERIALS AND METHODS

Measurements of FEM

Subjects

Eight healthy young adults (mean age 23.4, ranging from 22 to 25 years, all men) participated in the experiment. All subjects had normal or corrected to normal vision. They received monetary rewards (4,800 Japanese Yen) for their participation. The experiment was approved by the local ethics committee of Osaka University and was conducted under the Declaration of Helsinki. All participants gave written informed consent.

Experimental Systems

Binocular eye positions were obtained using a fast video-based eye movement monitor system (a dark pupil eye tracking system; iView X Hi-Speed, SensoMotoric Instruments, Teltow, Germany) with a sampling frequency of 500 Hz. A standard 13-point calibration was performed to align the eye and computer display coordinate systems. Subjects were seated in a chair in a black room, and their head was supported on a chin/forehead rest that included the support for the camera for eye tracking. A bite bar was also used for additional support for head fixation. A computer screen with a refresh rate of 120 Hz and an area of 1,920 pixels × 1,080 pixels for 52.4 cm × 29.5 cm width and height was placed 72.1 cm from the eyes. The display was filled with a uniform white background of constant illumination (42.1 lux), regardless of the appearance and disappearance of the small visual target used in the task described below.

Experimental Protocol

To investigate the dependence of FEM on horizontal GZ direction, we prepared a small fixation target on the display at five locations that differed only in the horizontal direction (**Figure 1A**). The target was persistently located at 0 in the vertical direction, and at −15.2°, −7.76°, 0°, 7.76°, and 15.2° in

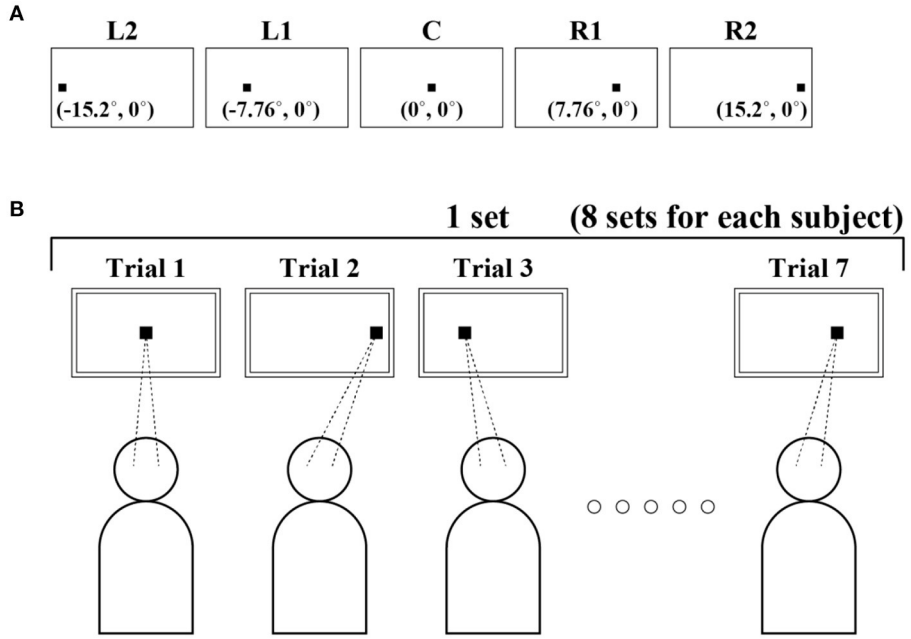

FIGURE 1 | Schematic diagram of the experiment. **(A)** Five target positions from the left to right, which were referred to as L2, L1, C, R1, and R2, respectively. **(B)** An experimental protocol. A small target was projected at 0 in the vertical direction and at −15.2°, −7.76°, 0°, 7.76°, and 15.2° in the horizontal direction. Fixational eye movement (FEM) was measured to obtain gaze (GZ) time series for each of these five positions of the fixation target. Single trials lasted 35 s, which were interrupted by several eye blinks. The target position for each trial was chosen pseudo-randomly from the five locations. Each subject performed 56 trials in total.

the horizontal direction. Five target locations (conditions) from the left to right were referred to as L2, L1, C, R1, and R2, respectively. We measured FEM to acquire the corresponding GZ time series for those five locations of the fixation target. The fixation target was a small black square with a size of 7 pixels × 7 pixels (0.15°). The target location was randomly chosen and presented to each subject. Subjects were informed that the fixation target appeared somewhere in the horizontal position at the vertical center of the display, and were asked to fixate on the target while it appeared as accurately as possible. Subjects were allowed to blink freely during the fixation task. One session was composed of seven fixation trials. Each single trial lasted 35 s, which was interrupted by several eye blinks, for a fixed target position that was chosen pseudorandomly from the five positions. Each subject performed eight sessions, i.e., 56 trials in total on a single experimental day. A pseudorandom sequence of 56 target positions used in 56 trials for the eight sessions was predetermined, in which the randomness was manipulated so that each of the four positions was chosen 11 times and the remaining one position was chosen 12 times. We provided a break of 10 s between trials and of 10–30 min rest between sessions. Data acquisition for each subject lasted for ∼4 h. The schematic view of the experimental protocol is shown in **Figure 1B**.

Data Analysis

Preprocessing

The first and last 2.5-s segments of the GZ time series of each trial were removed to avoid possible effects of the initial transient and the expectation of the end of the trial. Blinks were detected by referring to the known properties of blinks (Caffier et al., 2003), automatically for complete blinks and manually with visual inspections for incomplete blinks. For automatic detection, the onset and offset of each blink were detected based on the vertical pupil diameter, where a value of 2/3 of the mean diameter of each GZ series was used as the threshold for detecting the onset and offset of each blink. We removed a 1.0-s long segment of the GZ time series, as a blink segment, from the pre-blink time of 0.22 s (±0.074 s) before onset to the post-blink time of 0.53 s (±0.18 s) after offset. Pre-blink and post-blink intervals were determined such that the sum of pre-blink, post-blink, and blink intervals was 1.0 s, and the ratio between pre-blink and post-blink intervals was 1:2.4. By removing the data segments during the detected blinks, the GZ series of each trial was divided into short segments corresponding to the inter-blink intervals. Each of the short segments obtained represents a sample path of the GZ time series. We excluded data segments (typically corresponding to very short inter-blink interval cases) that did not contain any MS events that were identified by the method described below. In this study, we focused on the binocular aspects of FEM only in the horizontal direction. Thus, we computed the average time series of the left and right GZ positions in the horizontal direction for further analysis. Note that, the version components are emphasized through the averaging of the left and right GZ time series, because the vergence components cancel and would be almost absent from the averaged binocular GZ time series. Note also that the version position was defined as the average between the left and right eye positions, as in previous studies

(Collewijn et al., 1997; Quinet et al., 2020). Because the center of the GZ direction is not decided by the dominant eye, but is located between the two eyes as the cyclopean eye (Ono and Barbeito, 1982), the average binocular GZ values approximate the center of the GZ direction. In this way, any GZ time series hereafter for further analysis was redefined as the binocular GZ time series averaged for an inter-blink interval.

Decomposing GZ Time Series Into DRT and MS Series

A GZ time series can be decomposed into DRT components and MS components using an algorithm summarized here (see the **Supplementary Material** for a detailed mathematical description of the algorithm). After decomposition, we analyzed DRT and MS components of the GZ time series separately. To this end, we defined the DRT time series $X_{DRT}(t)$ and the MS time series $X_{MS}(t)$ consisting of only DRT and MS components, respectively, for a given GZ time series that was referred to as the raw gaze (raw-GZ) time series $X_{rGZ}(t)$, where t represents the discrete time of the data with a sampling time interval of $\delta_s = 0.002$ s. **Figure 2** shows a representative example of the experimental time series $X_{DRT}(t)$ and $X_{MS}(t)$ with the corresponding $X_{rGZ}(t)$. The origins (0) of those time series represented the front-facing position of the GZ, and the right and left directions for the subject were defined as the positive and negative values of the GZ positions. We defined the MS time series $X_{MS}(t)$ by eliminating overshoot components as well as a ballistic transient component of each MS from the raw-MS time series (Ozawa and Nomura, 2019), and analyzed it for making relationships between DRT and MS clear, because we were not interested in the detailed temporal structure of each MS waveform. Note that an overshoot is a small overrun component that is followed by a small return in the opposite direction to MS immediately after MS, after which the GZ position settles at the beginning of subsequent DRT motion. In other words, the MS time series $X_{MS}(t)$ was obtained by replacing each transient ballistic component plus overshoot of MS in the raw-MS time series by an instantaneous jump in amplitude determined by the onset and offset of MS from the raw-MS time series [see Equation (3)]. Using $X_{MS}(t)$, we defined the simplified GZ time series $X_{GZ}(t)$, referred to simply as the GZ time series in this sequel.

In this study, we would show that each of $X_{DRT}(t)$ and $X_{MS}(t)$ exhibited a unidirectional linear trend that diffuses in the opposite direction to each other, and the slopes of their linear trend altered depending on the degree of small eccentricity of the horizontal fixation position, i.e., L2, L1, C, R1, and R2. To this end, we characterized such trends in $X_{DRT}(t)$ and $X_{MS}(t)$, and the variation of $X_{GZ}(t)$ as the sum of those two types of time series. In particular, we quantified the slopes of the linear trend of $X_{DRT}(t)$ and $X_{MS}(t)$ by the least-squares linear regression of $X_{DRT}(t)$ and $X_{MS}(t)$, denoted by $\mu_{DRT,k}$ and $\mu_{MS,k}$, respectively, for the kth sample path. Then, subject-wise mean values of the slopes, denoted $\hat{\mu}_{DRT}$ and $\hat{\mu}_{MS}$, were computed for each target position. The mean slope values across the eight subjects were summarized as boxplots for L2, L1, C, R1, and R2 to elucidate how the $\hat{\mu}_{DRT}$ and $\hat{\mu}_{MS}$ altered depending on the degree of eccentricity of the horizontal fixation point.

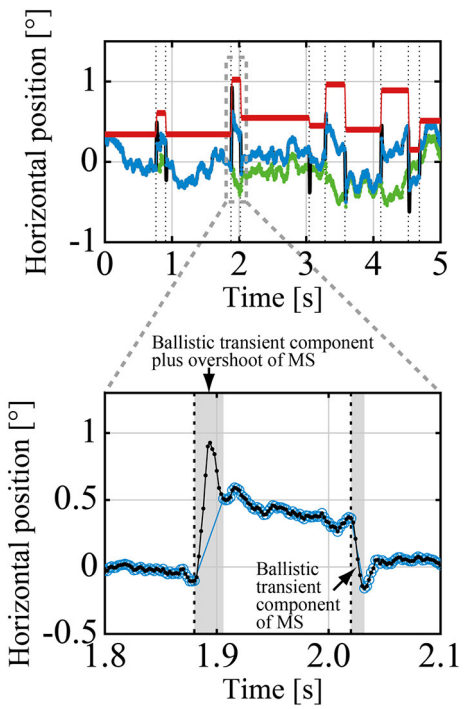

FIGURE 2 | A representative example of the raw-GZ time series $X_{rGZ}(t)$ (black curve, mostly behind the blue curve), the GZ time series $X_{GZ}(t)$ (blue curve), which was decomposed into the drifts-tremor (DRT) time series $X_{DRT}(t)$ (green curve), and the microsaccade (MS) time series $X_{MS}(t)$ (red line). The vertical dotted lines indicate the time instances when MS events (MS onset and offset) occurred. The enlarged view compares the details of the raw-GZ time series $X_{rGZ}(t)$ (small black filled circles) with the transient and overshoot ballistic components of two MS events and the GZ time series $X_{GZ}(t)$ (blue open circles). The transient and overshoot ballistic components were eliminated from the raw GZ to obtain the GZ time series.

Random-Walk Analysis of the GZ and DRT Time Series

The diffusion properties of $X_{DRT}(t)$ and $X_{GZ}(t)$ were characterized by the mean squared displacements (MSD) as functions of the time lag $\tau \cdot \delta_s$ defined as follows:

$$\left\langle (\Delta x_{GZ}(\tau))^2 \right\rangle = \frac{1}{N-\tau} \sum_{j=1}^{N-\tau} \left| x_{GZ}(j+\tau) - x_{GZ}(j) \right|^2, \quad (1)$$

$$\left\langle (\Delta x_{DRT}(\tau))^2 \right\rangle = \frac{1}{N-\tau} \sum_{j=1}^{N-\tau} \left| x_{DRT}(j+\tau) - x_{DRT}(j) \right|^2, \quad (2)$$

where N is the total number of data included in the time interval of T_{GZ} for a given sample path. Note that MSD is also known as the stabilogram diffusion analysis (Collins and De Luca, 1993; Engbert and Kliegl, 2004). Double-log plots of MSD as a function of τ for each target position were obtained by performing an ensemble average over all sample paths for each subject. From

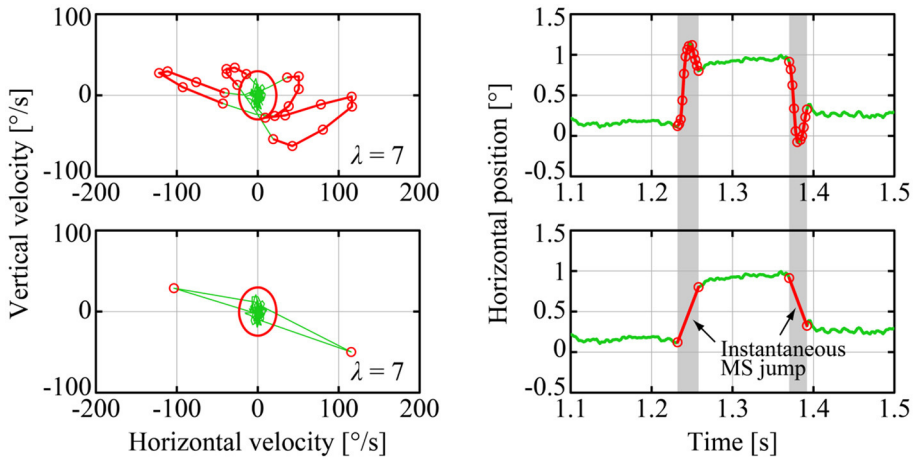

FIGURE 3 | Detection and simplification of MS events. The upper panels show an example of raw-GZ data with an MS event detected by the Engbert and Kliegl (E&K) method in the $v_x - v_y$ plane (left panel) and the corresponding time profile (right panel), where the red curves are MS components and the green curves are DRT components. The lower panels are for the corresponding GZ data, in which MS events were simplified, referred to simply as MS in this paper, by eliminating the transient and overshoot ballistic components from the raw-MS waveforms for further analysis performed in this paper.

the estimated MSD scaling exponent, we characterized the degree of diffusion of $X_{DRT}(t)$ and $X_{GZ}(t)$ in comparison with the Brownian motion that exhibits the unit scaling exponent (which is equal to $2H$ for the Hurst exponent H) with its variance determined as the averaged variance of the increment per second of the DRT time series.

Detection and Simplification of MS

We detected MS events using the method of Engbert and Kliegl, referred to as the E&K method (Engbert, 2006) as illustrated in **Figure 3**. In the E&K method, a parameter λ was introduced to determine the velocity ellipse size in the v_x-v_y plane, where v_x and v_y were the velocities of the GZ motion in the horizontal and vertical directions, respectively [see Engbert and Kliegl (Engbert, 2006) for the definition of the parameter λ]. In this study, we used $\lambda = 7$ for all target position conditions. Some MS events acquired from eye movements measured by a pupil-based eye tracking system and detected by the E&K method might contain overestimated overshoot components (Otero-Millan et al., 2014; Nyström et al., 2016; Ozawa and Nomura, 2019). The validity of the MS events detected by the E&K method in the current study was confirmed by drawing the main sequence diagrams for the MS events (see **Supplementary Figure 1**).

As mentioned above, the MS time series $X_{MS}(t)$ for our analysis were obtained by replacing each transient trajectory plus the overshoot component of MS in the raw-MS time series $X_{rMS}(t)$ with an instantaneous jump (see **Figures 2**, **3**). More specifically, for an onset time of the ith MS of the kth sample path of the raw-MS series, denoted by $X_{rMS,k}(t)$, occurred at t^i_{on} and the corresponding offset time at t^i_{off}, the amplitude of the ith MS (size of the instantaneous jump) was defined as

$$w_{i,k} = X_{rMS,k}\left(t^i_{off}\right) - X_{rMS,k}\left(t^i_{on}\right) \tag{3}$$

where $t^i_{on} \cdot \delta_s$ and $t^i_{off} \cdot \delta_s$ were the time instances when GZ velocity trajectory in the v_x-v_y plane cut the velocity ellipse of the E&K method from inside to outside and from outside to inside, respectively. Note that, in $X_{MS}(t)$, any MS occurs in unit time step, because transient plus overshoot portions of the corresponding MS in $X_{rMS}(t)$ were eliminated by the definition of $X_{MS}(t)$. Positive and negative amplitudes $w_{i,k}$ for the ith MS in the kth sampling path means that the corresponding MS jumps to the right and left, respectively, and their absolute value represents the jump size. The rightward and leftward MS events in the kth sampling path were counted separately when necessary, by which the signed amplitude of the ith rightward MS and the jth leftward MS were denoted, respectively, by $w_{+,i,k}$, $w_{-,j,k}$. The total number of rightward and leftward MS events in the kth sampling path were denoted by $n_{+,k}$ and $n_{-,k}$, respectively. The subject-wise means of $w_{i,k}$, regardless of the jump direction, as well as the subject-wise means of $w_{+,i,k}$ and $w_{-,j,k}$, across all sampling paths were computed and denoted by $\hat{w}$, $\hat{w}_+$, and $\hat{w}_-$, respectively.

Temporal Structure of MS Time Series

The temporal structure of the MS time series was characterized by the histogram of the inter-microsaccadic intervals (IMSI) in the right and left directions. Because the probability of the occurrence of MS events has been approximated by a Poisson-point-process (Engbert, 2006), for which the IMSI obeys the exponential distribution with the exponential probability density function (PDF), we approximated the histograms of IMSI in each of the rightward (+) and leftward (−) directions by

$$p(x; \lambda_\pm) = \lambda_\pm e^{-\lambda_\pm x} \tag{4}$$

for IMSI values $x = \mathrm{IMSI}_+$ between subsequent rightward MS events with occurrence frequency λ_+ and for $x = \mathrm{IMSI}_-$ between subsequent leftward MS events with occurrence frequency λ_-.

For the kth sample path of $X_{GZ}(t)$ with the data length (the inter-blink interval) $T_{GZ,k}$, the estimates of the Poisson rates λ_+ and λ_-, denoted, respectively, by $\Lambda_{+,k}$ and $\Lambda_{-,k}$, were obtained as the inverse of the mean MS interval, i.e.,

$$\Lambda_{+,k} = \frac{n_{+,k}}{T_{GZ,k}}, \quad \Lambda_{-,k} = \frac{n_{-,k}}{T_{GZ,k}}, \tag{5}$$

where $n_{+,k}$ and $n_{-,k}$ were the numbers of rightward and leftward MS events, respectively. Moreover, we also computed the occurrence frequency of the total number of MS events, regardless of the direction of the jumps, as

$$\Lambda_k = \frac{n_{+,k} + n_{-,k}}{T_{GZ,k}}, \tag{6}$$

for the kth sample path. For those MS rate parameters, the subject-wise mean values, i.e., $\hat{\Lambda}_+$, $\hat{\Lambda}_-$, and $\hat{\Lambda}$, were computed. In addition to those estimates of MS occurrence, the slopes of the least-squares linear regression lines for semi-log plots of the $IMSI_+$ and $IMSI_-$ histograms were performed, by which alternative estimates of the Poisson rates for each subject, denoted by $\hat{\lambda}_+$ and $\hat{\lambda}_-$, respectively, were obtained, which should be consistent with the $\hat{\Lambda}_+$ and $\hat{\Lambda}_-$ obtained by Equation (5), if the occurrence of each of the rightward and the leftward MS events obeyed the Poisson-point-process. The consistency between $\hat{\Lambda}_\pm$ and $\hat{\lambda}_\pm$ confirms the assumption of the Poisson-point-process property of the MS events.

As described above, the unidirectional linear trend of the MS time series $X_{MS}(t)$ for the kth sample path was quantified by the slope $\mu_{MS,k}$ of the least-squares regression line. We computed the subject-wise mean values of $\mu_{MS,k}$, denoted by $\hat{\mu}_{MS}$. Alternatively, the linear trend of the stair-like MS time series for the kth sample path could be quantified using the mean jump sizes $\hat{w}_{+,k} > 0$ and $\hat{w}_{-,k} < 0$ and their mean occurrence frequency per second by introducing the parameter s_k defined as follows:

$$s_k \triangleq w_{+,k}\lambda_{+,k} + w_{-,k}\lambda_{-,k}. \tag{7}$$

Then, $\hat{s}$ as the subject-wise mean of s_k across all trials for each subject was also computed. Comparisons between those two types of quantifications, i.e., $\hat{\mu}_{MS}$ and $\hat{s}$ across subjects were made to elucidate the underlying mechanisms of the unidirectional linear MS trend as well as the DRT time series. Specifically, to elucidate the dominant contributing parameters, among $\hat{\lambda}_+$, $\hat{\lambda}_-$, $\hat{w}_+$, and $\hat{w}_-$, that characterize the temporal structure of the MS time series to the unidirectional linear trend of the MS time series, we compared the means of those four parameters across all subjects using boxplots of the parameters for the five fixation conditions, i.e., L2, L1, C, R1, and R2. Furthermore, the boxplots of the values of $\hat{s}$ across all subjects for the five fixation conditions were examined, which were compared with the boxplots of the slope $\hat{\mu}_{MS}$ of the least-squares linear regression line, to show that an appropriately biased balance of the rates and amplitudes between rightward and leftward MS events was the major cause of the unidirectional linear trend of the MS time series. We also performed comparisons between $\hat{\lambda}_+$ and $\hat{\lambda}_-$ and between $\hat{w}_+$ and $\hat{w}_-$ for each of the five target positions to examine the differences between rightward and leftward MS jumps.

Relationships Between the Onset Position of MS and Its Amplitude With the Direction of MS

The relationships between the onset position of MS and its amplitude were analyzed by examining their joint PDF, for which we calculated the corresponding two-dimensional histograms of the onset position and amplitude of MS with 0.25° and 0.20° bin widths, respectively. We then performed cubic spline interpolation of the histogram between the bins (meshes), which was displayed as a color map of the joint frequency of the onset positions and amplitudes of the MS events. Moreover, to investigate the relationships between the onset position and the jump direction of MS, we calculated a one-dimensional histogram with a bin width of 0.10° for each of the rightward and leftward MS events. To investigate the MS amplitude distribution, we calculated a one-dimensional histogram with a bin width of 0.10° for each of the rightward and leftward MS events. As **Supplementary Material**, we also calculated a one-dimensional histogram of the GZ time series for each fixation condition, corresponding to the PDF of the GZ time series, which was shown below the color map.

Examining the Balance Between the Linear Trends of DRT and MS

We hypothesized that the GZ fixation for each of the five target positions was established by the balance between the unidirectional linear trends of the DRT and MS time series in opposite directions. To examine such a balance, we examined scatter plots for s_k defied by Equation (7) against the unidirectional linear trend of DRT $\mu_{DRT,k}$ for all sample paths k across all subjects. Negative correlation with the slope of minus one in the scatter plot implies that the centripetal DRT and the centrifugal MS are completely balanced, as in the following equation

$$\mu_{DRT} = -s. \tag{8}$$

Moreover, we also computed the means of $\mu_{DRT,k}$ and the parameter s_k for all kth sample paths across all subjects, denoted by μ_{DRT} and s, respectively, for each target position, which were indicated on the scatter plots.

Target Position-Dependent Basic Properties of FEM

To characterize target position-dependent basic properties of FEM, other than the direct drift-related properties, we calculated statistical mean values of the following 14 metrics for the GZ time series $X_{GZ}(t)$, averaged across all trials (all sample paths) and all subjects for each target position: the data length T_{GZ} of $X_{GZ}(t)$ defined by **Supplementary Equation 15** in the **Supplementary Materials** that represents the inter-blink interval, the time average of GZ position $X_{GZ}(t)$, the standard deviation (SD) of $X_{GZ}(t)$, the absolute error between the target position and the GZ position, the amplitude of the total MS regardless of the direction, and the rightward MS and the leftward MS (i.e., $\hat{w}$, $\hat{w}_+$, and $\hat{w}_-$ as defined above), the occurrence

TABLE 1 | Dependence of horizontal gaze (GZ) position on the mean of each statistic for all subjects.

Mean values across 8 subjects	Horizontal fixation target				
	L2	**L1**	**C**	**R1**	**R2**
Data length, T_{GZ} [s]	15.6 (±8.08)	16.1 (±8.57)	16.7 (±8.78)	15.2 (±6.68)	14.5 (±8.40)
Gaze position, X_{GZ} [°]	−15.2 (±0.215)	−7.79 (±0.131)	0.0236 (±0.158)	7.77 (±0.121)	15.1 (±0.219)
SD of gaze position [°]	0.246 (±0.0406)	0.230 (±0.0250)	0.206 (±0.0152)	0.228 (±0.0354)	0.243 (±0.0271)
Absolute error from target [°]	0.363 (±0.0977)	0.299 (±0.117)	0.271 (±0.0743)	0.319 (±0.161)	0.347 (±0.0773)
Amplitude of total MS, $\hat{w}$ [°] *	−0.0514 (±0.0622)	−0.0258 (±0.0459)	0.0016 (±0.0370)	0.0164 (±0.0372)	0.0392 (±0.0532)
Amplitude of leftward MS, $\hat{w}_-$ [°]	−0.363 (±0.132)	−0.361 (±0.0996)	0.314 (±0.0875)	−0.315 (±0.103)	−0.326 (±0.105)
Amplitude of rightward MS, $\hat{w}_+$ [°]	0.354 (±0.105)	0.348 (±0.0842)	0.310 (±0.0763)	0.329 (±0.0867)	0.354 (±0.112)
Frequency of total MS, $\hat{\Lambda}$ [1/s]	1.66 (±0.499)	1.55 (±0.478)	1.47 (±0.560)	1.57 (±0.544)	1.67 (±0.512)
Frequency of leftward MS, $\hat{\Lambda}_-$ [1/s]	0.934 (±0.274)	0.842 (±0.291)	0.745 (±0.312)	0.803 (±0.333)	0.818 (±0.287)
Frequency of rightward MS, $\hat{\Lambda}_+$ [1/s]	0.738 (±0.250)	0.727 (±0.216)	0.745 (±0.263)	0.779 (±0.206)	0.891 (±0.209)
Frequency of leftward MS, $\hat{\lambda}_-$ [1/s]	1.21 (±0.374)	1.07 (±0.325)	0.967 (±0.411)	1.09 (±0.386)	1.02 (±0.423)
Frequency of rightward MS, $\hat{\lambda}_+$ [1/s]	0.854 (±0.462)	0.966 (±0.395)	0.902 (±0.367)	1.02 (±0.335)	1.12 (±0.322)
Relative Onset position of MS to mean gaze position [°]	0.0240 (±0.0497)	0.0182 (±0.0496)	0.0044 (±0.0320)	−0.0005 (±0.0180)	−0.0052 (±0.0308)
Relative offset position of MS to mean gaze position [°] *	−0.0400 (±0.0535)	−0.0141 (±0.0463)	0.0053 (±0.0354)	0.0186 (±0.0323)	0.0420 (±0.0432)

*The * symbol indicates that there was a significant difference ($p < 0.05$) between L2 and R2.*

frequency $\hat{\Lambda}$ for the total MS regardless of the direction using Equation (6), and the occurrence frequencies of the rightward and leftward MS events by $\hat{\Lambda}_+$ and $\hat{\Lambda}_-$ from Equation (5) as well as by $\hat{\lambda}_+$ and $\hat{\lambda}_-$ based on the exponential fitting of IMSI histograms, the onset position of MS relative to the mean GZ position, and the offset position of MS relative to the mean GZ position.

Statistical Analysis

To examine the target position dependence on any metrics characterizing the GZ, DRT, and MS time series, we performed Bartlett's test to examine the equality of variances among five target positions (L2, L1, C, R1, and R2), and confirmed it at the 5% significance level. The Tukey–Kramer test was then performed to examine the differences between them at the 5 and 1% significance level.

RESULTS

Basic Statistics

Table 1 shows the dependence of horizontal GZ position on the mean values of 14 metrics averaged across all subjects. There were no significant differences between horizontal GZ positions in the following 12 metrics: mean values of the data length T_{GZ} of $X_{GZ}(t)$, the GZ position, the SD of the GZ position, absolute value of the error from the target, amplitude of the rightward and the leftward MS events ($\hat{w}_+$ and $\hat{w}_-$), occurrence frequency of the rightward and the leftward MS events ($\hat{\Lambda}_+$ and $\hat{\Lambda}_-$ as well as $\hat{\lambda}_+$ and $\hat{\lambda}_-$), occurrence frequency of the total MS events $\hat{\Lambda}$, and the relative onset position of MS. Significant differences ($p < 0.05$) were found only in the amplitude $\hat{w}$ of total MS and relative MS offset position between L2 and R2. However, the SD of the GZ position and absolute error from the target tended to be large as the eccentricity was increased, although without no statistical significance.

GZ, DRT, and MS Time Series

The upper panels of **Figure 4** show all sample paths of the GZ time series $X_{GZ}(t)$, DRT time series $X_{DRT}(t)$, and MS time series $X_{MS}(t)$, for a representative subject. The least-squares linear regression line was superimposed on each of the $X_{GZ}(t)$, $X_{DRT}(t)$, and $X_{MS}(t)$ for each of the five fixation targets. For $X_{GZ}(t)$, the blue time series in the upper left panel of **Figure 4**, we could observe the time series fluctuating around the target

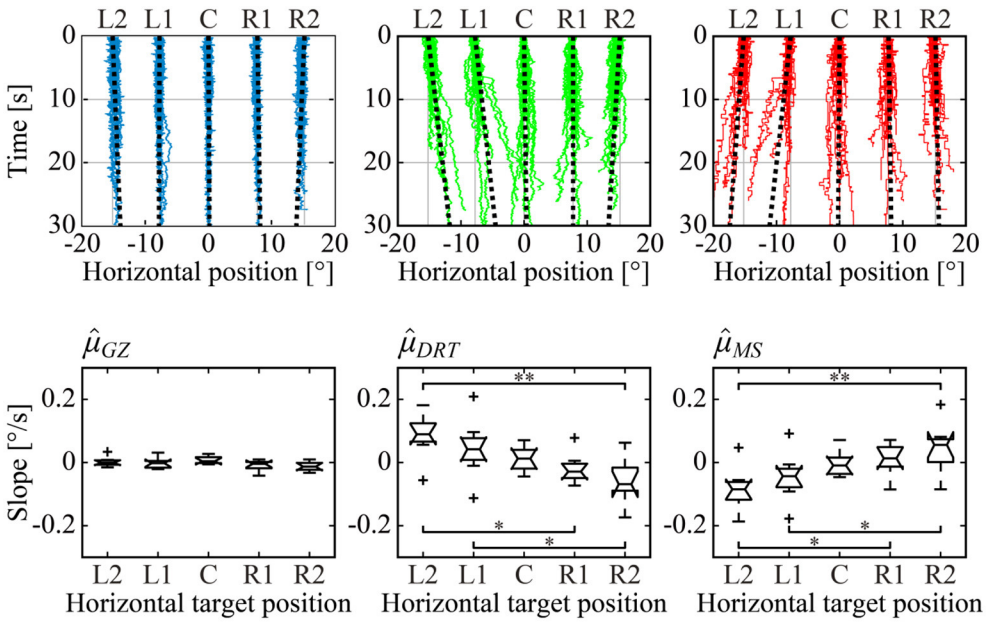

FIGURE 4 | Horizontal dependence of the target position on GZ, DRT, and MS time series and the slopes on their trend. Upper panels: All sample paths of GZ (left, blue), DRT (middle, green), and MS (right, red) time series of a representative subject were superimposed for each of the five target positions. Black dotted lines are the least-squares linear regression lines, representing the linear trend of the time series for each of the five target positions. Lower panels: box plots of the mean value of the subject-wise means of slopes for each time series across all subjects. Single and double asterisks indicate that there was a significant difference between groups at the 5 and 1% significance level, respectively.

position. Together with the fact that the SD of $X_{GZ}(t)$ and the absolute error were small, as shown in **Table 1**, with no dependence on target position, we confirmed that the GZ fixation was performed correctly, regardless of the horizontal target position. For $X_{DRT}(t)$, the green time series in the upper middle panel of **Figure 4**, the unidirectional linear trend toward the front-facing position (i.e., the horizontal center at 0°) was found for the target position of L2, L1, R1, and R2. That is, $X_{DRT}(t)$ exhibited the centripetal drift. On the other hand, in the upper right panel of **Figure 4**, the red time series of $X_{MS}(t)$ showed the unidirectional linear trend in the opposite direction to DRT, i.e., away from the front-facing position, were found for the target position of L2, L1, R1, and R2. In other words, $X_{MS}(t)$ exhibited a centrifugal trend. The linear trend of each time series was quantified by the slope of the least-squares linear regression line, and the mean slope averaged across all subjects for each of the five target positions as depicted in the lower panels of **Figure 4**. The slopes of $X_{GZ}(t)$ were close to 0 for all of the five target positions, and there were no significant differences in the slopes of $X_{GZ}(t)$ among the five target positions. That is, GZ fixation was performed correctly regardless of the fixation position. On the other hand, in the $X_{DRT}(t)$ and $X_{MS}(t)$ boxplots, the slope became steeper as the target GZ angle became larger, in the opposite direction from each other. That is, the centripetal drift of X_{DRT} (t) and the centrifugal trend of $X_{MS}(t)$ became faster as the target GZ angle increased. The differences between the slopes were significant between L2 and R2 ($p < 0.01$), between L2 and R1 ($p < 0.05$), and between L1 and R2 ($p < 0.05$) for both of X_{DRT} (t) and $X_{MS}(t)$. For the L2 and R2 conditions, the mean absolute values of the linear trend of $X_{DRT}(t)$ and $X_{MS}(t)$ were about 0.1°/s. Note that there were some subjects who did not exhibit the target position-dependent linear trends of $X_{DRT}(t)$ and $X_{MS}(t)$.

Random-Walk Analysis

Figure 5 shows the MSD of $X_{GZ}(t)$ and $X_{DRT}(t)$ for a representative subject for each of the five target positions. Over a wide range of time lag (0.002–10 s), regardless of the horizontal fixation condition, the scaling exponent of the DRT time series, which corresponds to $2H$ for the Hurst exponent H, was about 1, i.e., $H \sim 1/2$. That is, the MSD profile of the DRT time series was similar to the MSD of the Brownian motion, regardless of the target position, despite of the fact that the slope (i.e., the velocity) of the centripetal linear trend of the DRT time series exhibited a clear dependence on the target position. This means that the centripetal DRT linear trend was not caused by a positive persistence of the DRT time series (see Section Discussion). On the other hand, the MSD of the GZ time series $X_{GZ}(t)$ exhibited a crossover phenomenon, in which the critical point (critical time lag) was located around 0.1–0.2 s. The 2H scaling exponent of $X_{GZ}(t)$ for the short-time scale (0.002–0.1 s) was about 1, whereas that for the long-time scale (0.2–10 s) was between 0.1 and 0.3, regardless of the target position. In summary, the MSD of $X_{GZ}(t)$ and $X_{DRT}(t)$, i.e., the random-walk property of the GZ and DRT time series did not show the dependence on the target position,

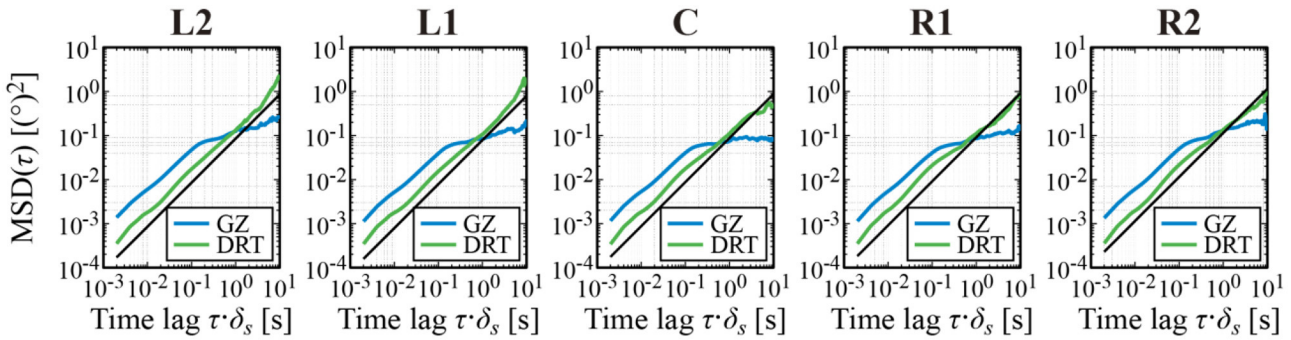

FIGURE 5 | Mean square displacement (MSD) analysis of the GZ and DRT time series. The blue and green curves represent, respectively, the MSDs of the GZ and DRT time series. The black lines are the MSD of the Brownian motion for comparison. The MSD curves depicted in each panel are the ensemble average of MSD for each sample path of a representative subject.

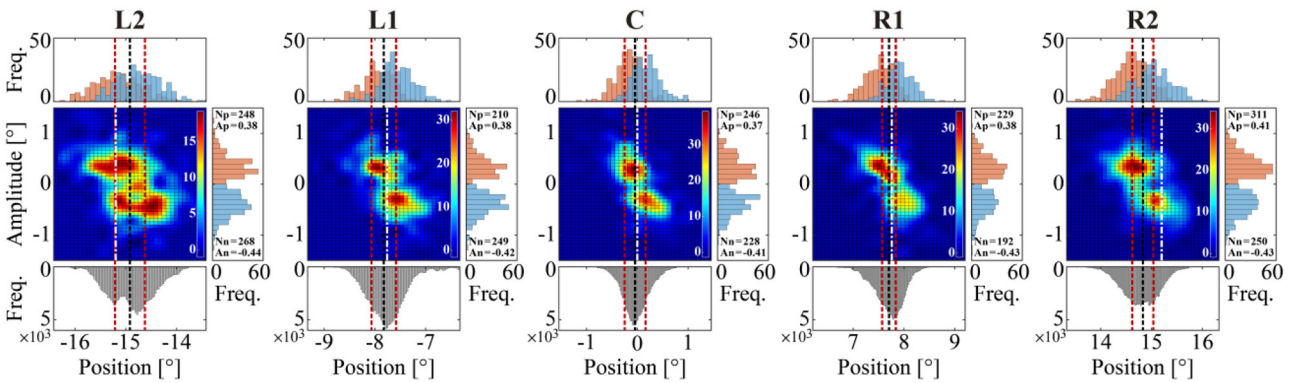

FIGURE 6 | Relationships between the onset position of MS and its amplitude for each of the five target positions. Color map: two-dimensional histograms of the onset position and amplitude of MS with 0.25° and 0.20° bin widths, respectively, representing the joint frequency of onset positions and amplitudes of MS events. Upper histograms: one-dimensional histograms with a bin width of 0.10° for each of the rightward (red) and leftward (blue) MS events. Right-side histograms: one-dimensional histograms with a bin width of 0.10° for each of the rightward (red) and leftward (blue) MS events. In the right-side histograms, N_p and N_n are the rightward and leftward MS counts, respectively. Similarly, A_p and A_n are the mean amplitude of rightward and leftward MS. For each target condition, the black dotted line represents the mean value of the GZ time series, and the red dotted lines on both sides of the black line represent ±SD away from the mean value of the GZ time series. The dashed white line represents the fixation target position in each target condition.

despite the fact that the slope (i.e., the velocity) of the centripetal linear trend of the DRT time series and the centrifugal linear trend of the MS time series exhibited a clear dependence on the target position.

Characterization of MS Time Series

Detailed characterizations of the MS time series are presented in **Figures 6**, **7** for a representative subject and in **Figure 8** obtained using data from all subjects. Regardless of the target position, we found a negative correlation between MS onset position and amplitude ($\hat{w}_+$ and $\hat{w}_-$), as represented in each panel of **Figure 6**. More specifically, the onset positions were localized at locations about 0.3° from the average GZ position, in both the negative (left) and the positive (right) directions, from which MS with an amplitude of about 0.3° occurred in the positive (rightward) and the negative (leftward) directions, respectively, regardless of the target position. The histograms of MS events tended to be more horizontally stretched and became asymmetric as the target position was more distant from the front-facing position. For the target positions on the left, particularly for the L2 condition, the peaks of the histograms (in the upper side of the color maps) for the leftward MS (the blue histograms) were slightly higher than those for the rightward MS (the red histograms). Moreover, the mean value of the MS onset (the dashed vertical black line in the color map) was slightly shifted to the right from the target position (the dash-dot vertical white line). In contrast, for the target positions on the right, particularly for the R2 condition, the peaks of the rightward MS histograms (the red histograms) were slightly higher than those of the leftward MS histograms (the blue histograms). Moreover, the mean value of the MS onset (the dashed vertical black line in the color map) was slightly shifted to the left from the target position (the dash-dot vertical white line). In this way, MS events occurred more frequently toward the centrifugal direction compared to the centripetal direction. However, these differences between rightward and leftward MS events were not statistically significant, as shown in **Table 1**.

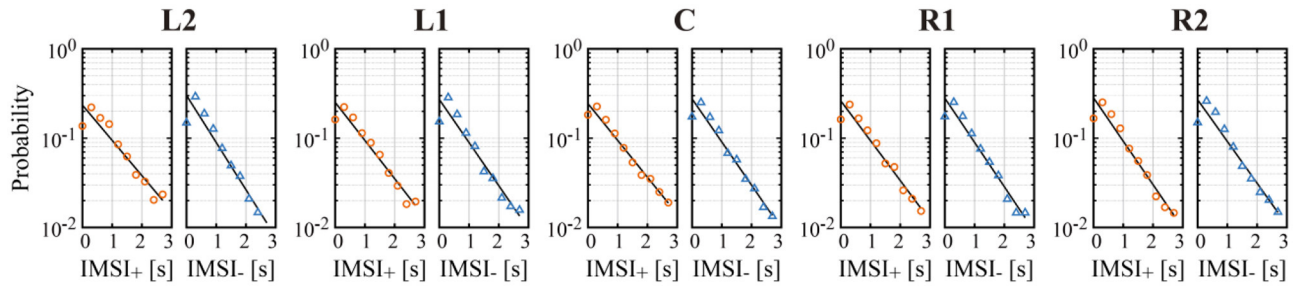

FIGURE 7 | Semi-log plot of the probability of inter-microsaccadic intervals (IMSI) of all left/right MS across all subjects, with a regression line (black line) in each condition. $IMSI_+$ plotted by the orange circles are the IMSI of rightward MS, and $IMSI_-$ plotted by the blue triangles are the IMSI of leftward MS.

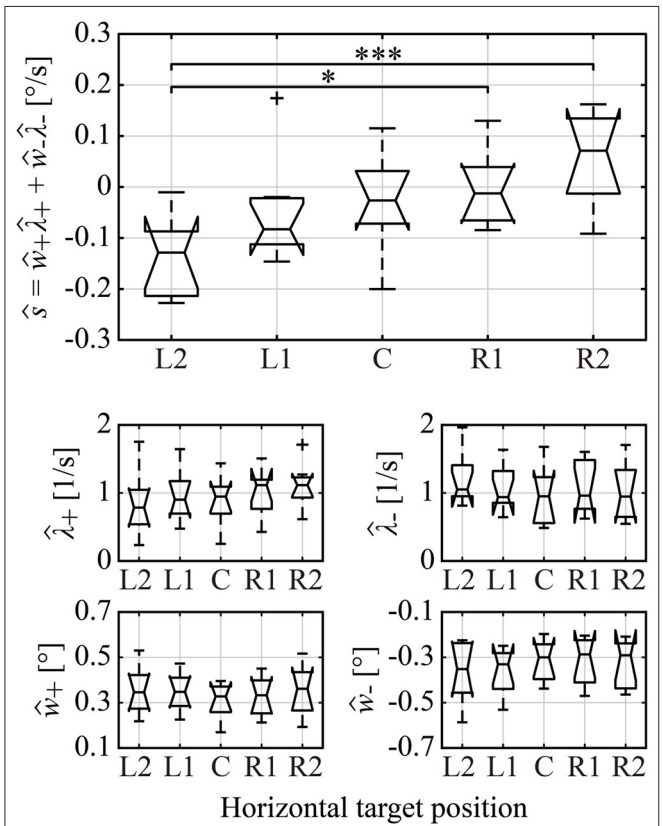

FIGURE 8 | Boxplots of the estimated amplitude and occurrence frequency of right/left MS, and the total trend generated by total MS across all subjects. $\hat{w}_+$, $\hat{w}_-$, $\hat{\lambda}_+$, and $\hat{\lambda}_-$ represent the subject-wise mean values of the right/left MS amplitude and occurrence frequency, respectively. $\hat{s} \triangleq \hat{w}_+\hat{\lambda}_+ + \hat{w}_-\hat{\lambda}_-$ is the estimated total trend of MS reconstructed from $\hat{w}_+$, $\hat{w}_-$, $\hat{\lambda}_+$, and $\hat{\lambda}_-$. Single and triple asterisks indicate a significant difference between the groups at the 5 and 0.1% significance level, respectively.

We confirmed in **Figure 7** that the occurrence probability of IMSI with both in the positive ($IMSI_+$) and negative ($IMSI_-$) directions obeyed the exponential distribution with the identical rate parameter, regardless of the target position (see **Table 1** for a comparison of the rates $\hat{\lambda}_+$ and $\hat{\lambda}_-$). **Figure 8** shows the boxplots of $\hat{s}$ as the mean of the subject-wise mean values of $s_k \triangleq w_{+,k}\lambda_{+,k} + w_{-,k}\lambda_{-,k}$, as well as $\hat{\lambda}_+$, $\hat{\lambda}_-$, $\hat{w}_+$ and $\hat{w}_-$ that characterize the target position dependency of the occurrence frequency and the amplitude of MS for each of the five target positions. The top panel of **Figure 8** shows that $\hat{s}$, representing the velocity of centrifugal trend of $X_{MS}(t)$, increased linearly from negative to positive values as the target location varied from the left to the right. This dependency was apparent and quantitatively the same as the target position dependency of the mean slope of the regression lines for the centrifugal linear tend of $X_{MS}(t)$ (the lower right panel of **Figure 4**), which counterbalanced with the opposite dependency of the mean slope of the regression line for the centripetal linear trend of $X_{DRT}(t)$ (the lower middle panel of **Figure 4**). Specifically, differences in $\hat{s}$ were significant between L2 and R2 ($p < 0.01$), and between L2 and R1 ($p < 0.05$). As described for the asymmetric shape of the histograms in **Figure 6**, the occurrence frequencies of the rightward $\hat{\lambda}_+$ and leftward $\hat{\lambda}_-$ MS events slightly increased and decreased, respectively, as the target position varied from the left to the right (the middle row panels of **Figure 8**), although the pairwise comparison between those values for the five target positions were not different significantly (**Table 1**). We also compared the values of $\hat{\lambda}_+$ and $\hat{\lambda}_-$ for each target position, because it seemed $\hat{\lambda}_+ < \hat{\lambda}_-$ for L2 and $\hat{\lambda}_+ > \hat{\lambda}_-$ for R2 by the visual inspection. However, the differences between the rates of rightward and leftward MS events within the same target position were not statistically significant. Moreover, there was no recognizable nor statistically significant target position dependency in the amplitude of the leftward $\hat{w}_-$ and rightward $\hat{w}_+$ MS events (the middle row panels of **Figure 8**). In any cases, each of the parameters $\hat{\lambda}_+$, $\hat{\lambda}_-$, $\hat{w}_+$, and $\hat{w}_-$ alone did not show significant dependency on the target position.

Balance Between the Unidirectional Trends of the DRT and MS Time Series

The linear trend of DRT quantified by the slope of the least-squares linear regression line $\mu_{DRT,k}$ and the linear trend of MS quantified by s_k defined by Equation (7) for the kth sample path were compared by the scatter plot for each target position across all sampling path from all subjects (**Figure 9**, in which the plotted points represent single sampling paths across all subjects). Negative correlations between them were apparent for all target positions. In addition, they were distributed along the line given

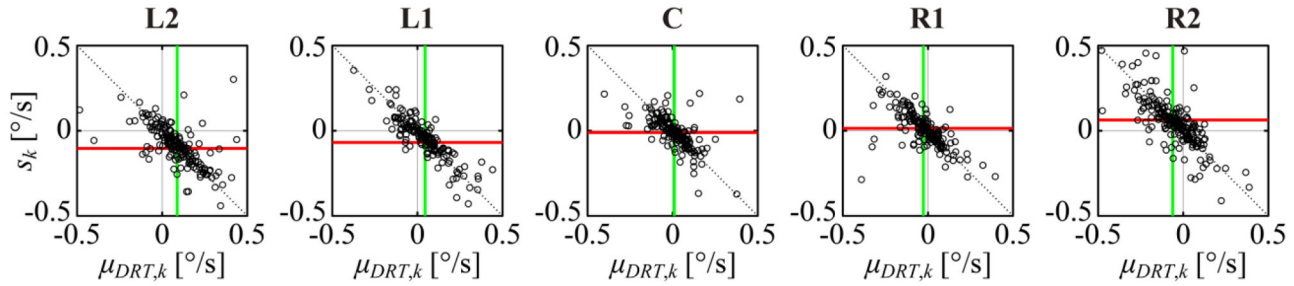

FIGURE 9 | Scatter plot of a DRT trend $\mu_{DRT,k}$ and the reconstructed MS trend s_k for the kth sample paths across all samples of all subjects for each target position. The green vertical line and the red horizontal line represent the mean value of $\mu_{DRT,k}$ and s_k, respectively. The dotted black line is the complete balanced condition defined by Equation (8).

by Equation (8) that is satisfied when the centripetal DRT and centrifugal MS are completely counterbalanced.

The vertical green line and the horizontal red line in each panel of **Figure 9** represent the mean values μ_{DRT} and s across all subjects. The green line μ_{DRT} shifted more to the right (positive direction) as the target was displayed more to the left (negative direction), and they shifted more to the left (negative direction) as the target was displayed more to the right (positive direction), which was consistent with the lower middle panel of **Figure 4**. The red line s shifted more downward (negative direction) as the target was displayed more to the left (negative direction), and they shifted more upward (positive direction) as the target was displayed more to the right (positive direction), which was consistent with **Figure 4**, lower right panel and **Figure 8**, upper panel.

DISCUSSION

Summary

The GZ time series was decomposed into DRT and MS time series. The DRT and MS time series showed unidirectional linear trends in opposite directions. The slope (i.e., the velocity) of the linear trends altered depending on the horizontal position of the fixation target. DRT during inter-MS intervals tended to migrate toward the front-facing position, and MS pulled back the GZ position toward the fixation target intermittently. MSD analysis of the GZ and DRT time series clarified that the GZ time series (FEM) behaved like Brownian motion on the short-time scale (0.002–0.1 s) and exhibited antipersistence on the long-time scale (0.2–10 s), whereas the DRT time series was similar to the Brownian motion over the entire time scale (0.2–10 s). These diffusion characteristics were common for all conditions at the fixation target position, which means that the stochastic property of diffusion in DRT alone, such as positive persistence, might not be the major determinant of the unidirectional linear trend of DRT. In other words, the GZ relaxes very slowly ($\sim$ 0.1°/s) with the centripetal DRT toward the front-facing position during inter-MS intervals caused by a deterministic driving force, as if there always exists a quasi-stable equilibrium posture in the front-facing position.

Comparison of the Centripetal DRT Trend With Previous Studies

The linear trend (velocity) of the centripetal DRT was at most about 0.1°/s at the L2 and R2 conditions placed at 15.2° leftward and rightward shifted positions, respectively (**Figure 4**). Centripetal DRT velocity estimated by Bertolini et al. (2013) was about 0.3°/s at the corresponding eccentricity, i.e., for the L2 and R2 conditions, which was three times larger than the velocity estimated by the current study. One of the possible causes of this discrepancy is that Bertolini et al. measured DRT velocity in the transient state, that is, not during persistent GZ fixation but during GZ tracking of a quasi-fixation LED target that flashed briefly for 0.05 s every 2 s and shifted between −40° and 40° synchronously with the flash. Such an experimental setting might affect DRT velocity because the GZ in this case might not be able to settle to its steady state within the short time of 0.05 s.

Random-Walk Analysis

The unit slope of the centripetal DRT time series in the Brownian motion analysis (diffusion plot) suggests that the linear trend of the centripetal DRT is not caused by positive persistence of the DRT time series for the following reason, which can be clarified as follows. First, let us consider a random process with positive persistence, i.e., an increment of the process is followed by an increment in the same direction as the previous increment with probability greater than 1/2. Due to this property of positive persistence, the process with positive persistence tends to exhibit a drift-like behavior in one direction. Note that a process with positive persistence exhibits a Hurst exponent $H > 1/2$ and the scaling exponent (a slope of the diffusion plot) $2H > 1$. On the other hand, Brownian motion is neutral in terms of persistence. Namely, an increment of the Brownian motion is independent of the successive increment, and its scaling exponent (a slope of the diffusion plot) is 1, as in the DRT time series. Based on this consideration, we can conclude that the linear trend in the centripetal DRT is not caused by positive persistence of the DRT time series. This result suggests that the linear trend in the DRT time series is caused by a deterministic drifting component. Indeed, if we consider a random process $X(t) \equiv t + B(t)$, where t is a linear trend proportional to time and $B(t)$ is the Brownian

motion, it can be confirmed that $X(t)$ exhibits a linear trend and the scaling exponent (the slope of the diffusion plot) is 1.

The diffusion property of the GZ time series characterized by the MSD analysis showed a crossover phenomenon at the critical time lag around 0.1–0.2 s that separates the Brownian-motion-like behavior in the short-time scale and antipersistence on the long-time scale, regardless of the horizontal eccentricities (**Figure 5**). As the mean MS frequency was about 2 Hz, the Brownian-motion-like behavior of the GZ time series on the short-time scale must be dominated by that of the DRT time series. Indeed, the MSD of the GZ time series was similar to that of the DRT time series on the short-time period (0.002–0.1 s). As the scaling exponent ($2H$) of the DRT time series was close to 1 for both short- and long-time scales, we could conclude that the diffusion property of DRT can be modeled by the Brownian motion over the entire time period (0.002–10 s). On the other hand, the antipersistence with the scaling exponent less than 1 of the GZ time series on the long-time scale (0.2–10 s) might be caused by MS that counteracted the diffusion of DRT.

The result of our random-walk analysis was qualitatively consistent with the pioneering research by Engbert and Kliegl (2004), but quantitatively different. In their study, the critical point of FEM appeared around 0.02–0.04 s, whereas the critical point of this study was located at around 0.1–0.2 s in this study, i.e., about five times larger for the current study. Possible reasons for the difference could be the dimension and length of FEM of interest. They applied the random-walk analysis to a two-dimensional FEM measured for 3 s, whereas we used a one-dimensional (horizontal) FEM recorded up to 30 s with a typical length of T_{GZ} ∼16 s for the GZ time series. Thus, direct comparisons between our results and their study are less meaningful. However, the diffusion properties of FEM may change according to the spatial and temporal size of interest. Nevertheless, as discussed above, because the critical time lag (crossover point) of the MSD analysis of FEM must be closely related to the occurrence timing and amplitude of MS, the crossover point of our estimate might be more plausible from a mechanistic viewpoint.

FEM as GEN With More Randomness and a Slower Centripetal DRT Trend Compared to EPN

This study revealed that alternating repetitions between centripetal drifts and centrifugal saccades as in physiological GEN, also referred to as EPN during FEM with large horizontal eccentricities, even during FEM with small horizontal eccentricities, but with slower centripetal DRT and more stochasticity in the oscillation period. GEN stochasticity during FEM can be characterized by the SD of the inter-(micro)saccadic intervals. In this study, both the mean and SD of the leftward and the rightward IMSI were the inverse of the MS rate for the Poisson-point-process, which were about 1.25 s. In addition to this randomness, the major cause of GEN stochasticity during FEM was that MS occurred not only in the centrifugal direction against centripetal DRT, but also in the centripetal direction, which lowered the periodicity of GEN during FEM. On the other hand, EPN is much more periodic because MS-like jumps apparently occurred only in the centrifugal direction in EPN (Abel et al., 1978; Shallo-Hoffmann et al., 1990) although the SD of the oscillation period for EPN (Shallo-Hoffmann et al., 1990) is not much different from the SD of the IMSI during FEM. In this way, the stochasticity of the GEN-like behavior during FEM was much larger than EPN with large eccentricities. This finding is novel, which might contribute to a deeper understanding of both physiological GEN and FEM. The stochasticity of GEN can be argued as follows. In front-looking, MS drivers are influenced by a variety of factors, such as proper foveating, and peripheral attention. On the other hand, when looking far to the side, all of these factors are trumped by a bigger force favoring to relax the eye muscles back to the primary position (resulting in the centripetal drift followed by corrective centrifugal saccades). In other words, the properties of FEM may not be fully stochastic and are influenced by a variety of task demands; a demand of eccentric GZ fixation might add an extra factor of the eye relaxing back to its primary position, which might appear it somehow "reduces" stochasticity.

The time constant of the exponential centripetal DRT can be defined as the quotient of the difference between the target position and the equilibrium position divided by a DRT trend, which characterizes the leakiness of the oculomotor velocity-to-position neural integrator (Kheradmand and Zee, 2011). If the equilibrium point is assumed to be at the horizontal center of 0°, the time constant obtained from this study was very slow, which was about 250 s if calculated from the mean DRT trend, and about 85 s even in the smallest case. These time constants are much larger than the time constant of a DRT trend in the periodic EPN, and also larger than the time constant of the centripetal drifts in the previous studies (Becker and Klein, 1973; Robinson et al., 1984; Eizenman et al., 1990; Reschke et al., 2006). Particularly, in previous studies, subjects were required to memorize and fixate continuously on the position of the fixation target presented instantaneously in complete darkness, but in the present study, fixation target position was presented continuously in the presence of display light. To the best of our knowledge, this is the first study to show the existence of the slow centripetal DRT in FEM at small target angles other than in complete darkness with large eccentricities.

Possible Mechanisms of the Centrifugal MS Trend Generation

Linear regression analysis of the MS time series revealed that the centrifugal MS trend counterbalanced the centripetal DRT trend (**Figure 4**), and the MS trend was generated by the target position-dependent small modulation of the total MS amplitudes (**Table 1**) as well as the target position- and jump direction-dependent small modulation in the occurrence frequency of MS events (**Figure 8**), albeit without statistical significance in these modulations. Despite the absence of significant position-dependent differences in each of the rightward and leftward MS amplitudes, a significant dependence of the target position on the mean total MS amplitude, which averages the MS amplitudes without distinction between rightward and leftward jumps,

implies a non-negligible dependence of the target position on MS amplitude for each of the rightward and leftward MS.

A detailed analysis of the MS time series and their centrifugal trend was performed based on the four parameters of MS, i.e., $\hat{\lambda}_+$, $\hat{\lambda}_-$, $\hat{w}_+$, and $\hat{w}_-$, which represent the subject-wise means of rates and amplitudes of the rightward and the leftward MS events, together with the combination of those as $\hat{s}$, which is the slope of the centrifugal trend of MS (**Figure 8**). Such an analysis revealed the complex mechanism of how the centrifugal MS trend is generated. None of the four parameters did not show significant dependence on the target positions, while $\hat{s}$ reconstructed from the four parameters explained the dependence of the target position on the velocity of the centrifugal trend (**Figure 8**, top panel). This result implies that MS amplitude and frequency were co-modulated (though very slightly for each of them own) to generate the target position-dependent slope of the centrifugal trend of MS, which counterbalanced the centripetal DRT trend. It has been known that the occurrence frequency of MS is suppressed when subjects concentrate on the fixation intentionally (Winterson and Collewun, 1976; Bridgeman and Palca, 1980). A typical example of such an amplitude modulation occurs when subjects are asked to perform a macroscopic voluntary saccade to track a sudden change in the target position. In this case, the MS amplitude during GZ fixation becomes small prior to the onset of the voluntary saccade, suggesting that MS and voluntary saccades may share a common neural control mechanism. Recent studies have begun to elucidate a detailed MS generation and modulation mechanism by a cortical neural network (e.g., frontal eye field and primary visual cortex) and a subcortical neural network (e.g., superior colliculus and cerebellum), which adapt MS dynamics to a varied situation (Hafed et al., 2009, 2021; Hafed, 2011; Otero-Millan et al., 2011; Arnstein et al., 2015; Peel et al., 2016; Willeke et al., 2019; Buonocore et al., 2021). Such functional neuroanatomy could provide a mechanistic basis of the cooperative control and/or co-modulation of MS amplitude and frequency that were characterized in this study. Establishing a computational model for this mechanism is our future work.

Target Position-Dependent Counterbalance Between the Linear Trends of DRT and MS

The scatter plot between the linear trends of DRT characterized by $\mu_{DRT,k}$ and MS characterized by s_k showed that centripetal DRT and centrifugal MS satisfied Equation (8), and the counterbalance point between them (i.e., the point at which the mean linear trends of DRT and MS coincided in the $\mu_{DRT,k}$-s_k plane) in **Figure 9** was shifted from the origin along the line $\mu_{DRT} = -s$ of Equation (8), depending on the target position. This target position-dependent shift of the counterbalance point along the line of Equation (8) explains the GZ control mechanism during GZ fixation with eccentricities because the GZ fixation might lose its stability if the counterbalance point between DRT and MS was shifted away from the line of Equation (8). Interestingly, it seems that eye blinks might reset the GZ position to the desired target position when the counterbalance between DRT and MS was shifted away from the line of Equation (8) based on a visual inspection of the upper middle and right panels of **Figure 4**, where the DRT and/or the MS series tended to be terminated by eye blink, making the length of those sample paths shorter than the others.

Oculomotor Control Perspective

Fixation on a target shifted to the left or right from the center position is an attention-demanding motor task. Therefore, it is expected that the motor center and motor neurons need to maintain the tonic balance of the tension between the medial and lateral rectus muscles of each eyeball. The existence of migration trends in DRT implies that the tonic control of these antagonist muscles is lost intermittently, and the GZ diffuses away from the fixation target position during "resting" intervals. Furthermore, in this situation, it is conceivable that a stable eyeball posture appears transiently somewhere in the front-facing-side, toward which the eyeball posture may be relaxed, leading to the generation of centripetal DRT. From the viewpoint of motor control, when one fixates on a target position deviated from the center to the left or right, his/her eyeballs are always drawn to their most stable postures by the DRT, which is internal noise, and the errors that increase continuously during the DRT interval are intermittently and stochastically reduced by MS reflecting the control input for correction. This is consistent with existing research with respect to the role of MS in improving fixation stability (Cornsweet, 1956; Engbert and Kliegl, 2004; Ko et al., 2010).

The intermittent loss of tonic balance between antagonist muscles could be due to neuronal fatigue or more strategic optimization, such as to minimize energy expenditure or to increase flexibility in preparation for oculomotor demands.

DATA AVAILABILITY STATEMENT

The raw data supporting the conclusions of this article will be made available by the authors, without undue reservation.

ETHICS STATEMENT

The studies involving human participants were reviewed and approved by the Ethical Committee of the Graduate School of Engineering Science at Osaka University. The patients/participants provided their written informed consent to participate in this study.

AUTHOR CONTRIBUTIONS

MO and TN conceived, designed the research, and interpreted the results of the experiments. MO performed the experiments, analyzed the data and drafted this manuscript. YS and TN advised on the analytical methodologies. MO and YS prepared the figures. TN edited and revised this manuscript. MO, YS, and TN approved the final version of this manuscript.

FUNDING

This study was supported by the following grants from the Ministry of Education, Culture, Sports, Science and Technology (MEXT)/Japan Society for the Promotion of Science (JSPS) KAKENHI: 20H05470 (TN), 26242041 (TN), and 20J13713 (MO). MO was supported in part by Program for Leading Graduate Schools of MEXT and the scholarship for human resources development granted by Sumitomo Chemical Co., Ltd., Japan.

ACKNOWLEDGMENTS

We thank Drs. Yasushi Kobayashi and Ken-ichi Okada for their initial guidance for the experimental setup.

SUPPLEMENTARY MATERIAL

The Supplementary Material for this article can be found online at: https://www.frontiersin.org/articles/10.3389/fnhum.2022.842883/full#supplementary-material

REFERENCES

Abel, L. A., Parker, L., Daroff, R. B., and Dell'Osso, L. F. (1978). End-point nystagmus. *Investigat. Ophthalmol. Visual Sci.* 17, 539–544.

Arnstein, D., Junker, M., Smilgin, A., Dicke, P. W., and Thier, P. (2015). Microsaccade control signals in the cerebellum. *J. Neurosci.* 35, 3403–3411. doi: 10.1523/JNEUROSCI.2458-14.2015

Becker, W., and Klein, H. M. (1973). Accuracy of saccadic eye movements and maintenance of eccentric eye positions in the dark. *Vision Res.* 13, 1021–1034. doi: 10.1016/0042-6989(73)90141-7

Bertolini, G., Tarnutzer, A. A., Olasagasti, I., Khojasteh, E., Weber, K. P., Bockisch, C. J. et al. (2013). Gaze holding in healthy subjects. *PLoS ONE.* 8, e61389. doi: 10.1371/journal.pone.0061389

Bridgeman, B., and Palca, J. (1980). The role of microsaccades in high acuity observational tasks. *Vision Res.* 20, 813–817. doi: 10.1016/0042-6989(80)90013-9

Buonocore, A., Tian, X., Khademi, F., and Hafed, Z. M. (2021). Instantaneous movement-unrelated midbrain activity modifies ongoing eye movements. *Elife* 10, e64150. doi: 10.7554/eLife.64150.sa2

Büttner, U., and Grundei, T. (1995). Gaze-evoked nystagmus and smooth pursuit deficits: their relationship studied in 52 patients. *J. Neurol.* 242, 384–389. doi: 10.1007/BF00868394

Caffier, P. P., Erdmann, U., and Ullsperger, P. (2003). Experimental evaluation of eye-blink parameters as a drowsiness measure. *Euro. J. Appl. Physiol.* 89, 319–325. doi: 10.1007/s00421-003-0807-5

Cannon, S. C., and Robinson, D. (1987). Loss of the neural integrator of the oculomotor system from brain stem lesions in monkey. *J. Neurophysiol.* 57, 1383–1409. doi: 10.1152/jn.1987.57.5.1383

Collewijn, H., Erkelens, C. J., and Steinman, R. M. (1997). Trajectories of the human binocular fixation point during conjugate and non-conjugate gaze-shifts. *Vision Res.* 37, 1049–1069. doi: 10.1016/S0042-6989(96)00245-3

Collins, J. J., and De Luca, C. J. (1993). Open-loop and closed-loop control of posture: a random-walk analysis of center-of-pressure trajectories. *Experiment. Brain Res.* 95, 308–318. doi: 10.1007/BF00229788

Cornsweet, T. N. (1956). Determination of the stimuli for involuntary drifts and saccadic eye movements. *JOSA.* 46, 987–993. doi: 10.1364/JOSA.46.000987

Cunitz, R. J., and Steinman, R. M. (1969). Comparison of saccadic eye movements during fixation and reading. *Vision Res.* 9, 683–693. doi: 10.1016/0042-6989(69)90125-4

Ditchburn, R. W., and Ginsborg, B. L. (1953). Involuntary eye movements during fixation. *The J. Physiol.* 119, 1–17. doi: 10.1113/jphysiol.1953.sp004824

Eizenman, M., Cheng, P., Sharpe, J. A., and Frecker, R. C. (1990). End-point nystagmus and ocular drift: an experimental and theoretical study. *Vision Res.* 30, 863–877. doi: 10.1016/0042-6989(90)90055-P

Engbert, R. (2006). Microsaccades: A microcosm for research on oculomotor control, attention, and visual perception. *Progr. Brain Res.* 154, 177–192. doi: 10.1016/S0079-6123(06)54009-9

Engbert, R., and Kliegl, R. (2004). Microsaccades keep the eyes' balance during fixation. *Phychol. Sci.* 15, 431–431. doi: 10.1111/j.0956-7976.2004.00697.x

Engbert, R., and Mergenthaler, K. (2006). Microsaccades are triggered by low retinal image slip. *Proceed. Nat. Acad. Sci.* 103, 7192–7197. doi: 10.1073/pnas.0509557103

Ezenman, M., Hallett, P. E., and Frecker, R. C. (1985). Power spectra for ocular drift and tremor. *Vision Res.* 25, 1635–1640. doi: 10.1016/0042-6989(85)90134-8

Findlay, J. M. (1971). Frequency analysis of human involuntary eye movement. *Kybernetik* 8, 207–214. doi: 10.1007/BF00288749

Hafed, Z. M. (2011). Mechanisms for generating and compensating for the smallest possible saccades. *Euro. J. Neurosci.* 33, 2101–2113. doi: 10.1111/j.1460-9568.2011.07694.x

Hafed, Z. M., Goffart, L., and Krauzlis, R. J. (2009). A neural mechanism for microsaccade generation in the primate superior colliculus. *Science* 323, 940–943. doi: 10.1126/science.1166112

Hafed, Z. M., Yoshida, M., Tian, X., Buonocore, A., and Malevich, T. (2021). Dissociable cortical and subcortical mechanisms for mediating the influences of visual cues on microsaccadic eye movements. *Front. Neural Circuit.* 15, 429. doi: 10.3389/fncir.2021.638429

Kheradmand, A., and Zee, D. S. (2011). Cerebellum and ocular motor control. *Front. Neurol.* 2, 53. doi: 10.3389/fneur.2011.00053

Ko, H. K., Poletti, M., and Rucci, M. (2010). Microsaccades precisely relocate gaze in a high visual acuity task. *Nat. Neurosci.* 13, 1549–1553. doi: 10.1038/nn.2663

Leigh, R. J., and Zee, D. S. (2015). *The Neurology of Eye Movements, fifth edition*. New York, NY: Oxford University Press.

Martinez-Conde, S., Macknik, S. L., and Hubel, D. H. (2004). The role of fixational eye movements in visual perception. *Nat. Rev. Neurosci.* 5, 229–240. doi: 10.1038/nrn1348

Martinez-Conde, S., Macknik, S. L., Troncoso, X. G., and Hubel, D. H. (2009). Microsaccades: a neurophysiological analysis. *Trends Neurosci.* 32, 463–475. doi: 10.1016/j.tins.2009.05.006

Nyström, M., Hansen, D. W., Andersson, R., and Hooge, I. (2016). Why have microsaccades become larger? investigating eye deformations and detection alg*orithms. Vision Res.* 118, 17–24. doi: 10.1016/j.visres.2014.11.007

Ono, H., and Barbeito, R. (1982). The cyclopean eye vs. the sighting-dominant eye as the center of visual direction. *Percept. Psychophysics.* 32, 201–210. doi: 10.3758/BF03206224

Otero-Millan, J., Castro, J. L. A., Macknik, S. L., and Martinez-Conde, S. (2014). Unsupervised clustering method to detect microsaccades. *J. Vision* 14, 18–18. doi: 10.1167/14.2.18

Otero-Millan, J., Macknik, S. L., Serra, A., Leigh, R. J., and Martinez-Conde, S. (2011). Triggering mechanisms in microsaccade and saccade generation: a novel proposal. *Annal. New York Acad. Sci.* 1233, 107–116. doi: 10.1111/j.1749-6632.2011.06177.x

Otero-Millan, J., Troncoso, X. G., Macknik, S. L., Serrano-Pedraza, I., and Martinez-Conde, S. (2008). Saccades and microsaccades during visual fixation, exploration, and search: foundations for a common saccadic generator. *J. Vision* 8, 21–21. doi: 10.1167/8.14.21

Ozawa, M., and Nomura, T. (2019). "Relationship between saccadic intrusions and a bimodal aspect of inter-microsaccadic intervals," in *2019 IEEE 1st Global Conference on Life Sciences and Technologies (LifeTech)*, p. 300–301.s doi: 10.1109/LifeTech.2019.8883966

Peel, T. R., Hafed, Z. M., Dash, S., Lomber, S. G., and Corneil, B. D. (2016). A causal role for the cortical frontal eye fields in microsaccade deployment. *PLoS Biol.* 14, e1002531. doi: 10.1371/journal.pbio.1002531

Quinet, J., Schultz, K., May, P. J., and Gamlin, P. D. (2020). Neural control of rapid binocular eye movements: Saccade-vergence burst neurons. *Proceed. Nat. Acad. Sci.* 117, 29123–29132. doi: 10.1073/pnas.2015318117

Reschke, M. F., Somers, J. T., Feiveson, A. H., Leigh, R. J., Wood, S. J., Paloski, W. H. et al. (2006). *Studies of the ability to hold the eye in eccentric gaze: measurements in normal subjects with the head erect. NASA Technical Reports Server*. Available at: https://ntrs.nasa.gov/citations/20080026117 (accessed December 20, 2021).

Robinson, D. A., Zee, D. S., Hain, T. C., Holmes, A., and Rosenberg, L. F. (1984). Alexander's law: Its behavior and origin in the human vestibul - ocular reflex. *Annal. Neurol. Offic. J. Am. Neurologic. Assoc. Child Neurol. Soc.* 16, 714–722. doi.org/10.1002/ana.410160614

Romano, F., Tarnutzer, A. A., Straumann, D., Ramat, S., and Bertolini, G. (2017). Gaze-evoked nystagmus induced by alcohol intoxication. *J. Physiol.* 595, 2161–2173. doi: 10.1113/JP273204

Rucci, M., and Poletti, M. (2015). Control and functions of fixational eye movements. *Ann. Rev. Vision Sci.* 1, 499–518. doi: 10.1146/annurev-vision-082114-035742

Shallo-Hoffmann, J., Schwarze, H., Simonsz, H. J., and Mühlendyck, H. (1990). A reexamination of end-point and rebound nystagmus in normals. *Investigat. Ophthalmol. Visual Sci.* 31, 388–392.

Tarnutzer, A. A., Weber, K. P., Schuknecht, B., Straumann, D., Marti, S., and Bertolini, G. (2015). Gaze holding deficits discriminate early from late onset cerebellar degeneration. *J. Neurol.* 262, 1837–1849. doi: 10.1007/s00415-015-7773-9

Versino, M., Hurko, O., and Zee, D. S. (1996). Disorders of binocular control of eye movements in patients with cerebellar dysfunction. *Brain* 119, 1933–1950. doi: 10.1093/brain/119.6.1933

Whyte, C. A., Petrock, A. M., and Rosenberg, M. (2010). Occurrence of physiologic gaze-evoked nystagmus at small angles of gaze. *Investigat. Ophthalmol. Visual Sci.* 51, 2476–2478. doi: 10.1167/iovs.08-3241

Willeke, K. F., Tian, X., Buonocore, A., Bellet, J., Ramirez-Cardenas, A., and Hafed, Z. M. (2019). Memory-guided microsaccades. *Nat. Commun.* 10, 1–14. doi: 10.1038/s41467-019-11711-x

Winterson, B. J., and Collewun, H. (1976). Microsaccades during finely guided visuomotor tasks. *Vision Res.* 16, 1387–1390. doi: 10.1016/0042-6989(76)90156-5

Conflict of Interest: The authors declare that the research was conducted in the absence of any commercial or financial relationships that could be construed as a potential conflict of interest.

Publisher's Note: All claims expressed in this article are solely those of the authors and do not necessarily represent those of their affiliated organizations, or those of the publisher, the editors and the reviewers. Any product that may be evaluated in this article, or claim that may be made by its manufacturer, is not guaranteed or endorsed by the publisher.

Copyright © 2022 Ozawa, Suzuki and Nomura. This is an open-access article distributed under the terms of the Creative Commons Attribution License (CC BY). The use, distribution or reproduction in other forums is permitted, provided the original author(s) and the copyright owner(s) are credited and that the original publication in this journal is cited, in accordance with accepted academic practice. No use, distribution or reproduction is permitted which does not comply with these terms.

frontiers | Frontiers in Human Neuroscience

ORIGINAL RESEARCH
published: 27 May 2022
doi: 10.3389/fnhum.2022.805452

Design of an Isometric End-Point Force Control Task for Electromyography Normalization and Muscle Synergy Extraction From the Upper Limb Without Maximum Voluntary Contraction

*Woorim Cho[1], Victor R. Barradas[2], Nicolas Schweighofer[2,3] and Yasuharu Koike[2]**

[1] School of Engineering, Tokyo Institute of Technology, Yokohama, Japan, [2] Institute of Innovative Research, Tokyo Institute of Technology, Yokohama, Japan, [3] Division of Biokinesiology and Physical Therapy, University of Southern California, Los Angeles, CA, United States

OPEN ACCESS

Edited by:
Jun Izawa,
University of Tsukuba, Japan

Reviewed by:
Qi An,
The University of Tokyo, Japan
Takeshi Sakurada,
Ritsumeikan University, Japan

***Correspondence:**
Yasuharu Koike
koike@pi.titech.ac.jp

Specialty section:
This article was submitted to Motor Neuroscience, a section of the journal Frontiers in Human Neuroscience

Received: *30 October 2021*
Accepted: *03 March 2022*
Published: *27 May 2022*

Citation:
Cho W, Barradas VR, Schweighofer N and Koike Y (2022) Design of an Isometric End-Point Force Control Task for Electromyography Normalization and Muscle Synergy Extraction From the Upper Limb Without Maximum Voluntary Contraction. Front. Hum. Neurosci. 16:805452. doi: 10.3389/fnhum.2022.805452

Muscle synergy analysis *via* surface electromyography (EMG) is useful to study muscle coordination in motor learning, clinical diagnosis, and neurorehabilitation. However, current methods to extract muscle synergies in the upper limb suffer from two major issues. First, the necessary normalization of EMG signals is performed *via* maximum voluntary contraction (MVC), which requires maximal isometric force production in each muscle. However, some individuals with motor impairments have difficulties producing maximal effort in the MVC task. In addition, the MVC is known to be highly unreliable, with widely different forces produced in repeated measures. Second, synergy extraction in the upper limb is typically performed with a multidirection reaching task. However, some participants with motor impairments cannot perform this task because it requires precise motor control. In this study, we proposed a new isometric rotating task that does not require precise motor control or large forces. In this task, participants maintain a cursor controlled by the arm end-point force on a target that rotates at a constant angular velocity at a designated force level. To relax constraints on motor control precision, the target is widened and blurred. To obtain a reference EMG value for normalization without requiring maximal effort, we estimated a linear relationship between joint torques and muscle activations. We assessed the reliability of joint torque normalization and synergy extraction in the rotating task in young neurotypical individuals. Compared with normalization with MVC, joint torque normalization allowed reliable EMG normalization at low force levels. In addition, the extraction of synergies was as reliable and more stable than with the multidirection reaching task. The proposed rotating task can, therefore, be used in future motor learning, clinical diagnosis, and neurorehabilitation studies.

Keywords: muscle synergy, EMG normalization, maximum voluntary contraction (MVC), isometric force control, electromyography (EMG)

INTRODUCTION

Electromyography (EMG) describes muscle activation by measuring the electrical activity of muscles (Wu et al., 2013). The EMG analysis is widely applied to monitor and evaluate the motor performance of neurotypical individuals (Brueckner et al., 2018; Singh et al., 2018) and the motor function and physiological condition of individuals with neurological deficits (Cheung et al., 2012; Singh et al., 2018; Pan et al., 2021). To measure EMG signals in a non-invasive way, surface EMG is measured by attaching electrodes on the skin. However, surface EMG relies on measurements of the electric activity of muscles through the skin, making it vulnerable to intrinsic and extrinsic factors such as motor unit properties, skin condition, and the placement of the electrode (Hsu et al., 2006; Gaudet et al., 2016). Therefore, raw EMG signals need to be normalized for quantitative comparisons between different muscles and experimental sessions within and between subjects (Burden, 2010).

Maximum voluntary contraction (MVC) is the most commonly used method for EMG normalization (Hsu et al., 2006). During an MVC task, EMG is measured to find the reference values that correspond to a maximal effort contraction (Konrad, 2005). These reference values are then used to normalize the EMG measured during the actual experimental task. However, one of the limitations of the MVC method is that generating maximal effort contractions may be difficult and is affected by muscle fatigue or pain, especially for elderly individuals and individuals with neurological deficits (Hsu et al., 2006; Sousa et al., 2012). Furthermore, because some upper limb muscles are involved in force generation in a direction perpendicular to the reaching plane (Roh et al., 2012), there is a concern that some force would be generated on the perpendicular direction when maximally producing force, even when the task only requires forces contained in the horizontal plan. Last, the reliability of MVC for intersession comparison is affected by the interval between sessions (Kollmitzer et al., 1999), which may be inadequate for monitoring changes in EMG during motor learning or rehabilitation, for instance. Thus, a method for normalizing EMG that does not rely on MVC is needed. EMG normalization is also a necessary processing step for analyses that establish relationships between muscles, such as muscle synergy analysis. Muscle synergies are groups of muscles that the central nervous system (CNS) activates in a coordinated way during the execution of a motor task (Tresch et al., 1999). Therefore, the analysis of muscle synergies is useful for describing and evaluating patterns of muscle activation during a given task (Gentner et al., 2013; Taborri et al., 2018). For example, a muscle synergy can serve as a low dimensional index for motor performance or skill training in neurotypical individuals (Kristiansen et al., 2015), as the muscle synergy may reflect adaptation to changes in neurological or external conditions, appearing as a change in muscle activation patterns (Carson and Riek, 2001; Shemmell et al., 2005; Safavynia et al., 2011; Brueckner et al., 2018; Li et al., 2019). In neurorehabilitation, muscle synergies can serve as a physiological marker of a patient's motor impairment or to describe the effect of a treatment (Cheung et al., 2012; Hesam-Shariati et al., 2017; Pan et al., 2018, 2021; Singh et al., 2018).

Isometric multidirection reaching tasks are commonly used for extracting synergies of upper extremity muscles (Dewald et al., 1995; Roh et al., 2012; Berger et al., 2013; Gentner et al., 2013; Barradas et al., 2020). In these tasks, subjects are instructed to move a cursor controlled by the subject's end-point force to targets distributed uniformly around a center point. However, these tasks suffer from two weaknesses for synergy analysis. First, these tasks demand relatively precise force generation in multiple directions, which can be difficult for individuals with motor impairments. As a result, such participants are excluded from the experiment (Dewald et al., 1995), or the missing data are excluded from the synergy analysis (Roh et al., 2013). For instance, in Dewald et al. (1995), ten out of twenty participants were excluded. In both cases, this data removal was prone to bias the results. Second, the validity of the extracted synergies is vulnerable to the number of the reaching directions in these tasks (Augenstein et al., 2020). This is because if only a few discrete directions are used in the task, the EMG data for missing directions must be interpolated, which could affect the shape of muscle synergy tuning curves. A continuous motor task in which the participants generate forces in all directions would be beneficial for the extraction of synergies that better represent the muscle activation patterns of subjects during a reaching task.

For these reasons, we proposed here a new continuous isometric end-point force control task that enables both EMG normalization without relying on an MVC task and muscle synergy extraction without precise force generation in different reaching directions. This new task consists of maintaining a cursor controlled by the arm's end-point force on a target that rotates at a constant angular velocity around a central position at a constant force magnitude. Therefore, the rotating task has continuous angular information in all directions of the reaching plane in an isometric condition. Additionally, to make the rotating task have looser motor control requirements, the target and the cursor are large and have blurry edges (Burge et al., 2008) to weaken the sense of their exact location, giving subjects fewer constraints to follow the cursor.

The rotating task allows the use of joint torque normalization (Shin et al., 2009) as a replacement for MVC normalization. Joint torque normalization uses the relationship between estimated joint torques from the end-point force and EMG. We showed that low levels of joint torque far from maximal effort levels are sufficient to conduct reliable normalization of the EMG signals. To confirm the reliability of EMG normalization, we compared the results of joint torque normalization using the rotating task and the results of an MVC task. Furthermore, to validate the muscle synergy extraction in the rotating task, we compared the synergy extraction results of the rotating task and a multidirection reaching task.

MATERIALS AND METHODS

Participants

Ten healthy subjects (all males, 28.6 years, SD: 5.4) participated in the experiment. All subjects were right-handed and used their right arm to perform the experimental tasks. Subjects performed the commonly used planar multidirection isometric reaching task, the MVC task, and the proposed rotating task. All experimental procedures were approved by the ethics board of the Tokyo Institute of Technology, and all subjects provided written informed consent before participating in the study.

Experimental Setup

Subjects sat on a chair facing a computer screen and held a handle attached to a force sensor centered at the body midline. The height of the seat was adjusted so that the sensor and the arm lay on a horizontal plane. The arm's weight was supported by a two-link elbow support, and the wrist was constrained by a splint. Based on previous studies (Berger et al., 2013), surface EMG signals from 10 shoulder and elbow muscles (i.e., trapezius, posterior deltoid, middle deltoid, anterior deltoid, pectoralis major, triceps brachii long head, biceps long head, triceps brachii lateral head, brachioradialis, and pronator teres) were measured using bipolar electrodes (Bagnoli system; Delsys). The arm end-point force was measured with a 6-axis force sensor (DynPick WEF-6A200; Wacoh-tech). Raw EMG and force data were sampled at 2,000 Hz using an analog-to-digital converter (USB-6363 BNC; National Instruments) and processed and analyzed using Matlab 2020. Filtered end-point force data were projected on a 30-inch LCD screen as a visual feedback cursor, so that subjects could control the cursor position according to the experiment instructions.

Experiment Protocol

Subjects performed three isometric tasks, namely, the proposed rotating task, the multidirection reaching task, and the MVC task. The tasks were performed on the same day. We grouped the MVC and the multidirection reaching tasks as one task unit, in which the MVC task was always conducted before the multidirection reaching task. The rotating task constituted a separate task unit. We counterbalanced the order of these two task units across subjects to reduce the effects of fatigue and any other task order effects. Furthermore, we asked subjects about their fatigue condition in every task transition to confirm that they were ready to move on to the next task. The next task was only conducted with the subject's agreement.

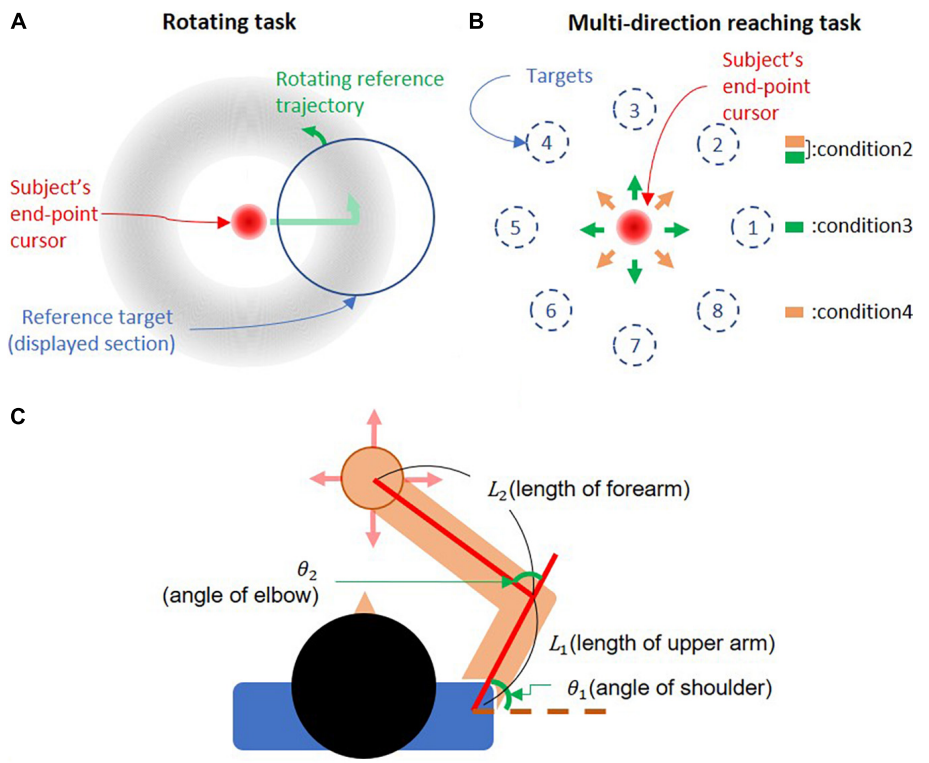

FIGURE 1 | Experimental setup. **(A)** Rotating task. The cursor is controlled by the subject's end-point force. Subjects move the cursor around a circular trajectory indicated by a doughnut-shaped silhouette. Only a portion of the silhouette enclosed by the reference target is visible during the task. The reference target rotates around the trajectory, setting the pace at which subjects move the cursor. **(B)** Multidirection reaching task. The cursor is controlled by the subject's end-point force, and targets are presented according to the trial condition (direction and force level). Subjects were instructed to move the cursor to target. **(C)** Subject's arm posture. The upper arm was set between 40° and 70° with respect to the frontal axis. The forearm was fixed to the handle, so that it formed an angle between 65° and 90° with the upper arm.

Rotating Task

In the rotating task, subjects controlled the cursor using their end-point force to keep the cursor near a reference target that followed a reference trajectory. The reference trajectory was circular and was displayed as a section of a doughnut-shaped silhouette, which gradually faded in shades of gray as the distance from the circular trajectory increased. The subjects were informed that the darkest color in the silhouette indicated the reference force level. The reference target was a circular "window" that revealed a section of the reference trajectory as it rotated around the trajectory (**Figure 1**). The cursor was a large red circle with a color gradient that gradually faded as the distance to the center of the cursor increased. The gradually fading visual feedback of the target and cursor weakened the sense of their exact position, reducing the pressure for precise motor control (Burge et al., 2008). At the beginning of a trial, subjects placed the cursor on the reference target, which prompted the reference target to start rotating. After the reference target completed a whole revolution around the screen, the trial ended, and subjects had to rest for 5 s. Subjects were able to rest for longer if they so desired. Each trial lasted 20 s. There was no condition to pause or stop during the trial even if subjects could not place the cursor on the target. The task is illustrated in **Figures 1A,C**.

The parameters of each trial were defined by 64 randomized trial conditions designed to prevent muscle co-contraction and motor planning for the next trial. The 64 conditions consisted of combinations of 2 rotating directions (i.e., CW and CCW), 8 uniformly distributed starting positions around the reference trajectory for the reference target, and 4 force levels (i.e., 5, 10, 15, and 20N), which indicated the necessary force to keep the cursor on the circular trajectory. These 64 trial conditions were divided into 8 blocks of 8 trials each, and subjects could rest freely between blocks. For all force levels, the diameter of the cursor was 3.1 cm, and the radius of the reference trajectory was kept at 6.9 cm (in 5, 10, 15, and 20N conditions, a distance of 1 cm in the virtual environment corresponded to 0.72, 1.45, 2.17, and 2.90N, respectively).

Maximum Voluntary Contraction Task

The MVC task was used to normalize the EMG signals measured in the multidirection reaching task. We also used the MVC task to normalize the EMG in the rotating task to conduct the muscle synergy analysis for comparison to the multidirection reaching task.

Subjects were instructed to produce the largest possible end-point force in eight uniformly distributed directions. At the beginning of the MVC task, a white ring was displayed at the center of the screen, and subjects moved the cursor into the ring. Later, a solid white circular target appeared in one of the directions, and the subject generated the largest possible force using only the upper limb for 2 s in the indicated direction. The target was set at a distance corresponding to 10N from the center of the virtual environment. The cursor could not move past the target. For applied forces exceeding 10N, the cursor remained at the same distance from the center of the virtual environment. While subjects generated their maximum voluntary force, EMG data were recorded to obtain the maximum EMG values to normalize EMG in the other tasks. This process was repeated twice for each target. Subjects could rest freely between trials.

Multidirection Reaching Task

In the multidirection reaching task, subjects controlled the cursor using their end-point force to reach a target that appeared at fixed positions on the screen (corresponding to specific force magnitudes and directions). There were 32 targets in the task, resulting from the combination of 8 uniformly distributed force directions and 4 force magnitudes (5, 10, 15, and 20% of the MVC's maximum force magnitude). Each target was presented 3 times, resulting in a total of 96 trials. At the beginning of a trial, a white empty circle appeared at the center of the screen, into which subjects moved the cursor. Next, a target was presented according to the trial condition (i.e., direction and magnitude of force), toward which subjects moved the cursor at their preferred speed and timing. If subjects succeeded to reach the target, visual feedback was removed for 2 s. Subjects were instructed to move the cursor to the target and hold the cursor at the target position until visual feedback reappeared. If subjects failed the trial, the trial was repeated. Subjects could rest freely between trials.

For all force levels, the cursor was a solid red circle with a 0.9 cm diameter, and targets were rings with a 4.5 cm diameter to induce precise reaching. The movement of the cursor and applied force from the end point were mapped such that 5% of the MVC's maximum force magnitude was projected as 3.6 cm on the screen.

Data Analysis

Electromyography Signal Processing

Electromyography data were processed offline. Raw EMG signals were rectified and filtered to obtain a linear envelope of the EMG signal. First, we used a Butterworth second-order high-pass filter with 20 Hz cutoff frequency. Second, the high-pass-filtered data were rectified and filtered with a Butterworth second-order low-pass filter with a 5 Hz cutoff frequency. Finally, the filtered data were normalized using two different methods, namely, MVC normalization and joint torque normalization.

End-Point Force Data Processing

Rotating Task

In the rotating task, to give visual feedback to subjects, the force was re-sampled at 100Hz and filtered using a moving average filter with a window size of 15 samples. This filter was used to avoid delays, since we found that control in the rotating task is more susceptible to delays than that in the multidirection reaching task. To analyze force trajectories on the plane, the force was filtered using a median filter with a window size of 15 samples. The scale of the force-position mapping on the screen was adjusted so that the size and position of elements on the screen remained constant across all conditions.

Maximum Voluntary Contraction Task

In the MVC task, a Butterworth second-order low-pass filter with a 1 Hz cutoff frequency was used to filter the raw force signals. We measured forces in the vertical direction to verify whether maximal force production in the horizontal plane was associated with forces outside of the horizontal plane. We calculated the

ratio of the magnitudes of the vertical force and the maximum force in the reaching plane.

Multidirection Reaching Task

In the multidirection reaching task, a Butterworth second-order low-pass filter with a 1 Hz cutoff frequency was used for filtering the raw force signals. The filtered force data were scaled to provide the position of the cursor on the screen according to the MVC task's maximum force magnitude.

Joint Torque Estimation

For the joint torque normalization, the torques around the elbow and shoulder were estimated from the end-point force using the virtual work principle according to Eqs 1, 2. A two-dimensional model of each subject was used, as seen in **Figure 1C**. We measured the length of the upper limb segments and the elbow and shoulder joint angles to define the two-dimensional model.

$$\mathrm{J} = \begin{bmatrix} -L_1 * \sin(\theta_1) - L_2 * \sin(\theta_1 + \theta_2) & -L_2 * \sin(\theta_1 + \theta_2) \\ L_1 * \cos(\theta_1) + L_2 * \cos(\theta_1 + \theta_2) & L_2 * \cos(\theta_1 + \theta_2) \end{bmatrix} \quad (1)$$

$$\begin{bmatrix} \tau_s \\ \tau_e \end{bmatrix} = \mathrm{J}^{\mathrm{T}} \times \begin{bmatrix} F_x \\ F_y \end{bmatrix} \quad (2)$$

where J is the Jacobian matrix according to a model of the forward kinematics of a planar two-joint arm, F_x and F_y are end-point forces on the reaching plane, and τ_s and τ_e are the estimated joint torques of the shoulder and elbow.

Joint Torque Normalization Method

The joint torque normalization method was used to normalize the filtered EMG signals using the relationship between joint torque and muscle activation (Shin et al., 2009). This method finds the relationship between joint torque and filtered EMG by performing a linear regression between these two variables. Next, the estimated filtered EMG value that corresponds to a torque magnitude of 80 Nm in the linear regression model was determined as the reference value for the normalization in each muscle. We followed Shin et al. (2009)'s assumption that 80 Nm is appropriate for estimating the reference value of the joint torque normalization.

To estimate the linear model for the filtered EMG data and joint torque, we only used EMG and torque data corresponding to the anatomical pulling direction of the analyzed muscle, that is, positive torques for joint flexors and negative torques for joint extensors. Then, the filtered EMG data were uniformly divided into 100 bins according to the range of the joint torque data. We defined the representative EMG values of each bin as the 5th percentile of the EMG values in the bin to eliminate surplus EMG activity due to co-contraction. The joint torque value of each bin and representative filtered EMG values were used in the linear regression. The estimated filtered EMG value when the joint torque of the linear function was –80 Nm or 80 Nm, according to the function of each muscle around the joint, was defined as the reference value for joint torque normalization:

$$EMG_{norm} = \frac{EMG - EMG_{min}}{EMG_{ref} - EMG_{min}} \quad (3)$$

where EMG_{ref} is the estimated value of EMG at the 80 Nm torque magnitude, and EMG_{min} is the smallest value of EMG in the whole rotating task trials. Thus, the range of the values of normalized muscle activation goes from 0 to 1.

Comparison of Normalization Methods

To compare the normalization results of the joint torque normalization method and the results of MVC normalization, we obtained the ratio of the normalization reference values for each muscle using both methods. The ratio was obtained by dividing the reference value obtained from the MVC task by the reference value obtained from the joint normalization method using the data from the rotating task.

Muscle Synergy Extraction

We used non-negative matrix factorization (non-NMF) to extract muscle synergies in the rotating task and the multidirection reaching task (Lee and Seung, 1999; Berger et al., 2013). For an ideal matrix factorization without residual EMG activity, non-NMF is represented as:

$$\mathbf{m} = \mathbf{W}\mathbf{c} \quad (4)$$

where $\mathbf{m}$ is a 10-dimensional vector of muscle activations measured during the experiment (normalized EMG by MVC normalization), $\mathbf{W}$ is a $10 \times N$ matrix of each muscle activation's weight vector in the extracted synergy, and $\mathbf{c}$ is an N-dimensional synergy activation vector, where N is the number of extracted synergies.

Since ten muscles were measured during the experiment, the possible values of N are between 1 and 10. For each value of N, we repeated the synergy extraction computation 100 times using a different initial condition for $\mathbf{W}$ to find the synergy set with the highest reconstruction quality R^2 of muscle activations $\mathbf{m}$.

To find the best number of synergies (N), R^2 and the slope function of the R^2 curve were used, as in Berger et al. (2013). First, the minimum best synergy number (N) was determined when N number of synergies in the synergy set could reproduce more than 90% of the EMG data variance. In parallel, N was determined as the smallest number for which the slope of a linear regression fit of the R^2 curve between N and $N = 10$ had a mean squared error less than 10^{-4} (D'Avella et al., 2006). In case the best synergy numbers N calculated using the above two criteria did not match, N was chosen as the value for which there was the least overlap between the preferred direction of the extracted synergies. When the best synergy number N could not be decided with this process, N was fixed to $N = 4$ as the default synergy number of the synergy set.

Muscle Synergy Extraction Result Comparison

We compared the synergy extraction results of the rotating task and the multidirection reaching task. To compare the synergy extraction result between tasks, we extracted synergies in four conditions. The first condition was the synergy extraction from the rotating task. The second condition was the synergy extraction from the multidirection reaching task. The third and

fourth conditions were synergy extractions from reduced data sets of the multidirection reaching task, in which 4 reaching directions were omitted. The third condition comprised the 4 directions aligned with the x- and y-axes of the reaching plane (target numbers: 1, 3, 5, and 7 in **Figure 1B**), The fourth condition comprised the 4 directions diagonal to the x- and y-axes of the reaching plane (target numbers: 2, 4, 6, and 8 in **Figure 1B**). These last two conditions helped to analyze the effects of synergy extraction in data sets that are missing information and how the generalizability of synergies may be affected by this.

We evaluated the suitability of the rotating task for synergy extraction by examining the reliability and stability of the synergy extraction results compared with those of the multidirection reaching task. We extracted muscle synergies by fixing the number of synergies from 3 to 5 in each of the 4 conditions defined in the previous section. We then attempted to reconstruct the EMG measured in the multidirection task conditions using synergies extracted from the rotating task and vice versa. We reconstructed the EMG data by estimating synergy activations of a reference synergy set that most adequately reconstructs the muscle activations in the target task:

$$\mathbf{m}_r = \mathbf{W}_{ref}\mathbf{c}_{est} \quad (5)$$

where $\mathbf{m}_r$ are the reconstructed muscle activities, $\mathbf{W}_{ref}$ is the extracted synergy set from the reference task, and $\mathbf{c}_{est}$ are the estimated synergy activations. We obtained $\mathbf{c}_{est}$ by performing a non-negative linear regression between the muscle activations of the target task ($\mathbf{m}$) and $\mathbf{W}_{ref}$. For example, to reconstruct the EMG in the multidirection task with the synergy set of the rotating task, we found $\mathbf{c}_{est}$ by applying a non-negative linear regression between the EMG in the multidirection reaching task and the synergy set of the rotating task. We quantified the goodness of reconstruction in each condition using the R^2 index.

Statistical Analysis

To find a reliable minimum force level of the rotating task for the joint torque normalization, we compared slopes estimated by joint torque normalization for each force level with slopes estimated using all force levels. We tested the null hypothesis that there would be no difference in estimated slopes between each force level and all force levels by an independent t-test (i.e., two-tailed).

To test the reconstruction result of the synergy set in the rotating task and the multidirection reaching task's conditions, the R^2 indices from the rotating task and each of the multidirection task conditions were compared. We tested the null hypothesis that there would be no difference in R^2 indices between the rotating task and each condition of the multidirection reaching task by using a paired t-test (i.e., two-tailed). We also tested the null hypothesis that there would be no difference in the variance of R^2 indices between task conditions by using an f-test (i.e., two-tailed). The significance threshold was set to $P < 0.05$. All analyses were performed using MATLAB R2019b.

RESULTS

Comparison Between Joint Torque and Maximum Voluntary Contraction Normalization

Figure 2 shows sample trials in the rotating and multidirection reaching task for a representative subject. In the rotating task, subjects produced cursor trajectories with a root mean square error (RMSE) of 12.3% (SD 5.7) of the reference force level with respect to the reference trajectory. All subjects completed all trials of the MVC task and the average resting time between MVC task trials was 4.96 s (SD 3.31, maximum resting time 31 s). We compared the results of joint torque normalization using the rotating task and the results of MVC normalization by calculating the ratio of reference values obtained in both normalization methods (**Figure 3**). The mean ratio of MVC and joint torque normalization reference values among subjects and muscles was 2.09 (SD 1.95) [Tra: 4.02 (SD 4.56), P.del: 1.61 (SD 0.48), M.del: 2.07 (SD 1.45), A.del: 2.21 (SD 0.63), Pec: 1.81 (SD 0.83), Tri.Lo: 1.55 (SD 0.84), Bi.Lo: 2.60 (SD 1.87), Tri.La: 1.20 (SD 0.66), Bra: 2.84 (SD 2.09), and Pro: 1.02 (SD 0.82)]. Four muscles displayed relatively larger variance in the ratio of reference values than other muscles across subjects (i.e., trapezius, middle deltoid, biceps long head, and brachioradialis). In high effort conditions, such as MVC, these four muscles may be involved in force generation outside of the horizontal plane defined in the isometric tasks. Given that some muscles may generate forces perpendicular to the defined reaching plane, we verified the magnitude of perpendicular forces during the MVC task. We quantified the size of perpendicular forces with respect to planar forces as the ratio of the magnitudes of the perpendicular and reaching plane forces for each target (**Figure 4**). The mean ratio across all subjects and targets was 0.41 (SE 0.024) [Target1: 0.20 (SE 0.049), Target2: 0.18 (SE 0.032), Target3: 0.36 (SE 0.049), Target4: 0.36 (SE 0.041), Target5: 0.67 (SE 0.084), Target6: 0.67 (SE 0.065), Target7: 0.48 (SE 0.029), and Target8: 0.35 (SE 0.067)]. This indicates that perpendicular forces comprised around 41% of the maximal forces produced on the horizontal plane.

Minimum Force Level for Joint Torque Normalization

We sought to determine the minimum force level that would still produce joint torque normalization results that are comparable to using higher force levels in the rotating task. To do this, we compared the slopes of the regression lines between estimated torque and EMG for every muscle in each level of force in the rotating task. We divided the data set of the rotating task according to each force level and estimated the slope for each force level from the divided data sets. As a result, we found that the slopes estimated for each force level starting from 10N were not statistically different to the slope estimated by combining data from all force levels: [5N: 0.00062[1/Nm] (SE 9.75e–05), $P = 0.001$; 10N: 0.00093[1/Nm] (SE 1.03e–04), $P = 0.21$; 15N: 0.00106[1/Nm] (SE 1.10e–04), $P = 0.70$; 20N: 0.00109[1/Nm] (SE 1.16e–04), $P = 0.87$; all force level: 0.00112 (SE 1.14e–04);

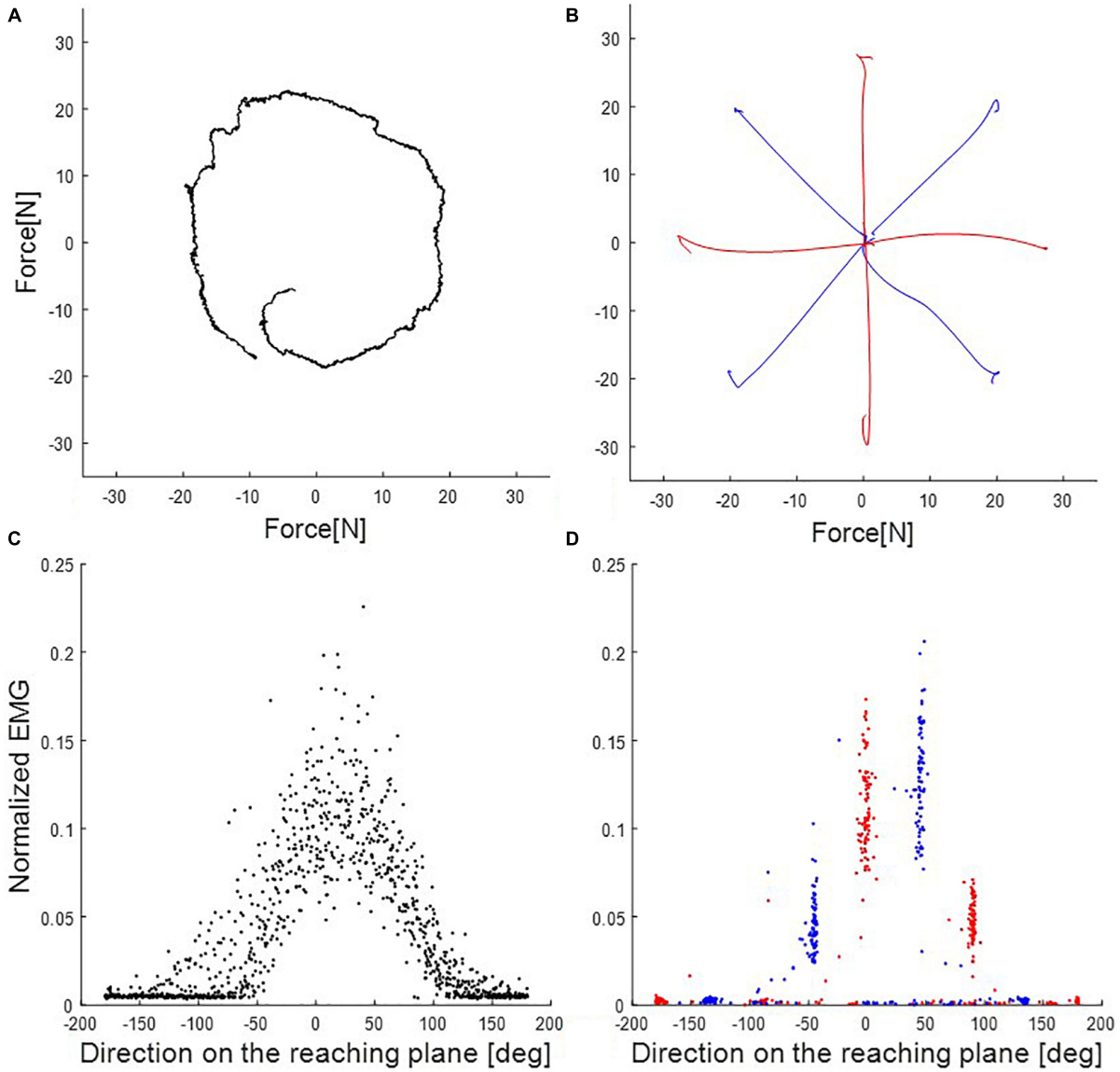

FIGURE 2 | End-point force trajectory and electromyography (EMG) activations in rotating and multidirection reaching tasks of the representative subject (subject 8). **(A)** Rotating task (condition 1) in one trial of 20N trials. **(B)** Multidirection reaching task in trials of 20% of Maximum voluntary contraction's (MVC's) maximum magnitude. Condition 2 used all eight targets. Conditions 3 and 4 (red and blue traces, respectively) used subsets of four targets each in different direction. **(C)** EMG activations of the posterior deltoid according to direction on the reaching plane (trials of 20N in the rotating task). Black dots are EMG activation in the rotating task (condition 1). **(D)** EMG activations of the posterior deltoid according to direction on the reaching plane (trials of 20% of the maximum value of MVC in the multidirection reaching task). Red and blue dots are EMG activation in the multidirection reaching task (condition 2). Red and blue dots are subsets, respectively, for conditions 3 and 4.

independent *t*-test]. The estimated slope for each force level and the corresponding standard error are shown in **Figure 5**.

Effect of Number and Direction of Targets on Synergy Extraction

We compared the results of the synergy extraction procedure using the rotating and the multidirection reaching tasks. We defined two additional sub-tasks based on the multidirection reaching task by varying the number and direction of targets in the tasks. Therefore, we defined four conditions for this analysis (**Figures 2A,B**): (condition 1: rotating task; condition 2: multidirection reaching task with all 8 targets; condition 3: multidirection reaching task with 4 targets lying on the x- and y-axes of the reaching plane; and condition 4: multidirection reaching task with 4 targets located diagonal to the x- and y-axes on the reaching plane). **Figure 6** shows the extracted synergy sets for a representative subject. **Table 1** shows the selected number of synergies for each subject and condition. In conditions 1–3, 4–5 synergies were extracted across subjects, whereas in condition

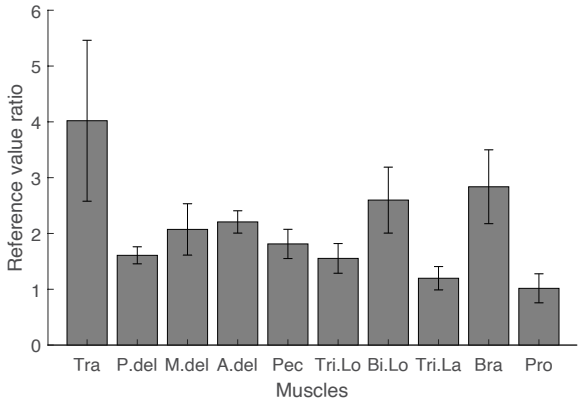

FIGURE 3 | Ratio of reference values of MVC and joint torque normalization. The reference values for EMG normalization of the MVC task and joint torque normalization were compared by dividing the reference value in the MVC task by the reference value in joint torque normalization for each muscle and every subject. The average ratio for every muscle across subjects was larger than 1. The variance of the ratio across subjects was large in trapezius, middle deltoid, biceps long head, and brachioradialis. Error bars indicate the standard error.

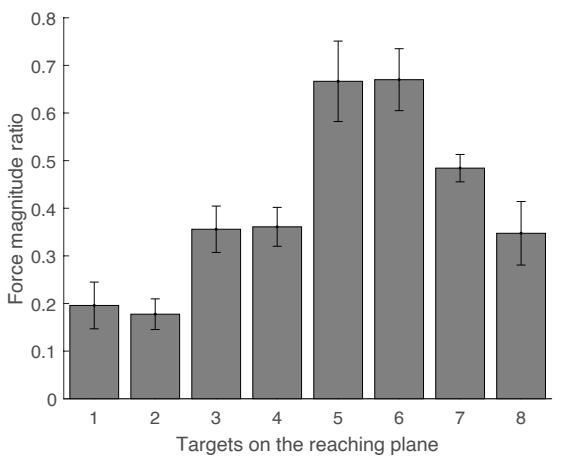

FIGURE 4 | Ratio of magnitudes of perpendicular and in-plane forces for each target during MVC task. Error bars indicate the standard error across subjects.

4, 3–5 synergies were extracted. The default synergy number $N = 4$ was used in only 3 out of 40 instances (10 subjects and 4 conditions) of muscle synergy extraction. For conditions 1 and 2, the number of extracted synergies within a subject was the same or fewer in condition 1 except for two subjects (fewer than condition 2 in 5 subjects, same as condition 2 in 3 subjects, and larger than condition 2 in 2 subjects). For conditions 2 and 3, the number of synergies was almost identical (fewer than condition 3 in 1 subject, same as condition 3 in 9 subjects). Finally, for conditions 2 and 4, the number of synergies was larger or the same in condition 2 (same as condition 4 in 3 subjects and larger than condition 4 in 7 subjects). Therefore, this analysis shows that in the multidirection reaching task with a reduced number of targets, synergy extraction was affected according to the directions of the targets.

Mutual Reconstruction Quality of Muscle Activations in Rotating and Multidirection Reaching Tasks

We quantified the goodness of reconstruction of the EMG measured in the multidirection task conditions by synergies extracted from the rotating task, and vice versa, by using the R^2 index (**Figure 7**). We compared the mutual reproducibility of EMG between both tasks. For a fixed number of synergies (i.e., 3–5), synergies extracted from the rotating task produced higher reconstruction qualities R^2 of the EMG in the multidirection reaching task than vice versa. **Table 2** contains the results of mutual reconstruction between condition 1 and the other conditions for fixed numbers of synergies and the statistical results. As a general tendency, the R^2 score increased as the number of synergies N increased from 3 to 5 in all conditions. The difference in R^2 of the mutual reproducibility between conditions 1 and 2 was not statistically significant. Nonetheless, the standard deviation of R^2 in the reconstruction by the rotating task synergies was smaller than in the reconstruction by the synergies of the multidirection reaching task for N = 3–5. The difference in variance between conditions was statistically significant when $N = 5$. In the case of conditions 1 and 3, the difference in R^2 was statistically significant when $N = 5$. However, there was no significant difference in the standard deviation of R^2 between both conditions. Last, in the case of conditions 1 and 4, the reconstruction qualities by the rotating task synergies were higher than the reconstruction qualities by the synergies of the multidirection reaching task for N = 3–5. There was statistical significance when $N = 3$. The standard deviation of R^2 in the reconstruction by the rotating task synergies was smaller than in the reconstruction by the synergies of the multidirection reaching task for N = 3–5. Furthermore, these differences were statistically significant when $N = 4$ and 5.

In summary, the average R^2 score of the rotating task was equivalent to the R^2 score of other conditions. Moreover, the standard deviation of the R^2 score of the rotating task was smaller than the standard deviation of the R^2 score of other conditions in most cases, reaching statistical significance in 3 cases.

DISCUSSION

Muscle Activations Related to Perpendicular Force Generation Produced a Difference Between Maximum Voluntary Contraction Normalization and Joint Torque Normalization

We found that the MVC and joint torque normalization methods produced different results in the normalization reference values. To our knowledge, previous studies

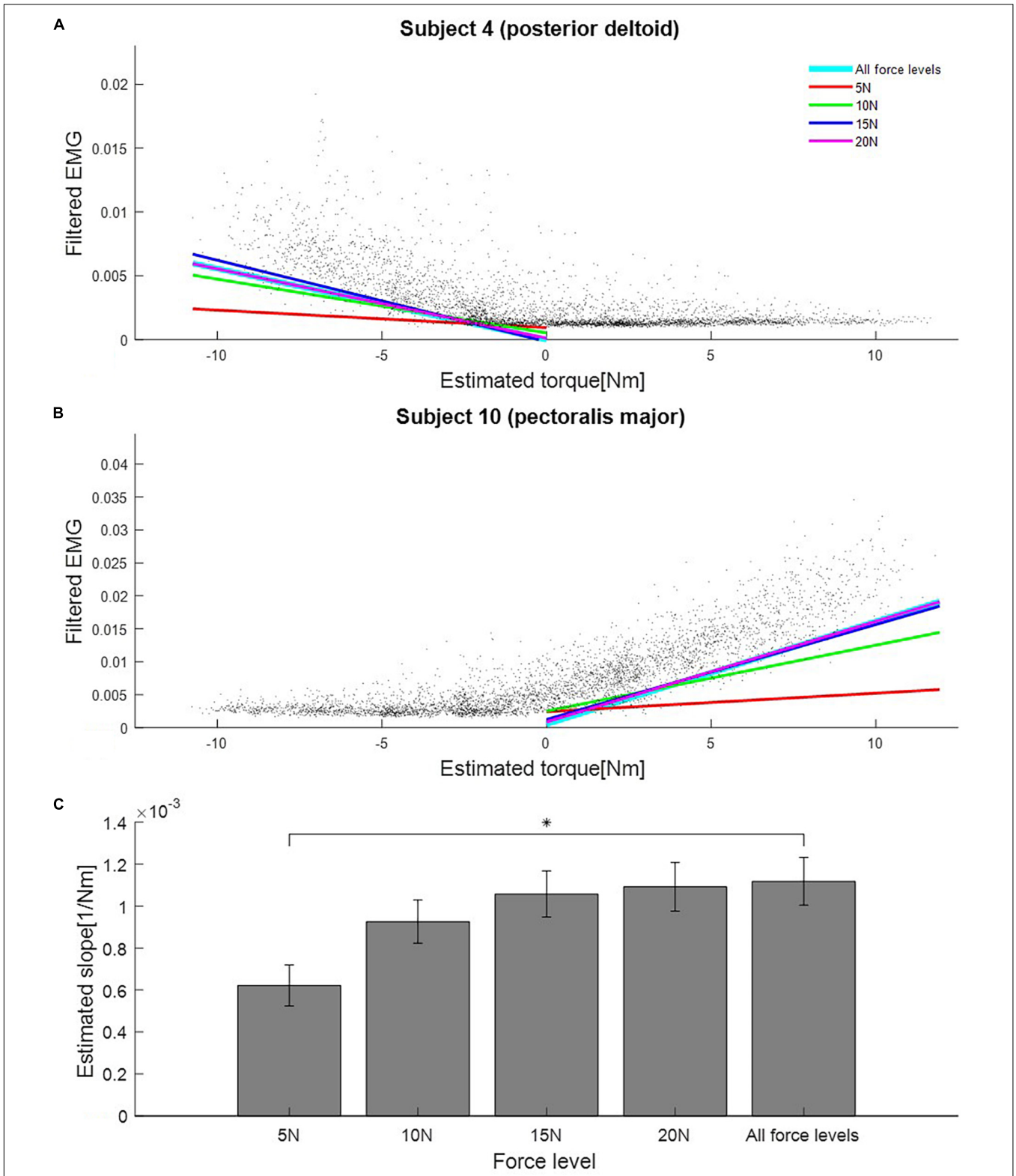

FIGURE 5 | Estimated slopes for joint torque normalization procedure at different force levels in the rotating task. **(A)** Slopes estimated from data of each force level in the rotating task (Subject 4, posterior deltoid). Black dots are samples of estimated torque and EMG. Colored lines represent regression lines between estimated torque and EMG for each force level. **(B)** Slopes estimated from data of each force level in the rotating task (Subject 10, pectoralis major). **(C)** Mean estimated slopes for joint torque normalization for all force levels in the rotating task. Asterisk indicates statistical significance. Error bars indicate the standard error across all muscles and subjects.

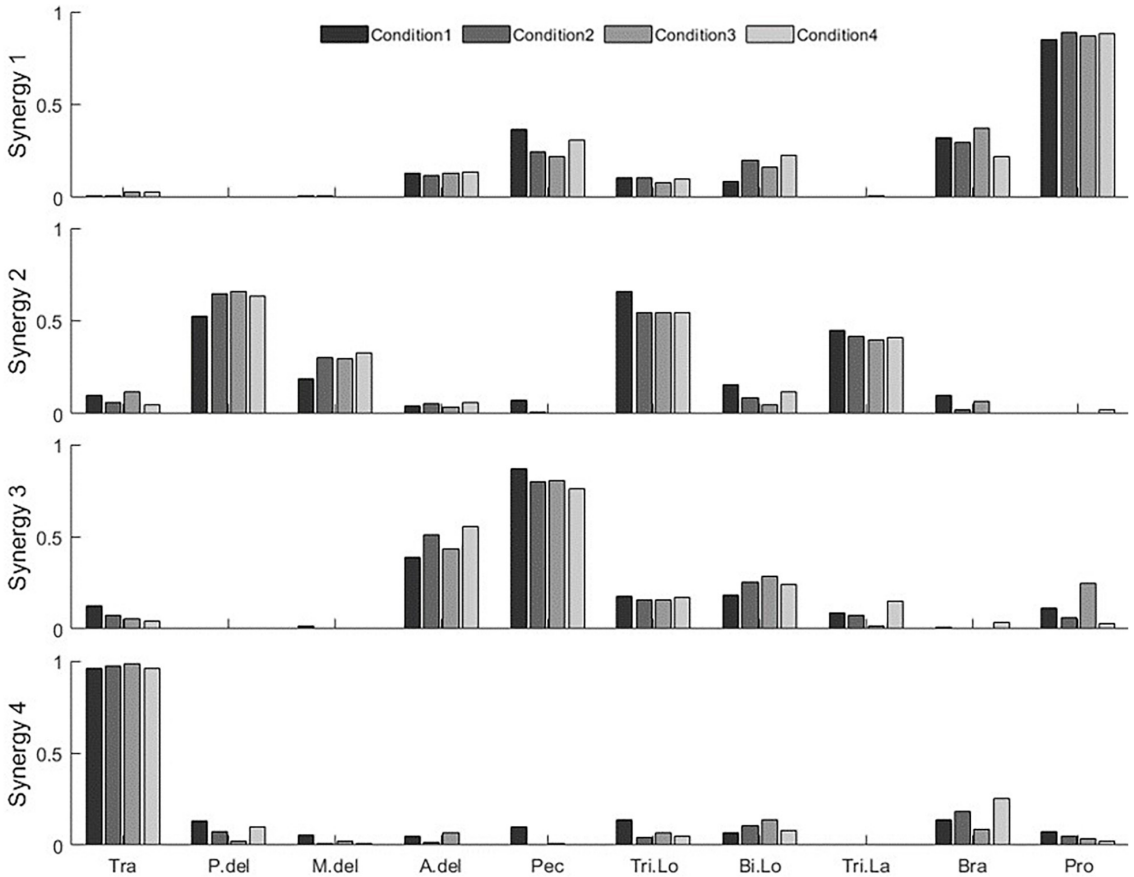

FIGURE 6 | Synergy set extracted in all conditions (condition 1—the rotating task, condition 2—the multidirection reaching task with 8 targets, condition 3—the multidirection reaching task with 4 targets, and condition 4—the multidirection reaching task with 4 targets in diagonal directions) from a representative subject (subject 8).

TABLE 1 | Number of synergies extracted in each task condition.

Condition	1	2	3	4
	Rotating task	**Multidirection reaching task (8 directions)**	**Multidirection reaching task (4 directions)**	**Multidirection reaching task (4 directions-diagonal)**
Mean (SD)	4.2 (SD 0.42)	4.5 (SD 0.53)	4.6 (SD 0.52)	3.8 (SD 0.63)
Subject 1	4	4	4	4
Subject 2	5	4	5	3
Subject 3	4	5	5	4
Subject 4	4	5	5	4
Subject 5	4	5	5	4
Subject 6	4	4	4	3
Subject 7	5	4	4	3
Subject 8	4	4	4	4
Subject 9	4	5	5	5
Subject 10	4	5	5	4

examining maximum voluntary isometric force generation in a horizontal plane have not considered the vertical force as a variable of interest. Mainly two-dimensional models and measurements of joint torques and end-point forces are used for tasks on the horizontal plane (Nijhof and Gabriel, 2006; Pinter et al., 2010; Sin et al., 2014; Gorkovenko, 2018; Gorkovenko et al., 2020). Furthermore, in studies that use virtual environments to guide force generation on the

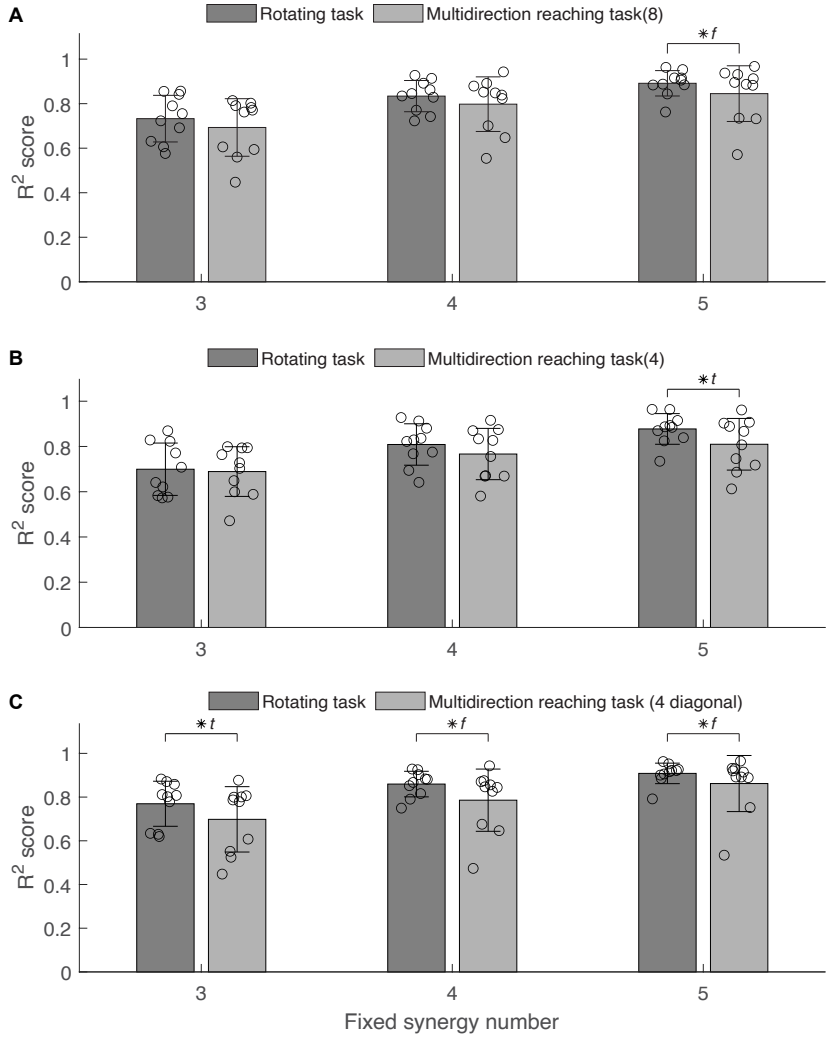

FIGURE 7 | Electromyography reconstruction R^2 score between the rotating task and multidirection reaching conditions. Error bars indicate the standard deviation. Scattered circles indicate R^2 score of each subject in each condition. Asterisk indicates statistical significance in the *t*-test and *f*-test. **(A)** Comparison between rotating task and multidirection reaching task (8 directions: condition 2). **(B)** Comparison between rotating task and multidirection reaching task with 4 targets (condition 3). **(C)** Comparison between rotating task and multidirection reaching task with 4 diagonal targets (condition 4).

two-dimensional plane, there are no reported instructions, feedback, or results related to perpendicular forces during the MVC task (Berger et al., 2013; Gentner et al., 2013; Barradas et al., 2020).

However, our results suggest that the difference between the two normalization methods arose due to sizeable perpendicular forces exerted during the MVC task (**Figure 4**). On average, the perpendicular force component had a magnitude that was around 41% the size of forces measured on the reaching plane. Consequently, this additional force could have made the MVC's reference value for some muscles higher than if forces had been applied only on the reaching plane. In particular, because our arm model is defined only for planar forces, increased EMG activity in some muscles due to perpendicular forces would not be associated with corresponding increases in the estimated joint torque. This would appear as a non-linearity in the relationship between estimated joint torque and EMG in the case of the MVC task. Such non-linearities would produce overestimations of the slope of the joint torque-EMG relationship, bringing about a discrepancy with the computed slope in the rotating task. Therefore, we also observed a discrepancy in the ratio of normalization reference values of both tasks across muscles. In other words, since the non-linearities caused by perpendicular forces exerted during the MVC task are different for each muscle, the reference values of MVC normalization and joint torque normalization may be different. However, the difference between the reference values of both normalization methods should be similar between subjects within the same muscle. Therefore, for reliable joint torque normalization between subjects, the variability of the ratio of normalization reference values of both tasks in the same muscle should be small.

TABLE 2 | The result of electromyography (EMG) activity reconstruction comparison between the rotating task (condition 1) and the multidirection reaching task (conditions 2, 3, and 4) in each fixed synergy number.

Fixed number of synergies		3		4		5	
Rotating task and Multidirection reaching task (8)	$mean_{con1}$	0.73 (SD 0.10)	P_t 0.179	0.83 (SD 0.07)	P_t 0.215	0.89 (SD 0.06)	P_t 0.095
	$mean_{con2}$	0.69 (SD 0.13)	P_f 0.539	0.80 (SD 0.12)	P_f 0.111	0.85 (SD 0.13)	**P_f 0.028**
Rotating task and Multidirection reaching task (4)	$mean_{con1}$	0.70 (SD 0.12)	P_t 0.762	0.81 (SD 0.09)	P_t 0.131	0.88 (SD 0.07)	**P_t 0.012**
	$mean_{con3}$	0.69 (SD 0.11)	P_f 0.879	0.77 (SD 0.11)	P_f 0.534	0.81 (SD 0.11)	P_f 0.137
Rotating task and Multidirection reaching task (4 diagonal)	$mean_{con1}$	0.77 (SD 0.10)	**P_t 0.016**	0.86 (SD 0.06)	P_t 0.052	0.91 (SD 0.05)	P_t 0.155
	$mean_{con4}$	0.70 (SD 0.15)	P_f 0.283	0.79 (SD 0.14)	**P_f 0.014**	0.86 (SD 0.13)	**P_f 0.006**

Paired t-test and f-test, bold P-values indicate < 0.05. For statistic comparison of the means of both tasks, non-statistical significance reveals that both tasks are equivalent when we reconstruct EMG activities of other tasks. In case the t-test result has statistical significance, the reconstruction by the rotating task is better because the rotating task has a higher mean than the multidirection reaching task. This implies that the rotating task is as reliable as or, in some cases, more reliable than the multidirection reaching task. For statistic comparison of the variances of both tasks, non-statistical significance reveals that both tasks are equally stable in EMG reconstruction. In case that they are significantly different, the reconstruction by the rotating task is more stable because the variability in the multidirection reaching task is larger than the rotating task in most cases. This suggests that synergies extracted from the rotating task are more stable for reconstructing EMG activities of other tasks.

Joint Torque Normalization Allows for Suitable Normalization in Low Force Conditions

Maximum voluntary contraction normalization requires maximal effort muscle contractions that are outside the range of forces produced in daily life. Some of the limitations of this technique are evidenced when applying it to motor-impaired patients, who may be unable to produce the required forces and decreasing reliability due to fatigue and pain (Sousa et al., 2012). Therefore, a reliable EMG normalization method that is easier to perform and improves accessibility is needed. Our results show that using the rotating task at forces as low as 10N can produce joint torque normalization results that are equivalent to results derived from larger forces. Therefore, our results strongly suggest that joint torque normalization in the rotating task enables reliable EMG normalization using low levels of force. This suggests that joint torque normalization is potentially useful as an EMG normalization method for subjects with motor impairments.

The Rotating Task Is as Reliable as the Multidirection Reaching Task for Synergy Extraction

Extracting synergies that are as general as possible in describing different motor behaviors is important for the analysis of muscle activation patterns. In other words, good synergy extraction is equivalent to extracting synergies that better reproduce various motor behaviors in the same workspace. To confirm the universality of synergies extracted in the rotating task proposed in this study, we tested the ability of these synergies to reconstruct the EMG measured in the multidirection reaching task and sub-tasks and vice versa.

We found that in 7 out of 9 pairings between the rotating task and each condition of the multidirection reaching task, the R^2 mutual reconstruction score was equivalent. In 2 out of 9 pairings, the mean R^2 score was significantly higher for the reconstruction by the rotating task than by the multidirection reaching tasks. This indicates that the mean R^2 score of the reconstruction of EMG in the multidirection reaching tasks by the rotating task across subjects was at least as good as in the reciprocal case. This supports that the generality of synergies in the rotating task was equivalent or better than synergies in the multidirection reaching task. Therefore, the generality of synergies in the rotating task allows the description of the same or more diverse motor behavior information in the reaching plane than multidirection reaching tasks.

Furthermore, we found that in 8 out of 9 pairings between the rotating task and each condition of the multidirection reaching task, the variance of R^2 in the reconstructions by the rotating task was smaller than in the reconstructions by the multidirection reaching tasks. In 3 out of these 8 pairings, the differences in reconstruction variance were significant. This suggests that the stability of EMG reconstruction by synergies in the rotating task was equivalent or higher than by synergies in the multidirection reaching task. Therefore, synergies in the rotating task reconstructed the muscle activations in the reaching plane with higher stability than the multidirection reaching tasks.

We also investigated whether the rotating task elicits muscle activation patterns as complex as the multidirection reaching task by examining the number of synergies extracted in each task. The average number of synergies in the rotating task and the multidirection reaching task were 4.2 (SD 0.42) and 4.5 (SD 0.53), respectively. This indicates that both tasks elicit muscle activation patterns that have a similar degree of complexity. We also investigated whether target number (angular resolution of target distribution on the reaching plane) and target direction

affect synergy extraction in the multidirection reaching task. The number of synergies extracted from the multidirection reaching task with 8 directions was usually larger than the number of synergies extracted from the task with diagonal target directions. This suggests that the complexity of the identified EMG activation patterns was higher for the task with a larger number of targets. This may be because the diagonal targets coincide with the directions of action of the shoulder and elbow joints in the examined posture, reducing simultaneous activation of muscles crossing these joints resulting in less complex activation patterns.

Therefore, tasks that rely on discrete reaching movements for synergy extraction are vulnerable to oversimplified muscle synergy descriptions if an inadequate distribution of targets is used. Our results are supported by Augenstein et al. (2020), who indicate that the number of reaching directions and selection of reaching directions in muscle synergy analysis affect the validity of the extracted muscle synergies. Thus, depending on the purpose of the experiment, the target distribution setting on the reaching plane should be carefully considered. This problem is bound to occur when testing subjects with motor impairments, for which some target directions may be excluded in the task or in data analysis due to the inability of the subjects to acquire these targets (Roh et al., 2013), which could bias the synergy analysis. This highlights the benefits of the rotating task, in which the force is generated continuously around the plane, allowing to more granularly identify the area where forces cannot be adequately produced due to subjects' motor performance. Furthermore, the rotating task allows considerable variability in the magnitude of the produced forces, possibly entailing the production of richer muscle activation patterns.

In conclusion, the rotating task has the potential to replace the multidirection reaching task as a synergy extraction task in the reaching plane of the upper limb. Furthermore, the rotating task has the advantage that EMG data can be normalized with low end-point forces. Additionally, because the area of the plane where patients are not able to adequately execute the task can be more narrowly identified due to the continuous task demands, it may allow to investigate the motor ability of individuals with neurological deficits in higher resolution than the discrete target reaching task. Moreover, one of the ideas of the rotating task was to reduce the pressure for precise motor control to prevent patient's frustration from failures in motor execution. Therefore, as a future plan, we intend to apply the rotating task to develop a muscle synergy extraction system for patients with motor impairments. In addition, we will compare the influence of the EMG normalization method in the muscle synergy extraction in both neurotypical and neuroatypical individuals. We also intend to extend the rotating task to a three-dimensional task involving force production around a sphere-shaped space, analogous to Roh et al.'s (2012) three-dimensional multidirection reaching task.

DATA AVAILABILITY STATEMENT

The data presented in this study are available from the corresponding author on reasonable request.

ETHICS STATEMENT

The studies involving human participants were reviewed and approved by Tokyo Institute of Technology Human Subjects Research Ethics Review Committee. The participants provided their written informed consent to participate in this study.

AUTHOR CONTRIBUTIONS

WC and VB performed the experiments. WC analyzed data, prepared figures, and drafted the manuscript. All authors conceived and designed the research, interpreted the results of experiments, edited and revised the manuscript, and approved the final version of the manuscript.

FUNDING

This work was supported by Japan Society for the Promotion of Science (JSPS) Grant KAKENHI 19H05728 (to YK) and Japan Science and Technology Agency (JST) Grant MIRAI JY300171 (to YK); NIH R21 NS120274 (to NS); and NIH R56 NS100528 (to NS).

REFERENCES

Augenstein, T. E., Washabaugh, E. P., Remy, C. D., and Krishnan, C. (2020). Motor modules are impacted by the number of reaching directions included in the analysis. *IEEE Trans. Neural Syst. Rehabil. Eng.* 28, 2025–2034. doi: 10.1109/TNSRE.2020.3008565

Barradas, V., Kutch, J., Kawase, T., Koike, Y., and Schweighofer, N. (2020). When 90% of the variance is not enough: residual EMG from muscle synergy extraction influences task performance. *J. Neurophysiol.* 123, 2180–2190. doi: 10.1152/jn.00472.2019

Berger, D. J., Gentner, R., Edmunds, T., Pai, D. K., and D'Avella, A. (2013). Differences in adaptation rates after virtual surgeries provide direct evidence for modularity. *J. Neurosci.* 33, 12384–12394. doi: 10.1523/JNEUROSCI.0122-13.2013

Brueckner, D., Kiss, R., and Muehlbauer, T. (2018). Associations between practice-related changes in motor performance and muscle activity in healthy individuals: a systematic review. *Sports Med. Open* 4:9. doi: 10.1186/s40798-018-0123-6

Burden, A. (2010). How should we normalize electromyograms obtained from healthy participants? What we have learned from over 25years of research. *J. Electromyogr. Kinesiol.* 20, 1023–1035. doi: 10.1016/j.jelekin.2010.07.004

Burge, J., Ernst, M. O., and Banks, M. S. (2008). The statistical determinants of adaptation rate in human reaching. *J. Vis.* 8, 20.1–19. doi: 10.1167/8.4.20

Carson, R. G., and Riek, S. (2001). Changes in muscle recruitment patterns during skill acquisition. *Exp. Brain Res.* 138, 71–87. doi: 10.1007/s002210100676

Cheung, V. C. K., Turolla, A., Agostini, M., Silvoni, S., Bennis, C., Kasi, P., et al. (2012). Muscle synergy patterns as physiological markers of motor cortical damage. *Proc. Natl. Acad. Sci. U.S.A.* 109, 14652–14656. doi: 10.1073/pnas.1212056109

D'Avella, A., Portone, A., Fernandez, L., and Lacquaniti, F. (2006). Control of fast-reaching movements by muscle synergy combinations. *J. Neurosci.* 26, 7791–7810. doi: 10.1523/JNEUROSCI.0830-06.2006

Dewald, J. P. A., Pope, P. S., Given, J. D., Buchanan, T. S., and Zev Rymer, W. (1995). Abnormal muscle coactivation patterns during isometric torque generation at the elbow and shoulder in hemiparetic subjects. *Brain* 118, 495–510. doi: 10.1093/brain/118.2.495

Gaudet, G., Raison, M., Dal Maso, F., Achiche, S., and Begon, M. (2016). Intra- and intersession reliability of surface electromyography on muscles actuating the forearm during maximum voluntary contractions. *J. Appl. Biomech.* 32, 558–570. doi: 10.1123/jab.2015-0214

Gentner, R., Edmunds, T., Pai, D. K., and d'Avella, A. (2013). Robustness of muscle synergies during visuomotor adaptation. *Front. Comput. Neurosci.* 7:120. doi: 10.3389/fncom.2013.00120

Gorkovenko, A. V. (2018). Theoretical analysis of the peculiarities of motor control at generation of two-joint isometric efforts by the human upper limb. *Neurophysiology* 50, 309–321. doi: 10.1007/s11062-018-9753-z

Gorkovenko, A. V., Tomiak, T., Pilewska, W., and Kostyukov, A. I. (2020). Synergetic control during generation of a maximal isometric effort by the human arm. *Neurophysiology* 52, 49–59. doi: 10.1007/s11062-020-09850-9

Hesam-Shariati, N., Trinh, T., Thompson-Butel, A. G., Shiner, C. T., and McNulty, P. A. (2017). A longitudinal electromyography study of complex movements in poststroke therapy. 2: changes in coordinated muscle activation. *Front. Neurol.* 8:277. doi: 10.3389/fneur.2017.00277

Hsu, W. L., Krishnamoorthy, V., and Scholz, J. P. (2006). An alternative test of electromyographic normalization in patients. *Muscle Nerve* 33, 232–241. doi: 10.1002/mus.20458

Kollmitzer, J., Ebenbichler, G. R., and Kopf, A. (1999). Reliability of surface electromyographic measurements. *Clin. Neurophysiol.* 110, 725–734. doi: 10.1016/S1388-2457(98)00050-9

Konrad, P. (2005). *The ABC of EMG A Practical Introduction to Kinesiological Electromyography*. Scottsdale, AZ: Noraxon U.S.A. Inc.

Kristiansen, M., Madeleine, P., Hansen, E. A., and Samani, A. (2015). Inter-subject variability of muscle synergies during bench press in power lifters and untrained individuals. *Scand. J. Med. Sci. Sports* 25, 89–97. doi: 10.1111/sms.12167

Lee, D. D., and Seung, H. S. (1999). Learning the parts of objects by non-negative matrix factorization. *Nature* 401, 788–791. doi: 10.1038/44565

Li, Z., Liu, H., Yin, Z., and Chen, K. (2019). Muscle synergy alteration of human during walking with lower limb exoskeleton. *Front. Neurosci.* 13:1050. doi: 10.3389/fnins.2018.01050

Nijhof, E. J., and Gabriel, D. A. (2006). Maximum isometric arm forces in the horizontal plane. *J. Biomech.* 39, 708–771. doi: 10.1016/j.jbiomech.2005.01.004

Pan, B., Huang, Z., Jin, T., Wu, J., Zhang, Z., and Shen, Y. (2021). Motor function assessment of upper limb in stroke patients. *J. Healthc. Eng.* 2021:6621950. doi: 10.1155/2021/6621950

Pan, B., Sun, Y., Xie, B., Huang, Z., Wu, J., Hou, J., et al. (2018). Alterations of muscle synergies during voluntary arm reaching movement in subacute stroke survivors at different levels of impairment. *Front. Comput. Neurosci.* 12:69. doi: 10.3389/fncom.2018.00069

Pinter, I. J., Bobbert, M. F., van Soest, A. J., and Smeets, J. B. (2010). Isometric torque-angle relationships of the elbow flexors and extensors in the transverse plane. *J. Electromyogr. Kinesiol.* 20, 923–931. doi: 10.1016/j.jelekin.2010.05.001

Roh, J., Rymer, W. Z., and Beer, R. F. (2012). Robustness of muscle synergies underlying three-dimensional force generation at the hand in healthy humans. *J. Neurophysiol.* 107, 2123–2142. doi: 10.1152/jn.00173.2011

Roh, J., Rymer, W. Z., Perreault, E. J., Yoo, S. B., and Beer, R. F. (2013). Alterations in upper limb muscle synergy structure in chronic stroke survivors. *J. Neurophysiol.* 109, 768–781. doi: 10.1152/jn.00670.2012.-Previous

Safavynia, S., Torres-Oviedo, G., and Ting, L. (2011). Muscle synergies: implications for clinical evaluation and rehabilitation of movement. *Top. Spinal Cord Inj. Rehabil.* 17, 16–24. doi: 10.1310/sci1701-16

Shemmell, J., Tresilian, J. R., Riek, S., Barry, B. K., and Carson, R. G. (2005). Neuromuscular adaptation during skill acquisition on a two degree-of-freedom target-acquisition task: dynamic movement. *J. Neurophysiol.* 94, 3058–3068. doi: 10.1152/jn.00671.2004

Shin, D., Kim, J., and Koike, Y. (2009). A myokinetic arm model for estimating joint torque and stiffness from EMG signals during maintained posture. *J. Neurophysiol.* 101, 387–401. doi: 10.1152/jn.00584.2007

Sin, M., Kim, W. S., Park, D., Min, Y. S., Kim, W. J., Cho, K., et al. (2014). Electromyographic analysis of upper limb muscles during standardized isotonic and isokinetic robotic exercise of spastic elbow in patients with stroke. *J. Electromyogr. Kinesiol.* 24, 11–17. doi: 10.1016/j.jelekin.2013.10.002

Singh, R. E., Iqbal, K., White, G., and Hutchinson, T. E. (2018). A systematic review on muscle synergies: from building blocks of motor behavior to a neurorehabilitation tool. *Appl. Bionics Biomech.* 2018:3615368. doi: 10.1155/2018/3615368

Sousa, A. S. P., Roberto Frias, R., and Tavares, J. R. M. S. (2012). "Surface electromyographic amplitude normalization methods: a review," in *Electromyography: New Developments, Procedures and Applications*, ed. H. Takada (New York, NY: Nova Science Publishers, Inc.), 85–102.

Taborri, J., Agostini, V., Artemiadis, P. K., Ghislieri, M., Jacobs, D. A., Roh, J., et al. (2018). Feasibility of muscle synergy outcomes in clinics, robotics, and sports: a systematic review. *Appl. Bionics Biomech.* 2018:3934698. doi: 10.1155/2018/3934698

Tresch, M. C., Saltiel, P., and Bizzi, E. (1999). The construction of movement by the spinal cord. *Nat. Neurosci.* 2, 162–167. doi: 10.1038/5721

Wu, Y., Martnez, M. A. M., and Orizaola Balaguer, P. (2013). "Overview of the application of EMG recording in the diagnosis and approach of neurological disorders," in *Electrodiagnosis in New Frontiers of Clinical Research*, ed. H. Turker (London: InTech). doi: 10.5772/56030

Conflict of Interest: The authors declare that the research was conducted in the absence of any commercial or financial relationships that could be construed as a potential conflict of interest.

Publisher's Note: All claims expressed in this article are solely those of the authors and do not necessarily represent those of their affiliated organizations, or those of the publisher, the editors and the reviewers. Any product that may be evaluated in this article, or claim that may be made by its manufacturer, is not guaranteed or endorsed by the publisher.

Copyright © 2022 Cho, Barradas, Schweighofer and Koike. This is an open-access article distributed under the terms of the Creative Commons Attribution License (CC BY). The use, distribution or reproduction in other forums is permitted, provided the original author(s) and the copyright owner(s) are credited and that the original publication in this journal is cited, in accordance with accepted academic practice. No use, distribution or reproduction is permitted which does not comply with these terms.

frontiers | Frontiers in Computational Neuroscience

ORIGINAL RESEARCH
published: 02 June 2022
doi: 10.3389/fncom.2022.784604

Reinforcement Learning Model With Dynamic State Space Tested on Target Search Tasks for Monkeys: Extension to Learning Task Events

Kazuhiro Sakamoto[1,2], Hinata Yamada[1], Norihiko Kawaguchi[2], Yoshito Furusawa[2], Naohiro Saito[2] and Hajime Mushiake[2]*

[1] Department of Neuroscience, Faculty of Medicine, Tohoku Medical and Pharmaceutical University, Sendai, Japan,
[2] Department of Physiology, Tohoku University School of Medicine, Sendai, Japan

Learning is a crucial basis for biological systems to adapt to environments. Environments include various states or episodes, and episode-dependent learning is essential in adaptation to such complex situations. Here, we developed a model for learning a two-target search task used in primate physiological experiments. In the task, the agent is required to gaze one of the four presented light spots. Two neighboring spots are served as the correct target alternately, and the correct target pair is switched after a certain number of consecutive successes. In order for the agent to obtain rewards with a high probability, it is necessary to make decisions based on the actions and results of the previous two trials. Our previous work achieved this by using a dynamic state space. However, to learn a task that includes events such as fixation to the initial central spot, the model framework should be extended. For this purpose, here we propose a "history-in-episode architecture." Specifically, we divide states into episodes and histories, and actions are selected based on the histories within each episode. When we compared the proposed model including the dynamic state space with the conventional SARSA method in the two-target search task, the former performed close to the theoretical optimum, while the latter never achieved target-pair switch because it had to re-learn each correct target each time. The reinforcement learning model including the proposed history-in-episode architecture and dynamic state scape enables episode-dependent learning and provides a basis for highly adaptable learning systems to complex environments.

Keywords: reinforcement learning, target search task, dynamic state space, episode-dependent learning, history-in-episode architecture

OPEN ACCESS

Edited by:
Jun Ota,
The University of Tokyo, Japan

Reviewed by:
Tetsuro Funato,
The University of Electro-Communications, Japan
Yuichi Kobayashi,
Shizuoka University, Japan

****Correspondence:***
Kazuhiro Sakamoto
sakamoto@tohoku-mpu.ac.jp

Received: *28 September 2021*
Accepted: *26 April 2022*
Published: *02 June 2022*

Citation:
Sakamoto K, Yamada H, Kawaguchi N, Furusawa Y, Saito N and Mushiake H (2022) Reinforcement Learning Model With Dynamic State Space Tested on Target Search Tasks for Monkeys: Extension to Learning Task Events. Front. Comput. Neurosci. 16:784604. doi: 10.3389/fncom.2022.784604

INTRODUCTION

Learning is a fundamental process that is crucial for biological systems to adapt to the real world. Real environments have diverse states, and situation-dependent learning is indispensable to adapt successfully to such complexity. A good example of situation-dependent learning in humans is a baseball game: to win, the batter needs to bat according to the situation of the game and batting order, i.e., according to whether the previous batter got a hit and got on base. However, the batter also needs to consider of his own episode, that is, how he played against the pitcher last few times to predict what kind of ball the pitcher will throw next. An episode, which is also referred to as

context in the field of neuroscience, is defined as a state (or framework) of the environment in which an agent gains experience and makes decisions or predictions (Maren et al., 2013; Yonelinas et al., 2019). Studies on episode-dependent learning provide a basis for understanding the high adaptability of living systems to real environments, and applying this to engineering.

The two-target search task used in our non-human primate neurophysiological experiments has advantages for building models that learn behaviors based on the sequence of episodes and history of each individual episode (Kawaguchi et al., 2013, 2015). The episodes of one trial of the task are shown in **Figure 1A** (i.e., the sequence of task events): the central fixation spot is presented, and the animal fixates on it (2nd episode); during fixation, four light spots appear around the fixation spot (3rd episode); the disappearance of the fixation spot is used as a go signal for gaze shift to one of the four spots. If the correct light spot is fixed on, a reward is given (4th episode). To be successful in the 4th episode, an action based on the history must be selected. In the task, two adjacent light points (the target pair) among the four should be alternately selected (**Figure 1B**). However, after a certain number of consecutive correct responses (exploitation phase), the target pair is switched without an instruction signal, and the animal must identify a new target pair through trial and error (exploration phase). To achieve a high correct response rate in this task, action selection must be based on the history of actions and outcomes of the previous two trials.

The first model of choice for learning action while inferring what cannot be directly observed, such as a target pair, would be a reinforcement learning model using a partially observable Markov decision process (POMDP; Jaakkola et al., 1995; Thrun et al., 2005). However, applied to a two-target search task, learning models using a POMDP have *a priori* knowledge of the target pairs. Models that require such knowledge will not be able to learn unassumed tasks, as our previous studies have shown (Katakura et al., 2022). Some models do not require prior knowledge and make decisions based on history, including models involving infinite hidden Markov processes, such as the hierarchical Dirichlet process (Beal et al., 2002; Teh et al., 2006; Mochihashi and Sumita, 2007; Mochihashi et al., 2009; Pfau et al., 2010; Doshi-Velez et al., 2015). However, models using such processes do not exhibit stable performance, because they generate many useless action-value functions due to a lack of criteria regarding the appropriateness of history length required for decision-making (Katakura et al., 2022).

The reinforcement learning model with a dynamic state space that we demonstrated in our previous study does not require prior knowledge of target pairs, and adheres to criteria regarding appropriate history length, and when that length should be increased for decision-making. The model showed high performance in a two-target search task, suggesting excellent generality (Katakura et al., 2022). However, in the model described above, one trial is equal to one-time step. Thus, it cannot learn appropriate behavior in a case involving a sequence of episodes (i.e., the task event sequence shown in **Figure 1A**).

In this study, we developed a reinforcement learning model with a dynamic state space to enable episode-dependent learning. Specifically, we added a "dynamic-state-within-episode," or "history-in-episode," architecture to the model. The model architecture dynamically generates a memory set when encountering a novel episode, namely, a task event (**Figures 2A,B**). Furthermore, the dynamic state space was used to generate a *Q*-table (action value function) for each episode (**Figure 2C**), according to the aforementioned criteria for appropriateness of determining state expansion: the experience saturation and decision uniqueness of action selection. These two mechanisms enable episode-dependent learning in the two-target search task. That is, the model autonomously determines that the previous state in the relevant episode is the last two trials (we refer to this as the "history" in this paper), and can find the correct new target pair in a short time without significant re-learning, resulting in high performance comparable to that exhibited by monkeys. Such learning greatly contributes to our understanding of the high adaptability of living systems to complex real environments and could lead to engineering applications.

MATERIALS AND METHODS

Model Architecture

Our proposed model has two types of time steps/sequences (**Figure 2**). The first type is the sequence of episodes, t, on which the changes of episode, E_t, depend. In this study, an episode is defined as a task event, specifically a display presented to an animal, rather than a sequence of events. Hence, episodes are explicit and directly observable, in the sense that the agent does not need to make any particular inferences. Temporally neighboring episodes interact when calculating reward prediction error (see below for details). The other type of step pertains to the history within an episode. Within this framework, the history at the N^{th} trial denotes the experience with the same task event, e_i, accrued over previous trials, and is represented as $H_N(e_i)$. A given history, h_j, is a state composed of a sequence of action–outcome pairs. Each history can include an arbitrary number of trials; however, they have a length of one trial when learning begins. Herein, we refer to this temporal structure of the model as history-in-episode architecture. The model generates a new set of memories, consisting of working memory and a dynamic *Q*-table (**Figure 2A**; episode-dependent memory set), when a novel task event is encountered (**Figure 2B**). Since our goal was to develop a learning model for a two-target search task consisting of a discrete sequence of events, the model has a simple mechanism to generate a memory set with probability 1 when a new display is exhibited. This history-in-episode architecture enables behaviors to be learned in each task period; this was not possible using the one trial-one time-step model in our previous paper (Katakura et al., 2022), in which one trial had one time unit and only the fourth task period in **Figure 1A** was considered.

Each episode-dependent memory set in the proposed model contained the same dynamic states as the one proposed in our previous paper (Katakura et al., 2022). The basic structure of the episode-dependent memory set was grounded in the

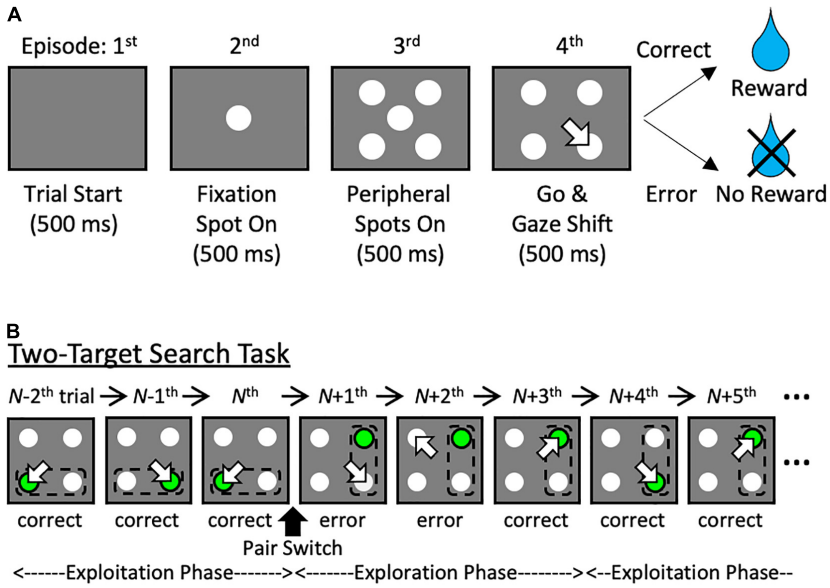

FIGURE 1 | The target search task. **(A)** The event sequence of the target search task. **(B)** A similar illustration of a valid-pair switch in the two-target search task. Green circle: correct target; arrow: choice; dashed line: valid pair. Note that the subjects were not instructed to move their eyes by the green spot before gaze shift.

conventional temporal difference (TD) learning (Sutton and Barto, 1998). The action value function, $Q_N(E_t = e_i, H_N = h_j, A_N = a_k)$ for the set of a particular episode, e_i, history, h_j, and an action, a_k, at the Nth trial were updated by the following equation:

$$Q_{N+1}\left(e_i, h_j, a_k\right) \leftarrow Q_N\left(e_i, h_j, a_k\right) + \alpha\delta_{t,N}\left(e_i, h_j, a_k\right) \quad (1)$$

where α is the learning rate, set to 0.1 in the range that showed desirable results revealed by the parameter search. $\delta_{t,N}$ is the reward prediction error, given by

$$\delta_{t,N}\left(e_i, h_j, a_k\right) \equiv r_t + \gamma Q_{t+1,N}(e_{i'}, h_{j'}, a_{k'}) - Q_{t,N}(e_i, h_j, a_k) \quad (2)$$

where r_t is the reward delivered for A_N taken at E_t and H_N at time t in the Nth trial, and the discount factor γ was set to 0.7 decided empirically. If the correct spot was selected, a reward $r = 1$ was delivered, otherwise $r = 0$ was given. $A_{t,N}$ was selected according to the stochastic function, $P^{\pi}(A_{t,N} = a_k \mid E_t = e_i, H_N = h_j)$, under the policy π. We used a softmax function for P^{π}, defined by

$$P^{\pi}\left(a_k \mid e_i, h_j\right) \equiv \frac{\exp(\beta Q\left(e_i, h_j, a_k\right))}{\sum_l^5 \exp(\beta Q\left(e_i, h_j, a_l\right))} \quad (3)$$

where the parameter β, termed the inverse-temperature, was set to 100 in the range that provided desirable results. 5 is the number of actions that the model can take. For action selection, the Q-table that refers to the longest history among generated Q-tables was used.

Our model was designed to avoid the need for stochastic decisions as much as possible. Specifically, when the model did not have a value function for a particular action that required a much larger value compared with others following extensive experience with the episode and history, it expanded the Q-table of the episode backward in sequence of trial (**Figure 2C**). We illustrate the algorithm of this expansion in **Supplementary Figure 1A**.

The initial *Q-table* was set as the one of a particular combination of the five possible actions, namely gazing at the right-up (RU), left-up (LU), left-down (LD), right-down (RD) spot, or center (C), which are represented by arrows and a black dot, and the outcome (correct or error), denoted by o and x in **Figure 3A** and **Supplementary Figure 1B**. The initial Q-value for each action was set to 0.5. The model monitored the stochastic mean policy for each episode e_i and history h_j, given by

$$P^{\pi}_{mean,N_{update,e_i,h_j}}\left(\mathbf{a}|e_i, h_j\right) \equiv \frac{1}{N_{update,e_i,h_j}} \sum_{m=1}^{N_{update,e_i,h_j}} P^{\pi}_m\left(\mathbf{a}|e_i, h_j\right) \quad (4)$$

where $N_{update,ei,hj}$ is the number of times that the Q-values for the episode e_i and history h_j were updated. Then, the information gain or the Kullback-Leibler divergence (KLD) obtained by updating the stochastic policy (step 1 in **Supplementary Figure 1A**) is calculated:

$$Update_KLD_{e_i,h_j}$$

$$\left(P^{\pi}_{mean,N_{update,e_i,h_j}}(\mathbf{a}|e_i, h_j)||P^{\pi}_{mean,N_{update,e_i,h_j}-1}(\mathbf{a}|e_i, h_j)\right)$$

$$\equiv \sum_l^5 P^{\pi}_{mean,N_{update,e_i,h_j}}\left(a_l|e_i, h_j\right) log\frac{P^{\pi}_{mean,N_{update,e_i,h_j}}\left(a_l|e_i, h_j\right)}{P^{\pi}_{mean,N_{update,e_i,h_j}-1}\left(a_l|e_i, h_j\right)} \quad (5)$$

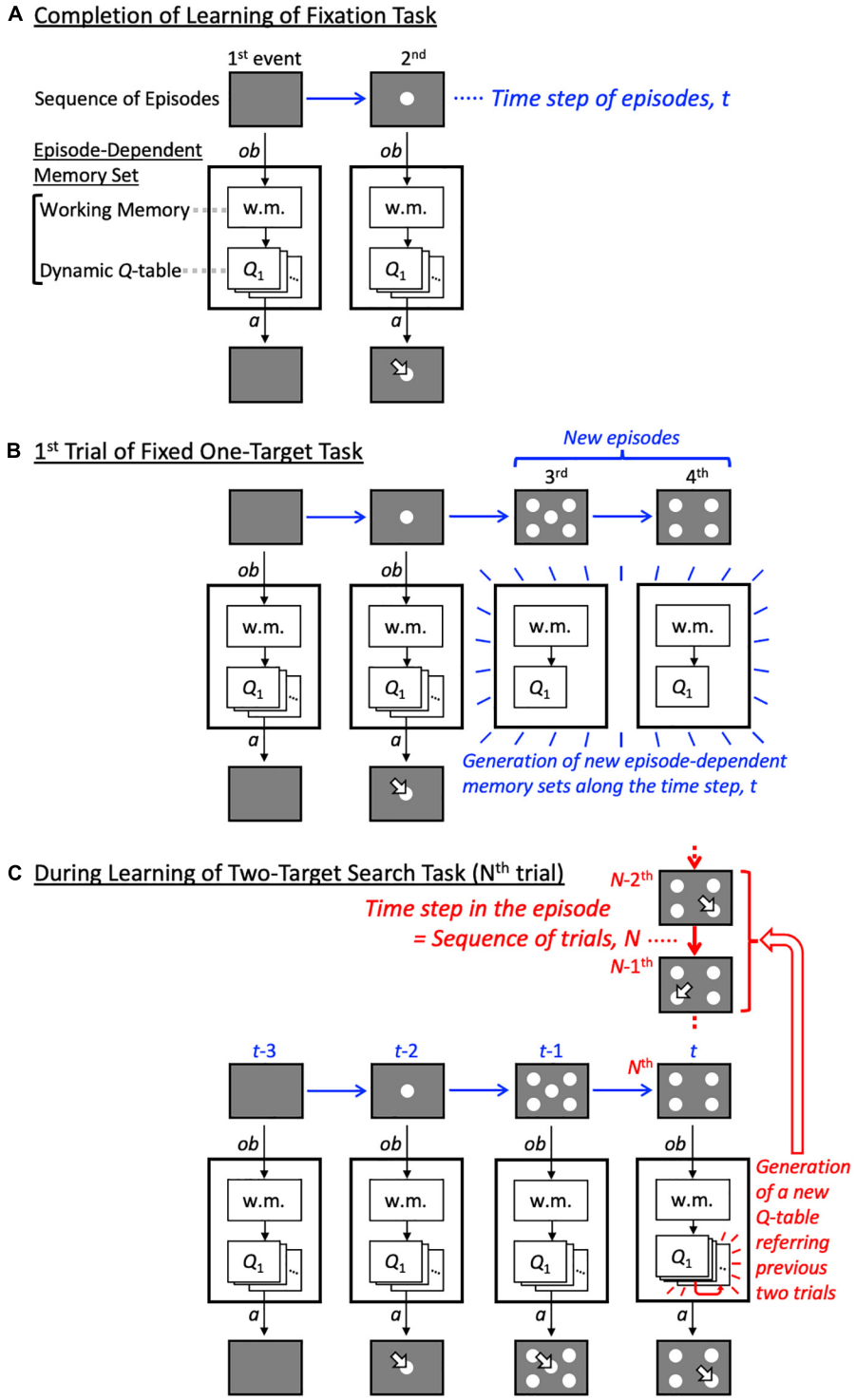

FIGURE 2 | Schematic diagram of model operations as training progresses. **(A)** Schematic diagram of the model after the most elementary task, the fixation task, has been completed. Some states and corresponding *Q*-tables are generated by reflecting on the previous action and its outcome in each episode. **(B)** Schematic diagram of the model in the first trial in which the fixed one-target task was performed after the fixation task. Since the fixed one-target task includes task events 3 and 4 that the fixation task did not include, episode-dependent memory sets corresponding to task events 3 and 4 are newly generated. **(C)** Schematic diagram of the model while it is learning the two-target search task. The figure illustrates that the number of states in task event 4 is still increasing, while those in task events 1 to 3 have already stopped increasing. w.m.: working memory; arrow: choice; ob: observation; a: action.

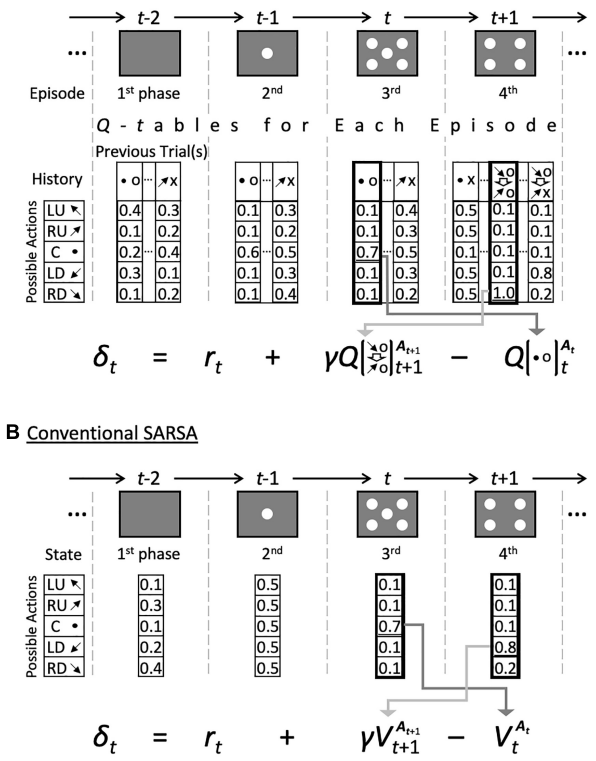

FIGURE 3 | Calculation of temporary difference learning by the proposed and control models. **(A)** A history-in-episode architecture using the dynamic state model (proposed method) as an example. The action value function is selected according to the history of each episode, and the reward prediction error is calculated. Fixed 5-, 10- and 10 by 10-state models also have a history-in-episode architecture, i.e., a *Q*-table generated for each episode. However, its size does not change dynamically. **(B)** The conventional SARSA model, which is the simplest control model. Since the previous actions are irrelevant in this model, the state value function *V* is used here. This model does not have a history-in-episode architecture, as only one state-value function can be assigned to each episode.

We referred to this as the Update_KLD. $N_{update,ei,hj} - 1$ indicates the number of trials since the model last encountered episode e_i and history h_j and calculated the mean $P^{\pi}(\boldsymbol{a}|\ e_i,\ h_j)$.

Next, the model judged whether the Update_KLD of the episode e_i and history h_j, fell below the criterion for experience saturation, ζ (step 2),

$$Update_KLD_{e_{i,h_j}} \leq \zeta \tag{6}$$

indicating that information can no longer be gained by updating. The value of ζ was determined to be 10^{-2} in the range that showed desirable results. When the Update_KLD$_{ei,hj}$ was < ζ, the distribution of $P^{\pi}_{mean,N_{update,e_i,h_j}}(\mathbf{a}|e_i, h_j)$ was compared with $P^{\pi}_{ideal}(\mathbf{a}|e_i, h_j)$. $P^{\pi}_{ideal}(\mathbf{a}|e_i, h_j)$ is the action selection probability that only one action will be selected and was obtained as follows. First, the ideal policy, $Q_{ideal}(\boldsymbol{a}|\ e_i, h_j)$, was obtained by setting the largest value within $Q(\boldsymbol{a}|\ e_i, h_j)$ to 1 and the other values to zero. For example, if the $Q(\boldsymbol{a}|\ e_i, h_j)$ were, {0.1, 0.4, 0.1, 0.2, 0.1}, the $Q_{ideal}(\boldsymbol{a}|\ e_i, h_j)$, would be set to {0, 1, 0, 0, 0}.

Thereafter, the $P^{\pi}_{ideal}(\mathbf{a}|e_i, h_j)$ was calculated from $Q_{ideal}(\boldsymbol{a}|\ e_i, h_j)$ using the softmax function in Eq. 3. For comparison, another KLD was calculated, as described below (step 3):

$$D_KLD_{e_i,h_j}\left(P^{\pi}_{mean,N_{update,e_i,h_j}}(\mathbf{a}|e_i, h_j)||P^{\pi}_{ideal}(\mathbf{a}|e_i, h_j)\right)$$

$$\equiv \sum_{l} P^{\pi}_{mean,N_{update,e_i,h_j}}(a_l|e_i, h_j) log \frac{P^{\pi}_{mean,N_{update,e_i,h_j}}(a_l|e_i, h_j)}{P^{\pi}_{ideal}(a_l|e_i, h_j)} \tag{7}$$

We called this the Decision-uniqueness KLD (D_KLD). When the D_KLD was below the criterion for a preference for deterministic action selection, η (step 4),

$$D_KLD_{e_{i,hj}} < \eta \tag{8}$$

the agent had uniquely selected an action for the episode e_i and history h_j, and the *Q*-table was not expanded any further. η was set to 2 within the range which produced fair performance revealed by the parameter search. These two criteria, ζ and η, guaranteed the appropriateness of state (history) expansion: the former is for the appropriate timing of expansion; the latter is for whether the *Q*-table should be expanded or not (Katakura et al., 2022). When the D_KLD did not meet the criterion, it was also compared to the parent D_KLD (step 5), defined as the D_KLD of the parent history from which the current history h_j had been expanded (e.g., **Supplementary Figure 1B**). In step 6, when the D_KLD is judged to be less than its corresponding parent D_KLD, as in Eq. 9,

$$D_KLD_{e_{i,h_j}} < Parent\ D_KLD_{e_{i,h_j}} + bias \tag{9}$$

the D_KLD value is saved as the parent D_KLD, and the history is expanded as depicted in the *Q*-table of **Supplementary Figure 1B** (step 7). That is, the new history (child history) is the combination of the parent history and the history of one more previous trial to which the parent history refers. In the schematic example in **Supplementary Figure 1B**, a new history is generated from one in which the agent looked at LD and was rewarded one trial ago; this is changed to one in which it looked at LD and was rewarded one trial ago after it looked at RD and was rewarded two trials ago. The initial *Q*-value for each action is set to 0.5. On the other hand, if Eq. 9 does not hold, the current history being processed (see flowchart in **Supplementary Figure 1A**) is pruned (step 6'). When the current history consists of only the previous one trial, it is not erased because there is no parent history with which it could be compared. The bias is set to be −1 in all calculation.

In the current study, we compared the proposed model, including the dynamic state space, to several models with fixed state-space using the two-target search task and related simpler tasks. However, these control models also generated a new episode-dependent memory set when they encountered a novel episode or task event. The models were classified depending on the type of fixed *Q*-table in the generated episode-dependent memory set. The fixed 10-state model had a *Q*-table of size 5

by 10 in each episode, meaning that it had five action choices in each of the 10 states (histories), which were the combinations of five actions and their outcomes in the previous trial. The fixed 10 by 10-state model had states consisting of the combinations of the actions and outcomes of the two previous trials, i.e., fixed 10 by 10 states (histories). The results for this model are not shown in the current study, but this model is the optimal model when created with prior knowledge of the task structure of the two-target search task. Our previous paper (Katakura et al., 2022) showed its performance as a fixed 8 by 8-model. The fixed 5-state model obviously had five states for each episode, corresponding to the actions in the previous trial. In other words, this model did not explicitly include the result of the previous trial in the state. This model is an instrumental learning model, the results for which are omitted from the current study. The conventional SARSA model had only one value function (V-table, since the state was independent of the agent's action) for each episode, and selected one action among the five choices based on the V-table. Therefore, this model did not include "history." That is, while the other models contained a history-in-episode architecture (**Figure 3A**), the conventional SARSA model did not have that architecture (**Figure 3B**). It should also be noted that the conventional SARSA model is a Pavlovian learning model in which each task event serves as a CS.

Behavioral Tasks and Simulation Framework

The target search task included the four task events "trial start," "fixation spot on," "peripheral spots on," and "go & gaze shift" (**Figure 1A**). During the "fixation spot on" period, the agent was required to fixate on the central spot (C). In the subsequent "peripheral spots on" period, the agent was required to keep fixating on C without being distracted by the four spots presented around it: left-up (LU), right-up (RU), left-down (LD), and right-down (RD). When C disappeared at the beginning of the "go & gaze shift" period, the agent shifted its focus to one of the four surrounding spots, and if it focused on the correct target spot, it was rewarded. Note that, in **Figure 1B** and **Supplementary Figure 2**, the correct target is shown in green to help readers identify the currently correct target. In actual calculations, the agent only observe correct or error after gaze shift and cannot directly observe the true target. If the agent chose the wrong target spot, the trial was repeated under the same condition, i.e., the correct target stayed the same. The duration of each task period in the experiments with primates was 500 ms (Kawaguchi et al., 2013, 2015). In our simulations, the time step for calculation was set to one task period for simplicity.

The one-target search task (**Supplementary Figure 2**) was easier than the two-target task, and was used as a pretraining task for monkeys. In this task, one out of four spots served as the correct target until the target was switched to another spot after seven successive successes without the provision of additional instructions. After the target switch, the subject was required to search for the new correct target.

In the two-target search task (**Figure 1B**), two neighboring spots, referred to as a valid pair, were used as correct targets alternately. A valid pair was switched after seven consecutive successes without additional instructions, followed by an exploration phase for the new valid pair. Details are described elsewhere (Kawaguchi et al., 2013, 2015).

We also tested fixed one- and two-target tasks, in which the correct target or valid pair was fixed throughout the simulations, respectively, to evaluate each learning model.

Animal Behavior

Our animal research was performed in accordance with National Institutes of Health guidelines and the guidelines of Tohoku University. All experimental protocols were approved by the Animal Care and Use Committee, Tohoku University (Permit No. ido-74). Two Japanese monkeys (*Macaca fuscata*; monkey K: 6.5 kg, monkey G: 6.1 kg) were trained to perform the two-target search task. The monkeys were kept in individual primate cages in an air-conditioned room with food available *ad libitum*. During the experiments, the monkeys sat in a primate chair with their heads restrained and faced a screen on which visual stimuli were presented. Eye position was monitored with an infrared corneal reflection system sampling at 250 Hz. Details are described elsewhere (Kawaguchi et al., 2013, 2015).

RESULTS

We tested the proposed dynamic state model using several behavioral tasks related to the two-target search task and compared it to other models with fixed sets of states or value functions. This comparison revealed fundamental differences between the compared models.

First, we tested all models using a fixed one-target search task with only one correct target spot during the entire simulation. All models exhibited almost perfect performance (**Figure 4A**; data not shown for the fixed 10 by 10- and 5-state models. The same applies to the following results). However, it is noteworthy that the simplest model, i.e., the conventional SARSA model, learned the fastest.

Figure 4B shows the results of the fixed two-target task. In this task, the correct valid target pair was not changed during the entire simulation, but two targets in the pair were the correct target alternately. This setup created additional difficulty since the correct strategy in the previous trial is not valid, and the models had to switch their behavior alternatively depending on the state, i.e., the history. Under these conditions, we expected the conventional SARSA model to exhibit poor performance because it was not able to make decisions based on the previous actions. As expected, all models except the conventional SARSA model showed almost perfect performance.

The one-target search task revealed additional differences between the tested models (**Figures 4C,D**). This task required the agent to adapt to a switched correct target after every seven consecutive successes. This requirement forced the conventional SARSA model, as well as the fixed 5-state model (data not shown), to re-learn the correct target after each switch. As a result, they exhibited much lower correct response rates (**Figure 4C**) and numbers of target switch (**Figure 4D**) than the dynamic state,

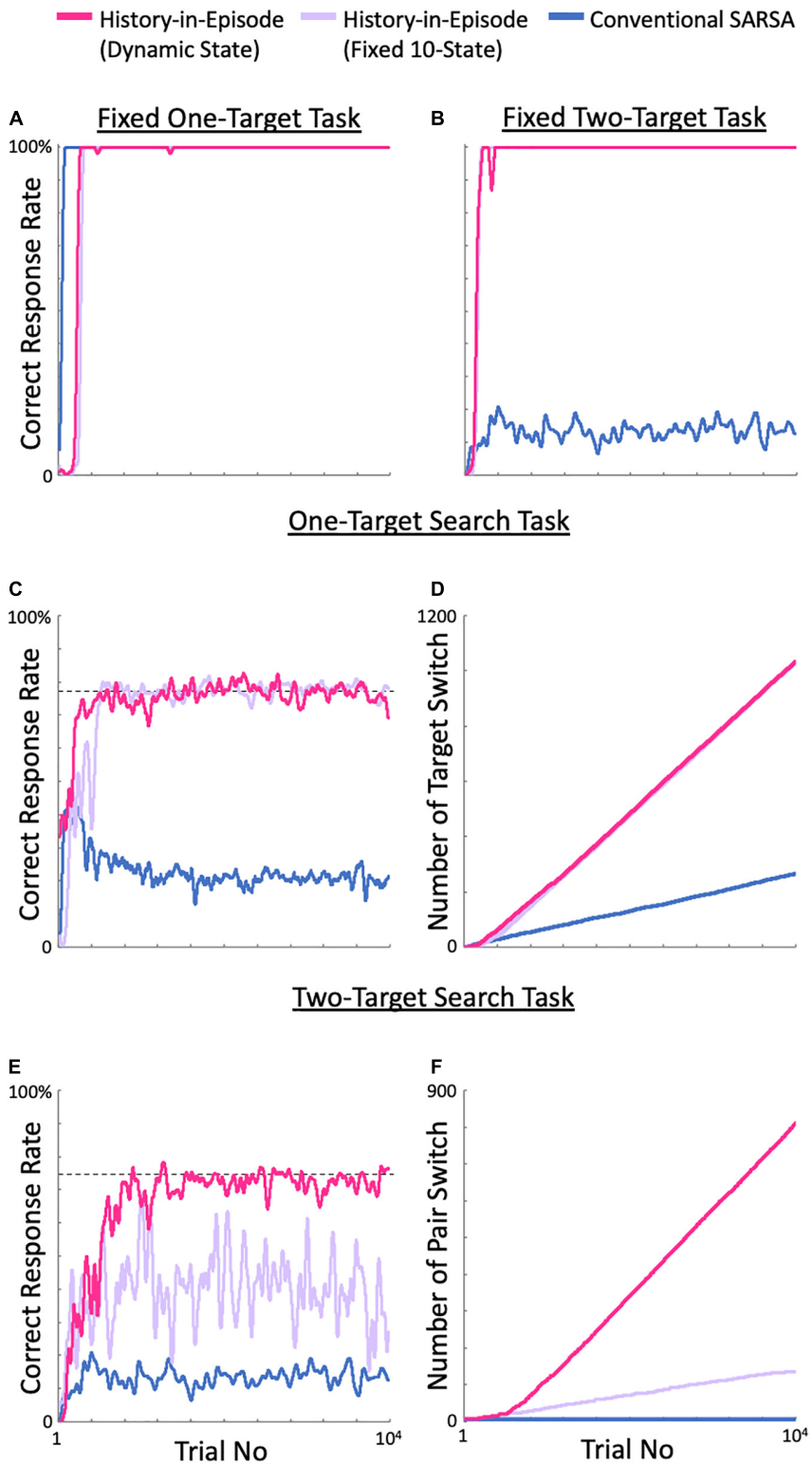

FIGURE 4 | Comparison of the performance on each task between the proposed and control models. **(A)** Evolution of the correct response rate in the fixed one-target task. **(B)** The fixed two-target task. **(C)** One-target search task. Dashed line: ideal performance. **(D)** Evolution of the number of target switches. **(E)** Two-target search task. Dashed line: ideal performance. **(F)** Number of valid-pair switches. All calculations started at the initial state.

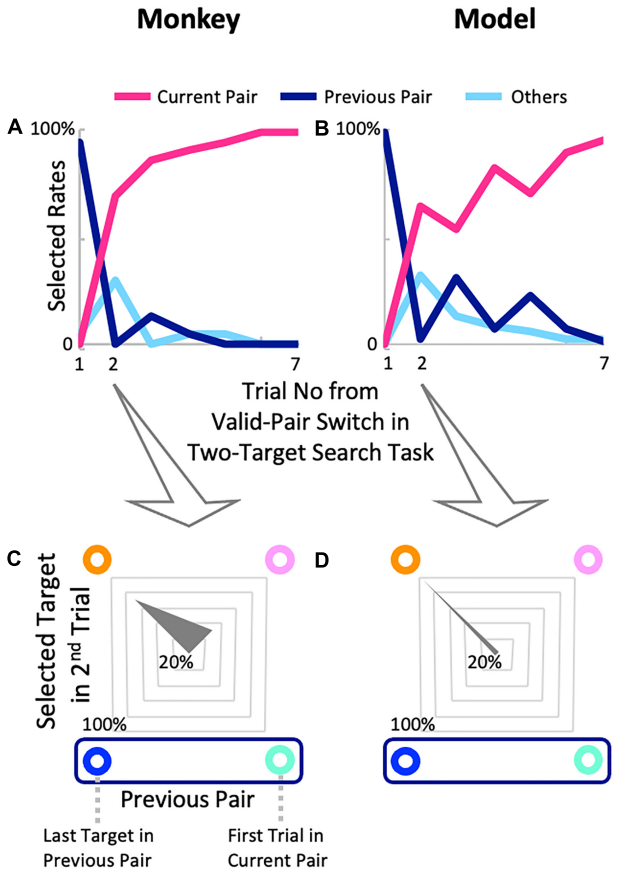

FIGURE 5 | Comparisons of model performance and the exploratory behavior of a monkey after valid-pair switches in the two-target search task. **(A)** Monkey G's exploratory behavior while recording the activity of a neuron (20509U1a2) after completing the training; there were 23 pair switches. **(B)** Exploration behavior of the model, with 774 pair switches. The gaze direction distributions of the monkey **(C)** and model **(D)** in the second trial, after switching the valid pairs.

fixed 10- and 10 by 10-state models. These superior models, in contrast, learned how to explore in the exploration phase after a target switch, because the state, i.e., history, explicitly included the previous outcome as well as the action, which led to almost ideal performance (dashed line in **Figure 4C**), although some delay in the increase in correct response rate was observed for the fixed 10-state model.

Finally, we tested all models on the two-target search task (**Figures 4E,F**). As expected, our dynamic state model reproduced the results of our previous paper (Katakura et al., 2022), and showing nearly ideal performance (dashed line in **Figure 4E**) and a high number of pair switches (**Figure 4F**); the same performance was obtained for the fixed 10 by 10-state model (data not shown), which was created as an ideal model with prior knowledge of the task structure. As for the fixed 10-state model, although it performed well for the one-target search task, its performance for the two-target search task was much worse than the ideal performance. This poor performance was expected because the model included only one previous trial in its history, while the ideal performance required inclusion of the two previous trials in its history. The fixed 5-state model showed similar performance to the fixed 10-state model. The conventional SARSA model exhibited a lower correct response rate than in the one-target search task and achieved no pair switch. Re-learning to focus on each of the spots of the valid pair never allowed the conventional SARSA model to achieve a pair switch.

The proposed model performed as well as a monkey in the two-target search task (**Figure 5**). The monkey quickly located new valid pairs after valid-pair switches (**Figure 5A**). Since valid pairs were switched without any explicit instruction, he inevitably gazed at the target of the previously valid pair in the first trial of the exploration phase (dark blue line in **Figure 5A**), whereas he was highly likely to gaze at the new pair target after the first trial (red line in **Figure 5A**). The rapid switching to the new pair displayed by the monkey was also seen in the proposed model (**Figure 5B**). Furthermore, to examine the exploratory behaviors of the monkey and model in detail, gaze directions in the second trials of the exploration phase were analyzed, and we found that both the monkey (**Figure 5C**) and model (**Figure 5D**) were highly likely to gaze at the target diagonal to the one in the first trial (orange circles in **Figures 5C,D**). These results indicate that the early detection of new pairs is achieved by sophisticated, non-random exploratory behavior.

Previously, we showed that good performance can be achieved over a wide range of meta-parameter, i.e., the learning rate, inverse temperature, threshold of experience saturation, and threshold of decision uniqueness, through parameter search (Katakura et al., 2022). Here, we examine model performance while varying the discount factor Eq. 2, which was not included in our previous one trial-one time-step model (**Figure 6**). When the high default value of 0.7 was reduced to 0.4, the model achieved a high correct response rate, although learning was relatively slow. However, when the default value was reduced further, the performance deteriorated rapidly (**Figure 6A**). This deterioration was not due only to the selection of the correct target in task event 4, but also to the inability to maintain fixation in the preceding task events. When the discount factor was reduced, the fixation error rate in each task event, i.e., the percentage of trials in the task event of interest that had fixation errors relative to the total number of trials on which task performance was maintained up to that task event, increased. In addition, the error rate in task event 3 was lower than that in task event 2, which is remote from task event 4 (in which the reward is actually delivered; **Figure 6B**). This implies that a high discount factor is required to learn a task involving a long sequence of events with a reward given only at the end of a trial.

Executing the two-target search task with a high correct response rate requires making decisions based on the actions of the previous two trials and their outcomes. However, this is only true for the action selection during task event 4. Other task events require the agent to only fixate to the central spot. The dynamic state model learns to execute the task while increasing the states consisting of actions and their outcomes. However, when learning to focus on only one spot regardless

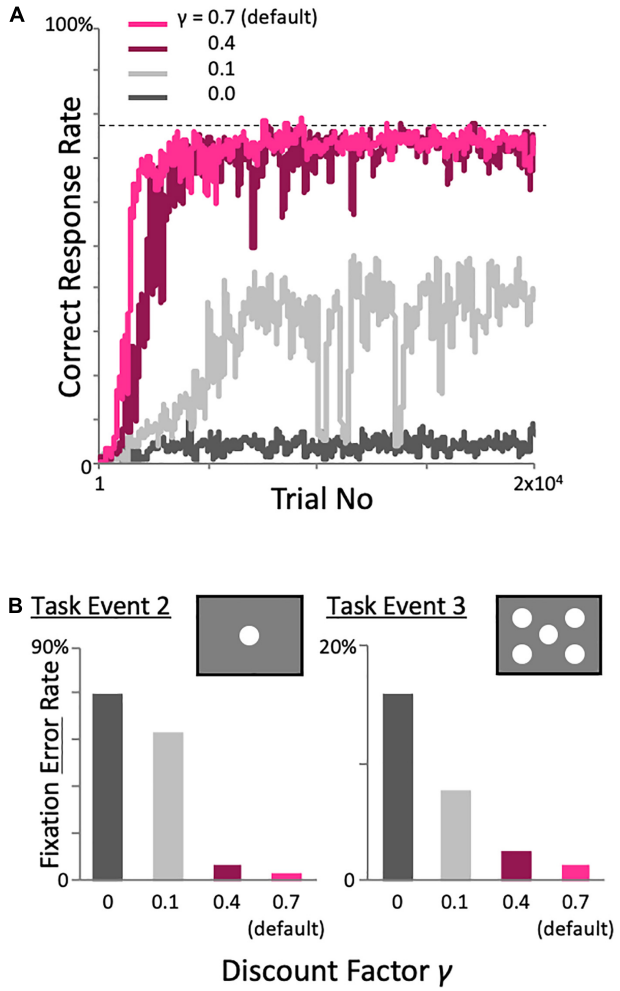

FIGURE 6 | Effects of varying the discount factor on performance in the two-target search task. **(A)** Changes in the percentage of correct trials with learning. The incorrect response rates during task events 2 **(B)** The incorrect response rates during task events 2 and 3 when varying the discount factor.

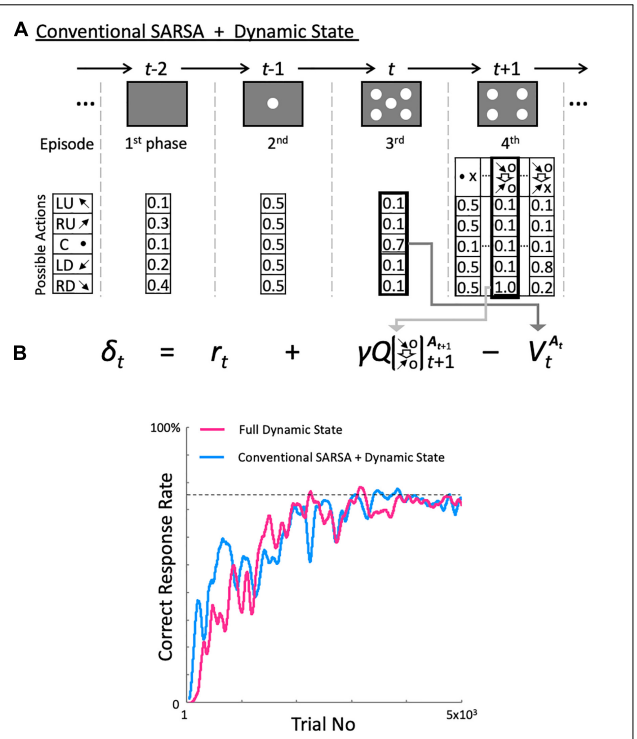

FIGURE 7 | Configuration and performance of the hybrid model. **(A)** Calculation of reward prediction error in the hybrid model. Dynamic state space is given only to task event 4. **(B)** Performance comparison between the hybrid and full dynamic state models (**Figure 3A**) in the two-target search task. All calculations started at the initial state.

of the previous actions, learning using a single state, i.e., Pavlovian learning, might not only be sufficient, but could even speed up learning.

To test this idea, we implemented a hybrid model in which we used a single *Q*-table for task events 1 to 3 and a dynamic *Q*-table for only task event 4 (**Figure 7A**). **Figure 7B** compares performances between the dynamic state and hybrid models on the two-target search task. Almost ideal correct response rates were obtained (dashed line in **Figure 7B**); however, the performance of the hybrid model increased earlier than that of the dynamic state model. These results support our idea that, by minimizing the number of states when learning how to fixate on the center spot, the hybrid model speeds up its learning during the first three task events.

To further confirm this, we developed a parallel model in which Pavlovian, fixed 5-state, and dynamic state models were calculated in parallel for each episode and an action was selected based on the *Q*-table exhibiting the highest decision uniqueness among the three models. After executing 10,000 trials, we examined the model used in each task event and found that the dynamic model was used in task event 4, while the Pavlovian model was used in the other three task events. This result indicated that the most appropriate learning model changes depending on the task requirements.

DISCUSSION

In this study, we proposed a history-in-episode architecture to extend a reinforcement learning model, enabling episode-dependent learning. In addition, we built a model that also included the dynamic state space proposed in our previous paper (Katakura et al., 2022), and tested its performance in a two-target search task. By having episode and history, the model was able to learn the appropriate action for each event in one trial based on the history of recent trials. The proposed model, which includes the dynamic state space and the history-in-episode architecture, is expected to be further developed and applied as a pioneering learning model with high adaptability to complex real environments, since it learns appropriate behaviors under various circumstances.

As shown in our previous paper (Katakura et al., 2022), the dynamic state model had a sufficient range of well-behaved

meta-parameters for its intrinsic parameters, such as experience saturation and decision uniqueness, as well as conventional parameters such as learning rate and inverse temperature of the softmax function for action selection. This robustness was also true for the model with the history-in-episode architecture presented in the current study. Unlike the one trial-one time-step model in our previous paper, the model including the history-in-episode architecture uses TD learning to learn the task events. In TD learning, the discount factor is used as a coefficient that is multiplied by the reward prediction at the next time step in calculating the reward prediction error in Eq. 2. The model exhibited desirable performance in a sufficiently wide range of discount factors as shown in **Figure 6**. When the discount rate was too low, TD learning was unsuccessful and the model did not learn to take any action, specifically not during the earlier task events. The desirability of a high discount rate is also consistent with Go and Shogi models (Silver et al., 2016, 2017), which learn behavior for long and complex orders of steps.

In recent years, machine learning and artificial intelligence (AI), as exemplified by learning models for Go and Shogi, have outperformed humans in some tasks (Silver et al., 2016, 2017). However, it is questionable whether these models can be implemented in field robots working in real environments. Although the models can outperform humans in a single task, they lack some basic structures that are crucial for flexible learning in a real environment with complex situations and multiple goals. As shown in **Figure 4**, when multiple targets must be achieved (fixed two-target task), or when targets are frequently switched (one-target search task), the conventional SARSA or Pavlovian model or exhibited poor performance. In contrast, the fixed 10-state model with history-in-episode architecture achieved high performance for these two tasks, although state space was fixed. Even the fixed 5-state, i.e., the conventional instrumental learning model, which did not explicitly include the outcome of the previous trial, showed high performance in the fixed two-target task by choosing an action depending on the action in the fourth task period of the previous trial. Therefore, the history-in-episode architecture proposed in the current study provided a framework for achieving multiple goals, which has recently been a research issue (Bai et al., 2019; Colas et al., 2019; Zhao et al., 2019; Pitis et al., 2020; Shantia et al., 2021).

However, that does not mean that Pavlovian learning is always inferior. Our proposed model dynamically generated states and corresponding *Q*-tables based on combinations of actions and their outcomes. However, in task events 1 to 3 of the two-target search task, it is sufficient to simply learn to fixate, and having multiple states in each task event seems redundant. The hybrid model, which learns in a Pavlovian fashion in all task periods except the fourth using only a single *V*-table, learned the task faster than the full dynamic model (**Figure 7B**). A similar observation is shown in **Figure 4A**: for the fixed one-target task, the conventional SARSA model with Pavlovian learning during all task periods learned the task faster than the other models. These computational examples show that when states are redundant, the frequency with which each state is encountered decreases, resulting in slower learning. These arguments are related to the debate about whether Pavlovian or instrumental learning is better (Rescorla and Solomon, 1967), and how they can be used differently (Cartoni et al., 2016). Dorfman and Gershman (2019) developed a model in which either Pavlovian or instrumental conditioning predominated, depending on the degree to which an action can control the reward. We also generated a parallel model that included Pavlovian, instrumental, and dynamic state models, computed them in parallel, and let it select an action via the model exhibiting the highest decision uniqueness. We found that in the two-target search task, the Pavlovian model was used in task events 1 to 3, which are independent of the previous action. These observations suggest that learning models that are as simple as possible, i.e., having only the necessary states, are preferable. Choosing a resource-saving learning method according to the task requirements can avoid the curse of dimensionality problem in reinforcement learning (Sutton and Barto, 1998) and increase the learning speed.

If an action and its outcome are not uniquely predicted, it is desirable to increase the number of states so that the action and outcome can be uniquely expected by incorporating new clues. When presented with an ambiguous CS, i.e., when a US follows a CS in an episode or experimental condition but not in another condition, rats can uniquely predict the US by considering the information available under each condition, i.e., some clues in the environment or the configuration between them (Fanselow, 1990). The first brain region that contributes to such episode-dependent learning is the hippocampus. For example, hippocampal lesions in rodents produce deficits in freezing behavior during exposure to a shock-paired condition (Selden et al., 1991; Kim and Fanselow, 1992; Phillips and LeDoux, 1992). The structure and function of the hippocampus should be taken into account when developing our proposed model into one more in line with the structure of the real brain.

Some readers may find similarities between assigning a different *Q*-table to each episode in our model and learning sub-tasks in hierarchical reinforcement learning (HRL) models (Barto and Mahadevan, 2003; Hengst, 2010; Al-Emran, 2015; Pateria et al., 2021). However, since the two-target search task has temporally discrete task events, we need only generate a new episode-dependent memory set when a new task event is presented, and avoid the difficult problem of generating sub-tasks by deciding how to divide a continuous scene, which is one of the main issues for HRL. Moreover, our model is not hierarchical in the same sense of HRL. That is, our model does not include a supervisor that overlooks the units learning the sub-tasks, and gives them sub-goals. For these reasons, our model is not meant to be considered alongside or compared with HRL models. Rather, the proposed model includes two types of time steps i.e., the time step across different task events and the dynamic history in the episode of interest, and has a structure that generates memory sets or *Q*-tables as required in each time direction, especially in the case of history, where the state is generated dynamically to refer to multiple steps in the past. We consider these to be two novel points of the proposed model, and to be indispensable for learning the two-target search task. In our previous physiological studies, we observed neuronal activities in the lateral prefrontal cortex of monkeys that reflected sub-task generation

(Saito et al., 2005; Mushiake et al., 2006; Sakamoto et al., 2008, 2013, 2020a). In the future, HRL will have to be considered when modeling those neural activities.

Other route to improvement of our proposed model is the involvement of finer time and space increments. To train a monkey to perform the two-target search task, it is necessary to start with the fixation task, in which the monkey is required to fixate on a single point in a continuous wide field of view and then complete simple tasks, such as the one-target search task used in the current study. In addition, it is necessary to gradually increase the length of each task period and gradually decrease the number of trials required to switch between targets or valid pairs in the pretraining trials. In contrast, in our computer simulations, the dynamic state model was able to learn the two-target search task without any pretraining. This is because we made the conditions of the simulations as simple as possible: one task period corresponded to one time step in the calculation and there were only five discrete choices of actions. In future, when the model becomes applicable to finer increments of time and space, the training of the model will require steps compatible to the training of monkeys.

However, it remains difficult to determine appropriate training steps. We have trained monkeys to perform many advanced behavioral tasks (Mushiake et al., 2001; Sakamoto et al., 2008, 2013, 2015, 2020a,b) and obtained empirical knowledge regarding appropriate training steps. This knowledge is crucial for effective training. A major focus for future work will be to determine appropriate training steps for the model. We will aim to develop a "coach" that outputs task parameters, such as the length of the task period or complexity of the task, depending on the task conditions and learner's behavior, etc. The coach, which also needs to be equipped with a model involving a dynamic state space and a history-in-episode architecture, and the learner then start co-learning. In developing such a coach, the main challenge will be formulating the task complexity and generating a new training step depending on the progress of the learner. However, if we can generate such a coach model, it will likely be the prototype of a new type of AI that co-develops with humans and draws out our potential abilities rather than "confronting" us. Such a system could be referred to as hyper-adaptable, and we hope to use such systems to create a new discipline called neuro-coaching (Sakamoto, 2019).

DATA AVAILABILITY STATEMENT

The raw data supporting the conclusions of this article will be made available by the authors, without undue reservation.

ETHICS STATEMENT

The animal study was reviewed and approved by the Animal Care and Use Committee, Tohoku University (Permit No. ido-74).

AUTHOR CONTRIBUTIONS

KS designed the research, analyzed the data, wrote the first draft of the manuscript, edited the manuscript, and wrote the manuscript. KS and HY performed the research. NS and HM designed the two-target search task. YF obtained the behavioral data. KS and NK analyzed the behavioral data. All authors contributed to the article and approved the submitted version.

FUNDING

This work was supported by the JSPS KAKENHI Grant Numbers 17K07060 and 20K07726 (Kiban C), MEXT KAKENHI Grant Number 15H05879 (Non-linear Neuro-oscillology), 26120703 (Prediction and Decision Making), and 20H05478 and 22H04780 (Hyper–Adaptability).

ACKNOWLEDGMENTS

We thank Y. Matsuzaka and Y. Nishimura of Tohoku Medical and Pharmaceutical University for advice and suggestions.

SUPPLEMENTARY MATERIAL

The Supplementary Material for this article can be found online at: https://www.frontiersin.org/articles/10.3389/fncom.2022.784604/full#supplementary-material

Supplementary Figure 1 | Expansion and contraction of the history. **(A)** Flowchart of the expansion and contraction process. **(B)** An example of expansion of a history derived from the parent history in *Q*-table. The direction of the arrow represents the target that the agent looked at, and o and x represent the correct answer and error, respectively. The example in the figure shows that a new history is generated from the history that the agent looked at LD and was rewarded one trial ago, to the history that it looked at LD and was rewarded one trial ago after it looked at RD and was rewarded two trials ago. The numbers in the *Q*-table represent *Q*-values. The initial *Q*-value for each action is set to 0.5.

Supplementary Figure 2 | A schematic example of a target switch in the one-target search task. The format is the same as the task shown in **Figure 1B**.

REFERENCES

Al-Emran, M. (2015). Hierarchical reinforcement learning: a survey. *Int. J. Comput. Dig. Syst.* 4:2. doi: 10.12785/IJCDS/040207

Bai, B., Liu, P., Zhao, W., and Tang, X. (2019). Guided goal generation for hindsight multi-goal reinforcement learning. *Neurocomput* 359, 353–367. doi: 10.1016/j.neucom.2019.06.022

Barto, A. G., and Mahadevan, S. (2003). Recent advances in hierarchical reinforcement learning. *Discr. Event Dyn. Syst.* 13, 41–77. doi: 10.1023/A:1025696116075

Beal, M. J., Ghahramani, Z., and Rasmussen, C. (2002). The infinite hidden Markov model. *Adv. Neural Inform. Proc. Sys.* 14, 577–584.

Cartoni, E., Balleine, B., and Baldassarre, G. (2016). Appetitive Pavlovian-instrumental transfer: A review. *Neurosci. Biobehav. Rev.* 71, 829–848. doi: 10.1016/j.neubiorev.2016.09.020

Colas, C., Fournier, P., Chetouani, M., Sigaud, O., and Oudeyer, P.-Y. (2019). "CURIOUS: Intrinsically motivated modular multi-goal reinforcement learning". *Proceedings of the 36th International Conference on Machine Learning*, Long Beach: ICML. 97, 1331–1340.

Dorfman, H. M., and Gershman, S. J. (2019). Controllability governs the balance between Pavlovian and instrumental action selection. *Nat. Commun.* 10:5826. doi: 10.1038/s41467-019-13737-7

Doshi-Velez, F., Pfau, D., Wood, F., and Roy, N. (2015). Bayesian nonparametric methods for partially-observable reinforcement learning. *IEEE Trans. Patt. Anal. Mach. Intell.* 37, 394–407. doi: 10.1109/TPAMI.2013.191

Fanselow, M. S. (1990). Factors governing one trial contextual conditioning. *Anim. Learn. Behav.* 18, 264–270. doi: 10.3758/BF03205285

Hengst, B. (2010). *Hierarchical reinforcement learning. In Encyclopedia of Machine Learning*. Boston, MA: Springer, 495–502. doi: 10.1007/978-0-387-30164-8_363

Jaakkola, T., Singh, S. P., and Jordan, M. I. (1995). Reinforcement learning algorithm for partially observable Markov decision problems. *Adv. Neural Inf. Proc. Syst.* 7, 345–352.

Katakura, T., Yoshida, M., Hisano, H., Mushiake, H., and Sakamoto, K. (2022). Reinforcement learning model with dynamic state space tested on target search tasks for monkeys: Self-determination of previous states based on experience saturation and decision uniqueness. *Front. Comput. Neurosci.* 15:784592. doi: 10.3389/fncom.2021.784592

Kawaguchi, N., Sakamoto, K., Furusawa, Y., Saito, N., Tanji, J., and Mushiake, H. (2013). Dynamic information processing in the frontal association areas of monkeys during hypothesis testing behavior. *Adv. Cogn. Neurodynam.* 4, 691–698. doi: 10.1007/978-94-007-4792-0_92

Kawaguchi, N., Sakamoto, K., Saito, N., Furusawa, Y., Tanji, J., Aoki, M., et al. (2015). Surprise signals in the supplementary eye field: rectified prediction errors drive exploration–exploitation transitions. *J. Neurophysiol.* 113, 1001–1014. doi: 10.1152/jn.00128.2014

Kim, J., and Fanselow, M. (1992). Modality-specific retrograde amnesia of fear. *Science* 256, 675–677. doi: 10.1126/science.1585183

Maren, S., Phan, K. L., and Liberzon, L. (2013). The contextual brain: implication for fear conditioning, extinction and psychopathology. *Nat. Rev. Neurosci.* 14, 417–428. doi: 10.1038/nrn3492

Mochihashi, D., and Sumita, E. (2007). The infinite Markov model. *Adv. Neural Inform. Proc. Syst.* 20, 1017–1024.

Mochihashi, D., Tamada, T., and Ueda, N. (2009). "Bayesian unsupervised word segmentation with nested Pitman-Yor language modeling," in *Proc. 47th Annual Meeting ACL 4th IJCNLP AFNLP*, Singapore. 100–108.

Mushiake, H., Saito, N., Sakamoto, K., Itoyama, Y., and Tanji, J. (2006). Activity in the lateral prefrontal cortex reflects multiple steps of future events in action plans. *Neuron* 50, 631–641. doi: 10.1016/j.neuron.2006.03.045

Mushiake, H., Saito, N., Sakamoto, K., Sato, Y., and Tanji, J. (2001). Visually based path planning by Japanese monkeys. *Cogn. Brain Res.* 11, 165–169. doi: 10.1016/S0926-6410(00)00067-7

Pateria, S., Subagdja, B., Tan, A.-H., and Quek, C. (2021). Hierarchical reinforcement learning: a comprehensive survey. *ACM Comput. Surv.* 54:109. doi: 10.1145/3453160

Pfau, D., Bartlett, N., and Wood, F. (2010). Probabilistic deterministic infinite automata. *Adv. Neural Inform. Proc. Syst.* 23, 1930–1938. doi: 10.1109/tpami.1982.4767292

Phillips, R., and LeDoux, J. (1992). Differential contribution of amygdala and hippocampus to cued and contextual fear conditioning. *Behav. Neurosci.* 106, 274–285. doi: 10.1037/0735-7044.106.2.274

Pitis, S., Chan, H., Zhao, S., Stadie, B., and Ba, J. (2020). "Maximum entropy gain exploration for long horizon multi-goal reinforcement learning". *Proceedings of the 37th International Conference on Machine Learning*, Paris: PMLR. 119, 7750–7761.

Rescorla, R. A., and Solomon, R. L. (1967). Two-process learning theory: relationships between Pavlovian conditioning and instrumental learning. *Psychol. Rev.* 74, 151–182. doi: 10.1037/h0024475

Saito, N., Mushiake, H., Sakamoto, K., Itoyama, Y., and Tanji, J. (2005). Representation of immediate and final behavioral goals in the monkey prefrontal cortex during an instructed delay period. *Cereb. Cor.* 15, 1535–1546. doi: 10.1093/cercor/bhi032

Sakamoto, K. (2019). *Brain science of creativity: beyond the complex systems theory of biological systems*. Tokyo: Univ Tokyo Press.

Sakamoto, K., Katori, Y., Saito, N., Yoshida, S., Aihara, K., and Mushiake, H. (2013). Increased firing irregularity as an emergent property of neural-state transition in monkey prefrontal cortex. *PLoS One* 8:e80906. doi: 10.1371/journal.pone.0080906

Sakamoto, K., Kawaguchi, N., and Mushiake, H. (2020b). Differences in task-phase-dependent time-frequency patterns of local field potentials in the dorsal and ventral regions of the monkey lateral prefrontal cortex. *Neurosci. Res.* 156, 41–49. doi: 10.1016/j.neures.2019.12.016

Sakamoto, K., Kawaguchi, N., Yagi, K., and Mushiake, H. (2015). Spatiotemporal patterns of current source density in the prefrontal cortex of a behaving monkey. *Neural Netw.* 62, 67–72. doi: 10.1016/j.neunet.2014.06.009

Sakamoto, K., Mushiake, H., Saito, N., Aihara, K., Yano, M., and Tanji, J. (2008). Discharge synchrony during the transition of behavioral goal representations encoded by discharge rates of prefrontal neurons. *Cereb. Cor.* 18, 2036–2045. doi: 10.1093/cercor/bhm234

Sakamoto, K., Saito, N., Yoshida, S., and Mushiake, H. (2020a). Dynamic axis-tuned cells in the monkey lateral prefrontal cortex during a path-planning task. *J. Neurosci.* 40, 203–219. doi: 10.1523/JNEUROSCI.2526-18.2019

Selden, N., Everitt, B., Jarrard, L., and Robbins, T. (1991). Complementary roles for the amygdala and hippocampus in aversive conditioning to explicit and contextual cues. *Neurosci* 42, 335–350. doi: 10.1016/0306-4522(91)90379-3

Shantia, A., Timmers, R., Chong, Y., Kuiper, C., Bidoia, F., Schomaker, L., et al. (2021). Two-stage visual navigation by deep neural networks and multi-goal reinforcement learning. *Robot. Autonom. Syst.* 138:103731. doi: 10.1016/j.robot.2021.103731

Silver, D., Huang, A., Maddison, C. J., Guez, A., Sifre, L., van den Driessche, G., et al. (2016). Mastering the game of Go with deep neural networks and tree search. *Nature* 529, 484–489. doi: 10.1038/nature16961

Silver, D., Schrittwieser, J., Simonyan, K., Antonoglou, I., Huang, A., Guez, A., et al. (2017). Mastering the game of Go without human knowledge. *Nature* 550, 354–359. doi: 10.1038/nature24270

Sutton, R. S., and Barto, A. G. (1998). *Reinforcement learning: An introduction*. Cambridge, MA: MIT Press.

Teh, Y. W., Jordan, M. I., Beal, M. J., and Blei, D. M. (2006). Hierarchical Dirichlet processes. *J. Amer. Statist. Assoc.* 101, 1566–1581. doi: 10.1198/016214506000000302

Thrun, S., Burgard, W., and Fox, D. (2005). *Probabilistic Robotics*. Cambridge, MA: MIT Press.

Yonelinas, A. P., Ranganath, C., Ekstrom, A. D., and Wiltgen, B. J. (2019). A contextual binding theory of episodic memory: systems consolidation reconsidered. *Nat. Rev. Neurosci.* 20, 364–375. doi: 10.1038/s41583-019-0150-4

Zhao, R., Sun, X., and Tresp, V. (2019). "Maximum entropy-regularized multi-goal reinforcement learning". *Proceedings of the 36th International Conference on Machine Learning*. Long Beach. 97, 7553–7562.

Conflict of Interest: The authors declare that the research was conducted in the absence of any commercial or financial relationships that could be construed as a potential conflict of interest.

Publisher's Note: All claims expressed in this article are solely those of the authors and do not necessarily represent those of their affiliated organizations, or those of the publisher, the editors and the reviewers. Any product that may be evaluated in this article, or claim that may be made by its manufacturer, is not guaranteed or endorsed by the publisher.

Copyright © 2022 Sakamoto, Yamada, Kawaguchi, Furusawa, Saito and Mushiake. This is an open-access article distributed under the terms of the Creative Commons Attribution License (CC BY). The use, distribution or reproduction in other forums is permitted, provided the original author(s) and the copyright owner(s) are credited and that the original publication in this journal is cited, in accordance with accepted academic practice. No use, distribution or reproduction is permitted which does not comply with these terms.

frontiers | Frontiers in Human Neuroscience

TYPE Original Research
PUBLISHED 20 January 2023
DOI 10.3389/fnhum.2022.805867

Check for updates

OPEN ACCESS

EDITED BY
Tomohiko Takei,
Tamagawa University, Japan

REVIEWED BY
Shota Hagio,
Kyoto University, Japan
Simon Giszter,
Drexel University, United States

*CORRESPONDENCE
Yasuharu Koike
✉ koike@pi.titech.ac.jp

SPECIALTY SECTION
This article was submitted to Motor Neuroscience, a section of the journal Frontiers in Human Neuroscience

RECEIVED 31 October 2021
ACCEPTED 30 December 2022
PUBLISHED 20 January 2023

CITATION
Barradas VR, Cho W and Koike Y (2023) EMG space similarity feedback promotes learning of expert-like muscle activation patterns in a complex motor skill.
Front. Hum. Neurosci. 16:805867.
doi: 10.3389/fnhum.2022.805867

COPYRIGHT
© 2023 Barradas, Cho and Koike. This is an open-access article distributed under the terms of the Creative Commons Attribution License (CC BY). The use, distribution or reproduction in other forums is permitted, provided the original author(s) and the copyright owner(s) are credited and that the original publication in this journal is cited, in accordance with accepted academic practice. No use, distribution or reproduction is permitted which does not comply with these terms.

EMG space similarity feedback promotes learning of expert-like muscle activation patterns in a complex motor skill

Victor R. Barradas[1], Woorim Cho[2] and Yasuharu Koike[1]*

[1]Institute of Innovative Research, Tokyo Institute of Technology, Yokohama, Japan, [2]School of Engineering, Tokyo Institute of Technology, Yokohama, Japan

Augmented feedback provided by a coach or augmented reality system can facilitate the acquisition of a motor skill. Verbal instructions and visual aids can be effective in providing feedback about the kinematics of the desired movements. However, many skills require mastering not only kinematic, but also complex kinetic patterns, for which feedback is harder to convey. Here, we propose the electromyography (EMG) space similarity feedback, which may indirectly convey kinematic and kinetic feedback by comparing the muscle activations of the learner and an expert in the task. The EMG space similarity feedback is a score that reflects how well a set of muscle synergies extracted from the expert can reconstruct the learner's EMG when performing the task. We tested the EMG space similarity feedback in a virtual bimanual polishing task that uses a robotic system to simulate the dynamics of a real polishing operation. We measured the expert's and learner's EMG from eight muscles in each arm during the real and virtual polishing tasks, respectively. The goal of the virtual task was to smoothen the surface of a virtual object. Therefore, we defined performance in the task as the smoothness of the object at the end of a trial. We separated learners into real feedback and null feedback groups to assess the effects of the EMG space similarity feedback. The real and null feedback groups received veridic and no EMG space similarity feedback, respectively. Subjects participated in five training sessions on different days, and we evaluated their performance on each day. Subjects in both groups were able to increase smoothness throughout the training sessions, with no significant differences between groups. However, subjects in the real feedback group were able to improve in the EMG space similarity score to a significantly greater extent than the null feedback group. Additionally, subjects in the real feedback group produced muscle activations that became increasingly consistent with an important muscle synergy found in the expert. Our results indicate that the EMG space similarity feedback promotes acquiring expert-like muscle activation patterns, suggesting that it may assist in the acquisition of complex motor skills.

KEYWORDS

motor learning, biofeedback, muscle synergies, complex motor skills, virtual reality

1. Introduction

Most complex motor skills involve interacting with objects in the environment. These motor skills require generating not only precise movements, but also precise forces. In fact, inappropriate forces may lead to failure in the task. For instance, an experienced nylon-string guitar player may face difficulties playing a familiar piece on a steel-string guitar due to the higher stiffness of steel strings. In this case, even though the required hand movements are kinematically equivalent, the kinetic (force) requirements differ considerably.

Therefore, to master such complex motor skills, the kinematic and kinetic components of the task must be learned concurrently. Appropriate sensory feedback about the execution of the task is essential for effective training (Kernodle and Carlton, 1992; Young and Schmidt, 1992; Zubiaur et al., 1999; Hinder et al., 2008). In particular, augmented feedback from a coach (Reid and Giblin, 2015) or an augmented reality system (Emken and Reinkensmeyer, 2004, 2005; Sigrist et al., 2013) may assist the learner in evaluating performance aspects that are not easy to self-evaluate (Lauber and Keller, 2014). Providing augmented kinematic feedback about task execution is relatively simple. A common coaching technique is to guide and/or evaluate motion trajectories that the learner generates. These evaluations may be verbal or visual, relying on in-person demonstrations, or on video recordings of an expert performer or of the learners themselves (Al-abood et al., 2001). In contrast, providing augmented kinetic feedback is in general a more complex problem, requiring especially instrumented equipment to measure forces or torques (Broker et al., 1993; Smith and Loschner, 2002). Without such equipment, augmented kinetic feedback is limited to verbal instructions about the desired forces in the task. However, verbal instructions may not be as effective in promoting learning of kinetic tasks as feedback derived from instrumented equipment (Dowling et al., 2010).

Here, we explore a new kind of augmented feedback based on electromyography (EMG) measurements. EMG from muscles involved in a task can be used to estimate the stiffness of their corresponding limb (Osu et al., 2002; Shin et al., 2009). According to the theory of impedance control, the CNS can concurrently satisfy kinematic and kinetic task goals by adjusting muscle activations to modulate the stiffness of the end-point of the limb (Hogan, 1985b). This allows the CNS to control the compliance of the limb to external forces and achieve successful interactions with the environment (Hogan, 1985a; Burdet et al., 2001). Muscles are also responsible for generating movement, and consequently EMG signals contain information about both the kinetics and the kinematics of movements in a task.

Therefore, we hypothesize that augmented feedback that quantifies the similarity of the muscle activations of a learner and the muscle activations of an expert in a task can enhance skill learning by promoting the acquisition of expert-like muscle activation patterns. This in turn may promote learning of the kinetic components of the task. We used muscle synergy analysis (D'Avella et al., 2003) to identify the muscle activation patterns of the expert, and used these patterns to reconstruct the learner's muscle activations. We defined the resulting reconstruction quality as the EMG space similarity, which we provided to the learner as a score during training in the task. Higher scores indicate that the muscle activations of the learner and the expert reside in spaces that overlap, which may be associated with the acquisition of expert-like muscle activation patterns.

We tested our hypothesis in the context of a simulated polishing operation. Expertise in polishing operations entails maintaining the attack angle between the grinder and the polished object as constant as possible (Tsujiai et al., 2015). This requires the generation of precise force patterns that counteract the interaction forces that arise when pressing the polished object against the grinder (Kodama et al., 2015). To test our hypothesis, we designed a virtual polishing task that simulates the dynamic environment of a polishing operation and provides the EMG space similarity score to learners in real time. The EMG space similarity score was computed based on the muscle activation patterns of a polishing expert.

2. Materials and methods

2.1. Subjects

Twenty-one subjects [20 learners: mean age, 28.2 yr (SD 8.9), 19 males, 19 right-handed (self-reported); 1 expert: 59 yr, male, right-handed] participated in the study after providing written informed consent. All procedures were approved by the Ethical Review Board of the Tokyo Institute of Technology.

2.2. Experimental setup

We designed a bimanual virtual task that simulates a polishing operation with a bench grinder. Participants sat facing a pair of planar robotic manipulanda (KINARM End-point Lab; BKIN Technologies) and held onto the handle of each manipulandum (**Figure 1A**). A virtual environment was displayed on a mirror placed on a horizontal plane above the participant's arms, occluding vision of the arms and the manipulanda. The mirror reflected images displayed on a screen placed above it. The virtual environment consisted of a polished object (object with irregular shape), a grinder (rectangular object), and score displays (EMG and smoothness scores or smoothness score only). Participants were able to control the position of the polished object by moving the manipulanda. Arm end-point movements were constrained to a horizontal plane at approximately the height of the xiphoid process of the sternum.

We recorded surface EMG activity from eight muscles in each arm: deltoid posterior (DeltP), pectoralis major (PectMaj), triceps brachii long head (TriLong), biceps brachii long head (BicLong), brachioradialis (BrRad), palmaris longus (PalmLong), extensor digitorum (ExtDig) and extensor carpi radialis (ExtCR). Active bipolar electrodes (Trigno, analog output mode; Delsys) were used to record EMG activity. EMG signals were bandpass filtered (20–450 Hz) *via* hardware, and digitized at 2 kHz using an analog-to-digital converter coupled to the KINARM's real time computer. Further EMG processing included rectification, low-pass filtering (second order Butterworth filter, 5 Hz) and normalization. EMG signals were normalized to the maximum EMG activity of each muscle during a maximum voluntary contraction (MVC) task, as described in the section "2.7. Experimental protocol."

2.3. Virtual environment

Participants experienced a dynamic virtual environment that simulated a polishing task (**Figure 1A**). The polished

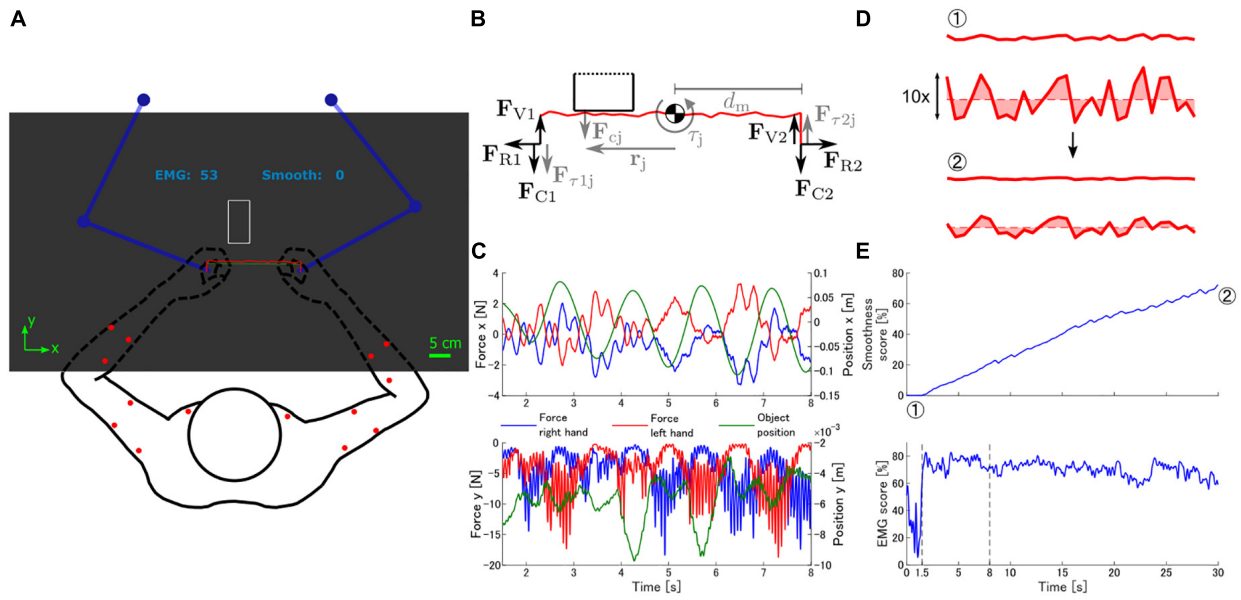

FIGURE 1
Virtual task environment. **(A)** Experimental setup. Participants held a pair of manipulanda (blue), and moved them to control the position of the polished object (red line). The main goal of the task was to smoothen the polished object by moving it against the grinder (white rectangle). Contact between both objects caused the manipulanda to generate forces simulating the contact interaction, which also changed the shape of the polished object. The EMG and smoothness scores were displayed above the task workspace. Red dots on the arms indicate the location of the EMG electrodes. **(B)** Simulation of polishing task dynamics. The robotic manipulanda applied forces on the participants' arms according to three components: forces to keep the distance between hands constant simulating a rigid object (F_{Ri}), contact between the polished object and the grinder (F_{Ci}), and vibration forces (F_{Vi}). Contact forces F_{cj} originated from the overlap of the vertices of the polished object and the grinder and were applied to both arms. Contact forces also generated torque (τ_j) around the centroid of the polished object according to the distance between the contact point and the centroid (r_j). The torque τ_j was simulated by a pair of forces applied to both arms ($F_{\tau ij}$). Black arrows represent the main force components (F_R, F_C, F_V). Gray arrows represent sub-components of the main forces. **(C)** Forces generated by the robotic manipulanda and position of the virtual object during a sample portion of a trial in the virtual polishing task. Notice that the magnitude of the vertical forces applied on each hand is coupled to the movement of the object along the horizontal axis. The position of the object is measured with respect to the center of the front edge of the grinder. **(D)** Deformation of the polished object by contact forces with the grinder. The polished object is shown with and without scaling in the vertical direction. The smoothness of the object was quantified as the area between the outline of the object and a horizontal line at the mean vertical position of all contact points. **(E)** Smoothness and EMG similarity scores throughout a trial. The objects in panel **(D)** correspond to the points indicated by circled numbers. Vertical dashed lines indicate the portion of the trial displayed in panel **(C)**.

object was represented as a jagged red line formed by connecting a set of randomly generated contact points. Thirty contact points were placed at uniform intervals along a 22 cm long straight line with a random perpendicular distance to the straight line taken from a uniform distribution (range: [−2.5, 2.5] mm). The grinder was represented as a 5 × 10 cm rectangular white outline fixed at the center of the display.

The robotic manipulanda generated forces onto the participant's hands to simulate the interaction between objects in the polishing task (Figure 1B). The generated forces were the sum of three components:

$$\mathbf{F}_{Ti} = \mathbf{F}_{Ri} + \mathbf{F}_{Ci} + \mathbf{F}_{Vi} \quad (1)$$

where $\mathbf{F}_T$ is the total force produced by the manipulandum, $\mathbf{F}_R$ is a force that simulates the rigidity of the polished object, $\mathbf{F}_C$ is a force arising from the contact forces between the polished object and the grinder, and $\mathbf{F}_V$ is a vibration force. The subindex i = 1, 2 indicates forces corresponding to the left and right manipulanda, respectively.

In order to approximate the sensation of holding a rigid body between both hands, the rigidity of the polished object was simulated as a pair of rigid spring-dampers. For each side, the spring-damper was attached between the end-point of the manipulandum and the end-point of the polished object:

$$\mathbf{F}_{Ri} = \mathbf{F}_{si} + \mathbf{F}_{di} \quad (2)$$

$$\mathbf{F}_{si} = k\left(\mathbf{p}_{hi} - \mathbf{p}_{oi}\right) \quad (3)$$

$$\mathbf{F}_{di} = b\left(\mathbf{v}_{hi} - \mathbf{v}_{oi}\right) \quad (4)$$

where $\mathbf{F}_s$ and $\mathbf{F}_d$ are the spring and damper forces, $\mathbf{p}_h$ and $\mathbf{p}_o$ are the positions of the manipulandum end-point and the polished object end-point, $\mathbf{v}_h$ and $\mathbf{v}_o$ are the velocities of the manipulandum end-point and the polished object end-point, and k and b are the stiffness and damping coefficients (k = 1000 N/m, b = 5 Ns/m). Therefore, the spring-damper produces equal and opposite forces on each hand that attempt to maintain the position of the manipulanda end-points close to the ends of the polished object (Figure 1C, horizontal forces).

Contact forces between the polished object and the grinder were computed based on the overlap between the polished object and the grinder. The overlap was detected when one or more contact points

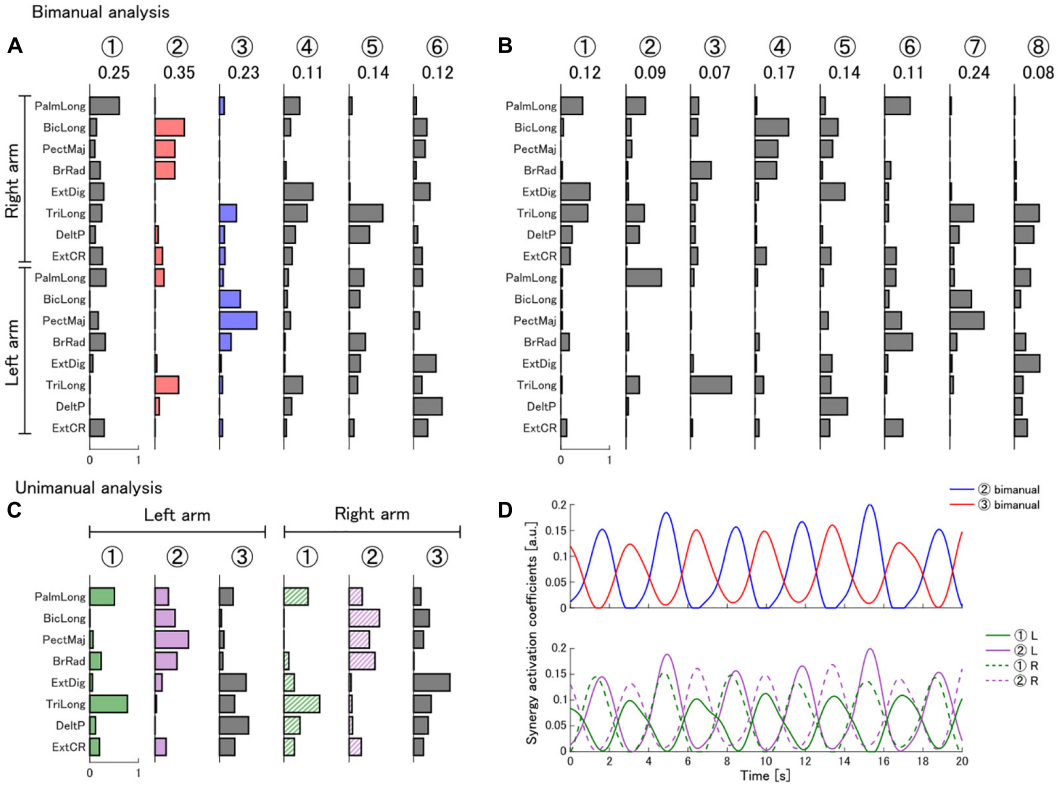

FIGURE 2
Muscle synergies extracted from the expert during a real polishing operation. **(A)** Bimanual muscle synergies extracted according to the synergy selection criteria ($R^2 > 0.90$). The number of synergies was determined as $N_b = 6$. Synergies were extracted from the palmaris longus (PalmLong), biceps brachii long head (BicLong), pectoralis major (PectMaj), brachioradialis (BrRad), extensor digitorum (ExtDig), triceps brachii long head (TriLong), deltoid posterior (DeltP), and extensor carpi radialis (ExtCR) muscles of both arms. **(B)** Bimanual muscle synergies used to compute the EMG similarity score in the virtual polishing task. We selected $N_{EMG} = 8$ to facilitate improvement in the task. Encircled numbers are labels indicating the synergy number. The value of the synergy importance metric within a synergy set is indicated below each synergy label. **(C)** Unimanual muscle synergies extracted separately from the left and right arms according to the synergy selection criteria. **(D)** Muscle synergy activation coefficients of a subset of synergies of the expert during a sample portion of a trial in the real polishing task. The upper and lower panels show the activations of bimanual and unimanual synergies, respectively. The color of the traces indicates the corresponding bimanual or unimanual synergy.

in the polished object entered the area defined by the outline of the grinder. Contact forces $\mathbf{F}_c$ were modeled as elastic forces proportional to the distance d_j between the front edge of the grinder and the contact point j:

$$\mathbf{F}_{cj} = kd_j\mathbf{y} \tag{5}$$

where k is the stiffness coefficient (k = 1000 N/m) and $\mathbf{y}$ is a unit vector along the y axis, indicating that contact forces were always perpendicular to the front edge of the grinder. Each of the contact forces $\mathbf{F}_{cj}$ also generated a torque $\boldsymbol{\tau}_j$ around the mid-point of the polished object. The torques were computed as the cross-product of the contact force and $\mathbf{r}_j$, the position vector of contact point j with respect to the mid-point of the polished object.

$$\boldsymbol{\tau}_j = \mathbf{r}_j \times \mathbf{F}_{cj} \tag{6}$$

The torques $\boldsymbol{\tau}_j$ were simulated by converting them to a pair of opposing forces perpendicular to the polished object applied at both manipulanda end-points,

$$\mathbf{F}_{\tau ij} = \frac{||\boldsymbol{\tau}_j||}{d_m}\mathbf{u}_i \tag{7}$$

where d_m is the distance between the midpoint and the end-point of the polished object, and $\mathbf{u}$ is a unit vector perpendicular to the polished object. Brackets indicate the magnitude of $\boldsymbol{\tau}_j$. The directions of $\mathbf{u}_i$ were determined according to the direction of $\boldsymbol{\tau}$. The contact-related force generated by each manipulanda was defined as the sum of contact forces from all overlapping contact points and their associated torque forces:

$$\mathbf{F}_{Ci} = \sum_j (\mathbf{F}_{cj} + \mathbf{F}_{\tau ij}) \tag{8}$$

Vibration forces were produced when the polished object contacted the grinder. The amplitude of the vibration on each manipulandum was proportional to the magnitude of the total contact forces on the manipulandum (gain, g = 0.15) and had a frequency f of 15 Hz. The direction of the vibration forces was perpendicular to the grinder:

$$\mathbf{F}_{Vi} = \mathbf{y}\,||\mathbf{F}_{Ci}||\,g\mathbf{sin}(2\pi ft) \tag{9}$$

where t is time. Forces along the vertical axis are mainly the sum of $\mathbf{F}_{Ci}$ and $\mathbf{F}_{Vi}$ (Figure 1C, vertical forces).

The polishing effect between the polished object and the grinder was simulated by deforming the polished object according to the computed contact forces on each contact point. Each contact point j was modeled as a two-dimensional point mass-damper system (m = 0.1 kg, b = 300 Ns/m^2) with the contact force $\mathbf{F}_{cj}$ as input (Equation 5), producing acceleration of the contact point. We used

the Euler method to integrate the computed acceleration and obtain the new position of each contact point at each simulation step.

2.4. Smoothness score

The main goal of the task was to use the grinder to transform the initially jagged polished object into a smooth and straight line. We provided learners with feedback about the smoothness of the polished object (aside from the shape of the object itself) in the form of a smoothness score during the task. We quantified smoothness as the area between the line defined by the polished object and a straight line crossing the polished object from end to end at the mean vertical position of the contact points (**Figures 1D, E**). We showed the smoothness score to participants as a number between 0 and 100 in a linear scale, with 0 indicating the smoothness at the start of a trial (before polishing), and 100 indicating a perfectly smooth and flat object (area between object line and straight line is zero).

2.5. EMG space similarity score

An additional objective during the polishing task was to maximize the EMG space similarity score (EMG score). The EMG score reflected the similarity between the spaces containing the muscle activations of the learners and of an expert in the polishing task. This score was defined as the quality of the reconstruction of the participant's EMG activity based on a set of muscle synergies extracted from the expert ("see the section 2.6. Expert muscle synergies"). Higher qualities of reconstruction indicate that participants generate muscle activations that could be generated by the expert during the polishing task with a high degree of plausibility, and vice versa. To calculate the quality of reconstruction we first solved a non-negative linear regression problem to find synergy activation coefficients $\mathbf{c}$ that approximate the measured muscle activations $\mathbf{m}$ based on the expert's muscle synergies $\mathbf{S}$

$$\min_{\mathbf{c}} ||\mathbf{m}_r - \mathbf{m}||^2 \; s.t. \; \mathbf{c}_i \geq 0 \tag{10}$$

$$\mathbf{m}_r = \mathbf{Sc}$$

where $\mathbf{m}_r$ are the reconstructed muscle activations. Only synergies $\mathbf{S}$ extracted using the bimanual analysis described in the section "2.8.1. Synergy extraction" were used. We used the lsqnonneg function in Matlab to solve this non-negative linear regression problem. We then defined the quality of reconstruction as

$$R^2 = 100\left(1 - \frac{\sum_j \sum_i (m_{ij} - m_{rij})^2}{\sum_j \sum_i (m_{ij} - \overline{m}_i)^2}\right) \tag{11}$$

where m_{ij} is the activation of the i^{th} muscle in the j^{th} sample, m_r are the reconstructed muscle activations, and $\overline{m}_i$ is the mean activation of the i^{th} muscle within a defined moving window. For a given time, the moving window contained the most recent 100 samples of $\mathbf{m}$ and their corresponding $\mathbf{c}$, which amounts to 50 ms of data. The reconstruction quality calculated from the window was stored in an additional window that held the results of the 200 most recently computed reconstruction quality values, containing information about the latest 150 ms of data. The average value of the reconstruction quality window was shown to the participants as feedback. The sizes of the windows were selected so that participants could perceive a causal relationship between muscle contractions and the EMG score. **Figure 1E** shows an example of the EMG space similarity score for one trial.

2.6. Expert muscle synergies

We used the muscle synergies extracted from an expert as a template of the muscle synergies that participants should learn to use during a polishing task. The expert has 35 years of experience in polishing operations, and has received the title of master from an industry regulatory organization. The expert continuously engages in training apprentices. The synergies were extracted from the expert performing a polishing operation on metal cylinders using an industrial bench grinder. The real polishing environment differs from the virtual environment in that motion and forces in the virtual environment are not constrained to a horizontal plane, and in the postures of the expert and participants during the task. In the real environment, the grinder is placed approximately at knee height, allowing the expert to support their forearms on their upper legs while performing the task. However, both environments require oscillatory movements of the arms to the sides to accomplish the task. The expert performed the polishing operation in 7 trials, each lasting 60 s. EMG signals were measured and processed using the same methods described in the sections "2.2. Experimental setup" and "2.8.1. Synergy extraction." We pooled the EMG data of all 7 trials for analysis.

2.7. Experimental protocol

Participants attended five experimental sessions of the virtual polishing task on different days. Sessions were scheduled according to participant availability. The mean time between sessions was 3.8 days (SD 3.0). The minimum and maximum times between sessions were 1 and 14 days, respectively. Participants completed the five sessions in 15.2 days (SD 9.3) on average. The minimum and maximum times of completion were 5 and 35 days, respectively.

Participants were divided into two groups: the real feedback and the null feedback groups (10 participants in each group). The real feedback group received veridic smoothness and EMG scores as described in the previous sections. The null feedback group received the veridic smoothness score, but did not receive the EMG score.

Each experimental session consisted of a maximum voluntary contraction task and the virtual polishing task. The MVC task was conducted before the virtual polishing task for EMG normalization purposes. In the MVC task, participants performed maximum voluntary contractions of their arm muscles by producing maximum isometric torques at the degrees of freedom of joints that are relevant to the motion in the task and the muscles used for EMG measurement (wrist flexion/extension and ulnar/radial deviation, elbow flexion/extension, and shoulder horizontal abduction/adduction). We asked participants to push with the corresponding arm segment (hand, forearm, or upper arm) against a fixed object that opposed motion around each degree of freedom of interest. The arm posture during the MVC task was similar to the baseline posture in the virtual polishing task.

In each session, before the virtual polishing task, participants were shown two videos. The first video showed the expert performing a real polishing operation. The second video showed an example participant performing a trial of the virtual polishing task. Both videos illustrated the polishing operation as a cyclic motion of the arms and the polished object from side to side while lightly contacting the grinder. Participants in the real feedback group were instructed to make the polished object as smooth as possible while also attempting to maximize the EMG score. Participants in the null feedback group were only instructed to make the polished object as smooth as possible. Additionally, participants in both groups were encouraged to explore different movement and force patterns to increase their scores. Participants in the real feedback group were informed that this exploration could influence the EMG score.

Each session of the virtual polishing task consisted of 60 trials, each with a duration of 30 s. Before each trial, participants moved each end-point of the manipulanda, indicated by white circles, to its initial position, indicated by red rings in the virtual environment. The initial position was centered on the display and close to the participant's torso. The distance between the initial positions of each manipulandum end-point corresponded to the size of the polished object. At this stage, only the initial position indicators were visible, and no forces were generated by the manipulanda. After holding the manipulanda for 5 seconds at their initial positions, the polished object and the grinder became visible, and the simulated physics of the task were activated. The shape of the polished object was randomly generated at the beginning of each trial. The appearance of the virtual objects prompted the participants to begin the task. At the end of the trial the simulated physics were deactivated and the grinder disappeared. Participants could observe the resulting shape of the polished object and rest before starting the next trial. Participants were required to rest at least 5 seconds between trials, but rested 10.2 seconds (SD 4.0) on average.

2.8. Data analysis

2.8.1. Synergy extraction

We used non-negative matrix factorization (NMF) (Lee and Seung, 1999) to extract muscle synergies from the EMG signals collected during the actual polishing task with the expert, and the virtual polishing task with the experiment participants. In our main analysis, the processed EMG signals from muscles of both arms were pooled together to extract bimanual synergies. In the case of the expert polisher, synergies were extracted for all number of synergies N from 1 to 16. We selected the number of synergies by finding the smallest N_b that resulted in a reconstruction quality R^2 of the processed EMG of at least 0.90 (Berger et al., 2013; Barradas et al., 2020). We used the expert's extracted synergies in the bimanual analysis to compute the EMG space similarity score during the experimental sessions. However, we decided to use a larger number of synergies N_{EMG} for the EMG score, as a pilot test showed that the EMG score was predominantly negative when N_b was used. We then extracted muscle synergies offline from each participant and experimental session. We set the number of synergies to N_{EMG} for each participant for comparison to the expert's synergies.

We also conducted a secondary synergy analysis in which the processed EMG signals from the muscles of each arm were analyzed separately to extract unimanual synergies for each arm. The number of synergies N_u for each arm of the expert polisher was selected as described above, except that N_u was taken from 1 to 8. The number of synergies from each participant, experimental session, and arm were set to N_u for comparison to the expert's synergies. Note that the unimanual synergies were not used to compute the EMG space similarity score.

2.8.2. Muscle synergy similarity metric

We performed a similarity analysis between the expert's muscle synergies and participants' synergies extracted from each experimental session to assess changes in the synergies in both the bimanual and unimanual analyses. We defined the similarity between two different set of synergies as the average cosine of the angle between individual corresponding synergies in the two sets:

$$sim = \frac{1}{N}\sum_{i=1}^{N}\cos\theta_i = \frac{1}{N}\sum_{i=1}^{N}\frac{\mathbf{s}_{i1}\cdot\mathbf{s}_{i2}}{||\mathbf{s}_{i1}||\,||\mathbf{s}_{i2}||} \quad (12)$$

where N is the number of synergies in the set, θ is the angle between two individual synergies when considering them as a vector, and $\mathbf{s}_{i1}$ and $\mathbf{s}_{i2}$ are matched individual synergies to be compared represented as vectors. For each session, we matched individual synergies of the expert and the participants by computing the cosine similarity between each synergy in the expert's synergy set and all other synergies in the participant's synergy set. The pair of synergies with the largest similarity was considered a match, and was removed from the synergy sets. The process was then repeated with the remaining synergies in each set until all synergies in one set had been matched to a synergy in the other set. For each participant, we computed the muscle synergy similarity metric separately for each session in the experiment.

2.8.3. Muscle synergy importance

We calculated the relative contribution of each extracted muscle synergy to the reconstruction of the EMG activity of the expert. Given that muscle synergies computed using NMF are not necessarily linearly independent, it is generally not possible to assess the contribution of each synergy by reconstructing the EMG using only the synergy of interest as in other matrix factorization algorithms like PCA. Instead, we defined the contribution of each synergy in terms of a synergy importance metric as

$$IMP_{si} = 1 - \frac{R^2{}_{sri}}{R^2{}_{sf}} \quad (13)$$

where IMP_{si} is the synergy importance of synergy $i = 1, \ldots, N$, $R^2{}_{sri}$ is the reconstruction quality achieved with a reduced synergy set, from which synergy i has been removed, and $R^2{}_{sf}$ is the reconstruction quality achieved with the full synergy set. Therefore, larger values of the importance metric indicate a larger contribution of the synergy of interest to EMG reconstruction. To compute $R^2{}_{sri}$, we recalculated the synergy coefficients for the reduced synergy set that optimally reconstruct the EMG by performing a non-negative linear regression, as described in Equation 10.

We also applied this metric to participants in the virtual task using the expert's muscle synergies. This allowed us to measure the degree to which the participants' EMG can be explained by individual synergies of the expert. For each participant, we computed the muscle synergy importance metric separately for every session in the experiment.

2.8.4. Polishing attack angle

The attack angle in a polishing operation is the angle formed between the grinder and the surface of the polished object. The variability of the attack angle is an indicator of the skill level in the polishing task (Kodama et al., 2015; Tsujiai et al., 2015). Therefore, we measured the attack angle that subjects used during the experiment. Given that the grinder in the virtual task is static and parallel to the horizontal in the task, the attack angle is determined by the orientation of the polished object with respect to the horizontal. For each participant, we calculated the standard deviation of the attack angle within each trial, and averaged the result of all trials within one session.

2.8.5. Statistical analysis

The main outcome variables of the experiment were the average smoothness and EMG space similarity scores across learners in both the real and null feedback groups. Secondary outcome variables were the average variability of the polishing attack angle, the muscle synergy similarity and the muscle synergy importance. We assessed differences in the outcome variables using mixed two-factor ANOVA tests with trial session as the within-subjects factor (with five levels: sessions 1–5), and feedback type as the between-subjects factor. In cases where the sphericity assumption of the mixed ANOVA test was not met, we used the Greenhouse-Geisser correction. Furthermore, in cases where the outcome variables did not satisfy the normality assumptions of the ANOVA test, we used the non-parametric ANOVA-type statistic (ATS) implemented in the nparLD package in R (Noguchi et al., 2012). The significance threshold was set at $p = 0.05$. We performed *post-hoc* tests with Bonferroni corrections.

3. Results

3.1. One muscle synergy of the expert predominantly contributes to EMG reconstruction

We analyzed the muscle activations of 8 muscles from both arms of an expert performing a real polishing operation. In the bimanual analysis, we identified 6 muscle synergies ($N_b = 6$), which achieved a reconstruction quality (R^2) of 0.90 of the original EMG signals. We also quantified the contribution of each extracted synergy to the reconstruction quality of the expert's EMG signals by calculating the synergy importance metric in the bimanual analysis. We found that synergy 2 played a predominant role in the reconstruction of the EMG signals (**Figure 2A**). Synergy 2 had an importance value of 0.35. which was 1.4 times larger than the synergy with the next highest importance (0.25).

3.2. Bimanual muscle synergies capture temporal coordination of unimanual synergies in the expert

In the unimanual analysis, we identified 3 muscle synergies in each arm ($N_u = 3$, $R^2_{left} = 0.91$, $R^2_{right} = 0.90$) (**Figure 2C**). The synergies in both arms had a largely equivalent composition, which we quantified as the cosine similarity between corresponding synergy pairs in both arms (syn 1: 0.95, syn 2: 0.93, syn 3: 0.87). A comparison between the bimanual and unimanual synergies revealed that unimanual left synergy 1 and unimanual right synergy 2 can be combined to form a bimanual synergy that highly resembles the important bimanual synergy 2 (cosine similarity: 0.92). Similarly, unimanual left synergy 2 and unimanual right synergy 1 can be combined to form a synergy that resembles bimanual synergy 3 (cosine similarity: 0.86). The activation coefficients of bimanual synergies 2 and 3 show that, during the task, the synergies are activated in an alternating pattern (**Figure 2D**). Furthermore, the activations of the unimanual synergies contained in bimanual synergies 2 and 3 are locked in phase with each other, and with their corresponding bimanual synergy (**Figure 2D**).

3.3. Real feedback group showed improvement in smoothness and EMG space similarity scores

Participants in the real feedback group showed an improvement in the mean smoothness score throughout the experiment [session 1: 57.0 % (SD 7.1), session 5: 62.2 % (SD 11.4)]. Participants in the null feedback group also showed an improvement in the mean smoothness score [session 1: 59.6 % (SD 7.1), session 5: 64.8 % (SD 9.0)]. A mixed two-factor ANOVA analysis showed that there was no statistically significant interaction between the effects of training session and feedback type (real or null) on the mean smoothness score [$F(2.14,38.55) = 0.323$, $p = 0.74$]. The ANOVA analysis also determined that there was a statistically significant main effect of training session [$F(2.14,38.55) = 5.79$, $p = 0.005$], but not of feedback type [$F(1,18) = 0.30$, $p = 0.59$]. A *post-hoc* analysis confirmed a statistically significant difference in the mean smoothness score between training sessions 1 and 2 [paired t-test with Bonferroni corrections, $p = 0.039$]. **Figure 3** shows the progression in the smoothness scores for all participants.

We used the extracted bimanual synergies from the expert with $N_{EMG} = 8$ to reconstruct the EMG signals of participants in the virtual polishing task and compute the EMG space similarity score (**Figure 2B**). The reconstruction quality R^2 of the expert's EMG by the synergy set with $N_{EMG} = 8$ was 0.94. Participants in the real feedback group showed an improvement in the mean EMG score throughout the experiment [session 1: 29.4% (SD 10.3), session 5: 37.7 % (SD 14.3)]. Participants in the null feedback group showed a smaller improvement in the mean EMG score [session 1: 23.6% (SD 9.1), session 5: 29.0% (SD 9.4)]. Due to the presence of outliers and non-normality in the data we used a non-parametric test (ATS). The ATS analysis (nparLD) showed that there was no statistically significant interaction between the effects of training session and feedback type on the mean EMG score [$F(3.06, \infty) = 0.35$, $p = 0.79$]. The ATS analysis also determined that there was a statistically significant main effect of feedback type [$F(1.00, \infty) = 9.70$, $p = 0.002$], but not of training session [$F(3.06, \infty) = 2.05$, $p = 0.10$]. **Figure 3** shows the progression in the EMG score for all participants.

We also measured the variability in the attack angle throughout the experiment as the standard deviation of the attack angle across all trials in a session. Participants in the real feedback group showed a decrease in the mean variability of the attack angle [session 1: 2.2° (SD 1.2), session 5: 1.3° (SD 0.5)]. Similarly, participants in the null feedback group showed a significant decrease in the mean variability

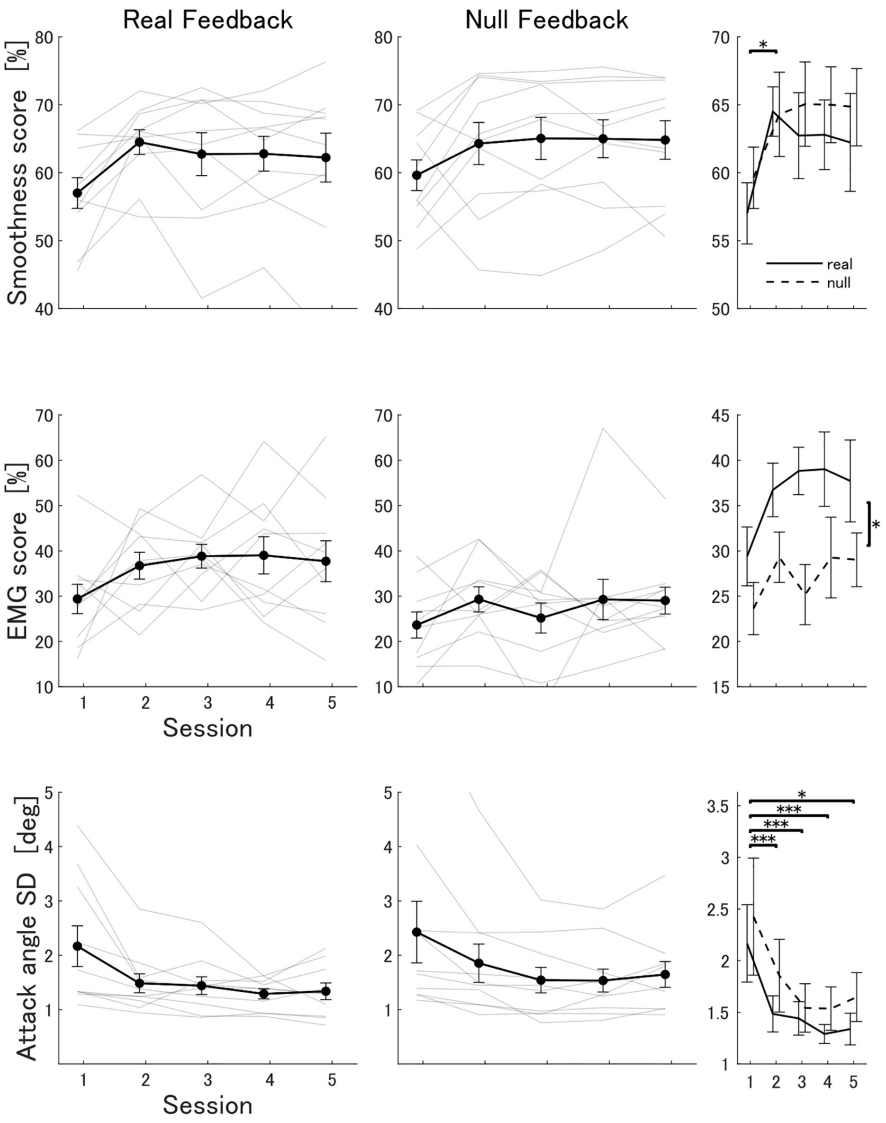

FIGURE 3
Progression of the smoothness score, EMG similarity score and attack angle variability in the real and null feedback groups. The attack angle variability was measured as the standard deviation of the attack angle across all trials in one session. Thick lines indicate the mean score across participants in each group. Light lines indicate scores for each participant. Error bars indicate the standard error. The third column summarizes statistical comparisons. Asterisks indicate significant differences between metrics: $^{***}p < 0.001$, $^{*}p < 0.05$.

of the attack angle [session 1: 2.4° (SD 1.8), session 5: 1.6° (SD 0.7)]. An ATS analysis showed that there was no statistically significant interaction between the effects of training session and feedback type on the variability of the attack angle [$F(2.01, \infty) = 0.31$, $p = 0.56$]. The ATS analysis also determined that there was a statistically significant main effect of training session [$F(2.01, \infty) = 6.22$, $p = 0.002$], but not of feedback type [$F(1.00, \infty) = 0.31$, $p = 0.58$]. A *post-hoc* analysis confirmed a statistically significant difference in the mean variability of the attack angle between training sessions 1 and 2 [ATS with Bonferroni corrections, $p < 1 \times 10^{-9}$], 1 and 3 [$p < 1 \times 10^{-4}$], 1 and 4 [$p < 1 \times 10^{-4}$], and 1 and 5 [$p = 0.04$], but no difference between the rest of the session pairs. **Figure 3** shows the progression in the variability of the attack angle for all participants. Interestingly, the variance across subjects of the standard deviation of the attack angle, that is, a measure of the variability across subjects of the variability of the attack angle within subjects, was significantly smaller in the real feedback group than in the null feedback group during session 4 (F-test for equality of variances, $p = 0.021$).

3.4. Real feedback group showed increased importance and similarity to one muscle synergy of the expert

The muscle synergies of participants in the real feedback group did not appreciably become more similar to the expert's bimanual synergies ($N_{EMG} = 8$) as a whole throughout the experiment according to the mean muscle synergy similarity metric [session 1: 0.54 (SD 0.05), session 5: 0.57 (SD 0.04)]. This was also true for participants in the null feedback group [session 1: 0.56 (SD 0.05), session 5: 0.57 (SD 0.03)]. A two-way ANOVA analysis showed that there was no statistically significant interaction between the effects of training session and feedback type on the mean synergy

similarity to the expert [$F(4,72) = 0.93$, $p = 0.45$]. Additionally, the analysis determined no statistically significant main effects of training session [$F(4,72) = 1.16$, $p = 0.34$] or feedback type [$F(1,18) = 0.04$, $p = 0.85$]. **Figure 4A** shows the progression of the synergy similarity metric of participants in the real feedback and null feedback groups. **Supplementary Figure 1** shows the synergies extracted from a representative participant in the real feedback group in sessions 1 and 5.

We also examined the cosine similarity of participant's individual muscle synergies to the corresponding expert synergy ($N_{EMG} = 8$) during each session of the experiment. In the bimanual analysis, we found that only synergy 3 showed a trend for increasing similarity in the real feedback group (**Figure 4B**). Participants in the real feedback group showed an increase in the cosine similarity of synergy 3 [session 1: 0.44 (SD 0.42), session 5: 0.70 (SD 0.29)], whereas participants in the null feedback group showed a decrease [session 1: 0.72 (SD 0.22), session 5: 0.55 (SD 0.36)]. An ATS analysis showed that there was a statistically significant interaction between the effects of training session and feedback type on the similarity of synergy 3 [$F(3.35, \infty) = 2.71$, $p = 0.037$]. A statistically significant main effect of feedback type was found [$F(1.00, \infty) = 4.02$, $p = 0.045$], but not of training session [$F(3.35, \infty) = 0.89$, $p = 0.45$].

Similarly, in the unimanual analysis we found that only synergy 1 of the left arm showed a trend for increasing similarity in the real feedback group (**Figure 5**). Participants in the real feedback group showed an increase in the cosine similarity of synergy 1 [session 1: 0.63 (SD 0.23), session 5: 0.74 (SD 0.19)], whereas participants in the null feedback group showed no increase [session 1: 0.69 (SD 0.11), session 5: 0.68 (SD 0.17)]. An ATS analysis showed that there was no statistically significant interaction between the effects of training session and feedback type on the similarity of synergy 1 [$F(3.74, \infty) = 1.08$, $p = 0.36$]. A statistically significant main effect of feedback type was found [$F(1.00, \infty) = 5.06$, $p = 0.025$], but not of training session [$F(3.74, \infty) = 0.68$, $p = 0.59$].

Additionally, we examined the importance of the expert's bimanual synergies in reconstructing the EMG of the participants in the virtual polishing task. In particular, we examined the importance of synergy 3 (IMP_{s3}), as it was the only synergy for which similarity increased throughout the experiment (**Figure 4C**). We found that IMP_{s3} increased for participants in the real feedback group [session 1: 0.03 (SD 0.05), session 5: 0.13 (SD 0.12)]. In contrast, IMP_{s3} did not increase for participants in the null feedback group [session 1: 0.14 (SD 0.26), session 5: 0.06 (SD 0.1)]. An ATS analysis showed that there was a statistically significant interaction between the effects of training session and feedback type on IMP_{s3} [$F(3.37, \infty) = 4.64$, $p = 0.002$]. Statistically significant main effects of feedback type [$F(1.00, \infty) = 4.41$, $p = 0.036$] and training session [$F(3.37, \infty) = 2.84$, $p = 0.031$] were found.

Interestingly, out of all synergies in the expert synergy set with $N_b = 6$, synergy 3 of the set with $N_{EMG} = 8$ is most similar to synergy 2, the predominant synergy (cosine similarities between synergy 3 from set $N_{EMG} = 8$ and synergies from set $N_b = 6$: syn 1: 0.37, syn 2: 0.71, syn 3: 0.15, syn 4: 0.60, syn 5: 0.30, syn 6: 0.35).

4. Discussion

Learning a new motor skill entails concurrently acquiring kinematic and kinetic movement patterns to satisfy the goals of a task. Augmented feedback that contains kinematic and/or kinetic information provided by a coach or an augmented reality system can facilitate motor skill learning (Young and Schmidt, 1992; Vander Linden et al., 1993; Lauber and Keller, 2014). Humans are able to simultaneously meet kinematic and kinetic task goals by appropriately modulating muscle activations, which control the stiffness of the limbs during a movement, and set the level of compliance in interactions with tools and other objects (Hogan, 1985b). Therefore, EMG from the muscles involved in the task can provide information about the kinematics and kinetics of the task. Here, we propose the EMG space similarity feedback, a new kind of augmented feedback that compares the EMG of learners to the EMG of an expert in the task. This kind of feedback could provide implicit comparisons between the kinematics and kinetics of movements of learners and the expert. The EMG space similarity feedback could be especially relevant for skills that have an important kinetic component, which in contrast to the kinematic component, is hard to evaluate by external observers without the use of special equipment.

We tested the EMG space similarity feedback in a virtual environment that simulates a polishing operation with a grinder, which requires precise kinematic and kinetic patterns of movement (Kodama et al., 2015). We divided participants into two groups: real and null feedback groups. The real feedback group was provided with the EMG space similarity feedback at all times, whereas the null feedback group was not. While both groups were able to improve the EMG score throughout the experiment, the real feedback group consistently showed larger EMG scores. However, we found that the groups did not differ significantly in their performance in the task, as measured by the smoothness score (**Figure 3**). This suggests that the smoothness objective of the virtual polishing task may be achievable independently of the way muscles are engaged in the task. Therefore, a variety of muscle activation strategies may be able to produce equivalent smoothness results in the virtual task. In any case, we have demonstrated that the EMG space similarity score can induce the use of muscle activation patterns that are increasingly consistent with a template synergy set.

Theories of motor skill learning posit that the acquisition of a skill is the result of the adjustment of a variety of processes and computations in the CNS (Willingham, 1998). Under this view, strategic and perceptual-motor integration processes must first transform the explicit goal of smoothening the polished object into lower level goals that correspond to suitable kinetics and kinematics for the task. Therefore, optimization of these processes may not directly cause improvements in task performance, especially in the early stages of learning, as other processes (i.e., sequential and/or dynamic processes) may need to be further tuned to exploit the output of the strategic and integration processes. The EMG space similarity feedback could contribute to these complex processes, as it can guide learners to generate muscle activations in a desired space, which can be associated to a corresponding kinetic and kinematic space that includes the goal actions. Thus, the EMG score may contribute to the overall process of motor skill learning.

We expected that the EMG score would reflect the similarity between the expert's and the learner's muscle synergies. Indeed, the EMG space similarity score is a local approximation to the global variance accounted for (VAF) metric, which has been described in previous research as a holistic measure of the similarity of two synergy

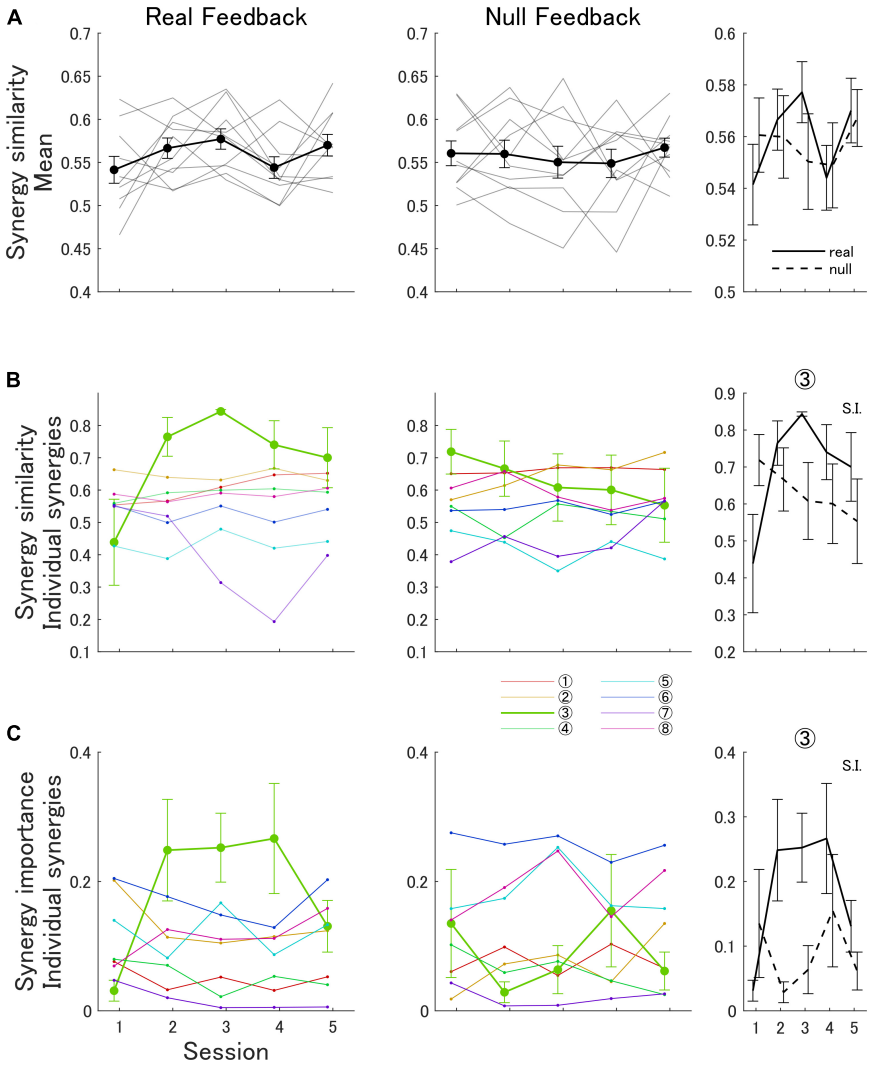

FIGURE 4
Bimanual synergy similarity and importance metrics in the real and null feedback groups. **(A)** Mean synergy similarity metric. Thick lines indicate the mean score across participants in each group. Light lines indicate scores for each participant. Error bars indicate the standard error. **(B)** Cosine similarity metric of individual synergies (1–8). **(C)** Synergy importance of individual expert synergies (IMP_{S1}–IMP_{S8}). The third column summarizes statistical comparisons. The S.I. legend indicates a significant interaction between session number and feedback type on the outcome variable.

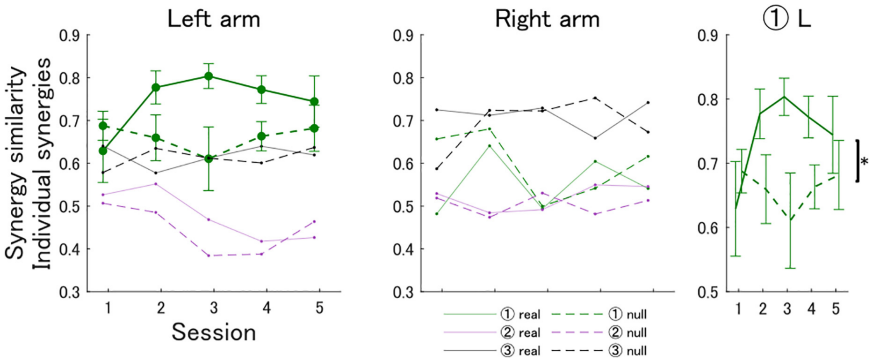

FIGURE 5
Cosine similarity metric of individual unimanual synergies in the real and null feedback groups. The first and second panels show the similarity metric for the left and right arms, respectively. Solid and dashed lines show the results for the real and null feedback groups, respectively. The third column summarizes statistical comparisons. The asterisk indicates a significant effect of feedback type on the similarity of synergy 1 of the left arm to the corresponding expert synergy.

sets (Perreault et al., 2008; Roh et al., 2013). The only difference is that our EMG score continuously evaluates the quality of reconstruction of EMG within short time windows, as opposed to using the whole data set at once. However, we did not find any improvements in the muscle synergy similarity metric that mirrored the improvements in the EMG score by the real feedback group. This underscores that both metrics quantify synergy similarity in different ways. Namely, two different synergy sets may produce muscle activations in increasingly overlapping regions of the muscle activation space without necessarily becoming more similar themselves. One way to visualize this is that a vector space may have multiple bases, and the bases can be orthogonal to each other. An additional reason is that the global VAF metric considers the variance of the data corresponding to each synergy to determine the similarity between synergy sets, whereas the muscle synergy similarity metric does not (Perreault et al., 2008). Therefore, the effect of individual synergies that explain larger portions of the variance is prioritized in the global VAF metric, as discussed below. These observations suggest that the EMG score cannot promote the directed learning of muscle synergies strictly, but instead allows to approximate the desired muscle activation space.

Illustrating the preference of the EMG score for important individual synergies, we found that participants in the real feedback group showed a tendency to improve the similarity of a single synergy to one of the expert's synergies (synergy 3 from the extended set with $N_{EMG} = 8$) (**Figure 4B** and **Supplementary Figure 1**). Moreover, we also found that synergy 3 of the expert became increasingly important (Equation 13) in reconstructing the EMG signals of participants in the real feedback group throughout the experiment (**Figure 4C**). However, we did not observe this effect in the null feedback group. Therefore, the real feedback group acquired an expert-like synergy during training.

We can further explain the nature of the synergy similarity and EMG space similarity metrics by considering the rest of the individual synergies. While one synergy increased in similarity to synergy 3 of the expert, another synergy decreased in similarity to synergy 7, and the rest of the synergies did not show appreciable changes (**Figure 4**). Therefore, any increase in the mean synergy similarity score was canceled. However, the importance of synergy 7 was very low throughout the experiment, suggesting that the observed increases in the EMG score reflected the acquisition of synergy 3 of the expert.

Interestingly, synergy 3 from the expert's set with $N_{EMG} = 8$ highly resembles synergy 2 from the set with $N_b = 6$, which is the synergy with the highest importance in the $N_b = 6$ set (**Figure 2**). In fact, synergy 2 in the set with $N_b = 6$ appears to have fragmented into synergies 3 and 4 in the set with $N_b = 8$, which is common when increasing N in the non-negative matrix factorization algorithm (Cheung et al., 2012; Barradas et al., 2020). This explains why the importance of synergies 3 and 4 in the set with $N_b = 8$ is reduced with respect to their parent synergy in the set with $N_b = 6$. That is, in our synergy importance metric, removing one of the fragmented synergies while leaving the other one in the set allows a better reconstruction of the EMG activity in the task than if both fragments were removed, reducing the importance metric of both fragments. However, synergy 3 (and not synergy 4) in the $N_{EMG} = 8$ set encodes a strong bimanual coordination pattern that is also characteristic of synergy 2 in the set with $N_b = 6$, and which may be essential to explain its high importance. Therefore, participants in the real feedback group not only acquired an expert-like synergy, but they acquired the most important synergy within the expert's synergy set.

It is possible that the expert-like synergy that participants in the real feedback group acquired is associated with kinematic and/or kinetic patterns that are relevant to both the actual and the virtual tasks. This synergy is composed mainly of the co-activation of the left triceps long head, an elbow extensor, and the right brachioradialis, an elbow flexor. Therefore, this synergy could be involved in producing a counter-clockwise torque around the center of the polished object when held bimanually. The grinder also produces torques around the object during contact with off-center spots on the object. Therefore, this synergy could be important to counter the torque from the grinder, stabilizing the object during contact. This is reasonable, as an important symmetric synergy that could stabilize the object in the opposite direction is present in the expert's synergy set with $N_b = 6$ (synergy 3). Synergy 7 in the synergy set with $N_{EMG} = 8$ (or synergy 3 in $N_b = 6$) is symmetric to synergy 2 in the set with $N_b = 6$, suggesting that the expert uses symmetric patterns to stabilize the object. However, subjects in the real feedback group did not show muscle activation patterns consistent with this synergy. This again highlights the fact that the EMG space similarity feedback does not seem to be able to promote learning desired muscle synergies directly.

Here, we computed the EMG space similarity feedback *via* a bilateral muscle synergy analysis that pools signals from both arms (Jarrassé et al., 2014; Botzheim et al., 2021). This analysis can capture timing relationships between synergies of both arms as a spatial structure, which enables the EMG score to provide information about the coordination of both arms (**Figure 2**). However, a large body of evidence indicates that limb-specific synergies are encoded in spinal circuits across species (Kargo and Giszter, 2008; Kargo et al., 2010; Giszter, 2015; Takei et al., 2017; Yang et al., 2019; Cheung and Seki, 2021). An EMG score based on a unimanual synergy analysis would not be able to convey the necessary information about bimanual coordination to effectively learn expert-like muscle activation patterns. However, a unimanual synergy analysis of both arms revealed that subjects in the real feedback group showed increased similarity to one of the left arm synergies of the expert. Interestingly, this learned unimanual synergy constituted the left arm component of the important bimanual synergy discussed above (synergy 2 in the set with $N_b = 6$, and synergy 3 in the set with $N_{EMG} = 8$). Therefore, the unimanual analysis allowed us to observe that, in addition to an increased interarm coordination, the acquisition of the important bimanual synergy was due to the acquisition of a left arm synergy, but not a right arm synergy (**Figure 5**). This warrants further research, as the EMG space similarity feedback may have an effect on arm specialization *via* interarm differences in synergy control (Sainburg, 2005).

The attack angle between the grinder and the polished object has been previously identified as a kinematic variable that reflects expertise in a polishing task (Kodama et al., 2015). Expert polishers show smaller variability in the attack angle than inexperienced people. Because of the interaction forces between the grinder and the polished object, reducing variability in the attack angle most likely also involves precise kinetic patterns. We found that participants in both the real and null feedback groups showed a reduction in the variability of the attack angle throughout the experiment. It is notable that participants tended to modify their kinematic

patterns in a way that characterizes expertise in the task without receiving explicit instructions to do so. Interestingly, the real feedback group appeared to be more consistent in reducing the variability in the attack angle during the experiment, as the variance among subjects in this metric was smaller than for the null feedback group. This may indicate increased stability in the motion against the grinder.

Training paradigms to shape muscle activations using EMG as both a control and an augmented feedback signal have been proposed previously. Feedback that promotes changing the timing of peak EMG of a single muscle during a cycling task has been shown to also promote time shifts in the activations of other muscles, resulting in novel muscle activation patterns (Torricelli et al., 2020). However, it is unclear whether these novel muscle activations can be shaped to a desired pattern, or bring about useful or even new kinematic or kinetic movement patterns. In a different kind of tasks, the position of objects in a virtual environment can be controlled as a function of EMG. The function can be defined so that successful completion of the task requires decorrelating the activity of two or more muscles (Wright et al., 2014; Mugler et al., 2019), or learning entirely new muscle activations patterns (Berger et al., 2021). Therefore, whereas learning in these tasks may reshape muscle activation patterns, it is unclear whether the newly learned patterns are transferable to more ecological tasks. In contrast, the EMG space similarity feedback can be used during actual ecological tasks, where it complements task performance feedback. Therefore, as long as the task constraints are reasonably met, it can assist in reshaping muscle activations in a task-relevant way.

One limitation of our study is that there are different task constraints in the actual and virtual polishing environments. Namely, in the actual polishing operation, the expert sat in front of the grinder, which was placed at the height of the hips in a sitting posture. This allowed him to perform the polishing operation while supporting his forearms on top of his upper legs. Consequently, the side-to-side polishing motion involves not only arm, but also leg movements. Additionally, contact between the grinder and the polished object produces friction forces in the vertical direction. In contrast, in the virtual polishing environment, the polishing movement was restricted to a horizontal plane located at approximately the height of the sternum when sitting upright. Therefore, in the virtual task the weight of the arms is not supported and the legs were not involved in the task. Furthermore, our robotic system only produced forces on the horizontal plane. Differences in the task biomechanics may entail differences in the optimal arm kinematics and kinetics in the actual and virtual tasks. Moreover, differences between the sizes of body parts of the expert and the learners may also entail different biomechanical constraints even within the same task, real or virtual. This suggests that the EMG space similarity feedback may contain information about the actual task that is inappropriate or irrelevant for the virtual task. However, even if the expert or template synergies corresponded to an arbitrary task unrelated to the task of interest, our results show that learners are able to use the EMG space similarity feedback to increasingly move their muscle activation patterns into the space spanned by the expert synergies.

This could offer an explanation to the observation that some participants in the real feedback group showed a decline in the smoothness score after reaching a peak, even though they were able to keep improving the EMG score. Because of the different biomechanical contexts of the actual and virtual tasks, attempting to further imitate the expert's EMG patterns could be difficult and even detrimental to performance. However, the positive results up to session 3, and the lack of evident differences in performance between the real and null feedback groups suggest that the EMG score conveys sufficiently compatible information between both tasks. This may involve force application patterns onto the grinder that are universally useful in polishing-like operations.

The emphasis on important synergies and the possible presence of inappropriate synergies for the virtual task in the expert's synergy set suggest an improvement to the implementation of the EMG space similarity score. Reducing the expert synergy set to appropriate and/or important synergies would produce a score that is more related to useful kinetic and kinematic movement patterns. However, it must be taken into account that reduced synergy sets cannot account for some important task-space components in some tasks (Barradas et al., 2020). Another improvement to the EMG score would be to include information about the timing of the expert synergies during the task. This would provide a more direct way to indicate the desired kinetic and kinematic patterns. However, this can only work under the assumption that the expert patterns of muscle activation have been previously acquired. Therefore, we envision the current EMG space similarity score as a way to promote the acquisition of expert-like muscle activation patterns, that is, the building blocks of movement. Upon the acquisition of these building blocks, further training on how to use these blocks is needed.

In the future we plan to study the transferability of the polishing skill within the virtual environment. Namely, it is necessary to verify whether subjects in the real feedback group are able to retain the improved performance levels after the removal of the EMG space similarity feedback in the virtual task. Next, we also plan to study the transferability of the polishing skill between the actual and virtual environments. In a first stage, the expert polisher would perform the task in the simulated environment. Such a study would allow us to directly measure the kinematic and kinetic patterns that the expert uses during the task and compare them to the patterns acquired by the learners. This would confirm whether the movement patterns of the expert are actually conveyed to the learners through the EMG space similarity feedback. In a second stage, the learners would perform a baseline session in the real environment followed by training in the virtual environment, and finally, a transfer test in the real environment. Improvements in the transfer test would not only further confirm that the EMG score teaches appropriate kinematic and kinetic patterns, but would also establish a basis for augmented reality training of highly skilled technicians.

Overall, our results suggest that augmented feedback in the form of an EMG space similarity score can facilitate the acquisition of expert-like muscle activation patterns. Thus, the EMG space similarity score may assist in learning a complex skill by placing the muscle activations of learners in a space that could facilitate producing expert-like motions. Thus, the EMG space similarity feedback could be a useful tool to facilitate motor training for technicians and athletes. Further research is necessary to determine its applicability in a broader range of tasks, and to investigate the mechanisms through which it operates. A promising feature of the EMG score is that it probably conveys feedback about desired task kinetics, which usually requires especially instrumented equipment. EMG measurement systems can be used in a wider range of contexts than such equipment. Therefore, it is possible that the EMG score could be used as a substitute or in parallel to more specialized equipment to provide kinetic feedback.

Data availability statement

The raw data supporting the conclusions of this article will be made available by the authors, without undue reservation.

Ethics statement

The studies involving human participants were reviewed and approved by the Tokyo Institute of Technology Human Subjects Research Ethics Review Committee. The patients/participants provided their written informed consent to participate in this study.

Author contributions

VB and YK conceived and designed the research, edited and revised the manuscript, and interpreted the results of experiments. VB and WC performed the experiments. VB analyzed the data and drafted the manuscript. All authors approved the final version of the manuscript.

Funding

This work was supported by the Japan Society for the Promotion of Science (JSPS) Grant KAKENHI 19H05728 (to YK), Japan Science and Technology Agency (JST) Grant MIRAI JY300171 (to YK), and Japan Society for the Promotion of Science (JSPS) Grant KAKENHI 21K17789 (to VB).

Acknowledgments

We thank Atsushi Takagi for providing the first version of the polishing task virtual environment.

Conflict of interest

The authors declare that the research was conducted in the absence of any commercial or financial relationships that could be construed as a potential conflict of interest.

Publisher's note

All claims expressed in this article are solely those of the authors and do not necessarily represent those of their affiliated organizations, or those of the publisher, the editors and the reviewers. Any product that may be evaluated in this article, or claim that may be made by its manufacturer, is not guaranteed or endorsed by the publisher.

Supplementary material

The Supplementary Material for this article can be found online at: https://www.frontiersin.org/articles/10.3389/fnhum.2022.805867/full#supplementary-material

References

Al-abood, S. A., Davids, K., and Bennett, S. J. (2001). Specificity of task constraints and effects of visual demonstrations and verbal instructions in directing learners' search during skill acquisition. *J. Mot. Behav.* 33, 295–305. doi: 10.1080/00222890109601915

Barradas, V. R., Kutch, J. J., Kawase, T., Koike, Y., and Schweighofer, N. (2020). When 90% of the variance is not enough: Residual EMG from muscle synergy extraction influences task performance. *J. Neurophysiol.* 123, 2180–2190. doi: 10.1152/jn.00472.2019

Berger, D. J., Borzelli, D., and Avella, A. (2021). Task space exploration improves adaptation after incompatible virtual surgeries. *bioRxiv* [Preprint]. *bioRxiv* 2021.08. doi: 10.1152/jn.00356.2021

Berger, D. J., Gentner, R., Edmunds, T., Pai, D. K., and D'Avella, A. (2013). Differences in adaptation rates after virtual surgeries provide direct evidence for modularity. *J. Neurosci.* 33, 12384–12394. doi: 10.1523/JNEUROSCI.0122-13.2013

Botzheim, L., Laczko, J., Torricelli, D., Mravcsik, M., Pons, J. L., and Barroso, F. O. (2021). Effects of gravity and kinematic constraints on muscle synergies in arm cycling. *J. Neurophysiol.* 125, 1367–1381. doi: 10.1152/jn.00415.2020

Broker, J. P., Gregor, R. J., and Schmidt, R. A. (1993). Extrinsic feedback and the learning of kinetic patterns in cycling. *J. Appl. Biomech.* 9, 111–123. doi: 10.1016/0021-9290(89)90134-6

Burdet, E., Osu, R., Franklin, D. W., Milner, T. E., and Kawato, M. (2001). The central nervous system stabilizes unstable dynamics by learning optimal impedance. *Nature* 414, 446–449. doi: 10.1038/35106566

Cheung, V. C. K., and Seki, K. (2021). Approaches to revealing the neural basis of muscle synergies: A review and a critique. *J. Neurophysiol.* 125, 1580–1597. doi: 10.1152/jn.00625.2019

Cheung, V. C. K., Turolla, A., Agostini, M., Silvoni, S., Bennis, C., Kasi, P., et al. (2012). Muscle synergy patterns as physiological markers of motor cortical damage. *Proc. Natl. Acad. Sci. U.S.A.* 109, 14652–14656. doi: 10.1073/pnas.1212056109

D'Avella, A., Saltiel, P., and Bizzi, E. (2003). Combinations of muscle synergies in the construction of a natural motor behavior. *Nat. Neurosci.* 6, 300–308. doi: 10.1038/nn1010

Dowling, A. V., Fisher, D. S., and Andriacchi, T. P. (2010). Gait modification via verbal instruction and an active feedback system to reduce peak knee adduction moment. *J. Biomech. Eng.* 132, 1–5. doi: 10.1115/1.4001584

Emken, J. L., and Reinkensmeyer, D. J. (2004). Accelerating motor adaptation by influencing neural computations. *Annu. Int. Conf. IEEE Eng. Med. Biol. Proc* 26, 4033–4036. doi: 10.1109/iembs.2004.1404126

Emken, J. L., and Reinkensmeyer, D. J. (2005). Robot-enhanced motor learning: Accelerating internal model formation during locomotion by transient dynamic amplification. *IEEE Trans. Neural Syst. Rehabil. Eng.* 13, 33–39. doi: 10.1109/TNSRE.2004.843173

Giszter, S. F. (2015). Motor primitives-new data and future questions. *Curr. Opin. Neurobiol.* 33, 156–165. doi: 10.1016/j.conb.2015.04.004

Hinder, M. R., Tresilian, J. R., Riek, S., and Carson, R. G. (2008). The contribution of visual feedback to visuomotor adaptation: How much and when? *Brain Res.* 1197, 123–134. doi: 10.1016/j.brainres.2007.12.067

Hogan, N. (1985b). The mechanics of multi-joint posture and movement control. *Biol. Cybern.* 52, 315–331. doi: 10.1007/BF00355754

Hogan, N. (1985a). Impedance control: An approach to manipulation. *J. Dyn. Syst. Meas. Control* 107, 1–24. doi: 10.1115/1.3140702

Jarrassé, N., Ribeiro, A. T., Sahbani, A., Bachta, W., and Roby-Brami, A. (2014). Analysis of hand synergies in healthy subjects during bimanual manipulation of various objects. *J. Neuroeng. Rehabil.* 11, 1–11. doi: 10.1186/1743-0003-11-113

Kargo, W. J., and Giszter, S. F. (2008). Individual premotor drive pulses, not time-varying synergies, are the units of adjustment for limb trajectories constructed in spinal cord. *J. Neurosci.* 28, 2409–2425. doi: 10.1523/JNEUROSCI.3229-07.2008

Kargo, W. J., Ramakrishnan, A., Hart, C. B., Rome, L. C., and Giszter, S. F. (2010). A simple experimentally based model using proprioceptive regulation of motor primitives captures adjusted trajectory formation in spinal frogs. *J. Neurophysiol.* 103, 573–590. doi: 10.1152/jn.01054.2007

Kernodle, M. W., and Carlton, L. G. (1992). Information feedback and the learning of multiple-degree-of-freedom activities. *J. Mot. Behav.* 24, 187–195. doi: 10.1080/00222895.1992.9941614

Kodama, K., Ioi, K., and Ohtsubo, Y. (2015). "Development of a new skill acquisition tool and evaluation of mold-polishing skills," in *Proceedings of the 34th Chinese control conference and sice annual conference*, Hangzhou, 139–142.

Lauber, B., and Keller, M. (2014). Improving motor performance: Selected aspects of augmented feedback in exercise and health. *Eur. J. Sport Sci.* 14, 36–43. doi: 10.1080/17461391.2012.725104

Lee, D. D., and Seung, H. S. (1999). Learning the parts of objects by non-negative matrix factorization. *Nature* 401, 788–791. doi: 10.1038/44565

Mugler, E. M., Tomic, G., Singh, A., Hameed, S., Lindberg, E. W., Gaide, J., et al. (2019). Myoelectric computer interface training for reducing co-activation and enhancing arm movement in chronic stroke survivors: A randomized trial. *Neurorehabil. Neural Rep.* 33, 284–295. doi: 10.1177/1545968319834903

Noguchi, K., Gel, Y. R., Brunner, E., and Konietschke, F. (2012). nparLD : An R software package for the nonparametric analysis of longitudinal data in factorial experiments. *J. Stat. Softw.* 50, 1–23. doi: 10.18637/jss.v050.i12

Osu, R., Franklin, D. W., Kato, H., Gomi, H., Domen, K., Yoshioka, T., et al. (2002). Short- and long-term changes in joint co-contraction associated with motor learning as revealed from surface EMG. *J. Neurophysiol.* 88, 991–1004. doi: 10.1152/jn.2002.88.2.991

Perreault, E. J., Chen, K., Trumbower, R. D., and Lewis, G. (2008). Interactions with compliant loads alter stretch reflex gains but not intermuscular coordination. *J. Neurophysiol.* 99, 2101–2113. doi: 10.1152/jn.01094.2007

Reid, M., and Giblin, G. (2015). Another day, another tennis coaching intervention, but does this one do what coaches purport? *Sport. Biomech.* 14, 180–189. doi: 10.1080/14763141.2015.1045549

Roh, J., Rymer, W. Z., Perreault, E. J., Yoo, S. B., and Beer, R. F. (2013). Alterations in upper limb muscle synergy structure in chronic stroke survivors. *J. Neurophysiol.* 109, 768–781. doi: 10.1152/jn.00670.2012

Sainburg, R. L. (2005). Handedness: Differential specializations for control of trajectory and position. *Exerc. Sport Sci. Rev.* 33, 206–213. doi: 10.1097/00003677-200510000-00010

Shin, D., Kim, J., and Koike, Y. (2009). A myokinetic arm model for estimating joint torque and stiffness from EMG signals during maintained posture. *J. Neurophysiol.* 101, 387–401. doi: 10.1152/jn.00584.2007

Sigrist, R., Rauter, G., Riener, R., and Wolf, P. (2013). Augmented visual, auditory, haptic, and multimodal feedback in motor learning: A review. *Psychon. Bull. Rev.* 20, 21–53. doi: 10.3758/s13423-012-0333-8

Smith, R. M., and Loschner, C. (2002). Biomechanics feedback for rowing. *J. Sports Sci.* 20, 783–791. doi: 10.1080/026404102320675639

Takei, T., Confais, J., Tomatsu, S., Oya, T., and Seki, K. (2017). Neural basis for hand muscle synergies in the primate spinal cord. *Proc. Natl. Acad. Sci. U.S.A.* 114, 8643–8648. doi: 10.1073/pnas.1704328114

Torricelli, D., De Marchis, C., d'Avella, A., Tobaruela, D. N., Barroso, F. O., and Pons, J. L. (2020). Reorganization of muscle coordination underlying motor learning in cycling tasks. *Front. Bioeng. Biotechnol.* 8:1–17. doi: 10.3389/fbioe.2020.00800

Tsujiai, M., Kodama, K., Ioi, K., and Ohtsubo, Y. (2015). "Characteristics of human skills about mold-polishing," in *Proceeding of the 12th international conference on ubiquitous healthcare*, Osaka, 8.

Vander Linden, D. W., Cauraugh, J. H., and Greene, T. A. (1993). The effect of frequency of kinetic feedback on learning an isometric force production task in nondisabled subjects. *Phys. Ther.* 73, 79–87. doi: 10.1093/ptj/73.2.79

Willingham, D. B. (1998). A neuropsychological theory of motor skill learning. *Psychol. Rev.* 105, 558–584. doi: 10.1037//0033-295x.105.3.558

Wright, Z. A., Rymer, W. Z., and Slutzky, M. W. (2014). Reducing abnormal muscle coactivation after stroke using a myoelectric-computer interface: A pilot study. *Neurorehabil. Neural Repair* 28, 443–451. doi: 10.1177/1545968313517751

Yang, Q., Logan, D., and Giszter, S. F. (2019). Motor primitives are determined in early development and are then robustly conserved into adulthood. *Proc. Natl. Acad. Sci. U.S.A.* 116, 12025–12034. doi: 10.1073/pnas.1821455116

Young, D. E., and Schmidt, R. A. (1992). Augmented kinematic feedback for motor learning. *J. Mot. Behav.* 24, 261–273. doi: 10.1080/00222895.1992.9941621

Zubiaur, M., Oña, A., and Delgado, J. (1999). Learning volleyball serves: A preliminary study of the effects of knowledge of performance and of results. *Percept. Mot. Skills* 89, 223–232. doi: 10.2466/pms.1999.89.1.223

Frontiers in
Systems Neuroscience

Advances our understanding of whole systems of the brain

Part of the most cited neuroscience journal series, this journal explores the architecture of brain systems and information processing, storage and retrieval.

Discover the latest Research Topics

See more →

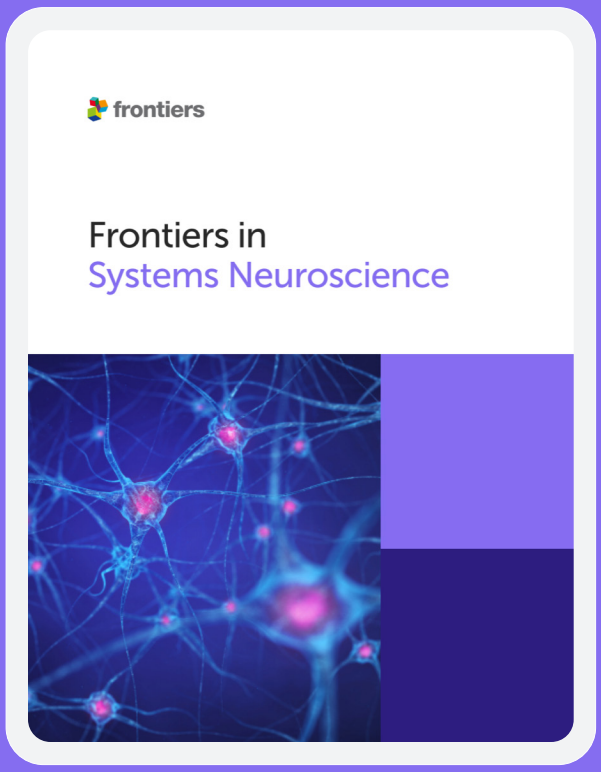

Frontiers

Avenue du Tribunal-Fédéral 34
1005 Lausanne, Switzerland
frontiersin.org

Contact us

+41 (0)21 510 17 00
frontiersin.org/about/contact